LOS ALAMOS
NATIONAL LABORATORY
IM-MU-64 DOCUMENT CONTROL

654

CONTROLLED DOCUMENT
(Uncontrolled Document: If not printed in red)

Users have the ultimate responsibility to ensure that they are working with the latest revision of the controlled document.

Copy Number
383

REPORT

PERFORMANCE ASSESSMENT AND COMPOSITE ANALYSIS FOR LOS ALAMOS NATIONAL LABORATORY MATERIAL DISPOSAL AREA G

REPORT-54G-013,R.2.1

EffectiveDate: 04/07/1997

HOLLIS, DIANA
EM-SWO
J595

JUN 10 1999

10756

LA-UR-97-85
Report-54G-013.R.2

PERFORMANCE ASSESSMENT AND COMPOSITE ANALYSIS FOR LOS ALAMOS NATIONAL LABORATORY MATERIAL DISPOSAL AREA G

MARCH 1997

Diana Hollis, EM-SWO, Project Leader
Erik Vold, EM-SWO
Rob Shuman, RAE Corp.

Kay Birdsell, EES-5
Kathleen Bower, EES-5
Wayne Hansen, EES-15
Don Krier, EES-1
Patrick Longmire, CST-7
Brent Newman, EES-15
David Rogers, ESH-18
Everett Springer, EES-15

ACKNOWLEDGMENTS

This work was conducted under the support of the U.S. Department of Energy, Waste Management Programs, Contract Number W-7405-ENG-36. It represents several years of dedication, perseverance, and cooperation on the part of many individuals, especially the contributing authors. The report itself reflects significant contributions from not only those listed individual, but also: Mary Olson, Patricia Leyba, Germaine Martinez, Carmen Velasquez, Madeline Romero, Shelly Meddles, Christine Salazar and Loretta Atencio (document publication); Maria Romero, Mark Valenzuela, and Scott Smith (document preparation); Rick O'Rear (graphics); Shelley Sussman and Mike Borduin (technical editing), and Wayne Hansen (technical direction). The authors wish to thank these individuals for their patience and hard work.

EXECUTIVE SUMMARY

This report describes the Performance Assessment (PA) and Composite Analysis (CA) for the current solid low-level radioactive waste (LLW) disposal facility at the Los Alamos National Laboratory(LANL), Material Disposal Area (MDA) G. The PA and CA satisfy the following DOE requirement documents:

- DOE Order 5820.2A, Radioactive Waste Management (September 1988);
- "Guidance for a Composite Analysis of the Impact of Interacting Source Terms on the Radiological Protection of the Public from DOE LLW Disposal Facilities" (April 1996);
- "Revised Interim Policy on Regulatory Structure for Low-Level Radioactive Waste Management and Disposal" (July 1996); and
- "Interim Format and Content Guide and Standard Review Plan for U.S. Department of Energy Low-Level Waste Disposal Facility Performance Assessments" (October 1996).

The purpose of the PA is to determine if LLW generated since September 26, 1988 has been, and will continue to be, disposed of at MDA G in a manner that will not result in radiation doses to members of the public that exceed performance objectives specified by the DOE. In a complementary fashion, the CA is used to evaluate options for ensuring that exposures from all waste disposed of at MDA G will not impart doses to future members of the public in excess of specified limits.

MDA G has been used for disposal of the Laboratory's radioactive waste since 1957. The chemical, physical, and radiological characteristics of waste disposed of after September 26, 1988 have been reported and documented in accordance with the requirements of DOE Order 5820.2A. Characteristics of the inventory buried prior to September 25, 1988 are uncertain, although electronic records exist for disposals after 1971. Together, the PA and CA provide a comprehensive evaluation of the potential radiological exposures to future members of the public from past, present, and future disposals at MDA G. Doses are projected beyond 1,000 years after facility closure, which is assumed to occur in 2044. The results are compared with performance objectives provided by the DOE. Radiological doses to future members of the public can result from the release and

transport of radioactivity via natural processes affecting the undisturbed disposal site, and from direct intrusion into the waste by humans. The latter can, in principle, be prevented, while the former can be controlled to only a limited extent.

The projection of future doses involves modeling releases of radioactivity from MDA G and transport of that radioactivity in air, water, soil, and biota at locations accessible to future members of the public for a period of at least 1,000 years. This requires an understanding of facility uses and natural processes affecting release and transport and assumptions about human use of the site and its surroundings.

This report first establishes the regulatory framework of the PA and CA, defining the performance objectives and summarizing the general approach followed to demonstrate compliance with those objectives, and then discusses the technical framework of the analysis. The technical framework includes detailed descriptions of the natural and man-made characteristics of the site that relate to its long-term radiological performance, and descriptions of the models used to analyze its long-term performance. Two conditions are evaluated: One considers doses to offsite members of the public following releases of radioactivity from the facility resulting from natural processes, while a second considers doses to individuals who may inadvertently intrude into the waste. Results of the dose projections are evaluated against performance objectives and are interpreted in the context of implications for disposal operations and further investigations.

The performance objectives for the PA are provided in DOE Order 5820.2A and the report "Interim Format and Content Guide and Standard Review Plan for U.S. Department of Energy Low-Level Waste Disposal Facility Performance Assessments." These performance objectives were interpreted as:

- Maximum effective dose equivalent of 25 mrem/yr to any member of the public resulting from external exposure and concentrations of radioactive material released into surface water, groundwater, soil, plants, and animals.
- Maximum effective dose equivalent of 10 mrem/yr to any member of the public from concentrations of radioactive material released to the atmosphere (excluding radon) from Area G and all other facilities at the LANL.

- Maximum flux of radon gas (i.e., ^{220}Rn and ^{222}Rn) from the undisturbed disposal site of 20 pCi/m^2/s (1.9 pCi/ft^2/s).
- Maximum effective dose equivalent of 100 mrem/yr for continuous exposures of individuals who inadvertently intrude into the facility after the loss of active institutional control (100 years).
- Maximum effective dose equivalent of 500 mrem/yr for acute exposures of individuals who inadvertently intrude into the facility after the loss of active institutional control (100 years).
- Maximum effective dose equivalent of 4 mrem/yr to any member of the public from the consumption of drinking water drawn from wells outside of the land-use boundary.

The performance objective for the CA is the DOE primary annual dose limit of 100 mrem effective dose equivalent for members of the public. If the projected dose exceeds 30 mrem/yr, an options analysis must be prepared to consider actions that could be taken to reduce exposures, taking into account the cost of such actions. Compliance with performance objectives is evaluated over a 1,000-year post-closure period.

To model release and transport of radioactivity from MDA G, waste characteristics and natural processes were examined. Most waste disposed of at MDA G is slightly contaminated laboratory trash (e.g., paper, packaging materials, glassware, etc.) and debris from cleanup activities (e.g., building rubble, conduit, soil, etc.). The inventory includes large quantities of tritium, ^{60}Co (in activated metals), and ^{137}Cs (in irradiation sources); special nuclear materials (e.g., ^{239}Pu, ^{241}Am, and ^{235}U); and residues from medical radioisotope separations (e.g., ^{95m}Tc and ^{94}Nb).

The waste inventory for the PA and CA was divided into four segments, each of which was characterized separately according to availability of information. The four segments and the general method of characterization are:

- 1957 - 1970 Inventory: Radionuclide content extrapolated from records from the early 1970s;
- 1971 - September 25, 1988 Inventory: Radionuclide content obtained from electronic database;
- September 26, 1988 - 1995 Inventory: Radionuclide content obtained from electronic database; and

- 1996 - 2044 Inventory: Radionuclide content extrapolated from records between 1990 and 1995.

This segmentation of waste inventory allowed the projected doses associated with separate PA and CA inventories to be evaluated against the applicable performance objectives. The PA addressed waste disposed of only after September 26, 1988, while the CA addresses all waste. When uncertainties arose for any segment of the inventory, a conscious effort was made to err on the side of conservatism and overestimate radionuclide content and potential release rates.

Radioactivity released by the source term processes was assumed to be transported within one or more of the following environmental media:

- Air;
- Surface soil;
- Surface water;
- Groundwater; and
- Vegetation.

Contact with or use of contaminated environmental media was assumed to cause radiation doses as a result of:

- Inhalation of contaminated air;
- Immersion within contaminated air;
- Incidental ingestion of contaminated soil;
- External exposure to contaminated soil;
- Ingestion of contaminated water;
- Consumption of milk and meat from animals that have ingested contaminated water; and
- Consumption of food crops grown in contaminated soils and subject to surface deposition of radioactivity.

The MDA G facility is situated atop a relatively flat narrow mesa named Mesita del Buey, about 30 m (99 ft) above two canyons, Cañada del Buey to the north and Pajarito Canyon to the south. Disposal units are excavated to depths of about 20 m (65 ft), set back a distance of 15 m (50 ft) from the sides of the mesa. The surface of Mesita del Buey is

about 275 m (900 ft) above the regional aquifer, which supplies the drinking water for area residents. The climate is semiarid, the ecosystem is Piñon-Juniper woodland. There are natural processes somewhat unique to this setting that have important implications with respect to exposure pathways considered in the PA and CA, including:

- Evaporation at depths within the mesa;
- Slow moisture flux through the mesa;
- Surface water runoff from the mesa into the canyons; and
- Channeled winds within the canyons.

The MDA G inventory includes many waste forms contaminated with a wide variety of radionuclides. Three source term models were developed to account for possible releases. For the purpose of the PA and CA, releases of radioactivity were assumed to result from the following processes:

- Gas-phase diffusion;
- Translocation of radioactive materials by burrowing animals and deep-rooting plants; and
- Aqueous-phase leaching of soluble radionuclides.

A gas-phase diffusion model was used to calculate the time-dependent flux of radionuclides in the inventory that are either characteristically volatile (i.e., krypton and radon) or form gases (i.e., ^{14}C as $^{14}CO_2$) or vapors (i.e., ^{3}H as $^{3}H_2O$, $H^{3}HO/HTO$). A biotic translocation model was used to account for time-dependent surface-soil radionuclide concentrations as a result of burrowing animals excavating waste and plants assimilating radioactivity through roots penetrating waste, then depositing radioactivity on the surface with natural defoliation. Finally, an aqueous-phase release model was developed to simulate dissolution of radioactive materials into water percolating through the disposal units.

Gas-phase releases were transported offsite in air, producing inhalation doses. Surface contamination resulting from biotic intrusion was transported offsite in air and subsequent redeposition and in surface water, resulting in inhalation, ingestion, and external exposures. Aqueous-phase releases were transported vertically downward toward the

regional aquifer and laterally toward the sides of Mesita del Buey, generating ingestion, inhalation, and external radiation doses.

Receptor Locations

Maximum offsite radiation doses were calculated at various times and locations consistent with the natural characteristics of the site, assumed facility life-cycle, and assumed future land use. MDA G lies along the LANL boundary, directly adjacent to land in Cañada del Buey owned by the San Ildefonso American Indians, and approximately 2 km (1.3 mi) from the small residential community of White Rock. White Rock is hydrologically downgradient from MDA G, while Cañada del Buey is effectively downwind of the facility. Consequently, potential offsite receptor locations for groundwater and air contamination are relatively close to the facility. The following time periods, land use assumptions, and receptor locations were considered in the PA and CA:

- 1957 - 2044: Operational period during which site access is strictly limited and environmental monitoring prevents offsite releases, causing no offsite doses;
- 2045 - 2046: Closure period during which surface structures are dismantled, disposal units are covered, site access is limited, and environmental releases are monitored;
- 2047 - 2146: Institutional-control period during which access is controlled according to existing boundaries, allowing potential exposures to a receptor in White Rock and within Cañada del Buey; and
- 2147 - 3046: Industrial-use period during which access is controlled over a smaller perimeter around the facility, allowing potential exposures at a receptor location in Pajarito Canyon directly adjacent to the facility.

The following table summarizes the maximum doses calculated over the 1,000-year compliance period for several pathways at various receptor locations and compares them with applicable performance objectives.

Inventory[a]	Analysis	Location	Calculated Peak Dose	Performance Objective
PA	Air Pathway	Cañada del Buey	6.6×10^{-2} mrem/yr	10 mrem/yr[b]

CA	All Pathways	Cañada del Buey	5.5 mrem/yr	30/100 mrem/yr
PA	Groundwater Protection	White Rock Pajarito Canyon	3.5×10^{-5} mrem/yr	4 mrem/yr
PA	All Pathways	White Rock Pajarito Canyon	1.0×10^{-4} mrem/yr	25 mrem/yr
CA	All Pathways	White Rock Pajarito Canyon	7.2×10^{-3} mrem/yr	30/100 mrem/yr
PA	Intruder	MDA G	12 to 30 mrem/yr	100 mrem/yr
PA	Radon Flux	MDA G	0.1 to 3.1 pCi/m^2/s	20 pCi/m^2/s

a. PA includes waste disposed of after September 26, 1988; CA includes all waste
b. Performance objective represents the maximum projected exposure from all releases at LANL.

Projected doses and radon fluxes were small in all cases considered, and well below the applicable performance objectives for the PA and CA. The peak PA dose for the air pathway analysis was a small contribution to the maximum annual dose of 3.5 mrem projected for other facilities at LANL. The projected doses for the CA were less than the 100 mrem/yr primary objective, as well as the 30 mrem/yr limit indicative of the need for an options analysis.

The uncertainties associated with the projected doses, and their impact on the ability of MDA G to comply with the performance objectives, are discussed. Uncertainties in inventory, environmental data, and modeling parameters are considered over a 10,000-year period to provide reasonable assurance that the performance objectives will be achieved. After accounting for the uncertainty in the dose analyses, all performance objectives are still likely to be met.

Analyses and field and experimental data will continue to be refined to support the maintenance of the site Performance Assessment, with an emphasis on reducing important uncertainties in the analysis. Waste Acceptance Criteria, waste characterization requirements, and waste disposal operations will be modified to reflect the results of the PA.

TABLE OF CONTENTS

EXECUTIVE SUMMARY ..... i-vii

1. INTRODUCTION 1-1

1.1 APPROACH 1-3
1.1.1 Source Terms and Related Processes 1-6
1.1.2 Exposure Pathways and Related Processes 1-6
1.1.3 Exposure Scenarios 1-7

1.2 FACILITY DESCRIPTION 1-8
1.2.1 Geographic Siting 1-10
1.2.2 Geologic Siting 1-11
1.2.3 Waste Management 1-11

1.3 SCHEDULES 1-13

1.4 RELATED DOCUMENTS 1-14
1.4.1 Site-wide Environmental Impact Statement 1-14
1.4.2 Environmental Restoration Project Documents 1-15
1.4.3 Land Use Plan 1-16
1.4.4 Site-wide Groundwater Protection Plan 1-16
1.4.5 Waste Management Documents 1-17

1.5 PERFORMANCE CRITERIA 1-19
1.5.1 Public Protection Performance Objectives 1-19
1.5.2 Intruder-Protection Performance Objective 1-21
1.5.3 Groundwater-Protection Performance Objective 1-22

1.6 SUMMARY OF KEY ASSESSMENT ASSUMPTIONS 1-22

2. DISPOSAL FACILITY CHARACTERISTICS 2-1

2.1 SITE CHARACTERISTICS 2-1
2.1.1 Geography and Demography 2-2
2.1.2 Meteorology and Climatology 2-7
2.1.3 Ecology 2-13
2.1.4 Geology, Seismology, and Volcanology 2-16
2.1.5 Hydrogeology 2-32
2.1.6 Geochemistry 2-56
2.1.7 Natural Resources 2-61
2.1.8 Natural Background Radiation 2-63

2.2 PRINCIPAL FACILITY DESIGN FEATURES 2-66
2.2.1 Water Infiltration 2-67
2.2.2 Disposal Unit Cover Integrity 2-71
2.2.3 Structural Stability 2-71

2.2.4 Inadvertent Intruder Barrier 2-73

2.3 WASTE CHARACTERIZATION 2-73
2.3.1 Historic Waste 2-73
2.3.2 Future Inventory 2-81
2.3.3 PA Inventory 2-85
2.3.4 CA Inventory 2-89
2.3.5 Summary of PA and CA Inventories 2-92

3. ANALYSIS OF PERFORMANCE 3-1

3.1 SOURCE TERM ANALYSIS 3-2
3.1.1 Air Pathways Analysis 3-3
3.1.2 Groundwater Protection Analysis 3-14
3.1.3 All-pathways Analysis 3-22

3.2 PATHWAYS AND SCENARIOS 3-23
3.2.1 Air Pathways Analysis 3-24
3.2.2 Groundwater Protection Analysis 3-25
3.2.3 All-pathways Analysis 3-27

3.3 ANALYSIS METHODOLOGY 3-29
3.3.1 Air Pathways Analysis 3-30
3.3.2 Groundwater Protection Analysis 3-34
3.3.3 All-pathways Analysis 3-68

4. RESULTS OF ANALYSES 4-1

4.1 RESULTS OF THE PA DOSE ANALYSES 4-1
4.1.1 Results of Air Pathway Analysis 4-1
4.1.2 Results of Groundwater Protection Analysis 4-5
4.1.3 Results of All Pathways Analysis 4-7

4.2 RESULTS OF THE CA DOSE ANALYSES 4-10
4.2.1 All Pathways Dose Analysis 4-12

4.3 SENSITIVITY AND UNCERTAINTY 4-14
4.3.1 Inventory Uncertainties 4-16
4.3.2 Source Term Uncertainties 4-21
4.3.3 Environmental Transport Modeling Uncertainties 4-23
4.3.4 Usage Factor Uncertainties 4-28
4.3.5 Dose Conversion Factor Uncertainties 4-30
4.3.6 Propagated Dose Assessment Uncertainties 4-31

4.4 ALARA ANALYSIS 4-43

5. INADVERTENT INTRUDER ANALYSIS 5-1

5.1 INTRUDER EXPOSURE SCENARIOS 5-1

5.2 INTRUDER ANALYSIS RESULTS 5-3
5.2.1 Intruder Analysis Results for Historic Waste 5-4
5.2.2 Intruder Analysis Results for Future Waste 5-6
5.2.3 Summary of Intruder Analysis Results 5-8

5.3 INTRUDER SENSITIVITY AND UNCERTAINTY ANALYSIS 5-8
5.3.1 Inventory Uncertainties 5-9
5.3.2 Disposal-Unit Cover Uncertainties 5-9

6. PERFORMANCE EVALUATION 6-1

6.1 COMPARISON OF RESULTS OF PERFORMANCE OBJECTIVES 6-1
6.1.1 Evaluation of Performance Assessment Results 6-1
6.1.2 Evaluation of Composite Analysis Results 6-5

6.2 USE OF RESULTS 6-6
6.2.1 Use of Performance Assessment Results 6-6
6.2.2 Use of Composite Analysis Results 6-11

6.3 MAINTENANCE PROGRAMS 6-12
6.3.1 Maintenance of the Performance Assessment 6-12
6.3.2 Maintenance of the Composite Analysis 6-15

7. QUALITY ASSURANCE 7-1

7.1 FIELD DATA 7-1

7.2 LABORATORY DATA 7-1

7.3 INVENTORY DATA 7-2

7.4 FACILITY CHARACTERISTICS 7-3

7.5 MATHEMATICAL MODELS 7-4
7.5.1 Atmospheric Transport Modeling 7-4
7.5.2 Surface Runoff and Soil Erosion Modeling 7-4
7.5.3 Subsurface Transport Modeling 7-4
7.5.4 Dose Assessment 7-5

8. PREPARERS 8-1

9. REFERENCES 9-1

LIST OF APPENDICES

Appendix 1a Resolution of PRP Comments on Draft Performance Assessment of LANL TA-54, Area G Low-Level Radioactive Solid Waste Disposal Facility

Appendix 1b Technical Justification for Excluding Sources from the MDA G Composite Analysis

Appendix 2a Geologic, Geohydrologic, and Geochemical Data Summary of Material Disposal Area G, Technical Area 54, Los Alamos National Laboratory

Appendix 2b Vadose Zone Water Movement at Area G, Los Alamos National Laboratory, TA-54: Interpretations Based on Chloride and Stable Isotope Profiles

Appendix 2c Analysis of Liquid Phase Transport in the Unsaturated Zone at a Mesa Top Disposal Facility

Appendix 2d Batch Sorption Results for Americium, Neptunium, Plutonium, Technitium, and Uranium Transport Through the Bandelier Tuff, Los Alamos, New Mexico

Appendix 2e Radioactive Waste Inventory for the TA-54, Area G Performance Assessment and Composite Analysis

Appendix 2f Isotopic Composition of Inventory Designations, "Mixed Fission Products" and "Mixed Activation Products"

Appendix 3a Evaluation of Atmospheric Release Sources for Gaseous Phase Contaminants Emanating from the Disposal Facility at Area G

Appendix 3b A Model for the Biotic Translocation of Buried Low-Level Radioactive Waste to the Ground Surface in the Presence of Surface Erosion

Appendix 3c Surface Water and Erosion Calculations to Support the MDA G Performance Assessment

Appendix 3d Source Release Modeling for the Los Alamos National Laboratory Material Disposal Area G Performance Assessment and Composite Analysis

Appendix 3e Radiological Dose Assessment for the TA-54, Area G Performance Assessment and Composite Analysis

Appendix 3f Atmospheric Transport in Complex Terrain at Los Alamos, Area G

Appendix 3g Simulations of Groundwater Flow and Radionuclide Transport in the Vadose and Unsaturated Zones Beneath Area G, Los Alamos National Laboratory

Appendix 3h Conceptual Model for Subsurface Transport at MDA G

LIST OF FIGURES

Figure 1-1 Conceptual Model of MDA G 1-5
Figure 1-2 Aerial Photograph of MDA G and Its Surroundings 1-8
Figure 1-3 Facility Characteristics Considered In Offsite Dose Assessments in the PA and CA 1-9
Figure 1-4 LANL Technical Area (TA) Map 1-10
Figure 2-1 Use of Disposal Facility Characteristics in Analyzing Disposal Facility Performance 2-1
Figure 2-2 Location of the Los Alamos National Laboratory 2-2
Figure 2-3 Map of MDA G Illustrating Mesa-canyon Topography and Current and Future Land-use Boundaries 2-4
Figure 2-4 a) Windroses from Mesita del Buey: daytime (top) nighttime (bottom) 2-11
Figure 2-4 b) Windrose from Pajarito Canyon: daytime (top) nighttime (bottom) 2-12
Figure 2-5 Generalized Stratigraphic Relationships of the Pajarito Plateau 2-17
Figure 2-6 Cross-referenced Stratigraphic Nomenclatures Used to Describe the Subsurface at MDA G 2-20
Figure 2-7 Boreholes Completed in 1996 around MDA G 2-22
Figure 2-8 Cross Sections of Stratigraphic Setting of MDA G 2-23
Figure 2-9 a) Surge Bed and Fractures in Unit 2, Pit 38, and b) Surge Beds at Base of Unit 2 in Outcrop Along South Wall of Mesita Del Buey 2-26
Figure 2-10 The Pajarito Fault System and The Rendija Canyon and Guaje Mountain Faults 2-30
Figure 2-11 Water Supply and Test Wells in the LANL Region 2-35
Figure 2-12 Flow Rate and Direction of Regional Aquifer across the Plateau 2-36
Figure 2-13 Representative Unsaturated Hydraulic Conductivity Curves for the Upper Subunits of Bandelier Tuff 2-42
Figure 2-14 Chloride Concentration Versus Depth in Porewater Extracted from Well 54-1117 2-46
Figure 2-15 Cumulative water versus Cumulative Chloride 2-47
Figure 2-16 Unsaturated Hydraulic Conductivity as a Function of Moisture for Tshirege Member Beneath MDA G 2-50
Figure 2-17 Measured Volumetric Moisture Content in Bandelier Tuff and Calculated Recharge Rates 2-51
Figure 2-18 Neutron-probe Moisture Profile of Borehole LGM-85-06, Near Pit 38 2-52
Figure 2-19 Vertical Flux and Source Term for Borehole LGM-85-06 2-53
Figure 2-20 Magnitudes of Liquid and Vapor Flux in Borehole 54-1117 2-56
Figure 2-21 Regional Surface Water and Soil Sampling Locations 2-65
Figure 2-22 Conceptualized Water Balance Components 2-67
Figure 2-23 Neutron Moisture Profiles Through Pit 37 2-70
Figure 2-24 Recorded Annual LLW Disposal Volumes (Top) and Radioactivities (Bottom) 2-74
Figure 2-25 Recorded Annual TRU Storage Volumes and Radioactivities 2-75
Figure 2-26 Disposal Units Contributing to the PA and CA Inventories 2-86
Figure 2-27 Annual Volumes of Pit and Shaft Waste Disposed of From September 26, 1988 through 1995 2-86
Figure 2-28 Total Annual Activities of Pit Shaft Waste Disposed of from September 26, 1988 through 1995 2-87
Figure 2-29 Volume and Activity of Waste in Each Inventory Category Disposed of from September 26, 1988 through 1995 2-87

Figure 2-30 Total Annual Volume of Waste Disposed of Between 1971 and 1988 2-91
Figure 2-31 Total Annual Activity of Waste Disposed of Between 1971 and 1988 2-92
Figure 3-1 Relationship Between Facility Characteristics and Analysis 3-1
Figure 3-2 Source Term Components Considered in the PA and CA 3-2
Figure 3-3 Conceptual Model of the Evolution and Release of ^{14}C-Labeled Biogases 3-5
Figure 3-4 Radium Isotope Activities in Historic (Top) and Future Waste (Bottom) 3-6
Figure 3-5 Conceptual Model of Gaseous-phase Source Release 3-7
Figure 3-6 Biotic Translocation Conceptual Model 3-9
Figure 3-7 Normalized Surface Contaminant Concentration Versus Time for the Base Case; Shown for Several Values of Plant Uptake Factor (B_l) 3-12
Figure 3-8 Conceptual Model for Aqueous-phase Dissolution of Radioactivity from Surface-contaminated Waste 3-17
Figure 3-9 Location of Evaluation of Exposure Scenarios 3-24
Figure 3-10 Coupling of Source Term and Environmental Transport Analyses 3-30
Figure 3-11 Atmospheric Release Computed from Three Point Sources Within Area G (Centered Near X=-1, Y=0) Showing a Convergence of the Plumes in Cañada del Buey to the Northwest of the Release 3-33
Figure 3-12 Region of Interest Identified for the Groundwater Pathways Computations 3-35
Figure 3-13 Three-dimensional Stratigraphy of Vadose Zone Grid 3-40
Figure 3-14 Pit Boundaries, Internal Pit Nodes, and Mesa Edge Nodes for the three-dimensional Vadose Zone Calculations 3-41
Figure 3-15 Saturation Profile of the Three-dimensional Vadose Zone Grid 3-43
Figure 3-16 Moisture Profiles from Transient Input Compared with 5mm/yr Steady-state Input 3-48
Figure 3-17 Simulated Solute Pathways for the Two-dimensional Parameter Study on Basalt Properties, A) Particle Release only at Mesa Top, Matrix-type Basalt Properties, B) Particle Release at Mesa Top and Canyon Floor, Matrix-type Basalt Properties, C) Particle Release at Mesa Top, Fracture-type Basalt Properties 3-51
Figure 3-18 Configuration of Model Used to Simulate Evaporation in Fractures 3-52
Figure 3-19 Resulting Saturation Profiles for Evaporation Along a Mesa Edge (Right Side) and from Fractures with 5 m and 10 m Spacing, Unit 2 3-53
Figure 3-20 Resulting Saturation Profile for Evaporation Along the "Surge Beds" at the Unit 2/1vu Interface Compared to that for Infiltration Alone 3-54
Figure 3-21 System Configuration for Fracture Fill and Coating Study 3-55
Figure 3-22 Total Flux of ^{14}C from the Vadose Zone to the Saturated Zone from the Four Source Regions 3-59
Figure 3-23 ^{129}I Fluxes at the Base of the Vadose Zone Grid for Several Variations in Flow Fields 3-60
Figure 3-24 Lateral ^{14}C Fluxes Along the North (Left) and South (Right) Walls of Mesita del Buey from the 4 CA Source Segments 3-61
Figure 3-25 Generic Fluxes at Base of Grid from Lateral Fluxes Through North and South Mesa Walls, Then Transported Vertically, Base Case 3-62
Figure 3-26 Computational Domain of the Puye Formation for Saturated Transport Calculations 3-64
Figure 3-27 Three-dimensional Finite Element Grid Used for the Saturated Zone Flow and Transport Calculations 3-65
Figure 3-28 Fluxes of ^{129}I Reaching the Base of the Vadose Zone Grid at 1,000 Years for the Four Different Source Regions, Base Case 3-66

Figure 3-29 ^{129}I Concentrations in the Saturated Zone for the Point of Maximum Concentration and the 100 m Downgradient Compliance point with the Base Case Vertical Transport Through the Vadose Zone 3-67
Figure 3-30 Groundwater Concentrations in the Saturated Zone Beneath Pajarito Canyon for Three Flow Fields 3-68
Figure 4-1 Offsite Air Pathway Doses During the Industrial-Use Period for the PA 4-4
Figure 4-2 Radionuclides Contributing to Offsite Air Pathways Dose During *Industrial-use Period for the PA*.... 4-4
Figure 4-3 Doses Projected for PA from Ingestion of Contaminated Water Drawn from the Regional Aquifer 100 m Downgradient of MDA G.... 4-6
Figure 4-4 Doses Projected for PA from Ingestion of Contaminated Water Drawn from the Regional Aquifer from Well in Pajarito Canyon 4-7
Figure 4-5 Doses Projected for the PA All-pathways Analysis from Use of Contaminated Water Drawn from the Regional Aquifer 100 m downgradient of MDA G 4-8
Figure 4-6 Doses Projected for the PA All-pathways Analysis from Use of Contaminated Water Drawn from a Well in Pajarito Canyon.... 4-9
Figure 4-7 Offsite doses from Air Pathway During Industrial-use Period for the CA....4-11
Figure 4-8 Radionuclides Contributing to Offsite Dose From Air Pathway During Industrial-Use Period for the CA....4-12
Figure 4-9 Doses Projected for CA All-Pathways Analysis from Use of Contaminated Water Drawn from Regional Aquifer 100 m Downgradient of MDA G....4-12
Figure 4-10 Doses Projected for CA All-Pathways Analysis from Use of Contaminated Water Drawn from Well in Pajarito Canyon....4-13

LIST OF TABLES

Table 2-1 Summary of Meteorological Data at MDA G 2-7
Table 2-2 Atmospheric Stability Class Frequencies 2-9
Table 2-3 Average Atmospheric Mixing Heights 2-10
Table 2-4 Average Rooting Depths of Piñon and Juniper Woodland Plants 2-14
Table 2-5 Maximum Recorded Depth of Burrows of Animals at MDA G 2-15
Table 2-6 Hydrologic Characteristics of Pajarito Field Water Supply Wells 2-37
Table 2-7 Hydraulic Characteristics of MDA G Vadose Zone 2-41
Table 2-8 Recharge and Moisture Source Summary for MDA G 2-54
Table 2-9 Comparison of Water Canyon Gallery and Bandelier Tuff Pore Water Chemistries 2-59
Table 2-10 Experimentally-determined Average Distribution Coefficients from Core Samples from Borehole 1107 2-60
Table 2-11 Calculated Speciation and Solubilities using Water Canyon Gallery and Synthetic Pore Water Chemistries 2-61
Table 2-12 Average Background Concentrations of Radioactivity in Air from Regional Stations 2-64
Table 2-13 Radiochemical Quality of Regional Soils 2-65
Table 2-14 Radiochemical Quality of Surface Water from Offsite Stations 2-66
Table 2-15 "Mixed Activation Product" Abundance 2-77
Table 2-16 Waste Categories for LANL Waste Codes 2-80
Table 2-17 LANL Technical Areas Identified as Major LLW Generators 2-83
Table 2-18 Waste Codes Excluded from Future Projections 2-84
Table 2-19 Projected Disposal Volumes and Activities for Future Inventory Categories 2-88
Table 2-20 Extrapolated Volumes and Activities for Each Inventory Category Disposed of from 1957 through 1970 2-90
Table 2-21 Pit and Shaft Waste-category Volumes and Activities Include in the PA Inventory 2-93
Table 2-22 Pit and Shaft Waste-category Volumes and Activities Include in the CA Inventory 2-94
Table 3-1 Approximate Gas-phase Source Term Inventory in 2044 3-4
Table 3-2 *In situ* Diffusion coefficients used to Calculate Gaseous Contributions to the Air Pathway 3-8
Table 3-3 Results of the Groundwater-pathway Inventory Screen 3-16
Table 3-4 Annual Values of Percolation, Runoff, and Soil Erosion 3-19
Table 3-5 Summary of Exposure Pathways and Scenarios 3-24
Table 3-6 Distribution of Inventory in Modeled Pits 3-42
Table 3-7 Hydrologic Properties used in the Vadose-zone Transport Model 3-44
Table 3-8 Sorption Coefficients used in the Vadose-zone Transport Calculations 3-46
Table 3-9 Statistics of Pit Percolation Used in the Four Transient Calculations 3-47
Table 3-10 Comparison of ^{14}C Arrival Times and Peak Concentrations for the Steady-state and Four Transient Flow Simulations 3-48
Table 3-11 Saturated Hydraulic Conductivity Ranges for Geologic Materials 3-57
Table 3-12 Scaling Factors to Correct Generic Concentration Breakthrough Curve for Each Nuclide and Waste Category for the Base Case, and Low- and High-flow Fields 3-63
Table 4-1 Summary of Exposure Pathways and Performance Objectives 4-2

Table 4-2 Projected Peak Radon Fluxes from Historic Waste During the 1,000 year Compliance Period for the PA 4-5
Table 4-3 Exposure Pathway Contribution to Peak All Pathways Dose During Institutional-control Period for the PA 4-10
Table 4-4 Exposure Pathways Contributing to Peak Dose Calculated to an Offsite Resident During the 1,000-year Compliance Period for the CA 4-14
Table 4-5 Ratio of Projected Performance-to-Performance Measure 4-16
Table 4-6 Correction Factors for Uncertainties in Air-pathway Dose Assessment 4-34
Table 4-7 Correction Factors for Uncertainties in Radon Flux for the PA 4-36
Table 4-8 Correction Factor s for Uncertainties in PA Groundwater Protection Doses 4-38
Table 4-9 Correction Factors for Uncertainties in Downgradient All-pathways Doses in the PA and CA 4-41
Table 4-10 Correction Factors for Uncertainties in Pajarito Canyon All-pathways Doses in the PA and CA 4-42
Table 4-11 Collective Population Doses for the Composite Analysis ALARA Analysis 4-44
Table 6-1 Summary Comparison of Air Pathways Doses With Performance Objective During the 1,000-year Compliance Period 6-2
Table 6-2 Comparison of Projected Radon Fluxes with the Flux Limit 6-3
Table 6-3 Intruder-agriculture Dose Assessment Compared with the Performance Objective 6-5
Table 6-4 Inventory Limits for Pit Waste Using Intruder Analysis Limits 6-7
Table 6-5 Inventory Limits for Shaft Waste Using Intruder Analysis Results 6-9
Table 6-6 Total Inventory Limits for LANL LLW 6-10

1. INTRODUCTION

This report describes the radiological performance assessment (PA) for Material Disposal Area (MDA) G, the disposal facility for low-level radioactive solid waste (LLW) at Los Alamos National Laboratory (the Laboratory, LANL). The PA mathematically projects the potential radiological dose posed by LLW disposed of at MDA G after September 26, 1988 to a hypothetical member of the public over a period of 1,000 years.[1] To supplement the PA, a composite analysis (CA) projects the potential cumulative impacts of all radioactive materials in the ground at LANL that may interact with releases calculated in the MDA G PA.[2] The results of the PA are used to set limits on the radioactivity content of LLW that can be safely disposed of at MDA G. Results of the CA provide evidence that continued disposals at MDA G will not require future corrective or remedial actions to protect the public even when other sources are considered. Both analyses are required by the U S Department of Energy (DOE) and must be approved by the Deputy Assistant Secretary for DOE Waste Management, and once approved, form the technical basis for the MDA G Disposal Authorization Statement.[3]

The analyses described in this report reflect the resolution of comments provided by the DOE Peer Review Panel (PRP) upon review of preliminary work.[4] Those comments, and how each was addressed in the present analysis, are contained in Appendix 1a *Resolution of PRP Comments on Draft Performance Assessment for LANL TA-54, Area G Low-Level Radioactive Waste Disposal Facility*. One of the major comments provided by the PRP recognized the issuance of *Recommendation 94-2* of the Defense Nuclear Facilities Safety Board (DNFSB), which concluded that all waste should be included in the PA for LLW disposal facilities:[5]

> (I)nstructions should be issued to insure that: (a) performance assessments are based upon the total inventories (past, present, and future) emplaced or planned for the burial site; and (b) performance objectives (dose criteria) of DOE Order 5820.2A are achieved for the composite of all low-level waste disposal facilities at the site.

Pursuant to the DOE's acceptance of the DNFSB recommendation, the *Implementation Plan* for DNFSB Recommendation 94-2 was issued.[6] This plan specified the requirement for the CA::

> (T)he Department will conduct a composite analysis that accounts for other source terms that add to the dose to a hypothetical future member of the public projected for the disposal facilities.

This report fulfills the requirement for the completion of the LANL PA and CA. The PA portion of the analysis focuses on LLW disposed of after September 26, 1988, when DOE facilities implemented rigorous waste characterization requirements.[7] The CA considers waste disposed of before and after these requirements were implemented, at locations where potential releases might combine with projected releases from MDA G within 1,000 years after disposal operations at MDA G cease. Of the pre-1988 disposals at LANL, only those occurring at MDA G itself are considered likely to interact with releases from post-1988 disposals. The technical justification supporting this conclusion is presented in Appendix 1b *Technical Justification for Excluding Sources from the MDA G Composite Analysis*

Since both the PA and CA analyses involve the projection of future events, the results are not predictions of certain impacts; rather, the PA/CA process is a systematic method of demonstrating reasonable expectation that MDA G will not exceed performance measures defined by the DOE.[1,2] The results of the analyses indicate that the natural features of the site provide long-lasting protection against significant releases of radioactivity into the accessible environment. Exposures to radiation from waste disposed of at MDA G can be kept as low as reasonably achievable (ALARA), and well below performance measures prescribed by the DOE, if the waste is left in place and not disturbed. Furthermore, the performance measures can be met even if other sources of radioactivity remain in place.

The analyses supporting these conclusions are described in subsequent sections of this report. To limit the length of this report, it borrows information from other sources to the extent possible. Documents available from LANL or in the open literature that provided

supplemental information considered in the PA or CA are included in the References section. The main body of this document was written to be generally accessible to interested and informed readers. It contains the minimum technical language and mathematical expressions possible without compromising the quality of information required by *Interim Format and Content and Standard Review Plan for U.S. Department of Energy Low-Level Waste Performance Assessments*,[1] and *Guidance for a Composite Analysis of the Impact of Interacting Source Terms on the Radiological Protection of the Public from Department of Energy Low-Level Waste Disposal Facilities*.[2] Readers with interest in technical formalisms and intermediate results are directed to the extensive appendix section. The appendices include independent reports prepared for the PA and CA by subject-matter experts. They provide complete descriptions of methodology, input parameters, assumptions, uncertainties, and results of work conducted for the Disposal Facility Characteristics (Section 2), Analysis of Performance (Section 3), Results of Analysis (Section 4), and Inadvertent Intruder Analysis (Section 5) sections of this report.

This is the first iteration of what will become a "living" document. It will be continuously evaluated and revised in accordance with *Maintenance of U.S. Department of Energy Low-Level Waste Performance Assessments*.[8] The PA and CA will be considered final only after MDA G is closed, other sources of potentially interacting radioactivity are remediated and/or stabilized in place, and the boundaries of institutional control over contaminated sites are established.

1.1 APPROACH

MDA G has been used for the disposal of the Laboratory's radioactive waste since 1957. While several other sites at the Laboratory have also been used for radioactive waste disposal, MDA G is the only LLW disposal facility currently operating and is expected to be the only facility used in the future. While interactions from potential releases from formerly used sites are not expected within 1,000 years, releases from past, present, and future disposals at MDA G will be additive. Therefore, the entire MDA G inventory was

rigorously modeled, while other sources were analyzed in a semi-quantitative manner to accomplish the objectives of the PA and CA.

An extensive body of data was collected to evaluate the potential for releases of radioactivity from MDA G and to project subsequent exposures to members of the public due to such releases. Information on the MDA G geologic setting, facility characteristics, and waste inventory, for example, was collected, reviewed, and interpreted to identify processes and conditions that could potentially lead to releases of radioactivity from MDA G (referred to as *source terms*), and move it to locations that could be accessed by members of the public (referred to as *exposure pathways*). Source term(s) and exposure pathway(s) were coupled with realistic human activities that might lead to contact with contaminated soil, air, water, or foodstuffs to define *exposure scenarios*. Taken together, all source terms, exposure pathways, and exposure scenarios form the *conceptual model* of MDA G, which is illustrated in Figure 1-1.

The diagram illustrates the topographic setting of MDA G on Mesita del Buey, bounded by Cañada del Buey to the north and Pajarito Canyon to the south; the geologic setting of MDA G, consisting of subsurface layers of various volcanic depositions (i.e., Units 2, 1vu, 1vc, and 1vg of the Tshirege Member of the Bandelier Tuff; the Otowi Member of the Bandelier Tuff; and the Cerros del Rio Basalt); and the hydrologic setting of MDA G, incorporating intermittent surface streams in Pajarito Canyon and Cañada del Buey, liquid- and vapor-phase water moving through the subsurface within the intact rock (i.e., the *matrix*), within fractures in the rock, and along interfaces between layers (i.e., *interbeds* and *contacts*), and from vegetation (i.e., *transpiration*). The solid arrows emanating from the mesa surface and vegetation represent the movement of water as a liquid (straight arrows) and as a vapor (serpentine arrows).

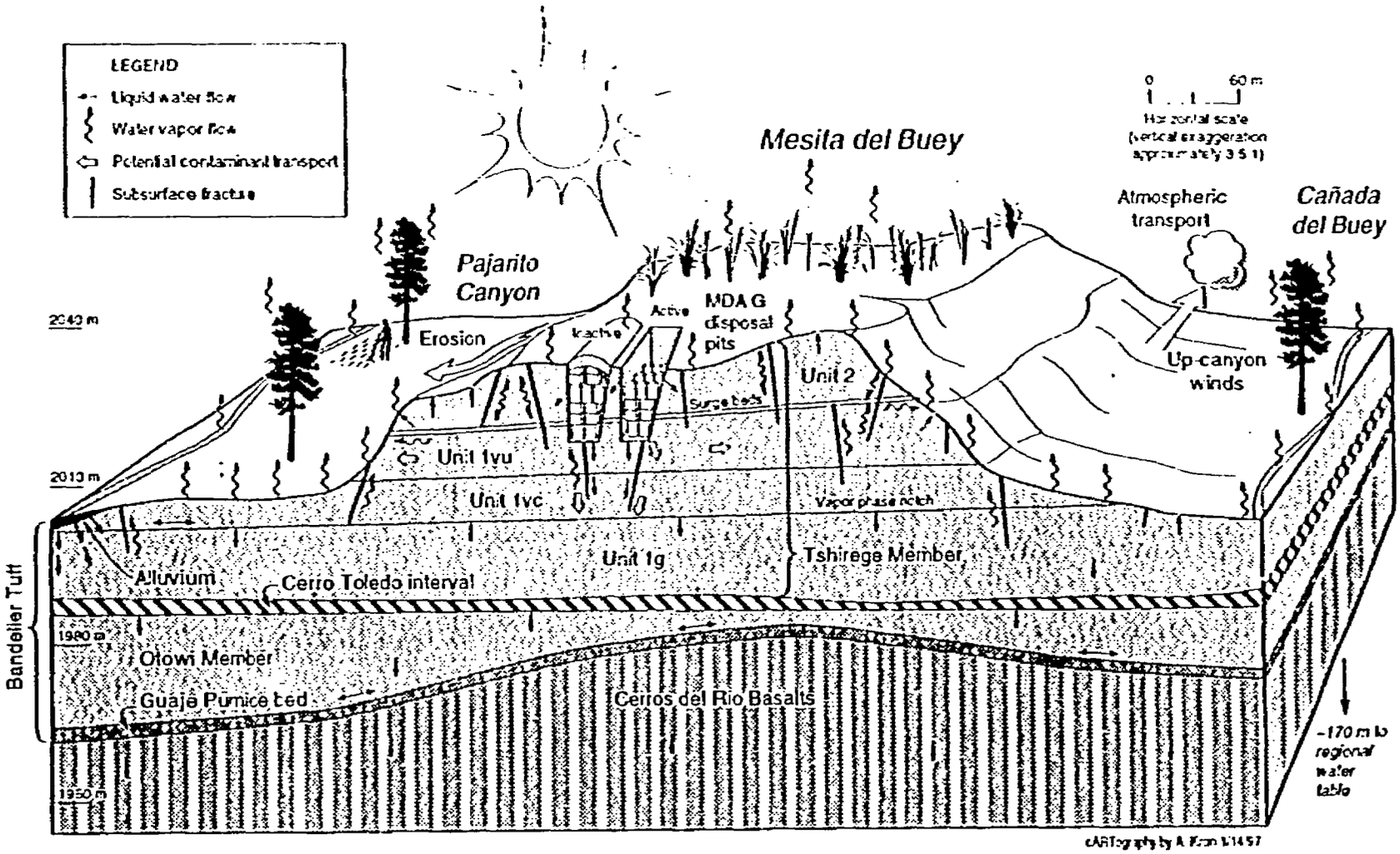

Figure 1-1 Conceptual Model of MDA G

The natural characteristics of the site have important implications regarding the source terms and exposure pathways analyzed for the PA and CA. This is especially true for exposures associated with contamination of the regional water-supply aquifer. When combined with the semiarid climate, the Bandelier Tuff is in general very dry. Much of the moisture from precipitation that is absorbed by the matrix is removed by evaporation and transpiration (collectively termed *evapotranspiration*) from the surface of the mesa. Evapotranspiration is effective to depths of 1 to 2 m (3 to 7 ft), where plant roots are abundant. In addition to this near-surface drying, evaporation appears to occur along the sides of the mesa, and in fractures and surge beds, which are layers within the mesa that appear to allow air flow. This relative absence of moisture practically eliminates the possibility that radioactivity will be carried down through the tuff to the regional water table, which is about 275 m (900 ft) below the surface of the mesa. The movement of radioactivity through the tuff is further reduced by natural minerals in the tuff that bind many radionuclides. These and other natural features of the site, along with man's uses of the facility and its environs, are described in Section 2 Disposal Facility Characteristics. The mathematical models for source term and pathways' analyses are described in Section 3 Analysis of Performance.

1.1.1 Source Terms and Related Processes

The source terms illustrated Figure 1-1 are identified by straight and serpentine arrows around the disposal units. The straight arrows represent dissolution of radioactivity in liquid water percolating through the disposal units (i.e., *aqueous-phase* source term). The serpentine arrows suggest releases of radioactivity into the air, either as gases (i.e., *gas-* or *vapor-phase* source term) or as dust particles (i.e., *resuspended particulates*). The actual source term for resuspended particulates involves processes that lead to surface contamination, including erosion and intrusion by plants and animals (i.e., *biotic translocation*).

1.1.2 Exposure Pathways and Related Processes

The exposure pathways combine a source release with air or water, which can transport radioactivity away from the disposal facility to locations where it might be accessed by

future members of the public (i.e., *receptor locations*). Contaminant transport is identified by open arrows on Figure 1-1. Aqueous-phase releases are transported through the rock beneath the disposal units (i.e., the *vadose zone*) toward the regional aquifer (i.e., the *saturated zone*) with liquid water in the matrix by gravity and other natural forces (e.g., vapor pressure, water pressure, etc.). Gas-phase releases and resuspended particulates are transported in air to downwind receptors. Finally, surface contamination resulting from biotic translocation is transported off of the mesa by stormwater runoff.

Exposure pathways can combine one or more source terms and transport media. For example, radioactivity contained in water (either below ground or on the surface) can be assimilated by plants; resuspended radioactivity in air can be deposited onto plants; and contaminated surface soils can be splashed onto plants.

1.1.3 Exposure Scenarios

The exposure scenarios considered in the PA and CA include internal exposures due to the consumption of water contaminated through aqueous-phase release and transport; inhalation of air contaminated with radioactive gases and radioactive particles; ingestion of foods cultivated in contaminated soils, and contaminated by redeposited radioactive particles; and direct external exposure to contaminated air, water, and soil. To project doses to hypothetical future members of the public for the PA and CA, these exposure scenarios were assumed to occur at locations away from MDA G.

In addition to the offsite exposures considered in the PA and CA, another scenario was performed as part of the PA only. This scenario projects doses to a hypothetical inadvertent intruder who may actually come into contact with radioactivity through activities at MDA G. While not a likely scenario, the intrusion analysis was performed to establish upper limits for the radioactivity content of LLW disposed of in the future at MDA G; this is called out as the development area in the figure.

1.2 FACILITY DESCRIPTION

The current configuration of MDA G with respect to the entire mesa and bordering canyons is shown in Figure 1-2.

Figure 1-2 Aerial photograph of MDA G and its surroundings

Of the 40 hectares (100 acres) comprising MDA G, 26 hectares (65 acres) have already been used for waste disposal. A portion of the remaining available acreage is expected to be developed as necessary to meet the LLW disposal needs of the Laboratory.

The geographic and geologic siting of MDA G provide natural features that enhance the suitability of MDA G for LLW disposal. The waste management and disposal activities provide further assurance of safe disposal operations. Section 2 of this report describes the characteristics of the site and facility that affect the analyses that are described in

Section 3. Figure 1-3 is a graphical depiction of how the information in Section 2 supports the analyses implemented for offsite dose projections described in Section 3.

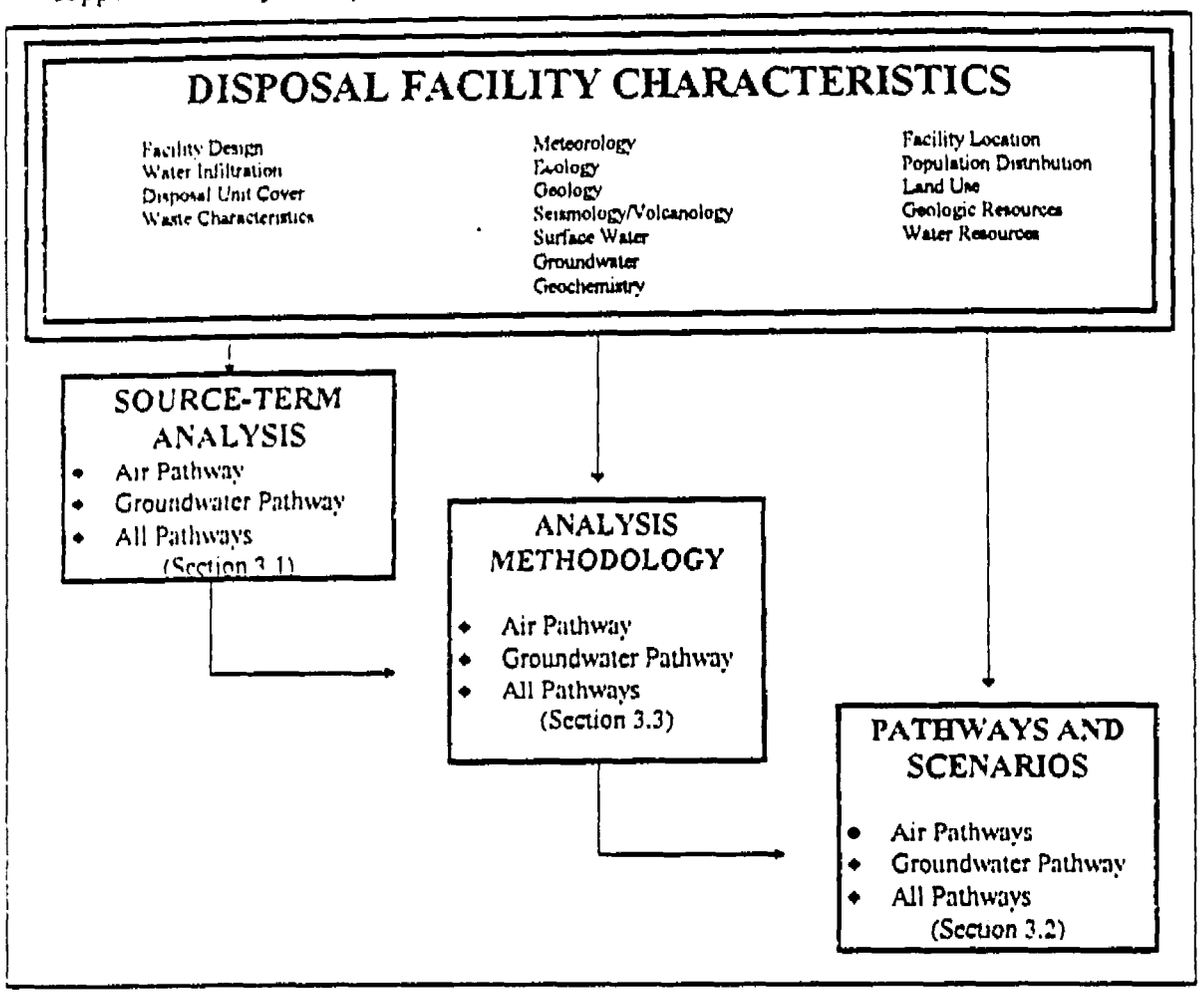

Figure 1-3 Facility characteristics considered in offsite dose assessments in the PA and CA

On the top of Figure 1-3, the disposal facility characteristics that are described in Section 2 are listed. Subjects are grouped according to the general portion of the performance analysis that they support, either source term, environmental transport analysis, or dose analysis. The three blocks in the middle of the figure indicate the organization of Section 3 of the report. Section 3 discusses the source term, environmental transport, and offsite dose analyses that were selected to simulate the performance of MDA G in light of the site-specific information presented in Section 2. Each phase of the overall analysis is presented in terms of air-, groundwater-, and all-pathways.

1.2.1 Geographic Siting

Mesita del Buey is located in the east-central portion of the LANL complex, which is separated into Technical Areas (TAs). Mesita del Buey and MDA G are located in TA-54. As Figure 1-4 shows, the TA-54 perimeter is coincident with the LANL boundary on its north and east edges.

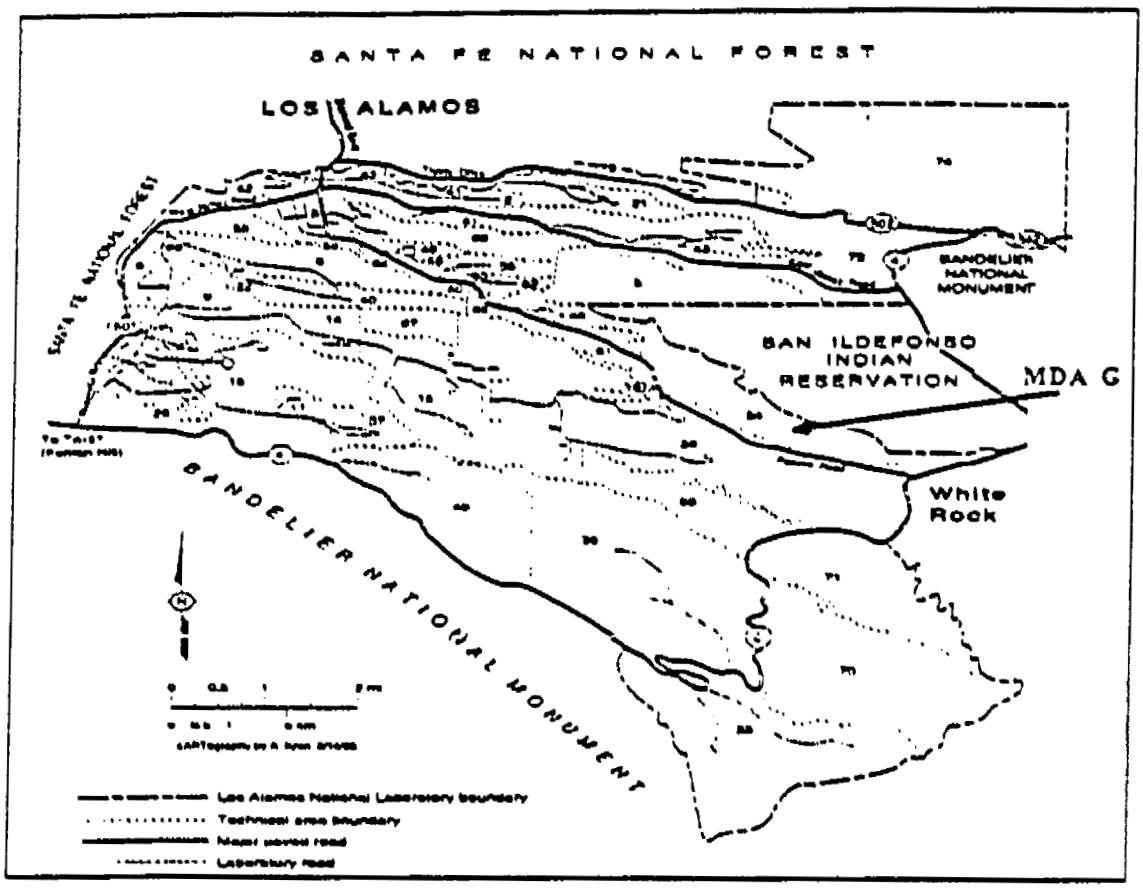

Figure 1-4 LANL Technical Area (TA) map

The nearest residential community to MDA G is White Rock, which is located directly east of the TA-54. The land adjacent to the north perimeter is owned by the San Ildefonso Indian Tribe. Tribal land extends into Cañada del Buey, the canyon directly north of Mesita del Buey. The people of San Ildefonso Pueblo regard a portion of land adjacent to LANL as sacred hunting grounds. In addition to hunting wildlife for food, Pueblo people also harvest the fruit of piñon and juniper trees native to the area. Hunting and gathering

activities, as well as use of the canyon stream, occur on the land directly adjacent to MDA G.

1.2.2 Geologic Siting

Mesita del Buey is composed of several distinct layers of porous rock, known as Bandelier Tuff, the layers are identified in Figure 1-1. Bandelier Tuff was deposited by volcanic eruptions in the Jemez Mountains to the west; two major eruptions resulted in the deposition of the lower 25 m (82 ft) thick Otowi Member, and the upper 55 m (175 ft) thick Tshirege Member. Between the two massive deposits are two relatively thin layers called the Tsankawi pumice bed and the Cerro Toledo interval. The uppermost layers of the Tshirege Member of the Bandelier Tuff are visible on exposed mesa sides.

On average along its centerline, the surface of Mesita del Buey is about 30 m (100 ft) above the adjacent canyon floors, and about 275 m (900 ft) above the regional aquifer. The depositional units thin and dip gently along the length of the mesa toward the east and south.

A considerable amount is known about the properties of the Tshirege Member of the Bandelier Tuff into which disposal units at MDA G are excavated. Much less is known about deeper units, most notably the Cerros del Rio Basalt between the Bandelier Tuff and the regional aquifer. As mentioned in Section 1.1, the Bandelier Tuff contains minerals that are known to hold, or sorb, certain radionuclides. The moisture content of the tuff the mesa is low, containing on average about 5 percent water on a volume basis. However, the moisture content is quite variable depending on the location. Measurements taken from boreholes at several locations around MDA G suggest a complicated process of wetting and drying throughout the mesa, apparently influenced by fractures and certain interbeds.

1.2.3 Waste Management

Current waste management operations at MDA G include permanent disposal of LLW, temporary storage of transuranic (TRU)[9] waste awaiting final disposal at the Waste

Isolation Pilot Plant (WIPP), and temporary storage of Mixed LLW (MLLW)[10] awaiting final treatment under the Federal Facilities Compliance Act (FFCA).[11] The LANL radioactive waste management program is consistent with the specifications of DOE Order 5820.2A.[7] The physical, chemical, and radiological characteristics of all waste stored and disposed of at MDA G are described by the waste generator on several forms. These forms are reviewed by waste management personnel prior to shipment of waste to ensure that all waste meets applicable acceptance criteria regarding waste form, packaging, chemical content, and radioactivity content. Once approved, these documents become permanent quality records. Both paper copies and electronic data are retained indefinitely. The LLW disposal records are used to develop the PA and CA inventories and to compare projected inventory with actual disposals.

Once received by MDA G, waste packages and documentation are checked for consistency and acceptability. If any significant discrepancies are identified, the receiving technician issues a nonconformance report to the waste generator describing the problem. The generator is then responsible for correcting the problem, either at MDA G or, if necessary, after the waste is returned to the generating facility. Nonconformance reports are also permanent quality records. They are reviewed to identify trends that indicate either inadequate guidance or surveillance on the part of waste management or recalcitrant waste generators. The documentation, review, approval, and acceptance processes are all elements of the generator certification program implemented for LLW.[12]

The largest *volume* of LLW disposed of at MDA G is routine LLW, which includes slightly contaminated refuse like paper and personnel protective equipment generated on a routine basis. The majority of the *radioactivity* disposed of is associated with a relatively small volume of nonroutine LLW, which includes highly activated metals disposed of periodically. Routine LLW is disposed of in unlined pits, while nonroutine LLW is disposed of in lined and unlined vertical shafts, which provide additional personnel protection and/or segregation.

Typically, pits are rectangular, about 20 m wide × 150 m long × 21 m deep (~65 ft × 500 ft × 65 ft), a notable exception is Pit 39, which is approximately hemispherical, about 20 m (65 ft) in diameter and 20 m (65 ft) deep. Shafts are typically cylindrical, about 20 m (~65 ft) deep and ranging in diameter from 0.5 to 1 m (~1.5 to 3 ft); one exception is a 4 m (~12 ft) diameter "triple-augered shaft" used solely for the disposal of activated components from the LANL Neutron Science Center and Meson Physics Facility. Pits are filled with waste to within 1 to 2 m (3.3 to 6.6 ft) of the ground surface, then backfilled and covered with consolidated crushed tuff. Topsoil and native grass seeds are emplaced over the tuff to form a vegetative cover that prevents erosion and water infiltration, and provides an esthetic appearance. Shafts are filled to within 1 m (3.3 ft) of the rim, then backfilled with tuff. Until this year, filled shafts were capped with concrete. The current operational closure procedure for filled shafts is to cover them with mounded tuff and allow for settlement for a period of up to 5 years before capping with concrete.

1.3 SCHEDULES

As noted earlier, the CA considers waste disposed of at MDA G in the past, present, and future, while the PA addresses inventory disposed of since September 26, 1988 and waste that will require disposal in the future. The analysis is performed over a period of 1,000 years after facility closure. For the purposes of the analysis, it is assumed that MDA G will be used through 2044. Once the disposal capacity is exhausted, all disposal units will be closed, and surface structures dismantled. Final site closure is expected to require one to two years (between 2045 and 2046). Active institutional control will continue for a period of 100 years (between 2047 and 2146). During institutional control, site access will be controlled, environmental monitoring will be performed, and closure cap integrity will be maintained. After the institutional-control period, it is assumed the site will be maintained by the DOE or its equivalent for as-yet undefined industrial uses. This industrial-use period is assumed to prevail for the 900 years remaining in the compliance period (between 2147 and 3046). In summary, for the purposes of the PA and CA, the MDA G lifecycle is defined as follows (all dates are inclusive):

- 1957-2044: Active waste disposal period;
  - 1957-2044: CA inventory disposal;
  - September 26, 1988-2044: PA inventory disposal;
- 2045-2046: Site closure period;
- 2047-2146: Institutional-control period; and
- 2147-3046: Industrial-use period.

1.4 RELATED DOCUMENTS

The results of the PA and CA impact several ongoing programmatic and planning activities at LANL. In addition, the results of the PA provide technical information that is integrated into many waste management documents. The relationship between these documents and the PA/CA are described below.

1.4.1 Site-Wide Environmental Impact Statement

The DOE is currently preparing a site-wide environmental impact statement (SWEIS) pursuant to the National Environmental Policy Act (NEPA),[13] which evaluates the potential environmental and economic effects of continued and proposed operations at the Laboratory. Continued operations at MDA G are among the activities addressed in the SWEIS. The PA team and SWEIS personnel have coordinated activities to ensure that the analyses have been approached in a consistent and efficient manner with respect to the following aspects of MDA G:

- General facility and site description;
- Existing waste inventory;
- Projected future LLW inventory;
- Proposed future disposal-unit development;
- Disposal unit closure; and
- Results of transport calculations.

The current SWIES schedule allows for consideration of PA details reported herein.

1.4.2 Environmental Restoration Project Documents

The Laboratory's Environmental Restoration (ER) Project has many documents that are related to both the PA and CA. Those documents and their relationship to the MDA G analyses are briefly discussed below.

1.4.2.1 Installation Workplan

The Installation Workplan (IWP) establishes the regulatory framework, programmatic structure, and lifecycle for the Laboratory's ER Project.[14] It also identifies the project scope and schedule for all sites described as Solid Waste Management Units (SWMUs), Operable Units (OUs), and Field Units (FUs) under consideration for remediation under the Resource Conservation and Recovery Act (RCRA). Certain aspects of the IWP are important to the development of the CA, and the results of the CA will, in turn, provide information that is important to the implementation of activities described in the plan. Examples of mutual interest and benefit include:

- Radioactively contaminated sites identified in the IWP as potentially interacting sources considered in the CA;
- Schedules for completing site characterization studies that may impact the maintenance of the CA; and
- Results of the CA that can be used as a tool to prioritize activities and schedules in the IWP.

1.4.2.2 RCRA Facilities Investigations Workplans

The detailed plans and schedules for individual OUs within the ER Project are described in RCRA Facilities Investigation (RFI) Workplan documents. The portion of MDA G that contains waste disposed of before 1988 is part of the ER Project's OU 1148. Many activities described in the *RFI Workplan for OU 1148* are specifically related to the MDA G PA and CA.[15] Both the workplan and this document describe natural features of the site, facility uses, and conceptual models for contaminant transport. The RFI workplan describes field investigations to measure releases from historic disposals, while the CA models the same releases. Those field investigations have provided a substantial body of data used in the PA and CA. In turn, the results of the CA will be used to evaluate alternative remediation and/or closure options for OU 1148.

In addition to the RFI workplan for OU 1148, additional ER plans describing sites with potentially interacting sources have been very useful in developing the CA. The descriptions of the natural setting and uses of other MDAs in various RFI Workplans were used directly to identify, and ultimately exclude, sources of radioactivity that could interact with projected releases from MDA G within a period of 1,000 years. In turn, it is anticipated that the results of the CA will be used to prioritize field investigations at other sites

1.4.3 Land Use Plan

The Laboratory's ER Project has developed a site-wide future land use plan in cooperation with the New Mexico Environment Department, the U.S. Environmental Protection Agency, and the DOE.[16] Annex E of that document describes the future scenario for MDA G, which is designated for future industrial use on DOE property. Access to the site will be limited to workers or authorized visitors and general facility surveillance will be instituted. Additional institutional controls will be defined and implemented as needed to prevent or limit exposure to contaminants. This Document of Understanding has important implications regarding exposure pathways and scenarios used in the PA and CA to evaluate compliance with specific performance objectives.

1.4.4 Site-Wide Groundwater Protection Plan

The Site-Wide Hydrogeologic Workplan relates to the prediction of hydrologic flow paths and resultant contaminant movement on a Laboratory-wide scale. One purpose of the workplan is to perform hydrogeologic modeling to answer contaminant pathway and hydrologic questions at ER sites. All of the ER sites considered in the CA are considered in the Hydrogeologic Workplan. Thus, the results of the PA and CA will be reviewed for consistency with existing conceptual models of the hydrogeology of the LANL site. Furthermore, results will be integrated with any regional analyses to be performed.

1.4.5 Waste Management Documents

There are many documents describing administrative, programmatic, and/or operational aspects of the LLW management program that are related to the PA. These relationships are summarized below. Each of the documents described, along with the PA, are integral elements of the formal configuration management program to ensure consistency throughout the facility lifecycle.[17]

1.4.5.1 Safety Analysis Report

MDA G is identified as a Hazard Category 2 non-reactor nuclear facility due to the TRU waste storage activities that occur there. A Safety Analysis Report (SAR) is maintained to understand and minimize the hazards associated with various facility uses.[18] To support the SAR for MDA G, the natural features and uses of the facility are described, and a hazard analysis is performed. A considerable degree of overlap exists between the information contained in the SAR and the PA; both are considered companion documents that ensure the safety of the facility during the operational (SAR) and post-closure (PA) periods.

1.4.5.2 Waste Acceptance Criteria

The results of the PA will be used to set limits on the future waste inventory so as to establish reasonable assurance that human health and environmental impacts will be below applicable performance objectives. These limits will become integrated into the *Waste Acceptance Criteria for CST Treatment, Storage, and Disposal Facilities* (WAC).[19] The relationship between the results of the PA and the WAC is discussed in Section 6 of this report.

1.4.5.3 Waste Certification Program

The requirements for waste characterization as described in the *Waste Acceptance and Certification Program* are based on the results of the PA.[12] This use of the PA results in the waste certification program will be performed in accordance with the Data Quality Objectives process endorsed by the U.S. EPA and DOE.[20]

1.4.5.4 Closure Plan

The operational closures for pits and shafts were briefly discussed previously in this section. Operational closures will be used until the site undergoes final closure, which is assumed to occur between 2045 and 2046. The *Closure Plan for LANL MDA G* describes final conceptual closure designs for the site.[21] Two options are included: one for the pits containing TRU waste, and one for pits containing only LLW. Both options incorporate layers of materials specifically engineered to minimize water percolation and prevent deep-rooting plants and burrowing animals from penetrating the cover, as demonstrated over several years in experimental and field investigations performed at LANL. The source term analyses for the PA and CA, and intruder analysis for the PA, modeled the operational cover. The results of the PA and CA will be used to evaluate options for final cover designs, including the operational cover.

1.4.5.5 Environmental Monitoring Plan

The *Environmental Monitoring Plan for TA-54, Area G* describes activities related to the MDA G PA.[22] Routine sampling and analysis of air, sediment, soils, plants, and animals performed around MDA G in support of the Laboratory-wide program are supplemented with additional field work that specifically support the PA. As detailed later in this report, additional field investigations are planned to provide information for reducing the uncertainty in the PA and CA evaluations.

1.4.5.6 Stormwater Pollution Prevention Plan

The *Stormwater Pollution Prevention Plan for TA-54, Area G* describes the natural and manmade features that control water runoff from the surface of MDA G into the adjacent canyons.[23] As such, it provides information useful in describing and modeling surface water movement related to transport of radioactivity both above and below ground. It also provides information for assessing the potential for water erosion that may impact the ability of the site to contain radioactivity over the long term.

1.5 PERFORMANCE CRITERIA

This section outlines the criteria used to judge the performance of MDA G over a period of 1,000 years. To provide a comprehensive analysis, the DOE has established performance objectives against which the results of the PA are compared to demonstrate lasting protection of:

- Future members of the public;
- Inadvertent intruders; and
- Groundwater.

In addition to the explicit performance objectives, the PA and CA evaluate the costs and benefits of alternatives designed to maintain releases to the environment at ALARA levels. The DOE is committed to managing MDA G (and other waste disposal areas) as long as necessary to ensure lasting protection of the public and the environment. Long-term institutional control of MDA G is considered a best management practice and will ensure that releases from the site are ALARA. Current LANL land-use plans project that MDA G will be an industrial site. Institutional control will be consistent with current Laboratory operations and procedures and will limit access to workers and authorized visitors.

The following sections define the performance objectives for the MDA G PA and CA, and identify the point of compliance where each performance objective is evaluated. Each numerical objective is applied at a location consistent with the long-term institutional control assumed for MDA G. At the same time, locations are chosen where maximum doses are likely to occur.

1.5.1 Public Protection Performance Objectives

The public-protection analysis is described fully in Section 3 of this report, while results are presented in Section 4. It was conducted to assess compliance with the public-protection performance objective as stated in DOE Order 5820.2A:

> Assure that external exposure to the waste and concentrations of radioactive material which may be released into surface water, groundwater, soil, plants and animals results in an effective dose equivalent that does not exceed 25 mrem/yr to any member of the public. Releases to the atmosphere shall meet the requirements of 40 CFR 61. Reasonable effort should be made to maintain releases of radioactivity in effluents to the general environment as low as reasonably achievable.

To demonstrate compliance with the first part of this statement, the "all-pathways" dose to a hypothetical member of the public is calculated at the point of highest dose. The all-pathways dose is then compared with the 25 mrem/yr performance objective to evaluate the long-term ability of the site to control the migration of radioactivity offsite. The all-pathways dose includes exposures to radioactivity in air, water, soil, and foodstuffs. The point of assessment for the all-pathways analysis during the 100-year institutional-control period is near the town of White Rock, which is the nearest offsite receptor downgradient from the facility. During the 900-year industrial-use period, two groundwater receptors are considered, one 100 m (330 ft) east-southeast (i.e., downgradient) of the MDA G fenceline, and another in Pajarito Canyon, opposite MDA G, which is assumed to be accessible if the land-use boundary is reduced to the MDA G fenceline.

The air pathway is considered alone in demonstrating compliance with the second statement in the public-protection performance objective. The numerical objective is based on the National Emission Standards for Hazardous Air Pollutants, which limits doses from radioactivity in air at offsite locations to 10 mrem/yr; this limit applies to the Laboratory as a whole[24] Two points of assessment are evaluated, one in Cañada del Buey, which has been demonstrated as being the location of maximum potential offsite airborne concentrations, and another in White Rock, which is the nearest population center.

Neither the all-pathways nor the air-pathways dose assessment includes the effect of radon-series radioisotopes in air. Separate controls for the emission of radon have been developed:[1]

- Average ground-surface emission from the disposal facility not to exceed 20 $pCi/m^2/s$, or
- Incremental increase in the air concentration of radon not to exceed 0.5 pCi/l at the point of public access.

The point of assessment for the radon performance objective is MDA G.

Results of the composite analysis must be compared with the DOE's primary annual dose limit for public protection of 100 mrem/yr at the point of public access. In addition, if the projected dose from CA sources exceeds 30 mrem/yr, there is a requirement to analyze alternatives for reducing the public dose ALARA.[2]

1.5.2 Intruder-Protection Performance Objective

For the purposes of establishing radioactivity limits for LLW to be disposed of in the future at MDA G, the PA uses the concept of the "inadvertent intruder." The inadvertent-intruder analysis is fully described in Section 5 of this report. The inadvertent-intruder performance objective is found in DOE Order 5820.2A:

> Assure that the committed effective dose equivalents received by individuals who inadvertently may intrude into the facility after the loss of active institutional control (100 years) will not exceed 100 mrem/yr for continuous exposure or 500 mrem for a single acute exposure.

The inadvertent intruder analysis establishes radioactivity limits by calculating the dose to a person who inadvertently intrudes into the waste. Upper limits for concentrations of radionuclides in the disposal unit are those that result in an intruder dose equal to the applicable numerical objective. Again, this is a modeling construct and not an anticipated occurrence, as institutional controls will prevent such events.

For the purpose of the analysis, intrusion is assumed to occur no sooner than 100 years following facility closure, and not beyond 1,000 years after closure. The 100 mrem/yr objective is used to assess exposure from a person accessing the disposal site. Doses are assumed to occur from direct radiation, ingestion of contaminated soils and foodstuffs, and inhalation of airborne radioactivity. Intruder doses are evaluated for PA waste only and are assumed to occur on or into a representative existing pit and/or shaft, as well as a future pit and/or shaft; there is no intruder dose assessment required for the CA inventory.

1.5.3 Groundwater-Protection Performance Objective

The groundwater protection analysis is discussed in Section 3 of this report, and the results are presented in Section 4. The applicable performance objective is found in DOE Order 5820.2A; "Protect groundwater resources, consistent with Federal, State and local requirements."

The point of assessment for the groundwater protection criterion is the point of maximum exposure beyond the land-use boundary. During the 100-year institutional-control period, the current TA-54 boundary is assumed to apply, which places the point of compliance at a water well near White Rock. During the 900-year industrial-use period, two points of assessment are evaluated consistent with the assumption that the land-use boundary during this period will be reduced to the current MDA G fenceline. One point of assessment is 100 m downgradient of the fenceline, and another is in Pajarito Canyon, adjacent to MDA G.

1.6 SUMMARY OF KEY ASSESSMENT ASSUMPTIONS

Exposures to future members of the public will be minimized if radioactivity is locally contained, and if intrusion into the waste is prevented. The ability to contain radioactivity locally depends largely on nature, while the ability to prevent intrusion depends solely on man. It follows, then, that two key assumptions in the MDA G PA and CA are that, throughout the 1,000-year compliance period:

- The current natural conditions of the site will prevail, and
- A government entity will maintain the site and control access to it.

Certain reasonably-expected extremes in precipitation are evaluated, and intrusion into the waste is also considered. The results provide additional assurance that human exposures will be below the performance objectives even under worst-credible cases.

2. DISPOSAL FACILITY CHARACTERISTICS

Numerous site, facility, and waste characteristics are important to model potential releases of radioactivity from Material Disposal Area (MDA) G, and to assess the potential consequences of such releases. Figure 2-1 summarizes these characteristics and identifies their relationships to aspects of the analysis described in Section 3.

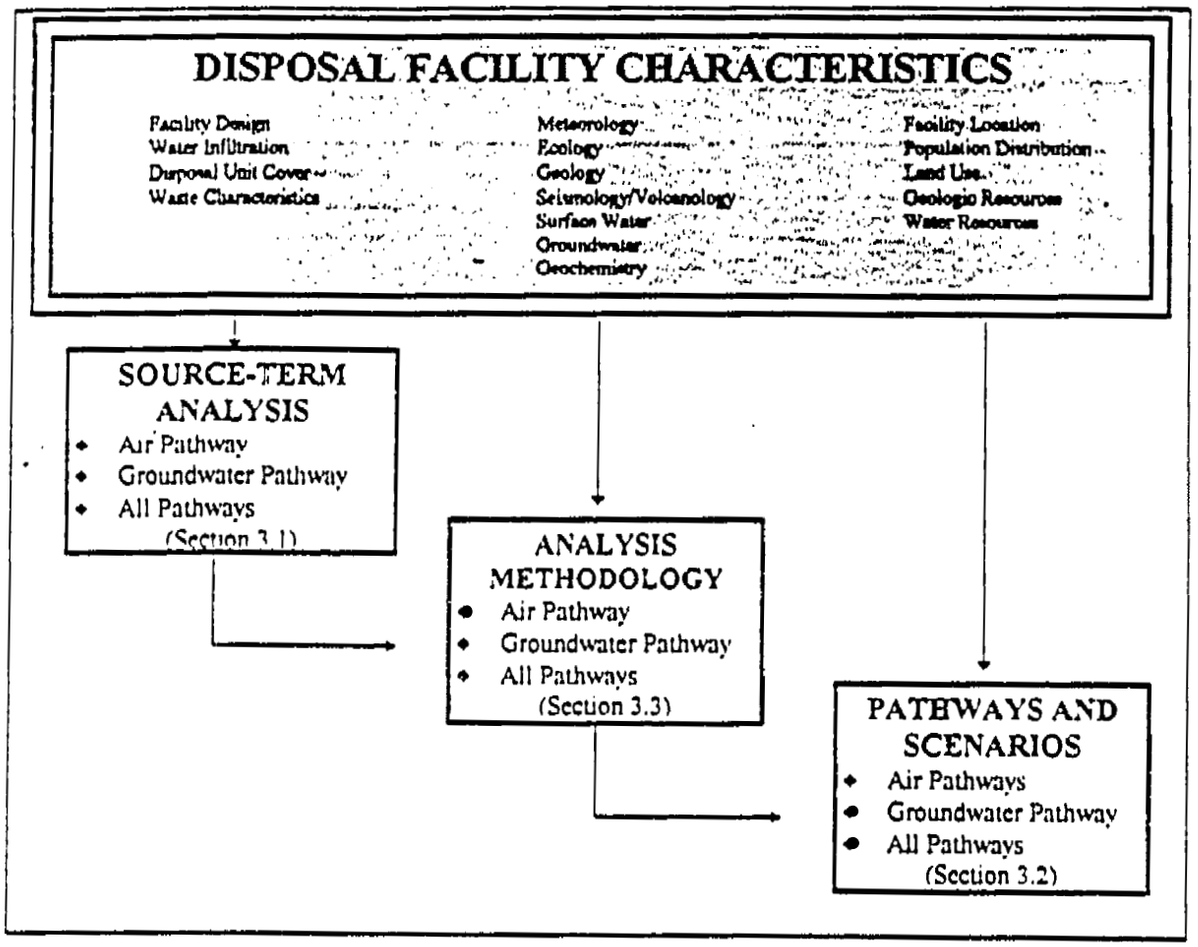

Figure 2-1 Use of disposal facility characteristics in analyzing disposal facility performance

2.1 SITE CHARACTERISTICS

The potential for releases of radioactivity from MDA G to affect human health will rely on the likely proximity of future members of the public to the facility and their anticipated use of potentially-contaminated environmental media. The consequence of such releases will depend on the type of radioactivity released, the quantity of radioactivity released, the rate

of release, and the environmental medium through which the release occurs. Important aspects of the site geography, meteorology, ecology, geology, geochemistry, background radiation environment, and natural resources that impact the performance assessment (PA) and composite analysis (CA) are characterized below.

2.1.1 Geography and Demography

LANL is located in northwestern New Mexico, about 45 km (29 mi) northwest of the state capitol, Santa Fe, and about 100 km (60 mi) north-northwest of Albuquerque, the state's largest city. A regional map is shown in Figure 2-2. The Laboratory owns and occupies some 111 km^2 (48 mi^2).

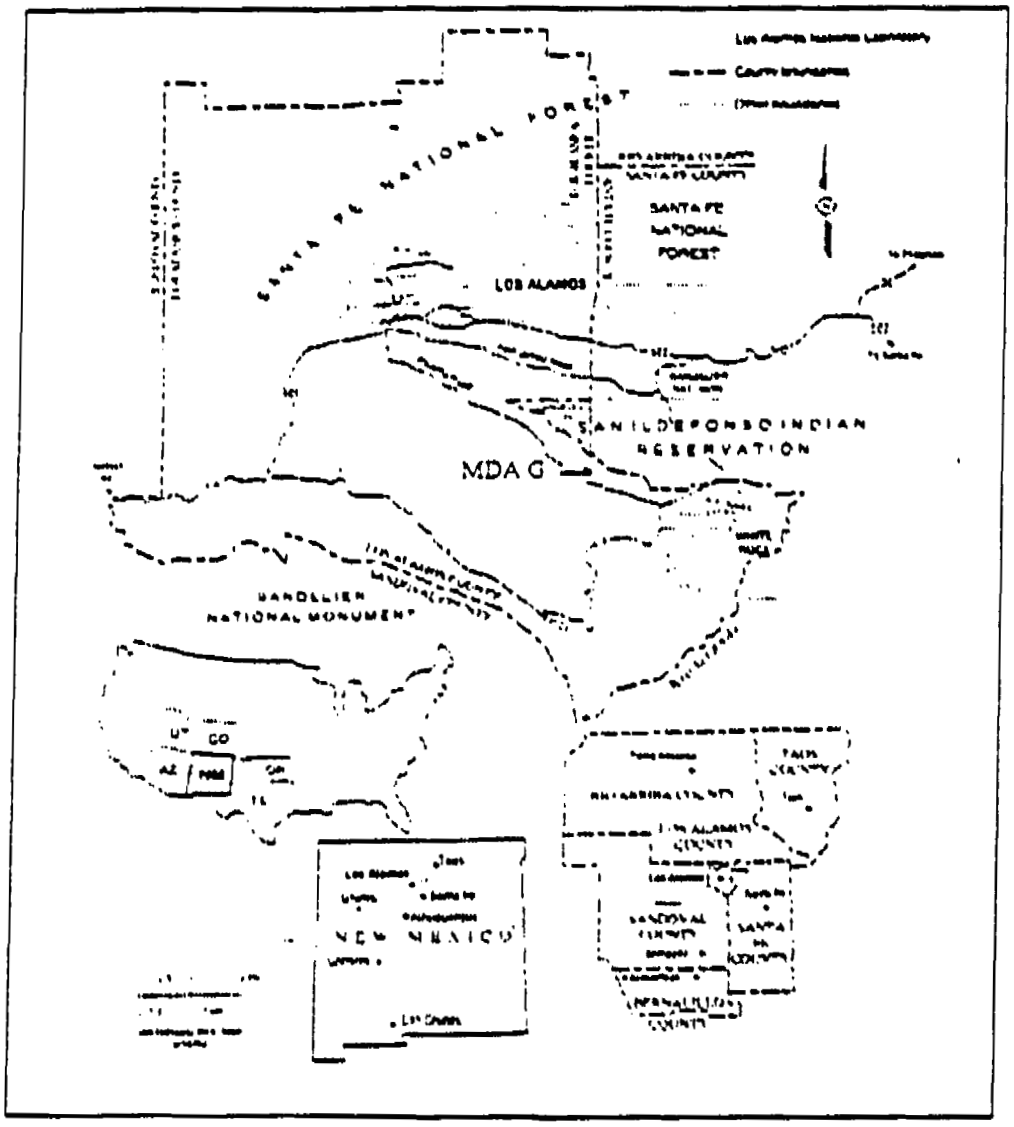

Figure 2-2 Location of the Los Alamos National Laboratory

2.1.1.1 Disposal Site Location

MDA G is located on Mesita del Buey at TA-54, which is in the east-southeast portion of the Laboratory complex. The north and east borders of TA-54 are coincident with the LANL property boundary. Mesita del Buey was identified in 1956 by the U.S. Geological Service for radioactive waste disposal due to its favorable hydrogeologic properties, which are described in detail later in this section. The majority of TA-54 was identified in the initial site survey as suitable for radioactive waste disposal. Since 1957, about 26 hectares (65 acres) have been used for this purpose; an additional 40 hectares (100 acres) are expected to provide sufficient LLW disposal capacity to support the mission of the Laboratory in the future.

For the purposes of projecting doses to future members of the public, it is assumed that the current MDA G boundary will remain through the 100-year institutional-control period. Thereafter, during the 900-year industrial-use period, it is assumed that the boundary will be reduced to coincide with the perimeter currently defined by the fence around MDA G.

2.1.1.2 Disposal Site Description

The geometry and placement of disposal units, and the types of waste they contain, influence potential release and transport processes, and, ultimately, the projected radiological impacts. Figure 2-3 is a facility map of MDA G superimposed on a topographical map. The figure calls out the approximate current boundary used in the analysis of the 100-year institutional-control period and the assumed future boundary used in the 900-year industrial-use period. Also identified is the future development area assumed to be filled over a period of 50 years. As the topographical map shows, the mesa is relatively flat and narrow running east-southeast, with steep sides draining into Cañada del Buey to the north and Pajarito Canyon to the south. The northern side of the mesa is more gently sloping than the south side. The south faces of Mesita del Buey are almost vertical near the rim, becoming more sloped toward the canyon floor some 30 m (100 ft) below. Perennial water flows in Pajarito Canyon are a result of rainfall and snowmelt

events. Cañada del Buey is much drier than Pajarito Canyon, with a small stream that flows only a few days out of the year. Stormwater runoff from Mesita del Buey feed the streams in both canyons. The major natural drainages are evident in the Figure 2-3 as incisions along the south wall of the mesa.

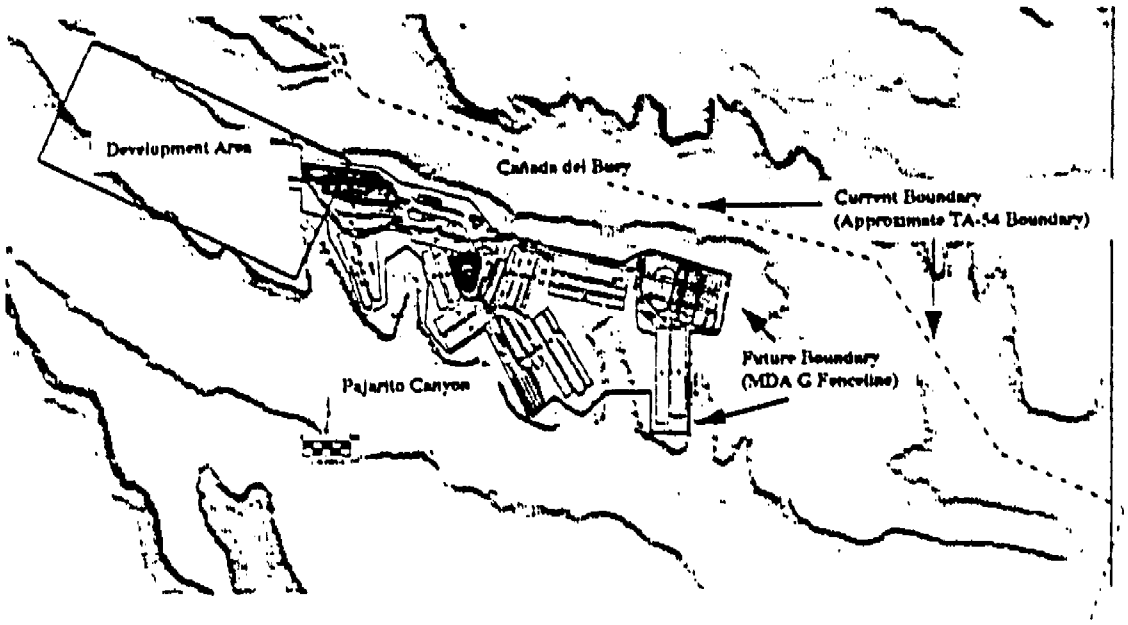

Figure 2-3 Map of MDA G illustrating mesa-canyon topography and current and future land-use boundaries

The natural drainage pattern is locally disturbed as a result of waste management activities at MDA G. Erosion controls are used to divert water away from waste management activities and disposal units. These controls include graded drainage channels, installed culverts, riprap, silt fences, asphalt channels, asphalt curbing, earthen berms, and weirs. As a practice, runoff controls are designed to guide surface water into the natural drainages. Certain surface structures at MDA G also alter the natural erosion patterns along the mesa, but only on a very local scale. Signs of erosion are identified and corrected as a part of the quarterly storm water compliance process.

Disposal units are excavated into the Bandelier Tuff using backhoes, while shafts are drilled using augers. All disposal units are set back at least 15 m (50 ft) from the nearest

canyon rim and are dug no deeper than 3 m (10 ft) above the adjacent canyon floor.[25,26] The intact Bandelier Tuff and the "crushed tuff" used to backfill and cover disposal units provide effective containment and isolation of radioactivity because of the hydrologic and geochemical properties discussed in section 2.1.4.

2.1.1.3 Population Distribution

The number of people living around MDA G is important for evaluating potential impacts of disposal operations there. This is especially true in the ALARA analysis, which compares costs and benefits of alternatives on the basis of population risk. The projected population of Los Alamos County in 1994 was approximately 18,200.[27] Two residential and associated commercial areas exist in the county, Los Alamos with a population of 11,400 and White Rock with a population of 6,800. White Rock borders the LANL boundary to the east, and is approximately 2 km (1.3 mi) east of MDA G. Other major residential population centers within an 80-km (53 mi) radius of LANL include Española to the northeast and Santa Fe to the southeast. Santa Fe, with a population of about 80,000, is expected to remain the major urban center of the region. In all, approximately 224,000 persons live within an 80-km (53-mi) radius of the Laboratory.

2.1.1.4 Uses of Adjacent Lands

Ownership of land surrounding LANL is indicated in Figure 2-2. State and federal government agencies and local Indian tribes control land surrounding Los Alamos County. Of these, three federal agencies (i.e., Bureau of Indian Affairs, U.S. Forest Service, and Bureau of Land Management) control the majority of land in the area.

The Santa Fe National Forest comprises 634,486 hectares (1,567,181 acres) of land in several counties. The Española District of the Santa Fe National Forest includes 142,521 hectares (352,170 acres) that border DOE land to the northwest and southeast. The Bandelier National Monument borders the southwest portion of the LANL complex and is managed by the National Park Service. The monument includes 12,950 hectares (32,000 acres) of land, 9,308 hectares (23,000 acres) of which are designated wilderness. All access routes to the monument pass through or along the Laboratory property.

Thirteen Native American Pueblos are located within 80 km (53 mi) of LANL. Each is governed by its own tribal government, with technical and administrative assistance from the Bureau of Indian Affairs. The San Ildefonso Pueblo owns a triangular piece of land that directly borders MDA G within Cañada del Buey to the north of the facility. The total area owned by the Pueblo is 10,600 hectares (26,192 acres). As stated in Section 1, the people of San Ildefonso Pueblo regard a portion of land adjacent to LANL as sacred hunting grounds. In addition to hunting wildlife for food, Pueblo people also harvest the fruit of piñon and juniper trees indigenous to the area. Hunting and gathering activities occur on the land directly adjacent to Mesita del Buey.

Within Los Alamos County, vacant land dominates all categories of land use, accounting for 49 percent of the area. Agricultural activities in the vicinity of LANL have been declining for the past several decades and are no longer considered an important economic activity in terms of cash income to area residents. Livestock (primarily cattle) provides nearly 75 percent of the cash revenue from farm commodities in the region; crops (including hay, corn, chile, and apples) provide the remaining 25 percent. Small farms remain an important means of supplemental income and domestic food in the northern New Mexico region. The San Ildefonso Pueblo grows crops for domestic consumption and some local marketing. Among the crops grown are corn, chile, squash, beans, and tomatoes. The following points summarize local agricultural activity:

- A small percentage of land (1 to 2 percent) is used for growing crops;
- Hay, corn, and chile are the most common crops in Los Alamos, Rio Arriba, and Santa Fe counties;
- Most of the agricultural acreage is irrigated;
- Surface-water irrigation is much more common than groundwater irrigation in Sandoval and Rio Arriba Counties; the opposite is true in Santa Fe County; and
- Livestock density is low (1 per 300 acres).

All cattle are range fed in northern New Mexico, livestock forage primarily on native short-grass species. Much of the land now occupied by LANL was historically used for grazing. The people of the Pueblos in the region also graze livestock on their lands near

LANL, and numerous private land owners in rural areas keep small numbers of livestock on land that surrounds Los Alamos County.

2.1.2 Meteorology and Climatology

The local and regional atmospheric conditions influence radionuclide transport in several ways. In terms of subsurface transport, water from rain and snow is important as the source of *recharge*, water flowing through the ground to the water table. Summer rains and spring snowmelt also cause erosion of the mesa surface, and have the potential to carry radioactive materials into adjacent canyons. Finally, the atmospheric conditions determine the extent to which airborne radioactivity will be transported away from the disposal site.

Los Alamos County has a semiarid, temperate mountain climate that is extensively monitored and well described.[28] There are four permanent meteorological towers LANL that collect data on precipitation, temperature, humidity, evapotranspiration, and wind speed and direction. The main Los Alamos gauge was initially installed at TA-59, west of TA-54 and at a higher elevation. In 1990, the main gauge was moved to TA-6, just south of TA-59 but at a comparable elevation. Additional gauges have been installed at TA-49, TA-53, and TA-54. The permanent towers are all sited on mesa tops. Table 2-1 summarizes pertinent data measured since 1989 at the TA-54 tower. It lists both monthly and average annual parameters.

Table 2-1 Summary of Meteorological Data at MDA G

Data	Jan	Feb	Mar	Apr	May	Jun	Jul	Aug	Sep	Oct	Nov	Dec	Avg
Ave Max Temp (F)	41	46	53	61	70	81	84	81	75	64	51	42	63
Ave Min Temp (F)	16	20	26	33	42	51	56	54	47	36	25	17	35
Total Precip (cm)	5.1	3.3	2.5	0.10	2.8	0.86	3.4	10.0	1.8	1.4	2.5	1.8	36
Ave Rel Humidity (%)	61	61	53	42	40	38	45	50	52	54	57	64	51
Total Evapo-transpiration (cm)	0.56	0.99	2.2	3.3	4.1	4.8	6.4	5.3	4.8	1.5	1.0	0.71	36

2.1.2.1 *Precipitation and Evapotranspiration*

The data in Table 2-1 indicate that about 40 percent of the annual average precipitation occurs during July and August, which is referred to as the monsoon season. Snowfall is greatest from December through March. Variations in precipitation from year to year can be quite large, with annual extremes ranging from 17 to 77 cm (6.8 to 30.3 in.) over the 9-year record from TA-54. Evaporation is generally high. The data in Table 2-1 indicate that an equal amount of moisture was lost through evaporation and transpiration as well as precipitation. Evapotranspiration is highest in the summer months, when vegetation is lush, temperatures are high, and relative humidity (i.e., the amount of moisture present in air compared with the amount of moisture that can be in air) is low.

The average annual precipitation measured over a period of 30 years at the Los Alamos gauge is 46 cm (18 in.), which is considerably higher than the 36 cm (14 in.) average measured over 9 years at TA-54. The 30-year pluviometric record from the Los Alamos precipitation gauge has been used for predicting annual precipitation in the region, including a 100-year daily rainfall extreme of 6.4 cm (2.5 in.) and a 100-year annual precipitation event for Los Alamos of 84 cm (33 in.).[29] Daily rainfall extremes of 2.5 cm (1.0 in.) or more occur in most years.

Additional longer-term evidence of local precipitation history is available through dendroclimatology, which compares modern meteorological records with contemporaneous tree growth (tree rings).[30] Semiarid climates like Los Alamos have very strong dendroclimatic correlation between precipitation and tree-ring width. The best correlations have been found for long-lived coniferous species that survive arid cycles, including ponderosa pine.[31] While ponderosa pine do not grow at Mesita del Buey, they are abundant at slightly higher elevations on the Pajarito Plateau, including TA-59 and TA-6, where the Los Alamos weather gauge has been stationed. Dendroclimatology has been used to estimate annual precipitation in years predating the pluviometric record, back to the year 1510. The analysis indicates the following precipitation extremes:

- The maximum annual precipitations were 101 cm (40 in.), 58 cm (23 in.), and 79 cm (31 in.), occurring in 1597, 1794, and 1919, respectively.
- The minimum annual precipitations were 14 cm (5.5 in.), 11 cm (4.3 in.), and 6 cm (0.79 in.), occurring in 1523, 1585, and 1685, respectively.

These numbers compare well with the estimated maximum precipitation based on pluviometric records. Both suggest that a maximum annual precipitation of about 80 cm (31 in.) can be expected every century. Again, these annual precipitation extremes are based on pluviometric and dendroclimatic records at TA-59/TA-6, where rainfall generally exceeds that at TA-54 by about 10 cm (3.9 in.).

2.1.2.2 Wind Speed and Direction

For the purposes of modeling atmospheric transport of radioactivity from MDA G, several characteristics about wind speed and direction are required. Two of these are *stability classes* and *mixing height*. Stability classes A through F characterize the ability of the atmosphere to disperse or spread contamination, from unstable (A) to stable (F). Unstable conditions are good for dispersing (and therefore diluting) airborne contamination, while stable conditions tend to keep the contamination in a more localized volume of air. Stability category frequencies are based on variations in wind direction and speed as a function of height above the ground. Stability class frequencies over Mesita del Buey and in Pajarito Canyon based on the 1995 meterological gauge data are listed in Table 2-2. The data suggest that canyon winds and mesa winds are both dominated by unstable (favorable) conditions.

Table 2-2 Atmospheric Stability Class Frequencies

Stability Class	Conditions	Mesita del Buey	Pajarito Canyon
A through C	Unstable (Favorable)	48%	48%
D	Neutral	22%	15%
E and F	Stable (Unfavorable)	30%	37%

The mixing height is related to the vertical thickness of the unstable atmosphere. Large mixing heights are "favorable" for dispersing or diluting airborne contamination. Average mixing heights for the Laboratory region are listed in Table 2-3.

Table 2-3 Average Atmospheric Mixing Heights[32]

Season	Average Mixing Height (m)
January	710
July	3,300
Average	2,000

The wind patterns across the Pajarito Plateau are greatly influenced by the mesa-canyon topography, which is evident in Figure 2-3. Data from 6 portable meteorological gauges installed in 1994 to monitor wind around MDA G are indicative of the strong channeling that occurs in canyons. Figure 2-4 shows the average *wind roses* (diagrams of wind speed, frequency, and direction) for daytime and nighttime hours during 1995 over Mesita del Buey and within Pajarito Canyon.[33] The wind roses indicate "wind from" directions, speeds, and frequencies. While mesa-top winds flow predominantly from the south to southwest during the day, canyon winds flow almost exclusively upcanyon (north northwest) during the day and drain downcanyon (south-southeast) at night. The strongest winds at MDA G are out of the south-southwest, up the Rio Grande valley. During the nighttime, westerly winds from the Jemez Mountain downslope are common, tending to follow the canyon drainage winds.[34] Winds speeds are less than 3 m/sec (10 ft/sec) most of the time, and are slower in the canyon than across the mesa.

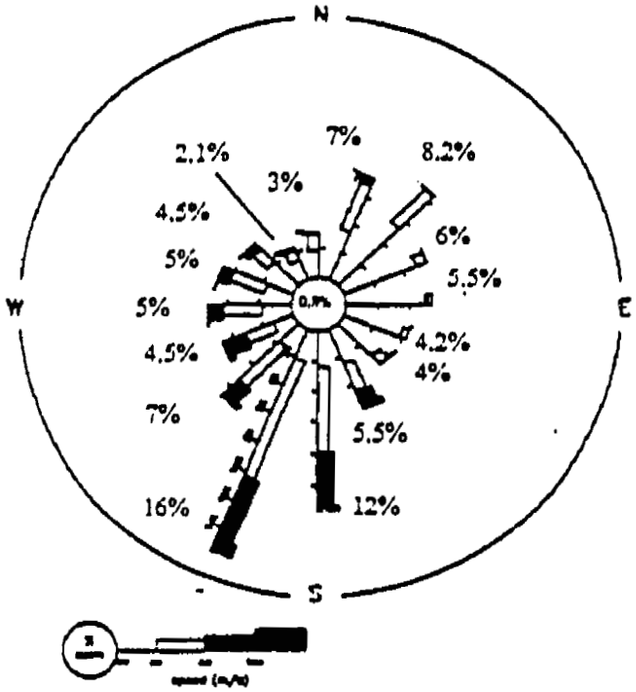

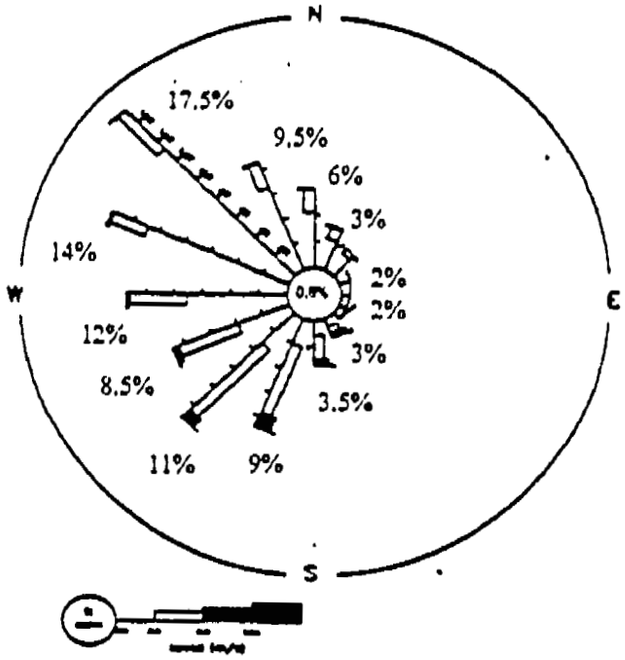

Figure 2.(a)

Figure 2-4 a Windroses from Mesita del Buey: daytime (top) nighttime (bottom)

2.1.4.1.1 Surface Deposits

Soils of the surface of Mesita del Buey arise from Tshirege colluvium and wind-blown sources. Native soils have been disturbed by waste-management operations over much of the surface of the mesa. In less disturbed portions of Mesita del Buey, native soils are thickest near the center of the mesa and thinner toward the edges. More highly developed soils on the north-facing slopes are richer in organic matter. Surface soils tend to be sandy in texture near the surface and are more clay-like beneath the surface. Soil-forming processes have been identified along fractures in the upper part of the mesa, and the translocation of clay minerals from surface soils into fractures has been described at MDA G.[41]

While certain soil components (including iron oxides and clay minerals) are very important in understanding the fate and transport of surface contamination (e.g., spills and effluent discharges) they have not been extensively studied to support MDA G modeling because the radioactivity is below ground. Greater consideration has been paid to the geochemical constituents of the subsurface, as discussed next. However, both modeling and field data suggest that surface soils do affect subsurface contaminant transport through their physical characteristics related to water flow. Recent geophysical tests have been performed on surface soils, but the data have not yet been analyzed.

2.1.4.1.2 Bandelier Tuff, Tshirege Member Unit 2

Unit 2 of the Tshirege Member of the Bandelier tuff is competent, resistant caprock that forms the level top of Mesita del Buey. It is about 12 m (39 ft) thick over much of MDA G. Unit 2 forms nearly vertical cliffs on the sides of the mesa where it is exposed. The rock is composed of crystal-rich, devitrified pumice fragments in a matrix of ash, shards, and phenocrysts.

Unit 2 is extensively fractured as a consequence of contraction upon postdepositional cooling. The "cooling-joint" fractures are visible on mesa edges and on the walls of pits, as shown in Figure 2-9a. In general, the fractures dissipate at the bottom of Unit 2.

Observation and detailed mapping show that most fractures in Unit 2 are nearly vertical. Mean spacing between fractures is about 1 m (3.3 ft), and fracture width ranges from less than 1 to 13 mm (<0.03 to 0.51 in.) with a median of 3 mm (0.12 in.). Fractures are typically filled with smectite clays to a depth of about 3 m (10 ft); smectite clays are known for their tendency to swell when water is present, and for their ability to strongly bind certain elements, both of which have implications for transport of radioisotopes in fractures. At greater depths in fractures, opal and calcite have been observed, usually in the presence of tree and plant roots; both the minerals and the roots suggest that some water occurs at depth in fractures.

At the base of Unit 2 is a series of thin [less than 10 cm (3.9 in.) thick], crystal-rich, fine and sand-sized surge deposits. The surge beds mark the base of Unit 2; they are identified along the wall of a pit in Figure 2-9a, and on an outcrop along the south wall of Mesita del Buey in Figure 2-9b. As discussed below, data obtained from boreholes and cores show that the surge beds at the base of Unit 2 appear to have an important local effect on moisture flux.

2.1.4.1.3 Bandelier Tuff, Tshirege Member Unit 1vu

Tshirege Member Unit 1v is a vapor-phase cooling unit beneath Unit 2. This unit forms sloping outcrops, which contrast with the more vertical cliffs of Unit 2. The uppermost portion of Unit 1v is devitrified and vapor-phase altered ash-fall and ash-flow tuff and has been designated Unit 1vu, where "u" signifies "upper." It is about 14 m (46 ft) thick near MDA G, is slightly welded at its base, and becomes moderately welded nearer the overlying Unit 2. Only the more prominent cooling fractures originating in Unit 2 continue into the more welded upper section of Unit 1vu but die out in the less-consolidated lower section. More typically, fractures in Unit 2 do not extend into Unit 1vu, as illustrated in Figure 2-9a.

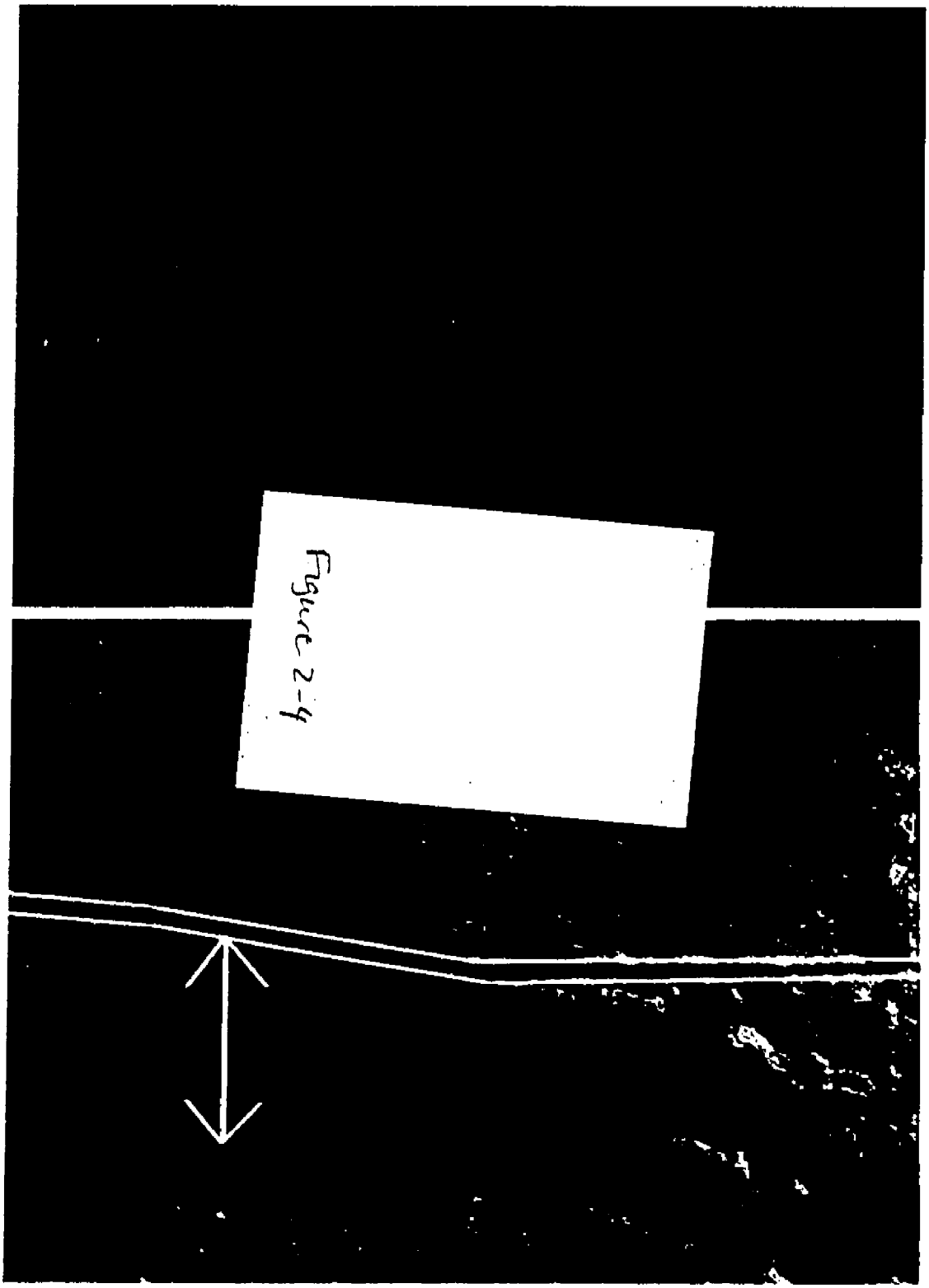

Figure 2-9 a) Surge bed and fractures in Unit 2, Pit 38, and b) surge beds at base of Unit 2 in outcrop along south wall of Mesita del Buey

2.1.4.1.4 Bandelier Tuff, Tshirege Member Unit 1vc

Beneath Unit 1vu is Unit 1vc, where "c" stands for "colonnade," characterizing the columnar jointing visible in cliffs formed in this unit. Unit 1vc is a slightly welded, devitrified ash-flow tuff at its base and top, becoming more welded in its interior. Unit 1vc is 7 to 8 m (23 to 26 ft) thick in the eastern reaches of Mesita del Buey and 15 m (49 ft) thick in the western reaches.

The basal contact of Unit 1vc is marked by a rapid change (i.e., 0.2 m vertical) from devitrified to vitrified pumice. Vitrified pumices below this interval, in Unit 1g, stand out in relief on weathered outcrops, while devitrified pumices above this interval are highly weathered. Near the base of this interval is a preferentially-eroded recess named the "vapor-phase notch." There is no depositional break associated with the vapor-phase notch; the abrupt transition suggests that this feature is the base of the devitrification that occurred in the hot interior of the cooling ash-flow sheet after emplacement. As discussed in greater detail below, the vapor-phase notch shows interesting local characteristics with respect to moisture flux.

2.1.4.1.5 Bandelier Tuff, Tshirege Member Unit 1g

Unit 1g is a vitric, pumiceous, nonwelded ashflow tuff underlying the devitrified Unit 1vc. It is about 15 m (49 ft) thick beneath MDA G. Few fractures are observed in the visible outcrops of this unit, and weathered cliff faces have a distinctive swiss-cheese appearance due to the softness of the tuff. Only the uppermost surface of Unit 1g is resistant to erosion, helping to define the vapor-phase notch described above. A distinctive pumice-poor surge deposit forms the base of Unit 1g.

2.1.4.1.6 Bandelier Tuff, Tshirege Member, Tsankawi Pumice Bed

The Tsankawi pumice bed is a thin bed of gravel-sized vitric pumice. It is about 0.6 m (2 ft) thick beneath MDA G.

2.1.4.1.7 Cerro Toledo Interval

The Cerro Toledo Interval comprises thin beds of tuffaceous sandstones, siltstones, ash, and pumice falls, which separate the upper Tshirege and lower Otowi Members of the Bandelier Tuff. The Cerro Toledo Interval also includes mixed gravel and cobble deposits derived from lava; it is either not reported or not present in older core logs, but has been identified as a 7 m (22 ft) interval in recent core samples recovered from drilling on the eastern portion of MDA G.

2.1.4.1.8 Bandelier Tuff, Otowi Member

The Otowi Member tuffs are about 30 m (98 ft) thick in the northwestern portion of Mesita del Buey and become thinner toward MDA G. Although the Otowi has been penetrated by recent boreholes, its thickness has not been measured at MDA G. The tuffs are massive, nonwelded, pumice-rich, and mostly vitric ash-flow. The pumices are fully inflated, supporting tubular structures that have not collapsed as a result of any postdepositional welding. The matrix is an unsorted mix of glass shards, phenocrysts, perlite clasts, and minute, broken pumice fragments.

2.1.4.1.9 Bandelier Tuff, Otowi Member, Guaje Pumice Bed

The presence of the Guaje Pumice Bed beneath MDA G can be inferred from core logs, but its thickness has not been measured there. The thickness of the unit has been measured as 3 m (10 ft) in the northwestern reaches of Mesita del Buey, and as 3.7 m (12 ft) in Pajarito Canyon south of MDA G. It is absent or not identified in core taken from the eastern part of the mesa. The pumice bed is nonwelded but brittle. Pumice tubes are partially filled with silica cement.

2.1.4.1.10 Cerros del Rio Basalt

Few data exist to describe the Cerros del Rio Basalt directly beneath MDA G. Local borehole cores show that the basalt consists of both angular rubble and dense, fractured masses, with zones of moderately to very porous lavas. The thickness of the basalt beneath MDA G is extrapolated to be between 80 and 150 m (262 and 492 ft).

2.1.4.1.11 Puye Formation

The depth to, and thickness of, the Puye Formation beneath MDA G has not been determined. However, 533 m (1,750 ft) of Puye Formation sedimentary rocks were encountered beneath 24 m (82 ft) of basalt in a water-supply well in Pajarito Canyon, about 1.5 km (0.9 mi) west of MDA G.[42] The lower part of the Puye Formation hosts the regional aquifer beneath Mesita del Buey.

2.1.4.2 Seismology

The LANL is locating within the northern Rio Grande rift, a seismically active region undergoing east-west extension. MDA G is located west of the Pajarito Fault system, which includes the Pajarito, Rendija Canyon, and Guaje Mountain faults. These faults are identified in Figure 2-10, in relation to some of the TAs comprising the LANL complex including TA-54, the location of MDA G. The heavy lines on the figure represent the traces of the three major faults included in the Pajarito Fault system, and the lesser Sawyer Canyon fault. The main east-dipping Pajarito fault has an average vertical slip rate of 0.07 mm/yr (2.7×10^{-4} in./yr) for the past 1.2 mA, whereas the shorter west-dipping Rendija Canyon and Guaje Mountain faults have average vertical slip rates of 0.02 and 0.01 mm/yr (7.8×10^{-5} and 3.9×10^{-5} in./yr), respectively.[43] Given the proximity of MDA G to the Pajarito Fault system, a seismic hazard evaluation was performed to support the PA and CA.[44] The results of that analysis are summarized in this section. Two potential seismic hazards were identified as having a possible impact on the ability of MDA G to contain and isolate radioactivity: 1) the potential for small displacements or deformation of the disposal unit cover due to surface faulting on minor secondary faults; and 2) the potential disturbance or deformation of the disposal unit cover due to ground shaking. Other potential earthquake hazards were not considered a risk at MDA G for a variety of reasons. Most important among these is that the subsurface excavation of disposal units into bedrock precludes the potential for liquifaction of sediments or earth-quake induced slope failures. While there is a potential for earthquake induced mass wasting of the cliff walls, there have been no large landslides or other large slope-failures identified near MDA G. Should such events occur, the 15 m (50 ft) setback from the edge of the cliffs is judged to provide good protection against loss of integrity of disposal units due to mass wasting.

The Rendija Canyon fault is the nearest of the Pajarito Fault system to MDA G, located [illegible] 6 km (3.6 mi) to the west-northwest of the site. The most recent surface [illegible] fault occurred at least 8,000 years ago, and possibly

23,000 years ago.[45] In either case, the most recent event did not rupture the southern end of the fault, which is the end nearest to MDA G. Estimates of average recurrence intervals for surface-faulting earthquakes (i.e., Richter magnitude greater than 6.5) range from 33,000 to 66,000 years.

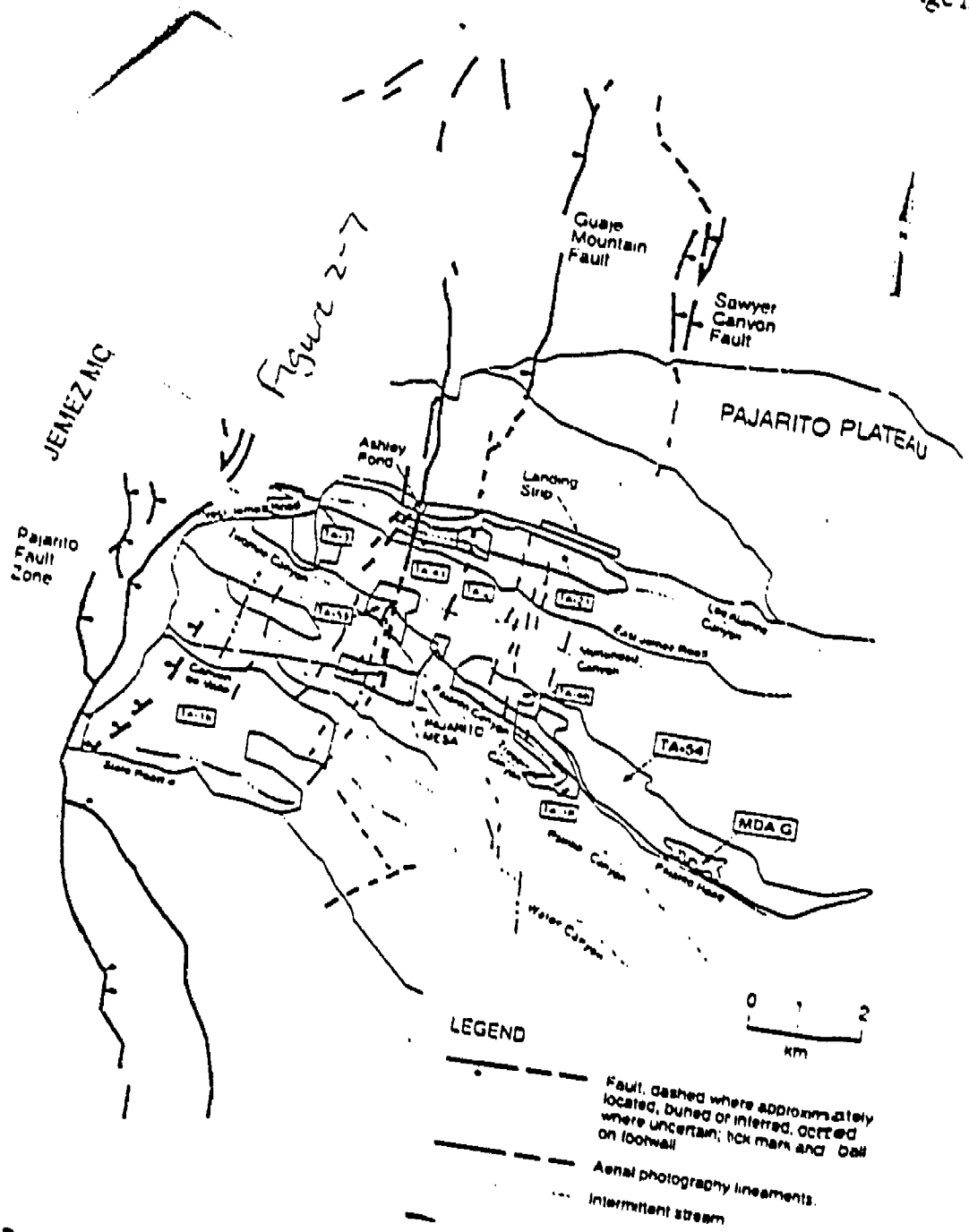

Figure 2-10 The Pajarito Fault System and the Rendija Canyon and Guaje Mountain Faults

2.1.7.2 Water Resources

Under normal operating conditions, the majority of water from the Guaje and Otowi well fields serves only the town of Los Alamos. Approximately 5 percent of the water from the Otowi well serves LANL. Of the 5 wells in the Pajarito field, 2 serve the town of White Rock and 3 serve LANL. Under unusual circumstances, water from any well can be routed to any destination. The LA well field was transferred to San Ildefonso in 1991. Currently only LA-2 and LA-5 are used for water supply. The wells are no longer used for drinking water but do provide nonpotable water for irrigation. In addition, nonpotable industrial water is obtained from the spring gallery in Water Canyon.

The Cochiti reservoir dam is located on the Rio Grande, about 15 km (9.3 mi) from the southernmost point of the LANL boundary. It provides the area with flood control, sediment retention, recreation, and fishery development. The permanent pool extends upstream some 12 km (7.4 mi), reaching a point about 5 km (3.1 mi) from the southernmost point of the LANL boundary. The dam is estimated to trap at least 90 percent of the sediments carried by the Rio Grande.

No municipal water supplies are taken directly from the Rio Grande river between LANL and the Cochiti Dam. The river is used primarily for recreation. Irrigation water is taken from the Rio Grande downstream from LANL at numerous diversions starting at the Cochiti Dam.

2.1.8 Natural Background Radiation

To evaluate contamination of environmental media (including air, soil, water, plants, and animals) as a result of waste management activities at MDA G, it is necessary to know the natural background radiation environment. The LANL publication *Environmental Surveillance at Los Alamos during 1994* reports that the annual effective dose equivalents due to background radiation in Los Alamos townsite and White Rock were 348 and 336 mrem, respectively.[69] Naturally-occurring radon accounts for nearly half of the total, with the remainder contributed by cosmic and terrestrial radioactivity, and self-irradiation.

While data describing the pre-operational background environment at MDA G are unavailable, regional background information is available. Representative background concentrations of radioactivity in air from the Laboratory region are listed in Table 2-12.

Table 2-12 Average Background Concentrations of Radioactivity in Air from Regional Stations

Radioactivity	Concentration
Gross Beta (10^{-15} mCi/mL)	18.0+/- 4.2*
^{3}H (10^{-12} mCi/mL)	0.5 +/- 1.3
Uranium (pg/m^3)	114.0 +/- 117.0
^{238}Pu (10^{-18} mCi/mL)	0.7 +/- 0.7
$^{239,240}Pu$ (10^{-18} mCi/mL)	0.9 +/- 0.7
^{241}Am (10^{-18} mCi/mL)	2.9 +/- 1.0

* +/- represents two standard deviations

Soil and water samples are collected at several regional stations, which are shown in Figure 2-21. The samples are analyzed for radioactivity generally associated with Laboratory operations. The LANL Environment, Safety, and Health Division is responsible for sampling and analysis, and presents results in annual environmental surveillance reports, such as that cited above. All data summarized here were taken from 1994 sampling and analysis.

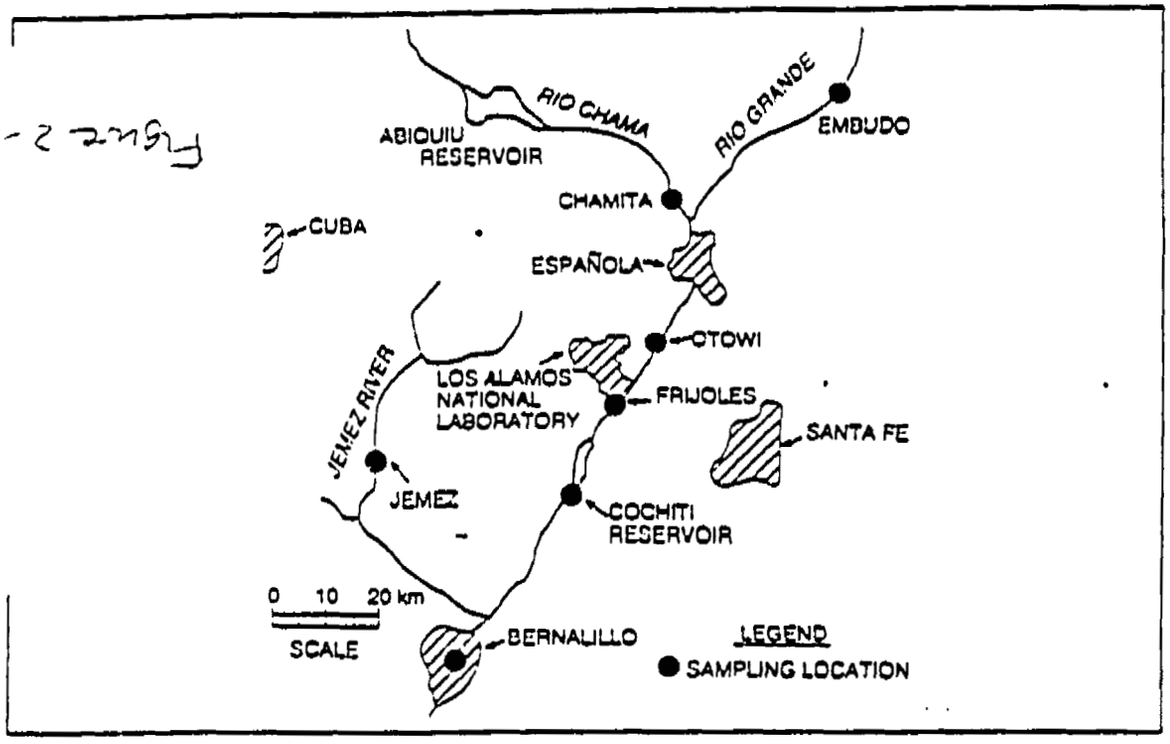

Figure 2-21 Regional surface water and soil sampling locations

Samples of soils north (Chamita sampling station), east (Otowi sampling station), and south (Frijoles sampling station) of the Laboratory have been analyzed for radioactivity. Results representing regional background radioactivity in soils are listed in Table 2-13.

Table 2-13 Radiochemical Quality of Regional Soils

Radioactivity	Chamita Station	Otowi Station	Frijoles Station
^{3}H (nCi/L)	0.2 +/- 0.3	-0.3 +/- 0.3	0.3 +/- 0.4
^{90}Sr (pCi/g)	-1.7 +/- 1.9	0.2 +/- 0.3	0.4 +/- 0.3
^{137}Cs (pCi/g)	0.1 +/- 0.0	7.7+/- 0.7	0.0 +/- 0.1
Uranium (µg/g)	1.0 +/- 0.4	1.5 +/- 0.4	2.0 +/- 0.5
^{238}Pu (pCi/g)	0.001 +/- 0.030	0.000 +/-0.030	0.005 +/- 0.001
$^{239,240}Pu$ (pCi/g)	0.001 +/- 0.020	0.001 +/- 0.020	0.005 +/- 0.001
^{241}Am (pCi/g)	0.004 +/- 0.030	0.004 +/- 0.030	0.008 +/- 0.003
Gross Gamma (pCi/g)	2 +/-0	0 +/- 0	3 +/- 0

* +/- represents two standard deviations

Surface water samples collected at offsite stations provide baseline information for water quality in the region. Radiochemical quality of water in the Rio Grande river upstream from (Embudo sampling station), adjacent to (Otowi sampling station), and downstream from (Cochiti sampling station) the Laboratory are listed in Table 2-14.

Table 2-14 Radiochemical Quality of Surface Water from Offsite Stations

Radioactivity	Embudo Station	Otowi Station	Cochiti Station
^{3}H (nCi/L)	0.1 +/- 0.3#	0.2 +/- 0.3	0.0 +/- 0.3
^{90}Sr (pCi/L)	0.4 +/- 0.7	0.1 +/- 0.7	0.3 +/- 0.8
^{137}Cs (pCi/L)	1.9 +/- 0.7	<0.6*	1.9 +/- 0.7
Uranium (mg/L)	1.6 +/- 0.2	2.4 +/- 0.2	1.6 +/- 0.2
^{238}Pu (pCi/L)	0.012 +/- 0.030	-0.014 +/- 0.030	-0.017 +/- 0.030
$^{239,240}Pu$ (pCi/L)	0.033+/- 0.020	0.035 +/- 0.022	-0.014 +/- 0.020
^{241}Am (pCi/L)	0.004 +/- 0.030	N/A	0.017 +/- 0.030
Gross Gamma (cpm/L)	60 +/-50	20 +/- 50	10 +/- 50

+/- represents two standard deviations
* Measurement below detection limit

2.2 PRINCIPAL FACILITY DESIGN FEATURES

The long-term radiological consequence of LLW disposals at MDA G will be negligible if two conditions can be met: Radioactivity does not become distributed in the environment, and humans do not come into direct contact with the radioactive waste. The ability to isolate radioactivity from the environment depends largely on natural processes and conditions, while the ability to control human intrusion depends on human factors. The previous section described many of the natural characteristics of the disposal site that must be considered in the PA for MDA G to evaluate the likelihood that the aforementioned conditions will be met. This section discusses the man-made features of the disposal facility that must also be considered in making this determination.

The design of MDA G takes advantage of the natural ability of the site to contain radioactivity. The very dry host rock effectively decouples radioactivity in LLW from the

main aquifer for thousands of years. Pits and shafts are excavated in the Tshirege Member of the Bandelier tuff. Crushed tuff removed during excavation is used to line, backfill, and cover pits. As a liner, the crushed tuff absorbs moisture and leachate. As backfill, the crushed tuff compacts to stabilize the pits, and also absorbs moisture. As a cover, the crushed tuff provides a stable, absorptive barrier, and supports natural vegetation that controls erosion and transpires moisture. These and other facility design features are described below.

2.2.1 Water Infiltration

Water infiltrating from the surface of the mesa through the disposal units is potentially problematic, particularly if the infiltration is of sufficient quantity to leach radioactivity from the waste and transport the contamination down through the vadose zone. As discussed earlier, the unsaturated upper units of the Bandelier Tuff tend to retain water (providing an opportunity for evaporation) as opposed to transmitting it. The amount of infiltration realized depends upon several components of the hydrologic cycle. Figure 2-22 depicts the water balance components that influence infiltration through a disposal unit.

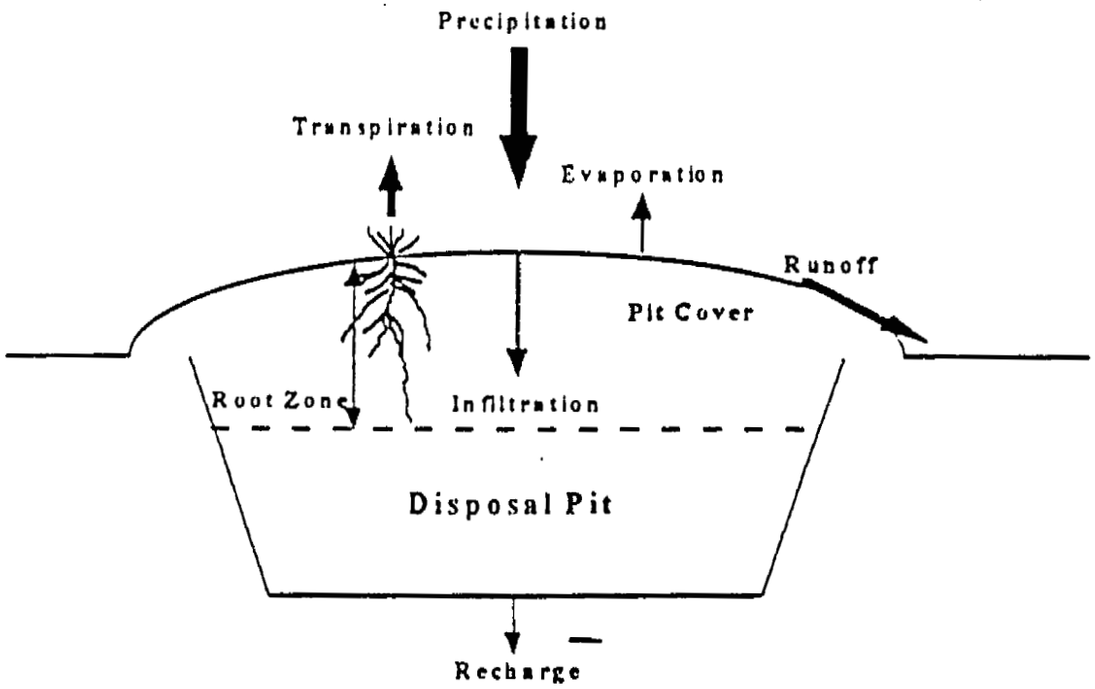

Figure 2-22 Conceptualized water balance components

Infiltration is the moisture remaining in the ground (or the pit cover) after runoff, evaporation, and transpiration remove some fraction of the precipitation (or snowmelt). Several components of the water-balance system have been discussed on a regional scale earlier in this section. As mentioned, precipitation, evaporation, and transpiration vary throughout the year. Evaporation generally occurs within several centimeters of the surface and appears to be effective over greater depths in fractured or very permeable rock. Transpiration is a result of root uptake and occurs throughout the root zone. Due to the inter-relationships among the water-balance components, infiltration varies with climate, ecology, and topography. Natural recharge through the Bandelier Tuff also varies, according to climate and local rock characteristics.

Manmade disturbances at MDA G interact with the naturally variable water balance components, making infiltration difficult to quantify with a high degree of certainty. Throughout much of the year, evapotranspiration keeps the disposal units quite dry; recharge occurs with snowmelt, when evapotranspiration is low. Efforts are made to maintain the high evapotranspiration potential on site by maintaining vegetative covers over filled disposal pits. However, waste management operations require features such as roads, asphalt pads, fire breaks, and stormwater diversions that interfere with evapotranspiration. In addition, while pits are in use, they may retain additional moisture from rainfall or snowmelt because transpiration is absent.

Studies of test plots at LANL have measured water-balance components through covers resembling the operational pit cover used at MDA G.[70] Data show that 87 percent of precipitation is lost to evapotranspiration, while about 6 percent remains as infiltration below the root zone (the remainder is retained in surface soil). Data also indicate that percolation through a conventional vegetated crushed-tuff cover was greatest in the late winter and early spring when snowmelt occurred and evapotranspiration was low because the vegetation was not active. Additional information on infiltration is available from field measurements of moisture within well-established covers at MDA G.[71] In 1973,

measurements were taken in holes augered into the covers over Pit 1 and Pit 2, which were closed in 1961 and 1963, respectively. Measured volumetric moisture content was quite variable, with individual measurements of 4 and 8 percent by volume in Pit 2, and 12 and 17 percent by volume in Pit 1. In all measurements, peak water concentrations occurred at depths of 2 m (6.6 ft), and decreased between 2 and 3 m (6.6 and 10 ft). The variation in moisture contents observed between the pits was tentatively attributed to variations in soil conductivity or differences in surface slope.

As discussed in Section 2.1.5, a common approach to estimating infiltration (or moisture flux) is to equate flux with the unsaturated hydraulic conductivity of the rock using the unit-gradient assumption.[72] Applied to the above moisture measurements, this method indicates infiltration within the Pit 1 and Pit 2 covers between several millimeters to several centimeters per year. Clearly, many factors influence infiltration through pit covers. Among those as recognized as important are surface-soil properties, depth of the root zone, vegetation density, and slope. All of these factors differ between disturbed covers and the undisturbed natural setting.

To better understand infiltration through disposal units at MDA G, the moisture content within Pit 37 has been measured periodically over the past three years. Pit 37 is expected to have moisture contents in excess of most pits at MDA G. While most pits are excavated, filled, and covered within two to four years, Pit 37 has been receiving waste since 1990, and has still not yet been covered. Multiple measurements from Pit 37 indicate a maximum moisture content of about 11 percent by volume, with a mean of about 8 percent.[73] Figure 2-23 is a composite plot showing volumetric moisture as a function of depth for several measurements taken over a period of a year. Using the unit approximation, the average infiltration rate through Pit 37 is 5 mm/yr (0.2 in./yr) at the average pit moisture content.

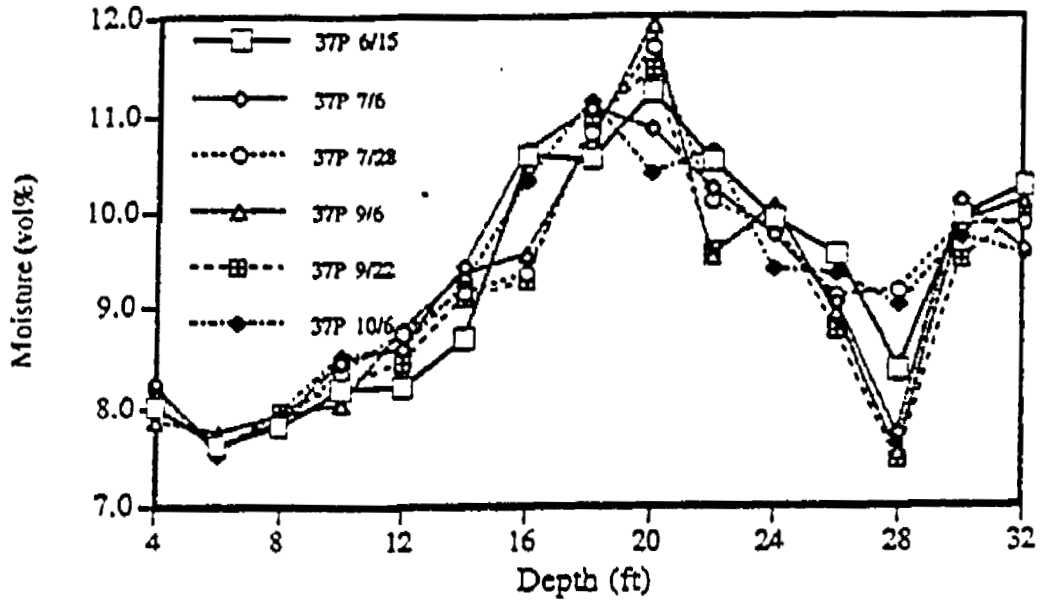

Figure 2-23 Neutron moisture profiles through Pit 37

While moisture content data collected within pit fill has generally shown moisture levels higher than for surrounding undisturbed tuff, the ultimate effect on recharge beneath the pits is not known.[31,74] In 1976 cores were collected from horizontal boreholes drilled to pass through Tshirege Unit 2 about 1 m (3.3 ft) beneath a pit that had been closed in 1966.[41] Analysis of these cores indicated that concentrations of ^{90}Sr, ^{137}Cs, ^{238}Pu, $^{239,240}Pu$, and ^{241}Am were below the minimum detection limits, suggesting that none of these radionuclides had migrated from the pits. In 1992 the boreholes were re-entered and moisture measurements made with a neutron probe.[75] Volumetric moisture content values beneath the pits were in the range of 1 to 4 percent, and were generally 1 to 2 percent higher beneath the pit than moisture levels away from the pit. These measurements suggest that pit excavation has a small effect on moisture contents beneath the pits.

—

This discussion has focused on infiltration through pit covers, and not shaft covers. This is largely because more data are available for pits. The conditions measured in pits are

expected to bound the infiltration in shafts, however. Pits provide a much larger surface area for infiltration than shafts. In addition, pits remain open during disposal operations, while shafts are covered between disposals, and, once filled, are generally covered with concrete.

2.2.2 Disposal Unit Cover Integrity

Considerable research has been conducted at LANL regarding the effectiveness of landfill covers in arid environments.[76] Many important aspects of relevant field studies and analyses were used in developing a conceptual multi-layer engineered cover for MDA G, which is described in the *Closure Plan for LANL MDA G*. While an engineered cover has been contemplated for final site closure, the simple interim cover seems to perform adequately, and has some advantages over an engineered design. The most obvious of these advantages include ease of installation and maintenance, and cost-effectiveness. Another important consideration that any uncertainties regarding the performance of the simple crushed-tuff cover are exacerbated in a multilayer barrier. The nominal 1 or 2 m (3 or 6 ft) operational cover described below is the base-case design in the PA models; alternative designs will be evaluated on the basis of the results of the PA and CA.

The operational closure cap for pits at MDA G consists of 1 to 2 m (3.3 to 6.6 ft) of consolidated crushed tuff, 10 cm (4 in.) topsoil, and native grass vegetation. Crushed tuff is emplaced with earthmovers or scrapers, then consolidated in place using a 50-ton bulldozer The general topography of the surface of the cap over a given pit is matched to the natural local topography. Until this year, pits were filled to within 1 m (3.3 ft) of the "spill point," or the lowest point along the surface perimeter of the pit. Current specifications require that pits be filled to within 2 m (6.6 ft) of the nearest rim. For pits filled according to the spill-point restriction, the operational closure cap may be several meters thick.

2.2.3 Structural Stability

The waste packaging requirements and disposal pit operations used throughout the history of MDA G confer structural stability to the pits. The 35 years of practical field

applications suggest that the design is effective at providing an interim barrier to water percolation, a critical aspect with respect to long-term disposal-unit performance. There has been no significant subsidence, only infrequent and minor local settlements, which have been filled with tuff. The performance is attributed largely to overall disposal-unit stability conferred by the operational practices of burying waste in compacted, parallel lifts separated by consolidated crushed tuff.

Pit disposal methodology was developed to minimize the potential for subsidence, promote consolidation within the disposal pits, and minimize the potential for shear failure. This is achieved by layering and compacting waste. Both modeling and field evidence support that the system is stable. Waste is emplaced in parallel horizontal layers or "lifts" using dump trucks, cranes or forklifts. Sufficient crushed-tuff backfill is used to fill void spaces between waste, to cover waste in one lift, and to provide an even, consolidated surface for the next lift. Earthmovers and scrapers are used to emplace the backfill, and 50-ton bulldozers are used to consolidate the crushed-tuff layer and the emplaced waste. On a volume basis, a typical disposal pit is at least 60 percent consolidated, crushed tuff. Compression measurements of crushed tuff show extremely fast consolidation; minimal settlement is observed because consolidation is immediate and occurs cumulatively during each loading.[77]

While liberal use of large quantities of backfill is a good practice in terms of disposal unit stability, it is not an efficient use of limited disposal capacity. To increase pit efficiency, waste management is now using large containers to package most LLW disposed of in pits and MDA G. Efforts are made to ensure that the boxes are full and contents compacted to the extent possible, both to maximize efficiency and to minimize the potential for subsidence. These objectives will be more easily achieved when LANL begins operating its 200-ton supercompactor to compact waste directly into large metal boxes. To date, one pit (Pit 38) has been used for disposal of waste contained in large metal boxes. The disposal efficiency of that pit is expected to be substantially higher than previously-filled pits.

2.2.4 Inadvertent Intruder Barrier

The only structural barriers to human intrusion at MDA G are concrete caps place over filled disposal shafts. There are no structural barriers to prevent inadvertent intrusion into disposal pits at MDA G. Rather, site access controls such as those currently used are assumed to be in place throughout the 100-year active institutional-control period and into the industrial-use period.

2.3 WASTE CHARACTERIZATION

This section discusses the approach used to characterize the waste disposed of at MDA G and summarizes the results of the characterization effort. The methods used to characterize the historic and future waste inventories are addressed in Section 2.3.1 and 2.3.2, respectively. Complete descriptions of the inventory projection methodology and results may be found in Appendix 2e *Radioactive Waste Inventory for the TA-54, Area G Performance Assessment and Composite Analysis.*[78]

2.3.1 Historic Waste

Historic waste refers to the material disposed of at MDA G from 1957 through 1995. The characterization effort considered this waste in three segments, based on the period over which it was disposed of. These periods include:

- 1957 to 1970,
- 1971 to September 25, 1988, and
- September 26, 1988 through 1995.

This approach was used because the level of information available for each waste segment differs, and because it allowed clear delineation between the PA and CA inventories. The methodology used to estimate the radiological characteristics of the historic waste are summarized below.

2.3.1.1 Inventory Development

Detailed records describing the radiological characteristics of waste disposed of at MDA G between 1957 and 1970 are unavailable. While the early inventory is largely LLW, it

also includes some TRU waste and mixed LLW (MLLW). TRU waste was segregated from LLW prior to disposal starting in 1971, and MLLW was segregated from LLW prior to disposal in the mid-1980s. Lacking detailed disposal records, the waste disposed of between 1957 and 1970 was characterized by extrapolating waste data for material generated after 1971 back to the earlier period. Adjustments were made to the extrapolation-based estimates to account for shortcomings in the projection method.

The periods from which the 1957 to 1970 waste characteristics were extrapolated were selected following an evaluation of LLW and TRU waste disposal data in the post-1971 period. The recorded annual volumes and activities disposed of as LLW, and stored as TRU waste, between 1971 and 1995 are plotted in Figure 2-24 and Figure 2-25, respectively.

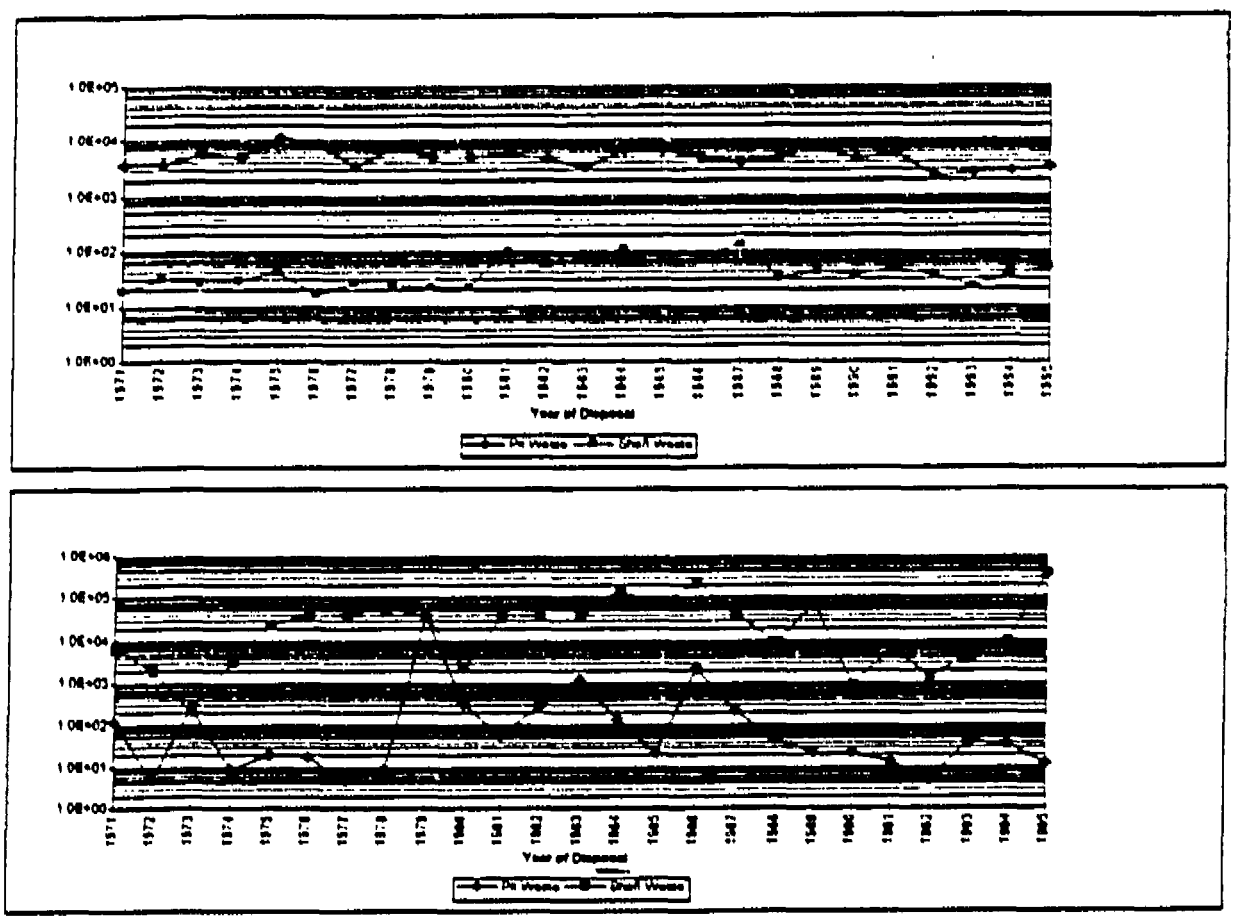

Figure 2-24 Recorded annual LLW disposal volumes (top) and radioactivities (bottom)

Referring to Figure 2-24, annual LLW disposal volumes have been relatively constant over time. In contrast, LLW activities have varied widely, most notably in 1979. For TRU waste, Figure 2-25 shows that volumes of waste placed in storage ranged over an order of magnitude, while radioactivity content ranged over about 3 orders of magnitude. In light of these trends and variations, efforts were made to select the most representative time frame to extrapolate back to the 1957 to 1970 period.

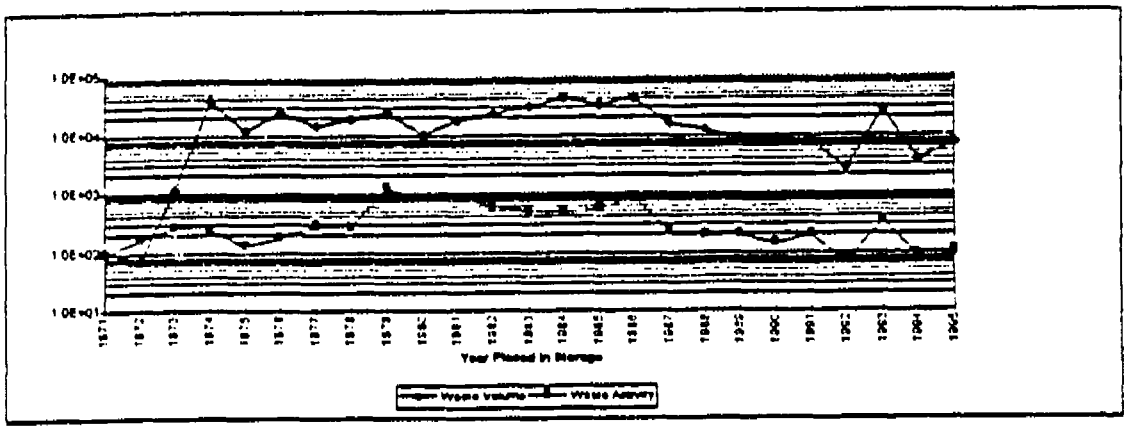

Figure 2-25 Recorded annual TRU storage volumes and radioactivities

The LLW disposal and TRU waste storage records from the early 1970s were judged to be most representative of waste disposed of before 1970 based on information provided by former LANL waste management personnel.[79] For waste disposed of in pits, the period from which the 1957 to 1970 waste characteristics were extrapolated was 1971 to 1977; for shaft waste, the period was 1971 to 1975. The 1971 to 1977 pit data and the 1971 to 1975 shaft data were used to develop average annual disposal quantities for estimating the pre-1971 inventory. These averages were multiplied by the number of years MDA G accepted waste for disposal in the respective disposal units between 1957 and 1970. The average annual pit inventories were multiplied by 12, to account for the 12 years that "routine" waste was disposed of at MDA G; records indicate that only "non-routine" waste was disposed of during 1957 and 1958. For shafts, the average annual inventory was multiplied by 5, reflecting the fact that shafts began accepting waste in 1966.

The fundamental assumption of the extrapolation approach used to characterize the pre-1971 disposal inventory is that waste disposed of between 1971 and 1977 resembles the waste disposed of prior to 1971. While this assumption is generally expected to be valid, some of the wastes generated from 1957 to 1970 and 1971 to 1977 are unique to those periods. To account for waste that was unique to either period, individuals familiar with the Laboratory's waste-generating and waste management programs during the periods of interest were interviewed. As a result of those interviews, waste in the recorded inventory that was determined to have been generated only after 1971 was removed from the data used to extrapolate the 1957 to 1970 inventory. Waste that was unique to the 1957 to 1970 period was added to the inventory estimated using the extrapolation approach. Examples of inventory associated only with the post-1971 period include the waste generated by the Los Alamos Neutron Scattering Center (LANSCE; TA-53) and the new plutonium-processing facility (at TA-55). An example of waste that is associated only with the pre-1971 period is the material generated during the decommissioning of the old nuclear-material processing laboratories at TA-21.

The historic waste inventories for the 1971 to September 25, 1988 and September 26, 1988 to 1995 periods were estimated using disposal data in the LANL LLW disposal database and the TRU waste database. The majority of the MDA G inventory for this period was derived from the LLW disposal records. The TRU waste that was non-retrievably disposed of in pits and shafts was added to the LLW inventory to arrive at the total inventory for the period.

2.3.1.2 Radionuclide Allocations

Radionuclide inventories in the historic waste were estimated using the appropriate waste disposal records. In recent years, waste generators have been required to list each radionuclide present in the waste, along with its activity. However, up until 1991, generators were permitted to use acronyms and material codes to report radioactivity in a more generic manner. Since the quantity of specific radionuclides is needed to conduct

for release, transport, and dose calculations, it was necessary to relate these entries to individual radionuclides. The methods used to convert generic coded activities to radionuclide-specific activities are discussed in the following paragraphs.

A portion of the waste disposed of at MDA G is characterized in the LLW and TRU waste databases as mixed activation products (MAP) or mixed fission products (MFP). Radionuclide allocations for these acronyms were performed according to the analysis described in Appendix 2f *Isotopic Compositions of Inventory Designations "Mixed Fission Product" and "Mixed Activation Product."*[60] The MAP designation has been used primarily by generators at the LANSCE, where high-energy particle beams are projected onto targets which, in turn, become activated. Three major waste streams are generated at LANSCE including trash, targets, and beam-line inserts. The fractional abundance of each radionuclide in the MAP waste was determined through discussions with the generator. These abundances are shown in Table 2-15. The data in the last column in this table were multiplied by the activity reported as MAP to determine radionuclide-specific activities. The majority of the MFP waste included in the databases was generated through the processing of contaminated specimens retrieved from underground nuclear weapons test-beds. When elements' fission, they produce other elements (i.e., fission products), some of which are themselves radioactive. The amount of each fission product (or fission yield) generated depends upon how fission is induced (by fast or thermal neutrons) and what radionuclide fissions (e.g., ^{235}U or ^{239}Pu).

Table 2-15 "Mixed Activation Product" abundance

Radionuclide	Mass Fraction	Activity Concentration (Ci/g)	Activity Fraction
^{7}Be	3.0E-02	1.1E-04	6.9E-01
^{22}Na	1.0E-01	6.3E+02	4.1E-02
^{54}Mn	1.8E-01	1.5E+03	9.5E-02
^{57}Co	1.2E-01	1.0E+03	6.7E-02
^{60}Co	4.4E-01	5.0E+02	3.3E-02
^{65}Zn	1.3E-01	1.1E+03	7.1E-02

The allocation of radionuclides present in MFP was based on thermal and fast neutron fission yields for ^{235}U and ^{239}Pu. All radionuclides with an atomic mass number between 78 and 160 and a half-life of at least one year were included in the calculations. In using these fission yields, it was conservatively assumed that the yield of a given isotope was the maximum of that provided for thermal and fast neutrons. In cases where several isotopes of a given element were generated by fission, it was assumed that the entire yield consisted of the long-lived species. When two long-lived isotopes were generated, it was assumed that the yield of each isotope was half of the total.

Nuclear material codes were used at LANL to describe uranium and plutonium isotope blends on waste characterization forms during the cold war. These codes continued to be used by many generators through 1991. In order to characterize historic waste inventories, it was necessary to convert the activities recorded for each code into radionuclide-specific activities. The information needed to perform the conversion is available from the nuclear materials processing facilities. The fractional abundances used to allocate material-code activities to radionuclide activities are included in Appendix 2e.

2.3.1.3 Inventory Categories

The chemical, physical, and radiological characteristics of waste determine how radioactivity may be released from the material. For example, surface contamination on glass may be quickly rinsed from the waste as water percolates through the disposal units, whereas radionuclides sorbed to soils or concrete may be released from the waste gradually over time. Under certain conditions (e.g., ^{14}C in organic waste), releases may occur in the form of gases. Source-term modeling for the PA and CA accounts for the predominant modes of release.

Assignment of the historic waste inventory to specific waste forms was based on "waste codes" assigned by generators to describe their waste. These waste codes were divided among four generic waste forms including:

- Surface-Contaminated Waste;
- Soils;
- Concrete/Sludge; and
- Bulk-Contaminated Waste.

This categorization allowed implementation of a fairly detailed aqueous-phase source release analysis described in Section 3.1.2. If a characteristic release process could not be determined for a given type of waste, the material was assumed to be Surface-Contaminated Waste. Modeled rates of release are greatest from this waste form. The categories to which the different waste codes were assigned are presented in Table 2-16.

2.3.1.4 Radionuclide Screening

As discussed earlier, active institutional-control over MDA G is expected to last 100 years after the end of disposal operations and the two-year closure period. During this period, persons will be prevented from intruding onto the site and measures will be taken to maintain proper facility function. Consequently, there will be little or no potential for exposures from radionuclides that undergo significant levels of decay during the 100-year period. Consistent with this reasoning, the PA and CA inventories were screened to eliminate radionuclides with half-lives of 5 years or less that decay to stable products. Radionuclides with half-lives of 5 years or less that decay into radioactive isotopes with half-lives greater than 5 years were maintained. All radionuclides with half-lives greater than 5 years were maintained.

Table 2-16 Waste categories for LANL waste codes

Waste Code	Waste Description	Release Mechanism: Rapid Release	Soil Sorption	Sludge/ Concrete Sorption	Corrosion
10	Graphite Solids	X			
11	Graphite Powder	X			
14	Combustible Decon Waste	X			
15	Cellulosics (paper, wood, etc.)	X			
16	Plastics	X			
17	Rubber Materials	X			
18	Combustible Lab Trash (paper, plastic, rubber)	X			
181	Non- Combustible Lab Trash (glass, metal)	X			
19	Combined Combust./Non-Combust. Lab Trash	X/50%(a)			50%(a)
20	Hydrocarbon Oil - Liquid	X			
21	Silicon Based Oil - Absorbed - No Free Liquid	X			
201	Hydrocarbon Oil - Absorbed - No Free Liquid	X			
211	Silicon Based Oil - Absorbed - No Free Liquid	X			
22	Petroleum Contaminated Soil		X		
23	Aqueous Solution - Absorbed - No Free Liquid	X			
24	Cemented/Immobilized Residues/Powders			X	
25	Leached Process Residues	X			
26	Evaporator Bottoms/Salts	X			
28	Chloride Salts	X			
30	PN Equipment	X			
31	Non-PN Equipment	X			
32	PN Oversize Equipment	X			
33	Non-PN Oversize Equipment	X			
35	Combustible Building Debris	X			
36	Non-Combustible Building Debris	50%(b)	25%(b)	25%(b)	
40	Combustible Hot Cell Waste	X/50%(a)			50%(a)
41	Non-Combustible Hot Cell Waste	X/50%(a)			50%(a)
45	Uranium Chips and Turnings in Diesel Fuel				X
46	Skull and Oxide	X			
47	Slag and Porcelain	X			
49	Sanitary Sludge			X	
50	Metal Crucibles, Scrap, Dies	X			
51	Precious Metals	X			
52	Scrap Metal	X/50%(a)			50%(a)
53	Lead	X			
55	Filter Media	X			
56	Filter Media Residue	X			
60	Other Combustibles	X			

Waste Code	Waste Description	Rapid Release	Soil Sorption	Sludge/ Concrete Sorption	Corrosion
61	Other Non-Combustibles	X			
62	Molecular Sieves	X			
65	Animal Tissue	X			
68	Asbestos	X			
69	Asbestos-Contaminated Debris	50%(b)	25%(b)	25%(b)	
70	Chemical Waste	X			
71	Beryllium	X			
72	Beryllium-Contaminated Debris	50%(b)	25%(b)	25%(b)	
73	Scintillation Vials	X			
74	Ion Exchange Resins	X			
75	Chemical Treatment Sludge -			X	
76	Cement Paste			X	
77	PCB-Contaminated Materials	X			
78	PCB-Contaminated Equipment	X			
79	PCB-Contaminated Soil		X		
791	PCB-Contaminated Concrete			X	
80	Irradiation Sources	X			
801	Irradiation Sources in Lead Shielding	X			
85	Firing Point Residues		X		
90	Radioactively-Contaminated Soil		X		
95	Glass	X			
99	Unidentified Material	X			

a. Release of all radionuclides except MAP is assumed to occur via rapid rinse; release of MAP is assumed to occur via rapid rinse (50%) and corrosion (50%).
b. Assumed distribution.
c. Property Numbered (i.e., accountable)

2.3.2 Future Inventory

Future waste includes all LLW expected to require disposal at MDA G between 1996 and the end of facility operations in the year 2044. For the purposes of estimating the future inventory, three categories of waste were evaluated:

- Operational waste;
- ER and D&D waste (including facility upgrades); and
- Mixed-waste treatment residues.

The information and assumptions used to project future inventories of these wastes are discussed below.

2.3.2.1 *Operational Waste*

Operational waste refers to material generated by ongoing programs at the Laboratory. In general, LANL programs are grouped according functions in TAs. The waste generated by programs within a given TA is similar in a broad sense. For example, nuclear weapons and fuel operations are performed at TA-55, and the radioactive waste generated there is generally contaminated with actinides. Given these similarities, the projected operational LLW inventory was developed based on the assumption that, barring any unforeseeable changes in Laboratory programs, the waste streams generated at a given TA in the past would generally reflect operational waste generated in the future by the same TA. Accordingly, recorded data for major waste generators at LANL were analyzed to estimate average annual waste volumes, activities, and radionuclide-specific concentrations (i.e., radioactivity in waste divided by volume of waste for each radionuclide). Separate projections were developed for waste disposed of in pits and shafts. These average waste characteristics were assumed to remain constant over the remainder of the operational lifetime of MDA G.

The major generators of LLW at LANL were identified using screening calculations based on total volume, total activity, and radionuclide-specific activities disposed of during the 1990 through 1995 period. Generators contributing to 95 percent of the total volume, activity, or radionuclide-specific activity of waste disposed of at MDA G in one or more years were identified as major generators of waste. All screening calculations were based on the total waste disposed of at MDA G, with no distinction being made between waste buried in pits and shafts.

A total of 19 TAs were identified as major generators of LLW on the basis of total volumes of waste shipped for disposal. Only 7 TAs were identified as major generators on the basis of total waste activity, all of which were identified as major waste generators on the basis of waste volume as well. The screening calculation based on radionuclide-specific activities identified twenty-eight TAs as major generators of waste during the 1990 through 1995 period. All told, 26 TAs were identified as major generators of LLW.

The remaining TAs at the LANL generated less than 5 percent of the volume and activity of LLW disposed of at MDA G in any given year between 1990 and 1995. These TAs were not considered in the development of the future operational LLW inventory.

Once the major LLW generating sites were identified, associated program and facility managers were interviewed to validate the assumption that waste-generating activities at the TAs are expected to continue. The results of these surveys revealed that operations are expected to continue essentially unchanged for the foreseeable future at several TAs; these generators were included in projected inventories for operational LLW. Waste generated at 5 TAs is expected to consist primarily of ER and D&D waste as closed sites and facilities are remediated. These TAs were eliminated from the list of major generators of operational waste. Table 2-17 lists the TAs identified as major generators of waste.

Table 2-17 LANL technical areas identified as major LLW generators

TA-3 South Mesa Site	TA-36 Kappa Site
TA-8 Anchor Site West	TA-39 Ancho Canyon Site
TA-9 Anchor Site East	TA-41 W-Site
TA-11 K-Site	TA-43 Health Research Lab
TA-15 R-Site	TA-46 WA-Site
TA-16 S-Site	TA-48 Radiochemistry Site
TA-18 Pajarito Laboratory	TA-50 Waste Management Site
TA-21 DP-Site	TA-51 Radiation Exposure Facility
TA-35 Ten Site	TA-53 Meson Physics Facility
TA-59 OH-Site	TA-55 Plutonium Facility

A portion of the 1990 to 1995 LLW data used to project future operational waste inventories was generated during *de facto* ER and D&D activities. Because projections of LLW generated by ER and D&D activities were developed separately, the ER and D&D waste records were removed to avoid double-counting this waste in the MDA G inventory. Although it is not possible to extract all records for ER and D&D LLW from the database, it is reasonable to assume that waste identified by certain waste codes was generated as a result of clean-up activities. Thus, 11 waste streams, shown in Table 2-18,

were assumed to represent ER and D&D waste and were excluded from projections of future operational waste inventories.

Table 2-18 Waste codes excluded from future projections

Waste Code	Waste Description
22	Petroleum-Contaminated Soil
35	Combustible Building Debris
36	Noncombustible Building Debris
68	Asbestos
69	Asbestos-Contaminated Debris
72	Beryllium-Contaminated Debris
77	PCB-Contaminated Materials
78	PCB-Contaminated Equipment
79	PCB-Contaminated Soil
791	PCB-Contaminated Concrete
90	Radioactively-Contaminated Soil

2.3.2.2 ER and D&D Waste

Waste generated as a result of ER and D&D activities at LANL generally consists of soil, concrete, asphalt, metals, ductwork, electrical conduit, and piping. A number of TAs scheduled to undergo ER or D&D were identified in the screening process discussed above. Estimates of LLW volumes provided by the ER Project Office were used in the future waste projections.[81]

Detailed characterization of ER and D&D LLW has not been undertaken at LANL. However, when LANL was considering the development of a RCRA disposal facility for ER waste, a survey was completed to characterize the potential MLLW inventory expected to require disposal in that RCRA facility.[82] Assuming that the radiological characteristics of the MLLW to be generated by ER would apply equally well to the LLW

inventory, this information was used to estimate the ER and D&D radionuclide inventories in the future waste.

2.3.2.3 MLLW Treatment Residues

A variety of MLLW streams are in storage or are generated at LANL. Treatment of this waste in compliance with the RCRA Land Disposal Restriction (LDR) is expected to result in some of this waste being reclassified as LLW (i.e., waste without any hazardous components). While a portion of the LLW generated through treatment could be disposed of at MDA G, this quantity is expected to be small. This is because the preferred alternative for dealing with the MLLW, as provided in the fiscal year 1995 update to the LANL Draft Site Treatment Plan, is to send the material offsite for treatment and disposal. Based on these considerations, LLW generated from the treatment of MLLW was not included in inventory projections.

In addition to the MLLW that will undergo treatment, depleted uranium chips and turnings generated during ongoing machining operations must be treated before disposal at MDA G. These chips and turnings are pyrophoric and, therefore, fail to meet the waste acceptance criteria for disposal at MDA G. In the past, this waste was stored above ground at MDA G. The stored inventory was recently stabilized in a solidified clay matrix in 0.1-m^3 (30-gal) drums and is staged for disposal in a pit. Chips and turnings generated in the future will be similarly stabilized and disposed of. The projected future uranium-chip inventory includes waste already staged for disposal, and waste expected to be generated in the coming years.[83]

2.3.3 PA Inventory

The results of the waste characterization effort are summarized below for the PA inventory. The disposal pits containing waste that contribute to the PA are identified in Figure 2-26. While the general location of disposal units expected to receive waste between 1996 and 2044 is shown, the dimensions of these units are not known at this time. Historic disposal shafts are also indicated in the figure, but are not identified in terms of their contribution to the PA inventory.

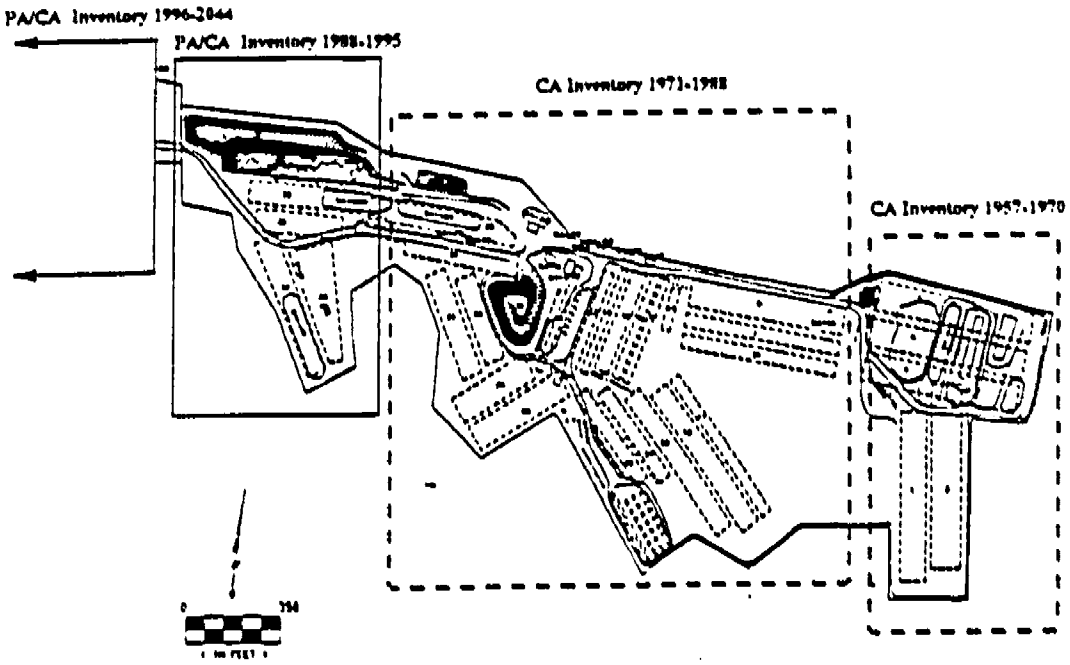

Figure 2-26 Disposal units contributing to the PA and CA inventories

2.3.3.1 September 26, 1988 through 1995 PA Waste

The volumes of waste disposed of at MDA G between September 26, 1988 and the end of 1995 are shown in Figure 2-27. Pit disposals averaged about 4,000 m^3 (140,000 ft^3), while shaft disposals averaged about 40 m^3 (1,000 ft^3). All told, almost 30,000 m^3 (1,000,000 ft^3) of waste was disposed of during the period.

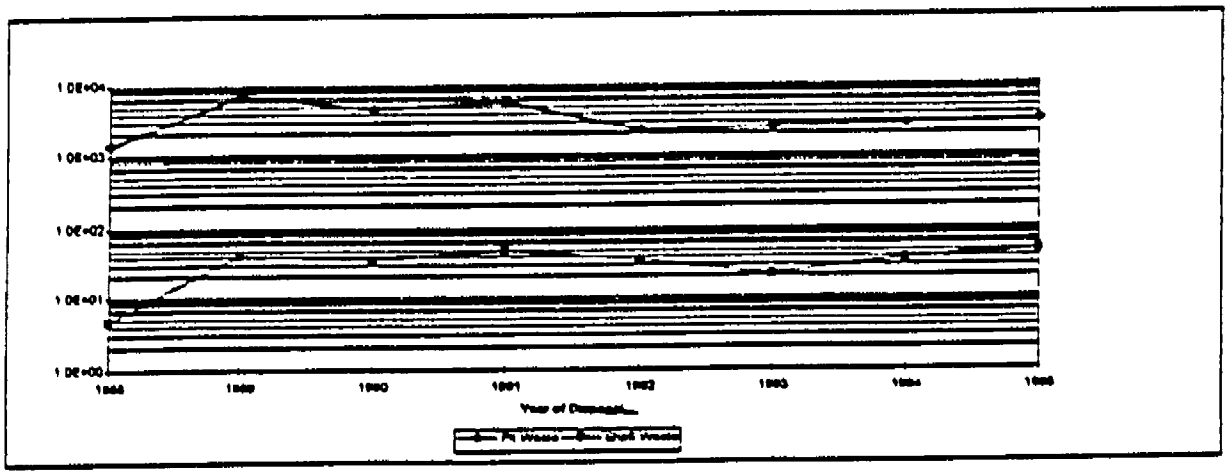

Figure 2-27 Annual volumes of pit and shaft waste disposed of from September 26, 1988 through 1995

The total as-disposed activities in pit and shaft waste for the September 26, 1988 to 1995 period are shown in Figure 2-28. Annual disposal activities are greatest for the shafts, averaging about 40,000 Ci. Annual disposal activities for the pits average around 20 Ci. Approximately 440,000 Ci was disposed of during the period, more than 99 percent of which was placed in shafts, nearly all of which was tritium.

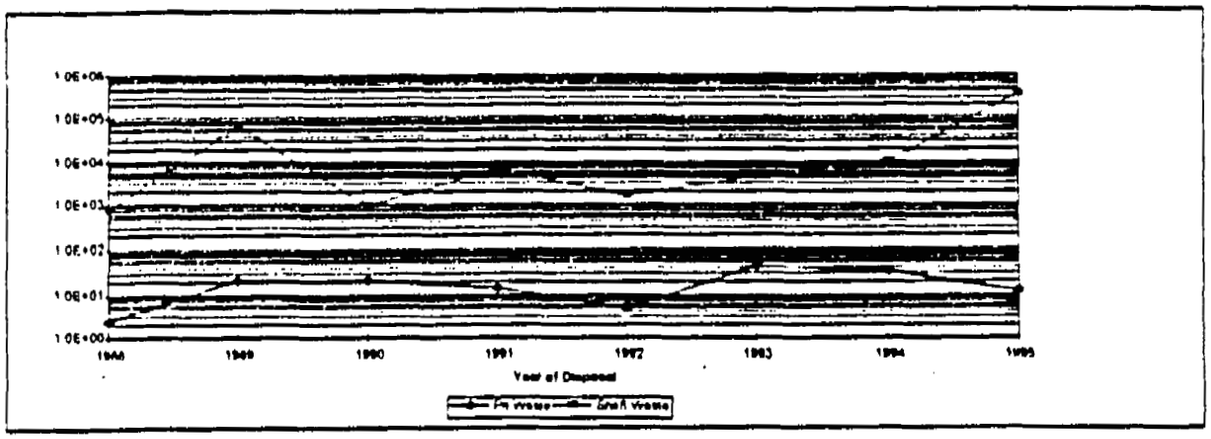

Figure 2-28 Total annual activities of pit and shaft waste disposed of from September 26, 1988 through 1995

The distribution of the historic PA inventory among the four waste forms used in source term modeling is shown in Figure 2-29 for waste volumes and activities. More than 75 percent of the waste volume consists of surface-contaminated waste. Approximately 75 percent of the pit activity, and more than 99 percent of shaft activity, is associated with surface-contaminated waste.

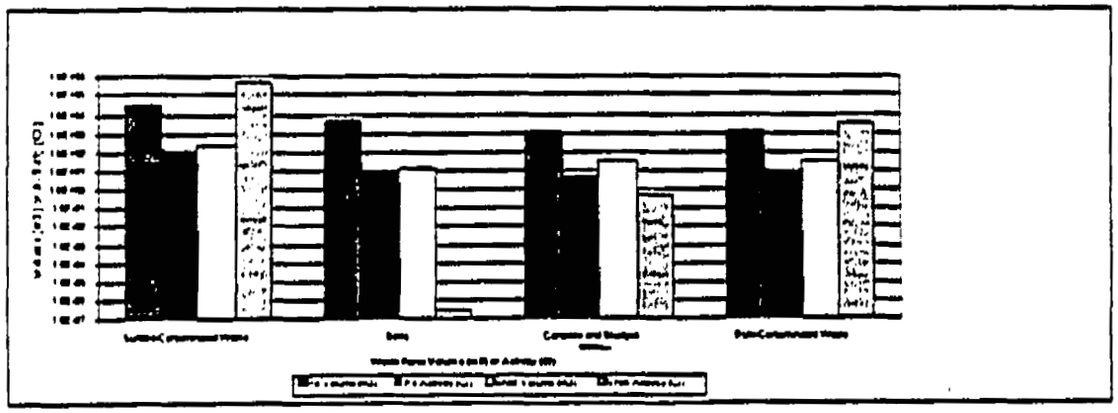

Figure 2-29 Volume and activity of waste in each inventory category disposed of from September 26, 1988 through 1995

The predominant radionuclides present in the pit include ^{3}H, ^{60}Co, and ^{238}U with activities ranging from about 5 to 16 Ci in surface-contaminated waste. These activities are small, however, compared to the activities of the predominant radionuclides in shaft waste, where ^{3}H, ^{60}Co, and ^{137}Cs activities range from 83 to 430,000 Ci in the surface-contaminated waste.

2.3.3.2 1996 through 2044 PA Waste

The total volumes and as-disposed activities of waste projected to require disposal at MDA G from 1996 through 2044 are shown in Table 2-19.

Approximately 150,000 m^3 (5,200,000 ft^3) of waste is projected for disposal, almost 99 percent of this volume is expected to be disposed of in pits. In contrast, the vast majority of the total activity will be disposed of in shafts. In terms of the pits, 88 percent of the total waste volume consists of surface-contaminated waste; surface-contaminated waste comprises 94 percent of the total pit activity. Seventy-eight percent of the total shaft waste volume consists of surface-contaminated waste, this same waste form accounts for essentially all of the shaft activity. With the exception of high-activity ^{3}H waste, the future waste is projected to be disposed uniformly over the remainder of the operational lifetime of MDA G. Larger amounts of the ^{3}H waste will be disposed of early in the 1996 to 2044 period as backlogged waste is buried.

Table 2-19 Projected disposal volumes and activities for future inventory categories

Inventory Category	Volume (m^3)		Activity (Ci)	
	Pits	Shafts	Pits	Shafts
Surface Contaminated	1.3E+05	1.1E+03	1.6E+03	6.2E+06
Soil	9.3E+03	0.0E+00	3.4E+01	0.0E+00
Concrete/Sludge	5.6E+03	1.9E+02	3.9E+01	3.5E+00
Bulk Contaminated	2.5E+03	1.1E+02	1.7E+01	1.6E+04
Total	**1.5E+05**	**1.4E+03**	**1.6E+03**	**6.2E+06**

The radionuclide-specific inventories for the future PA waste are listed in Tables 3-28 and 3-29 of Appendix 2e. The predominant radionuclides in the future pit waste are ^{3}H, ^{60}Co, ^{238}U, ^{239}Pu, and ^{241}Pu with activities in surface-contaminated waste ranging from 20 to 700 Ci. Activities of ^{238}Pu, ^{234}U, and ^{238}U in soils or concrete and sludges are similar to the activities of ^{60}Co and ^{239}Pu in surface-contaminated waste. Future shaft waste activities are dominated by ^{3}H, ^{60}Co, ^{90}Sr, and ^{137}Cs which have activities ranging from 34 to 6,200,000 Ci. Tritium accounts for nearly all of the total shaft inventory.

2.3.4 CA Inventory

The inventory included in the MDA G CA is discussed below. As stated earlier, this inventory includes all waste disposed of at MDA G since 1957 and all waste expected to require disposal through the end of operations in 2044.

2.3.4.1 1957 through 1970 CA Waste

The estimated volumes and as-disposed activities of waste placed in pits and shafts from 1957 through 1970 are summarized in Table 2-20. The table lists the contributions made by extrapolated LLW and TRU waste. The methods used to estimate the 1957 to 1970 pit and shaft inventories are such that totals for individual disposal units cannot be derived nor can the year of disposal be discerned.

On a volume basis, LLW accounts for approximately 90 percent of the pit waste and essentially all of the shaft waste disposed of during this period. The activity of the waste estimated to be disposed of in pits is dominated by TRU waste, however, which accounts for 93 percent of the total. TRU waste comprises only 2 percent of the total shaft waste activity. Similar to the pattern noted earlier with respect to the PA inventory, surface-contaminated waste comprises the bulk of the pit and shaft waste. In terms of the pits, surface-contaminated waste accounts for about 75 percent of the total volume and approximately 85 percent of the total activity. Practically all of the shaft waste (volume and activity) is contributed by the surface-contaminated component of the waste.

Table 2-20 Extrapolated volumes and activities for each inventory category disposed of from 1957 through 1970

Inventory Category and Disposal Unit	LLW		TRU		Total	
	Volume (m^3)	Activity (Ci)	Volume (m^3)	Activity (Ci)	Volume (m^3)	Activity (Ci)
Pit Waste						
Surface Contaminated	4.0E+04	7.4E+02	1.7E+03	1.5E+04	4.2E+04	1.6E+04
Soil	6.0E+03	1.9E+01	1.1E+01	3.7E+01	6.1E+03	3.9E+01
Concrete/Sludge	4.5E+03	4.1E+02	3.0E+03	2.4E+03	7.5E+03	2.8E+03
Bulk Contaminated	1.1E+01	7.8E-02	0.0E+00	0.0E+00	1.1E+01	7.8E-02
Shaft Waste						
Surface Contaminated	1.4E+02	3.8E+04	1.2E+00	8.3E+02	1.5E+02	3.6E+04
Soil	2.1E-02	0.0E+00	0.0E+00	0.0E+00	2.1E-02	0.0E+00
Concrete/Sludge	4.4E-01	0.0E+00	0.0E+00	0.0E+00	4.4E-01	0.0E+00
Bulk Contaminated	5.3E-01	5.5E+01	0.0E+00	0.0E+00	5.3E-01	5.5E+01

The radionuclide-specific inventories for the 1957 to 1970 CA waste are provided in Appendix 2e. The pit waste activity is dominated by several transuranic radionuclides, reflecting the contributions made by the TRU waste disposed of during the period. Several plutonium isotopes and ^{241}Am are present at activities ranging from 44 to 8,100 Ci in one or more waste forms. The shaft waste is dominated by ^{3}H, which accounts for almost 99 percent of the total activity.

2.3.4.2 1971 to September 25, 1988 CA Waste

The volumes of waste disposed of at MDA G from 1971 through September 25, 1988 are shown in Figure 2-30. Annual disposal volumes during this period ranged from 2,000 to 11,000 m^3 (70,000 to 385,000 ft^3) for the pits, volumes of shaft waste ranged from 10 to 140 m^3 (350 to 4,900 ft^3). Annual disposal volumes for the pits were relatively constant during the period, averaging about 5,000 m^3 (175,000 ft^3). Shaft waste disposal was more

erratic, and increased noticeably between 1981 and 1988. Approximately 128,000 m^3 (4,500,000 ft^3) of waste was disposed of during the period.

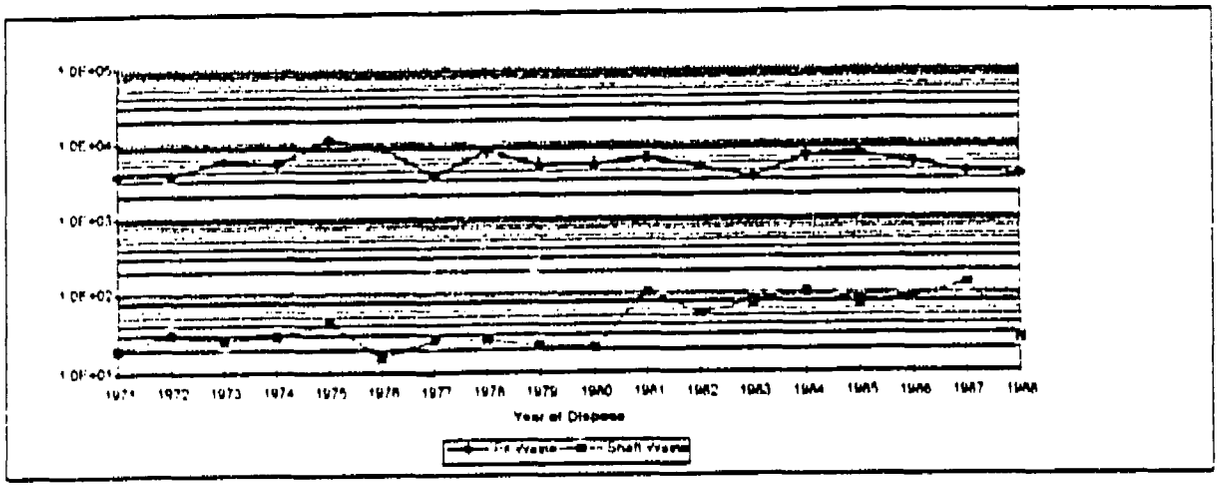

Figure 2-30 Total annual volume of waste disposed of between 1971 and 1988

The estimated as-disposed waste activities placed in pits and shafts at MDA G between 1971 and September 25, 1988 are shown in Figure 2-31. Approximately 870,000 Ci was disposed of in the 23 pits and almost 100 shafts active during the period. Annual disposal activities for the pits ranged from 4 to 35,000 Ci, while shaft activities ranged from 250 to 350,000 Ci The activities placed in individual pits were highly variable, ranging from less than 1 Ci (Pit 12) to about 30,000 Ci (Pit 18) Four pits (Pits 10, 18, 28, and 29) account for 98 percent of the total activity The total activity of waste disposed of during the period was dominated by the shafts, which received almost 830,000 Ci.

Several pits and shafts were used for the disposal of TRU waste in the 1970s. The total volume of non-retrievable TRU waste disposed of in 4 pits was 71 m^3 (2,500 ft^3), an additional 4.4 m^3 (150 ft^3) of waste was disposed of in shafts. The activity associated with this waste totaled about 3,400 Ci. This waste is included in the projections shown above.

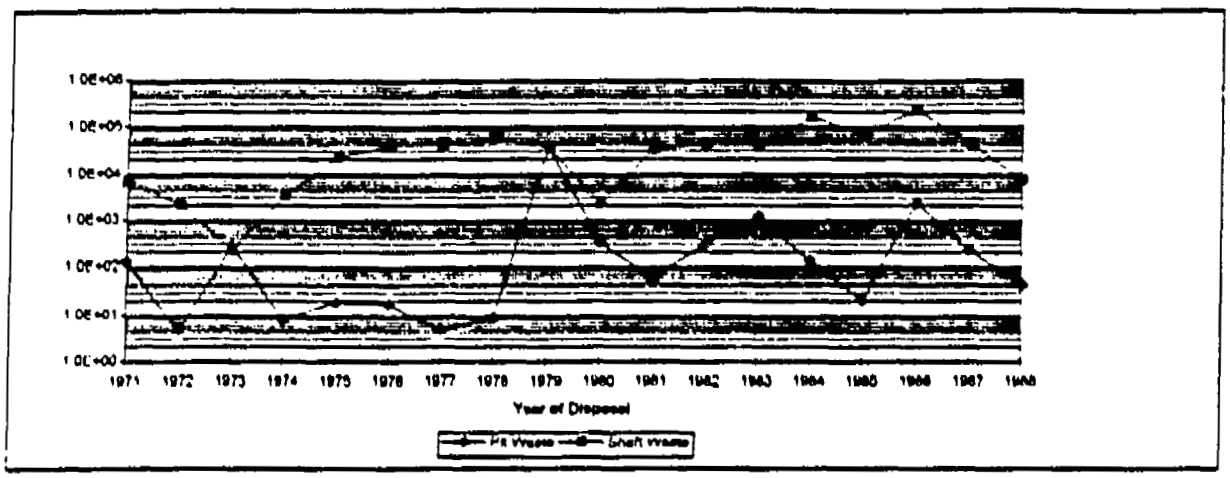

Figure 2-31 Total annual activity of waste disposed of between 1971 and 1988

Surface-contaminated waste and soils are the major forms of pit waste on a volume basis, accounting for 56 and 36 percent of the total, respectively. In terms of activity, however, the surface-contaminated waste is the major contributor, accounting for more than 98 percent of the total activity. Surface-contaminated waste accounts for almost 85 percent of the projected shaft inventory and over 99 percent of the total activity.

Radionuclide-specific activities are tabulated in Appendix 2e. Similar to more recent waste inventories, ^{3}H, ^{60}Co, ^{90}Sr, and ^{137}Cs are the major contributors to the total pit activity, with activities ranging from about 1,100 to 7,500 Ci in surface-contaminated waste. Disposal shaft waste is dominated by ^{3}H, with an activity of almost 800,000 Ci in surface-contaminated waste. Contributions from other radionuclides drop off rapidly, ^{60}Co, ^{85}Kr, ^{90}Sr, ^{133}Ba, ^{137}Cs, and ^{239}Pu contribute 100 to 3,000 Ci each.

2.3.5 Summary of PA and CA Inventories

As discussed earlier, the MDA G PA and CA address different portions of the waste that has been disposed of and expected to require disposal in the future. This section summarizes the radioactive waste inventories included in the two analyses. The inventories of the PA and C are very briefly summarized here. These final inventories were the basis of the source-term analysis presented in Section 3.1. The detailed radionuclide-

specific waste volumes and activities for each of the 4 waste categories are found in Tables 3-32 through 3-36 in Appendix 2e.

2.3.5.1 Total PA Inventory

The PA inventory includes the waste disposed of at MDA G since September 26, 1988 and the waste expected to require disposal over the remainder of the facility's lifetime. The total volumes and activities of waste projected to be disposed of over this period are provided in Table 2-21 for the disposal pits and shafts. These quantities are provided for the four waste forms that are considered in source-term modeling and are summed over all pits and shafts receiving waste during this period.

Table 2-21 Pit and shaft waste-category volumes and activities include in the PA inventory

Inventory Category	Total Volume (m^3)	Total Activity (Ci)
Pits		
Surface Contaminated	1.5E+05	1.6E+03
Soil	1.4E+04	4.0E+01
Concrete/Sludge	6.8E+03	4.4E+01
Bulk Contaminated	3.5E+03	2.4E+01
Shafts		
Surface Contaminated	1.3E+03	6.6E+06
Soil	1.3E+01	2.7E-07
Concrete/Sludge	2.2E+02	3.9E+00
Bulk Contaminated	1.4E+02	1.9E+04

Surface-contaminated waste is the major contributor to the PA inventory on a volume and activity basis. In terms of the pits, this waste form comprises 86 percent of the projected volume and 94 percent of the projected activity of PA waste. Surface-contaminated waste comprises 77 percent of the shaft waste on a volume basis and more than 99 percent of the projected activity.

2.3.5.2 *Total CA Inventory*

The inventory for the CA includes waste disposed of at MDA G since it opened in 1957 and the waste expected to require disposal over the remainder of the facility's lifetime. The total volumes and activities of waste projected to be disposed of over this period are provided in Table 2-22 for the disposal pits and shafts. These quantities are provided for the waste forms that are considered in source-term modeling and are summed over all pits and shafts receiving waste during this period.

Table 2-22 Pit and shaft waste-category volumes and activities include in the CA inventory

Inventory Category	Total Volume (m^3)	Total Activity (Ci)
Pits		
Surface Contaminated	2.4E+05	5.9E+04
Soil	5.4E+04	1.0E+02
Concrete/Sludge	2.0E+04	2.9E+03
Bulk Contaminated	4.4E+03	5.7E+02
Shafts		
Surface Contaminated	2.2E+03	7.4E+06
Soil	3.5E+01	1.0E+02
Concrete/Sludge	2.2E+02	1.0E+02
Bulk Contaminated	2.6E+02	2.6E+04

The predominant waste form in the CA inventory is surface-contaminated waste. It accounts for 76 and 94 percent of the pit waste on volume and activity bases, respectively. Surface-contaminated waste comprises 81 percent of the shaft waste on a volume basis and more than 99 percent on an activity basis.

3. ANALYSIS OF PERFORMANCE

This section describes the methods used to analyze the radiological performance of MDA G in terms of the potential for future exposures from the release and transport of radioactivity to locations and media accessible to members of the public. The objective is to compare projected doses to future members of the public with the prescribed DOE performance measures which s done in section 4. There are three parts to the overall analysis corresponding to the three shaded boxes in Figure 3-1. The Source Term defines how and at what rate radioactivity might be released into air, water, and soil; Analysis Methodology describes how the amount of radioactivity in air, water, and soil was modeled as a function of time, and how doses due to use of contaminated air, water, and soil were calculated; and Pathways and Scenarios discusses where and how exposures to radioactivity in air, water, and soil might occur. Each part of the analysis is related to site-specific information provided in Section 2, as suggested in the figure.

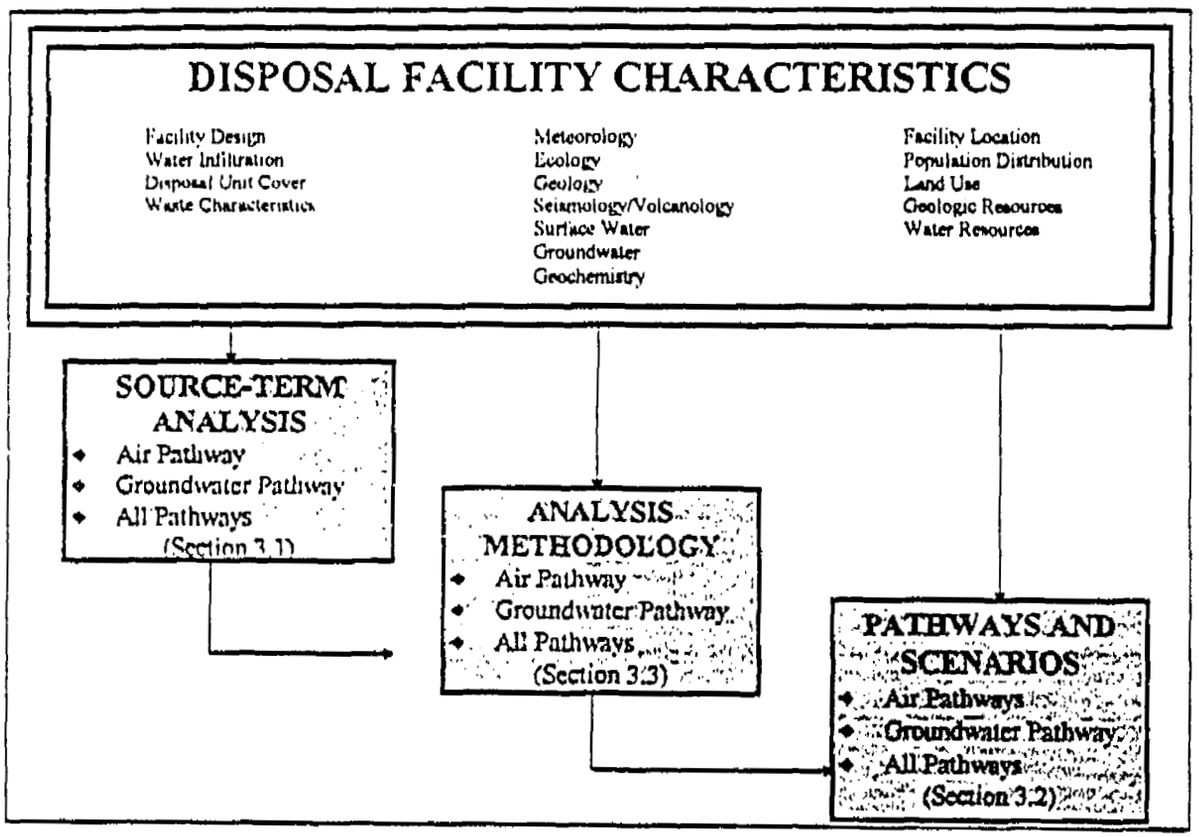

Figure 3-1 Relationship between facility characteristics and analysis

3.1 SOURCE TERM ANALYSIS

This section describes the natural processes by which radioactivity may be released from the LLW disposed of at MDA G after disposal operations cease. The mathematical models used to estimate rates of release of radioactivity into air, water, and soil over time are summarized below, while detailed descriptions are provided in appendices to this section as noted.

Figure 3-2 illustrates the various natural processes considered in the source term analysis as having a potential for releasing radioactivity from disposal units at MDA G. These processes include:

- Dissolution of radioactivity in water percolating through the waste;
- Diffusion of radioactive gases;
- Biotic translocation of radioactive material to the surface by plants rooting and animals burrowing into the waste; and
- Exposure of radioactive material by erosion and cliff retreat.

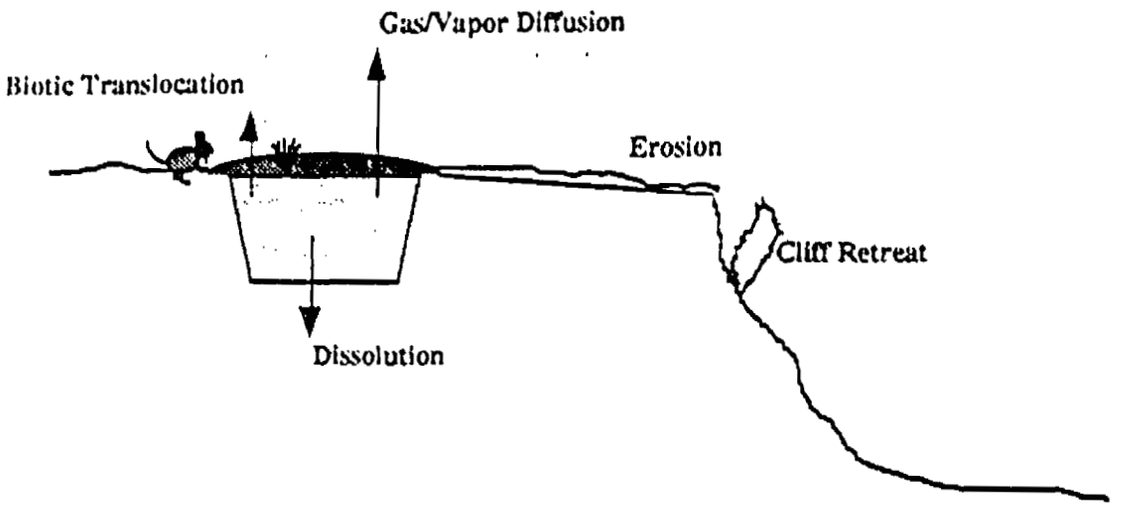

Figure 3-2 Source term components considered in the PA and CA

In general, the source term processes illustrated in Figure 3-2 do not apply equally to all radionuclides in the MDA G inventory. Different models were invoked to account for the inventory characteristics discussed in Section 2.3, as well as the natural and man-made characteristics of the site discussed in Section 2.1 and Section 2.2. Most radionuclides in the inventory will dissolve in water infiltrating the disposal units, but the rate of dissolution will depend on the waste form, the radionuclide, and geochemical factors. In contrast, only a few radionuclides will be released in a gas phase, including those that are either characteristically volatile (e.g., ^{85}Kr, ^{220}Rn, and ^{222}Rn) or those that become incorporated into gases or vapors under certain circumstances (e.g., ^{3}H and ^{14}C). All radionuclides in the inventory may be translocated from the disposal unit to the ground surface by plants and animals that penetrate disposal-unit covers, but the rate may be radionuclide specific. Finally, the exposure of waste by erosion and cliff retreat will, over geologic time, affect all waste equally.

The following paragraphs summarize the source term models used to quantify releases of radioactivity to support the air-, groundwater-, and all-pathways analyses for the PA and CA. For each, the relevant information presented in Section 2 will be referred to.

3.1.1 Air Pathways Analysis

The air-pathways analysis addresses the potential impacts of radioactivity released from MDA G to the atmosphere. Releases may occur as a result of gases diffusing from the disposal facility or resuspension of contamination exposed at the surface as a result of biotic intrusion, erosion, or cliff retreat. The release mechanisms for gases and particulates are discussed below.

3.1.1.1 Gas-phase Source Term

The gas-phase source term analysis accounts for that fraction of the MDA G inventory that can be expected to be released as either a gas or a vapor. Modeling radioactive gas generation within disposal units is based on the characteristics of the inventory described in Section 2.3, while the rates at which radioactive gases and vapors diffuse from the disposal

units account for disposal unit design features discussed in Section 2.2. The following paragraphs summarize the detailed gas-phase source term analysis reported in Appendix 3a, *Evaluation of Atmospheric Release Sources for Gaseous Phase Contaminants Emanating from the Disposal Facility at Area G.*[86]

3.1.1.1.1 Gas-Phase Radionuclide Inventories

A total of 6 radionuclides were considered in the development of source release models for gaseous species including ^{3}H, ^{14}C, ^{81}Kr, ^{85}Kr, ^{220}Rn, and ^{222}Rn. The inventories of ^{3}H, ^{14}C, ^{81}Kr, and ^{85}Kr available for release as gases at the assumed time of facility closure are listed in Table 3-1; radon is discussed later in this section. The activities are decay-corrected to the year 2044, when disposals are assumed to cease.

Table 3-1 Approximate gas-phase source term inventory in 2044

Radionuclide	2044 Inventory (Ci)
^{3}H	2.0E+06
^{14}C	6.0E-01
^{81}Kr	5.0E-03
^{85}Kr	7.0E+00

Much of the MDA G ^{3}H inventory is in the form of tritiated water absorbed in a solid matrix (e.g., molecular sieves). In this form, ^{3}H can be leached by water percolating through the disposal units, or can diffuse in vapor-phase following oxidation. Vapor-phase releases were calculated by dividing the ^{3}H concentration in the waste by the 8 percent pit moisture content (measured in Pit 37; refer to Section 2.2.1), then partitioning this concentration between liquid and vapor phases based on the vapor pressure of the gas.

Production rates of ^{14}C-labeled gases were estimated assuming that the ^{14}C inventory associated with organic waste will be incorporated into methane and carbon dioxide as the waste biodegrades. This process is illustrated in Figure 3-3. All ^{14}C present in the form of combustible laboratory trash and half of the inventory present as combined combustible/non-combustible laboratory trash was assumed to be available for biodegradation and the evolution of ^{14}C-labeled gas. Two rates of generation for $^{14}CH_4$ and $^{14}CO_2$ were evaluated. In the analytic model used for final calculations, all ^{14}C gas was conservatively assumed to be generated within a single year. In a numerical model used to verify the conservatism of the analytic approach, more realistic gas generation rates were

and $^{14}CO_2$ were evaluated. In the analytic model used for final calculations, all ^{14}C gas was conservatively assumed to be generated within a single year. In a numerical model used to verify the conservatism of the analytic approach, more realistic gas generation rates were used, based on degradation rates of paper and wood, which biodegrade over 17 and 500 years, respectively.[87]

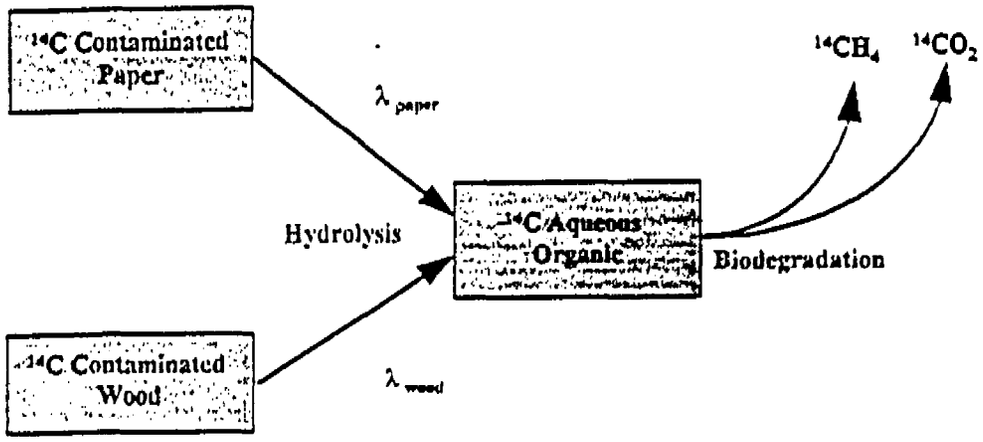

Figure 3-3 Conceptual model of the evolution and release of 14C-labeled biogases

Two isotopes of krypton ,^{81}Kr and ^{85}Kr, occur in the MDA G inventory as fission products. These isotopes are noble gases that will readily diffuse from waste. The entire projected inventories of these gases were assumed to be available for immediate release from the disposal facility.

The only other characteristically volatile radionuclides in the MDA G inventory are ^{220}Rn and ^{222}Rn. These gases are generated by the radioactive decay of ^{228}Ra and ^{226}Ra, respectively, and are available for immediate release from the disposal facility upon generation. The projected inventories of ^{220}Rn account for the inventory of ^{228}Ra in the disposed waste and the generation of ^{228}Ra following the decay of ^{232}Th, ^{236}U, and ^{240}Pu. Similarly, the projected ^{222}Rn inventories account for the ^{226}Ra disposed of in the pits and shafts and the ^{226}Ra generated by the decay of ^{230}Th, ^{234}U, ^{238}Pu, ^{238}U, and ^{242}Pu.

The projected inventories of ^{226}Ra and ^{228}Ra in pit and shaft waste are shown in Figure 3-4 for the September 28, 1988 - 1995 and 1996 - 2044 PA inventories. Insofar as the radon isotopes are in secular equilibrium with their respective parents, the inventories shown in the figure are equivalent to the activities of ^{220}Rn and ^{222}Rn. The ^{220}Rn inventories are dominated by the ^{230}Th in the waste. Given the long half-life of the ^{230}Th, the radon inventory remains constant over the period of time shown in the figure. Projected inventories of ^{222}Rn are more variable over time as ^{226}Ra present in the waste initially decays, inventories rise at later times due to daughter ingrowth.

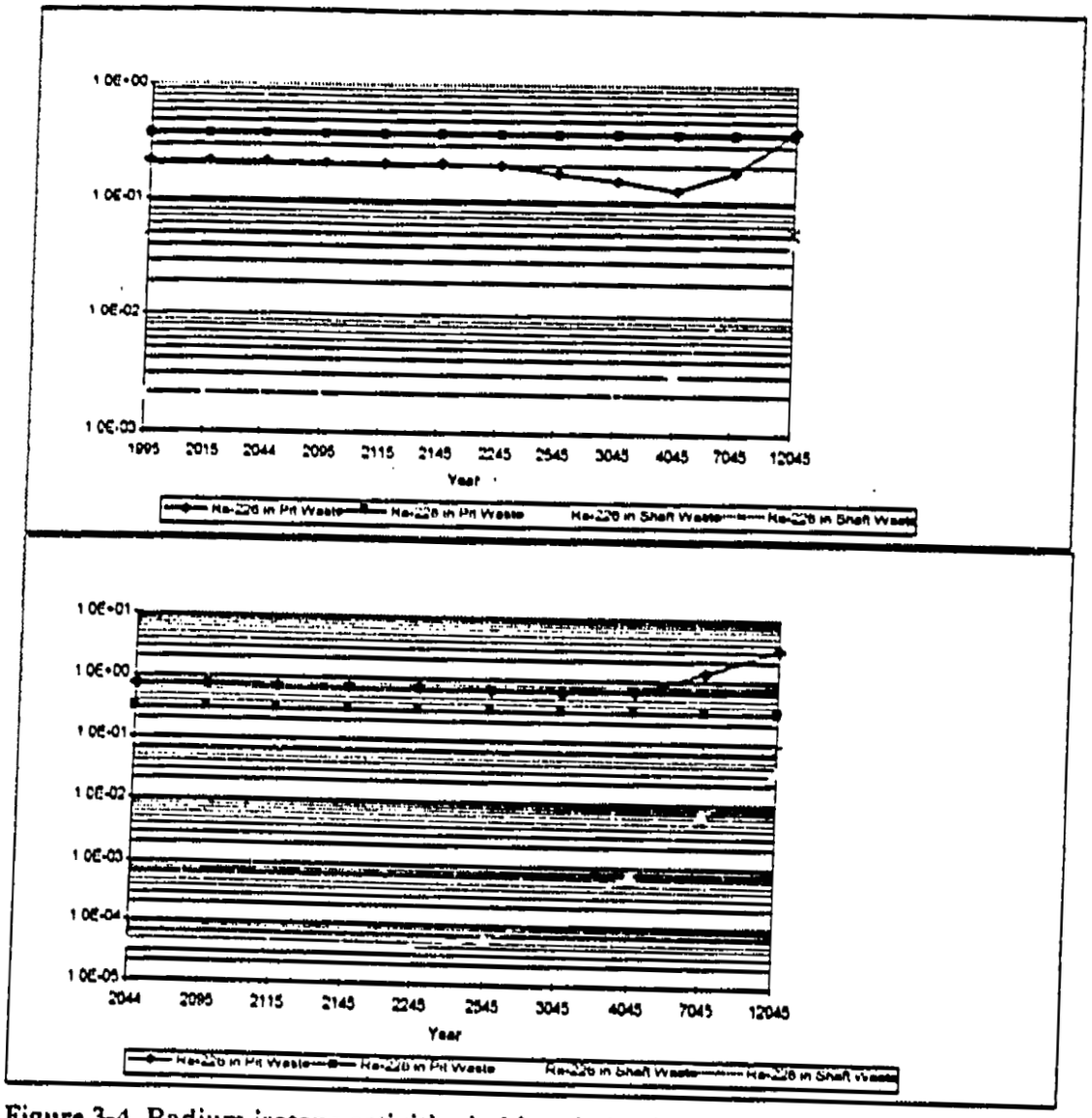

Figure 3-4 Radium isotope activities in historic (top) and future waste (bottom)

3.1.1.1.2 Gas-Phase Source Term Modeling

Figure 3-5 is a conceptual model of the gas-phase source releases. It represents the gas-phase inventory as "waste," and illustrates the gas diffusing through the disposal unit and cover. The gas concentration gradient is a measure of the change in gas concentration with depth; it is the driving force for diffusion. The magnitude of the concentration gradient is a function of the source inventory and the diffusion coefficient. The amount of gas diffusing through a given area of the cover into the atmosphere as a function of time is the flux, which is the source term for that gas.

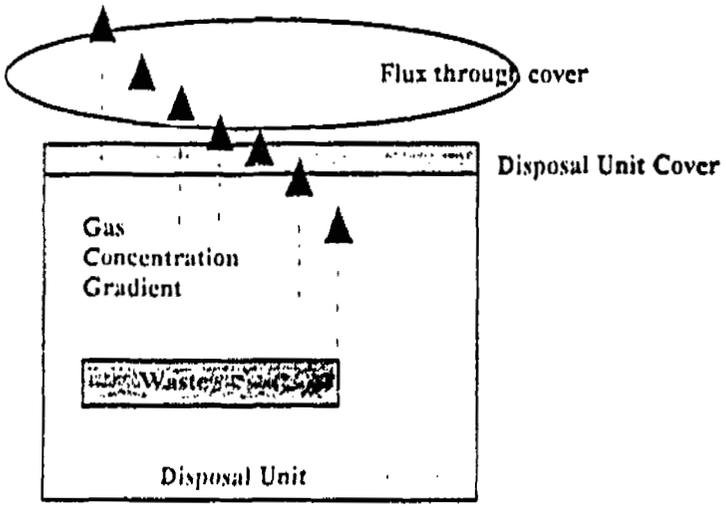

Figure 3-5 Conceptual model of gaseous-phase source release

The fluxes of ^{3}HHO, $^{14}CH_4$, $^{14}CO_2$, ^{85}Kr, ^{220}Rn, and ^{222}Rn were estimated using standard diffusion theory. The diffusion coefficient used for waste disposed of in shafts was derived from field measurements of tritium flux around the tritium shafts at MDA G. The diffusion coefficient indicated by these measurements, 5.0×10^4 m^2/yr (4.6×10^3 ft^2/yr), is about 60 times larger than expected values based on standard diffusion models.[88] This enhancement has been attributed to advection due to pressure changes (*barometric pumping*) communicated within the mesa through fractures, consistent with the discussion of vapor-phase drying in Section 2.1.5.

The enhanced diffusion coefficient is expected to apply to all gases diffusing from the disposal shafts due to the proximity of the disposed waste to the surrounding fractured tuff. A diffusion coefficient of 1.0×10^2 m^2/yr (1.1×10^3 ft^2/yr) was used to model ^{14}C, ^{81}Kr, ^{85}Kr, ^{220}Rn, and ^{222}Rn diffusion in the pits. This diffusion coefficient is based on the free diffusion coefficient of the gases, adjusted to account for porosity and tortuosity effects. The diffusion coefficient used to estimate ^3HHO fluxes from the pits was 6.0×10^2 m^2/yr (6.5×10^3 ft^2/yr). This higher coefficient accounts for the effects of thermal gradients on the diffusion of water vapor in porous media. The diffusion coefficients used to model gas-phase diffusion from pits and shafts are listed in Table 3-2.

Table 3-2 *In situ* diffusion coefficients used to calculate gaseous contributions to the air pathway

Gas or Vapor	Diffusion Coefficient (m^2/yr)	
	Pits	Shafts
$^{14}CH_4$, $^{14}CO_2$, $^{81,85}Kr$, $^{220,222}Rn$	100	50,000
^3HHO	600	50,000

3.1.1.2 Surface Soil Releases

The second source of atmospheric release is the resuspension of radioactivity in soils at MDA G. Surface contamination may result from biological and physical processes. Based on the information provided in Tables 2-4 and 2-5, animals and plants native to the region may penetrate disposal unit covers in a relatively short time if left unchecked, translocating contaminated material to the surface either directly through excavation or indirectly through root-uptake and subsequent defoliation. Over a longer period of time, surface erosion due to runoff may reduce the thickness of the disposal unit covers, and lateral erosion (or cliff retreat) may disrupt the disposal units. Based on information presented in Section 2.1, over a period of 1,000 years, surface erosion and cliff retreat will not expose waste directly. However, surface erosion will thin the cover, making it easier for deep-rooting plants and burrowing animals to penetrate contaminated regions.

Plant and animal intrusion and surface erosion are currently controlled at MDA G as part of ongoing site maintenance. For the PA and CA, it is assumed that disposal unit covers will be similarly inspected and maintained throughout the 1,000-year compliance period to ensure that damage from settlement or erosion is corrected. While this level of maintenance is also assumed to prevent extensive intrusion into the waste by plants and animals, biotic intrusion was included in the source term analysis for the PA and CA. The approaches taken in modeling releases due to biotic intrusion, erosion, and cliff retreat are summarized below.

3.1.1.2.1 Biotic Intrusion

The conceptual model for biotic intrusion is depicted in Figure 3-6 . As illustrated in the figure, plants may assimilate radioactivity from the disposed waste and deposit it on the surface as a result of leaf-fall or succession. Radioactivity may also be brought to the surface during burrow excavation and mixed with clean cover soil. The implementation of the biotic intrusion model is summarized below. Complete model details may be found in Appendix 3b *A Model for the Biotic Translocation of Buried Low-Level Radioactive Waste to the Ground Surface in the Presence of Surface Erosion.*[89]

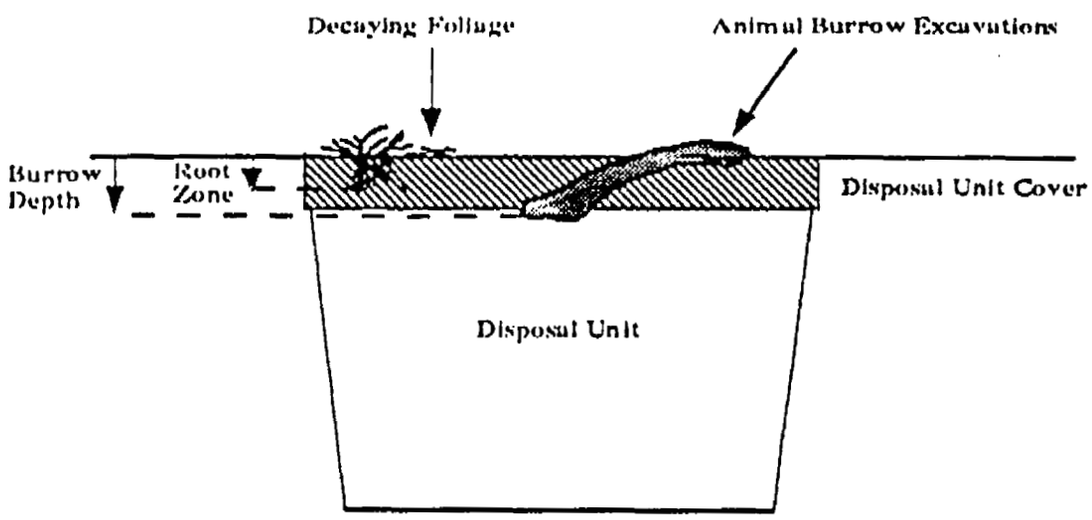

Figure 3-6 Biotic translocation conceptual model

Key parameters in the biotic translocation model include:

- The waste cover thickness;
- The intrusion depth;
- The waste volume translocated;
- The rate at which waste is translocated; and
- The ratio of the waste volume to the total volume (waste plus cover) translocated.

Rooting and burrowing depths for native plants and animals, presented in Tables 2-4 and 2-5, provide site-specific data on intrusion depth. The base case considered a single plant and single animal species. The representative burrowing animal was the deer mouse, which is the small animal most frequently trapped at MDA G.[90] While harvester ants have deeper burrowing depths, the volume excavated by them is insignificant compared with that excavated by a deer mouse. A generic arid plant with a 2 m (6.6 ft) rooting depth bounds the plant intrusion expected at MDA G. While some plants may extend tap roots to greater depths, the root mass responsible for radionuclide uptake has been found to be within the top 2 m (6.6 ft), which is consistent with the information in 2.1.3.

The relative volumes of contaminated and uncontaminated materials brought to the surface were approximated with a single bounding value for plants and a second value for animals, which represent a net penetration into the disposed waste volume. Data used to evaluate parameters for the burrowing-animal translocation calculations were taken from the BIOPORT code documentation.[91] Much of the data cited there originated from studies on pocket gophers, done at LANL, and are considered to be directly relevant to the MDA G.[92]

Deer mice were assumed to excavate 0.05 $kg/m^2/yr$ (0.01 $lb/ft^2/yr$), of which 10 percent was considered waste. All radioactivity present in the top layer of waste was assumed to be equally susceptible to translocation by burrowing animals. (Tables 3-3 through 3-38 are in Appendix 2e with Ci/m^3.) Plants were assumed to contribute biomass at a rate of

0.1 $kg/m^2/yr$ (0.02 $lb/ft^2/yr$), [93] with 30 percent of the rooting volume extending into the waste volume. This latter value is conservative, compared to site specific data, and could be considered to account for a contribution from plants such as chamisa which extend well below the maximum 2 m (6.6 ft) rooting depth used in the model. To bound the root uptake factors for all radionuclides in the inventory without modeling each one individually, a range of root uptake values was modeled, including 0.001, 0.01, 0.1, 1.0, and 10.

The biotic translocation model calculated a surface concentration normalized to initial waste concentration. Each intruding plant or animal contributed to a time-dependent surface contamination concentration. Plants were assumed to biodegrade and deposit biomass in the soil surface locally, as supported by a study conducted at LANL.[94] Plants add biomass to the soil, which is assumed to be primarily drawn from biosynthesis and not from the original soil mass. Therefore, the contaminant concentrations will be continually diluted in new biomass and the waste and surface concentrations will eventually approach zero if only plants are considered. Over very long periods of time (i.e., >10,000 years) surface concentrations approach that of the waste due to translocation by burrowing animals.

The normalized surface contaminant results for the base case parameter values are shown in Figure 3-7. The vertical axis is a measure of the ratio of the surface soil contaminant concentration (C_s) to the original waste concentration (C_{w0}); the horizontal axis is time. Different symbols represent the time-dependent normalized surface concentrations for the root uptake factors (B_l) considered; animals are represented by an uptake factor of 1. For fractional root uptake, surface soil concentrations remain below the waste concentration for all time. For uptake factors larger than unity, surface soil concentrations exceed waste concentrations until such time that the waste concentration is depleted, and uncontaminated biomass dilutes the surface soil concentrations, occurring between 1,000 and 10,000 years on Figure 3-7. Beyond 10,000 years , the surface concentration is limited by the animal excavation.

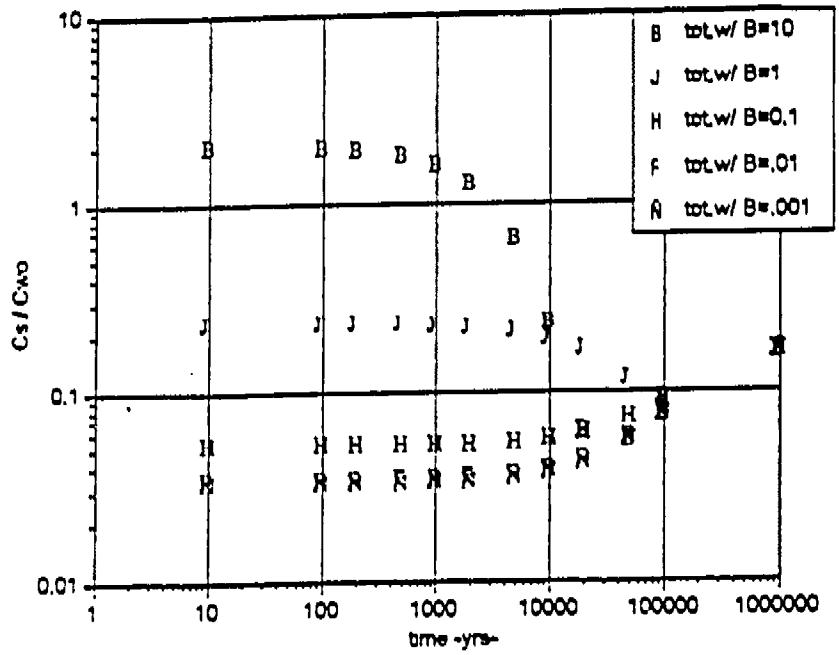

Figure 3-7 Normalized surface contaminant concentration versus time for the base case; shown for several values of plant uptake factor (B_i).

The soil concentrations over 1,000 years were relatively constant for uptake factors less than about 1. The maximum normalized surface contaminant concentration value was about 0.07 or 7 percent. For the 5 elements in the waste inventory with uptake factors greater than or equal to about 1, maximum concentration constants were determined from the model as follows:

Element	Uptake Factor	Soil Concentration Factor
Tc	9.5	2.0
Sr	2.5	0.6
C	1.3	0.25
H	0.9	0.25
Cd	0.5	0.1

These concentrations were used to evaluate exposures due via air and surface-water pathways, discussed in section 3.2.1.

3.1.1.2.2 Erosion and Cliff Retreat

A surface water balance model was performed for the PA and CA, which estimated, among the other components of the water balance equation discussed in Section 2.2, rates of surface sediment transport. The model is summarized later in this section, and is completely reported in Appendix 3c *Surface Water and Erosion Calculations to Support the Area G Performance Assessment.*[95] The surface water balance model indicates that the surface of Mesita del Buey (including closure caps) is subject to sheet erosion, at a rate of 4×10^{-7} m/yr (1.3×10^{-6} ft/yr). The model assumed a 1 m (3.3 ft) layer of crushed-tuff over the waste, with a gravel-mulch layer over the tuff supporting dense grassy vegetation. While not all of the disposal units at MDA G currently have a gravel-mulch layer, the final closure design will incorporate one based on these results. Soil erosion studies on surface covers at Los Alamos showed that soil erosion was greatest on plots that were recently disturbed and had little or no cover.[96] Substantially less erosion occurred when gravel-mulch was applied to the recently-disturbed cover.[97] Another factor of 2 reductions in soil loss was suggested when vegetation was used in conjunction with the gravel mulch. Erosion rates calculated in that study are assumed to be valid for the purposes of modeling the long-term performance of the disposal pit covers.

Erosion at the rate of 4×10^{-7} m/yr (1.3×10^{-6} ft/yr) over the 1,000-year compliance period will remove less than 1 percent of the total cover depth placed over any of the disposal units. Consequently, erosion does not pose a direct threat to the integrity of the disposed waste during this period.

Referring to the information in section 2.1.4, lateral erosion or cliff retreat occurs to variable degrees along the mesa walls across the Pajarito Plateau. In theory, erosion of Mesita del Buey may, over time, expose waste disposed of in the pits and shafts closest to the mesa edges. The 15 m (50 ft) minimum set-back distance between disposal units and the edge of the mesa was established to delay disruption of the waste by lateral erosion.

The rate of lateral erosion is difficult to predict because it is a discontinuous process. Independent estimates of cliff retreat rates made by several investigators at LANL were

presented in Section 2.1.4. Applying them to MDA G, the 15 m (50 ft) setback distance at MDA G will not erode before 40,000 to 400,000 years. Thus, it is unlikely that waste disposed of at MDA G will be exposed by lateral erosion during the 1,000-year compliance period, therefore cliff retreat was not included in the PA and CA as a viable mechanism of radionuclide release.

3.1.2 Groundwater Protection Analysis

Source term modeling for the groundwater pathway quantifies the rates at which radionuclides may be dissolved into water percolating through the disposal units. The model described in this section accounts for many of the natural and designed features of MDA G presented in Sections 2.1 and 2.2, and addresses the characteristics of the inventory described in Section 2.3. First, the inventory is summarized, then the source term model and the assumptions upon which it is based are discussed.

3.1.2.1 Groundwater Pathway Inventory

In Section 2.3, 4 waste categories were identified: Surface Contaminated, Concrete/Sludge, Soil, and Bulk Contaminated. These categories account for differences in the rates at which radioactivity in or on the waste would be dissolved or leached into water percolating through a disposal unit. In the aqueous-phase source term model, unique release rates were developed for each category based upon the quantity of water contacting the waste, the geochemistry of that water, the contact time between the water and the waste, and the chemical form of the radionuclides present.

The number of radionuclides initially considered in the aqueous-phase source term was 68, each generally present in 38 disposal units. To reduce this number, a conservative screen was performed to identify radionuclides that could be eliminated from the aqueous-phase source term without compromising the dose analysis. The screen was performed as follows:

- The total inventory of each radionuclide in the MDA G CA was assumed to be dissolved instantaneously in moisture within a disposal unit. (The amount of water into which the total inventory was dissolved was 8 percent, based on data presented in Section 2.2.)
- The contaminated water was assumed to be ingested at a rate of 2 L/day (0.52 gal/day) for an entire year by a single person.
- The dose resulting from each radionuclide was compared to the 4 mrem/yr groundwater protection standard.
- Radionuclides for which the dose was less than 4 mrem/yr were eliminated from the aqueous-phase source term analysis.
- Radionuclides for which the dose was equal to or greater than 4 mrem/yr were maintained in the aqueous-phase source term analysis.

This screening scenario bears no basis in fact. It is a modeling construct that allowed for the identification and elimination of radionuclides that present no significant radiological risk via groundwater even when ingested at their highest possible concentrations. The moisture within disposal units is not available for human consumption and, at 8 percent, is not even extractable. During the time that radionuclides are transported from the disposal units to the regional aquifer, concentrations would be greatly reduced as a result of radioactive decay, dispersion and sorption within the vadose zone, and dilution in the regional aquifer. Thus, the screen is very conservative, leading to much higher doses on a radionuclide-specific basis than would otherwise be projected in the groundwater protection analysis.

A total of 68 radionuclides, excluding daughter products, were initially considered in the aqueous-phase source term analysis. Twenty-two of these radionuclides, considered individually, resulted in maximum doses less than 4 mrem/year and were excluded from further consideration in the groundwater protection analysis. The collective dose resulting from all radionuclides eliminated by the screen was 15 mrem/yr. The results are presented in Table 3-3.

Table 3-3 Results of the groundwater-pathway inventory screen

Radionuclide	Maintained	Eliminated
Ac-227	X	
Ag-108m	X	
Al-26		X
Am-241	X	
Am-243	X	
Ba-133	X	
Bi-207		X
Bk-247		X
C-14	X	
Cd-113m	X	
Cf-249	X	
Cf-251		X
Cf-252	X	
Cl-36		X
Cm-244	X	
Co-60	X	
Cs-135		X
Cs-137	X	
Dy-154		X
Eu-152	X	
Eu-154	X	
Gd-148	X	
Gd-150		X
H-3	X	
Hf-182	X	
Ho-163		X
I-129	X	
K-40	X	
Kr-81		X
Kr-85		X
La-137		X
Mo-93	X	
Nb-92		X
Nb-94	X	
Ni-59		X
Ni-63		X
Np-237	X	
Pa-231		X
Pb-210	X	
Pd-107		X
Pm-145		X
Pu-238	X	
Pu-239	X	
Pu-240	X	
Pu-241	X	
Pu-242	X	
Ra-226	X	
Se-79		X

Radionuclide	Maintained	Eliminated
Si-32	X	
Sm-146		X
Sm-147	X	
Sm-151	X	
Sr-90	X	
Tb-157	X	
Tb-158	X	
Tc-97		X
Tc-99	X	
Th-229	X	
Th-230	X	
Th-232	X	
Ti-44	X	
U-232	X	
U-233	X	
U-234	X	
U-235	X	
U-236	X	
U-238	X	
Zr-93		X

3.1.2.2 Groundwater Pathways Source Term Model

The conceptual model for aqueous-phase source term is shown in Figure 3-8. The left side of the figure represents a pit containing a relatively homogeneous distribution of waste, with the 4 categories initially represented. The right site of the figure shows one unit of a particular waste category, with infiltration entering the waste at the top, and leachate leaving the waste at the bottom. A portion of the radioactivity in the waste remains as a solid-phase concentration (C_s), while the liquid-phase concentration moves with the leachate (C_l).

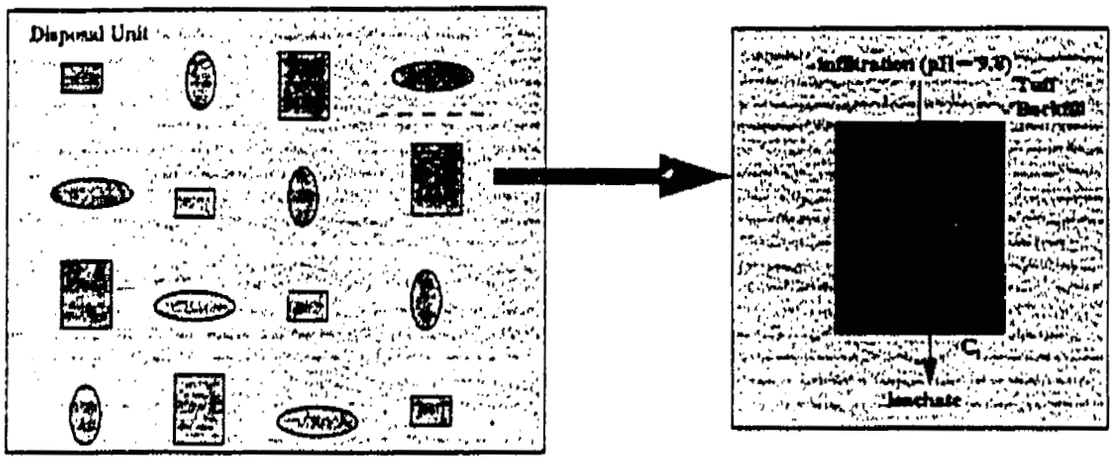

Figure 3-8 Conceptual model for aqueous-phase dissolution of radioactivity from surface-contaminated waste

The concentration in the solid phase relative to the liquid phase is related to the speciation, solubility, and distribution coefficients associated with each waste form, which depend on the chemistry of the infiltrating water and the contact time between the water and the waste. The following subsections describe these characteristics for each of the 4 waste forms. In general, release rates are greatest for the surface-contaminated waste. The rates of release for soils, concrete, and sludges are controlled by the geochemistry of the water percolating through the disposal units and the chemical forms of the radionuclides. Releases from the bulk-contaminated waste are retarded by physical factors such as the rate of corrosion of activated steel. The models used to estimate radionuclide releases from each waste-form category are summarized below. More detailed information is provided in Appendix 3d *Modeling of the Aqueous Phase Source Release to the*

Unsaturated Zone from the Los Alamos Area G Disposal Facility.[98] The appendix report summarizes a two-phase analysis, a preliminary analysis modeled releases from all 4 waste categories in detail. The final analysis addresses only the surface-contaminated waste category. With this simplification in the source term analysis, it was possible to model releases of multiple radionuclides from each of 38 disposal units independently.

Before describing the source term modeling, the surface-water balance model performed to estimate a percolation or recharge rate through the pits is briefly discussed. The complete report of the surface water balance model summarized below is available in Appendix 3c.

3.1.2.2.1 Percolation Modeling

The ability to model water balance is essential to projecting long-term facility performance. In support of the PA, surface runoff, soil erosion, and percolation through a 1-m (3.3 ft) thick vegetated crushed-tuff cover was simulated. The base-case simulation modeled the anticipated disposal-unit cover configuration during the active institutional-control period at MDA G. The pit for this simulation was given a surface area of 0.41 ha (1ac) with a length to width ratio of 2 to 1. The pit was assumed to be sloped along the width dimension for runoff and erosion calculations. The surface slope was 3 percent, consistent with the degree of dip of the stratigraphic layers, described in Section 2.1.4. The pit with cover was assumed to be 16 m (53 ft) deep, with water balance calculated for the upper 1 m (3.3 ft). A 10 cm (4 in.) clay loam surface topsoil layer was modeled at the top of the pit, which supported a uniform vegetative layer with an average root depth of 1 m (3.3 ft), and a thin gravel-mulch layer. The remaining depth (90 cm) of the pit was filled with crushed Bandelier Tuff.

Percolation through the 1-m (3.3-ft) covers were predicted using a Monte Carlo approach. A total of 100 realizations that were 10,000 years long were generated, giving a total of 1,000,000 annual percolation calculations. The average annual precipitation from the stochastic weather generator was constrained to the site-specific value of 36 cm (14 in.) cited in Section 2.1.2; the maximum was 71 cm (28 in.), and the minimum was 12 cm (5

in.). These values compare well with the estimated 100-year precipitation event based on the 30-year pluviometric record, which is consistent with the 400-year dendroclimatic record. Table 3-4 shows the statistics for annual values of percolation, runoff, and soil erosion for the 1,000,000 observations modeled. The average percolation through a nominal operational closure cap calculated in the 1,000,000 Monte Carlo realizations was 1 mm (0.04 in.), with zero percolation occurring for 80 percent of the 1,000,000 realizations; the maximum single-year percolation was 130 mm (5 in.).

Table 3-4 Annual values of percolation, runoff, and soil erosion

Variable	Mean	Standard Dev.	Maximum	Minimum
Percolation (mm)	0.99	5.15	129	0.0
Runoff (mm)	0.78	1.65	67.5	0.0
Erosion (t/ac-yr)	0.002	0.005	0.23	0.0

While the final closure condition of MDA G is expected to be well represented by the surface water balance model, the current state of vegetation and other surface conditions is highly variable between pits. To be conservative in the groundwater protection, the 5 mm/yr (0.2 in./yr) infiltration rate suggested by Pit 37 *in situ* moisture measurements was used to calculate aqueous-phase source releases rather than the lower 1 mm/yr (0.04 in./yr) value calculated by the water-balance model. The higher recharge rate is also consistent with the near-surface fluxes estimated in several independent investigations, as discussed in Section 2.1.5. The higher *in situ* measurements and inferred moisture fluxes are consistent with the absence of vegetation in open pits, confirming the results that transpiration is very important in removing water from the system.

3.1.2.2.2 Surface-Contaminated Waste Source Term

Release from surface-contaminated waste was assumed to occur as water dissolves the contamination. The rate of dissolution and the magnitude of radionuclide releases depend upon the amount of water contacting the waste, the length of contact time, the geochemical characteristics of the water, and the chemical form of the radionuclides. The

amount of infiltrating water and the rate of infiltration were based on *in situ* pit-moisture measurements referred to in Section 2.2.1. A moisture content of 8 percent was assumed, with an infiltration rate of 5 mm/yr (2.0×10^{-1} in./yr) through the disposal units. Assuming an average waste package thickness of 1 m (3.3 ft), a water transit time of 16 years through the waste was estimated. The infiltrating water was assumed to have the geochemical characteristics of the Water Canyon Gallery, reported in Section 2.1.6. The dominant chemical forms (speciation) of the radionuclides were modeled assuming dissolution in water of that chemistry; these are listed in Table 12 in Appendix 2a.

The maximum concentration of an element in water, or the solubility limit, was also determined using Water Canyon Gallery chemistry; the solubility limits applied in the analysis are listed in Table 13 of Appendix 2a. For most radionuclides in the MDA G inventory, solubility limits are never reached; those radionuclides are termed "inventory limited." Those radionuclides whose calculated leachate concentrations do reach the solubility limit are termed "solubility limited."

Solubility limits apply to elements, and therefore are compared to the total concentration of all radioisotopes of a given element in a given volume of water. To realistically model the contributions of several radioisotopes of a single element to the elemental solubility limit, the distribution of the radioisotopes in individual disposal units must be known. While data are available to support such modeling, the effort required to evaluate thousands of disposal records was judged to be greater than the benefit derived. To simplify the aqueous-phase source term model in a conservative way, each radionuclide was assumed to be available at its elemental solubility limit on a disposal-unit basis. This approach is clearly conservative since it allows more radioactivity to be released under solubility-limited conditions. An exception to this is uranium, which is abundant as several isotopes. For uranium, correction factors were derived for the isotopes in each package and among all packages in a disposal unit. This is detailed in Appendix 3d.

For inventory-limited radionuclides, releases modeled in this manner increase over a period of 16 years until a short-term peak release rate was attained, then decline until the inventory is depleted thereafter. Releases of most radionuclides in the MDA G inventory are inventory limited. For radionuclides that are solubility-limited, releases remain at a level dictated by the solubility limit until the entire inventory within a single disposal unit is leached.

3.1.2.2.3 Soil Source Term

The soil source term model accounts for radionuclide releases from soils and soil-like materials, taking into account the sorption behavior of the contaminants. Sorption was characterized by the soil distribution coefficients. These coefficients were based on site-specific studies using crushed tuff and values adopted from the open literature, accounting for chemical speciation under the conditions imposed by the assumed Water Canyon Gallery pore water geochemistry. Radionuclide concentrations were compared with the appropriate solubility limits. The data used in the analysis are presented in Tables 7 and 13 in Appendix 2a.

3.1.2.2.4 Concrete and Sludge Source Term

Releases from concrete and sludges were estimated based on the sorption of radionuclides in high pH environments. Many radionuclides, actinides in particular, sorb strongly to cementitious material, due to the abundance of minerals in cement, as well as its alkalinity (pH > 10).[99] Sludges generated at the LANL liquid waste treatment facility (TA-50) are highly alkaline due to the addition of lime during the treatment process. The chemistry of the dewatered sludge is similar to cement, resulting in similar modes of release.[100] For the concrete/sludge source term, chemical speciation and radionuclide solubilities were estimated based on an alkaline, oxidizing environment. The sorption values and solubility limits used to model releases from cement and sludge waste forms are included in Tables 9 and 14 in Appendix 2a. The time-dependent concentrations of radionuclides released from concrete/sludge waste were compared with the solubility limits for the isotopes under alkaline conditions.

3.1.2.2.5 Bulk-Contaminated Waste Source Term

The bulk-contaminated waste form consists largely of activated metals from the Los Alamos Neutron Scattering Center, including stainless-steel target mounts and metal beam-line inserts. The release of contamination from this waste form was modeled using a steel corrosion rate of 2.0×10^{-3} m/yr (7.0×10^{-3} ft/yr).[101] Quantities of radioactivity released from the metals were assumed to enter into solution in the pore water within the disposal units. The radionuclide concentrations in the leachate were compared with solubility limits for intact tuff and releases were limited as appropriate.

3.1.2.3 Groundwater Pathways Source Term Summary

The results of the groundwater pathway source term model revealed that the projected radionuclide concentrations in the leachate were dominated by the surface-contaminated waste inventories. This was the case for all radionuclides and disposal units included in the PA and CA. Based on these results, the final source term model implemented for the groundwater protection analysis included only the surface-contaminated waste. This simplification made it possible to allocate pit inventories to the individual units; ultimately, the analytic release model was added to the numerical model used to calculate subsurface transport in Section 3.3. Furthermore, it allowed consideration of the effects of solubility limits on a disposal-unit basis, with 38 pits being modeled in a realistic geometry. Source terms were developed using this model for the four inventory segments: 1957 - 1970; 1971 - September 25, 1988; September 26, 1988 - 1995; and 1996 - 2044.

3.1.3 All-Pathways Analysis

The mechanisms and processes that were considered in the all-pathways analysis include gas release, biotic intrusion, and leaching by water percolating through the disposal units. The models and assumptions used in estimating rates of release by these mechanisms have been discussed.

3.2 PATHWAYS AND SCENARIOS

Pathways and scenarios are used to define how and where exposures to radioactivity released from MDA G will occur. Specific scenarios are defined to evaluate the ability of MDA G to comply with the performance measures presented in Section 1. The performance measures are interpreted such that exposures are evaluated in terms of the air pathway and the groundwater pathway independently, and then all pathways combined. The pathways link releases of radioactivity to air, water, and surface soil to offsite locations, where exposures to future members of the public are evaluated assuming various air, water, and surface soil usage scenarios. The pathways and scenarios invoked in the PA and CA differ somewhat depending on which period of the MDA G lifecycle is considered. For the purposes of defining appropriate pathways and scenarios, the facility lifecycle and access boundaries are defined as follows:

- Operational/Closure Period: 1957 - 2046, when public access is assumed to be limited by the existing TA-54 boundary, and offsite releases are assumed to be prevented.
- Institutional-Control Period: 2047 - 2146, when public access is assumed to be limited by the existing MDA G fenceline, and disposal site is actively maintained to ensure integrity of the disposal unit covers.
- Industrial-Use Period: 2147-3046, when public access is assumed to be limited by the existing MDA G fenceline, and site is passively maintained such that biotic intrusion into disposal units may occur.

The pathways and scenarios to be described in this section are summarized in Table 3-4, and the locations at which each scenario is evaluated are indicated in Figure 3-5. Since offsite releases are assumed to be controlled during the operational and closure periods, offsite exposures are not considered until the onset of institutional-control. Complete descriptions of the pathways and scenarios discussed below are available in Appendix 3e *Radiological Dose Assessment for the TA-54, Area G Performance Assessment and Composite Analysis.*[102]

Table 3-5 Summary of exposure pathways and scenarios

Time Period	Pathway	Scenario
Institutional-control (2047-2146)	Air Groundwater All	Inhalation of gases Ingestion of groundwater Inhalation of gases, direct and indirect ingestion of groundwater
Industrial-use (2147-3046)	Air Groundwater All	Inhalation of and immersion in gases and particulates; ingestion of and exposure to redeposited particulates Ingestion of groundwater Inhalation of and immersion in gases and particulates; ingestion of and exposure to redeposited particulates; direct and indirect ingestion of groundwater; direct and indirect consumption of contaminated sediment

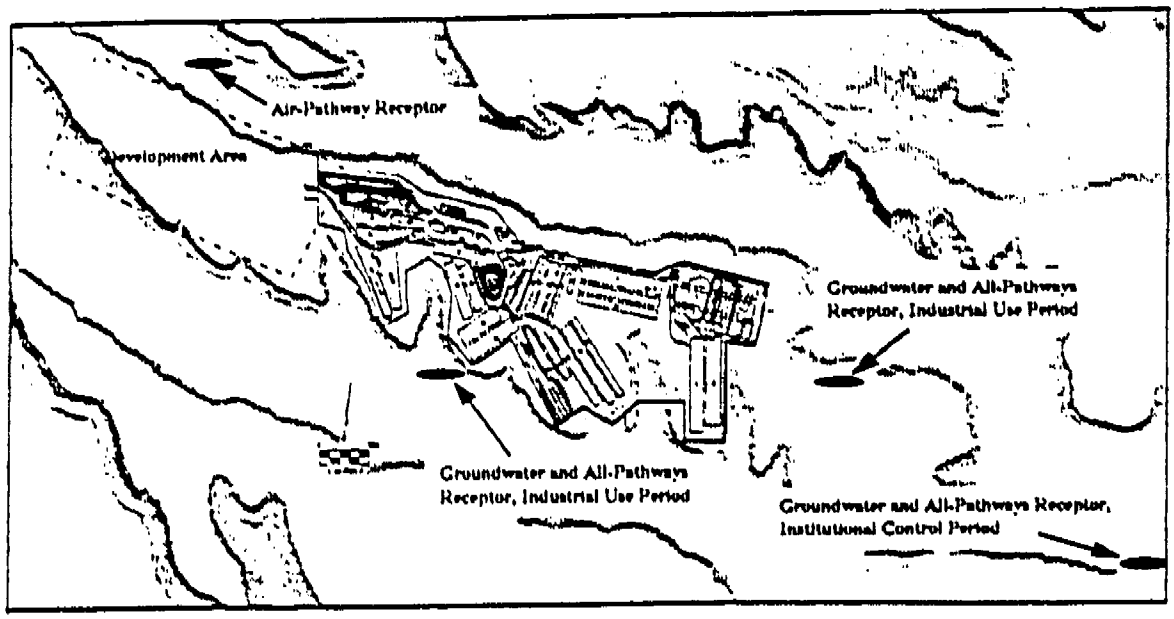

Figure 3-9 Location of evaluation of exposure scenarios

3.2.1 Air Pathways Analysis

The air pathway analysis was performed to assess the ability of MDA G to comply with offsite dose limit of 10 mrem/yr for the PA and 100 mrem/yr for the CA, and with the radon flux limit of 20 pCi/m^2/s (1.9 pCi/ft^2/s). For the offsite dose assessment, the air pathway analysis projected exposures due to radioactive gases and suspended particulates

translocated to the surface by biota, as described in Section 3.1.1. Doses from the air pathway were calculated at the town of White Rock and at the point of maximum atmospheric exposure. The point of maximum exposure was located about 500 m (1,600 ft) north of MDA G in Cañada del Buey, identified on the basis of prevailing meteorological conditions and the complex terrain in the vicinity of MDA G. Because active site maintenance is assumed to prevent biotic intrusion throughout institutional-control, exposures during that period were assumed to result from the inhalation of only radioactive gases (except radon and its daughters) released from MDA G. During the industrial-use period, site maintenance is assumed to be more passive, allowing for some biotic intrusion to occur. Therefore, contaminated soils suspended from the disposal site following biotic intrusion were included in the dose projections during the industrial-use period. The receptor was assumed to inhale airborne dust, ingest crops contaminated by radioactivity deposited on plants, and receive external radiation from contaminated soils and airborne radioactivity. While the cultivation of crops in Cañada del Buey is not considered to be likely due to the lack of available water, the scenario is assumed to conservatively bound exposures received by persons harvesting native foodstuffs, such as Piñon nuts and juniper berries.

3.2.2 Groundwater Protection Analysis

The groundwater protection analysis projected doses to future members of the public due to radioactivity leached from MDA G, transported through the vadose zone, and entering the regional aquifer. It was performed to assess the ability of MDA G to comply with the 4 mrem/yr performance objective for doses received by a future member of the public due to consumption of contaminated groundwater. Groundwater ingestion doses were projected at the point of maximum offsite groundwater concentration, which differed during the institutional-control and industrial-use periods. Referring to the discussion of local and regional hydrology in Section 2.1.5, and recalling the assumed landuse boundaries reviewed above, maximum groundwater concentrations at locations accessible to members of the public are expected to occur near the town of White Rock during the institutional-control period. During the industrial-use period, the assumed current

fenceline boundary allows access to groundwater at locations nearer to MDA G. Two locations were identified for evaluation of groundwater doses during the industrial-use period, one downgradient from MDA G approximately 100 m south-southeast of the facility, and another in Pajarito Canyon directly adjacent to the facility. The downgradient receptor was identified to evaluate doses from radioactivity transported down through the vadose zone directly beneath MDA G, then out into the regional aquifer. The Pajarito Canyon location was selected to evaluate the lateral transport pathway, where radioactivity is transported in the aqueous phase laterally out towards the mesa side, where radioactivity may then be rinsed by runoff into the alluvial groundwater in Pajarito Canyon and subsequently transported to the regional aquifer. Since recharge beneath the alluvial aquifer in Pajarito Canyon is faster than recharge through Mesita del Buey, this pathway was evaluated as a potential "fast path" for radioactivity to reach the regional aquifer.

While the alluvial aquifer in Pajarito Canyon was evaluated in terms of its potential effect on accelerating vadose zone transport, it was not considered to be a drinking water source. The source of water used as the basis for evaluated compliance with the groundwater protection performance objective must meet three criteria:

1. The water must have a potential for being contaminated by radioactivity leached from MDA G, as modeled in the aqueous-phase source term.
2. The aquifer must be of adequate quality and supply to meet the needs of the user.
3. The aquifer must be accessible to the receptor within the constraints of the DOE land-use boundaries.

Of the groundwater sources in the area described in Section 2.1.5 (i.e., alluvial water in Cañada del Buey and Pajarito Canyon and the saturated aquifer in the Puye Formation) only the regional aquifer meets all of these criteria. Water in Pajarito Canyon and Cañada del Buey may become contaminated by radioactivity transported laterally from the disposal units to the sides of the mesa and washed into the canyon by surface runoff. Consistent with the assumed boundaries during the facility lifetime, water in Pajarito Canyon will not

be accessible as a source of drinking water in the location immediately adjacent to MDA G during the operational and active institutional-control periods. However, this water may be accessed for drinking water near White Rock approximately 2 km (1.2 miles) away. Alluvial water in this canyon is accessible to members of the public during the industrial-use period; water within Cañada del Buey is accessible to individuals at all times as this canyon lies on the border of LANL and San Ildefonso Indian lands. According to data presented in Section 2.1.5, neither source of water in the canyons is capable of supporting average household water use. The alluvial water in Pajarito Canyon, the more substantial of the two sources, would most likely be pumped dry during most seasons of the year.

The regional aquifer situated in the Puye Formation beneath MDA G is the only body of water that is suitable for evaluating the compliance with the 4 mrem/yr PA performance objective. Radioactivity leached from the waste disposed of at MDA G will eventually discharge into the regional aquifer. This aquifer is accessible to members of the general public during all phases of the facility's lifetime. Groundwater within the aquifer is of sufficient quality and quantity to meet all water needs of an individual.

3.2.3 All-Pathways Analysis

The all pathways analysis was performed to evaluate the ability of MDA G to comply with the 25 mrem/yr public-protection performance objective for the PA, and the 100 mrem/yr public dose limit for the CA. It considered doses from airborne radioactivity as previously described. Direct ingestion doses via the groundwater pathway were expanded to include indirect ingestion of groundwater through foodstuffs raised on contaminated water. In addition to the air and groundwater pathway doses, the all-pathways analysis included doses associated to the transport of contaminated surface soil (resulting from biotic translocation) off of the mesa into Pajarito Canyon by runoff.

The all-pathways analysis was implemented in Cañada del Buey and near White Rock during the institutional-control period, and in Pajarito Canyon and 100 m downgradient of the MDA G fenceline during the industrial-use period. The receptor near White Rock was

assumed to receive exposures from the ingestion and inhalation of radioactivity and direct radiation. Ingestion doses occur from the consumption of crops irrigated with water drawn from the resident's well, milk and meat from animals raised using water from the well, and drinking water. Inhalation doses result from the intake of dust suspended from contaminated soil surfaces. Exposures to direct radiation from airborne contamination and radioactivity deposited on the soil add to the internal exposures. Exposure pathways for the receptor at the point of maximum atmospheric exposure were discussed in Section 3.2.1.

During the industrial-use period, exposure pathways modeled at the location of maximum groundwater exposure were identical to those described above for the receptor location near the town of White Rock. The receptor location in Pajarito Canyon was used to estimate potential doses resulting from the transport of contamination from Mesita del Buey to the canyons below. Sources of contamination included radioactivity brought to the surface of the mesa by plants and burrowing animals, and contamination transported laterally to the sides of the mesa and downward to the regional aquifer. Surface runoff was assumed to transport each source of contamination into the canyon.

The receptor in Pajarito Canyon was assumed to receive exposures from the ingestion of small amounts of soil, food crops grown in contaminated soils and irrigated with water drawn from the alluvial aquifer, and milk and meat from animals raised using the same source of water. Additionally, exposures were modeled from the inhalation of suspended particulates and direct radiation from airborne and soil contamination.

The assessment of exposures to the offsite resident at the locations discussed above is expected to provide reasonably conservative dose estimates. By definition, the location of maximum atmospheric exposure will bound doses to offsite individuals resulting from airborne releases from the facility. Concentrations of airborne contaminants will diminish as the distance from the disposal facility increases or as the location of the receptor relative to the site changes. Groundwater pathway doses will decline at locations further

downgradient than those evaluated as the concentrations of groundwater contamination abate due to dilution and dispersion. Exposures to persons living in Pajarito Canyon are expected to be greatest immediately below MDA G, as transport of surface runoff further down the canyon will tend to dilute soil contaminant concentrations.

3.3 ANALYSIS METHODOLOGY

This section summarizes the approaches used to model the transport of radioactivity from MDA G to offsite receptor locations and to project doses for each of the exposure scenarios discussed above. The discussion follows the organization of the previous sections, describing the air pathway analysis methodology first, the groundwater protection analysis methodology second, and the all-pathways methodology third. For each pathway, the methods used to simulate transport of radioactivity released by one or more of the source terms discussed in Section 3.1 to locations identified in Section 3.2 are described, followed by a summary of the methods used to project doses according to the scenarios presented in Section 3.2. Figure 3-10 illustrates the connection between source term and environmental transport. Source terms, described in Section 3.1, are indicated as dashed lines, while the environmental transport mechanisms (and media) with which source terms are coupled are indicated as solid lines. Referring to the figure, the gas-phase source term diffusing through the cover into air is coupled directly with the atmospheric dispersion transport pathway; the aqueous dissolution source term is coupled directly to the lateral and vertical unsaturated transport pathways, which are coupled with the surface-water and saturated transport pathways, respectively. The biotic translocation source term is coupled directly with the surface-water sediment transport pathway, and indirectly, through resuspension, with the atmospheric diffusion pathway. The relationships shown in the figure will be discussed in detail below.

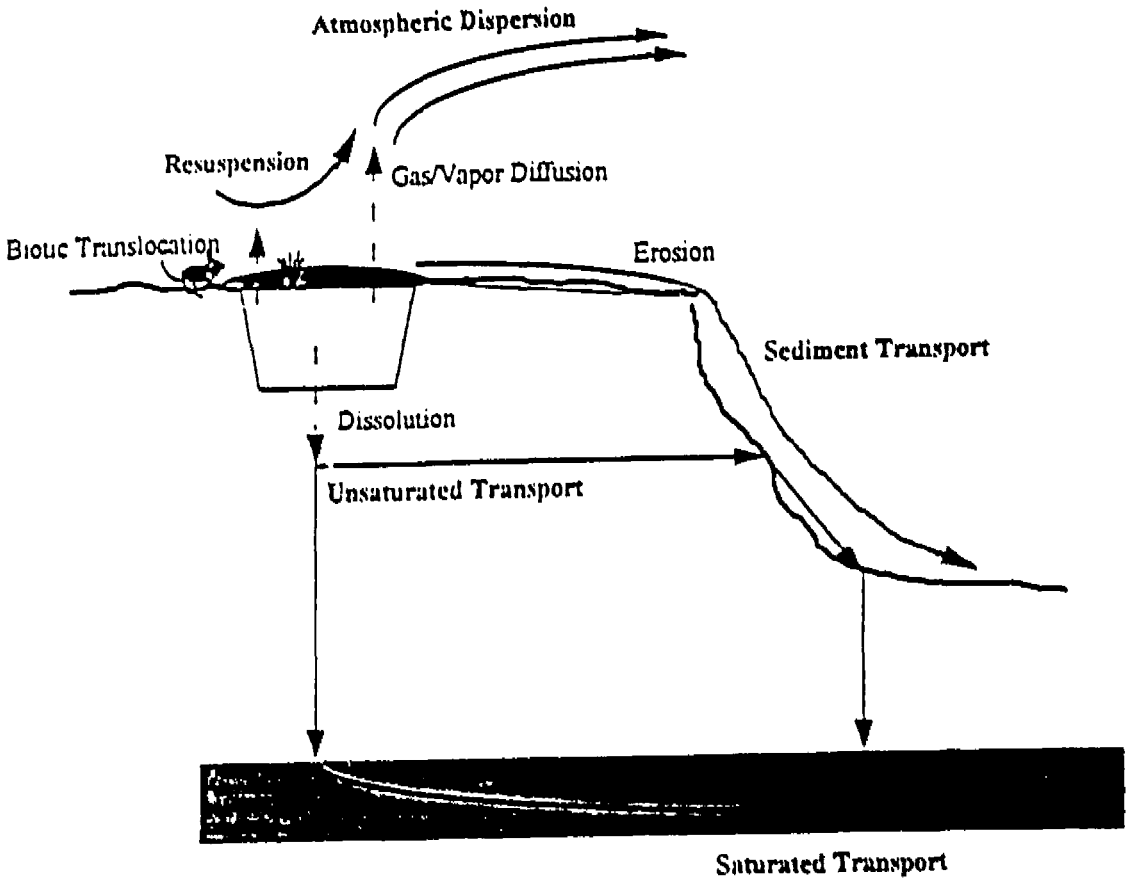

Figure 3-10 Coupling of source term and environmental transport analyses

3.3.1 Air Pathway Analysis

The air pathway analysis addressed the transport of gas-phase releases and resuspended particulates to locations downwind of MDA G. The paragraphs to follow describe how the meteorological data presented in Section 2.1.2 were used to quantify atmospheric concentrations at the Cañada del Buey receptor location, and how those atmospheric concentrations were used to estimate doses to an individual residing in Cañada del Buey.

3.3.1.1 Atmospheric Transport Model

The information summarized here is presented in detail in Appendix 3f *Atmospheric Transport in Complex Terrain at Los Alamos, Area G.*[103] As presented in Section 3.1.1, releases of radioactivity to the atmosphere may be expected to occur as a result of gases diffusing from MDA G and the resuspension of contaminated dust exposed at the surface

following biotic intrusion. Resuspension occurs as a result of winds across the mesa, and converts surface-soil concentrations calculated using the biotic translocation model into airborne particulated concentrations. The resuspension rate used in the analysis was 1.8×10^{-9} kg/m^2/sec (3.7×10^{-10} lb/ft^2/sec), which was determined at MDA G.[104] The transport analysis was based on standard Gaussian plume models generally used to calculate concentration maxima of airborne contamination. However, the dispersion factors were modified to account for winds channeling through canyons.

The air pathways transport model made use of the wind speed, wind direction, atmospheric stability, and mixing height data discussed in Section 2.1.2. The model used measured windrose data like that presented in Figure 2-4 to identify wind sectors on the mesa top (where releases would occur) that coalesce into winds in Cañada del Buey (where concentrations would be greatest). To calculate airborne concentrations from MDA G sources, wind speeds and frequencies measured at the MDA G meteorological station were compiled. The data indicate that 68 percent of the southerly winds that blow across Mesita del Buey annually contribute to winds in Cañada del Buey during the daytime. It was determined that the maximum air pathways releases are transported by winds within sectors from WSW to ESE. Gaussian plume dispersion values for those sectors were obtained from a previous analysis performed using standard EPA methodology.[105,106] That analysis calculated dispersion at a location 500 m (1,600 ft) downwind of MDA G, the minimum distance allowed for distributed source (i.e., 60 acres).

Wind rose data from Cañada del Buey, Pajarito Canyon, and another canyon stations at TA-41 were used to calculate an average canyon wind velocity of 1.6 m/s (5.1 ft/s). Data from four mesa-top canyons were used to calculate an average mesa-top wind velocity of 2.6 m/s (8.6 ft/s). Stability-class and mixing-heights were determined from the mesa-top meteorological data. (More recent information, unavailable at the time that this analysis was performed, show that canyon winds are stable and unstable in roughly equal proportions, and that neutral conditions occur relatively infrequently.)

Summing the SWS-ESE quadrant dispersion parameters at 500 m (1,600 ft), multiplying by the mesa-to-canyon wind-speed ratio of 1.7, and by the daytime frequency of 0.68, a dispersion value within Cañada del Buey at the location of the maximum concentration was calculated to be 5.5×10^{-5} s/m^3 (1.6×10^{-6} s/ft^3). Gas-phase concentrations at that location were calculated by multiplying the dispersion value by the gas-phase fluxes. For airborne particulates, the surface-soil concentrations (see Section 3.1) were multiplied by a resuspension velocity consistent with an average mass loading of 1.0×10^{-7} kg/m^3 (6.3×10^{-9} lb/ft^3) from measurements performed at MDA G.[104] Consistent with these data, the maximum offsite concentrations were calculated 500 m (1,600 ft) north of MDA G in Cañada del Buey under daytime conditions.

To illustrate the effect of channeling of winds within Cañada del Buey, Figure 3-11 shows the result of an atmospheric release computed from three point sources within MDA G, which is located near x = -1, y = 0 in the figure.[107] The plumes converge in Cañada del Buey to the northwest of the release site at the location of the maximum offsite receptor, and then diverge as the plumes disperse above the adjacent mesas and canyons. The results are in good agreement with the empirically observed wind flow fields, and with the assumptions for determining the maximum offsite receptor location used in the PA and CA.

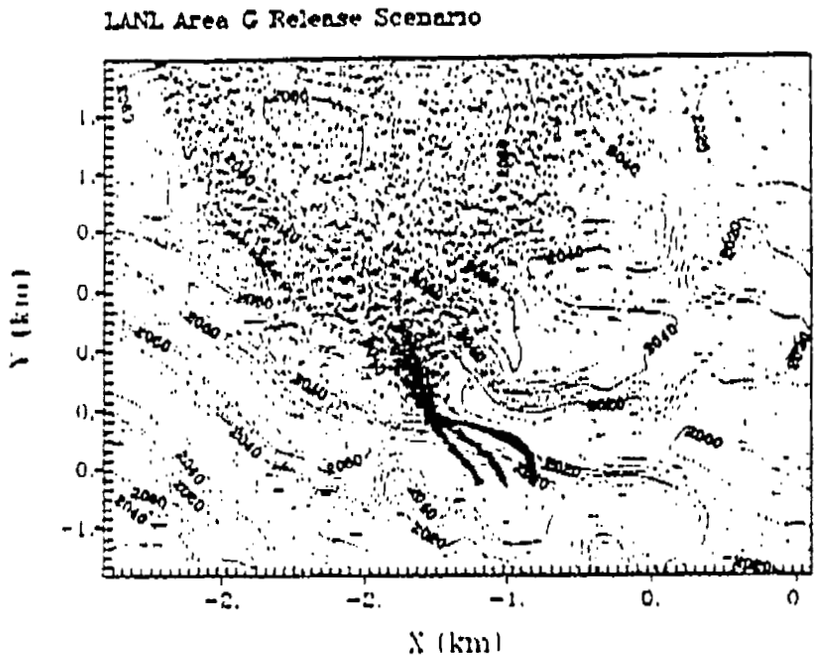

Figure 3-11 Atmospheric release computed from three point sources within Area G (centered near x = -1, y = 0.) showing a convergence of the plumes in Cañada del Buey to the northwest of the release.

3.3.1.2 Air Pathway Dose Projections

The projected doses for the air pathway analysis accounted for exposures from airborne concentrations of radioactive gases and contaminated dust. Airborne concentrations of radioactivity used in the dose projections were taken directly from the atmospheric transport modeling results described above. Suspended contamination was assumed to deposit on the surfaces of food crops grown by a resident and on surface soils. Plants were assumed to assimilate a portion of the radioactivity deposited on the foliage, and a portion of radioactivity present in contaminated soils. The details of the approach are presented in Appendix 3e.

The level of resource utilization assumed for the receptor is expected to provide very conservative estimates of potential doses. As stated previously, the raising of food crops in Cañada del Buey is not considered likely based on the limited availability of water. Rather, exposures might occur due to the ingestion of native foodstuffs harvested within the

canyon. This more realistic scenario is bounded by the modeled one, wherein The receptor was assumed to be present at the site approximately 70 percent of the time and crops grown at the residence were assumed to comprise 50 percent of the individual's food requirements. An average inhalation rate of 8,000 m^3 (280,000 ft^3) was assumed.

Direct exposures from contaminated soil surfaces were estimated using the MICROSHIELD computer code.[108] MICROSHIELD simulations were conducted for unit concentrations of all parent and daughter radionuclides included in the air pathway analysis. These unit-concentration exposure rates were scaled using the projected surface soil concentrations at the receptor locations to determine the projected doses to the receptor.

3.3.2 Groundwater Protection Analysis

A 3-dimensional groundwater model was used to simulate the transport of radioactivity from the disposal units to the regional aquifer. The source term described in Section 3.1.2 for surface-contamination dissolution was implemented directly in the vadose-zone transport model, with releases from 38 disposal units being modeled independently. This level of complexity was required to incorporate releases from many sources containing multiple radionuclides, to account for the complex vadose-zone hydrology of the site described in Section 2.1.5., the large area over which waste has been disposed of at MDA G, and to account for the unique topography of the disposal site. The vadose-zone model was used to calculate radionuclide fluxes at the base of the Cerros del Rio Basalt section. Those fluxes were directly input into a three-dimensional model of the regional aquifer, which calculated groundwater concentrations at the offsite locations identified in Section 3.2.2.

A region of interest, shown in Figure 3-12, was determined that would include the distributed sources within the mesa, account for the prevailing groundwater flow direction beneath MDA G, (see Figure 2-12), and contain the appropriate offsite locations where radionuclide concentrations and doses would be calculated.

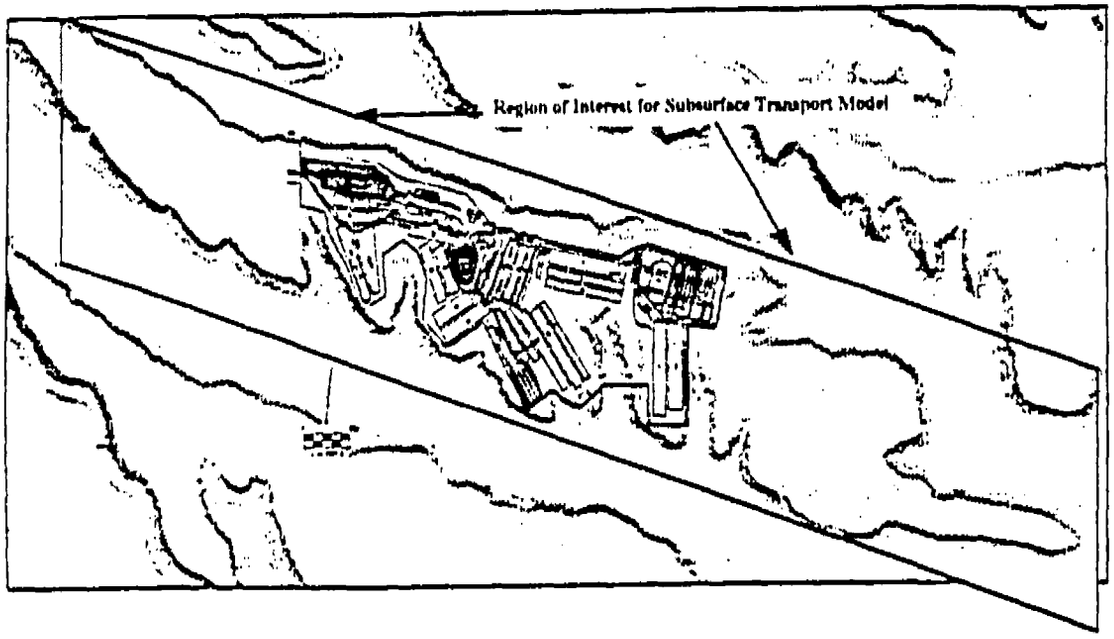

Figure 3-12 Region of interest identified for the groundwater pathways computations

This section describes the modeling approaches used for the groundwater protection analysis. It summarizes models used to simulate the transport of radioactivity in the aqueous phase through the vadose zone and regional aquifer. The details of the methodologies summarized below are presented in Appendix 3g *Simulations of Groundwater Flow and Radionuclide Transport in the Vadose and Saturated Zones Beneath Area G, Los Alamos National Laboratory.*[109] The manner in which radiological doses were projected from use of contaminated water are also summarized below, with details of the dose assessment available in Appendix 3e.

3.3.2.1 Vadose Zone Transport Model

The vadose zone transport model used in the groundwater protection analysis accounted for hydrogeologic and geochemical characteristics and processes that are expected to dominate contaminant transport in the unsaturated zone. The interpretation of the extensive body of data presented in Sections 2.1.5 represents the conceptual model of vadose-zone transport. The conceptual model necessarily invokes simplifications regarding the complex hydrologic system to allow the system to be mathematically

modeled. The effect of some of the more important simplifications are evaluated in short parameter studies.

3.3.2.1.1 Conceptual Model of Vadose Zone Transport

The conceptual model of vadose zone hydrology is a simplification of the complex hydrologic system at MDA G. The model is fully detailed in Appendix 3h *Conceptual Model for Subsurface Transport at MDA G.*[110] An important simplification in the conceptual model is a steady-state moisture recharge rate through Mesita del Buey. This simplification reflects the relative lack of data required to rigorously model vapor-phase moisture flow, evaporation through fractures and surge beds, and variable hydraulic parameters, all of which have been hypothesized on the basis of analyses on the available data set described in Section 2.1.5.3. The magnitude of the steady-state recharge rate used in the groundwater protection analysis was chosen to be conservative based on modeling and field data. Water balance modeling summarized in Section 3.1.2.2.1 and detailed in Appendix 3b indicates an average recharge rate of about 1 mm/yr (0.04 in./yr) through the disposal units in their closed configuration, assuming an average annual precipitation of 36 cm (14 in./yr), a fully vegetated cover with a maximum rooting depth of 1 m (3.3 ft). The modeled recharge rate is less than the 5 mm/yr (0.2 in./yr) indicated by moisture measurements in an open pit. This discrepancy reflects the importance of transpiration in water balance at MDA G, which is absent in open pits. While the lower recharge rate modeled may be anticipated when pits are closed and the vegetative cover is fully developed, the larger recharge rate consistent with *in situ* measurements was selected for the base case unsaturated transport model. Steady state recharge of this magnitude was considered to be a reasonable simplification based on the information available, which is briefly summarized below.

The recharge fluxes through the Bandelier Tuff have been estimated using a variety of field, laboratory, and computational techniques, the most relevant of which were summarized in Section 2.1.5.3. Interpretation of the available data supports the conceptual model of aqueous-phase transport that recognizes that moisture recharge is generally slow within the mesa, but is also quite variable. Recharge is affected by natural

characteristics and manmade alterations. Seasonal wetting and drying cycles maintain moisture contents (up to 20 percent) in the top few meters of the mesa that are higher than those found at greater depths (less than 5 percent). While recharge through fractures near the mesa surface may occasionally occur, fracture flow does not appear to result in increased recharge at depths below Unit 2.

Surface disturbances associated with waste management activities may increase the moisture content near the top of the mesa, but a lasting effect of this increased moisture on deeper recharge has not been demonstrated. Extremely low moisture contents found 10 to 15 m (50 to 60 ft) below the mesa surface are likely to be the result of evaporation caused by air flow through fractures and surge beds, as supported by data on moisture content, matric suction, stable isotope ratios, and chloride content. The hydraulic properties of each unit of the Tshirege Member and the Otowi Member of the Bandelier Tuff are relatively uniform, with larger differences between units.

There are several aspects of the hydrology that, while potentially important, were ignored in the computational model of vadose-zone transport, due to a lack of data. Several simplifying assumptions were invoked in the computational model. As stated, the model assumes a uniform rate of infiltration through the mesa; this may be reasonable, considering that the disposal units themselves do not contain fractures, and are excavated either within or through the surge bed at the base of Unit 2, and the apparent effects that these features have on removing water from *undisturbed* mesa may not apply to the *disturbed* system. Each stratigraphic unit is modeled with uniform hydraulic characteristics corresponding to the arithmetic mean of the field data summarized in Table 2-7; spatial variability of hydrologic properties within units is ignored in the model.

While not explicitly included in the final three-dimensional computations, several potentially important features of the hydrologic system were evaluated to understand their effect on the overall analysis. The effect of fractures on moisture flow was considered, as was evaporation through in fractures and surge beds.

In addition, uncertainties in material properties and structure were evaluated. The details of the geology beneath MDA G were shown in Figure 2-8. The base of the Bandelier Tuff lies directly over the Cerros del Rio Basalt and has a westerly dip beneath the mesa. The Guaje Pumice Bed at the bottom of the Bandelier Tuff appears to thin and may disappear completely toward the east end of the mesa. The characteristics of the interface may have significant consequences for lateral diversion of groundwater. The hydrologic characteristics of the Cerros del Rio Basalt, which makes up a substantial portion of the vadose zone, are not known. Variations in basalt properties and Guaje Pumice Bed dip and thickness were evaluated to ensure that the 3-dimensional model was conservative.

3.3.2.1.2 Mathematical Model Selection

The FEHM (Finite Element Heat and Mass) computer code was used to implement the conceptual model of vadose-zone transport. The code was developed at LANL to simulate the flow of subsurface air and water, and the transport of heat and mass (e.g., radionuclides). It has been applied to the proposed high-level nuclear waste repository site at Yucca Mountain in Nevada, which is hydrogeologically similar to MDA G. FEHM can be run in one-, two-, or three-dimensional geometries to represent flow and transport in heterogeneous porous fractured media of varying degrees of saturation. To calculate flow and transport through the vadose zone, FEHM solves mathematical equations that describe the conservation of mass for air, water, and contaminant radionuclides, and of energy. FEHM accounts for solute transport by advection and dispersion. The advection-dispersion equation accounts for sorption of solutes to materials.

The parameters used to describe flow and transport within regions of the grid include many of the characteristics of the vadose zone discussed in Section 2.1, including: radionuclide distribution coefficient, saturated hydraulic conductivities, and the matric potential and relative conductivities described by the van Genuchten parameters. The code parameters and previous calibration studies are described in detail elsewhere.[111] Although FEHM has the capability to calculate water vapor flow and transport which have

been suggested as potentially important, the data required to support such modeling are not yet available. The grid and material properties used to model the vadose zone within the region considered in the PA and CA are described below.

3.3.2.1.3 Computational Grid

The 3-dimensional grid used to model vadose-zone transport relied on field data to realistically portray the surface and subsurface geology of the region. The surface topography was defined using 0.6 m (2 ft) topographic contours from the LANL Facility for Information Management and Display (FIMAD). The top and bottom surfaces of the Otowi and Tshirege Members were defined at 15.2 m (50 ft) spacings (northing and easting) obtained from the LANL site-wide geologic model.[112] Data from many of the cores recovered from boreholes at MDA G were used to define Units 2, 1vc, the Cerro Toledo Interval, and the Guaje Pumice Bed.[112] These data were supplemented by outcrop observations to define the Unit 2/Unit 1vu contact. In all, 149 data points were available for defining the Bandelier Tuff in the three-dimensional grid. Not all stratigraphic units were equally-well defined; a parameter study was performed to evaluate the sensitivity of the calculations to the definition of the more poorly-defined layers. The number of points available to define each unit were as follows:

- 76 points for Unit 2;
- 30 points for Unit 1vc;
- 25 points for Unit 1g;
- 14 points for the Cerro Toledo Interval; and
- 4 for the Guaje Pumice Bed.

These points were interpolated to form surfaces using the Stratigraphic Geocellular Modeling (SGM) software.[113] Unit 1vu, which is poorly represented by core logs, was defined as a parallel 7.6 m (25 ft) layer above Unit 1vc. In the absence of specific field data, the Puye Formation was defined as a flat 30 m (100 ft) thick layer at the base of the vadose-zone model. The water table occurs at the bottom grid boundary, at an elevation

Pits were defined in the grid with nodes outlining the surface perimeter, and with a set of internal nodes down the centerline at a depth of 7.6 m (25 ft). These internal nodes were assigned the properties of crushed tuff and the radionuclide flux terms calculated using the surface-contaminated waste source term model. Figure 3-14 shows the pit boundaries, internal pit nodes, and mesa edge nodes used in the grid. A comparison of this figure and Figure 2-26 indicates the realistic manner in which the site was simulated in the model.

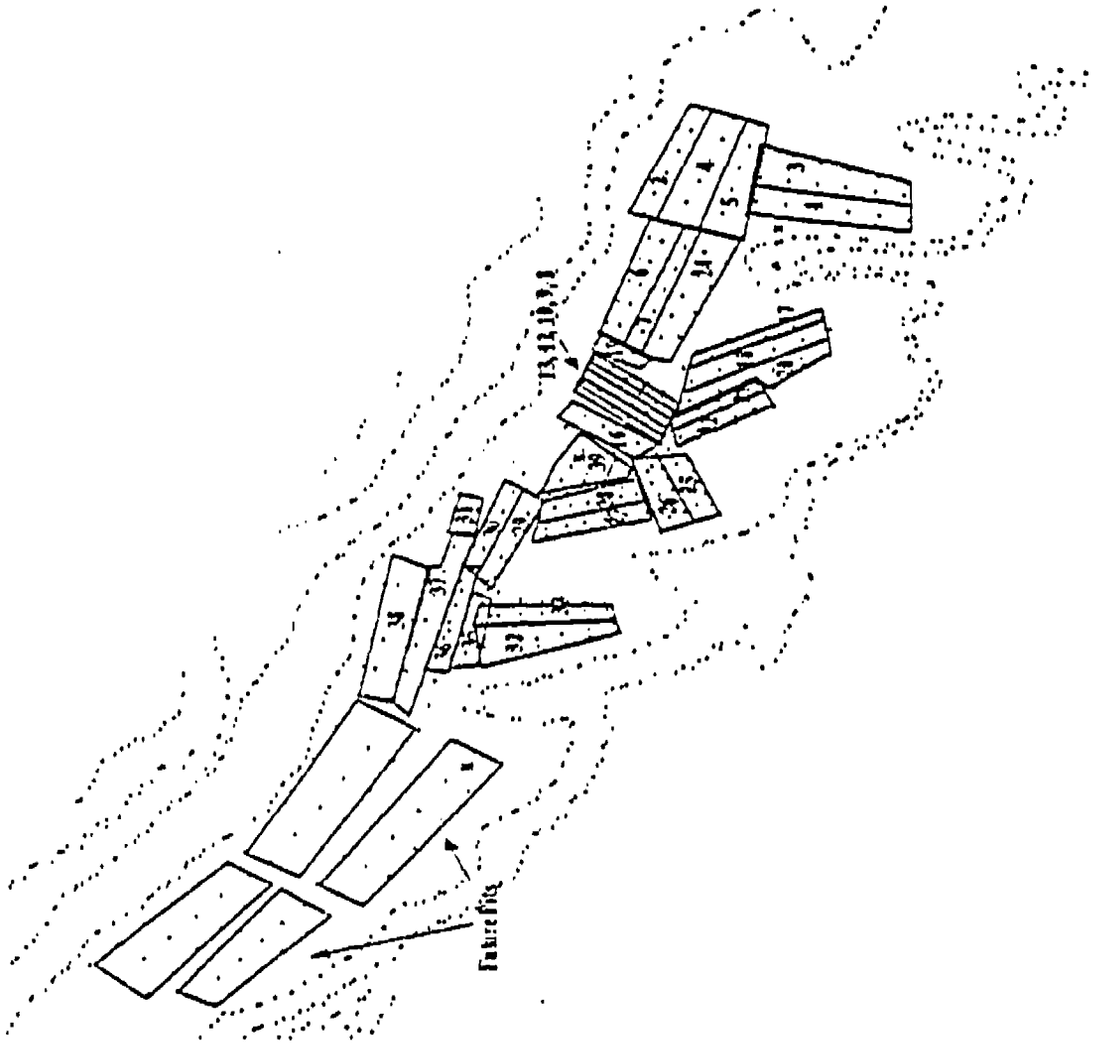

Figure 3-14 *Pit boundaries, internal pit nodes, and mesa edge nodes for the three-dimensional vadose zone calculations*

Table 3-6 lists how the various segments of the inventory discussed in Section 2.3 and Appendix 2e were distributed among the pits shown in Figure 3-14. The aqueous dissolution source term described in Section 3.1.2.2.1 and Appendix 3d was imbedded within FEHM, and computed directly in the transport calculations.

Table 3-6 Distribution of inventory in modeled pits

Inventory Segment	Modeled Pits Containing Inventory
1957 - 1970	Pits 1- 6; shafts located west of Pits 2 and 4
1971 - September 25, 1988	Pits 7 - 36, except pits 30 and 31; shafts west of Pit 16
September 26, 1988 - 1995	Pits 30, 31 and 36 - 39; shafts west of Pit 22
1996 - 2044	Four large pits shafts west of Pits 37 and 38

3.3.2.1.4 Boundary Conditions

A relatively complicated set of boundary conditions was required to define the region of interest described in Figure 3-12, which includes not only Mesita del Buey but also the adjacent canyons, all to the depth of the regional aquifer. For the base case, the surface of Mesita del Buey was assigned a 5 mm/yr (0.2 in./yr) infiltration rate, while Pajarito Canyon and Cañada del Buey had recharge rates of 50 mm/yr (2 in./yr) and 1 mm/yr (0.4 in./yr), respectively. These values were chosen on the basis of field data described in Section 2.1.5. The sides of the mesa were represented as evaporative boundaries. The bottom of the grid, representative of the regional aquifer, was assigned a fixed saturation of 99 percent. Figure 3-15 shows the background saturation field resulting from these boundary conditions. The outline of the mesa is well defined, reflecting the general topographic contours seen in Figure 3-12. The relatively moist alluvium in Pajarito Canyon shows up as green, as does the saturated boundary condition at the bottom of the grid.

To understand the potential sensitivity of the results to the 5 mm/yr (0.2 in./yr) steady-state percolation, two variations on steady-state infiltration rate through Mesita del Buey were considered, 1 mm/yr (0.04 in./yr) and 10 mm/yr (0.4 in./yr). Transient input was also evaluated in preliminary 2-dimensional calculations; the results will be reviewed later in this section.

3.3.2.1.5 Transport Properties

Each node of the computational grid (identified in Figure 3-15) was assigned the hydrologic values characteristic of the specific geologic material being modeled. These values are summarized in Table 3-7.

Table 3-7 Hydrologic properties used in the vadose-zone transport model

Geologic Material	Ksat (cm/s)	Porosity	van Genuchten Parameters		
			θ r	α	N (cm^{-1})
Unit 2	4.27E-04	4.81E-01	1.3E-02	6.0E-03	1.9E+00
Unit 1vu	1.48E-04	5.17E-01	2.0E-03	3.0E-03	1.9E+00
Unit 1vc	1.67E-04	5.09E-01	9.0E-03	3.3E-03	1.6E+00
Unit 1g	1.88E-04	4.80E-01	6.0E-03	5.3E-03	1.7E+00
Cerro Toledo	8.65E-04	4.73E-01	8.0E-03	1.5E-02	1.5E+00
Otowi Member	2.49E-04	4.35E-01	1.9E-02	5.9E-03	1.7E+00
Guaje Pumice	1.5E-04	6.67E-01	0.0E-00	8.1E-04	1.0E+00
Basalt Matrix	9.7E-05	1.0E-04	6.6E-06	3.8E-02	1.4E+00
Basalt Fractures	9.7E+02	1.0E-04	3.0E-06	3.8E-02	1.4E+00
Puye Formation	4.6E-03	2.5E-01	4.5E-02	1.5E-01	2.6E+008

Very little hydrogeologic data are available to characterize the Cerros del Rio Basalt. Samples collected from the basalt layer are extremely variable in texture, and indicate the layer may be highly fractured. To compensate for the lack of site-specific data, hydrologic properties were conservatively assigned to the basalt to reflect a one year travel time through the layer. The basalt was modeled as an "equivalent continuum," which combines hydrologic features of matrix and fracture flow.

Few data are available for the Puye Formation, although the general flow characteristics are more certain than the Cerros del Rio Basalt. The Puye Formation is a sandy conglomerate with cobble and gravel, whose hydrologic properties are expected to resemble those of coarse sand. The hydrologic properties assigned to the Puye Formation are typical of coarse sand, with a reduced porosity to account for the larger cobbles.

The distribution coefficients used in the vadose-zone transport calculations included the site-specific values derived experimentally for several radionuclides, as discussed in Section 2.1.6. Sorption coefficients measured for Am, Np, Pu, Tc, and U using synthetic pore water were used to model transport of those nuclides through all units of the Bandelier Tuff. Sorption coefficients measured for Np, Pu, Tc, and U using Water Canyon Gallery water and Unit 2 core samples taken from depths ranging from 3.3 to 3.7 m (11 to 12 ft) were used to model transport within the disposal units. Distribution coefficients measured in devitrified tuff from Yucca Mountain[22] were assigned to all of the remaining radionuclides. No sorption was assumed in the region of the grid representing the Cerros del Rio Basalts. The upper section of the Puye Formation was assigned measured sorption coefficients for Water Canyon Gallery on the assumption that the upper section of the Puye Formation, while unsaturated, would still have pore water similar to saturated samples. These same values were used in the three-saturated transport calculations. Table 3-8 summarizes the sorption coefficients used in the vadose-zone transport calculations. The radionuclides in the table are those that were identified in Section 3.1.2.1 as being maintained in the groundwater pathway analysis inventory.

The liquid diffusion coefficient used in the vadose-zone transport model varied with the degree of moisture saturation, reflecting the results of studies showing that diffusion decreases with decreasing saturation. In the calculations described here, the diffusion coefficient decreased from 10^{-9} m^2/s (1.1×10^{-8} ft^2/s) at saturation to 10^{-5} m^2/s (1.1×10^{-4} ft^2/s) at a moisture content of 0.1 percent. To account from hydrodynamic dispersion, the model assumed a vertical dispersivity of 1 m (3.3 ft) and a horizontal dispersivity of 0.1 m (0.33 ft).

3.3.2.1.6 Parameter Studies

The base case vadose-zone transport model described in the previous sections was characterized by a steady-state recharge rate, specific boundary conditions, and unit-average hydrologic properties. Several one- and two-dimensional parameter studies were performed using FEHM to investigate how the base case parameters might affect the outcome of the analysis, and to ensure that the base case was conservative in that it would result in the fastest and largest fluxes into the saturated zone grid (described later in this

section), while using parameters that are reasonable for the site. Each parameter study summarized below (and detailed in Appendix 3g) used the properties and dimensions applied in the 3-dimensional base-case model, unless otherwise indicated.

Table 3-8 Sorption coefficients used in the vadose-zone transport calculations

Radionuclide	Kd (mL/g)	
	Intact Tuff	Disposal Pits
Ac-227	130	130
Ag-108m	90	90
Am-241, -243	2359	2050
Ba-133	946	946
C-14	0	0
Cd-113m	80	80
Cf-249, -252	130	130
Cm-244	50	50
Co-60	0.45	0.45
Cs-137	428	428
Eu-152, -154	50	50
Gd-148	50	50
H-3	0	0
Hf-182	500	500
I-129	0	0
K-40	15	15
Mo-93	4	4
Nb-93m, -94	100	100
Np-237	2.25	7.5
Pa-231	50	50
Pb-210	25	25
Pu-238, -239, -240 -241, 242	4.13	711
Ra-226, -228	200	200
Si-32	35	35
Sm-147, -151	50	50
Sr-90	116	116
Tc-95m, -99	0	0
Th-229, -230, -232	500	500
Ti-44	500	500
U-233, -234, -235, -236, -238	2.43	2.61

Transient Infiltration

The effects of transient infiltration through pits were investigated to ensure that the steady-state approximation was applicable. These calculations simulated transient infiltration events by adding year-long "pulses" of moisture at the top of the computational

grid (i.e., into the disposal units). Four cases were considered, taken from the Monte Carlo percolation calculations performed for the surface-water balance model reported in Appendix 3c. Four high-percolation cases were selected for input in the two-dimensional FEHM transient-input parameter study; two cases (Case 6 and Case 17) had the highest number of years with consecutive percolation, and were selected as a worst-case. The maximum single-year percolation calculated in the water balance model was 105 mm (4.1 in.), with an associated percolation rate of 5.8 mm/yr (0.23 in./yr). The values and relevant statistics describing the four transient cases considered are shown in Table 3-9.

Table 3-9 Statistics of pit percolation used in the four transient calculations

Parameter	Case 1	Case 2	Case 6	Case 17
Average Pit Percolation Rate (mm/yr)	5.49	5.27	5.50	5.81
Maximum Pit Percolation Rate (mm/yr)	99.2	88.1	90.8	105.4
Percentage of years with no percolation	73.6	73.9	73.6	72.6

Transport times for the 5.81 mm/yr (0.229 in./yr) percolation rate matched the base-case steady-state 1 mm/yr infiltration rate to within three percent. The average pit percolation was 5.5 mm/yr (0.22 in./yr), with a maximum of nearly 10 cm/yr (4 in./yr). Most years showed zero net infiltration. Several transient moisture pulses representing wet years in the Monte Carlo simulations were used as boundary conditions for the pits and results were compared with the 5.5 mm/yr (0.22 in./yr) steady-state case. The results are compared in Table 3-10.

Table 3-10 Comparison of ^{14}C arrival times and peak concentrations for the steady-state and four transient-flow simulations

Case	First Arrival (yr)	Cumulative Moles to Pumice at 5000 years
Steady	800	8.05E+06
Case 1	940	7.81E+06
Case 2	1080	7.55E+06
Case 6	1000	7.88E+06
Case 17	950	7.99E+06

The results of the transient-recharge parameter study showed that the effects of the high annual percolation were reflected in transport times only for the first few hundred years, and only in the upper-most units of the Tshirege Member of the Bandelier Tuff. As Figure 3-16 shows, by the time the moisture reaches the base of the Otowi Member, the effects of the transient input (dashed lines) on saturation within the matrix are within 3 percent of the steady-state case (solid horizontal line). An important outcome of this study is that the steady-state boundary condition resulted in a faster groundwater travel time through the grid. Also, concentrations of tracer contaminants (i.e., ^{14}C) were about 10 percent higher in the steady-state case. These results suggest that the steady-state approximation is both valid and conservative for modeling transport through the vadose zone at MDA G.

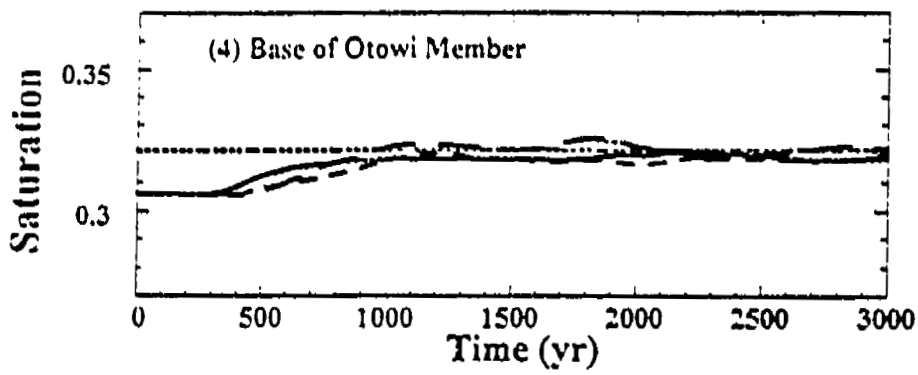

Figure 3-16 Moisture profiles from transient input compared with 5 mm/yr steady-state input.

Material Properties

Several 2-dimensional steady-state simulations were performed using FEHM to determine the sensitivity of contaminant transport to variations in hydrologic properties and in boundary conditions. The importance of uncertainties in the material properties of the Guaje Pumice Bed, the Cerros del Rio Basalt, and the Puye Formation were analyzed. The effect of moisture boundary conditions in Cañada del Buey and Pajarito Canyon was also investigated, to examine the uncertainty in moisture content in the canyon alluvium.

To examine the potential importance in uncertainties in material properties, hydrologic properties determined from a single core sample of the Guaje Pumice Bed were used, and associated uncertainties were evaluated. Without any credible site-specific characterization data for the Cerros del Rio Basalt, they were assigned the properties used to characterize the basalt beneath the Radioactive Waste Management Complex at the Idaho National Engineering Laboratory;[115] no transport properties were assigned to these lower units. The characteristics that were varied in this study included:

- The thickness of the Guaje Pumice Bed (0, 1, 3.7 and 12 m);
- The slope of the Guaje Pumice Bed (0, 0.5, 1, and 2 degrees);
- The saturated hydraulic conductivity of the Guaje Pumice Bed (1.33×10^{-4} and 8.7×10^{-3} cm/sec) ; and
- The saturated hydraulic conductivity of the Cerros del Rio Basalt (8.7×10^{-5} and 8.7×10^{-3} cm/sec).

A potentially significant outcome of this study is that the Guaje Pumice Bed, which dips 0.5 to one degree to the southeast, can promote significant lateral flow of moisture toward Pajarito Canyon. The lateral flow depends upon the degree of dip, the boundary conditions applied to Cañada del Buey and Pajarito Canyon, and the permeability of the underlying basalts. The thickness of the pumice layer had a relatively small effect on lateral flow, with thicker layers resulting in slower flows. Similarly small effects were found with variations in slope of the pumice layer.

Of the properties and boundary conditions investigated, the saturated hydraulic conductivity of the basalt underlying the Guaje Pumice Bed had the strongest influence on

flow. When the basalt conductivity data were used, the basalt served as a barrier to downward vertical flow, resulting in almost exclusively lateral flow in the Guaje Pumice Bed. When the basalt conductivity was increased (to account for open fractures, for example), moisture flowed down into the basalt from the pumice, and lateral flow was greatly diminished. Figure 3-17 illustrates the result of varying the basalt properties. The blue in the figure shows the flow of water, with the red background representing the solid matrix. All of the geologic units with their unique properties are represented in the calculations; this plow is simplified to illustrate the water plume. The top figure shows that, when basalt matrix properties are modeled, water entering from the top of the mesa spreads laterally within the basalt. The center figure shows the effect of a source of moisture (e.g., beneath Pajarito Canyon) added laterally (e.g., along the Guaje Pumice Bed; although not evident in this figure, lateral flow from the center of the mesa stagnates when it encounters the lateral flow from Pajarito Canyon. Finally, the bottom figure illustrates the effect that fracture properties (modeled as a equivalent continuum) have on moving water downward through the basalt.

As a result of this analysis, it was determined that the fracture properties for the basalt would be used in the final three-dimensional computations, given that this would affect the shortest travel times to the regional aquifer.

Evaporation along Fractures and Surge Beds

As discussed in some detail in Section 2.1.5, there appears to be evaporation occurring deep within Mesita del Buey, most likely along fractures and the surge beds at the base of Unit 2 of the Tshirege Member of the Bandelier Tuff. A set of two-dimensional FEHM calculations was conducted to model the effects of evaporation from the mesa sides, within fractures in Units 2 and 1vu, and within the surge beds at the base of Unit 2. The computational grid represented a 25 m wide, 5 m tall block of tuff, either Unit 2 or Unit 1vu, using the average properties previously discussed. The general configuration is shown in Figure 3-18. The top boundary represents the mesa top, the right boundary represents the mesa wall, and the left boundary represents the interior of the mesa.

evaporation case. This corresponded with an order-of-magnitude decrease in the net steady infiltration rate.

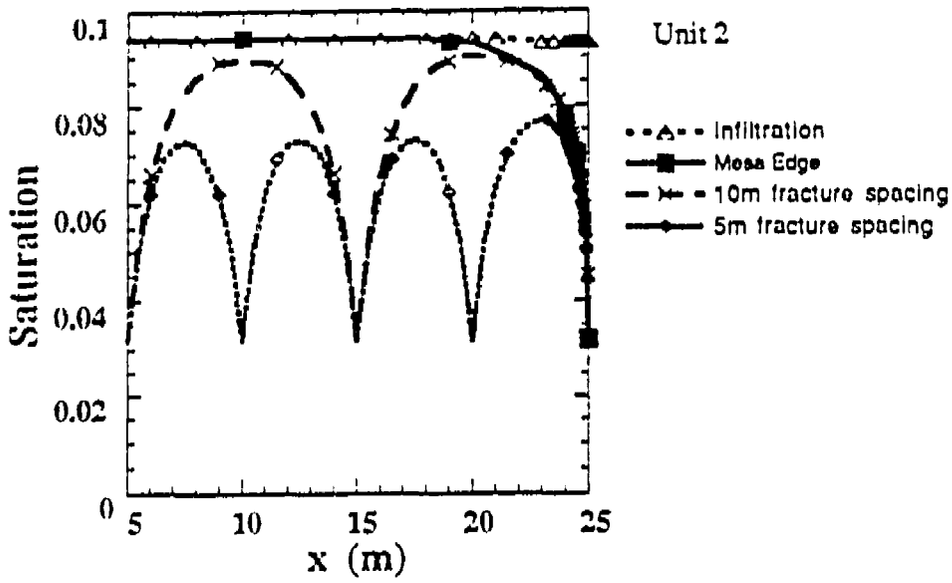

Figure 3-19 Resulting Saturation Profiles for Evaporation along a Mesa Edge (right side) and from fractures with 5-m and 10-m spacing, Unit 2.

Another calculation was performed to mimic evaporation within the surge beds at the base of Unit 2, abutting Unit 1vu. The two layers were modeled with their appropriate hydrologic properties and thicknesses. Uniform infiltration at a rate of 0.1 cm/yr (0.4 in./yr) was applied along the upper boundary. The surge bed was modeled as a region of low saturation again corresponding to a relative humidity of 50 percent. Figure 3-20 shows the steady-state saturation for this case compared with a no-evaporation case. Saturation values throughout both units were significantly lowered by the fixed low saturation at the interface.

These simulations indicate that evaporation along fractures and surge beds can contribute to significant drying of Units 2 and 1vu, possibly causing the very low saturations seen in these units.

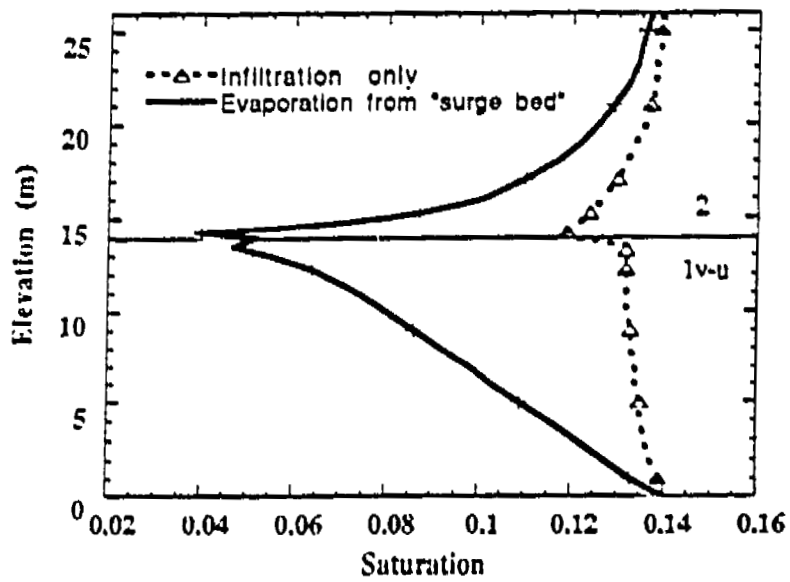

Figure 3-20 Resulting saturation profile for evaporation along the "surge beds" at the Unit 2/1vu interface compared to that for infiltration alone.

Single-Fracture Fills and Coatings

A study was conducted using FEHM to investigate the effect of fracture fills and coatings on moisture flow through the MDA G subsurface.[116] The model is illustrated in Figure 3-21 with a single vertical fracture centered in an otherwise uniform block of matrix assigned the properties of Unit 1vu. There were four parts of the system: the matrix, the fracture, the fracture coating and the fracture fill. The fracture aperture and spacings are average values from local measurements. The fracture was modeled with hydrologic properties of a highly porous and highly permeable sand.

When present, fracture coating and fracture fills were assigned clay parameters from the literature because there are no values available for the local clays and caliches.

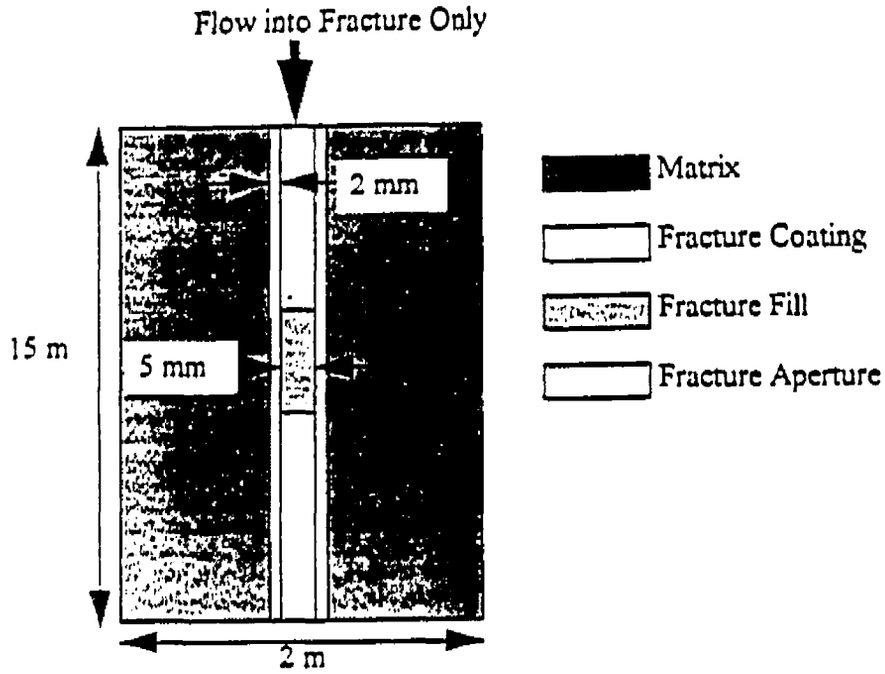

Figure 3-21 System configuration for fracture fill and coating study

Two different inflow conditions were used at the top of the fracture. One assumed a constant rate of 5 cm/day (2 in./day) to represent an extreme event for a single day. However, this inflow rate was applied for the entire time period of the simulations, often up to 100 days. The other inflow condition used was a ponded condition at the top of the fracture applied for 0.5 days, followed by removal of the source. This was effectively an infinite source of water for 0.5 days.

The following variations were considered, with the results indicated:

- No coating, no fill: no fracture flow;
- Continuous fracture coating, no fill: fracture flow only when hydraulic conductivity of the coating was four orders-of-magnitude less than the conductivity of the matrix;
- Discontinuous fracture coating, no fill: insignificant fracture flow beyond breaks in coating;
- Continuous fracture coating, fill within fracture: no fracture flow;
- Continuous fracture coating, fill at top of fracture: no fracture flow; and
- No coating, fill within fracture: no fracture flow beyond fill.

This study supports the conclusion that fractures will not sustain liquid flow under the conditions modeled, which represent conditions at MDA G.

Dual Permeability Matrix/Fracture Flow

A 1-dimensional sensitivity analysis was conducted with FEHM to determine whether including fractures in the upper units of Mesita del Buey would result in faster flows.. Both steady-state and transient infiltration patterns were evaluated. Also, the hydraulic conductivities of each geologic unit (no fractures) in the 1-dimensional column were varied within the range of field data to establish the minimum and maximum travel times through the units.

These parameter studies were performed using a 1 m (3.3 ft) wide, 1-dimensional cross-sectional column of the three-dimensional grid. Two base-case calculations were performed using the unit-average matrix properties assigned in the 3-dimensional computations; one calculation represented the undisturbed tuff with a 1 mm/yr (0.04 in./yr) infiltration rate, while a second represented the disposal pits with a 5.5 mm/yr (0.22 in./yr) infiltration rate.

The steady-state, matrix-only (i.e., no fractures) calculations based on the assumption that the unit-average hydraulic properties listed previously applied. The results represent the average travel time through the entire column. Minimum groundwater travel times through each unit were calculated by assigning the maximum measured saturated hydraulic conductivity; maximum travel times through each unit were calculated by using the minimum measured value. Each unit was evaluated separately, with all other units maintaining the average values. Maximum travel times through the entire column were also calculated, by assigning all units their respective minimum conductivities. The average, minimum, and maximum hydrologic properties used in the analysis are listed in Table 3-11.

Table 3-11 Saturated hydraulic conductivity ranges for geologic materials

Geologic Material	Ksat (m^2)		
	Minimum	Mean	Maximum
Crushed Tuff	1.05E-13	2.95E-13	9.40E-13
Unit 2	9.63E-14	4.46E-13	4.01E-12
Unit 1vu	8.48E-14	1.51E-13	1.01E12
Unit 1vc	2.18E-14	1.70E-13	1.49E-12
Unit 1g	3.44E-14	1.92E-13	4.47E-12
Cerro Toledo	5.39E-14	8.82E-13	4.93E-12
Otowi Member	1.26E-14	2.53E-13	8.94E-12
Guaje Pumice	no data	1.53E-13	no data
Basalt	no data	1.00E-13	no data

After base-case flow fields were established for the two columns, fracture parameters were added to Unit 2 and Unit 1vu in the undisturbed tuff column, and to Unit 1vu in the pit column (Unit 2 is generally entirely excavated for disposals). Fractures were modeled using the dual porosity/dual permeability option of FEHM. The fracture spacing and aperture were assigned values of 1.15 m (3.8 ft) and 3 mm (0.1 in), respectively, based on field measurements. Several values for van Genuchten properties for fractures were evaluated. In all but one case, the moisture flow in the matrix was larger (by 10 to 100,000 times) than the flow in the fracture. The van Genuchten parameters producing the greatest fracture flow, which was within the same order of magnitude as the matrix flow, were $\alpha = 0.03\ cm^{-1}$, $N = 1.5$, and $K = 7.5 \times 10^{-6}\ cm^2$. The moisture profiles for the unfractured and fractured intact tuff columns were nearly identical (within three percent), as were the groundwater travel times to the basalts (less than 300 years, slower in the fractured column).

Once a steady-state flow field was established for the fractured columns, transient infiltration simulations were conducted. The transient infiltration case with the greatest annual percolation referred to previously provided input to these calculations. Transient

infiltration into fractured and unfractured columns was calculated for a period of about 5,000 years. Moisture as a function of depth was compared between the fractured steady-state and fractured transient cases, between the transient fractured and non-fractured simulations, and between fractures and the matrix in the fractured transient simulations. The results of this study showed that fracture flow was not significant in the steady-state simulations. Nor did fracture flow significantly alter flow fields or transit times in the transient simulations. Based on these results, it was determined that the two-dimensional models used in other parameter studies, and the three-dimensional model used to calculate vadose-zone transport, could rely on the steady-state approximation. While fractures in the upper tuff units were shown to be inconsequential to the final results in the one-dimensional column studies, the three-dimensional model did include fracture-type properties for the basalt to force rapid transport through this uncharacterized layer.

3.3.2.2 Results of the Vadose Zone Transport Calculations

The 3-dimensional vadose zone transport calculations were run on a subset of radionuclides that were expected to be transported in the shortest period of time due to their low sorption coefficients. This subset included ^{14}C (Kd=0), ^{129}I (Kd=0), ^{237}Np (Kd=0.151-7.5), ^{99}Tc (Kd=0), and ^{238}U (Kd=2.43-4.83). The base case featured a steady flow field: 5 mm/yr (2 in./yr) for the mesa top, 1 mm/yr (0.4 in./yr) in Cañada del Buey, and 50 mm/yr (20 in./yr) in Pajarito Canyon. The calculations were run for a period of 10,000 years to ensure an understanding of the long-term potential for aqueous-phase transport. Both vertical flux to the water table and lateral flux to the mesa sides were examined. This calculation showed that only the completely nonsorbing (i.e., Kd=0) nuclides were transported to either the water table or to the mesa side over a 10,000-year time frame. This result enabled the elimination of the remaining nuclides from further consideration, because their sorption coefficients are larger than those of either ^{237}Np or ^{238}U. This screening technique includes the consideration of all daughter products in the radionuclide decay chains.

Transport calculations with different flow fields using the maximum flow field were performed to understand the sensitivity of the results to the percolation boundary conditions. (10 mm/yr for the mesa top, 5 mm/yr in Cañada del Buey, and 100 mm/yr in Pajarito Canyon) were performed to ensure conservatism in the model. Again, neither radionuclide was transported to the regional aquifer or to the sides of the mesa within 10,000 years.

3.3.2.2.1 Vertical Transport toward the Water Table

Figure 3-22 shows the total time-dependent flux of ^{14}C from the vadose zone to the saturated zone for the 4 inventory segments considered in the CA, referred to as: 1957 - 1970 (Oldest), 1971 - 1988 (71-88), 1988 - 1995 (Historic), and 1996 - 2044 (Future). These results are from the base case, steady flow field. The time of arrival and shape of the flux curves for ^{99}Tc and ^{129}I are qualitatively similar to and bounded by ^{14}C curves.

For each nuclide and each waste category, the flux increases through the 1,000-year compliance period. Beyond 1,000 years out to 10,000 years, peak fluxes have been captured for all nonsorbing radionuclides. No other radionuclides reach the saturated zone within 10,000 years.

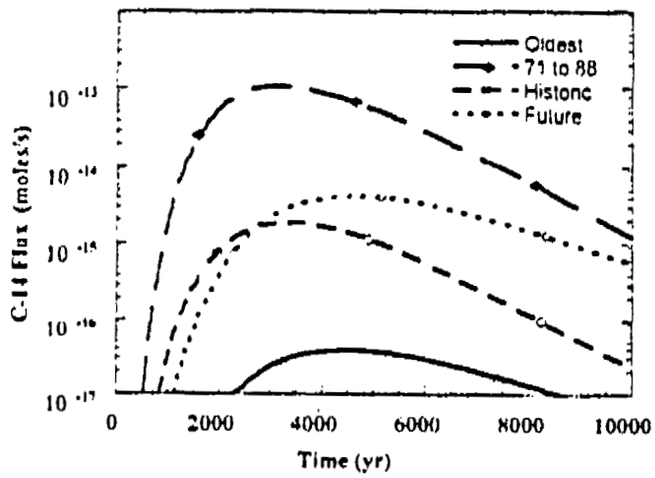

Figure 3-22 Total Flux of ^{14}C from the vadose zone to the saturated zone from the four source regions.

Figure 3-23 illustrates the effects of the various flow conditions considered to bound the base case, using ^{129}I flux curves as an example. The legend on the figure lists the infiltration boundary conditions, in mm/yr, on Mesita del Buey, in Cañada del Buey, and in Pajarito Canyon. For example, the base case of 1 mm/yr (0.04 in./yr) in Cañada del Buey, 5 mm/yr (0.2 in./yr) on Mesita del Buey, and 10 mm/yr (0.4 in./yr) in Pajarito Canyon would be identified as 5_1_10. The peak flux for the high-flow case (i.e., 10_5_100) occurred at about 1,000 years compared with about 2,5000 years in the base case, and had higher concentrations than the base case. Conversely, the peak flux in the low-flow (i.e., 1_1_20) calculation occurred several thousand years later than the base case, and the lower-concentration flux was dispersed over a much longer period of time.

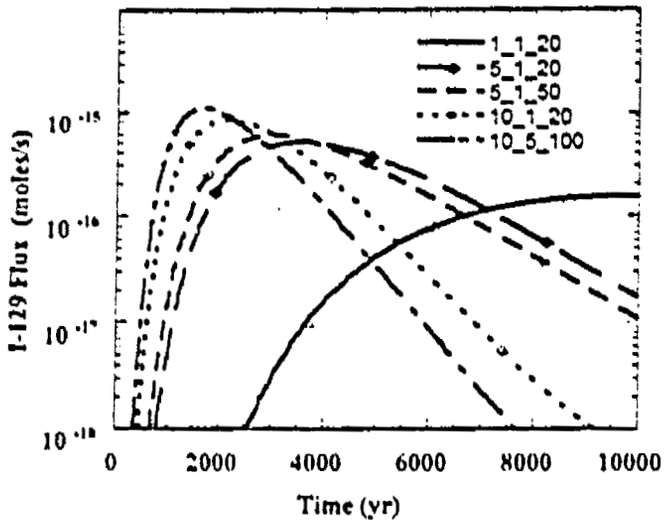

Figure 3-23 ^{129}I fluxes at the base of the vadose zone grid for several variations in flow fields

3.3.2.2.2 Lateral Transport toward the Mesa Sides

The lateral flux through the mesa sides adjacent to Cañada del Buey (north) and Pajarito Canyon (south) for the base case are shown in Figure 3-24, using ^{14}C as an example; fluxes for ^{99}Tc and ^{129}I are qualitatively similar. Fluxes associated with the lateral

transport of radioactivity from the 4 individual source terms considered in the CA [i.e., oldest (1957-1970), 1971-1988, historic (1988-1995), and future (1996-2044)], which includes the 2 considered in the PA [i.e., historic (1988-1995) and future (1996-2044). These calculated flux values are expected to greatly overestimate the true flux that might occur. The simulated lateral transport of the nuclides occurs because of the evaporative boundary condition imposed along the mesa sides. The very low, fixed saturation along the mesa sides causes a strong lateral pressure gradient which pulls water from the mesa interior toward the edges. This model ignores the evaporative processes that apparently occur within the fractures and surge beds, as discussed in Section 2.1.5. The effects of these deep-mesa evaporative processes would be expected to weaken the lateral pressure gradient caused by evaporation at the mesa side.

Additional conservatism in the lateral-flux pathway is introduced by the assumption that, immediately upon reaching the edge of the mesa, the radioactivity is instantaneously transported to the canyon alluvium. In reality, radionuclides would accumulate along the mesa edge rather than moving beyond, as water evaporates leaving the heavy, non-volatile solutes behind.

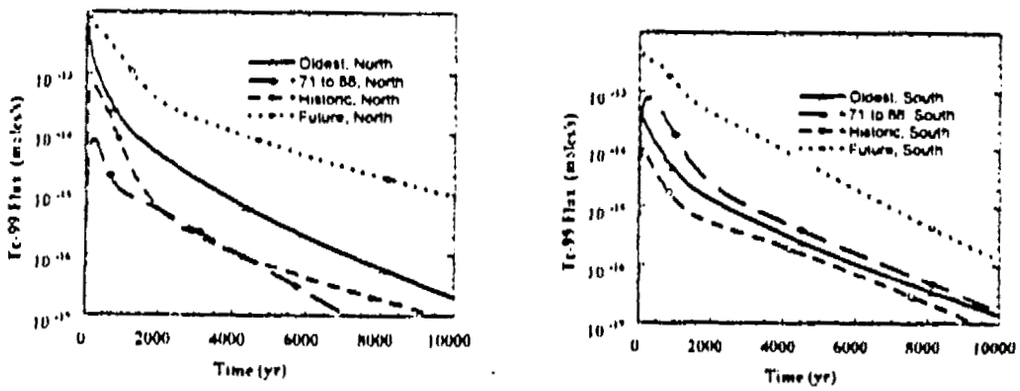

Figure 3-24 Lateral ^{14}C fluxes along the north (left) and south (right) walls of Mesita del Buey from the 4 CA source segments

Figures 3-25 shows the generic water fluxes calculated at the base of the vadose zone following lateral transport toward the south rim of the mesa adjacent to Pajarito Canyon and toward the north rim adjacent to Cañada del Buey. Separate calculations were performed for the two canyons. For Pajarito Canyon the percolation rate was 50 mm/yr (2 in./yr), and for Cañada del Buey the percolation rate was 1 mm/yr (0.4 in./yr). The flux was applied over areas in the two canyons adjacent to the historic pits. Figure 3-25 shows the resulting flux histories at the base of the vadose zone for the base case. As the figure indicates, much larger fluxes occur along the south wall adjacent to Pajarito Canyon.

In addition to the base case, high- and low-flow boundary conditions were considered in the lateral-transport pathway analysis. Larger and smaller fluxes occurred earlier and later for the high- and low-flow cases, respectively. These two cases, along with the base case, were run to bound the possible conditions at the site. Again, even the low-flow case, which produces the smallest fluxes, is considered conservative relative to what might really be expected to occur.

The generic fluxes shown in Figure 3-25 were multiplied by the scaling factors listed in Table 3-12 to determine the fluxes for the ^{14}C, ^{99}Tc, and ^{129}I. The table lists the scaling factors for the low-flow, base case, and high-flow boundary conditions.

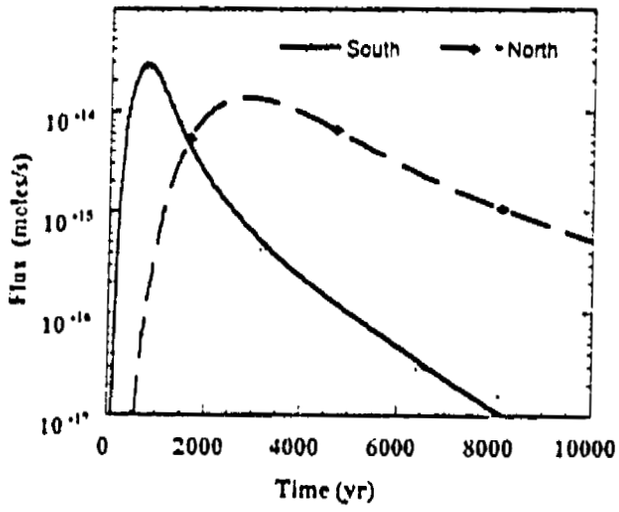

Figure 3-25 Generic fluxes at base of grid from lateral fluxes through north and south mesa walls, then transported vertically, base case

Table 3-12 Scaling factors to correct generic concentration breakthrough curve for each nuclide and waste category for the base case, and low- and high-flow fields

Inventory	^{14}C			^{129}I			^{99}Tc		
	Base	Low	High	Base	Low	High	Base	Low	High
1957-1970	1E-04	6E-05	1E-04	2E-01	4E-02	3E-01	4E-01	9E-02	5E-01
1971-1988	1E+00	5E-01	2E+00	5E-01	2E-01	6E-01	8E-01	4E-01	9E-01
1988-1995	4E-02	1E-02	6E-02	2E-02	5E-03	3E-02	1E-01	5E-02	1E-01
1996-2044	9E-02	3E-02	2E-01	5E-03	2E-03	7E-03	4E+00	1E+00	6E+00

3.3.2.3 Saturated Zone Transport Model

The characteristics of the regional aquifer considered in modeling saturated transport of radionuclides in the aquifer were presented in Section 2.1.5. A 3-dimensional computational grid was developed for aquifer flows in a southeasterly direction toward the Rio Grande river. The FEHM code was used to calculate saturated transport through the grid. The regional aquifer is assumed to be contained by the Puye Formation, this formation consists of volcanic debris with cobbles, rocks, and boulders in a matrix of silts, clays, and sands.

The model of the saturated zone was simple, commensurate with the relatively limited data available for regional aquifer beneath MDA G. Only the upper 100 m (330 ft) of the regional aquifer was modeled. A 3-dimensional rectangular box was defined that extended from the western end of MDA G to the Rio Grande river. The box was oriented approximately perpendicular to the assumed groundwater flow potential. The region modeled was 9,800 m (32,000 ft) long, 1,300 m (4,000 ft) wide, and 100 m (330 ft) deep. Figure 3-26 is a diagram of the computational domain.

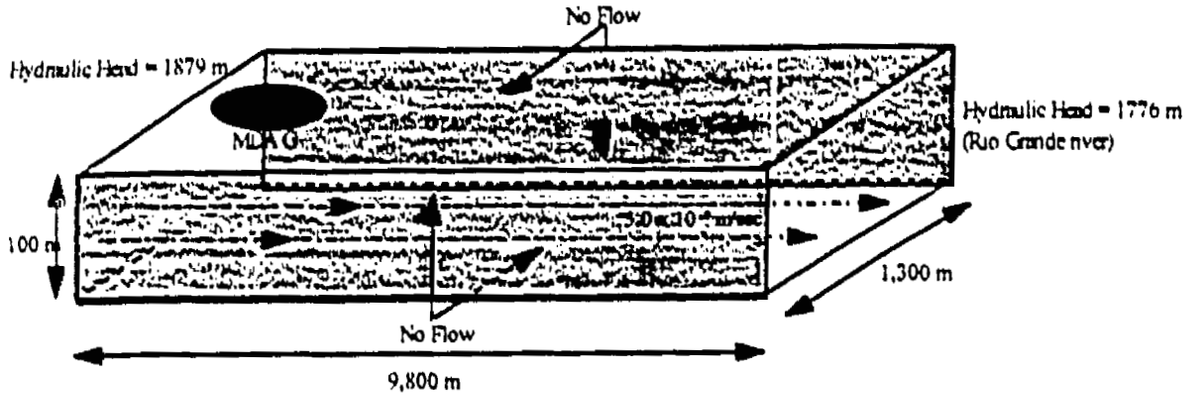

Figure 3-26 Computational domain of the Puye Formation for saturated transport calculations

The computational grid was rectangular, defined by a total of 19,580 nodes. The top, bottom, north side, and south side of the grid were assigned no-flow boundary conditions to minimize lateral dispersion and dilution. The east and west sides of the grid were assigned fixed hydraulic pressures corresponding to the assumed gradient. Figure 3-27 shows the computational grid used in the 3-dimensional saturated zone calculations.

Flow was modeled as homogeneous and isotropic with a velocity of 5.0×10^{-7} m/sec (52 ft/yr). Hydrologic properties of a coarse sand were assigned to the Puye Formation, with an intrinsic permeability of 4.7×10^{-12} m^2 (5.1×10^{-11} ft^2) and a porosity of 0.25. The diffusion coefficient for the saturated zone was assumed to be 1.0×10^{-9} m^2/sec (1.0×10^{-7} ft^2/sec), with a dispersivity of 20 m (66 ft) in the direction of flow and 2 m (6.6 ft) transverse to the flow. The area beneath MDA G was represented by grid elements that are 20 m (65 ft) wide in the direction of flow and 44 m (144 ft) wide in the direction perpendicular to the flow.

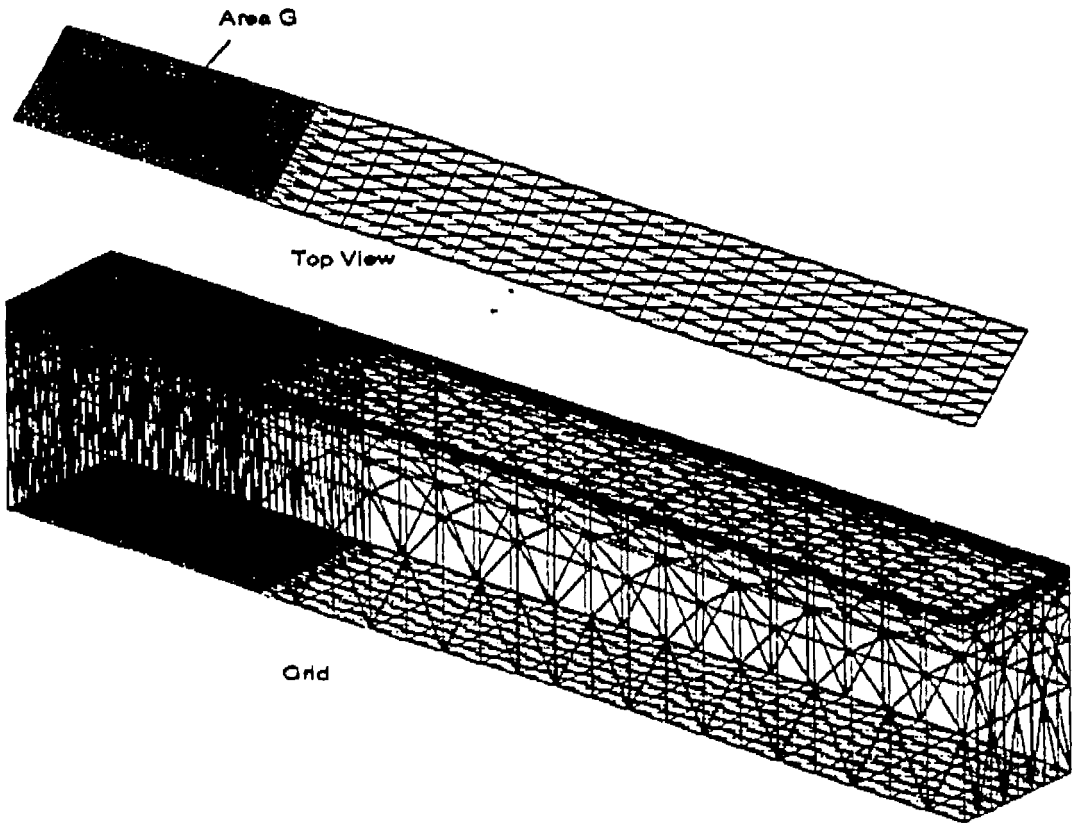

Figure 3-27 Three-dimensional finite element grid used for the saturated zone flow and transport calculations.

The flux of radionuclides calculated by the vadose zone transport model was input into the nodes representing MDA G. The fluxes were described by 28 spatial footprints, so that the spatial distribution produced by the various source regions was maintained. As an illustration of the interface of the vadose zone and saturated zone calculations, Figure 3-28 shows the concentrations of ^{129}I arriving at the base of the vadose-zone grid at 1,000-years. Concentrations for the 4 inventory segments considered in the CA are represented separately. Similar results were calculated for ^{14}C and ^{99}Tc. The plume from the oldest inventory is largest at this time, as the disposal units containing this inventory are on the eastern end of Mesita del Buey and are lowest in the stratigraphy.

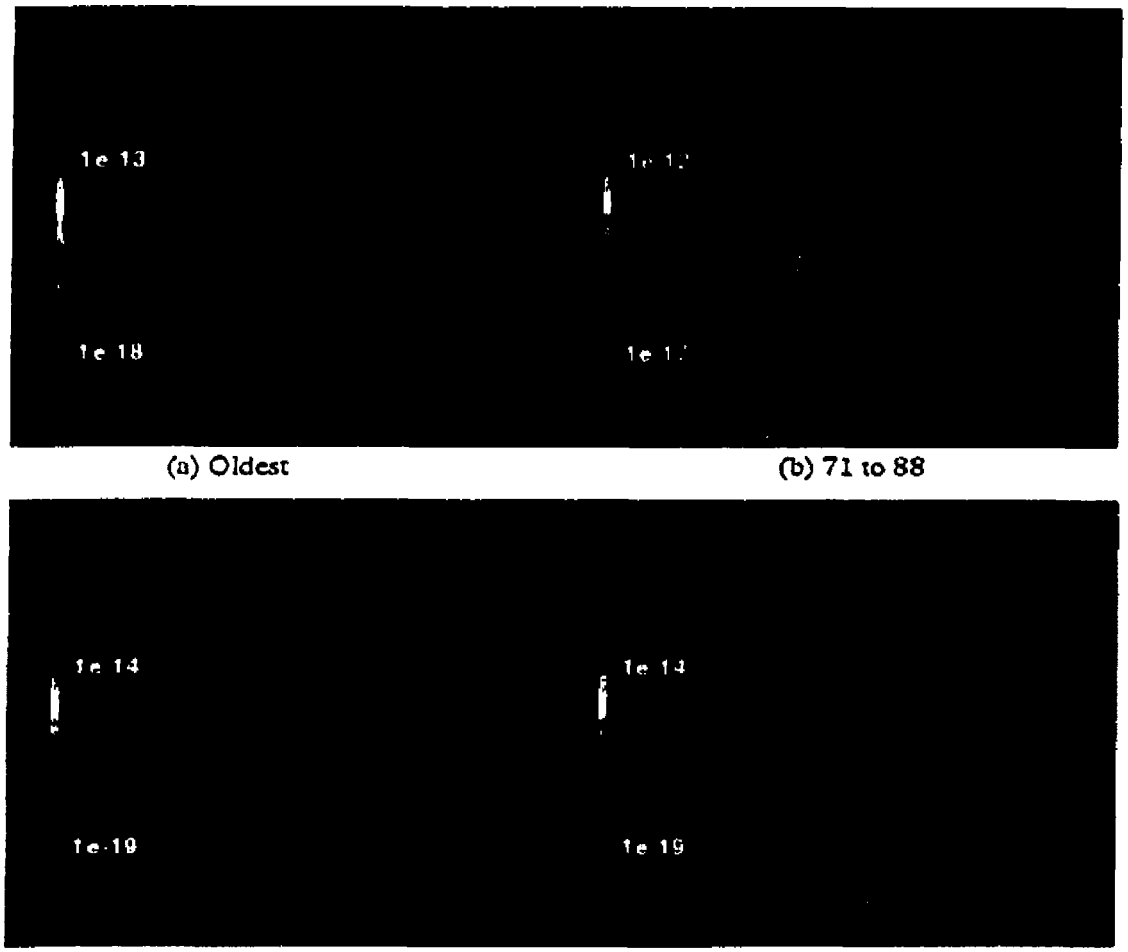

(a) Oldest (b) 71 to 88

(c) Historic (d) Future

Figure 3-28 Fluxes of ^{129}I reaching the base of the vadose zone grid at 1,000 years for the four different source regions, base case

3.3.2.4 Results of the Saturated Zone Transport Calculations

Figure 3-29 shows concentration profiles at two locations in the saturated zone, using the base-case vertical flux of ^{129}I from the historic inventory as an example. The two curves represent the point of maximum dose and the 100 m (330 ft) downgradient compliance point. The two curves have the same shape, but the lower concentrations 100 m (330 ft) downgradient location reflect the additional dilution and mixing that occurs. Aquifer dilution of vadose zone concentrations is approximately a factor of 500 between the maximum vadose zone concentration and the concentration at the 100 m (330 ft) downgradient compliance point.

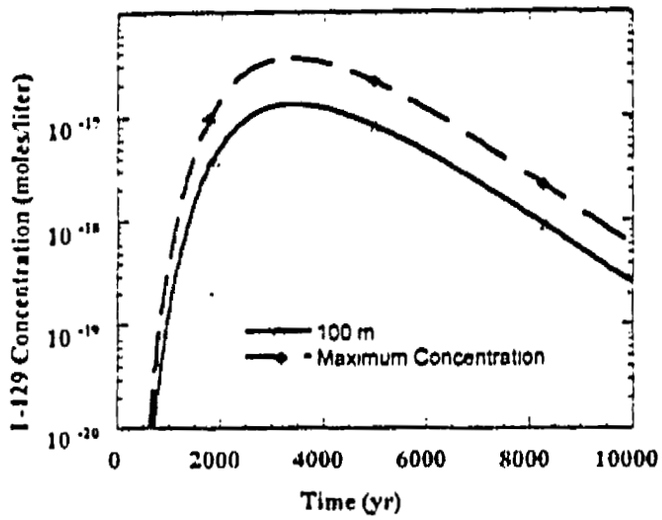

Figure 3-29 ^{129}I concentrations in the saturated zone for at the point of maximum concentration and at the 100-m downgradient compliance point with the base-case vertical transport through the vadose zone.

Figure 3-30 shows the groundwater concentrations resulting from the lateral transport pathway. The three groundwater flux curves represent the time-dependent aquifer concentrations at the location of maximum dose for the base case (5_1_50), low-flow case (1_1_20), and high-flow case 10_5_100. These generic fluxes were scaled by the approximate peak flux values listed in Table 3-12. The base case breakthrough curve resembles the mesa-side fluxes, with a lag time of approximately 50 years for radioactivity to travel through the vadose zone at the canyon flow rate of 50 mm/yr (2 in./yr). For each of the three vadose zone flow cases, this pathway results in higher aquifer concentrations than the downward pathway during the first 1,000 years because of the assumption of instantaneous transport from the mesa side to the canyon alluvium.

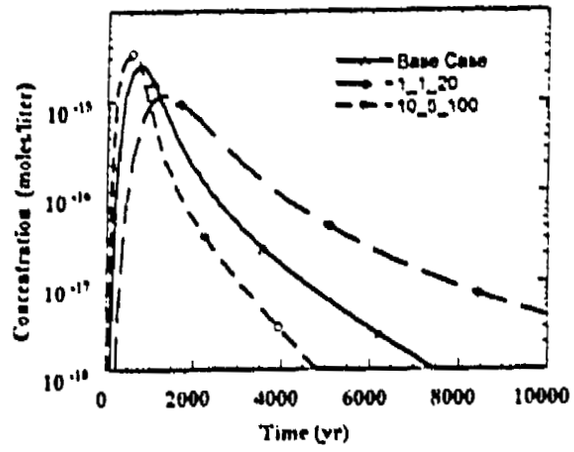

Figure 3-30 Groundwater concentrations in the saturated zone beneath Pajarito Canyon, for three flow fields

3.3.2.5 Groundwater Protection Analysis Dose Projections

The dose projections for the groundwater protection analysis estimated the radiation dose received by a hypothetical person assumed to use the regional aquifer as a source of drinking water. The potential doses depend upon the radionuclide concentrations in the aquifer, the quantity of water consumed, and the radionuclide dose conversion factors. The radionuclide concentrations in the aquifer were taken directly from the results of the saturated zone modeling. The aquifer modeling results were evaluated to identify the location where the potential dose from the consumption of water was greatest, taking into account all radionuclides present in the water.

The receptor was assumed to consume 730 L (189 gal) of water annually, all of which was assumed to come from the contaminated aquifer. This consumption rate is consistent with the levels of usage prescribed by safe drinking water regulations.

3.3.3 All Pathways Analysis

The all pathways analysis considered the potential impacts of radioactivity released from MDA G for three receptors. The approaches used to model the transport of radioactivity

to two of these locations, the points of maximum groundwater exposure and atmospheric exposure, have been discussed above. The third all pathways receptor location, in Pajarito Canyon, was assumed to become contaminated when surface runoff transported contamination from the top and sides of Mesita del Buey into the canyon. The thickness of contamination removed annually from the top of the mesa was set equal to the surface erosion rate of 7.0×10^{-6} m (2.3×10^{-5} ft), which was calculated in the surface-water transport model discussed earlier. The contaminated sediment was assumed to be spread over an area in the canyon equivalent to the area of contamination on the mesa top, and mixed to a depth of 0.15 m (5.9 in.) in the uncontaminated canyon soils.

All radioactivity transported laterally from the disposal units to the sides of the mesa was assumed to be carried by surface runoff into the canyon below. The radionuclides in the water were transported to the regional aquifer, which was assumed to be the receptor's sole source of water.

The modeling approach used to estimate doses for the all pathway analysis at the point of maximum atmospheric exposure has been discussed in Section 3.3.1. The projected doses for the all pathways analysis at the point of maximum groundwater exposure depend upon the radionuclide concentrations in the aquifer, the level of usage of this resource by the resident, and the radionuclide dose conversion factors. The level of resource utilization assumed for the analysis was identical to that discussed earlier for the air pathway analysis. The dose conversion factors and the application of the MICROSHIELD computer code to the dose analysis are also the same. The assumptions regarding resource utilization and the application of the dose factors were the same for the canyon resident as well. Detailed discussions of the models and data used in the all pathways analysis can be found in Appendix 3e.

4. RESULTS OF ANALYSES

This section presents the dose projections for the members of the public living in the vicinity of MDA G. The results of the dose analyses for both the PA and CA are discussed, along with a sensitivity and uncertainty analysis performed to better understand the resultant changes. Finally, the application of an ALARA analysis to MDA G is discussed, which evaluates certain options to further minimize projected doses from the facility.

4.1 RESULTS OF THE PA DOSE ANALYSES

The results of the PA dose analyses are discussed in terms of the various exposure pathways considered to demonstrate compliance with the public-protection and groundwater-protection performance objectives. The inventory addressed in the PA dose analyses is waste disposed of since September 26, 1988 projected through the year 2044. The characteristics of these wastes were summarized in Section 2.3.3. For each exposure pathway evaluated, Table 4-1 summarizes the time, location, and exposure routes considered in each phase of the analysis, along with the applicable performance objective(s).

4.1.1 Results of Air Pathway Analysis

The air pathway analysis was performed to evaluate the potential dose to a future member of the public as a result of airborne releases from MDA G and of the flux of radon gas from the surface of the disposal facility. The source terms for the air pathways were presented in Section 3.1.1, and include radioactive gases and resuspended surface contamination resulting from biotic intrusion.

The modeling of atmospheric dispersion of radioactive gases (excluding radon) and surface contaminants described in Section 3.3.1 identified the channeling effects of the complex mesa-canyon terrain, discussed in Section 2.1. Doses were calculated at the point of maximum atmospheric concentrations and in White Rock, which is the nearest

Table 4-1 Summary of exposure pathways and performance objectives

Pathway	Time of Assessment	Location of Assessment	Exposure Routes	Performance Objective
Air	Operational, Institutional-Control, and Industrial-Use Periods	LANL boundary near White Rock	Ingestion of food crops grown in contaminated soils and contaminated by airborne radioactivity Ingestion of contaminated soils Inhalation of airborne radioactivity Direct radiation from airborne radioactivity Direct radiation from contaminated soils	10 mrem/yr
	Operational, Institutional-Control, and Industrial-Use Periods	Not applicable	Radon flux from the undisturbed disposal site	20 pCi/m^2/yr
Groundwater	Operational and Institutional-Control Periods	LANL boundary near White Rock	Ingestion of drinking water	4 mrem/yr
	Industrial-Use Period	100 m east-southeast of MDA G and Pajarito Canyon	Ingestion of drinking water	4 mrem/yr
All	Operational and Institutional-Control Periods	LANL boundary near White Rock	Ingestion of food crops irrigated with well water Ingestion of meat and milk from animals watered with well water Ingestion of contaminated soils Direct radiation from airborne dust Direct radiation from contaminated soils	25 mrem/yr
	Industrial-Use Period	100 m east-southeast of MDA G and Pajarito Canyon	Ingestion of drinking water Ingestion of food crops grown in contaminated soils and/or irrigated with well water Ingestion of meat and milk from animals watered with well water. Ingestion of contamined soils Direct radiation from airborne dust Direct radiation from contaminated soils	25 mrem/yr

a Performance objective includes contributions from other LANL facilities.

population center; these locations were identified in Section 3.2.1. Maximum concentrations of airborne radioactivity were in Cañada del Buey approximately 500 m (1,600 ft) to the north of MDA G during both the 100-year institutional-control period and the subsequent 900-year industrial-use periods. The source term during the institutional-control period was limited to radioactive gas and vapors, assuming that site maintenance activities would protect against biotic intrusion. During the industrial-use period, biotic translocation as a source of surface contamination was included in the air-pathway analysis, assuming that the site is less rigorously maintained.

During the institutional-control period, the projected dose due to inhalation of contaminated gas was 6.6×10^{-2} mrem in Cañada del Buey and 1.6×10^{-2} mrem in White Rock. The projected doses were due almost exclusively to inhalation of ^{3}H (as water vapor), with ^{14}C (as carbon dioxide) contributing only 1 percent to the dose. The peak doses occurred at the end of disposal operations, in the year 2044, because inventories of ^{3}H were highest at this time.

Projected air pathway doses were considerably higher during the industrial-use period, due to resuspended surface contamination resulting from biotic translocation. The projected doses from atmospheric transport of suspended surface contamination during the industrial-use period are shown in Figure 4-1. Peak projected doses in Cañada del Buey and White Rock were 9.1×10^{-3} mrem and 2.2×10^{-3} mrem, respectively, occurring at the beginning of the industrial-use period.

The radionuclides that contributed to the peak dose during the 1,000-year compliance period are shown in Figure 4-2. Isotopes of americium, plutonium, and uranium account for more than 95 percent of the total dose. Inhalation of contaminated dust accounts for essentially all of the projected exposure.

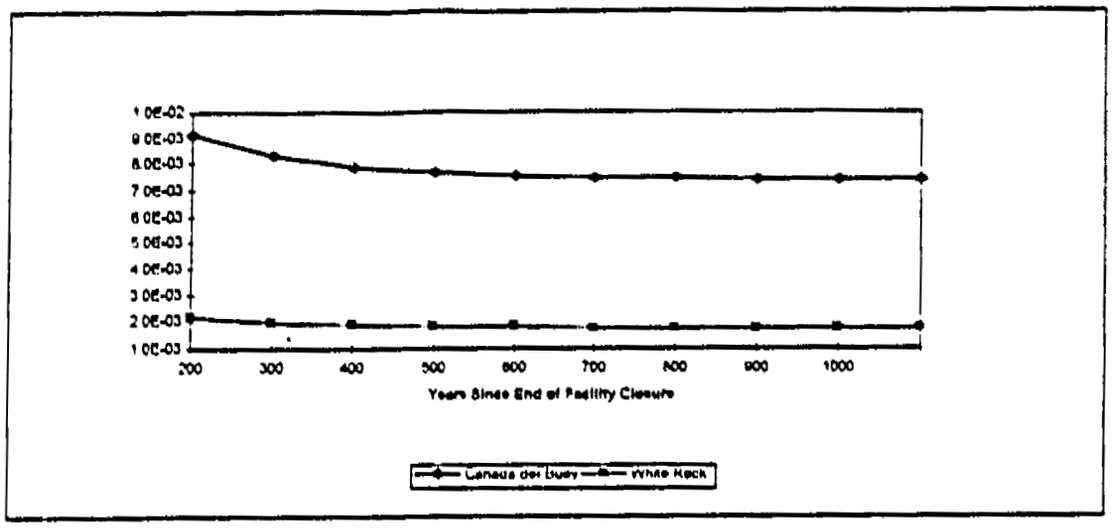

Figure 4-1 Offsite air pathway doses during the industrial-use period for the PA

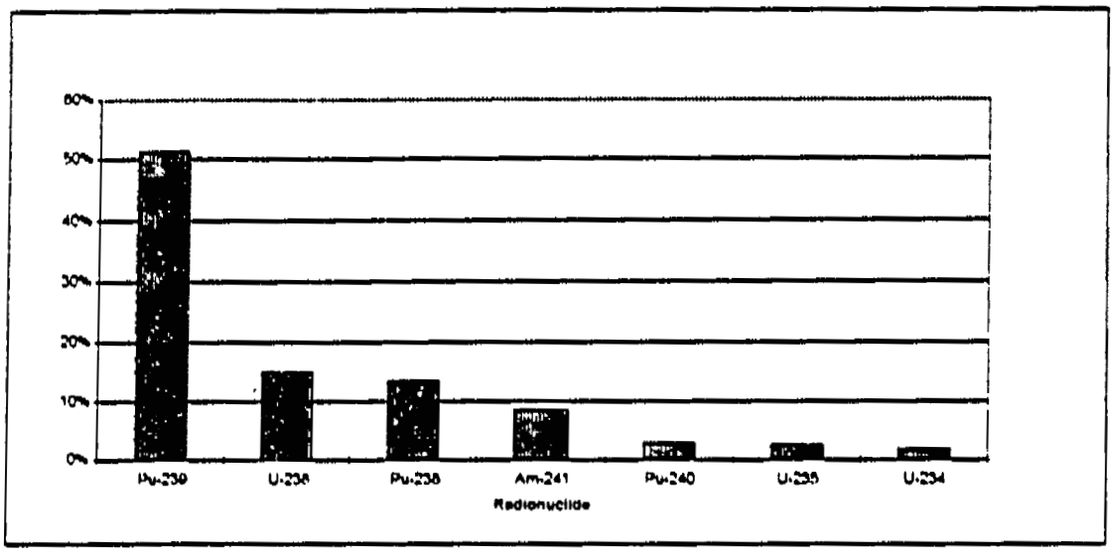

Figure 4-2 Radionuclides contributing to offsite air pathways dose during industrial-use period for the PA

The radon fluxes calculated for the PA inventory are presented in Table 4-2. Results are listed for both ^{222}Rn and ^{220}Rn calculated grow into the inventory as ^{226}Ra and ^{228}Ra decay. For waste already disposed of in pits, ^{222}Rn fluxes remained relatively constant at 1.1×10^{-1} pCi/m^2/s (1.0×10^{-2} pCi/ft^2/s) over the remainder of disposal facility operations

(i.e., until 2046), declining thereafter throughout the 1,000-year compliance as the ^{226}Ra decays. Very slightly higher ^{222}Rn fluxes were projected for the future pit waste, with the peak flux of 1.7×10^{-1} pCi/m^2/s (1.6×10^{-2} pCi/ft^2/s) occurring at the end of disposal operations. While ^{222}Rn fluxes dominated the radon emanations from pits, ^{220}Rn dominated the radon flux from shafts. The maximum projected flux of ^{220}Rn was 3.1 pCi/m^2/s (2.9×10^{-1} pCi/ft^2/s), from the existing shaft inventory, compared with a maximum ^{222}Rn flux of 2.5×10^{-2} pCi/m^2/s (2.3×10^{-3} pCi/ft^2/s). Smaller radon fluxes were projected for shaft waste extrapolated to require disposal in the future.

Table 4-2 Projected peak radon fluxes from historic waste during the 1,000 year compliance period for the PA

Disposal Inventory	^{220}Rn (pCi/m^2/s)	^{222}Rn (pCi/m^2/s)	Total (pCi/m^2/s)
Disposal Pits			
Existing waste	0.0E+00	1.1E-01	1.1E-01
Future waste	0.0E+00	1.7E-01	1.7E-01
Disposal Shafts			
Existing waste	3.1E+00	2.5E-02	3.1E+00
Future waste	8.1E-01	2.0E-03	8.1E-01

4.1.2 Results of Groundwater Protection Analysis

The source term model for the PA groundwater protection analysis was described in Section 3.1.2 as the surface-contaminated segment of the inventory summarized in Section 2.3.3. Doses due to the direct ingestion of groundwater extracted from the regional aquifer were calculated at the point of maximum offsite radionuclide concentration and in Pajarito Canyon, as identified in the Section 3.2.2 and Section 3.3.2. The projected doses for the groundwater protection analyses performed 100-m downgradient from MDA G and in Pajarito Canyon opposite MDA G are shown in Figures 4-3 and 4-4, respectively. The analysis was performed over a period of 10,000 years post closure to provide

reasonable assurance that the groundwater protection performance objective could be met despite significant uncertainties in the modeling. Project groundwater ingestion doses are small, with only three contributing radionuclides, ^{14}C, ^{99}Tc and ^{129}I. There were no offsite doses from the groundwater pathway during the institutional-control period, because no radionuclides were transported beyond the current TA-54/LANL boundary within 100 years.

At the location 100 m (330 ft) downgradient from MDA G, the peak annual dose was 1.4 × 10-5 mrem. The peak occurred beyond the 1,000-year compliance period, at 4,000 years. Ninety-eight percent of the dose at this location was due to ^{14}C and ^{99}Tc, each contributing equally. The remaining 2 percent was due to ingestion of ^{129}I.The maximum annual dose calculated in the groundwater protection analysis was 4.5 × 10-5 mrem, occurring at 700 years at the Pajarito Canyon location. About 67 percent of the peak dose was due to ^{14}C, with ^{99}Tc contributing 31 percent and 129I contributing the remainder.

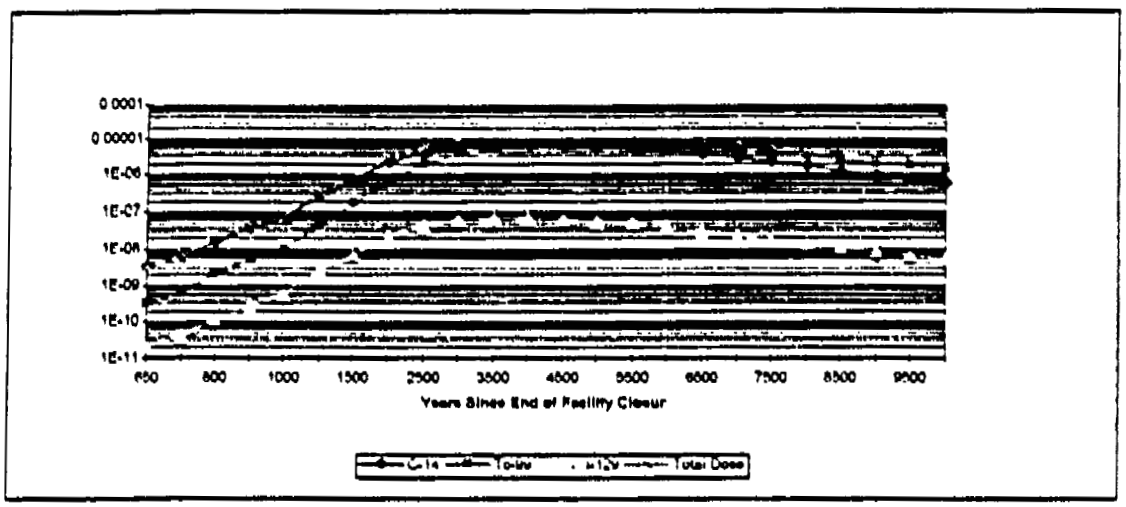

Figure 4-3 Doses projected for PA from ingestion of contaminated water drawn from the regional aquifer 100 m downgradient of MDA G.

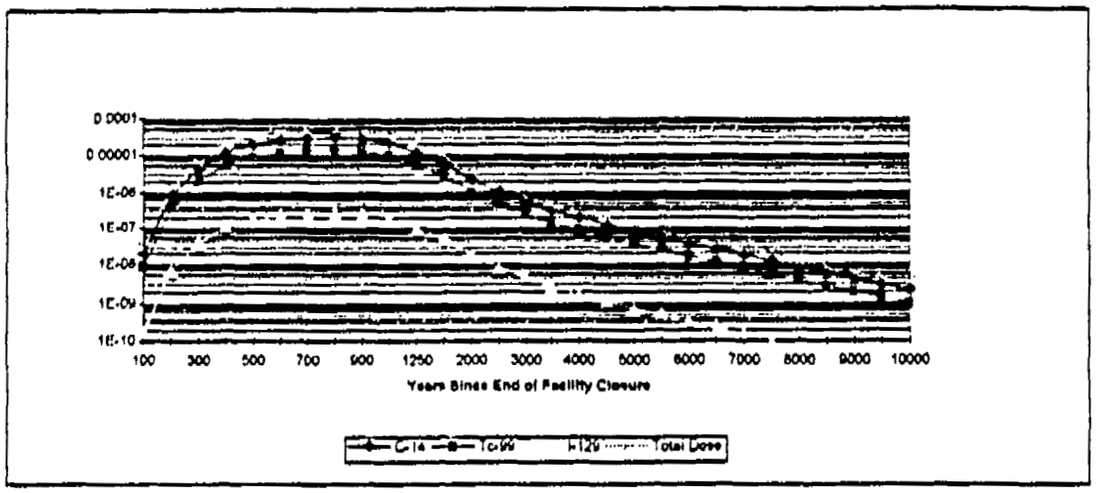

Figure 4-4 Doses projected for PA from ingestion of contaminated water drawn from the regional aquifer from well in Pajarito Canyon.

4.1.3 Results of All Pathways Analysis

The all pathways analysis examined the potential impacts upon members of the public as a result of radioactive releases to groundwater and to surface runoff. As described in Section 3.3.3, surface runoff was assumed to transport surface contamination resulting from biotic translocation as sediment into Pajarito Canyon. The all pathways analysis was performed where exposures would be maximized, which differed during the institutional-control and industrial-use periods according to assumed landuse boundaries. Exposure routes considered in the all pathways analysis were: direct ingestion of contaminated water drawn from the regional aquifer, ingestion of foodstuffs raised on contaminated water, inhalation of airborne radioactivity, immersion in airborne radioactivity, ingestion of redeposited airborne radioactivity, and direct exposure from redeposited airborne radioactivity. The projected doses were dominated by the groundwater pathway.

During the institutional-control period, potential doses were projected for a receptor located near the town of White Rock. Two locations were considered during the industrial-use period, one at the point of maximum groundwater concentration downgradient of MDA G, the other in Pajarito Canyon opposite MDA G.

No exposures are projected to occur for the all pathways analysis during the institutional-control period, as groundwater travel times from MDA G to White Rock exceed 100 years. The doses projected for two receptor locations considered during the industrial-use period are shown in are shown in Figures 4-5 and 4-6, respectively. Annual doses at the downgradient location increase to a peak of 4.2×10^{-5} mrem at 4,500 years post-closure, with ^{14}C and ^{99}Tc making approximately equal contributions to this dose. The peak dose at this location during the 1,000-year compliance period is 2.3×10^{-7} mrem/yr due largely to ^{14}C and to a lesser extent to ^{99}Tc. These two radionuclides are also responsible for the groundwater doses projected in all pathways analysis in Pajarito Canyon. Since the travel time to the aquifer is shorter via the "out and down" pathway, peak dose occurs earlier, at 700 years. Doses decline from the 1.3×10^{-4} mrem maximum for the remainder of the 10,000-year period. In addition to the dose associated with the use of contaminated water drawn from the regional aquifer is a small dose (roughly 2 percent of the maximum) due to exposures associated with ^{239}Pu in canyon soils.

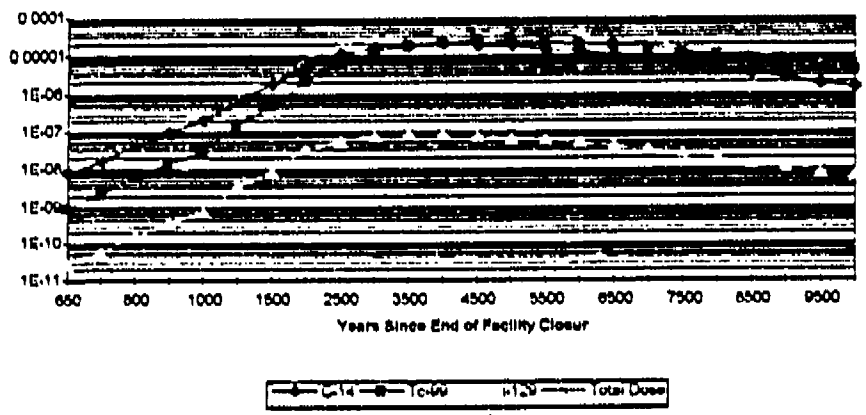

Figure 4-5 Doses projected for the PA all-pathways analysis from use of contaminated water drawn from the regional aquifer 100 m downgradient of MDA G.

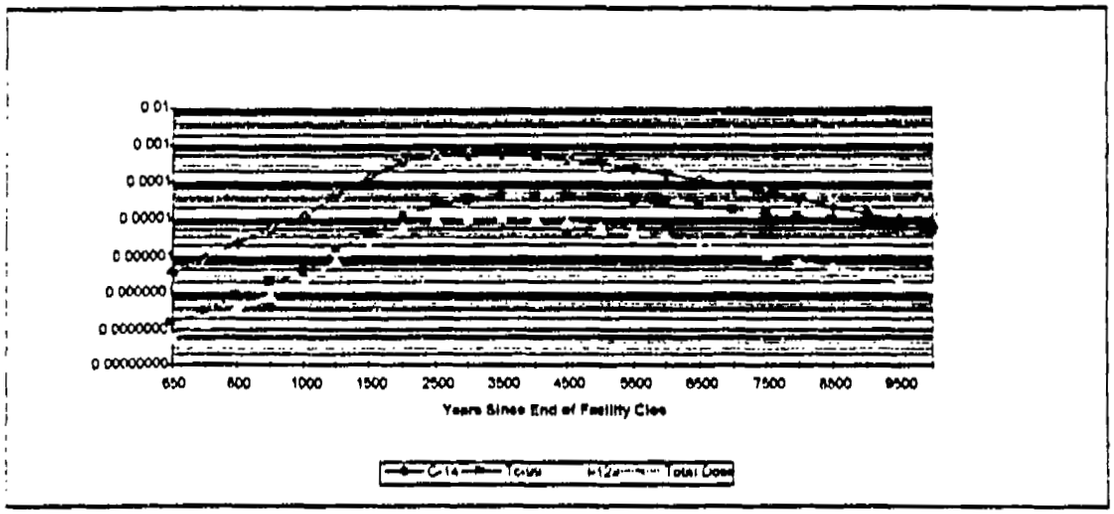

Figure 4-6 Doses projected for the PA all-pathways analysis from use of contaminated water drawn from a well in Pajarito Canyon.

The contributions of the various exposure pathways to this peak dose are shown in Table 4-3. At both receptor locations, the highest dose contribution is due to the ingestion of crops irrigated with contaminated water drawn from the regional aquifer. The second highest contributing pathway is direct ingestion of grounwater from the regional aquifer. The contribution of the consumption of irrigated crops to the total dose is expected to be over-estimated. Radionuclide concentrations in the crops are dominated by radioactivity taken up via the roots following the deposition of radioactivity in irrigation water on surface soils. While the three radionuclides projected to occur in the irrigation (i.e., ^{14}C, ^{99}Tc, and ^{129}I) water are highly mobile, their concentrations are projected assuming a buildup time in the soil of 15 years. A more reasonable period of buildup for highly mobile radionuclides is expected to be on the order of one year. Under these conditions, doses from the consumption of crops would decline about 15 times. At these levels, the consumption of drinking water would be the primary contributor to the projected doses.

Table 4-3 Exposure pathway contribution to peak all pathways dose during institutional-control period for the PA

Exposure Pathway	Contribution to Peak Dose (mrem)		Percent Peak Dose	
	Downgradient	Pajarito Cyn	Downgradient	Pajarito Cyn
Ingestion of Water	8.3E-08	4.5E-05	37%	34%
Ingestion of Soil	1.6E-10	1.1E-06	0%	1%
Ingestion of Crops	1.4E-07	8.0E-05	60%	60%
Ingestion of Meat	3.4E-09	1.4E-06	1%	1%
Ingestion of Milk	4.1E-09	1.5E-06	2%	2%
Inhalation of Particulates	3.83E-12	2.2E-06	0%	2%
Direct Radiation from Soils	1.8E-12	2.4E-06	0%	1%
Direct Radiation from Air	3.0E-18	1.6E-13	0%	0%
All pathways	**2.3E-07**	**1.0E-04**	**100%**	**100%**

4.2 RESULTS OF THE CA DOSE ANALYSES

The source term for the CA included the PA inventory, plus waste disposed of before September 26, 1988; the characteristics of the CA inventory were discussed in Section 2.3.4. The performance objective for the CA is a maximum dose of 100 mrem/yr to a future member of the public from all exposure pathways. The results of the CA are qualitatively similar to the results of the PA, with air-pathway doses associated with the biotic-intrusion source term being dominant. Cumulative air pathway doses were calculated in Cañada del Buey and White Rock, and cumulative all-pathway doses were projected at the location of maximum groundwater concentration downgradient of MDA G and in Pajarito Canyon.

The maximum dose to the air-pathway receptor in Cañada del Buey during the 100-year institutional-control period was 7.5×10^{-2} mrem/yr. The maximum dose via air at the White Rock location during the institutional-control period was 1.8×10^{-2} mrem/yr. The

air-pathway dose during this period is due to gas-phase releases (^3HHO, $^{14}CO_2$, and $^{14}CH_4$) from MDA G, and is projected to occur at the end of facility operations when ^3H inventories are greatest. The inhalation of tritiated water vapor is responsible for 90 percent of the total projected dose. Figure 4-7 shows the projected air-pathway doses calculated during the industrial-use period for the CA. Peak doses are projected to occur during the industrial-use period, as the radioactivity in air increases as a result of suspension and transport of surface contamination from biotic intrusion. The peak annual dose projected for the air pathway is 5.5 mrem in Cañada del Buey, and 1.3 mrem in White Rock. Doses decline to about 3.2 mrem by the end of the 1,000-year compliance period as radionuclides in the waste decay.

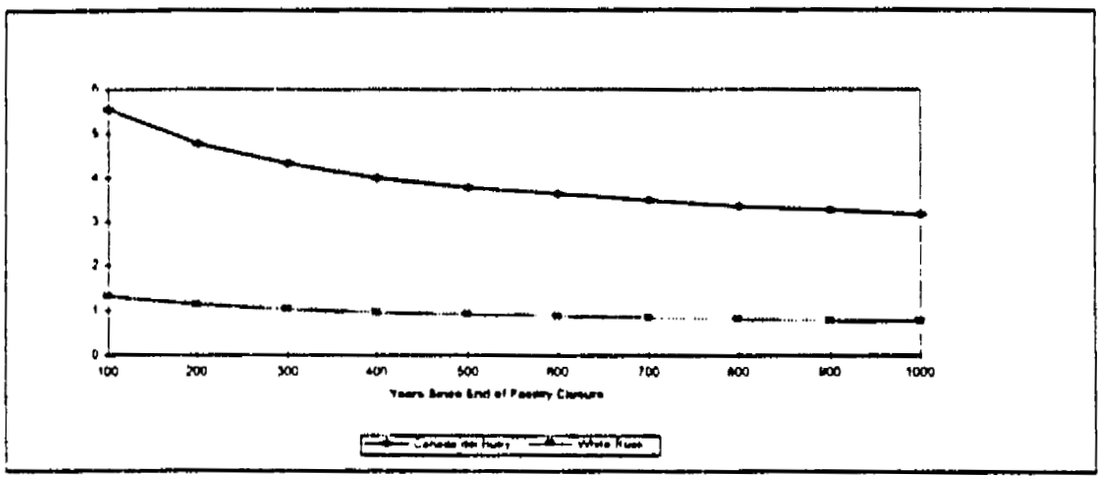

Figure 4-7 Offsite doses from air pathway during industrial-use period for the CA.

The radionuclides that contribute to the peak dose for the air pathway analysis are shown in Figure 4-8. Isotopes of americium and plutonium account for more than 95 percent of the total dose. Inhalation of contaminated dust accounts for essentially all of the projected dose.

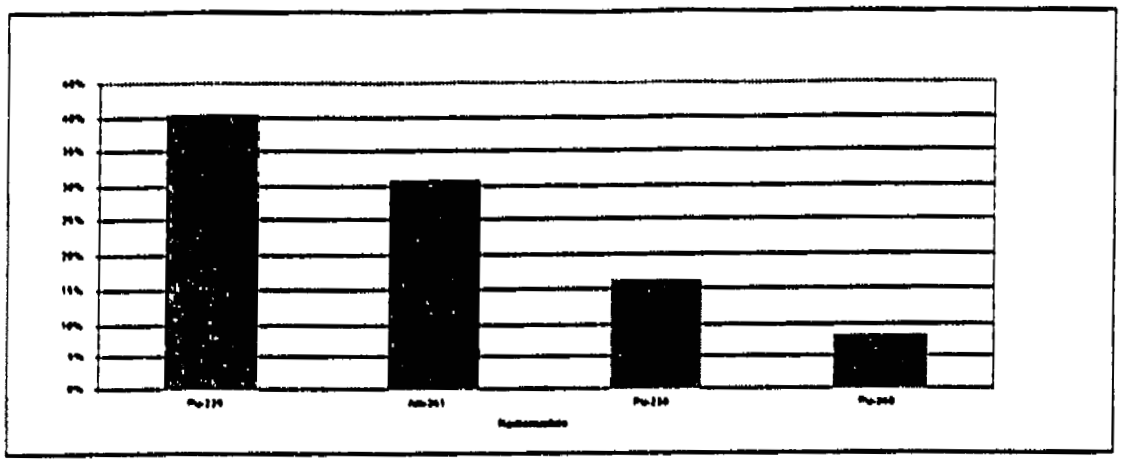

Figure 4-8 Radionuclides contributing to offsite dose from air pathway during industrial-use period for the CA

4.2.1 All Pathways Dose Analysis

The projected doses for the all-pathways receptors located 100 m downgradient of MDA G and in Pajarito Canyon are shown in Figures 4-9 and 4-10, respectively, for a period of 10,000 years. The downgradient doses peak at 7.3×10^{-4} mrem/yr approximately 3,000 years after the end of facility operations, coincident with the arrival of ^{14}C. The peak dose occurs after the 1,000-year compliance period. During the compliance period, the maximum annual all-pathways dose is 1.2×10^{-5} mrem, 98 percent of which is contributed by ^{14}C and ^{99}Tc.

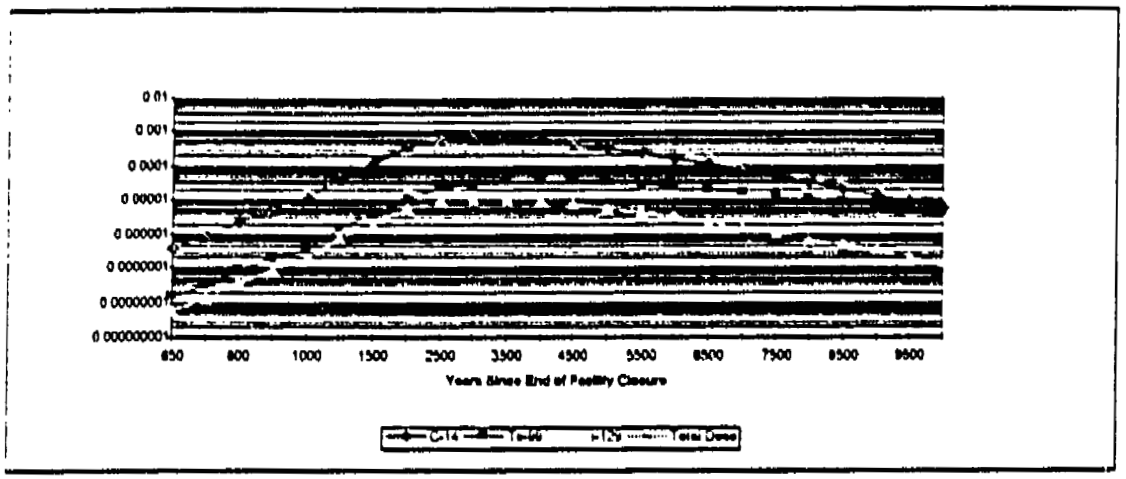

Figure 4-9 Doses projected for CA all-pathways analysis from use of contaminated water drawn from regional aquifer 100 m downgradient of MDA G

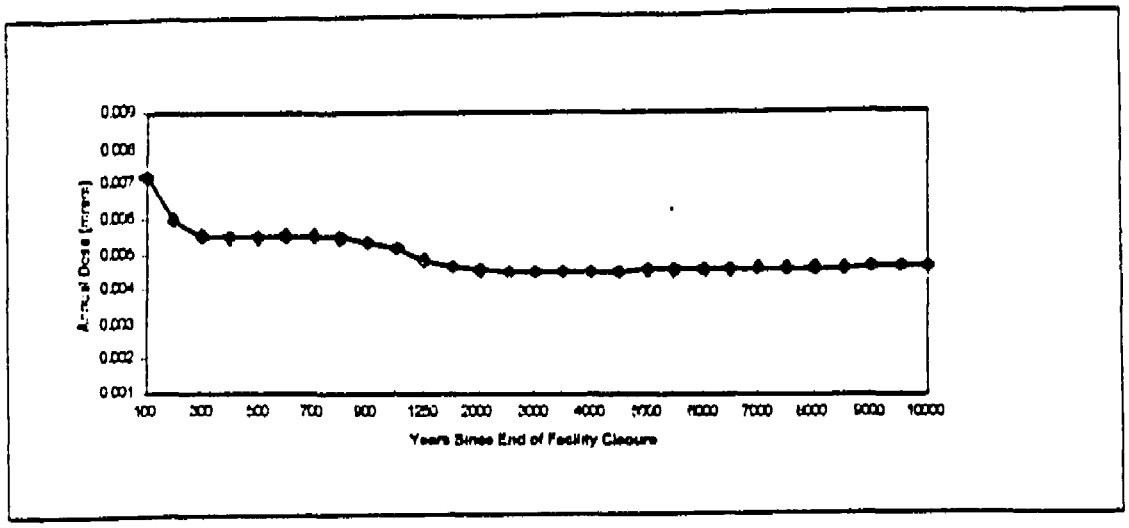

Figure 4-10 Doses projected for CA all-pathways analysis from use of contaminated water drawn from well in Pajarito Canyon

The peak annual dose for the receptor in Pajarito Canyon is 7.2×10^{-3} mrem, projected to occur early during the 900-year industrial-use period. Radioactivity brought to the surface by plants and animals and transported in sediment from the surface of Mesita del Buey into the alluvium in Pajarito Canyon is the major contributor to the peak dose. Several radionuclides contribute to the CA all-pathways dose, most importantly, ^{239}Pu (37 %), ^{108m}Ag (19 %), ^{182}Hf (18 %), and ^{241}Am (8 %). Important exposure pathways include the inhalation of suspended dust, the ingestion of soil, and direct radiation from contaminated soils, shown in Table 4-4.

Table 4-4 Exposure pathways contributing to peak dose calculated to an offsite resident during the 1,000 year compliance period for the CA

Exposure Pathway	Contribution to Peak Dose (mrem)		Percent Peak Dose	
	Downgradient	Pajarito Cyn	Downgradient	Pajarito Cyn
Ingestion of Water	4.6E-06	1.9E-07	38%	0%
Ingestion of Soil	8.8E-09	1.3E-03	0%	18%
Ingestion of Crops	7.2E-06	3.7E-04	59%	5%
Ingestion of Meat	2.0E-07	7.9E-09	2%	0%
Ingestion of Milk	2.3E-07	9.5E-09	2%	0%
Inhalation of Particulates	1.5E-10	2.4E-03	0%	34%
Direct Radiation from Soils	3.7E-10	3.1E-03	0%	43%
Direct Radiation from Air	2.2E-16	3.6E-10	0%	0%
All pathways	**1.2E-05**	**7.2E-03**	**100%**	**100%**

4.3 SENSITIVITY AND UNCERTAINTY

The dose projections presented in Section 4.1 and 4.2 are subject to uncertainties in various elements of the analysis supporting those projections. Some of the uncertainties are associated with the site characterization data summarized in Section 2, while others are inherent in the mathematical and computational approximations described in Section 3 used to simulate source terms, environmental transport, and dose consequence. Specifically, important uncertainties were identified by subject-matter experts who conducted work in support of the PA and CA; the appendices written by those experts include an evaluation of uncertainties in the context of their analysis. This section addresses these uncertainties and discusses the sensitivity of the dose projections to them. The material summarized below is presented in greater detail in Appendix 3e.

The purpose of the sensitivity and uncertainty analysis is to provide reasonable assurance that the performance measures will be met when uncertainties in the supporting analyses are propagated through the final dose assessment. Quantifying the potential for the

projected doses to be *underestimated* by uncertainties in the analyses is important in terms of demonstrating reasonable assurance, but it is important to recognize that uncertainties also lead to *overestimates* of projected doses. Both effects will be discussed.

The sensitivity and uncertainty analysis focused on the projected performance of the disposal facility during the 1,000-year compliance period. However, in some instances, sources of uncertainty are discussed here in terms of their impact over periods of up to 10,000 years because certain aspects of the analysis are insensitive to uncertainties in the 1,000-year period but are quite sensitive to uncertainties at later times.

The discussion to follow is organized in terms of these modeling components, which consistently affect dose projections for the air, groundwater, and all-pathways scenarios:

- The waste inventory, which defines the total amount of radioactivity buried in the disposal facility.
- Source release mechanisms, which define the mode and rate at which radioactivity is released to the environment from the disposed waste.
- Transport mechanisms, through which radionuclides are transported through the environment to locations accessible to humans.
- Usage factors, which describe the rate of usage of, or time exposed to, contaminated resources.
- Dose conversion factors, which relate intakes of radioactivity to absorbed doses in the receptor.

The importance of uncertainties is related to the safety margin implied by the ratio of the projected dose to the applicable performance measure(s). That ratio is provided in Table 4-5 for each pathway analyzed. The projected performance listed in the Table 4-5 is for the 1,000-year compliance period. For each pathway considered in the PA and CA, the dose (or flux, for radon) calculated during the 1,000-year compliance period is listed as projected performance. The applicable performance measure for each projected dose is then identified. Finally, in the last split column, the ratio of the projected dose to the performance measure is shown. This ratio is an indication of the margin of safety in the

projected performance. The smaller the margin of safety, the more important the uncertainties in the pathway analysis become.

Table 4-5 Ratio of projected performance to performance measure

Pathway	Projected Performance		Performance Measure		Ratio	
	PA	CA	PA	CA	PA	CA
Air	6.6E-02 mrem/yr	5.5 mrem/yr	10 mrem/yr	100 mrem/yr	7E-04	6E-02
Groundwater	8.3E-03 mrem/yr	n/a	4 mrem/yr	n/a	2E-03	n/a
All-pathways	1.3E-04 mrem/yr	7.2E-03 mrem/yr	25 mrem/yr	100 mrem/yr	5E-06	7E-05
Radon Flux	3.1 Ci/m2/s	n/a	20 Ci/m2/s	n/a	2E-01	n/a

4.3.1 Inventory Uncertainties

There are several sources of uncertainty in the inventories used in the PA and CA source term analyses. Recall from Section 2.3 that the total MDA G inventory was characterized in three segments. Two of these inventory segments, accounting for disposals between 1971 and September 25, 1988, and between September 26, 1988 and 1995, were characterized directly using electronic records. The two other segments, representing unrecorded disposals between 1957 and 1970, and future disposals between 1996 and 2044, were extrapolated using subsets of the electronic data. Assuming that the information in the database accurately reflects the information reported by generators, potential errors in the PA and CA inventories include: Errors intrinsically associated with measuring the activity present in waste, and inaccuracies in the extrapolation methods. Both of these sources of error or uncertainty are discussed below for each pathway analyzed in the PA and CA. A comprehensive discussion of the information summarized below can be found in Chapter 4 of Appendix 3e.

4.3.1.1 Air Pathway

The air pathway analysis included the projection of radon fluxes (PA only) and the projection of offsite doses associated with airborne radioactivity (PA and CA). Projected

peak fluxes of radon gas from the historic pit and shaft waste are 1.1×10^{-1} pCi/m2/s (1.0×10^{-2} pCi/ft^2/s) and 3.1 pCi/m^2/s (2.9×10^{-1} pCi/ft^2/s), respectively. The maximum flux for the future pit waste is 1.7×10^{-1} pCi/m^2/s (1.6×10^{-2} pCi/ft^2/s), while the peak flux for the future shaft waste is 8.1×10^{-1} pCi/m^2/s (7.5×10^{-2} pCi/ft^2/s). The projected radon fluxes are due to ^{222}Rn from ^{226}Ra, and ^{220}Rn from ^{228}Ra, a decay product of ^{232}Th. The peak air-pathway dose calculated for the PA inventory is 6.6×10^{-2} mrem/year in Cañada del Buey is, due to the inhalation of radioactive gases at the end of disposal operations. Dust resuspended from the site at the end of institutional control results in a peak dose of 9.2×10^{-3} in Cañada del Buey. The peak air-pathway dose projected for the CA inventory is 5.5 mrem/year in Cañada del Buey, projected to occur at the end of the institutional control period. The radionuclides contributing the the outcome of the air pathways analysis are: ^{226}Ra, ^{232}Th (radon flux); ^{3}H, ^{14}C (radioactive gases), and ^{235,238}U, ^{238,239}Pu, and ^{241}Am (radioactive particulates). The uncertainties in each of these radionuclides in the PA and CA inventory introduced by measurement errors and extrapolation errors are summarized below.

Radium-226 is relatively easy to detect to with a factor of 2. Similarly, ^{232}Th (the primary source of ^{220}Rn in the air pathway inventory) is relatively easy to detect because its short-lived daughters emit relatively high-energy gamma radiation. Errors associated with non-destructive analysis are typically within 200 to 300 percent.

Tritium is difficult to detect in small quantities without performing radiochemical analysis. Measurement errors decline as the activity of the waste increases. For samples with activities on the order of a few curies, off-gassing measurements may be accurate to within a factor of 10. Waste containing hundreds to thousands of curies of ^{3}H are readily characterized using ion chamber measurements and calorimetry, which are accurate to within a factor of 2 and less than 20 percent, respectively. In Section 2.3, it was identified that ^{3}H accounts for greater than 90 percent of the total activity inventory at MDA G. The majority of this ^{3}H was contains hundreds to tens of thousands of curies. Thus, measurements errors are expected to be less than 20 to 100 percent.

Measurement errors for ^{14}C can be significant because it emits low-energy beta particles. However, the ^{14}C inventory at MDA G is dominated by irradiation sources, which are accurately characterized. Thus, the uncertainty in the recorded activity is considered insignificant. However, there is some uncertainty in the extrapolation for future disposals of this potentially important radionuclide. The future inventory is based on an annual disposal rate applied for 50 years, which was based on only two disposals of irradiation sources within a period of 5 years. For this reason, the projected ^{14}C inventory is expected to be overestimated by as much as 50 percent.

The 235 and 238 isotopes of uranium can be detected using non-destructive techniques with errors on the order of 200 percent. This factors applies to the depleted and enriched uranium in the PA and CA inventory.

Nearly all of the plutonium-contaminated LLW disposed of at MDA G is generated by the nuclear weapons program, and is generated at TA-3 and TA-55. The same programs generate TRU waste. The LLW stream is generally low-density materials packaged in cardboard boxes. It is characterized using a sensitive gamma-ray detector calibrated to measure ^{241}Am, which is used as a scaling factor for estimating the quantity of various plutonium isotopes in the waste. Americium-241 is relatively easy to detect in low-density matrices; measurement errors for this low-density LLW are generally less than 100 to 200 percent. The relative proportions of ^{240}Pu and ^{239}Pu are reasonably well know. Thus, the errors in the reported ^{241}Am, ^{240}Pu, and ^{239}Pu from TA-3 and TA-55 are considered accurate to within a factor of 2 to 3.

The plutonium inventories (and projected air-pathway doses) for the CA are dominated by the extrapolated 1957-1970 disposals. Subject-matter experts maintain that this extrapolation vastly overestimates the actual activities, perhaps by as much at 300 percent.[79]

A substantial fraction of the recorded MDA G ^{241}Am inventory is contained in dewatered sludges from the liquid radioactive waste treatment facility at TA-50. This waste is radiochemically assayed and is therefore well characterized, with errors on the order of 10 to 50 percent. The amount of the ^{241}Am in the pre-1971 extrapolated may be significantly overestimated. A total of 2.2×10^3 Ci of the isotope was extrapolated based on 1971 - 1975 records, while the waste projected from 1971 through the end of disposal operations in 2044 was projected to contain only 34 Ci. The very large difference between these activities suggests that the 1957 to 1970 inventory of the radionuclide is overstated.

4.3.1.2 Groundwater Protection

A peak dose of 8.3×10^{-3} mrem/year is projected for the groundwater protection analysis for the PA at the receptor location 100 m (330 ft) east-southeast of the Area G fenceline during the 1,000-year compliance period. The peak annual dose projected for the receptor in Pajarito Canyon during this period is 4.5×10^{-5} mrem. In both cases, ^{14}C, ^{99}Tc, and ^{129}I are the only radionuclides that contribute to these projected doses; no other radionuclides reach the aquifer during the compliance period, or through the 10,000-year analysis period. Of these, ^{14}C is the primary contributor to the peak doses, accounting for 68 to 88 percent of the totals.

Measurement errors for ^{14}C, ^{99}Tc, and ^{129}I can be significant, because they emit low-energy beta particles and x-rays. Errors associated with measurements in low-density waste may be on the order of 100 to 200 percent unless the waste is subjected to radiochemical analysis, an approach seldom used to characterize LLW. The ^{14}C inventory is dominated by irradiation sources, which are very accurately characterized. Thus, the uncertainty in the recorded activity is considered insignificant. However, there is some uncertainty in the extrapolation for future disposals of this potentially important radionuclide.

The inventories of ^{14}C, ^{99}Tc, and ^{129}I included in the groundwater protection analysis are dominated by waste projected to be disposed of in the future. Annual future disposal

estimates were based on the annual disposals between 1990 to 1995. Approximately 60 percent of the projected annual disposal of ^{14}C over the next 50 years is based on two disposals since 1990, both of which were irradiation sources. Irradiation sources are not considered routine waste. Thus, the projected ^{14}C inventory is expected to be overestimated by as much as 50 percent. Both ^{99}T and ^{129}I are fission products. Their presence in the PA inventory is based on the method used to allocate activities reported as MFP to specific radionuclides, which is included as Appendix 2g. The major uncertainty in that allocation is the assumed age of the waste at the time of disposal. The effect of that uncertainty in the projected future inventory may not be important insofar as the programs responsible for generating MFP-contaminated waste are no longer in existence (i.e., reactors, weapons testing).

4.3.1.3 All Pathways

Two all-pathways exposure scenarios were included in the PA. One considered a receptor 100 m (330 ft) hydrologically downgradient from MDA G, and another in Pajarito Canyon. The maximum dose projected to occur within 1,000 years was 1.3×10^{-4} mrem/year. The consumption of water and ingestion of food crops irrigated with water drawn from a supply well in Pajarito Canyon accounted for 34 and 60 percent of the peak dose, respectively. The maximum annual dose projected for CA all-pathways analysis was 7.2×10^{-3} mrem, also occurring in Pajarito Canyon. The inhalation of resuspended dust and direct radiation from contaminated soil account for 77 percent of this dose. The radionuclides contributing to the all-pathways Pajarito Canyon receptor dose include: ^{90}Sr, ^{108m}Ag, ^{137}Cs, ^{182}Hf, $^{235,238}U$, $^{238,239}Pu$, and ^{241}Am. The uncertainties in the inventory of many of these radionuclides has been discussed.

Three of the radionuclides contributing significantly to the all-pathways dose emit high-energy photons and are thus easily measured: ^{108m}Ag, ^{137}Cs, and ^{182}Hf. Measurement errors for these radionuclides, using non-destructive analysis, will typically fall within 100 to 200 percent. In contrast, ^{90}Sr is a pure beta emitter and may be difficult to detect in waste matrices. Consequently, it is possible that generators have overlooked, or otherwise

underestimated, activities associated with this radionuclide, unless it is present with other easy-to-detect fission products (e.g. ^{137}Cs), whose abundance can be used as a scaling factor for ^{90}Sr.

As stated above, the majority of fission-products in the inventory results from the method used to allocate MFP activities among contributing radioisotopes. While the ^{137}Cs inventory is dominated by irradiation sources, the entire ^{108m}Ag inventory is based solely on the MFP allocation process. It is expected that all the projected quantities of radionuclides determined in the MFP allocation process are overestimated, since the programs that generated MFP waste in the past are no longer viable at LANL.

4.3.2 Source Term Uncertainties

The known or unknown uncertainties in the analyses developed to estimate time-dependent releases of the radionuclides discussed above are summarized below.

4.3.2.1 Air Pathway

Two mechanisms of release were considered in the source-term modeling for the air pathway analysis: the diffusion of radioactive gases from waste, and the resuspension of contamination transported to the surface by plants and burrowing animals. Potentially important uncertainties in the air-pathway source term analyses are discussed below.

The release of radon gas from the disposed waste is directly proportional to the emanation coefficient. This coefficient is the fraction of radon that is released from the waste matrix into the pore space. While the actual coefficient will be affected by the characteristics of the waste matrix, the value of 0.35 used in the dose assessment is expected to reasonably represent the soils at LANL.[115] Lacking actual measurements from the site, however, it was assumed that the error associated with the emanation coefficient was 20 percent.

The ^{3}H fluxes projected for the scenario are expected to overestimate the actual rates of release observed at the disposal site. The analytical model assumed that all tritiated water vapor in the disposal units at a given time was released from the disposal site within 1

year, that no depletion of the ^{3}H inventory occurred from groundwater leaching or diffusive losses, and that the entire ^{3}H inventory was located immediately below the earthen cover placed over the disposal units, thereby minimizing the distance over which the vapor must diffuse. An analysis of site-specific data suggest that the ^{3}H inventory is actually diffusing over a much longer period of time. The empirical data suggest that the modeled 3H fluxes are approximately 200 times greater than are presently occurring. Similar assumptions were made in modeling the diffusion of ^{14}C and $^{81,85}Kr$. Consequently, those fluxes are judged to be overestimated.

Potentially important sources of uncertainty in the biotic intrusion source release model relate to whether plants or animals are responsible for the translocation. For the radioactinides responsible for the majority of the air-pathway dose, burrowing animals were the primary transport vector. As modeled, the projected releases of radioactivity due to the intrusion of animals depend upon the burrow distributions and the densities of the burrows at the site. The source-release model was based on a burrow distribution representative of the pocket mouse. The burrow characteristics of this species were used to estimate those of the deer mouse, a species of small mammal commonly observed at MDA G. Burrow densities used in the model were consistent with densities observed for deer mice. In the base case, the depth of burrowing was 2 m (6.6 ft), with 10 percent of the burrows assumed to occur below a depth of 1 m (3.3 ft). Deeper and more extensive burrowing examined as an extreme case resulted in contamination levels almost 3 times greater than the base case.

4.3.2.2 Groundwater Protection

The uncertainties in the surface-contamination dissolution source term relate directly to the flux rate of moisture percolating through the disposal units. The base-case infiltration rate of 5 mm/year (0.2 in./year) used to calculate both contact time and release rate is relatively uncertain, but well within the range of anticipated values. The two bounding infiltration rates considered, 1 and 10 mm/year (0.04 and 0.4 in./year) lead to release rates that are 4 and 300 percent of those projected, respectively, to occur for base case. There is

very little likelihood that release rates would be otherwise underestimated for the three radionuclides of interest in the groundwater pathway analysis, since all radionuclides were assumed to be surface contaminated, and since ^{14}C, ^{99}Tc, and ^{129}I are nonsorbing.

4.3.2.3 All Pathways

Uncertainties associated with groundwater transport modeling of radionuclides to the receptor locations east-southeast of the MDA G disposal units and in Parajito Canyon are discussed in Section 4.1.1.3. These uncertainties, and their expected impact, apply to the "all pathways" scenarios as well. The following discussion addresses additional sources of uncertainty unique to the All Pathways - Groundwater and All Pathways - Parajito Canyon scenarios.

4.3.3 Environmental Transport Modeling Uncertainties

There are several sources of uncertainty that affect the environmental transport analyses described in Section 3.3. The most important of these were investigated by the analysts performing the modeling of various pathways and are included in the detailed appendices. The following sections summarize the potentially important uncertainties in the environmental transport models used in the air-, groundwater-, and all-pathways analyses.

4.3.3.1 Air Pathway

The atmospheric transport model may be characterized by the values of the resuspension factor and dispersion factor used in the dose calculations. These values are based on site-specific information and assumptions about the effects of complex terrain in the vicinity of MDA G. While there are uncertainties associated with the resuspension and dispersion factors, the magnitude of any error introduced into the projected atmospheric concentrations by these uncertainties is difficult to quantify without additional site data. Subject-matter experts expect that the overall uncertainty in the resuspension factor is less than an order of magnitude. Errors introduced by uncertainties associated with the dispersion factor are expected to be on the order of 100 to 200 percent.

4.3.3.2 Groundwater Protection

In the groundwater protection analysis, radioactivity dissolved from the surface of waste into water percolating through the disposal units was transported both vertically and laterally through the vadose zone. Radioactivity transported vertically followed a straight-down path into the regional aquifer, while radioactivity transported laterally was instantaneously rinsed from the mesa edge into the alluvial system into the canyon and then transported down to the regional aquifer. Once reaching the regional aquifer, the vertically-transported radioactivity was transported within the saturated zone to a downgradient receptor well; laterally-transported radioactivity was assumed to be accessed by a supply well directly beneath the Pajarito Canyon receptor location. Important factors in evaluating compliance with the groundwater protection performance objective relate to the time required for radioactivity to reach the receptor well, and the concentration of radioactivity at the location of the receptor well.

Radionuclide travel time is a function of the groundwater travel time, the sorption behavior of the contaminants, and the degree of dilution that occurs in the regional aquifer. Uncertainties in sorption are not important, since none of the radionuclides contributing to the drinking-water dose were sorbed within the vadose zone. Uncertainties in groundwater travel time, or recharge, and aquifer dilution are recognized and have an effect on the groundwater pathway analysis.

Groundwater travel times in the unsaturated zone are proportional to the amount of water percolating through the disposal site and to the hydraulic conductivities and moisture retention characteristics of the vadose zone. As reported in Appendix 3g, groundwater travel times were affected by only about 25 percent to uncertainties in hydraulic conductivity. Larger differences were found when extreme flow fields were considered. To bound the uncertainty in the base-case flow field, a set of high-flow and low-flow boundary conditions were considered in the vadose zone transport calculations. The high-flow case modeled infiltration rates of 10 mm/year (0.4 in./year) atop Mesita del Buey, 5 mmy/r (0.2 in./year) in Cañada del Buey, and 100 mm/year (0.2 and 4 in./year) in Pajarito

Canyon; the low-flow case modeled rates of 1, 1, and 20 mm/year (0.04, 0.04, and 0.8 in./year) at the top of the mesa, in Cañada del Buey, and in Pajarito Canyon, respectively. The high-flow case resulted in earlier and larger fluxes to the regional aquifer for both lateral and vertical transport, while the low-flow case resulted in later and smaller fluxes. Compared with the base-case peak flux at 2,500 years and 600 years for vertical and lateral-then-vertical groundwater flux to the saturated zone, breakthrough occurred at about 1,000 and 300 years, respectively.

Groundwater simulations indicate that the total mass of contamination exiting the sides of the mesa over 10,000 years is approximately 30 percent of the mass discharged to the aquifer. Based on these results, doses received by the receptor located east-southeast of Area G would be no more than 30 percent greater if all contamination were transported vertically to the regional aquifer.

4.3.3.3 All Pathways

The uncertainties discussed above for the groundwater pathway analysis apply to all-pathway environmental transport. In addition, uncertainties in sediment transport of surface contamination into Pajarito Canyon also apply, as do uncertainties in factors related to contamination of foodstuffs due to radionuclides present in irrigation water.

The mean erosion rate of 4.0×10^{-7} m/year (1.3×10^{-6} ft/year) calculated in the surface-water balance model described in Appendix 3b was used to transport contamination from the surface of Mesita del Buey into Pajarito Canyon in the all-pathways analysis. This erosion rate has a standard deviation of about 1×10^{-6} m/year (3.3×10^{-6} ft/year), and a maximum value of almost 5×10^{-5} m/year (1.6×10^{-4} ft/year). Based on these statistics, the actual erosion rate would be expected to fall within an order of magnitude of the mean rate. Hence, doses to the canyon resident would increase by 10 times or less due to errors in the erosion rate estimate.

Radioactivity transported into the canyons by surface runoff was assumed to uniformly disperse over an area that is equivalent to the area of contamination on the mesa. In actuality, relatively high contaminant concentrations are expected to occur in local depressions where surface runoff collects, while little or no contamination may occur in other areas. Though the actual distribution of contamination across the landscape will influence the projected exposures for the canyon resident, it is not readily projected. Consequently, the error introduced by this source of uncertainty was not considered further in the sensitivity and uncertainty analysis.

The contamination transported to the canyon floor was assumed to be mixed to a depth of 15 cm (6 in.) over the resident's entire lot. This depth is expected to be reasonable for the individual's garden, but may overestimate the mixing depth over the remainder of the lot and therefore, radionuclide concentrations in surface soil. Under worst-case conditions, however, reduced mixing depths will result in no more than a ten-fold increase in the projected doses.

The food crops considered in the all-pathways analysis were assumed to be contaminated by radioactivity deposited on plant surfaces during irrigation, as a result of rainsplash, and by root uptake of contamination in water reaching the ground. All radioactivity deposited on plants was assumed to be transferred to the edible portions of leafy vegetables grown by the resident, while 10 percent of the activity deposited on protected produce, fruit, and grain was assumed to be assimilated into the edible portion. Moderate increases in the translocation factor for protected produce, fruit, and grain will have limited impacts on the projected ingestion doses, given the small contribution that contamination deposited directly on the plants makes to the peak projected doses. For example, a five-fold increase in the translocation factor for non-leafy vegetables results in food pathway doses that are about 20 percent greater than those projected for the nominal case. The amount of radioactivity initially retained by a plant during irrigation and the rate at which it is weathered from plant surfaces are not easily quantified. The fraction of activity initially retained will depend largely upon the rate at which water is applied to the crops and the

morphology of the plants. The rate of weathering will vary with meteorological conditions at the site and characteristics of the food crops. While the magnitude of the error introduced by these uncertainties is unknown, it is not expected to be significant.

The root uptake pathway was the more significant of the three, accounting for more than 85 percent of the dose projected for the food ingestion pathway. The soil concentrations of ^{14}C, ^{99}Tc, and ^{129}I due to irrigation are expected to be overestimated by the models used in the dose assessment. A soil buildup time of 15 years was assumed to apply to all radionuclides in irrigation water. While accounting for buildup may be appropriate for radionuclides that sorb to soils, these highly mobile radionuclides will tend to be transported downward with water percolating through the garden. As the contamination is rinsed from the soils, it will become unavailable for root uptake by plants. Under these conditions, the plant radionuclide concentrations of ^{14}C and ^{99}Tc would be 19 and 16 percent, respectively, of the projected values. Concentrations of ^{129}I would be about 80 percent of the modeled values.

The uptake factors used in the dose assessment for ^{14}C and ^{99}Tc both exceed 1.0, indicating plant radionuclide concentrations exceeding those observed in soils. Moderately higher uptake factors for these radionuclides (e.g., 2 times the nominal values) would result in food pathway doses that are almost 2 times higher than projected. However, these higher doses would increase the peak scenario doses by less than 20 percent. The uptake factors for ^{129}I would need to increase by 100 times or more to have significant effects on the peak.

The plant radionuclide concentrations resulting from the assimilation of radioactivity directly from the irrigation water are a function of the amount of water applied to the crops, crop yields, the plant translocation factor, the fraction of the radioactivity deposited on the plant that is initially retained, and the rate at which radioactivity deposited on plant surfaces is removed due to weathering. The amount of water that was assumed to be applied to the crops is based on information for the greater Los Alamos area and, as such,

is expected to reasonably approximate the amount of water applied to food crops. While rates of water application could vary for short periods, the total amount of water applied to the crops over the course of a growing season is not expected to change substantially.

4.3.4 Usage Factor Uncertainties

The usage factors applied in the dose assessments for the PA and CA were taken from standard references. The effect of known uncertainties in these factors on the air-, groundwater-, and all-pathways analysis are discussed below.

4.3.4.1 Air Pathway

The quantity of radioactivity inhaled is determined by the rate of inhalation and duration of exposure. An annual inhalation rate of 8,000 m^3 (2.8×10^5 ft^3) was used in the dose assessment, based on the assumption that the individual spends 16 hr of each day engaged in light activity and 8 hr resting. This value is 10 percent greater than the annual inhalation rate of 7,300 m^3 (2.6×10^5 ft^3) recommended by the EPA but less than the EPA's reasonable worst-case inhalation rate of almost 11,000 m^3/year (3.9×10^5 ft^3).[116]

The offsite resident was assumed to be at home and inhale airborne radioactivity for almost 6,200 hr per year. Data summarized by the EPA) indicate that, on average, an adult spends 64 percent of their time at home or in the yard. This equates to approximately 5,600 hours per year, about 9 percent less than the values used in the PA and CA.

4.3.4.2 Groundwater Protection

The sole source of exposure for the groundwater protection analysis is the consumption of contaminated water drawn from the well. The individual is assumed to ingest 2 L (5.3×10^{-1} gal) of water per day, including water consumed in the form of juices and other beverages containing tap water. This water consumption rate is consistent with the methodology used to develop the groundwater protection standards and, as such, is appropriate for use in the MDA G dose assessment; however, it is expected to overestimate actual rates of consumption for an average individual. The National Academy of Sciences calculated an average per capita water consumption rate of 1.6

L/day (4.2×10^{-1} gal/day) based on a survey of nine literature sources. This source and several others chosen by the EPA to determine a recommended consumption rate indicate an average adult drinking water consumption rate of 1.4 L/day (3.7×10^{-1} gal/day) and a reasonable worst-case value of 2 L/day (5.3×10^{-1} gal/day).

4.3.4.3 All Pathways

In addition to the inhalation of contaminated air and the consumption of contaminated drinking water that were already discussed, the two all pathways receptors were assumed to consume food crops and animal products raised on a contaminated environment. The incidental ingestion of and exposure to contaminated soil also play important roles in the projected all pathways doses. While the consumption of contaminated food crops contributes as much as 60 percent of the projected peak doses, the consumption of milk and beef is responsible for less than 4 percent of the total doses. Consequently, the following discussion addresses the uncertainties associated with the food-crops usage.

The crop yields used in the dose assessment are expected to be reasonable for the northern New Mexico region. While decreased yields could result in higher concentrations of radionuclides in plants, these differences are expected to be minor. The assumption that one-half of the resident's food requirements are met by crops and animals raised at the site is expected to overestimate the actual amount of food raised by a typical individual. The EPA indicates that, on average, 25 percent of vegetables is home grown, while 20 percent of fruit is grown at home. Reasonable worst-case values cited by the EPA for the amount of home grown vegetables and fruit in the intruder's diet are 40 and 30 percent, respectively.

The rate of inadvertent soil ingestion used in the dose assessment, 100 mg/day (3.5×10^{-3} oz/day), reflects an adult with a high tendency to ingest soil. More reasonable ingestion rates would be low to moderate, in the range of 1 to 10 mg/day (3.5×10^{-5} to 3.5×10^{-4} oz/day). The rates of ingestion used for leafy vegetables, grain, and produce are based on national averages for the United States.[117] These consumption rates generally agree with

the annual consumption rate of 190 kg (420 lb) of fruit, grain, and vegetables cited by the NRC for an average individual.[118] The rates also generally agree with data which indicate annual consumption rates of vegetables, other produce, and grains of about 18, 140, and 35 kg (40, 310, and 77 lb), respectively.[119] Finally, the total consumption rate used in the dose assessment is similar to the consumption rate of 190 kg/year cited by the NRC, but is 3 to 4 times smaller than that cited for modeling doses received by the maximally exposed individual.

Direct radiation exposures will be attenuated by the individual's house during the time spent indoors. A shielding factor of 0.7 was used in the dose assessment to account for these shielding effects. In essence, this means that 70 percent of the direct radiation incident upon the house contributes to the resident's projected exposure. This shielding factor, which is expected to overestimate the exposure of the individual, is suggested by the NRC for projecting doses to the maximum individual; the value suggested for the average individual is 0.5.

4.3.5 Dose Conversion Factor Uncertainties

As in the case of usage factors, dose conversion factors used in the PA and CA dose projections came from standard references. The effect that uncertainties in dose conversion factors have in the air-, groundwater-, and all-pathways analyses are discussed below.

4.3.5.1 Air Pathway

The radioactivity inhaled by the receptor in the air-pathway analysis is related to doses by inhalation dose conversion factors. The projected doses for the scenario are committed effective dose equivalents, representing the total dose equivalent received by the body over a 50-year period after the intake of radioactivity. The dose conversion factors are based on the recommendations of the ICRP.[120] While uncertainties in the dose conversion factors used to project these doses do exist, these uncertainties are difficult to quantify and were not considered in the analysis.

4.3.5.2 Groundwater Protection

The only exposures evaluated in the groundwater protection analysis is the consumption of contaminated water drawn from the well into the regional aquifer. Uncertainties and their effects were discussed in Section 4.3.4.2.

4.3.5.3 All Pathways

All-pathways doses were estimated using 50-year committed effective dose equivalents for internal exposures[121] and external dose conversion factors for exposures to penetrating radiation in contaminated soils. The dose conversion factors used to estimate exposures from direct radiation from contaminated soils were developed using the MICROSHIELD computer code. This code accounts for the source geometry and shielding configuration (i.e., excluding the individual's house) appropriate for the "all pathways" scenarios and, as such, is expected to provide reasonable estimates of the actual exposures. The exposures calculated by the code were converted to radionuclide doses using a conversion factor of 0.75 mrem/mR. This factor was adopted from ICRP 51 and pertains to a rotational geometry for a photon energy of 0.2 MeV. While the precise conversion factor will depend upon the photon energy and exposure geometry, it is not expected to vary by more than 20 percent for expected exposure conditions.

4.3.6 Propagated Dose Assessment Uncertainties

Considered alone, no single source of uncertainty identifed above is expected to compromise the ability of the MDA G disposal facility to comply with the performance measures. However, the errors introduced by the uncertainties in each segment of the analysis for each pathway will propagate through the different modeling stages. To demonstrate reasonable assurance of compliance, the potential impact of these propagated errors on the dose assessments must be evaluated.

4.3.6.1 Air Pathway Analysis

The uncertainties that may cause the projected air-pathway doses to be underestimated include:

- Those associated with the projected inventories of several radionuclides;

- The extent of animal burrowing at the site;
- The values used for the resuspension and dispersion factors; The inhalation rate of the receptor; and
- The time the receptor is exposed to airborne radioactivity.

The composite analysis inventory for ^{241}Am was assumed to be subject to a 30 percent measurement uncertainty, consistent with the detection errors associated with radiochemical measurement techniques. The plutonium isotopes were assigned errors of 1.0 to account for measurement errors and the vast overestimation of inventories that is expected to result from the extrapolation-based projection method. The error of 2.9 assigned to animal burrow distributions reflects uncertainty about the extent of intrusion into the disposed waste. An error of 3.2 was assigned to the resuspension and dispersion factors to reflect a total error of 900 percent. This error was assumed to apply to the point of maximum exposure in Cañada del Buey and to the receptor location in the town of White Rock. An error of 1.4 was assigned to the inhalation rate based on a comparison of the inhalation rate used in the dose assessment to a reasonable worst-case value. Finally, an error term of 1.1 was assigned to the time of exposure to reflect an 80 percent occupancy rate at the disposal site.

Uncertainties associated with the projected radionuclide inventories, the resuspension and dispersion factors used in atmospheric modeling, the inhalation rate of the resident, and the amount of time the individual spends at home may cause the projected doses to be overestimated. Errors assigned to the projected inventories for the PA reflects a reduction in the operational period of the disposal facility and accurate measurement of radionuclide activities. Plutonium inventories are estimated to be overstated by at least a factor of 3. Errors were assigned to the resuspension and dispersion factors to reflect a total uncertainty of 900 percent for the Cañada del Buey and White Rock receptor locations. An error factor of 0.9 was assigned to the inhalation rate and the time of exposure to reflect average breathing rates and occupancy times. Table 4-6 identifies the uncertainty factors applied in the propagation of errors for the air-pathway dose assessment.

The propagated errors shown in Table 4-6 indicate that the PA doses projected to occur from the inhalation of radioactive gases may be underestimated by about 10 times and overestimated by 4.5 times. When applied to the projected peak doses, these errors translate into annual doses of 6.5 × 10-1 and 1.5 × 10-2 mrem at the point of maximum exposure in Cañada del Buey. Corresponding doses for the White Rock location are 1.5 × 10-1 and 3.4 × 10-3 mrem/year. Doses resulting from the inhalation of resuspended dust may be underestimated by 130 times under worst-case conditions, or may be overestimated by a factor of about 15 times under conditions approaching best-case. These estimated errors yield a maximum dose of 1.2 mrem/year, and a minimum dose of 6.3 × 10-4 mrem/year in Cañada del Buey. The worst-case dose projected for the receptor location at White Rock is 2.8 × 10-1 mrem/year, while a dose of 1.5 × 10-4 mrem/year is estimated for optimal conditions. None of these projected doses threaten the ability of the disposal facility to comply with the 10-mrem/year performance objective.

The total errors listed in Table 4-6 indicate that the air-pathway doses projected for the CA may be underestimated by 9.8 and 49 times for radioactive gases and resuspended dust, respectively. Based on these worst-case conditions, the maximum annual doses projected to occur following the release of radioactive gases from the disposal site are 7.4 × 10^{-1} mrem at the point of maximum exposure and 1.7 × 10^{-1} mrem at White Rock. The maximum doses from the resuspension of contaminated dust are estimated to be 2.7 × 10^{2} and 64 mrem/year in Cañada del Buey and at White Rock, respectively. Doses projected for the gas and dust inhalation pathways may overestimate actual doses by about 4.5 and 23 times, respectively. These errors translate into doses of 1.6 × 10^{-2} and 3.9 × 10^{-3} for radioactive gases for the receptor locations in Cañada del Buey and White Rock, respectively. The dust inhalation dose is reduced to 2.4 × 10^{-1} mrem/year in Cañada del Buey and 5.8 × 10^{-2} mrem/year in White Rock.

Table 4-6 Correction factors for uncertainties in air-pathway dose assessment

Source of Uncertainty	Factor for Underestimates[a]		Rationale for Correction Factor	Factor for Overestimates[b]		Rationale for Correction Factor
	PA	CA		PA	CA	
Radionuclide Inventories						
Am-241	3.0E+00	1.3E+00	Detection error of 200% for PA and 30% for CA	8.5E-01	1.0E+00	No detection error, inaccurate projection for PA
H-3	2.0E+00	2.0E+00	Detection error of 100%	8.5E-01	8.5E-01	No detection error, inaccurate projection for PA
Pu-238	3.0E+00	1.0E+00	Detection error of 200 % for PA; equal detection and projection errors for CA	8.5E-01	3.3E-01	No detection error, inaccurate projection for PA; 3-fold overestimate inventory for CA
Pu-239	3.0E+00	1.0E+00	Detection error of 200 % for PA; equal detection and projection errors for CA	8.5E-01	3.3E-01	No detection error, inaccurate projection for PA; 3-fold overestimate inventory for CA
Pu-240	3.0E+00	1.0E+00	Detection error of 200 % for PA; equal detection and projection errors for CA	8.0E-01	3.3E-01	No detection error, inaccurate projection for PA; 3-fold overestimate inventory for CA
Pu-241	3.0E+00	1.0E+00	Detection error of 200 % for PA; equal detection and projection errors for CA	8.5E-01	3.3E-01	No detection error, inaccurate projection for PA; 3-fold overestimate inventory for CA
Th-232	3.0E+00	c	Detection error of 200 %	8.5E-01	c	Projection inaccurate, no detection error.
U-234	2.0E+00	c	Detection error of 100 %	8.0E-01	c	Projection inaccurate, no detection error.
U-235	2.0E+00	c	Detection error of 100 %	8.5E-01	c	Projection inaccurate, no detection error.
U-238	2.0E+00	c	Detection error of 100 %	8.5E-01	c	Projection inaccurate, no detection error.
Source Releases						
Burrow Distrib	2.9E+00	2.9E+00	Ratio of maximum to base-case distribution	1.0E+00	1.0E+00	No overestimate assumed
Environmental Transport						
Resuspension	3.2E+00	3.2E+00	Error of 10 in resuspension and dispersion factors	3.2E-01	3.2E-01	Error of 10 in resuspension and dispersion factors
Dispersion	3.2E+00	3.2E+00	Error of 10 in resuspension and dispersion factors	3.2E-01	3.2E-01	Error of 10 in resuspension and dispersion factors
Resource Utilization						
Inhalation Rate	1.4E+00	1.4E+00	Ratio of worst-case to base-case	9.0E-01	9.0E-01	Ratio of EPA average to base-case
Exposure Time	1.1E+00	1.1E+00	Ratio of worst-case to base-case	9.0E-01	9.0E-01	Ratio of expected-case to base-case
Total Propagated Error						
Gas Inhalation	9.8E+00	9.8E+00		2.2E-01	2.2E-01	
Dust Inhalation	1.3E+02	4.9E+01		6.9E-02	4.4E-02	

a. Factors represent degree to which projected scenario doses may be underestimated due to errors in models and parameters under conditions approaching worst-case.
b. Factors represent degree to which projected scenario doses may be overestimated due to errors in models and parameters under optimal conditions.
c. No error assigned as parameter did not make significant contribute to dose.

While several sources of uncertainty are associated with the projected CA doses for the air pathway analysis, certain characteristics of the portion of MDA G used for the disposal of pre-1971 waste may significantly limit atmospheric pathway doses. Transuranic waste storage facilities have been constructed over the pits used for waste disposal between 1957 and 1970. As part of the construction of these facilities, a total of 3.3 m (10 ft) of cover material was placed over the disposal units. If maintained over this portion of MDA G, this additional cover would effectively prevent biotic intrusion into the 1957 to 1970 waste inventory. Given that this portion of the CA inventory contributes approximately 98 percent of the peak CA dose projected for the air pathway analysis, peak exposures would decline to about 0.1 mrem/year. This reduction would, in turn, significantly reduce the worst-case dose of 270 mrem/year reported above. Under these conditions, the 30-mrem/year performance objective would easily be met.

Sources of uncertainty that may cause the projected radon fluxes to be underestimated include those associated with the projected inventories of ^{226}Ra and ^{232}Th and the emanation coefficient. The errors assigned to the projected radionuclide inventories are based on the measurement uncertainties discussed earlier. An error term of 1.2 was assigned to the radon emanation coefficient in lieu of site-specific data for this parameter. Uncertainties associated with these same parameters may also overestimate the actual radon fluxes. The propagated errors shown in Table 4-7 indicate that the radon fluxes for the historic PA waste may be underestimated by 2.4 times, while fluxes for the future waste inventories may be 3.6 times higher. Applying these errors to the projected peak fluxes, radon fluxes of 2.6×10^{-1} and 6.1×10^{-1} pCi/m^2/s (2.4×10^{-2} and 5.7×10^{-2} pCi/ft^2/s) are projected for the historic and future pit waste, respectively. The worst-case fluxes for the historic and future disposal shafts are 7.4 and 2.9 pCi/m^2/s (6.9×10^{-1} and 2.7×10^{-1} pCi/ft^2/s), respectively. Fluxes may be overestimated by factors ranging from 1.2 to 1.6 times. These errors translate into projected fluxes of 8.8×10^{-2} and 1.1×10^{-1} pCi/m^2/s (8.2×10^{-3} and 1.0×10^{-2} pCi/ft^2/s) for the historic and future disposal pits, respectively. The corresponding fluxes for the historic and future shaft waste are 2.5 and 5.1×10^{-1} pCi/m^2/s (2.3×10^{-1} and 4.8×10^{-2} pCi/ft^2/s), respectively.

Table 4-7 Correction factors for uncertainties in radon flux for the PA

Source of Uncertainty	Correction Factor for Underestimated Flux		Correction Factor for Overestimated Flux	
Inventory	**Past**	**Future**	**Past**	**Future**
^{226}Rn	2.0	2.0	1.0	0.8
^{232}Th	3.0	3.0	1.0	0.8
Source Term				
Emanation	1.2	0.8	1.2	0.8
Total Radon Flux Uncertainty	2.4	3.6	0.8	0.64

4.3.6.2 Groundwater Protection Analysis

Uncertainties that may cause doses for the groundwater protection analysis for the PA to be underestimated include:

- Those associated with radionuclide inventories,
- Rates of water infiltration on the mesa and in the adjacent canyons, the water transit time in the waste, radionuclide travel times, and
- The modeling approach used to estimate rates of lateral transport.

An error term of 3 was assigned to ^{14}C, ^{99}Tc, and ^{129}I based on the assumptions that all future waste projections were correct and that measured activities always underestimate the actual activities by 200 percent. The error term associated with the water infiltration rate was 2.2, based on high flow calculations and the conservative assumption that water passes through the waste packages in the disposal units in a year's time. More rapid transit times may occur if the moisture content of the waste was greater than projected or the amount of infiltration in the disposal units was increased. Finally, an error of 1.3 was assigned to lateral flow modeling for the receptor location east-southeast of MDA G, based on the assumption that, in the event that no lateral transport occurs, all radioactivity leached from the waste may reach this receptor's well.

A number of sources of uncertainty may cause the actual doses for the groundwater protection analysis to be overestimated. Some error terms included were assigned to account for this possibility. The error terms assigned for inventory uncertainties are based on the assumptions that all waste activities were measured accurately and that the MDA G disposal facility ceases operation after 40 years rather than 49 years. This error term was reduced further for ^{14}C to account for the possibility that no ^{14}C sources, the dominant contributor to the projected inventory, will be generated at the Laboratory. The error terms associated with the water infiltration rates take into account the results of the groundwater simulations for low-flow conditions. These same error terms are listed for radionuclide travel times, but were considered only once in error propagation.

The error term of 0.75 for water transit time was estimated based on the assumption that the time required for water to travel through the waste packages is greater than 16 years but less than 50 years. Such a condition may exist, for instance, if drier conditions prevailed in the disposal units. Uncertainties associated with aquifer dilution modeling may overestimate the actual dose by a factor of two or more, a factor of two was assumed for the sensitivity and uncertainty analysis. An error term of 0.6 was assigned to the Parajito Canyon receptor location to account for uncertainties introduced by combining lateral releases from the historic and future performance assessment inventories. This factor was estimated as the ratio of the dose contributed by the future inventory to the total peak dose from the entire performance assessment inventory. Finally, the rate of water consumption was assigned an error of 0.7 to account for the fact that the 2-L/day (0.5-gal/day) consumption rate is higher than average per capita consumption rates. Table 4-8 lists the correction factors applied to the groundwater pathways doses to account for uncertainties that may underestimate or overestimate doses. The results shown in Table 4-8 indicate that the parameters and modeling approaches used in the PA may underestimate doses to the downgradient by as much as 360 times, and by as much as 18 times at the Parajito Canyon location. Based on these results and on the doses projected for the receptor located 100 m downgradient of MDA G, the peak annual dose expected under worst-case conditions during the 1,000-year compliance period is

Table 4-8 Correction factors for uncertainties in PA groundwater protection doses

Source of Uncertainty	Factor for Underestimates[a]	Rationale for Correction Factor	Factor for Overestimates[b]	Rationale for Correction Factor
Radionuclide Inventory				
C-14	3.0E+00	Projection accurate; detection error of 200%	4.2E-01	Projection inaccurate; no detection error.
Tc-99	3.0E+00	Projection accurate; detection error of 200%	8.4E-01	Projection inaccurate; no detection error.
I-129	3.0E+00	Projection accurate; detection error of 200%	9.0E-01	Projection inaccurate; no detection error.
Infiltration Rate				
Downgradient	4.2E+01	Ratio of high- flow field dose to base-case dose	5.3E-05	Ratio of low-flow field dose to base-case dose
Parajito Cyn	2.7E+00	Ratio of high- flow field dose to base-case dose	1.2E-01	Ratio of low-flow field dose to base-case dose
Waste Transit Time	2.2E+00	Ratio of 1 year to base case (16 years)	7.5E-01	Ratio of 50 years to base case (16 years)
Environmental Transport				
Radionuclide Travel Time				
Downgradient	4.2E+01	Ratio of high- flow field dose to base-case dose	5.3E-05	Ratio of low-flow field dose to base-case dose
Parajito Cyn	2.7E+00	Ratio of high- flow field dose to base-case dose	1.2E-01	Ratio of low-flow field dose to base-case dose
Lateral Transport Modeling				
Downgradient	1.3E+00	Proportion of lateral flux to vertical flux	1.0E+00	c
Aquifer Dilution	1.0E+00	c	5.0E-01	Ratio of calculated-to-observed aquifer velocity
Combination of Lateral Sources				
Parajito Cyn	1.0E+00	c	6.0E-01	Ratio of doses due to historic and future inventories
Resource Utilization				
Water Consumption Rate	1.0E+00	c	7.0E-01	Ratio of EPA's *per capita* rate to assumed rate
Total Propagated Error				
Downgradient	3.6E+02		7.7E-06	
Parajito Cyn	1.8E+01		1.0E-02	

a. Factors represent degree to which projected scenario doses may be underestimated due to errors in models and parameters under conditions approaching worst-case.
b. Factors represent degree to which projected scenario doses may be overestimated due to errors in models and parameters under optimal conditions.
c. No error assigned as parameter did not make significant contribution to doses.

expected to be 3.0×10^{-5} mrem/year. Similarly, the peak annual dose under worst-case conditions for the receptor in Parajito Canyon is expected to be 8.1×10^{-4} mrem. Even under these unfavorable conditions, the projected peak doses for the groundwater protection analysis still constitute only small fractions of the 4-mrem/year performance objective.

Based on the results shown in the table, doses for the downgradient receptor may be overestimated by several orders of magnitude, while doses for the Parajito Canyon resident may be overstated by a factor of 100. Hence, under conditions approaching best-case, the peak projected dose for the receptor east-southeast of the disposal facility is 6.4×10^{-13} mrem/year. Similarly, the peak annual dose projected for the person in Parajito Canyon is 4.5×10^{-7} mrem.

4.3.6.3 All-Pathways Analysis

The all-pathways doses propagated at the 100-m downgradient receptor location are sensitive to the uncertainties in the groundwater protection analysis already discussed, and also to other factors associated with doses due to exposures to contaminated foodstuffs and soil. In terms of the latter factors, uncertainties in plant uptake factors and the amount of radioactivity in irrigation water that is assimilated by crops may cause projected doses to be underestimated. An error of 1.9 was assigned to plant uptake factors to reflect the impact a two-fold increase in the plant uptake factors for ^{14}C, ^{99}Tc, and ^{129}I will have on projected food pathway doses. The error of 1.1 assigned to plant uptake from irrigation reflects a five-fold increase in the translocation factor for non-leafy vegetables.

Sources of uncertainty that may cause the projected all-pathways doses to be overestimated include soil radionuclide concentrations resulting from irrigation, the rate of soil consumption, and the proportion of the resident's food requirements that is raised by the individual. An error of 0.2 is assigned to the soil radionuclide concentrations, which is consistent with a more reasonable buildup time of 1 year for ^{14}C, ^{99}Tc, and ^{129}I. The error of 0.1 assigned to the soil consumption rate is based on average soil consumption rates in

adults that have a low tendency to eat soil. The proportion of food requirements grown at the resident's home is assigned an error of 0.5 based on the national averages for this parameter. Table 4-9 and 4-10 list the correction factors applied to the all-pathways doses to account for uncertainties that may underestimate or overestimate doses calculated in the PA and CA at the downgradient and Pajarito Canyon receptor locations, respectively.

The propagated errors listed in Table 4-9 indicate that the doses for the all-pathways analysis performed for the downgradient receptor may be underestimated by a factor of 630 for the PA and 710 for the CA. The products of these errors and the projected peak doses yield worst-case doses of 6.1×10^{-3} and 4.1×10^{-1} mrem/year, respectively. These doses are small fractions of the performance objectives pertinent to these analyses. Due to various uncertainties, the all-pathways doses may also be overestimated by several orders of magnitude.

Additional sources of uncertainty include the rate of erosion, the soil mixing depth in the canyon, and the soil consumption rate. An error of 10 was assigned to the first two parameters based on previous discussion. The error of 0.1 assigned to the soil consumption rate takes into account the intake of soil in adults with a low tendency to ingest soil.

Referring to Figure 4-10, the propagation of errors in dose assessment for the all-pathways receptor in Pajarito Canyon indicates that the PA doses may be underestimated by a factor of 27 and overestimated by 1.1×10^{-1} times. These propagated errors yield annual doses of 3.5×10^{-3} and 1.64×10^{-5} mrem, respectively. CA doses for this scenario may be underestimated by 540 times, and overestimated by 3.6 times. The doses corresponding to these errors are 3.9 and 2.0×10^{-3} mrem/year. The worst-case doses are all much less than the appropriate performance objectives.

Table 4-9 Correction factors for uncertainties in downgradient all-pathways doses in the PA and CA

Source of Uncertainty	Factor for Underestimates[a]		Rationale for Correction Factor	Factor for Underestimates[b]		Rationale for Correction Factor
	PA	CA		PA	CA	
Radionuclide Inventories						
C-14	3.0E+00	3.0E+00	Accurate projection; detection error 200 %	4.2E-01	9.4E-01	Inaccurate projection; no detection error.
Tc-99	3.0E+00	3.0E+00	Accurate projection; detection error 200 %	8.4E-01	8.7E-01	Inaccurate projection; no detection error.
I-129	3.0E+00	3.0E+00	Accurate projection; detection error 200 %	9.0E-01	1.0E+00	Inaccurate projection; no detection error.
Source Releases						
Infiltration Rate	4.2E+01	4.8E+01	Ratio of high-flow conditions dose to base-case dose	5.2E-05	4.4E-06	Ratio of low-flow conditions dose to base-case dose
Water Transit Time	2.2E+00	2.2E+00	Ratio of 1 year to base case	7.5E-01	7.5E-01	Ratio of 50 years to base case
Environmental Transport						
GW Travel Time	4.2E+01	4.8E+01	Ratio of high-flow conditions dose to base-case dose	5.2E-05	4.4E-06	Ratio of low-flow conditions dose to base-case dose
Lateral Transport	1.3E+00	1.3E+00	Ratio of lateral mass flux to total mass flux	1.0E+00	1.0E+00	n/a
Aquifer Dilution	1.0E+00	1.0E+00	n/a	5.0E-01	5.0E-01	Ratio of observed aquifer velocity to base case
Concentrations from Irrigation	1.0E+00	1.0E+00	15 yr buildup time of contaminants in soil with no migration	2.0E-01	2.0E-01	Ratio of soil buidup for 2 years to base case
Plant Uptake Factors	1.9E+00	1.9E+00	2-fold increase in plant uptake factors for C-14, Tc-99, and I-129.	1.0E+00	1.0E+00	n/a
Plant Uptake from Irrigation	1.2E+00	1.2E+00	5-fold increase in translocation factor for non-leafy vegetables.	1.0E+00	1.0E+00	n/a
Resource Utilization						
Soil Consumption	1.0E+00	1.0E+00	n/a	1.0E-02	1.0E-02	Ratio of expected soil ingestion to base case
Water Consumption	1.0E+00	1.0E+00	n/a	7.0E-01	7.0E-01	Ratio of estimated *per capita* rate to base case
Vegetable Consumption	1.0E+00	1.0E+00	n/a	1.0E+00	1.0E+00	n/a
Proportion of Garden Crops Eaten	1.0E+00	1.0E+00	n/a	6.0E-01	6.0E-01	Ratio of estimated home-grown foodstuffs ingestion to base case
Total Propagated Error	6.3E+02	7.1E+02		3.5E-06	5.0E-07	

a. Factors represent the degree to which projected scenario doses may be underestimated due to errors in models and parameters under conditions approaching worst-case.

b. Factors represent the degree to which projected scenario doses may be overestimated due to errors in models and parameters under optimal conditions.

Table 4-10 Correction factors for uncertainties in Pajarito Canyon all-pathways doses in the PA and CA

Source of Uncertainty	Factor for Underestimates[a]		Rationale for Correction Factor	Factor for Underestimates[b]		Rationale for Correction Factor
	PA	CA		PA	CA	
Radionuclide Inventories						
C-14	3.0E+00	3.0E+00	Accurate projection; detection error 200 %	4.2E-01	9.4E-01	Inaccurate projection; no detection error.
Tc-99	3.0E+00	3.0E+00	Accurate projection; detection error 200 %	8.4E-01	8.7E-01	Inaccurate projection; no detection error.
I-129	3.0E+00	3.0E+00	Accurate projection; detection error 200 %	9.0E-01	1.0E+00	Inaccurate projection; no detection error.
Source Releases						
Infiltration Rate	4.2E+01	4.8E+01	Ratio of high-flow conditions dose to base-case dose	5.2E-05	4.4E-06	Ratio of low-flow conditions dose to base-case dose
Water Transit Time	2.2E+00	2.2E+00	Ratio of 1 year to base case	7.5E-01	7.5E-01	Ratio of 50 years to base case
Environmental Transport						
GW Travel Time	4.2E+01	4.8E+01	Ratio of high-flow conditions dose to base-case dose	5.2E-05	4.4E-06	Ratio of low-flow conditions dose to base-case dose
Lateral Transport	1.3E+00	1.3E+00	Ratio of lateral mass flux to total mass flux	1.0E+00	1.0E+00	n/a
Aquifer Dilution	1.0E+00	1.0E+00	n/a	5.0E-01	5.0E-01	Ratio of observed aquifer velocity to base case
Concentrations from Irrigation	1.0E+00	1.0E+00	15 yr buildup time of contaminants in soil with no migration	2.0E-01	2.0E-01	Ratio of soil buidup for 2 years to base case
Plant Uptake Factors	1.9E+00	1.9E+00	2-fold increase in plant uptake factors for C-14, Tc-99, and I-129.	1.0E+00	1.0E+00	n/a
Plant Uptake from Irrigation	1.2E+00	1.2E+00	5-fold increase in translocation factor for non-leafy vegetables.	1.0E+00	1.0E+00	n/a
Resource Utilization						
Soil Consumption	1.0E+00	1.0E+00	n/a	1.0E-02	1.0E-02	Ratio of expected soil ingestion to base case
Water Consumption	1.0E+00	1.0E+00	n/a	7.0E-01	7.0E-01	Ratio of estimated *per capita* rate to base case
Vegetable Consumption	1.0E+00	1.0E+00	n/a	1.0E+00	1.0E+00	n/a
Proportion of Garden Crops Eaten	1.0E+00	1.0E+00	n/a	6.0E-01	6.0E-01	Ratio of estimated home-grown foodstuffs ingestion to base case
Total Propagated Error	6.3E+02	7.1E+02		3.5E-06	5.0E-07	

a. Factors represent the degree to which projected scenario doses may be underestimated due to errors in models and parameters under conditions approaching worst-case.

b. Factors represent the degree to which projected scenario doses may be overestimated due to errors in models and parameters under optimal conditions.

4.4 ALARA ANALYSIS

As stated earlier, the primary performance objective for the CA is 100 mrem/yr to a hypothetical member of the public. A dose constraint of 30 mrem/yr is also applied to the results of the CA. If the projected doses exceed 30 mrem/yr, an options or ALARA analysis shall be performed to identify cost-effective ways in which the potential exposures to the public can be reduced.

The projected peak doses for the exposure scenarios included in the CA do not exceed the 30 mrem/yr limit. Under these conditions, an ALARA analysis is not required but may still be warranted.[2] The following paragraphs discuss the process used to determine if, indeed, a quantitative ALARA assessment is justified.

The ALARA analysis considers the cost of the actions taken to reduce exposures relative to the reduction achieved. To conduct the analysis, a monetary equivalence is assigned to the reduction in doses. Having done this, the ALARA process is considered to be optimized when the cost of the action is less than, or in the range of, the monetary valuation of the avoided dose. The monetary equivalence recommended by DOE for the dose reduction is in the range of $1,000 to $10,000 per person/rem potentially avoided.

To evaluate whether an action taken to reduce collective population dose is cost-effective or ALARA, the potentially exposed population must be quantified. Then, the collective dose is the individual dose calculated in the CA multiplied by the number of potentially exposed people, integrated over a period of 300 years. In terms of the groundwater pathway, the size of the population exposed is conservatively set equal to the total number of people living in White Rock and in the Cochiti Pueblo. This population totals about 15,000 people. The peak exposure projected for the resident in Parajito Canyon depends upon the individual's presence directly below MDA G. Consequently, the total population that may be exposed is much less than that estimated for the groundwater pathways and is assumed to be 10. The peak air pathway exposure is to a hypothetical person in Cañada

del Buey, approximately 500 m north of MDA G. While the number of persons that would be exposed to these conditions will be small, it is conservatively assumed to be 100. The entire population of White Rock, 6,800 people, is assumed to be exposed to the air pathway concentrations projected for that location. The collective doses calculated for the CA ALARA analysis are listed in Table 4-11. Applying a $1,000 monetary valuation to the projected peak population doses listed, an action that eliminated the population exposure projected via the air pathway in Cañada del Buey would be ALARA if it cost less than $160,000, while eliminating the projected air-pathway dose in White Rock would be ALARA if it cost less than or equal to $2,700,000. In contrast, the all-pathways doses are so small that actions taken to reduce them are not highly valued in the ALARA sense.

Table 4-11 Collective population doses for the composite analysis ALARA analysis.

Exposure Scenario	Projected Peak Population Dose (person-rem)
All Pathways - Downgradient	5.4E-02
All Pathways - Parajito Canyon	2.2E-02
Air Pathway - Canada del Buey	1.6E+02
Air Pathway - White Rock	2.7E+03

Any of several options that would decrease the potential for biotic intrusion into disposal units at MDA G would substantially reduce the collective air-pathway doses in both Cañada del Buey and in White Rock. Among these options are a thicker cover and active maintenance of the site to eliminate the potential for biotic intrusion. The passive solution is attractive for several reasons. The estimated cost for 250,000 m^3 of crushed tuff (40 acres, 1 m thick) is $1,500,000. This cost would be augmented by the cost to prepare the existing covers, to emplace the new covers, to recontour the surface, and to revegetate the new cover. Even so, it may be ALARA to emplace an additional 1 m of crushed tuff over the closed disposal units. However, before such a decision is made, it is prudent to evaluate the results of the sensitivity and uncertainty analysis and to refine the air pathway analysis accordingly.

The results of the sensitivity and uncertainty analysis show that projected air pathway doses are sensitivite to the actinide inventory extrapolated for the period 1957 through 1971. That inventory is expected to be grossly overestimated. A more thorough characterization of the pre-1971 inventory is warranted if the results are going to be used as a basis for the closure plan. The air-pathway doses are also sensitive to the extent of biotic intrusion and subsequent translocation. In the biotic translocation model, actinides are extracted by deer mice rather than plants. No material will be excavated by deer mice if their burrows do not penetrate through the cover and into the waste. Assuming a 1 m (3.3 ft) cover and a 2 m (6.6 ft) burrowing depth, contamination will be translocated to the surface. The radionuclide content of the material will not likely be what was modeled, which assumed a homogeneous mix and distribution of all radionuclides contained in a given disposal unit. Certain records for the pre-1971 inventory suggest that much of the more highly contaminated plutonium waste is buried at the bottom of pits, thereby making it unavailable for extraction from the top-most lift. Again, a more careful consideration of the pre-1971 inventory is warranted before any decision is made on the basis of this analysis.

Two other considerations should be noted regarding the potential for biotic translocation. It is likely that several of the older pits are covered with more than 1 m (3.3 ft) of crushed tuff because, until 1996, disposal units were determined to be full on the basis of the spill point, the lowest point along the perimeter of a given pit. On excavation, the spill point was identified, and a line was projected from the spill point around the pit to create the fill line. Waste was not placed to within 1 m of the fill line. Given the topography of the mesa and the length of pits, the fill line may be more than 1 m (3.3 ft) lower than the opposite wall. Another fact to recognize is that the oldest disposal units (Pits 1-5) are responsible for the largest air-pathway doses, assuming a 1 m cover. In reality, however, these pits are covered with approximately 3 m (10 ft) of overburden and surface structures supporting a TRU waste management project. It is unlikely that all of the overburden will be removed. It is possible that the surface structures will be dismantled and removed, and that the bare surface will be recontoured and revegetated like the rest of the mesa.

5. INADVERTENT INTRUDER ANALYSIS

The inadvertent intruder analysis was performed to establish upper limits on radioactivity concentrations for LLW to be disposed of at MDA G. The DOE intends to exercise control of MDA G until it can be safely released for public use, and intrusion is a hypothetical event modeled to address the following performance objective in DOE 5820.2A, applicable to the PA inventory:

> Ensure that the committed effective dose equivalents received by individuals who inadvertently intrude into the facility after the loss of active institutional control (100 years) will not exceed 100 mrem/yr for continuous exposure or 500 mrem for a single acute exposure.

For the purposes of the analysis, accidental, temporary intrusion was assumed to be due to a lapse in control at the site during the industrial-use period.[1] Several intruder scenarios were considered to model events that could reasonably occur and result in chronic or acute exposures.

The intruder analysis and results are discussed in the following sections. First, the the acute and chronic exposure scenarios considered for the analysis are summarized, then the doses resulting from the scenarios analyzed are presented. Finally, a supplemental analysis performed to understand the sensitivity of the calculations to uncertainties in the model is discussed. A detailed description of the inadvertent intruder analysis summarized below is included in Appendix 3e.

5.1 INTRUDER EXPOSURE SCENARIOS

Three intruder exposure scenarios—1) Intruder Agriculture, 2) Intruder Construction, and 3) Intruder Discovery— were initially considered in the PA. In general, these exposure scenarios resemble those used by the U.S. Nuclear Regulatory Commission (NRC) in support of 10 CFR Part 61.[122]

Intrusion into the disposal pits at MDA G was assumed to be feasible at all times after the end of the 100-year active institutional-control period. It was assumed that waste containers and waste forms would not limit the potential for intrusion into the waste. While steel boxes and drums used for waste disposal, and some waste forms (e.g., metals and grouted waste) may be recognizable after 100 years, their rates of degradation under local disposal conditions are unknown. Inadvertent intrusion into the disposal shafts was assumed to be prevented for 300 years following the closure of MDA G. The disposal shaft design incorporates concrete caps to better isolate the waste from the surface environment. Although the expected lifetime of these concrete caps is unknown, it was assumed that the concrete caps will resist intrusion for 300 years.

Well drilling was not modeled primarily because it was not considered realistic. Foremost, an accidental, unnoticed siting of a water well is not likely in that the regional aquifer is located at a significant depth beneath MDA G. Similarly, exploratory wells will not likely be pursued in this area, due to the lack of exploitable natural resources.

Among the three intruder exposure scenarios, the intruder-agriculture scenario was chosen to demonstrate compliance. For usually, potential exposures will be greatest for the agricultural intruder under all conditions, when the concentration of radioactivity encountered, the times of exposure, and the level of resource use are considered. Generally, the exposure routes include ingestion of contaminated food and soil, inhalation of airborne contaminants (expect radon and its daughters), and direct radiation from airborne contaminants and contaminated soils. In the intruder-agriculture scenario, a "standard reference man" builds and resides in a basement home over a disposal unit, spreads contamination excavated during basement construction over the construction lot and garden area, and consumes crops grown in the garden.

The construction scenario considers exposures received by an individual constructing a house at the disposal site. The projected dose for this scenario is less than that projected for the agricultural intruder because of fewer routes and shorter exposure times.

In the discovery scenario, while constructing a house at disposal site, an individual discovers intact waste in the course of excavating a basement and abandons all efforts. The concentrations of radioactivity encountered by the intruder are greater than those contacted in the previous scenarios because the waste is not mixed with clean soil. However, the time of exposure is far less (less than 100 hours), and the number of exposure routes leading to potential doses are fewer.

The nature of the intruder scenario is such that intrusion into one type of disposal unit (i.e., pits or shafts) precludes simultaneous intrusion into the other. Similarly, intrusion into the historic waste by an individual is not consistent with intrusion into the future inventory at the same time. Consequently, separate intruder dose projections were calculated for the historical and future inventories, and for the disposal pits and shafts. These projections accounted for the inventories disposed of, or projected to be disposed of, at MDA G and the specific characteristics of the disposal units.

The results of the intruder analysis were used to assess compliance with DOE Order 5820.2A and to establish radionuclide concentration limits for waste disposed of at MDA G. Both of these analyses were based on the 100-mrem/yr performance objective for chronic intruder exposures. The NRC defines acute exposure events as those that occur for less than 1 year.[123] Based on this definition and on the assumption that complacency on the part of the site custodian could last as long as two years, it was assumed that the intruder-agriculture scenario constitutes a chronic exposure.

5.2 INTRUDER ANALYSIS RESULTS

The dose projections for the intruder-agriculture exposure scenario are presented and discussed below, first considering intrusion into waste disposed of between September 26, 1988, and the end of 1995, and then for waste expected to require disposal between 1996 and 2044, the assumed end of disposal operations at MDA G.

5.2.1 Intruder Analysis Results for Historic Waste

The doses projected for the intruder-agriculture exposure scenario for the disposal units filled from September 26, 1988 through 1995 are shown in Figure 5-1 for the period between 100 and 1,000 years following the end of disposal operations. In calculating the doses, it was assumed that pits filled before 1996 were covered with 0.9 m (3 ft) of crushed tuff and 0.1 m (0.3 ft) of topsoil; the shafts filled before 1996 were covered with 0.9 m (3 ft) of crushed tuff and 0.5 m (1.5 ft) of concrete.

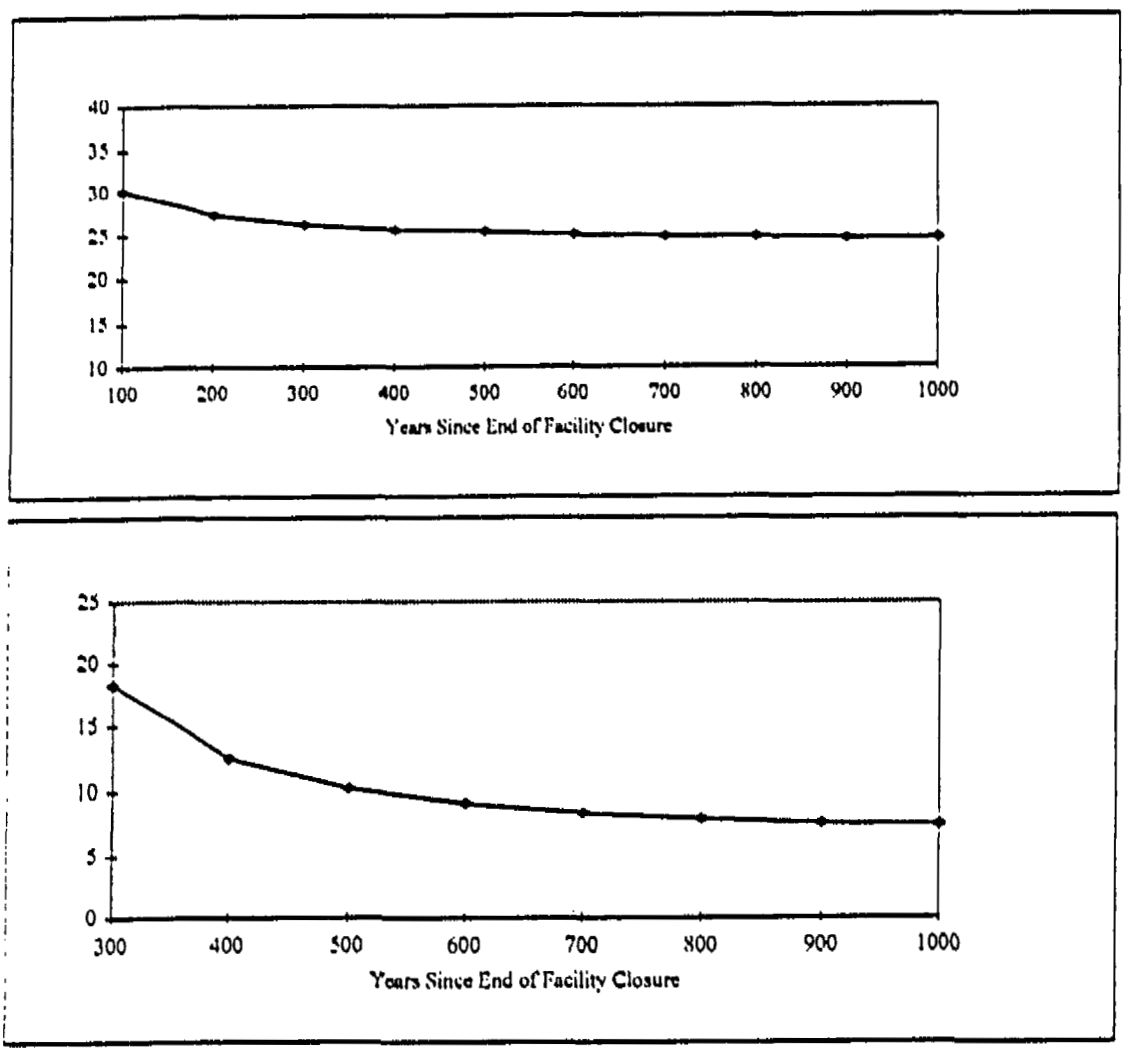

Figure 5-1 Doses calculated for intrusion into pits and shafts (top and bottom, respectively) filled from September 26, 1988 through 1995

The peak dose resulting from intrusion into historic pit waste was calculated to be 30 mrem/yr, while the peak dose from intrusion into historic shaft waste was 18 mrem/yr. For both pits and shafts, the peak dose occurred at the earliest time of intrusion, which was 100 years for pits and 300 years for shafts (because of the presumed stability of the concrete barrier). Thereafter, annual doses decreased with the decay of the shorter-lived radionuclides in the waste. The radionuclides making major contributions to the projected dose after intrusion are shown in Figure 5-2.

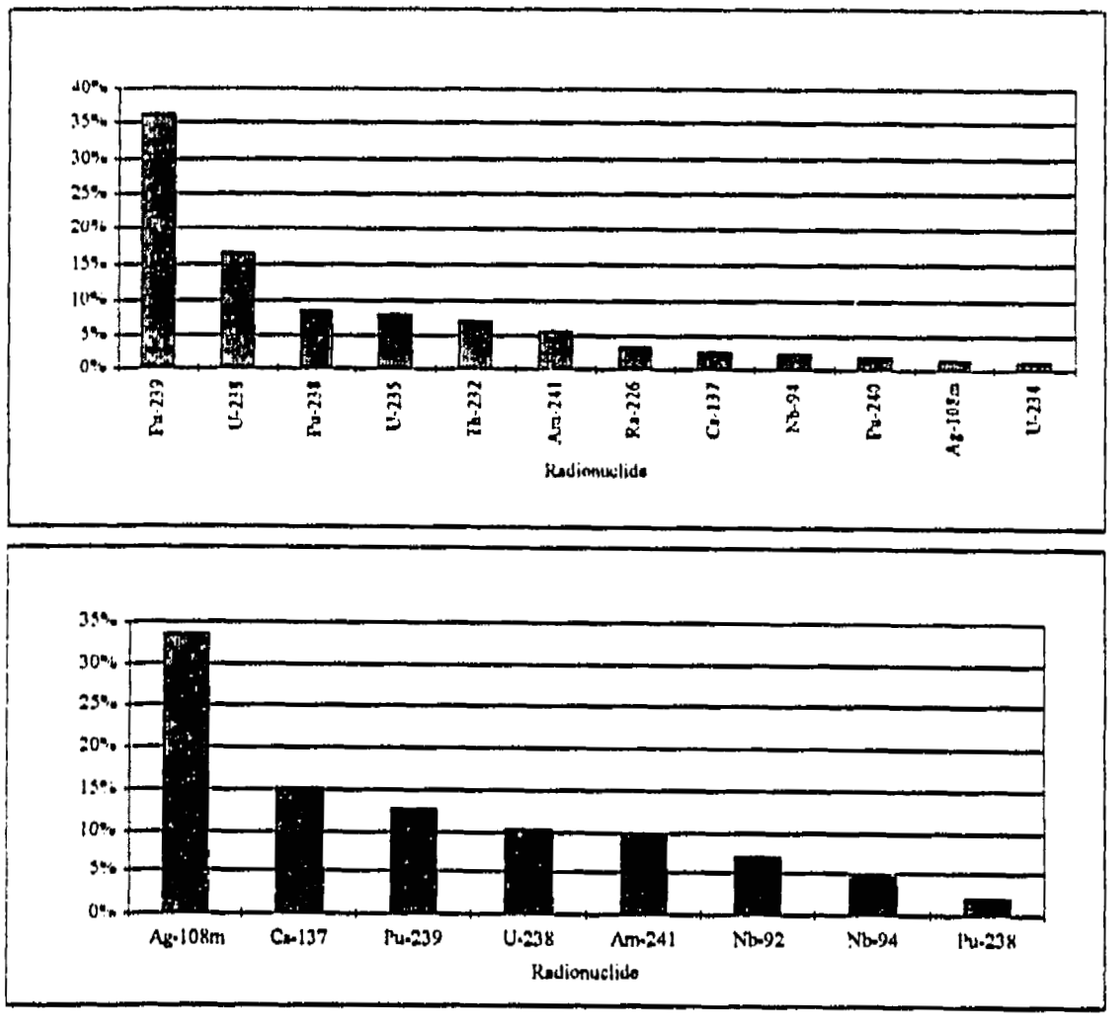

Figure 5-2 Radionuclides contributing to the doses from inadvertent intrusion into historic waste in pits and shafts (top and bottom, respectively)

Two long-lived radionuclides, ^{239}Pu and ^{238}U, account for about 52 percent of the peak dose projected for the historic pit waste; four others, ^{241}Am, ^{238}Pu, ^{232}Th, and ^{235}U, each contribute 6 to 9 percent of the peak dose. The inhalation of suspended dust and direct radiation from contaminated soil are responsible for 42 and 28 percent of the peak dose, respectively. For intrusion into shafts, ^{108m}Ag and ^{137}Cs are responsible for almost 50 percent of the projected dose; ^{241}Am, ^{92}Nb, ^{94}Nb, ^{238}Pu, and ^{238}U each contribute 5 to 13 percent of the dose. Important exposure pathways include direct radiation from contaminated soils, which accounts for 66 percent of the total dose, and the inhalation of airborne radioactivity, which contributes 21 percent of the dose.

5.2.2 Intruder Analysis Results for Future Waste

The intruder analysis for the future waste inventory assumed that pits will be covered with 2 m (6.6 ft) of crushed tuff and topsoil, and that shafts will be covered with 1.5 m (5.1 ft) of crushed tuff and 0.5 m (1.5 ft) of concrete. Doses projected for the intruder-agriculture exposure scenario for the future disposal pits and shafts are shown in Figure 5-3 for the 1,000-year compliance period. Similar to the historic inventory, peak doses occurred at the earliest time of intrusion, 100 years for pits and 300 years for shafts. The peak annual dose for the pit waste was 30 mrem, which remained relatively constant throughout the compliance period. The peak intruder dose for the future shaft waste was 12 mrem/yr. Annual doses for the shaft waste decline after the initial intrusion event at 300 years to less than 6 mrem by the end of the compliance period. Radionuclide contributions to the peak doses projected for the future pit and shaft waste are shown in Figure 5-4. Plutonium-239 and ^{238}U account for about 50 percent of the projected peak dose for the disposal pits; ^{241}Am, ^{238}Pu, ^{240}Pu, ^{226}Ra, and ^{238}U are each responsible for 5 to 7 percent of the total dose. Inhalation of airborne particulates and direct radiation from the ground surface are the dominant exposure pathways, accounting for 68 percent of the peak dose. In terms of the future shafts, ^{137}Cs accounts for 38 percent of the projected intruder dose; ^{241}Am, ^{92}Nb, ^{239}Pu, and ^{238}U each contribute 10 to 17 percent of the total dose. Inhalation of airborne ^{241}Am, ^{239}Pu, and ^{238}U and direct radiation from soil contaminated with ^{137}Cs account for 83 percent of the projected exposure.

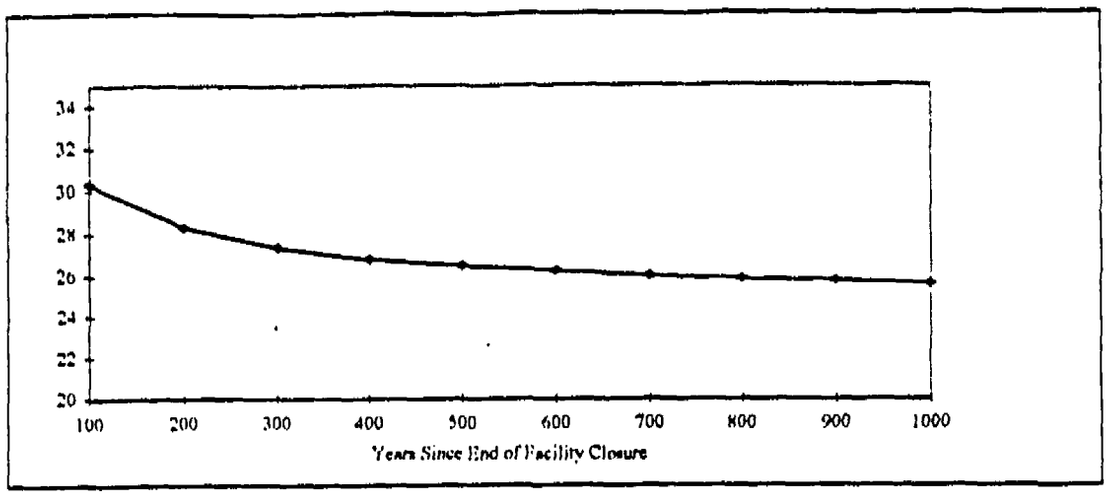

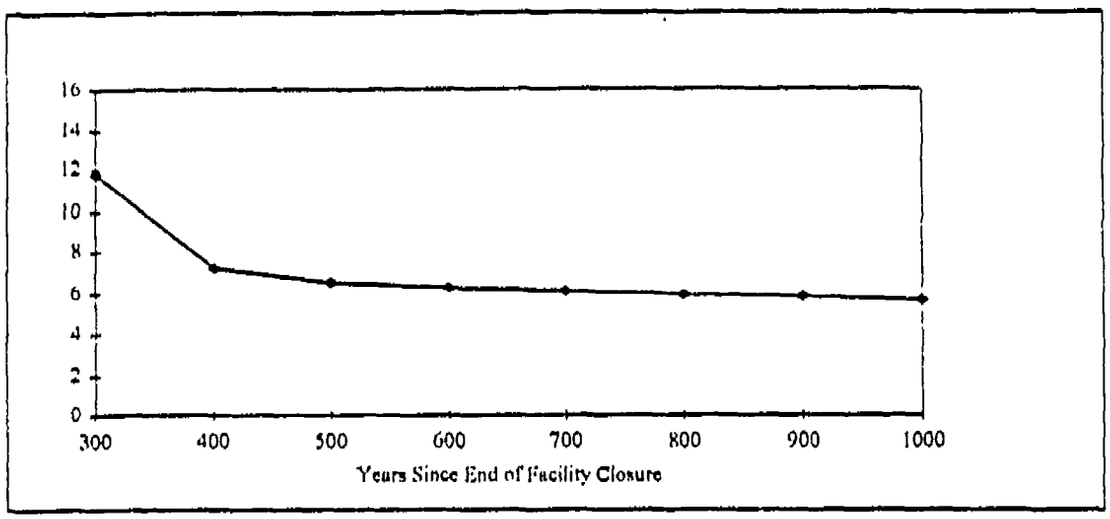

Figure 5-3 Doses calculated for intrusion into future pits and shafts (top and bottom, respectively)

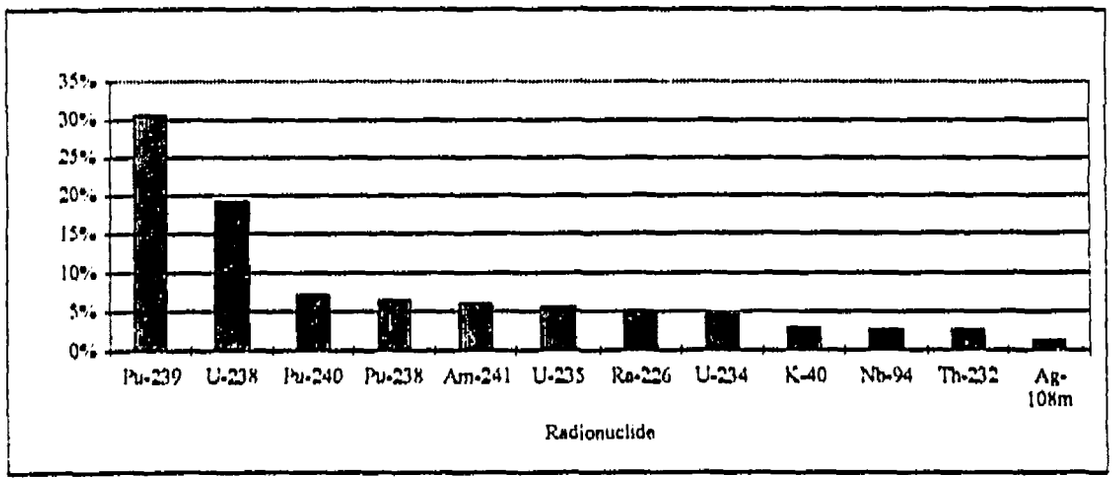

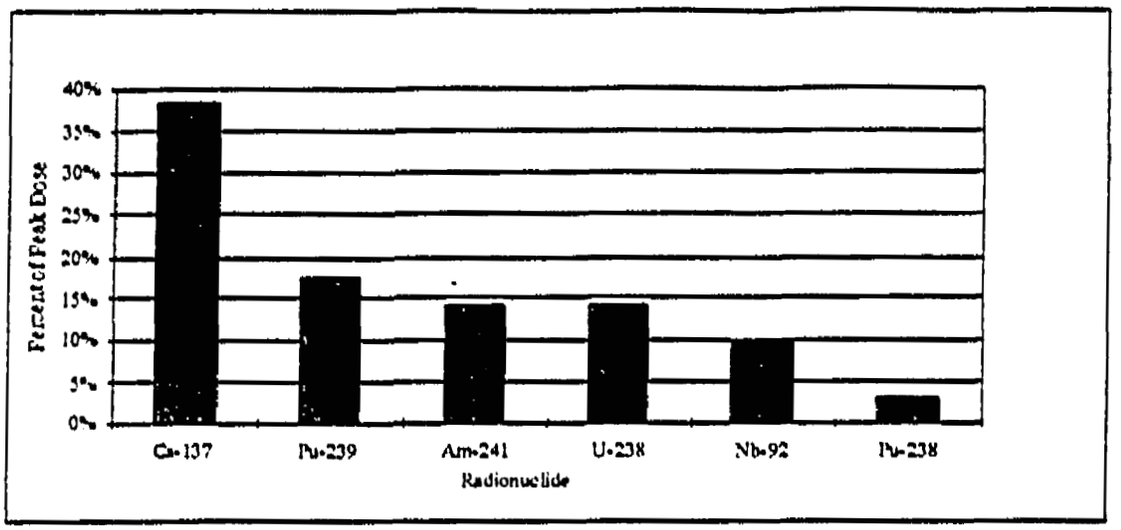

Figure 5-4 Radionuclides contributing to the doses from inadvertent intrusion into future waste, pits and shafts (top and bottom, respectively)

5.2.3 Summary of Intruder Analysis Results

In the inadvertent intruder analysis, waste disposed of in pits resulted in larger intruder doses than waste disposed of in shafts. The radionuclides contributing most of the pit-intrusion dose were long-lived radioactinides (uranium, americium, and plutonium), primarily through the particulate-inhalation pathway. Direct radiation from soils, ingestion of soils, and ingestion of crops also produced small but non-zero doses. Doses from intrusion into shafts, both historic and future, were due mainly to direct radiation from soil contaminated with gamma emitters including ^{108m}Ag, ^{137}Cs, ^{92}Nb, and ^{94}Nb, with inhalation of actinide-contaminated particulates and ingestion of actinide-contaminated soil also being important. Doses due to direct radiation from air and inhalation of ^{3}H, ^{14}C, and krypton were insignificant contributors to calculated intruder doses.

5.3 INTRUDER SENSITIVITY AND UNCERTAINTY ANALYSIS

The purpose of the intruder-scenario sensitivity and uncertainty analysis is to determine how the projected intruder doses change when uncertainties in data used in the analysis are considered. The uncertainties affecting the inadvertent-intruder analysis include the assumed radionuclide concentrations in the disposal units, the stability of the concrete shaft cover, and the thickness of the cover. The modeling parameters used in the analysis

were obtained from standard reference sources; however, the parameters were not considered in the sensitivity and uncertainty analysis not only because they are industry-standard values, but also because the scenario itself is considered very conservative with respect to regional norms. The sensitivity of the results to uncertainties in inventory are discussed in Section 5.3.1, while the effects of uncertainties regarding disposal-unit cover designs are characterized in Section 5.3.2.

5.3.1 Inventory Uncertainties

The intruder dose assessment indicates that relatively few radionuclides in the MDA G would have any significant radiological impact on an agricultural intruder. Those radionuclides were shown to be ^{241}Am, ^{239}Pu, ^{238}Pu, ^{238}U, ^{235}U, ^{232}Th, ^{137}Cs, ^{108m}Ag, ^{94}Nb and ^{92}Nb. The uncertainty in the recorded and projected inventories differs somewhat for these radionuclides, ranging from very low for easy-to-measure ^{137}Cs to very high for difficult-to-measure ^{238}Pu. Uncertainties in inventory only become important when projected doses are near the performance objective. The information presented in Section 4.3 on the inventory uncertainties apply to the intruder analysis.

5.3.2 Disposal-Unit Cover Uncertainties

The projected doses to hypothetical persons who may at some point in the future accidentally intrude into disposal pits and shafts at MDA G depend on the thickness and integrity of the disposal unit covers. The relative effect of 1 m (3.3 ft) and 2 m (6.6 ft) covers over disposal pits reflects the degree of mixing of contaminated waste and clean cover materials. This effect can be quantified in terms of the 2:3 ratio of contaminated to clean material excavated with a 1 m (3.3 ft) cover, compared with the ratio of 1:3 for a 2 m (6.6 ft) cover.

The effect of the assumed, but uncertain, 300-year integrity of the concrete shaft cover can be analyzed by comparing the relative radioactivity present at 100 years post closure (the earliest time that intrusion is considered feasible) to that present at 300 years, after 200 years of decay. The value used in the analysis is consistent with values generally assumed.

6. PERFORMANCE EVALUATION

The purpose of the PA is to determine if LLW generated since September 26, 1988 has been, and will continue to be, disposed of at MDA G in a manner that will not result in radiation doses to members of the public that exceed specified performance objectives. In a complementary fashion, the CA is used to evaluate options for ensuring that exposures from all waste disposed of at MDA G will not impart doses to future members of the public in excess of permissible levels. This is accomplished by comparing the results of the PA and CA to the applicable performance objectives for each exposure scenario modeled, as discussed in Section 6.1. The comparison provides information that is integrated directly into LANL waste management and environmental restoration activities, as described in Section 6.2. The results of the PA and CA are also evaluated to determine whether additional work is required to enhance the models and data used, and to ensure the continued applicability of the models and results, as discussed in Section 6.3.

6.1 COMPARISON OF RESULTS TO PERFORMANCE OBJECTIVES

The results of the PA dose calculations presented in Sections 4 and 5 are compared with the public-protection and intruder-protection performance objectives, respectively, as specified in DOE Order 5820.2A. The results of the CA included in Section 4 are compared against the offsite dose limits also specified by the DOE.[1] This section compares the results of the PA and CA dose projections with their respective performance objectives.

6.1.1 Evaluation of Performance Assessment Results

The PA modeled several exposure pathways and scenarios to determine compliance with public-protection and intruder-protection performance objectives within the 1,000-year compliance period. This section evaluates the results of the analyses by comparing each pathway with its applicable performance objective(s).

6.1.1.1 Air Pathways Analysis

The air pathways analysis projected doses resulting from the release of radioactive gases from the disposal facility during the operational, institutional-control, and industrial-use periods, as well as the resuspension of contaminated dust following the end of institutional control. Radon fluxes from the undisturbed site were projected for all three periods as well.

The dose objective for the air pathways analysis is 10 mrem/yr at an offsite receptor location. Table 6-1 shows the calculated doses for the institutional-control and industrial-use periods. The 10 mrem/yr performance objective for the air pathway analysis represents the maximum effective dose a member of the public may receive from all facilities at the LANL. To demonstrate compliance with this objective, the projected doses for MDA G must be added to those projected as a result of releases from other LANL facilities. In compliance with 10 CFR Part 61, the LANL environmental surveillance program includes the projection of maximum individual doses from airborne emissions from LANL facilities. Dose calculations based on monitoring data collected in 1994 project a maximum individual dose of 3.5 mrem/yr at a location north of TA-53, the Los Alamos Neutron Scattering Center.

Table 6-1 Summary comparison of air pathways doses with performance objective during the 1,000-year compliance period

Compliance Period	Radionuclides Contributing to Peak Dose	Peak Dose (mrem)	Fraction of Limit
Institutional Control	^{3}H, ^{14}C	6.6E-02	0.007
Industrial Use	^{239}Pu, ^{238}U, ^{238}Pu, ^{241}Am, ^{235}U	9.2E-03	0.0005

Summing the atmospheric contributions is incorrect because doses from emissions from TA-53 are not coincident (in time or space) with projected doses from TA-54. The dose contribution from MDA G corresponds to the time of projected facility closure at a location northwest of MDA G (south of TA-53), while the dose calculated to demonstrate compliance with 10 CFR Part 61 is based on data collected in 1994 north of TA-53.

However, the projected dose for the MDA G disposal facility is expected to bound the actual exposures received by a receptor at the point of maximum atmospheric exposure in 1994 and, generally speaking, for at least the next 100 years. To the extent that the doses from the other facilities at the LANL do not rise significantly above the 1994 dose estimate, the 10 mrem/yr performance objective will be satisfied.

The flux objective for radon from the undisturbed disposal site is 20 pCi/m^2/s (1.9 pCi/ft^2/s). Table 6-2 presents the results of the flux projection as fractions of this limit. Relative to the performance objectives, the projected radon fluxes are very low. The largest flux, projected for the historic disposal shafts, is only 16 percent of the flux objective. Fluxes calculated from the other disposal units and inventory segments are all less than five percent of the limit.

Table 6-2 Comparison of projected radon fluxes with the flux limit

Disposal Inventory	Projected Flux (pCi/m^2/s)			Fraction of Limit
	^{220}Rn	^{222}Rn	Total	
Disposal Pits				
Historic waste	0.0E+00	1.1E-01	1.1E-01	0.006
Future waste	0.0E+00	1.7E-01	1.7E-01	0.009
Disposal Shafts				
Historic waste	3.1E+00	2.5E-02	3.1E+00	0.16
Future waste	8.1E-01	2.0E-03	8.1E-01	0.04

6.1.1.2 Groundwater Protection Analysis

The performance objective for the groundwater protection analysis is 4 mrem/yr at the point of maximum groundwater exposure outside of LANL or MDA G boundaries. Doses were projected for a location near White Rock during the operational and institutional-control periods. Two locations, 100 m (330 ft) east-southeast of MDA G and Pajarito Canyon, were considered for the industrial-use period. No groundwater concentrations were calculated prior to the end of the 100-year institutional-control period. The peak annual doses within 1,000 years at the point of maximum exposure

east-southeast of MDA G and in Pajarito Canyon were 7.5×10^{-8} and 3.5×10^{-5} mrem, respectively. These doses are more than 100,000 times smaller than the dose objective.

6.1.1.3 All Pathways Analysis

The results for the all pathways analysis are compared against a performance objective of 25 mrem/yr. Locations for projected doses include the receptor location near White Rock prior to the end of institutional control and the receptor locations 100 m (330 ft) east-southeast of MDA G, and in Pajarito Canyon thereafter. No significant exposures were found to occur at the location near White Rock. The peak dose projected for the receptor 100 m (330 ft) east-southeast of MDA G was 2.0×10^{-7} mrem. While this is 60 percent greater than the dose for the groundwater pathway analysis, it is still a small fraction of the performance objective. Larger doses were calculated for the Pajarito Canyon receptor. The maximum dose during the 1,000-year compliance period was 1.0×10^{-4} mrem, which is a factor of 250,000 less than the performance objective.

6.1.1.4 Intruder Protection Analysis

The intruder-protection performance objective for chronic exposures is 100 mrem/yr. The results of the intruder-agriculture dose assessment are compared with this dose limit in Table 6-3. All projected doses are a small fraction of the dose objective.

Table 6-3 Intruder-agriculture dose assessment compared with the performance objective

Waste	Projected Dose (mrem)	Fraction of Performance Objective	Significant Pathways (>10% of dose)	Significant Radionuclides (>10% of dose)
Historic Pits	30	0.30	Inhalation of dust; ingestion of soil and crops; direct radiation from soil	^{239}Pu, ^{238}U
Historic Shafts	18	0.18	Inhalation of dust; direct radiation from soil	^{108m}Ag, ^{137}Cs, ^{239}Pu, ^{238}U, ^{241}Am
Future Pits	30	0.30	Inhalation of dust; ingestion of soil and crops; direct radiation from soil	^{239}Pu, ^{238}U
Future Shafts	12	0.12	Inhalation of dust; ingestion of soil; direct radiation from soil	^{92}Nb, ^{137}Cs, ^{239}Pu, ^{238}U, ^{241}Am

6.1.2 Evaluation of Composite Analysis Results

The results of the composite analysis are compared to an all pathways dose limit of 100 mrem/yr to demonstrate compliance. If the projected doses exceed 30 mrem/yr, an options analysis must be prepared to consider cost-effective actions that could be taken to reduce exposures. Groundwater-based doses were projected for a receptor near White Rock during the operational and institutional-control periods. Exposures were also projected for a receptor located at the point of maximum atmospheric exposure (i.e., outside of LANL boundaries) during these periods. Receptors located 100 m (330 ft) east-southeast of MDA G, at the point of maximum atmospheric exposure outside of MDA G boundaries, and in Pajarito Canyon were considered during the industrial-use period. No doses were projected to occur at the location near White Rock. The maximum annual dose for the receptor 100 m (330 ft) down-gradient of MDA G through the 1,000-year compliance period was 1.2×10^{-5} mrem. The peak projected dose for the receptor located at the point of maximum atmospheric exposure was 5.5 mrem/yr, after the end of institutional control. The maximum annual dose to the Pajarito Canyon

receptor was 7.2×10^{-3} mrem. The peak atmospheric pathway dose is 5.5 and 18 percent of the 100 and 30 mrem/yr limits, respectively. The peak projected doses for the other receptors are all much less than these dose objectives.

6.2 USE OF RESULTS

The results of the dose assessment over the 1,000-year compliance horizon provide useful information for ensuring lasting containment and isolation of radioactivity. This section discusses the likely and potential uses of the results of the PA (Section 6.2.1) and the CA (Section 6.2.2).

6.2.1 Use of Performance Assessment Results

The results of the PA are instrumental in the development of Waste Acceptance Criteria for MDA G and a closure plan for the facility. The results are also expected to contribute to the ongoing SWEIS. The application of the results to these areas is discussed in the following sections.

6.2.1.1 Waste Acceptance Criteria

As required by the DOE, the results of the dose projections in the PA are used to set limits on the amount of radioactivity that will be disposed of at MDA G. The results of the intruder analysis, in particular, are used to set radionuclide concentration limits for waste disposed of in a near-surface configuration.

The waste acceptance criteria for pit and shaft waste are calculated on the basis of the radionuclide-specific intruder doses projected for the future disposal unit inventories. In the first step of this calculation, the 100 mrem/yr intruder performance objective is divided by the projected dose for a given radionuclide. This ratio is subsequently multiplied by the as-disposed radionuclide concentration in the waste used as the basis for the dose assessment. The result is the concentration limit for that radionuclide. The application of this methodology to all radionuclides in the PA inventory is summarized in Table 6-4 for pits, and Table 6-5 for shafts. These inventory limits apply to all waste disposed of within 3 m (10 ft) of the surface of a disposal unit. There are no PA-based concentration limits

for waste disposed of at depths greater than 3 m (10 ft), as no intruder exposures are projected to occur as a result of this waste within 1,000 years of facility closure. The NRC Greater-Than-Class C and the DOE TRU limits still apply, however.

Table 6-4 Inventory limits for pit waste using intruder analysis limits

Radionuclide	Peak Dose (mrem)	PA Pit Concentration (Ci/m3)	Pit Limit (Ci/m3)
H-3	1.48E-05	4.98E-03	3.36E+04
C-14	3.47E-02	9.63E-07	2.77E-03
Al-26	2.10E-06	2.17E-12	1.03E-04
Si-32	6.99E-03	3.02E-06	4.33E-02
Cl-36	1.62E-02	2.16E-08	1.34E-04
K-40	9.05E-01	9.60E-06	1.06E-03
Ti-44	1.98E-03	1.73E-08	8.76E-04
Ni-59	1.18E-05	2.73E-07	2.30E+00
Co-60	2.89E-05	1.47E-04	5.07E+02
Ni-63	4.22E-07	9.31E-09	2.20E+00
Se-79	2.15E-08	2.80E-11	1.30E-01
Kr-81	1.11E-06	3.03E-10	2.74E-02
Kr-85	4.81E-06	1.49E-05	3.10E+02
Sr-90	1.44E-01	2.13E-05	1.48E-02
Nb-92	1.66E-05	2.96E-11	1.79E-04
Mo-93	8.43E-05	9.85E-08	1.17E-01
Zr-93	3.65E-08	3.12E-10	8.53E-01
Nb-94	8.24E-01	1.48E-06	1.79E-04
Tc-97	3.17E-07	2.28E-10	7.19E-02
Tc-99	9.69E-03	1.24E-06	1.28E-02
Pd-107	9.42E-10	4.20E-11	4.46E+00
Ag-108m	3.97E-01	1.39E-06	3.49E-04
Cd-113m	9.84E-04	5.67E-06	5.76E-01
I-129	9.32E-07	1.71E-11	1.83E-03
Ba-133	6.83E-05	4.98E-05	7.30E+01
Cs-135	1.17E-06	1.44E-09	1.23E-01
Cs-137	2.22E-01	2.04E-05	9.16E-03
La-137	5.89E-08	4.93E-09	8.37E+00
Pm-145	8.67E-07	3.31E-08	3.81E+00
Sm-146	1.83E-08	2.28E-12	1.25E-02
Sm-147	1.31E-11	1.80E-15	1.38E-02
Gd-148	1.90E-02	2.41E-06	1.27E-02

Radionuclide	Peak Dose (mrem)	PA Pit Concentration (Ci/m3)	Pit Limit (Ci/m3)
Sm-151	2.51E-06	7.70E-07	3.07E+01
Eu-152	1.58E-03	3.15E-06	2.00E-01
Eu-154	2.03E-03	8.98E-07	4.42E-02
Tb-157	5.59E-06	2.82E-08	5.04E-01
Tb-158	9.80E-07	1.21E-08	1.23E+00
Hf-182	1.41E-01	3.71E-07	2.63E-04
Bi-207	1.64E-04	5.42E-09	3.31E-03
Pb-210	8.57E-03	2.16E-06	2.52E-02
Ra-226	1.60E+00	1.94E-06	1.21E-04
Ac-227	1.62E-02	8.22E-07	5.08E-03
Th-229	4.54E-04	2.19E-09	4.84E-04
Th-230	1.39E-01	4.26E-07	3.07E-04
Pa-231	3.61E-07	5.20E-13	1.44E-04
Th-232	8.15E-01	8.08E-07	9.91E-05
U-232	2.16E-09	1.16E-14	5.35E-04
U-233	1.37E-03	4.42E-08	3.22E-03
U-234	1.57E+00	1.16E-04	7.36E-03
U-235	2.16E+00	3.20E-05	1.48E-03
U-236	4.99E-02	4.41E-06	8.84E-03
Np-237	9.66E-03	3.58E-08	3.70E-04
Pu-238	2.01E+00	1.37E-04	6.79E-03
U-238	5.85E+00	3.34E-04	5.71E-03
Pu-239	9.31E+00	2.07E-04	2.23E-03
Pu-240	2.21E+00	4.98E-05	2.25E-03
Pu-241	2.93E-01	2.16E-04	7.37E-02
Am-241	1.91E+00	4.31E-05	2.26E-03
Pu-242	3.44E-05	8.06E-10	2.34E-03
Am-243	1.33E-04	1.41E-09	1.06E-03
Bk-247	1.18E-07	3.20E-12	2.71E-03
Cf-252	7.78E-10	8.30E-10	1.07E+02

Table 6-5 Inventory limits for shaft waste using intruder analysis results

Radionuclide	Peak Dose (mrem)	PA Shaft Concentration (Ci/m3)	Shaft Limit (Ci/m3)
H-3	3.53E-04	4.39E+03	1.24E+09
C-14	7.15E-09	1.53E-11	2.14E-01
Co-60	2.30E-13	3.65E+00	1.59E+15
Ni-63	1.08E-08	1.73E-07	1.60E+03
Kr-85	4.40E-13	5.76E-06	1.31E+09
Sr-90	6.21E-02	2.41E-02	3.89E+01
Nb-92	1.15E+00	2.30E-05	2.00E-03
Ba-133	7.59E-16	1.43E-06	1.89E+11
Cs-135	1.11E-06	2.59E-08	2.34E+00
Cs-137	4.45E+00	4.72E-01	1.06E+01
Pm-145	1.54E-19	2.28E-16	1.48E+05
Sm-147	4.72E-15	8.64E-18	1.83E-01
Eu-152	1.05E-08	1.29E-05	1.23E+05
Eu-154	1.93E-05	5.56E-04	2.88E+03
Bi-207	6.30E-07	2.30E-08	3.66E+00
Pb-210	3.40E-12	1.35E-11	3.98E+02
Ra-226	6.89E-05	1.15E-09	1.67E-03
Th-229	5.59E-06	3.11E-10	5.56E-03
Th-232	2.07E-01	2.32E-06	1.12E-03
U-234	7.42E-04	7.01E-07	9.46E-02
U-235	4.44E-02	7.59E-06	1.71E-02
U-236	2.89E-05	3.34E-08	1.15E-01
Pu-238	3.78E-01	1.39E-03	3.68E-01
U-238	1.64E+00	1.16E-03	7.04E-02
Pu-239	2.03E+00	5.18E-04	2.56E-02
Pu-240	6.14E-02	1.61E-05	2.62E-02
Pu-241	2.38E-02	2.44E-04	1.03E+00
Am-241	1.65E+00	6.07E-04	3.68E-02
Pu-242	3.48E-06	9.29E-10	2.67E-02
Cf-252	2.98E-11	2.62E-10	8.77E+02

The concentration limits will be applied as WAC for "routine" LLW on a per-package basis, using the sum-of-fractions rule for wastes contaminated with more than one

radionuclide. Characterization requirements will be developed using the EPA DQO process. It is important to realize that these limits are based on the total volumes of pit and shaft waste disposed of in the future, 140,000 and 1,400 m^3 (5.0×10^6 and 5.0×10^4 ft^3), respectively. For this reason, packages with activities exceeding the limits may be safely disposed of provided that the *average* disposal unit concentration does not exceed the limit, and provided that neither TRU nor NRC Greater-Than-Class-C[124] waste is disposed of at MDA G. Waste packages with measured concentrations in excess of the limits listed in Table 6-4 and Table 6-5 may be accepted on a case-specific basis, with care being taken so as not to exceed the threshold over the disposal unit volume.

The results of the groundwater protection and all pathways analyses performed in the PA are used to establish total inventory limits for the average disposal unit. The methodology used to set total inventory limits based on the groundwater pathway analysis is analogous to that used in setting concentration limits based on the intruder analysis. Radionuclides that are projected to enter the regional aquifer within the 1,000-year compliance period are those for which inventory limits will be established. These include ^{14}C, ^{99}Tc, and ^{129}I. Table 6-6 lists the total inventory limits for those radionuclides that have the potential to be transported through the vadose zone within the compliance period based on the results in Section 4. Disposal of these radionuclides will be automatically tracked (at the pre-approval stage) so that total inventories listed in Table 6-6 are not exceeded.

Table 6-6 Total inventory limits for LANL LLW

Radionuclide	PA Inventory (Ci)	Inventory Limit (Ci)
^{14}C	1.62E-01	8.74E+06
^{99}Tc	7.71E+00	6.09E+10
^{129}I	4.39E-06	2.93E+04

6.2.1.2 MDA G Closure Plan

Because the air pathway analysis produced the highest doses in the PA/CA analyses during the industrial-use period when biotic translocation was modeled suggests that maintenance

and design of closure caps to minimize the potential for biotic intrusion is a relatively important consideration. The final cover designs considered in the *Closure Plan for LANL MDA G* incorporate a layer of heavy cobble-rocks to prevent biotic intrusion. These "biobarriers" have proven to be more effective for discouraging burrowing animals than plants, however, and are not perfectly effective. The results of the PA/CA will be used to re-evaluate the final cover options, in light of the ALARA analyses discussed in Section 4.4, which suggests that a fully engineered closure cap incorporating a biobarrier to prevent intrusion of most animals and some plants may not be cost effective. Rather, it may be equally as effective to add a second 1-m (3.3-ft) layer of crushed tuff over the older disposal units, whose nominal cover thickness is 1 m (3.3 ft). Before any decision is made on final cover design, however, the uncertainties in the biotic intrusion and atmospheric dispersion models must be better understood. In addition, engineering drawings and other records will be reviewed to determine the actual thickness of the closure caps over pits; it is likely that many pits already have cover thickness in excess of 1 m (3.3 ft).

In evaluating final cover options, the importance of the gravel mulch layer included in the surface water-balance model (Appendix 3b) will be considered. This is a feature of the simple crushed-tuff cover that has a potentially significant impact on site performance by controlling surface erosion.

6.2.1.3 Site-Wide Environmental Impact Statement

The results of the CA will also be made available to the SWEIS Office. Discussions with SWEIS personnel indicate that the results will be extremely useful in characterizing the likely impact of ongoing waste management operations in the context of NEPA.

6.2.2 Use of Composite Analysis Results

The results of the CA will be made available to ER Project field unit managers. Preliminary discussions indicate that the results may be used to support closure plans for certain sites. For other sites, aspects of the CA may be used as the technical framework for additional modeling.

6.3 MAINTENANCE PROGRAMS

The PA and CA will be maintained in accordance with DOE guidance to ensure the continued applicability of the models and interpretation of results. The PA maintenance program includes periodic evaluation of LLW disposal records and operating conditions to ensure consistency with the assumptions made in the PA, and identifies future work to be performed to improve the realism of the models used in the PA.[5] The elements of the PA maintenance program are presented in Section 6.3.1. Similarly, the CA will be reassessed as new information on other potentially interacting sources of radioactivity becomes available. The CA maintenance program is discussed in Section 6.3.2.

6.3.1 Maintenance of the Performance Assessment

The purpose of the PA maintenance program is to ensure the continued applicability of the PA. The PA will be revised every five years, or more frequently if new information becomes available that may alter the outcome of the analysis. The PA maintenance program has two key components. One is field and experimental work and additional analyses conducted to reduce the uncertainty in the models used in the PA. The second is the preparation of semiannual reports that summarize aspects of the waste management program and disposal operations related to the PA.

6.3.1.1 Further Work

The scope of the analyses, and field and experimental work required to support the PA is largely defined by the outcome of the sensitivity and uncertainty analysis. The program will focus on obtaining data that are expected to have an impact on the results and conclusions of the PA and that will provide additional assurance that the site is effective at containing and isolating radioactivity.

The analyses indicate that surface processes related to biotic intrusion affect the outcome of the PA and CA. There remains substantial uncertainty regarding moisture flux through the mesa; further work to enhance the understanding of processes and properties related to vadose zone flow and transport.

6.3.1.1.1 Inventory Characteristics

Uncertainties associated with the projected inventories of ^{241}Am and ^{238,239,240}Pu are important influences on the dust inhalation doses projected for the CA, as indicated in Section 4.3. While the error terms assigned to the projected inventories are small, it is evident that the actual inventories of americium and plutonium disposed of prior to 1971 are highly uncertain. For example, the projected inventory of ^{239}Pu in the pre-1971 waste may be overestimated by more than three-fold. Based on the relative activities of ^{241}Am disposed of before and after 1971, the inventories for this isotope also appear to vastly overstated. It is apparent from these results and the sensitivity of the atmospheric dose modeling to the pre-1971 inventory projections that better characterization of this early waste is warranted.

6.3.1.1.2 Surface Processes

Since biotic translocation, resuspension, and atmospheric transport of radioactivity was the pathway identified as having the greatest potential radiological impact on future members of the public, work will be performed to enhance the understanding of processes related to that pathway. Further evaluation of cover designs will be tied to additional investigations discussed to here. The actual potential for biotic transport by plant and animal vectors will be evaluated as site-specific data become available from annual sampling at MDA G. The complex-terrain correction to Gaussian dispersion model will continue to be evaluated relative to site-specific data.

The sensitivity and uncertainty analysis discussed in Section 4.3 assigned an error of ±900 percent to account for uncertainties associated with the resuspension and dispersion factors used in the atmospheric modeling. Given their potential impact on the projected doses when the total error of these parameters is constrained to ± 900 percent, further investigation into these uncertainties are necessary.

The surface water balance model will be calibrated to enhance the accuracy in simulations of long term cover performance. Several variables are particularly important, yet not fully characterized on a site-specific basis, including evapotranspiration and sediment transport.

The meteorological tower east-southeast of MDA G in White Rock began collecting evapotranspiration data in October of 1996. In addition, sediment traps have been installed at several locations around the MDA G perimeter. As data become available, including geophysical data from the recent analysis of MDA G surface-soil samples, the information will be used to calibrate the surface-water balance model.

Improvements in the understanding of surface processes, water balance in particular, has important implications for surface water flux boundary conditions, which drive subsurface processes related to transport of radioactivity. Additional work planned to enhance the understanding of subsurface processes is discussed below.

6.3.1.1.3 Vadose Zone Flow and Transport

While the groundwater pathway was not shown to be important during the 1,000-year compliance period, the peak doses for some nuclides at 2,000 to 3,000 years are very sensitive to uncertainties in the modeling. Therefore, it is important to understand, at least conceptually, how that pathway might impact the biosphere over a longer time horizon. The confidence in the long-term performance of MDA G with respect to groundwater protection would be greatly enhanced if additional data were available to characterize the vadose zone. The most valuable data are those that will enhance the ability to realistically model potentially important processes such as evaporation, vapor-phase water movement, and percolation transients through fractures and surge beds. Lateral transport along fractures or interbeds, and lateral movement of moisture toward the mesa along the Guaje Pumice Bed may be important in terms of the subsurface sources of moisture apparent in the recharge analyses. In addition, uncertainties associated with the model would be reduced if the deep stratigraphy of the subsurface (from the Otowi Member down to the Puye Formation) is defined.

Several core logs are still available from boreholes at MDA G. These will be used in additional natural tracer analyses. Results from these analyses will be valuable in substantiating the occurrence of deepevaporation within, and the very small recharge rates through, the mesa. The results will also better define the spatial variability in evaporative

effects and recharge. Geophysical analyses of samples from MDA G surface soils, basalt core, from the 'vapor phase notch' region, and from other core have been completed recently and need to be incorporated in the PA and CA.

Depending on the outcome of the field work, additional data will be required to support the modeling of processes that become better defined, such as deep evaporation. For example, the effect of barometric changes on vapor-phase flow within the fractures and surge beds must be quantified to provide boundary conditions for the model.

The *in situ* volumetric moisture content of several boreholes at MDA G will be regularly measured and used to estimate local recharge rates as part of the PA maintenance program. The current schedule calls for six boreholes to be monitored on a monthly basis using neutron probes, another twenty will be monitored annually.

6.3.1.2 Semiannual Reports

A report will be provided twice yearly to the Albuquerque Operations Office of the DOE summarizing information accumulated in the interim period that may affect the assumptions, outcome, or interpretation of the PA. This report will include a review of disposal records compared with the future inventory modeled in the PA and with the inventory limits established in the PA. The status of the waste certification program will also be discussed, insofar as it may have important implications with respect to inventory uncertainties. The bi-annual report will also summarize field and laboratory studies and analyses conducted in support of the PA, such as those described above, as well as site-specific environmental monitoring data. Finally, the report will describe any changes in operations at MDA G that may impact the analyses performed in support of the PA. Such changes may include new cover designs, new waste streams, or new pit designs.

6.3.2 Maintenance of the Composite Analysis

Most of the MDAs initially considered in, but ultimately eliminated from, the CA are in various stages of characterization in accordance with the RCRA Facilities Investigation process. Information regarding the source term, hydrogeologic setting, potential releases,

and closure plans will become available over the course of the next several years. All information will be evaluated to ensure the continued validity of the data used to perform the screening of these MDAs. If new information invalidates the technical justification(s) used to eliminate one or more MDAs from the CA, new analyses will be performed.

7. QUALITY ASSURANCE

This section summarizes quality assurance (QA) as related to the PA and CA. The QA program supports the credibility and validity of assumptions, data, and analytical methods used to demonstrate compliance with the performance objectives. This section and associated appendices of this report were peer reviewed for technical accuracy.

7.1 FIELD DATA

The *Quality Program Plan for the ER Program* describes the QA requirements for collecting, analyzing, and documenting field samples.[125] Much of the field data used to characterize the regional and local geology, geochemistry, hydrology, and hydrogeology were obtained by the LANL Environmental Restoration Project and compiled in the LANL Facility for Information Management Analysis and Display database (FIMAD). Using FIMAD ensures the availability of accurate and consistent geologic, hydrologic, meteorologic, and geochemical data. FIMAD was the source of most of the geohydrological data used in characterizing the setting of other MDAs initially considered in the CA, as discussed in Appendix 1b.

Meteorological, ecological, and radiological data used in the PA were obtained through LANL's Environment, Safety, and Health (ES&H) Division. The ES&H Division is also responsible for the Laboratory's groundwater protection program, and as such obtains and maintains data regarding surface water and groundwater. All monitoring and compliance activities sponsored and undertaken by the ES&H Division adhere to a QA program (QAP) with specific requirements for sampling and analysis.

7.2 LABORATORY DATA

The processes necessary to measure natural tracer content and radionuclide sorption were conducted in accordance with QA procedures implemented in analytical laboratories both at LANL and at the New Mexico Institute of Mining and Technology. Sample custody of core samples used in both analyses followed QA procedures at the Laboratory's ER core

storage facility. Chloride analyses were conducted using EPA traceable standards and techniques. Stable isotope analyses were conducted using gas standards calibrated against an international stable isotope standard, which were also applied in the isotope extraction process.

7.3 INVENTORY DATA

Quality assurance related to LLW inventory data applies to the quality of the records maintained by waste management personnel, and to the quality of the data provided by the generators. The *TA-54, Area G Quality Assurance Program Description* establishes the QA requirements for MDA G as a nonreactor nuclear facility.[126] With respect to records maintained at MDA G, waste characterization data provided by generators on waste profile forms and waste disposal request forms are thoroughly reviewed by trained personnel, and must be approved prior to waste shipment. After approval but prior to shipment, data is entered into an electronic database. After waste has been accepted for disposal, data is reentered into the database for double-data entry quality control. Data entry personnel are automatically alerted when discrepancies occur between the first and second data entries. In this manner, the accuracy of the data transcription is ensured.

The accuracy of the waste characterization data provided by the generators is variable, and depends largely on quality programs instituted at the generating facilities. Several of the larger-volume waste-generating sites are designated nuclear facilities (including the Plutonium Facility, the Chemistry and Metallurgy Research Building, and the Isotope Production Facility), and as such have QA programs consistent with 10 CFR 830. As previously mentioned, the ER Project (another high-volume LLW generator) has a robust QA program, with a sampling and analysis plan specific for waste characterization.[127]

The approach used to characterize the 1957 through 1970 inventory data was peer-reviewed by current and retired LANL personnel familiar with the generation, characterization, and disposition of radioactive waste through the Laboratory's history.

The inventory characterization report included as Appendix 2e was prepared by Rogers and Associates Engineering Corporation (RAE). All data used by RAE were provided electronically by LANL personnel. Those data were maintained and manipulated in Excel spreadsheets to provide the inventory segments (e.g., 1957-1970) and categories (e.g., surface contaminated). Results of spreadsheet computations were reviewed in accordance with RAE QA requirements.

Data used to assess other sources for inclusion in the CA were obtained from LANL references, many of which were provided by the ER Project.

7.4 FACILITY CHARACTERISTICS

Many of the methods for assuring quality at MDA G are described in the *Conduct of Operations* and other work-control procedures.[128] For example, the construction, use, closure, and maintenance of pits and shafts are performed under specific procedures by trained individuals. Data on the configurations of the disposal units modeled in the PA and CA were obtained from as-built records. Records have been historically maintained (either engineering drawings or photographs), and have been recently made available electronically from FIMAD, a database maintained by the LANL ER Project under its QAPP.

7.5 MATHEMATICAL MODELS

Much of the data described above was used in the mathematical models for source release, environmental transport, and dose impact. As described in this section, the major computational models used in the PA and CA have undergone extensive and well-documented verification. Analytical equations were derived from standard technical references.

7.5.1 Source Term Modeling

The quality of the inventory data used to develop and implement the source releases has been discussed. Analytical methodologies were based on standard sources, and parameters were taken either from standard references cited in appendices to section 3, or were based on site-specific data provided by the ES&H Division. Analyses and results were reviewed by subject-matter experts.

7.5.2 Atmospheric Transport Modeling

The computer code used to calculate transport of radioactivity in air was CAP-88, approved by the EPA for modeling contaminant dispersion in air. The standard dispersion calculations were performed by ES&H personnel in accordance with that Division's QA procedures. The complex terrain enhancements to the standard Gaussian plume results were based on meteorological data obtained from the ES&H Division. The analytical approach and results are fully described in Appendix 3a and have undergone technical peer review, both by LANL personnel and the American Meterological Society.

7.5.3 Surface Runoff and Soil Erosion Modeling

The code used in the surface runoff and erosion simulations reported in Appendix 3c was based on the SPUR model[129] and the CREAMS code developed by the U.S. Department of Agriculture.[130] The water-balance routines were validated on watersheds in southwestern Idaho.[131] The SPUR code has been successfully used to predict soil water dynamics on lysimeters at Hanford.[132] Parameters for the simulations were obtained from observations (weather and soils data), from handbook and suggested parameter values (snow parameters), and previous simulations at Los Alamos, as cited in Appendix 3c.

7.5.4 Subsurface Transport Modeling

The FEHM numerical model used to calculate aqueous-phase transport through the vadose zone and regional aquifer in support of the groundwater protection analysis has undergone extensive verification and validation as part of the Yucca Mountain Site Characterization Project. The mathematical models and numerical methods are described in *Models and Methods Summary for the FEHM Application*. A complete suite of

verification problems is documented in *Software Verification Report for FEHM Version 1.0*. Data used to generate the grids and to define initial and boundary conditions were taken from LANL references or open-literature sources, as cited in Appendix 3g.

7.5.5 Dose Assessment

The dose projections for the PA and CA were performed by RAE. Excel spreadsheets were used to implement standard dose-assessment calculations. All parameters used in the calculations were taken from standard references or were based on site-specific data, as cited in Appendix 3e. Results were reviewed in accordance with RAE QA procedures.

8. PREPARERS

The analyses conducted in support of the PA and CA were performed by subject-matter experts. Each member of the team is identified in this section, along with their qualifications and contributions.

Diana Hollis

Technical Staff Member, Solid Waste Operations Group, Environmental Management Division, Los Alamos National Laboratory

B.S., Physics and Biology, M.S. Radiopharmacy & Radiation Protection Engineering

Diana was the team leader and primary author for the PA and CA. She also directed the inventory characterization efforts described in Appendix 2e, and is the author of Appendix 1a *Resolution of PRP Comments on Draft Performance Assessment of LANL TA-54, Area G Low-Level Radioactive Waste Disposal Facility*, and Appendix 1b *Technical Justification for Excluding Sources from the MDA G Composite Analysis*.

Diana has six years of experience in LLW management at LANL, and eight years of experience in fluid-dynamics modeling in support of the DoD underground nuclear weapons program.

Erik Vold

Technical Staff Member, Solid Waste Operations Group, Environmental Management Division, Los Alamos National Laboratory

M.S. Health Physics, M.S. Environmental Engineering, Ph.D. Mechanical Engineering

Erik provided technical oversight for the PA team, ensuring integration and consistency among the mathematical models. He conducted analyses of *in situ* moisture data to understand the role of vapor phase and liquid phase water transport in the vadose zone in support of the hydrogeological model, as detailed in Appendix 2c *Analysis of Liquid Phase Transport in the Unsaturated Zone at a Mesa Top Disposal Facility*, and 2f *Isotopic Compositions of Inventory Designations "Mixed Fission Product," and "Mixed Activation Product."* He developed all source term analytical models for the PA, which are reported in Appendix 3a *Evaluation of Atmospheric Release Sources for Gaseous Phase Contaminants Emanating from the Disposal Facility at Area G*, Appendix 3b *A Model for the Biotic Translocation of Buried Low-Level Radioactive*

Waste to the Ground Surface in the Presence of Erosion, and Appendix 3d *Modeling of the Aqueous Phase Source Release to the Unsaturated Zone from the Los Alamos Area G Disposal Facility*. In addition, he performed the atmospheric dispersion analysis as described in Appendix 3f *Atmospheric Transport in Complex Terrain at Los Alamos, Area G*.

Erik has more than 10 years' experience in radiologic environmental analysis and is currently the project leader for environmental monitoring at MDA G.

Rob Shuman

Principal Scientist, Rogers and Associates Engineering Corporation

B.S. Zoology, M.S. Health Physics/Radioecology

Rob prepared the inventory used in the source term modeling for the PA, which is described in Appendix 2e *Radioactive Waste Inventory for the TA-54, Area G Performance Assessment and Composite Analysis*, and conducted the dose assessments, which are reported in Appendix 3e *Radiological Dose Assessment for the TA-54, Area G Performance Assessment and Composite Analysis*. In addition, Rob assisted in many other aspects of the PA, including source term modeling, exposure pathways and scenarios development, and interpretation and integration of results.

Rob has many years' experience in radiological performance assessments, and human and ecological risk assessment. He assisted in the technical review of the INEL and ORNL PAs, and the DOE's Performance Evaluation methodology.

Kay Birdsell

Technical Staff Member, Geoanalysis Group, Earth and Environmental Sciences Division, Los Alamos National Laboratory

B.S., M.S. Chemical Engineering

Kay was responsible for the subsurface flow and transport modeling for the PA and conducted the unsaturated transport calculations. She is the primary author of Appendix 3g *Simulations of Groundwater Flow and Radionuclide Transport in the Vadose and Saturated Zones beneath Area G, Los Alamos National Laboratory*.

Kay has 11 years' experience at LANL in modeling flow and transport in the unsaturated and saturated media. For eight years, she performed model verification support for the Yucca Mountain Project at LANL.

Kathleen Bower

Technical Staff Member, Geoanalysis Group, Earth and Environmental Sciences Division, Los Alamos National Laboratory

B.S., M.S. in Geological Engineering, M.S. Education, Ph.D. Civil Engineering

Kathleen developed the saturated zone model used in the PA, and performed the calculations of radionuclide transport in the regional aquifer, and contributed to Appendix 3g *Simulations of Groundwater Flow and Radionuclide Transport in the Vadose and Saturated Zones beneath Area G, Los Alamos National Laboratory.*

Kathleen has extensive field and modeling experience related to rock mechanics, groundwater hydrology, and solute transport.

Don Krier

Technical Staff Member, Earth and Environmental Sciences Division, Los Alamos National Laboratory

B.S. Earth Sciences, M.S. Geology

Don compiled the geologic and hydrologic data of Mesita del Buey for use in the PA and is the primary author of Appendix 2a *Geologic, Geohydrologic, and Geochemical Data Summary of Material Disposal Area G, Technical Area 54, Los Alamos National Laboratory.* He assisted in the development of the three-dimensional grid used in the vadose zone transport calculations.

Don is the manager of Field Unit 5 of the Laboratory's ER Project, which includes a portion of MDA G as Operable Unit 1148.

Patrick Longmire

Technical Staff Member, Chemical Science and Technology Division, Los Alamos National Laboratory

B.S., M.S., Ph.D. Geology with Geochemistry emphasis

Pat was responsible for characterizing the geochemistry of the MDA G subsurface, which included literature searches, modeling, and experimental work. He is a co-author of Appendix 2a, and the primary author of Appendix *2d Batch Sorption Experiments for*

Americium, Neptunium, Plutonium, Technetium, and Uranium Transport through the Bandelier Tuff, Los Alamos, New Mexico.

Pat has 18 years' experience in hydrogeochemistry, including fate and transport of inorganic contaminants, soil chemistry, and contaminant sorption. He is a Certified Groundwater Professional and an instructor for the Association of Ground Water Scientists and Engineers.

Brent Newman

Technical Staff Member, Environmental Sciences Group, Earth and Environmental Sciences Division, Los Alamos National Laboratory

B.S., M.S., Ph.D. Geochemistry

Brent conducted the natural tracers analyses in support of the subsurface characterization and modeling for the PA, and is the author of Appendix 2b *Vadose Zone Water Movement at Area G, Los Alamos National Laboratory, TA-54" Interpretations Based on Chloride and Stable Isotope Profiles.*

Brent has applied the geochemical and isotopic tracer analyses to vadose zone processes at several locations on the Pajarito Plateau.

David Rogers

Technical Staff Member, Water Quality and Hydrology Group, Environment, Safety, and Health Division, Los Alamos National Laboratory

B.A. Physics, M.S. Geophysics, Ph.D. Earth Sciences

David prepared the hydrogeological conceptual model for the performance assessment, detailed in Appendix 3h *Conceptual Model for Subsurface Transport at MDA G.* He assisted in data collection, evaluation, interpretation, and analyses in support of the hydrogeological conceptual and mathematical models.

David is involved in the development of the site-wide hydrology model for the Laboratory.

Everett Springer

Deputy Group Leader, Environmental Sciences Group, Earth and Environmental Sciences Division, Los Alamos National Laboratory

B.S., Ph.D. Watershed Science

Everett performed the surface water balance modeling in support of the source term, subsurface transport, and sediment transport analyses. He is the author of Appendix 3c *Surface Water and Erosion Calculations to Support the MDA G Performance Assessment.*

Everett has many years' experience in simulation and assessment of surface and subsurface arid and semiarid hydrologic systems. He is involved in Field Unit 1 of the ER Project. Everett is the lead modeler for the ecosystem-level model of the western U.S. rangeland ecosystems.

RESOLUTION OF PRP COMMENTS ON DRAFT PA FOR LOS ALAMOS AREA G DISPOSAL FACILITY

1. The PRP appreciates the open sharing of information between the preparers and the Panel, and the PRP commends the PA preparers on the preparation of the qualify draft PA.

   No resolution required.

2. In finalizing the PA, there needs to be concerted effort to integrate the various parts into a cohesive whole. For example, interpretations lent to site data in forming the conceptual model need to be carried through from detailed appendices to conclusions of the analyses. There needs to be a closer coordination among the team members.

   There are several reports included as appendices that contributed to the formulation of the conceptual model for subsurface transport, and supported the implementation of the numerical model subsurfact transport. These reports describe independent analyses that suggest a very complex geohydrology that involves evaporative processes deep within the mesa. Each of these analyses are reviewed and interpreted as the basis of the conceptual model described in Appendix 3g Conceptual Model for Subsurface Transport. The simplifications assumed in implementing the numerical model for subsurface transport are summarized in Section 3.3.2.1.1 Conceptual Model of Vadose Zone transport.

3. The process of developing waste acceptance criteria from PA results must be presented in the final PA.

   Section 6.2.1 Use of Performance Assessment Results describes the methodology of interpreting the results of the PA dose analyses in the context of waste acceptance criteria.

4. The site-specific information available at Los Alamos, that has lead to the general understanding of how the site works, is not well reflected in the modeling to date. For example, stresses that drive the natural system at LANL are highly variable and transient, yet steady-state assumptions are made in the groundwater analyses.

   A concerted effort has been made to collect and assess new and existing data regarding the natural processes related, in particular, to moisture fluxes within the mesa. The interpretation of those data formed the hydrogeologic conceptual model.

As discussed at length in Section 2.1.5 Hydrogeology, it is recognized that the moisture fluxes within the natural system are spatially and temporally variable. However, data required to resolve the variability are not available, and may not be attainable without perturbing that natural system. Several parameter studies, described in Section 3.3.2 Groundwater Protection Analysis, were performed to examine the validity of the steady-state approximation of recharge through the vadose zone. It was found that transients as modeled were damped within the vadose zone, and that the steady state infiltration rate used in the vadose zone transport calculations was a conservative approximation of actual conditions.

5. The PA is focused on selected mechanisms and pathways. Finalization will require consideration of other pathways and the associated rationale (lateral migration, lateral migration coupled with cliff retreat, upward migration, episodic events, surface water transport, migration to groundwater through canyon floor, etc.).

   All of these mechanisms and pathways were addressed, and are discussed in Section 3.3.2 Groundwater Protection Analysis of the report.

6. Upward migration and lateral migration (individually and in combination) of contaminants needs to be addressed.

   Upward migration was discounted on the basis of in situ moisture profiles, which indicate that liquid-phase moisture flow is downward to the depths of the surge beds at the base of Unit 2, which is approximately 15 m below the surface. Upward migration of gases and vapors was calculated, as reported in Section 3.1.1.1 Gas-Phase Source Term and Appendix 2a Evaluation of Atmospheric Release Sources for Gaseous Phase Contaminants Emanating from the Disposal Facility at Area G. Lateral aqueous-phase migration was included in the vadose-zone transport calculations It is discussed in Section 3.3.2 Groundwater Protection Analysis of the report, and is recognized as a viable pathway.

7. Calculations are based on sheet erosion; however, this may not be the most appropriate runoff model for such complex terrain.

   Field investigations of the surface of MDA G performed by the surface water balance modeling team indicate that sheet erosion of disposal pit covers is a valid assumption. Erosion is discussed in Section 2.1.4.1 Regional and Site-Specific Geology and Topography and Section 2.1.5.1 Surface Water.

8. Surface water transport off the mesa to the canyon floor and then to the aquifer should be considered. Experience at LANL indicates that contamination at the surface of the mesa readily moves via surface water runoff to the mesa edge, then to the canyon bottom. Thus, contamination at the surface from cover erosion and-or biotic pathways would then bypass the unsaturated tuff deposit of the mesa, and move to the aquifer through sediments in the canyon floor.

This pathway was modeled in the all pathways analysis of the PA, Section 3.2.3 All Pathways Analysis. The source term for this transport pathway was biotic intrusion; at the estimated erosion rate, the effect of surface erosion on biotic translocation was insignificant. Even a higher rate of erosion that was coupled into the detailed biotic translocation model did not affect surface contamination levels appreciably, as reported in Appendix 3b Model for the Biotic Translocation of Buried Low-Level Radioactive Waste to the Ground Surface in the Presence of Surface Erosion.

9. The fastest rate of cliff retreat (7,000 years to expose the waste) should not be summarily dismissed. Cliff retreat should be coupled with horizontal and lateral migration rates.

   Cliff retreat is addressed in the report in Section 3.1.1 Air Pathways Analysis. Given the change in compliance period to 1,000 years, even the fastest estimated cliff retreat rate referred to by the PRP is not considered an imminent threat to containment of radioactivity, however.

10. To better understand the hydrological system, some consideration and simulation of transient event should be done. Efforts should be made to factor the basalt into the model to provide a better representation of the physical system (the higher water content of the Otowi formation). Even if the water flow and contaminant transport through the basalt were not factored into the overall result (i.e., the breakthrough monitoring point were retained), a different water retention relationship for the Guaje pumice or Cerros del Rio basalts could be used to bring about higher water contents in the Otowi formation. More effort is also needed to represent the influence of air movement within the vadose zone (Tshirege member).

    All of these items were explicitly addressed in the modeling discussed in Section 3.2.2 Groundwater Protection Analysis. The parameter study performed to evaluate the effects of the Guaje Pumice Bed and the Cerros del Rio Basalt is summarized in the main body of the report, and is reported in detail in Appendix 3g Simulations of Groundwater Flow and Radionuclide Transport in the Vadose and Saturated Zones Beneath Area G, Los Alamos National Laboratory.

    Unfortunately, sufficient data are not presently available to realistically model air flow in the vadose-zone transport model, although the model does have a dual-phase transport capability. As reported in Section 2.1.5.6.4 Vapor Flux Studies, the water flux in mid-depth region of the mesa apparently occurs in the vapor phase. This vapor-phase flux occurs in the fractured Unit 2, and the highly permeable surge beds at the base of that stratum. Barometric pumpings has been identified as a driving force for vapor-phase transport. Thus, while the role of vapor-phase drying and deep evaporation appear to play a critical role in vadose-zone hydrology, additional field data are required to define boundary conditions in the vadose-zone transport model.

11. The use of field studies such as TDR probes, weighing lysimeter, etc., should be considered to gain a better understanding of water flow in the vadose zone. Incorporate the data from appropriate existing field studies and discuss plans for conducting additional field studies in the future work section of the PA.

    Additional data have been obtained from new boreholes at MDA G. Several boreholes are being maintained and used for routine neutron-probe moisture measurements. The data obtained to date from boreholes and recovered core are included in Section 2.1.5 Hydrogeology. If funding is secured, there are plans to install moisture gauges along the bottom of Pit 38 and Pit 39, through access pipes that are already installed.

12. The PRP is concerned that the new method of waste emplacement may enhance subsidence. LANL may wish to consider elimination of voids by compaction or filling.

    The PA analysts share this concern. The use of large metal containers do enhance disposal efficiency, but this must be weighed against the potential consequences of probable void spaces associated with the use of large containers. An option being evaluated is the emplacement of large containers without their covers, then backfilling the containers with crushed tuff to ensure that void spaces are filled. To date, only single lifts within two pits (Pit 37 and Pit 38) have been completed with large containers.

13. The "all-pathways" dose is dominated by consumption of crops which have been contaminated by irrigation. It is counter-intuitive that the dose from drinking water is so much less than that from eating.

    This issue is discussed in Section 4.3 Sensitivity and Uncertainty, which is a summary of the more detailed discussion in Appendix 3e Radiological Dose Assessment for the TA-54, Area G Performance Assessment and Composite Analysis. The contribution of the consumption of irrigated crops to the total dose is expected to be over-estimated. Radionuclide concentrations in the crops are dominated by radioactivity taken up via the roots following the deposition of said radioactivity on surface soils by irrigation. While the radionuclides projected to occur in the irrigation water are highly mobile, their concentrations are projected assuming a buildup time in the soil of 15 years. A more reasonable period of buildup for highly mobile radionuclides is expected to be on the order of one year. Under these conditions, doses from the consumption of crops would decline about 15 times. At these levels, the consumption of drinking water would be the primary contributor to the projected doses.

14. The assessment of biotic transport does not seem to be consistent with data provided on plant rooting depth and animal burrow depth.

This apparent discrepancy results from the fact that, while some plants and animals native to the region do root and burrow to depths greater than those modeled, the amount of material brought to the surface is dominated by shallower processes. In particular, studies have shown that root mass decreases almost exponentially with depth, and is largest within the top one or two meters of the surface. Regarding burrowing animals, site-specific studies reveal that the most prevalent burrowing animal is the deer mouse. The modeling of biotic translocation is discussed in Section 3.1.1 Air Pathways Analysis Source Term, which summarizes the analysis detailed in Appendix 3b Model for the Biotic Translocation of Buried Low-Level Radioactive Waste to the Ground Surface in the Presence of Surface Erosion.

15. The information presented for atmospheric transport does not seem to support the location of the maximum receptor.

    Discussion of the location of the maximum offsite air concentrations is summarized in Section 3.3.1 Air Pathways Analysis, and detailed in Appendix 3f Atmospheric Transport in Complex Terrain at Los Alamos, Area G. The placement of the maximally-exposed offsite individual for the air-pathway analysis in Cañada del Buey is well supported by site-specific meteorological data (i.e., wind direction and frequency on mesas and in canyons). The particular location, 500 m upcanyon.

16. The bar graphs representing radionuclide concentrations, presented in Chapter II, page 50, Figure 2.3-2 of the PA, should be checked for accuracy. In addition, radionuclide concentrations provided in Tables 10 and 11 of Appendix 2C, "Area G LLW Inventory Over Facility Lifetime." Indicate how these corrections will affect the dose projections presented in the PA.

    All inventory data and graphs have been revised, and are presented in Section 2.3 Waste Characteristics.

17. Per the May 31, 1995, memorandum from Jill E. Lytle, EM-30, "Inclusion of Pre-1988 Source Term and Other Sources of Radioactive Contamination in Low-Level Waste Disposal Facility Performance Assessments," legacy waste and other potential sources of radioactive contamination will have to be included as the PA is finalized.

    The PA analysis included the entire disposal inventory at MDA G to meet this requirement. Other potential sources were excluded, based on technical justifications provided in Appendix 1b Technical Justification for Excluding Sources from the MDA G Composite Analysis.

18. Care should be taken in developing inventories of legacy and historical wastes to consider uncertainties in older waste characterization.

The methodology and results of the older waste characterization effort were peer reviewed by current and former LANL personnel familiar with the Laboratory's past waste generating and waste management practices.

19. The PRP suggest that an effort be undertaken to interview long-term LANL employees and available retirees to help determine process history for legacy waste.

    See response for Comment 18, above.

20. The PRP suggest that a broader set of radionuclides should be initially considered in the screening process, i.e., all of the nuclides listed in the DOE dose conversions factors documents, July 1988.

    The future inventory considered in the PA is based on information provided by facility and program managers at LANL. While radionuclides not considered in the analysis are not expected, if a situation arises where a new waste stream is generated that contains radionuclides not included in the PA, the waste stream will be certified and accepted for disposal only after PA analysts have approved it. The characteristics of the new waste stream that are relevant to release and transport will be reviewed, including radionuclide speciation, solubility, and sorption.

21. Uncertainty analysis has only been done in a qualitative manner to date. A more rigorous study of uncertainty is needed. The analysis should also consider coupled mechanisms rather that just one mechanism at a time. This will help in the planning of future work.

    The sensitivity and uncertainty analyses for the offsite and intruder dose projections have been updated to address the PRP's comment. These analyses, discussed in Sections 4 and 5 of the main report and Appendix 3e Radiological Dose Assessment for the TA-54, Area G Performance Assessment and Composite Analysis, were performed in accordance with current DOE guidance.

22. Justification or rationale must be presented for the selection of parameter values and scenarios, such as 10^{-7} dust loading and 10,000-year compliance period.

    All parameters used in the analyses are justified, either within the body of the report or within the appendices.

23. Solubility limited data for certain radionuclides needs to be presented on the basis of all isotopes in the element; for example, uranium and thorium.

    Solubility limits as modeled in the PA are discussed in Section 3.1.2 Groundwater Protection Analysis Source Term

24. The radon flux values should also be presented in terms of air concentration or dose to make the values meaningful.

In accordance with current DOE guidance, radon fluxes were calculated as discussd in Section 3.1.2 Air Pathways Analysis Source Term and compared with the radon-flux performanc objective in Section 4.1.1 Results of Air Pathway Analysis. The performance objective used to evaluate the projected MDA G fluxes was 20 pCi/m^2/s.

25. The effective diffusion coefficient for the vapor phase is about 10 times lower than that used in NRC Regulatory Guide 3.64. This should be justified.

Diffusion coefficients used in the air pathways analysis were measured at MDA G. As discussed in.Section 3.1.1 Air Pathways Analysis Source Term , the diffusion coefficient for water vapor from the shafts was based on site-specific data, the coefficient for the pits was estimated from the free diffusion coefficient adjusted to account for the effects of porosity, tortuosity, and thermal gradients. The revised coefficients are larger than that used in NRC Regulatory Guide 3.64

26. The final documents needs to be consistent among the various parts, i.e., a consistent rooting depth should be used in each of the various analyses that use it, and moisture content should be used in each of the various analyses that use it, and moisture content should be reported and discussed in a single unit (i.e., % by volume) rather than by the three units of % by weight, % by volume, and saturation.

Attempts were made to ensure consistency to the extent possible. However, certain measured values cannot easily be converted into other units.

27. In finalizing the PA, attention should be given to technical editing to produce a quality document (define terms, provide units in equations, present legible graphics, coordinate text titles and paragraph numeration with the table of contents, etc.).

The main body of the report has undergone a complete technical edit. Individual authors were responsible for the format of their appendices.

TECHNICAL JUSTIFICATION FOR EXCLUDING SOURCES FROM THE MDA G COMPOSITE ANALYSIS

DIANA HOLLIS, LANL EM-SWO

TABLE OF CONTENTS

1. INTRODUCTION 1

2. SUMMARY OF MDA G ANALYSES 1

3.1 AIR-PATHWAY SCENARIO FOR MDA G CA 3
3.2 GROUNDWATER-PATHWAY SCENARIO FOR MDA G CA 4
3.3 ALL-PATHWAYS ANALYSIS FOR THE MDA G PA 6

3. SOURCES TO BE CONSIDERED 7

3.1 MDA AB 7
3.2 MDA A 7
3.3 MDA B 7
3.4 MDA C 8
3.5 MDA T 8

4. CRITERIA FOR SOURCE EXCLUSION 8

4.1 DATA QUALITY OBJECTIVES 9
4.2 POTENTIAL AIR-PATHWAY SOURCES 10
4.3 POTENTIAL GROUNDWATER-PATHWAY SOURCES 11
4.4 POTENTIAL ALL-PATHWAYS SOURCES 14

5. CONCLUSIONS 14

6. REFERENCES 17

LIST OF FIGURES AND TABLES

FIGURE 1 MDA G LAYOUT SUPERIMPOSED ON A TOPOGRAPHIC CONTOUR MAP 2
FIGURE 2 STRATIGRAPHY OF MESITA DEL BUEY 5
FIGURE 5 STRATIGRAPHY OF BANDELIER TUFF AT MDA G, MDA C, AND MDA T 12
FIGURE 3 TOPOGRAPHIC SETTING OF POTENTIALLY SIGNIFICANT SOURCES 15
FIGURE 4 ISOPRESSURE CONTOURS OF THE REGIONAL AQUIFER 16

TABLE 1. FEATURES OF THE MDA G GROUNDWATER TRANSPORT ANALYSIS 6
TABLE 2. COMPARISON OF MDA G INVENTORY WITH OTHER SOURCES 10

1. INTRODUCTION

The DOE requires that a composite analysis (CA) be prepared to assess the cumulative future impacts of active low-level radioactive solid waste (LLW) disposal facilities and other sources of radioactivity that could interact with projected releases from the active facility.[1] Material Disposal Area (MDA) G is the only active LLW disposal facility at the Los Alamos National Laboratory (LANL). Projected releases of radioactivity from waste disposed of at MDA G after September 26, 1988 have been evaluated in the radiological performance assessment (PA) for MDA G, as required by DOE Order 5820.2A.[2]

Radioactive waste has been disposed of at MDA G since about 1957. Before the mid-1970s, radioactive waste was also disposed of at at several other facilities across the 111-km^2 (43 mi^2) LANL complex . While MDA G continues to be used for LLW disposal, other radioactive waste disposal sites are inactive and are managed by the LANL Environmental Restoration (ER) Project pursuant to the Hazardous and Solid Waste Amendments (HWSA) of the Resource Conservation and Recovery Act (RCRA).[3] In terms of a composite effect of potential future releases from MDA G and formerly-used MDAs, the waste disposed of at MDA G between 1957 and September 26, 1988 are likely to interact with potential releases from waste disposed of after September 26, 1988. For this reason, all waste disposed of at MDA G since 1957 and projected to be disposed of through 2044 was included in the source term for the MDA G PA. The composite impact of past, present, and future disposals at MDA G have been analyzed and reported in the *Performance Assessment and Composite Analysis for the Los Alamos National Laboratory Material Disposal Area G.*[4]

Due to the favorable meteorologic, hydrogeologic, and geochemical characteristics of the natural environment in the Los Alamos area, potential releases from formerly-used MDAs across the LANL complex are unlikely to interact with modeled releases from MDA G. This report presents the technical justification for eliminating other sources from consideration in the MDA G CA. Potential releases from other sources are compared with the modeled releases from MDA G.

The modeling approach and dose estimates for the MDA G CA analyses are summarized in Section 2. Other sources of radioactivity that were initially considered in, but eventually excluded from, the CA are described in Section 3. The technical basis for excluding these sources is discussed in Section 4. Finally, conclusions drawn from the preceding sections are presented in Section 5.

2. SUMMARY OF MDA G ANALYSES

The performance measure for the MDA G CA is that the projected dose to a hypothetical future member of the public resulting from releases from MDA G and all other potentially interacting sources should not exceed a dose limit of 100 mrem/yr. If the projected dose exceeds a dose constraint of 30 mrem/yr, an analysis should be performed to consider the actions that can be taken to reduce the calculated dose. The period of assessment is 1,000 years after closure of MDA G, which is assumed to occur after disposals cease in the year 2044.

As Figure 1 illustrates, MDA G is located on Mesita del Buey, a narrow east-southeast trending mesa bounded by Cañada del Buey to the north and Pajarito Canyon to the south. The topography of the site important effects on release and transport and, ultimately, consequences of radioactivity contained by the facility.

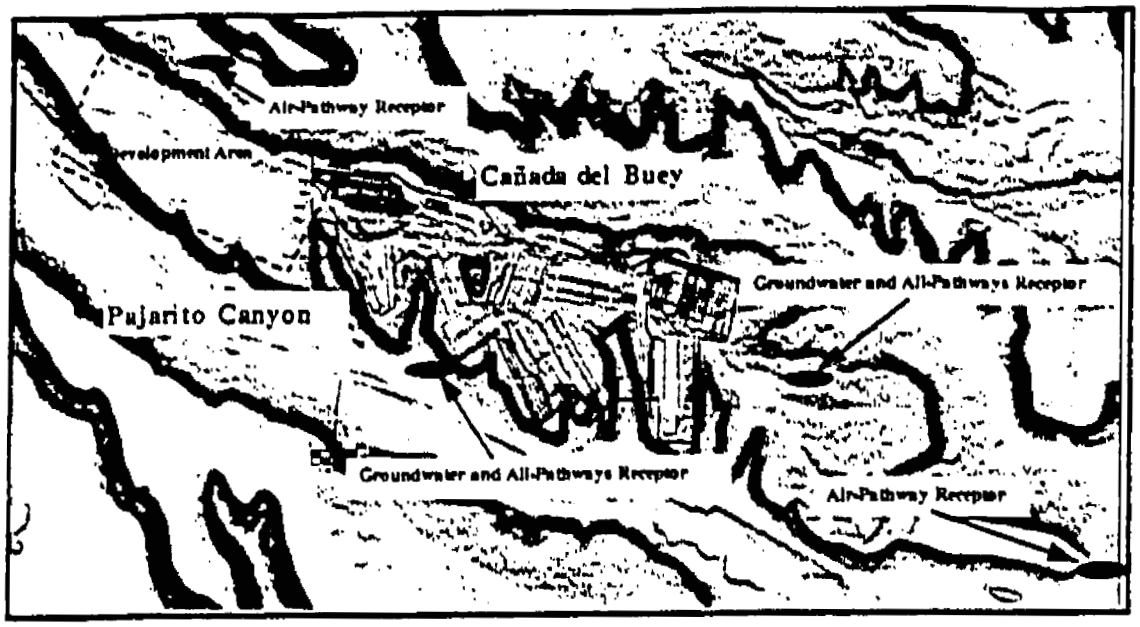

Figure 1 MDA G layout superimposed on a topographic contour map

At MDA G, LLW is disposed of in pits and shafts excavated into bedrock to depths of about 20 m (65 ft). The bedrock is of volcanic origin, and forms a 275 m (900 ft) vadose zone. The mesa consists of Bandelier Tuff, a compound cooling unit of variable degrees of welding. The canyons are about 30 m (100 ft) below the surface of the mesa.

The disposal facility has been filled from east to west, with future disposals anticipated to occur in the development area called out in Figure 1. As stated in the Introduction, past, present, and future disposals at MDA G were included in the source term for the MDA G PA to evaluate compliance with the CA performance measure. The following offsite exposure scenarios were evaluated for the CA inventory:

Air-pathway scenario: Burrowing animals excavate contaminated material from disposal units at MDA G; contaminated material is suspended in air above the disposal facility and transported to an offsite receptor; a portion of the airborne radioactivity is redeposited at the receptor site, while the the rest remains airborne; an individual receptor receives doses from the radioactivity in air, on soil, and on foodstuffs.

Groundwater-pathway scenario: Radioactivity is dissolved by water percolating through disposal units at MDA G; leachate is transported vertically down through the vadose zone directly to the regional aquifer, and laterally into semi-saturated alluvium located near the disposal facility, from which it is transported directly downward to the regional aquifer; radioactivity is mixed into the regional aquifer; an individual receptor at an offsite location receives doses due to the consumption and use (irrigation) of contaminated water drawn from the regional aquifer.

All-pathway scenario: The all-pathways scenario combines portions of the air- and groundwater-pathway scenarios. Burrowing animals excavate contaminated material from disposal units at MDA G; contaminated material is transported offsite by surface-water runoff; an individual offsite receives doses from contaminted water (via the groundwater pathway) and from contaminated sediment.

The approach to modeling these scenarios is summarized below. This information will be used to evaluate, and ultimately dismiss, the potential for releases from other formerly-used MDAs to increase the projected doses from MDA G.

2.1 Air-Pathway Scenario for MDA G CA

The maximum air-pathway dose projected in the MDA G CA was 5.5 mrem/yr, the result of:

- burrowing animals penetrating through 1-m (3.3-ft) disposal-unit covers and excavating material contaminated with actinides;
- suspension of actinides in air; dispersion of airborne actinides into Cañada del Buey north of MDA G; and
- inhalation of airborne actinides.

According to *Radiological Dose Assessment for the TA-54, Area G Performance Assessment and Composite Analysis*,[5] the inventory responsible for the great majority of the air-pathway dose was the oldest waste in the inventory, the characteristics of which were extrapolated from existing records, as described in *Radioactive Waste Inventory for the TA-54, Area G Performance Assessment and Composite Analysis*.[6] The model used for biotic translocation is reported in *A Model for the Biotic Translocation of Buried Low-Level Radioactive Waste to the Ground Surface in the Presence of Surface Erosion*, which assumes a maximum burrowing depth was assumed to be 2 m (6.6 ft) based on site-specific data.[7] It assumes that waste contaminated with actinides is readily excavated by burrowing animals. This is conservative based on information suggesting that the largest amount of plutonium-bearing waste in that portion of the inventory is dewatered sludge that is buried at the bottom of only a single pit.

The atmospheric dispersion model used to simulate the transport of airborne radioactivity is reported in *Atmospheric Transport in Complex Terrain at Los Alamos, Area G*.[8] The identification of the air-pathway receptor location was based on data collected from six meteorological stations operated on the mesas and in the canyons immediately around MDA G. These data indicate that winds flowing across Mesita del Buey are channeled into Cañada del Buey. Thus, groundsurface releases suspended in winds blowing from several sectors across the mesa are expected to coalesce into channeled winds within the canyon. Prevailing mesa-top winds are generally from the south-southwest during the day, following the Rio Grande valley. During the night, downdrafts from the mountains from to the west cause winds to flow towards the east. Mesa top winds vary, however, particularly during the day. In contrast to mesa-top winds, flow in the canyons is strictly bimodal: Winds flow up-canyon (west) during the day, and down-canyon (east) at night.

To calculate air-pathway doses in Cañada del Buey, the dispersion of suspended particulates was characterized by site-specific dispersion parameters χ/Q [i.e., air concentrations (Ci/m^3) normalized to source release (Ci/s)] at two receptor locations. One receptor was defined at the point of maximum offsite concentration, which was 500 m (1,600 ft) north of MDA G in Cañada del Buey. A second receptor was defined at the nearest downwind population center, White Rock, which is about 2 km (1.3 mi) east of MDA G. These air-pathway receptor locations are called out in Figure 1. Values of χ/Q were calculated for 16- 22.5° wind sectors using the CAP-88 computer code. The

calculated values reflect the dominant wind direction on the mesa tops, which is from south-southwest and apply to open, flat terrain. They were modified to account for the complex mesa and canyon terrain surrounding the MDA G site to ensure that maximum offsite concentrations were modeled realistically for the site.

The atmospheric model conservatively assumed that all ground level releases from MDA G which blow out across an adjacent canyon become entrained in the canyon flow. Several wind sectors were combined into a single canyon flow, which was upstream during the day and downstream at night. Using this method, it was determined that the maximum off-site airborne concentrations would occur in Cañada del Buey during the daytime. At that location, the maximum dispersion parameter was calculated to be 5.5×10^{-5} s/m^3. The maximum dispersion parameter in White Rock was associated with nighttime down-canyon flow, with a value of 1.3×10^{-5} s/m^3. At both receptor locations, the complex terrain correction increased projected plume concentrations by a factor of 2.4 over that expected in any single downwind sector. Concentrations are increased by a factor of 1.7 as a result of lower average wind velocities in the canyons.

2.2 Groundwater-Pathway Scenario for MDA G CA

The maximum annual groundwater-pathway dose calculated during the 1,000-year compliance period in the MDA G CA was 1.2×10^{-5} mrem at the downgradient receptor location. Groundwater doses were due to the ingestion of the three radionuclides of the 60-plus in the inventory that were non-sorbing: ^{14}C, ^{99}Tc, and ^{129}I. Carbon-14 was responsible for most of this dose. The source term used in the groundwater-pathway analysis was based on the assumption that all of the radioactivity surface contamination, which is thought to be conservative for at least the ^{14}C based on knowledge of the dominant waste form for that radionuclide.

The MDA G groundwater pathway analysis is fully described in *Simulations of Groundwater Flow and Radionuclide Transport in the Vadose and Unsaturated Zones Beneath Area G, Los Alamos National Laboratory.*[9] The three-dimensional grid was a fairly accurate representative of the stratigraphy illustrated in Figure 2. A good set of data is available to support modeling within the upper 100 m (330 ft) of the Bandelier Tuff. Each stratigraphic unit comprising the Bandelier Tuff was modeled with uniform hydraulic characteristics corresponding to the arithmetic mean of the field data summarized in *Geologic, Geohydrologic, and Geochemical Data Summary of Material Disposal Area G, Technical Area 54, Area G, Los Alamos National Laboratory.*[10]

The conceptual model of vadose zone hydrology is a simplification of the complex hydrologic system at MDA G. The model is fully detailed in Appendix *Conceptual Model for Subsurface Transport at MDA G.*[11] An important simplification in the conceptual model is a steady-state moisture recharge rate through Mesita del Buey. This simplification reflects the relative lack of data required to rigorously model vapor-phase moisture flow, evaporation through fractures and surge beds, and variable hydraulic parameters, all of which have been hypothesized on the basis of analyses on the available data set. The magnitude of the steady-state recharge rate used in the groundwater protection analysis was chosen to be conservative based on modeling and field data. Water balance modeling

reported in *Surface Water and Erosion Calculations to Support the MDA G Performance Assessment*[12] indicates an average recharge rate of about 1 mm/yr (0.04 in./yr) through the disposal units in their closed configuration, assuming an average annual precipitation of 36 cm (14 in./yr), a fully vegetated cover with a maximum rooting depth of 1 m (3.3 ft). The modeled recharge rate is less than the 5 mm/yr (0.2 in./yr) indicated by moisture measurements in an open pit at the site. This discrepancy reflects the importance of transpiration in water balance at MDA G, which is absent in open pits. While the lower recharge rate modeled may be anticipated when pits are closed and the vegetative cover is fully developed, the larger recharge rate consistent with *in situ* measurements was selected for the base case unsaturated transport model. Steady state recharge of this magnitude was considered to be a reasonable simplification based on the information available, which is briefly summarized below.

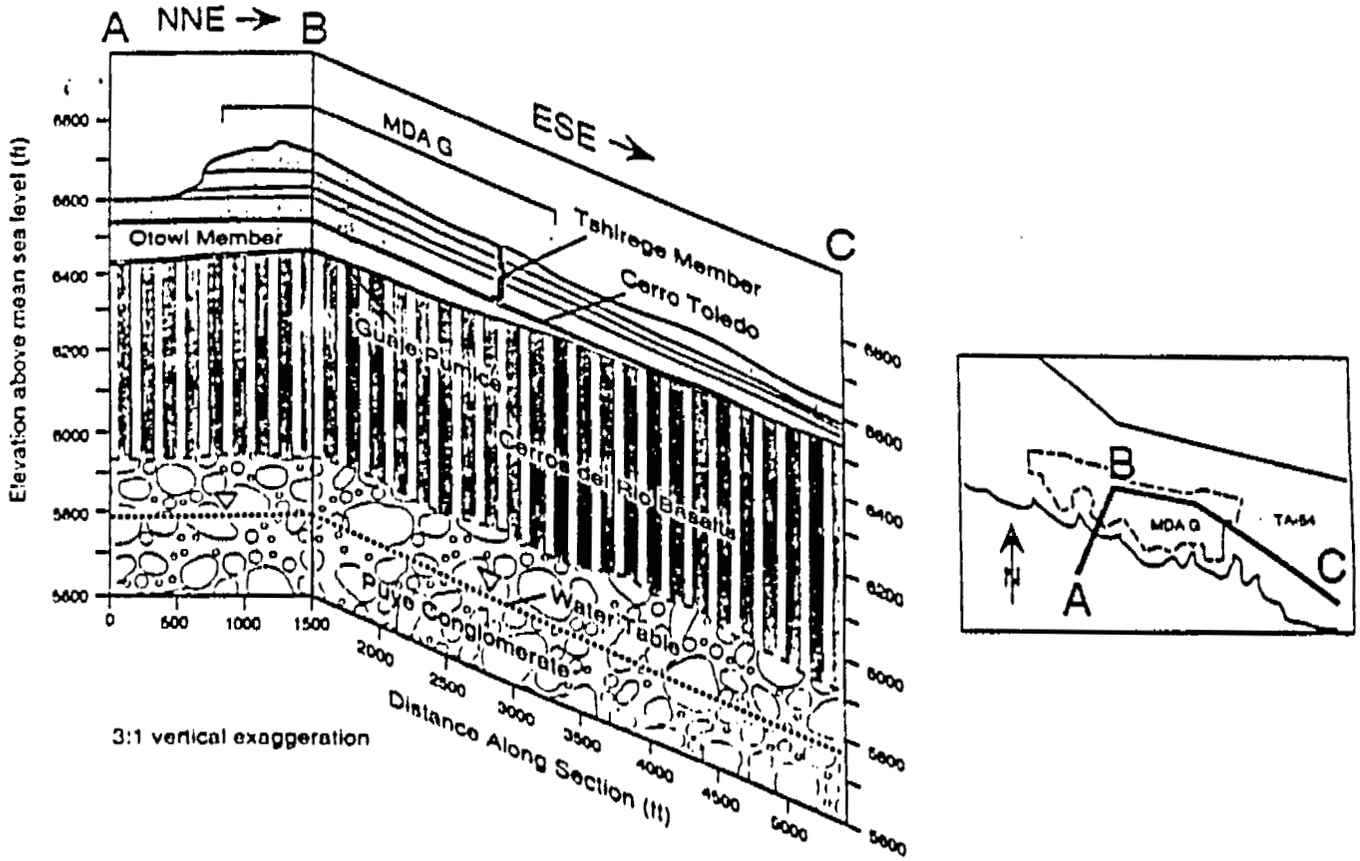

Figure 2 Stratigraphy of Mesita del Buey

The recharge fluxes through the Bandelier Tuff have been estimated using a variety of field, laboratory, and computational techniques. Recharge is affected by natural characteristics

and manmade alterations. Seasonal wetting and drying cycles maintain moisture contents (up to 20 percent) in the top few meters of the mesa that are higher than those found at greater depths (less than 5 percent). While recharge through fractures near the mesa surface may occasionally occur, fracture flow does not appear to result in increased recharge at depths below Unit 2. Surface disturbances associated with waste management activities may increase the moisture content near the top of the mesa, but a lasting effect of this increased moisture on deeper recharge has not been demonstrated. Extremely low moisture contents found 10 to 15 m (50 to 60 ft) below the mesa surface are likely to be the result of evaporation caused by air flow through fractures and surge beds, as supported by data on moisture content, matric suction, stable isotope ratios, and chloride content.

There are several aspects of the hydrology that, while potentially important, were ignored in the computational model of vadose-zone transport, due to a lack of data. Several simplifying assumptions were invoked in the computational model. As stated, the model assumes a uniform rate of infiltration through the mesa; this may be reasonable, considering that the disposal units themselves do not contain fractures, and are excavated either within or through the surge bed at the base of Unit 2, and the apparent effects that these features have on removing water from *undisturbed* mesa may not apply to the *disturbed* system. While not explicitly included in the final three-dimensional computations, several potentially important features of the hydrologic system were evaluated to ensure conservatism in the the final analysis. The effect of fractures on moisture flow was considered, as was evaporation through in fractures and surge beds. In addition, uncertainties in material properties and structure were evaluated.

The analysis used a conservative but reasonable steady-state infiltration rate of 5 mm/yr to simplify the complex vadose-zone hydrology. The computation represented the regional stratigraphy and geology in a realistic three-dimensional configuration, capturing the physical, hydrologic, hydraulic, and geochemical properties of the Bandelier Tuff.

Table 1 lists several features of the MDA G groundwater transport analysis.

Table 1. Features of the MDA G groundwater transport analysis

Unit of Bandelier Tuff Hosting Facility	Unit 2/Unit 1 vu
Depth of Disposal Units	<20 m (65 ft)
Thickness of Bandelier Tuff	82 m (270 ft)
Depth to regional aquifer	Approximately 305 m (1,000 ft)
Recharge Rate through Mesita del Buey	Approximately 5 mm/yr (0.2 in./yr)
Moisture Transit Time to Regional Aquifer	>600 years

2.3 All-Pathways Analysis for the MDA G PA

The maximum all-pathways dose calculated during the 1,000-year compliance period considered in the CA was 7.2×10^{-3} mrem/yr, received by the receptor in Pajarito Canyon. The majority of the dose was attributed to inhalation of resuspended contaminated sediments and ingestion of vegetables contaminated with sediment (via rainsplash). Contributing radionuclides were ^{239}Pu, ^{108m}Ag, and ^{241}Am. As in the air-pathway analysis, the source term was burrowing animals. The transport pathway was sediment transport at a rate of 4.0×10^{-7} m/yr (1.3×10^{-6} ft/yr), as modeled in *Surface Water and Erosion Calculations to Support the MDA G Performance Assessment*. The conservatism in the actinide inventory and biotic translocation model stated previously in reference to the air-pathway analysis apply equally to the dominant all-pathway source term. The inventory of the dominant fission products was extrapolated using the methodology described in

Isotopic Compositions of Inventory Designations "Mixed Fission Products" and "Mixed Activation Products."[13]

3. Sources to be Considered

In terms of physical dimensions and radiological inventory, the largest potentially-interacting sources at LANL are formerly-used MDAs. Figure 3 illustrates the distribution and size of these other sources on a topographical map. With the exception of MDA AB, these other MDAs generally resemble MDA G. MDAs A,B, and T about 6 km (4 mi) northwest of MDA G and MDA C about 6 km (4 mi) west-northwest of MDA G are all formerly-used radioactive waste disposal sites. MDA AB 5 km (3 mi) west-southwest of MDA G was used for below-ground test detonations. As Figure 3 illustrates, the area occupied by MDA G is 405,000 m^2 (100 ac), while the combined area of the other sources is only about 83,690 m^2 (20 ac). Like MDA G, the formerly-used MDAs are on mesas.

In addition to the formerly-used MDAs, some smaller zones of contamination are known to exist in Pueblo Canyon, Los Alamos Canyon, Mortandad Canyon, and Pajarito Canyon. The canyon contamination is the result of past liquid effluent discharges from nuclear materials processing (Pueblo and Los Alamos Canyons), liquid waste treatment (Mortandad Canyon), and test reactors (Pajarito Canyon). Canyon contamination is associated with sediment and alluvium. Information regarding the inventory of other sources was compiled in 1977.[14] Very little is known about the total extent of contamination within the canyons identified above. It is certain that the amount of contamination in canyon alluvium and sediment is far less than the mesa-top sources, however. The following paragraphs discuss the history and inventory of formerly-used mesa-top MDAs.

3.1 MDA AB

MDA AB is located at Technical Area (TA) 49, which is about 5 km (3 mi) west-southwest of MDA G. It was used for below-ground hydronuclear experiments in 1960 and 1961. Experiments were conducted in shafts and chambers at depths between 18 and 24 m (60 and 80 ft). The total volume of contaminated tuff has been estimated at about 30,000 m^3 (1,000,000 ft^3).[15] The radiological inventory has been estimated as 0.2 Ci ^{235}U and 2,450 Ci ^{239}Pu.

3.2 MDA A

MDA A is located at TA-21, some 6.7 km (4.2 mi) north-northwest of MDA G. MDA A ccupies an area of 5,060 m^2 (1.25 ac). Between 1944 and 1947, two shallow pits that were about 4 m (13 ft) deep were used to dispose of about 1,020 m^3 (36,000 ft^3) of "solid wastes with alpha contamination accompanied by small amounts of beta and gamma."[16, 17] During this period, two underground storage tanks were installed to store a total of 185,494 L (49,000 gal) of a sodium hydroxide solution containing 334 g of ^{239}Pu at the time of emplacement (circa 1947).[18] The liquid from these tanks was recovered, treated, and solidified in cement in 1975. The contaminated cement was buried at MDA A for several years, but was retrieved in the late 1980s and moved to Pit 29 at MDA G. In 1969, a 9 m (30 ft) deep pit was excavated at MDA A for the disposal of ^{235}U, ^{238}Pu, and ^{239}Pu-contaminated building debris from demolition work at TA-21. The actinide inventory of MDA A is judged to be much smaller than the MDA G inventory.

3.3 MDA B

MDA B is also located at TA-21. The approximate area occupied by MDA B is 24,000 m^2 (6.0 ac). Engineering drawings show that a single large pit comprises MDA B, but there is

conflicting evidence that 4 smaller pits were excavated. Solid waste was disposed of at MDA B between 1947 and 1950. The radiological inventory includes "plutonium, polonium, uranium, americium, curium, lanthanum, (and) actinium."[19] The disposal capacity of the pits is estimated to be about 21,000 m^3 (760,000 ft^3). The entire pit area is estimated to contain no more than 100 g (6.13 Ci) of ^{239}Pu.

In 1984, MDA B was resurfaced with a variety of cover systems during a pilot study conducted in support of the National Low Level Waste Management Program and the EPA's Land Pollution Control Division, Contaminant Branch. Its present state incorporates several variations of a nominal 1 m (3.3 ft) thick crushed-tuff cover, which is placed over the original crushed-tuff cover. Variations include cobble and gravel bio-barriers between the old and new covers, as well as shrub, grass, and gravel-mulch surface treatments. The total cover thickness at MDA B is nominally 2 m (6.6 ft).

3.4 MDA C

MDA C is located at TA-50 on a mesa about 6 km (4 mi) west-northwest of MDA G. MDA C occupies an area of about 48,500 m^2 (12 ac). Radioactive and hazardous (chemical) waste was disposed of in six pits and 107 shafts at MDA C between 1948 and 1965. The average depth of the MDA C disposal pits was 6 m (20 ft), while the average depth of shafts was about 5 m (16 ft). The pits were filled between 1948 and 1959, and the shafts were filled between 1958 and 1965. Log books were used to record limited information about waste disposals after 1954. Estimates of the total radiological inventory at MDA C are 196 Ci in pits and 49,483 Ci in shafts. This estimate includes 28 Ci of uranium (i.e., ^{233}U, ^{234}U, ^{235}U, ^{236}U, and ^{238}U); 49,136 Ci of ^{137}Cs; 31 Ci of ^{90}Sr; 26 Ci of ^{239}Pu; 149 Ci of ^{241}Am; 50 Ci of Mixed Fission Products (MFP); and 200 Ci of Mixed Activation Products (MAP). Many of these radioisotopes are important, based on the results of the MDA G analyses. Important fission products include ^{99}Tc, ^{129}I, and ^{108m}Ag. Using the conversion factors used in the MDA G analysis, 50 Ci of MFP would include $1x10^{-5}$ Ci ^{99}Tc and $5x10^{-7}$ Ci ^{129}I and $5x10^{-2}$ Ci ^{108m}Ag.

3.5 MDA T

MDA T is located at TA-21, along with MDA A and MDA B. MDA T includes four absorption beds where radioactively contaminated liquid waste from the plutonium processing laboratories at TA-21 was disposed of between 1945 and 1952. In 1952, a liquid-waste treatment plant was installed to remove plutonium and other radionuclides. Thereafter, the absorption beds received relatively small quantities of LLW, until 1967, when a new liquid-waste treatment process was initiated. Between 1968 and 1975, treated liquid waste was mixed with cement pumped into shafts at MDA T for disposal. After 1975, the cement paste was poured into corrugated metal pipes, and retrievably buried at MDA T. There were 62 shafts at MDA T used for the permanent disposal of cement-treated liquid waste.

Approximately 69,000 m^3 (18,300,000 gal) of liquid waste was disposed of the MDA T absorption beds between 1945 and 1967. "As of January 1973, the absorption beds contained... 10 Ci of ^{239}Pu... As of July 1976, the disposal shafts contained 7 Ci of ^{233}U, 47 Ci of ^{238}Pu, 3,761 Ci of ^{241}Am, and 3 Ci of MFP." In terms of mobile radionuclides, this translates into $6x10^{-7}$ Ci ^{99}Tc and $3x10^{-8}$ Ci ^{129}I and $3x10^{-3}$ Ci ^{108m}Ag The total volume of cement paste permanently disposed of in shafts at MDA T was 3,500 m^3 (122,500 ft^3).

4. CRITERIA FOR SOURCE EXCLUSION

Sources can be excluded from consideration in the CA if sufficient justification is provided, and the rationale for exclusion is explained.[1] At LANL, sources were excluded on the basis

of radioactivity inventory relative to the total inventory at MDA G, availability of that inventory for release via biotic translocation or leachate, potential for atmospheric dispersion toward MDA G, potential for contamination of the regional aquifer at a receptor near White Rock, and potential for sediment transport into Pajarito Canyon. The MDA G CA is used as a basis for comparison. This approach invokes the fundamental assumption that the models used to project release and transport from disposal pits at MDA G are applicable to other mesa-top sources, which is judged to be reasonable. It uses an all-other-things-being-equal approach for such things as recharge rates, erosion rates, and complex-terrain effects, which is generally valid among the sources being considered.

The rationale used to exlude formerly-used MDAs is consistent with DOE guidance[1] stating that sources may be excluded from the CA if:

- the radionuclide inventory of the source is small enough that, given reasonable release mechanisms, the source could contribute only a very small fraction to the dose attributed to MDA G; or
- the distance from the source to the location where potential exposures are projected to occur is sufficiently long that dispersion into the environment would reduce the contribution from the source to a small fraction of that projected from MDA G.

The DOE also recommends that the first iteration of the CA be based on information readily at hand. The information presented above is consistent with this guidance. The determination as to its acceptability as a bases for exclusion presented in this Section can be made in the context of Data Quality Objectives (DQOs), in the manner summarized below.

4.1 Data Quality Objectives

The EPA developed the Data Quality Objective Process to determine the type, quantity, and quality of data needed to support decisions regarding environmental restoration options for contaminated sites.[20] The DQO Process consists of six steps, which were applied as follows:

1. State the Problem: Cumulative doses to future members of the public due to releases from MDA G and MDAs AB, A, B, C, and T must be kept below 100 mrem/yr, and should be maintained below 30 mrem/yr if ALARA.
2. Identify the Decision: Do projected environmental releases from MDAs AB, A, B,C, and T have the potential to interact with offsite doses calculated in the MDA G CA so that the cumulative dose exceeds 30 mrem/yr primary dose constraint?
3. Identify the Inputs to the Decision: The maximum air-pathway dose from the MDA G CA (5.5 mrem/yr), the maximum groundwater-pathway dose (1.2×10^{-5} mrem/yr), and the maximum all-pathways dose (7.2×10^{-3} mrem/yr); the radionuclides contributing to those doses (^{240}Pu, ^{239}Pu, ^{238}Pu, ^{241}Am ^{108m}Ag, ^{182}Hf, ^{129}I, ^{99}Tc, and ^{14}C); contributing source terms (biotic intrusion, aqueous-phase dissolution); readily-available information on the inventory, meteorologic, geologic, and geohydrologic characteristics of MDAs AB, A, B,C, and T.
4. Define the Boundaries: Regional aquifer 100 m (330 ft) downgradient from MDA G; air in White Rock; air 500 m (1,640 ft) in Cañada del Buey, and soil in Pajarito Canyon; MDAs G, AB, A, B, C, and T.
5. Develop a Decision Rule: The primary dose constraint is 30 mrem/yr, and the dose limit is 100 mrem/yr. The maximum air-pathway dose from the MDA G CA is 5.5 mrem/yr, the maximum groundwater pathway dose is 1.2×10^{-5} mrem/yr, and the maximum all-pathways dose is 7.2×10^{-3} mrem/yr. To meet the 30 mrem/yr dose constraint, doses from other MDAs must be shown to be less than 24.5 mrem/yr via air in Cañada del Buey, less than 99.999988 mrem via groundwater, and less than 99.993 mrem via all-pathways.

6. Specify Limits on Decision Errors: The very low groundwater doses and all-pathways doses from MDA G allow very large errors to be acceptable in the inventories of ^{239}Pu, ^{241}Am ^{108m}Ag, ^{182}Hf, ^{129}I, ^{99}Tc, and ^{14}C at the formerly-used MDAs, and very large errors in the vadose-zone travel times beneath those MDAs. Uncertainties affected estimated releases from other sources more important when considering the air pathway. The propagated uncertainties in the ^{240}Pu, ^{239}Pu, ^{238}Pu, ^{241}Am inventories, the potential for biotic translocation of contaminated materials, and the potential for atmospheric dispersion into Cañada del Buey must be more carefully evaluated to ensure compliance with the 30 mrem/yr primary dose constraint and the 100 mrem/yr dose limit.

4.2 Potential Air-Pathway Sources

Based on the DQO Process, potentially-interacting source terms must have the following properties:

- Significant ^{240}Pu, ^{239}Pu, ^{238}Pu, and ^{241}Am inventories;
- Disposal unit covers less than 2 m (6.6 ft) thick; and
- Wind directions toward Cañada del Buey.

Table 2 lists the inventory of important radionuclides for all of the formerly used MDAs combined. The data in the table were presented above, in Section 3.

Table 2. Comparison of MDA G inventory with other sources

Isotope	Total Inventory (Ci)	
	MDA G	Other MDA (max)
^{14}C	3.8E-1	n/a
^{99}Tc	7.7E+0	1.1E-5 (MDA C)
^{108m}Ag	3.1E+1	5.0E-2(MDA C)
^{129}I	4.6E-5	5.3E-7 (MDA C)
^{238}Pu	4.2E+3	4.7E+1 (MDA T)
^{239}Pu	1.8E+3	2.5E+3 (MDA AB)
^{241}Am	2.2E+3	3.8E+3 (MDA T)

The table lists the MDA G inventory for comparison. At most sites, the known inventories of most important radionuclides are between two and five orders of magnitude less than the MDA G inventory. There are two notable exceptions, however: The inventories of ^{239}Pu and ^{241}Am at MDA AB and MDA T, respectively, are larger than the MDA G inventories. While they are not listed on the table because their inventory is difficult to quantify given the readily-available information, it can be assumed on the basis of process knowledge that both MDA AB and MDA T are contaminated with fission products associated with many uranium and plutonium isotopes; this assumption will be carried through in the discussion to follow.

The data in Table 2 suggest that MDA AB and MDA T have the potential inventory to increase air-pathway doses calculated in the MDA G CA. It then remains to be determined whether these inventories have the potential to be released to the surface, where they can be resuspended and transported in air. The MDA G CA showed that actinides are translocated to the surface by burrowing animals, and not by plants whose roots penetrate into disposal units. This is due to the fact that the actinides have very small root-uptake coefficients. Thus, MDA AB and MDA T are evaluated in terms of the potential for burrowing animals

with a maximum burrowing depth of 2 m (6.6 ft) to access contamination. As stated above, the source of contamination at MDA AB is at least 18 m (60 ft). This is nine times the nominal burrowing depth for the region. Thus, MDA AB can be excluded from further consideration as a potential air-pathways source.

Based on information provided by the ER Project, the disposal unit covers at MDA T are very similar to those at MDA G.[27] Thus, the potential for biotic translocation as a source term at MDA T is considered equal to that at MDA G. The ^{241}Am inventory is the quantity of interest. All other things being equal, the source term from MDA T might be about twice as large as that at MDA G.

Next, the potential for ground-level releases at MDA T to coalesce with releases from MDA G within Cañada del Buey is evaluated. The wind roses shown on the right-hand side of Figure 3 can be used to evaluate this potential. The data shown for TA-53 are considered to be representative of conditions at MDA T. During a typical year, winds at MDA T blow toward MDA G about 10 percent of the time. Assuming that those winds *are not* intercepted within the several canyons between MDA T and MDA G (which *is* expected), airborne contaminants may be carried toward Cañada del Buey about 10 percent of the time.

The dispersion distance between MDA T and Cañada del Buey is about 6 km (4 mi). Assuming Pasquill Category D (i.e., neutral dispersion), a groundlevel release will be dispersed by 1.6×10^{-6} s/m^3 (i.e., χ/Q) over this distance. As stated in Section 2.1, releases from MDA G are dispersed by a factor of 5.5×10^{-5} s/m^3 at the receptor location.

All of this information can be used to estimate the amount be which projected air-pathway doses calculated in the MDA G CA may be enhanced by releases from MDA T. Due to their relative inventories, it is assumed that the ^{241}Am releases from MDA T are approximately twice those at MDA G. In the MDA G PA, ^{241}Am accounted for about 30 percent of the 5.5 mrem/yr air-pathway dose. All other things being equal, the MDA T releases would increase doses by 60 percent. Taking into account the wind frequency, this factor would be reduced to 6 percent. Finally, accounting for relative dispersion, the potential dose increase due to airborne ^{241}Am released from MDA T and dispersed into Cañada del Buey would be about 0.1 percent of 5.5 mrem, or 5.5×10^{-3} mrem. To cause the composite air-pathway doses from MDA G and MDA T to approach the 30 mrem/yr primary dose constraint, the uncertainties in this estimate would have to exceed 4.5×10^{3}.

The uncertainty in the air-pathway dose assessment performed for the MDA G CA was relatively large. Several individual sources of uncertainty contributed to the overall propagated uncertainty, including inventory, source term, environmental transport, resource utilization, and dose conversion factors. Each of these is discussed at length in *Dose Assessment for the TA-54, Area G Performance Assessment and Composite Analysis*. In summary, the total propagated error that may lead to underestimates of air-pathway doses in the CA is 540, while the total propagated error that may lead to overestimates of air-pathway doses in 0.28. The two greatest individual sources of uncertainty were associated with radionuclide inventory and the potential for biotic intrusion. It is expected that similar uncertainties will apply at MDA T. The potential worst-case uncertainty of 5.4×10^{2} is nearly an order of magnitude less than the the acceptable uncertainty of 4.5×10^{3}.

4.3 Potential Groundwater-Pathway Sources

The radionuclides of interest in the groundwater-pathway are ^{14}C, ^{99}Tc, and ^{129}I. Based on the information in Table 2, MDA C has a potentially important inventory of at least ^{129}I. This radionuclide was a very small contributor to groundwater-pathway doses in the MDA G CA. It is also likely that MDA AB and MDA T also contain fission products due to the uranium and plutonium processes leading to the contamination at those sites. The amount, however, is difficult to quantify. Thus, MDA C, MDA T, and MDA AB were all considered as viable groundwater-pathway sources. The potential for nonsorbing fission

products entering the regional aquifer from MDA C, MDA T, and MDA AB to be transported to a receptor between MDA G and White Rock over a period of 1,000 years was evaluated.

Figure 4 shows iso-pressure contours of the regional aquifer beneath many of the LANL MDAs, including those under consideration here, namely, MDA G, MDA AB, MDA C, and MDA T. The contours show the general direction of the groundwater flow, from west to east. The figure shows that MDA C is clearly upgradient from MDA G. MDA T is generally upgradient, but the direction of groundwater flow is less clear do to the width between contours. MDA AB appears to have a parallel flow path to MDA G. For the purposes of this evaluation, it was considered possible that contaminants released from these three formerly-used MDAs, once reaching the regional aquifer, might be carried toward White Rock.

Next, the vadose zone groundwater travel time was evaluated. This was accomplished by comparing the "modelable stratigraphy" beneath these sites, as illustrated in Figure 5. The figure indicates the thickness of the Tshirege Member of the Bandelier Tuff, the stratigraphic unit for which reliable geohydrologic data are available to support credible vadose zone transport modeling. The Tshirege Member is the uppermost compound cooling unit of the Bandelier Tuff. It is composed of Unit 2 and Unit 1 at MDA G; Unit 3, Unit 2, and Unit 1 at MDA C and MDA T; and Unit 5/6, Unit 4, Unit 3, Unit 2, and Unit 1 at MDA AB. At each site, the Otowi Member of the Bandelier Tuff is present at different thicknesses, generally thinning from west to east. Beneath the Otowi Member, the Cerros del Rio Basalt can be found beneath MDA G and MDA C. The source of the basalt is east, near the Rio Grande River, and flows may not have reached MDA T or MDA AB. The stratigraphy beneath MDA AB is well known to depths of about 210 m (700 ft); no basalt was encountered in a borehole penetrating that depth. In the MDA G CA, the thick section (200 m) section of Cerros del Rio Basalt underlying the Otowi Member of the Bandelier Tuff was not modeled. It was given properties that allowed it to transmit water over a period of one year.

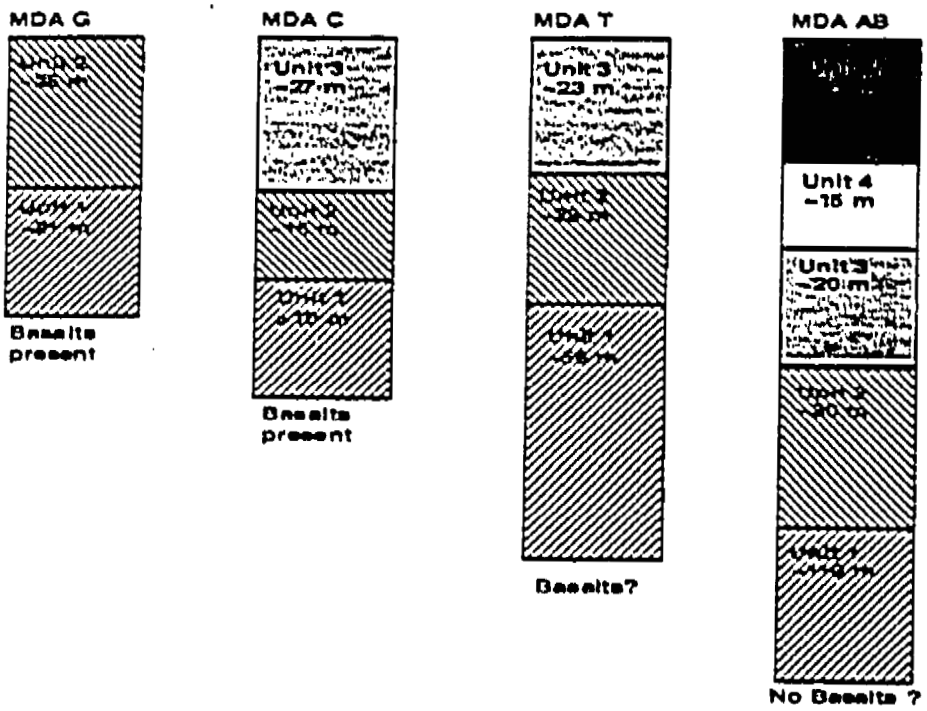

Figure 5 Stratigraphy of Bandelier Tuff at MDA G, MDA C, and MDA T

Groundwater travel time vertically down through the vadose zone to the regional aquifer was 600 years in the MDA G CA. That time was decreased to 100 years when a lateral path was followed out the mesa side, then through the Pajarito-Canyon subsurface. However, only 30 percent of the mass was transported laterally, contributing a very small percentrage of the groundwater-pathway dose. The vertical-downward travel path is therefore used as a basis of comparison with other sources. It is clear from Figure 5 that the downward vadose-zone groundwater travel time will be far less from MDA G than for any of the other sources under consideration, all other things being equal.

This comparison assumes that the hydrology modeled in the MDA G CA is representative of MDA C, MDA T, and MDA AB. Hydrology is affected by precipitation, vegetation, and geology, among other things. The vegetation is about the same at all of these disturbed sites, with the exception of MDA AB, which was covered with asphalt many years ago. Precipitation varies across the LANL complex, and is somewhat higher to the west of MDA G. MDA C is very near MDA G, and on the same mesa, and has similar precipitation. MDA AB is on the same isopleth as MDA G. However, MDA T receives higher annual average precipitation. However, that does not necessarily imply higher recharge rates. In fact, *in situ* moisture content of mesas across the LANL complex is relatively constant, even in areas that receive higher annual precipitation. This supports the assumption that recharge rates are probably similar, also.

The assumption that the recharge rate used in the MDA G CA applies to MDA T may not be considered appropriate at MDA T, based on the fact that liquid waste was disposed of at MDA T. As stated in Section 3.5, some 70,000 m^3 (18,000,000 gal) of liquid waste was disposed of at MDA T over a period of 22 years. At MDA G, an infiltration experiment was performed in the field to estimate the rate of liquid migration *in situ*. Over a period of 22 months, about 42 m^3 of water was pumped into a pit dug 1 m (3.3 ft) into the tuff;[22] this is about half the annual discharge into the sorption beds at MDA T. When moisture content was measured about 10 months after the infiltration has ceased, it was found that the moisture content had reached a steady state of about four percent at a depth of about 7 m (24 ft), which is typical of undisturbed regions. This information can be used to support the fact that, despite its higher initial moisture content, recharge beneath MDA T may be expected to revert to background conditions at a depth that it shallow relative to the thickness of the Bandelier Tuff.

Given the fact that MDA G has the shortest groundwater travel distance and perhaps the largest inventory of nonsorbing radionuclides, it is highly unlikely that releases from other sources will reach the main aquifer and combine with modeled releases from MDA G within 1,000 years. It is virtually impossible that such interacting releases would increase the doses projected in the MDA G CA by six or seven orders of magnitude, which would be required to exceed the performance measure. Modeled releases from MDA G will reach an offsite receptor (e.g., White Rock) sooner, and in a less dilute concentration, than releases from other sites, given the groundwater gradient. In addition, given available information, the inventory of mobile radionuclides is much larger at MDA G than at the formerly-used MDAs. In addition, significant dilution of releases from MDA C would occur within the regional aquifer before interacting with releases from MDA G, since MDA G is downgradient from these other sources.

4.4 Potential All-Pathways Sources

The MDA G CA identified several radionuclides as potentially important in terms of the all-pathways analysis for a receptor in Pajarito Canyon. The most important of these were ^{239}Pu, ^{108m}Ag, and ^{241}Am. The data in Table 2 suggest that MDAs C, T, and AB may have significant inventories of these species. It is not possible that sediment will be transported from the surface of MDA T or MDA AB into Pajarito Canyon. However, it is possible that surface contamination transported into Pajarito Canyon from MDA C could move in the perennial alluvial aquifer downstream toward MDA G. However, the inventory of ^{239}Pu, ^{108m}Ag, and ^{241}Am at MDA C is much smaller than that at MDA G.

5. Conclusions

This analysis indicates that releases from other large sources of radioactivity in the ground at LANL will not contribute significantly to releases projected in the MDA G CA, which projected releases from past, present, and future disposal activities. The most important pathway in the MDA G CA was identified as air, at a receptor location in Cañada del Buey. This receptor location is site-specific for MDA G, reflecting the channeling of winds into canyons. There is very little potential for groundlevel airborne releases at other sites to disperse into Cañada del Buey. Rather, airborne releases from other mesa-top facilities are expected to be channeled into canyons north and south of the facility in question.

The all-pathways scenario considered in the MDA G CA produced doses several orders of magnitude less than the 30/100 mrem/yr performance measures. The dominant pathway in the MDA G all-pathways analysis was sediment transport. Here, too, the receptor location is unique to MDA G, in Pajarito Canyon just south of the facility. There is no real potential for radionuclides to be transported in surface sediment from other sources except MDA C, which also borders Pajarito Canyon. However, the apparent inventory at MDA C is much smaller than the inventory at MDA G. Furthermore, it is not likely that contamination potentially transported into Pajarito Canyon from MDA C would be carried 6 km (4 mi) by downstream by the perennial waters in Pajarito Canyon. Finally, the long groundwater travel time through the vadose zone beneath MDA G and other locations effectively precludes the possibility that the regional aquifer will be contaminated by potential groundwater releases from any or many sources of radioactivity in the ground at LANL.

6. REFERENCES

[1] U.S. DOE 1996, "Guidance for a Composite Analysis of the Impact of Interacting Source Terms on the Radiological Protection of the Public from Department of Energy Low-Level Waste Disposal Facilities," April 1996, Washington, D.C.

[2] U.S. DOE 1988, *Radioactive Waste Management*, U.S. DOE Order 5820.2A, September 26, 1988, Washington, D.C.

[3] Title 40 CFR Subpart S, 1986, U.S. Environmental Protection Agency

[4] Hollis, D. et al. 1997, "Performance Assessment and Composite Analysis for the LANL MDA G," Los Alamos National Laboratory Report LA-UR-97-85, Los Alamos, NM

[5] Shuman, R. 1997, "Radiological Dose Assessment for the TA-54, Area G Performance Assessment and Composite Analysis," Rogers and Associates Engineering Corp. Report to LANL, RAE-9148/82-2, Salt Lake City, UT

[6] Shuman, R. 1996, "Radioactive Waste Inventory for the TA-54, Area G Performance Assessment and Composite Analysis," Rogers and Associates Engineering Corporation Report to LANL, RAE-9148/82-1, Salt Lake City, UT

[7] Vold, E.L. 1997, "A Model for the Biotic Translocation of Buried Low-Level Radioactive Waste to the Ground Surface in the Presence of Surface Erosion," Los Alamos National Laboratory Report LA-UR-97-84, Los Alamos, NM

[8] Vold, E.L. 1996, "Atmospheric Transport in Complex Terrain at Los Alamos, Area G," Los Alamos National Laboratory Report LA-UR-96-4870, Los Alamos, NM

[9] Birdsell, K. et al 1997, "Simulations of Groundwater Flow and Radionuclide Transport in the Vadose and Unsaturated Zones Beneath Area G, Los Alamos National Laboratory," Los Alamos National Laboratory Report LA-UR-97-157, Los Alamos, NM

[10] Krier, D. et al., 1997, "Geologic, Geohydrologic, and Geochemical Data Summary of Material Disposal Area G, Technical Area 54, Los Alamos National Laboratory," Los Alamos National Laboratory Report LA-UR-95-2696, February 1997 Revision

[11] Rogers, D. B. et al., 1997, "Conceptual Model for Subsurface Transport at MDA G," Los Alamos National Laboratory Report LA-UR-97-179, Los Alamos, NM

[12] Springer, E. 1996, "Surface Water and Erosion Calculations for the MDA G PA," Los Alamos National Laboratory Report LA-UR-96-4894, 1996

[13] Vold, E. 1996, "Isotopic Compositions of Inventory Designations 'Mixed Fission Products' and 'Mixed Activation Product'," Los Alamos National Laboratory Report LA-UR-96-4872

[14] Rogers, Margaret Anne, "History and Environmental Setting of the LASL Near-Surface Land Disposal Facilities for Radioactive Wastes (Areas A, B, C, D, E, F, G, and T), A Source Document," LA-6848-MS, June 1977

[15] Los Alamos National Laboratory ER Project 1995, "Installation Work Plan for Environmental Restoration," Los Alamos National Laboratory Report LA-UR-95-4048, Los Alamos, NM

[16] Los Alamos Scientific Laboratory internal memorandum from Dean Meyer to Jack Cully, Subject: Disposal of Contaminated Materials at Los Alamos, June 14, 1949

[17] Los Alamos Scientific Laboratory internal memorandum from John Bolton to Carroll L. Tyler, USAEC, Subject: Location of Classified and Contaminated Dumps in the Los Alamos Area, January 30, 1952

[18] Los Alamos Scientific Laboratory internal memorandum from W.B. Gibson to W.J. Maraman, Subject: General's Tanks- Memo from Dean D. Meyer, December 3, 1971

[19] Los Alamos Scientific Laboratory internal memorandum from Dean Meyer to Salvatore Russo, Subject: Location of Contaminated Waste Burial Pits, January 31, 1952

[20] U.S. EPA 1993 "Guidance for Planning in Support of Environmental Decision Making Using the Data Quality Objectives Process"

[21] Springer, E. 1997, Personal communication between Everett Springer, LANL EES-15, and Diana Hollis, LANL EM-SWO, March 1997

[22] Abrahams, J.G. Jr. 1963, "Physical Properties of and Movement of Water in the Bandelier Tuff, Los Alamos and Santa Fe Counties, New Mexico," U.S. Geological Survey unpublished report

February 1997
Revised Edition

LAUR-95-2696

GEOLOGIC, GEOHYDROLOGIC, AND GEOCHEMICAL DATA SUMMARY OF MATERIAL DISPOSAL AREA G, TECHNICAL AREA 54 LOS ALAMOS NATIONAL LABORATORY

DONATHON KRIER, PATRICK LONGMIRE,
ROBERT H. GILKESON, AND H. J. TURIN

Contents

1.0 INTRODUCTION ____ 1

2.0 GEOLOGY OF THE MDA G AREA ____ 2

2.1 Introduction ____ 2

2.2 Stratigraphy and Stratigraphic Nomenclature ____ 2

2.3 Description of Stratigraphic Units at Mesita del Buey ____ 4
2.3.1 Bandelier Tuff ____ 4
2.3.1.1 Tshirege Member Unit 2b ____ 4
2.3.1.2 Tshirege Member Unit 2a ____ 7
2.3.1.3 Tshirege Member Unit 1b ____ 9
2.3.1.4 Tshirege Member Unit 1a ____ 9
2.3.1.5 Tsankawi Pumice Bed and Cerro Toledo Interval ____ 9
2.3.1.6 Otowi Member ____ 10
2.3.1.7 Guaje Pumice Bed ____ 10
2.3.2 Pre-Bandelier Tuff Units ____ 10
2.3.3 Alluvium and Canyon Bottoms ____ 11
2.3.4 Structure Sections Through the MDA G Area ____ 12

3.0 HYDROGEOLOGY OF THE MDA G AREA: FACTORS PERTAINING TO SUBSURFACE CONTAMINANT TRANSPORT ____ 12

3.1 Introduction ____ 12

3.2 Material Properties ____ 14
3.2.1 Density and Porosity ____ 16
3.2.2 Characteristic Curves ____ 16
3.2.2.1 Tuff ____ 28
3.2.2.2 Alluvium ____ 28
3.2.2.3 Pre-Bandelier Units ____ 28
3.2.3 Saturated Conductivity and Unsaturated Conductivity Curves ____ 28
Table 3 ____ 29
3.2.3.1 Tuff ____ 31
3.2.3.1.1 Intact Tuff ____ 31
3.2.3.1.2 Crushed Tuff ____ 32
3.2.3.2 Alluvium ____ 33
3.2.3.3 Pre-Bandelier Tuff Units ____ 33
3.2.4 Hysteresis ____ 34
3.2.5 Geohydrologic Properties of Rock Units beneath MDA G ____ 34

3.3 Hydrologic Conditions Below MDA G ____ 34
3.3.1 In Situ Moisture Content ____ 34
3.3.2 Perched Aquifers ____ 35
3.3.3 In Situ Matric Tension ____ 35

3.4 Areas for Further Investigation ____ 35

4.0 GEOCHEMICAL BASELINE INFORMATION AND DATA ____ 36

4.1 Introduction 36

4.2 Source-Term Inventory and Geochemistry 37

4.3. Geochemical Transport Parameters 40
4.3.1 Element-Radionuclide Adsorption Behavior 42
4.3.2 Element-Radionuclide Rock/Water Interactions 50
4.3.3 Element-Radionuclide Solubility Limits 51

4.4. Uncertainties and Further Investigations 53

ACKNOWLEDGMENTS 55

REFERENCES 57

APPENDIX A A-1

APPENDIX B B-1

APPENDIX C C-1

LIST OF FIGURES

1	Stratigraphic correlation chart for Bandelier Tuff, Pajarito Plateau	3
2	Location map for MDA G and nearby boreholes	5
3	Frequency distributions of fracture spacings (above) and fracture apertures (below) in Pit 39, Unit 2b	6
4	Map of elevations of basal surge deposit outcrop, Unit 2b, MDA G area	8
5	Location map for geologic structure sections, MDA G	13
6	Structure section A-C along a northwest-southeast transect, MDA G	14
7	Structure sections D-E and F-G along north-south transects, MDA G	15
8	Volumetric moisture vs. depth for 12 boreholes	20
9	Geochemical conceptual model for TA-54	39
B-1	Boreholes with moisture content profiles located in MDA L and in the proposed expansion area for Area G	B-2
B-2	Location map of boreholes and 54-1110, 54-1111, and G-5	B-3
B-3	Gravimetric core moisture content for borehole 54-1001 (angled 22°)	B-10
B-4	Gravimetric core moisture content for borehole 54-1002 (angled 22°)	B-10
B-5	Gravimetric core moisture content for borehole 54-1003 (vertical)	B-11
B-6	Gravimetric core moisture content for borehole 54-1004 (vertical)	B-11
B-7	Gravimetric core moisture content for borehole 54-1005 (angled 22°)	B-12
B-8	Gravimetric core moisture content for borehole 54-1006 (angled 27°)	B-12
B-9	Gravimetric core moisture content for borehole 54-1007 (vertical)	B-13
B-10	Gravimetric core moisture content for borehole 54-1008 (vertical)	B-13
B-11	Gravimetric core moisture content for borehole 54-1009 (vertical)	B-14
B-12	Gravimetric core moisture content for borehole 54-1010 (angled 45° below Pit A)	B-14
B-13	Gravimetric core moisture content for borehole 54-1011 (angled 35° below Pit A)	B-15
B-14	Gravimetric core moisture content for borehole 54-1012 (angled 35° below Pit B)	B-15
B-15	Gravimetric core moisture content for borehole 54-1013 (angled 35° below Pit C)	B-16
B-16	Gravimetric core moisture content for borehole 54-1014 (angled 35° below Pit D)	B-16
B-17	Gravimetric core moisture content for borehole 54-1110 (vertical)	B-17

LIST OF FIGURES

B-18	Gravimetric core moisture content for borehole 54-1111 (vertical)	B-17
B-19	Gravimetric core moisture content for borehole G-5 at MDA G (vertical)	B-18
B-20	Locations of drill holes in MDAs G and L, TA-54	B-26
B-21	TA-54 Material Disposal Area G neutron probe hole (54G-NPH) locations	B-28
B-22	Neutron moisture profile for background hole 54G-NPH-2	B-29
B-23	Neutron moisture profile for hole 54G-NPH-1, MDA G, during July–October 1994	B-29
C-1	Anemometry and permeability results, borehole 54-1001	C-15
C-2	Anemometry and permeability results, borehole 54-1002	C-15
C-3	Anemometry and permeability results, borehole 54-1003	C-16
C-4	Anemometry and permeability results, borehole 54-1004	C-16
C-5	Anemometry and permeability results, borehole 54-1005	C-17
C-6	Anemometry and permeability results, borehole 54-1006	C-17

LIST OF TABLES

1	Hydraulic properties data for MDA G stratigraphy from selected boreholes	17
2	Pressure head vs. moisture data from listed sources	22
3	Summary of geohydrologic properties beneath MDA G, Mesita del Buey	29
4	Saturated conductivity values for pre-Bandelier Tuff units	33
5	Summary of radionuclide half-lives and total activity in Pit 37 at MDA G, TA-54, November 1994	38
6	Analytical results of Water Canyon gallery groundwater, Los Alamos, New Mexico, and well J-13 groundwater, Yucca Mountain, Nevada	42
7	Average sorption ratio, K_D or R_D (ml/g) for volcanic rock, Yucca Mountain tuffs, oxidizing conditions, pH 7, 25°C	44
8	Sorption and desorption ratios, K_D or R_D (ml/g) for volcanic rock, Yucca Mountain tuffs	46
9	Average sorption ratio, K_D or R_D (ml/g) for cement [Ca(OH)2], oxidizing conditions, pH 12.5, 25°C	47
10	Ranges of sorption ratios per surface area of fractured rock, K_A (cm) for volcanic rock, Yucca Mountain tuffs and Bandelier Tuff	49
11	Ranges of retardation factors for fractured volcanic rock, K_A (cm) for volcanic rock, Yucca Mountain and Bandelier Tuff	50
12	Results of speciation investigations (measured and calculated) for selected elements at pH 7 with PCO_2 equal to $10^{-3.5}$ atm under oxidizing conditions at 25°C	52
13	Preliminary measured and calculated solubilities for selected elements in volcanic tuff at pH 7, 25°C	53
14	Preliminary measured and calculated solubilities for selected elements at pH 12, 25°C	54
B-1	Gravimetric moisture content for boreholes 54-1001 to 54-1009	B-4
B-2	Gravimetric moisture content for boreholes 54-1010 through 54-1014	B-8
B-3	Gravimetric core moisture content for boreholes 54-1110, 54-1111, and G-5	B-9
B-4	In situ gravimetric moisture content in boreholes located in natural terrain settings	B-20
B-5	Dry bulk density and calculated volumetric moisture content in core from Mesita del Buey	B-24
B-6	In situ volumetric moisture content for core from borehole LGM-85-06	B-25

LIST OF TABLES

B-7	Summary of neutron probe access holes, MDA G	B-27
C-1	Air permeability values determined from air vacuum tests and air injection tests	C-2
C-2	In situ soil-gas permeability data	C-4
C-3	In situ soil-gas permeability data	C-6
C-4	In situ soil-gas permeability data	C-8
C-5	In situ soil-gas permeability data	C-9
C-6	In situ soil-gas permeability data	C-11
C-7	In situ soil-gas permeability data	C-13
C-8	Effective air permeability determined from straddle packer tests (air extraction)	C-18
C-9	Intrinsic air permeability values on core samples	C-20

GEOLOGIC, GEOHYDROLOGIC, AND GEOCHEMICAL DATA SUMMARY OF MATERIAL DISPOSAL AREA G, TA-54, LOS ALAMOS NATIONAL LABORATORY

by

Donathan Krier, Patrick Longmire,
Robert Gilkeson, and H. J. Turin

1.0 INTRODUCTION

This report provides geologic, geohydrologic, and geochemical descriptions of rock units surrounding Material Disposal Area (MDA) G at Technical Area (TA) 54 on Mesita del Buey at Los Alamos National Laboratory (LANL), New Mexico. This information is used in the LANL performance assessment of MDA G. The assessment, which is required by Department of Energy Order 5820.2A, is an evaluation of the long-term performance of the low-level radioactive waste disposal facility and will provide dose estimates as a function of time for radionuclides migrating from the facility to various depths and available to different exposure pathways, including to the regional aquifer. We reviewed the literature, laboratory, and field data of physical and geochemical properties for lithologic units that compose the stratigraphic section beneath MDA G. The physical properties data for the rock units hosting MDA G vary in quality and in applicability to the numerical flow and transport modeling effort, which will model MDA G as specifically as possible. This report attempts to compile the most reliable and consistent data for use in the performance assessment modeling and analysis.

This report is composed of four sections and three appendices. Section 2.0 presents summary geologic information of the stratigraphic units that underlie Mesita del Buey and host, at great depth, the regional aquifer for the Pajarito Plateau. New observations from recent drilling activities are included. Section 3.0 is a compilation and discussion of the hydraulic properties of these rock units. The hydrologic information focuses on stratigraphic unit hydraulic properties measured in drill core from Mesita del Buey and adjacent canyons and follows the approach of Rogers (1994) and Rogers and Gallaher (1994a, 1994b, and 1995). The Rogers and Gallaher technical memorandums are valuable source documents for the present work and a resource for calculations of matric potential [$\theta(\Psi)$] and hydraulic conductivity [$\theta(K)$] as functions of volumetric moisture content and other physical properties of the rock matrix. The data presented draw from the measurements chosen by Rogers and Gallaher based on data reliability, but differences exist because additional data were included in this report. Section 4.0 is a review of relevant geochemical data required for solute-transport calculations and for input to the numerical model FEHM (finite element heat and mass transfer) (Zyvoloski et al. 1988) used for the performance assessment effort in modeling subsurface flow and contaminant transport. Appendix A is a reference source listing of publications cited in Sections 1, 2, and 3 and of related papers for which no journal references or LANL reports exist; reproductions of each publication are provided to the principal investigator for the MDA G performance assessment. Data from these publications were used as input to the MDA G

performance assessment modeling. Appendix B describes in situ moisture in drill cores from beneath MDA G and adjacent areas. Appendix C presents subsurface air-permeability measurements at various locations on Mesita del Buey.

2.0 GEOLOGY OF THE MDA G AREA

2.1 Introduction

Mesita del Buey is composed of layers of volcanic materials that vary in thickness from a few feet to many tens of feet. Deeper stratigraphic units include rocks of sedimentary origin. Section 2.3 describes each layer and includes discussions of transition zones between layers. An important feature is the occurrence of numerous fractures in the uppermost volcanic layers of the mesa. Descriptions of the adjacent canyons are included; they are useful for compiling a complete hydrogeologic picture of MDA G.

Geologic descriptions of the MDA G area are drawn from numerous sources. Rosenberg and Turin (1993) provide a recent summary of MDA G geologic, hydrologic, and seismologic observations. Numerous characterization studies have been undertaken over the years, and most are referenced in Rosenberg and Turin (1993) and in this report. Some of the more important studies on specific topics are by Baltz et al. (1963), Smith and Bailey (1966), Purtymun and Kennedy (1971), Kearl et al. (1986a, b), Heiken et al. (1990), and Rogers and Gallaher (1995). More recent or less available sources have been included in Appendix A.

2.2 Stratigraphy and Stratigraphic Nomenclature

Mesita del Buey is composed of a complex series of nonwelded to moderately welded rhyolitic ash-flow and ash-fall tuffs called the Bandelier Tuff (Smith and Bailey 1966, Smith et al. 1970, Heiken et al. 1990). The tuff was deposited during violent eruptions of volcanic ash from the Valles caldera, located about 18 km (11 mi.) west of MDA G. The Bandelier Tuff has two members: the Tshirege Member (upper) and the Otowi Member (lower), and both are present beneath Mesita del Buey.

Different stratigraphic systems for the Tshirege Member have been developed over the years because of local variations in lithologies. Broxton and Reneau (1995) present a correlation chart for the systems developed since 1963 for Pajarito Plateau and propose a general system that can be used across the plateau (Figure 1). That system can be applied at Mesita del Buey and currently is in use for Environmental Restoration (ER) Project drilling at TA-54. For simplicity and ease in tracking historical properties data, however, we have chosen to utilize Baltz et al. (1963) (Figure 1) because of its widespread use in many physical properties investigations related to MDA G and to other waste disposal and hydrologic issues at the Laboratory.

From the surface downward, stratigraphic units beneath TA-54 consist of the Tshirege Member of the Bandelier Tuff (Units 2b, 2a, 1b, and 1a, and the basal Tsankawi pumice bed) and the Otowi Member of the Bandelier Tuff with its basal Guaje pumice bed. The members are separated by an ash-fall/fluviatile sedimentary interval (Cerro Toledo interval). Underlying the tuff is a thin deposit of poorly sorted coarse sandstones alternating with ashy layers, assigned to the Puye Formation; a thick sequence of basalt

flows and breccias of the Cerros del Rio basalts; and conglomerates and sandstones of the Puye Formation, which host the regional aquifer. From the region surrounding MDA G, Units 2b through 1b crop out on the tops and sides of Mesita del Buey, and all rocks that predate Unit 1b are observed only in boreholes penetrating below the base of the mesa. At Mesita del Buey, the potentiometric surface of the regional aquifer is at an elevation of about 1768 m (5800 ft) (Purtymun 1984). The mesa top elevation at MDA G is approximately 2048 m (6720 ft).

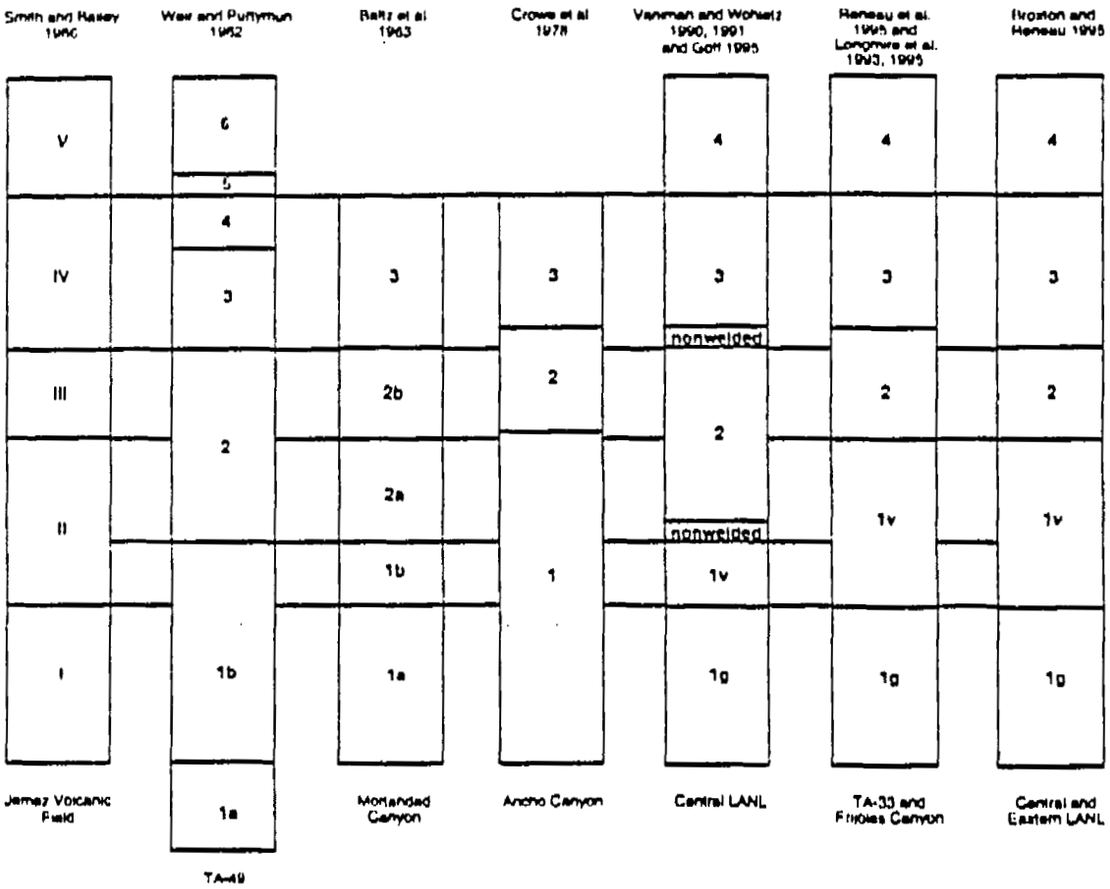

Figure 1. Stratigraphic correlation chart for Bandelier Tuff, Pajarito Plateau (Broxton and Reneau 1995).

The scope of available data specific to MDA G is limited. Hydraulic data do not exist for units deeper than the Otowi Member. Data on fractures are limited to Units 1b, 2a and 2b, which crop out on the top and sides of the mesa, and these data are incomplete because of limited exposure. A few boreholes in the area adjacent to MDA L extend to depths of about 100 m (328 ft), but within MDA G no boreholes extend deeper than about 45 m (148 ft).

2.3 Description of Stratigraphic Units at Mesita del Buey

The following sections contain descriptions of the stratigraphic units at Mesita del Buey. These units have wide distribution across the Pajarito Plateau except for the deeper basaltic lava flows section. The basaltic lava flows are limited to the eastern and southeastern plateau. Some descriptions are drawn from recent lithologic logging in boreholes near MDA L by F. Caporuscio (1994) and J. Marin (LANL, in progress). Broxton et al. (in progress) give detailed petrographic and geochemical descriptions of the units beneath the mesa. Figure 2 gives location information for MDA G and nearby boreholes.

2.3.1 Bandelier Tuff

2.3.1.1 Tshirege Member Unit 2b

Unit 2b is a brittle resistant caprock that forms the top of Mesita del Buey and adjacent mesas. It is the distal part of an extensive ash-flow sheet that is moderately welded and about 12 m (39 ft) thick at MDA G. This uppermost stratigraphic unit hosts the disposal pits and shafts that are the focus of the performance assessment.

Unit 2b is composed of crystal-rich devitrified pumice fragments in a matrix of ash, shards, and abundant phenocrysts. The rock is extensively fractured because of the contraction of the welded ash matrix as it cooled after deposition. The vertical cooling fractures have been described in several studies, but most thoroughly in studies of Disposal Pit 39 (Reneau and Vaniman 1994) and of the north wall of Pajarito Canyon (Reneau et al. 1995).

Maps of Pit 39 show that the mean fracture spacing in Unit 2b ranges between 0.6 and 0.8 m (1.9 and 2.6 ft), and apertures range between <1 and 13 mm (<0.03 and 0.51 in.) with a median of 3 mm (0.1 in.) (Figure 3). Previous fracture mapping in disposal pits (Purtymun and Kennedy 1971, Purtymun et al. 1978) indicated larger spacing (about 2.2 m, 7.1 ft); this may be attributable to incomplete mapping of minor fractures on the pit walls. Fracture orientations vary in Pit 39, but greatest frequencies are in the N 50° E and east-west directions. Fracture dip in Unit 2b averages 90° (vertical).

In Pit 39, fractures are typically filled with smectite clays to a depth of 3 to 4 m (9.8 to 13.1 ft) and with opal and calcite below this depth. Opal and calcite deposition is associated with presence of tree root molds. The association suggests that biological activity or its cessation results in mineral precipitation, which works to partially occlude transport pathways. In a root study, Martens and Barnes (1993) found the distal ends of roots of living piñon trees in thin joints at depths of 14 m (46 ft) in Pit 39, a fact often cited as evidence of moisture availability to this depth in the tuff. Living roots were observed to the bottom of the pit at a depth of 14.2 m (45 ft) (Reneau and Vaniman); their maximum depth is unknown. Observations in neighboring Pit 38 reveal one set of live roots at a depth of about 20 m (66 ft). The 3- to 4-mm-diameter (~0.1 in.) roots have grown downward within a prominent, near vertical fracture that is filled with clay and extends from the surface to below the bottom of the pit.

Deposition by wind and/or water of clays and carbonates in fractures is demonstrated by Davenport (1993) in a study at MDA J, about 2 km (1.2 mi.) northwest of MDA G. In

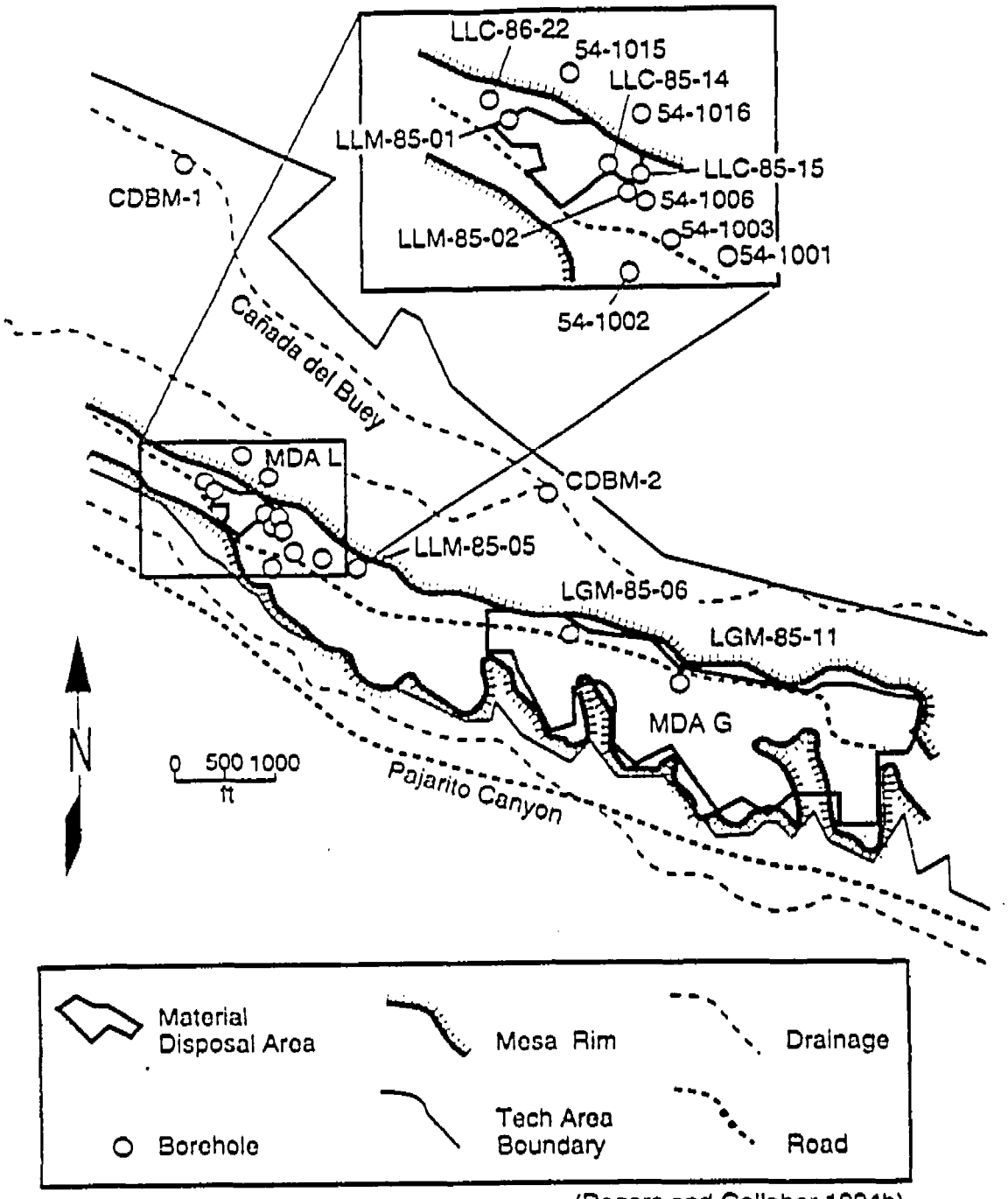

(Rogers and Gallaher 1994b)

Figure 2. Location map for MDA G and nearby boreholes.

detail, calcium carbonate deposition is usually interior to clay deposition where they coexist within a fracture. In Davenport's model, calcium carbonate precipitates from percolating water trapped in smectite shrinkage cracks as the clays rehydrate and swell. The swelling lowers fracture permeability within the upper several meters of fractured tuff. He concludes that the presence of calcite within clay fillings suggests that "clay fill alone does not completely seal the fractures or preclude water movement through them."

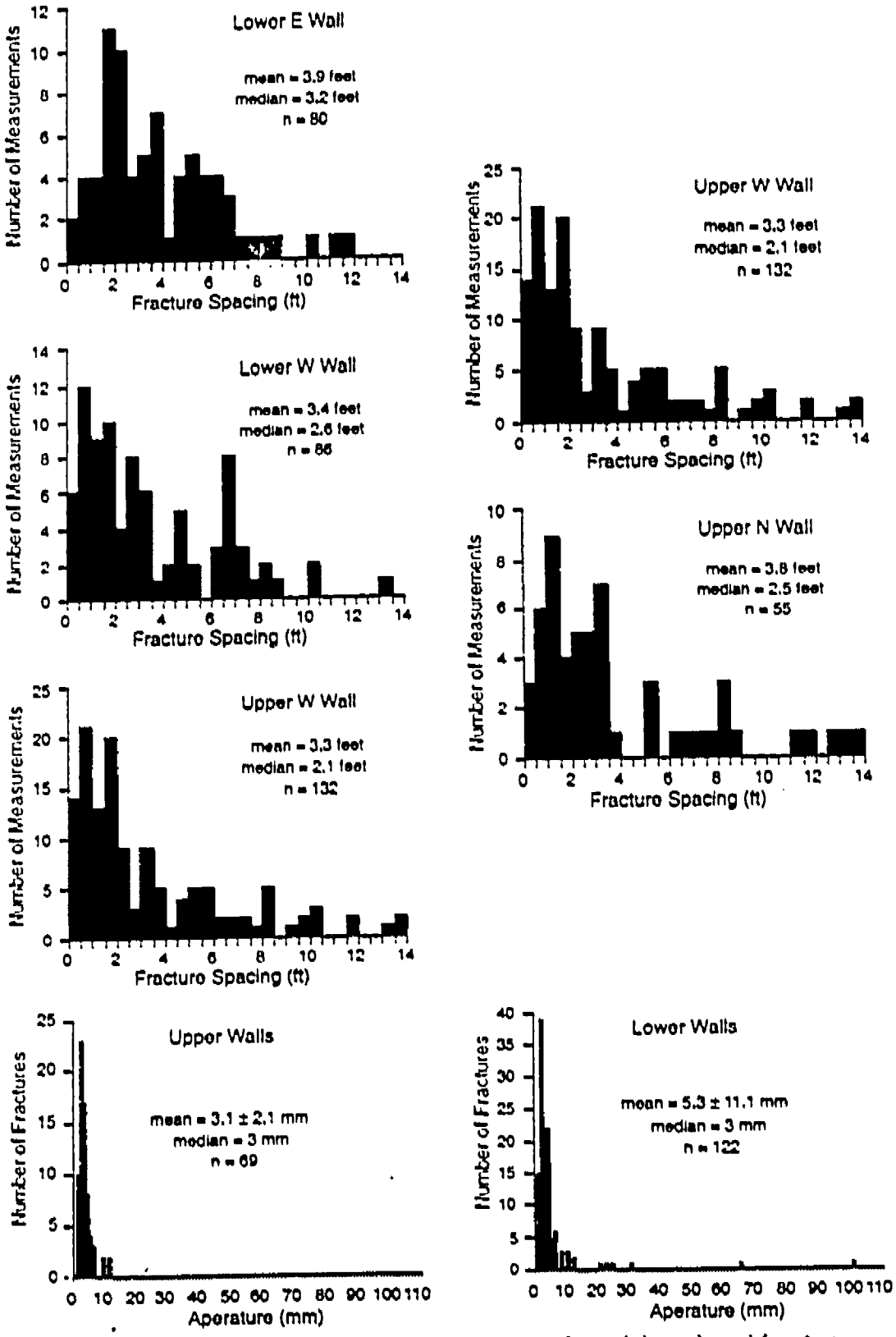

Figure 3. Frequency distributions of fracture spacings (above) and fracture aperatures (below) in Pit 39, Unit 2b (Reneau and Vaniman 1994).

Kearl et al. (1986a, b) report an increase in the number of fractures within more welded portions of Units 2b and in underlying Units 2a and 1b. A much smaller population of fractures is observed in the nonwelded to slightly welded Unit 1a. They describe one case of a dense lining (*case hardening*) along a cored fracture in Unit 2b at a depth of 10.0 to 13.4 m (35 to 44 ft), which they suggest may indicate preferential flow of water or water vapor in the fracture at that depth. Furthermore, their gravimetric moisture content data show increases in moisture associated with two specific fractures at depths of 11.6 m and 13.8 m (38 and 55 ft).

Recent ER Project drilling at the TA-73 landfill (airport site) has revealed elevated moisture associated with fractures at depths to 41 m (135 ft). Detailed fracture mapping along outcrops at TA-73 has demonstrated intervals of increased fracture density for tuff in cliff exposures. The development of these intervals is attributed to the strain response of brittle, moderately welded tuff to tectonic movement in the deeper subsurface rather than to cooling contraction immediately after deposition (Matt Walters, personal communication, 1995). Differential block motion along cooling fractures or planes of weakness is also evident. Along Mesita del Buey, this type of detailed fracture mapping has not been done.

A thin (<10 cm, <4 in.) interval of crystal-rich, fine sand-sized material is commonly found at the base of Unit 2b. This interval of lenticular and sometimes cross-bedded layers is attributed to deposition from the basal surge associated with violent eruptions. It rises in stratigraphic position 1 to 3 m (3 to 10 ft) toward the west (Broxton et al., in progress). In eastern TA-54, these layers (surge beds) occupy the highest levels of Unit 2a and progressively climb in stratigraphic position westward beyond MDA G where they occupy the basal portion of Unit 2b. The elevations of the surge beds have been surveyed on the edges of Mesita del Buey and are shown in Figure 4 (D. Broxton, personal communication, June 1995). The surge beds are displaced by small faults; displacements range between 5 cm (2 in.) and 60 cm (23.6 in.), with relative motions down to the west. Twenty-six such faults were measured along the north wall of Pajarito Canyon, but the number may be greater because of poor exposure in some areas. These small faults appear along cooling joints in the upper part of Unit 2b, but they have no aperture at the elevation of the surge beds. It is not known whether the faults die out in underlying poorly welded tuffs, as the majority of cooling joints do. There is evidence from borehole packer tests (Appendix C) that the thin surge beds allow higher air flow within the mesa interior because of impinging winds and fluctuations in barometric pressure.

2.3.1.2 Tshirege Member Unit 2a

Tshirege Member Unit 2a underlies Unit 2b and consists of devitrified ash-fall and ash-flow tuff (Purtymun and Kennedy 1971, Kearl et al. 1986a, b). The unit is about 14 m (46 ft) thick near MDA G, is slightly welded at its base, and becomes moderately welded up section. In outcrop, it has a massive and unjointed appearance, but its upper parts host downward extensions of more prominent cooling fractures that originate in Unit 2b. In outcrop and limited angled borehole data, the fractures die out downward as the tuff becomes less consolidated. Because of the very weak nature of the unit, attempts at retrieving core from Unit 2a near MDA L during ER Project investigations (Fall 1993, Summer 1994) invariably resulted in unconsolidated material.

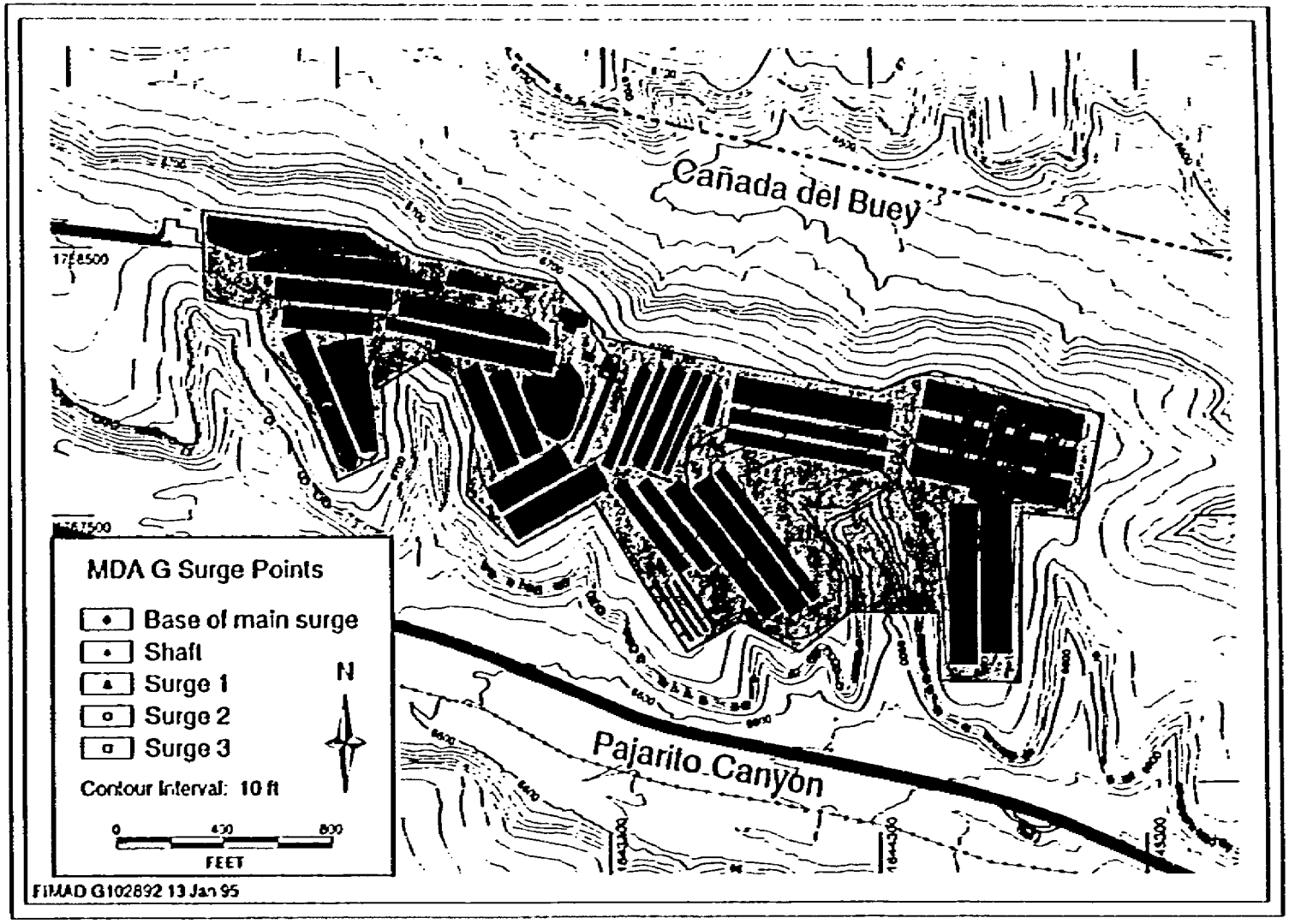

Figure 4. Map of elevations of basal surge deposit outcrop, Unit 2b, MDA G area.

2.3.1.3 Tshirege Member Unit 1b

Kearl et al. (1986a, b) describe Unit 1b as a slightly welded, devitrified ash-flow tuff at its base and top that becomes more welded in its center. However, the unit never exhibits the jointing characteristics of moderate welding shown by Unit 2b, which caps the mesa. Unit 1b is 7 to 8 m (23 to 26 ft) thick in eastern MDA G and 15 m (49 ft) thick near MDA L. It has a greater content of unflattened (nonwelded) pumice lapilli (size of 4 to 32 mm, 0.1 to 1.3 in.) than the overlying tuff (Unit 2a), which may contribute to a decreased density (Kearl et al. 1986a, b). The pumices are devitrified and show spherulitic cristobalite structures but become slightly more vitric with depth.

Unit 1b is more resistant to erosion that overlying Unit 2a and can form a small ledge in weathered outcrops. In the outcrop, the tuff hosts closely spaced (7.6 to 12.7 cm, 3 to 5 in.) vertical fractures that give the tuff an appearance of vertical colonnades.

Unit 1b is exposed at the base of the south-facing slope of Mesita del Buey. In drill core, its basal contact is marked by a rapid change [vertical distance of ~0.2 m (~0.7 ft)] from devitrified to vitric glass in underlying Unit 1a. Vitric pumices below this interval stand out in relief on weathered surfaces; devitrified pumices above this interval are eroded out leaving holes that wind, water, and ice continue to enlarge. This transition results in a preferentially eroded recess defined by alignment of small caves, some as tall as 1.5 m (5 ft); this recess is named the vapor-phase notch by Baltz et al. (1963). Characteristics of this interval at TA-21 are summarized by Broxton et al. (1995).

2.3.1.4 Tshirege Member Unit 1a

Unit 1a is the oldest unit of the Tshirege Member. It is a vitric, pumiceous, nonwelded ash-flow tuff that has a thickness of about 15 m (49 ft) beneath MDA G. Purtymun (1995) observed thicknesses in drill holes ranging between 15 m (49 ft) east of MDA G and 13 m (43 ft) west of MDA G. Further west, drilling beneath MDA L has penetrated 36 m (118 ft) of Unit 1a. Outcrops on south-facing slopes near MDA G suggest 15 m (49 ft) as a minimum thickness, perhaps because of local thickening from north to south through the mesa. There is little information about extent or characteristics of fractures in this unit. Kearl et al. (1986a, b) report encountering only 2 fractures in 11 holes cored into Unit 1a, although the entire thickness of the unit was never penetrated. Typically, nonwelded tuffs do not support fractures because of their weak matrix properties and relatively cool temperature at deposition.

2.3.1.5 Tsankawi Pumice Bed and Cerro Toledo Interval

The Tsankawi pumice bed near MDA G is a thin (<0.3 m, <1.0 ft) layer of gravel-sized, vitric, nonwelded pumice. Its presence is widespread across the Pajarito Plateau at the base of the Tshirege Member. The Cerro Toledo interval stratigraphically underlies the Tsankawi pumice bed and is composed of interbedded and lenticular beds of tuffaceous sandstones, siltstones, ash and pumice falls, and intercalated gravel and cobble deposits derived from mafic to intermediate lavas of the Tshicoma Formation. Some layers show evidence of reworking by running water during or soon after deposition.

The distinct Tsankawi pumice bed and the Cerro Toledo interval separate the upper and lower tuff members of the Bandelier Tuff but were often included as part of the top of the

underlying Otowi Member tuffs during past core logging at TA-54. In recent drilling beneath MDA L, 9 m (29 ft) of Cerro Toledo interval and <0.5 m (1.6 ft) of overlying Tsankawi pumice bed were encountered. Because the Cerro Toledo interval thins eastward across the Pajarito Plateau, we assign a 5-m (16-ft) thickness to this interval beneath MDA G. Physical properties of this interval would probably be dominated by Cerro Toledo sedimentary beds because the Tsankawi pumice bed is very thin. In borehole 54-1015 (Figure 2), Cerro Toledo interval core was damp with moisture and was the shallowest visible moisture encountered in the borehole (elevation 1994.3 m, 6543 ft). No contaminants have been measured with field instruments or in core sample analysis in this interval.

2.3.1.6 Otowi Member

Otowi Member tuffs are about 30 m (98 ft) thick beneath MDA L and thin eastward toward MDA G. No complete thickness has been measured for MDA G. The tuffs are composed of a massive, nonwelded, pumice-rich, mostly vitric ash-flow tuff. Pumices are fully inflated, meaning that the tubular pumice structures are not collapsed by any postdepositional welding. Beneath MDA L, the pumice makes up about 20% of the tuff, ranges in size between 0.5 and 7.0 cm (0.2 and 2.8 in.), and is vitric. The matrix is an unsorted mix of glass shards, phenocrysts, perlite clasts, and minute broken pumice fragments. Lithic fragments make up about 2% of the rock, and rare pumice swarms (with up to 30% pumice) occupy intervals as much as 0.6 m (2 ft) thick. No visible moisture has been observed in cored Otowi Member beneath Mesita del Buey.

2.3.1.7 Guaje Pumice Bed

The Otowi Member overlies 3 m (10 ft) of the Guaje pumice bed at a depth of 117.6 m (386 ft) beneath MDA L, corresponding to an elevation of 1955 m (6414 ft). The unit is composed entirely of pumices ranging between 0.3 and 1.5 cm (0.1 and 0.6 in.) in diameter. The pumice fragments are nonwelded but silicified and brittle beneath MDA L. Pumice tubes are partially filled with silica cement and may have reduced matrix permeability near that locality. The Guaje pumice bed is reported as 3.7 m (12 ft) thick in well T-5, located in Pajarito Canyon south of MDA G. Correlations between boreholes at MDA G suggest a shallow southward component of dip to the Guaje pumice bed.

2.3.2 Pre-Bandelier Tuff Units

In borehole 54-1015 at MDA L, the base of the Guaje pumice bed overlies about 3 m (10 ft) of poorly consolidated, interbedded, coarse sand, silt, and ashy layers that are probably related to the Puye(?) Formation. The thin finer-grained layers in the core were damp, but the basalt immediately below the contact was dry.

Layers of thick mafic lava flows and flow breccias of the Cerros del Rio basalts underlie the thin interval of Puye Formation. Little is known about fractures and internal contacts within the Cerros del Rio basalts beneath MDA G. Exposed basaltic flows in steep canyons on the Pajarito Plateau are highly fractured; discontinuous fractures form a jagged network with unfilled open apertures. Flow breccias are found separating individual flows and occupying the toes of flow fronts. Breccias are more easily eroded in outcrop and do not support fractures extending through the denser lava flows.

9. REFERENCES

[1] U.S. Department of Energy October 1996, "Interim Format and Content Guide and Standard Review Plan for U.S. Department of Energy Low-Level Waste Disposal Facility Performance Assessments," Washington D.C.

[2] U.S. Department of Energy April 1996, "Guidance for a Composite Analysis of the Impact of Interacting Source Terms on the Radiological Protection of the Public from DOE LLW Disposal Facilities," Washington D.C.

[3] U.S. Department of Energy Memorandum July 1996, "Revised Interim Policy on Regulatory Structure for Low-Level Radioactive Waste Management and Disposal," Washington D.C.

[4] Hollis, D.J. et al. 1995, "Performance Assessment for the LANL LLW Disposal Facility at TA-54, Area G," Los Alamos National Laboratory Preliminary Draft, Report-54G-013, Los Alamos, NM

[5] DNFSB September 1994, "Recommendation 94-2, Conformance with Safety Standards at Department of Energy Low-Level Nuclear Waste and Disposal Sites," Washington D.C.

[6] U.S. DOE April 1996, "Implementation Plan: Defense Nuclear Facilities Safety Board Recommendation 94-2," Revision 1, Washington D.C.

[7] U.S. Department of Energy Order 5820.2A September 26, 1988, "Radioactive Waste, Management," Washington D.C.

[8] U.S. Department of Energy, September 1996, "Maintenance of U.S. Department of Energy Low-Level Waste Performance Assessments," Washington D.C.

[9] U.S. Atomic Energy Commission 1970, Directive AEC-IAD-0511-21," Washington, D.C.

[10] U.S. Environmental Protection Agency, "Resource Conservation and Recovery Act," Code of Federal Regulations, Title 40, Part 261, Washington D.C.

[11] U.S. Environmental Protection Agency 1994 "Federal Facilities Compliance Act" Washington D.C.

[12] LANL January 1997, "Waste Acceptance, Characterization, and Certification Program," Los Alamos National Laboratory Interim Laboratory Implementation Requirements ILIR404-00-01.0, Los Alamos, NM

[13] U.S. Environmental Protection Agency, "National Environmental Policy Act," Code of Federal Regulations Title 40

[14] LANL November 1995, "Installation Workplan for Environmental Restoration Program, Revision 5," Los Alamos National Laboratory Report LA-UR-95-4048, Los Alamos, NM

[15] LANL January 1992, "RCRA Facilities Investigation Workplan for Operable Unit 1148," Los Alamos National Laboratory Report, Environmental Restoration Program, Los Alamos, NM

[16] New Mexico Environment Division 1995, Environmental Restoration Document of Understanding among New Mexico Environment Division, US Environmental Protection Agency, US Department of Energy, Los Alamos National Laboratory, and Sandia National Laboratories-New Mexico, Santa Fe, NM

[17] LANL 1995, "TA-54 Area G FMU-64 Operational Configuration Management Plan," Los Alamos National Laboratory Draft Waste Management Plan Plan-TA54-XXXX, Los Alamos, NM

[18] LANL August 1995, "Safety Analysis Report for TA-54, Area G," Los Alamos National Laboratory Report Waste Management Report CST14G-Report-009, Los Alamos, NM

[19] LANL December 1994, "CST Waste Management Facilities Waste Acceptance Criteria and Certification," Los Alamos National Laboratory Waste Management Plan Wastemgt-Plan-002, as revised, Los Alamos, NM

[20] U.S. DOE September 1994, "Institutionalizing the Data Quality Objective Process for EM's Environmental Data Collection Activities," U.S. DOE Memorandum, Washington, D.C.

[21] LANL 1995. "Closure Plan for LANL Material Disposal Area G," Los Alamos National Laboratory Waste Management Document Plan-54G-014, R0, Los Alamos, NM

[22] LANL 1996, ""TA-54 , Area G Environmental Monitoring Program," EM-SWO Plan-54G-011, R.2 Los Alamos National Laboratory, Los Alamos, NM

[23] LANL 1996, "Storm Water Pollution Prevention Plan for Technical Area 54, Material Disposal Area G," Los Alamos National Laboratory Waste Management Plan Plan-54G-004, R.1, Los Alamos, NM

[24] U.S. Environmental Protection Agency, "National Emission Standards for Hazardous Air Pollutants," Code of Federal Regulations, Title 40, Part 10, Washington D.C.

[25] Johnson, LaMar J. 1975, "Guidelines for Construction and Use of Solid Waste Disposal Facility," Los Alamos Scientific Laboratory Office Memorandum, Los Alamos, NM

[26] LANL 1996, "Pit Construction, Use and Closure," Los Alamos National Laboratory Detailed Operating Procedure DOP-54G-013, Los Alamos, NM

[27] U.S. Bureau of Census 1991, "Provisional Data for 1990 for New Mexico Counties," US Bureau of the Census Report

[28] Bowen, B.M.1990, "Los Alamos Climatology," Los Alamos National Laboratory Report LA-11735-MS, Los Alamos, NM

[29] Nyhan, J. et al. 1989, "Field Evaluation of Two Shallow Land Burial Trench Cap Designs for Long-Term Stabilization and Closure of Waste Repositories at Los Alamos, New Mexico,"

[30] Schulman, E. 1951 "Tree-Ring Indices of Rainfall, Temperature, and River Flow," Compendium of Meteorology, Americal Meteorological Society, Boston MA

[31] Abeele, W. V. et al., 1981, "Geohydrology of Bandelier Tuff," Los Alamos National Laboratory Report LA-8962-MS, Los Alamos NM

[32] Slade, D.H. ed., 1968, "Meteorology and Atomic Energy, U.S.. Atomic Energy Commission report TID-24190, NTIS

[33] Baars, Jeff 1997, Personal communication between J. Baars (LANL ESH-17) and D. Hollis (LANL EM-SWO), February 5, 1997

[34] Vold, E. et al. 1995, "Preliminary Results from the Los Alamos TA-54 Oomplex Terrain Atmospheric Transport Study," Los Alamos National Laboratory Report LA-UR-95-2222, Los Alamos, NM

[35] Tierney, G.D. and T.S. Foxx 1987, "Root Lengths of Plants on Los Alamos National Laboratory Lands," Los Alamos National Laboratory Report, LA-10865-MS, Los Alamos, NM

[36] Biggs, James 1995 Personal communications ESH-20, Ecology Group, LANL, Los Alamos, NM.

[37] Spell, T.L. et al. 1990, "40Ar/39Ar Dating of the Bandelier Tuff and San Diego Canyon Ignimbrites, Jemez Mountains, New Mexico: Temporal Constraints on Magmatic Evolution," J. Volcan. and Geothermal Research, V. 43

[38] Broxton, D.E. and S.L. Reneau 1996, "Buried Early Pleistocene Landscapes Beneath the Pajarito Plateau, Northern New Mexico," 1996 New Mexico Geologic Society Field Trip Guidebook

[39] Reneau, S.L. 1995, "Geomorphic Studies at DP Mesa and Vicinity," in *Earth Science Investigations for Environmental Restoration-- Los Alamos National Laboratory Technical Area 21*, Los Alamos National Laboratory Report LA-19934-MS, Los Alamos, NM

[40] Longmire et al. 1996, "Natural Background Geochemistry, Geomorphology, and Pedogenesis of Seleced Soil Profiles and Bandelier Tuff, Los Alamos, New Mexico," Los Alamos National Laboratory Report LA-12913-MS, Los Alamos, NM

[41] Purtymun, W.D., et al. 1978 "Geologic Description of Cores from Holes P-3 MH-5, Technical Area 54," Los Alamos Scientific Laboratory Report LA-7308-MS, Los Alamos, NM

[42] Purtymun, W.D. 1995 "Geologic and Hydrologic Records of Observation Wells, Test Holes, Test Wells, Supply Wells, Springs, and Surface Water Stations in the Los Alamos Area," Los Alamos National Laboratory Report LA-12883-MS,, Los Alamos, NM

[43] Olig, Susan S. 1996, et al., "The earthquake potential of the Pajarito fault system, New Mexico," New Mexico Geological Society Guidebook, 47

[44] Olig, S.S. 1997, Letter-report to D. Hollis, LANL, from S. Olig, Senior Project Seismologist, Woodward-Clyde Federal Services, March 21, 1997, Oakland, CA

[45] Kelson, K.I. et al., 1996, "Late Pleistocene and possibly Holocene displacement along the Rendija Canyon fault, Los Alamos County, New Mexico, New Mexico Geological Society Guidebook 47

[46] Reneau, S. et al., 1995, "Structure of the Tshirege Member of the Bandelier Tuff at Mesita del Buey," Draft LANL report

[47] Woodward-Clyde 1995 "Seismic Hazard Evaluation of the Los Alamos National Laboratory," Woodward-Clyde Engineers Report to LANL, San Francisco, CA

[48] Heiken, G. et al. 1986, "Intracaldera Volcanic Activity, Toledo Caldera and Embayment, Jemez Mountains, New Mexico," J. Geophys. Res. 99

[49] Devaurs, M., and W. D. Purtymun 1985, "Hydrologic characteristics of the alluvial aquifers in Mortandad, Cañada del Buey, and Pajarito Canyons," Los Alamos National Laboratory Report LA-UR-85-4002, Los Alamos, NM

[50] Purtymun et al. 1980, "Geohydrology of White Rock Canyon of the Rio Grande from Otowi to Frijoles Canyon," Los Alamos National Laboratory Report LA-8635-MS, Los Alamos, NM

[51] Abrahams, J.H. 1963, "Physical Properties of and Movement of Water in the Bandelier Tuff, Los Alamos and Santa Fe Counties, New Mexico," U.S. Geological Survey Admin. Report

[52] van Genuchten, M. 1980, "A Closed-Form Equation for Predicting the Hydraulic Conductivity of Unsaturated Soils," Soil Science Society of America Journal 44

[53] Rogers, David B. and Bruce M. Gallaher 1995, "The Unsaturated Hydraulic Characteristics of the Bandelier Tuff," Los Alamos National Laboratory Report LA-12968-MS, Los Alamos, NM

[54] Rogers, D. B., B. M. Gallaher, and E. L. Vold 1996, "Vadose zone infiltration beneath the Pajarito Plateau at Los Alamos National Laboratory," New Mexico Geological Society Guidebook, 47th Field Conference, The Jemez Mountains Region

[55] Rogers, D. B., E. L. Vold, and B. M. Gallaher 1995, "Bandelier Tuff Hydraulic Characteristics from Los Alamos National Laboratory Borehole G-5 at MDA G, TA-54," Los Alamos National Laboratory Report LA-UR-95-3129, Los Alamos, NM

[56] Newman, B. 1996, "Vadose Zone Water Movement at Area G, Los Alamos National Laboratory, TA-54: Interpretations Based on Chloride and Stable Isotope Profiles," Los Alamos National Laboratory Report LA-UR-96-4682, Los Alamos, NM

[57] Allison, G.B, et al. 1994, "Vadose-Zone Techniques for Estimating Groundwater Recharge in Arid and Semiarid Regions," Soil Sci. Soc. of Am. J.V. 58

[58] Newman, B. D., A. R. Campbell, and B. P. Wilcox. 1996. "Investigations of Soil-Water Movement in Semiarid and Subhumid Forests Using Stable Isotope and Halogen Tracers," J. of Hydrology (accepted).

[59] Maulem, Y.1976, "A New Model for Predicting Hydraulic Conductivity of Unsaturated Porous Media," Water Resources Research 12

[60] Vold, E.L. 1996, "Analysis of Liquid Phase Transport in the Unsaturated Zone at a Mesa Top Disposal Facility," Los Alamos National Laboratory Report LA-UR-96-370, Los Alamos, NM

[61] Vold, E. 1996, "An Analysis of Vapor Phase Transport in the Unsaturated Zone with Application to a Mesa Top Disposal Facility, Part I," Los Alamos National Laboratory Report LA-UR-96-973, Los Alamos, NM

[62] Vold, E. and B. Eklund 1996, "Determination of an In-Situ Vapor Diffusion Coefficient at a Mesa Top Waste Disposal Facility," Los Alamos National Laboratory Report LA-UR-96-1848, Los Alamos, NM

[63] Philip, J.R. and D.A. deVries 1957, "Moisture Movement in Porous Materials Under Temperature Gradients," Trans., Amer. Geophys. Union, 38

[64] Science and Engineering Associates 1996, "Open Borehole Anemometry and Air Permeability Measurements, Area G, TA-54," Science and Engineering Associates report, Santa Fe, NM

[65] D.B. Stephens and Associates 1996, "Laboratory Analysis of Soil Hydraulic Properties of G-5 Soil Samples," report no. DBSA/3854/195-1, Albuquerque, NM

[66] Broxton et al. 1995, "Stratigraphy, Petrography, and Mineralogy of Bandelier Tuff and Cerro Toledo Deposits" in Broxton, D.E. and P.G. Eller, eds., "Earth Science Investigations for Environmental Restoration- Los Alamos National Laboratory, Technical Area 21," Los Alamos National Laboratory Report LA-12934-MS, Los Alamos, NM

[67] Longmire, P. et al. 1995, "Batch Sorption Results for Americium, Neptunium, Plutonium, Technetium, and Uranium Transport through the Bandelier Tuff, Los Alamos, New Mexico," Los Alamos National Laboratory Report LA-UR-96-4716, Los Alamos, NM

[68] Longmire, P. et al. 1996 "Batch Sorption Results for Americium, Neptunium, Plutonium, Technetium, and Uranium Transport through the Bandelier Tuff, Los

Alamos, New Mexico," Los Alamos National Laboratory Report LA-UR-96-4716, Los Alamos, NM

[69] LANL 1996, "Environmental Surveillance at Los Alamos during 1994, Los Alamos National Laboratory Report LA-13047-ENV, Los Alamos, NM

[70] Nyhan, J. et al., 1990 "A Water Balance Study of Two Landfill Cover Designs for Semiarid Regions," J. Env. Qual. 19

[71] Wheeler, M.1974, "Moisture and Tritium Concentrations in Fill Material, Area G, TA-54," Los Alamos Scientific Laboratory internal memorandum, HS-WM-112

[72] Black, T.A. et al., "The Prediction of Evaporation, Drainage, and Soil Water Storage for a Bare Soil," Soil Sci. Soc. Am. Proc. 33

[73] Loaiza, D. and Vold, E. 1995, "Moisture Profile Measurements in Subsurface Monitor Holes at the Los Alamos LLRW Disposal Site," Los Alamos National Laboratory Report LA-UR-95-1922, Los Alamos, NM.

[74] Rogers, M. A. 1976, "History and environmental setting of LASL near-surface land disposal facilities for radioactive wastes (Areas A, B, C, D, E, F, G, and T)," Los Alamos National Laboratory Report LA-6848-MS, Los Alamos, NM

[75] McLin, S. G 1994., Horizontal borehole data gathered with SEAMIST, Los Alamos National Laboratory Memo ESH-8/WQ&H-94-571 to Erik Vold, Los Alamos, NM.

[76] Nyhan, J. et al., "A Study of Four Landfill Cover Designs Varying in Slope for Semiarid Regions," LA-UR-095-4396, 1995

[77] Nyhan J. et al. 1986, "Consolidation and Shear Failure Leading to Subsidence and Settlement," Los Alamos National Laboratory Report LA-10576-MS, Los Alamos, NM

[78] Shuman, Rob 1997, "Radiological Dose Assessment for TA-54, Area G Performance Assessment and Composite Analysis," Rogers and Associates Engineering Report to LANL RAE-9629/91B-2

[79] Warren, J.L. 1996, "Report on Review of Proposed Method for Characterizing 1959-1971 MDA G Disposal Inventory," Nuclear Filters Technology Report to LANL, July 1996

[80] Vold, E.L. 1996, "Isotopic Compositions of Inventory Designations "Mixed Fission Product" and Mixed Activation Product," Los Alamos National Laboratory Report LA-UR-96-4872, Los Alamos, NM

[81] Maassen, L. 1996, written communication From L. Maassen (LANL to D. Hollis, Los Alamos National Laboratory, Los Alamos, NM

[82] ERM/Golder 1995, "Estimated Inventory of Waste Materials for Disposal at the LANL Mixed Waste Disposal Facility," Report for Los Alamos National Laboratory, Los Alamos, NM

[83] Hodges, W.W. 1990, written communication from W. Hodges (LANL) to R. Shuman, Rogers and Associates Engineering Corp. July 1996

[84] Vold, E.L. 1996, "Evaluation of Atmospheric Release Sources for Gaseous Phase Contaminants Emanating from the Disposal Facility at Area G," Los Alamos National Laboratory Report LA-UR-97-155, Los Alamos, NM

[85] Kunz, C.O. 1982, "Radioactive Gas Production and Venting at a Low-Level Radioactive Waste Burial Site," Nucl. Chem. Waste Management, Vol. 3

[86] Vold, E.L. et al. 1995, "Preliminary Results from the Los Alamos TA-54 Complex Terrain Atmospheric Transport Study," LA-UR-95-2222, Los Alamos, NM

[87] Vold, E.L. and Rob Shuman (RAE) 1997, "A Model for the Biotic Translocation of Buried Low-Level Radioactive Waste to the Ground Surface in the Presence of Surface Erosion," Los Alamos National Laboratory Report LA-UR-97-84

[88] J.K. Biggs, K.D. Bennett, and P.R. Fresquez 1995, "Radionuclide Contaminant Analysis of Small Mammals at Area G, TA-54, 1994," Los Alamos National Laboratory report LA-13015-MS, Los Alamos, NM

[89] D.H. McKenzie et al. October 1982, "Relevance of Biotic Pathways to the Long-Term Regulation of Nuclear Waste Disposal", Pacific Northwest Laboratory, Topical Report on Reference Western Arid Low-Level Sites, U.S. Nuclear Regulatory Commission Report NUREG/CR-2675, Vol. 2

[90] T.E. Hakonson et al. 1982, "Some Interactive Factors Affecting Trench Cover Integrity of Low-level Waste Sites", *Proc. Low-level Waste Disposal: Site Characterization and Monitoring*, Arlington, VA, June 16-17, 1982, NUREG/CP-0028, CONF-820674, Vol. 2

[91] W.J. Arthur et al. 1987, "Radionuclide export by deer mice at a solid radioactive waste disposal area in southeastern Idaho", *Health Phys.*, Vol. 52

[92] P.R. Fresquez, T.S. Foxx and L. Naranjo, Jr. November 1995, "Strontium Concentrations in Chamisa (Chrysothamnus nauseous) Shrub Plants Growing in a Former Liquid Waste Disposal Area in Bayo Canyon", Los Alamos National Laboratory Report, LA-13050-MS, Los Alamos, NM

[93] Springer, E.P. 1996, "Surface Water and Erosion Calculations to Support the Area G Performance Assessment," Los Alamos National Laboratory Report LA-UR-97-, Los Alamos, NM

[94] Nyhan, J. et al.1984, "Erosion of Earth Covers used in Shallow Land Burial at Los Alamos, New Mexico," J. Environmental Quality 13(3)

[95] Nyhan, J.R. and L.J. Lane 1986 "Rainfall Simulator Studies of Earth Covers used in Shallow Land Burial at Los Alamos, New Mexico," Proceedings of the Rainfall Simulator Workshop, Society for Range Management

[96] Vold, Erik 1996, "Modeling of the Aqueous Phase Source Release to the Unsaturated Zone from the Los Alamos Area G Disposal Facility," Los Alamos National Laboratory Report LA-UR-96-, Los Alamos, NM

[97] Bradbury, M.H. and F-A Sarott 1995, "Sorption Databases for the Cementitious Near-Field of a L/ILW Repository for Performance Assessment," PSI Bericht Nr. 95-06,

[98] Moss, David January 5, 1994, Letter to Diana Hollis, Subject: LANL Liquid Waste Treatment Plant at TA-50

[99] Mughabghab, M.F. and T.M. Sullivan 1989, "Evaluation of the Pitting Corrosion of Carbon Steels and Other Ferrous Metals in Soil Systems," Waste Management, Vol. 9

[100] Shuman R. 1997, "Radiological Dose Assessment of the TA-54, Area G Performance Assessment and Composite Analysis," Rogers and Associates Engineering Corporation Report to LANL RAE-9148.82-2, Salt Lake City, UT

[101] Vold, E.L. 1996, "Atmospheric Transport in Complex Terrain at Los Alamos Area G," Los Alamos National Laboratory Report LA-UR-96-4870, Los Alamos, NM

[102] Kowalevsky, K. et al. 1995, "Air Quality Impacts Analysis for Area G," final report from RADIAN, Inc. to LANL, Los Alamos, NM

[103] CAP-88, Available from Radiation Shielding and Information Center, Oak Ridge National Laboratory, Oak Ridge, TN, ref. CCC-542

[104] U.S. Environmental Protection Agency 1986, "Guidelines on Air Quality Modeling (Rev.)," EPA-450/2-78-027R, July 1986

[105] K.R. Costigan, J.E.Bossert, 1996 "Three-dimensional modeling study of atmospheric circulations and dispersion at TA-54", Los Alamos National Laboratory report LA-UR-96-4793, Los Alamos, NM

[106] MICROSHIELD Grove Engineering, 1992

[107] Birdsell et al., 1997, "Simulations of Groundwater Flow and Radionuclide Transport in the Vadose and Saturated Zones Beneath Area G, Los Alamos National Laboratory," Los Alamos National Laboratory Report LA-UR-97-157, Los Alamos, NM

[108] Rogers, D. B. et al., 1997, "Conceptual Model for Subsurface Transport at MDA G," Los Alamos National Laboratory Report LA-UR-97-179, Los Alamos, NM

[109] Zyvolosky, G.A. et al. 1992, "FEHMN 1.0: Finite Element Heat and Mass Transfer Code," Los Alamos National Laboratory Report LA-12062-MS, Rev. 1, Los Alamos, NM

[110] Vaniman, D., G. et al. 1996, "Development of a Site-Wide Geologic Model for Los Alamos National Laboratory", Los Alamos National Laboratory report LA-UR-96-? , Los Alamos, NM

[111] Stratimodel, Inc., Version 3.10, Copyright 1994

[112] Gable, C.W. et al. 1995, "GEOMESH Grid Generation", Los Alamos National Laboratory Report LA-UR-95-4143, Los Alamos, NM

[113] Bishop, C.W. 1991, "Hydrologic Properties of Vesicular Basalt," Master's Thesis, University of Arizona, Tucson, AZ

[114] Soll, W.E. 1995, "Influence of Fracture Fills and Fracture Coatings on Flow in Bandelier Tuff", Los Alamos National Laboratory report LA-UR-95-2695, Los Alamos, NM

[115] NRC, 1989, "Regulatory Guide 3.64, Calculation of Radon Flux Attenuation by Earthen Uranium Mill Tailings Covers," U.S. Nuclear Regulatory Commission, June 1989

[116] EPA, 1989, "Exposure Factors Handbook," U.S. Environmental Protection Agency, EPA/600/8-89/043

[117] Yang, Y.Y. and C.B. Nelson, 1986, "An Estimation of Daily Food Usage Factors for Assessing Radionuclide Intakes in the U.S. Population," Health Physics, 50(2)

[118] NRC 1977, "Regulatory Guide 1.109, Calculation of Annual Doses to Man from Routine Release of Effluents for the Purpose of Evaluating Compliance with 10 CFR 50, Appendix I," U.S. Nuclear Regulatory Commission, Revision 1, October 1977

[119] Rupp, E.M., 1980, "Age-Dependent Values of Dietary Intake for Assessing Human Exposures to Environmental Pollutants," Health Physics, 39

[120] ICRP 1977, "Recommendations of the International Commission of Radiologcal Protection," ICRP Publication 26, Pergamon Press New York, NY

[121] ICRP 1977, "Data for Use in Protection Against External Radiation," ICRP Publication 51, Pergamon Press New York, NY

[122] U.S. Environmental Protection Agency, "Licensing Requirements for Land Disposal of Radioactive Waste," Code of Federal Regulations Title 10, Part 61, of 12-27-82.

[123] NRC 1986, "Update of Part 61 Impact Analysis Methodology, Methodology Report," U.S. Nuclear Regulatory Commission, NUREG/CR-4370, Vol. 1, January 1986.

[124] U.S Department of Energy 10CFR61

[125] "Los Alamos National Laboratory Quality Program Plan for Environmental Restoration Activities," LA-UR-91-1844, Los Alamos, NM

[126] LANL 1996, "TA-54, Area G Quality Assurance Program Description," Los Alamos National Laboratory Waste Management Plan Plan-54G-006, R.1, pursuant to Title 10, Part 830.120 of the Code of Federal Regulations (10 CFR 830).

[127] LANL 1996, "Management of Environmental Restoration Project Waste," Los Alamos National Laboratory ER Project Safe Operating Procedure LANL-ER-SOP-01.06, Rev. 1, Los Alamos, NM

[128] LANL 1995, "Conduct of Operations," Los Alamos National Laboratory Waste Management Plan Plan-54G-013, Los Alamos, NM

[129] Wight, J.R. and J.W. Skiles 1987, "SPUR: Simulation of Production and Utilization of Rangelands, Documentation and Users Guide," U.S. Dept. of Agriculture, ARS 63, Washington D.C.

[130] Knisel, W.G. 1980, "CREAMS: A Field-scale Model for Chemicals, Runoff, and Erosion from Agricultural Management Systems," U.S. Dept. of Agriculture Conservation Res. Rep. No 26, Washington D.C.

[131] Springer, E.P. et al. 1984, "Testing the SPUR hydrology component on rangeland watersheds in southwest Idaho", Trans. Amer. Soc. Agri. Engin. 27(4)

[132] Link, S.O. et al. 1995, "The Role of Plants and Animals in Isolation Barriers at Hanford, Washington," PNL-10788, Richland, WA

The Cerros del Rio basalts have been cored in boreholes 54-1015 and 54-1016 in the canyon north of MDA L. They consist of rubbly flow breccias and dense fractured microporphyritic lava flows with up to 10% vesicles, with zones of moderately vesicular to very frothy lavas (as much as 60% open vesicles) in the uppermost 21 m (69 ft). In borehole 54-1015, the circulation of drill air and retrieval of cuttings were lost when the drill encountered the frothy basaltic lava from about 100 to 105 m (328 to 345 ft); this indicated high permeability of the frothy basalts. On the other hand, drill air and cuttings were returned in the denser basaltic lavas, and little loss of circulation occurred through these intervals. However, during drilling of borehole 54-1016 at a depth of 33 m (108 ft) below the top of the basalt, the drill air was observed blowing out from borehole 54-1015, 107 m (351 ft) east of 54-1015. Both holes were uncased within the basalt. An ~500 ft^3/min. blower had been used for drilling borehole 54-1016, but the borehole had completely lost circulation, and an estimated 5 to 10% of the injection air had flowed to the distant well (J. Eddy, personal communication, March 1995). The observed flow of drill air horizontally through the basalt indicates high permeability in the frothy basaltic section.

Total thickness of the Cerros del Rio basalts beneath MDA G is unknown. In borehole 54-1015, a thickness of 48 m (157 ft) of basalts were drilled with no lower contact encountered. Puye Formation sedimentary rocks were encountered beneath 82 m (269 ft) of basalt in well PM-2, located south of MDA L. No basal contact was encountered in well T-5, south of MDA G, after drilling through 28 m (92 ft) of basalt.

Elevation of the top of the basalt directly beneath MDA L in borehole 54-1015 is 1949.5 m (6396 ft) above sea level. Hole LGC-89-32 in western MDA G encountered basalt at 1967.2 m (6454 ft) elevation; hole LGC-89-33 in eastern MDA G encountered basalt at 1980.7 m (6498 ft) elevation; and well T-6, south of MDA L, encountered basalt at 8133 m (6015 ft) elevation (Purtymun 1995). These elevations indicate that the basalt dips about 5° toward the west and possibly steepens east of MDA G toward basalt outcrops at State Road 4 and Pajarito Road. Basalt rock textures similar to those found near surface volcanic vents have been located near this intersection, about 1 km (0.6 mi.) east of MDA G.

Underlying and interfingering with the basalts are sedimentary conglomerates and fanglomerates of the main body of the Puye Formation. The upper approximately 200 m (656 ft) are composed of coarse basaltic, latitic, and quartzite gravels in a poorly sorted matrix of sand- and silt-sized grains. Well PM-2, located about 1.5 km (0.93 mi.) west of MDA G, is the nearest hole to intercept the Puye Formation and underlying Tesuque Formation, which host the regional aquifer (Cooper et al. 1965, Purtymun and Cooper 1969). No boreholes at MDA G extend deep enough to encounter these deeper units.

2.3.3 Alluvium and Canyon Bottoms

The canyons that bound Mesita del Buey in the region of MDA G are Pajarito Canyon to the south and Cañada del Buey to the north (Figure 2). Canyon alluvium is composed of unconsolidated silty to coarse sands of quartz and sanidine feldspar crystals, crystal fragments, and broken pumice fragments weathered from the surrounding mesa tops and sides. Occasionally, fragments of latite or similar composition lava are incorporated, as are cobble- or smaller-size fragments of welded tuff. Alluvial packages are lensoid in cross section and reach 3 to 4 m (10 to 13 ft) in thickness (Purtymun 1995).

The canyons transport water and loose sediment by way of surface runoff from the mesa and flow originating upstream from MDA G. Pajarito Canyon, on the south side of Mesita del Buey, transmits water intermittently throughout seasons of heavy precipitation. Cañada del Buey, on the north side, drains a much smaller area and flows only during heavy snowmelt or heavy rains. Pajarito Canyon hosts a known narrow alluvial aquifer system in an area near but upstream of MDA G. However, drilling within Cañada del Buey near MDA G shows that these canyon sediments contain no perched water, although thin moist lenses of silt and clay are reported (Devaurs 1985, Devaurs and Purtymun 1985, Purtymun 1995). (Perched water, probably related to discharge from a nearby water supply well, is reported in two boreholes in Cañada del Buey approximately 1800 m (6000 ft) upstream from MDA G; see Purtymun 1995, p. 114.).

2.3.4 Structure Sections Through the MDA G Area

Figure 5 indicates the lines of structure sections shown in Figures 6 and 7. Geologic controls for the sections are from boreholes shown on the figures. Bandelier Tuff units thin from west to east and dip about 3° to the east; borehole data suggest very little southeast component of dip to these sheet-like deposits, but measurements on outcrops at MDA G indicate a strike and dip on Unit 2b of approximately N 68° E 3° SE. The Bandelier Tuff is about 90 m (295 ft) thick beneath the west boundary of MDA G and 44 m (144 ft) thick beneath the east boundary. The thickness of Unit 2a in hole LGM 85-11 suggests a southerly component of dip to its upper contact, but other unit thicknesses are consistent with a gentle eastward dip. The Guaje pumice bed has been identified in the western map area, but the unit, if present, is very thin in the east.

Other than the minor faults described above at the base of Unit 2b of the Tshirege Member, no geologic faults or surface expressions of buried structure have been identified at Mesita del Buey. Cooling joints in the tuffs provide the only known fracture flow paths within the Bandelier Tuff.

3.0 HYDROGEOLOGY OF THE MDA G AREA: FACTORS PERTAINING TO SUBSURFACE CONTAMINANT TRANSPORT

3.1 Introduction

The portion of the performance assessment to which this document pertains is concerned with radionuclide contaminant transport beneath MDA G. If such subsurface transport is significant, it will be controlled by flow processes. The processes that drive flow and transport at MDA G are extremely complex, involving two phases (liquid and gas) in a variably saturated medium. The system is further complicated by the presence of open to filled fractures. Liquid flow in the partially-saturated (vadose) zone above the water table is driven by energy gradients and controlled by the hydraulic conductivity and structure of the medium. At the same time, the gradients and the conductivity are strongly affected by the moisture content distribution. This interrelated feedback system results in complex nonlinear behavior that is described by nonlinear partial differential equations. These equations cannot be solved analytically, so to accurately predict fluid movement and distributions, it is almost always necessary to use a numerical modeling approach. The accuracy of the numerical model depends on the accuracy of the characterization of the system. This includes knowing the values of the different material properties and

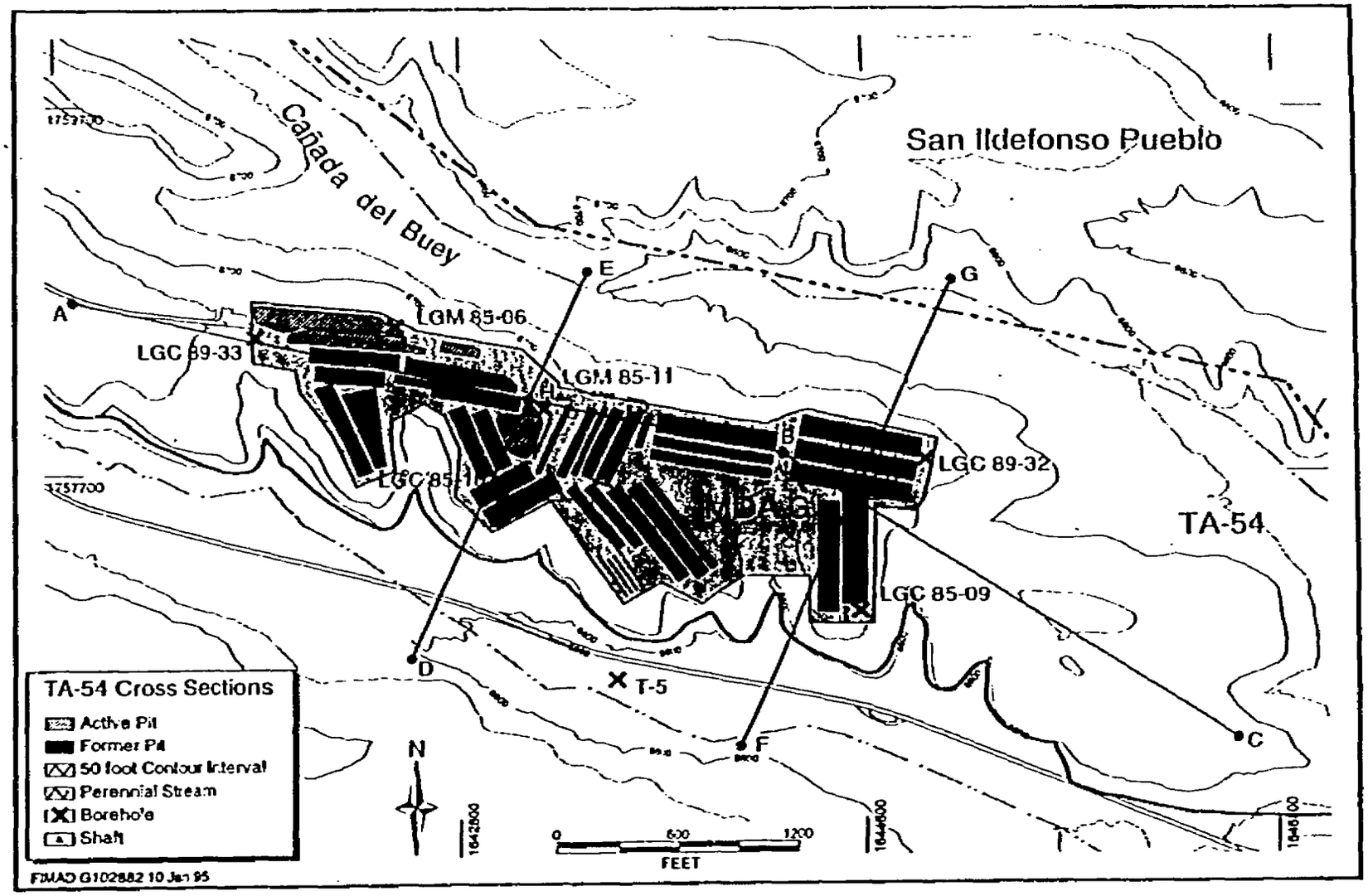

Figure 5. Location map for geologic structure sections, MDA G.

relationships called for in the equations. The purpose of this section is to summarize available data on material properties, report values that are representative of the different hydrogeologic units under MDA G, and provide references to the original data sources.

Most of the data presented or referenced in this section pertain to the upper Bandelier Tuff units because those are the units in which virtually all of the cores and measurements have been taken. The approximately 190 m (623 ft) of basaltic and underlying sedimentary rocks between the Bandelier Tuff and the water table have never been cored beneath MDA G and have rarely been cored elsewhere on the Pajarito Plateau, and thus, the hydraulic properties are largely unknown. Once measured, they would provide additional information on radionuclide transport times away from the disposal areas.

3.2 Material Properties

Some material properties and relationships are needed to characterize the subsurface system. Rock properties include porosity, bulk density, and saturated hydraulic conductivity. Properties that characterize the fluid/rock relationships in the vadose zone include θ, the volumetric moisture content (a measure of the amount of water present); ψ, the matric potential (suction, tension) (a measure of the energy state of the water); and K, the hydraulic conductivity (a measure of the ability of a fluid to flow). These three properties are strongly interrelated. The relationships between them are called *constitutive relationships* and include the θ-ψ relationship, the *characteristic curve*, and the K-θ and K-ψ relationships, the *unsaturated conductivity curves*. In the following tables, we have compiled values for those properties and relationships.

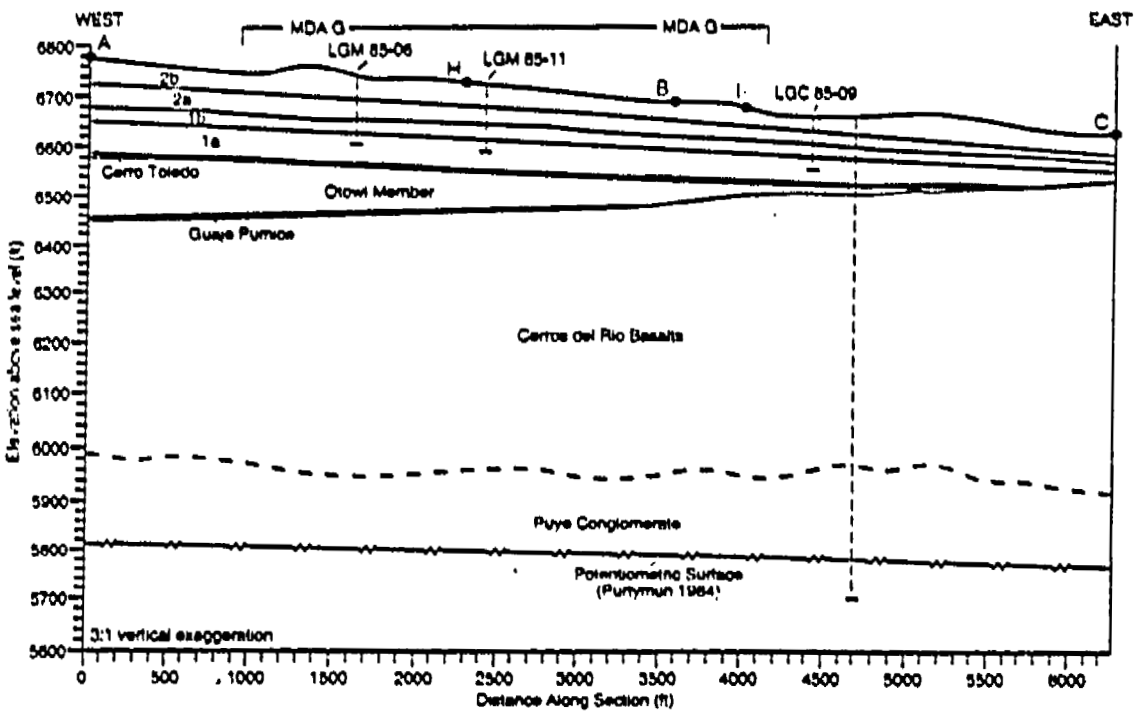

Figure 6. Structure section A-C along a northwest-southeast transect, MDA G.

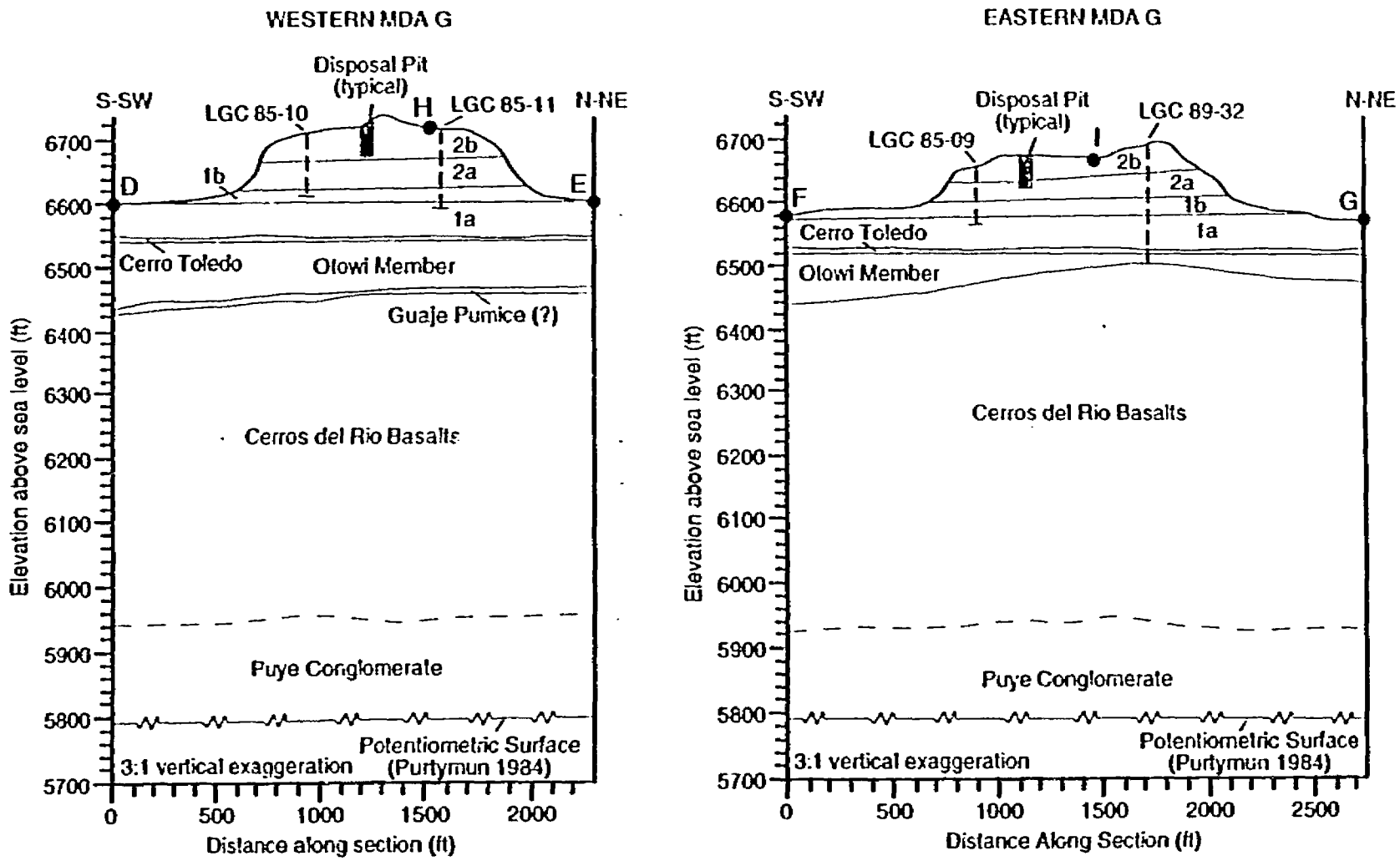

Figure 7. Structure sections D-E and F-G along north-south transects, MDA G.

Table 1 lists published and unpublished hydraulic property data measured from selected cores of MDA G and the vicinity. The data listed represent the best available based on the stratigraphic assignments of the samples, the analytical procedure used, and traceability of the data. However, in the case of stratigraphic assignments in Kearl et al. (1986a, b), we have reassigned a thickness of 8 m (26 ft) to Unit 1b, based on measured thicknesses in several outcrops and comparisons between the section originally described at Mortandad Canyon (Baltz et al. 1963) and Mesita del Buey. In doing so, we moved core measurements from upper Unit 1b (Kearl et al. 1986a, b) to their correct assignment in lower Unit 2a. This reassignment affects only three samples.

Individual sample data in Table 1 come from a variety of sources. For 16 of the samples in Table 1, volumetric water content was estimated from core moisture profiles reported in Kearl et al. (1986a, b). The original plots of the core moisture data as a function of depth are reproduced in Figure 8. The estimated data are sufficiently similar among the holes and agree sufficiently well with recently measured values that this approximation is acceptable for characterization of these layers.

3.2.1 Density and Porosity

Porosity is used in equations for flow and transport. Both porosity and bulk density are needed when converting moisture content to saturation, which is the form used in the model calculations. Numerous density and porosity measurements on Bandelier Tuff in the vicinity of MDA G have been reported by Kearl et al. (1986a, b) and in various reports by Stephens and Associates, Inc. (1994a, 1992b, 1992a, 1991), as summarized by Rogers and Gallaher (1994b).

In general, the best published descriptions of the pre-Bandelier units in the vicinity of MDA G are the drilling logs from water supply wells PM-1 and PM-2, (Cooper et al. 1965). However, no density or porosity measurements are reported.

3.2.2 Characteristic Curves

The characteristic curve (θ vs. ψ) is needed for any numerical prediction of flow in the unsaturated zone and can also be used for estimating field head (ψ) gradients from more readily available θ measurements. The determination of the characteristic curve for a core sample can be found in Bear (1972) and Klute (1986) and provides the types of data listed in Table 2.

Table 2 lists the moisture characteristics of drainage curves (water displaced by air), as measured in laboratory experiments on 45 samples of tuff. Data sources are shown after the table. The values reported in Table 2 use pressure-plate-derived data up to pressures of about 1 bar (-1021 cm) and psychrometer-derived data at the higher values of tension. Rogers and Gallaher (1994b) discuss the rationale for accepting measurements in reports from the geotechnical laboratory of Daniel B. Stephens and Associates and from Bendix (Kearl et al. 1986a, b). Because pressure-plate measurements do not equilibrate above ~0.5 bar (-511 cm water), psychrometer measurements should be used in high-tension regimes (Stephens and Associates 1992a).

TABLE 1
HYDRAULIC PROPERTIES DATA FOR MDA G STRATIGRAPHY FROM SELECTED BOREHOLES

Tshirege Member, Unit 2b

Borehole	Depth (ft)	ρ_b (g/cm^3)	θ (vol. %)	Porosity (%)	Saturation (%)	K_{SAT} (cm/sec)	θ_r (%)	N	α
LGM 85-11	3	—	—	54.0	—	5.4×10^{-4}	—	—	—
LLM 85-02	7	—	—	41.5	—	4.4×10^{-4}	—	—	—
5 LLC 85-15	10.0	1.46	1.0	46.4	2.2	1.6×10^{-3}	3.8	2.044	.0060
LLM 85-05	15	—	0.7*	52.6	1.3	5.4×10^{-4}	—	—	—
LGM 85-06	29	—	1.0*	42.5	2.4	4.8×10^{-4}	—	—	—
8 LLC 85-14	29.0	1.39	2.0	44.1	4.5	4.2×10^{-4}	0.0	1.890	.0060
LGM 85-11	30	—	1.9*	51.5	3.7	2.8×10^{-4}	—	—	—
LLM 85-01	30	—	3.8*	39.6	9.6	1.1×10^{-4}	—	—	—
LLM 85-02	36	—	3.7*	46.5	8.0	1.2×10^{-4}	—	—	—
LLM 85-05	36	—	2.0*	73.6	2.7	2.2×10^{-4}	—	—	—
54-1006	41.5	1.28	4.7	44.9	10.5	4.1×10^{-4}	0.0	1.760	.0064
LGM 85-06	51	—	1.3*	40.2	3.2	8.4×10^{-5}	—	—	—

Tshirege Member, Unit 2a

Borehole	Depth (ft)	ρ_b (g/cm^3)	θ (vol. %)	Porosity (%)	Saturation (%)	K_{SAT} (cm/sec)	θ_r (%)	N	α
LLM 85-01	52	—	1.3*	64.4	2.0	2.7×10^{-4}	—	—	—
2A LLC 86-22	54.5	1.26	1.3*	51.0	2.5	8.2×10^{-5}	2.0	2.238	.0037
2B LLC 86-22	54.5	1.26	1.3	48.3	2.7	2.5×10^{-4}	0.0	1.932	.0045
7 LLC 86-22	65.0	1.27	1.4*	48.7	2.9	1.4×10^{-4}	0.0	2.347	.0026
LLM 85-02	67	—	1.3*	43.3	3.0	9.8×10^{-5}	—	—	—
54-1001	67.8	1.20	1.9	41.4	4.6	1.3×10^{-4}	0.0	1.894	.0034
LLM 85-05	76	—	2.6	74.2	3.5	1.3×10^{-4}	—	—	—
54-1006	76.2	1.28	0.6	44.5	1.3	9.8×10^{-5}	0.0	1.880	.0030
54-1001	82.5	1.25	2.6	46.0	5.7	1.1×10^{-4}	0.0	2.225	.0022
54-1002	91.8	1.26	1.5	46.0	3.3	8.1×10^{-5}	0.0	2.213	.0012
LLM 85-01	101	—	3.4*	62.1	5.5	2.5×10^{-4}	—	—	—
54-1001	101.5	1.19	3.9	51.4	7.6	1.6×10^{-4}	0.0	1.782	.0034
54-1003	101.5	1.22	1.5	51.0	2.9	1.3×10^{-4}	0.0	1.733	.0030

* Moisture content (θ) estimated from moisture profiles in Kearl et al. (1986a, b).

TABLE 1 (continued)

Tshirege Member, Unit 1b									
Borehole	Depth (ft)	ρ_b (g/cm^3)	θ (vol. %)	Porosity (%)	Saturation (%)	K_{SAT} (cm/sec)	θ_r (%)	N	α
LGM 85-11	94	—	14.6*	64.3	22.7	1.1×10^{-4}	—	—	—
LLM-85-06	99	—	11.0*	52.6	20.9	1.3×10^{-3}	—	—	—
LLM 85-02	117	—	8.4*	48.5	17.3	1.7×10^{-4}	—	—	—
54-1003	119.0	1.22	6.4	59.9	10.7	9.9×10^{-5}	—	—	—
54-1001	121.5	1.18	9.0	46.4	19.4	2.2×10^{-5}	0.0	1.583	.0041
54-1002	121.5	1.23	3.2	49.5	6.5	4.6×10^{-5}	0.0	1.773	.0031
54-1006	124.0	1.22	2.5	43.5	5.7	4.5×10^{-5}	0.0	1.721	.0035
1 LLC 86-22	131.5	1.05	20.0*	50.7	39.4	1.9×10^{-5}	1.2	1.586	.0021
1BLLC 86-22	131.5	1.05	22.0	50.8	43.3	2.7×10^{-5}	4.4	1.709	.0021
54-1006	136.0	1.28	6.3	47.2	13.3	5.7×10^{-5}	0.0	2.087	.0014
54-1001	141.5	1.20	15.6	48.2	32.4	8.2×10^{-5}	0.0	1.429	.0037
54-1002	142.5	1.19	11.5	49.1	23.4	2.5×10^{-5}	1.7	1.393	.0154

Tshirege Member, Unit 1a									
Borehole	Depth (ft)	ρ_b (g/cm^3)	θ (vol. %)	Porosity (%)	Saturation (%)	K_{SAT} (cm/sec)	θ_r (%)	N	α
CDBM-1	23.5	1.17	2.7	48.8	5.5	6.2×10^{-5}	0.0	1.939	.0029
CDBM-1	34.0	1.07	5.8	46.2	12.7	2.2×10^{-4}	0.0	1.634	.0055
CDBM-2	38.0	0.94	8.3	48.4	17.2	4.5×10^{-4}	2.6	1.791	.0071
CDBM-1	44.0	1.26	9.3	44.5	20.8	7.0×10^{-5}	0.0	1.682	.0041
CDBM-1	54.0	1.09	8.9	44.6	20.1	4.6×10^{-4}	0.0	1.519	.0070
CDBM-1	64.0	1.23	11.2	45.1	24.9	1.2×10^{-4}	0.5	1.724	.0053
LLM 85-06	115	—	—	56.3	—	9.1×10^{-5}	—	—	—
LLM 85-11	115	—	—	60.1	—	1.8×10^{-4}	—	—	—
LLM-85-05	123	—	—	65.6	—	1.6×10^{-4}	—	—	—
LLM-85-01	124	—	—	48.9	—	2.2×10^{-4}	—	—	—
54-1003	156.0	1.14	4.9	43.2	11.3	1.3×10^{-4}	2.5	1.765	.0040
54-1006	160.5	1.13	1.8	52.6	3.4	1.2×10^{-4}	—	—	—
54-1002	178.5	1.16	6.6	39.3	16.8	6.5×10^{-5}	0.0	1.815	.0043
54-1003	206.0	1.18	8.0	42.8	18.7	1.5×10^{-4}	—	—	—
54-1002	243.5	1.14	27.0	39.3	19.1	1.7×10^{-4}	0.0	1.745	.0062
54-1003	260.5	1.11	9.6	48.8	19.7	2.7×10^{-4}	—	—	—
54-1003	270.5	1.31	12.1	41.0	29.5	2.6×10^{-4}	—	—	—

* Moisture content (θ) estimated from moisture profiles in Kearl et al. (1986a, b).

TABLE 1 (concluded)

Borehole	Depth (ft)	ρ_b (g/cm^3)	θ (vol. %)	Porosity (%)	Saturation (%)	K_{SAT} (cm/sec)	θ_r (%)	N	α
Tsankawi/Cerro Toledo									
CDBM-1	89.0	1.20	17.6	44.3	39.9	2.3×10^{-4}	0.0	1.428	.0131
CDBM-1	94.0	1.05	10.4	50.3	20.8	1.5×10^{-3}	1.6	1.585	.0173
Otowi Member									
Borehole	Depth (ft)	ρ_b (g/cm^3)	θ (vol. %)	Porosity (%)	Saturation (%)	K_{SAT} (cm/sec)	θ_r (%)	N	α
CDBM-2	66.5	1.16	11.6	44.6	26.1	5.0×10^{-4}	1.7	1.598	.0084
CDBM-2	67.5	1.22	12.3	44.0	27.9	2.7×10^{-4}	3.9	1.987	.0060
CDBM-1	104.0	1.20	15.1	44.6	33.8	2.3×10^{-4}	0.0	1.489	.0064
CDBM-1	114.0	1.29	15.6	45.1	34.6	1.6×10^{-4}	2.5	1.778	.0045
CDBM-1	124.0	1.10	11.0	43.7	25.1	2.9×10^{-4}	0.0	1.447	.0082
CDBM-1	134.0	1.24	11.7	44.7	26.2	1.6×10^{-4}	1.2	1.646	.0057
CDBM-1	144.0	1.14	10.2	42.8	23.9	4.2×10^{-4}	4.2	2.307	.0055
CDBM-1	154.0	1.29	11.1	41.0	27.1	1.0×10^{-4}	2.7	1.890	.0039
CDBM-1	164.0	1.21	10.6	43.6	24.2	1.7×10^{-4}	0.0	1.485	.0061
CDBM-1	174.0	1.18	10.1	41.2	24.4	2.1×10^{-4}	3.0	1.897	.0053
CDBM-1	184.0	1.18	9.3	43.2	21.4	3.0×10^{-4}	2.6	1.894	.0062
CDBM-1	189.0	1.19	9.4	43.0	21.9	1.8×10^{-4}	0.8	1.648	.0057

The laboratory method for determining characteristic curves involves the measurement of θ at discrete values of ψ, while for most purposes, some sort of continuous function [either $\theta(\psi)$ or $\psi(\theta)$] is desired. Various curve-fitting functions have been proposed, ranging from simple power-law fits to more complex multiparameter models. One multiparameter model that has met with wide acceptance is the van Genuchten curve (van Genuchten et al. 1980), given by the following function:

$$\tilde{\theta} = \frac{\theta - \theta_r}{\theta_s - \theta_r} = \frac{1}{\left[1 + |\alpha\psi|^N\right]^M} , \qquad (1)$$

where $\tilde{\theta}$ = effective saturation,
θ = moisture content (cm^3/cm^3),
θ_r = residual moisture content,
θ_s = saturated moisture content (porosity),

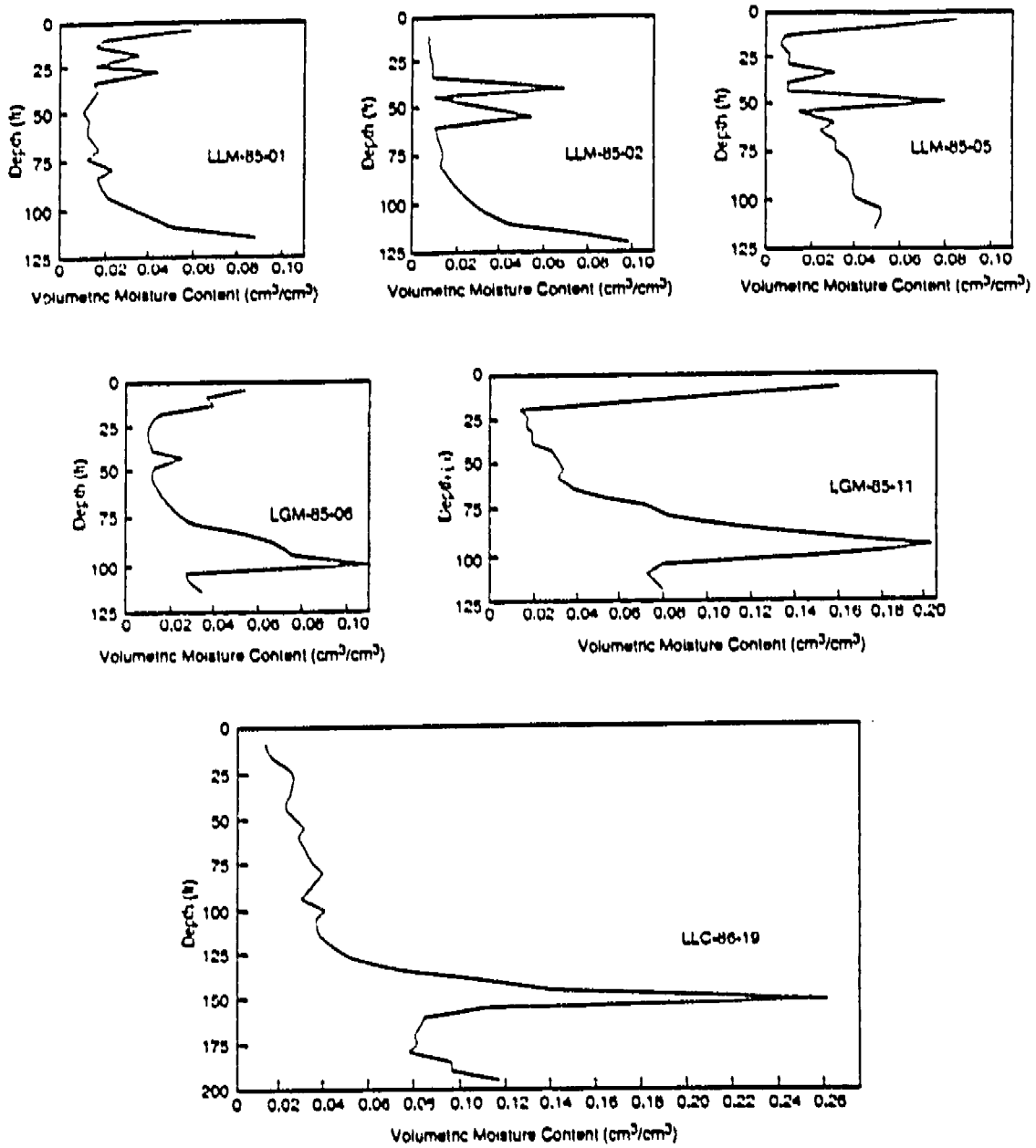

Figure 8. Volumetric moisture vs. depth for 12 boreholes (Kearl et al. 1986a,b).

ψ = matric suction,
α, N = van Genuchten fitting parameters, and
$M = 1-1/N$.

The van Genuchten curve is fit to the measured data by varying the two parameters, α and N.

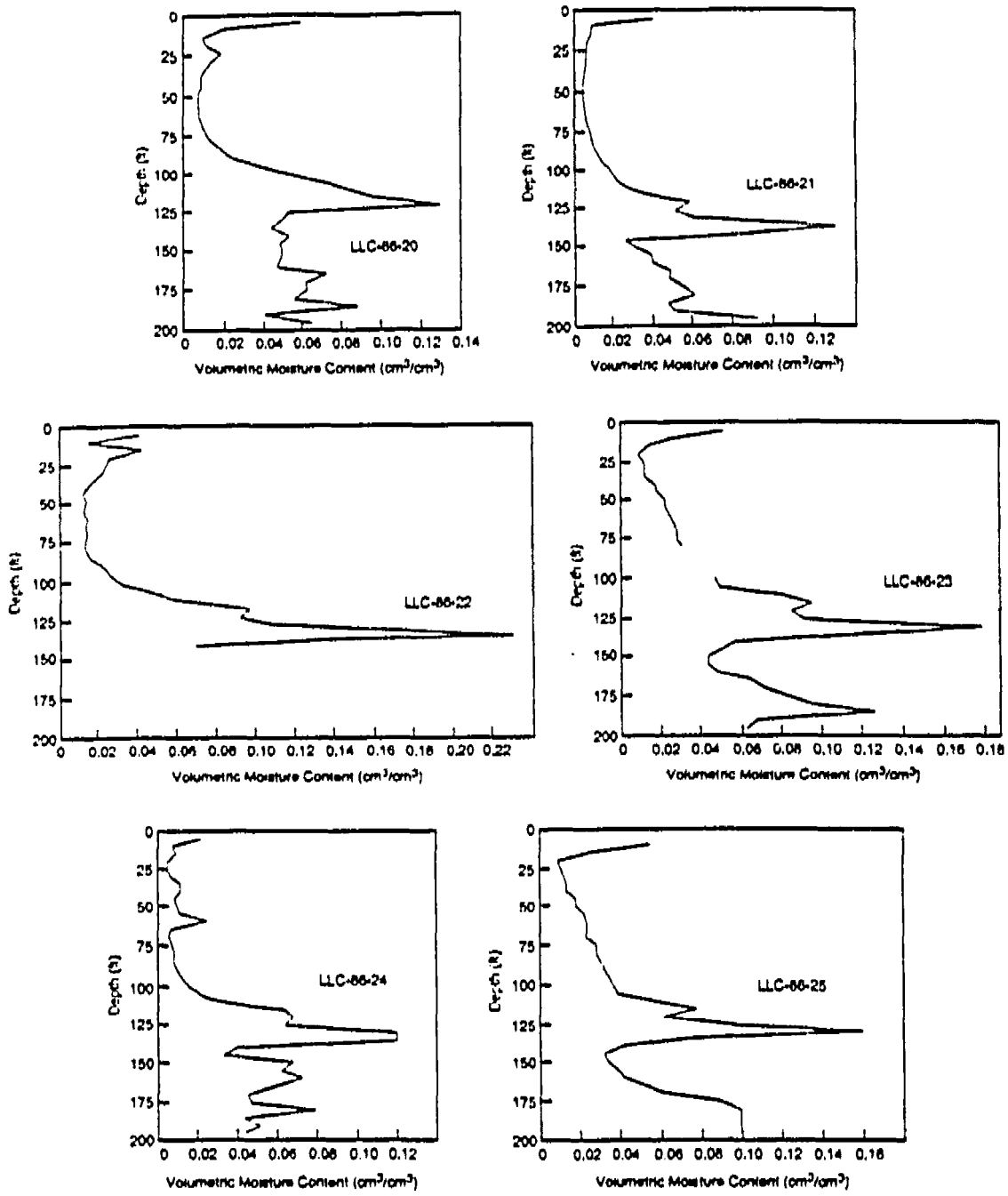

Figure 8 (concluded). Volumetric moisture vs. depth for 12 boreholes (Kearl et al. 1986a,b).

TABLE 2
PRESSURE HEAD VS. MOISTURE DATA FROM LISTED SOURCES[a]

54-1001, 67.8[b] Pressure Head (-cm water)	Moisture (vol. %)	54-1001, 82.5 Pressure Head (-cm water)	Moisture (vol. %)	54-1001, 101.5 Pressure Head (-cm water)	Moisture (vol. %)
0.1	41.4	0.1	46	0.1	51.4
51	38.6	51	43.3	51	46.8
112	37.3	112	41.3	112	44.1
326	29.3	326	38.1	326	37.3
918	25.7	918	35.1	918	21.4
6884	1.3	4304	2	6333	1.9
18101	1.2	14012	1.1	12656	1.2

54-1001, 121.5 Pressure Head (-cm water)	Moisture (vol. %)	54-1001, 141.5 Pressure Head (-cm water)	Moisture (vol. %)	54-1002, 91.8 Pressure Head (-cm water)	Moisture (vol. %)
0.1	46.4	0.1	48.2	0.1	46
51	42.4	51	44.6	51	43.6
99	40.4	112	43.1	112	42.4
306	34.6	326	37.7	311	38.4
920	21.7	918	28.8	903	32.3
5304	6.5	5599	11.2	5915	2.1
12074	3.8	21283	7.8	17948	0.7

54-1002, 121.5 Pressure Head (-cm water)	Moisture (vol. %)	54-1002, 142.0 Pressure Head (-cm water)	Moisture (vol. %)	54-1002, 178.5 Pressure Head (-cm water)	Moisture (vol. %)
0.1	49.5	0.1	49.1	0.1	39.3
51	45.3	61	43.6	51	37.7
112	43.6	102	33.9	102	35.2
311	37.4	301	27.8	306	25.9
903	22.5	923	26.6	918	20.9
6884	1.9	7118	9	5721	2
20886	1.2	17071	7	25495	1.6

a. Stephens and Associates 1991, Stephens and Associates 1992b, Stephens and Associates 1994a
b. Hole designation, sample depth (ft)

TABLE 2 (continued)

54-1002, 243.5		54-1003, 101.5		54-1003, 156.0	
Pressure Head (-cm water)	Moisture (vol. %)	Pressure Head (-cm water)	Moisture (vol. %)	Pressure Head (-cm water)	Moisture (vol. %)
0.1	39.3	0.1	51	0.1	43.2
51	37.3	51	46.1	51	41.7
102	33.1	112	44.4	102	40
306	22	311	37.8	306	30.2
918	20.7	903	27.7	918	28.1
5283	2.2	5599	1.7	7169	5.3
14094	1.9	27769	0.7	14818	4.6

54-1006, 41.5		54-1006, 76.2		54-1006, 124.0	
Pressure Head (-cm water)	Moisture (vol. %)	Pressure Head (-cm water)	Moisture (vol. %)	Pressure Head (-cm water)	Moisture (vol. %)
0.1	44.9	0.1	44.5	0.1	43.5
51	40.8	51	42.1	51	39.8
102	38.5	112	40.9	102	38.7
296	24.8	311	34.4	296	33.3
918	15.5	903	29.3	923	20.5
7536	2	6098	2.5	6557	3.8
13257	1.1	21630	0.9	14104	2.2

54-1006, 136.0		54-1006, 160.5		8LLC85-14, 29.0	
Pressure Head (-cm water)	Moisture (vol. %)	Pressure Head (-cm water)	Moisture (vol. %)	Pressure Head (-cm water)	Moisture (vol. %)
0.1	47.2	0.1	52.6	0.1	44.1
51	45.3	51	42.3	53	39.6
112	44.3	102	40.5	104	38.1
311	40.7	306	34	512	16.1
903	29.8	918	32	1030	8.2
4691	4	6853	0.8	3040	2.8
14746	1.9	13961	0.9	5080	1.4
—	—	—	—	15200	1

TABLE 2 (continued)

5LLC85-15, 10.0		2ALLC8622, 55.0		2BLLC8622, 55.0	
Pressure Head (-cm water)	Moisture (vol. %)	Pressure Head (-cm water)	Moisture (vol. %)	Pressure Head (-cm water)	Moisture (vol. %)
0.1	48.2	0.1	51	0.1	48.3
0.1	46.4	53	49.3	53	45.8
53	48.2	104	48.5	104	43.3
104	39.1	512	21.8	512	21.3
512	16.6	1030	11.1	1030	10.4
1030	10.1	3040	4.7	3040	4.1
3040	5.8	5080	3.1	5080	2.8
5080	5.1	15200	2.3	15200	0.1
15200	4.1	—	—	—	—

7LLC8622, 65.0		1LLC8622, 132.0		1BLLC8622, 132.0	
Pressure Head (-cm water)	Moisture (vol. %)	Pressure Head (-cm water)	Moisture (vol. %)	Pressure Head (-cm water)	Moisture (vol. %)
0.1	48.7	0.1	50.7	0.1	50.8
53	47.7	53	49.7	53	50.9
104	46.1	104	48.3	104	49.9
512	27	512	37.7	512	37.1
1030	11.6	1030	31.8	1030	30.9
3040	3.4	3040	17.1	3040	16.6
5080	1.4	5080	12.1	5080	11.7
15200	0.7	15200	8.7	15200	9.3

CDBM1, 23.5		CDBM1, 34.0		CDBM1, 44.0	
Pressure Head (-cm water)	Moisture (vol. %)	Pressure Head (-cm water)	Moisture (vol. %)	Pressure Head (-cm water)	Moisture (vol. %)
0.1	48.82	0.1	46.18	0.1	44.53
34	47.59	31	44.7	31	43.68
111	44.59	107	40.5	107	41.44
308	35.54	306	27.84	306	30.77
714	24.26	714	20.68	714	19.25
2295	21.33	1632	18.8	1632	13.94
5303	18.35	4875	16.96	4875	11.26
15348	14.8	15909	15.93	15909	10.06
2917	3.63	3885	4.99	5354	4.43
6200	3.07	11208	3.3	14400	2.49
19519	2.1	22517	2.56	—	—

TABLE 2 (continued)

CDBM1, 54.0		CDBM1, 64.0		CDBM, 89.0	
Pressure Head (-cm water)	Moisture (vol. %)	Pressure Head (-cm water)	Moisture (vol. %)	Pressure Head (-cm water)	Moisture (vol. %)
0.1	44.6	0.1	45.12	0.1	44.25
34	42.43	31	43.42	68	35.91
111	37.31	107	39.53	134	30.96
308	25.24	306	27.41	207	26.56
714	22.51	714	17.3	301	25.71
2295	20.49	1632	14.26	707	22.26
5303	18.81	4875	11.69	1448	19.74
15348	16.3	15909	10.79	5252	17.12
4120	5.6	4304	4.25	15042	13.09
18428	3.09	20212	2.64	2774	7.79
—	—	—	—	7791	6.04
—	—	—	—	20835	4.89

CDBM1, 94.0		CDBM1, 104.0		CDBM1, 114.0	
Pressure Head (-cm water)	Moisture (vol. %)	Pressure Head (-cm water)	Moisture (vol. %)	Pressure Head (-cm water)	Moisture (vol. %)
0.1	50.25	0.1	44.58	0.1	45.08
31	44.11	69	41.39	31	43.61
107	32.6	136	37.39	107	40.27
306	18.93	208	31.4	306	30.52
714	16.59	301	29.27	714	18.38
1632	15.59	707	21.31	1632	14.15
4875	13.15	1448	18.53	4875	11.49
15909	12.21	5252	17.21	15909	10.4
5792	4.94	15042	15.47	4171	6.83
24118	3.06	7506	6.07	15746	4.23
—	—	20743	4.43	—	—

TABLE 2 (continued)

CDBM1, 124.0		CDBM1, 134.0		CDBM1, 144.0	
Pressure Head (-cm water)	Moisture (vol. %)	Pressure Head (-cm water)	Moisture (vol. %)	Pressure Head (-cm water)	Moisture (vol. %)
0.1	43.73	0.1	44.7	0.1	42.84
69	39.33	68	41.07	31	41.18
134	35.48	135	37.63	107	38.04
207	28.64	207	32.31	306	20.57
301	25.97	301	28.02	714	18.63
707	22.46	707	18.44	1632	18.47
1448	17.97	1448	15.32	4875	18.04
5252	16.85	5252	13.98	15909	17.63
15042	13.92	15042	12.39	4395	5.37
6037	6.46	2499	6.38	19978	3.59
13359	4.68	5242	5.91	—	—
—	—	16857	3.66	—	—

CDBM1, 154.0		CDBM1, 164.0		CDBM1, 174.0	
Pressure Head (-cm water)	Moisture (vol. %)	Pressure Head (-cm water)	Moisture (vol. %)	Pressure Head (-cm water)	Moisture (vol. %)
0.1	41.03	0.1	43.56	0.1	41.22
31	39.52	68	40.27	31	40.08
107	37.23	136	37.02	107	36.6
306	28.71	209	30.55	306	23.9
714	16.68	301	27.74	714	18.77
1632	14.96	707	24.8	1632	16.64
4875	13.24	1448	22.11	4875	14.28
15909	12.37	5252	20.61	15909	13.41
4395	5.64	15042	18.31	2978	6.47
16378	3.89	5374	5.3	5711	4.7
—	—	25128	3.95	21895	3.41

TABLE 2 (concluded)

CDBM1, 183.5		CDBM1, 188.5		CDBM2, 27.5	
Pressure Head (-cm water)	Moisture (vol. %)	Pressure Head (-cm water)	Moisture (vol. %)	Pressure Head (-cm water)	Moisture (vol. %)
0.1	43.23	0.1	43	0.1	47.9
70	39.44	28.4	41.81	34	41.13
137	34.35	97	38.4	111	28.3
210	27.1	316	25.8	308	22.76
301	24.35	714	17.66	714	20.95
707	20.81	1530	16.06	2295	19.47
1448	18.07	5150	13.61	5303	18.25
5252	16.79	15297	12.26	15348	16.45
15042	14.33	7448	4.17	6608	9.65
2458	5.39	13250	3.31	19019	7.71
4151	4.67	24531	2.86	—	—
21487	3.67	—	—	—	—

CDBM2, 37.5		CDBM2, 66.5		CDBM2, 67.5	
Pressure Head (-cm water)	Moisture (vol. %)	Pressure Head (-cm water)	Moisture (vol. %)	Pressure Head (-cm water)	Moisture (vol. %)
0.1	48.39	0.1	44.56	0.1	43.97
34	45.63	34	42.12	34	42.43
111	39.58	111	36.69	111	37.72
308	24.94	308	22.13	308	23.02
714	19.53	714	17.69	714	19.02
2295	16	2295	14.22	2295	17.43
5303	11.89	5303	13.11	5303	16.38
15348	9.37	15348	11.74	15348	14.76
2580	6.77	4956	5.82	4844	5.75
4752	5.5	16847	3.91	18214	3.88
16266	3.88	—	—	—	—

Rogers and Gallaher (1994b and 1995) provide a compendium of moisture retention curve fits for the tuff core data and include data from measurements made on crushed tuff (Abeele 1979a, 1984). Mean α and N values for Bandelier Tuff core samples beneath TA-54, as compiled by Rogers and Gallaher (1994b), are listed in Table 3, along with other physical properties of tuff; the properties help constrain the performance assessment models. The software program RETC (van Genuchten et al. 1991) was used for the curve fitting. Full details of the θ-ψ measurements are contained in the original references cited above. The data and references in Table 2 are provided to enable the reader to critically evaluate the quality of the data and to use curve-fitting methods other than van Genuchten, if desired.

3.2.2.1 Tuff

Numerous characteristic curve calculations have been made for crushed Bandelier Tuff (Abeele 1979a, Abeele et al. 1981, Abeele 1984, Abeele et al. 1986) and intact core samples from beneath TA-54 (Rogers and Gallaher 1994b).

3.2.2.2 Alluvium

No characteristic curve data exist for alluvial units on the Pajarito Plateau. Alluvial cover on Mesita del Buey and MDA G is less than 1 m (3.3 ft) thick and is highly disturbed by human activity. Application of crushed tuff, asphalt roads and parking lots, cement pads and caps on shafts, heavy truck traffic on unpaved roads, and maintenance of natural or replanted vegetation have created a unique soil environment over the disposal units. Any influence on infiltration of moisture by the alluvium must be evaluated in future modeling efforts when data are available.

3.2.2.3 Pre-Bandelier Units

To date, there has been only one characteristic curve measured for units other than the Bandelier Tuff. This is a curve measured in the geotechnical laboratory (Stephens and Associates 1994b) on a basalt core sample taken from borehole SHB-1. This single curve cannot be considered in any way representative of the heterogeneous basaltic flows and flow breccias beneath TA-54.

3.2.3 Saturated Conductivity and Unsaturated Conductivity Curves

Saturated hydraulic conductivity, K_{sat}, is a measure of how readily a single fluid moves through a porous medium at saturation. Laboratory measurements are part of the typical analysis suite performed on core samples in geotechnical laboratories. Conductivity values for the stratigraphic units presented in Table 3 are taken from Stephens and Associates (1994a, 1992) and Kearl et al. (1986a, b).

The unsaturated conductivity curve relates the hydraulic conductivity of a fluid to its saturation in the system and must also be known for making numerical predictions of flow. The K-θ curve can also be used to estimate in situ infiltration rates from field moisture content measurements, given a number of simplifying assumptions. If the θ-ψ characteristic curve relationship is known, then given either the K-θ or K-ψ curve, the other can be calculated.

TABLE 3

SUMMARY OF GEOHYDROLOGIC PROPERTIES BENEATH MDA G, MESITA DEL BUEY

	Description				
Stratigraphic Unit	Unit 2b, Tshirege Member	Unit 2a, Tshirege Member	Unit 1b, Tshirege Member	Unit 1a, Tshirege Member	Tsankawi Pumice/Cerro Toledo
Thickness (typical)	12.2 m (40 ft)	13.7 m (45 ft)	7.6 m (25 ft)	15.2 m (50 ft)	Tsankawi: 1.8 m (6 ft); Cerro Toledo: 5 m (16 ft)
Lithology Summary (aft: ash-flow tuff)	Massive crystal-rich slightly welded aft, devitrified, vapor-phase altered, local pumice swarms, thin (0.2 m) basal surge	Massive crystal-rich nonwelded aft, devitrified, pumice-rich, gray-brown crystal-rich lapilli (>12% by vol.)	Massive crystal-rich nonwelded aft, devitrified, pumice-rich, brown crystal-rich lapilli (>12% by vol.), local pumice swarms, ash falls	Massive nonwelded nonindurated aft, vitric, pumice-rich, pumice are silky and vitreous, crystal-rich lapilli	Tsankawi: Massive air-fall tuff of 1-10 cm white pumice lapilli, 0.3-m surge bed of crystals and ash on top. Cerro Toledo: Moderately bedded, medium- to fine-grained tuffaceous sandstone and siltstone, moderately to poorly sorted.
Fracture Spacing	1.0-1.3 m, fractures continuous into upper Unit 1v	1.0-1.3 m (upper 3 m), fewer fractures deeper	No data, few fractures observed in outcrop	No data, few fractures observed in outcrop	No data, rare fractures in outcrop
Fracture Dip and Aperature	87° median, 3 mm median (3.1 ± 2.1 mm), max 13 mm	84° median, 3 mm median (5.3 ± 11.1 mm), max 100 mm	No data, assumed vertical fractures	No data, assumed vertical fractures	No data, assumed vertical fractures
Fracture Fill (XRD)	72% are filled, 9% plated, 19% open. Feldspar> trid-Q-crist> calcite>> gyp, hematite. Smectite> feldspar-Q-trid-crist>calcite	82% are filled or plated with brown clays, 18% are open. No caliche fracture-fill observed in this unit.	No data	No data	No data
Density (g/cm^3) • median • mean	1.37 1.37±.09 (n = 3)	1.26 1.24±.03 (n = 9)	1.20 1.16±.08 (n = 9)	1.14 1.15±0.09 (n = 13)	1.12 1.12±.10 (n = 2)
Porosity (%) -median • mean	45.7 48.1±9.33 (n = 12)	48.7 51.7±9.53 (n = 13)	49.3 50.9±5.80 (n = 12)	46.2 48.0±7.22 (n = 17)	47.3 47.3±4.24 (n = 2)
Vol. moisture (%) -median • mean	2.00 2.57±1.91 (n = 3)	1.50 1.89±0.95 (n = 13)	10.0 10.88±0.20 (n = 12)	8.3 8.94±6.22 (n = 13)	14.0 14.00±5.09 (n = 2)
K_{sat} (cm/s) • median • mean	4.15×10^{-4} 4.37×10^{-4} $\pm4.02\times10^{-4}$ (n = 12)	1.30×10^{-4} 1.48×10^{-4} $\pm6.59\times10^{-5}$ (n = 13)	5.15×10^{-5} 1.670×10^{-4} $\pm3.60\times10^{-4}$ (n = 12)	1.60×10^{-4} 1.88×10^{-4} $\pm1.19\times10^{-5}$ (n = 17)	8.65×10^{-4} 8.65×10^{-4} $\pm8.98\times10^{-4}$ (n = 2)
Saturation (%) -mean	5.7±4.29 (n = 3)	3.7±1.73 (n = 13)	21.3±12.06 (n = 12)	16.9±7.22 (n = 13)	30.3±13.50 (n = 2)
van Genuchten Fitting Parameters -median • mean	θ_r = 0.0 1.3±2.19 (n = 3)	θ_r = 0.0 0.2±0.67 (n = 9)	θ_r = 0.0 0.9±1.56 (n = 8)	θ_r = 0.0 0.6±1.11 (n = 9)	θ_r = 0.8 0.8±1.13 (n = 2)
	α = .0060 .0061±.0002 (n = 3)	α = .0030 .0030±.0009 (n = 9)	α = .0033 .0044±.0045 (n = 8)	α = .0053 .0052±.0014 (n = 9)	α = .0152 .0152±.0030 (n = 2)
	n = 1.890 1.898±.1422 (n = 3)	n = 1.932 2.027±.2279 (n = 9)	n = 1.647 1.660±.2195 (n = 8)	n = 1.745 1.735±.1183 (n = 9)	n = 1.506 1.506±.1110 (n = 2)

TABLE 3 (concluded)

Stratigraphic Unit	Description				
	Otowi Member	Guaje Pumice	Cerros del Rio basalts	Puye Formation	Santa Fe Group
Thickness	36.6 m (120 ft)	3.7 m (12 ft)	>36.6 m (>120 ft)	~200 m (~650 ft)	>350 m
Lithology Summary (aft: ash-flow tuff)	Massive moderately crystal-rich nonwelded aft, vitric, rare pumice swarms, but may contain up to 30% pumice	Basal nonwelded pumice lapilli bed, vitric	Dense highly fractured multiple basaltic to andesitic lava flows, separated by 1-3 m thick flow breccias, interbedded with Puye Formation	Fanglomerates, conglomerates, fluviatile and debris-flow deposits, minor interbedded ash and pumice falls, interstratified basalt flows may dominate in upper half, includes 20 m of coarse poorly consolidated basal conglomerate (Totavi Lentil)	Fluvial sandstones, siltstones, conglomerates, with subordinate eolian and lacustrine deposits, and ash beds; interbedded basalt flows and breccias constitute 15-45% of the group beneath Mesita del Buey
Fracture Spacing	No data, few fractures observed in outcrop	No data, rare fractures observed in outcrop	No data, ~ 0.3 m estimated from outcrops	No data, poor fracture development in outcrops	No data
Fracture Dip and Aperature	No data	No data	No data, ~ 5 mm estimated from outcrops	No data	No data
Fracture Fill (XRD)	No data, some filled with caliche in outcrops	No data	None	No data	No data
Density (g/cm^3) • median • mean	1.20 1.20±.056 (n = 12)	No data	No data, estimated 2.4-3.1	No data	No data
Porosity(%) •median • mean	43.6 43.5±1.32 (n = 12)	No data	No data	No data	No data
Vol. Moisture (%) • mean	11.50±2.01 (n = 12)	No data	No data	No data	No data
K_{sat} (cm/s) • median • mean	2.20×10^{-4} 2.49×10^{-4} $\pm1.16\times10^{-4}$ (n = 12)	No data	No data	No data	No data
Saturation (%)	26.4±4.12 (n = 12)	No data	No data	No data	No data
van Genuchten Fitting Parameters (θ_r, α, n)	θ_r = 2.1 1.88±1.49 (n = 12) α = .0059 .0060±.0009 (n = 12)) n = 1.713 1.755±.2528 (n = 12)	No data	No data	No data	No data

In writing the governing equations for flow, the unsaturated conductivity is often factored into two terms: the saturated conductivity (K_{sat}) and the relative conductivity (or relative permeability) (K_{rel}), i.e.,

$$K_{unsat} = K_{sat} * K_{rel} \quad , \tag{2}$$

with $0 \leq K_{rel} \leq 1$.

Unsaturated conductivity curves can either be directly measured or can be estimated in a number of ways. Direct measurement techniques include both field and laboratory methods. Direct measurements of K_{unsat} tend to be difficult, time-consuming, and expensive and are therefore much less common than K_{sat} measurements. Examples of techniques include laboratory column and ultracentrifuge studies and field infiltrometer studies (Conca and Wright 1992).

A faster and less costly alternative to direct measurement of unsaturated hydraulic conductivity is to use a mathematical estimation technique for K_{rel} (θ). Candidate models have been proposed by Campbell (Abeele 1979b), Mualem (1976), and Burdine (van Genuchten et al. 1991). These models assume that the shape of the characteristic curve implies certain properties of the pore structure of the medium and, using characteristic curve-fitting parameters, predicts K_{rel} as a function of saturation. K_{unsat} is then computed as the product of the K_{rel} function and a measured value of K_{sat}.

$$K = K_{sat}\theta^{-1/2}\left[1-(1-\theta^{-1/m})^{m}\right]^{2} \quad . \tag{3}$$

In situ field permeability measurements form another category of directly measured conductivity data. These measurements, which include downhole air permeability tests, packer tests, slug tests, and aquifer tests, all measure conductivity (or some closely related parameter) at a single field moisture content. Therefore, they do not provide information on K-θ for other values of θ, which would have to be extrapolated by some other means. They are also more difficult to perform and interpret than laboratory tests. However, these tests are the only ones that provide data on field-scale properties that reflect large-scale heterogeneities and fractures, data for relatively undisturbed materials, and the only data for soft or unconsolidated geologic intervals that are impossible to core intact.

3.2.3.1 Tuff

3.2.3.1.1 Intact Tuff

Measurements on intact tuff by the geotechnical laboratory of Daniel B. Stephens and Associates have produced numerous relative permeability curves for Bandelier Tuff at TA-54 and elsewhere on the Pajarito Plateau. These curves were produced using the van Genuchten/Mualem model (van Genuchten et al. 1991), with laboratory characteristic

curve measurements on core samples. Results are summarized by Rogers (1994) and Rogers and Gallaher (1995).

As part of the current ER Project site characterization efforts at TA-54, a number of in situ air permeability measurements have been conducted. Details of these studies are summarized in Appendix C. One of the ER Project studies included the use of borehole dual packer methods to measure in situ air permeability values in six boreholes in the proposed expansion area for MDA G. The measured air permeability values in each borehole are presented in Tables C-1 to C-6 and are summarized in Table C-7. Borehole locations are shown on Figure B-1. All of the measurements were performed with the air extraction method at an open interval of 27 in. (69 cm) between the borehole packers. The stratigraphic units tested were 2b, 2a, 1b, and 1a of the Tshirege Tuff Member; the Tsankawi pumice bed; the Cerro Toledo interval; and the Otowi Tuff Member [only one measurement (0.55 darcies) was performed]. For all measurements, air permeability values ranged between 0.35 darcies and 172.47 darcies. The highest values were measured on borehole intervals with open joints that were identified from geologic description of the continuous core.

The greatest range in air permeability values was measured in Unit 1b (0.63–172.47 darcies). The low values are believed to reflect the low air permeability of the matrix while the high values are due to measurements on open joints. Air permeabilities measured in the central and lower section of Unit 1a were low, with a median value of 1.12 darcies (Table C-7). The Otowi Tuff is also believed to have low air permeability; a low value of 0.55 darcies was measured in the one straddle packer test performed in this stratigraphic unit.

Laboratory measurements of air permeability were conducted on core from four of the six boreholes where straddle packer measurements were performed (Table C-8). In general, the core measurements determined lower air permeability than the colocated straddle packer measurements. This is expected because the laboratory measurements were on unfractured 6-in. (15-cm) lengths of core whereas the straddle packer measurements were on 27-in. (69-cm) borehole intervals where features such as open joints, fractures, or changes in rock matrix could influence the measurement results.

3.2.3.1.2 Crushed Tuff

Crushed Bandelier Tuff has historically been used for lining new disposal pits to a depth of about 0.3 m (13.0 in.), for separating some disposed of containers within the pits, and for covering pits. Stephens and Associates (1994b) provide one analysis of the hydraulic properties of a crushed Bandelier Tuff sample; the method of analysis was the pressure-plate and thermocouple psychrometer. The following values were reported: density was 1.40 g/cm^3, initial moisture content was 7.5 vol.%, θ_{sat} equaled 38.3%, and saturation equaled 19.6%. Using Equations (1, 2, and 3) for curve fit to the retention data, van Genuchten parameters are α equals .0083 and N equals 1.779, with a residual saturation calculated at 0.0%. K_{sat} for this single sample is 8.2 x 10^{-4} cm/sec. Calculated unsaturated conductivity for moisture ranging from 10% to 20% apparently vary from 10^{-8} to 10^{-6} cm/sec (Rogers and Gallaher 1995).

3.2.3.2 Alluvium

Local hydraulic information on alluvial aquifer materials comes from slug tests. These are single-well aquifer tests that provide only gross, and sometimes inaccurate, K_{sat} estimates. One set of slug tests has been conducted for the alluvial aquifer in Pajarito Canyon (Los Alamos Technical Associates 1991). These tests show K_{sat} ranging between 4.2×10^{-6} and 1.2×10^{-5} cm/sec (0.012 and 0.035 ft/day). These numbers are surprisingly low, much lower than the results of nine slug tests in Los Alamos Canyon alluvium that indicated a range of 1.5×10^{-3} to 4.0×10^{-2} cm/sec (4.8×10^{-5} ft/sec to 1.3×10^{-3} ft/sec) with an average of 1.4×10^{-2} cm/sec (4.7×10^{-4} ft/sec) (LANL 1993). The Environmental Surveillance Group has also conducted slug tests of the alluvial aquifer in Mortandad Canyon, but results have not been finalized or released (D. B. Rogers, personal communication, 1995).

3.2.3.3 Pre-Bandelier Tuff Units

The only available hydrologic data on the pre-Bandelier units of the Pajarito Plateau consist of estimates of saturated conductivity within the regional aquifer; these data were derived from specific capacity tests in production wells and test wells. These data, summarized by Purtymun (1984) (Table 4), are limited to good production zones; less permeable units, such as massive parts of the Cerros del Rio basalts, are not represented.

TABLE 4
SATURATED CONDUCTIVITY VALUES FOR PRE-BANDELIER TUFF UNITS

Unit		Saturated Hydraulic Conductivity (gpd/ft^2)	(cm/sec)
Tesuque Formation (sedimentary)	mean	5.6	2.6×10^{-4}
	range	3–9.3	$1.4–4.4 \times 10^{-4}$
Tesuque Formation with interbedded basalts	mean	8.2	3.9×10^{-4}
	range	5.3–11.3	$2.5–5.3 \times 10^{-4}$
Tschicoma Formation (volcanic flows)	mean	19	9.0×10^{-4}
Mixed Tesuque Formation and Puye conglomerate	range	53–83	$2.5–3.9 \times 10^{-3}$
Puye conglomerate*	mean	98	4.6×10^{-3}

* Purtymun 1984

Pumping tests done at Test Area North (TAN) at the Idaho National Engineering Laboratory (now Lockheed Idaho) provide data for saturated permeabilities within a basalt aquifer. For TAN, saturated permeabilities were 1 m/day at TAN-20, 43 m/day at TAN-18, 8 m/day at TAN-21, and 177 m/day at TAN-24A. At TAN-23, permeability was estimated at >213 m/day, but the water level could not be drawn down for a long enough time for reasonable measurement (W. Soll, personal communication, 1995). We might expect similar large ranges for saturated conditions beneath the Pajarito Plateau. Conductivities for a piece of cored basalt from borehole SHB-1 west of Mesita del Buey gave values of 3×10^{-11} and 3×10^{-9} cm/sec (Stephens and Associates 1994b).

3.2.4 Hysteresis

One physical process that is not typically characterized or measured in the laboratory is hysteresis of parameter values. Hysteresis in the θ-ψ relationship is the difference in the saturation of a fluid at a given pressure as a function of the fluid displacement history. It is caused by a change in displacement behavior of a fluid depending on whether it is by a drainage displacement (air displacing water) or an imbibition displacement (water displacing air). It is worth mentioning because it can have a significant effect on θ-ψ values, as noted for Bandelier Tuff by Abrahams (1963), but is almost always ignored because it introduces major complications into the modeling and prediction effort and requires more than double the number of experiments. Furthermore, the same hysteresis that affects the θ-ψ curve will also affect the K-ψ curve, although the K-θ relationship is inherently less hysteretic. We will also ignore hysteresis, out of necessity, because there are no data available.

3.2.5 Geohydrologic Properties of Rock Units beneath MDA G

Table 3 lists representative properties of the geologic units beneath Mesita del Buey in the region of MDA G for the purpose of modeling performance of the disposal site. There are many properties, mostly for the deeper strata, for which no relevant data exist. The uncertainties produced by these data gaps should be alleviated by investigations below our current depth of sampling. The thick interval of unsaturated rock between the relatively well-known tuff and the deep aquifer provides additional delay of radionuclide transport to the water table, but current data limits any quantification.

3.3 Hydrologic Conditions Below MDA G

The previous sections focused on hydrologic properties intrinsic to the geologic materials in the vicinity of MDA G. From these properties, we can tell how the materials might behave under a wide range of hydrologic conditions, but we can only speculate about how these materials are behaving under the disposal pits. In this section, we look at information about present conditions and processes. Both types of information are critical because together they can provide an understanding of the processes that affect flow and transport today and also predictions of the effects of the processes in the future.

3.3.1 In Situ Moisture Content

Numerous measurements, both laboratory measurements of fresh core samples and neutron probe measurements, of in situ moisture content have been conducted in and around MDA G (Kearl et al. 1986a, b; Rogers and Gallaher 1994a). The data indicate a

fairly predictable moisture profile through the different stratigraphic units of the Bandelier Tuff. Generally, field moisture content in the upper 33 m (100 ft) of tuff is less than 2% by volume in areas that are undisturbed by disposal pits and shafts, and most notably, asphalt cover. Around disturbed settings caused by disposal activities, near-surface moisture content dramatically increases above the natural background state because of a loss of plant evapotranspiration and suppression of atmospheric venting by installation of large asphalt surfaces. There is evidence that the increased moisture content may occur to depths of 15 m (50 ft) beneath disturbed areas. Appendix B describes our current data for in situ moisture content measurements.

3.3.2 Perched Aquifers

There is no evidence of extensive perched aquifers under Mesita del Buey. Gardner et al. (1993) report wet samples and equipment from the Otowi section in borehole SHB-4 in Pajarito Canyon 2.4 km (1.5 miles) northwest of MDA G. During drilling near MDA L, moist fine-grained Puye Formation was encountered directly overlying the basalts. Within the basalt, thin zones (~0.3 m, 1.0 ft) of wet basalt were observed (1) in the drill air return from the drill hole during drilling, (2) when the drill air was first turned on in the morning after being shut down overnight, and (3) as saturated zones in vesicular basalt core. The drill holes were not cored continuously. The elevations where water was observed in the basalt in borehole 54-1015 were 6278 ft (1913 m), 6260 ft (1908 m), and 6250 ft (1905 m). The elevations where water was observed in the basalt for borehole 54-1016 were 6292 ft (1918 m), 6258 ft (1907 m), 6204 ft (1891 m), and 6201 ft (1890 m). Chemical analysis of the water samples collected from the drill air was not warranted because of the impromptu collection methods. Monitor ports to collect groundwater, if present, were installed in the Tsankawi pumice bed, the Puye Formation, and selected zones in the basalt. To the present time, sampling events have not found water to be present in any of the ports. We believe that small quantities of water were trapped either soon after basalt deposition or en route toward the deep aquifer (Section 2.3.2).

3.3.3 In Situ Matric Tension

Kearl et al. (1986a, b) measured downhole matric tension profiles in two holes at TA-54 using thermocouple psychrometer arrays. Rogers and Gallaher (1994a) present laboratory-derived matric tension profiles for five wells drilled at MDA G during 1994; the cores were measured using the chilled-mirror psychrometer method. These measurements, together with measured water content, can be used to infer a direction of liquid movement based on head gradients. Based on head calculations from such measurements, Rogers and Gallaher (1994a) show that moisture is driven toward a dry, high-suction interval that is associated with the pyroclastic basal surge deposits at the base of Unit 2b. This high-suction interval is present to a degree in nearly all MDA G holes where matric tension data exists.

3.4 Areas for Further Investigation

Tables 3 and 4 indicate that much critical information is lacking about the hydrogeologic system beneath the Pajarito Plateau and below MDA G, specifically. The following are areas for further investigation.

1. There is almost no information available for pre-Bandelier Tuff lithologies, including hydrologic properties, thicknesses of basalt, and elevation of the top of the sedimentary rocks that host the regional aquifer below MDA G. A carefully cored well east of MDA G that penetrated the deep aquifer could fill in some information. When completed as a groundwater monitoring well, it would be the nearest monitoring station downgradient of the disposal units at Mesita del Buey. Aquifer testing, laboratory analysis of hydraulic properties for selected deeper stratigraphic units, and long-term monitoring activity would provide tighter control on numerical modeling and checks on aquifer integrity.

2. Little is known about fracture presence, frequency, aperture, continuity, and coatings or fillings below Unit 2a. Definitive characterization of fracture fillings and coatings is missing for all units. The available information is insufficient to determine whether fractures may be a critical flow path in the system. Characterization of this site would benefit from study of fracture coatings and fills and their material properties to augment existing data on population, aperture, and orientation. This information is most accessible from existing and future disposal pit walls.

3. Final disposition of MDA G and the other disposal areas on Mesita del Buey awaits federal and state agreement on scientific, economical, and political issues. One potential outcome is capping and stabilization of wastes in place. A pilot study in the ER Project is looking at the feasibility of large-scale atmospheric air movement through permeable geologic layers beneath disposal units. Dry atmospheric air can absorb and vent moisture from porous media, thereby decreasing the mobility of contaminants and increasing the effectiveness of natural retardation effects of the matrix. Future performance assessments might take into account the benefits of such an engineered stabilization system, particularly if a passive system can be made reliable.

4.0 GEOCHEMICAL BASELINE INFORMATION AND DATA

4.1 Introduction

The purpose of this section is to provide a review of the relevant geochemical data and information required for solute-transport calculations that will be used in the performance assessment. These data will serve as input to the mass/heat transfer model FEHM (Zyvoloski et al. 1988). Specific geochemical data used as input to FEHM include sorption isotherm models, consisting of the linear (K_D), Freundlich, modified Freundlich, and Langmuir; Henry's Law constants for liquid and vapor species; chemical rate laws using the Arrhenius equation; and solubility data for solid phases.

A detailed discussion on water/rock processes is also presented in this section. Geochemical parameters, such as pH, Eh, solution composition, mineral solubility, and presence of competing and complexing ligands, have the greatest impact on the sorption behavior of the elements of concern present in the pits. The release of radionuclides from the pits will be controlled by hydraulic flux, pore-water chemistry, mineral solubility, and sorption behavior. The following data and information are needed to verify and quantify geochemical reactions: source-term characterization (types, forms, and amounts of contaminants); source-term geochemistry (mineralogy, speciation, solubility, sorption,

pore-water chemistry, and reaction rates); and hydrogeological/geochemical characterization (mineralogy, fracture distribution, fracture mineralogy, sorption capacity of fracture material, hydraulic conductivity, porosity, and moisture content) of Bandelier Tuff and other geologic media at the site.

Very little site-specific geochemical data on sorption capacities of the Bandelier Tuff are available (Polzer et al. 1992). Parameter data for Freundlich, modified Freundlich, and Langmuir isotherms generally are not available from Yucca Mountain experiments, and application of these isotherms to the existing sorption data is not possible. Geochemical and hydrological processes influencing solute-transport processes within the Bandelier Tuff are extremely complex; therefore, site-specific data used as input to FEHM will be required to obtain the most relevant and meaningful results for the performance assessment.

4.2 Source-Term Inventory and Geochemistry

Predicting the release of radionuclides from MDA G is complex because of the variety of contaminated material disposed of in the pits and shafts. Elements of concern include americium (Am), carbon (C), cesium (Cs), cobalt (Co), neptunium (Np), strontium (Sr), plutonium (Pu), technetium (Tc), tritium (^3H), and uranium (U). This list is based on waste inventories provided by CST-14. Specific isotopes of these elements and their associated activities are provided in Table 5. Contaminated material in Pit 37 includes metal, cellulosics (cardboard), concrete, soil, and sludge. In Pit 37, most of the activity is associated with U-contaminated metal (8.16 Ci) and Pu-contaminated cellulosics (4.37 Ci). In terms of activity per volume of contaminated material, U-contaminated metal (0.0198 Ci/m^3) and Pu-contaminated sludge (0.0218 Ci/m^3) are the most abundant waste forms in this pit. Other waste forms in Pit 37, which are not included in Table 5, are irradiation sources consisting of encapsulated materials. These materials are not considered leachable and are not included in the total inventory of radionuclides listed in Table 5. A separate investigation is being conducted to quantify the amounts of radionuclides potentially migrating from the pits. Radionuclides are characterized by different leach rates, which are controlled by desorption and dissolution processes.

Cement sludge that was processed at TA-50 is disposed of in Pit 37. The sludge consists of an alkaline (pH 12) mixture containing $Si(OH)_4$ (40 wt%), $Ca(OH)_2$ (31 wt%), and $Fe(OH)_3$ (19 wt%) with varying amounts (approximately 10 wt%) of $Al(OH)_3$, $Mg(OH)_2$, NaOH and other metal hydroxides, metal sulfates, and metal chlorides. Typical activities of radionuclides in the TA-50 sludge are as follows: Pu-239/240, 1.0×10^4 pCi/g; Pu-238, 6.5×10^4 pCi/g; Am-241, 1.0×10^4 pCi/g; U-235, < 5 pCi/g; and U-234, 200 pCi/g (Terry Filer, CST-9, personal communication, July 28, 1995). The radionuclide content and activities of older TA-50 sludge is characterized by the following: Pu-239/240, 4.0×10^4 pCi/g; Pu-238, 1.0×10^4 pCi/g; and Am-241, 5.0×10^4 pCi/g (personal communication with Terry Filer, CST-9 on July 28, 1995). The chemical composition (major ion) of this hydroxide-rich sludge is representative of hydrated cement containing $Ca(OH)_2$ and $Si(OH)_4$ (Berner 1992, Krupka and Serne 1995).

TABLE 5
SUMMARY OF RADIONUCLIDE HALF-LIVES AND TOTAL ACTIVITY IN PIT 37 AT MDA G, TA-54, NOVEMBER 1994

Nuclide	Mass (g)	Half-life (yr)	Total Inventory (Ci)
^{3}H	1.24×10^{-3}	12.33	1.2×10^{1}
^{14}C	2.02	5.73×10^{3}	9.0
^{60}Co	6.64×10^{-3}	5.27	7.5
^{90}Sr	2.34×10^{-4}	29	3.3×10^{-2}
^{99}Tc	1.55×10^{-7}	2.13×10^{5}	8.2×10^{-1}
^{129}I	5.76×10^{-7}?	1.59×10^{7}	1.0×10^{-10}?
^{137}Cs	2.76×10^{-3}	30.17	2.4×10^{-1}
^{233}U	1.05×10^{-1}	1.59×10^{5}	1.0×10^{-3}
^{234}U	1.52×10^{1}	2.44×10^{5}	9.5×10^{-2}
^{235}U	1.26×10^{5}	7.04×10^{8}	2.7×10^{-1}
^{236}U	4.81×10^{-1}	2.34×10^{7}	3.1×10^{-5}
^{238}U	2.13×10^{6}	4.47×10^{9}	7.1×10^{-1}
^{237}Np	1.42×10^{-2}	2.14×10^{6}	1.0×10^{-5}, ingrowth from ^{241}Am
^{238}Pu	5.87×10^{-2}	87.74	1.0
^{239}Pu	1.42×10^{1}	2.41×10^{4}	8.7×10^{-1}
^{240}Pu	3.18×10^{-2}	6.54×10^{3}	7.2×10^{-3}
^{241}Pu	1.09×10^{-3}	14.7	1.1×10^{-1}
^{242}Pu	2.12×10^{-5}	3.76×10^{5}	8.3×10^{-6}
^{241}Am	8.95×10^{-2}	432	2.9×10^{-1}

Source: Keller, D., personal communication with P. Longmire on November 21, 1994.

A geochemical conceptual model for MDA G is shown in Figure 9. This geochemical model is based on relevant geochemical and mineralogical data and information collected from the ER Project at the Laboratory and from the Yucca Mountain Project. The key features of this model are discussed below.

1. Surface water (snowmelt, rainwater, and/or storm runoff) enters the pits. Rainwater and snowmelt will have a low total dissolved solids (TDS) content and an acidic pH because of low concentrations of bicarbonate, calcium (Ca), sodium (Na), and magnesium. Storm runoff may have a higher TDS content and near-neutral pH because of its contact with soils, sediments, asphalt, fill, and Bandelier Tuff.

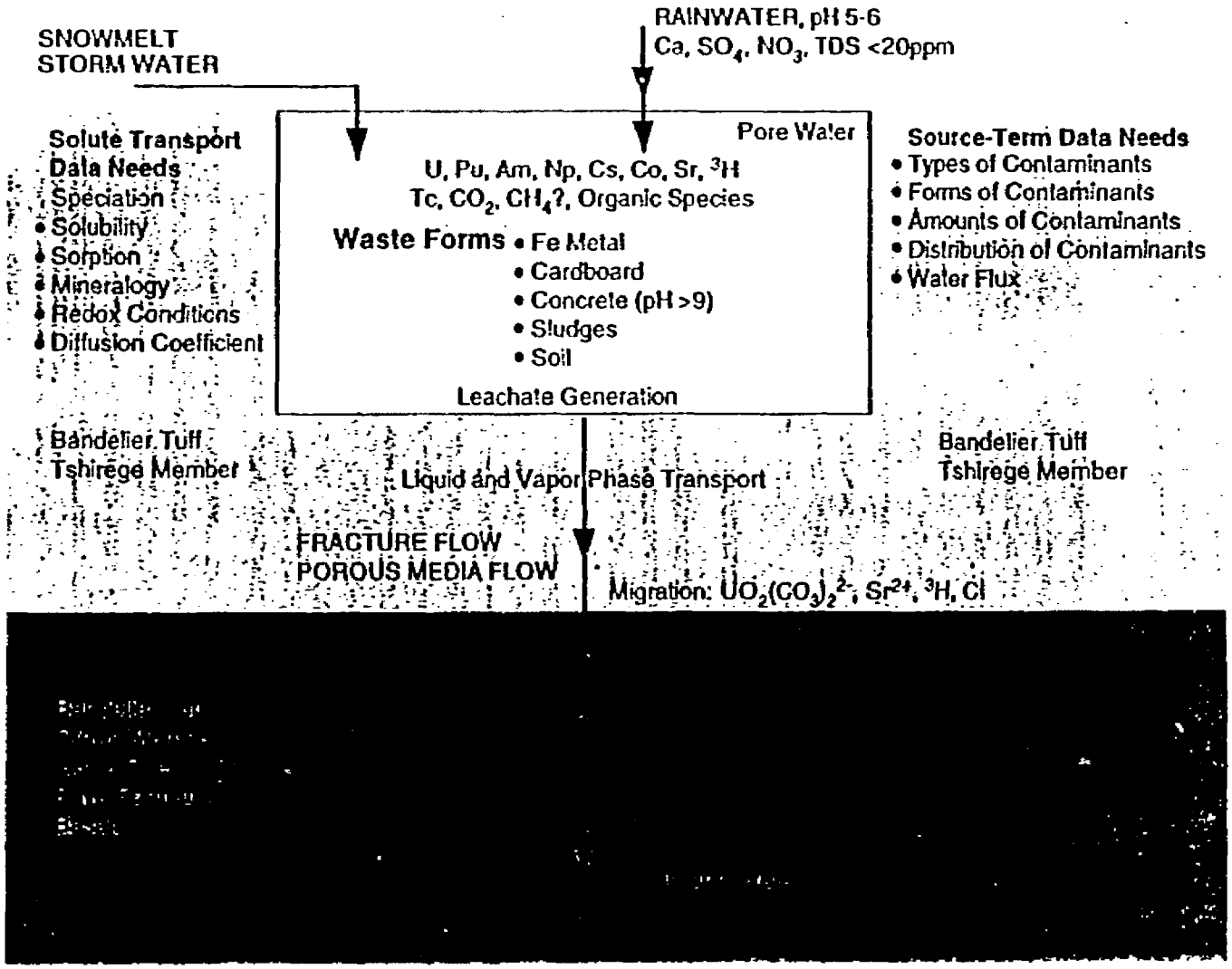

Figure 9. Geochemical conceptual model for TA-54.

2. Pore water will be generated as surface water enters the pits. This solution may approach equilibrium with crushed Bandelier Tuff, waste forms, dissolved gases, radionuclides, and other contaminants. The TDS content will increase in response to chemical reactions and pore-water residence time (mass/flux). Relatively oxidizing conditions probably prevail under unsaturated-flow conditions in areas deficient of chemical reductants, such as organic sludges, hydrogen sulfide, and methane. Localized reducing conditions are restricted to areas in the pits where reactive chemical reductants are present.

3. Important geochemical reactions controlling the release of contaminants from the pits include contaminant diffusion through waste forms, desorption of contaminants from waste forms, partial dissolution of waste forms, dissolution of contaminants, and gas generation. These geochemical reactions will be controlled by pH, Eh, speciation of contaminants, temperature, advection, and residence time of pore water. The pH may vary from near neutral to strongly alkaline values, especially if pore water comes in contact with concrete. Near-neutral pH values are expected to be dominant, however, because of the localized distribution of concrete and unsaturated-flow conditions within the pits. Contaminant leach rates will be controlled by the hydraulic flux, desorption, and equilibrium solubilities of the waste forms and contaminants.

4.3. Geochemical Transport Parameters

Release of contaminants (including radionuclides) from MDA G depends on the pit pore-water chemistry and the solubility and sorption behavior of the radionuclides. This section presents information and data derived from literature on sorption and equilibrium solubility for elements of concern at MDA G. Leach rates of radionuclides can be evaluated by considering equilibrium solubilities of solid phases containing the element of interest, e.g., U, Am, and Pu, and by determining ranges of the flux rate under unsaturated-flow conditions. Sorption values for devitrified tuff from Yucca Mountain are the primary focus of this discussion. Below MDA G, the Bandelier Tuff consists of both devitrified and vitrified rock. Other hydrogeologic units present beneath MDA G include basalts, Puye Formation, and the Santa Fe Group sediments, which are important to consider for the solute transport calculations. Unfortunately, very little hydrological and geochemical data have been collected on these strata, except for the Bandelier Tuff. Site-specific geochemical data for MDA G will make the calculations more technically defensible. Data needs are discussed in Section 4.4, Uncertainties and Future Investigations.

Distribution coefficient (K_D) values and solubility data from literature pertaining to Yucca Mountain were evaluated to estimate the potential for release of radionuclides from the pits and through the Bandelier Tuff. The Yucca Mountain experiments have relevance to MDA G because of similarities in mineralogy and sorption capacities of the Yucca Mountain tuffs and the Bandelier Tuff. The major controls of radionuclide adsorption include mineralogy and distribution of the adsorptive phases and major-ion chemistry of the solution containing the adsorbate(s). The mineralogy of devitrified volcanic tuffs at Yucca Mountain (Wolfsberg 1980) is similar to the bulk mineralogy of the Bandelier Tuff (Broxton et al. 1995). The Bandelier Tuff consists of devitrified and vitrified rock, which is assumed to have similar sorption capacities as Yucca Mountain tuffs for elements of concern based on similarities of bulk surface areas for devitrified and vitrified tuff. The dominant minerals

occurring in the devitrified tuff at Yucca Mountain include quartz, cristobalite, and feldspars with less than 5 wt% clay minerals and zeolites (Wolfsberg 1980). Devitrified sections of the Bandelier Tuff (Tshirege Member) are characterized dominantly by feldspar and quartz with some cristobalite and tridimite (Broxton et al. 1995). Clay minerals compose less than 2 wt% of the Tshirege Member (Broxton et al. 1995).

The groundwater chemistry of well J-13 at Yucca Mountain (Thomas 1987) is similar to the Water Canyon Gallery groundwater at Los Alamos (Table 6). There are some important differences, however, in temperature and major-ion chemistry, which may influence adsorption processes. The temperature of the J-13 groundwater (31.0°C) is higher than the temperature of the Water Canyon Gallery groundwater (11.3°C). The dominant cations and anions in both groundwaters are Na, calcium, and bicarbonate. The higher bicarbonate concentration in the J-13 groundwater probably accounts for the limited extent of adsorption of uranyl [U(VI)] species onto the Yucca Mountain tuffs. K_D values for U determined by Triay et al. (1994) under oxidizing conditions are less than 2 ml/g. The TDS content of the J-13 groundwater is higher than the TDS content of the Water Canyon Gallery groundwater by approximately a factor of 1.7. The J-13 groundwater may have a longer residence time within the tuff(s), which may account for the higher TDS content. The pH values for the Water Canyon Gallery and J-13 groundwaters are 7.6 and 6.9, respectively.

The geochemistry of soils is relevant to the migration of radionuclides in surface and near-surface environments at TA-54. Soils present on the Pajarito Plateau have extremely variable physical and chemical properties, including particle size, percent calcium carbonate, clay mineralogy, iron oxides, and trace element chemistry (Longmire et al. 1995). These properties influence the adsorption of potential contaminants that may be released to soils. Variations of element concentrations in soils are related to climate, topography, and to the parent materials, which include alluvial fans, sheet wash material, colluvium, wind-blown sediment, El Cajete pumice, and the Bandelier Tuff. Soils have higher concentrations of aluminum (Al), arsenic (As), barium (Ba), Ca, Cs, Co, chromium (Cr), and iron (Fe) than Bandelier Tuff samples because of the soil's higher sorptive capacity (Longmire et al. 1995). Bandelier Tuff has higher concentrations of beryllium (Be), lead (Pb), Na, potassium (K), thorium (Th), and U than the soils because of element partitioning during eruptive episodes.

A well-developed B horizon is a dominant characteristic of well-developed soil profiles. The B horizon contains a greater abundance of clay minerals and iron oxides than the A and C horizons. Clay minerals and iron oxides have relatively high surface areas that increase the adsorption capacity of a well-developed B horizon for trace elements. The B horizon contains higher concentrations of trace elements compared with A and C horizons. Distributions of the trace elements Th and U in soil horizons and in the Bandelier Tuff suggest that there has been little migration of these two elements from the soils.

TABLE 6

ANALYTICAL RESULTS OF WATER CANYON GALLERY GROUNDWATER, LOS ALAMOS, NEW MEXICO, AND WELL J-13 GROUNDWATER, YUCCA MOUNTAIN, NEVADA[a]

Element/Parameter	Water Canyon Gallery	Well J-13
Temperature (C)	11.3	31.0
pH (field)	7.6	6.9
Total dissolved solids	106[b]	278
Al	0.2[b]	0.03[b]
Ca	6.94[b]	11.5[b]
Cl	0.69[b]	6.4[b]
F	0.06[b]	2.1[b]
Fe	0.05[b]	0.04[b]
HCO_3	44.6[b]	124[b]
K	1.79[b]	5.3[b]
Mg	2.79[b]	1.76[b]
Na	4.9[b]	45[b]
NO_3 (N)	0.98[b]	0.23[b]
SiO_2	39.8[b]	64[b]
SO_4	2.85[b]	18.1[b]

a. Groundwater chemistry of Well J-13 is summarized by Thomas (1987). Input data for model simulations (speciation and mineral saturation index calculations) are described in the text using results of chemical analyses from Water Canyon Gallery, Los Alamos, New Mexico.

b. Concentration units reported in mg solute per kilogram water.

4.3.1 Element-Radionuclide Adsorption Behavior

Radionuclide-contaminated waste present in pits occurs as metals, cellulosics (cardboard), concrete, soil, and sludge. We assume that all radionuclides will be released from the waste forms and that partial sorption will only occur onto surfaces of pit fill material, Bandelier Tuff, and other hydrogeologic media. This assumption is applied to the geochemical-solute transport modeling because there is no site-specific data relevant to waste form radionuclide chemistry. In reality, some amount of each radionuclide will remain within or adsorbed onto waste-form surfaces.

Numerous batch and column adsorption studies of elements of concern and their associated radionuclides onto volcanic tuff have been performed at Yucca Mountain (Triay

et al. 1994, Wolfsberg 1980, Thomas 1987, Nitsche et al. 1993, Fuentes et al. 1987). Results of these investigations were used to select average values for batch K_D measurements, assuming that the Bandelier Tuff is the only reactive medium. Batch K_D or R_D values for Am, Cs, Np, Pu, Sr, Tc, and U were experimentally determined by Triay et al. (1994) and Wolfsberg (1980) using the following equation.

$$K_D = \frac{\text{moles or activity of radionuclide per g of solid phase}}{\text{moles or activity of radionuclide per ml of solution}} \quad . \qquad (4)$$

Other K_D values were selected from other literature references.

The dimensions for Equation (4) are $[M/M/M/L^3]$ or $[L^3/M]$, and the units of Equation (4) used in this report are ml/g or cm^3/g. R_D is the same as K_D, except that no approach to equilibrium is assumed. Average K_D values for the different elements are summarized in Table 7. Wolfsberg (1980) points out that, in an equilibrium situation, identical values for sorption should be obtained for all conditions intermediate between all activity initially on the solid (desorption) and all activity initially in solution (sorption). Wide ranges of sorption values for Cs and Sr are summarized in Wolfsberg (1980). Sorptive properties of the tuff vary with the abundance and composition of primary and secondary minerals, glass, and lithic fragments. Ranges of selected K_D values for Cs, Np, Sr, Pu, and U measured on devitrified tuff (Yucca Mountain) are summarized in Table 8.

Rundberg (1987) reports that Cs and Sr adsorb onto Yucca Mountain tuffs with moderately high K_D values and rapid kinetics. This suggests that the sorption kinetics for Cs and Sr are sufficiently fast so that equilibrium is reached for the retardation of these two elements under groundwater-flow velocities that would be reasonable for solute-transport simulations (Rundberg 1987). Rate constants for these two elements were high (for Cs, κ_1 ranged between 5.9×10^{-2} and $4.0 \times 10^{-1} s^{-1}$ and κ_2 ranged between 4.2×10^{-5} and $1.4 \times 10^{-4} s^{-1}$; for Sr, κ_1 ranged between 1.1×10^{-3} and $9.5 \times 10^{-3} s^{-1}$ and κ_2 ranged between 6.7×10^{-6} and $2.0 \times 10^{-7} s^{-1}$). The parameters, κ_1 and κ_2, are the rate constants of forward and backward reactions, respectively. The time-dependent sorption data suggest a two-step diffusional model, where diffusion inside the intracrystalline channels of zeolites and clay minerals proceeds much more slowly than does diffusion in the intercrystalline pore space (Rundberg 1987). The adsorption process at mineral surfaces, however, was rapid in the experiments simulating porous-media flow. However, the kinetics of adsorption under fracture-flow conditions are not well understood.

The actinides, specifically Pu, exhibit a slow time dependence for adsorption (Rundberg 1987). This effect is shown in Table 8, where the desorption K_D values for Am, Pu, and U are within a factor of 17 (greater than the adsorption K_D values for these elements). Rate constants κ_1 (6.37 x 10-7 s^{-1}) and κ_2 (6.37 x 10-9 s^{-1}) for Pu are smaller than the rate constants for Cs and Sr (Rundberg 1987). These higher desorption K_D values, however, may be reflective of mineral precipitation in addition to sorption reactions.

TABLE 7

AVERAGE SORPTION RATIO, K_D OR R_D (ML/G), FOR VOLCANIC ROCK, YUCCA MOUNTAIN TUFFS, OXIDIZING CONDITIONS, PH 7, 25°C

Element	Devitrified Tuff
Actinium[a]	130
Aluminum[a]	130
Americium[b]	130
Barium[b]	946
Cadmium[c]	80
Californium[a]	130
Carbon[d]	0
Chlorine[d]	0
Cesium[b]	428
Cobalt[e]	0.45
Curium[d]	50
Europium[d]	50
Gadolinium[d]	50
Hafnium[f]	500
Hydrogen (Tritium)[d]	0
Iodine[d]	0
Lead[d]	25
Molydenum[d]	4
Nickel[d]	50
Niobium[d]	100
Palladium[d]	50

a. K_Ds are estimated based on chemical similarities between americium (III) and californium (III), americium (III) and aluminum (III), and americium(III) and actinium (III).
b. Wolfsberg 1980
c. Thibault et al. 1990
d. Brookins 1984
e. Polzer et al. 1985
f. Hafnium (IV) is chemically similar to Zr (IV).

TABLE 7 (concluded)

Element	Devitrified Tuff
Plutonium[b]	110
Potassium[c]	15
Protactinium[d]	100
Radium[d]	200
Samarium[d]	50
Selenium[d]	2
Silicon[c]	35
Silver[c]	90
Strontium[b]	116
Neptunium[g]	0.007
Technetium[b]	0.3
Thorium[d]	500
Tin[d]	50
Uranium[b]	1.8
Zirconium[d]	500

b. Wolfsberg 1980
g. Thay et al. 1994
d. Brookins 1984
c. Thibault et al. 1990

The K_D values selected for the Bandelier Tuff (Table 7) represent a conservative set of values for soils forming on the Pajarito Plateau. The soils will have a higher sorptive capacity than the Bandelier Tuff for most of the elements of concern. This is because a higher abundance of geochemically active phases (clay minerals, ferric oxyhydroxide, calcium carbonate, and solid organic matter) is present in well-developed soils found at TA-54 (Davenport 1993) and throughout the Laboratory. In addition, soils have higher surface areas than the Bandelier Tuff, which enhances adsorption processes (Longmire et al. 1995).

Geochemical data for cement were provided by Bradbury and Sarott (1995) for source-term and transport analyses; the data consisted of K_D values for radionuclides measured under oxidizing conditions. These K_D values (Table 9) are the most current and critically reviewed data available from literature. Site-specific adsorption data for cement are not available for TA-54. The K_D values listed in Table 9 represent equilibrium values where

the contaminant has had adequate time to diffuse into all available internal surfaces of the fine-grained hydration gel minerals and related reaction products, such as silica and carbonate phases. These phases may be present within local alkaline conditions that may occur at the interface between alkaline sludge and the pore solution within the unsaturated zone.

TABLE 8

SORPTION AND DESORPTION RATIOS, K_D OR R_D, (ML/G) FOR VOLCANIC ROCK, YUCCA MOUNTAIN TUFFS

Element	Devitrified Tuff (Sorption)
Americium[a]	130
Cesium[a]	150–870
Neptunium[b]	0–3
Plutonium[a]	110
Strontium[a]	53–190
Uranium[a]	1.6–2.2

Element	Devitrified Tuff (Desorption)
Americium[a]	2200
Cesium[a]	310–630
Neptunium[b]	unknown
Strontium[a]	56–200
Plutonium[a]	1100
Uranium[a]	6–13

a. Wollsberg 1980
b. Triay et al. 1994

Krupka and Serne (1995) reviewed and generally agreed with the selected sorption data (Table 9) presented by Bradbury and Sarott (1995). Bradbury and Sarott (1995) provide detailed discussions on waste- and disposed-material-induced processes that influence the extent of sorption of different radionuclides under oxidizing and reducing conditions. We have selected values, based on observed mineralogy (Fe_2O_3, $Fe(OH)_3$, Fe_3O_4), of the sorption data for oxidizing conditions that prevail in the organic-poor unsaturated zone within the Bandelier Tuff.

TABLE 9

AVERAGE SORPTION RATIO, K_D OR R_D, (ML/G) FOR CEMENT [$CA(OH)_2$], OXIDIZING CONDITIONS, PH 12.5, 25°C[a]

Element	Cement
Actinium	2,000
Aluminum	5,000[b]
Americium	5,000
Barium	50.0[b]
Cadmium	500[b]
Californium	5,000[b]
Carbon (CO_3^{2-})	70,000
Cesium	20.0
Chlorine	20.0
Cobalt	100
Curium	5,000
Europium	5,000[b]
Gadolinium	5,000[b]
Hafnium	5,000
Hydrogen (tritium)	0
Iodine	0
Krypton	0
Lead	500
Molybdenum	0.1
Neptunium	5,000
Niobium	500
Nickel	100
Palladium	100
Plutonium	5,000
Potassium	0
Protactinium	5,000
Radium	50.0

a. Bradbury and Sarott 1995

b. Sorption ratios estimated as follows: Si(IV) is chemically similar to Sn(IV); Cd(II) is chemically similar to Pb(II); Ba(II) is chemically similar to Ra(II); and Al (III), Sm (III), Eu(III), Gd(III), and Cf(III) are chemically similar to Am(III). Hafnium (IV) is chemically similar to zirconium (IV).

TABLE 9 (concluded)

Element	Cement
Samarium	5,000[b]
Selenium	0.1
Silicon	1,000[b]
Silver	1.0
Strontium	1.0
Technetium	1.0
Thorium	5,000
Tin	1,000
Uranium	2,000
Zirconium	5,000

b. Sorption ratios estimated as follows: Si(IV) is chemically similar to Sn(IV); Cd(II) is chemically similar to Pb(II); Ba(II) is chemically similar to Ra(II); and Al (III), Sm (III), Eu(III), Gd(III), and Cf(III) are chemically similar to Am(III). Hafnium (IV) is chemically similar to zirconium (IV).

Fracture flow within the Bandelier Tuff and other hydrogeologic units may be significant beneath the pits at MDA G. Burkholder (1976) presents the following equation expressing the distribution coefficient, K_A, on a per unit of surface area basis.

$$K_A = \frac{\text{mass of solute on the solid phase per unit area of solid phase}}{\text{concentration of solute in solution}} \quad . \qquad (5)$$

The dimensions for Equation (5) are $[L^3/M \times M/L^2]$ or [L], and the units of Equation (5) are cm. Surface-area measurements (BET-N^2 gas method) of the Bandelier Tuff range between 0.4981 and 5.3856 cm^2/g (n = 21) with a mean of 1.5599 m^2/g (1.5599×10^4 cm^2/g) (Stephens and Associates 1994a). Using the K_D values listed in Tables 7 and 8 and an average surface area of 1.5599×10^4 cm^2/g for the Bandelier Tuff, K_A values were calculated (Table 10). These K_A values are quite low, suggesting that very little adsorption within fractures is likely based on the small surface area of the Bandelier Tuff.

A retardation equation for fracture flow presented by Freeze and Cherry (1979) is shown as Equation (6).

$$\frac{v}{v_c} = 1 + \frac{2K_A}{b} \quad . \qquad (6)$$

where v is the average flow velocity,
v_c is the average flow velocity of a given contaminant,
K_A is the distribution coefficient per unit of surface area, and
b is the aperture width of the fracture.

The ratio v/v_c is equivalent to the retardation factor. Equation (6) assumes that fracture surfaces are planer; however, some of the fracture surfaces at TA-54 are irregular and contain coatings of calcite, solid organic matter, smectite, kaolinite, and ferric oxyhydroxide(s) (Davenport, 1993). These coatings probably have higher surface areas than the Bandelier Tuff; therefore, the amount of sorption may be greater in filled or lined fractures than in unlined fractures. Fracture widths (parameter b) measured at MDA G consist of median apertures ranging between 0.2 and 0.4 cm (Reneau and Vaniman 1994). The mean fracture aperture on the lower walls of Pit 39 is 0.53 ± 1.11 cm (n = 122), although some fracture openings reached 10 cm in width (Reneau and Vaniman 1994).

Using the K_A values listed in Table 10 and a mean fracture aperture of 0.53 cm, retardation factors were calculated for fractured volcanic rock (Table 11). These retardation factors are quite low, suggesting that elements of concern will migrate at the same rate as water within the fractures.

TABLE 10

RANGES OF SORPTION RATIOS PER SURFACE AREA OF FRACTURED ROCK, K_A[a] (CM) FOR VOLCANIC ROCK, YUCCA MOUNTAIN AND BANDELIER TUFFS[b]

Element	Devitrified Tuff
Americium[c]	0.0083
Carbon	0
Cesium[c]	0.0096–0.0558
Cobalt[d]	0.00003
Iodine[c]	0
Neptunium[e]	0–0.00019
Plutonium[c]	0.0071
Strontium[c]	0.0034–0.0122
Technetium[c]	0.00002
Uranium[c]	0.00010–0.00014

a. $K_A = \frac{\text{mass of solute on the solid phase per unit area of solid phase}}{\text{concentration of solute in solution}}$

b. Average surface area of Bandelier Tuff is 1.5599 x 10^4 cm^2/g (Stephens and Associates 1994a).

c. Wolfsberg 1980

d. Polzer et al. 1985

e. Triay et al. 1994

Sorption and desorption ratios of Cs, Sr, Am, Pu, U, Np, I, Tc, and C are determined from Yucca Mountain tuffs, whereas the sorption ratio for Co is determined from the Bandelier Tuff.

TABLE 11

RANGES OF RETARDATION FACTORS[a] FOR FRACTURED VOLCANIC ROCK, K_A (CM) FOR VOLCANIC ROCK, YUCCA MOUNTAIN AND BANDELIER TUFFS

Element	Devitrified Tuff
Americium[b]	1.0313
Carbon	1.0
Cesium[b]	1.0362–1.2106
Cobalt[c]	1.0001
Iodine[b]	1.0
Neptunium[d]	1–1.0007
Plutonium[b]	1.0268
Strontium[b]	1.0128–1.0460
Technetium[b]	1.0001
Uranium[b]	1.0004–1.0005

a. Sorption and desorption ratios of Cs, Sr, Am, Pu, U, Np, I, Tc, and C are determined from Yucca Mountain tuffs, whereas the sorption ratio for Co is determined from the Bandelier Tuff. The retardation factor is given by $v/v_e = 1 + 2K_A/b$ where v is the average flow velocity, v_e is the average flow velocity of a given contaminant, K_A is the distribution coefficient per unit surface area, and b is the aperture width of the fracture. The mean fracture aperture on the lower walls of Pit 39, MDA G, is 0.53 cm (Reneau and Vaniman 1994).

b. Wolfsberg 1980

c. Polzer et al. 1985

d. Triay et al. 1994

4.3.2 Element-Radionuclide Rock/Water Interactions

The following discussion focuses on rock/water interactions, such as pH, Eh, solution composition, and presence of competing and complexing ligands, that have the greatest impact on the sorption behavior of the elements of concern present in the pits.

Knowledge of the redox conditions in the subsurface beneath MDA G is important. The Eh of solution in a rock/water system can influence the solubility and sorption behavior of a radionuclide. The sorption experiments cited in this report were conducted under relatively oxidizing conditions, which are likely to dominate at MDA G. Under these conditions, sorptive capacities of the Bandelier Tuff are predicted to decrease for U, Pu, Np, and Tc, which are stable in higher oxidation states, based on experimental results reported by Wolfsberg (1980) and Triay et al. (1994). Solubilities of these elements in solid phase are much lower under relatively reducing conditions than they are under relatively oxidizing conditions (Brookins 1988). Oxidizing Eh values should be used in any proposed experimental work and in model simulations.

The effect of ligand competition on the sorptive behavior of some elements of concern may be of secondary importance at MDA G. Radionuclides that adsorb/desorb by ion exchange, including ^{137}Cs and ^{90}Sr, may have higher affinities for ion-exchange sites available in the Bandelier Tuff than the major cations (Na^+, Ca^{2+}, Mg^{2+}, and K^+) present in Pajarito Plateau groundwaters. The sorptive capacities of the Bandelier Tuff for ^{137}Cs and ^{85}Sr, however, could be quite low (^{137}Cs at 0.661 ml/g and ^{85}Sr at 0.224 ml/g) (Polzer et al. 1985).

Changes in pH can have a major effect on the adsorption behavior of U, Pu, Am, and Np, where adsorption is controlled by surface complexation processes. When a net negative surface charge dominates on the adsorbent before the sorption reaction, sorption of cationic complexes is maximized above the pH of point of zero charge (pH_{pzc}). Conversely, when a net positive surface charge dominates on the adsorbent before the sorption reaction, sorption of anionic complexes is maximized below the pH_{pzc}. Anionic complexes of U, Am, Np, Pu, and Tc tend to adsorb less than cationic complexes at pH values greater than the pH_{pzc} for specific adsorbents. Cationic species of the elements of concern adsorb onto smectite and ferric oxyhydroxide to a greater extent than anionic species at pH 7 and higher (Triay et al. 1994, Brookins 1984, GCX 1994). Cationic adsorbates are expected to adsorb onto solid surfaces to a greater extent than anionic adsorbates.

For many of the elements of concern, the value of K_D is in part controlled by competition between the sorbent/surface site and complexing ligands (Cl^-, F^-, CO_3^{2-}, HCO_3^-, PO_4^{3-}, SO_4^{2-}) present in solution and dissociated organic anions such as humic and fulvic acids. By increasing the concentration of a complexing ligand in solution, the value of K_D is typically decreased. Aqueous speciation of elements of concern is provided in Table 12, with the listed values based on spectroscopy and/or thermodynamic calculations. Analytical results of groundwater samples collected on the Pajarito Plateau show that HCO_3^- is the anion found in highest concentration, typically exceeding millimolar concentrations. This ligand is important for radionuclide complexing of Np, Pu, and U in natural solutions (Clark et al. 1995). Increases in ligand concentration, however, may enhance precipitation of the element, e.g., the mineral UO_2CO_3, results in a decrease in solution concentration. Therefore, concentrations of ligands, including HCO_3^-, should be determined in porewaters for geochemical modeling simulations and experimental studies of MDA G.

4.3.3 Element-Radionuclide Solubility Limits

This section discusses solubility limits for the elements of concern in pits at TA-54. Solubilities of the elements of concern will be controlled by the degradation of wastes, e.g., corrosion of metal, breakdown of cardboard, and dissolution of soluble constituents within the concrete. Table 13 provides a summary of solubilities of solid phases for elements C, Sr, and U. Solid phases of U probably occur in waste as U metal and as U(IV) and U(VI). The values for C, Sr, and U are based on Yucca Mountain Project experiments and on thermodynamic calculations using the geochemical code MINTEQA2 (Allison et al. 1991). Solubility of $CoCO_3$ was estimated from thermodynamic data tabulated in Woods and Garrels (1987). These calculations were performed assuming an open system with CO_2 gas ($PCO_2 = 10^{-2.11}$ atm) (Kunkler 1969a, 1969b) to simulate

vadose-zone conditions within the Bandelier Tuff. Measured solubilities were available for Am, Pu, and Np (Triay et al. 1994, Nitsche et al. 1993). Molal solubilities for solid phases (Table 13) containing C, Co, Sr, and U were calculated using analytical results from native (background) groundwater discharging from the Bandelier Tuff in Water Canyon. Analytical results of groundwater collected at the Water Canyon Gallery are provided in Table 6. This native groundwater probably is representative of recharge (noncontaminated) pore water within the pits. Concentrations of Cl, NO_3, and PO_4 are less than 1 mg/kg, suggesting that anthropogenic species are not present. The TDS content is 106 mg/kg, which is relatively low compared to other groundwater samples collected on the Pajarito Plateau (Blake et al. 1995, Adams 1994).

TABLE 12

RESULTS OF SPECIATION INVESTIGATIONS (MEASURED AND CALCULATED) FOR SELECTED ELEMENTS AT PH 7 WITH PCO_2 EQUAL TO $10^{-2.11}$ ATM UNDER OXIDIZING CONDITIONS AT 25°C

Element	Aqueous Species
Americium[a]	$AmCO_3^+$, $Am(CO_3)_2^-$
Carbon[b]	HCO_3^- (35%), $CaHCO_3^+$ (58%)
Cesium	Cs^+
Cobalt[c]	Co^{2+}
Iodine	I^-
Neptunium[a]	NpO_2^+ (46%), $NpO_2CO_3^-$ (54%)
Plutonium[a]	III^+ + polymer, 5%; IV^+, 6%; V^+, 73% ; VI^+, 18%
Strontium[b]	Sr^{2+}
Technetium	TcO_4^-
Tritium	^3HHO
Uranium[b]	$UO_2(CO_3)_2^{2-}$ (81%), $(UO_2)_3(OH)_5^+$ (1%), $UO_2CO_3^0$(16%), $UO_2(CO_3)_3^{4-}$ (2%)

a. Speciation for Am, Np, and Pu were measured by Nitsche et al. (1993), Triay et al. (1994), and GCX (1994).

b. Speciation calculations for C, Sr, and U were performed using the geochemical computer program MINTEQA2 (Allison et al. 1991). Partial pressure of CO_2 gas set equal to $10^{-2.11}$ atmosphere for the computer simulations.

c. Speciation calculations for Co were performed using data from Brookins (1988). Input data for simulations are described in the text using chemical analyses from Water Canyon Gallery discharging from the Bandelier Tuff, Los Alamos, New Mexico.

Table 14 provides a summary of solubilities of solid phases at pH 12 using data provided by Ewart et al. (1989). Geochemical modeling was also performed on specific elements (Se, U, Cd, Al, and Si). The geochemical code MIMTEQA2 was used and equilibium with $Ca(OH)_2$ was assumed (Allison et al. 1991). Solubilities for nonredox sensitive elements are assumed to be constant, provided that the solid-phase controlling element solubility

reported by Ewart et al. (1989), which was measured under reducing conditions, applies for oxidizing conditions at TA-54.

TABLE 13

PRELIMINARY MEASURED AND CALCULATED SOLUBILITIES FOR SELECTED ELEMENTS IN VOLCANIC TUFF AT PH 7, 25°C[a]

Element	Solubility (mol/kg)	Element	Solubility (mol/kg)
Hydrogen	very large	Californium[d]	1.2×10^{-9}
Cesium	large	Europium[d]	1.2×10^{-9}
Strontium[b]	0.0014	Barium[b]	4.5×10^{-5}
Silicon[b]	2.8×10^{-4}	Aluminum[b]	3.5×10^{-11}
Americium[a]	1.2×10^{-9}	Curium[d]	1.2×10^{-9}
Plutonium[a]	2.3×10^{-7}	Protactinium[e]	1.3×10^{-4}
Thorium	1.9×10^{-10}	Radium[c]	5.5×10^{-11}
Samarium[a]	1.2×10^{-9}	Tin[c]	4.3×10^{-37}
Gadolinium[a]	1.2×10^{-9}	Molybdenum	large
Iodine	very large	Silver[b]	5.6×10^{-10}
Uranium[b]	1.1×10^{-4}	Palladium	1.0×10^{-5}
Carbon[a]	0.00034	Chlorine	very large
Technetium	large	Lead[b]	1.6×10^{-6}
Cobalt[c]	1.7×10^{-7}	Niobium[c]	2.0×10^{-54}
Zirconium[c]	1.0×10^{-15}	Selenium[b]	0.0079
Nickel[b]	1.0×10^{-5}	Neptunium[a]	1.3×10^{-4}
Cadmium[b]	5.0×10^{-8}	Actinium[d]	1.2×10^{-9}
Hafnium[c]	1.0×10^{-15}	—	—

a. Solubilities for Am, Np, and Pu were measured by Nitsche et al. (1993), Triay et al. (1994), and GCX (1994).

b. Solubilities for different elements were calculated using the geochemical computer program MINTEQA2 (Allison et al. 1991).

c. Solubilities for elements were calculated from thermodynamic data and redox information presented in Brookins (1988).

d. Solubilities were estimated based on chemical similarities with Am(III).

e. Solubilities were estimated based on chemical similarities with Np(V). Input data for simulations consist of chemical analyses from Water Canyon Gallery discharging from the Bandelier Tuff, Los Alamos, New Mexico.

4.4. Uncertainties and Further Investigations

Geochemical and hydrological processes influencing solute-transport processes in the Bandelier Tuff are extremely complex. Literature values from the Yucca Mountain Project (Triay et al. 1994) for geochemical calculations used in this report are reasonable

estimates for approximating solute transport in volcanic rock. There are uncertainties, however, associated with the application of these data to MDA G, which include

TABLE 14

PRELIMINARY MEASURED AND CALCULATED SOLUBILITIES[a] FOR SELECTED ELEMENTS AT PH 12, 25°C

Element	Solubility (mol/kg)	Element	Solubility (mol/kg)
Hydrogen	very large	Californium[b]	$3x10^{-11}$
Cesium[b]	large	Europium[b]	$1x10^{-10}$
Strontium[b]	$4x10^{-4}$	Barium[b]	$4x10^{-4}$
Silicon[c]	0.118	Aluminum[c]	0.250
Americium[b]	$3x10^{-11}$	Curium[b]	$3x10^{-11}$
Plutonium[b]	10^{-8} to 10^{-10}	Protactinium[b]	$1x10^{-10}$
Thorium[b]	$1x10^{-9}$	Radium[b]	$1x10^{-7}$
Samarium[b]	$1x10^{-10}$	Tin[b]	0.005
Gadolinium[b]	$1x10^{-10}$	Molybdenum[b]	large
Iodine[b]	very large	Silver[b]	$1x10^{-4}$
Uranium[b]	$4x10^{-7}$	Palladium[b]	$1x10^{-7}$
Carbon[b]	$3x10^{-5}$	Chlorine[b]	very large
Technetium[b]	large	Lead[b]	$4x10^{-4}$
Cobalt[d]	$8x10^{-17}$	Niobium[b]	$1x10^{-7}$
Zirconium[b]	$1x10^{-8}$	Selenium[c]	$3x10^{-5}$
Nickel[b]	$1x10^{-7}$	Neptunium[b]	10^{-5} to 10^{-7}
Cadmium[c]	0.069	Actinium	$1x10^{-10}$
Hafnium[e]	$1x10^{-6}$		

a. Input data for simulations consist of chemical analyses from Water Canyon Gallery discharging from the Bandelier Tuff, Los Alamos, New Mexico.

b. Solubility data are from Ewart et al. (1989).

c. Solubilities for Se, U, Cd, Al, and Si were calculated using the geochemical computer program MINTEQA2 (Allison et al. 1991). U(VI) is assumed to be in equilibrium with $CaUO_4$ (personal communication with R. J. Serne on April 26, 1995). Se(IV) is assumed to be in equilibrium with $CaSeO_3 \cdot H_2O$, based on moderate oxidizing conditions and a pore water enriched with Ca^{2+} from the dissolution of portlandite cement. Cd(II) is assumed to be in equilibrium with amorphous $Cd(OH)_2$ under high pH conditions. Al(III) is assumed to be in equilibrium with amorphous $Al(OH)_3$ under high pH conditions. Si(IV) is assumed to be in equilibrium with SiO_2 glass under high pH conditions.

d. Co(II, III) is assumed to be in equilibrium with Co_3O_4, (Brookins 1988) under high pH and oxidizing conditions (Eh = 250 mV).

e. Hafnium (IV) is chemically similar to zirconium (IV).

Solubilities for nonredox sensitive elements are assumed to be constant, provided that the solid phase controlling element solubility reported by Ewart et al. (1989) measured under reducing conditions apply for oxidizing conditions. Log PCO_2 gas set at -5 for model simulations.

application to field conditions at TA-54, laboratory-based sorption investigations as opposed to site-specific field calibrated investigations, mineralogy of waste/waste form(s), chemical characteristics of pore water, and sorption processes for matrix and fracture flow.

Site-specific data are required as input to FEHM (Zyvolski et al. 1988) to obtain the most relevant and meaningful results for the performance assessment. Geochemical data needs for model input using FEHM (Zyvoloski et al. 1988) include sorption isotherm models, consisting of linear (K_D), Freundlich, modified Freundlich, and Langmuir; Henry's Law constants for liquid and vapor species; chemical rate laws using the Arrhenius equation; and solubility data for solid phases. The release of elements-radionuclides from the pits will be controlled by hydraulic flux, pore-water chemistry, mineral solubility, and sorption behavior. Data and information needs to verify and quantify geochemical reactions occurring at MDA G include source-term characterization (types, forms, and amounts of contaminants); source-term geochemistry (mineralogy, speciation, solubility, sorption, pore-water chemistry, and reaction rates); and hydrogeological/geochemical characterization of Bandelier Tuff and other geologic media at the site (mineralogy, fracture distribution, fracture mineralogy, sorption capacity of fracture material, hydraulic conductivity, porosity, and moisture content).

ACKNOWLEDGMENTS

The authors appreciate the reviews of earlier drafts by and helpful discussions with David Rogers, Everett Springer, and Diana Hollis. The work was supported by Contract W-7405-ENG-36.

REFERENCES

Abeele, W. V., "Determination of Relative Hydraulic Conductivity from Moisture Retention Data Obtained in the Bandelier Tuff," Los Alamos Scientific Laboratory report LA-7625-MS (January 1979a).

Abeele, W. V., "Determination of Hydraulic Conductivity in Crushed Bandelier Tuff," Los Alamos Scientific Laboratory report LA-8147-MS (November 1979b).

Abeele, W. V., "Hydraulic Testing of Crushed Bandelier Tuff," Los Alamos National Laboratory report LA-10037-MS (March 1984).

Abeele, W. V., H. R. Fuentes, and J. Hosch, "Characterization of Soil Moisture Characteristic Curves in the 30 to 1000 kPa Tension Range for Bandelier Tuff in Waste Disposal Areas G and L, Technical Area 54, Los Alamos National Laboratory," Los Alamos National Laboratory report LA-UR-86-4360 (September 1986).

Abeele, W. V., M. L. Wheeler, and B. W. Burton, "Geohydrology of Bandelier Tuff," Los Alamos National Laboratory report LA-8962-MS (October 1981).

Abrahams, J. H., Jr., "Physical Properties of and Movement of Water in the Bandelier Tuff, Los Alamos and Santa Fe Counties, New Mexico," US Geological Survey Administrative Release, Albuquerque, NM (January 1963).

Allison, J. D., D. S. Brown, and K. J. Novo-Gradac, "MINTEQA2/PRODEFA2, A Geochemical Assessment Model for Environmental Systems: Version 3.0 User's Manual," EPA/600/3-91/021 (US Environmental Protection Agency, Athens, Georgia, 1991).

Baltz, E. H., J. H. Abrahams, Jr., and W. D. Purtymun, "Preliminary Report on the Geology and Hydrology of Mortandad Canyon near Los Alamos, New Mexico, with Reference to Disposal of Liquid Low-Level Radioactive Waste," USGS Open-File Report, Albuquerque, New Mexico (March 1963).

Bear, J., *Dynamics of Fluids in Porous Media* (American Elsevier Publishing, New York, 1972).

Berner, U. R., "Evolution of Pore Water Chemistry During Degradation of Cement in A Radioactive Waste Repository," *Waste Management* 12, 201–219 (1992).

Blake, W. D., F. Goff, A. I. Adams, and D. Counce, "Environmental Geochemistry for Surface and Subsurface Waters in the Pajarito Plateau and Outlying Areas, New Mexico," Los Alamos National Laboratory report LA-12912-MS (1995).

Bradbury, M. H. and F. A. Sarott, "Sorption Databases for the Cementatious Near-Field of a L/ILW Repository for Performance Assessment," (Paul Scherrer Institut, 1995) PSI Bericht Nr. 95-06.

Brookins, D. G., *Geochemical Aspects of Radioactive Waste Disposal* (Springer-Verlag, New York, 1984).

Brookins, D. G., *Eh-pH Diagrams for Geochemistry* (Springer-Verlag, New York, 1988).

Broxton, D. E. and P. G. Eller (eds.), "Earth Science Investigations for Environmental Restoration—Los Alamos National Laboratory Technical Area 21," Los Alamos National Laboratory report LA-12934-MS (June 1995).

Broxton D. and S. Reneau, "Stratigraphic Nomenclature of the Bandelier Tuff for the Environmental Restoration Project at Los Alamos National Laboratory," Los Alamos National Laboratory report LA-13010-MS (1995).

Broxton, D. E., C. LaDelfe, S. J. Chipera, and E. C. Kluk, "Stratigraphy, Mineralogy and Chemistry of Bedrock Tuffs at Mesita del Buey, Los Alamos National Laboratory, New Mexico," Los Alamos National Laboratory report (in progress).

Broxton, D. E., G. Heiken, S. J. Chipera, and F. M. Byers Jr., "Stratigraphy, Petrography, and Mineralogy of Tuffs at Technical Area 21, Los Alamos National Laboratory, New Mexico": in "Phase Report 1A, TA-21 Operable Unit RCRA Facility Investigation," Los Alamos National Laboratory report LA-UR-93-2028 (1995) pp. A1-A18.

Burkholder, H. C., "Methods and Data for Predicting Nuclide Migration in Geologic Media," in International Symposium Management of Wastes from the LWR Fuel Cycle, Denver, Colorado (1976).

Caporuscio, F. A., "Description of Rock Units in Drill Core at TA-54 Los Alamos National Laboratory," letter report (June 1994).

Clark, D. L., D. E. Hobart, and M. P. Neu, "Actinide Carbonate Complexes and Their Role in Actinide Environmental Chemistry," *Chem. Rev.* (1995), in press.

Conca, J. L. and J. Wright, "Direct Determination s of Unsaturated Flow and Transport," in Proceedings of the Twelfth Annual American Geophysical Union Hydrology Days Meeting (Hydrology Days Publications, Fort Collins, Colorado, March 1992).

Cooper, J. B., W. D. Purtymun, and E. C. John, "Records of Water-Supply Wells Guaje Canyon 6, Pajarito Mesa 1, and Pajarito Mesa 2, Los Alamos, New Mexico, Basic Data Report" USGS Administrative Release, Albuquerque, New Mexico (July 1965).

Crowe, B., G. Linn, G. Heiken, and M. Bevier, "Stratigraphy of the Bandelier Tuff in the Pajarito Plateau, Applications to Waste Management," Los Alamos National Laboratory report LA-7225-MS (1978).

Davenport, D. W., "Micromorphology, Mineralogy, and Genesis of Soils and Fracture Fills on the Pajarito Plateau, New Mexico," Ph. D. Dissertation, Texas Tech University (1993).

Devaurs, M., "Core Analyses and Observation Well Data from Mesita del Buey Waste Disposal Areas and in Adjacent Canyons," Los Alamos National Laboratory report LA-UR-85-4003 (1985).

Devaurs, M. and W. D. Purtymun, "Hydrologic Characteristics of the Alluvial Aquifers in Mortandad, Cañada del Buey, and Pajarito Canyons," Los Alamos National Laboratory report LA-UR-85-4002 (1985).

Ewart, F. T, S. Y. Pugh, S. J. Wisbey, and D. R. Woodwark, "Chemical and Microbial Effects in the Near Field: Current Status 1989," Harwell Laboratory, UKAEA, report G/111, (1989).

Freeze, R. A. and J. A. Cherry, *Groundwater*, (Prentice-Hall, Inc., Englewood Cliffs, New Jersey, 1979).

Fuentes, H. R., W. L. Polzer, J. Gruber, B. Lauctes, and E. H. Essington, "Preliminary Report on Sorption Modeling," Los Alamos National Laboratory report LA-10952-MS, (1987).

Gardner, J. N., T. Kolbe, and S. Chang, "Geology, Drilling, and Some Hydrologic Aspects of Seismic Hazards Program Core Holes, Los Alamos National Laboratory, New Mexico," Los Alamos National Laboratory report LA-12460-MS (January 1993).

GCX, "Groundwater Compositional Parameters Most Critical to the Sorption Behavior of Radionuclides-Of-Concern to the Yucca Mountain Project Milestone 4032 Letter Report," prepared for Los Alamos National Laboratory and Yucca Mountain Site Characterization Office (1994).

Goff, F., "Geologic Map of Technical Area 21," in "Earth Science Investigation for Environmental Restoration, Los Alamos National Laboratory Technical Area 21," D. E. Broxton and P. G. Eller, eds., Los Alamos National Laboratory report LA-12934-MS (1995).

Griggs, R. L., "Geology and Groundwater Resources of the Los Alamos Area, New Mexico, with a section of Quality of Water (John D. Hem)," US Geological Survey Water-Supply Paper 1753 (1964).

Heiken, G., F. Goff, J. N. Gardner, W. S. Baldridge, J. B. Hulen, D. L. Nielson, and D. Vaniman, "The Valles/Toledo Caldera Complex, Jemez Volcanic Field, New Mexico," in *Annual Review of Earth Planetary Science*, Vol. 18, pp. 27-53 (1990).

Kearl, P. M., J. J. Dexter, and M. Kautsky, "Vadose Zone Characterization of Technical Area 54, Waste Disposal Areas G and L, Los Alamos National Laboratory, New Mexico. Report 3: Preliminary Assessment of the Hydrogeologic System," Bendix Field Engineering Corp., Grand Junction Operations, Colorado, report GJ-44 (March 1986a).

Kearl, P. M., J. J. Dexter, and M. Kautsky, "Vadose Zone Characterization of Technical Area 54, Waste Disposal Areas G and L, Los Alamos National Laboratory, New Mexico. Report 4: Preliminary Assessment of the Hydrologic System Through Fiscal Year 1986," UNC Technical Services, Inc., Grand Junction, Colorado, report GJ-54 (December 1986b).

Klute, A., "Water Retention: Laboratory Methods," in *Methods of Soil Analysis, Part 1. Physical and Mineralogical Methods, Agronomy Monograph No. 9* (American Society of Agronomy-Soil Science Society of America, 1986), pp. 635-662.

Krupka, K. M. and R. J. Serne, "Performance Assessment of Low-Level Radioactive Waste Disposal Facilities: Effects on Radionuclide Concentrations by Cement/Ground-Water Interactions," Earth and Environmental Sciences Center, Pacific Northwest Laboratory, Richland, WA, Draft Document NUREG/CR, (1995).

Kunkler, J. L., "The Sources of CO_2 in the Zone of Aeration of the Bandelier Tuff Near Los Alamos, New Mexico," US Geological Survey Professional Paper 650-B (1969a), B185-B188.

Kunkler, J. L., "Measurement of Atmospheric Pressure and Subsurface-Gas Pressure in the Unsaturated Zone of the Bandelier Tuff, Los Alamos, New Mexico," US Geological Survey Professional Paper 650-D, (1969b), D283-D287.

LANL, "RFI Report for PRS 54-006," Los Alamos National Laboratory report (in progress).

LANL, "RFI Work Plan for Operable Unit 1098, Environmental Restoration Program," Los Alamos National Laboratory report LA-UR-92-3825 (May 1993).

Longmire, P., C. Duffy, and S. Reneau, "Preliminary Background Elemental Concentrations in Bandelier Tuff and Selected Soil Series, 1993," unpublished report, Los Alamos National Laboratory (1993).

Longmire, P., S. Reneau, P. Watt, L. McFadden, J. Gardner, C. Duffy, and R. Ryti, "Natural Background Geochemistry, Geomorphology, and Pedogenesis of Selected Soil Profiles and Bandelier Tuff, Los Alamos, New Mexico," Los Alamos National Laboratory report LA-12913-MS (1995) in press.

Los Alamos Technical Associates, "Assessment of Potential Shallow Groundwater Transport of Radionuclides at Critical Experiment Facility, TA-18, Los Alamos National Laboratory," (January 1991).

Martens, S. and F. Barnes, "Report on Activities for the Pilot Program for Root Distribution Studies FY 93," Los Alamos National Laboratory memorandum ESH15-93-533 to D. A. Neeper (September 1993).

Meijer, A., "Far-Field Transport of Carbon Dioxide: Retardation Mechanisms and Possible Validation Experiments," *in Proceedings of the Topical Meeting Site Characterization and Model Validation Focus '93, September 26-29, 1993, Las Vegas, Nevada* (American Nuclear Society, La Grange Park, Illinois) (1993), 110-112.

Mualem, Y., "A New Model for Predicting the Hydraulic Conductivity of Unsaturated Porous Media," *Water Resources Research* 12, 512–522 (1976).

Nitsche, H., R. C. Gatti, E. M. Standifer, S. C. Lee, A. Muller, T. Prussin, R. S. Deinhammer, H. Maurer, K. Becraft, S. Leung, and S. A. Carpenter, "Measured Solubilities and Speciations of Neptunium, Plutonium, and Americium in a Typical Groundwater (J-13) from the Yucca Mountain Region, Milestone Report 3010-WBS 1.2.3.4.1.3.1," Los Alamos national Laboratory report LA-12562-MS (1993).

Polzer, W. L., H. R. Fuentes, E. H. Essington, and F. R. Roensch, "Equilibrium Sorption of Cobalt, Cesium, and Strontium on Bandelier Tuff: Experiments and Analysis," Waste Management 1985 (1985), 175-181.

Polzer, W. L., M. G. Rao, H. R. Fuentes, and R. J. Beckman, "Thermodynamically Derived Relationships Between the Modified Langmuir Isotherm and Experimental Parameters," *Environmental Science and Technology*, **26**, 1780–1786 (1992).

Purtymun, W. D., "Hydrologic Characteristics of the Main Aquifer in the Los Alamos Area: Development of Ground Water Supplies," Los Alamos National Laboratory report LA-9957-MS (January 1984).

Purtymun, W. D., "Geologic and Hydrologic Records of Observation Wells, Test Holes, Test Well, Supply Wells, Springs, and Surface Water Stations in the Los Alamos Area," Los Alamos National Laboratory report LA-12883-MS (January 1995).

Purtymun, W. D., and J. B. Cooper, "Development of Ground-Water Supplies on the Pajarito Plateau, Los Alamos County, New Mexico," in Geological Survey Research 1969, US Geological Survey Professional Paper No. 650-B, pp. B149-B153 (1969).

Purtymun, W. D. and W. R. Kennedy, "Geology and Hydrology of Mesita del Buey," Los Alamos Scientific Laboratory report LA-4460 (May 1971).

Purtymun, W. D., E. A. Enyart, and S. G. McLin, "Hydrologic Characteristics of the Bandelier Tuff as Determined Through an Injection Well System," Los Alamos National Laboratory report LA-11511-MS (August 1989).

Purtymun, W. D., M. L. Wheeler, and M. A. Rogers, "Geologic Description of Cores from Holes P-3 MH-1 Through P-3 MH-5, Area G, Technical Area 54," Los Alamos National Laboratory report LA-7308-MS (May 1978).

Reneau, S. L. and D. T. Vaniman, "Fracture Characteristics in a Disposal Pit on Mesita del Buey, Los Alamos National Laboratory," Los Alamos National Laboratory unpublished report (March 21, 1994).

Reneau, S. L., T. Kolbe, D. Simpson, J. S. Carney, J. N. Gardner, S. S. Olig, and D. T. Vaniman, "Surficial Materials and Structure at Pajarito Mesa," in "Geological Site Characterization for the Proposed Mixed Waste Disposal Facility, Los Alamos National Laboratory," S. L. Reneau and R. Raymond, eds., Los Alamos National Laboratory report LA-13089-MS (1995).

Rogers, D. B., "Unsaturated Hydraulic Characteristics of the Bandelier Tuff at TA-54," Los Alamos National Laboratory memorandum ESH-18/WQ&H-94-565 (November 17, 1994).

Rogers, D. B. and B. M. Gallaher, "Moisture and Matric Suction Profiles for 1994 MDA G Wells," Los Alamos National Laboratory memorandum ESH-18/WQ&H-94-632 to J. Turin (December 19, 1994a).

Rogers, D. B. and B. M. Gallaher, "Unsaturated Hydraulic Characteristics of the Bandelier Tuff," Los Alamos National Laboratory memorandum ESH-18/WQ&H-94-525 (October 31, 1994b).

Rogers, D. B. and B. M. Gallaher, "The Unsaturated Hydraulic Characteristics of the Bandelier Tuff," Los Alamos National Laboratory report LA-12968-MS (September 1995).

Rogers, M. A., "History and Environmental Setting of LASL Near-Surface Land Disposal Facilities for Radioactive Wastes (Areas A, B, C, D, E, F, G, and T)", Los Alamos Scientific Laboratory report LA-6848-MS, Vol. 1 (June 1977).

Rosenberg, N. D. and H. J. Turin, "Summary of Area G Geology, Hydrology, and Seismicity for Radiological Performance Assessment," Los Alamos National Laboratory report LA-UR-93-3081 (August 1993).

Rundberg, R. S., "Assessment Report on the Kinetics of Radionuclide Adsorption on Yucca Mountain Tuff," Los Alamos National Laboratory report LA-11026-MS (1987).

Science and Engineering Associates, "Data Report: Open Borehole Anemometry and In Situ Gas Permeability Measurements in Boreholes 54-1001 Through 54-1006, Los Alamos Technical Area 54," performed for Los Alamos National Laboratory Contract 9-XZ3-2348K-1 (December 1994; revised March 1995).

Smith, R. L. and R. A. Bailey, "The Bandelier Tuff, a Study of Ash-Flow Eruption Cycles from Zoned Magma Chambers," *Bulletin Volcanique* 29, 83–104 (1966).

Smith, R. L., R. A. Bailey, and C. S. Ross. "Geologic Map of Jemez Mountains, New Mexico: US Geological Survey Miscellaneous Investigations Series, Map I-571, Washington, D.C (1970).

Stephens, D. B. and Associates, "Laboratory Analysis of Soil Hydraulic Properties of Boreholes 54-1001, -1002, -1003, and -1006," subcontract XT1-X1785-1 report prepared for Los Alamos National Laboratory (1994a).

Stephens, D. B. and Associates, "Laboratory Analysis of Soil Hydraulic Properties of SHB Soil Samples," prepared for Los Alamos National Laboratory (August 1994b).

Stephens, D. B. and Associates, "Laboratory Analysis of Soil Hydraulic Properties of PC4 Pressure Plate and SPOC Samples," prepared for Los Alamos National Laboratory (1992a).

Stephens, D. B. and Associates, "Laboratory Analysis of Hydraulic Properties of Volcanic Tuff Samples," report to E. P. Springer for Subcontract 9-XT1-X1785-1, Los Alamos National Laboratory (1991).

Stephens, D. B. and Associates, "Laboratory Analysis of Soil Hydraulic Properties of CDBM 2 and CDBM 3 Samples," report to Alan Stoker for Subcontract 9-XT1-X27EE-1, Los Alamos National Laboratory (1992b).

Thibault, D. H., M. I. Sheppard, and P. A. Smith, "A Critical Compilation and Review of Default Soil Solid/Liquid Partition Coefficients, K_d, for Environmental Assessments," Whiteshell Nuclear Research Establishment report AECL-10125, Pinawa, Manitoba, Cañada ROE 1L0 (1990).

Thomas, K. W., "Summary of Sorption Measurements Performed with Yucca Mountain, Nevada, Tuff Samples and Water from Well J-13," Los Alamos National Laboratory report LA-10960-MS (1987).

Triay, I. R., C. R. Cotter, S. M. Kraus, M. H. Huddleston, S. J. Chipera, and D. L. Bish, "Report on Radionuclide Sorption in Yucca Mountain Tuffs with J-13 Well Water: Neptunium, Uranium, and Plutonium Milestone #3338," Los Alamos National Laboratory draft (1994).

van Genuchten, M. T., "A Closed-Form Equation for Predicting the Hydraulic Conductivity of Unsaturated Soils," *Soil Science Society of America Journal* 44, 892–898 (1980).

van Genuchten, M. T., F. J. Leij, and S. R. Yates, "The RETC Code for Quantifying the Hydraulic Functions of Unsaturated Soils," US EPA report EPA/600/2-91/065 (December 1991).

Vaniman, D. and K. Wohletz, "Results of Geological Mapping/Fracture Studies: TA-55 Area," Los Alamos National Laboratory memorandum EES1-SH90-17. (November 14, 1990)

Vaniman, D. and K. Wohletz, "Revisions to Report EES1-SH90-17," Los Alamos National Laboratory memorandum EES1-SH91-12 (1991).

Weir, J. E., Jr., and W. D. Purtymun, "Geology and Hydrology of Technical Area 49, Frijoles Mesa, Los Alamos County, New Mexico," US Geological Survey Administrative Release, Albuquerque, New Mexico (1962).

Wolfsberg, K., "Sorptive Properties of Tuff and Nuclide Transport and Retardation," in "Evaluation of Tuff as a Medium for Nuclear Waste Repository: Interim Status Report on the Properties of Tuff," J. K. Johnstone and K. Wolfsberg, Eds., Sandia National Laboratory report SAND80-1464 (1980), pp. 39-48.

Woods, T. L. and R. M. Garrels, *Thermodynamic Values at Low Temperature for Natural Inorganic Materials: An Uncritical Summary* (Oxford University Press, New York, 1987).

Zyvoloski, G. A., Z. V. Dash, and S. Kelkar, "FEHM: Finite Element Heat and Mass Transfer Code," Los Alamos National Laboratory report LA-11224-MS (1988).

APPENDIX A
REFERENCE SOURCE LISTING

This appendix is a listing of relevant published and unpublished data sources. Reproductions of each publication are provided along with this report to the principal investigator for the MDA G performance assessment.

Abeele, W. V., "Determination of Hydraulic Conductivity in Crushed Bandelier Tuff," Los Alamos Scientific Laboratory report LA-8147-MS (November 1979).

Abeele, W. V., "Determination of Relative Hydraulic Conductivity from Moisture Retention Data Obtained in the Bandelier Tuff," Los Alamos Scientific Laboratory report LA-7625-MS (January 1979).

Abeele, W. V., "Hydraulic Testing of Crushed Bandelier Tuff," Los Alamos National Laboratory report LA-10037-MS (March 1984).

Abeele, W. V., H. R. Fuentes and J. Hosch, "Characterization of Soil Moisture Characteristic Curves in the 30 to 1000 kPa Tension Range for Bandelier Tuff in Waste Disposal Areas G and L, Technical Area 54, Los Alamos National Laboratory," Los Alamos National Laboratory report LA-UR-86-4360 (September 1986).

Abeele, W. V., M. L. Wheeler, and B. W. Burton, "Geohydrology of Bandelier Tuff," Los Alamos National Laboratory report LA-8962-MS (October 1981).

Abrahams, J. H., Jr., "Physical Properties of and Movement of Water in the Bandelier Tuff, Los Alamos and Santa Fe Counties, New Mexico," U.S. Geological Survey, Albuquerque, NM (January 1963).

Crowe, B. M., G. W. Linn, G. Heiken, and M. L. Bevier, "Stratigraphy of the Bandelier Tuff in the Pajarito Plateau: Applications to Waste Management," Los Alamos Scientific Laboratory report LA-7225-MS (April 1978).

Cushman, R. L., "An Evaluation of Aquifer and Well Characteristics of Municipal Well Fields in Los Alamos and Guaje Canyons, Near Los Alamos, New Mexico," US Geological Survey Water-Supply Paper 1809-D (1965).

Davenport, D. W., "Micromorphology, Mineralogy, and Genesis of Soils and Fracture Fills on the Pajarito Plateau, New Mexico," Ph. D. Dissertation, Texas Tech University (1993).

Department of Energy, "Expansion of Area G, Los Alamos National Laboratory," Department of Energy report DOE/EA-0866, LANL-90-012, Revision 5 (January 1994).

Devaurs, M., "Core Analyses and Observation Well Data from Mesita del Buey Waste Disposal Areas and in Adjacent Canyons," Los Alamos National Laboratory report LS-UR-85-4003 (November 1985).

Devaurs, M. and W. D. Purtymun, "Hydrologic Characteristics of the Alluvial Aquifers in Mortandad, Cañada del Buey and Pajarito Canyons," Los Alamos National Laboratory report LA-UR-85-4002 (1985).

Dransfield, B. J. and J. N. Gardner, "Subsurface Geology of the Pajarito Plateau, Espanola Basin, New Mexico," Los Alamos National Laboratory report LA-10455-MS (May 1985).

Griggs, R. L., "Geology and Groundwater Resources of the Los Alamos Area, New Mexico, with a section of Quality of Water (John D. Hem)," US Geological Survey Water-Supply Paper 1753 (1964).

Kearl, P. M., J. J. Dexter, and M. Kautsky, "Vadose Zone Characterization of Technical Area 54, Waste Disposal Areas G and L, Los Alamos National Laboratory, New Mexico. Report 3: Preliminary Assessment of the Hydrogeologic System," Bendix Field Engineering Corp., Grand Junction Operations, Colorado, report GJ-44, (March 1986).

Kearl, P. M., J. J. Dexter, and M. Kautsky, "Vadose Zone Characterization of Technical Area 54, Waste Disposal Areas G and L, Los Alamos National Laboratory, New Mexico. Report 4: Preliminary Assessment of the Hydrologic System through Fiscal Year 1986," UNC Technical Services, Inc., Grand Junction, Colorado, report GJ-54 (December 1986).

Kearl, P. M., R. J. Zinkl, J. J. Dexter, and T. Cronk, "Air Permeability Measurements of the Unsaturated Bandelier Tuff Near Los Alamos, New Mexico," *J. Hydrology* 117, 225–240 (1990).

Martens, S. and F. Barnes, "Report on Activities for the Pilot Program for Root Distribution Studies FY 93," Los Alamos National Laboratory memorandum ESH15-93-533, to D. A. Neeper (September 1993).

Mayfield, D. and W. R. Hansen, "Surface Reconnaissance Through 1980 for Radioactivity at Radioactive Waste Disposal Area G at the Los Alamos National Laboratory," Los Alamos National Laboratory report LA-9656-MS (March 1983).

Nyhan, J. W., B. J. Drennon, W. V. Abeele, G. Trujillo, W. J. Herrera, M. L. Wheeler, J. W. Booth, and W. D. Purtymun, "Distribution of Radionuclides and Water in Bandelier Tuff Beneath a Former Los Alamos Liquid Waste Disposal Site after 33 Years," Los Alamos National Laboratory report LA-10159-LLWM (July 1984).

Purtymun, W. D., "Underground Movement of Tritium from Solid-Waste Storage Shafts," Los Alamos Scientific Laboratory report LA-5286-MS (May 1973).

Purtymun, W. D., "Hydrologic Characteristics of the Main Aquifer in the Los Alamos Area: Development of Ground Water Supplies," Los Alamos National Laboratory report LA-9957-MS (January 1984).

Purtymun, W. D., E. A. Enyart, and S. G. McLin, "Hydrologic Characteristics of the Bandelier Tuff as Determined Through an Injection Well System," Los Alamos National Laboratory report LA-11511-MS (August 1989).

Purtymun, W. D., F. C. Koopman, S. Barr, and W. E. Clements, "Air Volume and Energy Transfer Through Test Holes and Atmospheric Pressure Effects on the Main Aquifer," Los Alamos National Laboratory report LA-5725-MS (October 1974).

Purtymun, W. D., M. L. Wheeler, and M. A. Rogers, "Geologic Description of Cores from Holes P-3 MH-1 Through P-3 MH-5, Area G, Technical Area 54," Los Alamos National Laboratory report LA-7308-MS (May 1978).

Purtymun, W. D., R. Garde, and R. Peters, "Movement of Fluids and Plutonium from Shafts at Los Alamos, New Mexico," Los Alamos Scientific Laboratory report LA-7379-MS (June 1978).

Rogers, D. B., "Unsaturated Hydraulic Characteristics of the Bandelier Tuff at TA-54," Los Alamos National Laboratory memorandum ESH-18/WQ&H-94-565 (November 17, 1994).

Rogers, D. B. and B. M. Gallaher, "Unsaturated Hydraulic Characteristics of the Bandelier Tuff," Los Alamos National Laboratory memorandum ESH-18/WQ&H-94-525 (October 31, 1994).

Rogers, D. B. and B. M. Gallaher, "Moisture and Matric Suction Profiles for 1994 MDA G Wells," Los Alamos National Laboratory memorandum ESH-18/WQ&H-94-632 to J. Turin, (December 19, 1994).

Rogers, M. A., "History and Environmental Setting of LASL Near-Surface Land Disposal Facilities for Radioactive Wastes (Areas A, B, C, D, E, F, G, and T)", Los Alamos Scientific Laboratory report LA-6848-MS, Vol. I (June 1977).

Rogers, M. A., "History and Environmental Setting of LASL Near-Surface Land Disposal Facilities for Radioactive Wastes (Areas A, B, C, D, E, F, G, and T)", Los Alamos Scientific Laboratory report LA-6848-MS, Vol. II (June 1977).

Rosenberg, N. D. and H. J. Turin, "Summary of Area G Geology, Hydrology, and Seismicity for Radiological Performance Assessment," Los Alamos National Laboratory report LA-UR-93-3081 (August 1993).

Rosenberg, N. D., W. E. Soll, and H. J. Turin, "Potential Transport of PCBs Through Fractured Tuff at Area G," Los Alamos National Laboratory report LA-UR-93-3081 (December 1993).

Springer, E. P. "Modeling of Organic Vapor Movement at Area L Disposal Site Los Alamos, New Mexico," Los Alamos National Laboratory report LA-UR-86-4359 (1986).

Stephens, D. B. and Associates, "Laboratory Analysis of Hydraulic Properties of Volcanic Tuff Samples," report to E.P. Springer for Subcontract 9-XT1-X1785-1, Los Alamos National Laboratory (1991).

Stephens, D. B. and Associates, "Laboratory Analysis of Soil Hydraulic Properties of CDBM 2 and CDBM 3 Samples," prepared for Los Alamos National Laboratory (December 1992).

Stephens, D. B. and Associates, "Preliminary Assessment of Numerical Data Requirements, TA-73 Landfill, Los Alamos, New Mexico," prepared for Los Alamos National Laboratory (November 1993).

Stephens, D. B. and Associates, "Laboratory Analysis of Soil Hydraulic Properties of Boreholes 54-1001, -1002, -1003, and -1006," subcontract XT1-X1785-1 report prepared for Los Alamos National Laboratory (1994).

Stephens, D. B. and Associates, "Laboratory Analysis of Soil Hydraulic Properties of SHB Soil Samples," prepared for Los Alamos National Laboratory (August 1994).

Stephens, D. B. and Associates, "Laboratory Analysis of Soil Hydraulic Properties of G-5 Soil Samples," prepared for Los Alamos National Laboratory (January 1995).

Stephens, D. B., P. M. Kearl, and R. W. Lee, "Hydrogeologic Review for the Environmental Restoration Program at Los Alamos National Laboratory, Los Alamos, New Mexico," prepared for Los Alamos National Laboratory (April 1993).

van Genuchten, M. T., "A Closed-Form Equation for Predicting the Hydraulic Conductivity of Unsaturated Soils," *Soil Science Society of America Journal* 44, 892–898 (1980).

Wenzel, W. J., W. D. Purtymun, J. M. Dewart, and J. C. Rodgers, "Los Alamos Low-Level Waste Performance Assessment Status," Los Alamos National Laboratory report LA-10768-MS (June 1986).

APPENDIX B

IN SITU MOISTURE FOR BANDELIER TUFF STRATIGRAPHY WITHIN THE MATERIAL DISPOSAL AREA G LOCATION

Analytical Techniques for Moisture Determination

Moisture content measurements were performed on core samples from boreholes drilled on Mesita del Buey [Material Disposal Areas (MDAs) G and L] to determine in situ water and to obtain the vertical moisture distribution. The boreholes were drilled in 1993 and 1994 as Environmental Restoration (ER) Project field investigations. The moisture measurements are gravimetric measurements that were performed in three laboratory settings: a fixed radiological analysis laboratory (FRAL), a mobile radiological analysis laboratory (MRAL), and a fixed geotechnical laboratory. The analytical procedure used in the FRAL was to heat 500-gram soil samples for 24 hours in a drying oven at 100°C, weigh the sample, and return the sample to the 100°C oven for an additional 4 hours. The sample weight after the additional 4 hours was compared to the weight after the initial 24 hours. If the weight changed during the 4-hour period, then the sample was heated for an additional 8 to 16 hours until repeated weighing showed zero weight change. The analytical procedure used in the MRAL was heating 10- to 15-gram samples at 200°C for 5 minutes in a Denver Instrument Company Model 1R-100 moisture analyzer. Select core samples sent to the geotechnical laboratory for determination of in situ moisture content on both a gravimetric and volumetric basis were sealed in metal sleeves and Protect Core laminated pouches. The analytical methods used for moisture content determination in the geotechnical laboratory were American Society for Testing and Materials (ASTM) D 2216-90 and ASTM D 4643-87. Analytical results from the geotechnical laboratory are reported in Stephens and Associates (1994, 1995).

The in situ moisture measurements presented here are for core from boreholes located within MDA G, MDA L, and east of MDA L in the proposed expansion area for MDA G. Boreholes located within MDA L and in the proposed expansion area are shown on Figure B-1. Boreholes located in MDA G are shown on Figure B-2. The boreholes at MDA G were a cooperative effort of the Los Alamos National Laboratory Environmental Surveillance Group and the ER Project. Tables B-1 to B-3 present gravimetric moisture content values for analyses in the FRAL and the MRAL. The in situ moisture content profiles at each of the boreholes are presented in Figures B-3 to B-19. The figures report whether analyses were performed by the FRAL or the MRAL. For comparison, Figures B-3, B-4, B-5, B-8, and B-19 also present results from gravimetric measurements in the geotechnical laboratory. The stratigraphy presented on each figure for correlation of units within the Tshirege Member of the Bandelier Tuff is that of Baltz et al. (1963). The stratigraphy of units below the Tshirege follows the correlation of Vaniman and Wohletz (1990) and Vaniman (1991).

Moisture Content Profiles for the Natural Terrain Setting of Mesita del Buey

Boreholes 54-1001, 54-1002, 54-1003, 54-1004, and 54-1005 are located in the proposed expansion area for MDA G. The moisture content profiles within these five boreholes are believed to be similar to moisture content profiles within the range for natural settings.

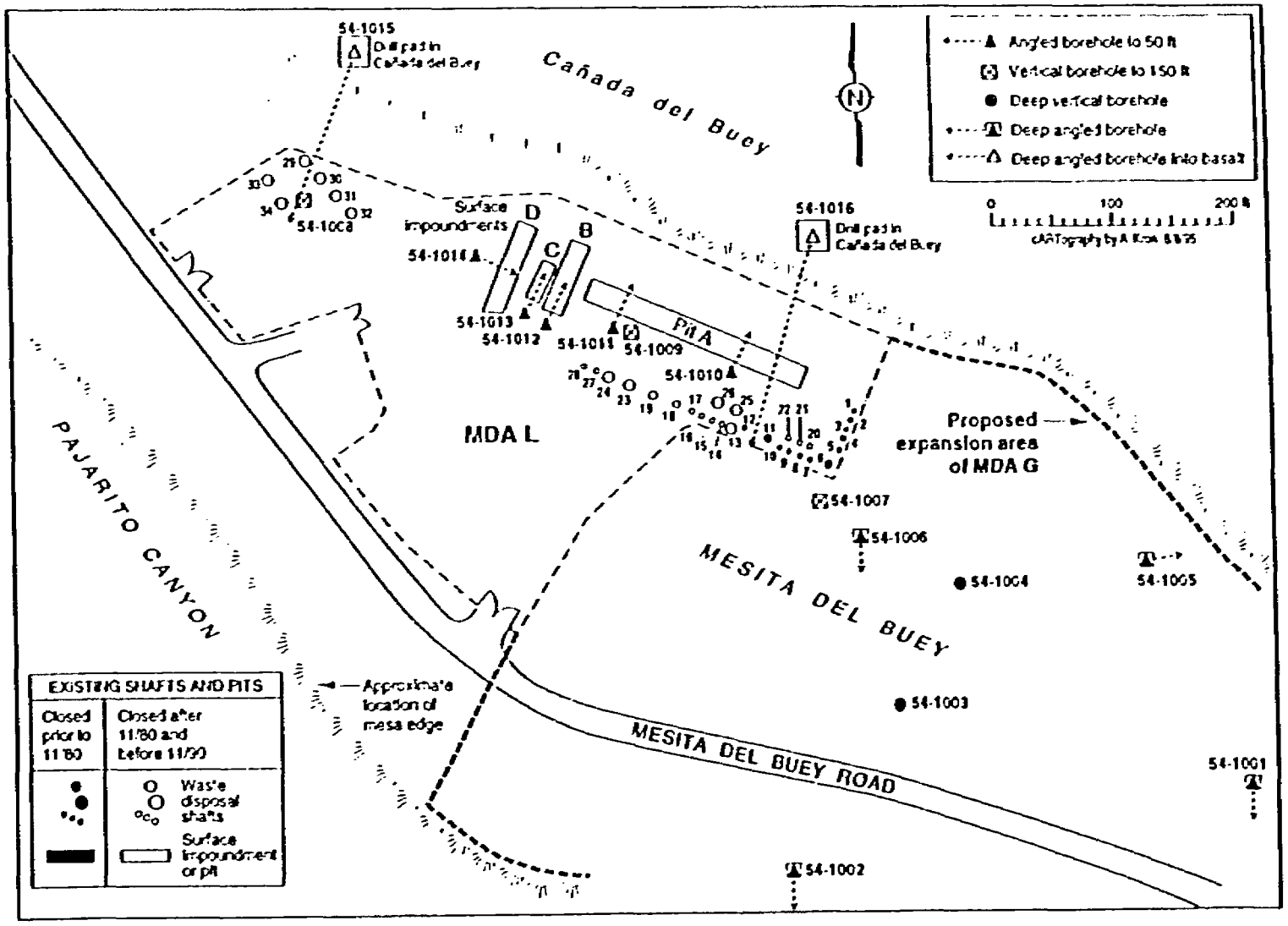

Figure B-1. Boreholes with moisture content profiles located in MDA L and in the proposed expansion area for MDA G.

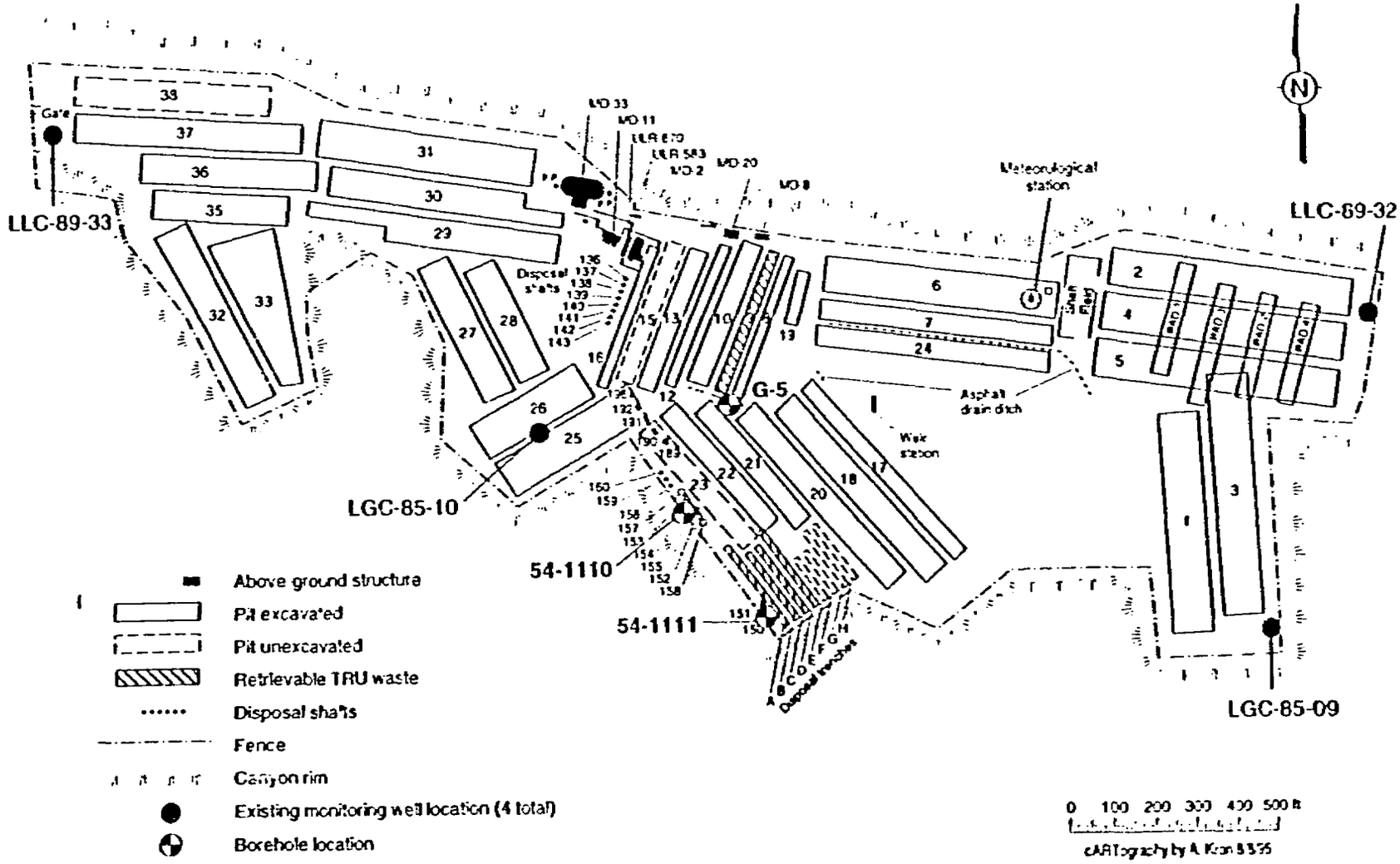

Figure B-2. Location map of boreholes and 54-1110, 54-1111, and G-5.

TABLE B-1

GRAVIMETRIC MOISTURE CONTENT FOR BOREHOLES 54-1001 TO 54-1009

54-1001		54-1002		54-1003		54-1004		54-1005		54-1006		54-1007		54-1008		54-1009	
Depth	%H_2O	Depth	%H_2O	Depth	%H_2O	Depth	%H_2O	Depth	%H_2O	Depth	%H_2O	Depth	%H_2O	Depth	%H_2O	Depth	%H_2O
3.3	1.9	4.3	4.87	4.3.9	0.33	4.4	1.66	4.1	3.37	3.3	3.06	6.3	5.87	2.0	7.86	4.25	6.29
6.5	1.40	8.8	4.17	46.0	0.12	8.8	0.34	9.2	3.34	6.5	1.27	16.25	10.38	5.9	7.14	6.5	5.37
10.4	0.65	13.6	1.82	53.9	0.31	11.7	2.44	13.8	2.55	12.3	0.5	21.15	8.22	11.35	5.29	11.35	5.72
17.8	0.29	15.4	1.42	56.9	0.53	22.1	0.34	18.8	0.65	16.8	0.39	31.5	7.44	15.15	5.13	16.75	4.7
21.1	0.25	22.6	0.35	67.6	0.16	26.0	0.52	29.2	1.15	21.5	1.31	43.1	0.3	21.75	0.39	21.15	5.32
29.1	0.28	27.3	0.39	73.2	0.43	31.5	0.72	32.5	0.67	26.9	2.51	54.8	1.43	25.6	0.69	27.25	5.41
33.25	0.39	32.9	1.06	76.5	0.59	37.9	0.39	37.2	0.63	33.0	4.2	57.9	1.02	31.4	0.39	34.15	3.83
35.0	.0.39	37.0	1.03	81.6	0.66	41.8	1.27	39.1	0.67	36.5	6.1	61.25	1.13	38.5	0.59	35.0	4.36
42.4	0.66	40.2	1.05	86.3	0.86	46.2	1.65	42.2	0.51	43.1	4.17	68.9	2.33	41.15	0.51	44.25	5.6
45.2	0.67	47.4	1.03	30.9	0.39	57.8	1.84	49.8	0.57	45.9	2.3	73.6	1.25	45.7	0.49	46.1	5.01
49.1	0.75	52.4	1.05	95.4	0.82	60.9	1.94	57.3	0.41	51.2	0.31	76.75	1.22	56.25	0.45	51.46	5.45
53.4	1.55	56.8	1.16	103.9	1.37	73.5	2.17	60.9	0.44	56.9	0.87	81.5	1.27	64.45	0.61	59.5	4.54
60.85	1.6	71.6	0.36	106.1	1.87	78.2	2.13	67.5	0.45	63.4	0.3	88.4	1.44	66.5	0.42	66.5	4.91
69.1	1.68	76.7	0.87	110.5	1.64	80.4	2.17	72.1	0.57	68.8	0.51	91.1	1.13	73.95	0.52	83.9	3.83
72.9	1.86	80.4	0.79	115.4	2.32	88.3	2.21	74.5	0.52	71.4	1.45	95.35	1.71	77.0	0.5	94.25	2.54
76.2	2.01	86.6	0.78	123.9	4.5	93.3	2.29	80.1	0.54	78.9	0.64	99.0	1.34	81.15	0.78	97.5	2.4

TABLE 8-1 (continued)

54-1001		54-1002		54-1003		54-1004		54-1005		54-1006		54-1007		54-1008		54-1009	
Depth	%H_2O	Depth	%H_2O	Depth	%H_2O	Depth	%H_2O	Depth	%H_2O	Depth	%H_2O	Depth	%H_2O	Depth	%H_2O	Depth	%H_2O
80.8	2.0	91.7	0.92	125.4	4.02	98.5	2.45	83.5	0.89	80.9	0.71	101.75	2.34	87.75	1.28	101.4	2.92
87.4	2.37	96.9	1.39	135.4	8.64	100.4	2.64	89.3	0.93	86.0	0.24	107.0	2.27	91.1	1.13	139.1	3.69
92.3	2.54	100.2	0.87	145.7	2.87	139.3	3.36	94.3	1.12	91.1	0.82	113.7	5.39	96.35	1.71	114.3	8.19
96.6	3.04	105.5	1.64	149.6	2.53	113.4	5.03	99.3	1.52	96.7	0.36	118.4	5.22	101.75	2.34	118.7	5.59
101.4	3.26	112.5	1.83	153.9	2.36	120.3	4.43	104.7	2.09	101.9	1.11	119.3	5.39	107.5	2.72	124.3	8.44
107.4	3.9	118.5	2.14	159.9	3.68	125.6	8.78	109.1	3.81	109.6	1.56	124.0	6.23	113.95	5.17	125.7	8.38
113.1	3.38	121.1	2.72	163.2	4.32	133.6	4.21	113.1	3.46	118.8	2.34	125.1	5.52	119.3	5.99	131.4	10.67
114.9	4.5	129.9	4.34	168.6	4.5	139.0	2.68	121.8	5.44	123.5	3.46	131.15	13.13	124.0	6.23	136.0	6.38
119.9	6.52	134.3	4.53	173.9	4.36	140.1	2.31	129.1	8.57	125.5	4.13	136.5	4.53	125.75	6.65	141.4	4.22
124.9	7.0	139.4	7.51	179.5	4.25	145.9	2.41	136.7	4.13	131.4	4.39	141.35	3.5	131.15	13.13	146.4	3.77
129.4	6.4	146.6	6.37	180.9	7.12	151.1	3.16	141.2	2.48	136.8	4.75	146.1	2.06	144.0	3.99	—	—
136.8	14.34	151.3	2.78	184.1	4.94	155.3	3.48	147.0	3.77	140.1	6.0	—	—	146.5	3.82	—	—
139.1	14.36	156.1	2.08	189.2	5.45	160.4	3.58	148.8	2.86	143.2	9.24	—	—	—	—	—	—
140.4	12.39	160.5	2.38	194.3	7.1	165.4	4.31	154.3	3.7	149.3	5.74	—	—	—	—	—	—
141.0	5.36	168.3	2.51	198.8	7.47	170.8	5.84	159.3	3.54	153.3	2.76	—	—	—	—	—	—
147.4	4.45	171.1	2.71	201.9	5.81	175.8	5.57	165.5	4.08	159.1	2.23	—	—	—	—	—	—
158.25	4.57	176.3	3.08	212.5	6.08	180.9	6.37	169.9	4.23	163.8	2.31	—	—	—	—	—	—

TABLE B-1 (continued)

54-1001		54-1002		54-1003		54-1004		54-1005		54-1006		54-1007		54-1008		54-1009	
Depth	%H_2O	Depth	%H_2O	Depth	%H_2O	Depth	%H_2O	Depth	%H_2O	Depth	%H_2O	Depth	%H_2O	Depth	%H_2O	Depth	%H_2O
157.1	4.39	180.3	3.58	215.3	5.4	185.8	6.17	174.1	4.95	168.9	2.73	—	—	—	—	—	—
160.4	4.83	185.8	3.81	220.9	6.14	190.6	6.62	179.4	5.3	173.6	2.89	—	—	—	—	—	—
166.0	5.05	196.4	4.53	222.3	6.16	195.9	6.48	185.2	5.21	182.1	3.56	—	—	—	—	—	—
174.4	5.38	200.4	4.55	225.9	5.56	200.9	6.49	189.1	6.02	184.1	3.69	—	—	—	—	—	—
176.0	5.53	206.2	4.98	231.7	5.97	205.8	6.74	197.1	6.39	187.6	4.21	—	—	—	—	—	—
181.0	6.33	210.7	5.1	235.8	6.24	210.8	6.39	201.9	6.99	192.7	4.51	—	—	—	—	—	—
186.0	6.07	215.9	5.12	240.1	5.99	215.7	6.37	204.9	7.02	196.9	5.32	—	—	—	—	—	—
191.0	6.55	223.4	4.98	246.0	6.15	221.4	6.43	209.4	7.35	200.9	5.62	—	—	—	—	—	—
199.4	7.08	226.1	4.96	251.0	6.5	225.7	6.59	214.8	7.52	205.8	5.87	—	—	—	—	—	—
206.9	7.05	230.9	4.81	256.2	6.94	230.3	6.98	221.9	4.37	211.8	5.97	—	—	—	—	—	—
215.0	7.11	235.8	4.98	261.0	10.34	235.6	7.06	227.0	8.30	215.4	6.1	—	—	—	—	—	—
220.0	6.9	240.4	5.12	266.3	4.92	240.4	7.13	229.8	8.14	220.9	6.08	—	—	—	—	—	—
224.4	7.03	245.6	4.9	271.7	7.39	246.1	7.55	237.2	8.48	224.0	6.25	—	—	—	—	—	—
228.9	7.18	250.9	4.94	276.2	11.82	250.9	8.06	236.8	8.55	229.3	6.03	—	—	—	—	—	—
230.0	6.9	255.7	4.89	281.9	11.83	255.1	5.32	245.0	8.30	233.4	6.21	—	—	—	—	—	—
233.8	5.02	266.0	5.15	285.9	13.0	261.1	8.84	250.0	9.08	238.7	6.39	—	—	—	—	—	—
235.0	7.02	270.7	5.23	291.0	10.11	266.4	10.31	257.0	9.22	240.9	6.22	—	—	—	—	—	—

TABLE B-1 (concluded)

54-1001		54-1002		54-1003		54-1004		54-1005		54-1006		54-1007		54-1008		54-1009	
Depth	%H_2O	Depth	%H_2O	Depth	%H_2O	Depth	%H_2O	Depth	%H_2O	Depth	%H_2O	Depth	%H_2O	Depth	%H_2O	Depth	%H_2O
241.0	7.11	275.2	6.56	295.8	4.31	273.5	7.45	259.2	10.12	244.3	6.34	—	—	—	—	—	—
244.4	7.07	278.6	9.32	—	—	278.5	10.68	264.4	13.06	249.1	6.5	—	—	—	—	—	—
249.4	7.18	290.1	16.42	—	—	290.9	12.52	269.2	9.1	254.2	6.14	—	—	—	—	—	—
256.4	7.42	296.1	10.39	—	—	296.0	4.23	278.1	5.97	261.6	5.36	—	—	—	—	—	—
266.4	7.82	291.2	4.62	—	—	295.6	7.58	283.5	11.74	253.8	6.45	—	—	—	—	—	—
276.1	8.47	298.2	13.44	—	—	300.9	6.87	296.2	8.65	299.0	6.97	—	—	—	—	—	—
281.3	12.69	301.1	9.57	—	—	306.1	7.66	289.4	8.85	275.4	6.9	—	—	—	—	—	—
286.2	9.11	306.0	10.19	—	—	316.1	7.68	—	—	277.2	6.8	—	—	—	—	—	—
291.1	9.76	309.2	6.54	—	—	320.9	8.47	—	—	291.1	7.17	—	—	—	—	—	—
295.7	10.64	311.0	10.43	—	—	325.9	8.41	—	—	293.6	7.46	—	—	—	—	—	—
300.2	10.45	312.9	9.08	—	—	331.8	9.33	—	—	295.9	11.71	—	—	—	—	—	—
303.8	7.35	—	—	—	—	336.0	9.51	—	—	296.8	4.48	—	—	—	—	—	—
305.8	7.39	—	—	—	—	—	—	—	—	299.3	3.91	—	—	—	—	—	—
—	—	—	—	—	—	—	—	—	—	296.4	10.35	—	—	—	—	—	—
—	—	—	—	—	—	—	—	—	—	300.6	5.35	—	—	—	—	—	—
—	—	—	—	—	—	—	—	—	—	306.3	6.34	—	—	—	—	—	—
—	—	—	—	—	—	—	—	—	—	310.6	13.17	—	—	—	—	—	—
—	—	—	—	—	—	—	—	—	—	318.2	4.73	—	—	—	—	—	—

TABLE B-2

GRAVIMETRIC MOISTURE CONTENT FOR BOREHOLES 54-1010 THROUGH 54-1014

54-1010		54-1011		54-1012		51-13		54-1014	
Depth	%H_2O	Depth	%H_2O	Depth	%H_2O	Depth	%H_2O	Depth	%H_2O
5.6	7.94	5.4	7.99	5.4	6.11	2.25	12.92	4.85	7.45
9.3	8.01	9.2	7.23	9.6	7.33	4.75	7.85	6.4	7.28
14.4	6.63	14.4	6.25	14.4	7.14	7.25	6.79	11.3	6.74
19.4	8.34	19.2	6.22	19.6	9.45	14.7	6.64	19.2	4.24
24.75	8.15	19.2	5.81	24.4	6.83	17.75	7.91	24.9	2.32
24.75	8.32	24.4	3.8	29.1	2.66	23.45	7.76	29.01	5.55
29.4	5.48	29.1	4.78	34.6	6.75	27.9	8.12	34.6	8.06
34.4	0.71	34.4	7.45	39.1	7.54	34.9	8.69	41.7	4.74
38.75	9.69	39.4	6.61	44.6	10.44	36.5	8.2	44.2	5.57
44.4	10.21	44.6	6.4	49.3	7.09	40.75	7.74	49.5	6.27
49.1	6.14	49.7	6.99	—	—	45.75	8.45	—	—
54.4	6.24	—	—	—	—	49.0	8.42	—	—
59.1	6.01	—	—	—	—	—	—	—	—

Boreholes 54-1006 and 54-1007 are located 60 ft and 25 ft, respectively, southeast of the southeast corner of MDA L. The moisture content profiles in these boreholes are elevated to a depth of approximately 50 ft, as compared to the profiles for natural settings, with the increase possibly due to the physical setting at MDA L.

For these seven boreholes, the gravimetric moisture content profiles for analyses in the FRAL are presented in Figures B-3 to B-9. A brief discussion of the physical setting of each borehole follows. A due-south drilling direction was selected for most deep angled holes because it had the greatest probability of intersecting near-vertical joints and fractures.

Borehole 54-1001. This angled borehole is located approximately 440 ft southeast of MDA L in the proposed expansion area for MDA G. It is drilled at an angle of 22° from vertical to the south to a total drilled depth of 314 ft.

Borehole 54-1002. This borehole is located approximately 330 ft south of the southeast boundary of MDA L in the proposed expansion area for MDA G. It is drilled at an angle of 22° from vertical to the south to a total drilled depth of 310 ft. This borehole was angled toward Pajarito Canyon to investigate the in situ moisture profile on the southern side of the mesa.

TABLE B-3

GRAVIMETRIC MOISTURE CONTENT FOR BOREHOLES 54-1110, 54-1111, AND G-5

54-1110		54-1111		G-5	
Hole Length	%H_2O	Hole Length	%H_2O	Hole Length	%H_2O
3.75	6.49	4.75	24.8	5	7.31
6.75	5.46	9.25	1.41	10.5	7.36
12.65	19	15	0.4	15	6.12
17	7.37	19.75	0.4	21.5	6.38
22.25	5.92	27.5	0.4	25	5.76
27	4.94	29.25	0.4	30	5.25
32.75	0.95	35.5	0.4	35	4.99
37	0.85	38.75	0.3	40	5.6
38.5	0.95	46	0.1	45	6.1
47	1.34	50.75	0.5	50	4.59
51.5	1.13	55.5	0.43	55	0.54
56.5	1.15	60.75	0.64	60	0.77
61.25	1.13	66.5	1.25	65	1.95
69.25	1.49	71.5	1.38	70	3.05
76	3.09	74.25	1.77	75	4.67
78.5	3.46	80.5	4.37	80	6.05
89	3.87	83.5	1.39	85	7.05
91.5	1.69	89.5	1.52	90	10.47
95.5	2.07	95.25	2.87	95	10.09
101.5	2.74	98.75	2.66	100	4.74
—	—	103.75	3.93	103	4.59
—	—	109	4.04	—	—
—	—	113.75	3.76	—	—
—	—	118.5	4.49	—	—
—	—	128.5	4.45	—	—
—	—	133.5	4.62	—	—
—	—	138.5	6.67	—	—
—	—	147.5	5.96	—	—
—	—	152.5	6.11	—	—

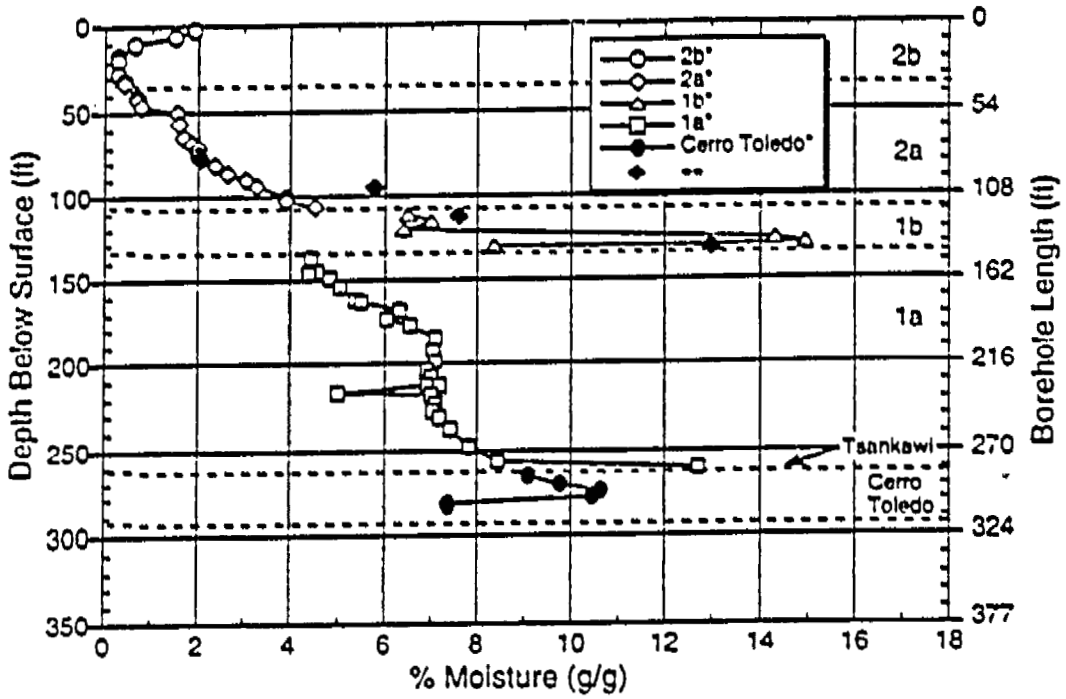

* Data from fixed radiological analysis laboratory
** Data from geotechnical laboratory

Figure B-3. Gravimetric core moisture content from borehole 54-1001 (angled 22°).

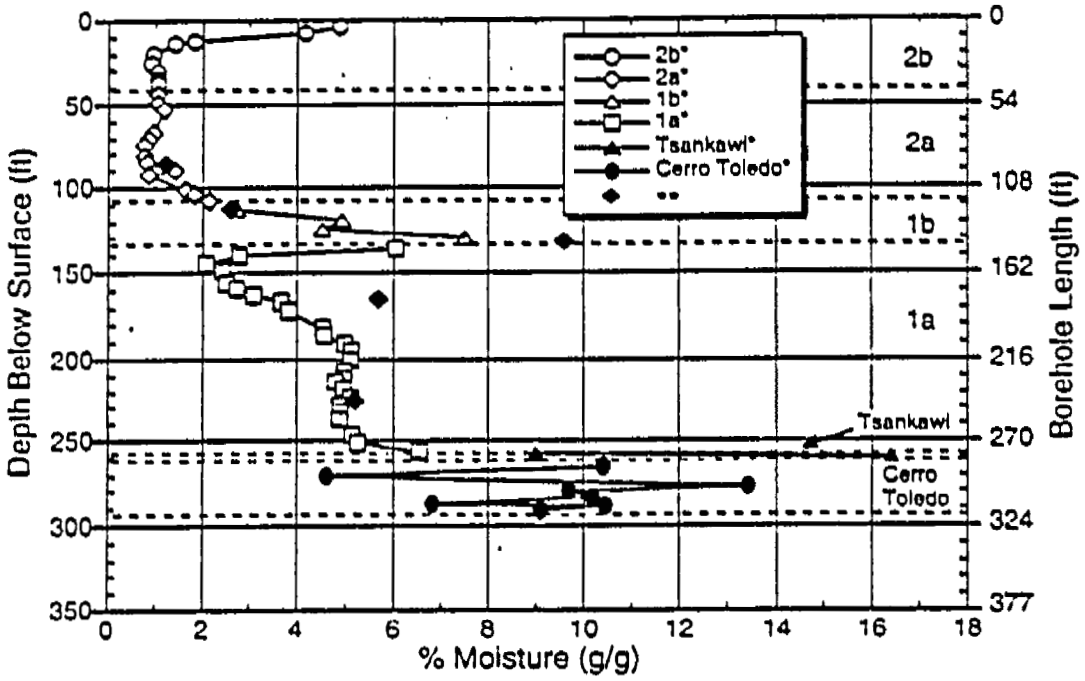

* Data from radiological laboratory
** Data from geotechnical laboratory

Figure B-4. Gravimetric core moisture content from borehole 54-1002 (angled 22°).

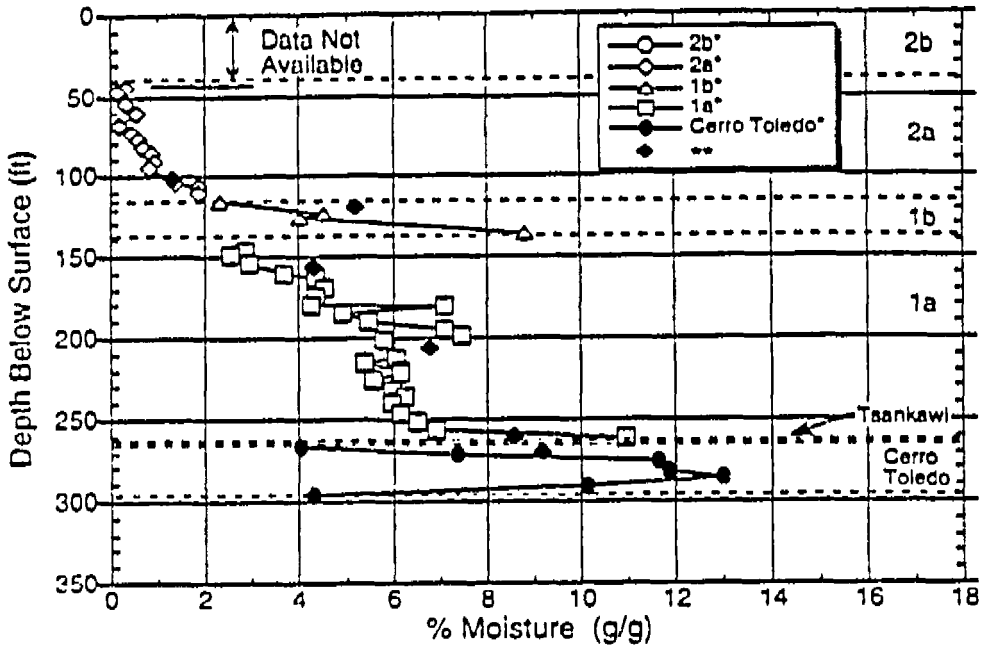

* Data from fixed radiological analysis laboratory
** Data from geotechnical laboratory

Figure B-5. Gravimetric core moisture content from borehole 54-1003 (vertical).

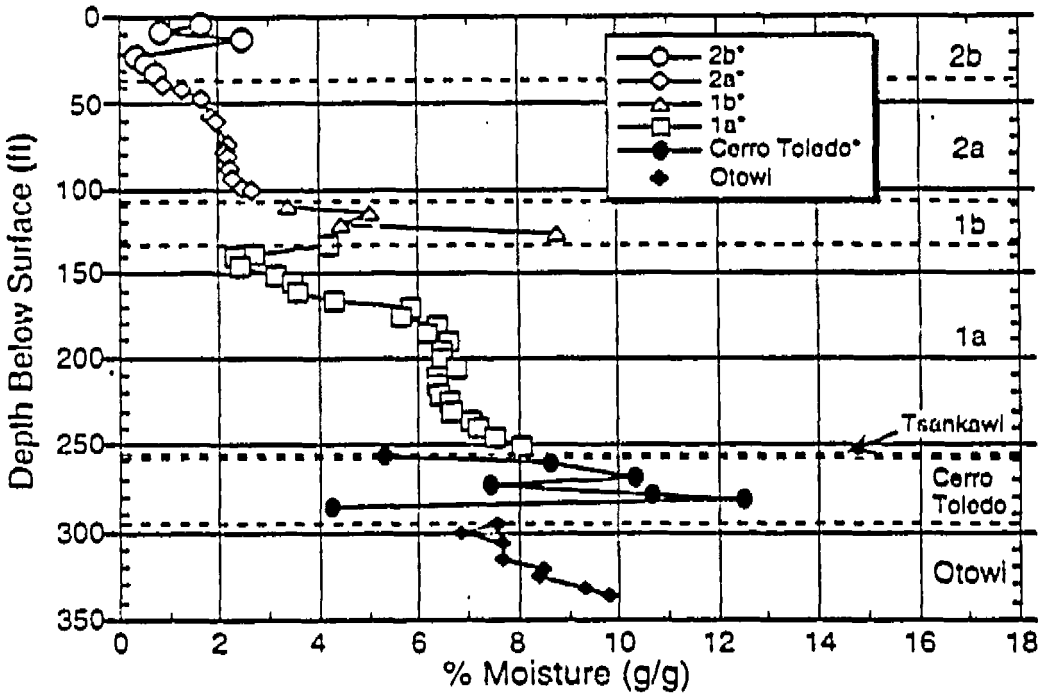

* Data from fixed radiological analysis laboratory

Figure B-6. Gravimetric core moisture content from borehole 54-1004 (vertical).

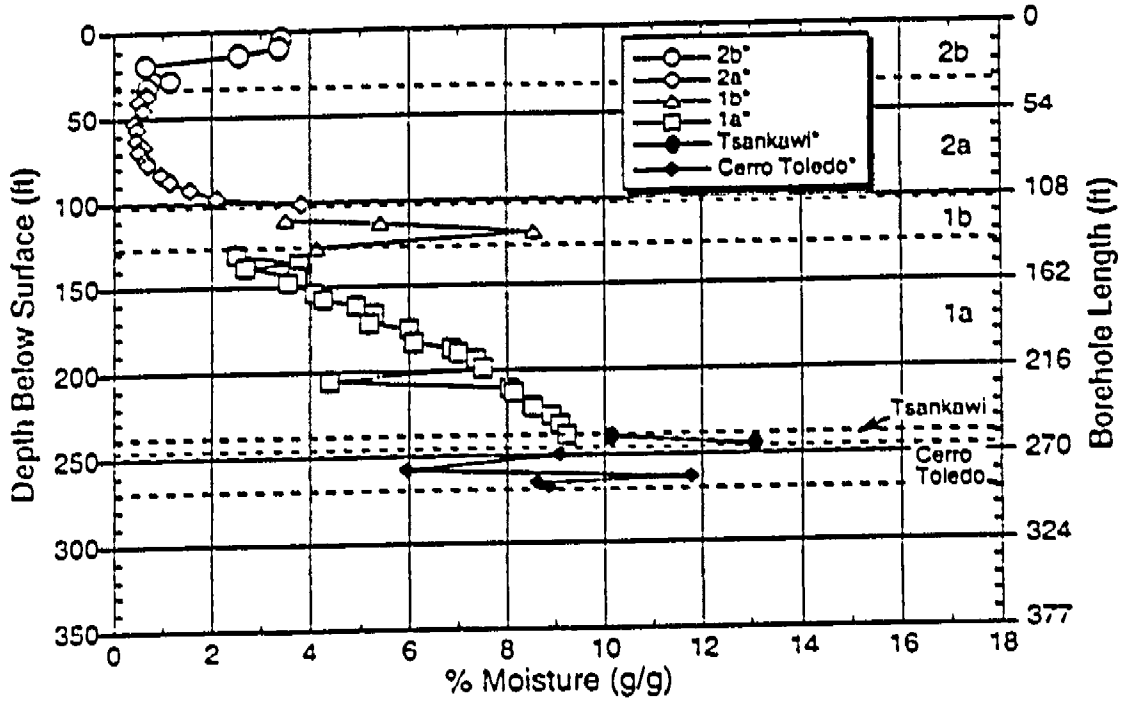

* Data from fixed radiological analysis laboratory

Figure B-7. Gravimetric core moisture content from borehole 54-1005 (angled 22°).

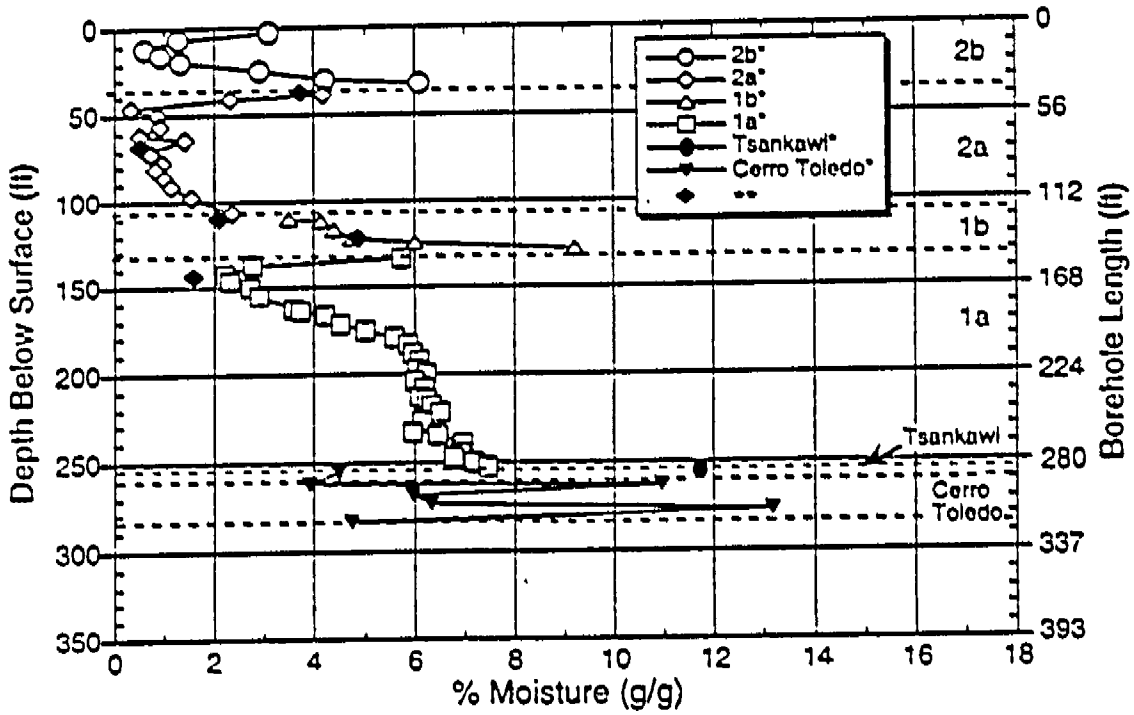

* Data from fixed radiological analysis laboratory
** Data from geotechnical laboratory

Figure B-8. Gravimetric core moisture content from borehole 54-1006 (angled 27°).

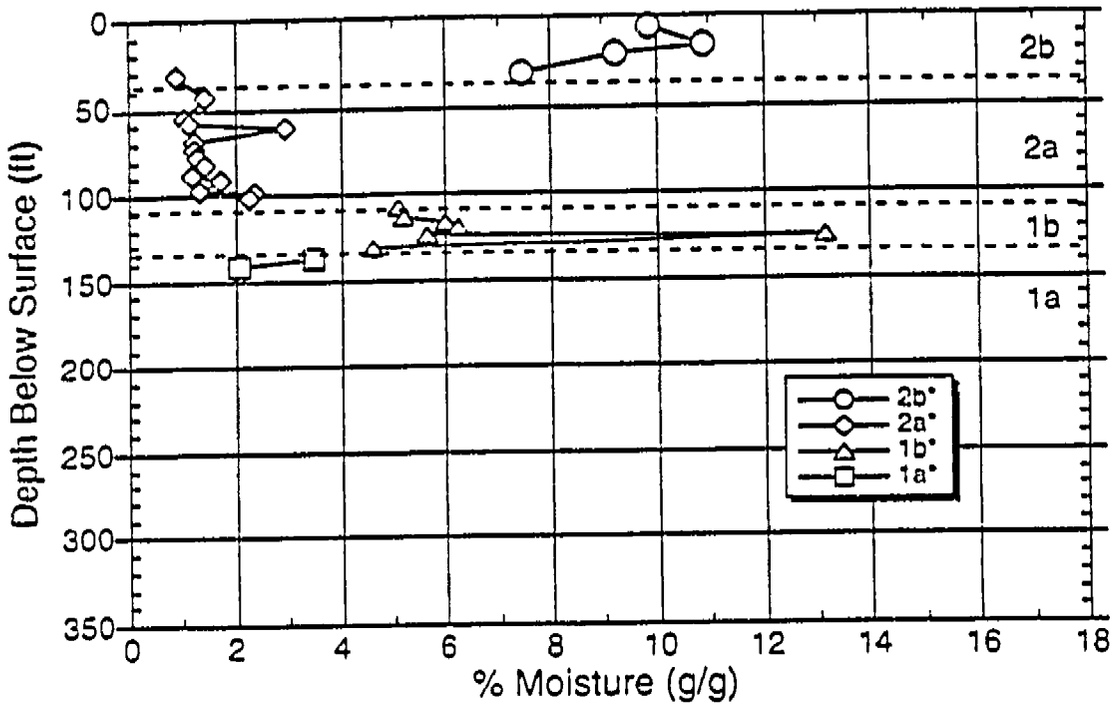

* Data from mobile radiological analysis laboratory

Figure B-9. Gravimetric core moisture content from borehole 54-1007 (vertical).

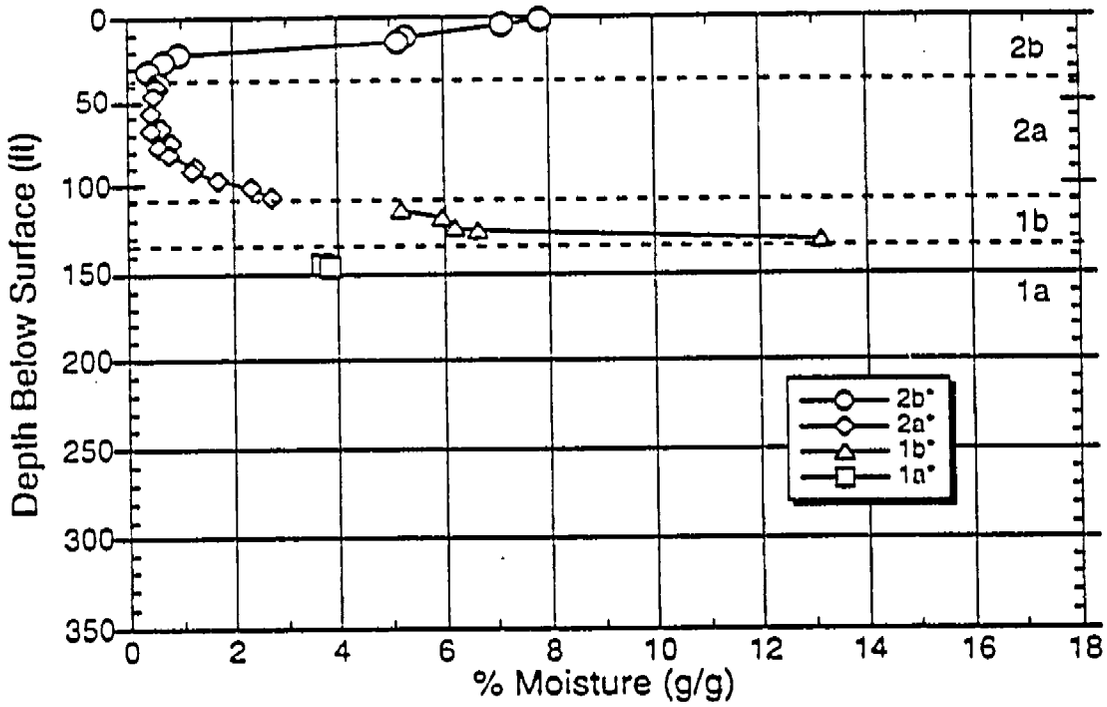

* Data from mobile radiological analysis laboratory

Figure B-10. Gravimetric core moisture content from borehole 54-1008 (vertical).

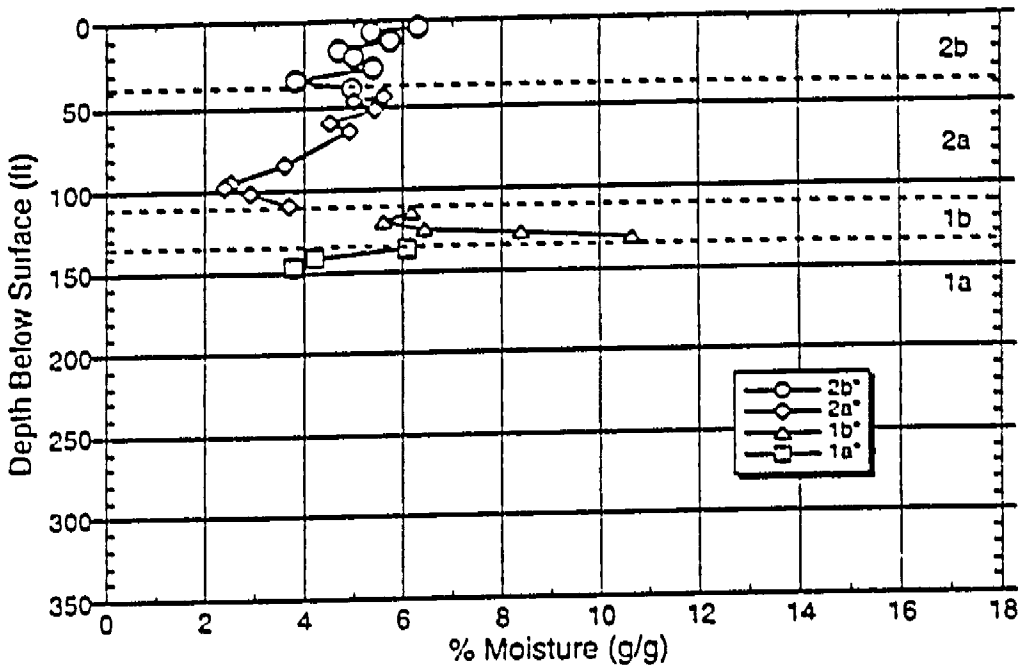

* Data from mobile radiological analysis laboratory

Figure B-11. Gravimetric core moisture content from borehole 54-1009 (vertical).

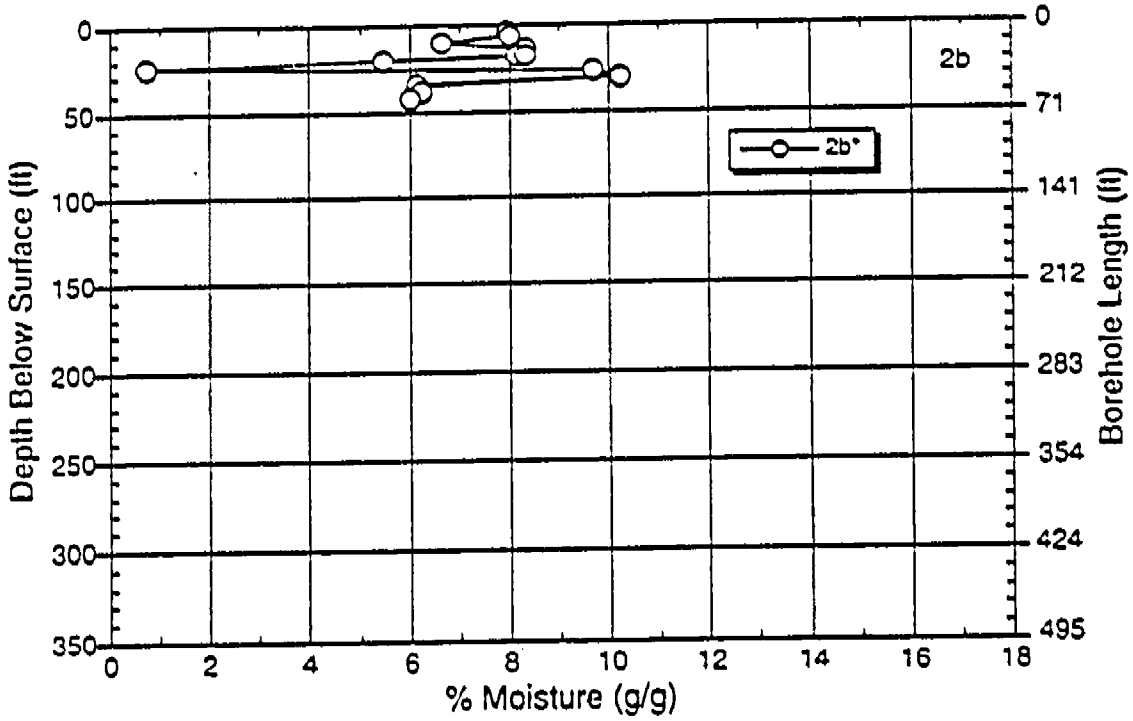

* Data from mobile radiological analysis laboratory

Figure B-12. Gravimetric core moisture content from borehole 54-1010 at MDA L (angled 45° below Pit A).

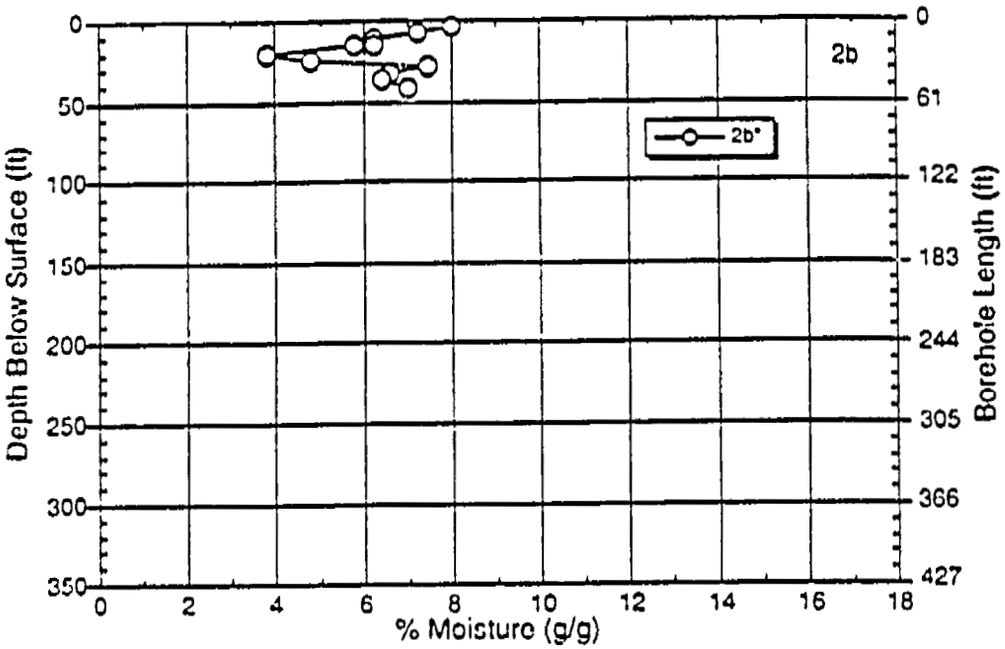

* Data from mobile radiological analysis laboratory

Figure B-13. Gravimetric core moisture content from borehole 54-1011 at MDA L (angled 35° below Pit A).

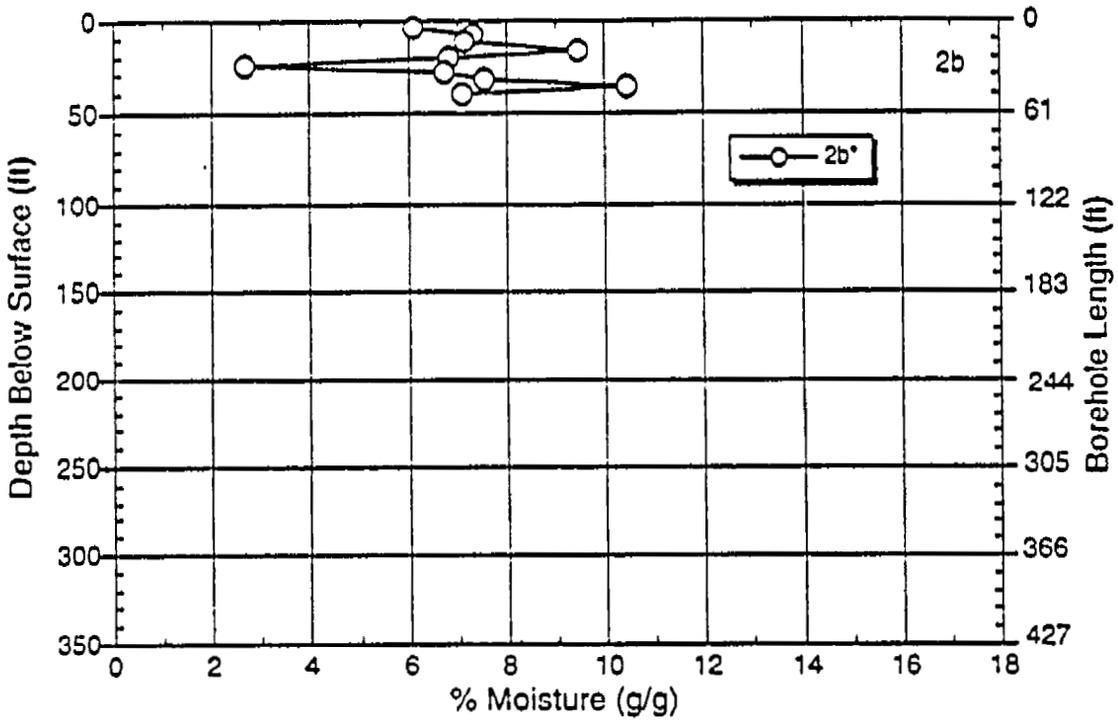

* Data from mobile radiological analysis laboratory

Figure B-14. Gravimetric core moisture content from borehole 54-1012 at MDA L (angled 35° below Pit B).

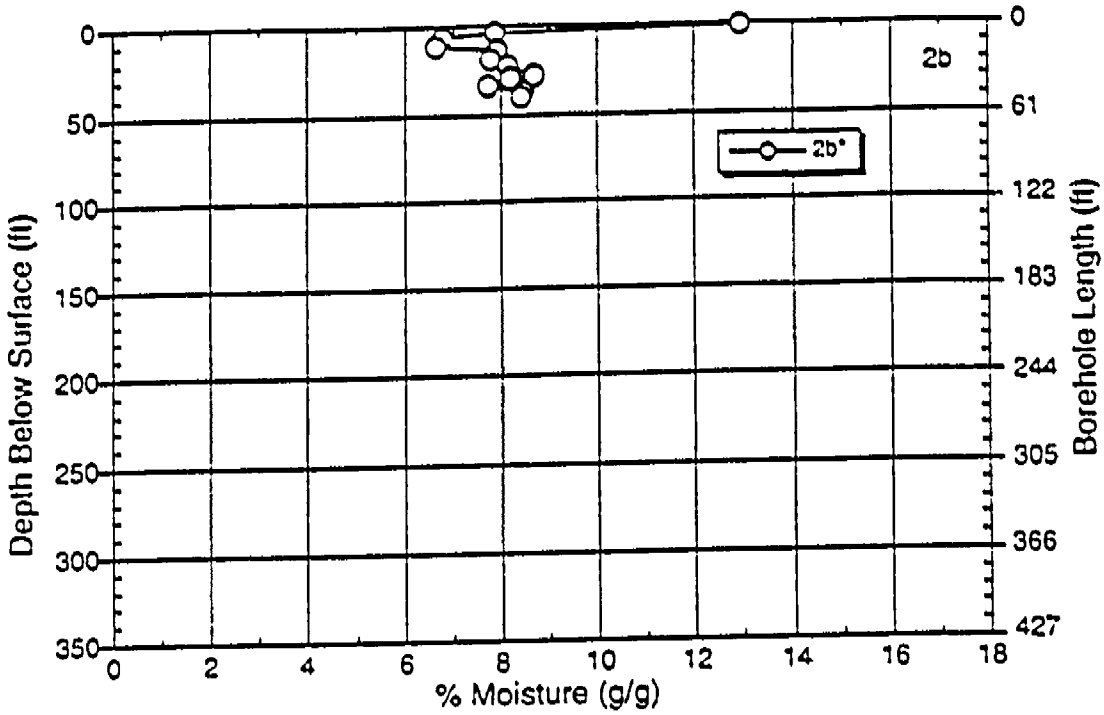

• Data from mobile radiological analysis laboratory

Figure B-15. Gravimetric core moisture content from borehole 54-1013 at MDA L (angled 35° below Pit C).

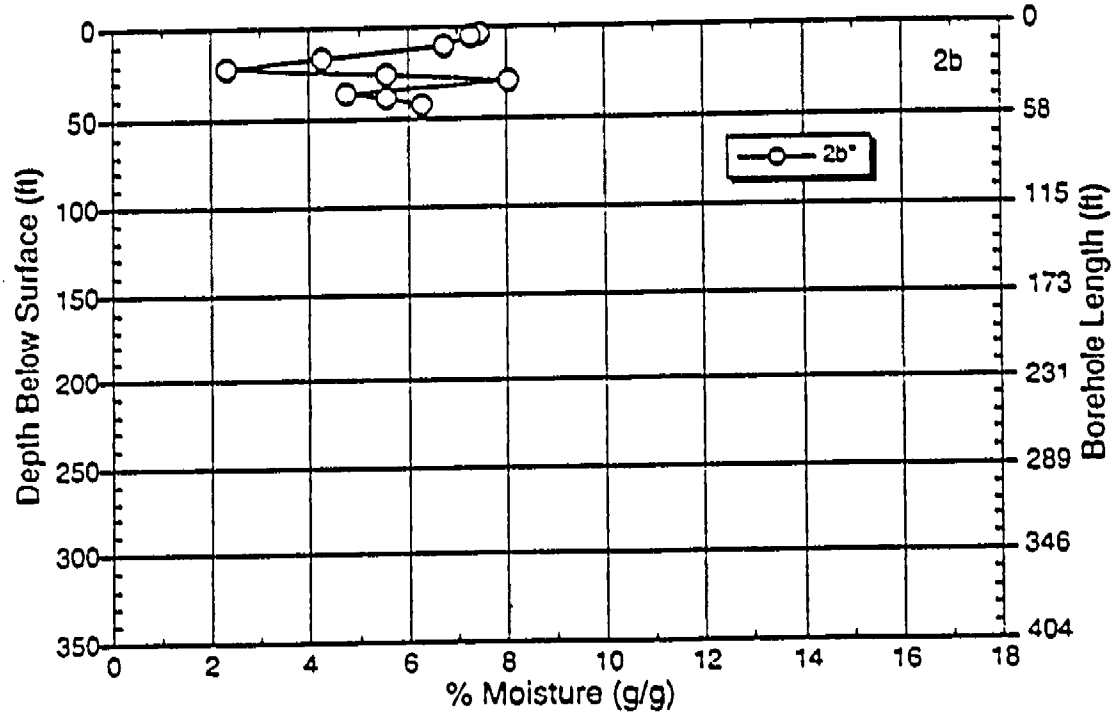

• Data from mobile radiological analysis laboratory

Figure B-16. Gravimetric core moisture content from borehole 54-1014 at MDA L (angled 35° below Pit D).

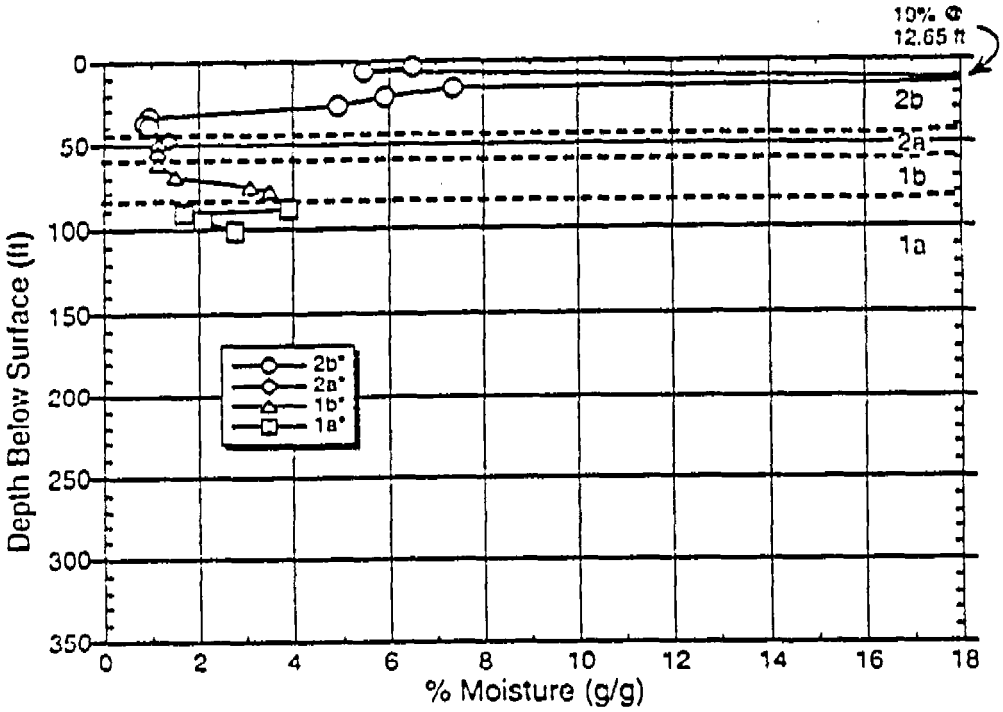

* Data from fixed radiological analysis laboratory

Figure B-17. Gravimetric core moisture content from borehole 54-1110 at MDA G (vertical).

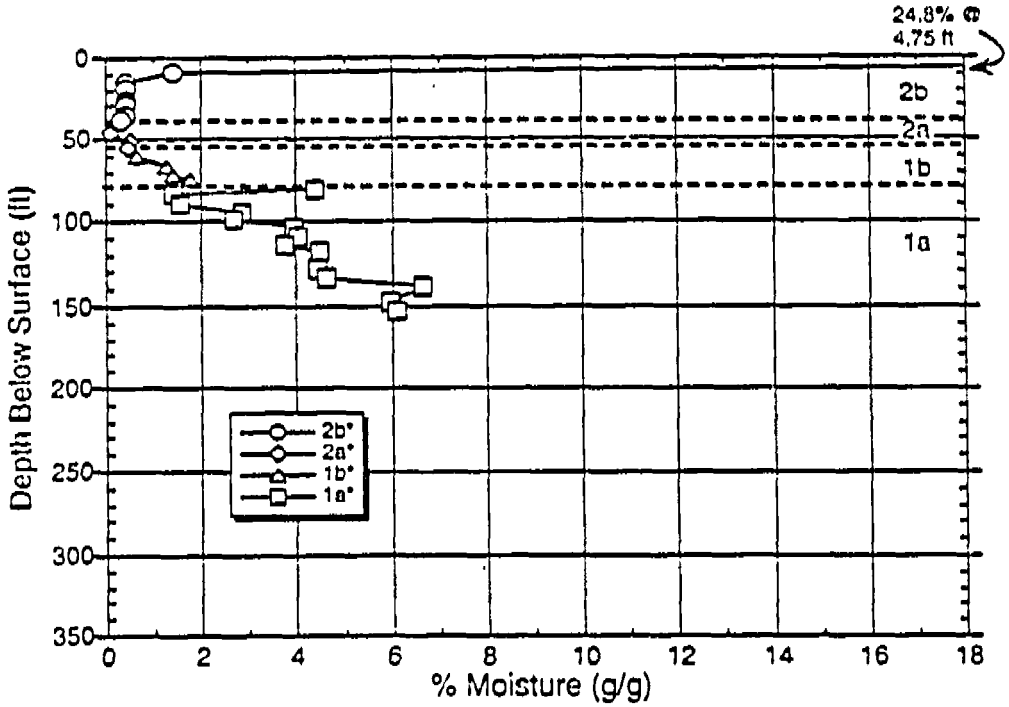

* Data from fixed radiological analysis laboratory

Figure B-18. Gravimetric core moisture content from borehole 54-1111 at MDA G (vertical).

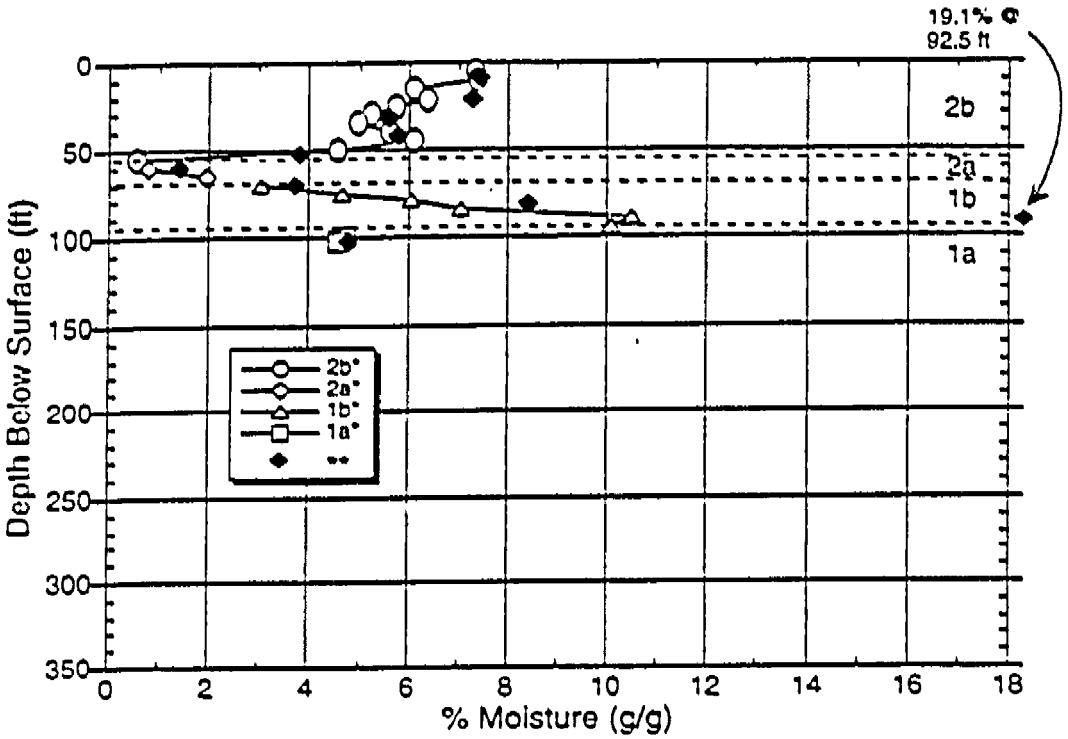

* Data from mobile radiological analysis laboratory
** Data from geotechnical laboratory

Figure B-19. Gravimetric core moisture content from borehole G-5 at MDA G (vertical).

Borehole 54-1002. This borehole is located approximately 330 ft south of the southeast boundary of MDA L in the proposed expansion area for MDA G. It is drilled at an angle of 22° from vertical to the south to a total drilled depth of 310 ft. This borehole was angled toward Pajarito Canyon to investigate the in situ moisture profile on the southern side of the mesa.

Boreholes 54-1003 and 54-1004. These two vertical boreholes are located in the proposed expansion area for MDA G. The boreholes were drilled vertically because of their future role as multiport soil-gas monitor holes in a pilot test to study active extraction of a subsurface plume of volatile organic compounds. Borehole 54-1003 is located approximately 200 ft southeast of the southeast boundary of MDA L and is drilled to a total depth of 296.5 ft. Borehole 54-1004 is located approximately 150 ft east of the southeast boundary of MDA L and is drilled to a depth of 340 ft.

Borehole 54-1005. This angled borehole is located approximately 400 ft east of MDA L in the proposed expansion area of MDA G. It is drilled at an angle of 21° in a northeast direction to an angled depth of 290.5 ft. This borehole was angled toward Cañada del Buey to investigate the in situ moisture profile in the northern side of the mesa.

Borehole 54-1006. This angled borehole is located within 60 ft east of the boundary of MDA L and is drilled at an angle of 26° from vertical to the south. The in situ moisture content to a drilled depth of approximately 50 ft is thought to be affected by the physical

setting at MDA L, that is, the proximity to the asphalt covered surfaces and past disposal practices at MDA L (discussed below).

Borehole 54-1007. This vertical borehole is located approximately 25 ft south of the southeast boundary of MDA L and is drilled to a depth of 150 ft. The in situ moisture content profile, measured in this borehole to a depth of approximately 50 ft, is also thought to be affected by the physical setting at MDA L.

Table B-4 is a statistical summary of the in situ gravimetric moisture content in stratigraphic units for the boreholes located in natural terrain settings.

Previous investigations of subsurface moisture profiles at MDA G (Abeele et al. 1981, Abeele 1986) report that seasonal changes in moisture content are limited to a depth of 15 ft. Inspection of the subsurface moisture profiles for boreholes (Figures B-3, B-4, B-6, and B-7) supports the 15-ft depth as the depth of seasonal infiltration. Table B-4 presents a statistical summary of moisture measured in the upper 15 ft of stratigraphic Unit 2b. Unit 2b is the uppermost stratigraphic unit in all of TA-54. In the subsurface, the lowest moisture (values less than 1.2% gravimetric) occurs in the depth interval from 15 ft to 40 ft below ground surface at borehole 54-1004 (Figure B-6) and to as great as 100 ft at borehole 54-1003 (Figure B-5).

Atmospheric venting (barometric pumping), an important mechanism related to the moisture content within the mesa, may occur to depths of approximately 110 ft. The local nature and extent of vertical fracturing is possibly an important control on the depth of the atmospheric venting. For example, there is a great difference in the subsurface moisture content profiles for borehole 54-1003 (Figure B-5) and borehole 54-1004 (Figure B-6). Both of the boreholes are located within the central region of Mesita del Buey at a separation distance of 125 ft. The low moisture extends to a much greater depth at borehole 54-1003 and may be due to atmospheric venting to a greater depth in the locality of this borehole. Boreholes 54-1002 (Figure B-4) and 54-1005 (Figure B-7) exhibit relatively low moisture to approximately the 100-ft depth. The low values observed in these boreholes may reflect greater atmospheric venting in the canyon wall regions of the mesa.

All of the subsurface profiles show a dramatic increase in moisture in the lower part of Unit 2a extending to the vapor-phase notch at the base of Unit 1b. Immediately below the vapor-phase notch there is a dramatic decrease in moisture in the top of Unit 1a. The measured gravimetric moisture content in core from Unit 1b ranges between 2.32% and 14.95%, with the highest values measured in borehole 54-1001 (Figure B-3).

Kearl et al. (1990) observed the increase in moisture content in Unit 1b and reported that it was probably due to a smaller average pore radius in the Unit 1b rock matrix compared to the overlying and underlying rock units, resulting in stronger moisture retention forces within Unit 1b.

TABLE B-4

IN SITU GRAVIMETRIC MOISTURE CONTENT[a] IN BOREHOLES[b] LOCATED IN NATURAL TERRAIN SETTINGS

Bandelier Tuff, Tshirege Member	n[c]	$\bar{x}$[d] (%)	m[e] (%)	SD[f]	r[g]	Range in Thickness of Stratigraphic Unit (ft)
2b (ground surface to 15-ft depth; 54-1001, -1002, -1004, -1005, -1006)	16	2.22	1.90	1.26	0.60–4.87	2b; 32–41
2b (depths greater than 15 ft; 54-1001, -1002, -1004, -1005)	15	0.68	0.67	0.33	0.29–1.15	—
2b/2a (depth interval with grav. moist. <1.2%; 54-1001, -1002, -1003, -1004, -1005)	52	0.67	—	0.27	0.12–1.16	2b/2a<1.2% grav. 25–85
2a (54-1001, -1002, -1003, -1004, -1005)	72	1.42	1.09	0.98	0.12–4.50	2a; 67–76
1b (54-1001, -1002, -1003, -1004, -1005, -1006)	30	6.31	4.99	3.27	2.32–14.95	1b[h]; 25
1a (54-1001, -1002, -1003, -1004, -1005, -1006)	156	5.61	5.97	1.79	2.08–12.69	1a; 112–128
Tsankawi Pumice Bed (1002, -1005, -1006)	5	12.07	11.71	2.88	9.02–16.42	Tsankawi; 1–7
Cerro Toledo Interval (54-1001, -1002, -1003, -1004, -1005, -1006)	40	8.62	9.09	2.82	3.91–13.44	Cerro Toledo[i]; 36
Otowi Tuff Member (54-1004)	8	8.23	8.04	0.98	6.87–9.81	Otowi[i]; >45

a. Analyses from MRAL and FRAL
b. Borehole locations shown on Figures B-1 and B-2
c. Number of samples
d. Mean
e. Median
f. Sample standard deviation
g. Range
h. Unit 1b is defined as 25 ft thick above base of vapor phase notch.
i. Borehole 54-1004 is the only borehole to completely penetrate the Cerro Toledo interval and drill 45 ft into the Otowi Member.

The subsurface profiles for each borehole show an increase in moisture content through Unit 1a with gravimetric moisture ranging between 2.08% and 12.69%. The lowest moisture occurs at the very top of this unit directly below the vapor-phase notch. The highest moisture occurs at the base of Unit 1a directly above the contact with the Tsankawi Pumice Bed. Table B-4 summarizes the distribution of subsurface moisture within the Tsankawi Pumice Bed, the Cerro Toledo Interval, and the Otowi Member. The Otowi Tuff Member was sampled in borehole 54-1004 only (Figure B-6).

Boreholes 54-1001, -1002, -1003, -1005, and -1006 all ended in the lower part of the Cerro Toledo interval. The Cerro Toledo exhibits a dramatic range of in situ moisture content over short vertical distances, with the range for all gravimetric measurements being between 3.91% and 13.44%. The observed great variation in moisture content over short vertical distances is probably due to changes in textural properties of the Cerro Toledo. Sedimentary rocks with relatively smaller pores would have greater moisture retention characteristics than immediately adjacent sediments with relatively coarser pore structure. Such textural changes in Cerro Toledo sedimentary rocks are noted in the geologic description of core from the boreholes at MDA G.

Moisture Content Profiles for Boreholes in MDA L

The measured in situ moisture content profiles for boreholes 54-1008, 54-1009, 54-1010, 54-1011, 54-1012, 54-1013, and 54-1014 are affected by the physical setting at MDA L. A brief discussion of the physical setting of each borehole follows.

Borehole 54-1008. This vertical borehole is located in the western part of MDA L within a region of inactive, closed chemical waste disposal shafts that extend to depths as great as 65 ft. The borehole was drilled to a depth of 150 ft and is located within 20 ft of disposal shaft 34, which extends to a depth of 63 ft. The land surface in the western disposal shaft field was bare soil with little vegetation and was not covered by asphalt when this borehole was drilled in 1993. In 1994, the western region of MDA L, including the location of borehole 54-1008, was paved with asphalt. As shown in Figure B-10, gravimetric water content values of less than 1% were measured for the depth interval of 21 ft to 81 ft. Many measured values in this depth interval were less than 0.5%. The low in situ moisture may be due in part to the disposal shafts, which served as an access to atmospheric air flow into and out of the mesa because of changes in atmospheric pressure and wind. A statistical summary of in situ moisture content in borehole 54-1008 correlated to stratigraphy and depth follows. The parameters presented in statistical summaries are the number of samples (n), the mean in situ moisture content ($\bar{x}$),and the range of in situ moisture content for the population (r).

Unit 2b (upper 15 ft): $n = 1$, $\bar{x} = 7.14\%$

Unit 2b (15 ft–39 ft): $n = 3$, $\bar{x} = 0.69\%$, $r = 0.39\%$ to 0.99%

Unit 2b/2a (31.4 ft–66.5 ft): $n = 7$, $\bar{x} = 0.49\%$, $r = 0.39\%$ to 0.61%

Unit 2a upper part (39 ft–85 ft): $n = 9$, $\bar{x} = 0.59\%$, $r = 0.41\%$ to 0.82%

Unit 2a lower part (85 ft–110 ft): $n = 5$, $\bar{x} = 1.85\%$, $r = 1.28\%$ to 2.72%

Unit 1b (110 ft–135 ft): $n = 5$, $\bar{x} = 7.43\%$, $r = 5.17\%$ to 13.13%

Unit 1a (135 ft–150 ft total depth): $n = 3$, $\bar{x} = 4.69\%$, $r = 3.77\%$ to 6.08%

Borehole 54-1009. This vertical borehole is located in the central region of MDA L between an inactive chemical waste disposal pit (Pit A) and inactive chemical waste disposal shafts. The area around the borehole is covered by asphalt. The in situ gravimetric moisture content profile for borehole 54-1009 is shown in Figure B-11. Compared to in situ moisture content profiles for boreholes in the natural terrain setting, the moisture content for borehole 54-1009 is elevated (to a depth of approximately 90 ft). We believe this is a result of the existence of the asphalt cover, which eliminates both plant evapotranspiration and solar evaporation, as well as any effects of drying caused by atmospheric venting through the ground surface. A statistical summary of in situ moisture content correlated to stratigraphic units and depth for borehole 54-1009 follows.

Unit 2b (upper 15 ft): $n = 1$, $\bar{x} = 5.37\%$

Unit 2b (15 ft–52 ft): $n = 6$, $\bar{x} = 5.19\%$, $r = 4.7\%$ to 5.6%

Unit 2a (52 ft–110 ft): $n = 7$, $\bar{x} = 3.52\%$, $r = 2.4\%$ to 4.91%

Unit 1b (110 ft–135 ft): $n = 5$, $\bar{x} = 7.45\%$, $r = 5.5.9\%$ to 10.67%

Unit 1a (135 ft–150 ft): $n = 3$, $\bar{x} = 4.69\%$, $r = 3.77\%$ to 6.08%

Boreholes 54-1010, 54-1011, 54-1012, 54-1013, and 54-1014. These five angled boreholes were drilled beneath inactive chemical waste disposal units in central and eastern MDA L. The area surrounding these boreholes is covered by asphalt. Boreholes 54-1010 and 54-1011 were angled beneath inactive asphalt-covered waste disposal Pit A. Boreholes 54-1012, 54-1013, and 54-1014 were angled beneath inactive asphalt-covered liquid waste surface impoundments B, C, and D, respectively. The elevated moisture content in these boreholes may be the result of the asphalt surface and may also be a result of the disposal of liquid wastes in these units. In addition, when these waste disposal units were in service, their open surfaces may have enhanced infiltration of precipitation. The moisture content profiles for these boreholes are shown in Figures B-12 to B-16. These boreholes were all completed in stratigraphic Unit 2b. A statistical summary of in situ moisture content in the five angled boreholes and in the Unit 2b section of borehole 54-1009 follows.

$n = 59$, $\bar{x} = 6.95\%$

$r = 2.66\%$ to 12.92%

The land surface in eastern MDA L is covered by asphalt, and the moisture in the angled boreholes and one vertical borehole (54-1009) drilled in that area is elevated compared to the moisture content in boreholes located in areas not covered by asphalt. The asphalt cover impedes removal of soil moisture by evapotranspiration and atmospheric venting. By the end of 1994, the entire land surface within MDA L was covered with asphalt. Two boreholes (54-1006 and 54-1007) located on open ground east of the boundary of MDA L have increased in situ moisture content to depths of approximately 50 ft. The cause for

the increased moisture is not known. Runoff of surface water from MDA L is currently controlled and directed north into the adjacent canyon. Controls on surface water runoff from MDA L in the past are not known.

In Situ Moisture Profiles for Boreholes near Waste Disposal Units at MDA G

Boreholes 54-1110, 54-1111, and G-5 are located within MDA G (54-1110 and 54-1111 are known also as G-3 and G-4). The locations of the three boreholes are shown on Figure B-2. The gravimetric moisture content profiles for the three boreholes are shown in Figures B-17 to B-19. The in situ moisture content for the three boreholes is believed to be affected by physical settings at MDA G. A brief discussion of the physical setting of each borehole follows. Borehole 54-1110 was located 14 ft from the center of tritium waste disposal shaft 153 and was drilled vertically to a depth of 103 ft. The disposal shaft extends to a vertical depth of 60 ft and has a diameter of 3 ft. Borehole 54-1111 was located a distance of 22 ft from the center of tritium waste disposal shaft 150 and was drilled vertically to a depth of 155 ft. The disposal shaft extends to a vertical depth of 60 ft and has a diameter of 6 ft. Borehole G-5 was located near disposal shafts for waste oils containing polychlorinated biphenyls (PCBs). The disposal shafts are 6 ft in diameter and most extend vertically to a depth of 60 ft. Three of the shafts extend vertically to a depth of 65 ft.

The in situ moisture content profile for borehole 54-1111 (Figure B-18) indicates very low gravimetric moisture content for the depth interval of 12.65 ft to 56.5 ft. The statistical summary for the gravimetric moisture content in this borehole over this depth interval follows.

Unit 2b/2a (12.65 ft–56.5 ft): $n = 10$, $\bar{x} = 0.40\%$, $r = 0.1\%$ to 0.65%

The low moisture content in this depth interval (12.65 ft to 56.5 ft) may be due to atmospheric venting in a permeable pathway created during the construction of disposal shaft 150. The atmospheric venting pathway may be the annular space between the shaft wall and the shaft borehole. However, such low moisture content values were not observed in the core samples analyzed from borehole 54-1110, which was located close to disposal shaft 153. The statistical summary for the gravimetric moisture content for this depth interval in borehole 54-1110 follows.

Unit 2b/2a (32.75 ft–61.25 ft): $n = 7$, $\bar{x} = 1.07\%$, $r = 0.85\%$ to 1.13%

The moisture content profile for borehole G-5 (Figure B-19) indicates that gravimetric moisture content values were greater than 4% over the depth interval of 5 ft to 50 ft. This borehole is located in one of the larger mesa-top landscapes, which is probably the reason for the higher moisture content in the 15- to 50-ft-depth interval. For this borehole, values of less than 1% were only measured in core samples from depths of 55 ft (0.54%) and 60 ft (0.77%). The in situ low moisture was measured in surge sediments that commonly occur at the base of Unit 2b. The surge deposits may be a laterally connected unit with a higher air permeability than the overlying and underlying stratigraphic units. The PCB disposal shafts extend in depth to 60 ft and their construction may be providing atmospheric venting to the surge deposits, which has resulted in the low in situ moisture measured at the 55-ft and 60-ft-depth interval in borehole G-5.

Table B-5 presents a summary of dry bulk density values measured in core from boreholes drilled in MDA G (borehole G-5 on Figure B-2) and in the proposed expansion area for MDA G (boreholes 54-1001, -1002, -1003, and -1006 on Figure B-1). The analyses are from reports by Stephens and Associates (1994, 1995). Measured dry bulk density values ranged from 1.11g cm^3 to 1.49 g/cm^3. The lowest density values were in stratigraphic Unit 1a, and the highest density values were in stratigraphic Unit 2b. Table B-5 also presents a calculated mean in situ volumetric moisture content for stratigraphic units in the natural terrain setting.

TABLE B-5

DRY BULK DENSITY[a] AND CALCULATED VOLUMETRIC MOISTURE CONTENT IN CORE FROM MESITA DEL BUEY

Borehole Number[b]	Stratigraphic Unit	n[c]	$\bar{x}$[d] g/cm^3	SD[e]	r[f]	Volumetric[g] Moisture Content (cm^3/cm^3)
G-5	Tshirege Mem., Unit 2b	5	1.42	0.06	1.35–1.49	0.97[h]
54-1001, -1002, -1003, -1006, and G-5	Tshirege Mem., Unit 2a	8	1.23	0.04	1.17–1.28	1.75
54-1001, -1002, -1003, -1005, and G-5	Tshirege Mem., Unit 1b	10	1.20	0.04	1.13-1.28	7.57
54-1002, -1003, -1006, and G-5	Tshirege Mem., Unit 1a	7	1.14	0.02	1.11-1.18	9.83
54-1003	Cerro Toledo interval	1	1.31			11.29

a. From Stephens and Associates (1994, 1995)

b. Borehole locations are shown on Figures B-1 and B-2.

c. Number of samples

d. Mean density

e. Sample standard deviation

f. Range

g. Volumetric moisture content calculated by multiplying the mean gravimetric moisture content (Table B-4) by the mean dry bulk density

h. Depth greater than 15 ft below ground surface in Unit 2b

Figure 8 in the main text of this paper presents subsurface in situ volumetric moisture content profiles for boreholes drilled on Mesita del Buey in 1985 and 1986 (Kearl et al. 1986a, b). The locations of the boreholes are shown on Figure B-20. Table B-6 presents in situ volumetric moisture content values related to depth and stratigraphic units from the borehole for monitor hole LGM-85-06.

TABLE B-6

IN SITU VOLUMETRIC MOISTURE CONTENT FOR CORE FROM BOREHOLE LGM-85-06*

Bandelier Tuff, Tshirege Tuff Mem.	In Situ Volumetric Moisture Content (cm^3/cm^3)	Depth (ft)
Unit 2b	4.21	13.6
Unit 2b	1.61	17.5
Unit 2b	1.16	22.8
Unit 2b	1.03	28.6
Unit 2b	1.24	33.5
Unit 2b	1.32	38.8
Unit 2b	2.81	42.2
Unit 2a	1.32	47.6
Unit 2a	1.24	52.9
Unit 2a	1.45	57.8
Unit 2a	1.78	63.1
Unit 2a	2.15	68.5
Unit 2a	2.56	7B
Unit 2a	3.26	78.2
Unit 1b	4.79	83.0
Unit 1b	7.27	87.9
Unit 1b	7.93	92.9
Unit 1b	11.61	99.0
Unit 1b	4.55	103.4
Unit 1a	3.06	108.7
Unit 1a	3.72	113.1

* (Kearl et al. 1986a, b) The borehole location is shown in Figure B-20, and the subsurface moisture profile is shown in Figure B-21.

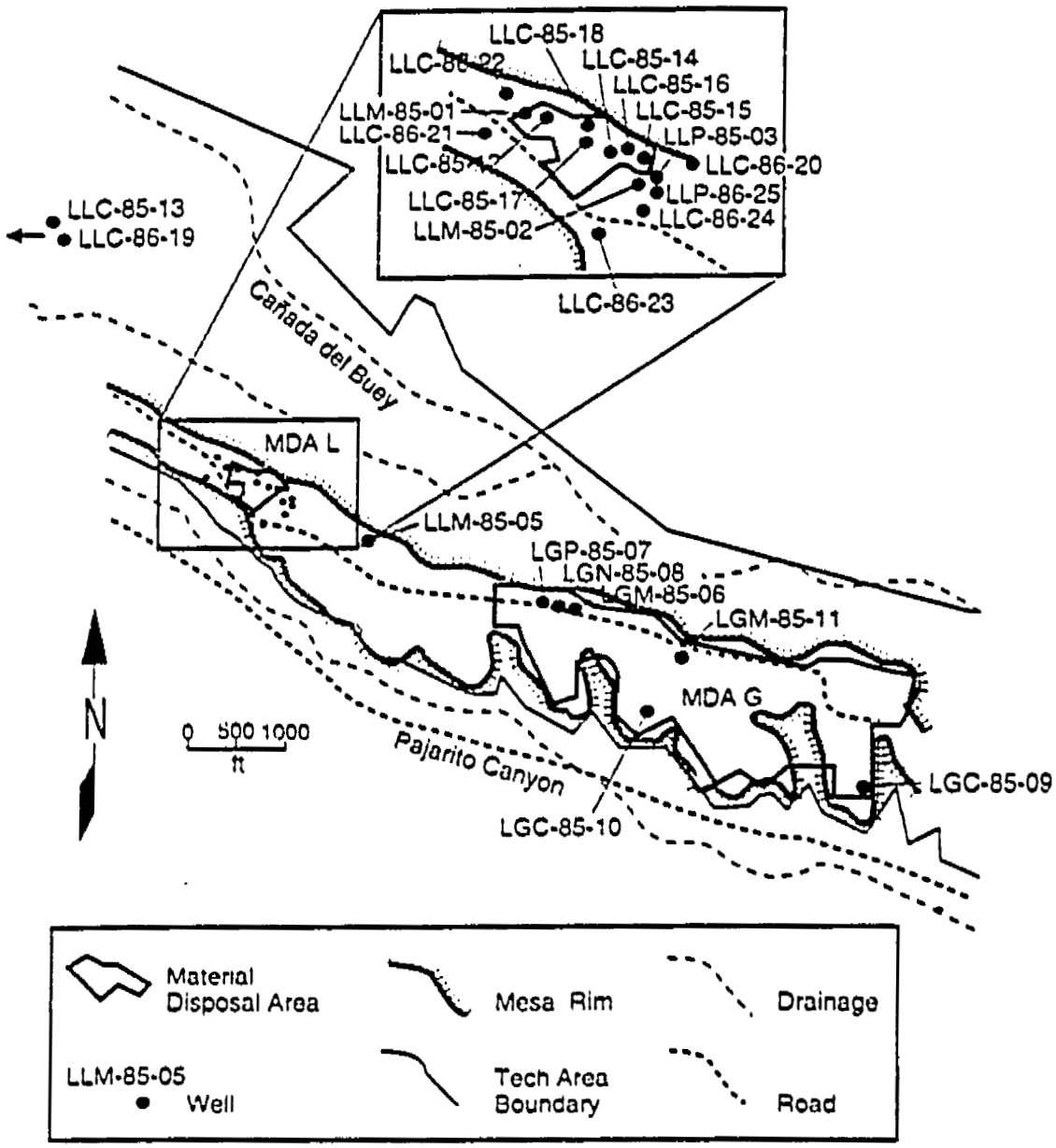

Figure B-20. Locations of drill holes in MDAs G and L, TA-54.

Subsurface moisture profiles are monitored with a neutron probe in several vertical monitor holes at MDA G (Loiza and Vold 1995). One monitor hole is located inside a disposal pit, some are located adjacent to disposal pits and shafts, and others are background monitor holes located away from disposal pits and shafts in the natural terrain setting. Neutron probe monitor hole locations are shown on Figure B-21. Table B-7 is a summary of monitor hole locations and depths. Background monitor holes in relatively undisturbed areas show a maximum volumetric moisture content ranging between 6 and 9% and commonly exhibit a constant volumetric content of approximately 2% below depths of 15

to 30 ft. Figure B-22, a subsurface moisture profile for background hole 54G-NPH-2, is a typical profile for the natural terrain setting (Loiza and Vold 1995). This background hole is located north of Pit 37 (Figure B-21).

TABLE B-7

SUMMARY OF THE NEUTRON PROBE ACCESS HOLES, MDA G

Hole ID	Depth (ft)	Casing/OD (in.)	Location
54G-NPH-1	32	Al/2 in.	Inside Pit 37
54G-NPH-2	60	Al/2 in.	North of Pit 37
54G-NPH-3	46	Al/2 in.	North of Pit 30
54G-NPH-4	66	PVC/4 in.	North of Bldg. 11
54G-NPH-5	96	Uncased/6 in.	PCB shafts
54G-NPH-6	54	PVC/4 in.	Southeast corner
54G-NPH-7a	46	PVC/4 in.	Tritium shaft area
54G-NPH-7b	42	PVC/4 in.	Tritium shaft area
54G-NPH-7c	64	PVC/4 in.	Tritium shaft area
54G-NPH-8	95	Uncased/5 in.	Tritium shaft area
54G-NPH-9	116	Uncased/5 in.	Tritium shaft area

Figure B-23 presents neutron volumetric moisture profiles measured on six dates over a 4-month period in monitor hole 546-NPH-1, which is located within Pit 37. The highest volumetric moisture content in the monitor hole is approximately 12% at the 20-ft depth. The higher moisture measured in the monitor hole located within the disposal pit compared to moisture content in background monitor hole 54G-NPH-2 (Figure B-22) may be a result of disposal operations or increased runoff of precipitation into the pit because of surface topography. Data from the neutron moisture monitor hole network at MDA G indicates that locations disturbed by excavation, engineering, and other disposal operations have resulted in increased moisture to depths greater than 50 ft (Loiza and Vold 1995).

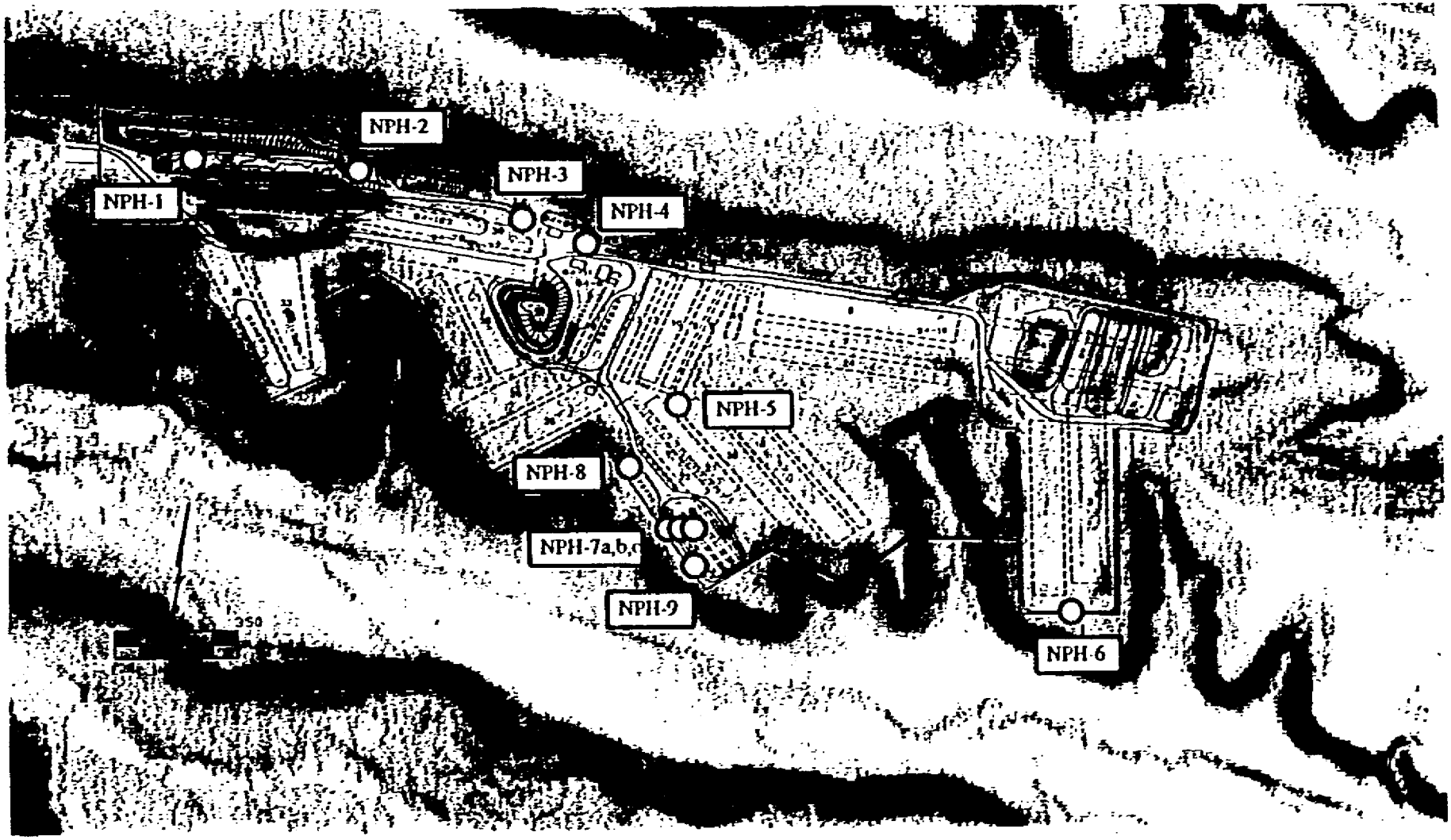

Figure B-21. TA-54 Material Disposal Area G neutron probe hole (54G-NPH) locations.

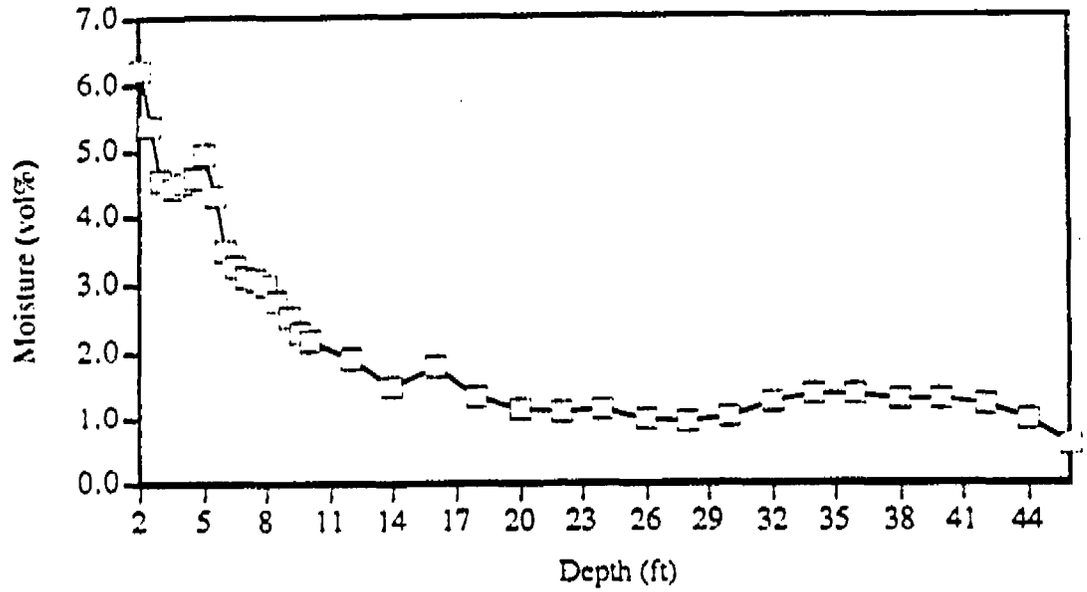

Figure B-22. Neutron moisture profile for background hole 54G-NPH-2.

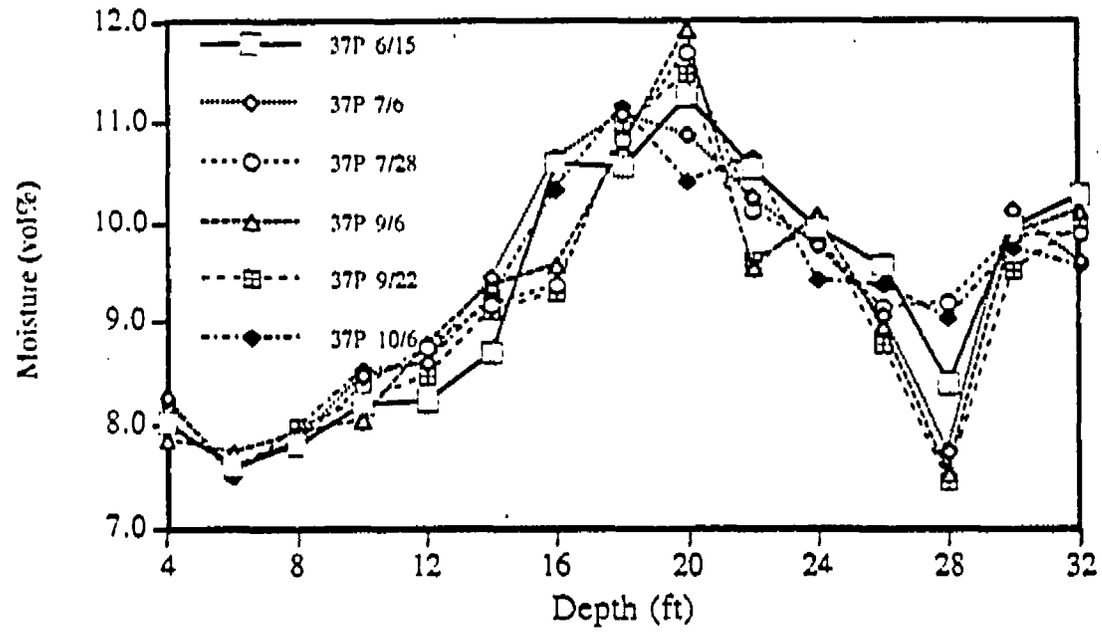

Figure B-23. Neutron moisture profiles for hole 54G-NPH-1, MDA G, during July–October 1994.

REFERENCES

Abeele, W. V., 1986. "Consolidation and Compaction as a Means to Prevent Settlement of Bentonite/Sandy Silt Mixes for Use in Waste Disposal Sites," in Geotechnical and Geohydrological Aspects of Waste Management, Geotechnical Engineering Program, Colorado State University, Fort Collins, Colorado, published by Rotterdam Boston Press, Boston, Massachusetts, pp. 255-264.

Abeele, W. V., M. L. Wheeler, and B. W. Burton, "Geohydrology of Bandelier Tuff," Los Alamos National Laboratory report LA-8962-MS (October 1981).

Kearl, P. M., J. J. Dexter, and M. Kautsky, "Vadose Zone Characterization of Technical Area 54, Waste Disposal Areas G and L, Los Alamos National Laboratory, New Mexico. Report 3: Preliminary Assessment of the Hydrogeologic System," Bendix Field Engineering Corp., Grand Junction Operations, Colorado, report GJ-44, (March 1986a).

Kearl, P. M., J. J. Dexter, and M. Kautsky, "Vadose Zone Characterization of Technical Area 54, Waste Disposal Areas G and L, Los Alamos National Laboratory, New Mexico. Report 4: Preliminary Assessment of the Hydrologic System through Fiscal Year 1986," UNC Technical Services, Inc., Grand Junction, Colorado, report GJ-54 (December 1986b).

Kearl, P. M., R. J. Zinkl, J. J. Dexter, and T. Cronk, "Air Permeability Measurements of the Unsaturated Bandelier Tuff Near Los Alamos, New Mexico," *J. Hydrology* 117, 225–240 (1990).

Loiza, D. and E. Vold, "Moisture Profile Measurements in Subsurface Monitor Holes at the Los Alamos LLRW Disposal Site," Los Alamos National Laboratory report LA-UR-95-1922 (June 1995).

Stephens, D. B. and Associates, "Laboratory Analysis of Soil Hydraulic Properties of Boreholes 54-1001, -1002, -1003, and -1006," prepared for Los Alamos National Laboratory (1994).

Stephens, D. B. and Associates, "Laboratory Analysis of Soil Hydraulic Properties of G-5 Soil Samples," prepared for Los Alamos National Laboratory (January 1995).

Vaniman, D., "Revisions to Report EES1-SH90-17," Los Alamos National Laboratory memorandum EES1-SH91-12 (July 29, 1991).

D. Vaniman and K. Wohletz, "Results of Geological Mapping/Fracture Studies, TA-55 Area," Los Alamos National Laboratory memorandum EES1-SH90-17 (November 14, 1990).

APPENDIX C
SUBSURFACE AIR PERMEABILITY MEASUREMENTS

Borehole straddle packer methods (air injection and air vacuum tests), open borehole anemometry methods, and laboratory methods were used to measure the air permeability of stratigraphic units in the Bandelier Tuff in boreholes located at Technical Area 54. Methods used for these measurements are described in Kearl et al. (1986a, b), Kearl et al. (1990), and Science and Engineering Associates, Inc. (1994).

Figure B-20 shows the location of five boreholes near Material Disposal Area (MDA) L and in MDA G where packer methods were used to determine air permeability values as reported in Kearl et al. (1986a, b; 1990). Appendix B reports the results of measurements of in situ moisture content, which were also performed on core from these boreholes. The borehole numbers and locations are as follows:

- Borehole LLM-85-01 is located immediately west of MDA L.
- Borehole LLM-85-02 is located outside of MDA L at the southeast boundary of the disposal site.
- Borehole LLM-85-05 is located approximately 700 ft east of the eastern boundary of MDA L in the proposed expansion area for MDA G.
- Borehole LGM-85-06 is located within MDA G in the northwestern part of the disposal facility.
- Borehole LGM-85-11 is located within MDA G in the north central part of the disposal facility.

Table C-1 presents the air permeability values for both air injection and air vacuum measurements in the five vertical boreholes. Packer separations of 6.0 ft were used in the air injection tests, and packer separations of 3.3 ft were used in the vacuum tests.

Table C-1 illustrates that the straddle packer tests by Kearl et al. (1986a, b) determined that intrinsic permeabilities for air injection tests ranged from 0.33 to 13.0 darcies whereas the permeabilities measured in the vacuum (air extraction) tests ranged from 0.084 to 4.3 darcies. There are large differences in permeability values determined with the two test methods in some depth intervals. The greatest difference is in borehole LGM-85-06 where a permeability of 12.0 darcies was measured for the air injection test in the depth interval of 60–66 ft and a permeability of 0.87 darcies was measured for the vacuum test in the depth interval of 60–63.3 ft. The difference may be because the greater open interval of the air injection test included local differences of air permeability within the stratigraphic unit, such as the presence of open fractures or changes in the air permeability of the matrix.

Borehole packer methods were used to measure in situ air permeabilities in six boreholes located in the proposed expansion area for MDA G. The locations of the boreholes (54-1001, 54-1002, 54-1003, 54-1004, 54-1005, and 54-1006) are shown on Figure B-1. The test methods and test results are presented in Science and Engineering Associates, Inc. (1994). The tests in each borehole included both open borehole anemometry and discrete in situ straddle packer gas permeability measurements. The open borehole anemometry

tests were performed first to identify relative differences in air permeability over the total footage in the open borehole. In this test, measurements were taken every 5 ft in the open borehole while a surface-mounted extraction blower applied approximately a 6-in. water column vacuum to the total borehole. The anemometry profiles were used to identify relative permeability differences within and between stratigraphic units in each borehole. The anemometry profiles and geologic information were used to select discrete depth intervals in each borehole for measurement of air permeability with the straddle packer system. With the straddle packer system, air was extracted from discrete open intervals of 27 in. between two packers that had a length of 6 ft each. During the extraction period,

TABLE C-1

AIR PERMEABILITY VALUES DETERMINED FROM AIR VACUUM TESTS AND AIR INJECTION TESTS[a]

Borehole Number	Depth Interval Tested (ft)		Bandelier Tuff, Tshirege Mem. Unit	Intrinsic Permeability (darcies)	
	Injection	Vacuum		Injection	Vacuum
LLM-85-01	30–36	30–33.3	2b	13.0	3.9
LLM-85-01	72–78	70–73.3	2a	1.9	4.3
LLM-85-01	—	80–83.3	2a	—	0.56
LLM-85-01	93–99	94–97.3	2a[b]	0.76	0.35
LLM-85-02	9–15	10–13.3	2b	1.0	1.5
LLM-85.02	24–30	25–28.3	2b	1.6	2.2
LLM-85-02	87–93	87–90.3	2a[b]	0.33	0.93
LLM-85-05	—	15–18.3	2b	—	2.4
LLM-85-05	—	40–43.3	2a	—	0.84
LLM-85-05	—	50–53.3	2a	—	0.86
LLM-85-05	—	60–63.3	2a	—	0.86
LGM-85-06	—	10–13.3	2b	—	3.8
LGM-85-06	60–66	60–63.3	2a[b]	12.0	0.87
LGM-85-06	81–87	82–85.3	2a/1b contact[b]	8.4	0.1
LGM-85-06	99–105	100–103.3	1b	0.33	0.084
LGM-85-11	35–41	35–38.3	2b/2a contact	1.7	0.55
LGM-85-11	77–83	77–80.3	2a/1b contact[b]	3.2	0.82
LGM-85-11	99–105	100–103.3	1b/1a contact	0.33	0.084
LGM-85-11	108–114	110–113.3	1a	0.72	0.27

a. Koari et al. 1986a, b

b. Stratigraphic units reported here are different from units reported in Koari et al (1986a, b) because thickness of Unit 1b is changed to a uniform 25 ft above the unit 1b/1a contact.

measurements were taken of the absolute pressure in the extraction zone, the temperature of the extracted air, and the airflow rate. For this application, air permeabilities were calculated using a spherical extraction geometry model. Tables C-2 to C-7 present the in situ soil-gas permeability measurements in each of the six boreholes. Figures C-1 to C-6 are subsurface profiles of the in situ effective gas permeabilities as a function of depth and stratigraphy. Each figure presents subsurface profiles of air production from the borehole anemometry tests, and for convenience, the figures also present the subsurface in situ moisture content profiles. See Appendix B for a discussion of subsurface moisture.

The effective air permeability measurements in boreholes 54-1001 to 54-1006 were all performed under air extraction with an open interval of 27 in. between the packers (Science and Engineering Associates 1994). For tests in the six boreholes, the measured effective air permeabilities ranged from 0.35 darcies to 172.47 darcies (Science and Engineering Associates 1994). The highest permeability values were measured in open-fracture intervals that were identified from continuous core collected during drilling of the six boreholes. Table C-8 is a statistical summary of the extraction tests performed in the six boreholes. The summary presents an analysis for boreholes 54-1001 to 54-1005 as a separate set from boreholes 54-1001 to 54-1006. Borehole 54-1006 is excluded from one set of statistical analysis because much higher permeabilities were measured in the tests conducted in borehole 54-1006 than were measured in the other five boreholes. The total borehole anemometry tests also determined a higher production of air from borehole 54-1006 than from the other five boreholes. The air production was higher from boreholes that were angled south to increase the probability of intersecting open fractures. Borehole 54-1006 was drilled at the greatest angle from vertical and had the greatest overall production of air in the extraction tests. The borehole anemometry tests were performed with completely different equipment and at different dates than the straddle packer permeability tests.

The total anemometry test for borehole 54-1006 indicated a high production of soil air extraction in the depth interval of 120 ft to 170 ft. This was supported by high effective permeability measurements in this interval with the straddle packer tests. The highest effective permeability (53.51 darcies) was measured on a 27-in. interval centered at 162 ft in a pumice bed in Unit 1a of the Tshirege Member.

The greatest range in effective air permeability values was recorded in Unit 1b of the Tshirege Member. This is possibly the result of more straddle packer measurements capturing air production from open fractures in this unit. The highest effective permeability measured in the straddle packer tests was 172.47 darcies in Unit 1b at a depth of 119.6 ft in borehole 54-1002.

The stratigraphic unit that was determined to have the lowest effective air permeability in the straddle packer tests is Unit 1a of the Tshirege Member with measurements of under 1.0 darcy, and the lowest value measured was 0.35 darcy at a depth of 134.4 ft in borehole 54-1005.

TABLE C-2
IN SITU SOIL-GAS PERMEABILITY DATA

Borehole 54-1301 Slant (deg off vert) 22

Date	Time	Depth in Borehole (ft)	Hole Diameter (in.)	Extr. Zone Height (in.)	Packer Pressure (psi)	Ambient DH[a] Pressure (mbar)	Extraction DP[b] (mbar)	Air Temperature (C)	Air Flowrate (scfm)[c]	Permeability (Darcies)	True Depth Below Ground (ft)	Stratigraphic Unit
3 Mar	1028	33.0	8.10	27	5.20	800.15	28.07	17.86	1.01	1.70	30.8	2b
3 Mar	1038	39.0	8.10	27	5.18	800.29	16.88	18.36	1.04	2.51	36.2	2a
3 Mar	1117	45.0	8.10	27	5.31	799.61	15.13	18.37	1.00	3.12	41.7	2a
3 Mar	1127	50.0	8.20	27	5.25	799.39	17.74	18.36	0.98	2.59	46.4	2a
3 Mar	1137	60.0	8.20	27	5.22	799.59	12.04	17.57	1.05	4.08	56.6	2a
3 Mar	1143	71.5	8.20	27	5.25	799.68	7.20	17.63	1.02	6.50	66.3	2a
3 Mar	1157	82.5	8.20	27	5.30	799.38	8.39	17.49	1.03	5.33	76.5	2a
3 Mar	1305	115.0	8.00	27	5.25	800.03	7.59	16.54	0.98	6.38	106.6	2a
3 Mar	1323	130.0	8.00	27	5.26	801.15	30.56	16.53	1.05	1.82	120.5	1b
3 Mar	1332	135.0	8.00	27	5.23	801.37	25.97	16.46	1.09	1.38	126.1	1b
3 Mar	1341	139.0	8.00	27	5.20	801.36	26.78	16.52	1.11	1.37	129.9	1b
3 Mar	1351	143.0	8.00	27	5.21	801.25	44.19	16.81	1.02	1.11	132.6	1b

a. DH = downhole
b. DP = drawdown pressure
c. scfm = standard cubic feet per minute

TABLE C-2 (concluded)

Borehole 54-1001 Slant (deg. off vert) 22

Date	Time	Depth In Borehole (ft)	Hole Diameter (in)	Extr. Zone Height (in)	Packer Pressure (psi)	Ambient DH Pressure (mbar)	Extraction DP (mbar)	Air Temperature (C)	Air Flowrate (scfm)	Permeability (Darcies)	True Depth Below Ground (ft)	Stratigraphic Unit
3 Mar	1401	150.0	8.00	27	5.16	800.54	113.13	17.30	1.03	0.45	139.1	ta
3 Mar	1410	160.0	8.00	27	5.23	800.74	87.36	17.31	1.00	0.57	148.3	ta
3 Mar	1420	175.0	8.00	27	5.26	801.00	38.96	17.15	0.36	1.23	162.3	ta
3 Mar	1431	190.0	8.00	27	5.24	801.48	54.50	17.50	1.08	0.36	176.2	ta
3 Mar	1440	198.0	8.00	27	5.23	800.91	28.95	17.35	1.03	1.70	183.6	ta
3 Mar	1450	216.0	8.00	27	5.29	801.92	37.92	17.56	0.94	1.19	200.3	ta
3 Mar	1506	233.0	8.00	27	4.96	802.31	72.33	18.02	1.11	0.75	216.0	ta
3 Mar	1519	256.0	8.10	27	5.26	812.79	74.19	18.06	1.07	0.71	236.4	ta
3 Mar	1528	274.0	8.10	27	5.18	803.16	74.36	18.19	0.32	0.61	254.0	ta
3 Mar	1537	292.0	8.00	27	5.23	802.36	52.13	18.24	1.06	0.39	261.5	ta
3 Mar	1545	297.0	8.00	27	5.22	802.83	7.65	18.08	1.02	6.29	298.1	CT

TABLE C-3
IN SITU SOIL-GAS PERMEABILITY DATA

Borehole 54-1002 Slant (deg off vert) 22

Date	Time	Depth In Borehole (ft)	Hole Diameter (in)	Extr. Zone Height (in)	Packer Pressure (psi)	Ambient DH[a] Pressure (mbar)	Extraction DP[b] (mbar)	Air Temperature (C)	Air Flowrate (scfm)[c]	Permeability (Darcies)	True Depth Below Ground (ft)	Stratigraphic Unit
7 Mar	1121	34.2	8.20	27	5.01	754.66	56.05	15.84	0.54	0.81	31.7	2b
7 Mar	1130	37.0	8.20	27	4.30	754.42	29.75	16.26	1.04	1.66	34.3	2b
7 Mar	1140	46.7	8.20	27	5.11	754.69	30.66	16.72	1.07	1.65	43.3	2a
7 Mar	1150	57.5	8.20	27	4.39	754.78	23.47	16.31	1.04	2.11	53.3	2a
7 Mar	1243	64.0	8.20	27	4.83	754.43	20.43	15.93	1.14	2.65	59.3	2a
7 Mar	1254	69.0	8.20	27	4.86	754.33	23.73	15.30	1.07	2.13	64.0	2a
7 Mar	1311	78.8	8.20	27	5.15	754.88	13.57	16.23	1.01	2.43	73.1	2a
7 Mar	1321	83.0	8.20	27	5.25	755.09	13.04	16.43	0.34	2.34	82.5	2a
7 Mar	1329	93.0	8.20	27	5.22	754.54	14.27	16.59	0.37	3.13	86.2	2a
7 Mar	1340	97.5	8.20	27	5.24	754.92	11.79	16.37	0.87	3.47	90.4	2a
7 Mar	1349	107.3	8.30	27	5.26	754.37	25.13	17.23	0.34	1.77	99.5	2a

a. DH = downhole
b. DP = drawdown pressure
c. scfm = standard cubic feet per minute

TABLE C-3 (concluded)

Borehole SS1302 Slant (deg off vert.) 22

Date	Time	Depth in Borehole (ft)	Hole Diameter (in.)	Extr. Zone Height (in.)	Packer Pressure (psi)	Ambient DH Pressure (mbar)	Extraction DP (mbar)	Air Temperature (C)	Air Flowrate (scfm)	Permeability (Darcies)	True Depth Below Ground (ft)	Stratigraphic Unit
7 Mar	1401	117.0	8.30	27	5.19	754.94	31.33	17.54	0.92	1.37	108.5	2a
7 Mar	1409	122.3	8.20	27	5.21	756.17	30.25	17.86	0.90	1.42	113.1	1b
7 Mar	1419	129.3	8.20	27	5.10	756.61	0.25	15.30	0.93	172.47	119.5	1b
10 Mar	917	135.0	8.20	27	4.90	801.00	30.73	7.22	0.92	1.37	125.2	1b
10 Mar	925	137.0	8.20	27	5.11	800.66	24.95	8.85	0.98	1.73	127.0	1b
10 Mar	934	141.0	8.20	27	5.26	800.32	12.78	10.08	1.06	3.73	130.7	1b
10 Mar	945	146.4	8.20	27	5.22	800.66	29.40	11.73	0.90	1.43	135.7	1a
10 Mar	952	159.0	8.20	27	5.39	801.10	30.27	12.64	0.94	1.45	145.5	1a
10 Mar	1001	168.0	8.20	27	5.47	800.68	19.23	13.33	0.90	2.28	155.8	1a
10 Mar	1009	179.0	8.30	27	5.44	801.34	11.52	14.02	0.99	3.95	166.0	1a
10 Mar	1021	202.0	8.30	27	5.42	802.74	10.09	14.88	1.04	4.72	187.3	1a
10 Mar	1032	225.0	8.30	27	5.24	802.72	40.24	15.80	1.04	1.21	208.6	1a
10 Mar	1041	250.0	8.30	27	5.48	803.57	63.20	16.50	0.96	0.73	231.8	1a
10 Mar	1052	275.0	8.10	27	5.26	803.87	60.17	17.05	1.02	0.82	255.0	1a
10 Mar	1110	277.3	8.10	27	5.07	803.18	37.28	17.58	1.11	1.42	257.3	T
10 Mar	1248	210.0	8.20	27	5.26	801.82	24.32	15.35	1.03	1.58	194.7	1a

TABLE C-4
IN SITU SOIL-GAS PERMEABILITY DATA

Borehole 54-1003 Slant (deg. off vert.) 0

Date	Time	Depth in Borehole (ft)	Hole Diameter (in.)	Extr. Zone Height (in.)	Packer Pressure (psi)	Ambient DH[a] Pressure (mbar)	Extraction DP[b] (mbar)	Air Temperature (C)	Air Flowrate (scfm)[c]	Permeability (Darcies)	True Depth Below Ground (ft)	Stratigraphic Unit
4 Feb	1021	36.0	8.40	27	4.82	734.30	62.77	15.39	1.79	1.36	36.0	2b
4 Feb	1037	48.6	8.50	27	4.85	734.58	30.97	15.95	3.39	4.65	48.6	2a
4 Feb	1049	51.0	8.50	27	5.05	734.73	65.34	16.44	1.35	1.43	51.0	2a
4 Feb	1100	65.5	8.50	27	4.82	735.02	56.34	16.84	2.40	2.03	65.5	2a
4 Feb	1114	72.7	8.50	27	5.17	735.03	48.73	17.09	2.50	2.42	72.7	2a
4 Feb	1135	80.0	8.70	27	5.02	735.04	63.36	17.77	2.07	1.56	80.0	2a
4 Feb	1146	95.2	8.70	27	4.30	735.36	63.73	17.91	1.79	1.33	95.2	2a
4 Feb	1237	102.0	8.60	27	5.01	735.54	78.79	16.67	1.17	0.71	102.0	2a
4 Feb	1316	117.5	8.40	27	5.09	735.46	70.54	17.07	0.37	0.96	117.5	1b
4 Feb	1329	125.0	8.30	27	5.14	735.25	58.52	17.30	2.27	1.87	125.0	1b
4 Feb	1343	137.0	8.20	27	5.20	735.32	59.88	17.68	2.34	1.30	137.0	1b
4 Feb	1356	157.0	8.40	27	5.23	735.29	66.03	18.06	1.13	0.97	157.0	1a
4 Feb	1406	175.0	8.60	27	5.23	735.76	68.34	18.42	1.55	1.08	175.0	1a
4 Feb	1418	192.0	8.50	27	5.22	737.20	68.16	18.66	2.00	1.41	192.0	1a
4 Feb	1444	207.0	8.50	27	5.25	737.34	64.36	20.25	1.97	1.48	207.0	1a
4 Feb	1456	230.0	8.50	27	5.25	738.65	66.72	20.38	1.67	1.21	230.0	1a

a. DH = downhole

b. DP = drawdown pressure

c. scfm = standard cubic feet per minute

TABLE C-5
IN SITU SOIL-GAS PERMEABILITY DATA

Borehole 54-1004 Slant (deg. off vert) 0

Date	Time	Depth in Borehole (ft)	Hole Diameter (in.)	Extr. Zone Height (in.)	Packer Pressure (psi)	Ambient DH[a] Pressure (mbar)	Extraction DP[b] (mbar)	Air Temperature (C)	Air Flowrate (scfm)[c]	Permeability (Darcies)	True Depth Below Ground (ft)	Stratigraphic Unit
11-Feb	1021	37.0	8.40	27	4.36	754.25	47.38	10.92	1.95	1.89	37.0	2b
11-Feb	1039	48.5	8.40	27	5.07	754.60	78.51	12.64	1.75	1.07	48.6	2a
11-Feb	1051	60.0	8.30	27	5.16	753.38	42.24	13.47	1.77	1.97	60.0	2a
11-Feb	1103	70.0	8.30	27	5.08	754.94	40.52	14.19	1.88	2.19	70.0	2a
11-Feb	1117	75.0	8.30	27	4.90	754.59	96.37	15.06	1.72	1.24	75.0	2a
11-Feb	1133	80.0	8.30	27	4.97	754.85	91.74	16.03	1.64	0.98	80.0	2a
11-Feb	1243	101.0	8.20	27	5.12	754.63	96.37	16.17	1.56	0.30	101.0	2a
11-Feb	1256	113.0	8.20	27	5.16	754.94	32.14	15.99	1.75	2.59	113.0	1b
11-Feb	1308	121.5	8.20	27	5.05	754.91	136.04	16.97	1.05	0.40	121.5	1b
11-Feb	1320	125.2	8.20	27	5.13	754.74	148.53	17.60	0.53	0.22	125.2	1b
11-Feb	1332	128.2	8.20	27	5.14	754.67	138.85	18.03	0.33	0.34	128.2	1b
11-Feb	1350	140.0	8.20	27	5.07	754.77	120.31	18.55	1.25	0.53	140.0	1a

a. DH = downhole
b. DP = drawdown pressure
c. scfm = standard cubic feet per minute

TABLE C-5 (concluded)

Borehole 54-1304 Slant (deg off vert) 0

Date	Time	Depth in Borehole (ft)	Hole Diameter (in.)	Extr. Zone Height (in.)	Packer Pressure (psi)	Ambient DH Pressure (mbar)	Extraction DP (mbar)	Air Temperature (C)	Air Flowrate (scfm)	Permeability (Darcies)	True Depth Below Ground (ft)	Stratigraphic Unit
11 Feb	1408	165.0	8.20	27	5.07	736.18	90.77	18.54	1.46	0.72	165.0	ta
11 Feb	1418	179.0	8.20	27	5.23	736.52	76.96	18.54	1.75	1.12	179.0	ta
11 Feb	1431	215.0	8.10	27	5.27	736.60	73.92	18.75	1.80	1.20	215.0	ta
11 Feb	1445	223.0	8.10	27	4.99	736.51	87.96	18.99	1.62	0.92	223.0	ta
11 Feb	1458	241.0	8.00	27	5.13	737.10	106.14	19.07	1.37	0.66	241.0	ta
11 Feb	1513	254.5	8.00	27	5.17	733.46	29.06	18.37	1.92	3.21	254.5	ta
11 Feb	1524	260.0	8.00	27	5.28	737.86	29.77	19.22	1.84	2.39	260.0	CT
12 Feb	916	280.5	7.80	27	5.15	736.76	39.38	5.75	1.76	2.11	280.5	CT
12 Feb	928	291.0	7.80	27	5.03	736.61	74.54	9.35	1.77	1.16	291.0	CT
12 Feb	943	305.0	7.80	27	4.92	736.58	112.24	12.74	1.23	0.55	305.0	O

TABLE C-6
IN SITU SOIL-GAS PERMEABILITY DATA

Borehole 54-1005 Slant (deg. off vert.) 22

Date	Time	Depth in Borehole (ft)	Hole Diameter (in.)	Extr. Zone Height (in.)	Packer Pressure (psi)	Ambient DH[a] Pressure (mbar)	Extraction DP[b] (mbar)	Air Temperature (C)	Air Flowrate (scfm)[c]	Permeability (Darcies)	True Depth Below Ground (ft)	Stratigraphic Unit
29-Feb	1452	36.5	8.00	27	4.38	791.13	4.36	13.46	1.00	10.74	33.8	2a
29-Feb	1512	42.5	8.00	27	5.29	790.54	17.78	14.27	1.01	2.89	39.4	2a
1-Mar	911	51.6	8.00	27	5.13	798.93	29.25	1.60	1.00	1.61	47.8	2a
1-Mar	935	54.2	8.00	27	5.32	797.56	20.67	3.47	0.35	2.08	50.3	2a
1-Mar	939	60.0	8.00	27	5.32	798.37	60.24	5.75	0.38	0.69	55.5	2a
1-Mar	959	70.0	8.00	27	5.25	799.00	56.09	7.57	0.34	0.77	64.9	2a
1-Mar	948	80.0	8.00	27	5.28	798.36	64.42	9.14	0.94	0.69	74.2	2a
1-Mar	1001	85.0	8.00	27	5.19	799.20	77.38	10.35	1.05	0.65	79.7	2a
1-Mar	1010	90.0	8.00	27	5.33	799.42	75.38	11.78	0.34	0.80	89.0	2a
1-Mar	1019	106.7	8.00	27	5.31	798.38	72.11	12.62	1.01	0.58	98.9	2a
1-Mar	1026	115.0	8.00	27	5.26	801.37	20.93	13.77	1.07	2.42	106.8	1b
1-Mar	1104	120.0	8.00	27	5.34	800.68	14.85	13.36	1.02	3.23	111.3	1b
1-Mar	1131	145.0	8.00	27	5.17	801.77	136.29	15.49	0.33	0.35	134.4	1a

a. DH = downhole
b. DP = drawdown pressure
c. scfm = standard cubic feet per minute

TABLE C-6 (concluded)

Borehole 54 1005 Slant (deg. off vert.) 22

Date	Time	Depth in Borehole (ft)	Hole Diameter (in.)	Extr. Zone Height (in.)	Packer Pressure (psi)	Ambient DH Pressure (mbar)	Extraction DP (mbar)	Air Temperature (C)	Air Flowrate (scfm	Permeability (Darcies)	True Depth Below Ground (ft)	Stratigraphic Unit
1 Mar	1140	165.0	8.00	27	5.32	801.25	66.81	15.53	1.01	0.76	153.0	1a
1 Mar	1151	185.0	8.00	27	5.27	800.30	50.43	15.78	1.00	0.36	171.5	1a
1 Mar	1242	210.0	8.00	27	5.29	801.69	43.82	15.78	0.99	1.09	134.7	1a
1 Mar	1254	242.0	8.00	27	5.22	802.32	57.61	15.92	1.03	0.86	224.4	1a
1 Mar	1304	256.0	8.00	27	5.31	802.59	65.61	16.14	0.95	0.71	237.4	1a
1 Mar	1316	263.3	8.00	27	5.34	802.16	47.43	16.52	0.92	0.33	244.1	T
1 Mar	1330	131.0	8.00	27	5.36	800.39	23.54	16.84	0.93	1.86	121.5	1b

TABLE C-7
IN SITU SOIL-GAS PERMEABILITY DATA

Borehole 54-1006 Slant (deg. off vert.) 27

Date	Time	Depth in Borehole (ft)	Hole Diameter (in.)	Extr. Zone Height (in.)	Packer Pressure (psi)	Ambient DH[a] Pressure (mbar)	Extraction DP[b] (mbar)	Air Temperature (C)	Air Flowrate (scfm)[c]	Permeability (Darcies)	True Depth Below Ground (ft)	Stratigraphic Unit
2 Mar	1015	36.5	8.00	27	5.07	801.39	13.58	20.24	1.09	3.53	34.3	2b
2 Mar	1025	42.0	8.00	27	5.23	799.42	5.50	19.74	1.12	9.73	37.4	2a
2 Mar	1036	48.4	8.00	27	5.30	801.06	4.12	19.27	0.97	11.16	43.1	2a
2 Mar	1048	56.7	8.00	27	5.19	801.32	3.11	18.98	1.03	15.99	50.5	2a
2 Mar	1057	66.0	8.00	27	5.39	801.06	6.83	18.24	0.95	6.52	56.8	2a
2 Mar	1109	72.0	8.00	27	5.36	801.52	8.05	17.89	1.09	8.50	64.2	2a
2 Mar	1122	78.8	8.00	27	5.06	801.86	5.76	17.15	1.09	8.36	70.2	2a
2 Mar	1130	86.0	8.00	27	5.40	801.52	10.34	16.94	1.05	4.79	78.4	2a
2 Mar	1140	96.0	8.00	27	5.29	802.23	11.46	16.32	1.06	4.39	87.3	2a
2 Mar	1149	106.0	8.00	27	5.33	802.11	10.93	16.98	1.08	4.65	97.1	2a
2 Mar	1240	116.4	7.90	27	5.20	801.56	4.75	15.45	1.07	10.56	103.7	2a
2 Mar	1251	124.0	7.90	27	5.19	802.29	4.41	14.95	1.13	12.07	110.5	1b
2 Mar	1300	136.0	7.90	27	5.33	802.76	9.58	15.02	1.04	5.11	120.3	1b

a. DH = downhole
b. DP = drawdown pressure
c. scfm = standard cubic feet per minute

TABLE C-7 (concluded)

Borehole 54-1306 Slant (deg. off vert.) 27

Date	Time	Depth in Borehole (ft)	Hole Diameter (in.)	Extr Zone Height (ft.)	Parker Pressure (psi)	Ambient DP Pressure (mbar)	Extraction DP (mbar)	Air Temperature (C)	Air Flowrate (scfm)	Permeability (Darcies)	True Depth Below Ground (ft)	Stratigraphic Unit
2 Mar	1312	130.2	7.20	27	5.18	802.19	11.87	15.15	1.14	4.54	124.0	1b
2 Mar	1323	145.0	7.20	27	5.22	802.53	23.70	15.41	1.12	2.25	125.2	1b
2 Mar	1336	151.0	7.20	27	5.27	802.36	3.11	15.67	1.09	16.53	134.5	1a
2 Mar	1345	158.7	8.10	27	5.25	802.29	0.25	15.79	1.10	53.51	141.4	1a
2 Mar	1356	162.0	8.10	27	5.25	802.71	4.14	16.20	1.08	12.18	144.3	1a
2 Mar	1407	172.0	8.10	27	5.19	801.63	16.13	16.51	1.15	3.35	153.3	1a
2 Mar	1416	198.0	7.20	27	5.36	802.14	19.67	16.78	1.10	2.68	167.5	1a
2 Mar	1429	206.0	8.10	27	5.19	802.30	31.69	17.08	1.12	4.49	192.7	1a
2 Mar	1440	217.0	8.10	27	5.29	803.37	17.89	17.21	1.10	2.33	123.3	1a
2 Mar	1452	231.0	8.10	27	5.28	802.79	31.78	17.49	1.08	1.81	206.8	1a
2 Mar	1502	250.0	8.10	27	5.36	801.75	12.38	17.61	1.04	3.26	222.8	1a
2 Mar	1512	254.0	8.10	27	5.28	803.67	30.79	17.82	1.09	1.68	236.2	1a
2 Mar	1525	264.2	8.20	27	5.25	801.38	2.28	18.04	1.10	17.19	253.2	1

Borehole #54-1001

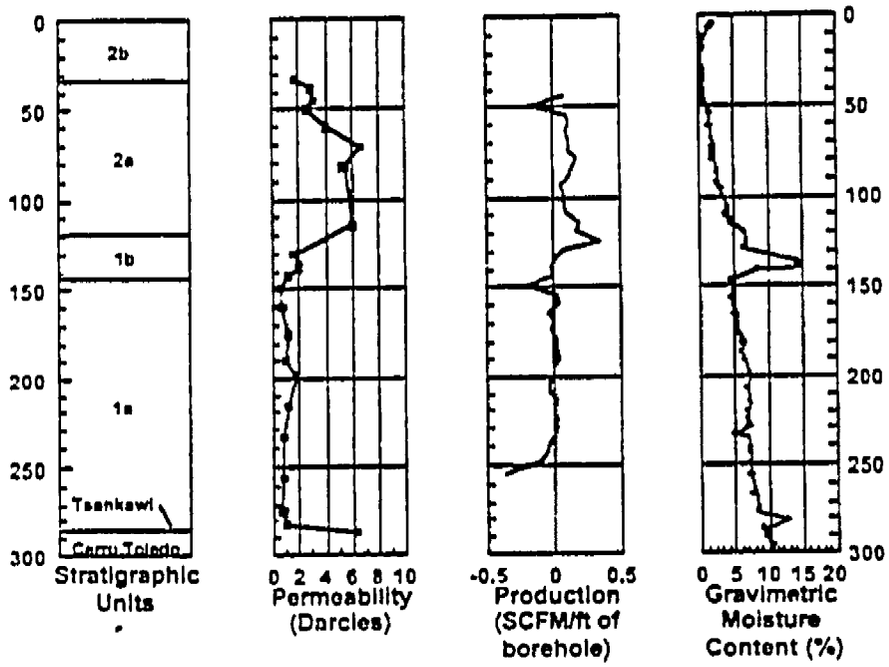

Figure C-1. Anemometry and permeability results, borehole 54-1001.

Borehole #54-1002

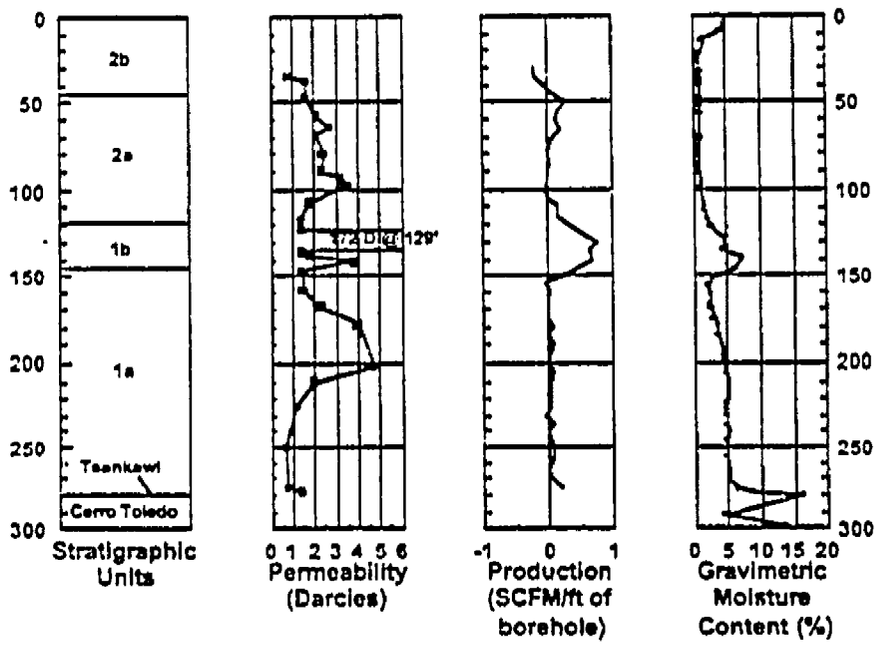

Figure C-2. Anemometry and permeability results, borehole 54-1002.

Borehole #54-1003

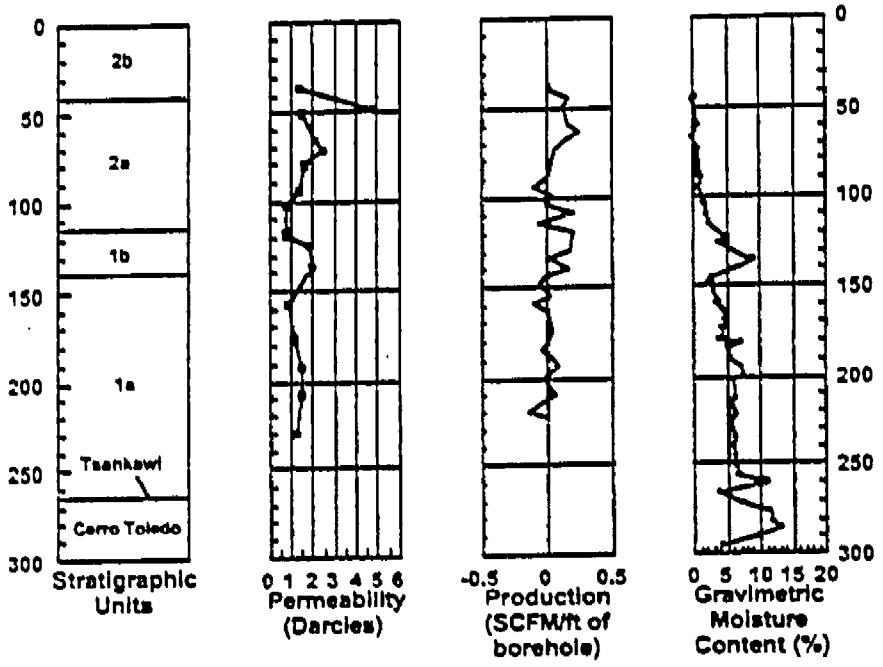

Figure C-3. Anemometry and permeability results, borehole 54-1003.

Borehole #54-1004

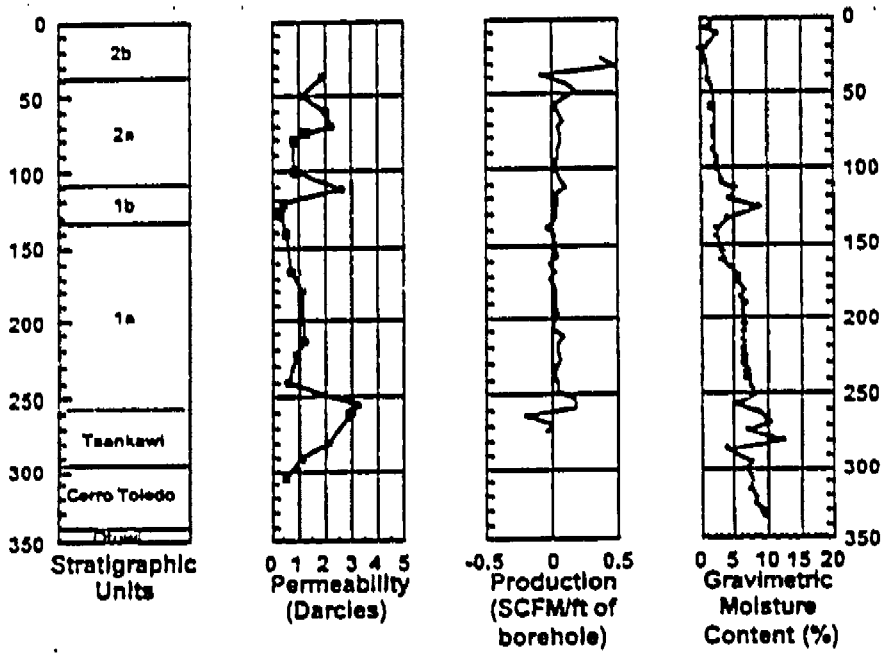

Figure C-4. Anemometry and permeability results, borehole 54-1004.

Borehole #54-1005

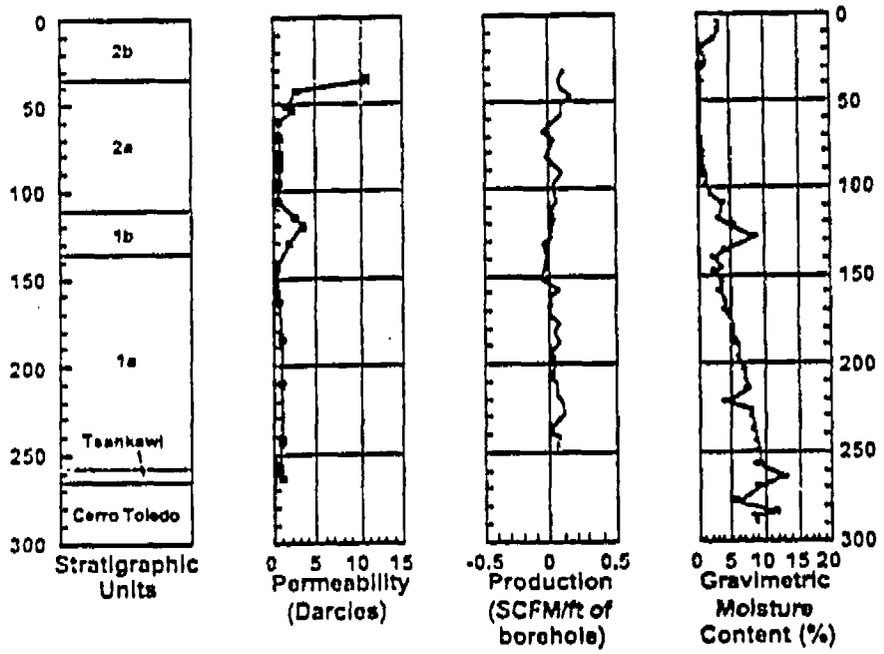

Figure C-5. Anemometry and permeability results, borehole 54-1005.

Borehole #54-1006

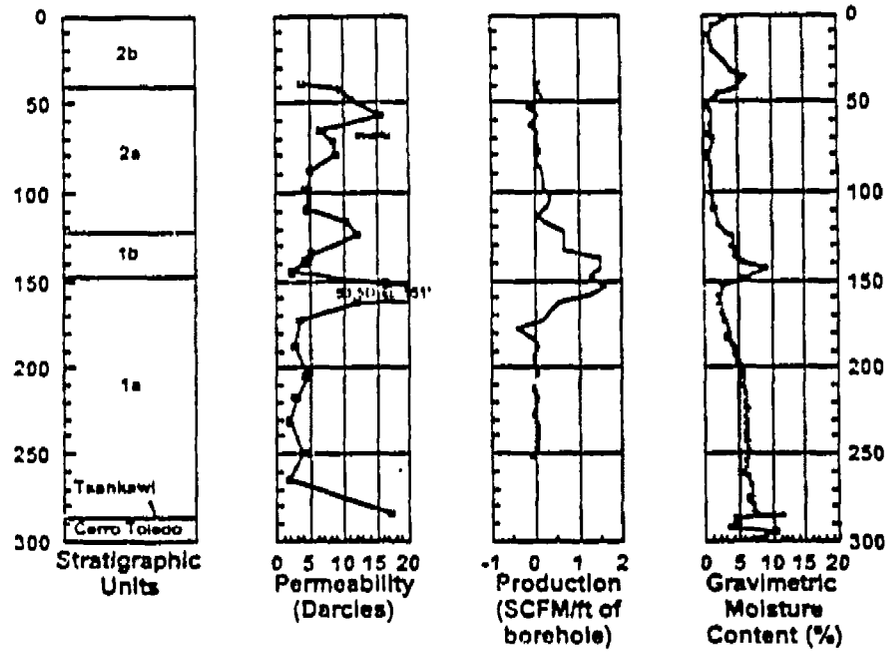

Figure C-6. Anemometry and permeability results, borehole 54-1006.

TABLE C-8
EFFECTIVE AIR PERMEABILITY DETERMINED FROM STRADDLE PACKER TESTS (AIR EXTRACTION)[a]

Bandelier Tuff, Tshirege Mem. Unit	Borehole Numbers[b]	n[c]	$\bar{x}$[d] (darcies)	m[e]	SD[f]	r[g] (darcies)	
2b	54-1001, -1002, -1003, -1004	5	1.48	1.66	0.42	0.81–1.70	
2b	54-1001, -1002,-1003, -1004,-1006	6	1.88	1.68	1.03	0.81–3.83	
2a	54-1001 to -1005	40	2.43	2.05	1.99	0.60–10.74	
2a	54-1001 to -1006	50	3.65	2.38	3.39	0.60–15.69	
1b	54-1001 to -1005	19	10.68	1.79	39.19	0.63–172.47	
1b	54-1001 to -1005	18	1.70	1.77	0.96	0.63–3.79	Minus 172.47 darcy value in 54-1002
1b	54-1001 to -1006	23	9.87	1.87	35.53	0.63–172.47	
1a	54-1001 to -1005	36	1.21	0.98	0.87	0.35-4.72	
1a	54-1001 to -1006	46	3.19	1.20	8.12	0.35–53.51	

a. From Stephens and Associates (1994)
b. Borehole locations are shown on Figures B-1 and B-2.
c. Number of samples
d. Mean permeability
e. Median permeability
f. Sample standard deviation
g. Range

TABLE C-8 (concluded)

Bandelier Tuff, Tshirege Mem. Unit	Borehole Numbers[b]	n[c]	$\bar{x}$[d] (darcies)	m[e]	SD[f]	r[g] (darcies)	
1a	54-1001 to -1006	43	1.50	1.12	1.11	0.35–4.72	Minus 53.51, 16.53 and 12.18 darcy values in upper 1b in 54-1006
Tsankawi Pumice Bed	54-1002, -1004, -1005, and -1006	4	5.69	2.32	7.73	0.93–17.19	
Cerro Toledo interval	54-1001 and -1004	4	3.14	2.55	2.23	1.16–6.28	
Otowi Mem.	54-1004	1	0.55	0.55			

b. Borehole locations are shown on Figures B-1 and B-2.
c. Number of samples
d. Mean permeability
e. Median permeability
f. Sample standard deviation
g. Range

Laboratory measurements of air permeability as a function of water content were performed on core samples from four boreholes that are located in the proposed MDA G expansion area (54-1001, 54-1002, 54-1003, and 54-1006) and from borehole G-5, which is located in the central part of MDA G south of a set of disposal shafts that received polychlorinated biphenyl wastes (Figures B-1 and B-2). Appendix B reports the results of measurement of in situ moisture content in core from these boreholes. Table C-9 presents the air permeability measurements on the core samples at the lowest water content used in the laboratory test. Table C-9 also identifies the stratigraphic unit for each discrete core sample. Air permeability values at other values of water content are presented in the geotechnical laboratory reports (Stephens and Associates 1994, 1995).

TABLE C-9
INTRINSIC AIR PERMEABILITY VALUES ON CORE SAMPLES[a]

Borehole Number	Depth[b] (ft)	Stratigraphic Unit[c]	Intrinsic Air Permeability (darcies)	Volumetric Water Content[d] (%)
54-1001	68	2a	0.45	0.3
54-1001	82.7	2a	0.30	0.2
54-1001	101.7	2a	2.95	0.3
54-1001	121.7	1b	2.34	0.1
54-1001	141.7	1b	1.06	0.4
54-1002	92.1	2a	0.29	0.12
54-1002	121.7	1b	0.17	1.0
54-1002	142.2	1b	0.30	0.44
54-1002	178.7	1a	1.11	0.63
54-1002	243.7	1a	2.68	0.57
54-1003	101.7	2a	1.69	0.11
54-1003	119.2	1b	0.22	0.26
54-1003	156.7	1a	1.84	0.44
54-1003	206.5	1a	1.06	1.02
54-1003	260.7	1a	1.13	0.72
54-1003	270.7	Cerro Toledo	3.29	1.11
54-1006	41.7	2a	4.67	0.18
54-1006	76.5	2a	0.32	0.03
54-1006	124.2	1b	1.18	0.10
54-1006	136.3	1b	0.46	0.18
54-1006	160.7	1a	0.26	0.60
G-5	9.0	2b	0.68	0.27
G-5	21.5	2b	0.49	0.34
G-5	32.5	2b	0.20	0.25
G-5	42.5	2b	0.13	0.19

a. Analytical methods and results from Stephens and Associates (1994, 1995)

b. Laboratory tests were performed on 5-in. lengths of core.

c. Units 2b, 2a, 1b, and 1a are within the Tshirege Member of the Bandelier Tuff.

d. Reported volumetric water are not in situ values.

TABLE C-9 (concluded)

Borehole Number	Depth[b] (ft)	Stratigraphic Unit[c]	Intrinsic Air Permeability (darcies)	Volumetric Water Content[d] (%)
G-5	52.5	2b	0.14	0.10
G-5	60.5	2a	0.31	0.13
G-5	70	2a/1b contact	0.33	0.23
G-5	82.5	1b	0.14	0.29
G-5	92.5	1b	1.21	0.61
G-5	102.5	1a	0.31	0.56

b. Laboratory tests were performed on 5-in. lengths of core.

c. Units 2b, 2a, 1b, and 1a are within the Tshirege Member of the Bandelier Tuff.

d. Reported volumetric water are not in situ values.

In general, the core measurements determined lower permeability values than the straddle packer tests in the same depth interval in the borehole. This is especially noted in borehole 54-1001 (Figure C-1) at the approximate depth interval of 60 ft to 110 ft. The laboratory tests were all performed on unfractured 6-in. lengths of core whereas the straddle packer tests included measurements across a 27-in. interval which could include features (fractures and changes in the rock matrix) that locally change the air permeability of the stratigraphic unit.

REFERENCES

Kearl, P. M., J. J. Dexter, and M. Kautsky, "Vadose Zone Characterization of Technical Area 54, Waste Disposal Areas G and L, Los Alamos National Laboratory, New Mexico. Report 3: Preliminary Assessment of the Hydrogeologic System," Bendix Field Engineering Corp., Grand Junction Operations, Colorado, report GJ-44, (March 1986a).

Kearl, P. M., J. J. Dexter, and M. Kautsky, "Vadose Zone Characterization of Technical Area 54, Waste Disposal Areas G and L, Los Alamos National Laboratory, New Mexico. Report 4: Preliminary Assessment of the Hydrologic System through Fiscal Year 1986," UNC Technical Services, Inc., Grand Junction, Colorado, report GJ-54 (December 1986b).

Kearl, P. M., R. J. Zinkl, J. J. Dexter, and T. Cronk, "Air Permeability Measurements of the Unsaturated Bandelier Tuff Near Los Alamos, New Mexico," *J. Hydrology* 117, 225–240 (1990).

Science and Engineering Associates, "Data Report: Open Borehole Anemometry and In Situ Gas Permeability Measurements in Boreholes 54-1001 Through 54-1006, Los Alamos Technical Area 54," performed for Los Alamos National Laboratory Contract 9-XZ3-2348K-1 (December 1994; revised March 1995).

Stephens, D. B. and Associates, "Laboratory Analysis of Soil Hydraulic Properties of Boreholes 54-1001, -1002, -1003, and -1006," subcontract XT1-X1785-1 report prepared for Los Alamos National Laboratory (1994).

Stephens, D. B. and Associates, "Laboratory Analysis of Soil Hydraulic Properties of G-5 Soil Samples," prepared for Los Alamos National Laboratory (January 1995).

LA-UR- 96-4682

Approved for public release; distribution is unlimited.

Title: VADOSE ZONE WATER MOVEMENT AT AREA G, LOS ALAMOS NATIONAL LABORATORY, TA-54: INTERPRETATIONS BASED ON CHLORIDE AND STABLE ISOTOPE PROFILES

Author(s): Brent D. Newman, EES-15

Submitted to: Deliverable Report to the Performance Assessment Project.

Los Alamos
NATIONAL LABORATORY

Los Alamos National Laboratory, an affirmative action/equal opportunity employer, is operated by the University of California for the U.S. Department of Energy under contract W-7405-ENG-36. By acceptance of this article, the publisher recognizes that the U.S. Government retains a nonexclusive, royalty-free license to publish or reproduce the published form of this contribution, or to allow others to do so, for U.S. Government purposes. Los Alamos National Laboratory requests that the publisher identify this article as work performed under the auspices of the U.S. Department of Energy. The Los Alamos National Laboratory strongly supports academic freedom and a researcher's right to publish; as an institution, however, the Laboratory does not endorse the viewpoint of a publication or guarantee its technical correctness.

Form 836 (

Vadose Zone Water Movement at Area G , Los Alamos National Laboratory, TA-54: Interpretations Based on Chloride and Stable Isotope Profiles

Brent D. Newman

Environmental Science Group, EES-15

Los Alamos National Laboratory

December 9, 1996

ABSTRACT

Natural chloride and stable isotope tracers were used to examine the vadose zone hydrology of Mesita del Buey in the vicinity of the Los Alamos National Laboratory, Area G, Low-Level Radioactive Waste Facility. Pore-water chloride concentrations were measured with depth from core samples from four wells. In addition, $\delta^{18}O$ and δD stable isotope profiles were determined for one of the wells. The objectives of the study were to (1) quantify flux rates and pore water ages using the chloride data; (2) compare water flux rates to those obtained from hydraulic methods in order to estimate the most appropriate values for use in performance assessment modeling; and (3) examine stable isotope profiles for evidence of deep evaporation in the mesa system. In general, the chloride results indicate flux rates of a few mm/yr in the upper and lower parts of the mesa. All the wells have a zone of high chloride concentration at approximately mid-depth. Fluxes in these chloride bulge areas range from 0.03 to 0.8 mm/yr. It is likely that the bulges and low flux values may be related to evaporative removal of water in the mesa. However, differences in maximum chloride concentrations (e.g., 232 mg/L in well 1107 vs. 4755 mg/L in well 1117) suggest that there may be substantial lateral variability in the amount of evaporation that occurs. The chloride-based fluxes are reasonably consistent with those from hydraulic approaches. The chloride results also suggest that there is substantial lateral and vertical variability in the mesa hydrologic system. Finally, the stable isotope results indicate the

presence of isotopically heavy water in the same region as the chloride bulge. Isotopically heavy water indicates that deep evaporation is likely because the largest values occur at depths much greater than the depths at which solar-driven surface evaporation takes place.

INTRODUCTION

Evaluating representative flux rates for the Mesita del Buey vadose zone is crucial for performance assessment of the Area G Low-Level Radioactive Waste Facility located at the LANL TA-54. The hydraulic approach (e.g., Birdsell et al., 1995; Rogers and Gallaher, 1995) is one way that vadose zone fluxes can be estimated. However, because of the difficulty in measuring hydraulic properties and accurately determining moisture content, suction, and hydraulic conductivity relationships, the hydraulic approach yields flux estimates with large uncertainties. Thus, even though the hydraulic approach provides useful information, additional estimates of the flux that do not rely on the same assumptions or parameters as the hydraulic approach is beneficial. The additional estimates would provide increased confidence that representative flux values are used in the performance assessment process. The current study was designed to provide estimates of flux based on the chloride mass balance method (Allison et al., 1994; Stone, 1984). Because this is a tracer-based, and not a hydraulic-based approach, it provides the independent estimates of flux that are needed.

In addition to flux estimates, conceptual models of mesa hydrology can be refined using natural tracer studies.] In particular, stable isotopes can be used to evaluate evaporation, both at the mesa surface and at depth. The isotopic composition of water is affected by evaporation, which preferentially extracts light isotopes into the vapor phase, leaving the remaining liquid enriched in heavy isotopes. The depth at which δD and $\delta^{18}O$ reach their maximum (heaviest) values coincides with the depth of evaporation (Barnes and Allison, 1983; Allison et al., 1983). Deep evaporation in Mesita del Buey, in contrast to surface evaporation, has been suggested by Rogers and Gallaher (1995); Rogers et al. (1996); and Vold et al. (1997) based on data from moisture content and matric potential measurements. The idea of evaporative removal of water from mid-mesa depths of approximately 15 to 100 ft is untested, and will significantly influence contaminant mobility affecting performance assessment calculations.

Based on the need for independent estimates of flux and for testing the deep evaporation hypothesis, the objectives of this study were to (1) use natural chloride tracers to estimate flux rates of water in mesas and the age of water in the vadose zone water; (2) compare the chloride-based fluxes to hydraulic-based fluxes currently used to model vadose zone behavior at Area G; and (3) examine stable isotope data for evidence of deep evaporative removal of water within the mesa.

MATERIALS AND METHODS

Chloride Sampling and Laboratory Analyses

Chloride profiles were determined from core samples from wells 54-1107, 54-1117, 54-1121, and 54-1123 at Area G. Samples were collected and analyzed at 5- or 10-ft intervals. Chloride concentrations were determined by leaching the core samples with DI water and analyzing the leachate using ion chromatography. The leaching and analyses were performed at the Los Alamos EES-1 geochemistry laboratory. For each sample, approximately 50 g of tuff was crushed using a mortar and pestle. The tuff was then oven dried for at least 12 hours at 100°C. The dry sample was weighed and added to an Erlenmeyer flask along with approximately 75 g of DI water. The flask was agitated for 24 hours on a rotary mixer. Once the mixer was turned off and the solid material settled, the supernatant was filtered and analyzed using a Dionex Ion Chromatograph. Analytical precision of the ion chromatograph is better than 5 %.

Pore water chloride concentrations were calculated using the leachate concentrations, volumetric moisture contents (from Vold, 1996), and bulk densities (from Krier et al., 1995) for each well (see Appendix 1). The pore water chloride concentrations were then used in the chloride mass balance approach described below to estimate vertical fluxes and vadose water ages.

Chloride Mass Balance Approach

The chloride mass balance approach has been successfully used to determine vadose zone fluxes in semiarid and arid locations worldwide. The approach involves measuring chloride concentrations in vadose zone water with depth. These concentrations serve as indicators of downward flux and water age (Stone, 1984; Allison et al., 1994). The downward flux is inversely proportional to the amount of chloride accumulation: high chloride concentrations indicate a low flux that represents many years of meteoric chloride accumulation coupled with evapotranspirative removal of water. Relatively low chloride contents indicate a high downward flux, or water that is able to move through the vadose zone at a fast enough rate to minimize evapotranspiration effects.

The chloride mass balance method is based on the following assumptions: 1) flow occurs largely as downward piston flow; 2) dispersive mixing of water and chloride is small; 3) atmospheric chloride deposition has been relatively constant and is the sole source of chloride to the system; and 4) chloride uptake by plants is negligible. Uncertainty related to these assumptions will be addressed in the Discussion section.

If vadose zone chloride concentrations are constant below the root zone, then the average annual flux (or recharge rate) can be estimated using

$$R = P \cdot Cl_p / C_{sw}, \quad (1)$$

were R is the flux (m/yr); P is the average annual precipitation rate (m/yr); Cl_p is the average concentration of chloride in bulk precipitation (g/m^3); and C_{sw} is the chloride concentration in vadose-zone water below the root zone (g/m^3). However, chloride concentrations in deep profiles are sometimes not constant below the root zone. In this case, plots of cumulative chloride as a function of cumulative water in the profile can be used to determine changes in recharge rates over time. Approximately linear segments on the cumulative-cumulative plots indicate zones of constant flux. The flux for a segment is given by

$$R = (Cl_p \cdot P) / Cl_{sw}, \quad (2)$$

where Cl_{sw} is the average chloride content of the samples represented by the segment (g/m^3). Chloride-based vadose water ages can also be estimated by first calculating the amount of chloride in each sample interval down to the depth of interest using the relationship

$$Cl_i = \theta \cdot C_{cl} \cdot Z \quad (3)$$

where Cl_i is the amount of chloride in the interval (g/m^2), θ is the volumetric moisture content in the interval, C_{cl} is the mass of chloride in the interval per volume of rock (g/m^3), and Z is the length of the sample interval (m). By calculating the cumulative sum of the Cl_i values down to the depth of interest, the age can be calculated using

$$A = Cl_{cum}/(Cl_p \cdot P), \quad (4)$$

where A is age in years, and Cl_{cum} is the cumulative sum of the Cl_i values (g/m^2) at a given depth. A value of 0.36 m/yr was used for the average annual precipitation (P) based on measurements at TA-54 (Bowen, 1990), and a value of 0.29 g/m^3 was used for the average concentration of chloride in bulk precipitation (Cl_p) based on Anderholm (1994).

Stable Isotope Analyses

Stable isotope analyses of pore waters from Area G were conducted using moisture-protected samples from well 54-1117. The moisture-protected system involves sealing core samples in gas impermeable plastic bags as the cores were removed from the core barrel during drilling. This procedure reduces the chance of pore water evaporation during the period between sampling and analysis which would alter the isotopic composition of the water.

The stable-isotope analyses were carried out at the New Mexico Tech Stable Isotope Laboratory. Soil water was extracted by high-temperature vacuum distillation, following Shurbaji et al. (1995), and $\delta^{18}O$ and δD measurements were made on a Finnegan-Mat, Delta-E stable-isotope-ratio mass spectrometer using OZ-Tech gas standards. The hydrogen and oxygen isotopes are reported in delta (δ) notation as per mil (‰) differences relative to the V-SMOW international standard:

$$\delta D \text{ or } \delta^{18}O = \left[\frac{R_{sample} - R_{SMOW}}{R_{SMOW}}\right] \times 1000, \qquad (5)$$

where R is the D/H or $^{18}O/^{16}O$ ratio. The value of $\delta^{18}O$ was measured from extractions made using the carbon dioxide equilibration technique of Socki et al. (1992). For the δD analyses, hydrogen was extracted using the hot uranium method of Bigeleisen et al. (1952), and the analyses were corrected by means of a linear equation ($\delta D_{actual} = 1.008\delta D_{measured} + 7.378$) based on regression analysis of V-SMOW and GISP standards. The analytical precision for the $\delta^{18}O$ and δD analyses by mass spectroscopy is better than ±0.2 ‰ and ±6 ‰, respectively. Two of the distillates (the 16.6 and 25.6 ft samples) did not yield reasonable δD values. It is likely that some hydrogen was produced from organic material, possibly from decayed roots, invalidating the water δD values.

RESULTS

Chloride profiles for the four wells are shown in Figure 1. The chloride concentrations are not constant with depth, and each profile shows a distinct bulge of high concentration between the 15 to 80 ft depths. The changes in chloride concentrations generally correspond to changes in volumetric moisture content where the chloride bulges occur in the zone of low moisture content (Figure 2).

Because the chloride concentrations were not constant with depth, the cumulative chloride-cumulative water approach was used to calculate fluxes (values used in the flux and age calculations are given in Appendix 1). Cumulative-cumulative plots for each well are shown in Figure 3. The figures show three approximately linear segments, with well 1107 having a possible fourth segment below the vapor phase notch. Flux rates were calculated for the three segments for each well (Table 1). For the upper segments that correspond to the shallowest depths, relatively high flux rates are indicated as compared to the middle segment. Wells 1107 and 1121 yield flux rates of 6 and 3 mm/yr, respectively, whereas the upper segments for wells 1117 and 1123 yield rates of 0.1 and 1.5 mm/yr. The reason that the 1117 and 1123 rates are so much lower than those of 1107 and 1121 is that shallow samples were not available for 1117 and 1123 and these would tend to have lower chloride concentrations which would increase the flux estimates. Flux rates are the lowest in each of the wells for the middle segments and range from 0.03 to 0.8 mm/yr. For the deepest segments, the flux rates increase to values similar to that of the upper segments. Again, there were no samples available deeper than about 90 ft for wells 1117 and 1123 and thus, the estimates of deep flux rates are substantially lower than those from 1107 and 1121 because only a few low chloride concentration samples were available.

Chloride accumulation ages for each well are also shown in Table 1. Ages for well 1107 suggest that it takes between one to two thousand years to

reach the 125 ft depth. Ages for the other wells suggest that it takes approximately six thousand years or more to reach the same depth.

The stable isotope profiles for well 1117 are shown in Figure 4. The trend is for the pore waters to become lighter in both $\delta^{18}O$ and δD with depth. Because there were no moisture-protected samples available for depths less than 16 ft, generalized curves for shallow isotope profiles at TA-51 (Newman et al., 1996) are also shown in Figure 4. TA-51 is on the same mesa as Area G, approximately 3 km upslope, and is probably a good proxy for undisturbed conditions at Area G. The TA-51 curves show that solar-induced surface evaporation is limited to shallow depths. By a depth of 1-2 meters, isotopic values become lighter (-9 to -10 $\delta^{18}O$ and -80 to -95 δD). At the depth that the well 1117 data start, isotopic values are substantially heavier than the 1-2 meter samples from TA-51. This difference is important for evaluating deep evaporative processes and will be explained further below.

DISCUSSION

Significance of the Chloride Bulges

The chloride bulges (Figure 1) are important features of the vertical profiles because the origin of these chloride accumulations will affect the development of conceptual and quantitative models of the mesa hydrologic system. One explanation is that the bulges represent a past period of low percolation rates and high evapotranspiration which was followed by a period

of higher percolation rates and lower evapotranspiration that displaced the chloride bulges to the ≈20-80 ft depth. However, the vadose water ages for the bulges are not concordant. If changing paleoclimate was the cause of the chloride bulges, roughly similar peak concentrations and ages would be expected. A further problem is that the climate for the last 20000 years, though variable, has tended to be wetter than the present (Phillips et al., 1986; Stute et al., 1992). This is in direct contrast to the interpretation that the bulges indicate drier past conditions. The most likely explanation is that the bulges represent a zone of evaporation and vapor phase transport which would cause chloride to accumulate. The possible pathways of vapor movement are discussed in the Deep Evaporation section below. Evaporation seems to be a plausible explanation given that other studies have suggested the possible presence of deep zones of vapor dominated transport (e.g., Rogers and Gallaher, 1995; Rogers et al., 1996; Vold et al. 1997). The evaporative zone, if present, may not always act as a barrier to flow as indicated by the profile and flux rates for well 1107 (Figure 1, Table 1). Even though there is a chloride bulge in well 1107, the mass accumulated is a fraction of that in the other wells and the estimated vertical flux is still fairly large (0.8 mm/yr). The differences in chloride accumulation between the wells suggests that if evaporation occurs, there may be substantial lateral heterogeneity where the evaporative flux is not uniform throughout the mesa. The changes in chloride concentration appear to be correlated to certain stratigraphic units and

features. The bulge in well 1107 occurs mainly within the lower part of unit 2b (surge beds), while the bulges in wells 1117, 1121 and 1123 occur within the stratigraphically lower units, 2a and 1b. These units may act as permeable zones that have a direct connection to the atmosphere. For example, the surge beds at the base of unit 2b have been suggested as a potential evaporative zone (Rogers and Gallaher, 1995; Rogers et al., 1996) which is consistent with the chloride bulge in well 1107. The bulges in wells 1117, 1121, and 1123 overlap the surge beds in some cases, but also the lithologic contacts between units 1v(c), 1v(u1), and 1v(u2) (following the suggested nomenclature of Broxton and Reneau, 1995). These units are fractured and contain pumice beds, either of which may have a connection to the atmosphere permitting deep evaporation.

The vapor-phase notch (Figure 3) is another stratigraphic feature that appears to control or at least correlate with changes in chloride concentrations and flux rates. Chloride concentrations at and below the vapor-phase notch are dilute and the decrease in concentration corresponds to a substantial increase in moisture content at the vapor phase notch. In wells 1121 and 1123 a large change in slope occurs between the middle segment and the deepest segment of the cumulative-cumulative plots (Figures 3c and 3d), that corresponds to the vapor-phase notch. The influence of the vapor phase notch in well 1107 is more subtle (Figure 3a). The cumulative-cumulative plot for well 1107 shows a small change in slope in the deepest segment close to the vapor phase notch. If there were samples deeper in the profile, a fourth

segment below the vapor phase notch might be more readily apparent. Only one sample from below the vapor phase notch was available for well 1117, so no assessment of its influence can be made for this well.

Uncertainty

With the various assumptions used in the chloride mass balance method there are some related uncertainties. The first uncertainty relates to the 1-D vertical flow assumption. If deep evaporative processes occur, then potentially large but unquantifiable errors in the flux estimates result. From a qualitative point of view, however, a large chloride concentration associated with an evaporative zone is consistent with a low flux. Lateral flow also violates the 1-D vertical flow assumption. If there is lateral flow in the deeper units at the base of the mesa (described in the Stable Isotope section, below) then the flux estimates are suspect because lateral flow can add or remove chloride from the system. Fracture flow is not considered in the chloride mass balance approach either and because of its possible importance, especially in the shallower tuff units, fracture flow adds additional uncertainty to the flux and age estimates. Another factor that contributes to uncertainty is the concentration of chloride entering the mesa. Unfortunately, there are no long term data available for the Los Alamos area, but short term data can be used to bound the problem. A value of 0.29 g/m^3 was used in the flux and age calculations based on a chloride mass balance study by Anderholm (1994) for the Sante Fe area. This

value may be higher than the Pajarito Plateau average value, and is probably a conservative value in that it may overestimate flux rates and underestimate the ages. Evaluation of chloride concentrations in precipitation from the National Atmospheric Deposition Program station at Bandelier National Monument (NADP, 1994) and various sampling stations on the Pajarito Plateau monitored by Adams et al. (1995) suggest that chloride concentrations in rainfall might be as low as 0.1 g/m^3. If this value is more representative of the Pajarito Plateau, then the fluxes in Table 1 would be about one third less than those shown and the ages would be about three times greater. The different chloride input values do not make order of magnitude changes in the flux rates, and thus do not result in much additional uncertainty, especially when compared to uncertainties from other factors such as deep evaporation. The effects of different chloride concentrations are important considerations for correlating ages and changes in flux with past periods of climate change because some paleoclimate changes have occurred over relatively short time periods.

Comparison of Chloride-Based Flux Estimates to Other Flux Estimates

Birdsell et al. (1995) used a modeling approach to estimate flux values in the vadose zone beneath Area G. They used generalized hydraulic parameters for the different stratigraphic units and varied the infiltration rate in order to match existing in-situ saturation data. They found that the saturation profile could not be simulated using a single flux value. Instead, they used three

different flux values to match three saturation zones in the profile. Their result is consistent with the chloride results in that three main flux zones were also identified. Unfortunately, the magnitudes of the chloride-based flux rates do not agree with the simulations in some cases. For example, Birdsell et al. found that a low flux of 0 to 0.1 mm/yr fit the saturation data from unit 2b best. For the same unit, the chloride-based flux rates are 3-6 mm/yr. This discrepancy results from differences in moisture contents used in the simulations versus those used in the chloride method. The moisture contents used by Birdsell et al. were based on values for the lower part of the unit where values range from 1 to 4% volumetric. The upper part of the unit is much wetter with moisture contents on the order of 7 to 14% and these values were used in the chloride-based estimates.

There was some consistency between the simulations and the chloride results for unit 2a, in that both studies indicate unit 2a is a zone of low flux. Again, however, the chloride method yields higher flux rates than the simulations, probably because of higher moisture contents than those used in the simulations. For units 1a and 1b, the chloride-based flux rates agree with the range of flux rates from the simulations. For the Cerro Toledo and Otowi units, the chloride-based estimate for well 1121 is consistent with the simulations. Wells 1107 and 1117 were not drilled into the Cerro Toledo and Otowi units, and only one sample was available from well 1123, so no comparisons can be made for these wells.

Another comparison can be made using the flux estimates for the upper part of unit 2b. Newman et al. (1996) estimated chloride-based flux rates through various soil profiles and into the first 10-50 cm of unit 2b for an undisturbed site at TA-51. For soils without clay-rich Bt horizons, which is representative of conditions at Area G, flux rates ranged from 0.5 to 10 mm/yr. Though these estimates are dominated by soil hydraulic properties, the majority of the estimates are consistent with the 3-6 mm/yr estimates for the upper part of unit 2b at Area G. Newman et al. also noted substantial lateral variability in flux rates, consistent with the results from this study.

A final comparison can be made with the results of Vold et al. (1997) who calculated the magnitude of liquid and vapor fluxes in the mesa. Overall, the Vold et al. results are in reasonable agreement with the chloride-based flux estimates. Vapor-flux rates dominate in the middle of the mesa, which corresponds to the zone of low chloride-based flux rates, and supports the hypothesis of deep evaporation. Liquid flux rates are dominant in the region near and below the vapor phase notch, which is consistent with the increase in chloride-based flux rates in the deeper parts of the mesa.

Stable Isotopes

Stable isotope data from well 1117 (Figure 4) provide additional evidence for deep evaporation. The TA-51 data show that surface evaporation effects disappear at depths less than 6 ft whereupon values reach relatively light $\delta^{18}O$

and δD values of -9 to -10 ‰ and -80 to -95 ‰, respectively. Unsaturated zone stable isotope theory predicts that a quasi-steady state value should be reached below the zone influenced by solar surface evaporation (Allison et al., 1983; Barnes and Allison, 1983). In other words, the approximately -9 ‰ $\delta^{18}O$ value, for example, should be maintained throughout the profile for all depths below about 6 ft. However, contrary to theory, the 1117 data show quite heavy values at depths below the zone influenced by surface evaporation.

A paleoclimate interpretation for the existence of isotopically heavy values deep in the profile does not seem plausible, as explained in the chloride bulge discussion. Instead, the isotope data are consistent with evaporative removal of water from within the mesa. At present, it is not clear how this process works or what the pathways for airflow and water removal might be. One hypothesis is that dry air travels down vertical fractures in the tuff, evaporates the water and moves back out of the fractures in response to thermal or barometric changes. Alternatively, the sides of the mesa could play a role in allowing dry air into the system and moving water vapor out. The Bandelier tuff is exposed on the mesa sides and is subject to a wide range of temperatures and barometric pressures. At this stage, the tracers and low moisture contents strongly indicate that deep evaporation occurs in the mesa. However, additional isotope data are needed to confirm the behavior seen in well 1117 and more work will be required to understand the mechanisms and pathways by which the evaporation occurs.

The existence of light isotope values at the vapor phase notch at the 85 ft depth in well 1117 leads to two explanations. The first is that water infiltrated during a higher precipitation period during the Pleistocene or early to mid Holocene, and was not subject to extensive evaporation. Studies by Phillips et al. (1986) and Stute et al. (1992) indicate that such periods occurred in the past 20,000 years, so this explanation appears to be reasonable for the light water at the bottom of the profile. The second explanation is that water may have been introduced by lateral flow along pathways that were not subject to evaporation of the same intensity that occurred in the middle of the mesa. It is possible that recharge in the adjacent canyons flows underneath Mesita del Buey, and Pajarito Canyon in particular contains saturated alluvial zones which could generate lateral flow. Unfortunately, we do not have enough information about the link between mesa and canyon hydrology to adequately evaluate if lateral flow really occurs. The stable isotope data however, can provide valuable clues regarding the validity of the lateral flow hypothesis. A meteoric water plot (Figure 5) shows a well-defined evaporation trend line extending from the local meteoric water line to the right. $\delta^{18}O$ and δD values of precipitation from the Pajarito Plateau plot along the local meteoric water line, and if evaporation occurs the isotopic values will become progressively heavier following a trend such as that shown for well 1117. The evaporative trend line suggests that all of the waters in the 1117 profile have the same source, including the light water at the vapor phase notch. Thus, if lateral flow occurs,

it would have to have the same original isotopic composition as the water that was evaporated from the middle of the mesa. In other words, the source of the lateral flow would need to plot on the same evaporation trend line as the 1117 waters. Measurements of the isotopic composition of potential lateral flow sources, such as the alluvial groundwater from Pajarito Canyon, would greatly aid in resolving this question.

SUMMARY AND CONCLUSIONS

Chloride flux estimates for wells 1107, 1117, 1121, and 1123 showed reasonable similarity in overall behavior where flux rates were highest in the shallow and deeper parts of Mesita del Buey and lowest in the middle of the mesa. Flux estimates for the shallow and deep zones are on the order of a few mm/yr. For the middle region of the mesa, flux estimates ranged from 0.03 mm/yr for well 1123 to 0.8 mm/yr for well 1107. The low mid-depth fluxes in the wells are related to large concentrations of chloride. It appears that these concentrations are related to deep evaporative processes, and a stable isotope profile from well 1117 supports this conclusion. One detail is that the bulge in well 1117 has a very high maximum chloride concentration (4755 mg/L), while the bulge for well 1107 has a much lower concentration (232 mg/L). The large differences in chloride concentrations suggest that there is substantial lateral variability in vertical flux and in the amount of evaporation that occurs. In summary, it appears that the Mesita del Buey vadose zone is characterized by

substantial lateral and vertical heterogeneities that control the rates of water movement in the mesa. In addition, water movement in the middle of the mesa is likely influenced by deep evaporation. Future work will involve measuring additional isotope profiles to verify the behavior seen in well 1117, and will also include analyses of shallow isotope data from Area G so that site specific values can be used instead of those from TA-51.

ACKNOWLEDGMENTS

The author gratefully appreciates the interest and support of Diana Hollis and Erik Vold. Thanks are given to Dale Counce for performing the leachings and chloride analyses, and to Andrew Campbell, Jeff Klein, and Christa Vindum for their work on the stable isotope analyses.

REFERENCES

Adams, A. I., F. Goff and D. Counce. 1995. Chemical and Isotopic Variations of Precipitation in the Los Alamos Region, New Mexico. Los Alamos National Laboratory Report, LA-12895-MS. 35 pp.

Allison, G. B., Barnes, C. J. and Hughes, M. W. 1983. The Distribution of Deuterium and ^{18}O in Dry Soils 2: Experimental. J. Hydrol. 64: 377-397.

Allison, G. B., G. W. Gee, and S. W. Tyler. 1994. Vadose-Zone Techniques for Estimating Groundwater Recharge in Arid and Semiarid Regions. Soil Sci. Soc. of Am. J. V. 58. pp. 6-14

Anderholm, S. K. 1994. Ground-water recharge near Sante Fe, north-central New Mexico. USGS Water-Res. Invest. Rep. 94-4078. 68 pp.

Barnes, C. J., and Allison, G. B., 1983. The Distribution of Deuterium and "O in Dry Soils. 1. Theory. J. Hydrol., 60: 141-156.

Bigeleisen, J., M. L. Perlman, H. C. Prosser. 1952. Conversion of Hydrogenic Materials to Hydrogen for Isotopic Analysis. Anal. Chem., V. 24. pp. 1356-1357.

Birdsell, K. H., W. E. Soll, N. D. Rosenberg, and B. A. Robinson. 1995. Numerical Modeling of Unsaturated Groundwater Flow and Radionuclide Transport at MDA G. . Los Alamos National Laboratory Report, LA-UR-95-2735. 49 pp.

Bowen, B. M. 1990. Los Alamos Climatology. Los Alamos National Laboratory Report LA-11735-MS. 254 pp.

Broxton, D. E. and S. L. Reneau. 1995. Stratigraphic Nomenclature of the Bandelier Tuff for the Environmental Restoration Project at Los Alamos National Laboratory. Los Alamos National Laboratory Report, LA-13010-MS. 21 pp.

Krier, D., P. Longmire, R. Gilkeson, and J. Turin. 1995. Geologic, Geohydrologic, and Geochemical Data Summary of MDA G, TA-54, Los Alamos National Laboratory, Los Alamos, New Mexico. in Performance Assessment of LANL, TA-54, Area G, Low-Level Radioactive Waste Disposal Facility (DRAFT). D. Hollis, E. Vold, K. Birdsell, J. Turin, P. Longmire, E. Springer, W. Hansen, D. Krier, and R. Shuman.

National Atmospheric Deposition Program (NADP). 1994. National Trends Network NADP/NTN (NRSP-3) Site Report, Precipitation and Chemistry Data. Natural Resource Ecology Laboratory, Colorado State, Ft. Collins, CO.

Newman, B. D., A. R. Campbell, and B. P. Wilcox. 1996. Tracer-based Studies of Soil Water Movement in Semi-Arid Forests of New Mexico. Accepted for Publication in the Journal of Hydrology

Phillips, F. M., L. A. Peters, M. K. Tansey, and S. N. Davis. 1986. Paleoclimatic Inferences from an Isotopic Investigation of Groundwater in the Central San Juan Basin, New Mexico. Quat. Res. V. 26. pp. 179-193.

Rogers, D. B, and B. M. Gallaher. 1995. The Unsaturated Hydraulic Characteristics of the Bandelier Tuff. Los Alamos National Laboratory Report, LA-12968-MS.

Rogers, D. B., B. M. Gallaher, and E. L. Vold. 1996. Vadose Zone Infiltration Beneath the Pajarito Plateau at Los Alamos National Laboratory. New Mexico Geological Society 1996 Guidebook, Geology of the Los Alamos-Jemez Mountains Region. In Press.

Shurbaji, A.-R.M., Phillips, F. M., Campbell, A. R. and Knowlton, R. G. 1995. Application of a Numerical Model for Simulating Water Flow, Isotope Transport, and Heat Transfer in the Unsaturated Zone. J. Hydrol. 171: 143-163.

Socki, R. A., Karlsson, H. R. and Gibson, E. K. 1992. Extraction Technique for the Determination of Oxygen-18 in Water Using Preevacuated Glass Vials. Anal. Chem., 64: 829-831.

Stone, W. J. 1984. Recharge in the Salt Lake Coal Field Based on Chloride in the Unsaturated Zone. New Mexico Bureau of Mines and Mineral Resources, Open-File Report 214. 64 pp.

Stute, M., P. Schlosser, J. F. Clark, and W. S. Broecker. 1992. Paleotemperatures in the Southwestern United States Derived from Noble Gases in Ground Water. Science, V. 256. pp. 1000-1002.

Vold, E. 1996. Unpublished Data. Los Alamos National Laboratory.

Vold, E., B. Newman, K. Birdsell, B. Gallaher, D. Krier, P. Longmire, D. Rogers, and E. Springer. 1997. Representative Recharge Rates in a Complex Unsaturated Hydrogeology. Waste Management 97. In preparation.

Vuataz, F.-D. and Goff, F. 1986. Isotope Geochemistry of Thermal and Nonthermal Waters in the Valles Caldera, Jemez Mountains, Northern New Mexico. J. Geophys. Res., 91(B2): 1835-1853.

Table 1. Flux Estimates and Soil Water Ages for Wells 1107 and 1121, Area G

Well 1107		
Depth interval (ft)	Flux (mm/yr)	Age at bottom of depth interval (yr)
0-31	6	120
31-58	0.8	1169
66-125	5	1345

Well 1117		
Depth interval (ft)	Flux (mm/yr)	Age at bottom of depth interval (yr)
15-30	0.1	482
35-60	0.03	8295
70-85	0.2	9674

Well 1121		
Depth interval (ft)	Flux (mm/yr)	Age at bottom of depth interval (yr)
0-42	3	323
42-84	0.06	17659
89-146	5	17862

Well 1123		
Depth interval (ft)	Flux (mm/yr)	Age at bottom of depth interval (yr)
9-20.3	1.5	118
25-62.5	0.1	5507
65-90.8	0.9	5852

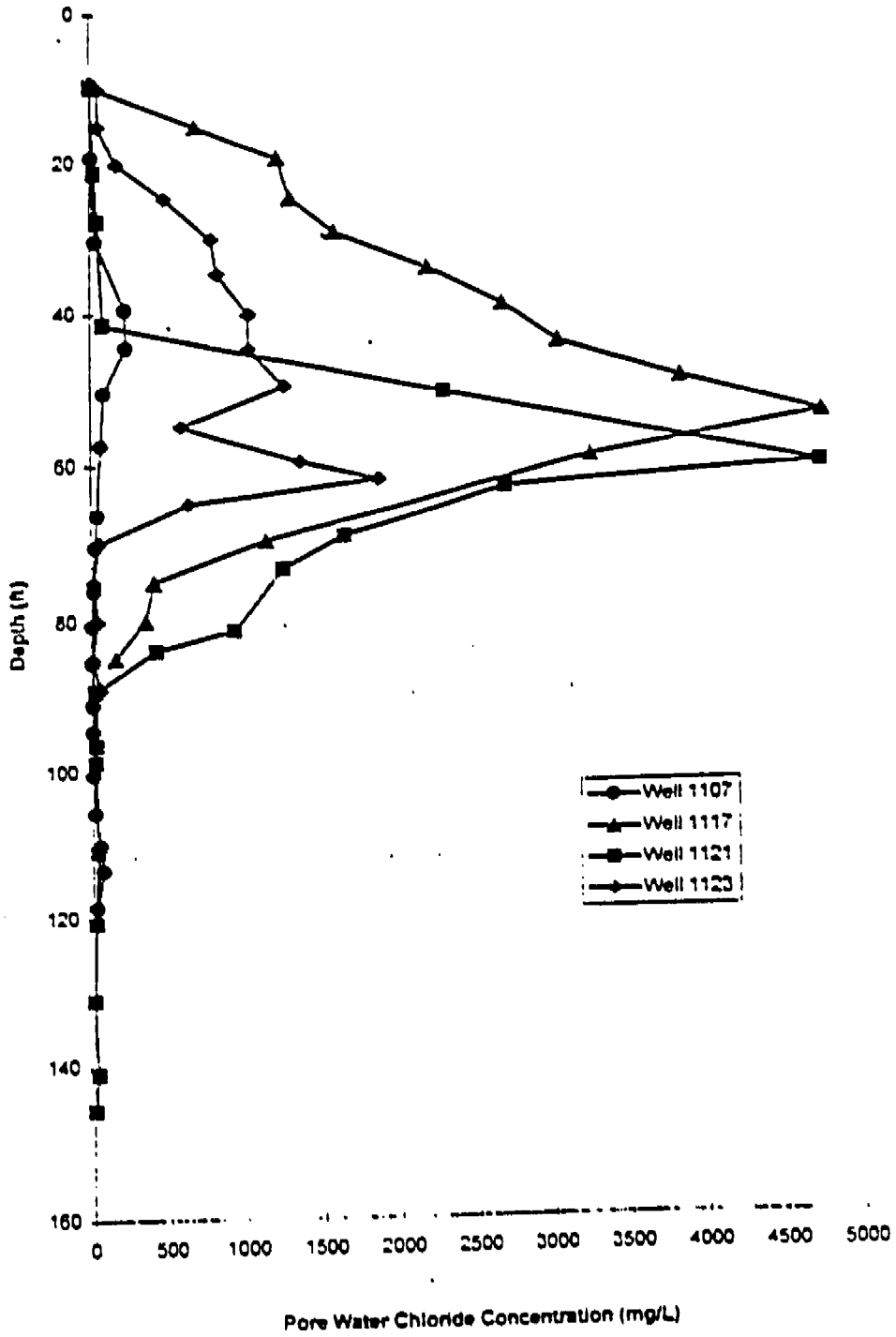

Figure 1. Chloride profiles for wells 1107, 1117, 1121, and 1123.

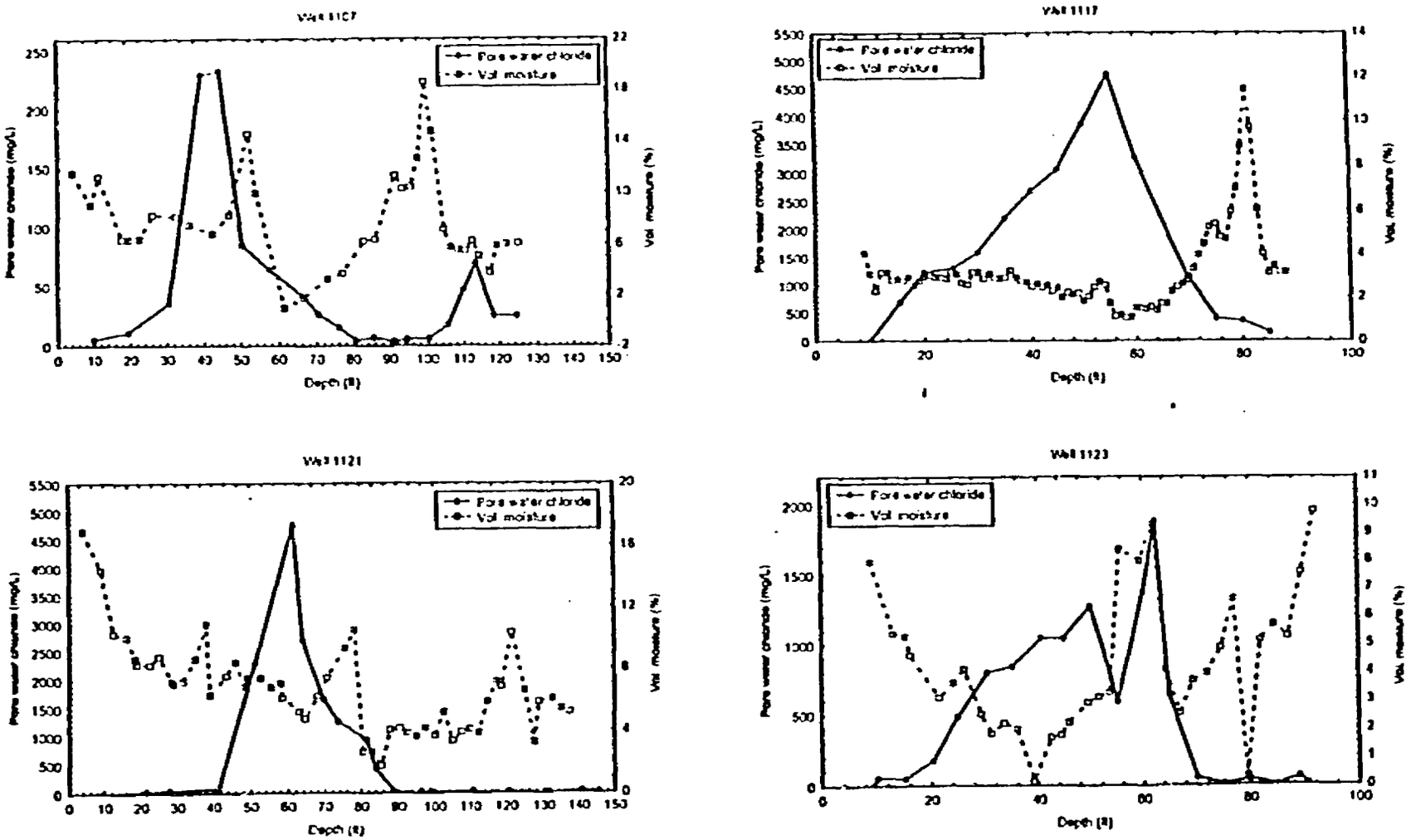

Figure 2. Comparison of pore water chloride and volumetric moisture profiles.

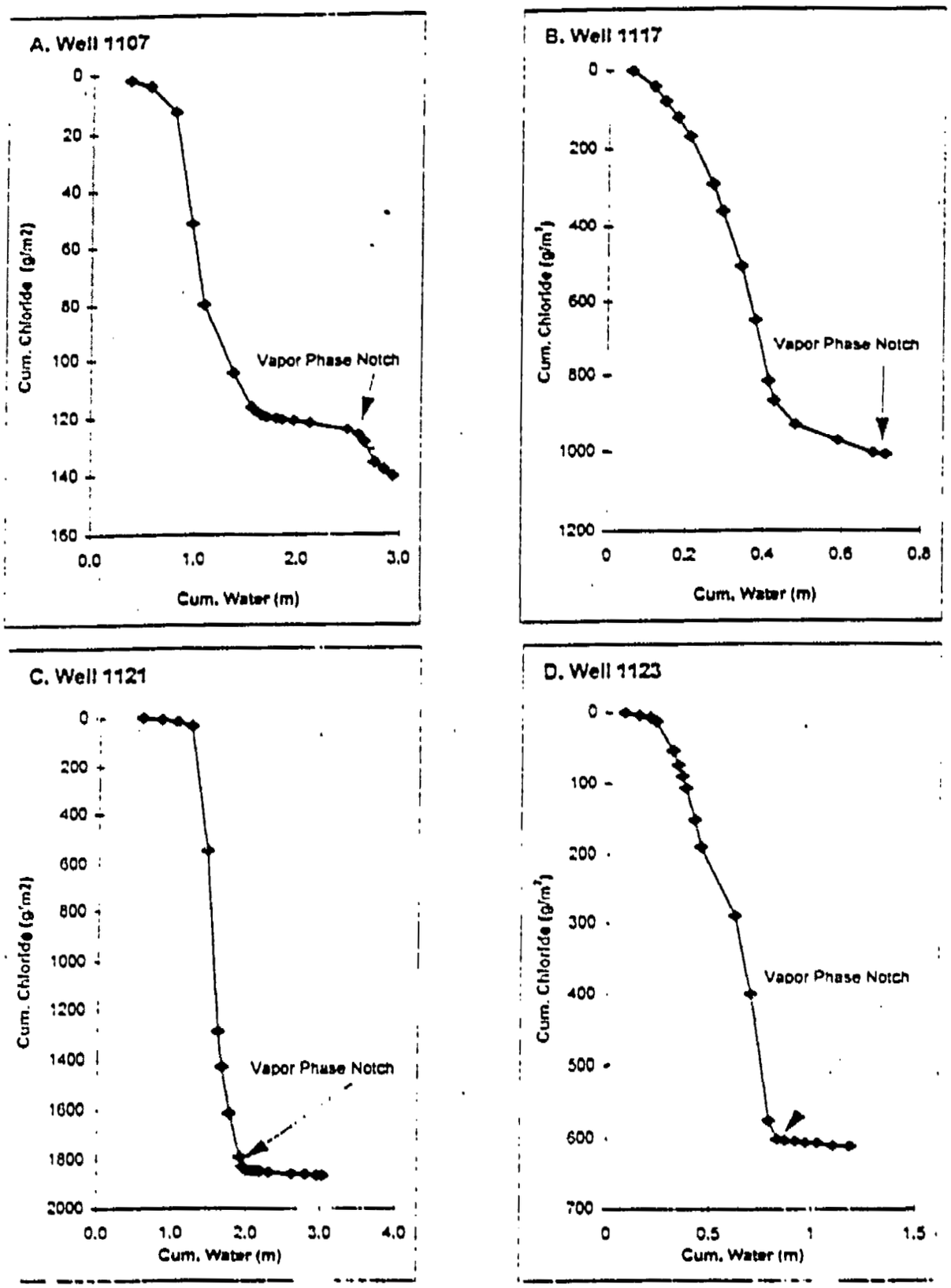

Figure 3. Cumulative water vs. cumulative chloride for wells 1101, 1117, 1121, and 1123.

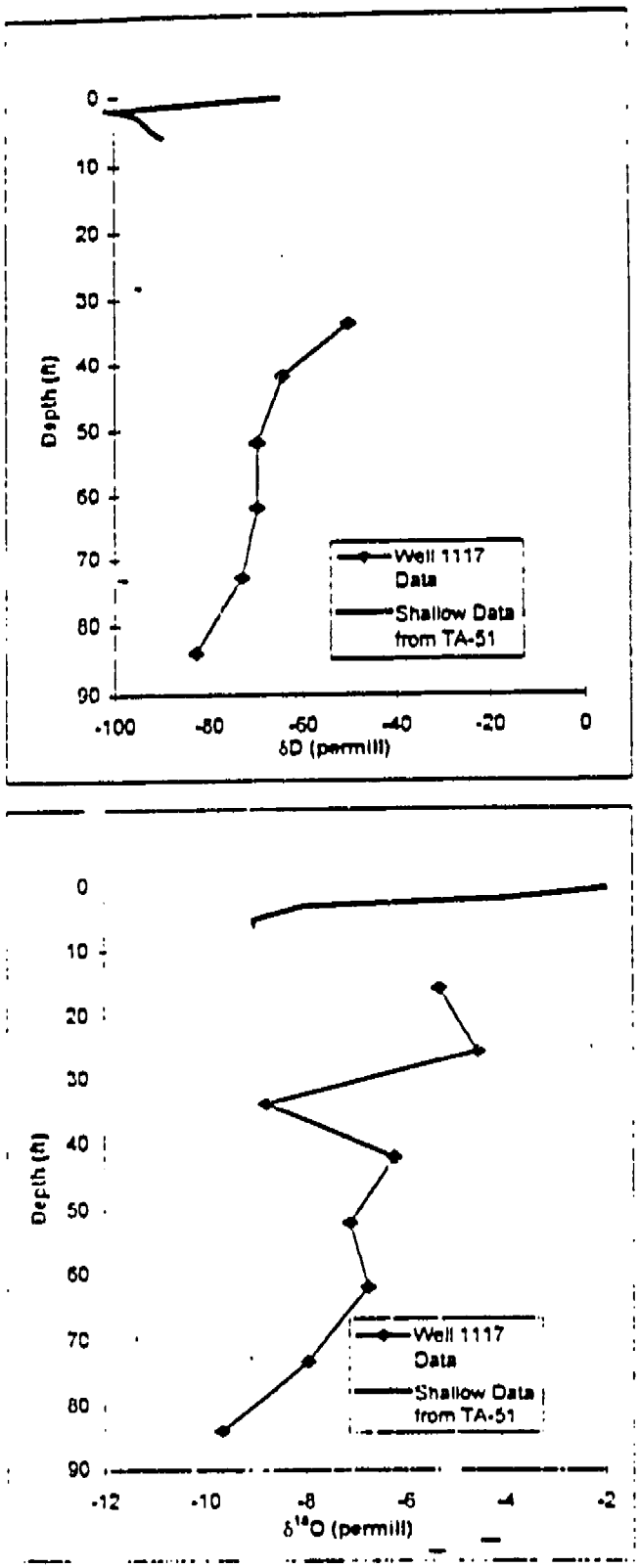

Figure 4. δD and $\delta^{18}O$ in well 1117 pore waters and TA-51 soils.

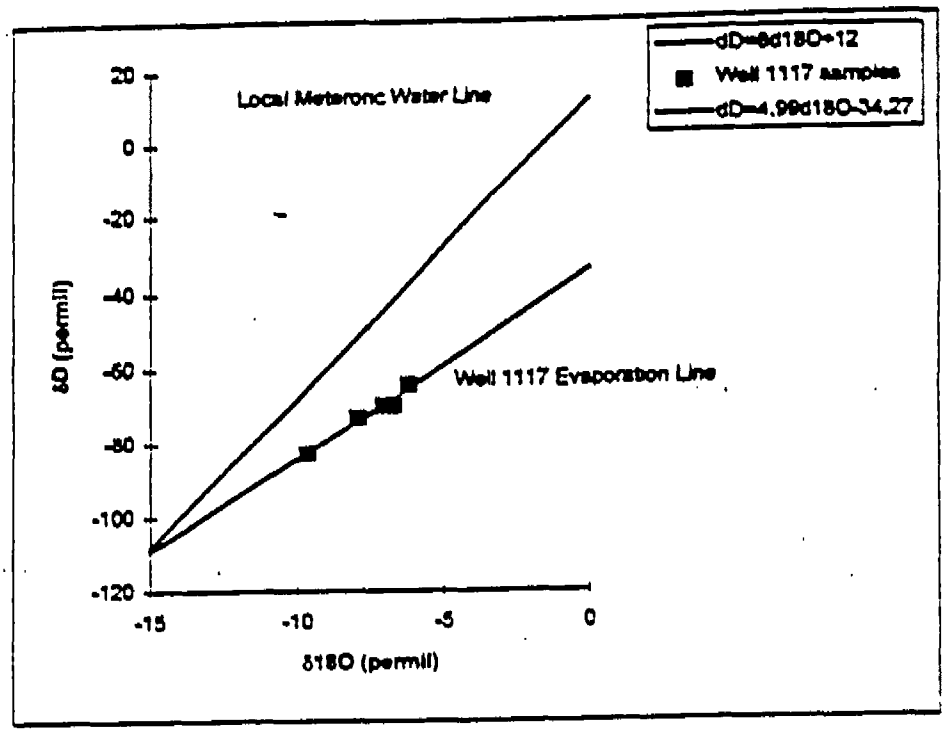

Figure 5. Meteoric water plot of well 1117 waters. The local meteonc water line is from Vuataz and Goff (1986).

Appendix 1a. Data for Area G Core 54-1107

Sampled Depth (ft)	Midpoint (m)	Cl- leachate conc. (mg/L)	DI added (g)	Cl- (mg)	Tuff Dry wt. (g)	θv (%)	ρb (g/cm3)	Pore H2O (L)	Clsw (mg/L)	Clswi (g/m3)	Interval (m)	Interval Clswi (g/m2)	Cum. Clswi (g/m2)	Interval θd (m)	Cum θd (m)
9.7	3.0	0.22	75.17	0.017	46.75	9.01	1.37	0.003	5.4	5.4	4.0	1.9	2	0.4	0.4
19.3	5.8	0.36	75.08	0.027	52.49	6.32	1.37	0.002	11.2	11.2	3.0	2.1	4	0.2	0.6
30.5	9.1	1.35	76.31	0.103	49.51	8.07	1.37	0.003	35.3	35.3	3.0	8.6	13	0.2	0.8
39.5	12.2	7.44	75.29	0.560	49.63	6.75	1.37	0.002	229.1	229.1	2.5	38.7	51	0.2	1.0
44.5	13.4	9.32	75.03	0.699	50.30	8.21	1.37	0.003	232.0	232.0	1.5	28.8	80	0.1	1.1
50.4	15.2	6.07	75.21	0.457	50.46	14.5	1.37	0.005	85.5	85.5	2.0	24.8	105	0.3	1.4
57.4	17.4	3.41	74.91	0.255	55.35	9	1.26	0.004	64.6	64.6	2.0	11.6	116	0.2	1.6
66.3	20.2	0.41	77.45	0.032	56.53	1.7	1.26	0.001	41.8	41.6	1.5	1.1	117	0.0	1.6
70.5	21.3	0.48	75.08	0.036	54.41	3.2	1.26	0.001	26.1	26.1	2.0	1.7	119	0.1	1.6
76	23.2	0.32	75.07	0.024	53.96	3.65	1.26	0.002	15.4	15.4	1.5	0.8	120	0.1	1.7
80.5	24.4	0.14	75.72	0.011	47.58	6.22	1.26	0.002	4.5	4.5	1.5	0.4	120	0.1	1.8
85.5	26.2	0.22	74.99	0.016	50.04	6.31	1.26	0.003	6.6	6.6	1.0	0.4	121	0.1	1.9
90.9	27.7	0.24	75.00	0.018	49.08	11.3	1.2	0.005	3.9	3.9	1.0	0.4	121	0.1	2.0
94.4	28.7	0.30	75.02	0.023	49.01	10.3	1.2	0.004	5.4	5.4	1.5	0.8	122	0.2	2.1
100.4	30.5	0.69	74.99	0.052	51.60	18.6	1.2	0.008	6.5	6.5	2.0	2.4	124	0.4	2.5
105.6	32.3	0.72	75.14	0.054	48.98	7.14	1.14	0.003	17.6	17.6	1.5	1.9	126	0.1	2.6
110	33.5	1.62	75.14	0.122	53.13	5.46	1.14	0.003	47.8	47.8	1.0	2.6	129	0.1	2.7
113.5	34.6	2.01	75.94	0.153	49.05	5.07	1.14	0.002	70.0	70.0	2.0	7.1	136	0.1	2.8
118.5	36.0	0.88	75.10	0.066	50.04	5.86	1.14	0.003	25.7	25.7	1.5	2.3	138	0.1	2.8
124.5	37.8	0.88	76.56	0.067	50.48	6.0534	1.14	0.003	25.1	25.1	1.5	2.3	140	0.1	2.9

Appendix 1b. Data for Area G Core 54-1117

Sampled Depth (ft)	Midpoint (m)	Cl- leachate conc. (mg/L)	DI Added (g)	Cl- (mg)	Tuff Dry Wt (g)	θv (%)	ρb (g/cm3)	Pore H2O (L)	Clsw (mg/L)	Clswi (g/m3)	Interval	Interval Clswi (g/m2)	Cum. Clswi (g/m2)	Interval θd (m)	Cum θd (m)
9.9	3.0	0.15	74.63	0.01	51.329	3.074	1.37	0.001	10	10	2.0	0.6	1	0.06	0.1
15.5	4.7	9.79	77.32	0.76	52.509	2.836	1.37	0.001	696	696	2.0	39.5	41	0.06	0.1
20	6.1	17.7	75.57	1.34	50.386	2.955	1.37	0.001	1231	1231	1.0	36.4	77	0.03	0.1
25.35	7.7	20.7	74.54	1.54	51.255	3.134	1.37	0.001	1316	1316	1.0	41.2	118	0.03	0.2
30	9.1	27.6	74.33	2.05	55.853	3.149	1.37	0.001	1598	1598	1.0	50.3	169	0.03	0.2
35	10.7	34.2	76.81	2.63	51.627	2.91	1.26	0.001	2203	2203	2.0	128.2	297	0.06	0.3
40	12.2	37.1	74.43	2.76	51.745	2.493	1.26	0.001	2697	2697	1.0	67.2	364	0.02	0.3
45	13.7	49.2	76.38	3.76	63.972	2.418	1.26	0.001	3061	3061	2.0	148.0	512	0.05	0.3
50	15.2	36.6	76.99	2.82	50.114	1.837	1.26	0.001	3856	3856	2.0	141.7	654	0.04	0.4
55	16.8	41.6	77.77	3.24	49.893	1.718	1.26	0.001	4755	4755	2.0	163.4	817	0.03	0.4
60	18.3	26.0	76.89	2.00	51.546	1.495	1.26	0.001	3270	3270	1.0	48.9	866	0.01	0.4
70	21.3	17.5	74.66	1.31	49.020	2.791	1.2	0.001	1146	1146	2.0	64.0	930	0.06	0.5
75.1	22.9	11.4	76.23	0.87	47.426	5.369	1.2	0.002	410	410	2.0	44.0	974	0.11	0.6
80	24.4	17.3	76.96	1.33	50.834	8.87	1.2	0.004	354	354	1.0	31.4	1005	0.09	0.7
85	25.9	3.00	76.48	0.23	53.021	3.149	1.14	0.001	157	157	1.0	4.9	1010	0.03	0.7

Appendix 1c. Data for Area G Core 54-1121

Sampled Depth (ft)	Midpoint (m)	Cl- leachate conc. (mg/L)	DI Added (g)	Cl- (mg)	Tuff Dry Wt (g)	θv (%)	ρb (g/cm3)	Pore H2O (L)	Clsw (mg/L)	Clswi (g/m3)	Interval (m)	Interval Clswi (g/m2)	Cum. Clswi (g/m2)	Interval θd (m)	Cum θd (m)
9.7	3.0	0.15	75.65	0.01	55.92	14.39	1.37	0.006	2	2	4.0	1.1	1	0.6	0.6
21.4	6.4	1.14	74.82	0.09	50.77	8.261	1.37	0.003	28	28	3.0	6.9	8	0.2	0.8
27.9	8.5	1.84	76.24	0.14	53.33	7.157	1.26	0.003	46	46	3.0	9.9	18	0.2	1.0
41.5	12.8	2.80	74.13	0.21	49.73	6.3	1.26	0.002	83	83	3.0	15.8	34	0.2	1.2
51.2	15.5	92.3	74.17	6.85	50.57	7.396	1.26	0.003	2306	2306	3.0	511.8	545	0.2	1.4
61.5	18.9	133	77.38	10.29	52.39	5.216	1.26	0.002	4744	4744	3.0	742.4	1288	0.2	1.6
63.7	19.5	75.7	75.74	5.73	51.21	5.216	1.26	0.002	2705	2705	1.0	141.1	1429	0.1	1.7
69.6	21.3	68.4	74.24	5.08	49.56	7.416	1.2	0.003	1658	1658	1.5	184.4	1613	0.1	1.8
73.7	22.6	63.6	75.87	4.83	49.34	9.324	1.2	0.004	1259	1259	1.5	176.0	1789	0.1	1.9
81.4	24.7	17.0	74.74	1.27	58.12	2.645	1.14	0.001	942	942	1.5	37.4	1827	0.0	1.9
84	25.6	7.37	74.18	0.55	55.76	2.633	1.14	0.001	425	425	1.5	18.8	1844	0.0	2.0
89.2	27.1	0.58	76.50	0.04	54.78	4.058	1.14	0.002	23	23	2.0	1.8	1845	0.1	2.1
96.3	29.3	0.66	74.28	0.05	60.26	3.648	1.14	0.002	25	25	1.5	1.4	1847	0.1	2.1
98.7	30.2	0.53	76.64	0.04	57.58	3.716	1.14	0.002	22	22	1.5	1.2	1848	0.1	2.2
110.9	33.8	0.82	75.43	0.06	49.00	4.081	1.14	0.002	35	35	3.0	4.3	1852	0.1	2.3
120.7	36.9	1.33	75.37	0.10	50.74	10.35	1.12	0.005	21	21	3.0	6.6	1859	0.3	2.6
131.2	39.9	0.17	75.24	0.01	49.32	6.037	1.12	0.003	5	5	3.0	0.9	1860	0.2	2.8
141	43.0	0.96	74.20	0.07	56.29	5.197	1.12	0.003	27	27	3.0	4.3	1864	0.2	2.9
145.7	44.5	0.26	74.79	0.02	48.78	5.197	1.2	0.002	9	9	1.5	0.7	1865	0.1	3.0

Appendix 1a. Data for Area G Core 54-1123.

Sampled Depth (ft)	Midpoint (m)	Cl- leachate conc. (mg/L)	DI Added (g)	Cl- (mg)	Tuff Dry Wt (g)	θv (%)	ρb (g/cm3)	Pore H2O (L)	Clsw (mg/L)	Clswi (g/m3)	Interval (m)	Interval Clswi (g/m2)	Cum. Clswi (g/m2)	Interval θd (m)	Cum θd (m)
9.2	2.80	0.135	75.66	0.010	47.6408	7.97	1.37	0.003	4	4	1.0	0.29	0.29	0.1	0.1
10.2	3.11	1.92	75.84	0.146	53.5126	7.00	1.37	0.003	53	53	1.0	3.7	4	0.1	0.1
15.2	4.63	1.47	76.22	0.112	55.4354	5.32	1.37	0.002	52	52	1.0	2.8	7	0.1	0.2
20.3	6.19	2.79	75.26	0.210	52.3217	3.12	1.37	0.001	176	176	1.0	5.5	12	0.0	0.2
25	7.62	10.4	76.97	0.800	54.6605	4.11	1.37	0.002	488	488	2.0	40.1	52	0.1	0.3
30.5	9.30	12.5	74.37	0.930	58.1434	2.52	1.26	0.001	799	799	1.0	20.1	73	0.0	0.3
35.1	10.70	10.0	75.22	0.752	56.9700	1.93	1.26	0.001	841	841	1.0	16.6	89	0.0	0.4
40.5	12.34	10.1	75.33	0.761	53.9021	1.70	1.26	0.001	1046	1046	1.0	17.8	107	0.0	0.4
45	13.72	13.0	77.95	1.013	55.1873	2.22	1.26	0.001	1043	1043	2.0	46.3	153	0.0	0.4
50	15.24	17.5	78.33	1.371	46.4465	2.92	1.26	0.001	1272	1272	1.0	37.2	190	0.0	0.5
55	16.76	29.6	76.09	2.252	54.1038	8.40	1.2	0.004	595	595	2.0	99.9	290	0.2	0.6
60	18.29	62.5	75.72	4.733	51.9046	7.98	1.2	0.003	1371	1371	1.0	109.4	400	0.1	0.7
62.5	19.05	115	77.23	8.881	60.8377	9.31	1.2	0.005	1881	1881	1.0	175.2	575	0.1	0.8
65	19.81	15.6	74.98	1.170	53.1470	4.12	1.2	0.002	642	642	1.0	26.4	601	0.0	0.8
70	21.34	1.17	75.52	0.088	50.7067	3.71	1.14	0.002	54	54	1.0	2.0	603	0.0	0.9
75	22.86	0.41	75.71	0.031	50.7688	4.89	1.14	0.002	14	14	1.0	0.7	604	0.0	0.9
80	24.38	1.31	74.71	0.098	53.8481	5.15	1.14	0.002	40	40	1.0	2.1	606	0.1	1.0
85	25.91	0.22	74.35	0.018	58.1223	5.70	1.14	0.003	6	6	1.0	0.3	606	0.1	1.0
89	27.13	2.40	77.50	0.188	49.8342	7.57	1.12	0.003	55	55	1.0	4.2	611	0.1	1.1
90.8	27.68	0.26	74.52	0.019	55.7523	8.00	1.12	0.004	5	5	1.0	0.4	611	0.1	1.2

LA-UR-96-320

Title: ANALYSIS OF LIQUID PHASE TRANSPORT IN THE UNSATURATED ZONE AT A MESA TOP DISPOSAL FACILITY

Author(s): Erik L. Vold

Submitted to: U.S. Department of Energy, as support documentation for the Los Alamos Area G Performance Assessment

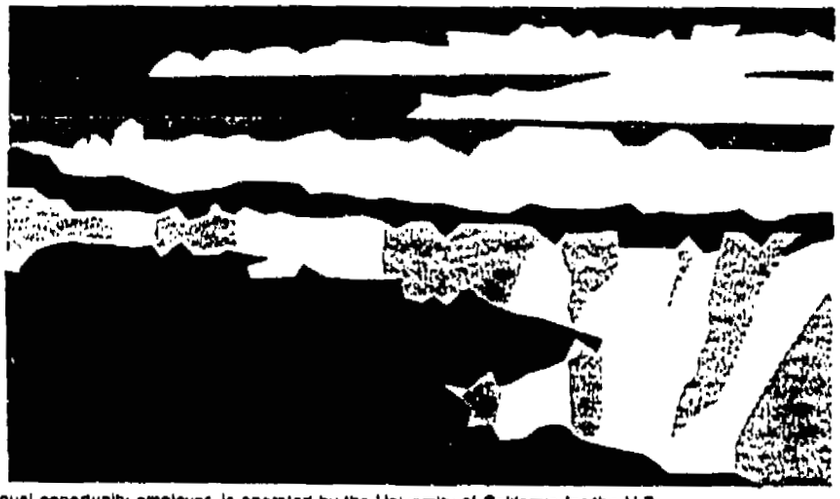

Los Alamos
NATIONAL LABORATORY

Los Alamos National Laboratory, an affirmative action/equal opportunity employer, is operated by the University of California for the U.S. Department of Energy under contract W-7405-ENG-36. By acceptance of this article, the publisher recognizes that the U.S. Government retains a nonexclusive, royalty-free license to publish or reproduce the published form of this contribution, or to allow others to do so, for U.S. Government purposes. The Los Alamos National Laboratory requests that the publisher identify this article as work performed under the auspices of the U.S. Department of Energy.

Appendix 2c

ANALYSIS OF LIQUID PHASE TRANSPORT IN THE UNSATURATED ZONE AT A MESA TOP DISPOSAL FACILITY

TABLE OF CONTENTS

ABSTRACT 1
INTRODUCTION 2
ANALYSIS 3
- Methods 3
- Application to Area G 6

RESULTS 8
- Matric Head and Unsaturated Conductivity Results 8
- Field Borehole Results 9
- Bounding Case Results 14

UNCERTAINTY 15
- Accuracy 15
- Error Analysis 16
- Minimum Detectable Flux 19

DISCUSSION 23
- Three Subsurface Transport Regions 23
- Source Term at Vapor Phase Notch 24
- Uncertainty Implications 25
- Flux Implications 26
- Disposal Operations 27
- Numerical Modeling Implications 27

CONCLUSIONS 28
ACKNOWLEDGMENTS 29
REFERENCES 29

Tables I - II 36

Figure 1-31 38

Appendix 2c

ANALYSIS OF LIQUID PHASE TRANSPORT IN THE UNSATURATED ZONE AT A MESA TOP DISPOSAL FACILITY

ABSTRACT

Analysis of liquid phase transport in the unsaturated zone beneath a mesa-top disposal facility is described. The analysis infers vertical moisture flux and a source term derived from the gradient of vertical flux, based on moisture profiles with empirical analytic forms for the moisture flux as a function of moisture content. The source term, expressed as a characteristic time scale for change in moisture content, varies from about one year in high flux regions to over one thousand years in low flux regions. Results show the moisture flux and source terms within the mesa fall into three regions. A 'near surface region' (<10m depth) is found to have an average net downward liquid phase flux of about 1 cm/yr and exhibits a significant evaporative loss, presumably from surface-connected fractures. This region has a large variation in flux characteristics and is influenced by disposal operations. Relatively large moisture content and inferred flux in this region at one location illustrates the potential for disposal operations to significantly alter the natural hydrology at least of the near surface on the mesa.

Beneath this is a 'low flux region' which extends downward at least to a horizon near the base of the mesa. In this region the average inferred vertical flux is 0.0017 cm/yr upward with a maximum downward flux at any location observed to be 0.006 cm/yr, suggesting there is negligible liquid phase movement through this region.

A third region near the base of the mesa is characterized by a peak in the vertical profile of moisture and is associated with a 'vapor phase notch', at the interface of the vitrified and the devitrified volcanic tuff. The analysis indicates a small average downward flux of 0.07 cm/yr in this region and suggests a local moisture source. This may indicate lateral flow, connectivity to alluvium of greater saturation in the adjacent canyon, or may signify the elevation of the bottom a network of surface-connected fractures. However, the apparent moisture source may be negligible if the local matric properties differ from the stratigraphic unit averaged values.

The flux magnitude indicated at most locations, including the apparent source at the vapor phase notch, is comparable to the uncertainty derived in an error analysis. Therefore, the results indicate trends in the flux profiles, while fluxes at specific points are best quantified as values below the derived detection limits. Results are ambiguous in the vapor phase notch region due to limited matric properties and indicate a need to determine the properties in this region, and thus to better understand the moisture flux to deeper horizons beneath the mesa.

ANALYSIS OF LIQUID PHASE TRANSPORT IN THE UNSATURATED ZONE AT A MESA TOP DISPOSAL FACILITY

INTRODUCTION

The Los Alamos National Laboratory (LANL) Low-Level Radioactive Waste (LLRW) Disposal Facility at Area G is being evaluated for subsurface transport of contaminants from the disposal site, as part of the Performance Assessment[1] required by the U.S. Department of Energy (US DOE) Order 5820.2A for US DOE facilities that dispose of radioactive waste. Environmental transport at the Area G disposal facility is complicated by the complex terrain consisting of finger-like mesas, typically 100' (30m) above the adjacent canyon floors. Figure 1 shows the site facilities imposed on a terrain map. The terrain is shaded to reflect the magnitude of the local slope so that the edges of the mesas are visible. Area G is located on top of a mesa, Mesita del Buey, with Pajarito Canyon to the south and Canada del Buey to the north. The mesa top, the canyon floors, and the water table (about 300m below the mesa top) are all sloping gently at about 3 percent grade downward towards the Rio Grande to the east.

Subsurface transport is complicated by the layered stratigraphy (Fig. 2) which has resulted from the deposition of multiple layers of volcanic flows and ash[2]. Site-specific hydrologic transport properties, defined in terms of van Genuchten parameters[3], porosity, and saturated hydraulic conductivity are available[2]. These are based on analyses by Rogers[4] and Rogers and Gallaher[5], for the upper layers of the Bandelier Tuff, Tshirege Member units 2b, 2a, 1b, 1a, (redesignated, respectively as 2, 1vu, 1vc, 1g) and Otowi Member, but there are no site-specific hydraulic or transport properties available for the deeper units. The upper layers of the Tshirege are fractured with an average fracture spacing of about 1m and aperture of about 3 mm reported at Area G[6].

This semi-arid region receives about 35 cm/yr of precipitation, mostly in brief intense summer thunderstorms and in winter snow fall. It has been hypothesized that transient infiltration events and long term evaporation from the surface-connected fractures play a dominant role in controlling the hydrologic transport, at least in the upper layers[7]. Modeling studies of the steady state moisture flux through the matrix (tuff) show that a single value for the vertical flux cannot match the field observations of moisture profiles at all depths simultaneously[8]. This suggests there are significant sources (or sinks) as a function of elevation in the upper layers of the Bandelier Tuff.

An early assessment of hydrology in the area[9] based on field studies[10,11] specified only a range for the magnitude of the vertical flux at Area G. A maximum downward flux was indicated to be near 0.4 ft/yr, or about 12 cm/yr. The uncertainty in field data allowed a range in the vertical flux estimate such that the net vertical flux may be a small upward quantity. The assessment of flux was based on intrinsic permeability, matric potential determinations on samples, and in-situ matric potential from thermocouple psychrometers placed in boreholes in and near to Area G. The methods did not fully resolve conditions in the range of the in-situ moisture content, so the flux estimates were maximum values estimated using higher moisture contents than observed in-situ. It was concluded[9] the actual flux is probably at least an order of magnitude less than their measured maximum value, or thus less than about 1.2 cm/yr downward. Neutron probe measurements of moisture content indicated that moisture profiles did not change appreciably in time below a depth of 1-2m.

Using typical values for the van Genuchten parameters for Bandelier Tuff and for in-situ moisture content observed in subsurface profiles, an unsaturated hydraulic conductivity for the disposal site was estimated to be less than or equal to 0.1 cm/yr[12]. In that study, it is noted that this conductivity equals the downward vertical flux under assumptions of unit gradient conditions. The vertical flux in a borehole at Area G (borehole G5 - to be discussed in the present study) was estimated as a function of depth[13] from in-situ moisture content data, with recovered core sample analyses for the matric characteristic curves and with measured values for the unsaturated conductivity. Their results showed a maximum magnitude for downward flux of about 1 cm/yr at 32', decreasing with greater depth to less than 0.2 cm/yr below 50', which was about the limit of resolution of those measurements and analyses.

From the previous studies, hydrolegic transport in the Area G unsaturated zone is still not well quantified nor even understood conclusively where or when the vertical flux is upward or downward. The present study examines field data from Area G in an analysis designed to address some of the present uncertainties in the unsaturated transport in the upper stratigraphic layers below this disposal site. Specifically, the vertical flux and its gradient (an effective source term) implied by field data from several monitoring bore holes throughout Area G (as seen in Fig. 1) are examined to help quantify our understanding of flux in the vadose zone.

ANALYSIS

Methods

In the complex stratigraphy within and beneath the mesa, an important step in understanding the subsurface transport, is to know if there are local sources or sinks to the liquid phase moisture flux or recharge rate in the tuff matrix. This would imply interactions with vapor phase or with a second permeable media, possibly a connected network of fractures. Without knowledge of specific subsurface sources, numerical models applied to subsurface transport in this region can only justify one source, a net infiltration at the surface. However, this source alone was seen to be inadequate to match all horizons within the mesa simultaneously[8]. The present analysis derives a vertically localized liquid-phase moisture flux (the vertical component of the Darcy flux) and a source term for the moisture content from field data to improve our understanding of the recharge rate and its variations within the mesa region. This is turn improves our understanding of the moisture movement within the mesa interior and its potential for contaminant transport.

A governing transport equation for moisture content in the unsaturated zone is discretized along the vertical axis. An inverse 'finite-difference' procedure is applied to field measurements of the moisture content to evaluate the vertical flux and its gradient. The empirical relationships defining the unsaturated hydrologic properties in terms of moisture content and its gradients are used in the finite discretized equations.

The vertical gradient of the moisture content is related to the vertical component of the divergence of flux. As such, it is an effective source term for vertical flux or recharge rate which includes effects of horizontal flux or time dependent change in the local moisture content. This source term is discussed in the following sections in terms of the possible physical mechanisms that may influence the vertical flux within the mesa subsurface.

A schematic summarizing the analysis is shown in Figure 3 for a cylindrical control volume. In brief, the divergence of flux includes a contribution from the differences in vertical flux, Γ_z, across the top and bottom faces, and from differences in horizontal flux, Γ_x, across the side areas. This

flux divergence equals the volumetric source term, $S_\theta(i)$, plus the change in local moisture content, $\frac{\partial \theta}{\partial t}(i)$, where i is the index of the discrete elevation at which the quantity is evaluated. The field data provide an estimate of the vertical component of the divergence of the flux. This estimate is a measure of an 'effective source term to the vertical flux' which may include contributions from horizontal flux, vapor or matrix volumetric exchange, or time dependent variations in the moisture storage. Terms are defined more rigorously and elaborated in the following analysis.

A continuity equation for moisture content, θ [volume fraction], can be written

$$\frac{\partial \theta}{\partial t} + \nabla \cdot \Gamma = S_\theta \qquad (1)$$

where Γ is the flux and S_θ is a source $(S_\theta>0)$ or sink $(S_\theta<0)$ term representing a volumetric addition to or loss from the matrix liquid phase. In the unsaturated zone, considering liquid phase transport only, the flux can be written

$$\Gamma = -K[\theta]\,(\,\nabla h_m[\theta] + z\,) \qquad (2)$$

where $[\theta]$ denotes a functional dependence upon the moisture content. Here, h_m is a matric head[14] representing the capillary suction forces. It is equal to the matric potential, Ψ_m expressed as a head, $h_m = \Psi_m/\rho g$. The matric head is a negative quantity since the matric potential, Ψ_m, is by convention a negative quantity. The unit vector in the vertical axis, z, is directed upward, so the vertical component of flux can be written

$$\Gamma_z = -K[\theta]\,(\,(\partial h_m[\theta]/\partial z) + 1.\,). \qquad (3)$$

Applying Eqn.(1) to flow in the matrix, the source term, S_θ, represents volumetric source or sink terms relative to the matrix liquid phase. The source can include moisture exchange with the vapor phase. In a matrix volume which is near surface-connected fractures open to the atmosphere, the moisture content can be significantly reduced from the conditions expected in the mesa interior. Therefore, this source term includes moisture exchanged with fractures or other surface-connected zones of high permeability distributed throughout the matrix. This term, S_θ, includes evaporative loss to the vapor phase when the source term is negative (a sink term), and could, for example, imply a net evaporative loss to a surface-connected feature within the local volume.

Combining terms above and accounting for one horizontal flux component, Γ_x, along an arbitrary horizontal axis, x, the continuity equation can be rewritten,

$$\frac{\partial \Gamma_z}{\partial z} = S_{zeff} = S_\theta - \frac{\partial \Gamma_x}{\partial x} - \frac{\partial \theta}{\partial t} \qquad (4)$$

where the left hand side is the vertical component of the divergence of flux, equal to an effective source term for the vertical flux, S_{zeff}. This source term equals the right hand side terms, respectively representing local exchange with another media (e.g., fractures) or with another phase (e.g., vapor), horizontal movement of liquid phase in the matrix, and transients which reflect the change in local storage of moisture content. The horizontal flux, Γ_x, could be evaluated using Eqn. 2 with the unit vertical vector equal to zero.

The term representing the volumetric source, S_θ, and the term for the horizontal gradient of flux in Eqn.(4) are expected to be physically related when the moisture at a specific location is influenced by horizontal movement towards or away from a fracture. In this case of a fractured medium, these two terms can be related to the same physical mechanism and need to be evaluated together to represent a moisture source or an evaporative loss.

In steady state, the last term in Eqn.(4) is negligible. In areas where recent disposal operations have disturbed the area, this last term is likely to be significant due to the increased moisture content associated with disturbances due to operations. The time scale where transients are likely to be important is evaluated in the results.

The left hand side of Eqn.(4) can be expressed in terms of a discretized approximation at a vertical point with index, i:

$$\frac{\partial \Gamma_z}{\partial z} = \frac{\{\, \Gamma_z(i+1/2) \;-\; \Gamma_z(i-1/2) \,\}}{\{\, z(i+1/2) \;-\; z(i-1/2) \,\}} \tag{5}$$

where the discretized vertical flux from Eqn. 2 evaluated at node, i+1/2, is

$$\Gamma_z(i+1/2) = -K[\theta]_{i+1/2}\left(\frac{(h_m[\theta]_{i+1} \;-\; h_m[\theta]_i)}{(z(i+1) \;-\; z(i))} + 1. \right) \tag{6}$$

and a similar expression with the indices decremented by one holds for the flux at i-1/2. The notation $h_m[\theta]_i$ means the matric head is evaluated at the moisture content at elevation, i, and $K[\theta]_{i+1/2}$ implies hydraulic conductivity is evaluated as an average between the two elevations at i and $i+1$. Empirical relations required to define $K[\theta]$ and $h_m[\theta]$ are discussed in the following section. Using field data and these empirical relations, Eqns. 6 and 5 can be evaluated for the vertical flux and its gradient, respectively.

It is convenient to express this gradient or effective source term to vertical flux in a number of ways. Multiplying Eqn. 5 through by $\Delta z = \{z(i+1/2) \;-\; z(i-1/2)\}$ gives the effective source term, $S1$ (as in Fig. 3), as

$$S1 = S_{zeff}\ \Delta z = \{\, \Gamma_z(i+1/2) \;-\; \Gamma_z(i-1/2) \,\} \tag{7}$$

expressed as an equivalent flux, in cm/yr for instance, which can be compared more directly to the local flux, to a net infiltration rate, or to the precipitation rate for comparison. This source term is not normalized per unit depth and so represents the total source (or sink) over the depth interval between the adjacent field data points at $z(i+1/2)$ and at $z(i-1/2)$.

The vertical gradient in flux, $\frac{\partial \Gamma_z}{\partial z}$, can also be considered as an effective source term, S_{zeff}, (in Eqns. 4 and 7) to the vertical flux or to the recharge rate. In this form, this effective source has units of inverse time and represents the change in vertical Darcy flux per unit vertical distance, with units for example as [yr^{-1} = (m^3_w/m^3) m/yr /m], where (m^3_w/m^3) represents the dimensionless volumetric water fraction, θ. In this form, we interpret the source term loosely to represent an inverse of the time scale over which the *vertical moisture flux* is changing. The

inverse of this S_{zeff} in Eqn. 4., the characteristic time scale for *moisture flux*, is denoted $S_{t\text{-}inv}$ in the Results figures.

The time scale for which the *moisture content* is changing is this effective source term for vertical flux times the moisture content. This effective vertical source for moisture content (denoted *Sinv* in Fig. 3, and denoted, $S_{t\text{-}inv}$*vol%, in the Result figures) is written in several equivalent forms

$$Sinv = \frac{\theta\,\Delta z}{S1} = \frac{\theta\,\Delta z}{(\,\Gamma_z(i+1/2) - \Gamma_z(i-1/2)\,)}$$

$$= S_{t\text{-}inv}{*}vol\% = S_{t\text{-}inv}\,\theta = (S_{zeff})^{-1}\,\theta. \qquad (8)$$

One can interpret this as a characteristic time scale for vertical movement, v_z, to change the moisture content, or, if the local source term is completely attributed to the time dependent change in moisture content (Eqn. 4) then this is the minimum time scale over which that moisture content is changing at the present flux rates.

The finite difference equations, 5 and 6, form the basis for the flux analysis with the alternate source term formulations in Eqns. 7 and 8. Each term in these equations has an associated error based on the field measurement and analysis uncertainty which contributes to the net uncertainty for the expression. This is an important consideration in interpretation of the results and will be discussed in a later section.

To summarize, the gradient of vertical flux implies a source term to the local recharge rate which can be expressed as a flux, *S1* (in Eqn. 7), or as a characteristic time scale, *Sinv* (Eqn.(8)). The flux source, *S1*, is interpreted as the moisture flux needed to account for the observed magnitude of the vertical flux gradient if steady state conditions prevail. The source term, expressed as a characteristic time scale, *Sinv*, is the minimum time over which the moisture content is changing if all of the vertical flux gradient is attributed to a time dependent change in moisture content at that location. In the field situation some combination of these two limiting cases is likely to apply. This combination will vary with location as discussed in the Results section for each of the field boreholes.

Application to Area G

The approach is to combine moisture content data with empirical fits for the functions, $K[\theta]$ and $h_m[\theta]$, to evaluate the vertical flux and its divergence. Moisture content data are examined from several monitor holes as indicated on Fig. 1. Data from most holes are from neutron probe measurements because these show good precision and, if properly calibrated, reasonable accuracy. Thus, moisture content gradients are determined relatively well, as discussed more quantitatively in the Uncertainty Section.

Moisture content profiles for each of the holes labeled *NPH#* (Neutron Probe Hole) in Fig. 1 were made during the summer to fall seasons of 1994. These were reported in Loaiza and Vold[15], as determined with a neutron moisture probe which measures directly in moisture content volume percent $(100\times\theta)$. Calibrations for each type of hole casing and hole diameter are documented[15]. Measurements in a monitor hole (NPH-1) into an active disposal unit confirmed earlier findings that moisture content does not change appreciably in time below 1-2m depth. The moisture content

in the two holes labeled LGM-85-# were taken from plots of results in a previous report[10] where the measurements were also made by neutron probe.

Borehole 54-1002 (in the LANL Environmental Restoration Program) is located on the mesa top about 1/2 km to the west of Area G, and is included because it is the deepest of the holes reported here. The moisture data are from gravimetric measurements of core samples from the borehole. Analytic determinations of the bulk density were averaged in each stratigraphic layer as summarized elsewhere[2] and used here to convert this moisture content to a volumetric basis. The values used for bulk density averaged for each stratigraphic unit are shown in Table I. Because of these extra steps in the analytic procedures, the gravimetric profiles contain more uncertainty than the neutron probe-determined profiles especially in the deeper layers where relatively few samples (2 in the Tsankawi-Cerro Toledo layers) were used to characterize the bulk density and unit-averaged hydrologic parameters.

Empirical relations required to define unsaturated moisture flux as functions of moisture content, $K(\theta)$ and $h_m(\theta)$, have been compiled by stratigraphic units at Area G[2] based on van Genuchten-Maulem analyses[3,16] as reported previously[4,5]. Stratigraphic unit mean values are used in the present study as summarized with their standard deviations in Table I. Although residual moisture content, θ-residual, is determined from curve fits, it is not applicable to the present analysis when field moisture data are less than the residual, $\theta(i) < \theta\text{-}residual$, therefore $\theta\text{-}residual$ was set equal to zero in this analysis. The stratigraphic unit interfaces in each borehole were determined from the borehole logs where borehole logs were available. Otherwise, a simple interpolation estimate was used by comparing depths of moisture profile peaks and inflection points, with those in logged holes.

Only one of the holes (54-1002) which was used to determine the mean stratigraphic unit transport parameters in Table I is the same as the holes examined in this present study. However, the moisture profiles in both sets are similar and so the transport properties used here are expected to be representative of the unit mean values. Recent data from borehole G5 [Ref.17] at Area G were not included in calculating the means used in this study, however, as seen in Table I, in the last column, by including the G5 data for Unit 2b, the van Genuchten-Maulem fits are not changed greatly.

Fitting parameters for the transport properties for the crushed tuff were taken from a separate reference[18] and are the same as the values used in the preliminary PA modeling and analyses[1]. (Note that these values have been revised for subsequent PA analyses, however, they provide a basis for comparisons here and for an understanding of the sensitivity of the flux results to the assumed matric properties.) The origin of the crushed tuff samples is Unit 3[4], not the same as the stratigraphic unit of interest here, Unit 2b. Unit 2b is the nearest surface stratum at Area G and therefore comprises most or all of the crushed tuff used in the disposal operations as fill for the waste disposal pits and shafts. The difference in the source of the crushed tuff samples led to comparison tests discussed in the Results Section.

Trends in the property variations within each unit have not yet been examined in detail and so possible systematic effects (e.g., a consistent vertical gradient of the fit parameters within a unit) are ignored in the field analyses, but considered to a limited extent in the uncertainty analyses. Matrix properties at a particular elevation, which deviate consistently from the mean value for the unit in which that elevation is included, can produce an error in the present analysis.

Unsaturated hydraulic conductivity was measured directly on several samples from hole G5[19] using the UFA centrifuge technique[20]. As discussed elsewhere[13,21] these measurements are in good agreement (factors of 2-3 difference near in-situ range of moisture content) with predictions from the van Genuchten-Maulem fits in some cases and in poor agreement (an order of magnitude or greater difference) in other cases. In several of the cases with poor agreement, the centrifuge measurements suggested that liquid phase flow does not occur at the in-situ moisture content.[19]

RESULTS

Results are presented in three similar plots for each monitor hole, which show (A) the moisture profile, (B) the vertical flux (Eqn. 6) with the effective source expressed as a flux (Eqn. 7), and (C) the inverse source term expressed as a characteristic time for the moisture flux (Eqn. 5) and for the moisture content (Eqn. 8). In the vertical flux plots, the flux is downward if negative and upward if positive, and the source term is into the matrix volume if positive and out from the matrix (e.g., evaporation) if negative. In the source term plots, the source term is a magnitude only on a log scale and does not indicate a direction in or out from the matrix. In several cases, the flux and effective sources are dominated by large values in limited ranges of depth and so these terms are then replotted over selected depth ranges to focus on the trends in the 'low flux' depth range.

Matric Head and Unsaturated Conductivity Results

Intermediate results used in this analysis are useful to understand the limitations in interpreting the results in the following figures. Moisture content, matric head and the unsaturated conductivity are shown in Fig. 4 for a particularly dry moisture profile, in hole NPH-9, ER-1111, as located in Fig. 1.

Fig. 4A identifies the interface locations between the stratigraphic units and shows the matric head with the moisture content for reference. The calculated values of matric head, h_m, over the two ranges of depth, 0-10m and below 26m, are most consistent with the in-situ psychrometer data previously reported[9] in the range, $h_m \sim 10\text{-}100m$. The higher matric potential values seen at the intermediate depth range are associated with a very low moisture content region, and there the matric potential fit curves may exaggerate the actual matric potential.

In Fig. 4B, the vertical flux is compared to the unsaturated hydraulic conductivity. Both values appear to be negligible throughout most of the depth range. The more significant peaks in vertical flux are not associated with peaks in conductivity, but are associated with maxima in the local head gradient.

The absolute magnitudes of conductivity and vertical flux are plotted together in Fig. 5A, to allow a log-scale presentation. Here one sees that the magnitude of the flux is generally 1-2 orders of magnitude larger than that of the hydraulic conductivity suggesting that a 'unit gradient assumption' holds at few if any of these specific points in this dry borehole. This is clear in Fig. 5B, which shows the absolute value of the vertical flux function, $(\partial h_m/\partial z + 1)$. At most points, this function is much greater than one, showing the differences in matric potential are critical in determining the magnitude of the moisture flux.

This becomes very important in the very low moisture region, where very small changes in moisture content are associated with large changes in matric potential through the unit-averaged

analytic fits. In actuality, small local changes in matric properties may smooth the matric potential profile. However, using the stratigraphic unit averaged properties, then small variations in moisture content increase the magnitude of the vertical flux above the unsaturated conductivity. For this reason, the results may be 'noisy', with spikes attributed to the limitations of the unit-averaged analyses. This effect is pronounced in these figures because this is a particularly dry borehole at Area G. An important implication is that it is necessary to look for trends common to many borehole profiles to 'smooth over' the noise of the analysis artifacts and to derive meaningful results.

Field Borehole Results

The field monitor holes are located as in Fig. 1 (with one hole not shown, 54-1002 located on the mesa top about 1/2 km to the west of Area G). The drainage divide along the mesa top runs NNW to SSE near the north mesa edge approximately through holes NPH-2, NPH-3, and LGM-85-11. These holes should be near the locations of maximum surface run-off and are expected to be among the drier boreholes.

The results from monitoring holes are presented roughly in order from drier to moister, looking first at a group of five shallower holes (<20m) which do not reach the depth of the adjacent canyon floors, and then at the deeper holes (>30m) which extend slightly below the depth of the Unit 1b-1a interface. This interface is nearly coincident with the elevation of the adjacent canyon floor (Pajarito Canyon). This layer is identified as the vapor phase notch, just at or above the 1b-1a unit interface, the transition region from vitrified tuff (1b) to devitrified tuff (2a). This notch has been identified at outcroppings as a layer of preferential weathering[22]. It may have unique hydrologic transport properties but these have not yet been determined.

Results for borehole NPH-2 (a background hole in relatively undisturbed tuff near pit 37) are shown in Fig. 6. This moisture curve in Fig. 6A is assumed to be a nominal 'undisturbed' case, with moisture decreasing somewhat linearly with depth from 6-7% near the surface and leveling out at about 1% below 6m. The inferred moisture flux in Fig. 6B is negligible below about 3m depth. In the upper most 3m interval, the vertical flux is predominantly downward, at 1-3 cm/yr. The associated moisture source is predominantly negative and of comparable magnitude to the flux suggesting a loss of the downward flux, possibly to evaporation in surface-connected fractures. The corresponding inverse sources in Fig. 6C suggest moisture content profiles are not changing within a 50 year time scale below 3m, and not changing within 500 years below 7m. In the top 2-3 m, the time scale for change is about 0.5 yr, consistent with a source term frequency of 2/yr, suggesting a seasonal source, possibly the summer rains and the winter snow melts.

Similar results are seen in Fig. 7 for hole NPH-3 another 'background hole' in a relatively undisturbed area also near the mesa top drainage divide. The moisture gradient and the flux become negligible at 4m depth. The flux is less than 1 cm/yr in the near-surface region (0.45 cm/yr average to depth of 4m). The time scales are slightly longer than in the previous case, with no changes seen here on a time scale shorter than 2 years even at 1m from the surface.

Fig. 8 expands the scale for flux and the flux source term over the depth range where the flux appears to be negligible in Fig. 7B. The flux and its source appear to be fluctuating with depth, with a maximum local magnitude of less than 0.4 mm/yr and an average flux of less than 10^{-3} cm/yr directed downward over this range in depth from 4m to 20m. The fluctuations may be artifacts of the analysis due to the large changes in matric potential implied by small changes in moisture at the dry end of the moisture range. The magnitude of implied moisture movement appears to be small compared to the error in the analysis as discussed later in the Uncertainty

Section. On the other hand, the apparent fluctuations may have a real physical basis, suggesting small localized 'pockets' of moisture flux moving at slow rates in different directions.

Results in hole NPH-7c are seen in Fig. 9. This hole is in the tritium disposal shaft area and adjacent to a series of old burial trenches. This is considered a 'disturbed area', and shows the increased moisture content relative to the previous two cases. The near surface moisture profile behaves similarly to the previous cases, but now decreases from about 12% near the surface and levels out at a depth of about 8m to 2% or less. The vertical flux in the top 6m is 2.4 cm/yr downward. The source in this region is negative on average (-0.7 cm/yr) indicating net loss from the matrix. A distinct positive spike in the source is seen in Fig. 9B at a depth of 3m, the location of a local maximum in moisture. This suggests a net influx of moisture either transported from a nearby moist region, a fracture or a disturbed trench excavation, or a time dependent residual related to previous surface wetting and more recent surface drying. The minimum time scale for moisture change is about once per two years as seen in Fig. 9C, suggesting that if the profile is attributed to recent drying, the previous wetting cycle was at least two years ago, perhaps during a 'wetter than average' year.

Results for hole NPH-6 in the southeast corner of Area G are shown in Fig. 10. Moisture is about 8% maximum and decreases from 3m to about 10m, similar to the previous case. The local maximum at 3m depth is again possibly related to horizontal migration from nearby disturbances or to a time dependent response of a previously greater rate of surface infiltration followed by more recent drying. The positive (upward) Darcy flux in the top 3m suggests that the moisture profile is relaxing by upward moisture flux driven by surface or near surface evaporation. The positive source term in this depth range shows moisture is now (or recently) moving towards this region. The minimum time scale for moisture change is about once per two years as seen in Fig. 10C.

A unique set of results are seen in Fig. 11 for hole NPH-4. This moisture content of 30% near the surface and the very slow decrease with depth were not observed at any other location. This hole is in an engineered drainage area where surface run-off is diverted towards this hole and so the infiltration is expected to be considerably higher than at any undisturbed location. Note that the monitor hole itself is cased and is not expected to be conducting water to the subsurface region. The average downward Darcy flux inferred in the upper depths is in the range of 100-200 cm/yr depending on the exact interval, corresponding to 3 to 6 times the annual average precipitation rate.

The average source term over the same depth is negative indicating a net evaporation or loss in the mesa top. The drying is not sufficient to reduce the moisture in the top 16m to the typical observed background levels below 2%. The time scales for moisture content change are seen in Fig. 11c to be well below one year at most depths, with a minimum value (at depth = 14m) of about 0.05 year or a frequency of about one per two weeks, and with several near surface points at 0.1 year or a frequency of about once per month. Thus, changes at this location (NPH-4) are rapid relative to any other monitor hole.

The monitor holes discussed up to this point did not extend deep enough to reach the elevation of the adjacent canyon floors. The remaining monitor holes are deeper than the adjacent canyon floors and show a characteristic moisture peak associated with the vapor phase notch near the unit 1b-1a interface. Fig. 12 shows the results in hole LGM-85-06, using the moisture profile previously reported[10]. Moisture content increases with depth beginning at about 20m, and shows a moisture peak at 30m. The borehole logging data shows this peak is in the 1b unit, with the 1b-1a interface at 32m. The profile in Fig. 12A is typical for a relatively undisturbed area near the surface.

The Darcy flux and associated source term flux (Fig. 12B) decrease rapidly near the surface and appear to be significant again near the moisture spike at 30m. In this region the Darcy vertical flux

and the source term flux show a trend which is seen in nearly all of the holes which penetrate this depth. The apparent source term exhibits a large positive value at the depth of the moisture peak suggesting net infiltration, in this case equivalent to about 5 cm/yr. To either side of this source spike, the source is negative suggesting net evaporative losses over a depth range of 1-3 m. The corresponding Darcy flux is positive above the source spike suggesting upward movement away from the spike and negative below the spike suggesting downward flux from the source.

This pattern suggests a source with movement away to either side and as the moisture moves away it evaporates as indicated by the negative sources to either side of the spike. Another interpretation of the data is possible, if there is a horizon near the moisture spike which has significantly different matric properties than the average values used for unit 1b (or 1a), then the moisture spike could still represent a static equilibrium, and correspond to negligible flux through the region.

In this hole, LGM-85-06, the average vertical flux from 25m to 35m depth is -0.43 cm/yr, and the average source in that range is 0.016 cm/yr, indicating a significant downward movement but a negligibly small net source. The minimum time scale for moisture content movement is about one year and occurs at the depth of the moisture peak as seen in Fig. 12C. There is a region from about 15m to almost 25m depth where the minimum time scale is almost 1000 years indicating negligibly slow changes in this 'low flux region'.

Hole LGM-85-11 (Fig. 13) shows higher moisture content compared to the previous case but similar trends with depth, decreasing from 15% near surface to 2% at 5m, and increasing slowly to 20-25m and then building to a local maximum or moisture spike at 28m, apparently the depth of the vapor phase notch at this location. The increased moisture content corresponds to much larger fluxes than the previous case, about 30 cm/yr near the surface and 10-20 cm/yr at the moisture spike at 28m. Except for one point at 5 m, the time scale for moisture content change (Fig. 13c) is one year or greater with the minimum values occurring near 28m. From 7 to 23m (a low flux region in this borehole) the source term time scale is greater than 100 years.

Each of the two previous cases showed negligible flux throughout the intermediate ranges of depth. In Fig. 14, the Darcy fluxes in the limited range are replotted to resolve this 'low flux' region for both holes. The vertical flux and source term in each case oscillate about zero with a maximum local magnitude of about 0.1-0.15 cm/yr. The average flux over this region is -0.0017 cm/yr and the average source is -0.013 cm/yr for hole LGM-85-06, and for hole LGM-85-11, these respective values are 0.01 and -0.07 cm/yr.

Results in Fig. 15 for hole NPH-8, near the tritium shaft field, show a modestly high near-surface moisture content consistent with profiles from other 'disturbed locations', falling to below 2% at depth 11m, more consistent with an 'undisturbed location' at depth. The maximum in moisture content at depth of 5m, with positive vertical flux and sources at shallower depths, is also consistent with a disturbed location as discussed for holes NPH-7c and NPH-6 in Figs. 9 and 10. The moisture peak at 27m is similar to that discussed for the previous two holes which penetrate the 1b-1a interface. The minimum time scale in Fig. 15C is about one year, with most points in the range of 20-1000 years. Fig. 16 shows the Darcy fluxes in this hole on an expanded scale over the 'low flux' region from 12 to 25 m depth. The maximum downward flux in this region is -0.033 cm/yr, the average flux over this range is -0.0038 cm/yr and the average sink over this range is -0.0024 cm/yr.

Fig. 17 shows results for hole NPH-9 (ER#1111) located near the high activity tritium shafts. The low moisture content throughout the profile suggests this area at least locally is relatively undisturbed by the nearby disposal operations, or it is dry due to its proximity to the mesa edge. The moisture spike at the 1b-1a interface is at about 25m depth at this location and small in magnitude, producing a minor perturbation in the vertical flux or flux source term. A moisture buildup at 10m depth does show the same trends as previously observed at the 1b-1a interface

moisture spike, a positive source dissipating with movement in the upward and downward directions and with adjacent negative sources possibly attributed to evaporation. Except for two points, the time scale in this hole is ten years or greater as seen in Fig. 17C.

Results are seen in Fig. 18 for hole NPH-5 (also identified as G-5[13,21]), located in a central portion of Area G between a shaft field and older disposal units. This hole was previously selected for detailed hydrologic transport assessments including complete matric characteristic curves[17] and UFA centrifuge measurements of the unsaturated hydraulic conductivity curves[19] on core samples removed at 10' intervals. These data have been discussed previously[13,21], and will be considered further in the Discussion Section.

The results in Fig. 18 reflect an atypical moisture profile, decreasing from about 10% to 7-8% in the top 15m, and then dropping precipitously to less than 2% at 16m. The interface of units 2b-2a occurs at this abrupt change in moisture content. Throughout the top 15m, the vertical flux is consistently downward with an average value over this interval of -1.1 cm/yr, and this average increases to -1.7 cm/yr in the top 17m, due to the large downward flux apparent at the abrupt drop in moisture. The net source term over these ranges are respectively, +0.36 cm/yr and +0.01 cm/yr. This condition may imply a significant connectivity between this hole and adjacent disturbed areas of increased moisture or adjacent surface-connected fractures which contribute to wetting the hole at certain depths and to drying the hole at other depths.

There is an apparent sink at 17m of -6.5 cm/yr (Fig. 16c) which seems to be removing the downward vertical flux above that depth. Surge beds at this depth have been proposed as a surface connected feature which may preferentially dry this horizon[23,13]. The source and flux values at this horizon are equal to that seen at 4m depth where the moisture profile undergoes a minor drying trend as evidenced by the local minimum in moisture content. In comparison to the profiles at other holes in this study, it appears that this is not a typical characteristic but is unique to this hole. [Note however, in a recently drilled borehole (Environmental Restoration Program, 54-1107) located near to G5, the moisture and matric potential profiles[24] are similar to that seen at G5 suggesting an area near the middle of Area G with similar characteristics, and similarly influenced by disposal operations and or by surface-connected fractures down through Unit 2b.]

The hole ER-1002 is located on the mesa top about 1/2 km to the west of Area G. It is included because it is deeper than any hole within Area G, penetrating into the Cerro-Toledo member at 78m depth. The hole was drilled at 22° from the vertical but all depths reported here are corrected to vertical. The moisture data is from gravimetric analyses on recovered bore hole samples corrected to a volumetric basis with stratigraphic unit averaged bulk densities (Table I) and is thus considered to have a larger uncertainty than the neutron probe measurements.

Results for hole 54-1002 in Fig. 19 show the trend expected for a relatively undisturbed area, 6-7% near surface moisture falling to 2% or less by 5m depth, with the moisture spike at the 1b-1a interface or vapor phase notch, at a depth of 40m at this location. Below this the moisture increases slightly until depths of 80-90 m where the moisture content increases and fluctuates significantly with depth. Using the limited data for the unit average properties at this depth, an apparent vertical flux and source term flux is seen (Fig. 19B) in the range 80-100 cm/yr at about 80m depth and several values near 10-20 cm/yr occur at points below 80 m.

If these data are valid, they suggest a moisture source at a very localized horizon at 80m which is primarily moving upward and evaporating or otherwise lost above 80m. This apparent flux may not be real however, it may be attributed to poor data in moisture content or to stratigraphic property variations at this depth which have not been resolved. The associated time scale in Fig.

19c is less than one year for several points in this range. The magnitude of the apparent source at first seems unlikely to represent a real physical source at this depth. However, similar apparent sources have been seen in recent analyses on moisture profiles underneath nearby canyon locations, suggesting the possibility of lateral mixing at this horizon.

Figure 20 (top) shows the rescaled Darcy fluxes down to 78m to avoid the erratic behavior near 80m and deeper. This now agrees well with data from previous holes, showing negligible flux or sources except near the surface and at the vapor phase notch (~40m here). Fig. 20 (bottom) shows the limited range of depth from 8 to 29m. Over this range, the average vertical flux is -0.0005 cm/yr and the derived sink is -0.0006 cm/yr. Deeper intervals have similarly negligible flux values until one includes the data below 76m. The vertical flux in this region is positive indicating an upward movement of 6.6 cm/yr which suggests the data and or analysis in this region are of questionable reliability. The average flux values over several intervals are included in the following table.

Average flux values for hole, 54-1002

depth interval	average vertical flux	average source term
	(cm/yr)	(cm/yr)
0 - 7 m	- 0.51	- 0.16
8 - 29 m	- 0.0005	- 0.0006
30 - 44 m	- 0.005	+ 0.0005
45 - 75 m	- 0.004	+ 0.0003
76 - 90 m	+ 6.6	+ 0.15

Results for hole NPH-1 are shown in Fig. 21. This is a cased hole going through a portion of an active and nearly filled disposal unit, pit #37. The zero depth in the figure is the current pit surface which is about 10m below grade, while the pit bottom is about 30m below grade or about 10m below the accessible 10m portion of this monitoring hole. The moisture profile is strongly inverted with a maximum at 6m depth consistent with on-going fill and disposal operations in the open pit.

The matric properties used in generating the fluxes and source terms in Fig. 21 B and C are for 'crushed tuff' as reported in [18,8]. Fig. 21B shows that in spite of a moisture gradient driving upward flux the net flux is gravity driven, downward throughout the profile. The source term expressed as a flux in Fig. 21B is small and only positive near the 5-6m depth, probably indicating moisture sources from recent disposal operations. Fig. 21c shows that the minimum characteristic time scale for moisture content movement is about 20 years, suggesting that seasonal or other short term fluctuations are dampened out in the crushed tuff matrix.

The crushed tuff used as fill at Area G is mostly from the unit 2b. However, the stratigraphic unit which served as the source of the 'crushed tuff' data is not from Unit 2b [p.17, Ref.5]. There have been some indications that crushed tuff and in-situ tuff do not behave too differently in unsaturated hydraulic conductivity[19], nor in matric properties[5]. Some differences in matric properties, expressed as different exponents in power law fits of matric potential as a function of moisture content, have been noted[25].

As a check on the sensitivity of these results to the actual matric properties used, the vertical flux and source terms were recalculated using the matric properties for in-situ unit 2b. These results, labeled (2b-i), are plotted with the previous results for the 'crushed tuff' properties, (2b-c), for comparison in Fig. 22. Using the in-situ matric properties it is seen that the upward slope of the moisture profile is now sufficient to drive a small upward flux (~1 cm/yr) between 4 and 5.5m depth, and a small upward spike at depth of 9m. For these properties, limited upward movement occurs. The extent could be examined in greater detail to determine if contaminant transport is

significant. Using the in-situ properties, the characteristic source term time scales in Fig. 22B are reduced from the previous 'crushed tuff' properties, and are now in the range of 1-2 years.

The van Genuchten values for crushed tuff used in the Results in Fig. 21 were used in the preliminary draft Area G Performance Assessment[1]. These parameter values have since been revised for subsequent PA work to a 'corrected' set of numbers for crushed tuff which are similar to those for the uncrushed Unit 2b average values used in this study. The results in Fig. 21 serve as a measure of the sensitivity of the vertical flux to the assumed matric properties, while results in Fig. 22 labeled *2b-i* represent expected field conditions.

Bounding Case Results

Results for two assumed profiles of moisture content are illustrated in Fig. 23, which bound the range in moisture content seen in the holes at Area G. The curves are useful to understand the limits of the basic analyses used here and to appreciate the nonlinear dependence of flux on the moisture content. Linear moisture profiles are assumed, one, from 6% near the surface decreasing to 1% at a depth of 15' (~5m), and two, 12% near the surface decreasing linearly to 2% at a depth of 30' (~10m), so that each has the same slope but in a different moisture range. These two profiles bracket the near surface profiles at Area G in all holes with one exception (NPH-4).

The slope in both profiles is $0.01 m^{-1}$, which was chosen as a 'typical value', close to an average of the observed vertical gradients in near-surface moisture. Many of the holes are seen to exhibit a near surface moisture gradient of about this magnitude independent of the near surface moisture content. Properties of Unit 2b are assumed in computing $K[\theta]$ and $h_m[\theta]$ in this example.

The associated Darcy flux in Fig. 23B shows the vertical flux as a curve and as a line segment for each of the two moisture curves. The drier moisture content corresponds to the smaller flux in Fig. 23B, which is less than 1 cm/yr, and the larger moisture profile corresponds to flux in the range of <1 - 7 cm/yr depending on the evaluation point. A curve and line segment for each moisture profile represent fluxes evaluated respectively, along the moisture profile curve (evaluated at each moisture point shown in Fig. 23A) and as an 'average' over the moisture profile curve (discretizing each moisture profile as a whole segment by evaluating Eqns.(4 - 6) using only the moisture profile endpoints and midpoint). The difference in flux in the continuous profiles and in these average segments is seen to be large. This indicates the sensitivity to the discretization in forming the non-linear difference expressions for the flux and for the source expressed as a flux. A reason for the sensitivity is that these flux expressions are 'integral measures between data points' and are not normalized per unit depth. This shows that the moisture profiles must be adequately resolved for meaningful results in these terms.

Similar considerations apply to the source term flux curves in Fig. 23B. The 'average' over each moisture range is now just a single point, using two values of vertical flux or three values of moisture content to evaluate the source term per Eqn. 5. The inverse of the source terms (Eqn. 7-8) are plotted as characteristic times in Fig. 23C. This source term is normalized per unit depth and so the difference between the source term calculated along the moisture profile and the source term calculated as an average over the moisture profile is in good agreement. The assumed linear moisture profiles lead to characteristic times for change in moisture content (indicated as *(St-inv)*vol%* in Fig. 3C) of 15 or more years at the lower moisture profile levels and about 5 years at the higher moisture content. The time scale for change in moisture flux in Fig. 23C is larger than that for the moisture content by the factor, θ^{-1}.

UNCERTAINTY

Accuracy

Accuracy of the results in this analysis depend on the accuracy of four main factors: the moisture profiles, the matric potential functions over the observed in-situ moisture range, the unsaturated conductivity function of moisture, and the application of stratigraphic unit average functions to all the data points within each unit. The application of unit averaged functions was discussed in relation to the vapor phase notch, with the implication that additional field data are required to resolve the hydraulic properties throughout that region. In other regions, the average stratigraphic unit properties seem to better represent the whole unit based on the results in the previous section.

The moisture profile accuracy is directly related to that of the neutron probe measurements for most of the data in this report. Neutron probe accuracy is estimated to be within 50% when properly calibrated, but the precision is expected to be better than 10%. In recent unpublished field data[26], it is seen in the dry regime in boreholes at Area G that the precision or reproducibility error, $\Delta\theta$, tends to about $\Delta\theta \sim 0.001$ or 0.1% (in moisture content volume percent), independent of moisture content. Thus at 1% moisture content, the relative error is $\Delta\theta/\theta \sim 0.001/0.01$ or 10% of the mean, and it is less at greater moisture content. It is the relative error or the difference between adjacent points as used in the moisture gradient determination which is important in this analysis and thus, 10% is a reasonable estimate for the error.

The accuracy of the van Genuchten fits for unsaturated conductivity has been discussed in several studies examining data from the G5 hole discussed in this report [13,19,21]. In that hole, unsaturated conductivity curves as a function of moisture content were measured by the UFA centrifuge method[19] and compared to van Genuchten fits using matric potential data[17] with the saturated conductivities. These curves were compared for 10 core samples, located approximately one every ten feet in the G-5 hole.

Of the 10 curve comparisons, two were based on unreliable data, one was ambiguous (at 9.5'), three were in relatively good agreement throughout the range of the curves and four were in poor agreement. This suggests almost half or 3 out of 7 of the reliable measurements are accurate based on comparable results from two different determinations for the unsaturated conductivity used in this study. Of the cases in poor agreement the tendency was for the experimental conductivity data (UFA determination) to asymptote at greater moisture content than expected[13,19]. In these cases, the actual conductivity at the in-situ moisture content was beyond the range of the experiment and therefore could not be determined. The discrepancy may have been attributed to experimental limitations, or to a real lack of liquid phase movement at the in-situ moisture content. The latter implies that the in-situ content could only be achieved by evaporation and vapor phase movement, a possibility considered further in a separate study[27].

Generally, the matric potentials (matric heads) found in this study are consistent with the range in the in-field psychrometer results reported previously[9-11]. A possible exception is at the driest moisture contents where the matric potential predicted from the van Genuchten fits in this study are of greater magnitude than previously observed. Matric potential results between van Genuchten fits and chilled mirror psychrometry (CMP) on recovered core samples from hole G5 were found in good agreement[13]. Matric potential from chilled mirror psychrometer measurements on recovered core samples compared well to van Genuchten fits with moisture data in horizontal

boreholes at Area G, at least at the dry range of moisture content[28]. Recent unpublished results on CMP matric potential from core recovered in Area G boreholes as part of the Environmental Restoration Program[24], agrees with results from moisture content combined with the unit-averaged van Genuchten functions within a factor of about two at most data points[27]. We find good agreement generally in matric potential observed in different studies and methods, however, it is difficult to quantify the overall accuracy of the matric potential determinations in these different studies without knowing which provides the 'right answer'.

Error Analysis

Assuming the overall validity of the analysis described in this report, an error analysis is used to understand the important contributions to error and the magnitude of the overall error associated with the analysis. The error or uncertainty associated with each variable is denoted as σ, subscripted with the appropriate variable name.

For a general function,

$$x = f(u,v,w,....),$$

the propagation of errors is based on the standard form[29],

$$\sigma_x^2 = \left(\frac{\partial f}{\partial u}\right)^2 \sigma_u^2 + \left(\frac{\partial f}{\partial v}\right)^2 \sigma_v^2 + \left(\frac{\partial f}{\partial w}\right)^2 \sigma_w^2 + ... \qquad (9)$$

which applies when there is no correlation between the independent variables. This is assumed in the present analysis.

We are interested in determining the error associated with the flux given by Eqn. 6. In this section, simple analytic forms are assumed for the transport properties (rather than the van Genuchten fits) which make it more convenient to analytically evaluate the uncertainty. Power law fits[30] for unsaturated transport properties over the low moisture content range [2%-20%] have proven to have high correlation coefficients [>98%] in Bandelier Tuff[25]. The unsaturated transport properties, expressed here as matric head, $h_m[\theta]$, and unsaturated conductivity, $K[\theta]$, are estimated in this uncertainty analysis as

$$h_m[\theta=2\text{-}20\%] = a_h\,\theta^{b_h} \quad and \quad K[\theta=2\text{-}20\%] = a_k\,\theta^{b_k} \qquad (10)$$

where a_h, b_h, a_k, and b_k are fitting parameters.

Equation 6, for the flux, is approximated by evaluating all functions at a moisture content, θ, at location, i, (index along the z axis), and the moisture gradient is estimated here as $d\theta/dz = (\theta - \theta_i)/\Delta z$ where θ_i is the adjacent moisture measurement. Hydraulic properties are assumed to be only a function of moisture so that, $\nabla h_m = (dh_m/d\theta)\nabla\theta$. This does not apply to the interface region between two dissimilar units, which must be considered separately, i.e., this applies only within a unit with average hydrologic properties. The vertical flux, Γ_z, can then be expressed in several equivalent forms for this analysis based on

$$\Gamma_z = -D_z - K, \tag{11}$$

where D_z is a 'diffusive part' of the flux, and K is the convective part. These can be written out as,

$$\begin{aligned}
\Gamma_z &= -K[\theta]\,\{\,(\partial h_m[\theta]/\partial z) + 1.\,\}, \\
&= -K[\theta]\left(\frac{\partial h_m[\theta](\theta - \theta_.)}{\partial\theta\quad\Delta z} + 1.\right), \\
&= -\frac{a_k a_h b_h}{\Delta z}\,\theta^{b_k+b_h} + \frac{a_k a_h b_h \theta_.}{\Delta z}\,\theta^{b_k+b_h-1} - a_k\,\theta^{b_k}, \\
&= -A + B - K.
\end{aligned} \tag{12}$$

Based on these simplified analytic forms, the derivatives, $\partial\Gamma/\partial a_k$, $\partial\Gamma/\partial\theta$, etc., needed in Eqn.(9) for the propagation of errors can be evaluated and combined to obtain an estimate for the error in the flux, expressed as σ_Γ/Γ. This is found to be given by

$$\begin{aligned}
\left(\frac{\sigma_\Gamma}{\Gamma}\right)^2 = {} & \left(\frac{\sigma_{a_k}}{a_k}\right)^2 + \left(\frac{D}{\Gamma}\frac{\sigma_{a_h}}{a_h}\right)^2 + \left(\frac{D}{\Gamma}\frac{\sigma_{\Delta z}}{\Delta z}\right)^2 + \left(\frac{B}{\Gamma}\frac{\sigma_{\theta_-}}{\theta_.}\right)^2 \\
& + \left(\ln\theta\,\sigma_{b_k}\right)^2 + \left(\frac{D}{\Gamma}\frac{\sigma_{b_h}}{b_h}\right)^2 + \left(\ln\theta\,\frac{D}{\Gamma}\sigma_{b_h}\right)^2 \\
& + \left(\left(-\frac{A}{\Gamma}(b_h + b_k) + \frac{B}{\Gamma}(b_h + b_k - 1) - \frac{K}{\Gamma}(b_k)\right)\left(\frac{\sigma_\theta}{\theta}\right)\right)^2.
\end{aligned} \tag{13}$$

Most of the terms have small uncertainties, probably about 10% (normalized) or better, considering a 'precision' error. Therefore the terms of the form $(\sigma_u/u)^2$, where u is any one of the independent variables, are each much less than unity. Similar terms including factors of D/Γ or B/Γ are also small since these factors are also less than one.

To simplify the term on the last line of Eqn. 13, we assume realistic values and evaluate these terms. Note that $|A/\Gamma|$, $|B/\Gamma|$, and $|K/\Gamma|$ are all less than or equal to one. Typical parameter values are $b_h = -1.3 \pm 0.3$ and $b_k \sim 7 \pm 0.5$ [Ref.25], and it is always true that $(b_h + b_k) < b_k$ since $b_h < 0$. This implies that the third line is less than $\left(b_k\left(\frac{\sigma_\theta}{\theta}\right)\right)^2$, which is approximately equal to 0.5 using $b_k = 7$, and $\sigma_\theta/\theta = 0.1$. The 'precision' error for neutron probe moisture measurements is better than 10% if the moisture volume content exceeds 1%, so this is a maximum magnitude for this term at most locations.

For $\theta = 0.02 - 0.2$, then $ln\theta \sim 2 - 4$, where 4 applies at the low moisture content end of the range. The two terms containing $ln\theta$ then both exceed unity and dominate the error propagation. Retaining these two terms, the total error is then approximately,

$$\left(\frac{\sigma_\Gamma}{\Gamma}\right)^2 \sim \left(ln\theta\ \sigma_{b_k}\right)^2 + \left(ln\theta\ \frac{D}{\Gamma}\sigma_{b_h}\right)^2, \tag{14}$$

which, in the low moisture content region, is estimated as

$$\left(\frac{\sigma_\Gamma}{\Gamma}\right)^2 \sim (4 \times 0.5)^2 + (4 \times 0.5 \times 0.3)^2 = 4 + 0.4 = 4.4,$$

or

$$\sigma_\Gamma^2 \sim 4.4\,\Gamma^2. \tag{15}$$

About 10% of the error comes from the uncertainty in the exponential parameter for the matric potential curve fit and the rest comes from the uncertainty in the exponential parameter describing the unsaturated hydraulic conductivity. While these exponents could be independently determined from experimental data, in the van Genuchten-Maulem model,[3,16] the exponents are not independent.

This uncertainty analysis shows that the error associated with each point is larger than the mean value. This is characteristic of a log-normal distribution, which in this analysis has $\sigma_g = \sqrt{4.4} \sim 2.1$ and is limited by the exponent of the moisture content used to characterize the unsaturated hydraulic conductivity. The implication, that the error for each point is larger than the mean, is that we need to interpret the results in terms of overall trends supported by each of the holes and by flux averages computed over large segments of the holes. In these average trends, the associated error is reduced in proportion to the number of observations included in the trend observation.

In this analysis, the error is dominated by a single term related to the uncertainty in the exponent for hydraulic conductivity. A direct analog in the van Genuchten-Maulem model does not exist, but in that case, the error must be related to the van Genuchten exponent, N, as confirmed in a numerical error analysis of the van Genuchten parameters[27], as summarized in the following section. Since N is typically $1.5 - 2$ and $b_k \sim 7$, it is reasonable to conclude that the error in the van Genuchten scheme is proportional to about four times the error in the exponent, N. The magnitude of the error does not depend upon the fitting scheme used to define the unsaturated transport functions, so the result that $\sigma_g \sim 2.1$ applies, independently of the fitting model used. Note that this value depends upon the assumption that $\sigma_{b_k} = 0.5$, which was an estimate, and was not quantitatively determined from site data.

As a final note, a moisture source term examined in this study was given by Eqns. 7 or 8. This source is the difference between flux at two adjacent points. The propagation of errors applied to the difference of two terms will double the magnitude of the error for the source term relative to that derived above for the flux at each point, giving an error for the source terms in this analysis expressed as a geometric deviation of $\sigma_g = 2x2.1 = 4.2$.

Minimum Detectable Flux

A minimum detectable flux of the liquid phase can be derived from the uncertainty or error analysis. In this section, we numerically evaluate the uncertainty in the flux derived from unit-averaged van Genuchten relations. This is described in detail for the vapor phase flux elsewhere[27]. The minimum detectable flux can be considered as that flux which is statistically discernible from a zero flux estimate, and as such, is related to the standard deviation or width of the uncertainty of the flux estimate. We consider a marginally detectable liquid phase flux, Γ_{min}, (to be denoted *LLDflux* in the subsequent result figures, where *LLD* refers to a lower limit of detection) and define it to be equal to the error expressed as one standard deviation of the flux estimate, σ_Γ. Thus,

$$\Gamma_{min} = \sigma_\Gamma . \tag{16}$$

To evaluate the uncertainty in our flux estimates, Eqn. 3 is rewritten for the magnitude of the liquid flux in the form,

$$\Gamma[cm/yr] = -K[\theta]\,(\nabla h_m + 1) = \frac{K[cm/yr]}{\Delta z}(h_{m1} - h_{m2} + \Delta z), \tag{17}$$

where h_{m1} and h_{m2} are matric potentials (heads) evaluated at adjacent points separated in space by vertical distance, Δz, each evaluated in the same units of length. The uncertainty in the flux, σ_Γ, is evaluated in terms of uncertainties in h_{m1}, h_{m2} and K, represented respectively by σ_{h1}, σ_{h2} and σ_K. Assuming these uncertainties are not correlated and that uncertainties in the distance, Δz, are negligible, this gives

$$\sigma_\Gamma^2 = \left(\frac{\partial\Gamma}{\partial K}\right)^2 \sigma_K^2 + \left(\frac{\partial\Gamma}{\partial h_1}\right)^2 \sigma_{h1}^2 + \left(\frac{\partial\Gamma}{\partial h_2}\right)^2 \sigma_{h2}^2 . \tag{18}$$

Evaluating the derivatives in Eqn. 18 from the flux given by Eqn. 17, and further simplifying with the reasonable assumption that matric potential uncertainties at adjacent points are comparable, or $\sigma_{h1} = \sigma_{h2} = \sigma_{hm}$, then the flux uncertainty becomes

$$\sigma_\Gamma^2 = \left(\frac{h_{m1} - h_{m2}}{\Delta z} + 1\right)^2 \sigma_K^2 + 2.\left(\frac{K}{\Delta z}\right)^2 \sigma_{hm}^2 . \tag{19}$$

The minimum detectable difference in matric potentials, $|h_{m1} - h_{m2}|_{min}$, is related to the uncertainties in matric potential, and again using a 'marginally detectable' criteria related to one standard deviation then

$$|h_{m1} - h_{m2}|_{min} = 2\,\sigma_{hm} , \tag{20}$$

and so the flux uncertainty becomes

$$\sigma_\Gamma^2 = \left(\frac{2\,\sigma_{hm}}{\Delta z} + 1\right)^2 \sigma_K^2 + 2.\left(\frac{K}{\Delta z}\right)^2 \sigma_{hm}^2 . \tag{21}$$

In deriving h_m with the unit-averaged van Genuchten parameters from the moisture content, then the uncertainty in h_m is assumed to depend primarily on the uncertainties associated with the parameters, N_{vg}, α_{vg}, and moisture content, θ. Uncertainty in the porosity and residual moisture contents are neglected. This is reasonable for porosity when in the dry regime far from saturation. It is a necessary simplification for the residual content, since the analyses proceeded under the simplification that residual content equals zero in order to assure that all field data values for moisture content are associated with a real matric potential in the van Genuchten fits. In this simplification, the matric potential uncertainty from the van Genuchten method, σ_{hm}, is written,

$$\sigma_{hm}^2 = \left(\frac{\partial h_{vg}}{\partial \theta}\right)^2 \sigma_\theta^2 + \left(\frac{\partial h_{vg}}{\partial N_{vg}}\right)^2 \sigma_{nvg}^2 + \left(\frac{\partial h_{vg}}{\partial \alpha_{vg}}\right)^2 \sigma_{\alpha vg}^2 . \qquad (22)$$

The hydraulic conductivity is assumed to depend primarily upon the saturated hydraulic conductivity, K_{sat}, the moisture content, and the van Genuchten parameter, N_{vg}. The uncertainty in the unsaturated conductivity derived from the moisture profile and the van Genuchten relations is then,

$$\sigma_K^2 = \left(\frac{\partial K_{vg}}{\partial \theta}\right)^2 \sigma_\theta^2 + \left(\frac{\partial K_{vg}}{\partial N_{vg}}\right)^2 \sigma_{nvg}^2 + \left(\frac{\partial K_{vg}}{\partial K_{sat}}\right)^2 \sigma_{Ksat}^2 . \qquad (23)$$

The derivatives in these Eqns, 22 and 23, are evaluated numerically from the van Genuchten relations in a spreadsheet analysis. The best estimates for the uncertainties in the dependent terms as applied to this study are, $\sigma_\theta = 0.001$ [volume fraction], $\sigma_{nvg} = 0.06$ and, expressed as fractions of the mean values, $\sigma_{\alpha vg} = 0.2\ \alpha_{vg}$ and $\sigma_{Ksat} = 0.2\ K_{sat}$. The values for σ_θ and for $\sigma_{\alpha vg}$ are discussed in [27], and σ_{nvg} and σ_{Ksat} values are discussed in the following.

The variation in saturated hydraulic conductivity, K_{sat}, within a given stratigraphic unit is typically 100% or more [2,4,5]. However, the uncertainty we wish to characterize here is not an overall result accuracy but the uncertainty in assuming K_{sat} is constant between two adjacent measured points. Thus, we need a measure of the variability of K_{sat} between adjacent profile measurement points as used in the flux analysis. This is estimated by considering the values measured at Area G [17] in borehole NPH-5 (G-5) as seen in Fig. 24. The uncertainty at a given point is estimated to be equal to a normalized difference in K_{sat} at adjacent spatial locations, $\delta K_{sat}/K_{sat}$, evaluated as the in-field observed gradient in K_{sat} times the distance, δz_m, between two points where the moisture profile measurements are typically made. These assumptions are written as

$$\frac{\sigma_{Ksat}}{K_{sat}} \sim \frac{\delta K_{sat}}{K_{sat}} \sim \frac{\frac{\partial K_{sat}}{\partial z}\delta z_m}{K_{sat}} \sim \frac{(K_{sat1} - K_{sat2})\ 2\ \delta z_m}{(z_1 - z_2)\ (K_{sat1} + K_{sat2})} . \qquad (24)$$

This estimate of the error in the saturated hydraulic conductivity is labeled *dKsat/Ksat*dzm/dz* in Fig. 24 and shown for the in-situ data, assuming $\delta z_m = 3' \sim 1m$. The value is less than or equal to about 0.2 at most points. At most locations then, it is expected that $\frac{\sigma_{Ksat}}{K_{sat}} < 0.2$.

The uncertainty in the van Genuchten exponent, σ_{nvg}, is seen in numerical evaluations[27] to dominate the errors especially at low moisture content, consistent with the analytic results in the previous section. Typically, the Bandelier Tuff stratigraphic unit average statistics show a standard deviation for the van Genuchten exponent of about $\sigma_{nvg} = 0.2$ [Ref.2] or about 10% of N_{vg} across each stratigraphic unit. The variation between two adjacent points is likely to be much smaller. This is seen in Fig. 25 where the van Genuchten exponent, N_{vg}, derived from core samples recovered from 10 ft depth intervals[13] is plotted verses depth in borehole NPH-5 (G-5).

A normalized gradient is used to estimate the variance expected in N_{vg} between two adjacent measurement points (separated by 1m) as discussed above for the K_{sat} error estimate. This is shown in Fig. 25, labeled, $dN/N*dzm/dz$. Most values are seen to less than 0.03 and since N is typically close to 2, then the magnitude of the error in N_{vg} is about, $\sigma_{nvg} = 0.03 \times 2 = 0.06$ at most field locations. This method is a simple means of estimating a spatial correlation scale length for the parameter.

A simpler but less conservative estimate of the variance between two measurement points is to take the variance associated with the stratigraphic unit[2] and simply assume the variance between two adjacent measurement points will be the total unit variance times the distance between two measurement points divided by the total unit thickness. For a 'typical unit thickness' in Area G of about 10m, and $dzm = 1m$, then for $\sigma_{nvg} = 0.2$ associated with the unit, we expect $\sigma_{nvg} \sim 0.02$ associated with the variation between two measurement points at 1m separation.

Using these estimates of uncertainty or error between adjacent measurements in the field then the error terms in Eqns. 22 and 23 are determined, the derivatives are evaluated numerically using the van Genuchten relations, and the equations are solved for σ_{hm} and σ_K. These values are combined in Eqn. 21 which is a measure of the flux detection limit per Eqn. 16. This flux detection limit is shown as a function of moisture content in Fig. 26 for the three values discussed above of uncertainty in the van Genuchten exponent, σ_{nvg} (and labeled dN in the Figures). The value $\sigma_{nvg} = 0.06$ is assumed to apply to the present study. The detection limited flux as a fraction of unsaturated flux is actually decreasing with moisture content, but not as fast as the unsaturated flux increases, thus the detection limit increases significantly with moisture content.

Results in Fig. 26 apply to the averaged van Genuchten parameters for the stratigraphic Unit 2b. These results are compared to the flux detection limit using van Genuchten parameters for Unit 1b in Fig. 27. In Unit 1b, a lower liquid phase flux is detectable at any given moisture content. Results for Unit 2a are similar to that for 2b. Results for the other Bandelier Units are expected to be approximately bracketed between results for Units 2b and 1b, by comparison to their hydraulic conductivity curves[27].

The detection limits derived from this uncertainty analysis can be compared to flux results predicted in the field boreholes. The region around the vapor phase notch was seen to exhibit an apparent moisture source and large moisture flux. In Fig. 28 the maximum magnitude of liquid phase flux observed near the vapor phase notch, for each of the six boreholes in this study which penetrated that region, is plotted against the peak value of moisture content in that region from that borehole. This is compared to the detection limit curve for Unit 1b (in which the vapor phase notch lies), and it is seen that the magnitudes of observed flux in each hole is consistent with the expected uncertainty in that Unit at that moisture content. This supports the notion that the apparent source at the vapor phase notch may not be a source of real moisture but may be an unresolved variation in

matric properties which consistently occurs near the notch region. This possibility is consistent with unique properties of the notch observed at other locations outside of Area G [22].

On the other hand, the points in Fig. 28 are plotted at the maximum moisture content associated with the borehole profile. In some cases, this maximum is a narrow peak and not aligned exactly with the position where the maximum moisture flux is indicated. If one assumes that the actual moisture content is slightly less at the borehole position where the maximum flux occurs, then the borehole points in Fig. 28 move slightly to the left. Most points would then indicate flux levels which are above the detection limit, and correspond to a real source. Thus, the 'source' indicated at the notch region remains ambiguous.

In Fig. 29, the magnitude of the moisture flux resulting from the analysis at all depths in two of the boreholes is shown verses the moisture content at that borehole location. These two boreholes were chosen because they bracket the field results where LGM-85-11 is an 'extreme moist case' and NPH-9 (ER1111) is an 'extreme dry case'. The field results are compared to the minimum detectable liquid phase flux in Unit 2b and in Unit 1b, using the best estimate of the uncertainty in the van Genuchten exponent, σ_{nvg} (labeled *dN* in Fig.) = 0.06. It is seen that most of the flux levels determined are below the flux detection limits, and therefore cannot be considered as accurate values, but rather are 'below detection limit' results. As above, those points which lie very near to the detection limit curves are ambiguous and may or may not be significantly determined flux levels. About 10% of the moisture flux determinations appear to the left of the detection limit curves and are likely to indicate real flux values.

Figure 30 compares the minimum detectable liquid phase flux in Unit 2b to the uncertainty in unsaturated hydraulic conductivity, σ_K, (labeled *sigmaK* in the Fig.), for the best estimate of the uncertainty in the van Genuchten exponent, σ_{nvg} (labeled *dN* in Fig.) = 0.06. The *(sigmaK)* value is an estimate of the recharge or vertical flux uncertainty under unit gradient conditions where the recharge rate is simply the unsaturated hydraulic conductivity evaluated at the in-situ moisture content. The comparison shows that the flux uncertainty is dominated by that of the unsaturated hydraulic conductivity at higher moisture contents where the two curves are comparable. The minimum detectable gradient in matric potential contributes significantly to the overall flux uncertainty in the dry range, where the two curves diverge.

In regions where it can be shown that the unit gradient assumption applies (e.g., where moisture content and matric properties are on the average constant with depth), then the detection limit for the vertical flux or recharge rate will be just (*sigmaK*). There is a substantial improvement in detection limit and therefore in estimating small recharge rates in the dry moisture range, when the unit gradient assumption can be justified.

The flux detection limits under unit gradient conditions, expressed as *(sigmaK)* derived from the van Genuchten averaged properties in three stratigraphic units are shown in Fig. 31. It is seen, for example, that in a region within the Otowi member where the unit gradient assumption applies, if the moisture content is 10-20%, then the respective flux uncertainties are about 0.4 - 10 cm/yr. Conditions similar to this example are observed in moisture profiles under some canyon locations at Los Alamos[5]. The flux uncertainties at these locations are large and may limit meaningful predictions of flux levels.

The minimum detectable flux described here relates to each flux determination in the profile as an independent measurement. Each flux estimate which can be grouped within a similar region (e.g., the low flux region) contributes to a mean flux estimate over that region (as summarized in Table II) which has its own associated uncertainty. Propagation of errors analysis shows that the error associated with the mean of *n* determinations, each with an error, σ, is equal to $\sigma\sqrt{n}$. A typical

borehole profile with 15 flux estimates throughout the 'low flux region' would then have an error in the average flux throughout that region of almost four times less than that associated with each flux determination.

The sum of all flux estimates over all boreholes (the summary mean values in Table II) involves about 100 points and therefore about a factor of ten reduction in the error associated with the mean estimated over that whole region. Referring to Fig. 29, one sees that a reduction by a factor of ten in detection limit puts us into the regime of most of the individual point flux estimates, e.g., the detection limit for a trend in flux averaged over 100 points in Unit 2b at 1.5% moisture content is about $1.x10^{-3}$ cm/yr. This suggests the region-averaged flux values are reasonable estimates of the region mean flux in spite of the high detection limits on each point. However, it is not clear if the variance throughout each region is associated with a real variation in flux or with variation in matric properties throughout the region.

DISCUSSION

Three Subsurface Transport Regions

The data and analyses reveal several trends. The Area G subsurface can generally be characterized by three regions. A 'near surface region' has a variable depth with hole location from about 5m to more than 10m and is characterized with a decreasing moisture content typically from 6-12% near the surface to < 2% at depth. Below this is a 'low flux region' characterized by low moisture content, and small vertical fluxes and source terms in this analysis which are typically less than 0.1 cm/yr locally (at any depth), less than 0.03 cm/yr in any hole, and less than 0.002 cm/yr averaged over the 'low flux' region and over all the holes. The third region is a moisture peak near the vapor phase notch or 1b-1a interface. This is apparently associated with a moisture source term and local flux although the average vertical flux over the range of this third region is small in most cases. Limited data below this third region makes it more uncertain, however, it appears in this analysis that below this 'notch region' the flux returns to a 'low flux regime'.

These trends are quantified in Table II which summarizes for each region, the depth intervals, the interval-averaged fluxes and source terms. The large variability associated with the 'near surface region' led to a geometric mean as the best characterization of the values in that region. The other regions were characterized with arithmetic means, required to meaningfully average the flux values of changing sign. Results at hole NPH-4, which was observed to be near an engineered drainage area and quite different from any other hole, were eliminated before taking the geometric mean because its inclusion skewed the results excessively.

The near surface region has a geometric mean depth of 7.8m (~25') with a geometric standard deviation of 1.6, suggesting that 'plus or minus one sigma' of the holes fall between 7.8/1.6 = 4.9m and 7.8*1.6 = 12.5m. The mean flux in this region is -0.94 cm/yr, about 1 cm/yr downward, with a geometric standard deviation of 3.9, characterizing a large variability in the results. The source term mean is -0.11 cm/yr, about 1 mm/yr net evaporative loss. The variability is huge (σ_g = 20.6) presumably skewed by two holes which have very small source terms (NPH5 and NPH9). Eliminating these holes from the statistical sum gives a reasonable source mean of -0.37 cm/yr, or about 40% of the vertical flux, and a more reasonable geometric deviation, σ_g = 4.2.

The depth, flux terms, and moisture content in this near surface region appear to be determined by the extent that the local site has been disturbed by adjacent engineered operations associated with

waste disposal. The natural distribution of surface-connected fractures in the immediate area of the monitor hole may also play a role in some holes, notably NPH-5 (G5), and in the nearby, recently drilled test hole, ER-1107 [ref.24].

A low flux region is characterized below the near surface region. In the Table II, this low flux region is characterized with a depth down to the 'vapor phase notch' region, however, the data are also consistent with a low flux region extending down to greater depths than examined in this study, with the vapor phase notch region imposed as a local perturbation on top of a low flux region continuing to greater depths. The depth of the vapor phase notch region has an arithmetic mean of 21 ± 5.4m. Over the low flux region, the maximum downward net flux in any hole is 0.007 cm/yr and the average flux over all the holes is 0.0017 cm/yr upward. The source term average is -0.013 cm/yr implying net evaporation, consistent with a net upward movement. The magnitude of these terms are all considered negligibly small, consistent with the large characteristic time scales for the source terms.

The vapor phase notch region, or units 1b-1a interface is somewhat arbitrarily identified in Table II as the range of depth for the moisture spike and the significant flux sources associated with this region, as seen in the earlier figures. This gives a mean range for the region from 21.3m to 34m. Though the local flux and source terms were seen to be significant in most cases, the integral flux and source terms over the region as shown in Table II, are small. The maximum region downward flux is 0.43 cm/yr calculated in two holes, while the average downward flux over all the holes over this region is 0.073 cm/yr or less than 1 mm/yr. The derived source magnitude is 0.032 cm/yr, for a small net influx. The standard deviations show a relatively large variability imposed on the small mean values, but the deviations are still small in terms of absolute values of flux, i.e., ±0.3 cm/yr for the vertical flux.

Source Term at Vapor Phase Notch

The vapor phase notch region shows interesting local characteristics in this analysis as seen in the previous figures. A positive source term, possibly influx from a localized horizon, is flanked by two horizons in which the moisture is moving away vertically (up above the source and down below the source) and simultaneously being lost to horizontal movement or evaporation in the two horizons adjacent to the source. The source average over the adjacent regions (in Table II) becomes a small net value for all of the boreholes examined. Alternatively, the results may reflect variable hydrologic properties in the region which are not well characterized.

One possible physical interpretation is that this source horizon is connected to a more saturated canyon region (Pajarito Canyon is the likely candidate at Area G) and the adjacent horizons are also surface-connected but to a less saturated region which thus acts as a sink. Another possible interpretation of the results is that this horizon is bringing in moisture from 'upstream' locations to the west (along the axis of the canyons), and the source represents a significant lateral moisture movement.

A third possibility to explain this apparent source as a real physical mechanism, is that there is a significant fracture network which is connected to the surface of the mesa and extends downward ending somewhat abruptly at the horizon of the vapor phase notch, or at the Units 1b-1a interface. This could allow infiltration through open fractures during heavy summer thunderstorms, which then moves rapidly downward to the bottom of the fracture network. The water sits there and is wicked horizontally into the Bandelier Tuff matrix at this horizon, producing the large local moisture peak. Simultaneously, the water spreads from the source horizon into the matrix and migrates back towards the fracture, driven by evaporation from the fracture. Eventually most of the water evaporates, leaving a small net source term when averaged over the region.

This possible source mechanism is consistent with the magnitude of the source term expressed as a characteristic time scale which was seen to be as small as one per year near this horizon in several borehole results. This supports the hypothesis of an annual influx. This mechanism would be consistent with stratigraphic unit properties which are approximately constant with elevation through the vapor phase notch region. This source mechanism seems a likely candidate to explain the field data and analyses, and will be tested against detailed field data to be collected in the near future. However, the moisture spike at the vapor phase notch is observed at other locations (e.g., TA-49) where the depth from the surface to the notch is much greater (~400'), making it less likely to be surface-connected by a fracture network, and more likely to be a region of significant lateral movement.

Another possibility is that the present analysis is giving erroneous results, and there is no significant source at this horizon. The analysis is based on the assumption that matric potential properties throughout a stratigraphic unit are approximated by the average value for the unit, although it is known there are large variations within a unit. If the variations are consistent in some way, e.g., the van Genuchten exponent, N, increases linearly with depth throughout unit 1b, then the present analysis can give erroneous results. If there exists a horizon near the vapor phase notch, where the matric properties are significantly different than the average values assumed (i.e., different from either unit 1b or 1a properties), then it would be possible to match the field observed moisture profiles while maintaining insignificant vertical flux and source term in these horizons. The flux detection limit analysis showed (Fig. 29) that the flux and source terms implied in the field near the notch region are within the range of uncertainty of the analysis, supporting the possibility that the apparent sources are not real but due to consistent matric property variations in the region.

The issue, whether or not a moisture source exists at the vapor phase notch, is important for understanding the unsaturated transport beneath the mesa. This will influence our understanding of the net vertical flux in and beneath the mesa top and therefore it is a critical issue for completing the Performance Assessment. The issue can be resolved by collecting core samples through the vapor phase notch region and doing a complete matric potential characteristic curve for each sample throughout this region. Care must be given in collecting the core to consider the possibility that the important controlling horizon may be very thin.

Below the vapor phase notch, there are limited data. In the present study, several holes (LGM-85-06, LGM-85-11, NPH-9, 54-1002) suggest a negligible vertical flux in the region below the vapor phase notch. The most data in this region included in the present study is from hole, 54-1002, (Fig. 19-20), which showed vertical flux << 0.1 cm/yr at all points (Fig. 20) and the average over the interval below the vapor phase notch (45-75m) of -0.004 cm/yr. The small average flux in that hole and the small average flux values over the vapor phase notch region as summarized in Table II each point to the possibility that the 'low flux region' actually extends deeper beyond the 'notch region' and that the 'notch region' is not more than a perturbation imposed on top of a continuous low flux region. The data in this hole, ER-1002, shows anomolously large flux magnitudes in the lowest interval, in the Cerro-Toledo unit. This needs further study to see if lateral flow or other effects are significant at that horizon.

Uncertainty Implications

The uncertainty analysis shows that the magnitudes of flux predicted at most borehole locations are within the range in the uncertainty in flux due to the variance in model parameters and field data. To some extent this variance is attributable to spatial variations in matric properties which could be resolved more carefully in field investigations. The potential moisture source term observed near the vapor phase notch region is significant enough to warrant such further investigation. At some

point where the variance due to real spatial variations is minimized, the flux detection limits derived from this analysis method will be limited by the experimental reproducibility in the determinations of the matric properties.

Most of the flux values implied at points throughout the borehole profiles in this analysis are not quantitatively accurate but are indications of flux below the 'detection limits', derived and quantified in this study. Thus it can be said that the flux at most points is less than the detection limits for a given moisture content as shown in Fig. 27. It is expected that the trends in moisture flux observed across the boreholes are qualitatively correct and that the average flux value determined for each of the different regions is a good 'representative value' of the 'expected flux' in each of those regions, as discussed at the end of the section on the Flux Detection Limits. This could be quantified more thoroughly in future work by evaluating in greater detail the reduction in error when estimating a mean quantity from a large number of independent estimates of that quantity.

Flux Implications

The results section presented the vertical flux source as a characteristic time scale for change in the moisture content. This value was seen to vary widely, with a minimum of about one year or more in the moist regions in most holes. A seasonal variation was evident in the near-surface of one hole (NPH-2). In an engineered drainage area, hole NPH-4 showed a time scale of less than one year. The magnitude of the source term in the low flux region of most holes increased to more than 1000 years reflecting the low turnover rate of moisture there by liquid phase movement.

Throughout the vertical profiles, and especially in the low moisture content region, the unit gradient assumption is not valid for estimating flux in this region. Small variations in moisture content correspond to large variations in matric potential which significantly change the vertical flux from that predicted as the unsaturated hydraulic conductivity. These small changes in moisture content often predict a small fluctuating moisture flux which may reflect real transport between local pockets or may reflect the error and uncertainty in this analysis.

Vapor phase loss by evaporation to surface connected features has been posited as a dominant mechanism in shaping the near-surface moisture profiles. Vapor phase transport, including effects of fractures in the matrix material, has not been analyzed in this report but will be the subject of a second report[27]. Anticipating those results, the vapor phase movement in the matrix is expected to play a role in the drier regions of the mesa top.

The present analysis showed that NPH-5 (G-5) did not exhibit the typical profile observed at many other locations, having a high moisture content which did not decrease appreciably with depth until below 17m. The observations may be consistent with a highly fractured region. The 17m horizon is coincident with the interface of units 2b and 2a (where 2b is more fractured) and also with the approximate depth of the adjacent disposal shafts and pits which could contribute to the flux and source terms seen at this hole. Moisture, including some infiltration from adjacent disturbed areas or from fractures, moves downward until the fractures end at the unit interface, and the remaining moisture at this depth evaporates to the fractures. This analysis shows that G-5 is not a good 'representative hole' for Area G profiles in general, however, it is similar to a recent profile in a nearby hole, ER-1107 [Ref.24], and may characterize a region in the central portion of Area G.

In previous analysis for hole G-5 [13], it was suggested that a unique horizon existed at the 2b-2a interface where vapor phase losses occur. The present analysis suggests that the horizon is not especially unique, but rather the increased moisture content and flux throughout the upper 2b layer is unique. This supports the notion of an effect from adjacent disposal operations or surface-

connected fractures. The impact of either could be reasonably expected to be limited to the Unit 2b layer. Vapor phase movement at this horizon will be discussed in a separate report[27], where it will be shown that vapor phase flux is significant under the moisture conditions observed in hole G5, only below the depth of 17m at the 2b-2a interface.

It is not clear that it would be worth applying the present analysis to moisture data in other deep holes due to the limited matric property data and therefore the large uncertainty in the results at the greater depths. On the other hand, it is important to pursue this type of analysis at greater depths for modeling calibrations and site characterization. It is expected that the flux at depths below possible canyon source terms is more characteristic of that through the bulk of the unsaturated zone, and therefore this is important to know for site performance. This can be examined in a future study.

Disposal Operations

Disposal operations appear to contribute to the moisture profiles in the near-surface layer and act to increase its variability above that expected in undisturbed locations. This was evidenced by increased moisture content and flux at locations adjacent to disposal units and trenches as discussed in the Results Section. At one location (NPH-4) the engineered drainage has increased the typical moisture content by 4-5 times corresponding to an increased vertical flux of 100-200 times that in the relatively 'undisturbed' locations. The borehole is not deep enough to determine if the increased infiltration has penetrated through the 'low flux region' at this location. The results show that the hydrology can be disturbed relatively easily by unchecked disposal operations, although long term effects are uncertain.

In relatively undisturbed areas, the mesa provides an excellent natural barrier to transport, however, in the disturbed locations the integrity of the natural transport barrier is compromised. A desirable goal in disposal operations is to minimize the potential for contaminant migration. This requires minimizing operations that add water to the mesa top and avoiding surface engineering which enhances local infiltration of natural precipitation or which reduces the large natural evapotranspiration. All surface paving, culverts, drainages, etc., should be designed to direct water away from covered and from open (actively used) disposal units. Adequate vegetative covers similar to the natural systems must be maintained to assure significant evapotranspiration. New and continuing operations should be reviewed regularly with respect to meeting specific requirements derived from these general considerations.

The depth of the low flux region or the top of the vapor phase notch region is comparable to the depth of the deeper disposal units in the area. As such, the low flux region may not provide a thick barrier to contaminants moving from the bottom of a disposal unit. This emphasizes the importance of determining if the 'low flux region' continues to greater depths with the vapor phase notch region as a small local perturbation.

Numerical Modeling Implications

These results have important implications for numerical modeling of the contaminant transport from the disposal unit and can be used to help calibrate numerical models to obtain realistic moisture flow fields which account for localized variations in recharge rate. Specifically, the source terms derived in this analysis can used to provide input to numerical models. This should provide better agreement between numerical models and the field data, than that obtained with the more restrictive source term assumptions of a net infiltration only at the mesa top surface. These results, in conjunction with other analyses on vapor transport[27], may be applied towards

completing a conceptual model of the complex flow in the mesa stratigraphy, and towards quantifying the contributions from liquid and vapor flux.

CONCLUSIONS

The flux analysis shows that unsaturated vertical transport in the mesa under the disposal site, Area G, can be characterized in three regions. A near surface region is influenced by infiltration and disposal operations and is spatially variable. It extends to 7.8m ± 1.6, has a downward vertical flux of 0.94 cm/yr ± 3.9, and a characteristic vertical flux source term of -0.37 cm/yr ± 4.2 (geometric means and standard deviations). The source term is about 40% of the vertical flux, with the difference assumed to be vapor transport, to be examined in a separate study. Below this variable near-surface region, a low moisture flux region exists to at least 21.3 ± 5.4 m with average vertical flux (upward) of +0.0017 ± 0.011 cm/yr (arithmetic values). These flux values are negligible and comparable to the analysis errors. At greater depths, the vapor phase notch region is characterized with a moisture peak and derived downward average flux of -0.073 ± 0.311 cm/yr. This large variability suggests the net flux from this region to greater depths depends strongly on location.

The data at the vapor phase notch suggest a moisture source which is dissipated by vertical motion and evaporation from the source horizon located at the peak in the moisture profile. A number of physical mechanisms were discussed which could contribute to this apparent source. One candidate mechanism, based on assessment to date, assumes a fracture network which is surface connected and ends abruptly near the Unit 1b-1a interface. Major storm events could potentially send water to the bottom of the fracture network where it will soak horizontally into the Bandelier Tuff matrix. This could produce the apparent source seen in the present analyses, and would represent a real and important source term possibly driving moisture flux at greater depths.

The apparent source may also be a non-physical artifact resulting from the analysis assumption of constant stratigraphic unit-averaged hydrologic properties. If this region has matric properties which are significantly different from the adjacent horizons, then the observed moisture profiles could be consistent with a flux which is everywhere negligible throughout the region. On the other hand, a horizon with distinct properties is likely to be associated with a real lateral moisture flux since the vertical variation in properties may act to interrupt vertical moisture flux. It is critical to distinguish these possibilities and determine if the apparent source term is physical or not, because this region may or may not provide a moisture source driving flux at greater depths throughout the unsaturated zone beneath the mesa. This controls the overall unsaturated transit time to the ground water and thus the impact on the site Performance Assessment depends critically upon resolving the hydrologic flows in this region. The source term derived in this analysis can be used in numerical studies to improve the accuracy in the Area G PA effort.

The large variability of moisture and flux in the near surface region indicates that operations may have a significant impact on the near surface unsaturated transport. Under extreme conditions as seen at the hole, NPH-4, near the drainage basin, operations could impact transport in deeper regions, and compromise the natural isolation provided by the low flux region. Any disposal operation which increases local moisture content or decreases evapotranspiration will degrade the natural integrity of the disposal site and degrade the site performance to some extent, and therefore, these operations should be reviewed regularly for impact.

The uncertainty analysis indicates that many of the flux result values are less than the estimate of the flux uncertainty, and therefore must be regarded as 'below the detection limits' of liquid flux

for this analysis method. While specific flux values are less than detectable, the flux trends indicated by the composite of values and by the averages over regions are good estimates of the average flux. The flux detection limits could be improved with additional field data, because the variance in the input parameters used in the present analysis reflects a real spatial variance in material properties which could be resolved in limited regions (e.g., in one or more selected boreholes). Ultimately, the flux detection limits in this type of analysis will be limited by the experimental uncertainty associated with the reproducibility in measuring the matrix properties needed to define the moisture characteristic curves and the saturated hydraulic conductivity.

ACKNOWLEDGMENTS

This work was sponsored by the U.S. Department of Energy, Waste Management Programs, as part of the Area G site Performance Assessment required per US DOE Order 5820.2A. The author wishes to thank Everett Springer and David Rogers for thorough and critical reviews of the draft manuscript, and David Broxton for helpful discussion on possible lateral flow at the vapor phase notch.

REFERENCES

[1] - D. Hollis, E. Vold, K. Birdsell, J. Turin, P. Longmire, E. Springer, W. Hansen, D. Krier, R. Shuman, "Performance Assessment of LANL TA-54, Area G, LLRW Disposal Facility - Preliminary Draft", Los Alamos National Laboratory, Los Alamos, NM, August, 1995.

[2] - D. Krier, P. Longmire, R. Gilkeson, H.J. Turin, "Geologic, Geohydrologic, and Geochemical Data Summary of MDA G, TA-54, LANL", Los Alamos National Laboratory Report LA-UR-95-2696, Los Alamos, NM, 1995.

[3] - van Genuchten, M. Th., "A closed-form equation for predicting the hydraulic conductivity of unsaturated soils", Soil Science Society of America Journal, 44, 892-898, 1980.

[4] - D. Rogers, "Unsaturated Hydraulic Characteristics of Bandelier Tuff at TA-54", Los Alamos National Laboratory Report LA-UR-95-1777, Los Alamos, NM, 1995.

[5] - Rogers, D. B., and B. M. Gallaher, "The Unsaturated Hydraulic Characteristics of the Bandelier Tuff'", 132 pp., Los Alamos National Laboratory Draft Report LA-12968-MS, May 1995.

[6] - Reneau, S. L. and D. T. Vanamin, "Fracture Characteristics in a Disposal Pit on Mesita del Buey, Los Alamos National Laboratory", Los Alamos National Laboratory informal report - unpublished - March 21,1994.

[7] - Turin, H. J., "Subsurface Transport Beneath MDA G: A Conceptual Model", Los Alamos National Laboratory Report LA-UR-94-1663, Los Alamos, NM, 1995.

[8] - K. Birdsell, W. Soll, N. Rosenberg, B. Robinson, "Numerical Modeling of Unsaturated Groundwater Flow and Radionuclide Transport at MDA G", Los Alamos National Laboratory Report LA-UR-95-2735, Los Alamos, NM, 1995.

[9] - International Technology Corporation, "Hydrologic Assessment of Technical Area 54, Areas G and L, Los Alamos National Laboratory", Final Report, Docket Number NMHWA 001007, Los Alamos National Laboratory, Los Alamos, NM, March, 1987.

[10] - Kearl, P. M., J. J. Dexter, and M. Kautsky, "Vadose zone characterization of Technical Area 54, waste disposal areas G and L, Los Alamos National Laboratory, New Mexico, Report 3: Preliminary assessment of the hydrologic system, Report GJ-44", Bendix Field Engineering Corp., March 1986a.

[11] - Kearl, P. M., J. J. Dexter, and M. Kautsky, "Vadose zone characterization of Technical Area 54, waste disposal areas G and L, Los Alamos National Laboratory, New Mexico, Report 4: Preliminary assessment of the hydrologic system through Fiscal Year 1986, Report GJ-54", UNC Technical Services, Inc., December 1986b.

[12] - Turin, H.J., Rosenberg, N.D., "Summary of TA-67 Geology, Hydrology, and Seismicity for Radiological Performance Assessment - FY93 Report", Los Alamos National Laboratory Report LA-UR-94-4399, Los Alamos, NM, 1994.

[13] - Rogers, D. B., Vold, E.L., Gallaher, B. M., "Bandelier Tuff Hydraulic Characteristics from Los Alamos National Laboratory (LANL) Borehole G-5 at MDA G, TA-54", draft, rev.1, completed July, 1995, Los Alamos National Laboratory Report, LA-UR-95-3129, Los Alamos, NM, 1995.

[14] - Koorevaar, P., Menelik,G., and Dirksen,C., Elements of Soil Physics, Elsevier Science, New York, 1983.

[15] - Loaiza, D. and Vold, E., "Moisture Profile Measurements in Subsurface Monitor Holes at the Los Alamos LLRW Disposal Site", Los Alamos National Laboratory Report LAUR-95-1922, Los Alamos, NM, submitted to the Journal, Environmental Monitoring, June, 1995.

[16] - Mualem, Y., "A new model for predicting the hydraulic conductivity of unsaturated porous media", Water Resources Research, 12, 513-522, 1976a.

[17] - Stephens, D. B., and Associates, "Laboratory analysis of soil hydraulic properties of G-5 soil samples, report no. DBSA/3854/195-1", prepared for Los Alamos National Laboratory, Los Alamos, New Mexico, January 1995.

[18] - E. Springer, "Area G Performance Assessment: Surface Water and Erosion", Los Alamos National Laboratory Report LA-UR-95-2497, Los Alamos, NM, 1995.

[19] - Conca, J., and T. J. Mockler, "Measurement of unsaturated hydraulic conductivity and recharge distribution in the Bandelier Tuff at Los Alamos", prepared for Los Alamos National Laboratory, Los Alamos, New Mexico, 24 pp., Northwest Environmental Services, March 1995.

[20] - Conca, J. L., and J. Wright, "Direct determinations of unsaturated flow and transport", Proceedings of the Twelfth Annual American Geophysical Union Hydrology Days Meeting, Fort Collins, 103-116, March 1992.

[21] - Turin, H.J., Rogers, D.B., Vold, E.L., "Determining unsaturated hydraulic conductivity of Bandelier Tuff; A comparison of characteristic curves and ultracentrifuge methods", Los Alamos National Laboratory report, LA-UR-95-1897, Los Alamos, NM, presented to the Kearney Foundation of Soil Science Conf., Davis, CA, June, 1995.

[22] - Broxton, D.E., Heiken, G.H., Chipera, S.,J., Byers, F.M., Jr., "Stratigraphy, petrography, and minerology of Bandelier Tuff and Cerro Toledo deposits", p.33 in Los Alamos National Laboratory report, LA-12934-MS, Los Alamos, NM, June, 1995.

[23] - Rogers, D. B., and B. M. Gallaher, "Moisture and Matric Suction Profiles for 1994 MDA G Wells", 7 pp. and 3 figures, Los Alamos National Laboratory Memo ESH-18/WQ&H-94-632, December 19, 1994.

[24] - Gilkeson, R., Kisiel, K., Marin, J. personnal communication, ERM/Golder Corp., unpublished moisture and matric potential data from Area G boreholes in series 1100-1125 for the LANL Environmental Restoration program (1996).

[25] - Abeele, W.V., "Hydraulic Testing of Crushed Bandelier Tuff", Los Alamos National Laboratory Report LA-10037-MS, March, 1984, and see also Abeele, W.V., Wheeler,M.L., Burton,B.W., "Geohydrology of Bandelier Tuff", Los Alamos National Laboratory report, LA-8962-MS, October, 1981.

[26] - Borduin, M., personnal communication, Los Alamos National Laboratory, CST14, plot of replicate neutron probe readings in borehole NPH-9 (ER1111), 1996.

[27] - Vold, E.L., "An Analysis of Vapor Phase Transport in the Unsaturated Zone with Application to a Mesa Top Disposal Facility, Part I", in preparation as a Los Alamos National Laboratory Report, January, 1996.

[28] - Puglisi, C., and Vold, E., "Low Impact Sampling under an Active Solid Low-level Radioactive Waste Disposal Unit Using Horizontal Drilling Technology", Los Alamos National Laboratory Report LA-UR-95-3691, in proceedings to Symposium on the Scientific Basis for Nuclerar Waste Management, Materials Research Society, Boston, MA, Nov.,1995.

[29] - Bevington, P.R., Data Reduction and Error Analysis for the Physical Sciences, McGraw Hill Book Co., New York, 1969.

[30] - Campbell, G.S., "A Simple Method for Determining Unsaturated Conductivity from Moisture Retention Data", Soil Sci., 117, 311-134 (1974).

Table 1. Hydrologic Transport Properties Used in the Analysis (from Ref.2 except as noted)

Property	Unit							
	2b	2a	1b	1a	Ts-CT [1]	Otowi	crushed tuff [2]	2b (w/G5) [3]
n = # of samples (vG[4] fits)	3	9	8	9	2	12	1	7
vG[4] alpha (cm-1)	0.0061 ± 0.0002	0.0030 ± 0.0009	0.0044 ± 0.0045	0.0052 ± 0.0014	0.0152 ± 0.0030	0.006 ± 0.0009	0.143	0.0047
vG[4] N	1.898 ± 0.142	2.027 ± 0.228	1.660 ± 0.220	1.735 ± 0.118	1.506 ± 0.111	1.755 ± 0.253	1.506	2.042
vG[4] M = 1-1/N	0.473	0.506	0.397	0.423	0.335	0.430	0.335	0.510
θ-residual (>0) [5]	1.3	0.2	0.9	0.6	0.8	1.9	1.0	
θ-saturation (%)	48.1	51.7	50.9	48	47.3	43.5	33	
Ksat (cm/s)	4.3E-04	1.5E-04	1.7E-04	1.9E-04	8.7E-04	2.5E-04	2.9E-04	
specific gravity-bulk-	1.37	1.26	1.2	1.14	1.12		1.2	

1 - (Tsankawi-Cerro Toledo)
2 - from Ref.18
3 - additional unit 2b data from hole G5 as reported in Ref.17
4 - van Genuchten fitting parameters
5 - θ-residual set equal to zero in present analysis to avoid inconsistencies where field data moisture is less than the average residueal, θ < θ-residual

Table II. Flux characteristics summary by monitor hole and by 'flux region'

hole	near surface region			low flux region			v.p.[1] notch (unit 1b-1a interface)		
	depth -m-	flux[2]	source[2]	depth -m-	flux[2]	source[2]	depth -m-	flux[2]	source[2]
nph-2 (bkg p37)	0 - 4	-0.41	-0.17	4 - 14	-0.0016	-0.0009	-		
nph-3 (bkg p30)	0 - 4	-0.45	-0.27	4 - 14	-0.0010	+0.0003	-		
nph-7c	0 - 8	-2.4	-0.65	8 - 19	-0.006	-0.0009	-		
nph-6	0 - 4 4 - 10	+0.87 - 0.74	1.4 -0.24	10 - 15	-0.007	-0.002	-		
nph-4	0 - 10 10 - 17	-178. -96.	-51. -6.8	-			-		
LGM-85-06	0 - 6	-0.29	-0.17	6 - 24	-0.0016	-0.013	24 - 35	-0.43	+0.016
LGM-85-11	0 - 7	-23.	-11.	8 - 24	+0.009	-0.070	24 - 37	-0.43	+0.10
nph-8	0 -4 5 - 11	+0.49 -1.42	+0.28 -0.17	11 - 25	-0.0038	-0.0024	25 - 29	+0.04	+0.004
nph-9 (ER1111)	0 - 5 6 - 12	-0.14 -0.21	-0.008 0.0001	12 - 24	0.0001	-0.0011	24 - 29-vp 29 - 35	0.0051 0.0084	0.0011 0.0019
nph-5(G5)	0 - 16	-1.68	0.0078	16 - 25	0.029	-0.038	25 - 30	+0.38	+0.069
ER-1002	0 -7	-0.51	-0.16	8 - 29	-0.0005	-0.0006	30 - 44	-0.0046	+0.0005
summary-									
mean[3]	7.8[4,5]	-0.94[5]	-0.11-0.37[5]	21.3[4]	0.0017	-0.013	34.0[4]	-0.073	0.032
std.dev[3]	1.6[4,5]	3.9[5]	20.6-4.2[5]	5.4[4]	0.011	0.023	5.9[4]	0.311	0.042

1 - vapor phase notch.
2 - average value over the indicated interval, units - cm/yr - 'flux' (vertical flux) and 'source' are terms plotted in Figs.#.B.
3 - arithmetic statistics used in low flux and vapor phase notch regions, geometric values used in near surface region (see text).
4 - mean values for maximum of the depth range.
5 - excludes data from hole NPH4, the second value also excludes NPH-5 (G-5) and NPH-9 (ER1111) data as discussed in the text.

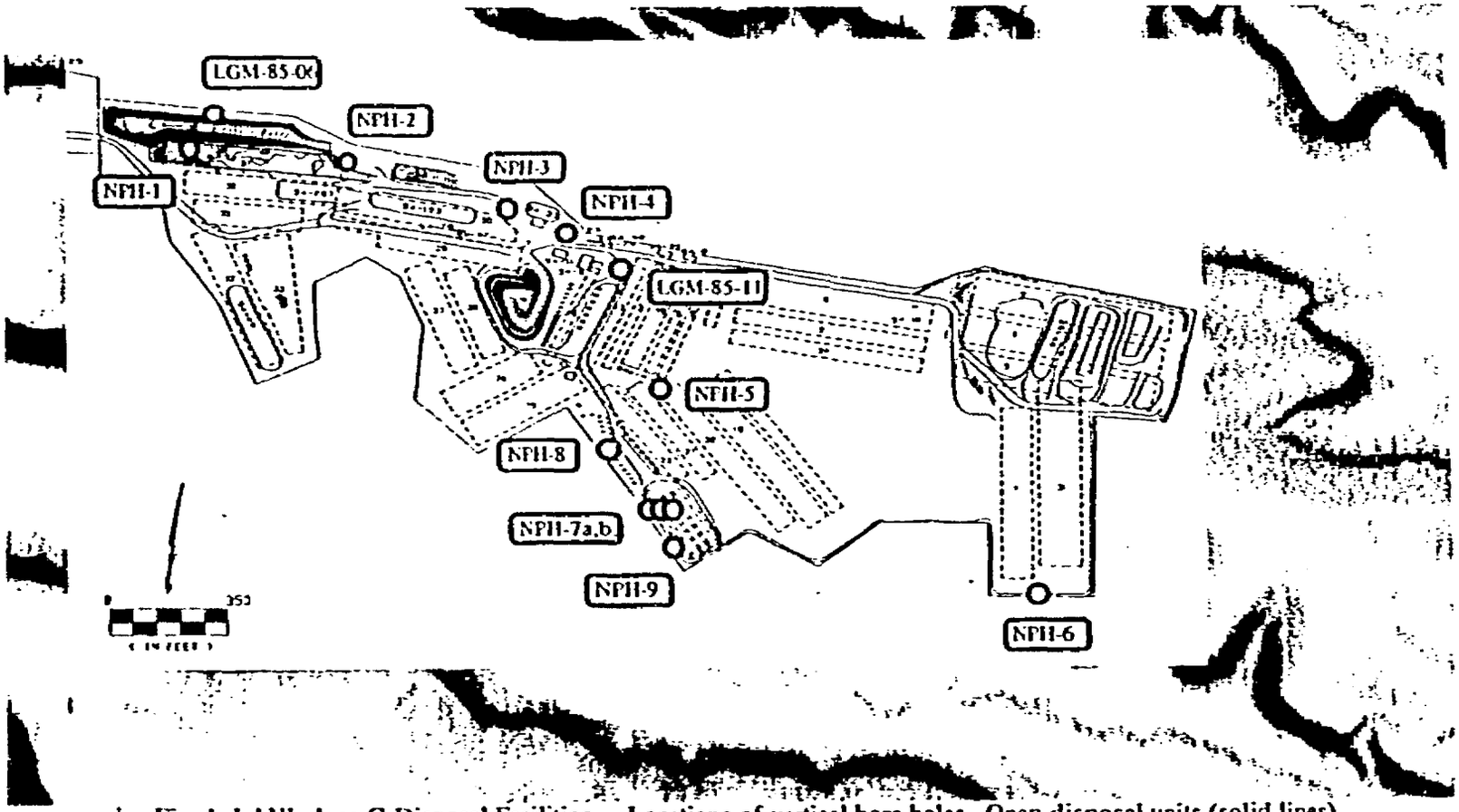

Fig. 1 LANL Area G Disposal Facilities - Locations of vertical bore holes. Open disposal units (solid lines), covered disposal units (dashed lines) and shafts (small cirles and boxes) are imposed on terrain contours of the mesa.

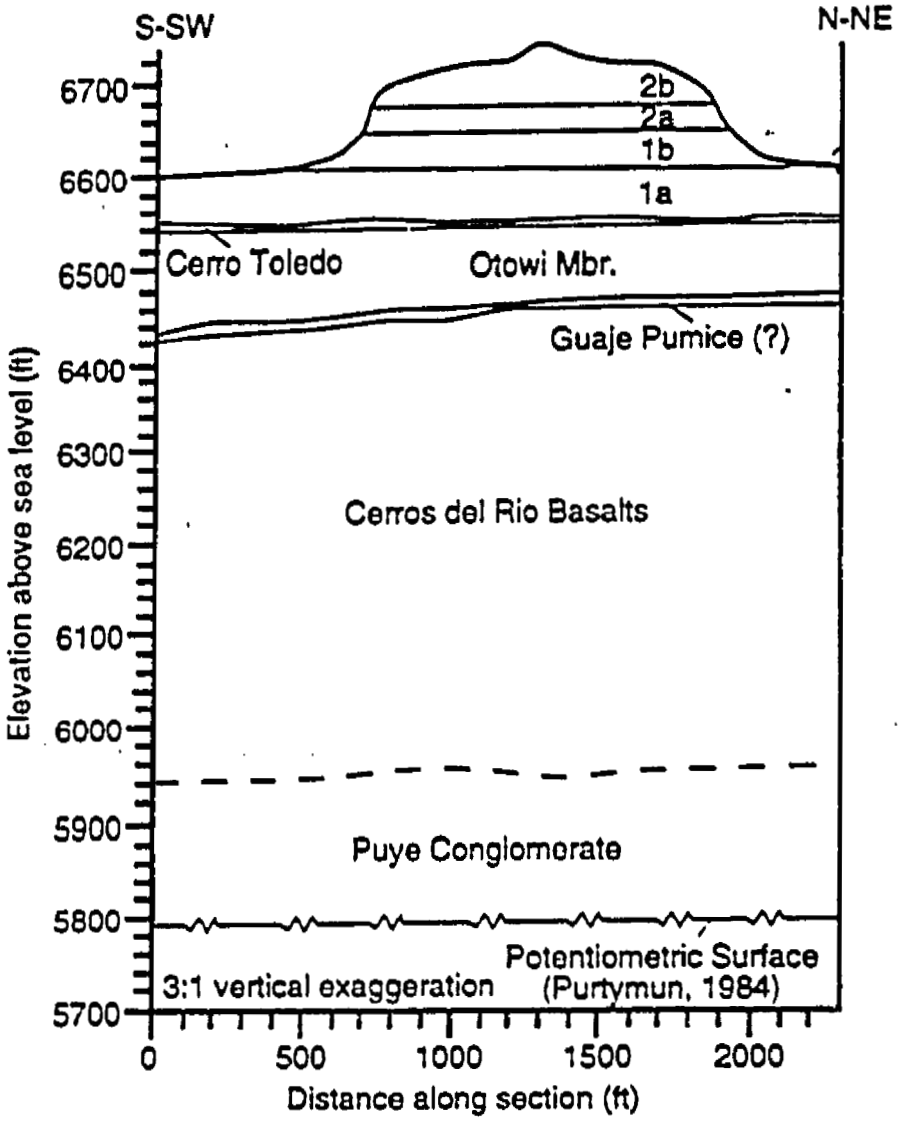

Fig.2 Stratigraphy cross-section (N-S) through the west end of the mesa-top disposal site at Area G (adapted from Krier, et.al. 1995).

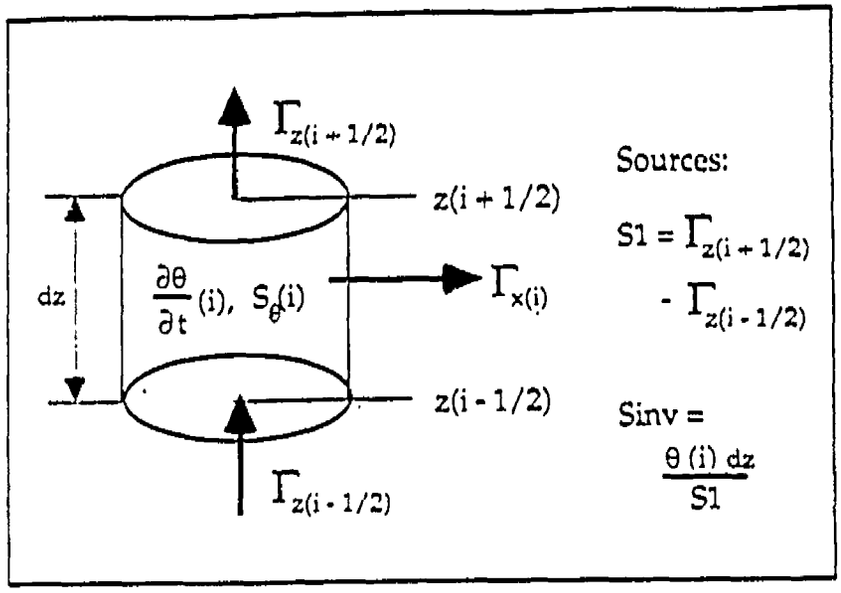

Fig.3 Schematic summary of analysis showing a control volume and flux elements through the control volume.

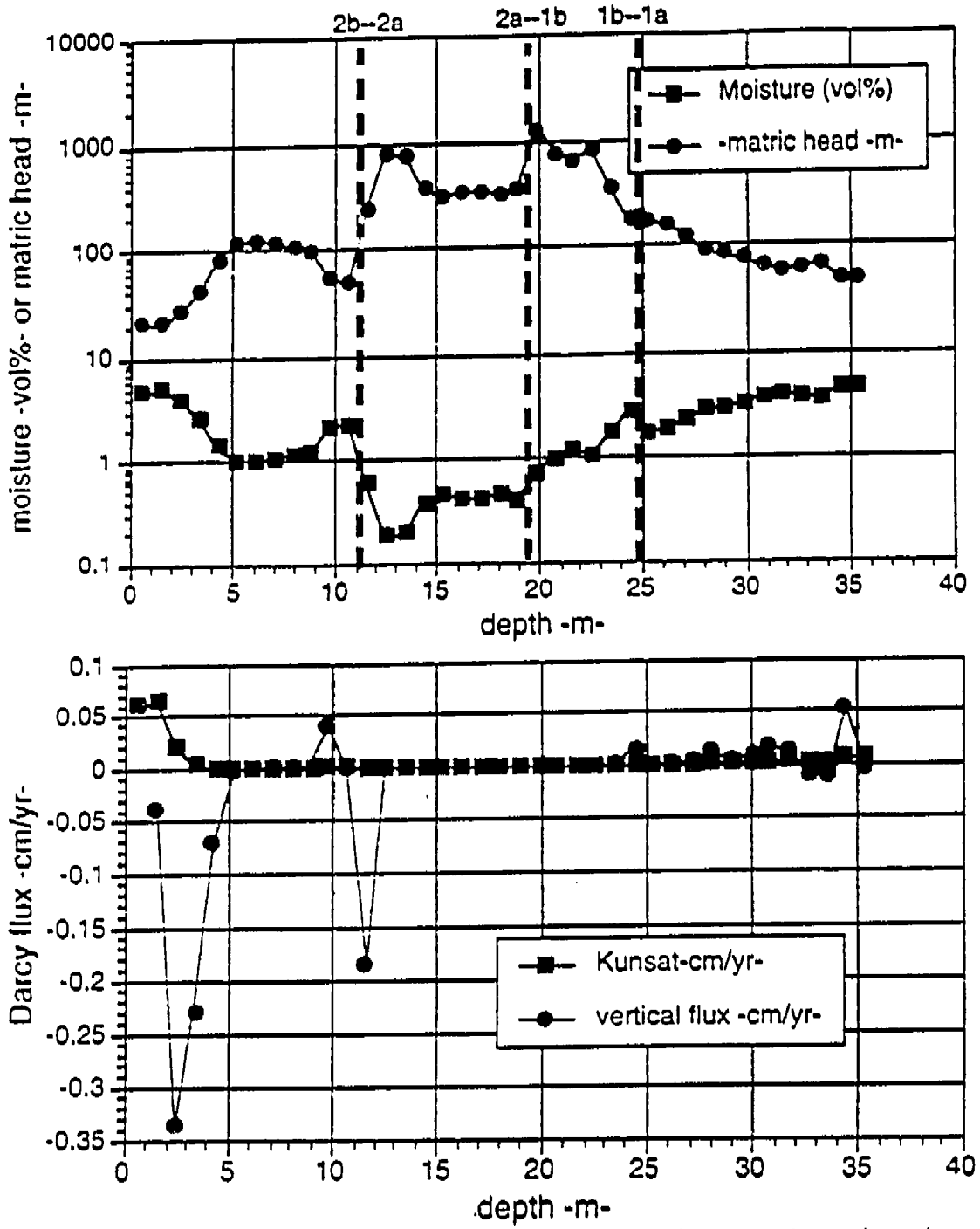

Fig. 4.A-B Vertical profiles for hole NPH-9 (ER1111) showing: A. volumetric moisture content (%) with the matric head (m) and stratigraphic unit interfaces indicated, and B. vertical flux and the local unsaturated hydraulic conductivity, Kunsat -cm/yr-.

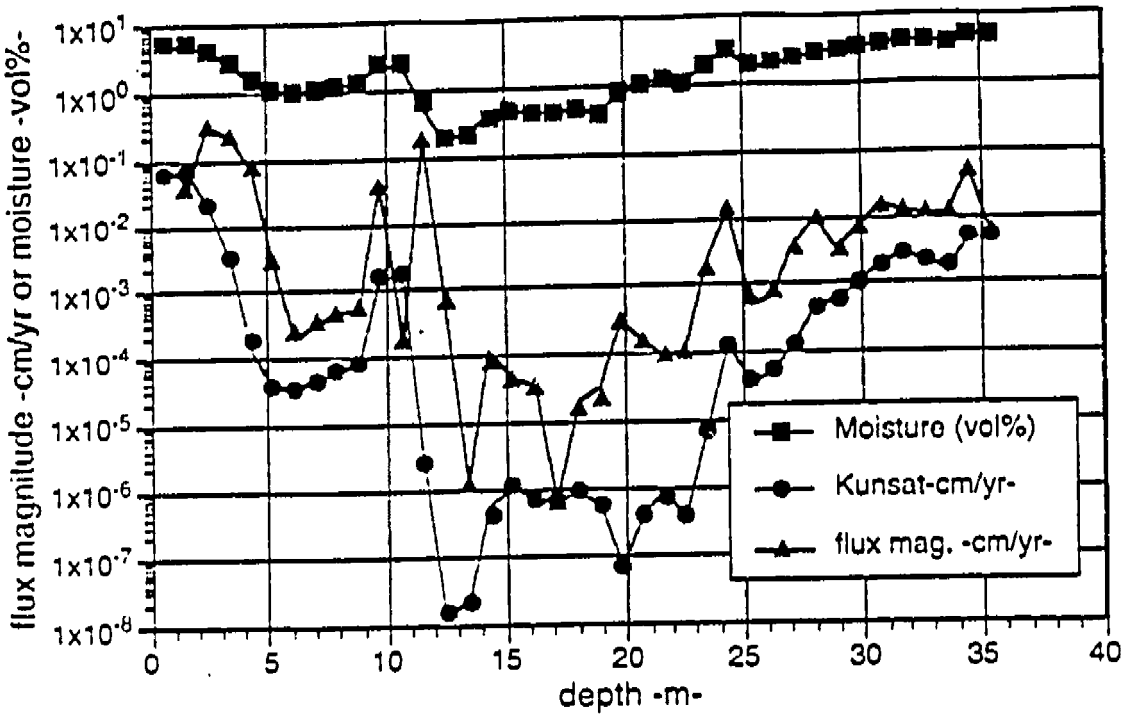

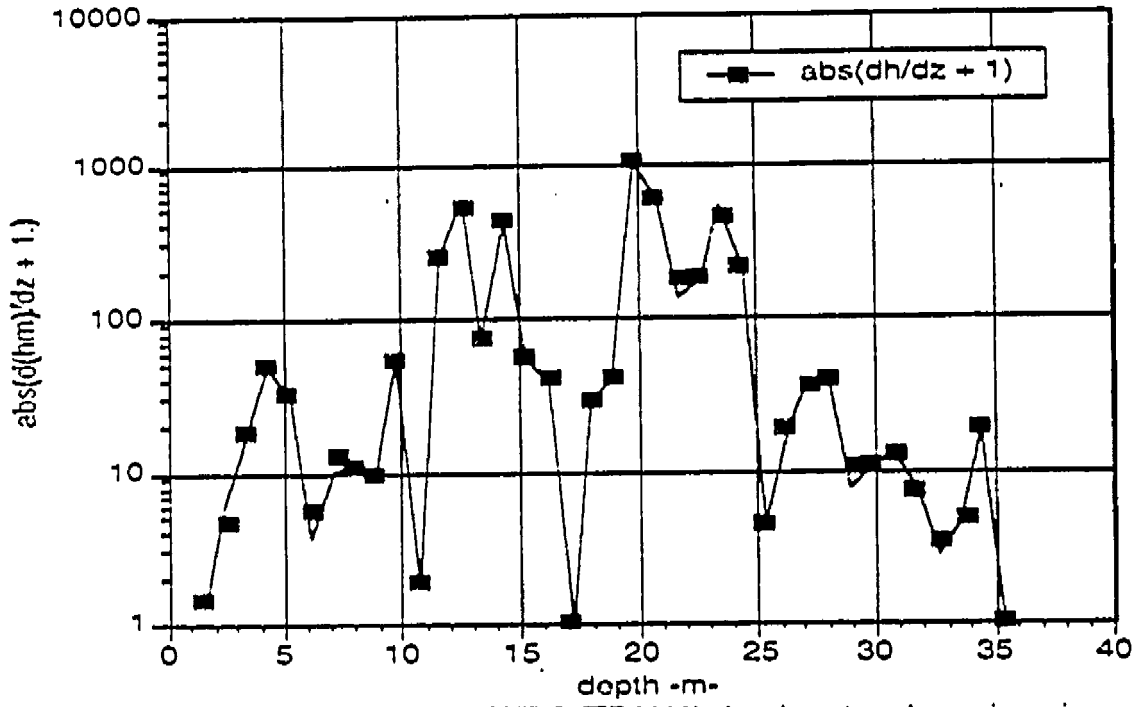

Fig. 5.A-B Vertical profiles for hole **NPH-9 (ER1111)** showing: A. volumetric moisture content (%), with the absolute magnitude of the vertical flux and the local unsaturated hydraulic conductivity, Kunsat -cm/yr-, and B. the vertical flux function, abs($d(h_m)/dz + 1$).

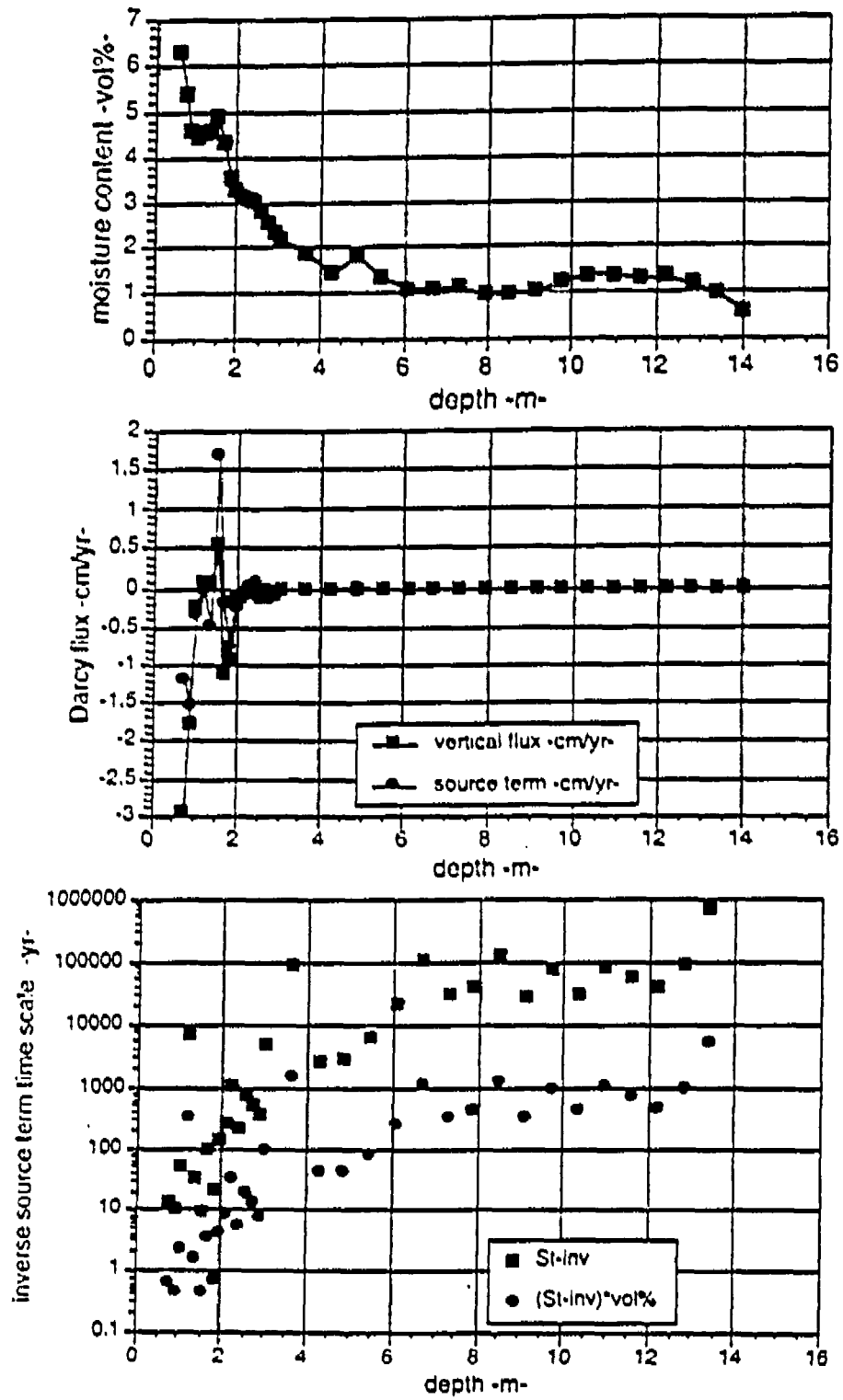

Fig. 6 Vertical profiles for hole NPH-2 (bkg near pit 37) showing: A. volumetric moisture content, B. vertical flux and the source term expressed as a flux, and C. source terms expressed as a characteristic response time.

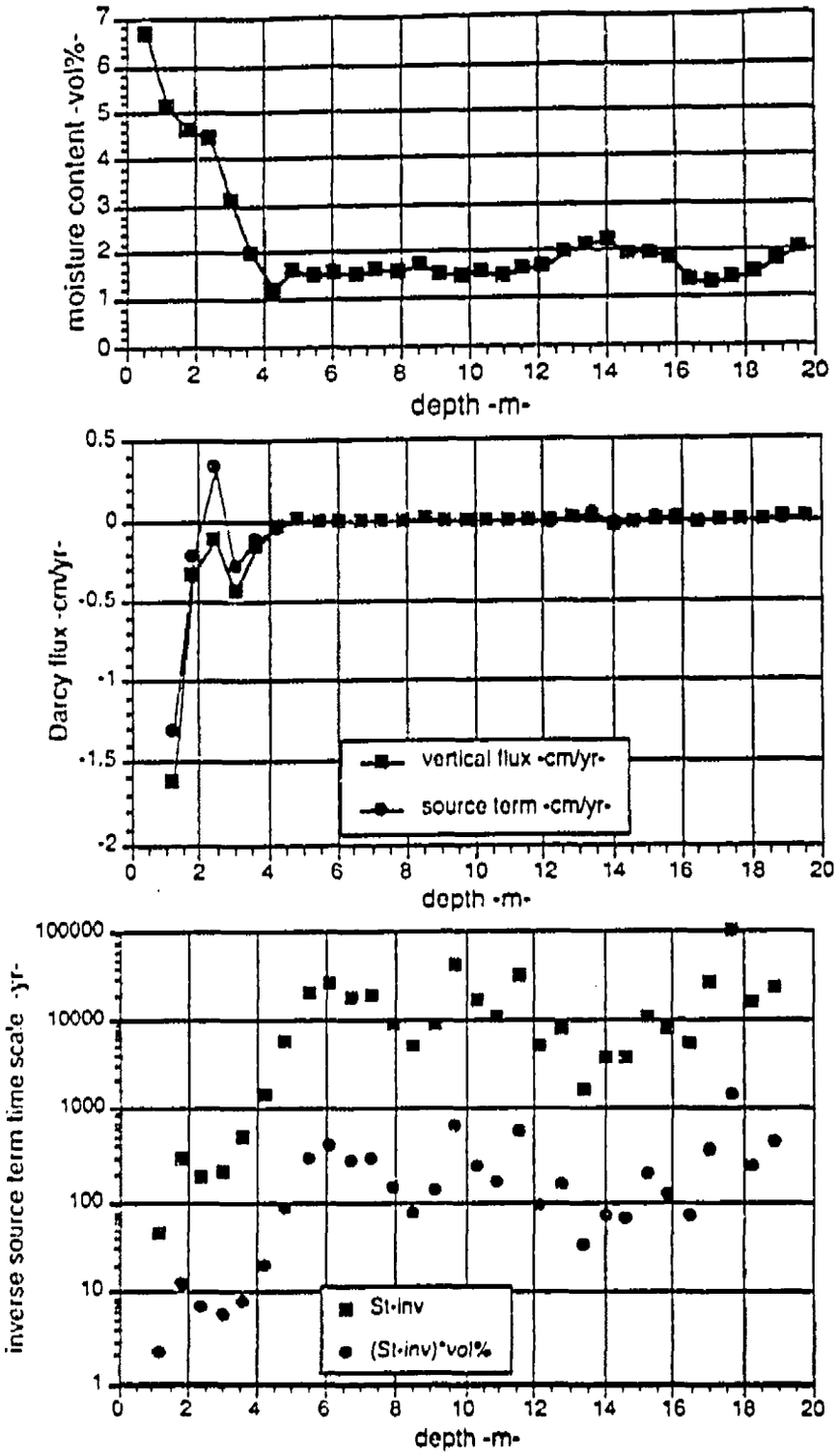

Fig. 7 Vertical profiles for hole NPH-3 (bkg near pit 30) showing: A. volumetric moisture content, B. vertical flux and the source term expressed as a flux, and C. source terms expressed as a characteristic

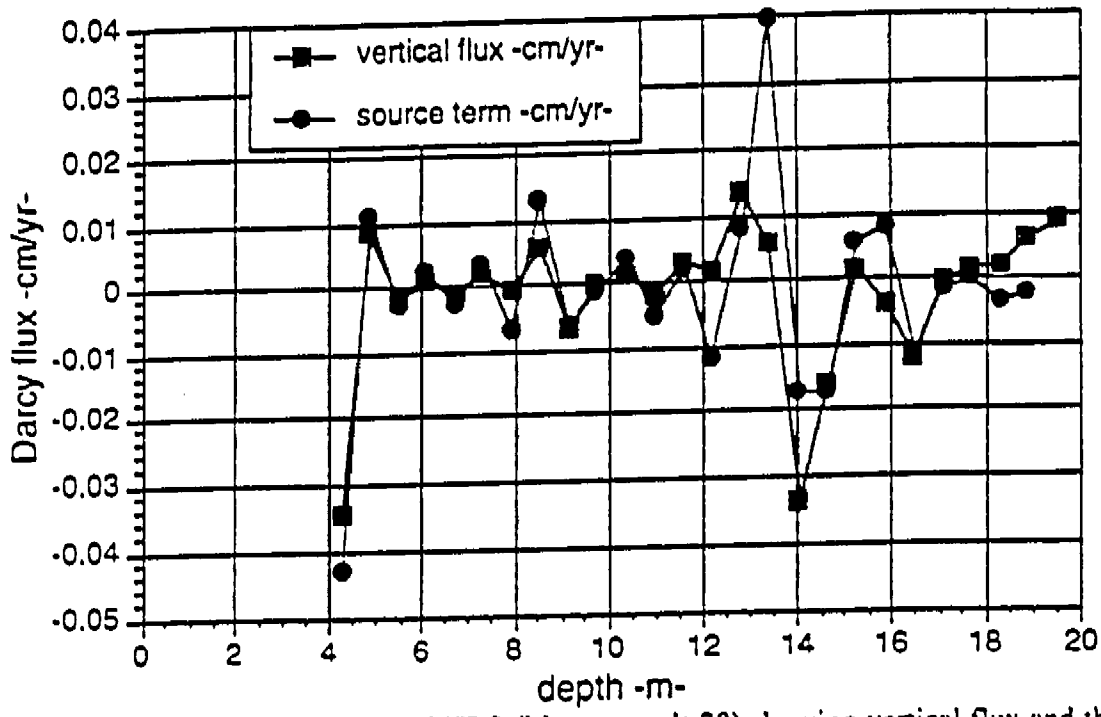

Fig. 8 Vertical profiles for hole NPH-3 (bkg near pit 30) showing vertical flux and the source term expressed as a flux in the limited range of depth from 4m to 20m.

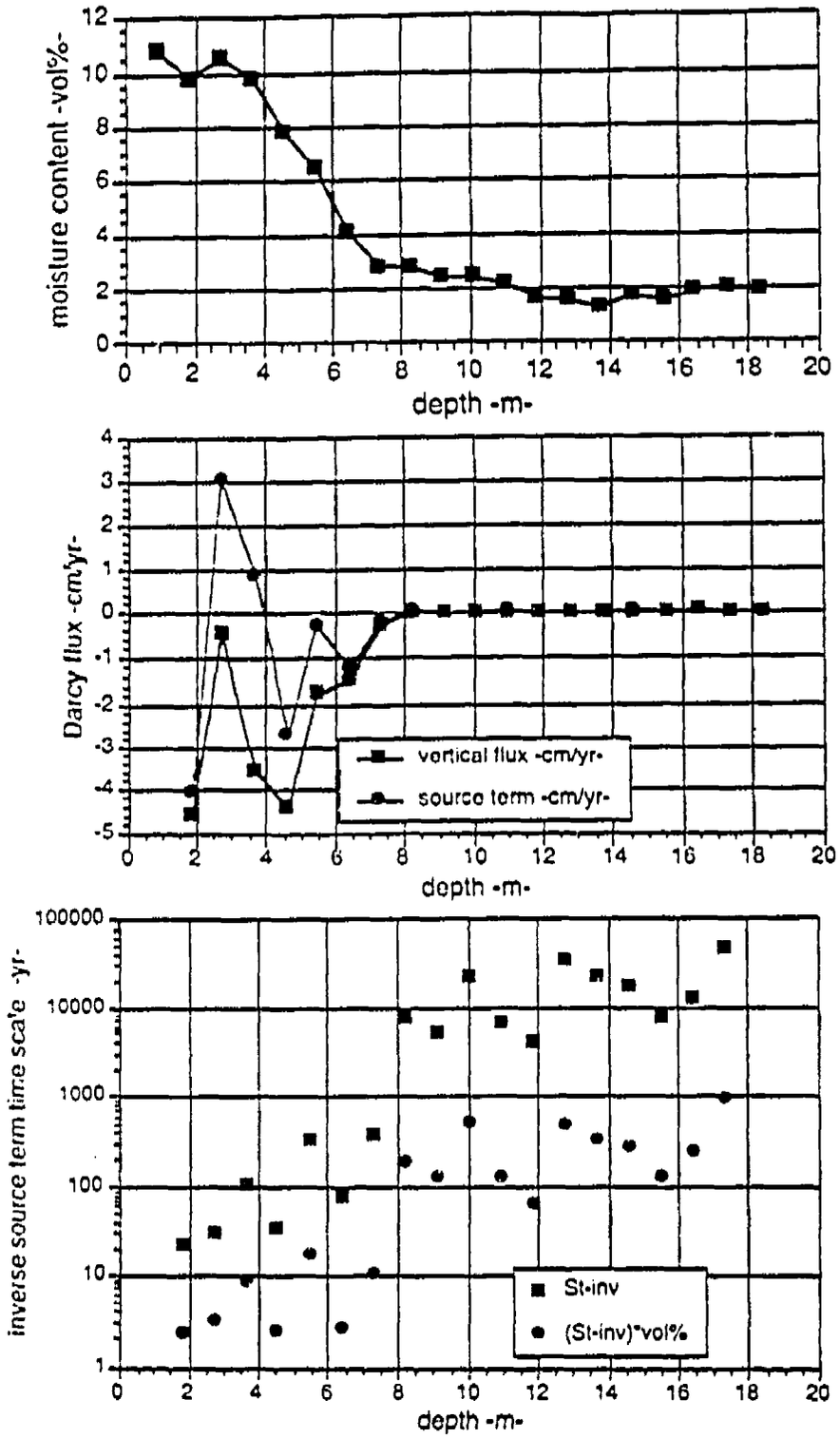

Fig. 9 Vertical profiles for hole NPH-7c (near trenches) showing: A. volumetric moisture content, B. vertical flux and the source term expressed as a flux, and C. source terms expressed as a characteristic response time.

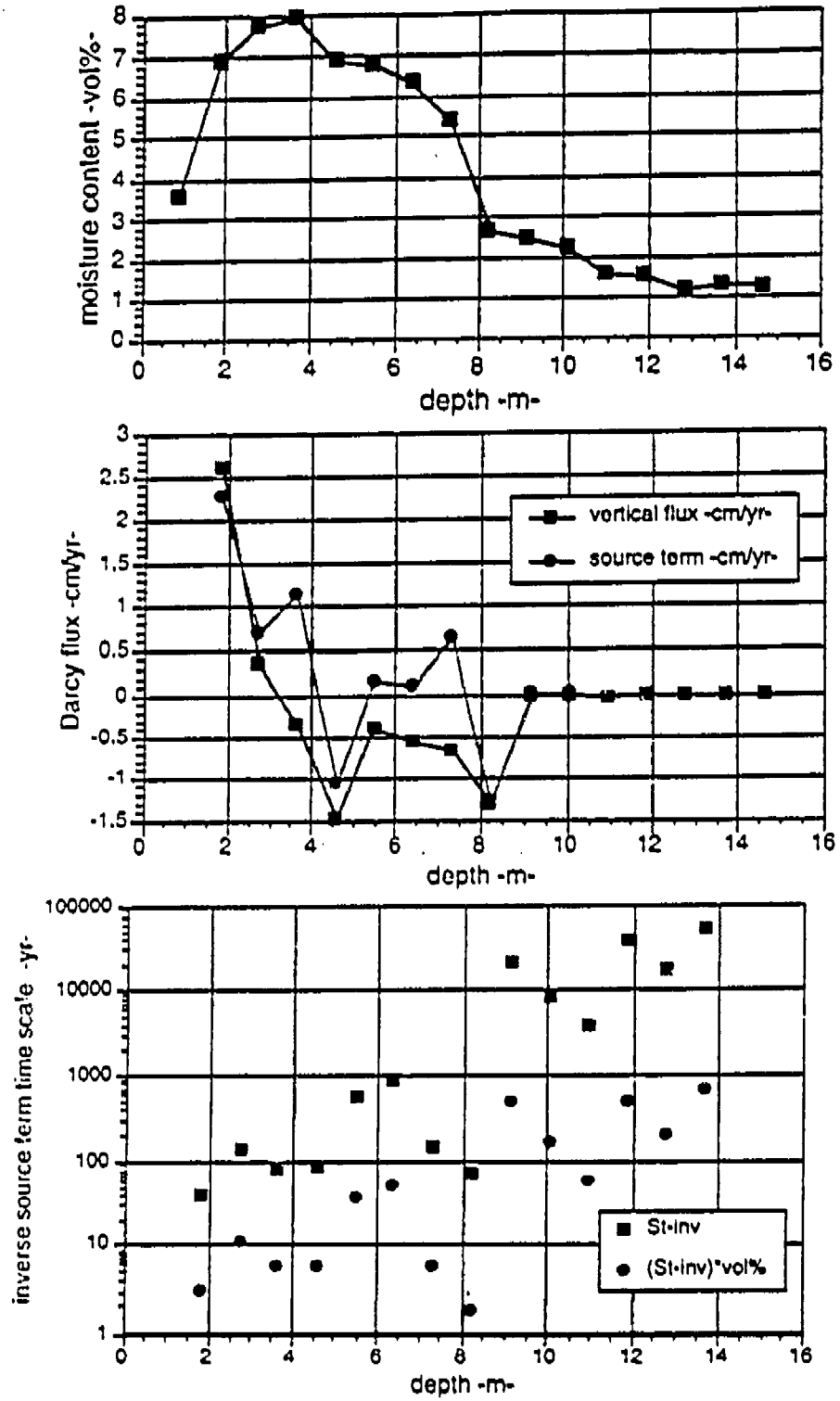

Fig. 10 Vertical profiles for hole **NPH-6 (SE corner of Area G)** showing: A. volumetric moisture content, B. vertical flux and the source term expressed as a flux, and C. source terms expressed as a characteristic response time.

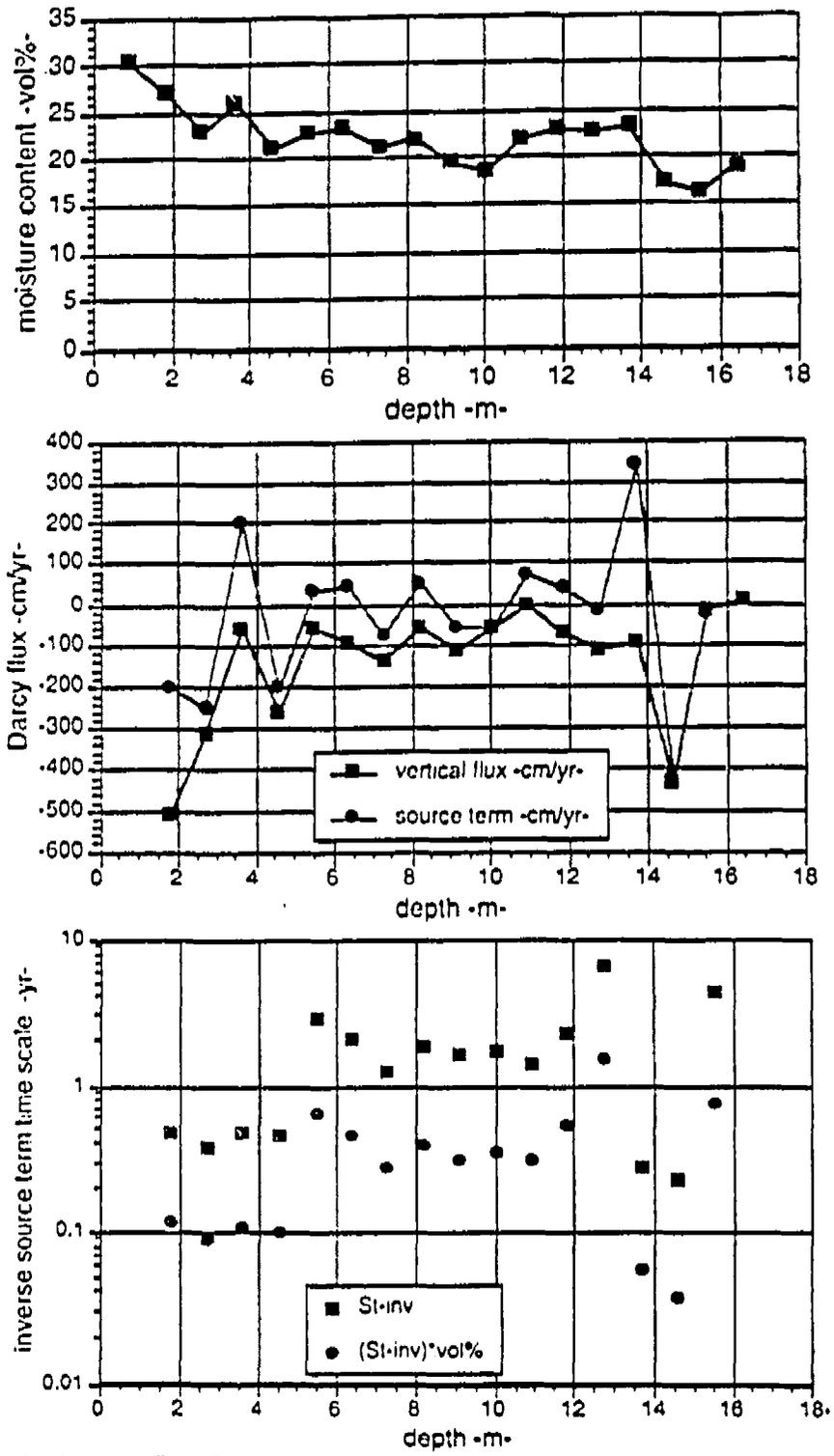

Fig. 11 Vertical profiles for hole **NPH-4** (near engineered drainage) showing: A. volumetric moisture content, B. vertical flux and the source term expressed as a flux, and C. source terms expressed as a characteristic response time.

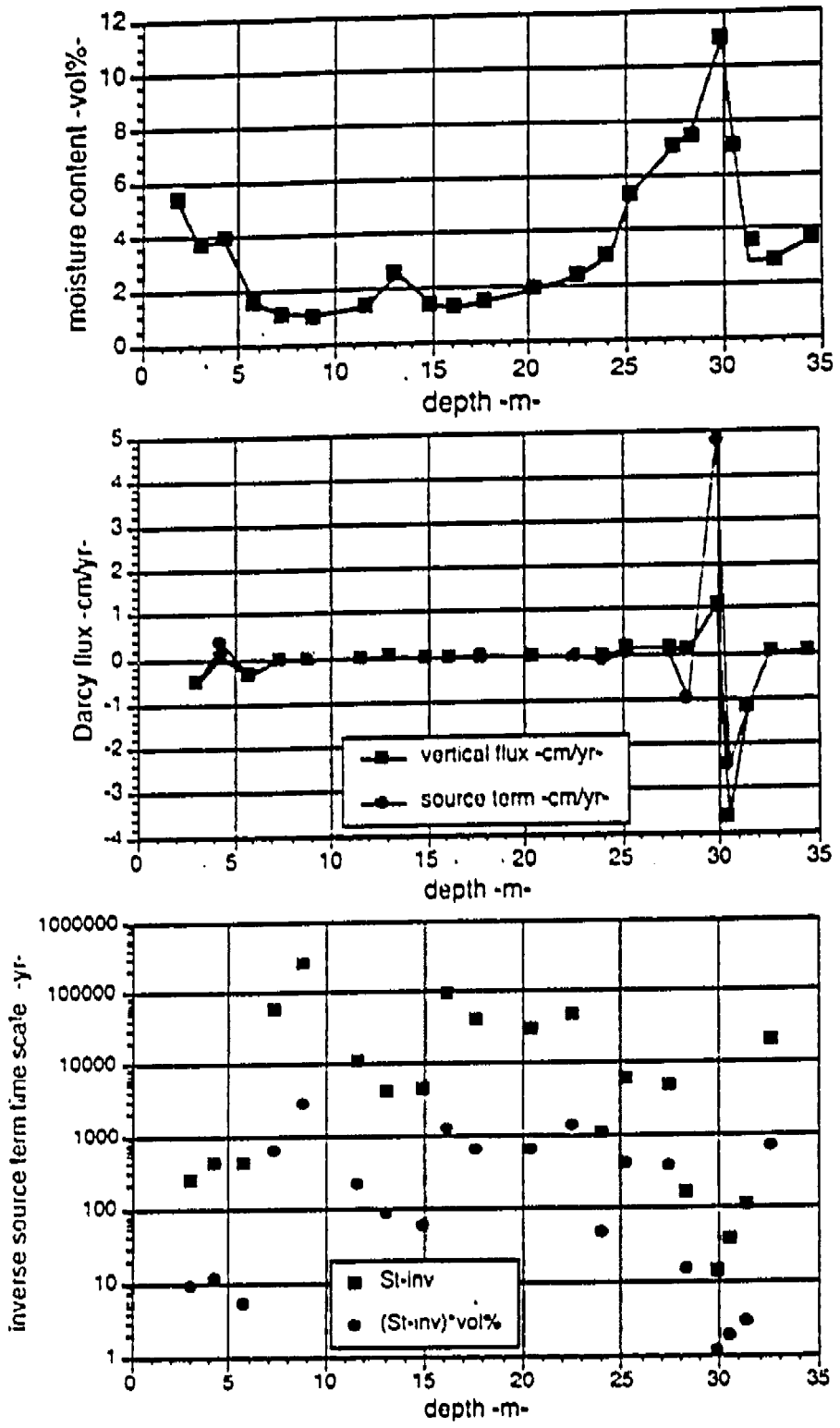

Fig. 12 Vertical profiles for hole **LGM-85-06** showing: A. volumetric moisture content, B. vertical flux and the source term expressed as a flux, and C. source terms expressed as a characteristic response time.

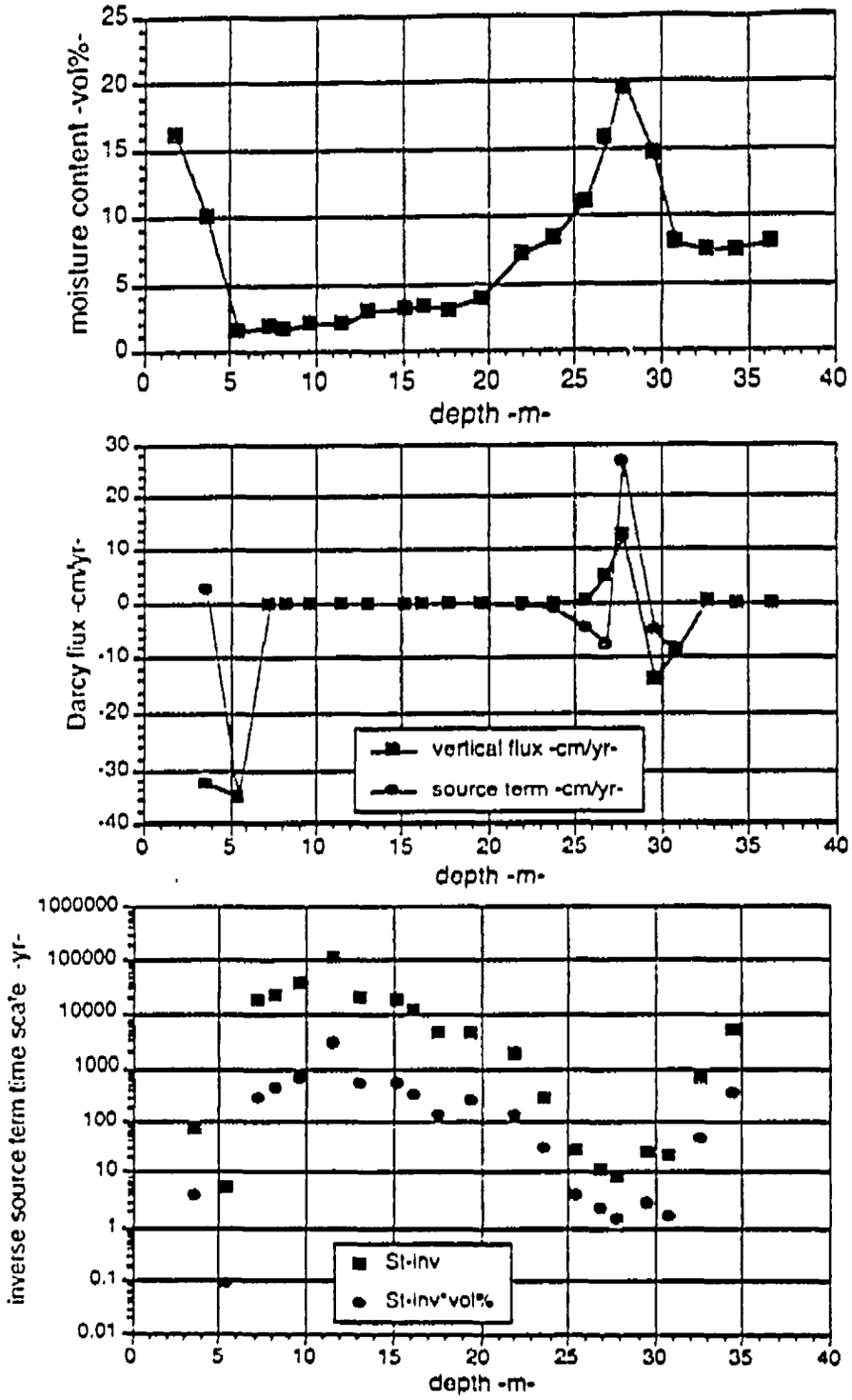

Fig. 13 Vertical profiles for hole LGM-85-11 showing: A. volumetric moisture content, B. vertical flux and the source term expressed as a flux, and C. source terms expressed as a characteristic response time.

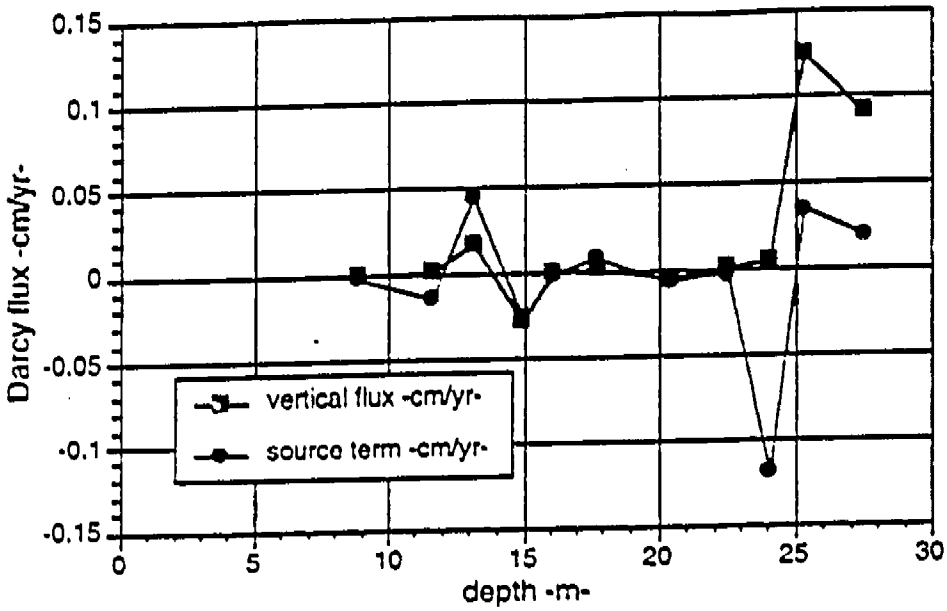

Fig. 14A Profiles for hole **LGM-85-06** showing vertical flux and the source term expressed as a flux in the 'low flux region' for the vertical range from 8m to 22m depth.

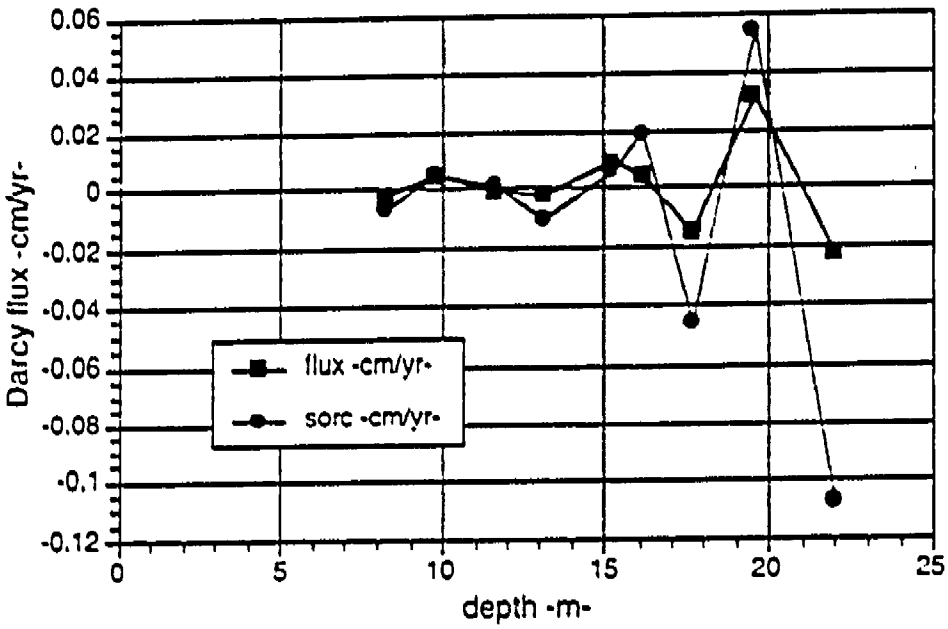

Fig. 14B Profiles for hole **LGM-85-11** showing vertical flux and the source term expressed as a flux in the 'low flux region' for the vertical range from 8m to 22m depth.

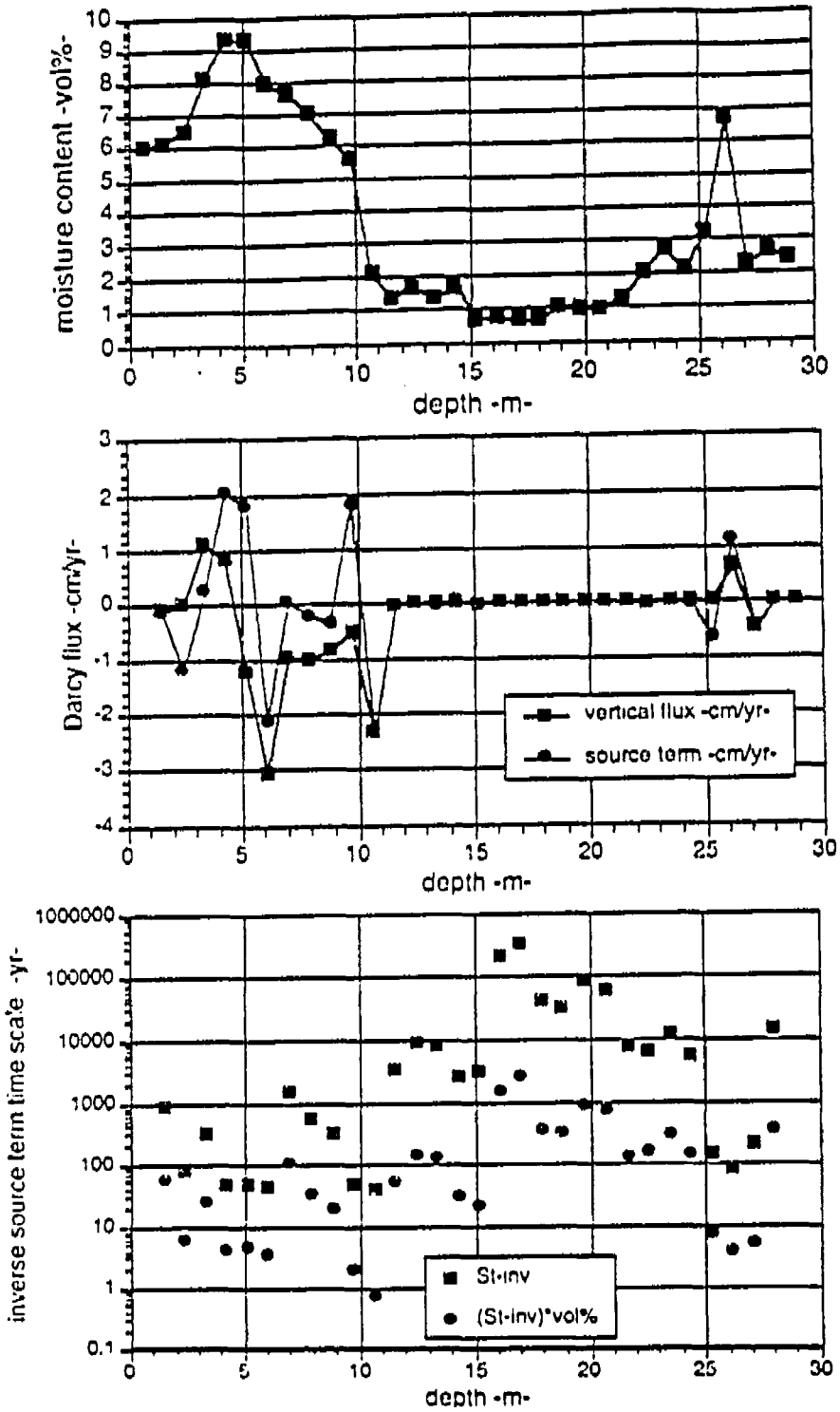

Fig. 15 Vertical profiles for hole NPH-8 (near tritium shafts) showing: A. volumetric moisture content, B. vertical flux and the source term expressed as a flux, and C. source terms expressed as a characteristic response time.

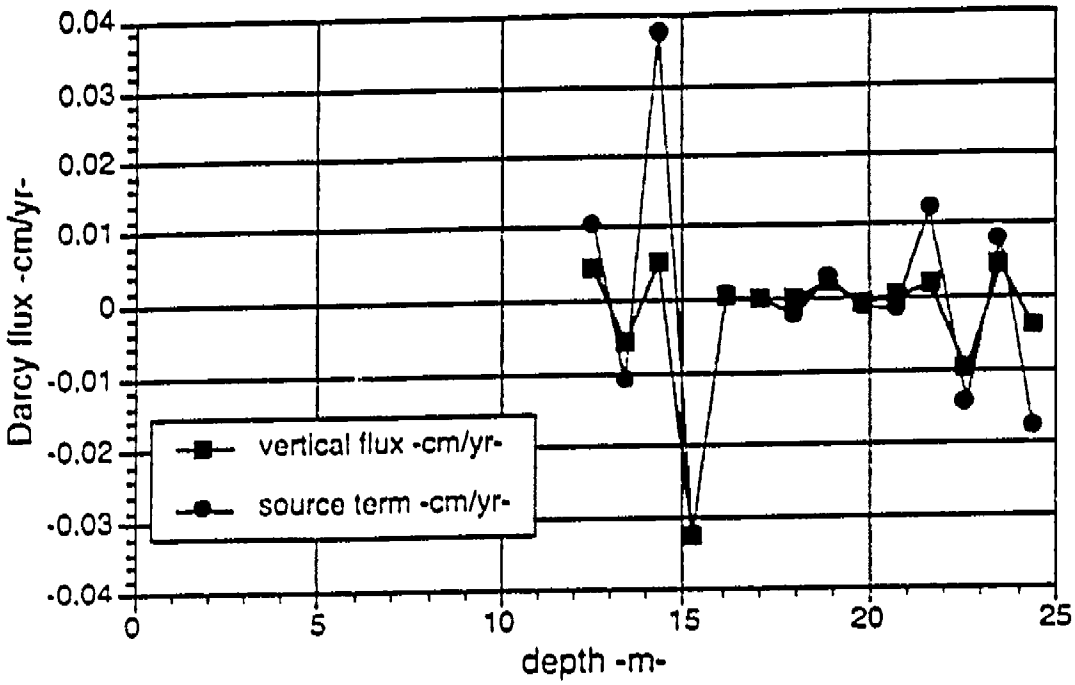

Fig. 16 Vertical profiles for hole **NPH-8 (near tritium shafts)** showing: A. volumetric moisture content, B. vertical flux and the source term expressed as a flux, and C. source terms expressed as a characteristic response time.

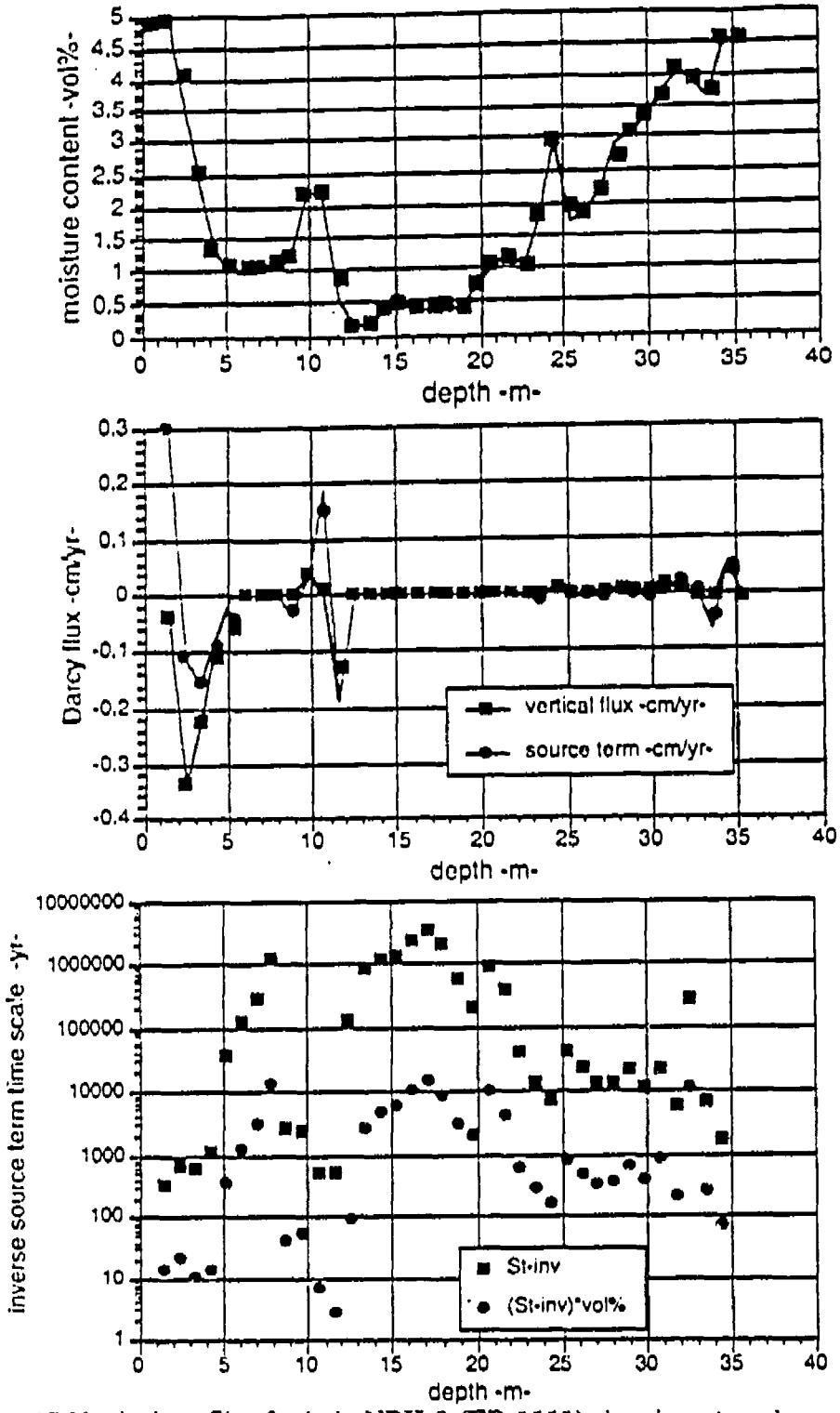

Fig. 17 Vertical profiles for hole NPH-9 (ER 1111) showing: A. volumetric moisture content, B. vertical flux and the source term expressed as a flux, and C. source terms expressed as a characteristic response time.

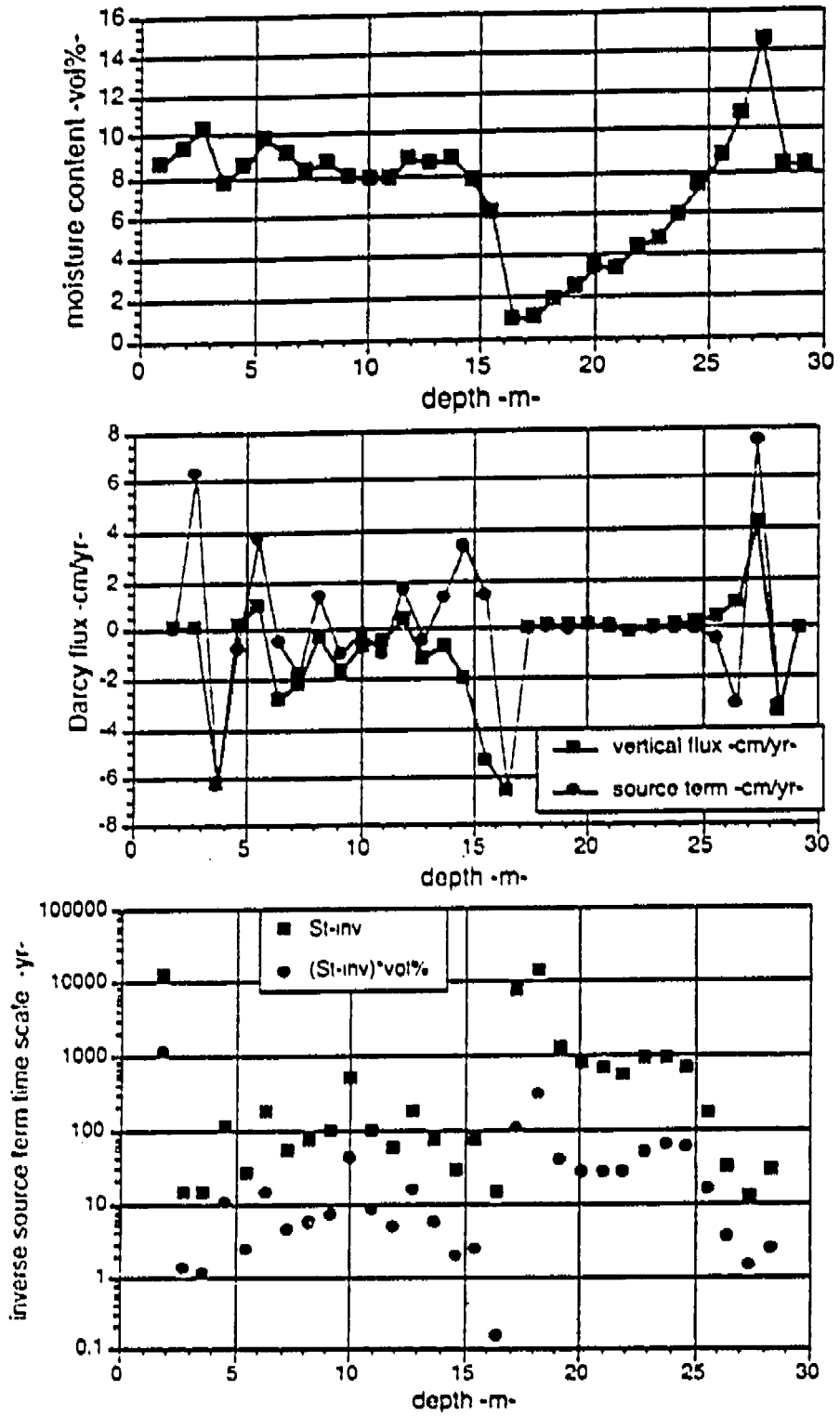

Fig. 18 Vertical profiles for hole NPH-5 (G5) showing: A. volumetric moisture content, B. vertical flux and the source term expressed as a flux, and C. source terms expressed as a characteristic response time.

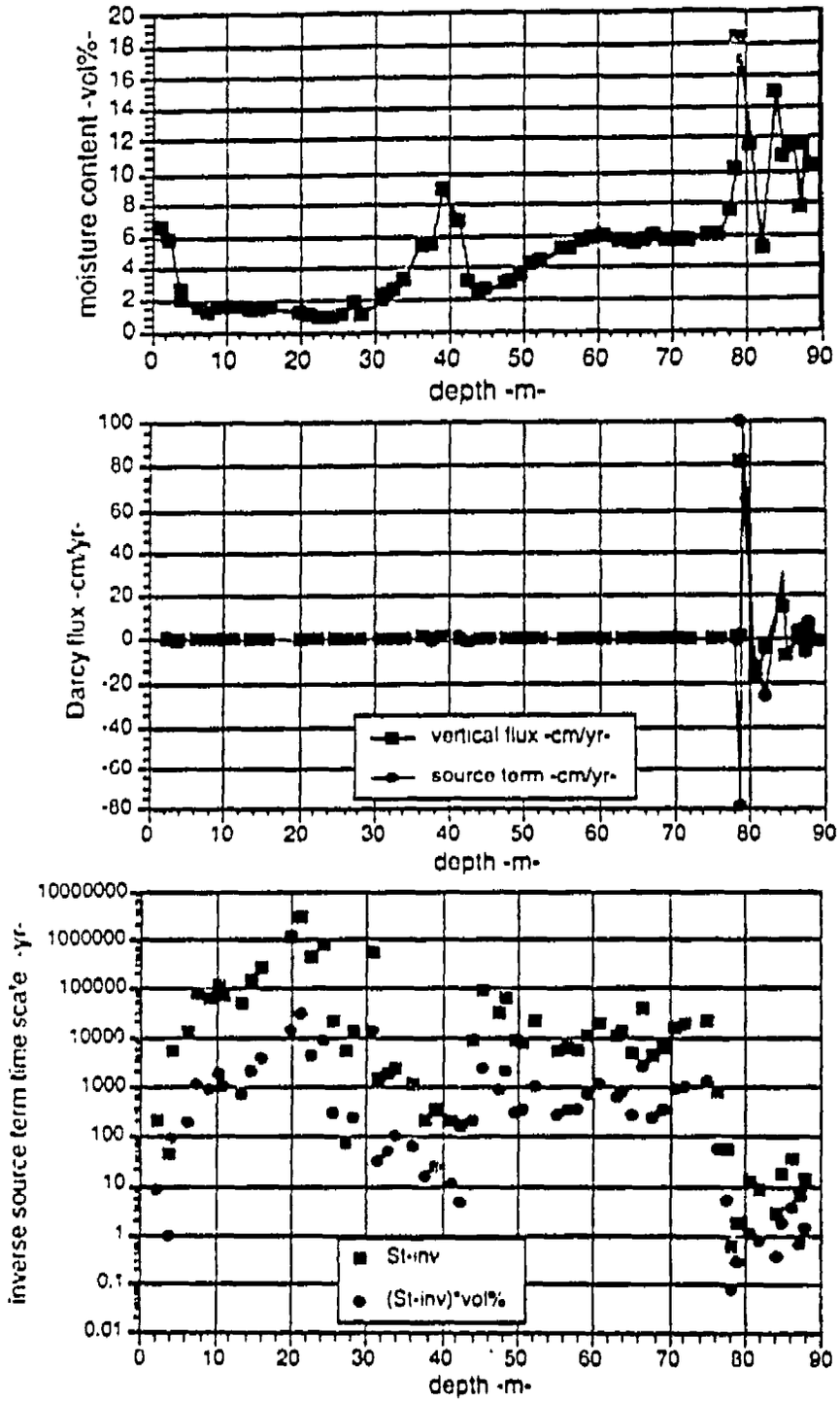

Fig. 19 Vertical profiles for hole 54-1002 (East of Area L) showing: A. volumetric moisture content, B. vertical flux and the source term expressed as a flux, and C. source terms expressed as a characteristic response time.

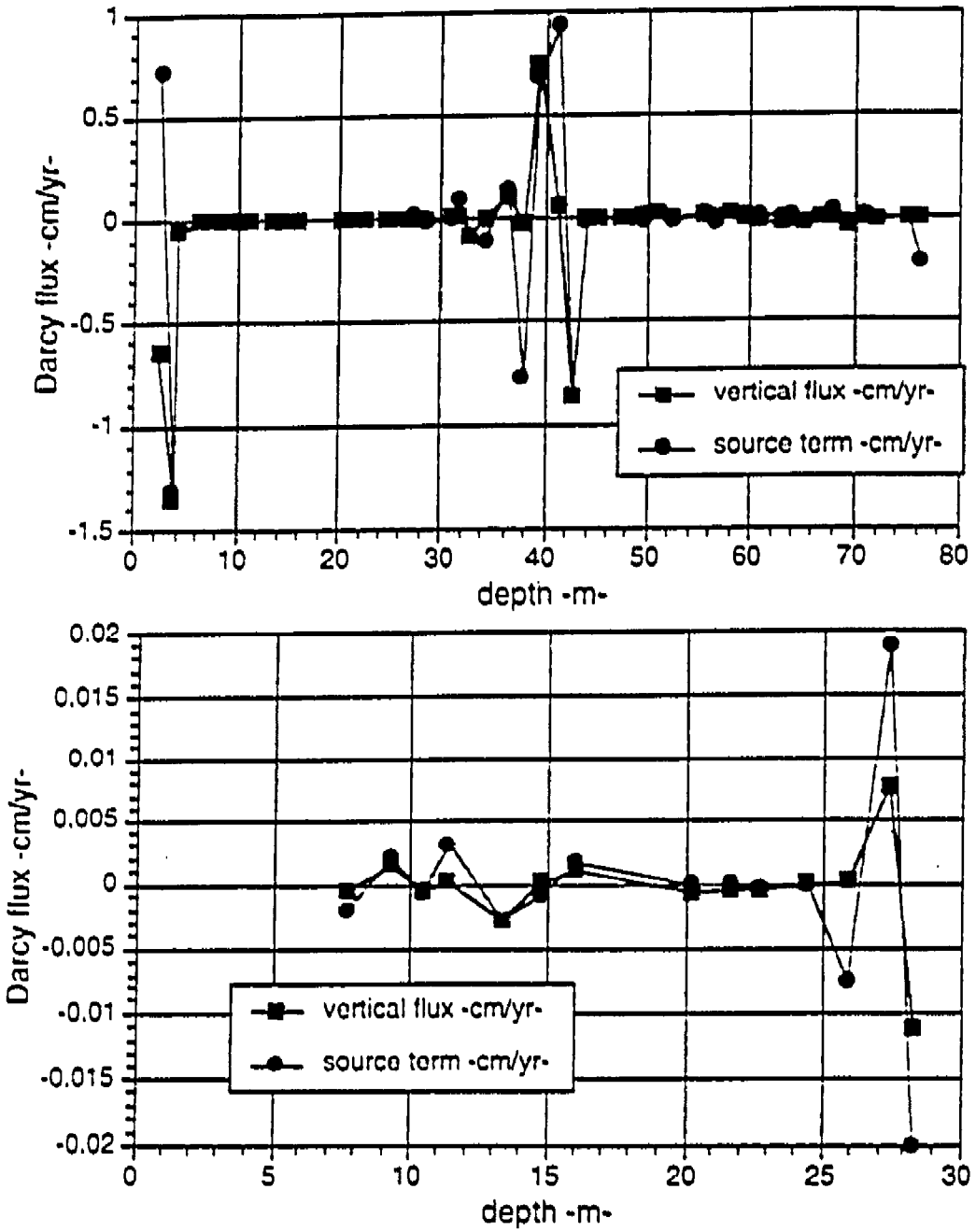

Fig. 20 Vertical profiles for hole 54-1002 (East of Area L) showing vertical flux and the source term expressed as a flux over two restricted intervals of depth.

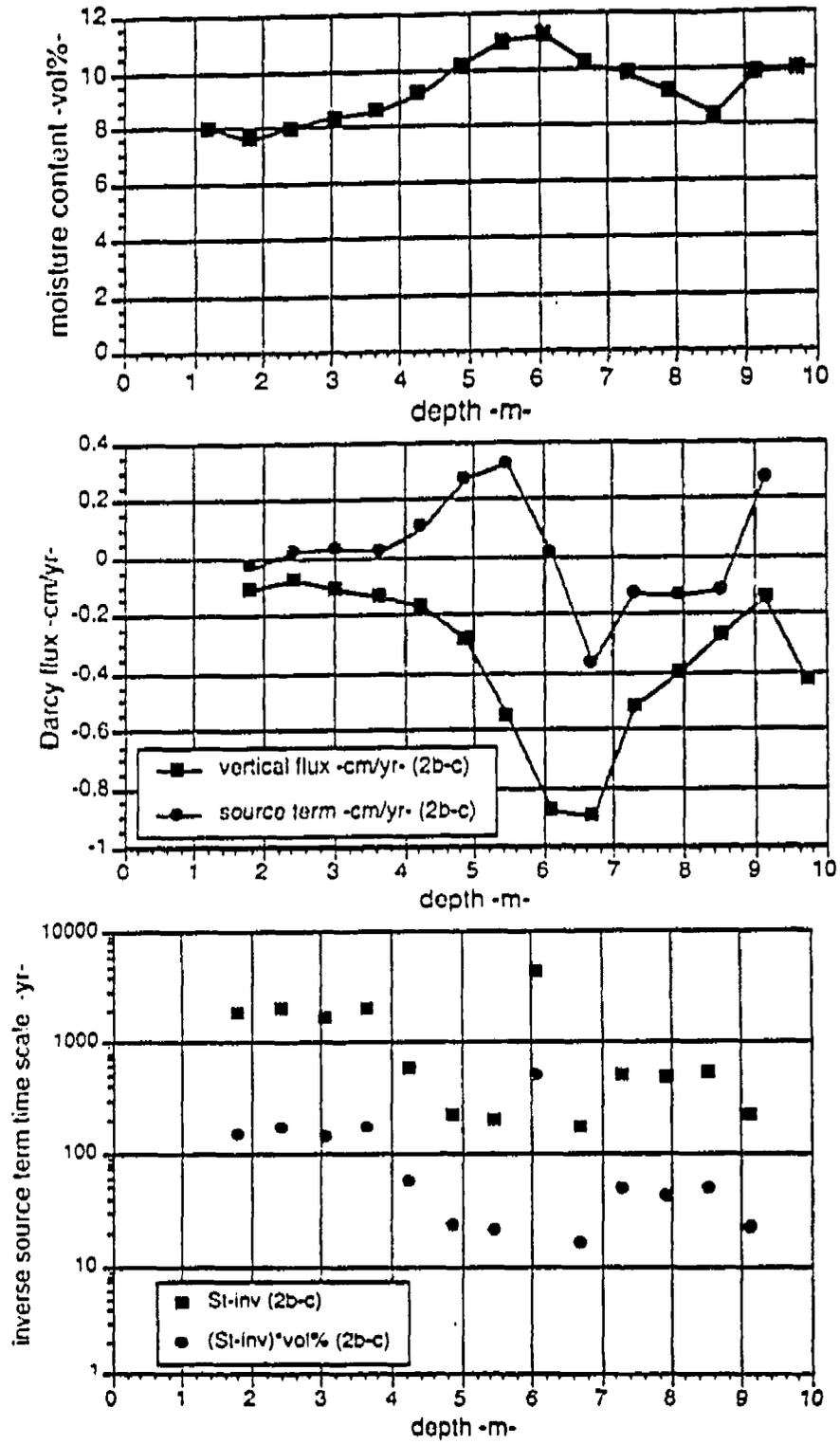

Fig. 21 Vertical profiles for hole NPH-1 (in pit 37) showing: A. volumetric moisture content, B. vertical flux and the source term expressed as a flux, and C. source terms expressed as a characteristic response time.

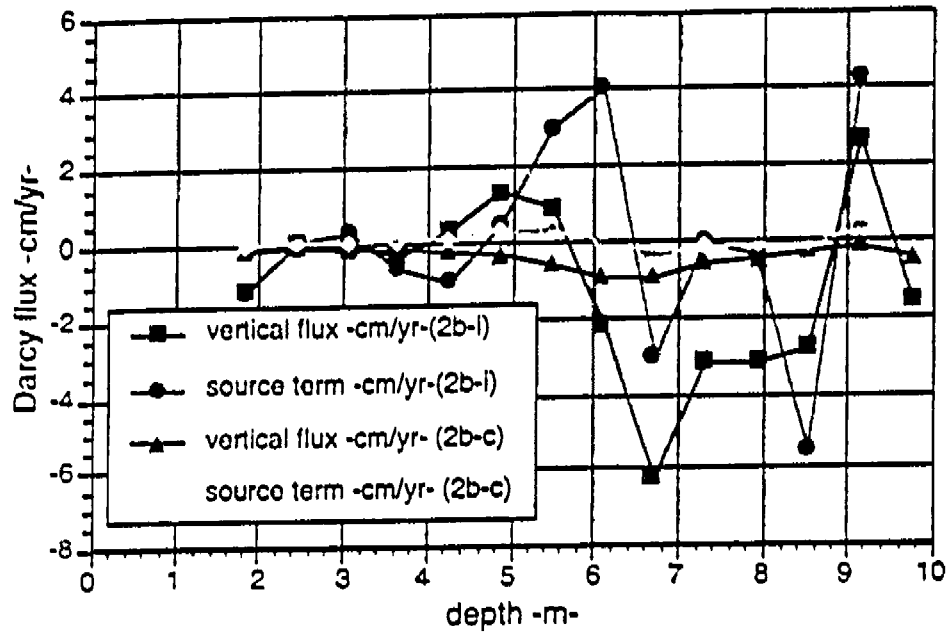

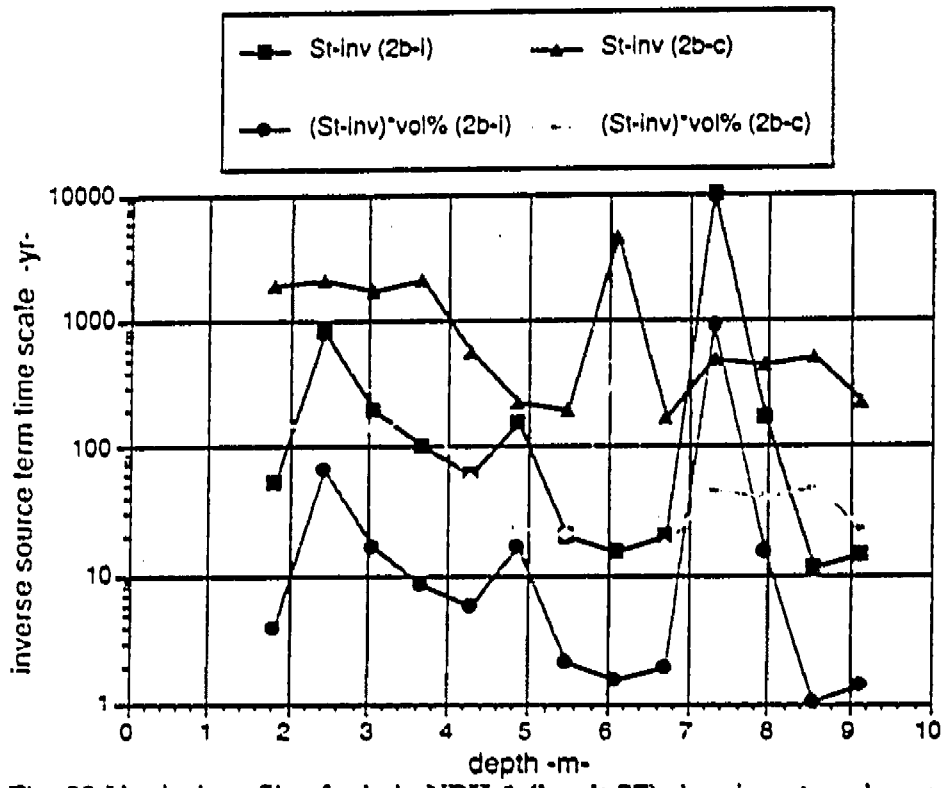

Fig. 22 Vertical profiles for hole NPE-1 (in pit 37) showing: A. volumetric moisture content, B. vertical flux and the source term expressed as a flux, and C. source terms expressed as a characteristic response time. (2b-i = Unit 2b intact, 2b-c = Unit 2b crushed, matric properties from Table 1.)

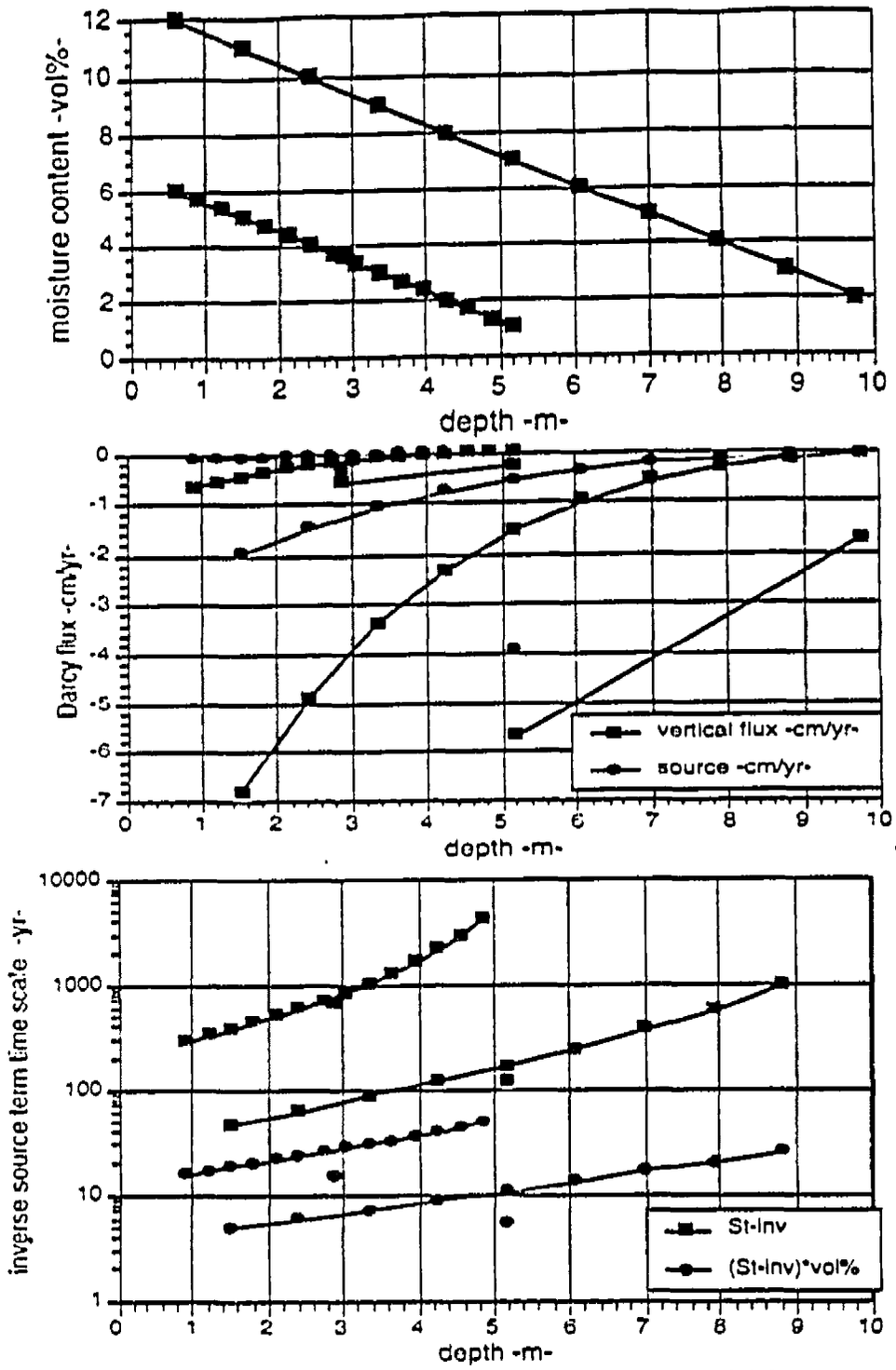

Fig. 23 Two generic linear vertical profiles for moisture content which bound the range typical for the near surface at Area G, showing: A. volumetric moisture content, B. vertical flux and the source term expressed as a flux, and C. source terms expressed as a characteristic response time.

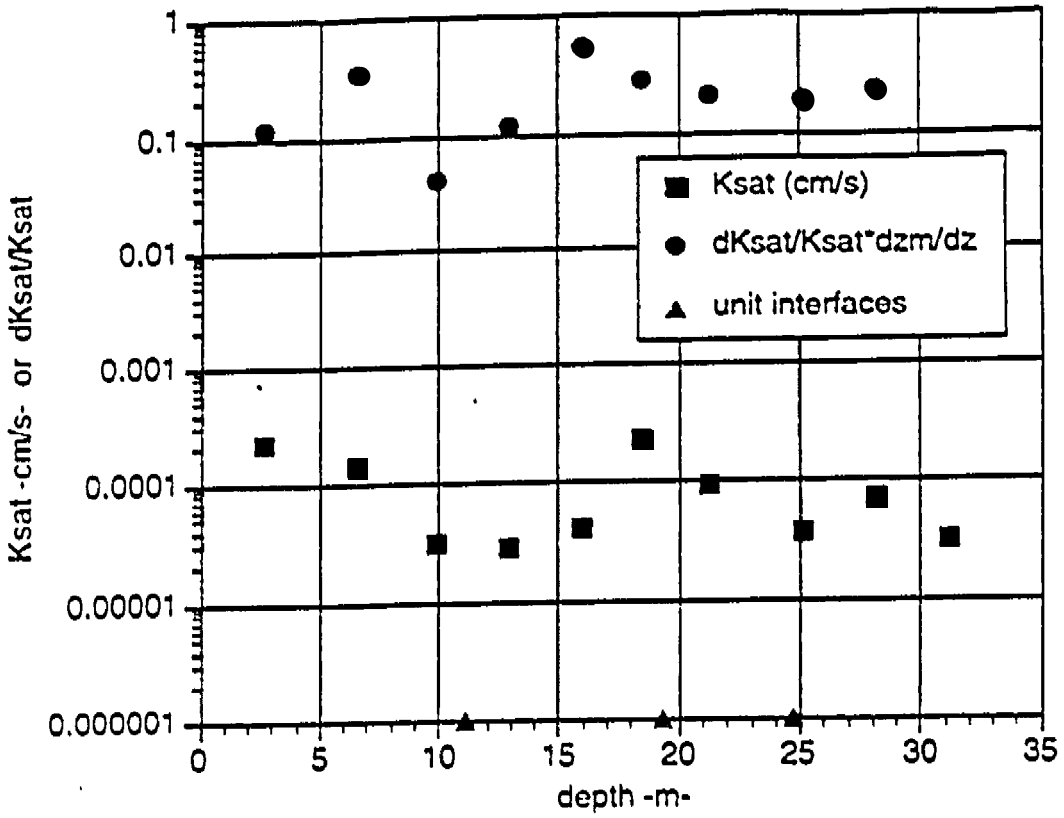

Fig.24 Variation with depth in hole NPH-5 (G-5) of the parameter, *Ksat* (data from Ref.[17]), and a measure of its error (*dKsat/Ksat*dzm/dz*) as described in the text.

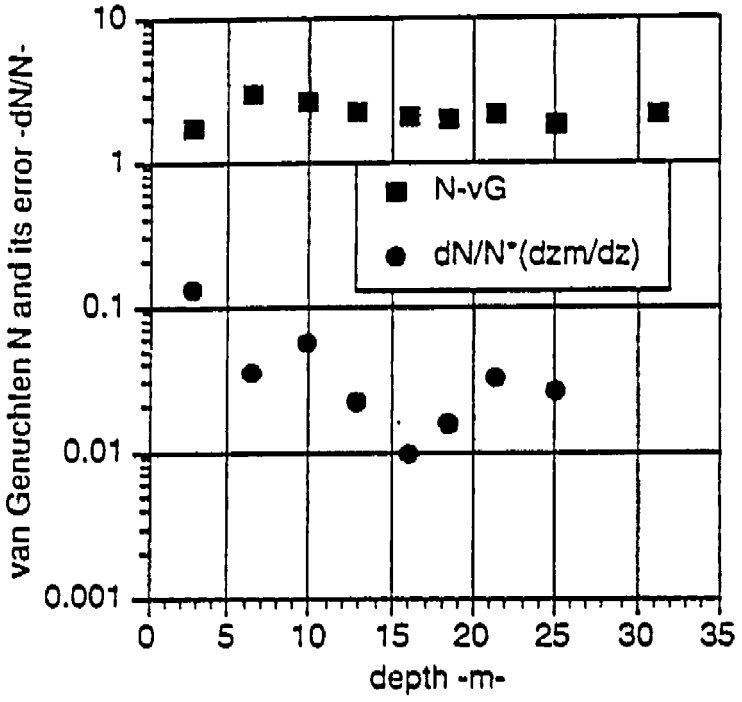

Fig.25 Variation with depth in hole NPH-5 (G-5) of the van Genuchten exponent parameter, *N* (data from Ref.[13]), and a measure of its error (*dN/N*dzm/dz*) as described in the text.

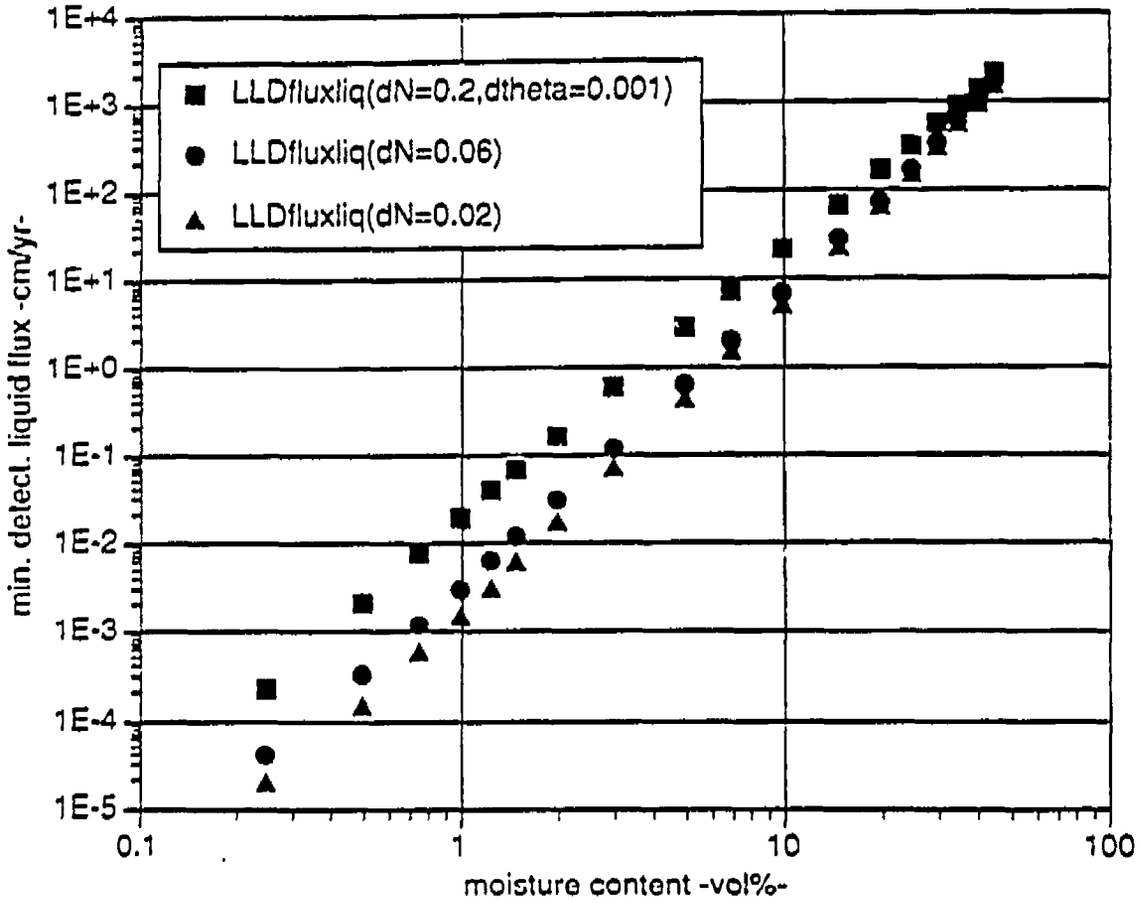

Fig.26 Flux uncertainty or minimum detectable liquid phase flux in Unit 2b from the flux analysis for three values of uncertainty in the van Genuchten exponent, dN = 0.2, 0.06, and 0.02. The best estimate for the present study conditions is dN = 0.06.

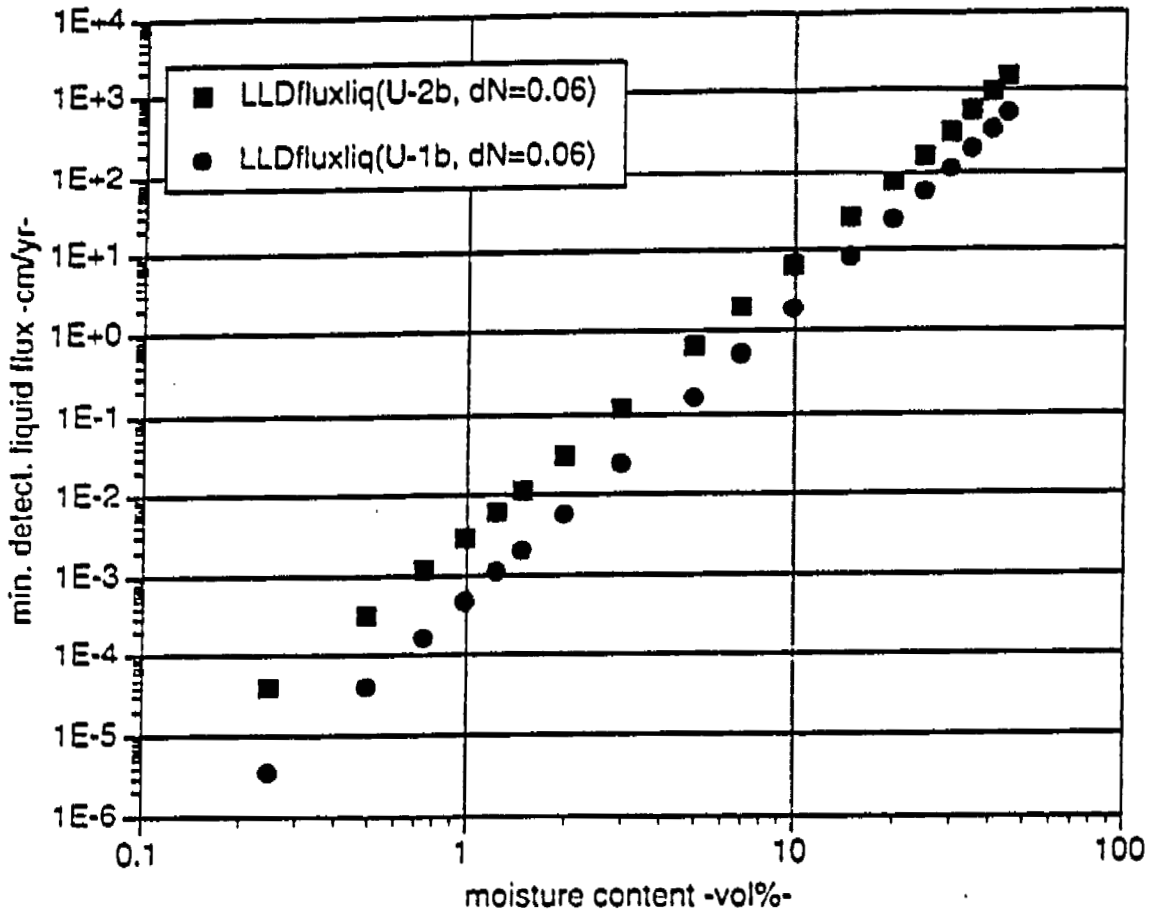

Fig.27 Flux uncertainty or minimum detectable liquid phase flux compared in Unit 2b and in Unit 1b for the best estimate of the uncertainty in the van Genuchten exponent, dN = 0.06, under the present study conditions.

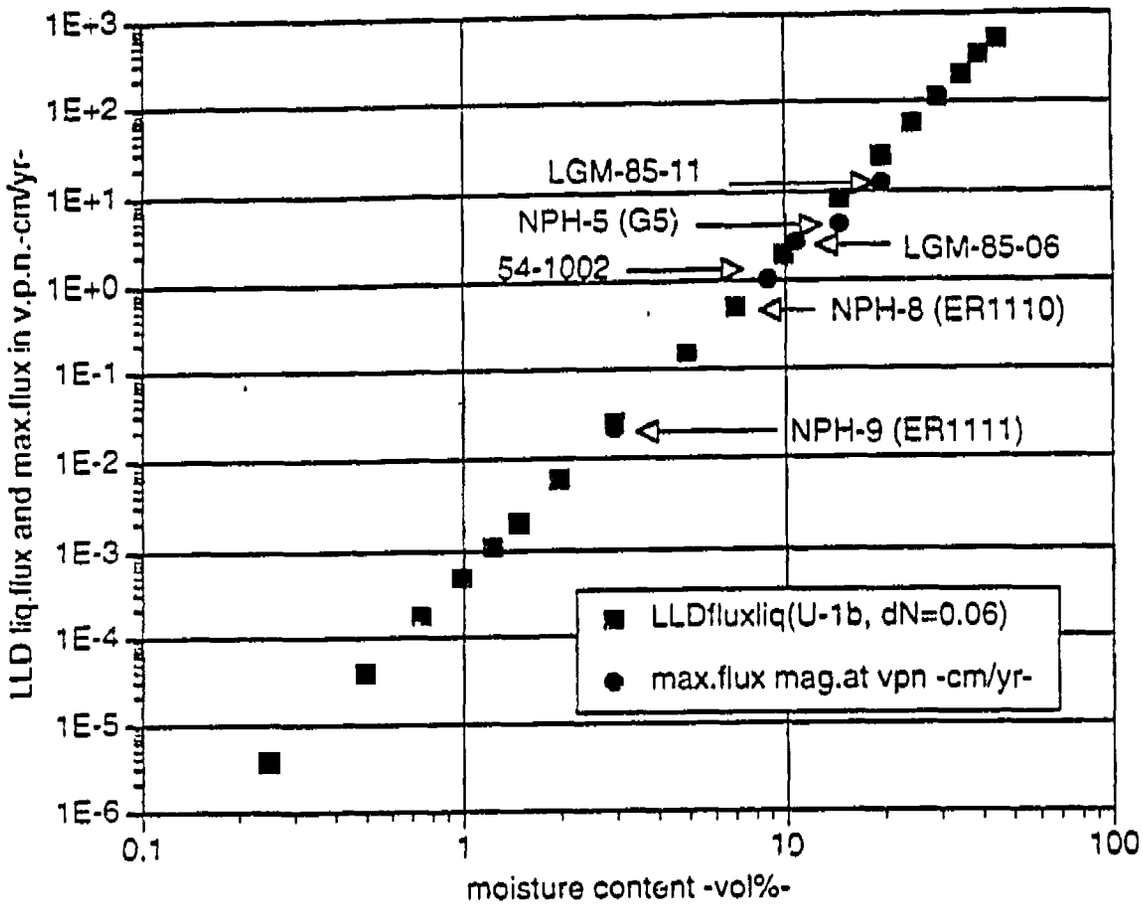

Fig.28 The maximum magnitude of the apparent flux resulting from this analysis at the vapor phase notch in 6 boreholes, compared to the minimum detectable liquid phase flux in Unit 1b for the best estimate of the uncertainty in the van Genuchten exponent, dN =0.06.

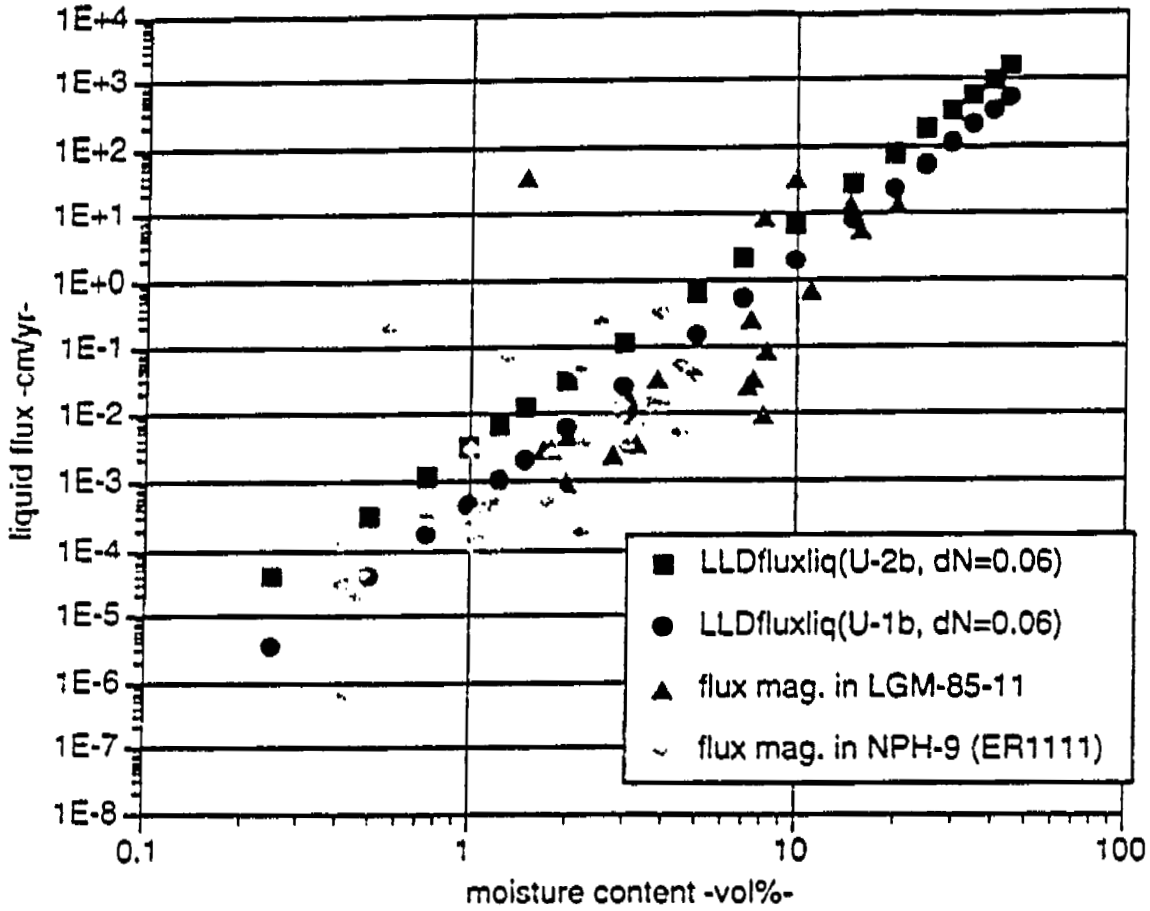

Fig.29 The magnitude of the apparent flux resulting from this analysis at all depths in 2 boreholes (where LGM-85-11 is an 'extreme moist case' and NPH-9 (ER1111) is an 'extreme dry case'), compared to the minimum detectable liquid phase flux in Unit 2b and in Unit 1b for the best estimate of the uncertainty in the van Genuchten exponent, dN =0.06.

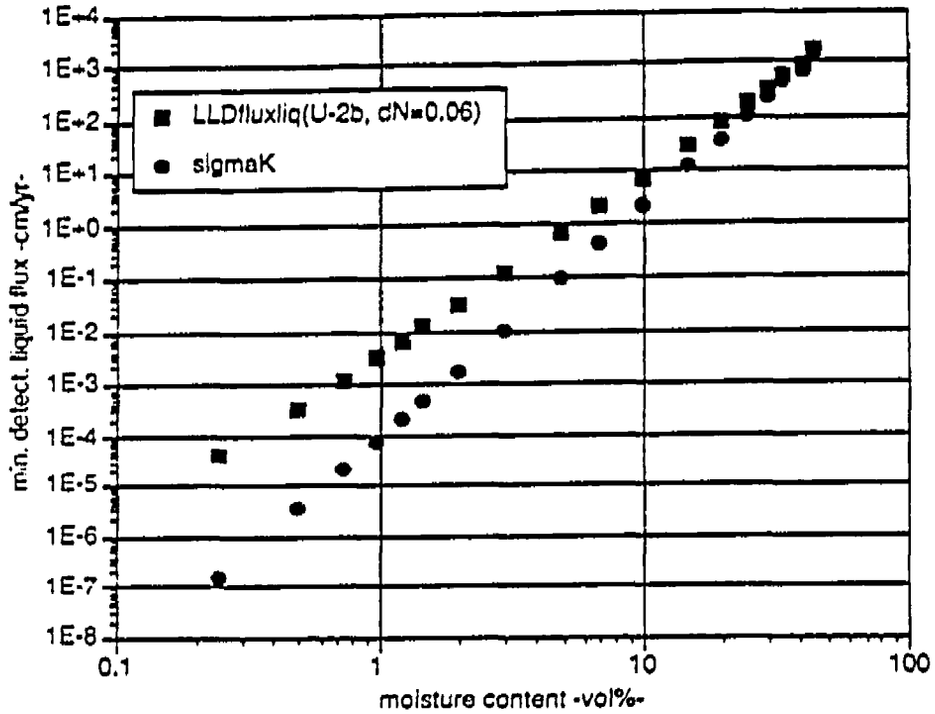

Fig.30 Flux uncertainty or minimum detectable liquid phase flux in Unit 2b compared to the uncertainty.. in unsaturated hydraulic conductivity (sigmaK = σ_K) for the best estimate of the uncertainty in the van Genuchten exponent, dN = σ_{nvg} = 0.06.

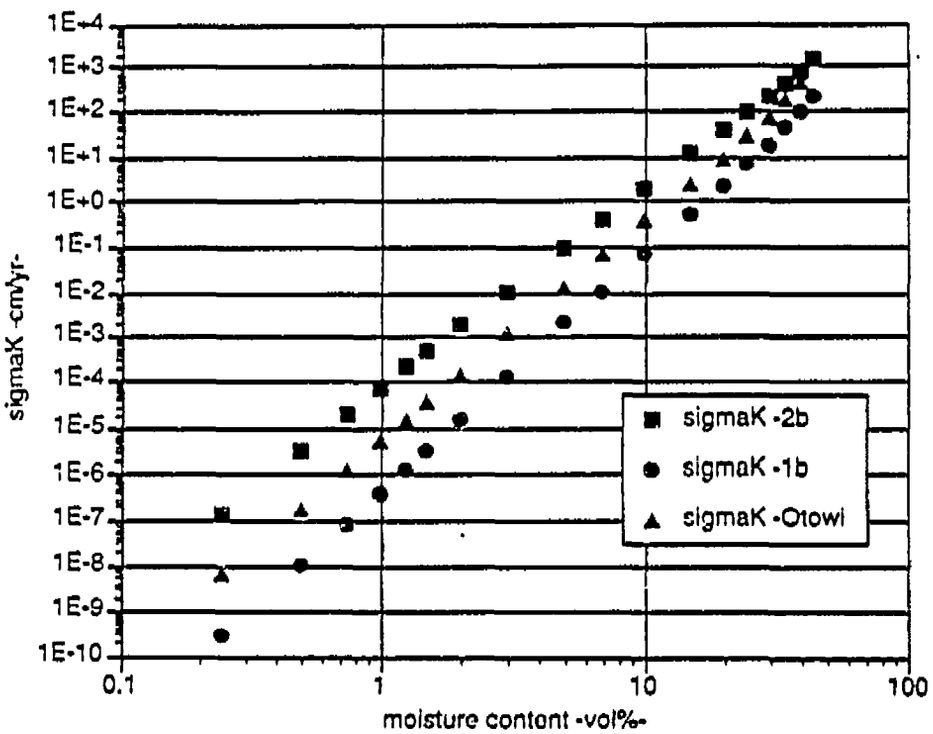

Fig.31 Uncertainty in unsaturated hydraulic conductivity (sigmaK) in each of three stratigraphic units (2b, 1b, Otowi) for the best estimate of the uncertainty in the van Genuchten exponent, dN = 0.06.

LAUR-96-4716 December 1996

Batch Sorption Results for Americium, Neptunium, Plutonium, Technetium, and Uranium Transport Through the Bandelier Tuff, Los Alamos, New Mexico

By

Patrick Longmire, Charles R. Cotter, Ines R. Triay, Jason J. Kitten, Colin Hall, Jessica Bentley, Diana J. Hollis, and Andrew I. Adams

Los Alamos

Los Alamos National Laboratory is operated by the University of California for the United States Department of Energy under contract W-7405-ENG-36.

BATCH SORPTION RESULTS FOR AMERICIUM, NEPTUNIUM, PLUTONIUM, TECHNETIUM, AND URANIUM TRANSPORT THROUGH THE BANDELIER TUFF, LOS ALAMOS, NEW MEXICO

by

Patrick Longmire, Charles R. Cotter, Ines R. Triay, Jason J. Kitten, Colin Hall, Jessica Bentley, Diana J. Hollis, and Andrew I. Adams

ABSTRACT

Quantifying the migration of radionuclides through the Bandelier Tuff is essential in conducting a performance assessment for Material Disposal Area-G, Technical Area-54, Los Alamos National Laboratory. The sorption of radionuclides on Bandelier Tuff is controlled by (1) the surface area and mineralogy of the tuff and (2) by the water chemistry of the solution in contact with the tuff. The dominant adsorbents within the Bandelier Tuff are inferred to include glass, hematite, smectite, amorphous $Fe(OH)_3$, kaolinite, and possibly calcite. Water Canyon Gallery (WCG) groundwater, discharging from the Bandelier Tuff, was used in the batch sorption experiments. This groundwater is relatively oxidizing and is characterized by a calcium-sodium-bicarbonate ionic composition with a TDS content less than 130 mg/L. The distribution coefficients for radionuclides measured on the Bandelier Tuff, at a pH value of 7.3, decrease in the following order: Am(III) >> Pu(V) > U(VI) >> Np(V) > Tc(VII). The distribution coefficients for Tc(VII) are all negative and therefore, they are assumed to be zero. Vadose-zone pore water was extracted from the Bandelier Tuff using an Unsaturated/Saturated Flow Apparatus. The pore water is characterized by a sodium-carbonate-bicarbonate solution with a TDS content of greater than 1300 mg/L. The pH values of the pore-water samples range from 9.2 to 9.8 and the solutions are oversaturated with respect to calcite. The distribution coefficients for radionuclides measured on the tuff samples using the synthetic pore water, at a pH value of 9.8, decrease in the following order: Am(III) >> Pu(V) > U(VI) > Np(V) >Tc(VII). The distribution coefficients for Am(III) and Np(V) using synthetic pore water are higher than the distribution coefficients for these two radionuclides using WCG groundwater. Based on MINTEQA2 simulations, the dominant aqueous complexes of Am(III) and Np(V) are predicted to include $Am(CO_3)_3^{3-}$ and $NpO_2(CO_3)_3^{5-}$, respectively. The synthetic pore water is predicted to be undersaturated with respect to $Am(OH)_3(s)$, $Am(OH)_3(am)$, $AmOHCO_3$, $NpO_2OH(am)$, $NpO_2OH(aged)$, $NaNpO_3 \cdot 3.5H_2O$, and $NaNpCO_3$. Enhanced sorption of Am(III) and Np(V) carbonato complexes on calcite is possible through surface exchange with carbonate and bicarbonate functional groups present on the calcite surface.

Introduction

Quantifying the migration of radionuclides through the Bandelier Tuff is essential in conducting a performance assessment (PA) of material disposal area (MDA)-G, technical area (TA)-54, Los Alamos National Laboratory. Adsorbates or radionuclides of interest at MDA-G include americium (Am), neptunium (Np), plutonium (Pu), technetium (Tc), and uranium (U). Neptunium, Tc, and U form soluble anionic species under oxidizing and near neutral pH conditions (Brookins, 1988; Brookins, 1984). These three elements are characterized by limited adsorption onto mineral surfaces in volcanic tuff (Triay et al., 1996; Thomas, 1987). The high solubilities of Np, Tc, and U make these three radionuclides a top priority in the transport investigations conducted as part of the PA for MDA-G.

The purpose of this report is to provide the results of batch-sorption experiments of Am, Np, Pu, Tc, and U performed on the Bandelier Tuff. Results obtained from these experiments are required for solute-transport calculations as part of the PA for MDA-G. These sorption data serve as input to the mass-heat transfer model FEHM (Finite Element Heat and Mass Transfer) (Zyvoloski et al., 1988).

The objectives of this investigation are:

1. identify the minerals and solid phases (silica glass, silicates, hematite, amorphous $Fe(OH)_3$) within the Bandelier Tuff;

2. characterize groundwater and pore-water chemistry most important to the sorption behavior of Am, Np, Pu, Tc, and U on Bandelier Tuff;

3. perform batch-sorption experiments with Bandelier Tuff (Tshirege Member) samples; and

4. determine statistical parameters of the distribution coefficients (K_d) for Am, Np, Pu, Tc, and U used in performance assessment calculations for MDA-G.

A detailed discussion on water-rock processes relevant to MDA-G is presented by Krier et al. (1995). Geochemical parameters, such as pH, Eh, solution composition, mineral solubility, and presence of competing and complexing ligands, have the greatest impact on the sorption behavior of the contaminants of concern found in the pits at MDA-G. The release of contaminants from the pits in MDA-G will be controlled by hydraulic flux, pore-water chemistry, mineral (radionuclide) solubility, and sorption behavior of the Bandelier Tuff and other underlying geological strata.

EXPERIMENTAL PROCEDURES

Groundwater

Groundwater from the Water Canyon Gallery (WCG), flowing from uppermost unit 4 in the Tshirege Member of the Bandelier Tuff, was used for the batch-sorption experiments. This solution is considered to be representative of groundwater flowing through the Bandelier Tuff. The most recent WCG groundwater sample was collected on February 1, 1996 via a pumping-distribution system at TA-16. Approximately 55 gallons of WCG groundwater were collected at the distribution system. Water Canyon Gallery groundwater was collected following procedures detailed in LANL-CP-CST-DP-99, R0 WCG-1. The measured pH and Eh of the WCG groundwater collected at the distribution point were 7.34 and +181 mV, respectively. The pH of the WCG groundwater is controlled by dissolved CO_2 gas under open conditions with the atmosphere. Analytical techniques for analyzing the groundwater include inductively coupled plasma emission spectroscopy (ICPES) (major cations and metals), ion chromatography (IC) (anions), carbonate alkalinity titration (CAT), cold vapor atomic absorption spectroscopy (CVAA) (mercury), and electrothermo vapor atomic absorption spectroscopy (ETVAA) (arsenic and selenium). Groundwater samples were analyzed at the EES-1 Laboratory, LANL and at the Department of Earth and Planetary Sciences, University of New Mexico using EPA-SW846 or equivalent methods. Results of chemical analyses of the WCG groundwater are provided in Appendix A.

The WCG groundwater collected in February, 1996 was filtered through 0.05-*um* filter prior to the chemical analyses and batch-sorption experiments. Prior to chemical analyses, the WCG groundwater samples collected by LANL staff were filtered through a 0.45 *um* membrane in the field. Filtration of the WCG groundwater removes any potential colloids that may bias experimental results. Groundwater analytical data from Yucca Mountain indicate that filtration does not cause changes in solute chemistry, which potentially may influence speciation of the adsorbates (radionuclides) (Triay et al., 1996).

Bandelier Tuff Samples and Mineralogy

The Bandelier Tuff samples used for batch-sorption experiments were obtained from the core hole 1107 drilled at TA-54, MDA-G, Los Alamos National Laboratory. Core samples were taken from split spoon, hollow-stem augers. Core samples selected for sorption experiments were collected from the Tshirege Member of the Bandelier Tuff from the following seven depth intervals (below ground surface, bgs): 10.8-12.0 ft; 65.0-66.0 ft, 74.0-75.0 ft, 79.1-79.7 ft, 79.9-80.0 ft, 91.0-91.5 ft, and 108.0-109.5 ft. The core sample collected from the

depth interval 10.8-12.0 ft is from the devitrified (crystal rich) unit 2. The core samples collected from 65.0 ft through 80.0 ft are from unit 1vu (vitric alteration, undifferentiated). The core samples collected from 91.0 ft through 91.5 ft are from unit 1vc (vitric alteration, collonnade, slightly welded). The core sample collected from 108.0 ft to 109.5 ft is from unit 1g (glass-rich). Geological characterization of the Bandelier Tuff at TA-54 is described in detail by Krier et al. (1995).

The mineralogy of the Bandelier Tuff was determined by x-ray diffraction (XRD) analysis and surface area of the tuff was determined by BET (Brunauer, Emmett, and Teller) analysis. The dry, partially disaggregated Bandelier Tuff samples were passed through a 500 *um* sieve prior to XRD and BET analyses. Crushing of the samples was performed prior to batch-sorption experiments. Details of the crushing and sieving procedures for the samples are given in LANL-CST-DP-63, R4, *Yucca Mountain Project Detailed Procedures*, Los Alamos National Laboratory. Data collected from the Yucca Mountain Project (YMP) indicate that crushing and sieving the tuff samples do not cause significant differences in the mineralogy of the tuff that may influence the sorptive capacity of the samples (Triay et al., 1996). Based on these results, the sorptive capacity of the Bandelier Tuff samples should not be biased by crushing and sieving.

Americium, Neptunium, Plutonium, Technetium, and Uranium Solutions

Acid stock solutions (4 N HNO_3) containing $^{241}Am(III)$, $^{243}Am(III)$, $^{237}Np(V)$, $^{239}Pu(V)$, $^{95m}Tc(VII)$, and $^{233}U(VI)$ were used in the batch-sorption experiments. The solutions were prepared by taking an aliquot of the well-characterized radionuclides and diluting them in the WCG groundwater or synthetic pore water. Radionuclide concentrations in the stock solutions used for the batch-sorption experiments are provided in Table 1. Nitsche et al. (1993) reported the solubility and speciation of Am, Np, and Pu in Yucca Mountain groundwater (well J-13) at room temperature at pH values 7 and 8.5. Based on these solubility measurements and similarities between the chemical compositions of WCG and J-13 groundwaters, the measured solubilities reported by Nitsche et al. (1993) were used to determine maximum concentrations of $^{241}Am(III)$, $^{243}Am(III)$, $^{237}Np(V)$, and $^{239}Pu(V)$ added to WCG groundwater and synthetic pore water.(Table 2). The high solubility of Tc(VII) is estimated from geochemical data (Eh-pH diagrams) presented by Brookins (1988). Grenthe et al. (1992) present chemical thermodynamic data of U and based on their solubility data, U probably occurs as U(VI) in both WCG groundwater and pore water extracted from the Bandelier Tuff. The mineral schoepite ($UO_2(OH)_2 \cdot H_2O$) is considered to be the most important U(VI) solid controlling the distribution of U(VI) carbonato and hydroxo species, based on XRD analysis of oxidized U metal found at firing sites within the Laboratory.

Table 1. Procedures for Sorption Experiments

Procedure	Reference*
Batch sorption (under atmospheric conditions)	LANL-CST-DP-86
Batch sorption (within the controlled atmosphere of a glove box)	LANL-CST-DP-100
pH measurement	LANL-CST-DP-35
Eh measurement	LANL-CST-DP-102
Liquid scintillation counting	LANL-CST-DP-79
Gamma scintillation counting	LANL-CST-NDK-95

*Yucca Mountain Project Detailed Procedures, Los Alamos National Laboratory.

Table 2. **Summary of Results for Solubility Experiments on Americium, Neptunium, Plutonium, Technetium, and Uranium in Yucca Mountain Groundwater (Well J-13) at pH 7 and Water Canyon Gallery Groundwater, Los Alamos, NM at pH 7.3 and 25°C.**

Radionuclide	Solubility (M)*	Initial Concentration (M)**
Am(III)	1.2×10^{-9}	3.2×10^{-9}
Np(V)	1.3×10^{-4}	4.3×10^{-5}
Pu(V)	2.3×10^{-7}	3.0×10^{-7}
Tc(VII)***	very large	$> 10^{-3}$
U(VI)	3.6×10^{-6}	3.6×10^{-6}

*From Nitsche et al., 1993. **Measured in Water Canyon Gallery groundwater prior to sorption experiments. The solid phases $AmOHCO_3$ and $NaNpO_2(CO_3) \cdot 2H_2O$ were identified by XRD analysis. For plutonium, amorphous material with some crystallinity containing carbonate and Pu(IV) polymer was suggested by Nitsche et al. (1993). $UO_2(OH)_2$ is predicted to control U(VI) solubility (Grenthe et al., 1992). ***Rard (1983) reports a solubility for $NaTcO_4$ of $10^{-1.52}$ molar.

Batch Sorption Procedure

Batch-sorption experiments consisting of three different sets were conducted as part of the PA for MDA-G. Data set 1 provides distribution coefficients for radionuclides using WCG groundwater (Appendix B) to model transport under saturated-flow conditions beneath the disposal pits at MDA-G using the computer program FEHM. Data set 2 provides distribution coefficients for radionuclides (Appendix B, 10.8-12.0 ft sample depth interval) to model transport under (un)saturated-flow conditions within the disposal pits at MDA-G. Chemical analyses of pore water extracted from the Bandelier Tuff, using an Unsaturated/Saturated Flow Apparatus (UFA) (Conca and Wright, 1995) are tabulated in Appendix C. The pore water chemistry provides the basis for the composition of the synthetic pore water, which is included as part of data set 3. Data set 3 provides distribution coefficients for radionuclides (Appendix D) to model transport under unsaturated-flow conditions beneath the disposal pits at MDA-G.

Results of the batch-sorption experiments, using WCG groundwater and synthetic pore water, are provided in Appendices B and D, respectively. All batch-sorption experiments were performed at room temperature, following the procedure detailed in Triay et al. (1996). The sorption procedure initially consisted of pretreating the Bandelier Tuff samples with WCG groundwater or synthetic pore water for approximately twelve days. The sorbent : solution ratio was 1 g of Bandelier Tuff to 20 mL of WCG groundwater or synthetic pore water. After twelve days, the pretreated Bandelier Tuff samples were then separated from the WCG groundwater or synthetic pore water by centrifugation and then equilibrated with 20 mL of ^{241}Am(III), ^{243}Am(III), ^{237}Np(V), ^{239}Pu(V), ^{95m}Tc(VII), and ^{233}U(VI) in separate solutions. After a sorption period of three weeks, the solid phase(s) was separated from each solution by centrifugation.

The amount of radionuclide in solution initially and after sorption was determined with scintillation counters (Packard tri-carb 2200-TR/AB for ^{233}U, ^{241}Am, and ^{243}Am; Packard tri-carb 2500-TR/AB for ^{239}Pu; Packard tri-carb 2550-TR/AB for ^{237}Np) and a gamma counter (Cobra-Canberra) for ^{95m}Tc. The amount of radionuclide sorbed on the solid phase(s) was determined by the difference. The liquid scintillation counting technique used can discriminate alpha activity from beta activity and consequently, no interferences from ^{233}Pa (the daughter of ^{237}Np) are expected. Because the efficiency of the liquid scintillation counters is approximately 100% for the radionuclides, excluding ^{95m}Tc, the counts per minute (cpm) provided in Appendices B and D are approximately equivalent to disintegrations per minute (dpm). The efficiency of the gamma scintillation counter for ^{95m}Tc (self calibrating) is approximately 70%. Containers without Bandelier Tuff (control tubes) were used to monitor

radionuclide precipitation and sorption onto container walls during the sorption experiment. The difference in the concentrations of ^{241}, ^{243}Am(III), ^{237}Np(V), ^{239}Pu(V), ^{95m}Tc(VII), and ^{233}U(VI) in the initial solutions and in the control tubes varied from 40% to 44%, -2% to 0.1%, 4% to 6%, -2% to 0.4%, 4% to 5%, respectively. The large concentration differences for ^{241}Am(III) and ^{243}Am(III) are due to the high sorption capacity of radionuclide on the control tubes.

The batch-sorption distribution coefficient, K_d, was calculated using

$$K_d = \frac{\text{moles of radionuclide per g of solid phase}}{\text{moles of radionuclide per mL of solution,}} \qquad (1)$$

and thus has units of mL/g.

Batch-sorption experiments were performed both under atmospheric conditions (synthetic Bandelier Tuff pore water, pH = 9.8) and inside glove boxes with a CO_2 gas overpressure (0.4% CO_2) to control the pH of the WCG groundwater. The initial pH values of the WCG groundwater, with the radionuclide solutions added, inside the glove boxes ranged from 7.08 to 7.55 (the CO_2 gas overpressure was adjusted to maintain pH values between 7.2 and 7.3). References describing the details of the experimental setup and analytical techniques used in the batch-sorption experiments are provided in Table 1.

Determination of very small or very large distribution coefficients result in large uncertainties in the calculated distribution coefficients (Triay et al., 1996). When little sorption occurs, calculations can yield negative K_d values; the error results from subtracting two large numbers (the initial radionuclide concentration in solution and the radionuclide concentration after sorption) to obtain a small number (the amount of radionuclide associated with the solid phase(s)). Therefore, small K_d values (in the range of ± 1) are not significant. When a great deal of sorption occurs, calculations can yield large uncertainties associated with measuring the small amount of radioactivity left in solution after sorption. Because sorption distribution coefficients for Np and Tc tend to be very small, most K_d values are only reported to two significant figures.

RESULTS AND DISCUSSION

Hydrochemistry and Geochemical Modeling of the Water Canyon Gallery Groundwater

The chemistry of WCG groundwater is shown in Figure 1 and all water chemistry data are presented in Appendix A. The most recent WCG sample was collected in February 1996. The WCG groundwater is a calcium-sodium-bicarbonate solution with magnesium, potassium, sulfate, and chloride present as the other major ions (Blake et al., 1995). The composition of this groundwater shows little variation in solutes over time, excluding bicarbonate (Figure 1). Dissolved silicic acid ($Si(OH)_4^0$) is the most abundant neutral species occurring in this groundwater, which is derived from the dissolution of soluble SiO_2 glass present in the Bandelier Tuff. The ionic strength of the WCG groundwater (February 1996 sample) is 0.0011 molal. The charge balance (sum of cations - sum of anions/sum of cations + sum of anions) calculated for this groundwater analysis is +2.39%, verifying accurate analytical results for this sample.

The WCG groundwater is considered to be relatively oxidizing, based on both near-surface, fracture flow conditions within the Bandelier Tuff and the lack of chemical reductants present in groundwater (for example H_2S aq) (Blake et al., 1995) and in the Bandelier Tuff (solid organic matter) (Longmire et al., 1995). In addition, ferric iron is the dominant form of this redox-sensitive element occurring in different minerals and solid phases including amorphous $Fe(OH)_3$, Fe_2O_3, and Fe_3O_4 (Broxton et al., 1995). The measured Eh value (+181 mV) further suggests that the WCG groundwater is relatively oxidizing. The batch-sorption experiments were performed under oxidizing conditions, based on the observed hydrochemical characteristics of the WCG groundwater and the mineralogy of the Bandelier Tuff.

Calculations of solute speciation, PCO_2, and solid phase saturation indices were made using the computer code MINTEQA2 (Allison et al., 1991), with single ion activity coefficients calculated using the Davies equation. MINTEQA2 quantifies possible rock-water and water-atmosphere reactions, however, modeling results should be interpreted with caution and are limited by the scope of our understanding of hydrologic flow conditions (saturated and unsaturated), possible reaction mechanisms, and kinetic constraints in a disequilibrium-dominated system.

Mineral saturation index (SI) and speciation calculations were performed, using the analytical results from the February 1996 WCG sample, with the computer code, MINTEQA2 (Allison et al., 1991). The WCG groundwater is predicted to be slightly oversaturated with respect to cristobalite (SI = +0.631). The solution is

FIGURE 1. CHEMISTRY OF WATER CANYON GALLERY GROUNDWATER.

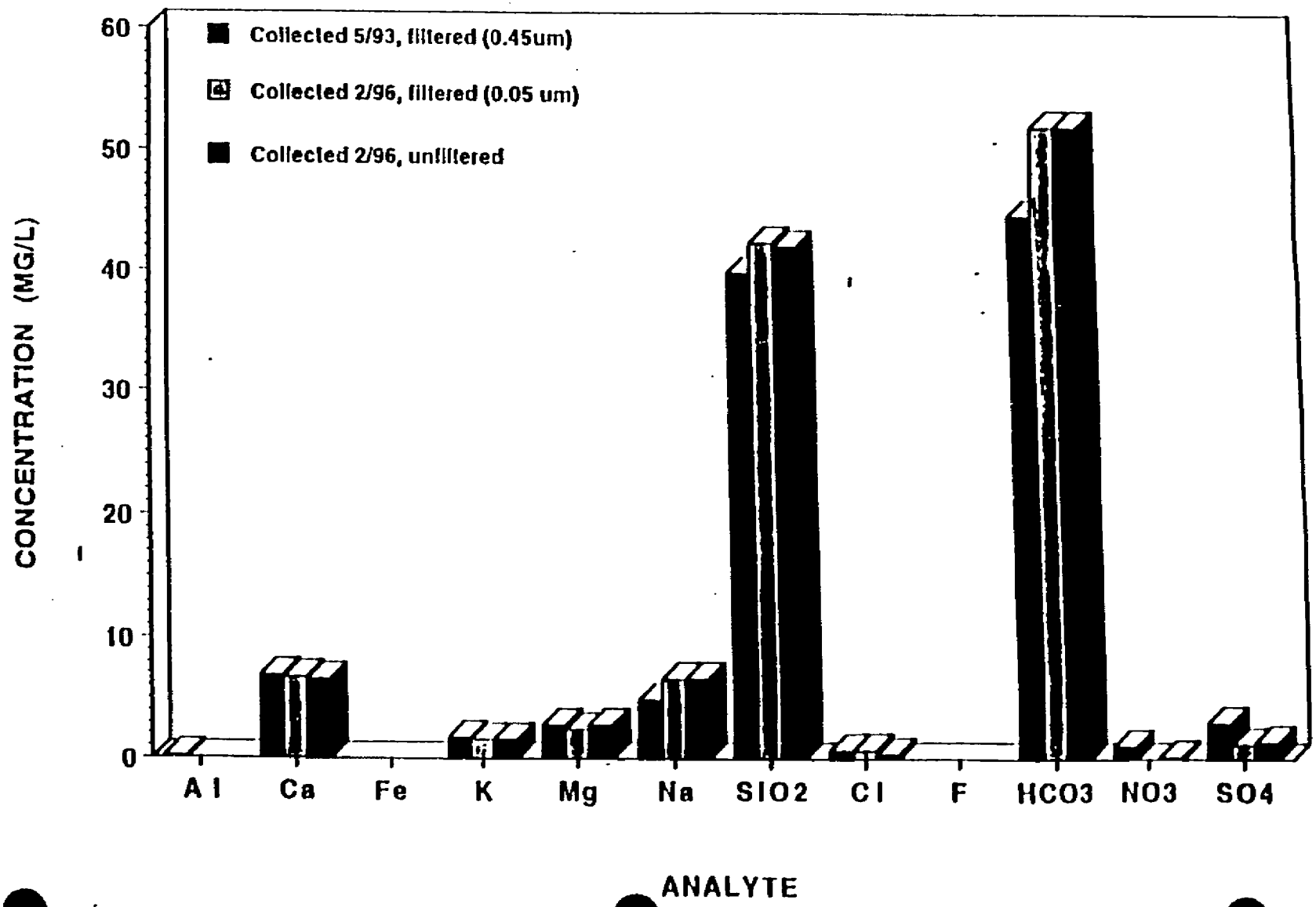

predicted to be in equilibrium (SI = 0.000 ± 0.500) with silica glass (SI = 0.025) and silica precipitate (SI = -0.302), which is consistent with results of mineralogical characterization studies of the Bandelier Tuff (Broxton et al., 1995). The solution is predicted to be undersaturated with respect to calcite (SI value for calcite = -1.674). This is consistent with the observation that only trace amounts of calcite typically occur in the matrix of unaltered Bandelier Tuff, excluding fracture fill material containing calcite and other soil constituents. In addition, calcite does not occur within non-contaminated alluvial aquifers consisting of Bandelier Tuff (for example upper Los Alamos Canyon), because native alluvial groundwater is undersaturated with respect to this mineral.

The oxidation states of Am, Np, Pu, Tc, and U in WCG groundwater and synthetic pore water are assumed to be III, V, V, VII, and VI, respectively, based on the following spectrophotometric and geochemical data. Americium(III) is the stable oxidation state of this actinide in Yucca Mountain groundwater (well J-13) (Nitsche et al., 1993). This is based on extractions with 0.5 M TTA at pH 0 and coprecipitation of Am(III) with LaF_3. The J-13 groundwater is a sodium and bicarbonate-rich solution similar to the ionic composition of WCG groundwater. Americium (III) is therefore, predicted to be the dominant oxidation state of this actinide in WCG groundwater and synthetic pore water. Results of absorption spectrophotometry studies conducted by Nitsche et al. (1993) suggest that Np is stable as Np(V) oxo and carbonato complexes in J-13 groundwater at a pH value of 7.0. The solution redox chemistry of Pu is very involved because several oxidation states (III, IV, V, and VI) can occur in aqueous solution. Nitsche et al. (1993) showed that at pH values of 7.0 and 8.5, Pu(V) is the dominant oxidation state of this actinide in J-13 groundwater. Nitsche et al. (1993) developed an indirect method to determine the oxidation states of Pu based on solvent extractions and coprecipitation. Technetium(VII) is stable as TcO_4^- at pH values ranging from 5 to 10 under oxidizing conditions (Brookins, 1988). Uranium (VI) is assumed to be the stable oxidation state of this element, based on relatively oxidizing conditions characteristic of both the WCG groundwater and pore water extracted from the Bandelier Tuff.

The chemistry of groundwater samples collected from well J-13 (summarized in Thomas, 1987) is similar to the WCG groundwater. There are some important differences, however, in temperature and major-ion chemistry that may influence adsorption processes in comparing the two groundwater chemistries to each other. The temperature of the J-13 groundwater (31.0°C) is higher than the temperature of the WCG groundwater (11.3°C). The dominant cations and anions in both groundwaters are sodium, calcium, and bicarbonate. The higher bicarbonate concentration in the J-13 groundwater probably influences the limited extent of adsorption of uranyl (U(VI)) species onto the Yucca Mountain tuffs. Subsequently, K_d values for uranium determined by Triay et al. (1994)

under oxidizing conditions are less than 2 mL/g. The total dissolved solids (TDS) content of the J-13 groundwater is higher than the TDS content of the WCG groundwater by approximately a factor of 1.7. The J-13 groundwater may have a longer residence time within the tuff(s) relative to the WCG groundwater, which may account for the higher TDS content. The pH values for the WCG and J-13 groundwaters are 7.3 and 6.9, respectively.

The speciated form(s) of the radionuclides of interest influence the extent of sorption that takes place with the adsorbent, in this case the Bandelier Tuff. Speciation versus pH diagrams for Am(III), Np(V), Pu(V), and U(VI) in WCG groundwater, using analytical results obtained from the February 1996 sample, were calculated using the computer program MINTEQA2. These diagrams are shown in Figures 2, 3, 4, and 5. Sources of thermochemical data used in the speciation calculations for the actinide elements include: Am (Kerrisk and Silva, 1986), Np (Lemire, 1984), Pu (Lemire and Tremaine, 1980), and U (Grenthe et al., 1992). At a pH value of 7.3, dissolved Am, Np, Pu, and U are predicted to be stable mainly as $AmCO_3^+$, NpO_2^+, PuO_2^+, and $UO_2(CO_3)_2^{2-}$, respectively (Figures 2, 3, 4, and 5). Technetium(VII) is stable as TcO_4^-, comprising 100% distribution of this element over pH values 6 to 10 (not shown as a figure). Depending on the pH_{pzc} for the different adsorbents present in the Bandelier Tuff, cationic solutes (radionuclides) tend to sorb to a greater amount than do anionic solutes under near-neutral pH conditions. Net-negative surface charge dominates above the pH_{pzc} for the different adsorbents, enhancing cation adsorption. Potential adsorbents in the tuff include glass, smectite, kaolinite, hematite, amorphous $Fe(OH)_3$, and possibly calcite.

Mineralogy and Surface Area of the Bandelier Tuff

The two major rock types of the Bandelier Tuff used in the batch-sorption experiments included vitric (glass) and devitrified (crystal rich) samples. Figure 6 summarizes the mineralogy of the Bandelier Tuff samples representative of the two rock types. The vitric Bandelier Tuff samples (unit 1g) are dominated by silica glass with varying amounts of alkali feldspar, quartz, and cristobalite. The devitrified Bandelier Tuff samples (units 1vu, 1vc, and 2) are characterized by alkali feldspar, quartz, tridymite, cristobalite with minor amounts of hematite and scapolite. Alkali feldspar is the dominant mineral present in the samples followed by quartz.

Figure 7 shows results of BET surface area measurements for the Bandelier Tuff samples. The surface area of the samples range from 1.294 m^2/g (sample depth interval 108.0-109.5 ft bgs) to 2.888 m^2/g (sample depth interval 10.8-12.0 ft bgs)(Figure 7). A correlation between surface area and mineralogy in the

FIGURE 2. RESULTS OF SPECIATION CALCULATIONS FOR WATER CANYON GALLERY WATER USING MINTEQA2, LOS ALAMOS, NEW MEXICO. LOG Am(III) = -8.62 M AND LOG CO3-2 = -3.07 M AT 25C.

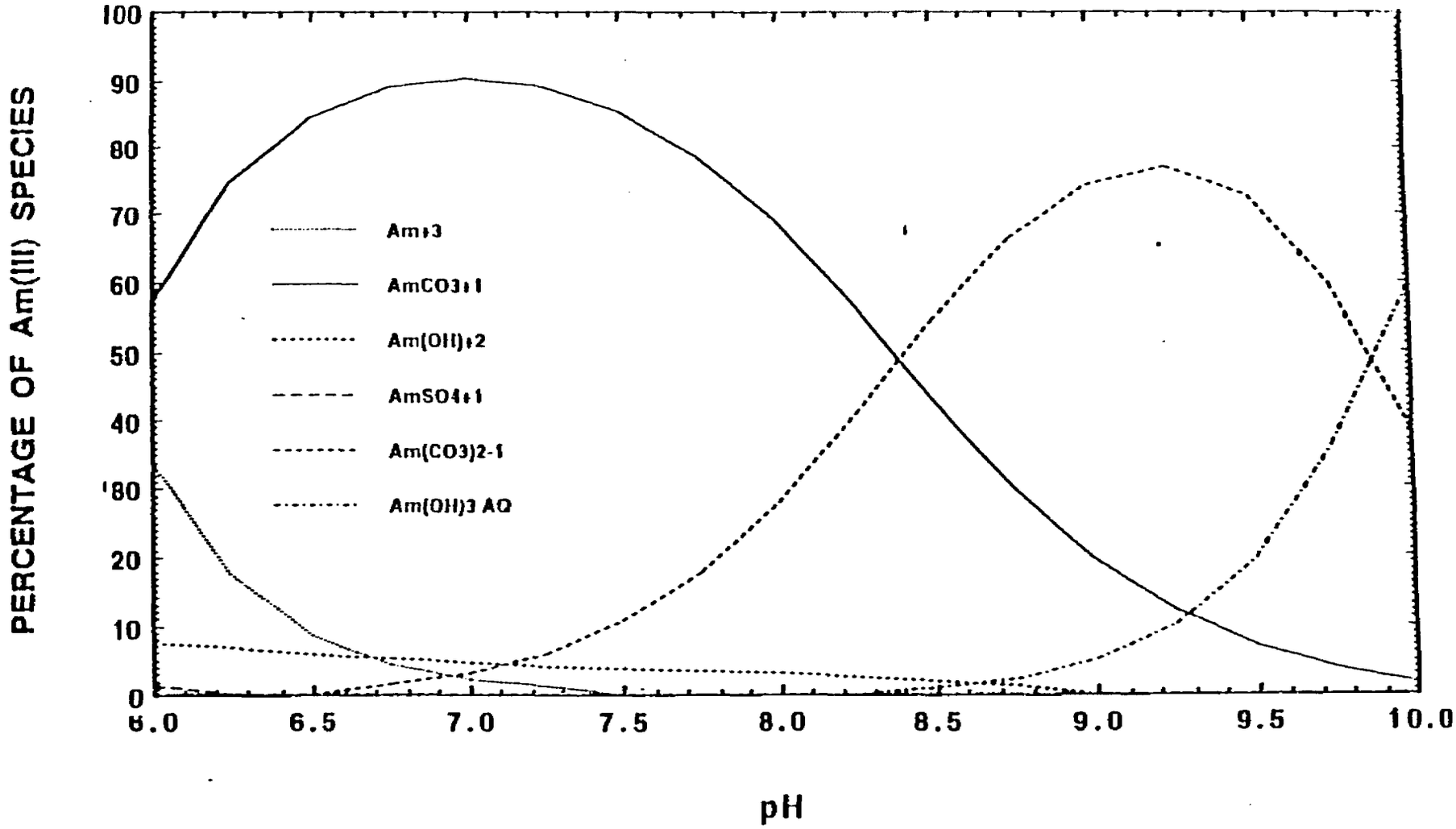

FIGURE 3. RESULTS OF SPECIATION CALCULATIONS FOR WATER CANYON GALLERY WATER USING MINTEQA2, LOS ALAMOS, NEW MEXICO. LOG Np(V) = -4.39 M AND LOG CO3-2 = -3.07 M AT 25C.

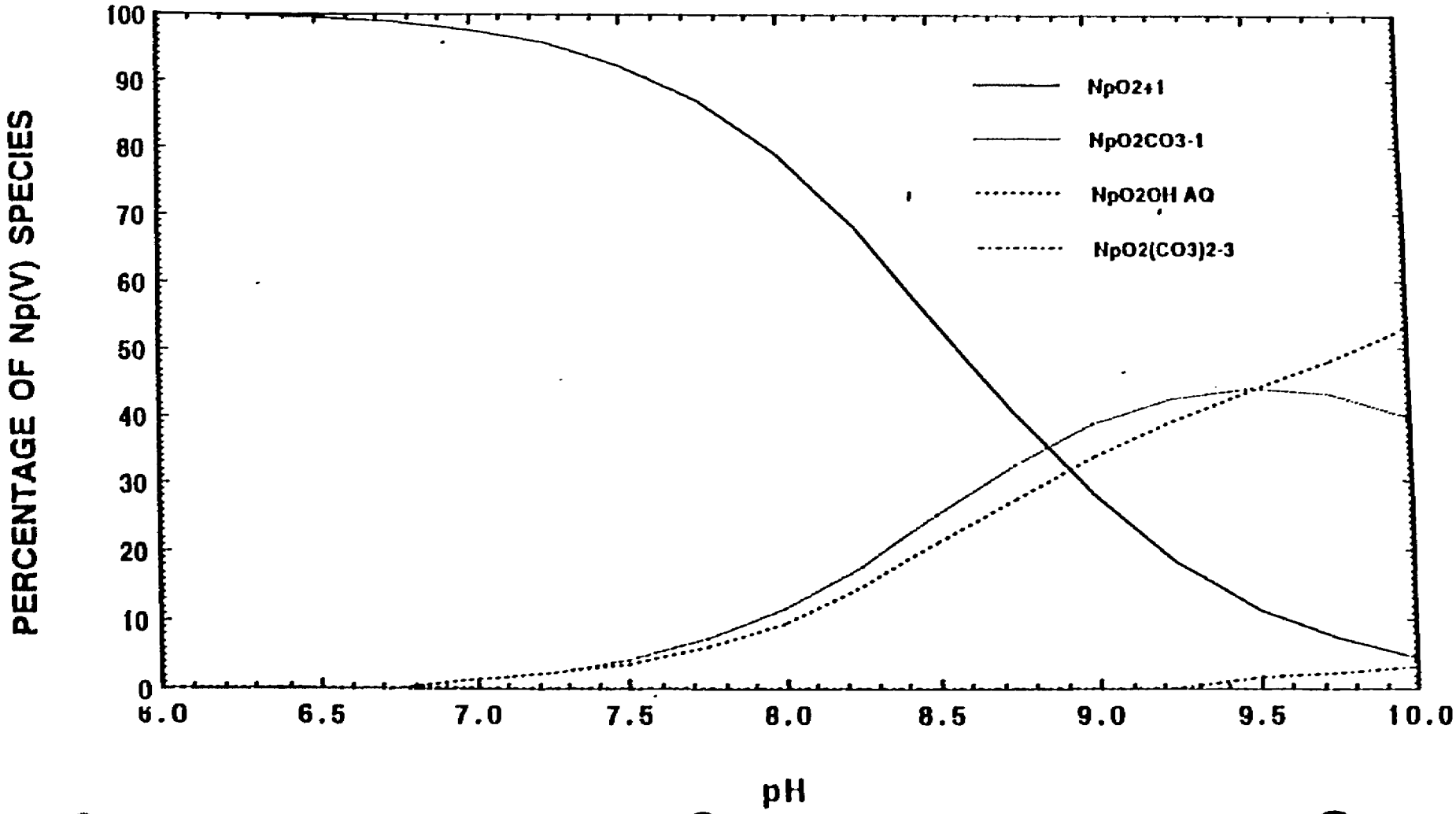

FIGURE 4. RESULTS OF SPECIATION CALCULATIONS FOR WATER CANYON GALLERY WATER USING MINTEQA2, LOS ALAMOS, NEW MEXICO. LOG Pu(V) = -6.54 M AND LOG CO3-2 = -3.07 M AT 25C.

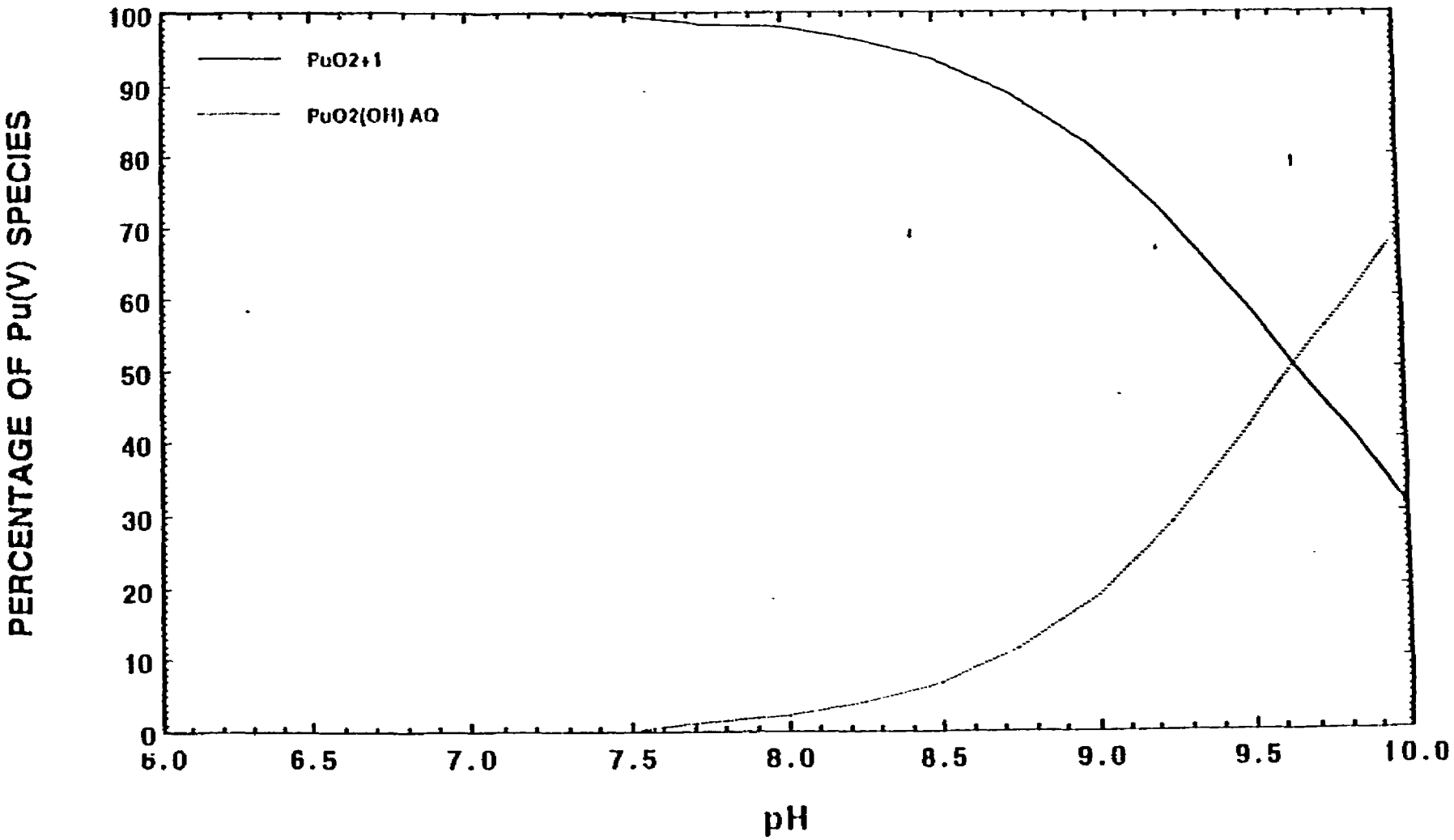

FIGURE 5. RESULTS OF SPECIATION CALCULATIONS FOR WATER CANYON GALLERY WATER USING MINTEQA2, LOS ALAMOS, NEW MEXICO. LOG U(VI) = -5.44 M AND LOG CO3-2 = -3.07 M AT 25C.

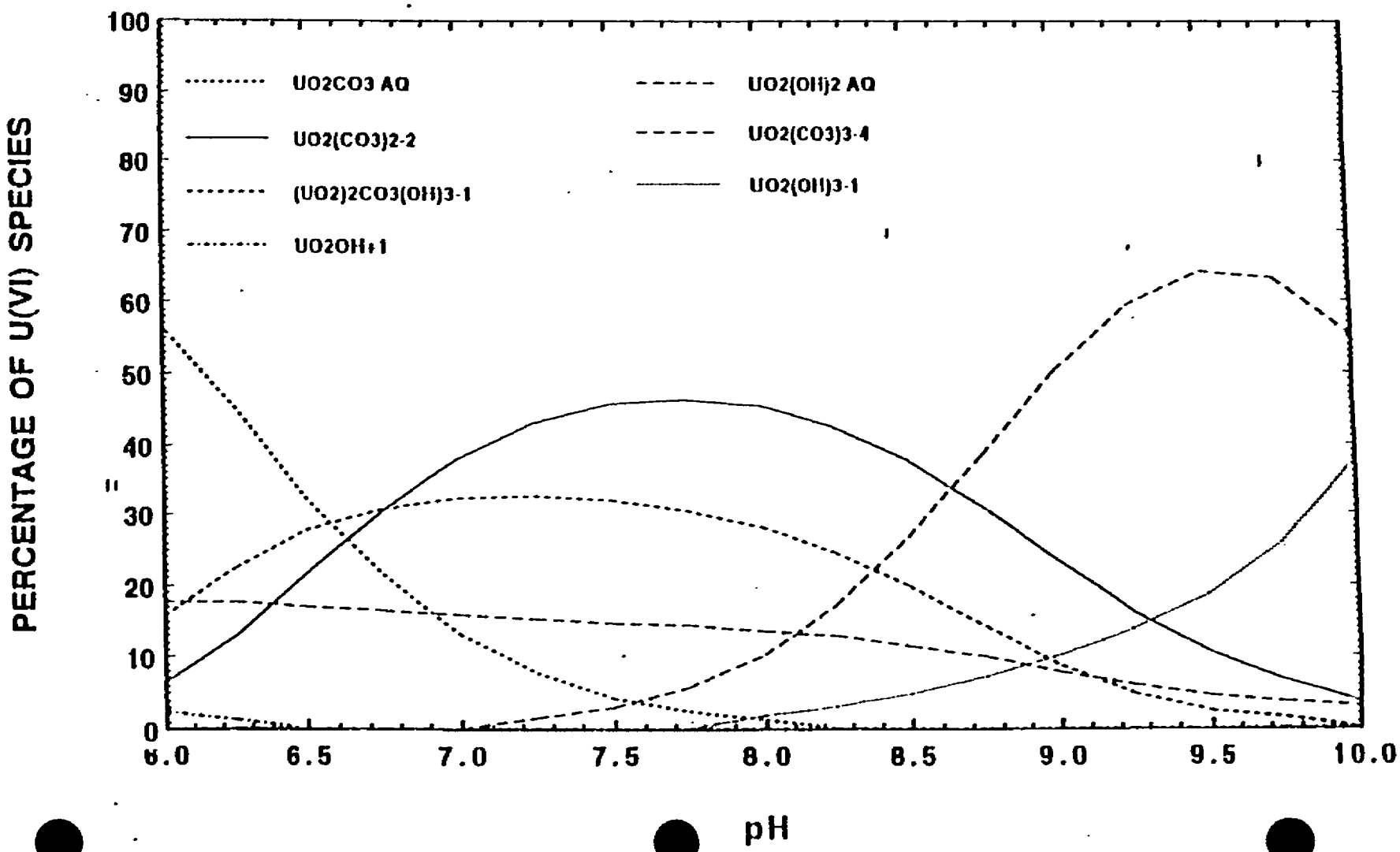

FIGURE 6. MINERALOGY OF CORE HOLE 1107, TA-54, LOS ALAMOS NATIONAL LABORATORY, NEW MEXICO.

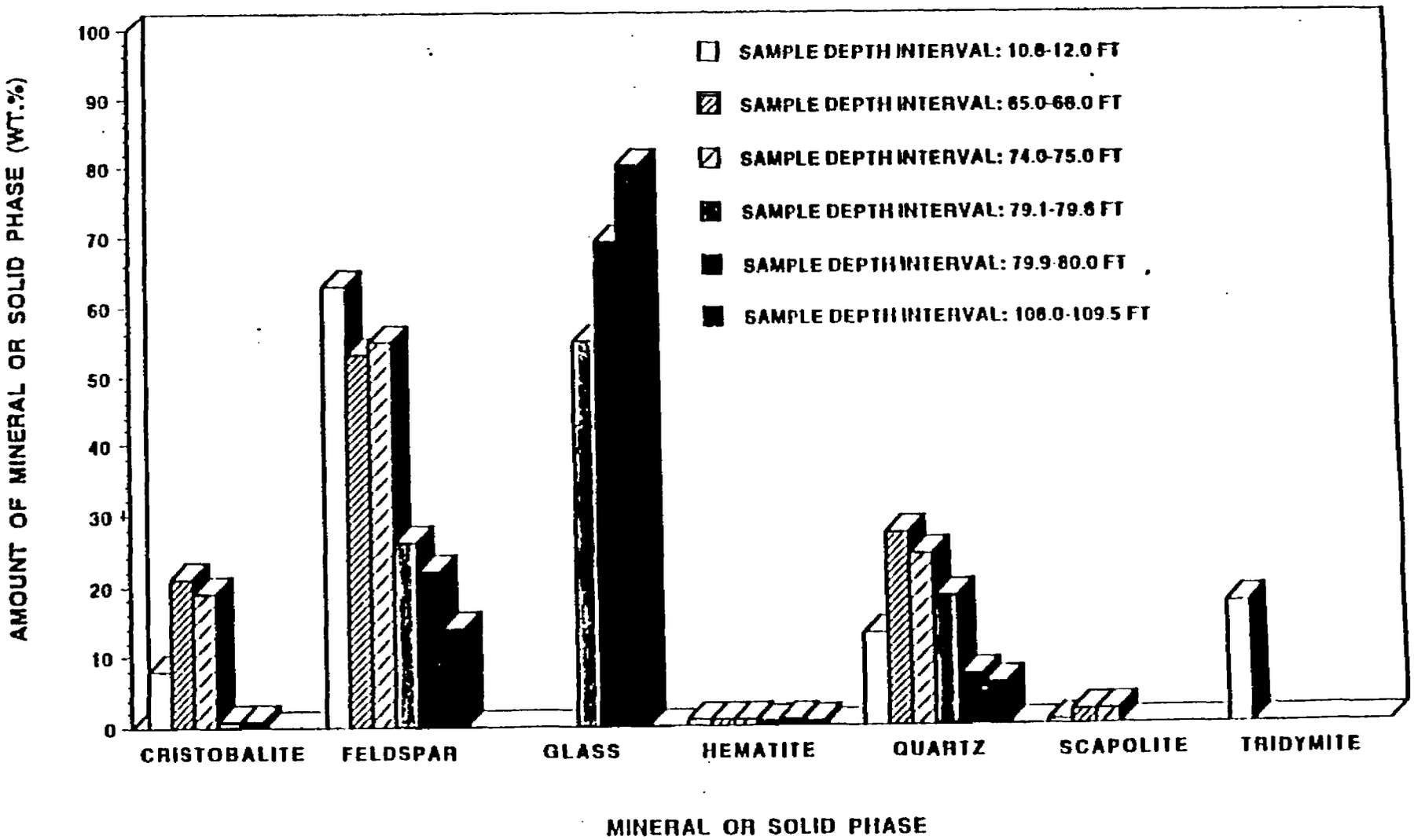

FIGURE 7. SURFACE AREA OF BANDELIER TUFF IN CORE HOLE 1107, MDA-G, TA-54, LOS ALAMOS NATIONAL LABORATORY, NEW MEXICO.

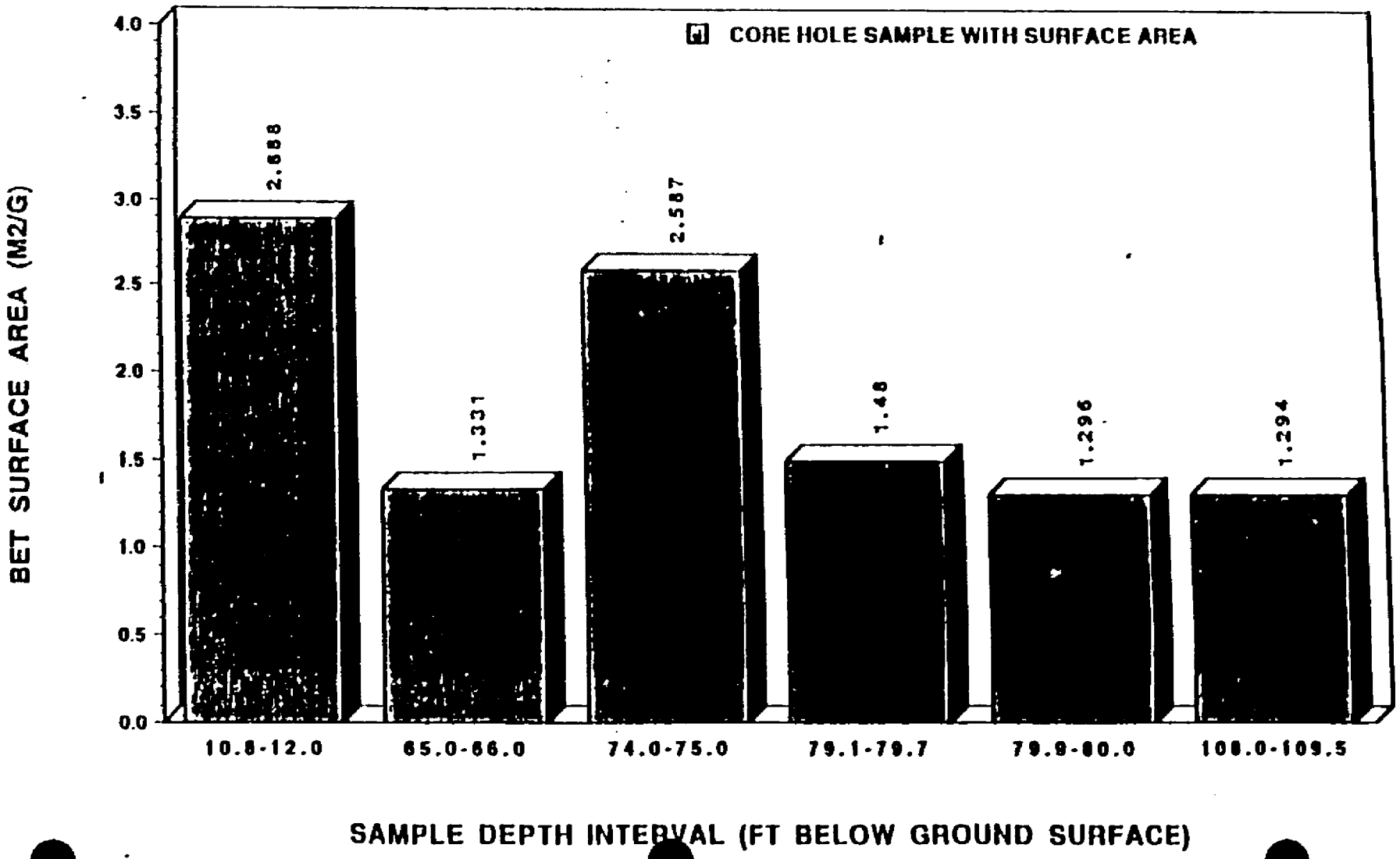

Bandelier Tuff is not possible with existing characterization data. Overall, the bulk surface area of the Bandelier Tuff is small (< 3 m^2/g) relative to specific surface areas of sorptive minerals or solid phases such as amorphous $Fe(OH)_3$ (600m^2/g)(Dzombak and Morel, 1990). Sorption of the radionuclides is in part controlled by the distribution of trace amounts of the highly sorptive phases (smectite, kaolinite, calcite, hematite, $Fe(OH)_3$) disseminated in the Bandelier Tuff. Increasing glass content of unit 1g does not contribute to increasing bulk surface area of the tuff (Figures 6 and 7).

Major and Minor Oxide Chemistry of the Bandelier Tuff

Major and minor oxide chemistry of the Bandelier Tuff (core hole 1107) is provided in Figure 8. The Bandelier Tuff is enriched in SiO_2, with values ranging from 72.00 to 74.89 weight percent (wt.%). The dominant silica phases present in the tuff include quartz, glass, cristobalite, and tridymite. The next most abundant oxide, Al_2O_3 ranges in concentration from 12.27 to 13.04 wt.%. Aluminum is a major structural constituent of alkali feldspars, smectite, kaolinite and amorphous $Al(OH)_3$ (Broxton et al., 1995). Concentration ranges of Fe_2O_3 and FeO in the tuff samples are 1.01 to 1.73 wt.% and 0.045 to 1.46 wt.%, respectively (Figures 8 and 9). The iron oxides Fe_2O_3 and FeO are representative of minor amounts of hematite (Fe_2O_3) and magnetite (Fe_3O_4). Hematite, however, is more abundant than magnetite in the Bandelier Tuff (Broxton et al., 1995). Magnetite increases in abundance below a depth of 79 ft bgs (increase in FeO concentration) in core hole 1107, which corresponds to the interface of lower unit 1g and upper unit 1v (Figure 9). Hematite is the dominant iron-rich phase within units 1v and 2 (Broxton et al., 1995). Abundances of CaO are generally less than 0.40 wt.% over most of the depth intervals sampled in core hole 1107 (Figure 9). Concentrations of CaO, however, increase to 2.48 wt.% in the depth interval 10.8-12.0 ft bgs within unit 2 of the Bandelier Tuff. This depth interval is also characterized by increasing concentrations of $H_2O(+)$ and CO_2, which suggest that calcite may be present in trace amounts (Figure 9). Broxton et al. (1995) report the occurrence of calcite in unit 2 within core samples drilled at TA-21, 1.5 miles northwest of TA-54. Calcite has a high sorptive capacity of Np (Triay et al., 1996) and other actinides.

Batch Sorption Experiments

The sorption of $^{243}Am(III)$, $^{237}Np(V)$, $^{239}Pu(V)$, $^{95m}Tc(VII)$, and $^{233}U(VI)$ on Bandelier Tuff samples was investigated and results of batch experiments (data set 1) are summarized in Table 3. All sorption data (data set 1) are tabulated in Appendix B. The distribution coefficients for the radionuclides (data set 1) are used to model transport under saturated-flow conditions beneath the disposal

FIGURE 8. OXIDE CHEMISTRY OF CORE HOLE 1107, MDA-G, TA-54, LOS ALAMOS NATIONAL LABORATORY, NEW MEXICO.

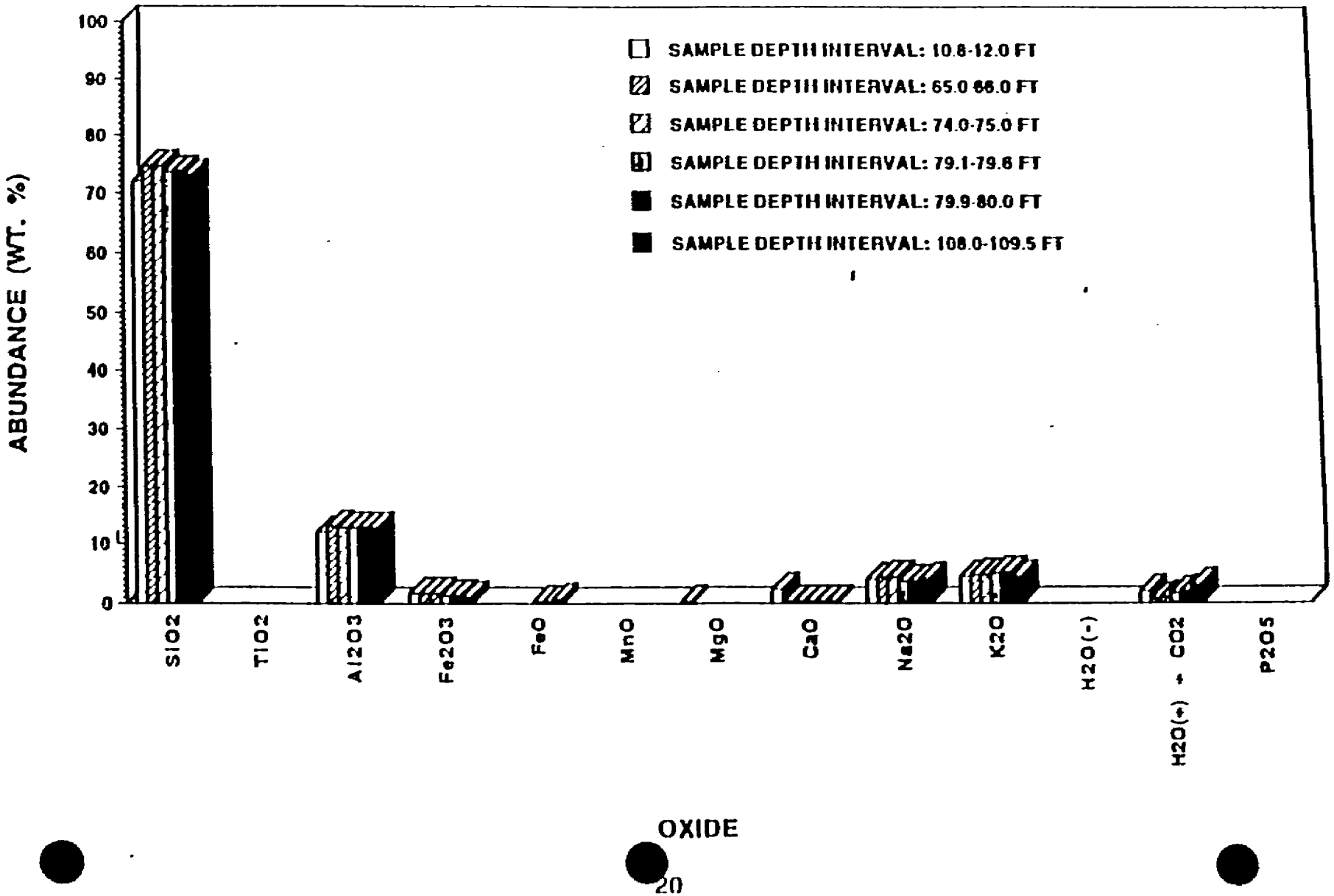

FIGURE 9. OXIDE CHEMISTRY OF CORE HOLE 1107, MDA-G, TA-54, LOS ALAMOS NATIONAL LABORATORY, NEW MEXICO.

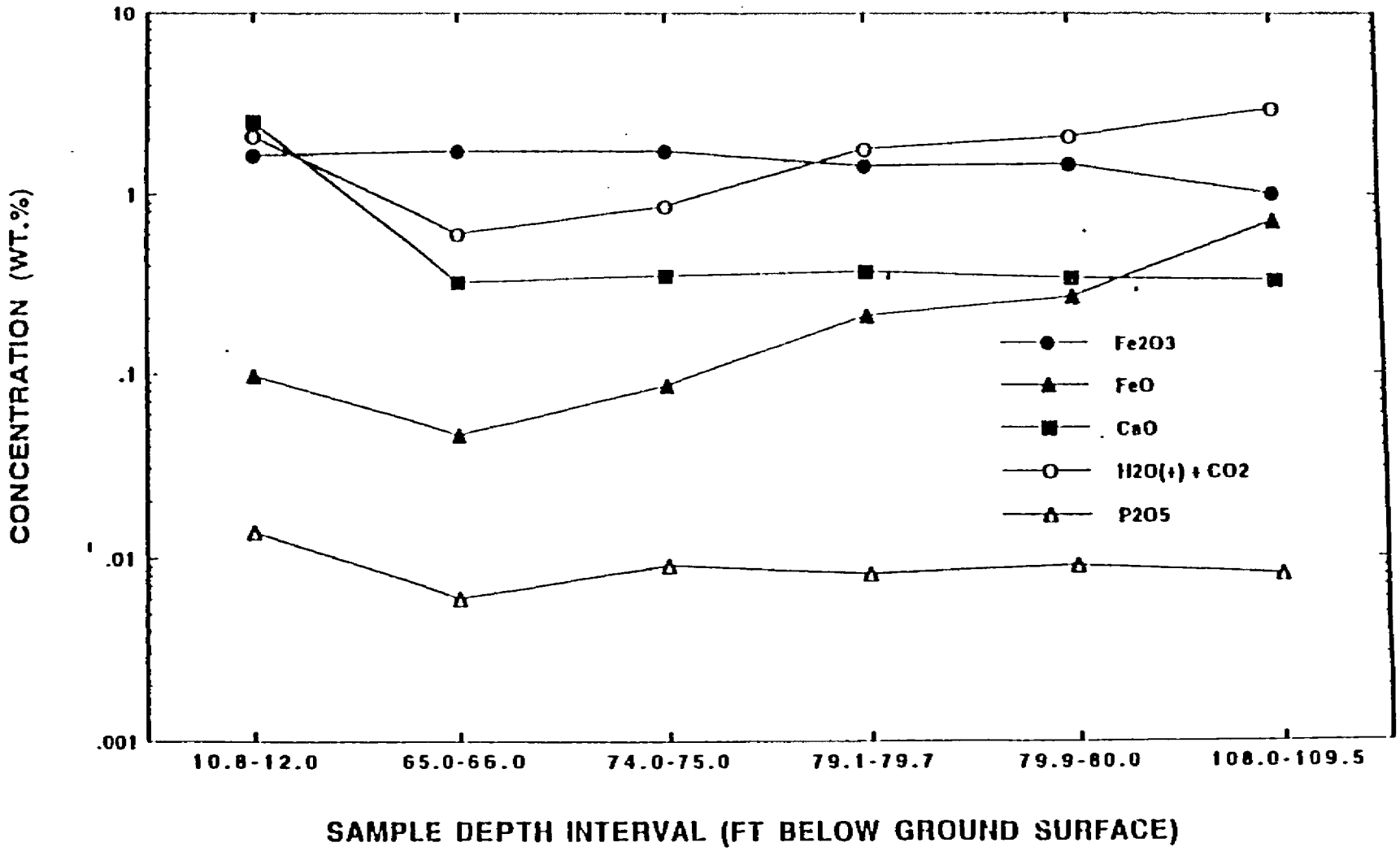

Table 3. Summary of Statistical Parameters for Distribution Coefficients (K_d) (mL/g) for the Bandelier Tuff (Core Hole 1107) using Water Canyon Gallery Groundwater (Data Set 1), Material Disposal Area G, Technical Area 54, Los Alamos National Laboratory, Los Alamos, New Mexico.

Statistic	Am-243	Np-237	Pu-239	U-233
Mean	144	0.253	20.41	5.14
Median	141	0.151	13.95	4.85
Stand. Dev.	13	0.239	18.78	2.98
Skewness	0.30	1.57	2.60	0.10
Minimum	122	0.082	7.64	1.33
Maximum	164	0.525	74.60	9.19
Sample No.	12	3	12	12

The pH of Water Canyon Gallery groundwater after sorption = 7.3 at 25 C. Sample depth intervals are 65.0-66.0 ft, 74.0-75.0 ft, 79.1-79.7 ft, 79.9-80.0 ft, 91.0-91.5 ft, and 108.5-109.0 ft BGS. Two rock samples from each depth interval were used in the sorption experiments. For ^{237}Np, nine sorption experiments yielded negative K_d values because of the low distribution coefficients for this radionuclide.

pits at MDA-G. Sample depth intervals listed in Table 3 include 65.0-66.0 ft, 74.0-75.0 ft, 79.1-79.7 ft, 79.9-80.0 ft, 91.0-91.5 ft, and 108.0-109.5 ft. The distribution coefficients measured on the Bandelier Tuff samples decrease in the following order: Am(III) >> Pu(V) > U(VI) >> Np(V) > Tc(VII). The distribution coefficients for Tc(VII) are all negative (Appendix B) and therefore, they are assumed to be zero. The distribution coefficients for the other radionuclides do not exhibit normal statistical distributions. This is based on differences between the mean and median values and a positive skewness characteristic of a right-sided distribution tail (Table 3). The average distribution coefficients (two sorption experiments per sample interval) for the different radionuclides, excluding Tc, are shown in Figure 10.

The distribution coefficients (data set 2) for the different radionuclides, using the Bandelier Tuff sample collected from the depth interval 10.8 to 12.0 ft bgs, are used to model transport under unsaturated-flow conditions within the disposal pits at MDA-G. The Bandelier Tuff, within the depth interval of 10.8-12.0 ft bgs, is used as pit fill material at MDA-G. Average distribution coefficients (two sorption experiments per sample) for Am(III), Np(V), Pu(V), and U(VI) measured on the tuff sample are 2050 mL/g, 7.5 mL/g, 711 mL/g, and 2.61 mL/g, respectively. The ranges in distribution coefficients for Am(III), Np(V), Pu(V), and U(VI) are 1550 to 2550 mL/g, 7.01 to 7.98 mL/g, 649 to 772 mL/g, and 1.43 to 3.78 mL/g, respectively (Figure 11). The distribution coefficients for Tc(VII) were negative and therefore, are assumed to be zero.

The distribution coefficients for Am(III), Np(V), and Pu(V), within sample depth interval 10.8-12.0 ft bgs, are larger than the distribution coefficients for these radionuclides at greater depths. This increase in the sorptive capacity of the Bandelier Tuff for Am(III), Np(V), and Pu(V) could be due to the presence of calcite, based on increasing concentrations of CaO and CO_2. This potential sorptive phase, however, was not quantified by XRD analysis. Distribution coefficients for U(VI), however, are smaller at this shallow depth interval relative to deeper sample intervals. Uranium is predicted to be stable as $UO_2(CO_3)_2^{2-}$ and this complex desorbs from ferric oxyhydroxide in equilibrium with solutions having a total carbonate concentration greater than 10^{-2} M (Hsi and Langmuir, 1985) at pH values greater than 6.

Figure 12 shows depth versus the distribution coefficients for ^{243}Am, ^{239}Pu, and ^{233}U and the BET surface area for the Bandelier Tuff (core hole 1107). The BET surface-area data correlate with the distribution coefficients for ^{243}Am and ^{239}Pu. The correlation, however, is not so obvious between ^{233}U and the BET surface area. Surface areas larger than 2 m^2/g may represent disseminated amorphous $Fe(OH)_3$, hematite, smectite, kaolinite, and calcite. Positive

FIGURE 10. AVERAGE DISTRIBUTION COEFFICIENT DATA FOR THE BANDELIER TUFF, TA-54, LOS ALAMOS NATIONAL LABORATORY, LOS ALAMOS, NEW MEXICO.

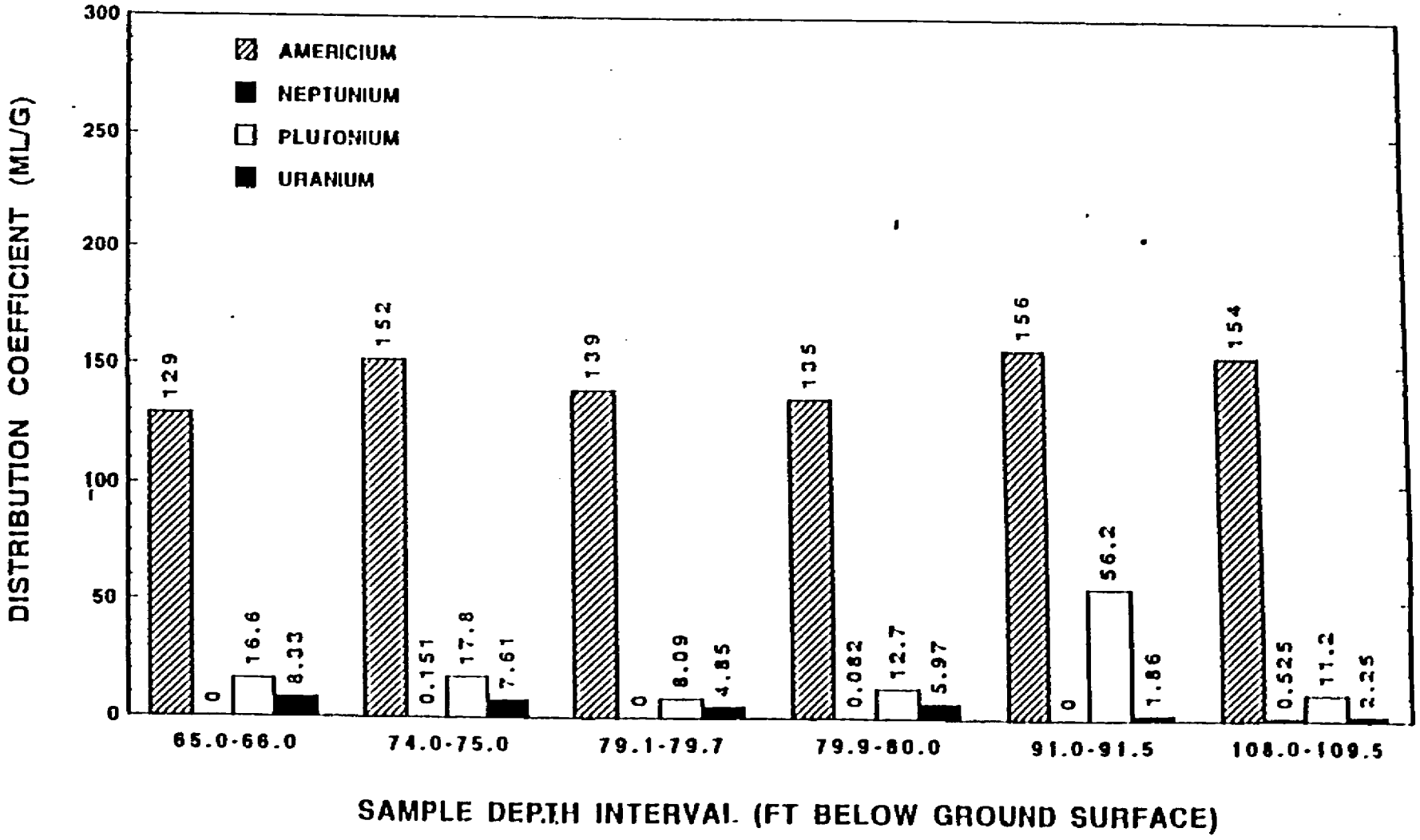

FIGURE 11. AVERAGE DISTRIBUTION COEFFICIENT DATA FOR THE BANDELIER TUFF, TA-54, LOS ALAMOS NATIONAL LABORATORY, LOS ALAMOS, NEW MEXICO.

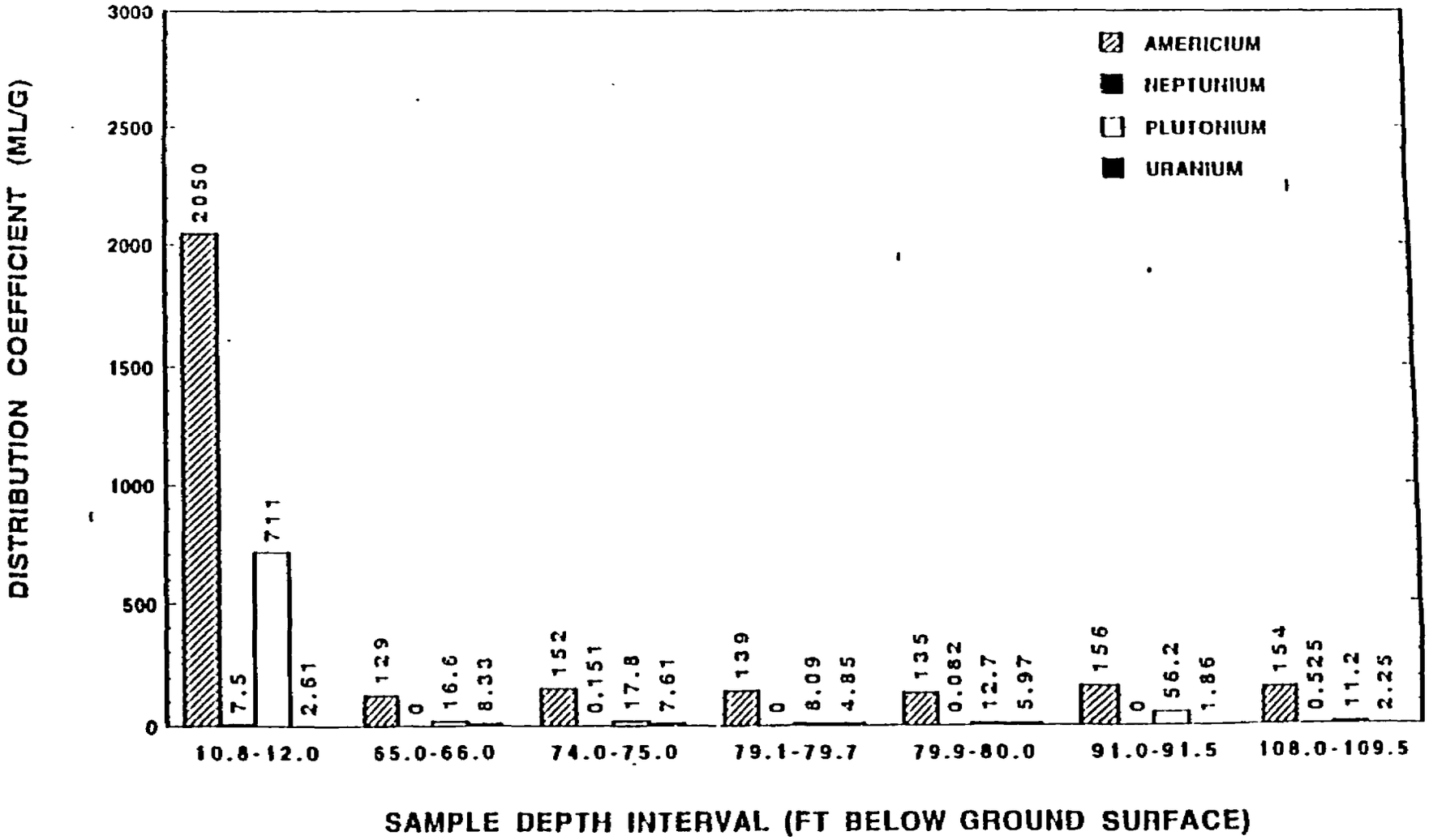

FIGURE 12. AVERAGE DISTRIBUTION COEFFICIENTS AND SURFACE AREA OF THE BANDELIER TUFF (CORE HOLE 1107), MDA-G, TA-54, LOS ALAMOS NATIONAL LABORATORY, LOS ALAMOS, NEW MEXICO.

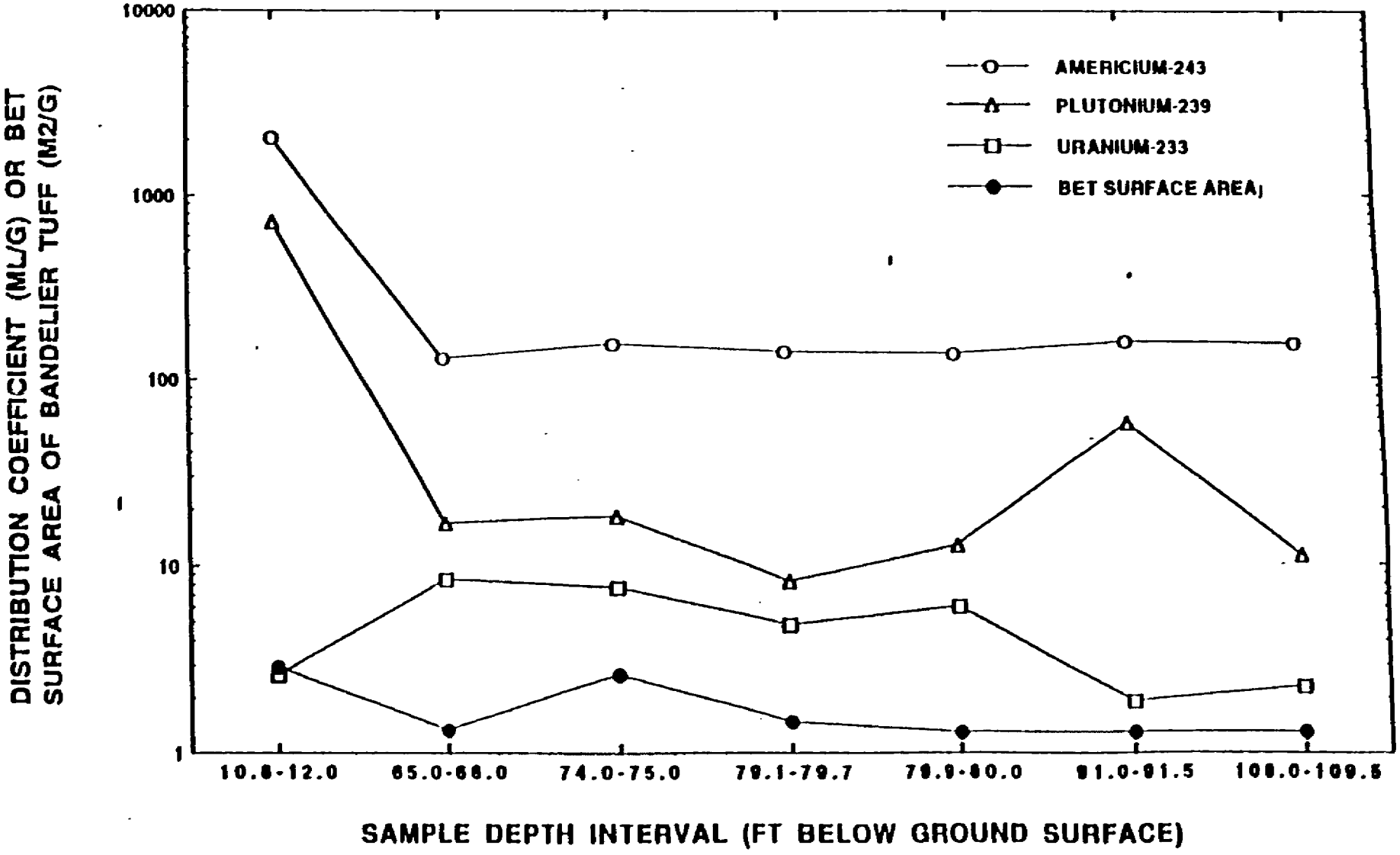

identification of these phases by XRD analysis, excluding hematite, has not been established in core hole 1107.

Figure 13 shows depth versus distribution coefficients for ^{243}Am, ^{239}Pu, and ^{233}U and oxide contents of the Bandelier Tuff (core hole 1107). Variation in abundances of FeO, CaO, and $H_2O(+) + CO_2$ generally correlate with the distribution coefficients for ^{243}Am and ^{239}Pu. This correlation, however, is reversed between the ^{233}U distribution coefficient and $H_2O(+) + CO_2$ content, which is consistent with experimental observations made by other researchers in that carbonate complexing of dissolved U decreases the distribution coefficient for this element (Triay et al., 1994; Hsi and Langmuir, 1985). The complex, $UO_2(CO_3)^{2-}$ is predicted to dominant between pH values 6.7 and 8.7 in WCG groundwater at an U(VI) concentration of $10^{-5.44}$ M (Figure 5).

Pore Water Chemistry of the Bandelier Tuff

Pore water was extracted from three core samples from core hole 1107 using an Unsaturated/Saturated Flow Apparatus (UFA) (Conca and Wright, 1995). This pore water is residual water trapped within pore spaces of the Bandelier Tuff within the vadose zone. The UFA is a new method, based on centrifugation, to obtain direct measurements of transport parameters for porous media and different fluids (Conca and Wright, 1995). The volumetric moisture content of the poorly indurated samples was less than 8%. Two more pore water samples were extracted from core holes 1121 (at 35 ft bgs) and1123 (at 59 ft bgs). The unconsolidated core samples were rotated at 10,000 rpm at a centrifugal force of 11,692 g for several days. The volume of pore water extracted from the core samples ranged from 1.5 to 6.0 mL. The solutions were diluted with ultrapure, double deionized water under controlled atmosphere conditions (argon gas) in glove boxes. The pH of each solution was then measured. The diluted samples were then analyzed from major cations and anions and trace elements. All pore-water chemistry data are provided in Appendix C.

Variation in pore-water chemistry of three core samples (1107) versus depth are shown in Figures 14 and 15. Overall, the pore water extracted from the Bandelier Tuff is characterized by a sodium-carbonate-bicarbonate solution. The pH of the pore-water samples ranges from 9.2 to 9.8, which is much more alkaline than the WCG groundwater (pH = 7.3). Accordingly, carbonate and bicarbonate concentrations are much higher in the pore waters relative to WCG groundwater. These two solutes increase in concentration with depth (Figure 14). Chloride and sulfate concentrations are also much higher in the pore-water samples relative to WCG groundwater and both of these solutes vary with depth in core hole 1107. Anion concentrations in the pore water generally decrease in the following order: chloride = bicarbonate > sulfate > carbonate >

FIGURE 13. AVERAGE DISTRIBUTION COEFFICIENTS AND OXIDE CONTRATIONS IN BANDELIER TUFF (CORE HOLE 1107), TA-54, LOS ALAMOS, NEW MEXICO.

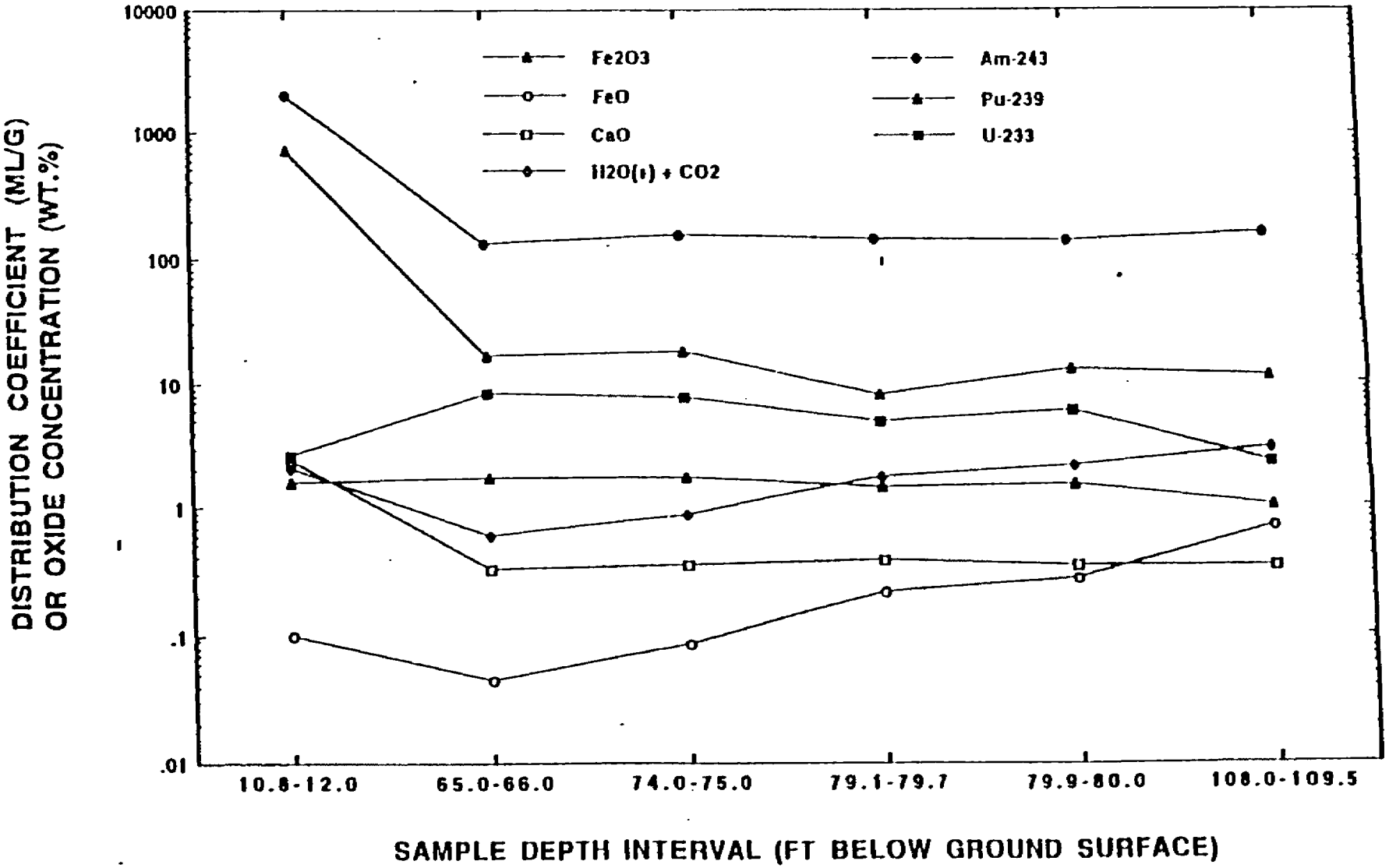

FIGURE 14. SOLUTE AND pH DISTRIBUTIONS WITHIN PORE WATER EXTRACTED FROM BANDELIER TUFF AT TA-54 (CORE HOLE 1107).

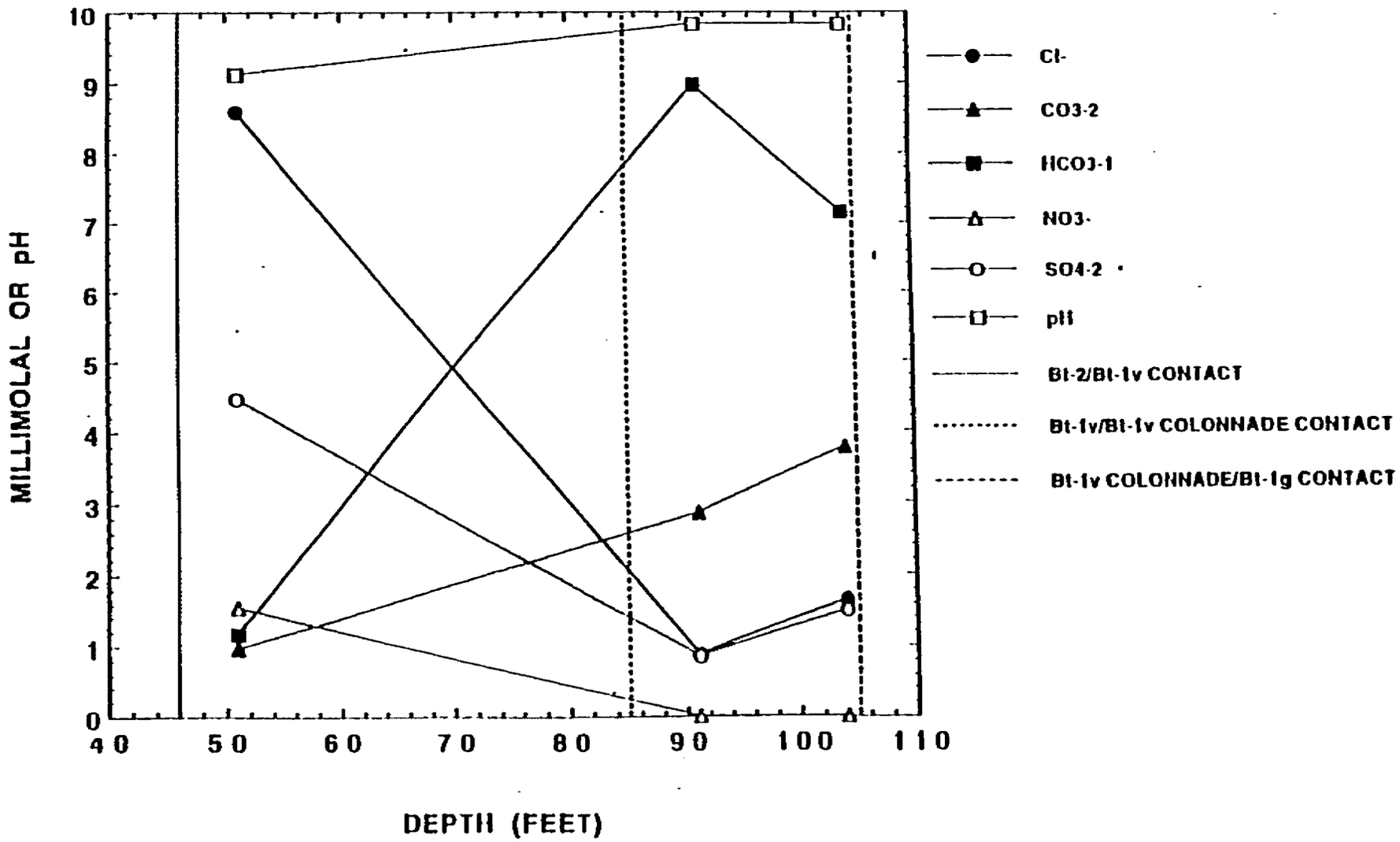

FIGURE 15. SOLUTE AND pH DISTRIBUTIONS WITHIN PORE WATER EXTRACTED FROM BANDELIER TUFF AT TA-54 (CORE HOLE 1107).

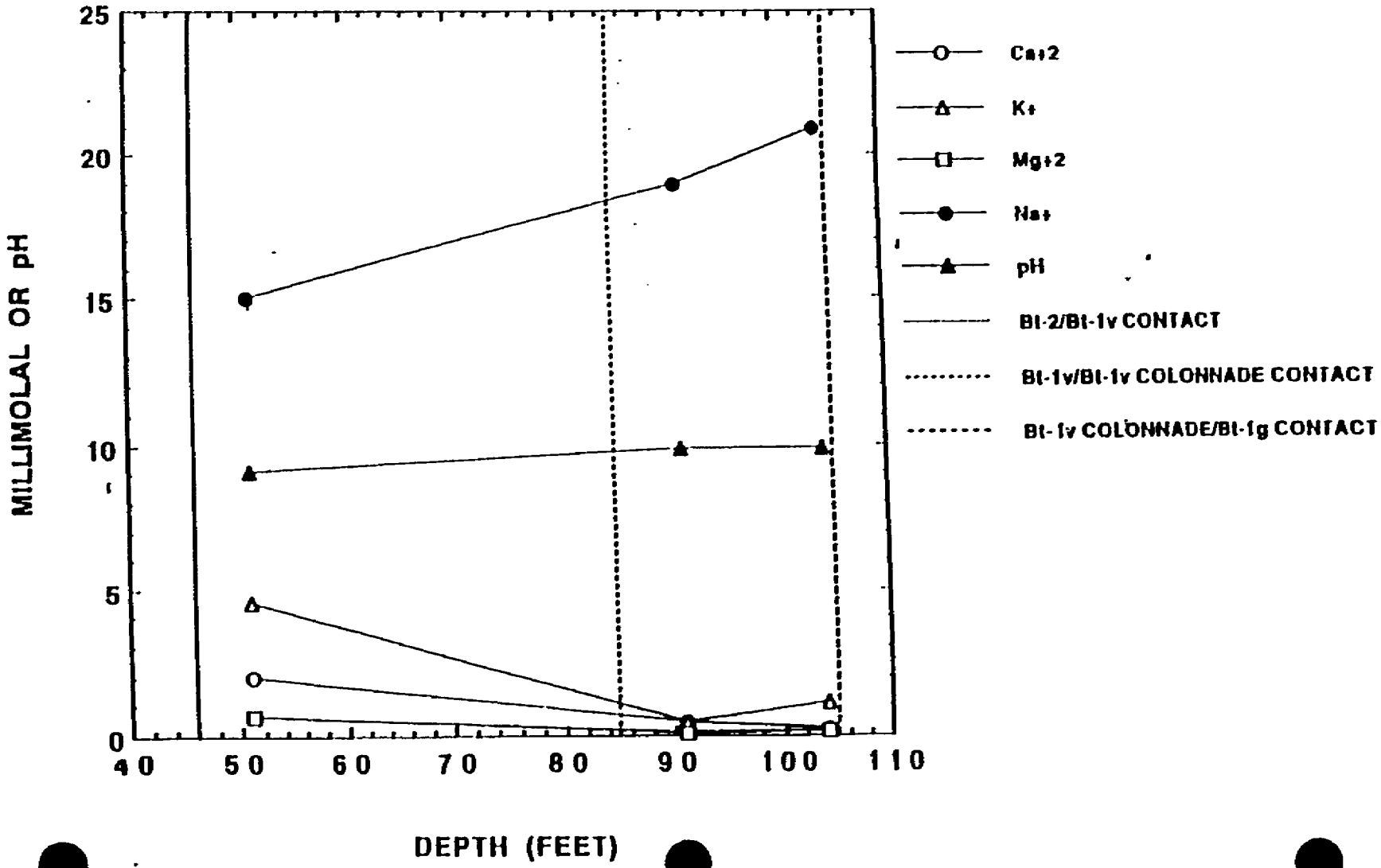

nitrate. Sodium is the most abundant cation in the pore-water samples and concentrations of this cation increase with depth. Concentrations of calcium, magnesium, and potassium are much lower than sodium and they decrease in concentration with depth (Figure 15). Cation concentrations in the pore water generally decrease in the following order: sodium >> potassium > calcium > magnesium.

Mineral-saturation index calculations were performed using the computer code, MINTEQA2 (Allison et al., 1991) on pore water extracted from core hole 1107 at 91 ft depth. The pH of this pore-water sample is 9.8 and the total carbonate (HCO_3^- plus CO_3^{2-}) is 718 ppm ($10^{-1.93}$ M as CO_3^{2-}). The extracted pore water is predicted to be oversaturated with respect to the mineral calcite (SI value for calcite = +1.718). Calcite was not observed by XRD analysis, however, this mineral could occur as surface coatings present at concentrations less than 1 wt.%.

The pore-water chemistry of core hole 1107 suggests that evaporation is an important process for concentrating dissolved species within the vadose zone of the Bandelier Tuff. Stable isotope and chloride leaching data collected at TA-54 (Newman, 1996) also suggest evaporation is an important process that occurs within the mesa. Vaniman and Chipera (1995) report the occurrence of evaporite minerals such as gypsum ($CaSO_4 \cdot 2H_2O$) and halite (NaCl) within fractures at TA-69. The chemical evolution of the pore water is also controlled by the low hydraulic flux, which allows for long residence times (mass of solute/flux of solute) of solutes within the Bandelier Tuff. Under ambient moisture conditions in the Bandelier Tuff, precipitation of sorptive phases, such as calcite and amorphous $Fe(OH)_3$ with high surface areas, is enhanced. These phases have been observed in fracture fill material across the Laboratory (Davenport, 1993; Longmire et al., 1995). Iron, in the forms of amorphous $Fe(OH)_3$ and hematite, and aluminum, concentrated within smectite, kaolinite, and possibly amorphous $Al(OH)_3$, are also elevated within the fracture fill material relative to the Bandelier Tuff at TA-46 (Longmire et al., 1995). Longmire et al. (1995) showed that naturally occurring trace elements (As, Be, Mn, and U) are concentrated within fracture fill material at TA-46, which is consistent with adsorption or possibly coprecipitation being an effective process for removing trace metals from solution.

Batch Sorption Experiments Using Synthetic Bandelier Tuff Pore Water

A synthetic pore water, based on the general composition of the pore water extracted from the Bandelier Tuff using the UFA, was prepared for the batch-sorption experiments to quantify the mobility of selected radionuclides within the

vadose zone. The synthetic solution consisted of a mixture of equal volumes of $10^{-1.26}$ M Na_2CO_3 and $10^{-1.23}$ M $NaHCO_3$ at 25°C. The total carbonate in the synthetic pore-water solution ($10^{-0.94}$ M) is greater than that measured in the extracted pore water ($10^{-1.93}$ M) to achieve a pH value of 9.8. pH is considered to be the master variable controlling sorption of radionuclides on Bandelier Tuff under vadose zone conditions. This variable, in addition to total carbonate, controls the speciation of the adsorbate and the solubility of the solid phase(s) containing the radionuclide of interest. The synthetic solution had an initial pH value of 10.3, which is slightly higher than the pH values (9.2-9.9) measured in the extracted solutions. At the conclusion of the batch-sorption experiments, the pH decreased to 9.8. The experiments were conducted under atmospheric conditions, with sealed sorption vessels, to maintain the alkaline pH conditions characteristic of the pore water within vadose zone.

Results of $^{241}Am(III)$, $^{237}Np(V)$, $^{239}Pu(V)$, $^{95m}Tc(VII)$, and $^{233}U(VI)$ sorption experiments, using the synthetic pore water, are summarized in Table 4. All sorption data are tabulated in Appendix D. Samples collected from depth intervals 10.8-12.0 ft, 65.0-66.0 ft, 74.0-75.0 ft, 79.1-79.7 ft, 79.9-80.0 ft, 91.0-91.5 ft, and 108.0-19.5 ft were used in the sorption experiments. The distribution coefficients measured on the tuff samples with the synthetic pore water decrease in the following order: Am(III) >> Pu(V) > U(VI) > Np(V). The distribution coefficients for Tc are all negative (Appendix D) and therefore, they are assumed to be zero. The distribution coefficients do not exhibit normal statistical distributions based on differences between the mean and median values. In addition, a positive skewness is characteristic of the right-sided distribution tails for $^{241}Am(III)$ and $^{239}Pu(V)$, whereas and a negative skewness is characteristic of the left-sided distribution tails for $^{237}Np(V)$ and $^{233}U(V)$ (Table 4). The average distribution coefficients (two sorption experiments per sample interval) for the different radionuclides, excluding $^{95m}Tc(VII)$, are shown in Figure 16. The distribution coefficients for $^{241}Am(III)$ and $^{239}Np(V)$ using synthetic pore water are larger than the distribution coefficients for these two radionuclides using WCG groundwater (Tables 3 and 4).

Results of speciation calculations for the synthetic pore-water solution, at a pH value equal to 9.8 using MINTEQA2, are shown in Figures 17 and 18. Based on the model simulations, the dominant aqueous complexes of $^{241}Am(III)$ and $^{237}Np(V)$ are predicted to include $Am(CO_3)_3^{3-}$ and $NpO_2(CO_3)_3^{5-}$, respectively. The dominant dissolved complexes of $^{239}Pu(V)$ and $^{233}U(VI)$ are predicted to include PuO_2OH^0 and $UO_2(CO_3)_3^{4-}$, respectively. The complex PuO_2^{1+}, however, is present at 49%. The synthetic pore-water solution is predicted to be undersaturated with respect to $Am(OH)_3(s)$, $Am(OH)_3(am)$, $AmOHCO_3$,

Table 4. Summary of Statistical Parameters for Distribution Coefficients (K_d) (mL/g) for the Bandelier Tuff (Core Hole 1107) Using Synthetic Pore Water Solution (Data Set 3), Material Disposal Area G, Technical Area 54, Los Alamos National Laboratory, Los Alamos, New Mexico.

Statistic	Am-241	Np-237	Pu-239	U-233
Mean	7611	1.88	8.06	2.44
Median	2359	2.25	4.13	2.43
Stand. Dev.	9754	1.15	7.89	0.66
Skewness	1.03	-0.41	0.66	-0.14
Minimum	198	0.17	1.23	1.38
Maximum	27300	3.07	19.40	3.44
Sample No.	12	12	12	12

Sample depth intervals are 10.8-12.0 ft, 65.0-66.0 ft, 74.0-75.0 ft, 79.1-79.7 ft, 79.9-80.0 ft, 91.0-91.5 ft, and 108.5-109.0 ft BGS. Two rock samples from each depth interval were used in the sorption experiments. pH = 9.8 using synthetic Bandelier Tuff pore water based on unsaturated flow apparatus (UFA) extractions.

FIGURE 16. AVERAGE DISTRIBUTION COEFFICIENT DATA FOR BANDELIER TUFF (SYNTHETIC PORE WATER, pH = 9.8), TA-54, LOS ALAMOS NATIONAL LABORATORY, NEW MEXICO.

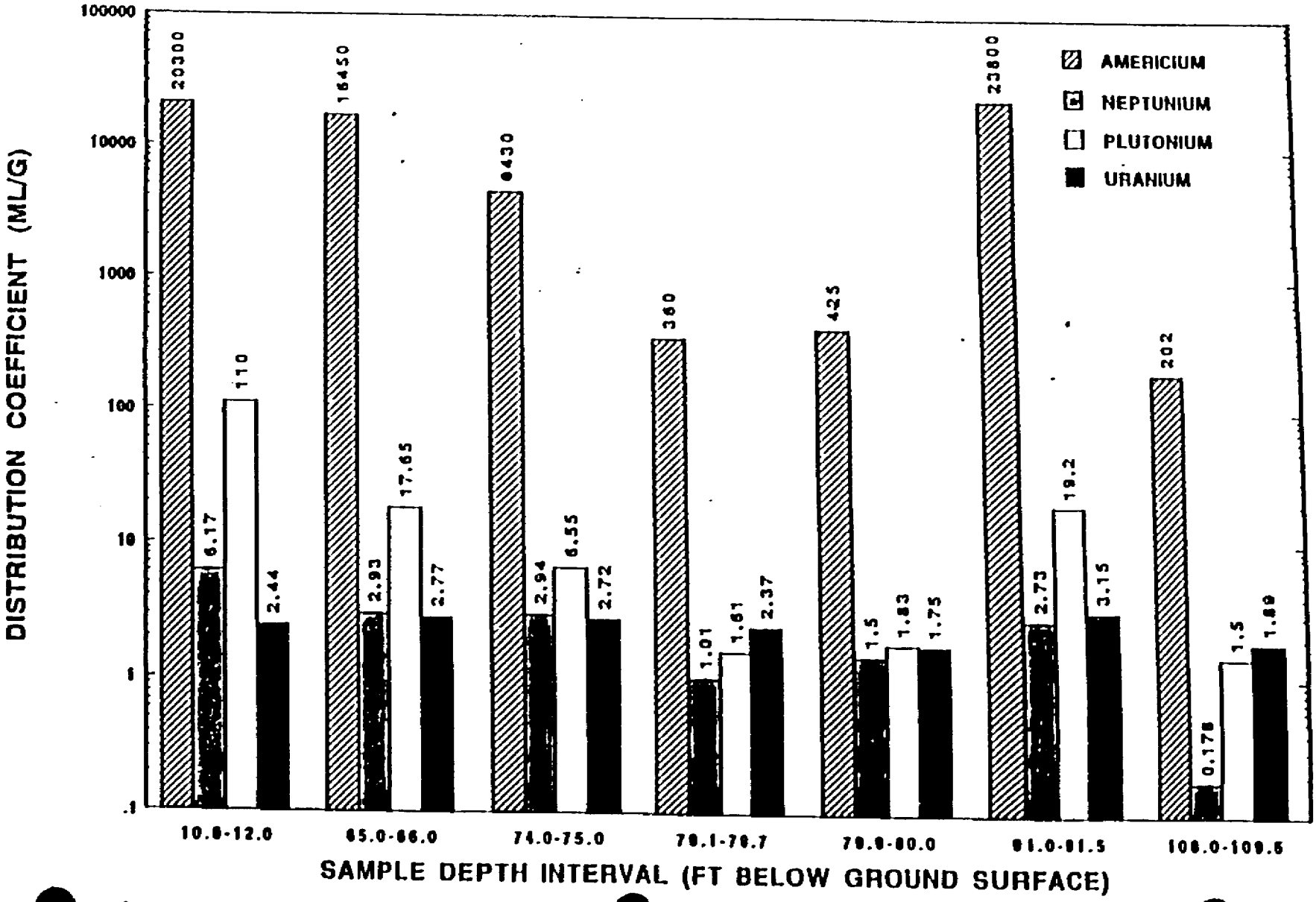

FIGURE 17. RESULTS OF SPECIATION CALCULATIONS USING MINTEQA2 FOR SYNTHETIC BANDELIER TUFF PORE WATER AT 25 C (LOG CO3-2 = -0.94 M, LOG Am(III) = -8.50 M, AND LOG Np(V) = -4.37 M).

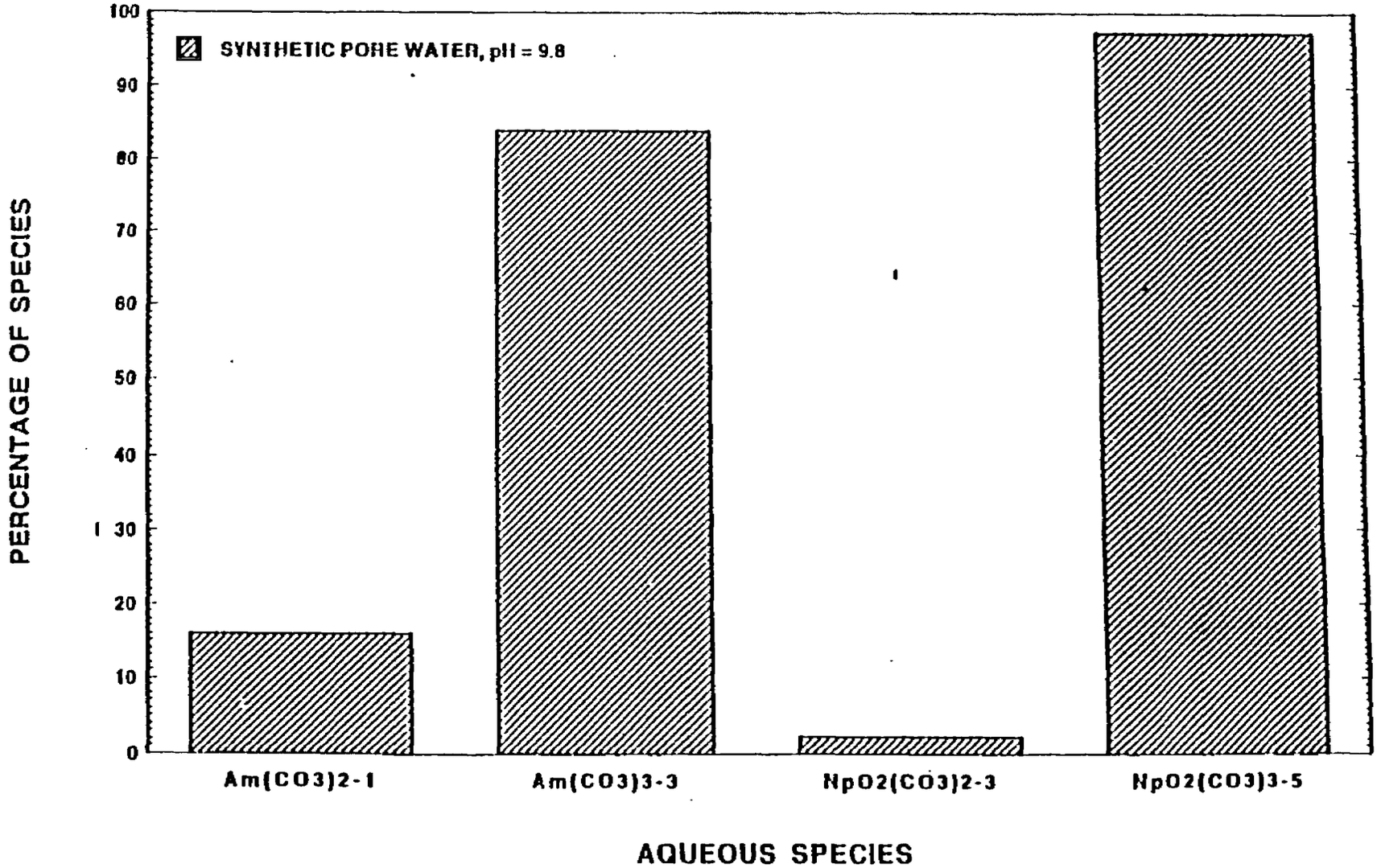

FIGURE 18. RESULTS OF SPECIATION CALCULATIONS USING MINTEQA2 FOR SYNTHETIC BANDELIER TUFF PORE WATER AT 25 C (LOG CO3-2 = -0.94 M, LOG Pu(V) = -6.53 M, AND LOG U(VI) = -5.45 M).

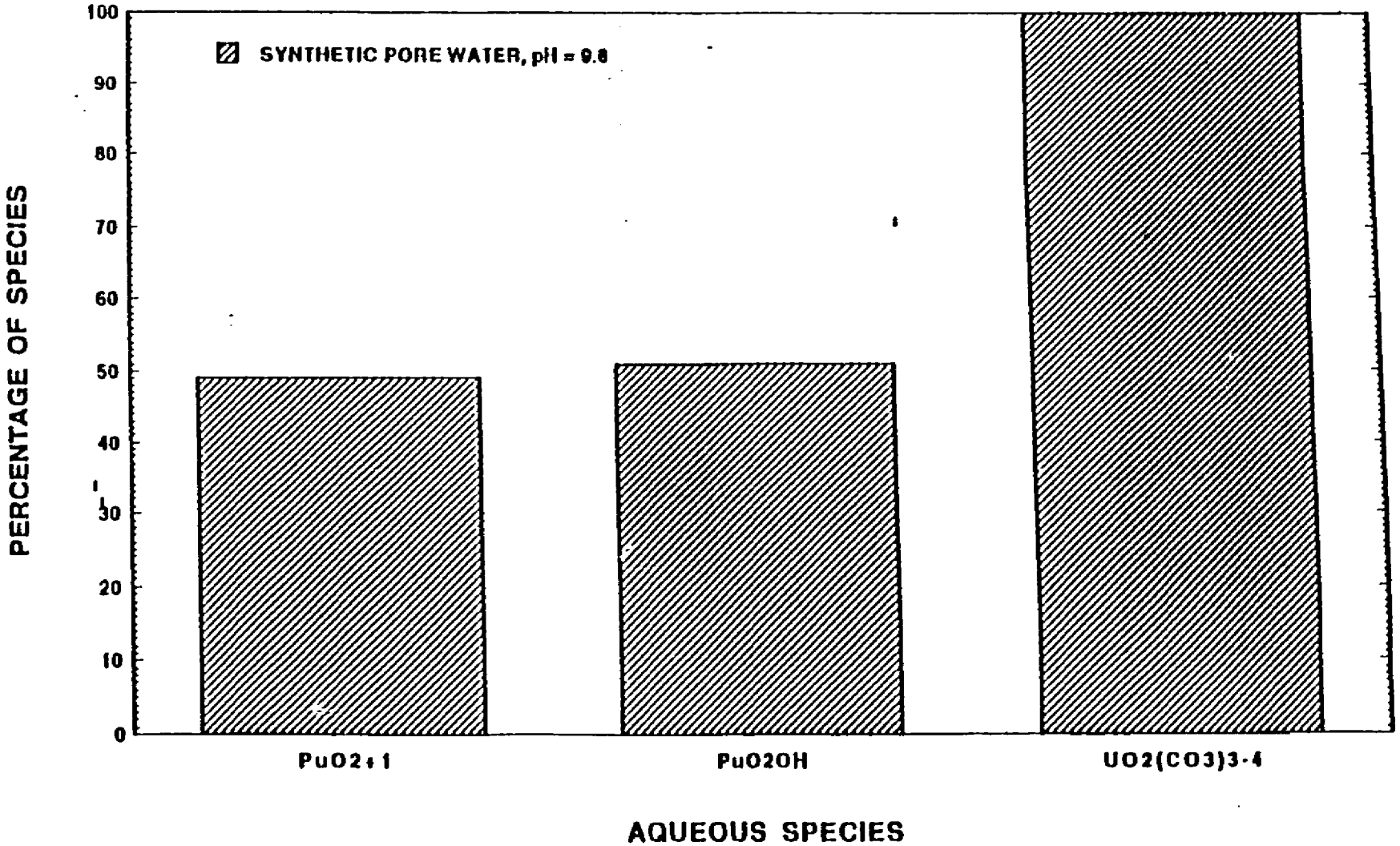

$NpO_2OH(am)$, $NpO_2OH(aged)$, $NaNpO_3 \cdot 3.5H_2O$, $NaNpCO_3$, $PuO_2OH(am)$, and $UO_2(OH)_2$ (Figures 19 and 20). Precipitation of these phases from the carbonate-rich solution is not likely from a thermochemical basis because of the strong complexing of Am(III), Np(V), and U(VI) with carbonate ligands.

Precipitation of calcite during the batch-sorption experiments using the synthetic pore water solution is possible. This solution containing $10^{-0.94}$ M total carbonate is predicted to be slightly oversaturated with respect to calcite (SI for calcite = +0.641), at Ca^{2+} concentrations equal to $10^{-4.60}$ M (1 ppm). Calcite has a strong affinity for sorbing Np(V) based on results of batch-sorption experiments conducted by Triay et al. (1996). Calcite, with a pH_{pzc} of 9.0 (saturated $CaCO_3$ solution with Log_{10} Ca = -4.4 M and Log_{10} PCO_2 = -3.5 atm) (Zachara et al., 1993), is characterized by a net-neutral surface charge at pH 9.0. As a comparison to the value provided by Zachara et al. (1993), Parks (1967) reports a pH_{zpc} value of 9.5 for calcite. Based on a net positive surface charge, calcite adsorbs anions at pH values below 9 or 9.5 and this phase can be an important adsorbent for anions in natural systems under near neutral to alkaline pH conditions. Conversely, the sorption of cationic metals on calcite is maximal above the pH_{pzc} for calcite (Zachara et al., 1993). At a pH value of 9.8, characteristic of pore water within the Bandelier Tuff, however, calcite contains a majority of negatively-charged surface sites consisting of O^{2-} (from dissociated surface H_2O), CO_3, and HCO_3. The positive charged surface sites on calcite consist of Ca and other substituted divalent metal cations.

Under the high alkalinity conditions (Log_{10} total CO_3^{2-} = -0.94 M) of the batch-sorption experiments, carbonate ligands attached to dissolved Am ($Am(CO_3)_3^{3-}$) and Np ($NpO_2(CO_3)_3^{5-}$) complexes may replace the CO_3 and HCO_3 surface sites on calcite through surface (ligand) exchange reactions. Sorption of Am(III) and Np(V) complexes directly onto calcite (as inner sphere complexes) at a pH value 9.8 under high carbonate conditions is possible based on geometries of the actinide(IV) and actinide(VI) carbonate species presented by Clark et al., (1994). The formation of bidentate surface complexes consisting of Am(III) and Np(V) carbonate adsorbates is consistent with the higher distribution coefficients measured for these two actinides using the synthetic pore water. The geometric configurations of the adsorbed $Am(CO_3)_3^{3-}$ and $NpO_2(CO_3)_3^{5-}$ complexes and their orientation on the adsorbing calcite surface have not been investigated as part of this study. An estimation based on the crystal radii of Am(III) and Np(V) carbonato ions, however, suggests that adsorbed $Am(CO_3)_3^{3-}$ and $NpO_2(CO_3)_3^{5-}$ complexes have cross sectional diameters larger than the cross sectional area of individual surface functional groups found on calcite consisting of CO_3 and HCO_3. It therefore seems likely that each adsorbed $Am(CO_3)_3^{3-}$ and $NpO_2(CO_3)_3^{5-}$ complex has exchanged more than one of its CO_3^{2-} ligands with

FIGURE 19. RESULTS OF SATURATION INDEX CALCULATIONS USING MINTEQA2 FOR WATER CANYON GALLERY GROUNDWATER AND SYNTHETIC PORE WATER, TA-54, LOS ALAMOS NATIONAL LABORATORY, LOS ALAMOS, NEW MEXICO.

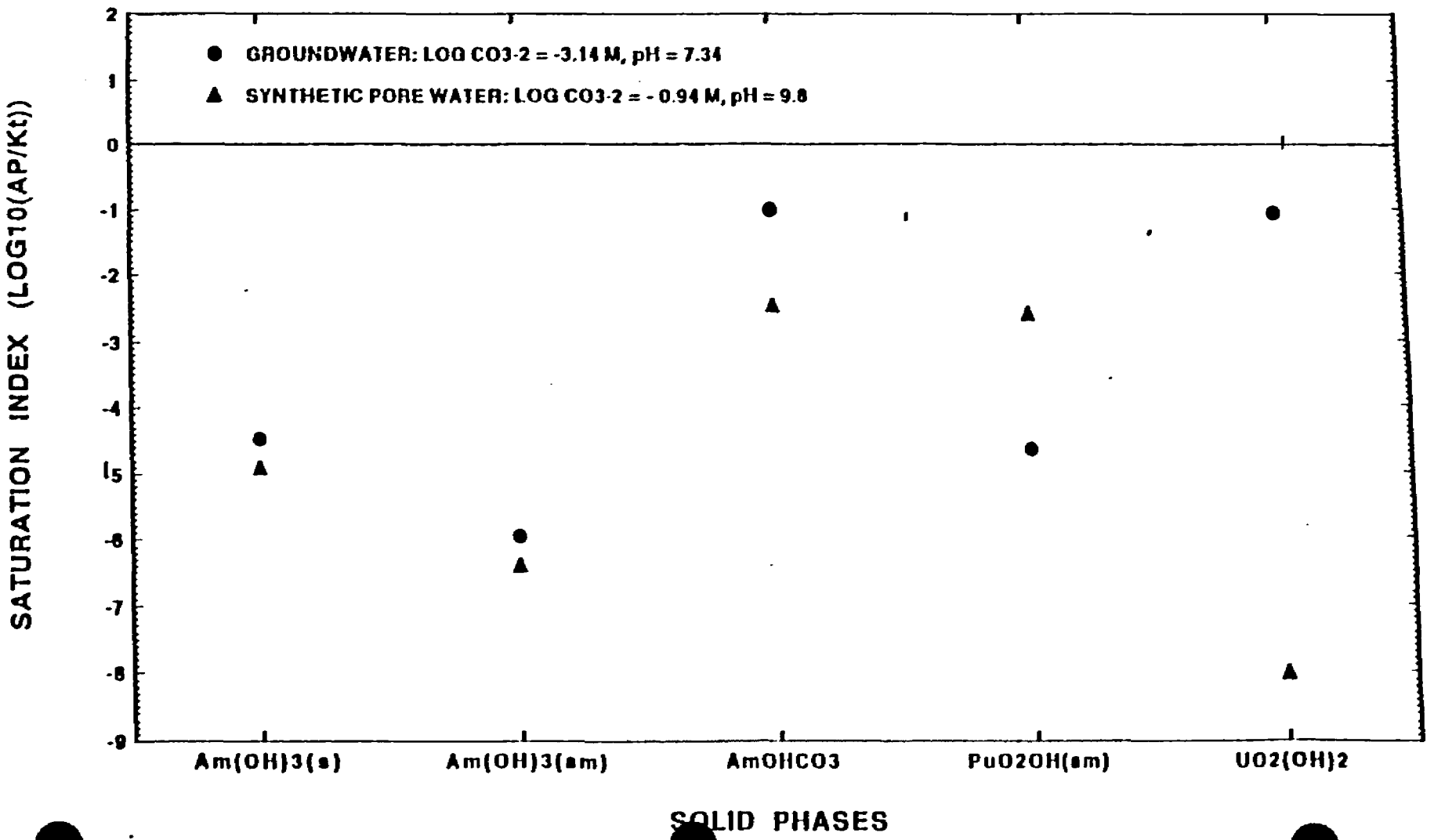

FIGURE 20. RESULTS OF SATURATION INDEX CALCULATIONS USING MINTEQA2 FOR WATER CANYON GALLERY GROUNDWATER AND SYNTHETIC POREWATER, TA-54, LOS ALAMOS NATIONAL LABORATORY, LOS ALAMOS, NEW MEXICO.

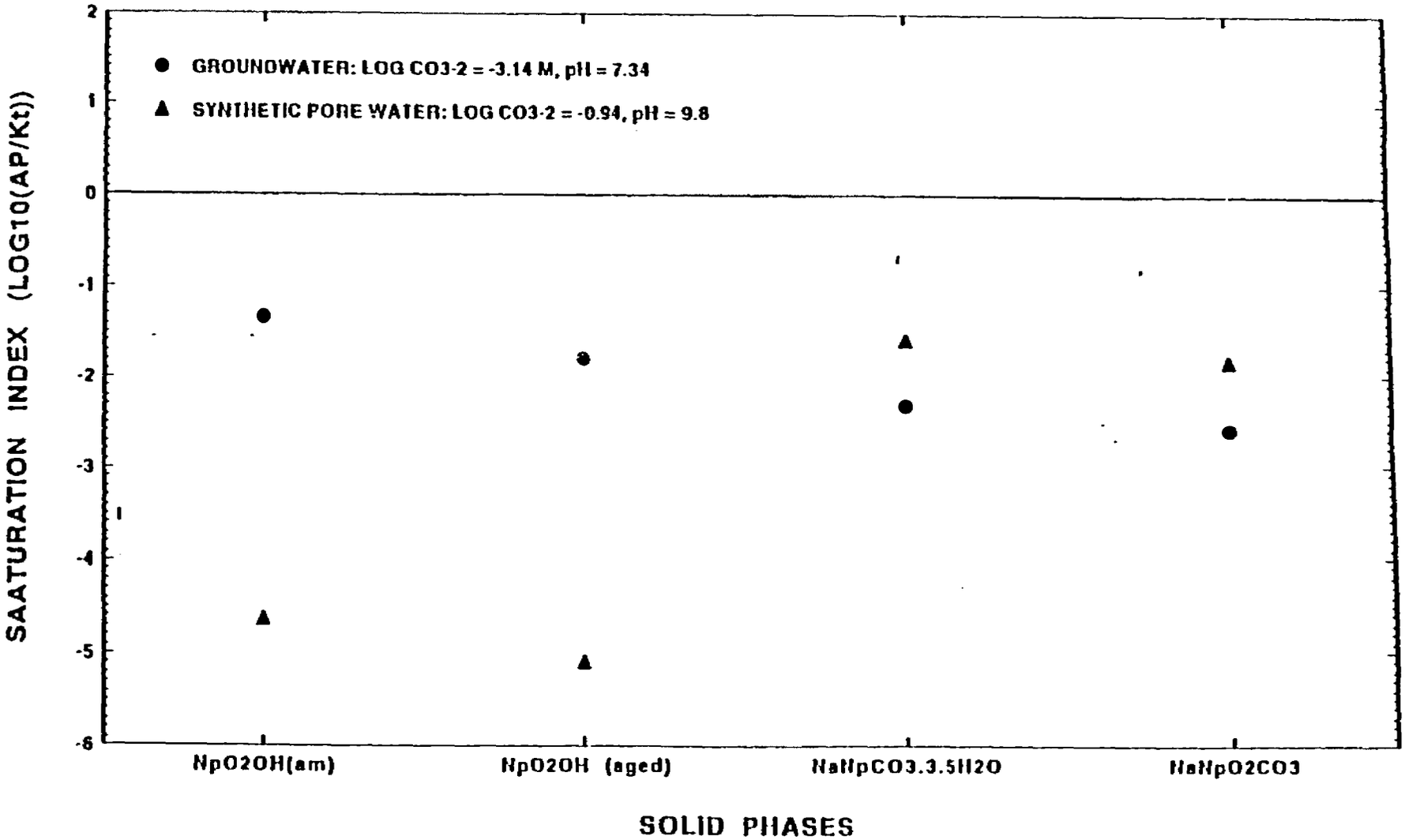

the surface functional groups. This supports the hypothesis that ligand exchange forms a bidentate surface complex, based on the geometry (hexagonal bipyramidal coordination geometry about the central actinide atom) of the basic structural unit of $AnO_2(CO_3)_3^{4-}$ reported by Clark et al. (1994). A tridentate complex is less likely than a bidentate complex because of the geometry of the three CO_3 ligands in $Am(CO_3)_3^{3-}$ and $NpO_2(CO_3)_3^{5-}$ complexes.

Based on carbon-13 nuclear magnetic resonance studies of carbonate exchange on plutonyl(VI) carbonate complexes conducted by Clark et al. (1994) and sorption modeling simulations for calcite presented by Zachara et al. (1993), ligand exchange of carbonato complexes of Am(III) and Np(V) with CO_3 surface sites (X'), forming a bidentate surface complex, are shown by the following reactions:

$$2X'\text{-}CO_3 + Am(CO_3)_3^{3-} = [2X'\text{-}(CO_3)_2AmCO_3]^{+} + 2CO_3^{2-} \qquad (2)$$

and

$$2X'\text{-}CO_3 + NpO_2(CO_3)_3^{5-} = [2X'\text{-}(CO_3)_2NpO_2CO_3]^{-} + 2CO_3^{2-}. \qquad (3)$$

X' represents the anion-specific surface sites for CO_3. These two reactions assume that $Am(CO_3)_3^{3-}$ and $NpO_2(CO_3)_3^{5-}$ are dominant complexes sorbing on the calcite surface.

Based on arguments made by Zachara et al. (1993) for other anionic complexes (SeO_3^{2-}) undergoing surface exchange reactions with calcite, the half reactions for the anionic complexes of Am(III) and Np(V) may require at least two different surface species (CO_3 and HCO_3) to successfully describe the batch-sorption data. Bicarbonate is considered as a surface-reactive species and competitor with $NpO_2(CO_3)_3^{5-}$ and $Am(CO_3)_3^{3-}$ because it is predicted to be the dominant non-complexed carbonate species (42.7%) present in the synthetic pore-water solution at a pH value of 9.8.

The distribution coefficients for $^{239}Pu(V)$ and $^{233}U(VI)$ using synthetic pore water, however, are smaller than the distribution coefficients for these two radionuclides using WCG groundwater (Tables 3 and 4). The decrease in sorption capacity of the Bandelier Tuff for Pu and U is most likely related to the speciation of these two actinides. The species PuO_2OH^0 may not undergo significant adsorption due to the lack of charge. In addition, ligand exchange is not effective for sorbing the complexes PuO_2OH^0 and PuO_2^{1+} on calcite. In the case of U(VI), the intrinsic surface exchange constants for $UO_2(CO_3)_3^{4-}$ with CO_3 surface sites must be smaller than those for $Am(CO_3)_3^{3-}$ and $NpO_2(CO_3)_3^{5-}$.

SUMMARY

Batch-sorption experiments were conducted to quantify the sorption capacity of the Bandelier Tuff (units 1g, 1v, and 2) for Am(III), Np(V), Pu(V), Tc(VII), and U(VI). The experiments were conducted using either WCG groundwater at a pH value of 7.3 or a synthetic pore-water solution at a pH value of 9.8. The WCG groundwater is characterized by a calcium-sodium-bicarbonate composition with a TDS content less than 130 mg/L. The synthetic pore water, representing pore water extracted from the Bandelier Tuff, is characterized by a sodium-bicarbonate-carbonate solution with a TDS content greater than 1300 mg/L.

At a pH value of 7.3 characteristic of WCG groundwater, the dominant aqueous complexes of Am(III), Np(V), Pu(V), Tc(VII), and U(VI) are predicted to occur as $AmCO_3^-$, NpO_2^+, PuO_2^+, TcO_4^-, and $UO_2(CO_3)_2^{2-}$, respectively. The WCG groundwater is predicted to be undersaturated with respect to calcite, $AmOHCO_3$, $Am(OH)_3$(am), $Am(OH)_3$(s), $NpO_2(OH)$(am), $NaNpCO_3 \cdot 3.5H_2O$, NpO_2OH(am), NpO_2OH(aged), $NaNpO_2CO_3$, PuO_2OH(am), and $UO_2(OH)_2$.

Based on model simulations using MINTEQA2, the dominant dissolved complexes of Am(III), Np(V), Pu(V), Tc(VII), and U(VI) in the synthetic pore water, at a pH value of 9.8 with a total carbonate concentration of $10^{-0.94}$ M, include $Am(CO_3)_3^{3-}$, $NpO_2(CO_3)_3^{5-}$, $PuO_2(OH)^0$, TcO_4^-, and $UO_2(CO_3)_3^{4-}$, respectively. The synthetic pore water is predicted to be undersaturated with respect to $AmOHCO_3$, $Am(OH)_3$(am), $Am(OH)_3$(s), $NpO_2(OH)$(am), $NaNpCO_3 \cdot 3.5H_2O$, NpO_2OH(am), NpO_2OH(aged), $NaNpO_2CO_3$, PuO_2OH(am), and $UO_2(OH)_2$. The synthetic pore water is predicted to be slightly oversaturated with respect to calcite.

Under the experimental conditions representing both transport under saturated (WCG groundwater) and unsaturated flow (synthetic pore water) conditions, the sorption capacity of the Bandelier Tuff for the radionuclides of interest decreases in the following order: Am(III) >> Pu(V) > U(VI) > Np(V) > Tc(VII). The distribution coefficients for Tc(VII) are assumed to be zero in all of the batch sorption experiments. The distribution coefficients for Am(III) and Np(V) using synthetic pore water are greater than those measured for these two actinides using WCG groundwater. It is postulated that calcite precipitated from the carbonate-rich synthetic pore water, which enhanced the sorptive capacity of the Bandelier Tuff for Am(III) and Np(V).

RECOMMENDATIONS FOR FURTHER RESEARCH

More studies should be conducted to characterize both the pore water chemistry of the Bandelier Tuff and sorption processes occurring in the vadose zone at MDA-G, TA-54. Transport under unsaturated flow conditions dominates beneath the disposal pits at MDA-G. The increased sorption of Am(III) and Np(V) on the Bandelier Tuff, at a pH value of 9.8 using synthetic pore water, with a total carbonate concentration of $10^{-0.94}$ M, has not been fully evaluated. Calcite is an important adsorbent for Np(V) carbonato species. Calcite is known to occur within the Bandelier Tuff where evaporation of matrix pore water and fracture fill solutions have occurred. Distribution coefficients for Am(III), Np(V), Pu(V), and U(VI) have not been determined using both glass-rich (unit 1g) samples of the Bandelier Tuff and buried soils potentially present beneath the disposal pits. More detailed mineralogical studies will be useful in identifying the adsorbents that are important in radionuclide transport at MDA-G. These investigations will be useful in quantifying the transport of mobile species including Np(V), under oxidizing and unsaturated flow conditions, for the performance assessment conducted at MDA-G.

ACKNOWLEDGEMENTS

The authors wish to thank Mr. John Husler (University of New Mexico) for the chemical analyses of the WCG groundwater used in the batch-sorption experiments; Dr. Phil Palmer (Materials and Chemical Design Group at LANL) for providing the acid stocks containing ^{241}Am(III), ^{243}Am(III), ^{237}Np(V), ^{239}Pu(V), ^{99m}Tc(VII), and ^{233}U(VI); Ms. Dale Counce (Geology and Geochemistry Group, EES-1 at LANL) for analyzing WCG groundwater and pore water extracted from the Bandelier Tuff; Mr. Steve Chipera (Geology and Geochemistry Group, EES-1 at LANL) for performing XRD analyses on the Bandelier Tuff samples;and Quantachrome Corporation for the BET analyses of the tuff samples.

This work was supported by the performance assessment for MDA-G, Chemical Science and Technology Group 14 at LANL. Support provided by Mr. Tony Stanford and Dr. Erik Vold, both of CST-14 group, is greatly appreciated.

REFERENCES

Allison, J. D., D. S. Brown, and K. J. Novo-Gradac, "MINTEQA2/PRODEFA2, A Geochemical Assessment Model for Environmental Systems: Version 3.0 User's Manual," EPA/600/3-91/021, U.S. Environmental Protection Agency, Athens, Georgia (1991).

Blake, W. D., F. Goff, A. I. Adams, and D. Counce, "Environmental Geochemistry for Surface and Subsurface Waters in the Pajarito Plateau and Outlying Areas, New Mexico.", Los Alamos National Laboratory Report LA-12912-MS, (1995), 43p

Brookins, D. G., "Eh-pH Diagrams for Geochemistry," Springer-Verlag, New York (1988), 176p.

Brookins, D. G., "Geochemical Aspects of Radioactive Waste Disposal," Springer-Verlag, New York (1984), 347p.

Broxton, D. E., G. Heiken, S. J. Chipera, and F. M. Jr. Byers, "Stratigraphy, Petrography, and Mineralogy of Bandelier Tuff and Cerro Toledo Deposits": *in* Earth Science Investigations for Environmental Restoration-Los Alamos National Laboratory, Technical Area-21, Los Alamos National Laboratory Report LA-12934-MS, (1995), pp. 33-63.

Clark, D. L., S. A. Ekberg, D. E., Morris, P. D. Palmer, and C. D. Tait, "Actinide (IV) and Actinide(VI) Carbonate Speciation Studies by PAS and NMR Spectroscopies", LA-12820-MS, Los Alamos National Laboratory (1995), 62 p.

Conca, J. and J. Wright, "Find Transport Data Faster", Soil and Groundwater Cleanup, December 1995, (1995), pp. 14-26.

Davenport, D. W., "Micromorphology, Mineralogy, and Genesis of Soils and Fracture Fills on the Pajarito Plateau, New Mexico", Ph.D. Dissertation, Texas Tech University, Lubbock (1993), 109p.

Dzombak, D. A. and F. M. M. Morel, "Surface Complexation Modeling", John Wiley & Sons, New York (1990), 393p.

Grenthe, I., J. Fuger, R. J. M. Konings, R. J. Lemire, A. B. Muller, C. Nguyen-Trung, and H. Wanner, Chemical Thermodynamics of Uranium," Nuclear Energy agency Thermochemical Data Base Project (Saclay: OECD Nuclear Energy Agency, (1992), pp. 29-62.

Hsi, C.-K. and D. Langmuir, "Adsorption of Uranyl Onto Ferric Oxyhydroxides: Application of the Surface Complexation Site-Binding Model," Geochim. Cosmochim. Acta, vol. 49 (1985), pp. 1931-1941.

Kerrisk, J. F. and R. J. Silva, "A Consistent Set of Thermodynamic Constants for Americium(III) Species with Hydroxyl and Carbonate": *in* Proceedings of the Workshop on Geochemical Modeling, Fallen Leaf Lake, California, (1986), pp. 167-175.

Krier, D., P. Longmire, R. Gilkeson, and J. Turin, "Geologic, Geohydrologic, and Geochemical Data Summary of MDA G, TA-54, Los Alamos National

Laboratory, Los Alamos, New Mexico", LA-UR-95-2696, Los Alamos National Laboratory (1995).

Lemire, R. J., "An Assessment of the Thermodynamic Behavior of Neptunium in Water and Model Groundwater from 25 to 150°C", AECL-7817, Pinawa, Manitoba: Atomic Energy of Canada Limited (AECL) (1984).

Lemire, R. J. and P. R. Tremaine, "Uranium and Plutonium Equilibria in Aqueous Solutions to 200°C", Jour. Chem. Eng. Data, vol. 25 (1980), pp. 361-370.

Longmire, P., S. Reneau, P. Watt, L. McFadden, J. Gardner, C. Duffy, and R. Ryti, "Natural Background Geochemistry, Geomorphology, and Pedogenesis of Selected Soil Profiles and Bandelier Tuff, Los Alamos, New Mexico ", LA-12913-MS, Los Alamos National Laboratory (1995), 176p.

Nitsche, H., R. C. Gatti, E. M. Standifer, S. C. Lee, A. Muller, T. Prussin, R. S. Deinhammer, H. Maurer, K. Becraft, S. Leung, and S. A. Carpenter, "Measured Solubilities and Speciations of Neptunium, Plutonium, and Americium in a Typical Groundwater (J-13) from the Yucca Mountain Region, Milestone Report 3010-WBS 1.2.3.4.1.3.1," LA-12562-MS, Los Alamos National Laboratory (1993), 127p.

Parks, G. A., "Surface Chemistry of Oxides in Aqueous Systems": *in* Stumm, W. (ed.), Equilibrium Concepts in Aqueous Systems, Adv. Chem. Ser. 67, Am. Chem. Soc., Washington (1967), pp. 121-160.

Rard, J. A., "Critical Review of the Chemistry and Thermodynamics of Technetium and Some of its Inorganic Compounds and Aqueous Species," UCRL-53440, Livermore, California (1983): LLNL.

Rundberg, R. S., "Assessment Report on the Kinetics of Radionuclide Adsorption on Yucca Mountain Tuff," LA-11026-MS, Los Alamos National Laboratory (1987), 93p.

Thomas, K. W., "Summary of Sorption Measurements Performed with Yucca Mountain, Nevada, Tuff Samples and Water from Well J-13", LA-10960-MS, Los Alamos National Laboratory (1987), 37p.

Triay, I. R., C. R. Cotter, M. H. Huddleston, D. E. Leonard, S. C. Weaver, S. J. Chipera, D. L. Bish, A. Meijer, and J. A. Canepa, "Batch Sorption Results for Neptunium Transport Through Yucca Mountain Tuffs: Yucca Mountain Site Characterization Program Milestone #3349," Los Alamos National Laboratory (1996), LA-12961-MS, 67p.

Triay, I. R., C. R. Cotter, S. M. Kraus, M. H. Huddleston, S. J. Chipera, and D. L. Bish, "Report on Radionuclide Sorption in Yucca Mountain Tuffs with J-13 Well Water: Neptunium, Uranium, and Plutonium Milestone #3338," Los Alamos National Laboratory (1994), draft, 12p.

Vaniman, D. and S. Chipera, "Mesa-Penetrating Fractures, Fracture Mineralogy, and Projected Fault Traces at Pajarito Mesa," *in* Geological Site Characterization for the Proposed Mixed Waste Disposal Facility, Los

Alamos National Laboratory, LA-13089-MS, Los Alamos National Laboratory (1995), pp. 71-85.

Zachara, J. M., C. E. Cowan, and C. T. Resch, "Metal Cation/Anion Adsorption on Calcium Carbonate: Implications to Metal Ion Concentrations in Groundwater":*in* Metals in Groundwater, H. E. Allen, E. M. Perdue, and D. S. Brown (eds.) , Lewis Publishers, Chelsea, MI, pp. 37-71.

Zyvoloski, G. A., Z. V. Dash, and S. Kelhar, "FEHM: Finite Element Heat and Mass Transfer Code," LA-11224-MS Los Alamos National Laboratory (1988).

APPENDIX A

CHEMICAL ANALYSES OF WATER CANYON GALLERY GROUNDWATER

Summary of Chemical Analysis of Groundwater Samples, Water Canyon Gallery, Los Alamos, New Mexico.

Date Analysis[a]	08/18/92*	05/20/93*	04/04/96**	04/04/96** (not filtered)
T(°C)	15.3	11.3	25	25
Al	<0.10	0.20	<0.1	<0.1
B	<0.05	<0.01	NA	NA
Ba	<0.05	<0.05	NA	NA
Ca	7.20	6.94	6.8	6.5
Cl	0.64	0.69	0.66	0.42
Cr	0.003	<0.002	NA	NA
F	0.05	0.06	0.04	0.05
Fe	<0.01	0.05	<0.1	<0.1
HCO_3	52.8	44.6	52.0	52.0
K	1.72	1.79	1.5	1.6
Mg	3.05	2.79	2.5	2.8
Mn	<0.01	<0.01	<0.01	<0.01
Na	6.30	4.90	6.60	6.60
NH_4	<0.05	<0.02	NA	NA
NO_3	0.48	0.98	0.05	0.18
pH[b]	7.4	7.6	7.40	7.60
SiO_2	43.7	39.8	42.4	42.0
SO_4	1.05	2.85	1.18	1.33
Sr	0.07	0.07	NA	NA
Zn	0.02	0.05	NA	NA
TDS[c]	117	106	114	NA

* Groundwater analyzed at Los Alamos National Laboratory, EES-1, Dale Counce analyst.
** Groundwater analyzed at University of New Mexico, Dept of Earth and Planetary Sciences, John Husler analyst.
a. All analyses are in mg/L, except where noted.
NA means not analyzed.
b. Standard units.
c. TDS is total dissolved solids.

APPENDIX B

RADIONUCLIDE BATCH SORPTION EXPERIMENTAL DATA AND RESULTS USING WATER CANYON GALLERY GROUNDWATER

AREA G SORPTION DATA INFORMATION SHEET	
Experiment Number	Bandelier Sorp.WCG
ID of Water Used in Experiment	WCG-1F.1
Notebook Reference	Area"G" Sorption Studies Opened 1/29/96 for Pat Longmire
Tracer Solution ID#	Am.SOR.BT.WCG.5/21/96 Pu.SOR.BT.WCG.5/21/96 Np.SOR.BT.WCG.5/21/96 U.SOR.BT.WCG.6/06/96 Tc.SOR.BT.WCG.5/21/96
Notebook with Information on Tracer Solution	LA-CST-NBK-95-027
YMP Balance ID# Used Before Addition of Tracer	METTLER PE 1600 757322
YMP Balance Calibration Due Date	11/29/96
YMP Balance ID# Used after Addition of Tracer	Sartorius
YMP Balance Calibration Due Date	12/8/96
YMP Balance ID# Used in Glovebox	Sartorius
YMP Balance Calibration Due Date	12/8/96
For Glovebox, YMP Balance ID# Used to Weigh Scintillation Vials and Aliquots	Sartorius
YMP Balance Calibration Due Date	12/8/96
Mineral Code IDs	Bandelier Tuff: 108.0'-109.5', 79.9'-80.0', 79.1'-79.7', 74.0'-75.0', 65.0'-66.0', 10.8'-12.0', 91.0'
Sieving Information	Dry
Notebook Reference for Information on Solid Samples	TWS-INC-01-93-09
Type of Oak Ridge Container Used for Sorption Experiment	POLYCARBONATE
Detailed Procedure Used - Sorption	LANL-CST-DP-86
DP Revision Number	R1
Glovebox Information	
Glovebox Temperature Before Adding Equilibration Water to OR Tubes, °F	69.4
Glovebox Humidity Before Adding Equilibration Water to OR Tubes, %	61
Glovebox Pressure Before Adding Equilibration Water to OR Tubes, Torr	586
Glovebox CO2 Reading Before Adding Equilibration Water to OR Tubes, %	0.405
Arbitrary Glovebox Air Pressure Gauge Input Reading Before Adding Equilibration Water to OR Tubes	N/A
Arbitrary Glovebox CO2 Pressure Gauge Input Reading Before Adding Equilibration Water to OR Tubes	N/A
Detailed Procedure Used - Glovebox	LANL-CST-DP-100
DP Revision Number	R0
Glovebox Humidity Before Adding Tracer Solution to OR Tubes, %	59.2
Glovebox Pressure Before Adding Tracer Solution to OR Tubes, Torr	580
Arbitrary Glovebox Air Pressure Gauge Input Reading Before Adding Tracer Solution to OR Tubes	N/A
Arbitrary Glovebox CO2 Pressure Gauge Input Reading Before Adding Tracer Solution to OR Tubes	N/A
Back-up Equilibration Water pH after Sorption	N/A
pH Meter Used YMP ID#	COLE PALMER Digi-Sense H93005911
pH Buffers Used/Manufacturer	7/Fisher,10/VWR
pH Buffer 7, Lot #/Expiration Date	953603-24/ June 96
pH Buffer 10, Lot #/Expiration Date	9409028, August 96
Detailed Procedure Used	LANL-CST-DP-35
DP Revision Number	R3
Glovebox Temperature after Sorption, °C	67.4
Glovebox Humidity after Sorption, %	67
Glovebox Pressure after Sorption, Torr	586
Glovebox CO2 Reading after Sorption, %	0.4
Arbitrary Glovebox Air Pressure Gauge Input Reading After Sorption	N/A
Arbitrary Glovebox CO2 Pressure Gauge Input Reading After Sorption	N/A
Glove Box Identification Code	GB 4
Hygrometer Used in Glovebox	No ID - Fisher Scientific in GB 4
Controlled Atmosphere Pressure Gauge Used in Glovebox	N/A
CO2 and Air Input Pressure Gauges Used in Glovebox	N/A

Notebook Reference for CO2/Air Input Pressure Gauge Calibration	YMP SORP/DESORP BINDER II VOL 2 TWS-INC-10-93-06
Volumetric Flow for Air Input, sccm	80
Volumetric Flow for CO2 Input, sccm	37
pH Measurement	
pH Meter Used, YMP ID#	COLE PALMER DigiSense H93005911
Detailed Procedure Used	LANL-INC-DP-35
DP Revision Number	R0
Tracer Solution pH Before Adding to OR Tubes	7.40, 7.40, 7.27, 7.25, 7.34
Glovebox Temperature Before Adding Tracer Solution to OR Tubes, °F	69.5
Glovebox Humidity Before Adding Tracer Solution to OR Tubes, %	62.4
pH Buffer 4, Manufacturer/Lot #/Expiration Date	N/A
Reading for pH 4 Buffer (Prior to Making Measurements)	N/A
Reading for pH 4 Buffer (after Making Measurements)	N/A
pH Buffer 7, Manufacturer/Lot #/Expiration Date	Fisher/ 953693-24/June 96
Reading for pH 7 Buffer (Prior to Making Measurements)	7.17
Reading for pH 7 Buffer (after Making Measurements)	7.18
pH Buffer 10 Manufacturer/Lot #/Expiration Date	VWR/ 9409028/ August 96
Reading for pH 10 Buffer (Prior to Making Measurements)	10.03
Reading for pH 10 Buffer (after Making Measurements)	10.06
Eh Measurement	
Detailed Procedure Used	LANL-CST-DP-102, R0
YMP ID# of Eh Meter	N/A
Electrodes Used for Eh Measurement	PLATINUM WIRE
Zobell Lot Number and Ideal Value	N/A
Zobell Solution Preparation Date	N/A
Eh of Zobell Solution (Prior to Making Measurements), mV	N/A
Eh of Zobell Solution (after making Measurements) mV	N/A
Temperature Range for Eh Measurements °C	N/A
Eh of Water Used in the Experiment, mV	N/A
Verification of Liquid Scintillation Counter	
YMP Counter ID#	841221, 901133, 764745
ID# of Low Standard Counted	St-Pu-1 & Np 2-4/94 A, Am 243 1/96 Mid, U233-1/96 Low
Expected CPM of Standard Counted	842, 233, 1462, 97
Total Activity (-Bkg)	776.15, 235.8, 1385.6, 100.05
ID# of High Standard Counted	ST-Pu-3, NIST Np1-4/94 A, Am 243 1/96 High, U233 Mid
Expected CPM of Standard Counted	8230, 1032, 46060, 1318
Total Activity (-Bkg)	8286.85, 1078.89, 43088.5, 1251.97
Detailed Procedure Used	LANL-CST-DP-79
DP Revision Number	R1
Explanation of Sample Coding	WC refers to the type of water used; BT refers to Bandelier Tuff; the number after BT is the core depth; the last number is a unique number assigned to each sample; GB refers to the Glove Box; CTR refers to the controls, STD refers to the standards.
Verification of Gamma Counter for Technetium 95m	
YMP Counter ID#	Auto-Gamma 5000 Counter
Detailed Procedure Used	Gamma Counter Tc 95m Notebook Proced
Notebook & Pages	LA-CST-NBK-95-015 E2-E21
Vendor Sample Analysis Information	
Vendor Analysis Notebook Reference	N/A
Acceptance Plan Notebook Reference	N/A
Location of Data	
Experimental Data (Notebook ID#)	Area G Sorption 1/29/96
Experimental Data (Page(s) #)	Section G
Reduced Data (Optical disk #)	TWS-INC-05-93-05
Reduced Data (Subdirectory)	AREA G SORPTION
Reduced Data (File name)	DATA SHEET NAT.WCG

	A	B	C	D	E	F	G	H	I	J	K
1	Sample Identification	Sorption Time	Experiment No	Atmosphere	Desired Pu, Am, Np, U, Tc Tracer Solution Activity, CFM/g	Description of Solid (Bandelier Tuff)	Particle Size, Micrometers (If Sieved)	Sieving Information	Type of Water Used if Wet Sieved	Tube + Cap Mass, g	Tube + Cap + Mineral Mass, g
2	WC.BT.109-2001.GB	3 weeks	Bandelier, Sorp WCG	0.4% CO_2	260 cf Am 243	108.0'-109.5'	< 500	Dry	N/A	23.05	24.05
3	WC.BT.109-2002.GB	3 weeks	Bandelier, Sorp WCG	0.4% CO_2	260 cf Am 243	108.0'-109.5'	< 500	Dry.	N/A	23.20	24.19
4	WC.BT.80-2003.GB	3 weeks	Bandelier, Sorp WCG	0.4% CO_2	260 cf Am 243	79.0'-80.0' Fe rich	< 500	Dry	N/A	22.74	23.75
5	WC.BT.80-2004.GB	3 weeks	Bandelier, Sorp WCG	0.4% CO_2	260 cf Am 243	79.0'-80.0' Fe rich	< 500	Dry	N/A	22.65	23.65
6	WC.BT.75-2005.GB	3 weeks	Bandelier, Sorp WCG	0.4% CO_2	260 cf Am 243	74.0'-75.0'	< 500	Dry	N/A	22.93	23.93
7	WC.BT.75-2006.GB	3 weeks	Bandelier, Sorp WCG	0.4% CO_2	260 cf Am 243	74.0'-75.0'	< 500	Dry	N/A	22.93	23.94
8	WC.BT.79-2007.GB	3 weeks	Bandelier, Sorp WCG	0.4% CO_2	260 cf Am 243	73.1'-73.7'	< 500	Dry	N/A	22.81	22.81
9	WC.BT.79-2008.GB	3 weeks	Bandelier, Sorp WCG	0.4% CO_2	260 cf Am 243	73.1'-73.7'	< 500	Dry	N/A	22.83	22.83
10	WC.BT.65-2009.GB	3 weeks	Bandelier, Sorp WCG	0.4% CO_2	260 cf Am 243	65.0'-66.0'	< 500	Dry	N/A	23.31	23.31
11	WC.BT.66-2010.GB	3 weeks	Bandelier, Sorp WCG	0.4% CO_2	260 cf Am 243	65.0'-66.0'	< 500	Dry	N/A	22.82	22.82
12	WC.BT.12-2011.GB	3 weeks	Bandelier, Sorp WCG	0.4% CO_2	260 cf Am 243	10.8'-12.0'	< 500	Dry	N/A	23.38	23.38
13	WC.BT.12-2012.GB	3 weeks	Bandelier, Sorp WCG	0.4% CO_2	260 cf Am 243	10.8'-12.0'	< 500	Dry	N/A	23.15	23.15
14	WC.BT.91-2061.GB	3 weeks	Bandelier, Sorp WCG	0.4% CO_2	260 cf Am 243	91.0	< 500	Dry	N/A	22.68	22.68
15	WC.BT.91-2062.GB	3 weeks	Bandelier, Sorp WCG	0.4% CO_2	260 cf Am 243	91.0	< 500	Dry	N/A	22.65	22.65
16	Am.SOR.BT.WCG 5/21/95_CTR 1	3 weeks	Bandelier, Sorp WCG	0.4% CO_2	260 cf Am 243	N/A	N/A	N/A	N/A	23.13	
17	Am.SOR.BT.WCG 5/21/95_CTR 2	3 weeks	Bandelier, Sorp WCG	0.4% CO_2	260 cf Am 243	N/A	N/A	N/A	N/A	23.12	
18	Am.SOR.BT.WCG 5/21/95_STD 1										
19	Am.SOR.BT.WCG 5/21/95_STD 2										
20											
21	WC.BT.109-2013.GB	3 weeks	Bandelier, Sorp WCG	0.4% CO_2	15000 cf Np 237	108.0'-109.5'	< 500	Dry	N/A	23.18	24.17
22	WC.BT.109-2014.GB	3 weeks	Bandelier, Sorp WCG	0.4% CO_2	15000 cf Np 237	108.0'-109.5'	< 500	Dry	N/A	23.00	23.99
23	WC.BT.80-2015.GB	3 weeks	Bandelier, Sorp WCG	0.4% CO_2	15000 cf Np 237	79.0'-80.0' Fe rich	< 500	Dry	N/A	22.93	23.93
24	WC.BT.80-2016.GB	3 weeks	Bandelier, Sorp WCG	0.4% CO_2	15000 cf Np 237	79.0'-80.0' Fe rich	< 500	Dry	N/A	22.97	23.96
25	WC.BT.75-2017.GB	3 weeks	Bandelier, Sorp WCG	0.4% CO_2	15000 cf Np 237	74.0'-75.0'	< 500	Dry	N/A	22.95	23.97
26	WC.BT.75-2018.GB	3 weeks	Bandelier, Sorp WCG	0.4% CO_2	15000 cf Np 237	74.0'-75.0'	< 500	Dry	N/A	23.03	24.10
27	WC.BT.79-2019.GB	3 weeks	Bandelier, Sorp WCG	0.4% CO_2	15000 cf Np 237	73.1'-73.7'	< 500	Dry	N/A	22.87	22.87
28	WC.BT.79-2020.GB	3 weeks	Bandelier, Sorp WCG	0.4% CO_2	15000 cf Np 237	73.1'-73.7'	< 500	Dry	N/A	22.67	22.67
29	WC.BT.65-2021.GB	3 weeks	Bandelier, Sorp WCG	0.4% CO_2	15000 cf Np 237	65.0'-66.0'	< 500	Dry	N/A	23.04	23.04
30	WC.BT.66-2022.GB	3 weeks	Bandelier, Sorp WCG	0.4% CO_2	15000 cf Np 237	65.0'-66.0'	< 500	Dry	N/A	22.64	22.64
31	WC.BT.12-2023.GB	3 weeks	Bandelier, Sorp WCG	0.4% CO_2	15000 cf Np 237	10.8'-12.0'	< 500	Dry	N/A	22.84	22.84
32	WC.BT.12-2024.GB	3 weeks	Bandelier, Sorp WCG	0.4% CO_2	15000 cf Np 237	10.8'-12.0'	< 500	Dry	N/A	23.01	23.01
33	WC.BT.91-2063.GB	3 weeks	Bandelier, Sorp WCG	0.4% CO_2	15000 cf Np 237	91.0	< 500	Dry	N/A	22.87	22.87

Bandelier Sorp NAT WCG

	A	B	C	D	E	F	G	H	I	J	K
1	Sample Identification	Sorption Time	Experiment No.	Atmosphere	Desired Pu, Am, Np, U, Tc Tracer Solution Activity, CPM/g	Description of Solid (Bandelier Tuff)	Particle Size, Micrometers (If Sieved)	Sieving Information	Type of Water Used If Wet Sieved	Tube + Cap Mass, g	Tube + Cap + Mineral Mass, g
34	WC.BT.91-2064.GB	3 weeks	Bandelier, Sorp WCG	0.4% CO_2	15000 cl Np 237	91 0	< 500	Dry	N/A	22.69	22.69
35	Np.SOR.BT.WCG 5/21/96_CTR 3	3 weeks	Bandelier, Sorp WCG	0.4% CO_2	15000 cl Np 237	N/A	N/A	N/A	N/A	22.61	
36	Np.SOR.BT.WCG 5/21/96_CTR 4	3 weeks	Bandelier, Sorp WCG	0.4% CO_2	15000 cl Np 237	N/A	N/A	N/A	N/A	22.95	
37	Np.SOR.BT.WCG 5/21/96_STD 3										
38	Np.SOR.BT.WCG 5/21/96_STD 4										
39											
40	WC.BT.100-2025.GB	3 weeks	Bandelier, Sorp WCG	0.4% CO_2	9600 cl Pu 239	100 0'-100.5'	< 500	Dry	N/A	22.84	23.85
41	WC.BT.100-2026.GB	3 weeks	Bandelier, Sorp WCG	0.4% CO_2	9600 cl Pu 239	100 0'-100.5'	< 500	Dry	N/A	22.85	23.87
42	WC.BT.80-2027.GB	3 weeks	Bandelier, Sorp WCG	0.4% CO_2	9600 cl Pu 239	79.8'-80.0' Fe rich	< 500	Dry	N/A	23.15	24.14
43	WC.BT.80-2028.GB	3 weeks	Bandelier, Sorp WCG	0.4% CO_2	9600 cl Pu 239	79.8-80.0' Fe rich	< 500	Dry	N/A	23.18	24.18
44	WC.BT.75-2029.GB	3 weeks	Bandelier, Sorp WCG	0.4% CO_2	9600 cl Pu 239	74.0'-75.0'	< 500	Dry	N/A	22.82	23.83
45	WC.BT.75-2030.GB	3 weeks	Bandelier, Sorp WCG	0.4% CO_2	9600 cl Pu 239	74.0'-75.0'	< 500	Dry	N/A	22.85	23.86
46	WC.BT.79-2031.GB	3 weeks	Bandelier, Sorp WCG	0.4% CO_2	9600 cl Pu 239	79.1'-79.7'	< 500	Dry	N/A	23.15	23.15
47	WC.BT.79-2032.GB	3 weeks	Bandelier, Sorp WCG	0.4% CO_2	9600 cl Pu 239	79.1'-79.7'	< 500	Dry	N/A	23.18	23.18
48	WC.BT.66-2033.GB	3 weeks	Bandelier, Sorp WCG	0.4% CO_2	9600 cl Pu 239	65.8'-66.0'	< 500	Dry	N/A	23.15	23.15
49	WC.BT.66-2034.GB	3 weeks	Bandelier, Sorp WCG	0.4% CO_2	9600 cl Pu 239	65.8'-66.0'	< 500	Dry	N/A	23.00	23.00
50	WC.BT.12-2035.GB	3 weeks	Bandelier, Sorp WCG	0.4% CO_2	9600 cl Pu 239	12.8'-12.0'	< 500	Dry	N/A	22.88	22.88
51	WC.BT.12-2036.GB	3 weeks	Bandelier, Sorp WCG	0.4% CO_2	9600 cl Pu 239	12.8'-12.0'	< 500	Dry	N/A	23.04	23.04
52	WC.BT.9-2065.GB	3 weeks	Bandelier, Sorp WCG	0.4% CO_2	9600 cl Pu 239	9.1 0	< 500	Dry	N/A	23.13	23.13
53	WC.BT.91-2066.GB	3 weeks	Bandelier, Sorp WCG	0.4% CO_2	9600 cl Pu 239	91 0	< 500	Dry	N/A	22.62	22.62
54	Pu.SOR.BT.WCG 5/21/96_CTR 5	3 weeks	Bandelier, Sorp WCG	0.4% CO_2	9600 cl Pu 239	N/A	N/A	N/A	N/A	22.95	
55	Pu.SOR.BT.WCG 5/21/96_CTR 6	3 weeks	Bandelier, Sorp WCG	0.4% CO_2	9600 cl Pu 239	N/A	N/A	N/A	N/A	22.72	
56	Pu.SOR.BT.WCG 5/21/96_STD 5										
57	Pu.SOR.BT.WCG 5/21/96_STD 6										
58											
59	WC.BT.100-2037.GB	3 weeks	Bandelier, Sorp WCG	0.4% CO_2	18200 cl U 233	100 0'-100.5'	< 500	Dry	N/A	23.03	23.03
60	WC.BT.100-2038.GB	3 weeks	Bandelier, Sorp WCG	0.4% CO_2	18200 cl U 233	100 0'-100.5'	< 500	Dry	N/A	23.00	23.00
61	WC.BT.80-2039.GB	3 weeks	Bandelier, Sorp WCG	0.4% CO_2	18200 cl U 233	79.8'-80.0' Fe rich	< 500	Dry	N/A	22.68	22.68
62	WC.BT.80-2040.GB	3 weeks	Bandelier, Sorp WCG	0.4% CO_2	18200 cl U 233	79.8'-80.0' Fe rich	< 500	Dry	N/A	23.08	23.08
63	WC.BT.75-2041.GB	3 weeks	Bandelier, Sorp WCG	0.4% CO_2	18200 cl U 233	74.0'-75.0'	< 500	Dry	N/A	22.93	22.93
64	WC.BT.75-2042.GB	3 weeks	Bandelier, Sorp WCG	0.4% CO_2	18200 cl U 233	74.0'-75.0'	< 500	Dry	N/A	23.04	23.04
65	WC.BT.79-2043.GB	3 weeks	Bandelier, Sorp WCG	0.4% CO_2	18200 cl U 233	79.1'-79.7'	< 500	Dry	N/A	23.05	23.05

	A	B	C	D	E	F	G	H	I	J	K
1	Sample Identification	Sorption Time	Experiment No	Atmosphere	Desired Pu, Am, Np, U, Tc Tracer Solution Activity, Ci/Mg	Description of Solid (Bandelier Tuff)	Particle Size, Micrometers (If Sieved)	Sieving Information	Type of Water Used If Wet Sieved	Tube + Cap Mass, g	Tube + Cap + Mineral Mass, g
66	WC.BT.79-2044.GB	3 weeks	Bandelier Sorp WCG	0.4% CO_2	18200 cf U 233	79.1-79.7	< 500	Dry	N/A	23.01	23.01
67	WC.BT.65-2045.GB	3 weeks	Bandelier Sorp WCG	0.4% CO_2	18200 cf U 233	65.0-65.0	< 500	Dry	N/A	22.74	22.74
68	WC.BT.65-2046.GB	3 weeks	Bandelier Sorp WCG	0.4% CO_2	18200 cf U 233	65.0-65.0	< 500	Dry	N/A	23.15	23.15
69	WC.BT.12-2047.GB	3 weeks	Bandelier Sorp WCG	0.4% CO_2	18200 cf U 233	10.8-12.8	< 500	Dry	N/A	23.03	23.03
70	WC.BT.12-2048.GB	3 weeks	Bandelier Sorp WCG	0.4% CO_2	18200 cf U 233	10.8-12.8	< 500	Dry	N/A	23.19	23.19
71	WC.BT.91-2067.GB	3 weeks	Bandelier Sorp WCG	0.4% CO_2	18200 cf U 233	91.0	< 500	Dry	N/A	22.75	22.75
72	WC.BT.91-2068.GB	3 weeks	Bandelier Sorp WCG	0.4% CO_2	18200 cf U 233	91.0	< 500	Dry	N/A	22.82	22.82
73	U.SOR.BT.WCG 5/21/98_CTR 7	3 weeks	Bandelier Sorp WCG	0.4% CO_2	18200 cf U 233	N/A	N/A	N/A	N/A	23.14	
74	U.SOR.BT.WCG 5/21/98_CTR 8	3 weeks	Bandelier Sorp WCG	0.4% CO_2	18200 cf U 233	N/A	N/A	N/A	N/A	22.76	
75	U.SOR.BT.WCG 5/21/98_STD 7										
76	U.SOR.BT.WCG 5/21/98_STD 8										
77											
78	WC.BT.109-2049.GB	3 weeks	Bandelier Sorp WCG	0.4% CO_2	34000 cf Tc 95	108.0'-109.5'	< 500	Dry	N/A	22.85	22.85
79	WC.BT.109-2050.GB	3 weeks	Bandelier Sorp WCG	0.4% CO_2	34000 cf Tc 95	108.0'-109.5'	< 500	Dry	N/A	23.16	23.16
80	WC.BT.80-2051.GB	3 weeks	Bandelier Sorp WCG	0.4% CO_2	34000 cf Tc 95	79.8'-80.0' Fe rich	< 500	Dry	N/A	22.93	22.93
81	WC.BT.80-2052.GB	3 weeks	Bandelier Sorp WCG	0.4% CO_2	34000 cf Tc 95	79.8'-80.0' Fe rich	< 500	Dry	N/A	22.93	22.93
82	WC.BT.75-2053.GB	3 weeks	Bandelier Sorp WCG	0.4% CO_2	34000 cf Tc 95	74.0'-75.0'	< 500	Dry	N/A	22.70	22.70
83	WC.BT.75-2054.GB	3 weeks	Bandelier Sorp WCG	0.4% CO_2	34000 cf Tc 95	74.0'-75.0'	< 500	Dry	N/A	22.69	22.69
84	WC.BT.79-2055.GB	3 weeks	Bandelier Sorp WCG	0.4% CO_2	34000 cf Tc 95	79.1'-79.7'	< 500	Dry	N/A	22.92	22.92
85	WC.BT.79-2056.GB	3 weeks	Bandelier Sorp WCG	0.4% CO_2	34000 cf Tc 95	79.1'-79.7'	< 500	Dry	N/A	22.79	22.79
86	WC.BT.65-2057.GB	3 weeks	Bandelier Sorp WCG	0.4% CO_2	34000 cf Tc 95	65.0'-65.0'	< 500	Dry	N/A	23.04	23.04
87	WC.BT.65-2058.GB	3 weeks	Bandelier Sorp WCG	0.4% CO_2	34000 cf Tc 95	65.0'-65.0'	< 500	Dry	N/A	22.85	22.85
88	WC.BT.12-2059.GB	3 weeks	Bandelier Sorp WCG	0.4% CO_2	34000 cf Tc 95	10.8'-12.8'	< 500	Dry	N/A	23.00	23.00
89	WC.BT.12-2060.GB	3 weeks	Bandelier Sorp WCG	0.4% CO_2	34000 cf Tc 95	10.8'-12.8'	< 500	Dry	N/A	22.87	22.87
90	WC.BT.91-2069.GB	3 weeks	Bandelier Sorp WCG	0.4% CO_2	34000 cf Tc 95	91.0	< 500	Dry	N/A	22.85	22.85
91	WC.BT.91-2070.GB	3 weeks	Bandelier Sorp WCG	0.4% CO_2	34000 cf Tc 95	91.0	< 500	Dry	N/A	22.76	22.76
92	Tc.SOR.BT.WCG 5/21/98_CTR 9	3 weeks	Bandelier Sorp WCG	0.4% CO_2	34000 cf Tc 95	N/A	N/A	N/A	N/A	23.09	
93	Tc.SOR.BT.WCG 5/21/98_CTR 10	3 weeks	Bandelier Sorp WCG	0.4% CO_2	34000 cf Tc 95	N/A	N/A	N/A	N/A	22.95	
94	Tc.SOR.BT.WCG 5/21/98_STD 9										
95	Tc.SOR.BT.WCG 5/21/98_STD 10										

Bentley Soap NAT WCG

	A	L	M	N	O	P	Q	R	S	T	U
1	Sample Identification	Mineral Mass, g (Col K-Col J)	Tube + Cap + Mineral + Water Mass, g	Water Mass, g (Col M-Col K)	Julian Date Pretreatment Started '96	Julian Date Pretreatment Ended '96	Period of Pretreatment, Days	Tube + Cap + Mineral + Water after Pretreatment Mass, g	% Evaporation during Pretreatment ((Col N-Col S) /Col N*100)	Tube + Cap + Mineral + Water after Decantation Mass, g	pH of Water after Pretreatment
2	WC.BT.109-2001.GB	0.93	43.91	19.86	150.6140	162.533	11.9250	43.88	0.07	25.12	7.46
3	WC.BT.109-2002.GB	0.93	43.92	19.73	150.6140	162.533	11.9250	43.83	0.07	25.22	N/A
4	WC.BT.80-2003.GB	1.01	43.50	19.75	150.6140	162.533	11.9250	43.43	0.02	24.97	7.25
5	WC.BT.80-2004.GB	1.00	42.93	19.25	150.6140	162.533	11.9250	42.65	0.59	24.82	N/A
6	WC.BT.75-2005.GB	1.00	43.79	19.83	150.6140	162.533	11.9250	43.77	0.05	25.26	7.29
7	WC.BT.75-2006.GB	1.01	43.73	19.79	150.6140	162.533	11.9250	43.70	0.07	25.23	N/A
8	WC.BT.78-2007.GB	0.93	43.56	20.75	150.6140	162.533	11.9250	43.53	0.07	25.11	7.28
9	WC.BT.78-2008.GB	1.00	43.55	20.73	150.6140	162.533	11.9250	43.53	0.07	25.15	N/A
10	WC.BT.66-2009.GB	1.01	44.03	20.78	150.6140	162.533	11.9250	44.05	0.10	25.57	7.27
11	WC.BT.66-2010.GB	1.01	43.60	20.78	150.6140	162.533	11.9250	43.57	0.07	24.93	N/A
12	WC.BT.12-2011.GB	0.93	44.12	20.74	150.6140	162.533	11.9250	44.03	0.20	25.13	7.28
13	WC.BT.12-2012.GB	1.00	43.78	20.63	150.6140	162.533	11.9250	43.77	0.02	24.95	N/A
14	WC.BT.91-2061.GB	1.01	43.37	20.69	150.6140	162.533	11.9250	43.35	0.05	24.85	7.38
15	WC.BT.91-2062.GB	1.00	43.30	20.65	150.6140	162.533	11.9250	43.28	0.05	24.85	N/A
16	Am.SOR.BT.WCG_5/21/96_CTR 1										
17	Am.SOR.BT.WCG_5/21/96_CTR 2										
18	Am.SOR.BT.WCG_5/21/96_STD 1										
19	Am.SOR.BT.WCG_5/21/96_STD 2										
20	[illegible]										
21	WC.BT.109-2013.GB	0.93	43.54	19.37	150.6140	162.533	11.9250	43.50	0.03	25.18	7.35
22	WC.BT.109-2014.GB	0.93	43.83	19.90	150.6140	162.533	11.9250	43.88	0.02	25.00	N/A
23	WC.BT.80-2015.GB	1.00	43.93	20.00	150.6140	162.533	11.9250	43.87	0.07	25.02	7.34
24	WC.BT.80-2016.GB	0.93	43.95	20.00	150.6140	162.533	11.9250	43.93	0.07	25.18	N/A
25	WC.BT.75-2017.GB	1.01	43.94	19.97	150.6140	162.533	11.9250	43.92	0.05	25.25	7.32
26	WC.BT.75-2018.GB	1.01	44.05	19.95	150.6140	162.533	11.9250	44.04	0.02	25.56	N/A
27	WC.BT.78-2019.GB	1.01	43.82	20.95	150.6140	162.533	11.9250	43.81	0.02	25.33	7.33
28	WC.BT.78-2020.GB	0.93	43.60	20.93	150.6140	162.533	11.9250	43.58	0.05	24.95	N/A
29	WC.BT.66-2021.GB	1.01	44.07	21.03	150.6140	162.533	11.9250	44.05	0.02	25.30	7.32
30	WC.BT.66-2022.GB	1.01	43.53	20.95	150.6140	162.533	11.9250	43.57	0.05	24.82	N/A
31	WC.BT.12-2023.GB	1.01	43.77	20.93	150.6140	162.533	11.9250	43.75	0.05	24.85	7.33
32	WC.BT.12-2024.GB	0.93	43.98	20.97	150.6140	162.533	11.9250	43.96	0.05	25.02	N/A
33	WC.BT.91-2063.GB	1.00	43.82	20.95	150.6140	162.533	11.9250	43.81	0.02	25.15	7.40

	A	L	M	N	O	P	Q	R	S	T	U
1	Sample Identification	Mineral Mass, g (Col K-Col J)	Tube + Cap + Mineral + Water Mass, g	Water Mass, g (Col M Col K)	Julian Date Pretreatment Started 95	Julian Date Pretreatment Ended 95	Period of Pretreatment, Days	Tube + Cap + Mineral + Water after Pretreatment Mass, g	% Evaporation during Pretreatment ((Col N Col S) /Col N*100)	Tube + Cap + Mineral + Water after Decantation Mass, g	pH of Water after Pretreatment
34	WC BT.91-2054 GB	1.00	43.65	20.97	150.6140	162.539	11.9250	43.64	0.05	24.91	N/A
35	Np SOR BT.WCG 5/21/95_CTR 3										
36	Np SOR BT.WCG 5/21/95_CTR 4										
37	Np SOR BT.WCG 5/21/95_STD 3										
38	Np SOR BT.WCG 5/21/95_STD 4										
39											
40	WC BT.109 2025 GB	1.01	43.78	19.93	150.6140	162.539	11.9250	43.76	0.05	24.93	7.66
41	WC BT.109-2026 GB	1.01	43.81	19.94	150.6140	162.539	11.9250	43.80	0.02	24.88	N/A
42	WC.BT.80-2027.GB	0.99	44.09	19.95	150.6140	162.539	11.9250	44.09	0.00	25.35	7.37
43	WC BT.80-2028 GB	1.00	44.11	19.93	150.6140	162.539	11.9250	44.10	0.02	25.62	N/A
44	WC BT.75-2029.GB	1.01	43.74	19.91	150.6140	162.539	11.9250	43.72	0.05	25.16	7.35
45	WC BT.75-2030 GB	1.00	43.76	19.90	150.6140	162.539	11.9250	43.74	0.05	25.25	N/A
46	WC.BT.79-2031 GB	0.99	44.04	20.89	150.6140	162.539	11.9250	44.03	0.02	25.55	7.34
47	WC BT.79-2032.GB	1.01	44.11	20.93	150.6140	162.539	11.9250	44.08	0.07	25.51	N/A
48	WC BT.65-2033 GB	1.00	44.05	20.90	150.6140	162.539	11.9250	44.03	0.05	26.26	7.31
49	WC BT.65-2034 GB	1.00	43.89	20.88	150.6140	162.539	11.9250	43.87	0.02	25.16	N/A
50	WC.BT.12-2035 GB	1.00	43.66	20.78	150.6140	162.539	11.9250	43.60	0.14	24.83	7.56
51	WC BT.12-2036 GB	0.99	43.91	20.87	150.6140	162.539	11.9250	43.90	0.02	24.97	N/A
52	WC BT.91-2065 GB	1.00	44.03	20.84	150.6140	162.539	11.9250	44.02	0.02	25.54	7.37
53	WC BT.91-2066 GB	0.99	43.42	20.80	150.6140	162.539	11.9250	43.41	0.02	24.82	N/A
54	Pu SOR BT.WCG 5/21/95_CTR 5										
55	Pu SOR BT.WCG 5/21/95_CTR 6										
56	Pu SOR BT.WCG 5/21/95_STD 5										
57	Pu SOR BT.WCG 5/21/95_STD 6										
58											
59	WC BT.109-2037 GB	1.00	43.87	20.78	150.6140	162.539	11.9250	43.87	0.00	25.15	7.35
60	WC BT.109-2038 GB	0.99	43.80	20.80	150.6140	162.539	11.9250	43.73	0.02	25.06	N/A
61	WC BT.80-2039 GB	0.99	43.45	20.77	150.6140	162.539	11.9250	43.43	0.05	24.84	7.37
62	WC BT.80-2040 GB	1.01	43.69	20.61	150.6140	162.539	11.9250	43.67	0.05	25.28	N/A
63	WC.BT.75-2041.GB	1.00	43.58	20.65	150.6140	162.539	11.9250	43.57	0.02	25.18	7.34
64	WC BT.75-2042.GB	1.01	43.55	20.51	150.6140	162.539	11.9250	43.52	0.07	25.38	N/A
65	WC BT.79-2043 GB	1.00	43.58	20.53	150.6140	162.539	11.9250	43.57	0.02	25.33	7.33

	A	L	M	N	O	P	Q	R	S	T	U
1	Sample Identification	Mineral Mass, g (Col K-Col J)	Tube + Cap + Mineral + Water Mass, g	Water Mass, g (Col M-Col K)	Julian Date Pretreatment Started '96	Julian Date Pretreatment Ended '96	Period of Pretreatment, Days	Tube + Cap + Mineral + Water after Pretreatment Mass, g	% Evaporation during Pretreatment ((Col N-Col S) /Col N*100)	Tube + Cap + Mineral + Water after Decantation Mass, g	pH of Water after Pretreatment
66	WC BT.79-2044 GB	0.99	43.85	20.85	150.6140	162.533	11.9250	43.85	0.02	25.31	N/A
67	WC BT.66-2045 GB	1.01	43.51	20.77	150.6140	162.533	11.9250	43.50	0.02	24.84	7.33
68	WC BT.66-2046 GB	1.00	43.91	20.76	150.6140	162.533	11.9250	43.88	0.07	25.28	N/A
69	WC BT.12-2047.GB	1.00	43.91	20.82	150.6140	162.533	11.9250	43.89	0.05	24.94	7.59
70	WC BT.12-2048 GB	1.01	44.00	20.81	150.6140	162.533	11.9250	43.98	0.05	25.09	N/A
71	WC BT.91-2067.GB	1.00	43.49	20.74	150.6140	162.533	11.9250	43.47	0.05	24.91	7.41
72	WC BT.91-2068 GB	0.99	43.54	20.72	150.6140	162.533	11.9250	43.52	0.05	25.08	N/A
73	U SOR BT.WCG 5/21/96_CTR 7										
74	U SOR BT.WCG 5/21/96_CTR 8										
75	U SOR BT.WCG 5/21/96_STD 7										
76	U SOR BT.WCG 5/21/96_STD 8										
77											
78	WC BT.103-2049.GB	0.93	43.93	150.00	150.6140	162.533	11.9250	43.68	0.05	25.17	7.37
79	WC BT.103-2050.GB	1.00	43.65	20.70	150.6140	162.533	11.9250	43.65	0.02	25.21	N/A
80	WC BT.83-2051.GB	1.01	43.77	20.78	150.6140	162.533	11.9250	43.77	0.00	25.15	7.35
81	WC BT.83-2052.GB	1.00	43.63	20.64	150.6140	162.533	11.9250	43.63	0.00	25.23	N/A
82	WC BT.75-2053.GB	1.00	43.46	20.76	150.6140	162.533	11.9250	43.45	0.02	24.91	7.34
83	WC BT.75-2054.GB	1.01	43.35	20.65	150.6140	162.533	11.9250	43.33	0.05	24.95	N/A
84	WC BT.79-2055.GB	1.01	43.58	20.66	150.6140	162.533	11.9250	43.57	0.02	25.07	7.31
85	WC BT.79-2056.GB	1.00	43.27	20.48	150.6140	162.533	11.9250	43.26	0.02	25.04	N/A
86	WC BT.66-2057.GB	1.01	43.48	20.44	150.6140	162.533	11.9250	43.46	0.05	25.25	7.23
87	WC BT.66-2058.GB	0.93	43.42	20.57	150.6140	162.533	11.9250	43.40	0.05	25.03	N/A
88	WC BT.12-2059.GB	0.93	43.55	20.55	150.6140	162.533	11.9250	43.54	0.02	24.77	7.57
89	WC BT.12-2060.GB	0.93	43.83	21.02	150.6140	162.533	11.9250	43.83	0.14	24.74	N/A
90	WC BT.91-2069.GB	0.93	43.82	20.97	150.6140	162.533	11.9250	43.82	0.00	25.00	7.32
91	WC BT.91-2070.GB	0.93	43.73	20.97	150.6140	162.533	11.9250	43.73	0.00	24.84	N/A
92	Tc SOR BT.WCG 5/21/96_CTR 9										
93	Tc SOR BT.WCG 5/21/96_CTR 10										
94	Tc SOR BT.WCG 5/21/96_STD 9										
95	Tc SOR BT.WCG 5/21/96_STD 10										

	A	V	W	X	Y	Z	AA	AB	AC	AD	AE
1	Sample Identification	Eh of Water after Pretreatment, mV	Julian Date Tracer Solution was Added, '96	Mass after Tracer Solution was Added, g	Mass of Tracer Solution Added, g	Julian Date Sorption Started '95	Julian Date Sorption Ended '95	Period of Sorption, Days	Mass after Sorption Ended, g	%, Evaporation during Sorption ((Col Y-Col AD) /Col.Y*100)	pH of tracer solution after sorption (pH'ed in glove box)
2	WC BT.109-2001.GB	N/A	163.5204	44.94	19.82	163.6504	184.6079	20.9575	44.78	0.35	7.15
3	WC BT.109-2002.GB	N/A	163.5204	45.24	20.02	163.6504	184.6079	20.9575	45.18	0.13	
4	WC BT.80-2003.GB	N/A	163.5204	44.78	19.81	163.6504	184.6079	20.9575	44.73	0.11	7.16
5	WC BT.80-2004.GB	N/A	163.5204	44.78	19.96	163.6504	184.6079	20.9575	44.70	0.18	
6	WC BT.75-2005.GB	N/A	163.5204	45.19	19.93	163.6504	184.6079	20.9575	45.13	0.13	7.13
7	WC BT.75-2006.GB	N/A	163.5204	45.19	19.95	163.6504	184.6079	20.9575	45.15	0.09	
8	WC BT.79-2007.GB	N/A	163.5204	45.01	19.90	163.6504	184.6079	20.9575	44.92	0.20	7.15
9	WC BT.79-2008.GB	N/A	163.5204	44.07	18.92	163.6504	184.6079	20.9575	44.01	0.14	
10	WC BT.66-2009.GB	N/A	163.5204	45.45	19.88	163.6504	184.6079	20.9575	45.37	0.18	7.22
11	WC BT.66-2010.GB	N/A	163.5204	44.83	19.84	163.6504	184.6079	20.9575	44.76	0.16	
12	WC.BT.12-2011.GB	N/A	163.5204	45.06	19.93	163.6504	184.6079	20.9575	44.99	0.16	7.14
13	WC BT.12-2012.GB	N/A	163.5204	44.82	19.87	163.6504	184.6079	20.9575	44.77	0.11	
14	WC.BT.91-2061.GB	N/A	163.5204	44.59	19.74	163.6504	184.6079	20.9575	44.53	0.13	7.18
15	WC.BT.91-2062.GB	N/A	163.5204	44.72	19.85	163.6504	184.6079	20.9575	44.65	0.16	
16	Am.SOR.BT.WCG 5/21/96_CTR 1		163.5204	43.03	19.90	163.6504	184.6079	20.9575	42.99	0.09	7.13
17	Am.SOR.BT.WCG 5/21/96_CTR 2		163.5204	42.99	19.87	163.6504	184.6079	20.9575	42.95	0.07	
18	Am.SOR.BT.WCG 5/21/96_STD 1										
19	Am.SOR.BT.WCG 5/21/96_STD 2										
20											
21	WC.BT.109-2013.GB	N/A	163.5204	45.26	20.08	163.6504	184.6079	20.9575	45.20	0.13	7.12
22	WC.BT.109-2014.GB	N/A	163.5204	44.94	19.94	163.6504	184.6079	20.9575	44.87	0.16	
23	WC.BT.80-2015.GB	N/A	163.5204	45.04	20.02	163.6504	184.6079	20.9575	44.97	0.16	7.11
24	WC.BT.80-2016.GB	N/A	163.5204	45.16	19.98	163.6504	184.6079	20.9575	45.10	0.13	
25	WC.BT.75-2017.GB	N/A	163.5204	45.15	19.90	163.6504	184.6079	20.9575	45.09	0.13	7.08
26	WC.BT.75-2018.GB	N/A	163.5204	45.48	19.92	163.6504	184.6079	20.9575	45.43	0.11	
27	WC.BT.75-2019.GB	N/A	163.5204	45.21	19.88	163.6504	184.6079	20.9575	45.14	0.15	7.18
28	WC.BT.79-2020.GB	N/A	163.5204	44.50	19.54	163.6504	184.6079	20.9575	44.43	0.15	
29	WC.BT.66-2021.GB	N/A	163.5204	45.18	19.83	163.6504	184.6079	20.9575	45.11	0.15	7.23
30	WC.BT.66-2022.GB	N/A	163.5204	44.84	20.02	163.6504	184.6079	20.9575	44.78	0.13	
31	WC.BT.12-2023.GB	N/A	163.5204	44.73	19.88	163.6504	184.6079	20.9575	44.65	0.15	7.40
32	WC.BT.12-2024.GB	N/A	163.5204	44.63	19.61	163.6504	184.6079	20.9575	44.56	0.16	
33	WC.BT.91-2063.GB	N/A	163.5204	45.03	19.88	163.6504	184.6079	20.9575	44.97	0.13	7.30

	A	V	W	X	Y	Z	AA	AB	AC	AD	AE
1	Sample Identification	Eh of Water after Pretreatment, mV	Julian Date Tracer Solution was Added, '96	Mass after Tracer Solution was Added, g	Mass of Tracer Solution Added, g	Julian Date Sorption Started '96	Julian Date Sorption Ended '96	Period of Sorption, Days	Mass after Sorption Ended, g	% Evaporation during Sorption ((Col Y-Col AD) /Col.Y*100)	pH of tracer solution after sorption (pH ed in glove Box)
34	WC.BT.91-2064.GB	N/A	163.5204	44.70	19.79	163.6504	184.6079	20.9575	44.62	0.18	
35	Np.SOR.BT.WCG 5/21/96_CTR 3		163.5204	42.71	19.93	163.6504	184.6079	20.9575	42.63	0.05	7.14
36	Np.SOR.BT.WCG 5/21/96_CTR 4		163.5204	42.79	19.84	163.6504	184.6079	20.9575	42.76	0.07	
37	Np.SOR.BT.WCG 5/21/96_STD 3										
38	Np.SOR.BT.WCG 5/21/96_STD 4										
39	[illegible]										
40	WC.BT.100-2025.GB	N/A	163.5204	45.04	20.05	163.6504	184.6079	20.9575	44.96	0.18	7.12
41	WC.BT.100-2026.GB	N/A	163.5204	44.92	20.04	163.6504	184.6079	20.9575	44.87	0.11	
42	WC.BT.80-2027.GB	N/A	163.5204	45.30	19.94	163.6504	184.6079	20.9575	45.22	0.18	7.14
43	WC.BT.80-2028.GB	N/A	163.5204	45.53	19.91	163.6504	184.6079	20.9575	45.45	0.18	
44	WC.BT.75-2029.GB	N/A	163.5204	45.05	19.90	163.6504	184.6079	20.9575	45.01	0.11	7.21
45	WC.BT.75-2030.GB	N/A	163.5204	45.25	19.93	163.6504	184.6079	20.9575	45.11	0.31	
46	WC.BT.78-2031.GB	N/A	163.5204	45.40	19.84	163.6504	184.6079	20.9575	45.33	0.15	7.23
47	WC.BT.78-2032.GB	N/A	163.5204	45.35	19.84	163.6504	184.6079	20.9575	45.28	0.15	
48	WC.BT.66-2033.GB	N/A	163.5204	45.05	18.79	163.6504	184.6079	20.9575	44.96	0.20	7.27
49	WC.BT.66-2034.GB	N/A	163.5204	44.97	19.81	163.6504	184.6079	20.9575	44.90	0.16	
50	WC.BT.12-2035.GB	N/A	163.5204	44.60	19.77	163.6504	184.6079	20.9575	44.54	0.13	7.53
51	WC.BT.12-2036.GB	N/A	163.5204	44.85	19.83	163.6504	184.6079	20.9575	44.80	0.13	
52	WC.BT.9-2065.GB	N/A	163.5204	45.45	19.91	163.6504	184.6079	20.9575	45.39	0.13	7.15
53	WC.BT.91-2066.GB	N/A	163.5204	44.65	19.83	163.6504	184.6079	20.9575	44.58	0.16	
54	Pu.SOR.BT.WCG 5/21/96_CTR 5		163.5204	42.75	19.80	163.6504	184.6079	20.9575	42.73	0.05	7.28
55	Pu.SOR.BT.WCG 5/21/96_CTR 6		163.5204	42.53	19.78	163.6504	184.6079	20.9575	42.51	0.05	
56	Pu.SOR.BT.WCG 5/21/96_STD 5										
57	Pu.SOR.BT.WCG 5/21/96_STD 6										
58	[illegible]										
59	WC.BT.100-2037.GB	N/A	163.5204	45.18	20.03	163.6504	184.6079	20.9575	45.11	0.15	7.13
60	WC.BT.100-2038.GB	N/A	163.5204	45.12	20.06	163.6504	184.6079	20.9575	45.04	0.18	
61	WC.BT.80-2039.GB	N/A	163.5204	[illegible]	19.98	163.6504	184.6079	20.9575	44.74	0.18	7.21
62	WC.BT.80-2040.GB	N/A	163.5204	45.14	19.85	163.6504	184.6079	20.9575	45.07	0.16	
63	WC.BT.75-2041.GB	N/A	163.5204	45.10	19.92	163.6504	184.6079	20.9575	45.02	0.18	7.10
64	WC.BT.75-2042.GB	N/A	163.5204	45.27	19.83	163.6504	184.6079	20.9575	45.21	0.13	
65	WC.BT.78-2043.GB	N/A	163.5204	45.30	19.97	163.6504	184.6079	20.9575	45.25	0.11	7.07

	A	V	W	X	Y	Z	AA	AB	AC	AD	AE
1	Sample Identification	Eh of Water after Pretreatment, mV	Julian Date Tracer Solution was Added, '95	Mass after Tracer Solution was Added, g	Mass of Tracer Solution Added, g	Julian Date Sorption Started '95	Julian Date Sorption Ended '95	Period of Sorption, Days	Mass after Sorption Ended, g	% Evaporation during Sorption ((Col Y-Col AD) /Col Y*100)	pH of tracer solution after sorption (pH'ed in glove box)
66	WC.BT.79-2044.GB	N/A	163.5204	45.25	19.94	163.6504	184.6079	20.9575	45.19	0.13	
67	WC.BT.66-2045.GB	N/A	163.5204	44.65	19.81	163.6504	184.6079	20.9575	44.59	0.13	7.19
68	WC.BT.66-2046.GB	N/A	163.5204	44.55	19.27	163.6504	184.6079	20.9575	44.46	0.20	
69	WC.BT.12-2047.GB	N/A	163.5204	44.74	19.83	163.6504	184.6079	20.9575	44.67	0.16	7.55
70	WC.BT.12-2048.GB	N/A	163.5204	44.67	19.58	163.6504	184.6079	20.9575	44.57	0.22	
71	WC.BT.91-2067.GB	N/A	163.5204	44.78	19.87	163.6504	184.6079	20.9575	44.71	0.16	7.10
72	WC.BT.91-2068.GB	N/A	163.5204	45.05	19.97	163.6504	184.6079	20.9575	44.98	0.16	
73	U.SOR.BT.WCG 5/21/95_CTR 7		163.5204	42.93	19.85	163.6504	184.6079	20.9575	42.97	0.05	7.08
74	U.SOR.BT.WCG 5/21/95_CTR 8		163.5204	42.63	20.43	163.6504	184.6079	20.9575	42.67	0.05	
75	U.SOR.BT.WCG 5/21/95_STD 7										
76	U.SOR.BT.WCG 5/21/95_STD 8										
77											
78	WC.BT.109-2049.GB	N/A	163.5204	45.21	20.04	163.6504	184.6079	20.9575	44.89	0.71	7.16
79	WC.BT.109-2050.GB	N/A	163.5204	45.16	19.95	163.6504	184.6079	20.9575	45.10	0.13	
80	WC.BT.83-2051.GB	N/A	163.5204	45.15	20.00	163.6504	184.6079	20.9575	45.03	0.13	7.16
81	WC.BT.83-2052.GB	N/A	163.5204	45.22	19.93	163.6504	184.6079	20.9575	45.17	0.11	
82	WC.BT.75-2053.GB	N/A	163.5204	44.88	19.97	163.6504	184.6079	20.9575	44.78	0.22	7.11
83	WC.BT.75-2054.GB	N/A	163.5204	44.93	19.95	163.6504	184.6079	20.9575	44.85	0.13	
84	WC.BT.78-2055.GB	N/A	163.5204	44.93	19.91	163.6504	184.6079	20.9575	44.92	0.13	7.33
85	WC.BT.78-2056.GB	N/A	163.5204	44.85	19.84	163.6504	184.6079	20.9575	44.82	0.13	
86	WC.BT.85-2057.GB	N/A	163.5204	45.19	19.94	163.6504	184.6079	20.9575	45.13	0.13	7.08
87	WC.BT.66-2058.GB	N/A	163.5204	44.83	19.86	163.6504	184.6079	20.9575	44.81	0.18	
88	WC.BT.12-2059.GB	N/A	163.5204	44.72	19.95	163.6504	184.6079	20.9575	44.65	0.13	7.09
89	WC.BT.12-2060.GB	N/A	163.5204	44.65	19.91	163.6504	184.6079	20.9575	44.57	0.18	
90	WC.BT.91-2069.GB	N/A	163.5204	44.85	19.85	163.6504	184.6079	20.9575	44.79	0.13	7.12
91	WC.BT.91-2070.GB	N/A	163.5204	44.57	19.73	163.6504	184.6079	20.9575	44.50	0.16	
92	Tc.SOR.BT.WCG 5/21/95_CTR 9		163.5204	42.87	19.78	163.6504	184.6079	20.9575	42.85	0.05	7.15
93	Tc.SOR.BT.WCG 5/21/95_CTR 10		163.5204	42.73	19.78	163.6504	184.6079	20.9575	42.71	0.05	
94	Tc.SOR.BT.WCG 5/21/95_STD 9										
95	Tc.SOR.BT.WCG 5/21/95_STD 10										

	A	AF	AG	AH	AI	AJ	AK	AL	AM	AN	AO	AP
1	Sample Identification	Mass after Sorption and Decantation, g	pH of Tracer Solution after Sorption	Eh of Tracer Solution after Sorption	Mass of Counting Vial, g	Mass of Counting Vial + Aliquot of Tracer Solution after Sorption, g	Mass of Counting Vial + Aliquot of Tracer Solution after Sorption + Scintillation Cocktail, g	Mass of Counted Tracer Solution after Sorption, g (Col AI-Col AH)	Total CFM in Counted Tracer Solution after Sorption	CFM/g in Counted Tracer Solution after Sorption (Col AL/ Col AK)	Kd (mL/g) of Original Tracer Solution Based on Standards	Kd (mL/g) of Original Tracer Solution Based on Controls
2	WC BT.169-2001.GB	24.95	N/A	N/A	6.52	12.73	26.77	6.21	55.20	9.05	2.97E+02	1.53E+02
3	WC.BT.169-2002.GB	24.93		N/A	6.57	12.58	26.62	6.01	60.95	10.14	2.65E+02	1.44E+02
4	WC.BT.80-2003.GB	25.25	N/A	N/A	6.53	12.46	26.50	5.93	64.45	10.87	2.38E+02	1.29E+02
5	WC.BT.80-2004.GB	24.74		N/A	6.52	12.47	26.52	5.95	61.00	10.25	2.53E+02	1.41E+02
6	WC.BT.75-2005.GB	25.22	N/A	N/A	6.52	12.52	26.57	6.00	54.15	9.03	2.95E+02	1.62E+02
7	WC.BT.75-2006.GB	25.19		N/A	6.52	12.48	26.53	5.95	60.55	10.16	2.53E+02	1.41E+02
8	WC.BT.79-2007.GB	25.15	N/A	N/A	6.5	12.47	26.51	5.97	60.10	10.07	2.64E+02	1.40E+02
9	WC.BT.79-2008.GB	25.31		N/A	6.49	12.44	26.48	5.95	58.70	9.87	2.58E+02	1.38E+02
10	WC.BT.66-2009.GB	25.59	N/A	N/A	6.51	12.33	26.43	5.88	66.95	11.33	2.28E+02	1.22E+02
11	WC.BT.66-2010.GB	25.05		N/A	6.55	12.57	26.61	6.01	62.50	10.40	2.50E+02	1.35E+02
12	WC.BT.12-2011.GB	25.21	N/A	N/A	6.5	12.49	26.52	5.93	3.93	0.65	4.42E+03	2.55E+03
13	WC.BT.12-2012.GB	25.21		N/A	6.51	12.47	26.50	5.95	6.25	1.05	2.70E+03	1.55E+03
14	WC.BT.91-2061.GB	25.00		N/A	6.52	12.52	26.55	6.00	52.35	8.73	3.00E+02	1.84E+02
15	WC.BT.91-2062.GB	24.85		N/A	6.48	12.48	26.51	6.00	58.65	9.78	2.70E+02	1.47E+02
16	Am SOR BT.WCG 5/21/96_CTR 1		N/A	N/A	6.51	12.45	26.50	5.94	503.05	84.63	N/A	N/A
17	Am SOR BT.WCG 5/21/96_CTR 2			N/A	6.49	12.43	26.45	5.94	483.95	81.47	N/A	N/A
18	Am SOR BT.WCG 5/21/96_STD 1				6.45	12.45	26.50	6.00	848.75	141.46	N/A	N/A
19	Am SOR BT.WCG 5/21/96_STD 2				6.48	12.43	26.43	5.95	867.50	145.80	N/A	N/A
20												
21	WC.BT.169-2013.GB	25.28	N/A	N/A	6.46	12.14	26.18	5.68	76381.60	13382.32	4.32E-01	6.25E-01
22	WC.BT.169-2014.GB	25.12		N/A	6.49	12.53	26.51	6.04	83174.10	13770.55	-1.74E-01	-8.42E-02
23	WC.BT.80-2015.GB	25.23	N/A	N/A	6.55	12.48	26.51	5.93	80611.60	13593.86	-9.17E-03	8.15E-02
24	WC.BT.80-2016.GB	25.24		N/A	6.47	12.44	26.48	5.97	82235.60	13774.97	-4.02E-01	-3.11E-01
25	WC.BT.75-2017.GB	25.38	N/A	N/A	6.57	12.45	26.48	5.88	78333.10	13435.22	6.12E-02	1.51E-01
26	WC.BT.75-2018.GB	25.55		N/A	6.51	12.54	26.58	6.03	83457.40	13840.35	-7.40E-01	-6.62E-01
27	WC.BT.79-2019.GB	25.25	N/A	N/A	6.56	12.24	26.27	5.68	76335.60	13433.54	-1.11E+00	-1.02E+00
28	WC.BT.79-2020.GB	25.01		N/A	6.48	12.43	26.43	5.92	80343.10	13572.48	-1.18E+00	-1.09E+00
29	WC.BT.66-2021.GB	25.33	N/A	N/A	6.55	12.47	26.50	5.91	80485.60	13618.78	-1.18E+00	-1.09E+00
30	WC.BT.66-2022.GB	24.97		N/A	6.51	12.43	26.45	5.92	81333.10	13851.20	-1.44E+00	-1.37E+00
31	WC.BT.12-2023.GB	24.75	N/A	N/A	6.56	12.51	26.54	5.95	58783.10	9880.52	6.83E+00	7.01E+00
32	WC.BT.12-2024.GB	24.93		N/A	6.48	12.44	26.47	5.95	55333.10	9563.61	7.85E+00	7.98E+00
33	WC.BT.91-2063.GB	25.04		N/A	6.52	12.54	26.57	6.02	82234.90	13570.25	-1.30E+00	-1.21E+00

	A	AF	AG	AH	AI	AJ	AK	AL	AM	AN	AO	AP
1	Sample Identification	Mass after Sorption and Decantation, g	pH of Tracer Solution after Sorption	Eh of Tracer Solution after Sorption	Mass of Counting Vial, g	Mass of Counting Vial + Aliquot of Tracer Solution after Sorption, g	Mass of Counting Vial + Aliquot of Tracer Solution after Sorption + Scintillation Cocktail, g	Mass of Counted Tracer Solution after Sorption, g (Col AI-Col AH)	Total CFM in Counted Tracer Solution after Sorption	CFM/g in Counted Tracer Solution after Sorption (Col AL/ Col AK)	Kd (mL/g) of Original Tracer Solution Based on Standards	Kd (mL/g) of Original Tracer Solution Based on Controls
34	WC BT.91-2054 GB	24.93		N/A	5.47	12.43	26.46	5.35	81711.60	13710.00	-1.29E+00	-1.20E+00
35	Np SOR BT.WCG 5/21/95_CTR 3		N/A	N/A	6.50	12.44	26.47	5.94	85565.80	14405.02	N/A	N/A
36	Np SOR BT.WCG 5/21/95_CTR 4			N/A	6.51	12.51	26.54	6.00	85915.80	14319.30	N/A	N/A
37	Np SOR BT.WCG 5/21/95_STD 3				5.48	12.53	26.53	6.05	85632.40	14154.12	N/A	N/A
38	Np SOR BT.WCG 5/21/95_STD 4				6.51	12.48	26.54	5.97	85249.10	14447.03	N/A	N/A
39												
40	WC BT.109-2025 GB	25.08	N/A	N/A	6.47	12.44	26.47	5.97	3.763.90	5156.09	1.38E+01	1.19E+01
41	WC BT.109-2026 GB	24.97		N/A	6.52	12.43	26.53	5.97	32205.40	5334.71	1.24E+01	1.05E+01
42	WC BT.83-2027 GB	25.60	N/A	N/A	6.55	12.47	26.52	5.91	29533.70	5014.16	1.49E+01	1.23E+01
43	WC BT.83-2028 GB	25.55		N/A	6.52	12.36	26.40	5.84	29333.00	5033.05	1.44E+01	1.24E+01
44	WC BT.75-2029 GB	25.16	N/A	N/A	6.56	12.54	26.59	5.98	26472.30	4426.81	1.91E+01	1.69E+01
45	WC BT.75-2030 GB	25.13		N/A	6.51	12.54	26.55	6.03	25635.60	4261.29	2.10E+01	1.87E+01
46	WC BT.79-2031 GB	25.57	N/A	N/A	6.5	12.51	26.55	6.01	34152.30	5682.58	9.38E+00	7.64E+00
47	WC BT.79-2032 GB	25.73		N/A	6.52	12.47	26.49	5.95	32727.30	5500.39	1.03E+01	8.54E+00
48	WC BT.65-2033 GB	25.52	N/A	N/A	6.48	12.44	26.45	5.95	25918.90	4349.81	1.71E+01	1.50E+01
49	WC BT.65-2034 GB	25.23		N/A	6.49	11.97	26.01	5.48	23149.20	4224.31	2.04E+01	1.81E+01
50	WC BT.12-2035 GB	24.72	N/A	N/A	6.48	12.48	26.52	6.00	1272.76	212.13	8.18E+02	7.72E+02
51	WC BT.12-2036 GB	25.03		N/A	6.5	12.50	26.54	6.00	1533.05	255.01	6.65E+02	6.43E+02
52	WC BT.9-2055 GB	25.41		N/A	6.5	12.00	26.03	5.50	15556.60	2830.23	4.12E+01	3.77E+01
53	WC BT.91-2056 GB	24.85		N/A	6.53	12.04	26.07	5.51	9712.91	1762.78	8.02E+01	7.46E+01
54	Pu SOR BT.WCG 5/21/95_CTR 5		N/A	N/A	6.47	12.00	26.05	5.53	47257.80	8545.71	N/A	N/A
55	Pu SOR BT.WCG 5/21/95_CTR 6			N/A	6.49	12.00	26.04	5.51	45796.70	8493.05	N/A	N/A
56	Pu SOR BT.WCG 5/21/95_STD 5				6.47	12.45	26.52	5.93	53572.30	8943.62	N/A	N/A
57	Pu SOR BT.WCG 5/21/95_STD 6				6.52	12.52	26.57	6.00	54432.30	9082.05	N/A	N/A
58												
59	WC BT.109-2037 GB	25.30	N/A	N/A	6.47	12.45	26.28	5.93	76963.80	12870.20	3.83E+00	2.62E+00
60	WC BT.109-2038 GB	25.24		N/A	6.52	12.49	26.54	5.97	77426.30	12969.23	3.69E+00	2.47E+00
61	WC BT.83-2039 GB	24.83	N/A	N/A	6.55	12.55	26.60	5.99	60797.90	10149.93	1.07E+01	9.19E+00
62	WC BT.83-2040 GB	25.27		N/A	6.55	12.55	26.61	6.00	76126.30	12687.72	3.97E+00	2.76E+00
63	WC BT.75-2041 GB	25.21	N/A	N/A	6.55	12.54	26.59	5.99	64179.20	10714.39	8.79E+00	7.34E+00
64	WC BT.75-2042 GB	25.33		N/A	6.52	12.53	26.58	6.01	62816.70	10452.03	9.34E+00	7.88E+00
65	WC BT.79-2043 GB	25.41	N/A	N/A	6.52	12.47	26.50	5.95	66400.00	11159.65	7.52E+00	6.13E+00

	A	AF	AG	AH	AI	AJ	AK	AL	AM	AN	AO	AP
1	Sample Identification	Mass after Sorption and Decantation, g	pH of Tracer Solution after Sorption	Eh of Tracer Solution after Sorption	Mass of Counting Vial, g	Mass of Counting Vial + Aliquot of Tracer Solution after Sorption, g	Mass of Counting Vial + Aliquot of Tracer Solution after Sorption + Scintillation Cocktail, g	Mass of Counted Tracer Solution after Sorption, g (Col AI-Col AH)	Total CPM in Counted Tracer Solution after Sorption	CPM/g in Counted Tracer Solution after Sorption (Col AL/ Col AK)	Kd (ml/g) of Original Tracer Solution Based on Standards	Kd (ml/g) of Original Tracer Solution Based on Controls
66	WC BT.79-2044 GB	25.35		N/A	6.49	12.48	26.52	5.99	73550.00	12278.80	4.64E+00	3.56E+00
67	WC BT.66-2045 GB	25.10	N/A	N/A	6.52	12.46	26.50	5.94	60637.60	10208.35	1.03E+01	8.78E+00
68	WC BT.66-2046 GB	25.63		N/A	6.53	12.52	26.55	5.99	62610.10	10452.44	9.31E+00	7.87E+00
69	WC BT.12-2047 GB	25.07	N/A	N/A	6.53	12.53	26.56	6.00	74161.40	12360.23	5.03E+00	3.78E+00
70	WC BT.12-2048 GB	25.03	N/A	N/A	6.56	12.55	26.53	5.99	81337.50	13578.88	2.64E+00	1.43E+00
71	WC BT.91-2067 GB	25.03	N/A	N/A	6.51	12.49	26.53	5.99	80775.00	13507.53	2.47E+00	1.33E+00
72	WC BT.91-2068 GB	24.88		N/A	6.51	12.50	26.54	5.99	77175.00	12883.97	3.62E+00	2.40E+00
73	U.SOR BT.WCG 5/21/96_CTR 7		N/A	N/A	6.54	12.50	26.54	5.96	94670.90	15884.38	N/A	N/A
74	U.SOR BT.WCG 5/21/96_CTR 8			N/A	6.50	12.48	26.52	5.98	94337.50	15775.50	N/A	N/A
75	U.SOR BT.WCG 5/21/96_STD 7				6.50	12.47	26.50	5.97	100088.00	16765.16	N/A	N/A
76	U.SOR BT.WCG 5/21/96_STD 8				6.61	12.62	26.65	6.01	98887.50	16453.83	N/A	N/A
77												
78	WC BT.100-2049 GB	25.27	N/A	N/A	3.24	3.97	N/A	0.73	18770.00	16123.23	-1.37E+00	-1.20E+00
79	WC BT.100-2050 GB	25.21		N/A	3.22	4.21	N/A	0.93	15855.00	16016.16	-1.21E+00	-1.04E+00
80	WC BT.80-2051 GB	25.27	N/A	N/A	3.22	4.24	N/A	1.02	16267.00	15948.04	-1.22E+00	-1.05E+00
81	WC BT.80-2052 GB	26.10		N/A	3.26	4.27	N/A	1.01	15862.00	15704.95	-1.00E+00	-8.23E-01
82	WC BT.75-2053 GB	25.02	N/A	N/A	3.23	4.24	N/A	1.01	16037.00	15878.22	-1.15E+00	-9.78E-01
83	WC BT.75-2054 GB	25.03		N/A	3.26	4.26	N/A	1.00	15825.00	15825.00	-1.15E+00	-9.87E-01
84	WC BT.78-2055 GB	25.41	N/A	N/A	3.25	4.25	N/A	1.00	15952.00	15952.00	-1.23E+00	-1.06E+00
85	WC BT.78-2056 GB	25.54		N/A	3.24	4.23	N/A	0.99	15675.00	15833.33	-1.18E+00	-1.01E+00
86	WC BT.66-2057 GB	25.47	N/A	N/A	3.25	4.25	N/A	1.00	15305.00	15305.00	-1.22E+00	-1.04E+00
87	WC BT.66-2058 GB	25.12		N/A	3.24	4.26	N/A	1.02	16280.00	15950.78	-1.27E+00	-1.09E+00
88	WC BT.12-2059 GB	24.93	N/A	N/A	3.22	4.23	N/A	1.01	16400.00	16237.62	-1.23E+00	-1.06E+00
89	WC BT.12-2060 GB	24.75		N/A	3.22	4.23	N/A	1.01	16366.00	16203.96	-1.27E+00	-1.09E+00
90	WC BT.91-2069 GB	25.16		N/A	3.25	4.24	N/A	0.99	15861.00	16021.21	-1.34E+00	-1.16E+00
91	WC BT.91-2070 GB	25.13		N/A	3.23	4.24	N/A	1.01	15953.00	15735.05	-9.64E-01	-7.83E-01
92	Tc.SOR BT.WCG 5/21/96_CTR 9		N/A	N/A	3.28	4.30	N/A	1.02	17052.00	16717.65	N/A	N/A
93	Tc.SOR BT.WCG 5/21/96_CTR 10			N/A	3.24	4.25	N/A	1.01	17008.00	16833.60	N/A	N/A
94	Tc.SOR BT.WCG 5/21/96_STD 9				3.22	4.19	N/A	0.97	16275.00	16778.35	N/A	N/A
95	Tc.SOR BT.WCG 5/21/96_STD 10				3.23	4.22	N/A	0.99	16337.00	16502.02	N/A	N/A

	A	AQ	AR	AS	AT	AU	AV	AW
1	Sample Identification	Water ID	Type of Scintillation Cocktail Used	ID of Tracer Solutions Used for Sorption Experiment	pH of Tracer Solutions Equilibrated in Glove Box	Disk where Raw Experimental Data are Located	Optical Disk where Reduced Data are Located	Subdirectory
2	WC.BT.109-2001.GB	WCG 1F.1	Ultima Gold AB	Am SOR BT WCG 5/21/96	7.35	Area G Sorption Studies 1/23/96	TWS INC 05 93 05	Area G Sorption
3	WC.BT.109-2002.GB	WCG 1F.1	Ultima Gold AB	Am SOR BT WCG 5/21/96	7.35	Area G Sorption Studies 1/23/96	TWS INC 05 93 05	Area G Sorption
4	WC.BT.80-2003.GB	WCG 1F.1	Ultima Gold AB	Am SOR BT WCG 5/21/96	7.35	Area G Sorption Studies 1/23/96	TWS INC 05 93 05	Area G Sorption
5	WC.BT.80-2004.GB	WCG 1F.1	Ultima Gold AB	Am SOR BT WCG 5/21/96	7.35	Area G Sorption Studies 1/23/96	TWS INC 05 93 05	Area G Sorption
6	WC.BT.75-2005.GB	WCG 1F.1	Ultima Gold AB	Am SOR BT WCG 5/21/96	7.35	Area G Sorption Studies 1/23/96	TWS INC 05 93 05	Area G Sorption
7	WC.BT.75-2006.GB	WCG 1F.1	Ultima Gold AB	Am SOR BT WCG 5/21/96	7.35	Area G Sorption Studies 1/23/96	TWS INC 05 93 05	Area G Sorption
8	WC.BT.79-2007.GB	WCG 1F.1	Ultima Gold AB	Am SOR BT WCG 5/21/96	7.35	Area G Sorption Studies 1/23/96	TWS INC 05 93 05	Area G Sorption
9	WC.BT.79-2008.GB	WCG 1F.1	Ultima Gold AB	Am SOR BT WCG 5/21/96	7.35	Area G Sorption Studies 1/23/96	TWS INC 05 93 05	Area G Sorption
10	WC.BT.65-2009.GB	WCG 1F.1	Ultima Gold AB	Am SOR BT WCG 5/21/96	7.35	Area G Sorption Studies 1/23/96	TWS INC 05 93 05	Area G Sorption
11	WC.BT.65-2010.GB	WCG 1F.1	Ultima Gold AB	Am SOR BT WCG 5/21/96	7.35	Area G Sorption Studies 1/23/96	TWS INC 05 93 05	Area G Sorption
12	WC.BT.12-2011.GB	WCG 1F.1	Ultima Gold AB	Am SOR BT WCG 5/21/96	7.35	Area G Sorption Studies 1/23/96	TWS INC 05 93 05	Area G Sorption
13	WC.BT.12-2012.GB	WCG 1F.1	Ultima Gold AB	Am SOR BT WCG 5/21/96	7.35	Area G Sorption Studies 1/23/96	TWS INC 05 93 05	Area G Sorption
14	WC.BT.91-2061.GB	WCG 1F.1	Ultima Gold AB	Am SOR BT WCG 5/21/96	7.35	Area G Sorption Studies 1/23/96	TWS INC 05 93 05	Area G Sorption
15	WC.BT.91-2062.GB	WCG 1F.1	Ultima Gold AB	Am SOR BT WCG 5/21/96	7.35	Area G Sorption Studies 1/23/96	TWS INC 05 93 05	Area G Sorption
16	Am.SOR.BT.WCG 5/21/96_CTR 1	WCG 1F.1	Ultima Gold AB	Am SOR BT WCG 5/21/96	7.35	Area G Sorption Studies 1/23/96	TWS INC 05 93 05	Area G Sorption
17	Am.SOR.BT.WCG 5/21/96_CTR 2	WCG 1F.1	Ultima Gold AB	Am SOR BT WCG 5/21/96	7.35	Area G Sorption Studies 1/23/96	TWS INC 05 93 05	Area G Sorption
18	Am.SOR.BT.WCG 5/21/96_STD 1	WCG 1F.1	Ultima Gold AB	Am SOR BT WCG 5/21/96	7.35	Area G Sorption Studies 1/23/96	TWS INC 05 93 05	Area G Sorption
19	Am.SOR.BT.WCG 5/21/96_STD 2	WCG 1F.1	Ultima Gold AB	Am SOR BT WCG 5/21/96	7.35	Area G Sorption Studies 1/23/96	TWS INC 05 93 05	Area G Sorption
20						Area G Sorption Studies 1/23/96	TWS INC 05 93 05	Area G Sorption
21	WC.BT.109-2013.GB	WCG 1F.1	Ultima Gold AB	Np SOR BT WCG 5/21/96	7.32	Area G Sorption Studies 1/23/96	TWS INC 05 93 05	Area G Sorption
22	WC.BT.109-2014.GB	WCG 1F.1	Ultima Gold AB	Np SOR BT WCG 5/21/96	7.32	Area G Sorption Studies 1/23/96	TWS INC 05 93 05	Area G Sorption
23	WC.BT.80-2015.GB	WCG 1F.1	Ultima Gold AB	Np SOR BT WCG 5/21/96	7.32	Area G Sorption Studies 1/23/96	TWS INC 05 93 05	Area G Sorption
24	WC.BT.80-2016.GB	WCG 1F.1	Ultima Gold AB	Np SOR BT WCG 5/21/96	7.32	Area G Sorption Studies 1/23/96	TWS INC 05 93 05	Area G Sorption
25	WC.BT.75-2017.GB	WCG 1F.1	Ultima Gold AB	Np SOR BT WCG 5/21/96	7.32	Area G Sorption Studies 1/23/96	TWS INC 05 93 05	Area G Sorption
26	WC.BT.75-2018.GB	WCG 1F.1	Ultima Gold AB	Np SOR BT WCG 5/21/96	7.32	Area G Sorption Studies 1/23/96	TWS INC 05 93 05	Area G Sorption
27	WC.BT.79-2019.GB	WCG 1F.1	Ultima Gold AB	Np SOR BT WCG 5/21/96	7.32	Area G Sorption Studies 1/23/96	TWS INC 05 93 05	Area G Sorption
28	WC.BT.79-2020.GB	WCG 1F.1	Ultima Gold AB	Np SOR BT WCG 5/21/96	7.32	Area G Sorption Studies 1/23/96	TWS INC 05 93 05	Area G Sorption
29	WC.BT.65-2021.GB	WCG 1F.1	Ultima Gold AB	Np SOR BT WCG 5/21/96	7.32	Area G Sorption Studies 1/23/96	TWS INC 05 93 05	Area G Sorption
30	WC.BT.65-2022.GB	WCG 1F.1	Ultima Gold AB	Np SOR BT WCG 5/21/96	7.32	Area G Sorption Studies 1/23/96	TWS INC 05 93 05	Area G Sorption
31	WC.BT.12-2023.GB	WCG 1F.1	Ultima Gold AB	Np SOR BT WCG 5/21/96	7.32	Area G Sorption Studies 1/23/96	TWS INC 05 93 05	Area G Sorption
32	WC.BT.12-2024.GB	WCG 1F.1	Ultima Gold AB	Np SOR BT WCG 5/21/96	7.32	Area G Sorption Studies 1/23/96	TWS INC 05 93 05	Area G Sorption
33	WC.BT.91-2063.GB	WCG 1F.1	Ultima Gold AB	Np SOR BT WCG 5/21/96	7.32	Area G Sorption Studies 1/23/96	TWS INC 05 93 05	Area G Sorption

	A	AQ	AR	AS	AT	AU	AV	AW
1	Sample Identification	Water ID	Type of Scintillation Cocktail Used	ID of Tracer Solutions Used for Sorption Experiment	pH of Tracer Solutions Equilibrated in Glove Box	Binder where Raw Experimental Data are Located	Optical Disk where Reduced Data are Located	Subdirectory
34	WC BT.91-2064 GB	WCG 1F.1	Ultima Gold AB	Np SOR BT WCG 5/21/96	7.32	Area G Sorption Studies 1/23/96 TWS INC 05 93 05		Area G Sorption
35	Np SOR.BT.WCG 5/21/96_CTR 3	WCG 1F.1	Ultima Gold AB	Np SOR BT WCG 5/21/96	7.32	Area G Sorption Studies 1/23/96 TWS INC 05 93 05		Area G Sorption
36	Np.SOR.BT.WCG 5/21/96_CTR 4	WCG 1F.1	Ultima Gold AB	Np SOR BT WCG 5/21/96	7.32	Area G Sorption Studies 1/23/96 TWS INC 05 93 05		Area G Sorption
37	Np SOR BT.WCG 5/21/96_STD 3	WCG 1F.1	Ultima Gold AB	Np SOR BT WCG 5/21/96	7.32	Area G Sorption Studies 1/23/96 TWS INC 05 93 05		Area G Sorption
38	Np.SOR BT.WCG 5/21/96_STD 4	WCG 1F.1	Ultima Gold AB	Np SOR BT WCG 5/21/96	7.32	Area G Sorption Studies 1/23/96 TWS INC 05 93 05		Area G Sorption
39						Area G Sorption Studies 1/23/96 TWS INC 05 93 05		Area G Sorption
40	WC BT.109-2025.GB	WCG 1F.1	Ultima Gold AB	Pu SOR BT.WCG 5/21/96	7.27	Area G Sorption Studies 1/23/96 TWS INC 05 93 05		Area G Sorption
41	WC BT.109-2026.GB	WCG 1F.1	Ultima Gold AB	Pu SOR BT.WCG 5/21/96	7.27	Area G Sorption Studies 1/23/96 TWS INC 05 93 05		Area G Sorption
42	WC.BT.80-2027.GB	WCG 1F.1	Ultima Gold AB	Pu SOR BT.WCG 5/21/96	7.27	Area G Sorption Studies 1/23/96 TWS INC 05 93 05		Area G Sorption
43	WC.BT.80-2028.GB	WCG 1F.1	Ultima Gold AB	Pu SOR BT.WCG 5/21/96	7.27	Area G Sorption Studies 1/23/96 TWS INC 05 93 05		Area G Sorption
44	WC.BT.75-2029.GB	WCG 1F.1	Ultima Gold AB	Pu SOR BT.WCG 5/21/96	7.27	Area G Sorption Studies 1/23/96 TWS INC 05 93 05		Area G Sorption
45	WC.BT.75-2030.GB	WCG 1F.1	Ultima Gold AB	Pu SOR BT.WCG 5/21/96	7.27	Area G Sorption Studies 1/23/96 TWS INC 05 93 05		Area G Sorption
46	WC.BT.78-2031.GB	WCG 1F.1	Ultima Gold AB	Pu SOR BT.WCG 5/21/96	7.27	Area G Sorption Studies 1/23/96 TWS INC 05 93 05		Area G Sorption
47	WC.BT.78-2032.GB	WCG 1F.1	Ultima Gold AB	Pu SOR BT.WCG 5/21/96	7.27	Area G Sorption Studies 1/23/96 TWS INC 05 93 05		Area G Sorption
48	WC BT.66-2033.GB	WCG 1F.1	Ultima Gold AB	Pu SOR BT.WCG 5/21/96	7.27	Area G Sorption Studies 1/23/96 TWS INC 05 93 05		Area G Sorption
49	WC.BT.66-2034.GB	WCG 1F.1	Ultima Gold AB	Pu SOR BT.WCG 5/21/96	7.27	Area G Sorption Studies 1/23/96 TWS INC 05 93 05		Area G Sorption
50	WC.BT.12-2035.GB	WCG 1F.1	Ultima Gold AB	Pu SOR BT.WCG 5/21/96	7.27	Area G Sorption Studies 1/23/96 TWS INC 05 93 05		Area G Sorption
51	WC BT.12-2036.GB	WCG 1F.1	Ultima Gold AB	Pu SOR BT.WCG 5/21/96	7.27	Area G Sorption Studies 1/23/96 TWS INC 05 93 05		Area G Sorption
52	WC.BT.9-2065.GB	WCG 1F.1	Ultima Gold AB	Pu SOR BT.WCG 5/21/96	7.27	Area G Sorption Studies 1/23/96 TWS INC 05 93 05		Area G Sorption
53	WC.BT.91-2066.GB	WCG 1F.1	Ultima Gold AB	Pu SOR BT.WCG 5/21/96	7.27	Area G Sorption Studies 1/23/96 TWS INC 05 93 05		Area G Sorption
54	Pu.SOR BT.WCG 5/21/96_CTR 5	WCG 1F.1	Ultima Gold AB	Pu SOR BT.WCG 5/21/96	7.27	Area G Sorption Studies 1/23/96 TWS INC 05 93 05		Area G Sorption
55	Pu.SOR BT.WCG 5/21/96_CTR 6	WCG 1F.1	Ultima Gold AB	Pu SOR BT.WCG 5/21/96	7.27	Area G Sorption Studies 1/23/96 TWS INC 05 93 05		Area G Sorption
56	Pu.SOR BT.WCG 5/21/96_STD 5	WCG 1F.1	Ultima Gold AB	Pu SOR BT.WCG 5/21/96	7.27	Area G Sorption Studies 1/23/96 TWS INC 05 93 05		Area G Sorption
57	Pu SOR BT.WCG 5/21/96_STD 6	WCG 1F.1	Ultima Gold AB	Pu SOR BT.WCG 5/21/96	7.27	Area G Sorption Studies 1/23/96 TWS INC 05 93 05		Area G Sorption
58						Area G Sorption Studies 1/23/96 TWS INC 05 93 05		Area G Sorption
59	WC.BT.109-2037.GB	WCG 1F.1	Ultima Gold AB	U SOR BT WCG 6/5/96	7.20	Area G Sorption Studies 1/23/96 TWS INC 05 93 05		Area G Sorption
60	WC BT.109-2038.GB	WCG 1F.1	Ultima Gold AB	U SOR BT WCG 6/5/96	7.20	Area G Sorption Studies 1/23/96 TWS INC 05 93 05		Area G Sorption
61	WC.BT.80-2039.GB	WCG 1F.1	Ultima Gold AB	U SOR BT.WCG 6/5/96	7.20	Area G Sorption Studies 1/23/96 TWS INC 05 93 05		Area G Sorption
62	WC BT.80-2040.GB	WCG 1F.1	Ultima Gold AB	U SOR BT WCG 6/5/96	7.20	Area G Sorption Studies 1/23/96 TWS INC 05 93 05		Area G Sorption
63	WC BT.75-2041.GB	WCG 1F.1	Ultima Gold AB	U SOR BT WCG 6/5/96	7.20	Area G Sorption Studies 1/23/96 TWS INC 05 93 05		Area G Sorption
64	WC BT.75-2042.GB	WCG 1F.1	Ultima Gold AB	U SOR BT WCG 6/5/96	7.20	Area G Sorption Studies 1/23/96 TWS INC 05 93 05		Area G Sorption
65	WC.BT.78-2043.GB	WCG 1F.1	Ultima Gold AB	U SOR BT WCG 6/5/96	7.20	Area G Sorption Studies 1/23/96 TWS INC 05 93 05		Area G Sorption

	A	AQ	AR	AS	AT	AU	AV	AW
	Sample Identification	Water ID	Type of Scintillation Cocktail Used	ID of Tracer Solutions Used for Sorption Experiment	pH of Tracer Solutions Equilibrated in Glove Box	Binder where Raw Experimental Data are Located	Optical Disk where Reduced Data are Located	Subdirectory
1								
66	WC BT.79-2044 GB	WCG 1F.1	Ultima Gold AB	U SOR BT WCG 6/5/96	7.20	Area G Sorption Studies 1/23/96	TWS INC 05 93 05	Area G Sorption
67	WC BT.65-2045 GB	WCG 1F.1	Ultima Gold AB	U SOR BT WCG 6/5/96	7.20	Area G Sorption Studies 1/23/96	TWS INC 05 93 05	Area G Sorption
68	WC BT.65-2046 GB	WCG 1F.1	Ultima Gold AB	U SOR BT WCG 6/5/96	7.20	Area G Sorption Studies 1/23/96	TWS INC 05 93 05	Area G Sorption
69	WC.BT.12-2047 GB	WCG 1F.1	Ultima Gold AB	U SOR BT WCG 6/5/96	7.20	Area G Sorption Studies 1/23/96	TWS INC 05 93 05	Area G Sorption
70	WC BT.12-2048 GB	WCG 1F.1	Ultima Gold AB	U SOR BT WCG 6/5/96	7.20	Area G Sorption Studies 1/23/96	TWS INC 05 93 05	Area G Sorption
71	WC BT.91-2067.GB	WCG 1F.1	Ultima Gold AB	U SOR BT WCG 6/5/96	7.20	Area G Sorption Studies 1/23/96	TWS INC 05 93 05	Area G Sorption
72	WC BT.91-2068 GB	WCG 1F.1	Ultima Gold AB	U.SOR BT WCG 6/5/96	7.20	Area G Sorption Studies 1/23/96	TWS INC 05 93 05	Area G Sorption
73	U SOR BT.WCG 5/21/95_CTR 7	WCG 1F.1	Ultima Gold AB	U SOR BT WCG 6/5/96	7.20	Area G Sorption Studies 1/23/96	TWS INC 05 93 05	Area G Sorption
74	U.SOR.BT.WCG 5/21/95_CTR 8	WCG 1F.1	Ultima Gold AB	U SOR BT.WCG 6/5/96	7.20	Area G Sorption Studies 1/23/96	TWS INC 05 93 05	Area G Sorption
75	U SOR BT.WCG 5/21/96_STD 7	WCG 1F.1	Ultima Gold AB	U SOR BT WCG 6/5/96	7.20	Area G Sorption Studies 1/23/96	TWS INC 05 93 05	Area G Sorption
76	U.SOR BT.WCG 5/21/95_STD 8	WCG 1F.1	Ultima Gold AB	U SOR BT WCG 6/5/96	7.20	Area G Sorption Studies 1/23/96	TWS INC 05 93 05	Area G Sorption
77						Area G Sorption Studies 1/23/96	TWS INC 05 93 05	Area G Sorption
78	WC BT.109-2049 GB	WCG 1F.1	Ultima Gold AB	Tc SOR BT WCG 5/21/96	7.22	Area G Sorption Studies 1/23/96	TWS INC 05 93 05	Area G Sorption
79	WC BT.109-2050.GB	WCG 1F.1	Ultima Gold AB	Tc SOR BT WCG 5/21/96	7.22	Area G Sorption Studies 1/23/96	TWS INC 05 93 05	Area G Sorption
80	WC BT.83-2051.GB	WCG 1F.1	Ultima Gold AB	Tc SOR BT WCG 5/21/96	7.22	Area G Sorption Studies 1/23/96	TWS INC 05 93 05	Area G Sorption
81	WC BT.83-2052 GB	WCG 1F.1	Ultima Gold AB	Tc SOR BT WCG 5/21/96	7.22	Area G Sorption Studies 1/23/96	TWS INC 05 93 05	Area G Sorption
82	WC.BT.75-2053 GB	WCG 1F.1	Ultima Gold AB	Tc SOR BT WCG 5/21/96	7.22	Area G Sorption Studies 1/23/96	TWS INC 05 93 05	Area G Sorption
83	WC BT.75-2054 GB	WCG 1F.1	Ultima Gold AB	Tc SOR BT.WCG 5/21/96	7.22	Area G Sorption Studies 1/23/96	TWS INC 05 93 05	Area G Sorption
84	WC BT.79-2055 GB	WCG 1F.1	Ultima Gold AB	Tc SOR BT WCG 5/21/96	7.22	Area G Sorption Studies 1/23/96	TWS INC 05 93 05	Area G Sorption
85	WC BT.79-2056.GB	WCG 1F.1	Ultima Gold AB	Tc SOR BT WCG 5/21/96	7.22	Area G Sorption Studies 1/23/96	TWS INC 05 93 05	Area G Sorption
86	WC BT.68-2057.GB	WCG 1F.1	Ultima Gold AB	Tc SOR BT WCG 5/21/96	7.22	Area G Sorption Studies 1/23/96	TWS INC 05 93 05	Area G Sorption
87	WC BT.68 2058.GB	WCG 1F.1	Ultima Gold AB	Tc SOR BT WCG 5/21/96	7.22	Area G Sorption Studies 1/23/96	TWS INC 05 93 05	Area G Sorption
88	WC BT.12-2059.GB	WCG 1F.1	Ultima Gold AB	Tc SOR BT WCG 5/21/96	7.22	Area G Sorption Studies 1/23/96	TWS INC 05 93 05	Area G Sorption
89	WC BT.12-2060 GB	WCG 1F.1	Ultima Gold AB	Tc SOR BT.WCG 5/21/96	7.22	Area G Sorption Studies 1/23/96	TWS INC 05 93 05	Area G Sorption
90	WC.BT.91-2069 GB	WCG 1F.1	Ultima Gold AB	Tc SOR BT WCG 5/21/96	7.22	Area G Sorption Studies 1/23/96	TWS INC 05 93 05	Area G Sorption
91	WC.BT.91-2070 GB	WCG 1F.1	Ultima Gold AB	Tc SOR BT WCG 5/21/96	7.22	Area G Sorption Studies 1/23/96	TWS INC 05 93 05	Area G Sorption
92	Tc.SOR.BT.WCG 5/21/95_CTR 9	WCG 1F.1	Ultima Gold AB	Tc SOR BT WCG 5/21/96	7.22	Area G Sorption Studies 1/23/96	TWS INC 05 93 05	Area G Sorption
93	Tc SOR BT.WCG 5/21/95_CTR 10	WCG 1F.1	Ultima Gold AB	Tc SOR BT WCG 5/21/96	7.22	Area G Sorption Studies 1/23/96	TWS INC 05 93 05	Area G Sorption
94	Tc.SOR BT.WCG 5/21/96_STD 9	WCG 1F.1	Ultima Gold AB	Tc SOR BT.WCG 5/21/96	7.22	Area G Sorption Studies 1/23/96	TWS INC 05 93 05	Area G Sorption
95	Tc.SOR BT.WCG 5/21/96_STD 10	WCG 1F.1	Ultima Gold AB	Tc SOR BT WCG 5/21/96	7.22	Area G Sorption Studies 1/23/96	TWS INC 05 93 05	Area G Sorption

Binder Sorp NAT WCG

	A	AX	AY	AZ	EA	EB
	Sample Identification	File Name				
1						
2	WC BT.109-2001 GB	Binder Sorp NAT WCG				
3	WC BT.109-2002.GB	Binder Sorp NAT WCG				
4	WC BT.83-2003.GB	Binder Sorp NAT WCG				
5	WC BT.83-2004 GB	Binder Sorp NAT WCG				
6	WC BT.75-2005.GB	Binder Sorp NAT WCG				
7	WC BT.75-2006 GB	Binder Sorp NAT WCG				
8	WC BT.79-2007.GB	Binder Sorp NAT WCG				
9	WC BT.79 2008.GB	Binder Sorp NAT WCG				
10	WC BT.66-2009 GB	Binder Sorp NAT WCG				
11	WC BT.66-2010 GB	Binder Sorp NAT WCG				
12	WC.BT.12-2011.GB	Binder Sorp NAT WCG				
13	WC.BT.12-2012.GB	Binder Sorp NAT WCG				
14	WC.BT.91-2061.GB	Binder Sorp NAT WCG				
15	WC BT.91-2062 GB	Binder Sorp NAT WCG				
16	Am.SOR BT.WCG 5/21/96_CTR 1	Binder Sorp NAT WCG				
17	Am.SOR BT.WCG 5/21/96_CTR 2	Binder Sorp NAT WCG				
18	Am SOR BT.WCG 5/21/96_STD 1	Binder Sorp NAT WCG				
19	Am SOR BT.WCG 5/21/96_STD 2	Binder Sorp NAT WCG				
20		Binder Sorp NAT WCG				
21	WC BT.109-2013 GB	Binder Sorp NAT WCG				
22	WC BT.109-2014 GB	Binder Sorp NAT WCG				
23	WC BT.60-2015.GB	Binder Sorp NAT WCG				
24	WC BT.83-2016 GB	Binder Sorp NAT WCG				
25	WC.BT.75-2017.GB	Binder Sorp NAT WCG				
26	WC BT.75-2018 GB	Binder Sorp NAT WCG				
27	WC BT.79-2019 GB	Binder Sorp NAT WCG				
28	WC BT.79-2020 GB	Binder Sorp NAT WCG				
29	WC BT.66-2021.GB	Binder Sorp NAT WCG				
30	WC BT.66-2022 GB	Binder Sorp NAT WCG				
31	WC BT.12-2023 GB	Binder Sorp NAT WCG				
32	WC BT.12-2024 GB	Binder Sorp NAT WCG				
33	WC BT.91-2063 GB	Binder Sorp NAT WCG				

	A	AX	AY	AZ	EA	EB
1	Sample Identification	File Name				
34	WC BT.91-2064 GB	Bander Sorp NAT WCG				
35	Np SOR BT.WCG 5/21/95_CTR 3	Bander Sorp NAT WCG				
36	Np SOR BT.WCG 5/21/95_CTR 4	Bander Sorp NAT WCG				
37	Np SOR BT.WCG 5/21/95_STD 3	Bander Sorp NAT WCG				
38	Np SOR BT.WCG 5/21/95_STD 4	Bander Sorp NAT WCG				
39		Bander Sorp NAT WCG				
40	WC BT.109-2025 GB	Bander Sorp NAT WCG				
41	WC BT.109-2026 GB	Bander Sorp NAT WCG				
42	WC.BT.83-2027.GB	Bander Sorp NAT WCG				
43	WC BT.83-2028.GB	Bander Sorp NAT WCG				
44	WC.BT.75-2029.GB	Bander Sorp NAT WCG				
45	WC BT.75-2030 GB	Bander Sorp NAT WCG				
46	WC.BT.78-2031.GB	Bander Sorp NAT WCG				
47	WC.BT.78-2032 GB	Bander Sorp NAT WCG				
48	WC.BT.66-2033.GB	Bander Sorp NAT WCG				
49	WC BT.66-2034 GB	Bander Sorp NAT WCG				
50	WC.BT.12-2035 GB	Bander Sorp NAT WCG				
51	WC.BT.12-2036.GB	Bander Sorp NAT WCG				
52	WC.BT.9 2065 GB	Bander Sorp NAT WCG				
53	WC.BT.91-2066.GB	Bander Sorp NAT WCG				
54	Pu SOR BT.WCG 5/21/95_CTR 5	Bander Sorp NAT WCG				
55	Pu SOR BT.WCG 5/21/95_CTR 6	Bander Sorp NAT WCG				
56	Pu SOR BT.WCG 5/21/95_STD 5	Bander Sorp NAT WCG				
57	Pu SOR BT.WCG 5/21/95_STD 6	Bander Sorp NAT WCG				
58		Bander Sorp NAT WCG				
59	WC BT.109-2037.GB	Bander Sorp NAT WCG				
60	WC.BT.109-2038 GB	Bander Sorp NAT WCG				
61	WC.BT.80-2039 GB	Bander Sorp NAT WCG				
62	WC BT.80-2040.GB	Bander Sorp NAT WCG				
63	WC BT.75-2041.GB	Bander Sorp NAT WCG				
64	WC BT.75-2042 GB	Bander Sorp NAT WCG				
65	WC BT.78-2043.GB	Bander Sorp NAT WCG				

	A	AX	AY	AZ	BA	BB
	Sample Identification	File Name				
1						
66	WC BT.79-2044.GB	Bander Sorp NAT. WCG				
67	WC BT.66-2045.GB	Bander Sorp NAT. WCG				
68	WC BT.66-2046.GB	Bander Sorp NAT. WCG				
69	WC BT.12-2047.GB	Bander Sorp NAT. WCG				
70	WC BT.12-2048.GB	Bander Sorp NAT. WCG				
71	WC BT.91-2067.GB	Bander Sorp NAT. WCG				
72	WC BT.91-2068.GB	Bander Sorp NAT. WCG				
73	U.SOR BT.WCG 5/21/96_CTR 7	Bander Sorp NAT. WCG				
74	U.SOR BT.WCG 5/21/96_CTR 8	Bander Sorp NAT. WCG				
75	U.SOR BT.WCG 5/21/96_STD 7	Bander Sorp NAT. WCG				
76	U.SOR BT.WCG 5/21/96_STD 8	Bander Sorp NAT. WCG				
77	[illegible]	Bander Sorp NAT. WCG				
78	WC BT.100-2049.GB	Bander Sorp NAT. WCG				
79	WC BT.100-2050.GB	Bander Sorp NAT. WCG				
80	WC BT.80-2051.GB	Bander Sorp NAT. WCG				
81	WC BT.80-2052.GB	Bander Sorp NAT. WCG				
82	WC BT.75-2053.GB	Bander Sorp NAT. WCG				
83	WC.BT.75-2054.GB	Bander Sorp NAT. WCG				
84	WC.BT.79-2055.GB	Bander Sorp NAT. WCG				
85	WC.BT.79-2056.GB	Bander Sorp NAT. WCG				
86	WC.BT.66-2057.GB	Bander Sorp NAT. WCG				
87	WC BT.66-2058.GB	Bander Sorp NAT. WCG				
88	WC BT.12-2059.GB	Bander Sorp NAT. WCG				
89	WC BT.12-2060.GB	Bander Sorp NAT. WCG				
90	WC BT.91-2069.GB	Bander Sorp NAT. WCG				
91	WC.BT.91-2070.GB	Bander Sorp NAT. WCG				
92	Tc.SOR BT.WCG 5/21/96_CTR 9	Bander Sorp NAT. WCG				
93	Tc.SOR BT.WCG 5/21/96_CTR 10	Bander Sorp NAT. WCG				
94	Tc.SOR BT.WCG 5/21/96_STD 9	Bander Sorp NAT. WCG				
95	Tc.SOR BT.WCG 5/21/96_STD 10	Bander Sorp NAT. WCG				

APPENDIX C

CHEMICAL ANALYSES OF PORE WATER EXTRACTED FROM BANDELIER TUFF

Summary of Chemical Analysis of Pore Water Samples, Bandelier Tuff, Los Alamos, New Mexico.

Date Analysis[a]	03/96*	06/96*	06/96*	06/96*	06/96*
CH	1107	1107	1107	1121	1123
D (ft)	91.0	51.0	104.0	35.0	59.0
Al	NA	0.23	0.15	0.14	0.90
B	NA	7.53	3.24	1.90	0.70
Br	1.07	4.28	1.00	2.58	22.6
Ca	17.3	78.0	8.79	23.8	853
Cl	31.4	306	58.3	161	1430
CO_3	171	58.2	225	239	<3
F	46.0	20.0	41.6	43.9	4.29
Fe	NA	<0.03	<0.03	<0.07	<0.03
HCO_3	547	71.2	436	176	<3
K	16.3	179	42.8	16.7	58.5
Mg	1.63	16.1	3.09	4.05	63.8
Na	435	345	481	567	920
NO_3	0.47	96.7	0.50	109	28.9
pH[b]	9.81	9.11	9.82	10.01	9.08
OH	NA	NA	NA	NA	52.1
SiO_2	NA	96.9	88.4	195	86.7
SO_4	81.1	429	143	279	1951
TDS[c]	1348	1708	1533	1819	5473

* Groundwater analyzed at Los Alamos National Laboratory, EES-1. Dale Counce analyst.
a. All analyses are in mg/L, except where noted.
CH means Core Hole Number.
D means depth of sample where pore water is extracted from (in feet).
NA means not analyzed due to insufficient sample volume.
b. Standard units.
c. TDS is total dissolved solids.

APPENDIX D

RADIONUCLIDE BATCH SORPTION EXPERIMENTAL DATA AND RESULTS USING SYNTHETIC PORE WATER

	A	B
1	AREA G SORPTION DATA INFORMATION SHEET	
2	Experiment Number	Bandelier.Sorp.SYN.WCG#2
3	ID of Water Used in Experiment	SYNWCG 9/17/96
4	Notebook Reference	Area"G" Sorption Studies
5	Tracer Solution ID#	Am.SORP.SYNWCG.9/23/96 Np.SORP.SYN.WCG. 9/17/96 U.SORP.SYNWCG. 9/17/96 Tc.SORP.SYNWCG.9/23/96 Pu.SORP.SYNWCG 9/17/96
6	Notebook with Information on Tracer Solution	Area"G" Sorption Studies
7	YMP Balance ID# Used Before Addition of Tracer	OHAUS GT4100 817457
8	YMP Balance Calibration Due Date	2/5/97
9	YMP Balance ID# Used after Addition of Tracer	OHAUS GT4100 817457
10	YMP Balance Calibration Due Date	2/5/97
11	YMP Balance ID# Used in Glovebox	N/A
12	YMP Balance Calibration Due Date	N/A
13	For Glovebox YMP Balance ID# Used to Weigh Scintillation Vials and Aliquots	N/A
14	YMP Balance Calibration Due Date	N/A
15	Mineral Code IDs	Bandelier Tuff: 108.0'-109.5', 79.9'-80.0', 79.1'-79.7', 74.0'-75.0', 65.0'-66.0', 10.8'-12.0', 91.0'
16	Sieving Information	Dry
17	Notebook Reference for Information on Solid Samples	Area"G" Sorption Studies
18	Type of Oak Ridge Container Used for Sorption Experiment	POLYCARBONATE
19	Detailed Procedure Used - Sorption	LANL-CST-DP-86
20	DP Revision Number	R1
21	Glovebox Information	
22	Glovebox Temperature Before Adding Equilibration Water to OR Tubes °C	N/A
23	Glovebox Humidity Before Adding Equilibration Water to OR Tubes, %	N/A
24	Glovebox Pressure Before Adding Equilibration Water to OR Tubes Torr	N/A
25	Glovebox CO2 Reading Before Adding Equilibration Water to OR Tubes, %	N/A
26	Arbitrary Glovebox Air Pressure Gauge Input Reading Before Adding Equilibration Water to OR Tubes	N/A
27	Arbitrary Glovebox CO2 Pressure Gauge Input Reading Before Adding Equilibration Water to OR Tubes	N/A
28	Detailed Procedure Used - Glovebox	N/A
29	DP Revision Number	N/A
30		
31	Glovebox Humidity Before Adding Tracer Solution to OR Tubes, %	N/A
32	Glovebox Pressure Before Adding Tracer Solution to OR Tubes, Torr	N/A
33	Arbitrary Glovebox Air Pressure Gauge Input Reading Before Adding Tracer Solution to OR Tubes	N/A
34	Arbitrary Glovebox CO2 Pressure Gauge Input Reading Before Adding Tracer Solution to OR Tubes	N/A
35		
36	Back-up Equilibration Water pH after Sorption	N/A
37	pH Meter Used YMP ID#	N/A
38	pH Buffers Used/Manufacturer	N/A
39	pH Buffer 4, Lot #/Expiration Date	N/A
40	pH Buffer 7, Lot #/Expiration Date	N/A
41	Detailed Procedure Used	N/A
42	DP Revision Number	N/A
43	Glovebox Temperature after Sorption, °F	N/A
44	Glovebox Humidity after Sorption, %	N/A
45	Glovebox Pressure after Sorption Torr	N/A
46	Glovebox CO2 Reading after Sorption, %	N/A
47	Arbitrary Glovebox Air Pressure Gauge Input Reading After Sorption	N/A
48	Arbitrary Glovebox CO2 Pressure Gauge Input Reading After Sorption	N/A
49		
50	Glove Box Identification Code	N/A

	A	B
51	Hydrometer Used in Glovebox	N/A
52	Controlled Atmosphere Pressure Gauge Used in Glovebox	N/A
53	CO_2 and Air Input Pressure Gauges Used in Glovebox	N/A
54	Notebook Reference for CO_2/Air Input Pressure Gauge Calibration	N/A
55	Volumetric Flow for Air Input, sccm	N/A
56	Volumetric Flow for CO_2 Input, sccm	N/A
57	**pH Measurement**	
58	pH Meter Used, YMP ID#	645399
59	Detailed Procedure Used	LANL-CST-DP-35
60	DP Revision Number	R3
61	Tracer Solution pH Before Adding to OR Tubes	Tc=10.03; Np=10.03; U=10.03; Pu=10.03; Tc=10.04
62	Glovebox Temperature Before Adding Tracer Solution to OR Tubes, °C	N/A
63	Glovebox Humidity Before Adding Tracer Solution to OR Tubes, %	N/A
64	pH Buffer 4, Manufacturer/Lot #/Expiration Date	Fischer/962222-24/4-98
65	Reading for pH 4 Buffer (Prior to Making Measurements)	4.01
66	Reading for pH 4 Buffer (after Making Measurements)	4.07
67	pH Buffer 7, Manufacturer/Lot #/Expiration Date	Fischer/953693-24/6-97
68	Reading for pH 7 Buffer (Prior to Making Measurements)	6.99
69	Reading for pH 7 Buffer (after Making Measurements)	7.03
70	pH Buffer 10, Manufacturer/Lot #/Expiration Date	Fischer/953243-24/5-97
71	Reading for pH 10 Buffer (Prior to Making Measurements)	10
72	Reading for pH 10 Buffer (after Making Measurements)	9.98
73	**Eh Measurement**	
74	Detailed Procedure Used	N/A
75	YMP ID# of Eh Meter	N/A
76	Electrodes Used for Eh Measurement	N/A
77	Zobell Lot Number and Ideal Value	N/A
78	Zobell Solution Preparation Date	N/A
79	Eh of Zobell Solution (Prior to Making Measurements), mV	N/A
80	Eh of Zobell Solution (after making Measurements), mV	N/A
81	Temperature Range for Eh Measurements, °C	N/A
82	Eh of Water Used in the Experiment, mV	N/A
83	**Verification of Liquid Scintillation Counter**	
84	YMP Counter ID#	841221, 901133, 754745
85	ID# of Low Standard Counted	Am243-1/96 Mid; Nist 2/4/94 A Np; U233-1/96 mid; St-Pu-1
86	Expected CPM of Standard Counted	Am243-1/96 Mid=1462; Nist 2/4/94 A Np=233; U233-1/96 mid=1318; St-Pu-1=842
87	Total Activity (-Bkg)	Am243-1/96 Mid=1398; Nist 2/4/94 A Np=239; U233-1/96 mid=1220; St-Pu-1=770
88	ID# of High Standard Counted	Am-243-1/96 high; Nist 1/4/94 A; U233-1/96 High; St-Pu-2
89	Expected CPM of Standard Counted	Am-243-1/96 high=45060; Nist 1/4/94 A Np=1032; U233-1/96 High42585; St-Pu-2=3650
90	Total Activity (-Bkg)	Am-243-1/96 high=42063; Nist 1/4/94 A Np=1073; U233-1/96 High 42368; St-Pu-2=3500
91	Detailed Procedure Used	LANL-CST-DP-79
92	DP Revision Number	R2
93	Explanation of Sample Coding	WC refers to the type of water used; BT refers to Bandelier Tuff; the number after BT is the core depth; the last number is a unique number assigned to each sample; GB refers to the Glove Box; CTR refers to the controls, STD refers to the standards.
94	**Verification of Gamma Counter for Technetium 95m**	

	A	B
95	YMP Counter ID#	Auto-Gamma 5000 Counter
96	Detailed Procedure Used	Gamma Counter Tc 95m Notebook Procedure
97	Notebook & Pages	LA-CST-NBK-95-015 E2-E21
98	Vendor Sample Analysis Information	
99	Vendor Analysis Notebook Reference	N/A
100	Acceptance Plan Notebook Reference	N/A
101	Location of Data	
102	Experimental Data (Notebook ID#)	Area G Sorption Studies
103	Experimental Data (Page(s) #)	Sorp. #2
104	Reduced Data (Optical disk #)	TWS-INC-05-96-05
105	Reduced Data (Subdirectory)	Area G Sorption
106	Reduced Data (File name)	Data Sheet SYN WCG #2

	A	B	C	D	E	F	G	H	I
1	Sample Identification	Sorption Time	Experiment No.	Atmosphere	Desired Pu, Am, Np, U, Tc Tracer Solution Activity, CPM/g	Description of Solid (Bandelier Tuff)	Particle Size, Micrometers (If Sieved)	Sieving Information	Type of Water Used If Wet Sieved
2	SYN.WCG BT.108-3101	2 weeks	Bandelier Sorp SYN WCG#2	.03%CO2	4300	108.0'-109.5'	< 500	Dry	N/A
3	SYN.WCG BT.108-3102	2 weeks	Bandelier Sorp SYN WCG#2	.03%CO2	4300	108.0'-109.5'	< 500	Dry	N/A
4	SYN.WCG.BT.79.9-3103	2 weeks	Bandelier Sorp SYN WCG#2	.03%CO2	4300	79.9'-80.0' Fe rich	< 500	Dry	N/A
5	SYN.WCG BT.79.9-3104	2 weeks	Bandelier Sorp SYN WCG#2	.03%CO2	4300	79.9'-80.0' Fe rich	< 500	Dry	N/A
6	SYN.WCG.BT.74-3105	2 weeks	Bandelier Sorp SYN WCG#2	.03%CO2	4300	74.0'-75.0'	< 500	Dry	N/A
7	SYN.WCG BT.74-3106	2 weeks	Bandelier Sorp SYN WCG#2	.03%CO2	4300	74.0'-75.0'	< 500	Dry	N/A
8	SYN.WCG.BT.79.1-3107	2 weeks	Bandelier Sorp SYN WCG#2	.03%CO2	4300	79.1'-79.7'	< 500	Dry	N/A
9	SYN.WCG BT.79.1-3108	2 weeks	Bandelier Sorp SYN WCG#2	.03%CO2	4300	79.1'-79.7'	< 500	Dry	N/A
10	SYN.WCG BT.65-3109	2 weeks	Bandelier Sorp SYN WCG#2	.03%CO2	4300	65.0'-66.0'	< 500	Dry	N/A
11	SYN WCG BT.65-3110	2 weeks	Bandelier Sorp SYN WCG#2	.03%CO2	4300	65.0'-66.0'	< 500	Dry	N/A
12	SYN.WCG BT.10-3111	2 weeks	Bandelier Sorp SYN WCG#2	.03%CO2	4300	10.8'-12.0'	< 500	Dry	N/A
13	SYN.WCG BT.10-3112	2 weeks	Bandelier Sorp SYN WCG#2	.03%CO2	4300	10.8'-12.0'	< 500	Dry	N/A
14	SYN.WCG.BT.91-3113	2 weeks	Bandelier Sorp SYN WCG#2	.03%CO2	4300	91.0	< 500	Dry	N/A
15	SYN.WCG BT.91-3114	2 weeks	Bandelier Sorp SYN WCG#2	.03%CO2	4300	91.0	< 500	Dry	N/A
16	Am.SOR BT.SYN.WCG 5/30/96 CTR 3101	2 weeks	Bandelier Sorp SYN WCG#2	.03%CO2	4300	N/A	N/A	N/A	N/A
17	Am.SOR BT.SYN.WCG 5/30/96 CTR 3102	2 weeks	Bandelier Sorp SYN WCG#2	.03%CO2	4300	N/A	N/A	N/A	N/A
18	Am.SOR.BT.SYN.WCG.5/30/96 STD 11								
19	Am.SOR BT.SYN.WCG 5/30/96 STD 12								

	A	J	K	L	M	N	O	P	Q	R
1	Sample Identification	Tube + Cap Mass, g	Tube + Cap + Mineral Mass, g	Mineral Mass, g (Col. K-Col. J)	Tube + Cap + Mineral + Water Mass, g	Water Mass, g (Col. M-Col. K)	Julian Date Pretreatment Started '95	Julian Date Pretreatment Ended '96	Period of Pretreatment, Days	Tube + Cap + Mineral + Water after Pretreatment Mass, g
2	SYN.WCG.BT.108-3101	22.93	23.93	1.00	44.11	20.18	250.6146	267.5417	16.9271	44.03
3	SYN.WCG.BT.108-3102	23.17	24.16	0.99	44.41	20.25	250.6146	267.5417	16.9271	44.20
4	SYN.WCG.BT.73.9-3103	23.11	24.11	1.00	44.34	20.23	250.6146	267.5417	16.9271	44.25
5	SYN.WCG.BT.73.9-3104	23.23	24.23	1.00	44.46	20.23	250.6146	267.5417	16.9271	44.35
6	SYN.WCG.BT.74-3105	23.04	24.04	1.00	44.22	20.18	250.6146	267.5417	16.9271	44.13
7	SYN.WCG.BT.74-3106	22.85	23.85	1.00	44.14	20.29	250.6146	267.5417	16.9271	44.06
8	SYN.WCG.BT.79.1-3107	23.11	24.12	1.01	44.35	20.23	250.6146	267.5417	16.9271	44.26
9	SYN.WCG.BT.79.1-3108	23.00	24.00	1.00	44.23	20.23	250.6146	267.5417	16.9271	44.19
10	SYN.WCG.BT.65-3109	22.83	23.83	1.00	44.04	20.15	250.6146	267.5417	16.9271	43.93
11	SYN.WCG.BT.65-3110	23.09	24.09	1.00	43.84	19.75	250.6146	267.5417	16.9271	43.74
12	SYN.WCG.BT.10-3111	23.28	24.27	0.99	44.32	20.05	250.6146	267.5417	16.9271	44.21
13	SYN.WCG.BT.10-3112	23.13	24.12	0.99	44.27	20.15	250.6146	267.5417	16.9271	44.17
14	SYN.WCG.BT.91-3113	22.91	23.92	1.01	44.08	20.16	250.6146	267.5417	16.9271	43.93
15	SYN.WCG.BT.91-3114	22.94	23.95	1.01	44.06	20.11	250.6146	267.5417	16.9271	43.95
16	Am SOR BT.SYN.WCG.5/30/96 CTR 3101	23.16								
17	Am SOR BT.SYN.WCG.5/30/96 CTR 3102	22.89								
18	Am SOR BT.SYN.WCG.5/30/96 STD 11									
19	Am SOR BT.SYN.WCG.5/30/96 STD 12									

	A	S	T	U	V	W	X	Y	Z	AA
1	Sample Identification	% Evaporation during Pretreatment ((Col N-Col S) /Col.N*100)	Tube + Cap + Mineral + Water after Decantation Mass, g	pH of Water after Pretreatment	Eh of Water after Pretreatment, mV	Julian Date Tracer Solution was Added, '96	Mass after Tracer Solution was Added, g	Mass of Tracer Solution Added, g	Julian Date Sorption Started '96	Julian Date Sorption Ended '96
2	SYN.WCG BT.108-3101	0.18	24.84	9.96	N/A	268.3431	44.96	20.12	268.3431	282.4167
3	SYN.WCG BT.108-3102	0.47	24.91		N/A	268.3431	45.01	20.10	268.3431	282.4167
4	SYN.WCG BT.79.9-3103	0.20	25.24	9.97	N/A	268.3431	45.34	20.10	268.3431	282.4167
5	SYN.WCG BT.79.9-3104	0.25	25.33		N/A	268.3431	45.48	20.18	268.3431	282.4167
6	SYN.WCG BT.74-3105	0.20	25.26	9.96	N/A	268.3431	45.46	20.20	268.3431	282.4167
7	SYN.WCG BT.74-3106	0.18	25.04		N/A	268.3431	45.09	20.05	268.3431	282.4167
8	SYN.WCG BT.79.1-3107	0.20	25.45	9.97	N/A	268.3431	45.64	20.19	268.3431	282.4167
9	SYN.WCG BT.79.1-3108	0.23	25.22		N/A	268.3431	45.33	20.11	268.3431	282.4167
10	SYN.WCG BT.65-3109	0.25	25.05	9.97	N/A	268.3431	45.17	20.12	268.3431	282.4167
11	SYN.WCG BT.65-3110	0.23	25.33		N/A	268.3431	45.46	20.16	268.3431	282.4167
12	SYN.WCG BT.10-3111	0.25	25.20	9.99	N/A	268.3431	45.30	20.10	268.3431	282.4167
13	SYN.WCG BT.10-3112	0.23	24.97		N/A	268.3431	45.05	20.08	268.3431	282.4167
14	SYN.WCG BT.51-3113	0.20	25.13	9.95	N/A	268.3431	45.23	20.10	268.3431	282.4167
15	SYN.WCG BT.51-3114	0.25	25.05		N/A	268.3431	45.00	19.95	268.3431	282.4167
16	Am.SOR.BT.SYN.WCG.5/30/96 CTR 3191					268.3431	43.29	20.13	268.3431	282.4167
17	Am SOR BT.SYN.WCG 5/30/96 CTR 3192					268.3431	42.81	19.92	268.3431	282.4167
18	Am SOR BT.SYN.WCG 5/30/96 STD 11									
19	Am SOR BT.SYN.WCG 5/30/96 STD 12									

	A	AB	AC	AD	AE	AF	AG	AH	AI	AJ
1	Sample Identification	Period of Sorption, Days	Mass after Sorption Ended, g	% Evaporation during Sorption ((Col.X-Col.AB) /Col.X*100)	pH of Tracer Solution after Sorption	Eh of Tracer Solution after Sorption	Mass of Counting Vial, g	Mass of Counting Vial + Aliquot of Tracer Solution after Sorption, g	Mass of Counted Tracer Solution after Sorption, g (Col AI-Col AH)	Total CFM in Counted Tracer Solution after Sorption
2	SYN.WCG.BT.108-3101	14.0735	44.84	0.27	9.79	N/A	6.17	7.20	1.03	391.35
3	SYN.WCG.BT.108-3102	14.0735	44.76	0.56		N/A	6.21	7.24	1.03	410.00
4	SYN.WCG.BT.79.9-3103	14.0735	45.19	0.33	9.8	N/A	6.17	8.23	2.06	421.10
5	SYN.WCG.BT.79.9-3104	14.0735	45.36	0.26		N/A	6.19	7.22	1.03	183.50
6	SYN.WCG.BT.74-3105	14.0735	45.36	0.22	9.79	N/A	6.2	7.22	1.02	20.55
7	SYN.WCG.BT.74-3106	14.0735	44.99	0.24		N/A	6.21	7.23	1.02	19.00
8	SYN.WCG.BT.79.1-3107	14.0735	45.40	0.53	9.79	N/A	6.18	7.21	1.03	242.85
9	SYN.WCG.BT.79.1-3108	14.0735	45.22	0.24		N/A	6.17	7.20	1.03	222.15
10	SYN.WCG.BT.65-3109	14.0735	45.02	0.33	9.79	N/A	6.2	7.22	1.02	4.95
11	SYN.WCG.BT.65-3110	14.0735	45.37	0.20		N/A	6.19	7.22	1.03	5.85
12	SYN.WCG.BT.10-3111	14.0735	45.19	0.24	9.81	N/A	6.18	7.19	1.01	4.80
13	SYN.WCG.BT.10-3112	14.0735	44.94	0.24		N/A	6.23	7.26	1.03	4.00
14	SYN.WCG.BT.91-3113	14.0735	45.06	0.38	9.79	N/A	6.2	7.20	1.00	4.20
15	SYN.WCG.BT.91-3114	14.0735	44.79	0.47		N/A	6.21	7.21	1.00	3.10
16	Am.SOR.BT.SYN.WCG.5/30/96 CTR 3101	14.0735	43.19	0.23	9.81	N/A	6.17	7.17	1.00	4305.05
17	Am.SOR.BT.SYN.WCG.5/30/96 CTR 3102	14.0735	42.70	0.26		N/A	6.17	7.18	1.01	4331.80
18	Am.SOR.BT.SYN.WCG.5/30/96 STD 11						6.65	7.62	0.97	4154.05
19	Am.SOR.BT.SYN.WCG.5/30/96 STD 12						6.65	7.62	0.97	4154.05

	A	AK	AL	AM	AN	AO	AP	AQ
1	Sample Identification	CPM/g in Counted Tracer Solution after Sorption (Col AL/ Col AK)	Kd (ml/g) of Original Tracer Solution Based on Standards	Kd (ml/g) of Original Tracer Solution Based on Controls	Water ID	Type of Scintillation Cocktail Used	ID of Tracer Solutions Used for Sorption Experiment	Binder where Raw Experimental Data are Located
2	SYN.WCG.BT.108-3101	373.95	2.26E+02	2.06E+02	SYN.WCG 9/17/96	Ultima Gold AB	Am.SOR.SYN.WCG 9/23/96	Area G Sorption Studies
3	SYN.WCG.BT.108-3102	398.06	2.18E+02	1.98E+02	SYN.WCG 9/17/96	Ultima Gold AB	Am.SOR.SYN.WCG 9/23/96	Area G Sorption Studies
4	SYN.WCG.BT.79.9-3103	204.42	4.20E+02	4.00E+02	SYN.WCG 9/17/96	Ultima Gold AB	Am.SOR.SYN.WCG 9/23/96	Area G Sorption Studies
5	SYN.WCG.BT.79.9-3104	183.98	4.69E+02	4.49E+02	SYN.WCG 9/17/96	Ultima Gold AB	Am.SOR.SYN.WCG 9/23/96	Area G Sorption Studies
6	SYN.WCG.BT.74-3105	20.15	4.29E+03	4.27E+03	SYN.WCG 9/17/96	Ultima Gold AB	Am.SOR.SYN.WCG 9/23/96	Area G Sorption Studies
7	SYN.WCG.BT.74-3106	18.63	4.61E+03	4.59E+03	SYN.WCG 9/17/96	Ultima Gold AB	Am.SOR.SYN.WCG 9/23/96	Area G Sorption Studies
8	SYN.WCG.BT.79.1-3107	235.78	3.62E+02	3.42E+02	SYN.WCG 9/17/96	Ultima Gold AB	Am.SOR.SYN.WCG 9/23/96	Area G Sorption Studies
9	SYN.WCG.BT.79.1-3108	235.68	3.98E+02	3.78E+02	SYN.WCG 9/17/96	Ultima Gold AB	Am.SOR.SYN.WCG 9/23/96	Area G Sorption Studies
10	SYN.WCG.BT.65-3109	4.85	1.76E+04	1.77E+04	SYN.WCG 9/17/96	Ultima Gold AB	Am.SOR.SYN.WCG 9/23/96	Area G Sorption Studies
11	SYN.WCG.BT.65-3110	5.68	1.52E+04	1.52E+04	SYN.WCG 9/17/96	Ultima Gold AB	Am.SOR.SYN.WCG 9/23/96	Area G Sorption Studies
12	SYN.WCG.BT.10-3111	4.75	1.83E+04	1.83E+04	SYN.WCG 9/17/96	Ultima Gold AB	Am.SOR.SYN.WCG 9/23/96	Area G Sorption Studies
13	SYN.WCG.BT.10-3112	3.88	2.24E+04	2.23E+04	SYN.WCG 9/17/96	Ultima Gold AB	Am.SOR.SYN.WCG 9/23/96	Area G Sorption Studies
14	SYN.WCG.BT.91-3113	4.20	2.03E+04	2.03E+04	SYN.WCG 9/17/96	Ultima Gold AB	Am.SOR.SYN.WCG 9/23/96	Area G Sorption Studies
15	SYN.WCG.BT.91-3114	3.10	2.73E+04	2.73E+04	SYN.WCG 9/17/96	Ultima Gold AB	Am.SOR.SYN.WCG 9/23/96	Area G Sorption Studies
16	Am.SOR.BT.SYN.WCG.5/30/96 CTR 3101	4305.05	N/A	N/A	SYN.WCG 9/17/96	Ultima Gold AB	Am.SOR.SYN.WCG 9/23/96	Area G Sorption Studies
17	Am.SOR.BT.SYN.WCG.5/30/96 CTR 3102	4288.91	N/A	N/A	SYN.WCG 9/17/96	Ultima Gold AB	Am.SOR.SYN.WCG 9/23/96	Area G Sorption Studies
18	Am.SOR.BT.SYN.WCG.5/30/96 STD 11	4282.53	N/A	N/A	SYN.WCG 9/17/96	Ultima Gold AB	Am.SOR.SYN.WCG 9/23/96	Area G Sorption Studies
19	Am.SOR.BT.SYN.WCG.5/30/96 STD 12	4282.53	N/A	N/A	SYN.WCG 9/17/96	Ultima Gold AB	Am.SOR.SYN.WCG 9/23/96	Area G Sorption Studies

	A	AR	AS	AT	AU	AV	AW	AX
1	Sample Identification	Optical Disk where Reduced Data are Located	Subdirectory	File Name				
2	SYN.WCG.BT.108-3101	TWS-INC-05-93-05	Area G Sorption	Syn Fl Sorp. #2				
3	SYN.WCG.BT.108-3102	TWS-INC-05-93-05	Area G Sorption	Syn Fl Sorp. #2				
4	SYN.WCG.BT.79.9-3103	TWS-INC-05-93-05	Area G Sorption	Syn Fl Sorp. #2				
5	SYN.WCG.BT.79.9-3104	TWS-INC-05-93-05	Area G Sorption	Syn Fl Sorp. #2				
6	SYN.WCG.BT.74-3105	TWS-INC-05-93-05	Area G Sorption	Syn Fl Sorp. #2				
7	SYN.WCG.BT.74-3106	TWS-INC-05-93-05	Area G Sorption	Syn Fl Sorp. #2				
8	SYN.WCG.BT.79.1-3107	TWS-INC-05-93-05	Area G Sorption	Syn Fl Sorp. #2				
9	SYN.WCG.BT.79.1-3108	TWS-INC-05-93-05	Area G Sorption	Syn Fl Sorp. #2				
10	SYN.WCG.BT.65-3109	TWS-INC-05-93-05	Area G Sorption	Syn Fl Sorp. #2				
11	SYN.WCG.BT.65-3110	TWS-INC-05-93-05	Area G Sorption	Syn Fl Sorp. #2				
12	SYN.WCG.BT.10-3111	TWS-INC-05-93-05	Area G Sorption	Syn Fl Sorp. #2				
13	SYN.WCG.BT.10-3112	TWS-INC-05-93-05	Area G Sorption	Syn Fl Sorp. #2				
14	SYN.WCG.BT.91-3113	TWS-INC-05-93-05	Area G Sorption	Syn Fl Sorp. #2				
15	SYN.WCG.BT.91-3114	TWS-INC-05-93-05	Area G Sorption	Syn Fl Sorp. #2				
16	Am.SOR.BT.SYN.WCG.5/30/96 CTR 3101	TWS-INC-05-93-05	Area G Sorption	Syn Fl Sorp. #2				
17	Am.SOR.BT.SYN.WCG.5/30/96 CTR 3102	TWS-INC-05-93-05	Area G Sorption	Syn Fl Sorp. #2				
18	Am.SOR.BT.SYN.WCG.5/30/96 STD 11	TWS-INC-05-93-05	Area G Sorption	Syn Fl Sorp. #2				
19	Am.SOR.BT.SYN.WCG.5/30/96 STD 12	TWS-INC-05-93-05	Area G Sorption	Syn Fl Sorp. #2				

	A	B	C	D	E	F	G	H	I
1	Sample Identification	Sorption Time	Experiment No.	Atmosphere	Desired Pu, Am, Np, U, Tc Tracer Solution Activity, CPM/g	Description of Solid (Bandelier Tuff)	Particle Size, Micrometers (If Sieved)	Sieving Information	Type of Water Used If Wet Sieved
20									
21	SYN.WCG.BT.108-3115	2 weeks	Bandelier Sorp SYN WCG#2	.03%CO2	16175 of Np 237	108.0'-109.5'	< 500	Dry	N/A
22	SYN.WCG.BT.108-3116	2 weeks	Bandelier Sorp SYN WCG#2	.03%CO2	16175 of Np 237	108.0'-109.5'	< 500	Dry	N/A
23	SYN.WCG.BT.79.9-3117	2 weeks	Bandelier Sorp SYN WCG#2	.03%CO2	16175 of Np 237	79.8'-80.0' Fe rich	< 500	Dry	N/A
24	SYN.WCG.BT.79.9-3118	2 weeks	Bandelier Sorp SYN WCG#2	.03%CO2	16175 of Np 237	79.8'-80.0' Fe rich	< 500	Dry	N/A
25	SYN.WCG.BT.74-3119	2 weeks	Bandelier Sorp SYN WCG#2	.03%CO2	16175 of Np 237	74.0'-75.0'	< 500	Dry	N/A
26	SYN.WCG.BT.74-3120	2 weeks	Bandelier Sorp SYN WCG#2	.03%CO2	16175of Np 237	74.0'-75.0'	< 500	Dry	N/A
27	SYN.WCG.BT.79.1-3121	2 weeks	Bandelier Sorp SYN WCG#2	.03%CO2	16175of Np 237	79.1'-79.7'	< 500	Dry	N/A
28	SYN.WCG.BT.79.1-3122	2 weeks	Bandelier Sorp SYN WCG#2	.03%CO2	16175 of Np 237	79.1'-79.7'	< 500	Dry	N/A
29	SYN.WCG.BT.65-3123	2 weeks	Bandelier Sorp SYN WCG#2	.03%CO2	16175 of Np 237	65.0'-66.0'	< 500	Dry	N/A
30	SYN.WCG.BT.65-3124	2 weeks	Bandelier Sorp SYN WCG#2	.03%CO2	16175 of Np 237	65.0'-66.0'	< 500	Dry	N/A
31	SYN.WCG.BT.10-3125	2 weeks	Bandelier Sorp SYN WCG#2	.03%CO2	16175of Np 237	10.8'-12.0'	< 500	Dry	N/A
32	SYN.WCG.BT.10-3126	2 weeks	Bandelier Sorp SYN WCG#2	.03%CO2	16175 of Np 237	10.8'-12.0'	< 500	Dry	N/A
33	SYN.WCG.BT.91-3127	2 weeks	Bandelier Sorp SYN WCG#2	.03%CO2	16175 of Np 237	91.0'	< 500	Dry	N/A
34	SYN.WCG.BT.91-3128	2 weeks	Bandelier Sorp SYN WCG#2	.03%CO2	16175 of Np 237	91.0'	< 500	Dry	N/A
35	Np SOR.BT.SYN.WCG 5/30/96 CTR 3115	2 weeks	Bandelier Sorp SYN WCG#2	.03%CO2	16175 of Np 237	N/A	N/A	N/A	N/A
36	Np SOR.BT.SYN.WCG 5/30/96 CTR 3116	2 weeks	Bandelier Sorp SYN WCG#2	.03%CO2	16175 of Np 237	N/A	N/A	N/A	N/A
37	Np SOR.BT.SYN.WCG 5/30/96 STD 13								
38	Np SOR.BT.SYN.WCG 5/30/96 STD 14								

	A	J	K	L	M	N	O	P	Q	R
1	Sample Identification	Tube + Cap Mass, g	Tube + Cap + Mineral Mass, g	Mineral Mass, g (Col. K-Col. J)	Tube + Cap + Mineral + Water Mass, g	Water Mass, g (Col. M Col. K)	Julian Date Pretreatment Started '95	Julian Date Pretreatment Ended '96	Period of Pretreatment, Days	Tube + Cap + Mineral + Water after Pretreatment Mass, g
20										
21	SYN.WCG.BT.108-3115	22.99	23.98	0.99	44.17	20.19	250.6146	267.5417	16.9271	44.09
22	SYN.WCG.BT.108-3116	23.05	24.04	0.99	44.24	20.20	250.6146	267.5417	16.9271	44.13
23	SYN.WCG.BT.79.9-3117	23.22	24.22	1.00	44.42	20.20	250.6146	267.5417	16.9271	44.32
24	SYN.WCG.BT.79.9-3118	22.97	23.97	1.00	44.16	20.19	250.6146	267.5417	16.9271	44.08
25	SYN.WCG.BT.74-3119	22.82	23.82	1.00	44.09	20.27	250.6146	267.5417	16.9271	44.09
26	SYN.WCG.BT.74-3120	23.17	24.17	1.00	44.41	20.24	250.6146	267.5417	16.9271	44.32
27	SYN.WCG.BT.79.1-3121	22.80	23.80	1.00	43.53	19.73	250.6146	267.5417	16.9271	43.43
28	SYN.WCG.BT.79.1-3122	23.14	24.14	1.00	44.19	20.05	250.6146	267.5417	16.9271	44.10
29	SYN.WCG.BT.65-3123	22.96	23.96	1.00	43.83	19.87	250.6146	267.5417	16.9271	43.74
30	SYN.WCG.BT.65-3124	23.25	24.25	1.00	44.17	19.92	250.6146	267.5417	16.9271	44.09
31	SYN.WCG.BT.10-3125	23.04	24.03	0.99	44.06	20.03	250.6146	267.5417	16.9271	43.97
32	SYN.WCG.BT.10-3126	22.94	23.95	1.01	44.09	20.13	250.6146	267.5417	16.9271	43.93
33	SYN.WCG.BT.91-3127	23.11	24.12	1.01	44.25	20.13	250.6146	267.5417	16.9271	44.16
34	SYN.WCG.BT.91-3128	23.22	24.23	1.01	44.30	20.07	250.6146	267.5417	16.9271	44.18
35	Np SOR.BT.SYN.WCG.5/30/96 CTR 3115	22.79								
36	Np SOR.BT.SYN.WCG.5/30/96 CTR 3116	22.73								
37	Np SOR.BT.SYN.WCG.5/30/96 STD 13									
38	Np SOR.BT.SYN.WCG.5/30/96 STD 14									

	A	S	T	U	V	W	X	Y	Z	AA
1	Sample Identification	% Evaporation during Pretreatment ((Col.N-Col.S)/Col.N*100)	Tube + Cap + Mineral + Water after Decantation Mass, g	pH of Water after Pretreatment	Eh of Water after Pretreatment, mV	Julian Date Tracer Solution was Added, '96	Mass after Tracer Solution was Added, g	Mass of Tracer Solution Added, g	Julian Date Sorption Started '96	Julian Date Sorption Ended '96
20										
21	SYN.WCG.BT.108-3115	0.18	25.25	9.96	N/A	268.3431	45.35	20.10	268.3431	282.4167
22	SYN.WCG.BT.108-3116	0.25	25.04		N/A	268.3431	45.11	20.07	268.3431	282.4167
23	SYN.WCG.BT.79.9-3117	0.23	25.50	9.96	N/A	268.3431	45.63	20.13	268.3431	282.4167
24	SYN.WCG.BT.79.9-3118	0.18	25.16		N/A	268.3431	45.31	20.15	268.3431	282.4167
25	SYN.WCG.BT.74-3119	0.20	25.13	9.97	N/A	268.3431	46.95	19.82	268.3431	282.4167
26	SYN.WCG.BT.74-3120	0.20	25.30		N/A	268.3431	45.42	20.12	268.3431	282.4167
27	SYN.WCG.BT.79.1-3121	0.23	25.24	9.97	N/A	268.3431	45.32	20.08	268.3431	282.4167
28	SYN.WCG.BT.79.1-3122	0.20	25.27		N/A	268.3431	45.39	20.12	268.3431	282.4167
29	SYN.WCG.BT.65-3123	0.21	25.87	9.96	N/A	268.3431	45.88	20.01	268.3431	282.4167
30	SYN.WCG.BT.65-3124	0.20	25.34		N/A	268.3431	45.27	19.93	268.3431	282.4167
31	SYN.WCG.BT.10-3125	0.20	25.98	9.98	N/A	268.3431	46.02	20.04	268.3431	282.4167
32	SYN.WCG.BT.10-3126	0.20	25.43		N/A	268.3431	45.47	20.04	268.3431	282.4167
33	SYN.WCG.BT.91-3127	0.20	25.88	9.97	N/A	268.3431	44.85	18.97	268.3431	282.4167
34	SYN.WCG.BT.91-3128	0.27	25.34		N/A	268.3431	45.40	20.06	268.3431	282.4167
35	Np SOR BT.SYN.WCG 5/30/96 CTR 3115					268.3431	42.81	20.02	268.3431	282.4167
36	Np.SOR BT.SYN.WCG 5/30/96 CTR 3116					268.3431	42.70	19.97	268.3431	282.4167
37	Np.SOR BT.SYN.WCG 5/30/96 STD 13									
38	Np.SOR BT.SYN.WCG 5/30/96 STD 14									

	A	AB	AC	AD	AE	AF	AG	AH	AI	AJ
1	Sample Identification	Period of Sorption, Days	Mass after Sorption Ended, g	% Evaporation during Sorption ((Col X-Col AB) /Col X*100)	pH of Tracer Solution after Sorption	Eh of Tracer Solution after Sorption	Mass of Counting Vial, g	Mass of Counting Vial + Aliquot of Tracer Solution after Sorption, g	Mass of Counted Tracer Solution after Sorption, g (Col AI-Col AH)	Total CFM in Counted Tracer Solution after Sorption
20										
21	SYN.WCG BT.108-3115	14.0736	45.13	0.49	9.8	N/A	6.17	7.18	1.01	16039.90
22	SYN.WCG BT.108-3116	14.0736	44.83	0.62		N/A	6.2	7.21	1.01	16273.20
23	SYN.WCG BT.79.9-3117	14.0736	45.44	0.42	9.8	N/A	6.18	7.19	1.01	15483.10
24	SYN.WCG BT.79.9-3118	14.0736	45.20	0.24		N/A	6.19	7.26	1.07	15553.30
25	SYN.WCG BT.74-3119	14.0736	44.84	0.24	9.79	N/A	6.19	7.19	1.00	13967.00
26	SYN.WCG BT.74-3120	14.0736	45.31	0.24		N/A	6.2	7.20	1.00	14043.30
27	SYN.WCG BT.79.1-3121	14.0736	45.08	0.53	9.8	N/A	6.2	7.21	1.01	15255.30
28	SYN.WCG BT.79.1-3122	14.0736	45.27	0.26		N/A	6.2	7.20	1.00	15379.60
29	SYN.WCG BT.65-3123	14.0736	45.73	0.33	9.8	N/A	6.19	7.20	1.01	13815.40
30	SYN.WCG BT.65-3124	14.0736	45.12	0.33		N/A	6.22	7.23	1.01	14214.20
31	SYN.WCG BT.10-3125	14.0736	45.91	0.24	9.8	N/A	6.2	7.21	1.01	12233.60
32	SYN.WCG BT.10-3126	14.0736	45.35	0.26		N/A	6.19	7.19	1.00	12154.00
33	SYN.WCG BT.91-3127	14.0736	44.74	0.25	9.79	N/A	6.19	7.19	1.00	13468.20
34	SYN.WCG BT.91-3128	14.0736	45.05	0.70		N/A	6.2	7.20	1.00	14524.70
35	Np SOR BT.SYN.WCG.5/30/96 CTR 3115	14.0736	42.70	0.26	9.81	N/A	6.25	7.26	1.01	16979.20
36	Np SOR BT.SYN.WCG.5/30/96 CTR 3116	14.0736	42.59	0.26		N/A	6.17	7.17	1.00	16859.90
37	Np SOR BT.SYN.WCG.5/30/96 STD 13						6.57	7.58	1.01	16511.40
38	Np SOR BT.SYN.WCG.5/30/96 STD 14						6.54	7.55	1.01	16230.30

	A	AK	AL	AM	AN	AO	AP	AQ
1	Sample Identification	CPM/g in Counted Tracer Solution after Sorption (Col AL/ Col AK)	Kd (mL/g) of Original Tracer Solution Based on Standards	Kd (mL/g) of Original Tracer Solution Based on Controls	Water ID	Type of Scintillation Cocktail Used	ID of Tracer Solutions Used for Sorption Experiment	Binder where Raw Experimental Data are Located
20								
21	SYN.WCG.BT.108-3115	15881.03	-6.04E-01	1.66E-01	SYN.WCG 9/17/96	Ultima Gold AB	Np SOR SYN/WCG 9/17/96	Area G Sorption Studies
22	SYN.WCG.BT.108-3116	16112.08	-5.68E-01	1.89E-01	SYN.WCG 9/17/96	Ultima Gold AB	Np SOR SYN/WCG 9/17/96	Area G Sorption Studies
23	SYN.WCG.BT.73.9-3117	15329.80	1.03E-01	8.94E-01	SYN.WCG 9/17/96	Ultima Gold AB	Np SOR SYN/WCG 9/17/96	Area G Sorption Studies
24	SYN.WCG.BT.79.9-3118	14541.43	1.27E+00	2.11E+00	SYN.WCG 9/17/96	Ultima Gold AB	Np SOR SYN/WCG 9/17/96	Area G Sorption Studies
25	SYN.WCG.BT.74-3119	13357.00	2.02E+00	2.88E+00	SYN.WCG 9/17/96	Ultima Gold AB	Np SOR SYN/WCG 9/17/96	Area G Sorption Studies
26	SYN.WCG.BT.74-3120	14043.30	2.13E+00	2.99E+00	SYN.WCG 9/17/96	Ultima Gold AB	Np SOR SYN/WCG 9/17/96	Area G Sorption Studies
27	SYN.WCG.BT.79.1-3121	15104.26	3.09E-01	1.11E+00	SYN.WCG 9/17/96	Ultima Gold AB	Np SOR SYN/WCG 9/17/96	Area G Sorption Studies
28	SYN.WCG.BT.79.1-3122	15379.60	8.14E-01	9.01E-01	SYN.WCG 9/17/96	Ultima Gold AB	Np SOR SYN/WCG 9/17/96	Area G Sorption Studies
29	SYN.WCG.BT.65-3123	13678.61	1.95E+00	2.87E+00	SYN.WCG 9/17/96	Ultima Gold AB	Np SOR SYN/WCG 9/17/96	Area G Sorption Studies
30	SYN.WCG.BT.65-3124	14073.47	2.13E+00	2.95E+00	SYN.WCG 9/17/96	Ultima Gold AB	Np SOR SYN/WCG 9/17/96	Area G Sorption Studies
31	SYN.WCG.BT.10-3125	12112.48	5.04E+00	6.04E+00	SYN.WCG 9/17/96	Ultima Gold AB	Np SOR SYN/WCG 9/17/96	Area G Sorption Studies
32	SYN.WCG.BT.10-3126	12154.00	5.32E+00	6.30E+00	SYN.WCG 9/17/96	Ultima Gold AB	Np SOR SYN/WCG 9/17/96	Area G Sorption Studies
33	SYN.WCG.BT.91-3127	13468.20	2.23E+00	3.07E+00	SYN.WCG 9/17/96	Ultima Gold AB	Np SOR SYN/WCG 9/17/96	Area G Sorption Studies
34	SYN.WCG.BT.91-3128	14524.70	1.56E+00	2.38E+00	SYN.WCG 9/17/96	Ultima Gold AB	Np SOR SYN/WCG 9/17/96	Area G Sorption Studies
35	Np SOR BT.SYN.WCG.9/30/96 CTR 3115	16811.09	N/A	N/A	SYN.WCG 9/17/96	Ultima Gold AB	Np SOR SYN/WCG 9/17/96	Area G Sorption Studies
36	Np SOR BT.SYN.WCG.9/30/96 CTR 3116	16863.90	N/A	N/A	SYN.WCG 9/17/96	Ultima Gold AB	Np SOR SYN/WCG 9/17/96	Area G Sorption Studies
37	Np SOR BT.SYN.WCG.9/30/96 STD 13	16347.92	N/A	N/A	SYN.WCG 9/17/96	Ultima Gold AB	Np SOR SYN/WCG 9/17/96	Area G Sorption Studies
38	Np SOR BT.SYN.WCG.9/30/96 STD 14	16129.01	N/A	N/A	SYN.WCG 9/17/96	Ultima Gold AB	Np SOR SYN/WCG 9/17/96	Area G Sorption Studies

	A	AR	AS	AT	AU	AV	AW	AX
1	Sample Identification	Optical Disk where Reduced Data are Located	Subdirectory	File Name				
20								
21	SYN.WCG.BT.108-3115	TWS-INC-05-93-05	Area G Sorption	Syn Rt Sorp. #2				
22	SYN.WCG.BT.108-3116	TWS-INC-05-93-05	Area G Sorption	Syn Rt Sorp. #2				
23	SYN.WCG.BT.79.9-3117	TWS-INC-05-93-05	Area G Sorption	Syn Rt Sorp. #2				
24	SYN.WCG.BT.79.9-3118	TWS-INC-05-93-05	Area G Sorption	Syn Rt Sorp. #2				
25	SYN.WCG.BT.74-3119	TWS-INC-05-93-05	Area G Sorption	Syn Rt Sorp. #2				
26	SYN.WCG.BT.74-3120	TWS-INC-05-93-05	Area G Sorption	Syn Rt Sorp. #2				
27	SYN.WCG.BT.79.1-3121	TWS-INC-05-93-05	Area G Sorption	Syn Rt Sorp. #2				
28	SYN.WCG.BT.79.1-3122	TWS-INC-05-93-05	Area G Sorption	Syn Rt Sorp. #2				
29	SYN.WCG.BT.65-3123	TWS-INC-05-93-05	Area G Sorption	Syn Rt Sorp. #2				
30	SYN.WCG.BT.65-3124	TWS-INC-05-93-05	Area G Sorption	Syn Rt Sorp. #2				
31	SYN.WCG.BT.10-3125	TWS-INC-05-93-05	Area G Sorption	Syn Rt Sorp. #2				
32	SYN.WCG.BT.10-3126	TWS-INC-05-93-05	Area G Sorption	Syn Rt Sorp. #2				
33	SYN.WCG.BT.91-3127	TWS-INC-05-93-05	Area G Sorption	Syn Rt Sorp. #2				
34	SYN.WCG.BT.91-3128	TWS-INC-05-93-05	Area G Sorption	Syn Rt Sorp. #2				
35	Np.SOR.BT.SYN.WCG.5/30/96 CTR 3115	TWS-INC-05-93-05	Area G Sorption	Syn Rt Sorp. #2				
36	Np.SOR.BT.SYN.WCG.5/30/96 CTR 3116	TWS-INC-05-93-05	Area G Sorption	Syn Rt Sorp. #2				
37	Np.SOR.BT.SYN.WCG.5/30/96 STD 13	TWS-INC-05-93-05	Area G Sorption	Syn Rt Sorp. #2				
38	Np.SOR.BT.SYN.WCG.5/30/96 STD 14	TWS-INC-05-93-05	Area G Sorption	Syn Rt Sorp. #2				

	A	B	C	D	E	F	G	H	I
	Sample Identification	Sorption Time	Experiment No.	Atmosphere	Desired Pu, Am, Np, U, Tc Tracer Solution Activity, CPM/g	Description of Solid (Bandelier Tuff)	Particle Size, Micrometers (if Sieved)	Sieving Information	Type of Water Used if Wet Sieved
39									
40	SYN.WCG BT.108-3129	2 weeks	Bandelier Sorp SYN WCG#2	.03%CO2	9710 cf Pu 239	108.0'-109.5'	< 500	Dry	N/A
41	SYN.WCG BT.108-3130	2 weeks	Bandelier Sorp SYN WCG#2	.03%CO2	9710 cf Pu 239	108.0'-109.5'	< 500	Dry	N/A
42	SYN.WCG BT.79.9-3131	2 weeks	Bandelier Sorp SYN WCG#2	.03%CO2	9710 cf Pu 239	79.9'-80.0' Fe rich	< 500	Dry	N/A
43	SYN.WCG BT.79.9-3132	2 weeks	Bandelier Sorp SYN WCG#2	.03%CO2	9710 cf Pu 239	79.9'-80.0' Fe rich	< 500	Dry	N/A
44	SYN.WCG BT.74-3133	2 weeks	Bandelier Sorp SYN WCG#2	.03%CO2	9710 cf Pu 239	74.0'-75.0'	< 500	Dry	N/A
45	SYN.WCG BT.74-3134	2 weeks	Bandelier Sorp SYN WCG#2	.03%CO2	9710 cf Pu 239	74.0'-75.0'	< 500	Dry	N/A
46	SYN.WCG BT.79.1-3135	2 weeks	Bandelier Sorp SYN WCG#2	.03%CO2	9710 cf Pu 239	79.1'-79.7'	< 500	Dry	N/A
47	SYN.WCG BT.79.1-3136	2 weeks	Bandelier Sorp SYN WCG#2	.03%CO2	9710 cf Pu 239	79.1'-79.7'	< 500	Dry	N/A
48	SYN.WCG BT.65-3137	2 weeks	Bandelier Sorp SYN WCG#2	.03%CO2	9710 cf Pu 239	65.0'-66.0'	< 500	Dry	N/A
49	SYN.WCG BT.65-3138	2 weeks	Bandelier Sorp SYN WCG#2	.03%CO2	9710 cf Pu 239	65.0'-66.0'	< 500	Dry	N/A
50	SYN.WCG BT.10-3139	2 weeks	Bandelier Sorp SYN WCG#2	.03%CO2	9710 cf Pu 239	10.8'-12.0'	< 500	Dry	N/A
51	SYN.WCG BT.10-3140	2 weeks	Bandelier Sorp SYN WCG#2	.03%CO2	9710 cf Pu 239	10.8'-12.0'	< 500	Dry	N/A
52	SYN.WCG BT.91-3141	2 weeks	Bandelier Sorp SYN WCG#2	.03%CO2	9710 cf Pu 239	91.0	< 500	Dry	N/A
53	SYN.WCG BT.91-3142	2 weeks	Bandelier Sorp SYN WCG#2	.03%CO2	9710 cf Pu 239	91.0	< 500	Dry	N/A
54	Pu.SOR BT.SYN.WCG.5/30/96 CTR 3129	2 weeks	Bandelier Sorp SYN WCG#2	.03%CO2	9710 cf Pu 239	N/A	N/A	N/A	N/A
55	Pu.SOR BT.SYN.WCG.5/30/96 CTR 3130	2 weeks	Bandelier Sorp SYN WCG#2	.03%CO2	9710 cf Pu 239	N/A	N/A	N/A	N/A
56	Pu SOR BT.SYN WCG 5/30/96 STD 15								
57	Pu SOR BT.SYN WCG 5/30/96 STD 16								

	A	J	K	L	M	N	O	P	Q	R
1	Sample Identification	Tube + Cap Mass, g	Tube + Cap + Mineral Mass, g	Mineral Mass, g (Col. K-Col. J)	Tube + Cap + Mineral + Water Mass, g	Water Mass, g (Col. M-Col. K)	Julian Date Pretreatment Started '96	Julian Date Pretreatment Ended '96	Period of Pretreatment, Days	Tube + Cap + Mineral + Water after Pretreatment Mass, g
39										
40	SYN.WCG.BT.108-3129	23.29	24.29	1.00	44.41	20.12	250.6146	267.5417	16.9271	44.32
41	SYN.WCG.BT.108-3130	23.03	24.03	1.00	44.17	20.14	250.6146	267.5417	16.9271	44.08
42	SYN.WCG.BT.79.9-3131	23.24	24.24	1.00	44.19	19.95	250.6146	267.5417	16.9271	44.10
43	SYN.WCG.BT.79.9-3132	22.97	23.97	1.00	43.89	19.91	250.6146	267.5417	16.9271	43.71
44	SYN.WCG.BT.74-3133	23.12	24.12	1.00	44.12	20.00	250.6146	267.5417	16.9271	44.02
45	SYN.WCG.BT.74-3134	22.86	23.86	1.00	43.81	19.95	250.6146	267.5417	16.9271	43.71
46	SYN.WCG.BT.79.1-3135	23.14	24.14	1.00	44.13	19.99	250.6146	267.5417	16.9271	44.03
47	SYN.WCG.BT.79.1-3136	23.07	24.07	1.00	44.16	20.09	250.6146	267.5417	16.9271	44.07
48	SYN.WCG.BT.65-3137	23.18	24.18	1.00	44.18	20.00	250.6146	267.5417	16.9271	44.09
49	SYN.WCG.BT.65-3138	22.89	23.89	1.00	47.57	23.68	250.6146	267.5417	16.9271	47.46
50	SYN.WCG.BT.10-3139	23.12	24.11	0.99	44.23	20.12	250.6146	267.5417	16.9271	44.14
51	SYN.WCG.BT.10-3140	23.08	24.08	1.00	44.06	19.98	250.6146	267.5417	16.9271	43.96
52	SYN.WCG.BT.91-3141	22.97	23.98	1.01	43.73	19.75	250.6146	267.5417	16.9271	43.63
53	SYN.WCG.BT.91-3142	22.95	23.97	1.01	43.70	19.73	250.6146	267.5417	16.9271	43.49
54	Pu SOR BT.SYN.WCG.5/30/96 CTR 3129	23.12								
55	Pu SOR BT.SYN.WCG.5/30/96 CTR 3130	23.14								
56	Pu SOR BT.SYN.WCG.5/30/96 STD 15									
57	Pu SOR BT.SYN.WCG.5/30/96 STD 16									

	A	S	T	U	V	W	X	Y	Z	AA
1	Sample Identification	% Evaporation during Pretreatment ((Col N-Col S)/Col N*100)	Tube + Cap + Mineral + Water after Decantation Mass, g	pH of Water after Pretreatment	Eh of Water after Pretreatment, mV	Julian Date Tracer Solution was Added, '96	Mass after Tracer Solution was Added, g	Mass of Tracer Solution Added, g	Julian Date Sorption Started '96	Julian Date Sorption Ended '96
39										
40	SYN.WCG BT.108-3129	0.20	25.69	10	N/A	268.3431	46.11	20.22	268.3431	282.4167
41	SYN.WCG BT.108-3130	0.20	24.90	N/A	N/A	268.3431	45.06	20.16	268.3431	282.4167
42	SYN.WCG BT.79.9-3131	0.20	25.77	9.96	N/A	268.3431	46.01	20.24	268.3431	282.4167
43	SYN.WCG BT.79.9-3132	0.39	26.02	N/A	N/A	268.3431	46.14	20.12	268.3431	282.4167
44	SYN.WCG BT.74-3133	0.23	27.06	9.96	N/A	268.3431	47.18	20.12	268.3431	282.4167
45	SYN.WCG BT.74-3134	0.23	26.28	N/A	N/A	268.3431	46.93	18.62	268.3431	282.4167
46	SYN.WCG BT.79.1-3135	0.23	25.81	9.97	N/A	268.3431	42.91	17.10	268.3431	282.4167
47	SYN.WCG BT.79.1-3136	0.20	26.44	N/A	N/A	268.3431	46.60	20.16	268.3431	282.4167
48	SYN.WCG BT.65-3137	0.23	25.89	10.02	N/A	268.3431	46.09	20.20	268.3431	282.4167
49	SYN.WCG BT.65-3138	0.23	26.36	N/A	N/A	268.3431	46.38	20.04	268.3431	282.4167
50	SYN.WCG BT.10-3139	0.20	25.48	9.98	N/A	268.3431	45.55	20.07	268.3431	282.4167
51	SYN.WCG BT.10-3140	0.23	25.94	N/A	N/A	268.3431	46.01	20.07	268.3431	282.4167
52	SYN.WCG BT.91-3141	0.23	26.92	9.93	N/A	268.3431	45.80	18.88	268.3431	282.4167
53	SYN.WCG BT.91-3142	0.48	26.13	N/A	N/A	268.3431	45.92	19.79	268.3431	282.4167
54	Pu SOR BT.SYN.WCG 5/30/96 CTR 3129					268.3431	43.15	20.03	268.3431	282.4167
55	Pu SOR BT.SYN.WCG 5/30/96 CTR 3130					268.3431	43.04	19.93	268.3431	282.4167
56	Pu SOR BT.SYN.WCG 5/30/96 STD 15									
57	Pu SOR BT.SYN.WCG 5/30/96 STD 16									

	A	AB	AC	AD	AE	AF	AG	AH	AI	AJ
1	Sample Identification	Period of Sorption, Days	Mass after Sorption Ended, g	% Evaporation during Sorption ((Col X-Col.AB) /Col.X*100)	pH of Tracer Solution after Sorption	Eh of Tracer Solution after Sorption	Mass of Counting Vial, g	Mass of Counting Vial + Aliquot of Tracer Solution after Sorption, g	Mass of Counted Tracer Solution after Sorption, g (Col AI-Col AH)	Total CFU in Counted Tracer Solution after Sorption
39										
40	SYN.WCQ.BT.108-3129	14.0736	45.91	0.43	9.8	N/A	6.2	7.21	1.01	8703.80
41	SYN.WCQ.BT.108.3130	14.0735	44.80	0.59		N/A	6.19	7.22	1.03	8971.95
42	SYN.WCQ.BT.73.9-3131	14.0736	45.83	0.26	9.8	N/A	6.2	7.20	1.00	8381.10
43	SYN.WCQ.BT.73.9-3132	14.0736	45.99	0.33		N/A	6.19	7.22	1.03	8475.50
44	SYN.WCQ.BT.74-3133	14.0736	47.03	0.32	9.8	N/A	6.18	7.21	1.03	8587.65
45	SYN.WCQ.BT.74-3134	14.0736	44.76	0.31		N/A	6.18	7.19	1.01	8533.30
46	SYN.WCQ.BT.73.1-3135	14.0736	42.79	0.28	9.8	N/A	6.2	7.21	1.01	8286.85
47	SYN.WCQ.BT.73.1-3136	14.0736	45.47	0.28		N/A	6.17	7.19	1.02	8359.55
48	SYN.WCQ.BT.65-3137	14.0736	45.97	0.26	9.8	N/A	6.27	7.29	1.02	5135.80
49	SYN.WCQ.BT.65-3138	14.0735	46.26	0.26		N/A	6.17	7.19	1.02	4932.05
50	SYN.WCQ.BT.10-3139	14.0736	45.35	0.44	9.8	N/A	6.24	7.25	1.01	1435.30
51	SYN.WCQ.BT.10-3140	14.0735	45.86	0.33		N/A	6.18	7.17	0.99	1492.20
52	SYN.WCQ.BT.91-3141	14.0736	45.51	0.63	9.79	N/A	6.19	7.21	1.02	4561.30
53	SYN.WCQ.BT.91-3142	14.0736	45.74	0.39		N/A	6.17	7.13	0.96	4515.60
54	Pu.SOR.BT.SYN.WCQ.5/30/96 CTR 3128	14.0736	43.05	0.23	9.81	N/A	6.18	7.19	1.01	9850.40
55	Pu.SOR.BT.SYN.WCQ.5/30/96 CTR 3139	14.0736	42.95	0.21		N/A	6.18	7.19	1.01	9791.40
56	Pu.SOR.BT.SYN.WCQ.5/30/96 STD 15						6.59	7.57	0.99	9580.20
57	Pu.SOR.BT.SYN.WCQ.5/30/96 STD 16						6.59	7.56	0.97	9456.50

	A	AK	AL	AM	AN	AO	AP	AQ
	Sample Identification	CPM/g in Counted Tracer Solution after Sorption (Col AL/ Col.AK)	Xd (ml/g) of Original Tracer Solution Based on Standards	Xd (ml/g) of Original Tracer Solution Based on Controls	Water ID	Type of Scintillation Cocktail Used	ID of Tracer Solutions Used for Sorption Experiment	Binder where Raw Experimental Data are Located
39								
40	SYN.WCG BT.108-3129	8617.62	1.67E+00	1.23E+00	SYN WCG 9/17/96	Ultima Gold AB	Pu SOR SYN WCG 9/17/96	Area G Sorption Studies
41	SYN WCG BT.108-3130	8710.63	1.71E+00	1.77E+00	SYN WCG 9/17/96	Ultima Gold AB	Pu SOR SYN WCG 9/17/96	Area G Sorption Studies
42	SYN.WCG BT.79.9-3131	8381.10	1.81E+00	1.87E+00	SYN WCG 9/17/96	Ultima Gold AB	Pu SOR SYN WCG 9/17/96	Area G Sorption Studies
43	SYN WCG BT.79.9-3132	8228.64	1.73E+00	1.79E+00	SYN WCG 9/17/96	Ultima Gold AB	Pu SOR SYN WCG 9/17/96	Area G Sorption Studies
44	SYN.WCG BT.74-3133	6587.04	6.31E+00	6.39E+00	SYN WCG 9/17/96	Ultima Gold AB	Pu SOR SYN WCG 9/17/96	Area G Sorption Studies
45	SYN.WCG BT.74-3134	6567.62	6.64E+00	6.71E+00	SYN WCG 9/17/96	Ultima Gold AB	Pu SOR SYN WCG 9/17/96	Area G Sorption Studies
46	SYN.WCG BT.79.1-3135	8204.80	1.59E+00	1.65E+00	SYN WCG 9/17/96	Ultima Gold AB	Pu SOR SYN WCG 9/17/96	Area G Sorption Studies
47	SYN.WCG BT.79.1-3136	8124.66	1.50E+00	1.56E+00	SYN WCG 9/17/96	Ultima Gold AB	Pu SOR SYN WCG 9/17/96	Area G Sorption Studies
48	SYN WCG BT.65-3137	5036.08	1.72E+01	1.73E+01	SYN WCG 9/17/96	Ultima Gold AB	Pu SOR SYN WCG 9/17/96	Area G Sorption Studies
49	SYN WCG BT.65-3138	4935.34	1.79E+01	1.80E+01	SYN WCG 9/17/96	Ultima Gold AB	Pu SOR SYN WCG 9/17/96	Area G Sorption Studies
50	SYN.WCG BT.10-3139	1481.43	1.11E+02	1.12E+02	SYN WCG 9/17/96	Ultima Gold AB	Pu SOR SYN WCG 9/17/96	Area G Sorption Studies
51	SYN.WCG BT.10-3140	1507.27	1.08E+02	1.09E+02	SYN WCG 9/17/96	Ultima Gold AB	Pu SOR SYN WCG 9/17/96	Area G Sorption Studies
52	SYN WCG BT.91-3141	4471.86	1.93E+01	1.94E+01	SYN WCG 9/17/96	Ultima Gold AB	Pu SOR SYN WCG 9/17/96	Area G Sorption Studies
53	SYN.WCG BT.91-3142	4703.75	1.85E+01	1.90E+01	SYN WCG 9/17/96	Ultima Gold AB	Pu SOR SYN WCG 9/17/96	Area G Sorption Studies
54	Pu SOR BT.SYN.WCG 5/30/96 CTR 3129	9782.57	N/A	N/A	SYN WCG 9/17/96	Ultima Gold AB	Pu SOR SYN WCG 9/17/96	Area G Sorption Studies
55	Pu SOR BT.SYN.WCG 5/30/96 CTR 3130	9534.45	N/A	N/A	SYN WCG 9/17/96	Ultima Gold AB	Pu SOR SYN WCG 9/17/96	Area G Sorption Studies
56	Pu SOR BT.SYN.WCG 5/30/96 STD 15	9576.97	N/A	N/A	SYN WCG 9/17/96	Ultima Gold AB	Pu SOR SYN WCG 9/17/96	Area G Sorption Studies
57	Pu SOR BT.SYN.WCG 5/30/96 STD 16	9748.97	N/A	N/A	SYN WCG 9/17/96	Ultima Gold AB	Pu SOR SYN WCG 9/17/96	Area G Sorption Studies

	A	AR	AS	AT	AU	AV	AW	AX
1	Sample Identification	Optical Disk where Reduced Data are Located	Subdirectory	File Name				
39								
40	SYN.WCG.BT.109-3129	TWS-INC-05-93-05	Area G Sorption	Syn Pt Scrp. #2				
41	SYN.WCG.BT.108-3130	TWS-INC-05-93-05	Area G Sorption	Syn Pt Scrp. #2				
42	SYN.WCG.BT.79.9-3131	TWS-INC-05-93-05	Area G Sorption	Syn Pt Scrp. #2				
43	SYN.WCG.BT.79.9-3132	TWS-INC-05-93-05	Area G Sorption	Syn Pt Scrp. #2				
44	SYN.WCG.BT.74-3133	TWS-INC-05-93-05	Area G Sorption	Syn Pt Scrp. #2				
45	SYN.WCG.BT.74-3134	TWS-INC-05-93-05	Area G Sorption	Syn Pt Scrp. #2				
46	SYN.WCG.BT.79.1-3135	TWS-INC-05-93-05	Area G Sorption	Syn Pt Scrp. #2				
47	SYN.WCG.BT.79.1-3136	TWS-INC-05-93-05	Area G Sorption	Syn Pt Scrp. #2				
48	SYN.WCG.BT.65-3137	TWS-INC-05-93-05	Area G Sorption	Syn Pt Scrp. #2				
49	SYN.WCG.BT.65-3138	TWS-INC-05-93-05	Area G Sorption	Syn Pt Scrp. #2				
50	SYN.WCG.BT.10-3139	TWS-INC-05-93-05	Area G Sorption	Syn Pt Scrp. #2				
51	SYN.WCG.BT.10-3140	TWS-INC-05-93-05	Area G Sorption	Syn Pt Scrp. #2				
52	SYN.WCG.BT.91-3141	TWS-INC-05-93-05	Area G Sorption	Syn Pt Scrp. #2				
53	SYN.WCG.BT.91-3142	TWS-INC-05-93-05	Area G Sorption	Syn Pt Scrp. #2				
54	Pu.SOR.BT.SYN.WCG.5/30/96 CTR 3129	TWS-INC-05-93-05	Area G Sorption	Syn Pt Scrp. #2				
55	Pu.SOR.BT.SYN.WCG.5/30/96 CTR 3130	TWS-INC-05-93-05	Area G Sorption	Syn Pt Scrp. #2				
56	Pu.SOR.BT.SYN.WCG.5/30/96 STD 15	TWS-INC-05-93-05	Area G Sorption	Syn Pt Scrp. #2				
57	Pu.SOR.BT.SYN.WCG.5/30/96 STD 16	TWS-INC-05-93-05	Area G Sorption	Syn Pt Scrp. #2				

	A	B	C	D	E	F	G	H	I
1	Sample Identification	Sorption Time	Experiment No.	Atmosphere	Desired Pu, Am, Np, U, Tc Tracer Solution Activity, CPM/g	Description of Solid (Bandelier Tuff)	Particle Size, Micrometers (if Sieved)	Sieving Information	Type of Water Used if Wet Sieved
58									
59	SYN.WCG.BT.108-3143	2 weeks	Bandelier Sorp SYN WCG#2	.03%CO2	49566 of U 233	108.0'-109.5'	< 500	Dry	N/A
60	SYN.WCG.BT.108-3144	2 weeks	Bandelier Sorp SYN WCG#2	.03%CO2	49566 of U 233	108.0'-109.5'	< 500	Dry	N/A
61	SYN.WCG.BT.79.9-3145	2 weeks	Bandelier Sorp SYN WCG#2	.03%CO2	49566 of U 233	79.9'-80.0' Fe rich	< 500	Dry	N/A
62	SYN.WCG.BT.79.9-3146	2 weeks	Bandelier Sorp SYN WCG#2	.03%CO2	49566 of U 233	79.9'-80.0' Fe rich	< 500	Dry	N/A
63	SYN.WCG.BT.74-3147	2 weeks	Bandelier Sorp SYN WCG#2	.03%CO2	49566 of U 233	74.0'-75.0'	< 500	Dry	N/A
64	SYN.WCG.BT.74-3148	2 weeks	Bandelier Sorp SYN WCG#2	.03%CO2	49566 of U 233	74.0'-75.0'	< 500	Dry	N/A
65	SYN.WCG.BT.79.1-3149	2 weeks	Bandelier Sorp SYN WCG#2	.03%CO2	49566 of U 233	79.1'-79.7'	< 500	Dry	N/A
66	SYN.WCG.BT.79.1-3150	2 weeks	Bandelier Sorp SYN WCG#2	.03%CO2	49566 of U 233	79.1'-79.7'	< 500	Dry	N/A
67	SYN.WCG.BT.65-3151	2 weeks	Bandelier Sorp SYN WCG#2	.03%CO2	49566 of U 233	65.0'-66.0'	< 500	Dry	N/A
68	SYN.WCG.BT.65-3152	2 weeks	Bandelier Sorp SYN WCG#2	.03%CO2	49566 of U 233	65.0'-66.0'	< 500	Dry	N/A
69	SYN.WCG.BT.10-3153	2 weeks	Bandelier Sorp SYN WCG#2	.03%CO2	49566 of U 233	10.8'-12.0'	< 500	Dry	N/A
70	SYN.WCG.BT.10-3154	2 weeks	Bandelier Sorp SYN WCG#2	.03%CO2	49566 of U 233	10.8'-12.0'	< 500	Dry	N/A
71	SYN.WCG.BT.91-3155	2 weeks	Bandelier Sorp SYN WCG#2	.03%CO2	49566 of U 233	91.0	< 500	Dry	N/A
72	SYN.WCG.BT.91-3156	2 weeks	Bandelier Sorp SYN WCG#2	.03%CO2	49566 of U 233	91.0	< 500	Dry	N/A
73	U.SOR.BT.SYN.WCG.5/30/96 CTR 3143	2 weeks	Bandelier Sorp SYN WCG#2	.03%CO2	49566 of U 233	N/A	N/A	N/A	N/A
74	U.SOR.BT.SYN.WCG.5/30/96 CTR 3144	2 weeks	Bandelier Sorp SYN WCG#2	.03%CO2	49566 of U 233	N/A	N/A	N/A	N/A
75	U.SOR.BT.SYN.WCG.5/30/96 STD 17								
76	U.SOR.BT.SYN.WCG.5/30/96 STD 18								

	A	J	K	L	M	N	O	P	Q	R
1	Sample Identification	Tube + Cap Mass, g	Tube + Cap + Mineral Mass, g	Mineral Mass, g (Col. K-Col. J)	Tube + Cap + Mineral + Water Mass, g	Water Mass, g (Col. M-Col. K)	Julian Date Pretreatment Started '96	Julian Date Pretreatment Ended '96	Period of Pretreatment, Days	Tube + Cap + Mineral + Water after Pretreatment Mass, g
58										
59	SYN.WCG BT.108-3143	23.21	24.21	1.00	43.88	19.67	250.6146	267.5417	16.9271	43.75
60	SYN.WCG BT.108-3144	23.02	24.02	1.00	43.95	19.93	250.6146	267.5417	16.9271	43.83
61	SYN.WCG BT.73.9-3145	23.14	24.15	1.01	43.97	19.82	250.6146	267.5417	16.9271	43.86
62	SYN.WCG.BT.73.9-3146	22.95	23.95	1.00	43.67	19.72	250.6146	267.5417	16.9271	43.57
63	SYN.WCG BT.74-3147	23.05	24.05	1.00	43.77	19.71	250.6146	267.5417	16.9271	43.65
64	SYN.WCG BT.74-3148	23.04	24.04	1.00	43.78	19.74	250.6146	267.5417	16.9271	43.68
65	SYN.WCG.BT.79.1-3149	22.95	23.95	1.00	43.79	19.84	250.6146	267.5417	16.9271	43.69
66	SYN.WCG BT.79.1-3150	22.73	23.73	1.00	43.61	19.88	250.6146	267.5417	16.9271	43.52
67	SYN.WCG BT.65-3151	22.99	23.99	1.00	43.25	19.26	250.6146	267.5417	16.9271	43.17
68	SYN.WCG.BT.65-3152	23.17	24.17	1.00	43.84	19.67	250.6146	267.5417	16.9271	43.41
69	SYN.WCG BT.10-3153	22.93	23.93	1.00	43.35	19.42	250.6146	267.5417	16.9271	43.26
70	SYN.WCG.BT.10-3154	22.64	23.64	1.00	43.65	20.01	250.6146	267.5417	16.9271	43.55
71	SYN.WCG BT.91-3155	22.61	23.61	1.00	43.33	19.72	250.6146	267.5417	16.9271	43.21
72	SYN.WCG BT.91-3156	22.92	23.93	1.01	43.73	19.80	250.6146	267.5417	16.9271	43.64
73	U.SOR BT.SYN.WCG.5/30/96 CTR 3143	23.05								
74	U.SOR BT.SYN.WCG 5/30/96 CTR 3144	22.83								
75	U.SOR BT.SYN.WCG 5/30/96 STD 17									
76	U.SOR BT.SYN.WCG 5/30/96 STD 18									

	A	S	T	U	V	W	X	Y	Z	AA
1	Sample Identification	% Evaporation during Pretreatment ((Col N-Col S) /Col N*100)	Tube + Cap + Mineral + Water after Decantation Mass, g	pH of Water after Pretreatment	Eh of Water after Pretreatment, mV	Julian Date Tracer Solution was Added, '96	Mass after Tracer Solution was Added, g	Mass of Tracer Solution Added, g	Julian Date Sorption Started '96	Julian Date Sorption Ended '96
58										
59	SYN.WCQ BT.108-3143	0.30	25.68	9.99	N/A	268.3431	45.86	20.18	268.3431	282.4167
60	SYN.WCQ BT.108-3144	0.27	25.37		N/A	268.3431	45.50	20.13	268.3431	282.4167
61	SYN.WCQ BT.79.9-3145	0.25	26.92	9.93	N/A	268.3431	47.03	20.11	268.3431	282.4167
62	SYN.WCQ BT.79.9-3146	0.23	26.02		N/A	268.3431	46.15	20.13	268.3431	282.4167
63	SYN.WCQ BT.74-3147	0.27	25.81	9.99	N/A	268.3431	45.95	20.14	268.3431	282.4167
64	SYN.WCQ BT.74-3148	0.23	26.18		N/A	268.3431	46.23	20.11	268.3431	282.4167
65	SYN.WCQ.BT.79.1-3149	0.23	26.52	9.97	N/A	268.3431	46.62	20.10	268.3431	282.4167
66	SYN.WCQ.BT.79.1-3150	0.21	26.11		N/A	268.3431	45.92	19.81	268.3431	282.4167
67	SYN.WCQ.BT.65-3151	0.18	25.79	9.96	N/A	268.3431	45.92	20.13	268.3431	282.4167
68	SYN.WCQ.BT.65-3152	0.98	26.16		N/A	268.3431	46.23	20.07	268.3431	282.4167
69	SYN.WCQ.BT.10-3153	0.21	25.55	9.98	N/A	268.3431	45.63	20.08	268.3431	282.4167
70	SYN.WCQ.BT.10-3154	0.23	25.22		N/A	268.3431	45.15	19.93	268.3431	282.4167
71	SYN.WCQ.BT.91-3155	0.28	26.11	9.97	N/A	268.3431	46.06	19.95	268.3431	282.4167
72	SYN.WCQ.BT.91-3156	0.21	26.03		N/A	268.3431	45.91	19.91	268.3431	282.4167
73	U.SOR.BT.SYN.WCQ 5/30/96 CTR 3143					268.3431	43.10	20.05	268.3431	282.4167
74	U.SOR.BT.SYN.WCQ 5/30/96 CTR 3144					268.3431	42.78	19.95	268.3431	282.4167
75	U.SOR.BT.SYN.WCQ 5/30/96 STD 17									
76	U.SOR.BT.SYN.WCQ 5/30/96 STD 18									

	A	AB	AC	AD	AE	AF	AG	AH	AI	AJ
1	Sample Identification	Period of Sorption, Days	Mass after Sorption Ended, g	% Evaporation during Sorption ((Col X-Col AB) /Col.X*100)	pH of Tracer Solution after Sorption	Eh of Tracer Solution after Sorption	Mass of Counting Vial, g	Mass of Counting Vial + Aliquot of Tracer Solution after Sorption, g	Mass of Counted Tracer Solution after Sorption, g (Col AI-Col AH)	Total CFM in Counted Tracer Solution after Sorption
58										
59	SYN.WCG BT.108-3143	14.0736	45.05	1.70	9.6	N/A	6.2	7.23	1.03	44443.00
60	SYN.WCG BT.108-3144	14.0736	45.35	0.31		N/A	6.20	7.19	0.99	43530.60
61	SYN.WCG BT.79.9-3145	14.0736	46.90	0.28	9.8	N/A	6.18	7.21	1.03	41606.20
62	SYN.WCG BT.79.9-3146	14.0736	46.01	0.30		N/A	6.17	7.18	1.01	42926.50
63	SYN.WCG BT.74-3147	14.0736	45.80	0.33	9.79	N/A	6.21	7.22	1.01	40342.00
64	SYN.WCG BT.74-3148	14.0736	45.18	0.28		N/A	6.22	7.23	1.01	41107.40
65	SYN.WCG BT.73.1-3149	14.0736	45.49	0.29	9.8	N/A	6.19	7.21	1.02	41670.50
66	SYN.WCG BT.73.1-3150	14.0736	45.80	0.26		N/A	6.21	7.21	1.00	39584.80
67	SYN.WCG BT.65-3151	14.0736	45.80	0.26	9.6	N/A	6.19	7.22	1.03	41134.80
68	SYN.WCG BT.65-3152	14.0735	45.74	1.06		N/A	6.2	7.19	0.99	41455.00
69	SYN.WCG BT.10-3153	14.0736	45.52	0.24	9.8	N/A	6.21	7.23	1.02	42026.50
70	SYN.WCG BT.10-3154	14.0736	45.01	0.31		N/A	6.19	7.20	1.01	42443.10
71	SYN.WCG BT.91-3155	14.0735	45.70	0.78	9.8	N/A	6.22	7.20	0.98	39013.40
72	SYN.WCG BT.91-3156	14.0736	45.77	0.30		N/A	6.17	7.18	1.01	39477.70
73	U.SOR.BT.SYN.WCG 5/30/96 CTR 3143	14.0736	42.93	0.26	9.81	N/A	6.20	7.19	0.99	49726.50
74	U.SOR.BT.SYN.WCG 5/30/96 CTR 3144	14.0736	42.68	0.23		N/A	6.25	7.27	1.02	50234.80
75	U.SOR.BT.SYN.WCG 5/30/96 STD 17						6.63	7.62	0.99	50046.50
76	U.SOR.BT.SYN.WCG 5/30/96 STD 18						6.59	7.56	0.97	47933.10

1	A	AK	AL	AM	AN	AO	AP	AQ
	Sample Identification	CPM/g in Counted Tracer Solution after Sorption (Col AU/ Col AK)	Kd (ml/g) of Original Tracer Solution Based on Standards	Kd (ml/g) of Original Tracer Solution Based on Controls	Water ID	Type of Scintillation Cocktail Used	ID of Tracer Solutions Used for Sorption Experiment	Binder where Raw Experimental Data are Located
58								
59	SYN.WCG BT.108-3143	43148.54	2.52E+00	2.39E+00	SYN WCG 9/17/95	Ultima Gold AB	U SOR.SYN WCG 9/17/95	Area G Sorption Studies
60	SYN.WCG BT.108-3144	44371.31	1.50E+00	1.38E+00	SYN WCG 9/17/95	Ultima Gold AB	U SOR SYN WCG 9/17/95	Area G Sorption Studies
61	SYN.WCG BT.79.9-3145	40394.37	2.13E+00	1.99E+00	SYN WCG 9/17/95	Ultima Gold AB	U SOR SYN WCG 9/17/95	Area G Sorption Studies
62	SYN WCG BT.79.9-3146	42501.43	1.63E+00	1.50E+00	SYN WCG 9/17/95	Ultima Gold AB	U SOR SYN WCG 9/17/95	Area G Sorption Studies
63	SYN.WCG BT.74-3147	40536.63	3.11E+00	2.97E+00	SYN WCG 9/17/95	Ultima Gold AB	U SOR SYN WCG 9/17/95	Area G Sorption Studies
64	SYN.WCG BT.74-3148	40700.40	2.59E+00	2.45E+00	SYN WCG 9/17/95	Ultima Gold AB	U SOR SYN WCG 9/17/95	Area G Sorption Studies
65	SYN.WCG BT.79.1-3149	40853.43	2.07E+00	1.93E+00	SYN WCG 9/17/95	Ultima Gold AB	U SOR SYN WCG 9/17/95	Area G Sorption Studies
66	SYN.WCG BT.79.1-3150	39584.80	2.95E+00	2.82E+00	SYN WCG 9/17/95	Ultima Gold AB	U SOR SYN WCG 9/17/95	Area G Sorption Studies
67	SYN.WCG BT.65-3151	39936.70	3.40E+00	3.26E+00	SYN WCG 9/17/95	Ultima Gold AB	U SOR SYN WCG 9/17/95	Area G Sorption Studies
68	SYN.WCG BT.65-3152	41873.74	2.40E+00	2.27E+00	SYN WCG 9/17/95	Ultima Gold AB	U SOR SYN WCG 9/17/95	Area G Sorption Studies
69	SYN.WCG BT.10-3153	41202.45	2.78E+00	2.65E+00	SYN WCG 9/17/95	Ultima Gold AB	U SOR SYN WCG 9/17/95	Area G Sorption Studies
70	SYN.WCG BT.10-3154	42022.87	2.35E+00	2.22E+00	SYN WCG 9/17/95	Ultima Gold AB	U SOR SYN WCG 9/17/95	Area G Sorption Studies
71	SYN.WCG BT.91-3155	39869.53	2.97E+00	2.84E+00	SYN WCG 9/17/95	Ultima Gold AB	U SOR SYN WCG 9/17/95	Area G Sorption Studies
72	SYN WCG BT.91-3156	39016.83	3.60E+00	3.46E+00	SYN WCG 9/17/95	Ultima Gold AB	U SOR SYN WCG 9/17/95	Area G Sorption Studies
73	U.SOR BT.SYN.WCG 5/30/96 CTR 3143	50228.79	N/A	N/A	SYN WCG 9/17/95	Ultima Gold AB	U SOR SYN WCG 9/17/96	Area G Sorption Studies
74	U.SOR BT.SYN.WCG 5/30/96 CTR 3144	49249.80	N/A	N/A	SYN WCG 9/17/95	Ultima Gold AB	U SOR SYN WCG 9/17/95	Area G Sorption Studies
75	U.SOR BT.SYN WCG 5/30/96 STD 17	50552.02	N/A	N/A	SYN WCG 9/17/95	Ultima Gold AB	U SOR SYN WCG 9/17/95	Area G Sorption Studies
76	U.SOR BT.SYN WCG 5/30/96 STD 18	49477.42	N/A	N/A	SYN WCG 9/17/95	Ultima Gold AB	U SOR SYN WCG 9/17/96	Area G Sorption Studies

	A	AR	AS	AT	AU	AV	AW	AX
1	Sample Identification	Optical Disk where Reduced Data are Located	Subdirectory	File Name				
58								
59	SYN.WCG.BT.108-3143	TWS-INC-05-93-05	Area G Sorption	Syn Pt Sorp. #2				
60	SYN.WCG.BT.108-3144	TWS-INC-05-93-05	Area G Sorption	Syn Pt Sorp. #2				
61	SYN.WCG.BT.79.9-3145	TWS-INC-05-93-05	Area G Sorption	Syn Pt Sorp. #2				
62	SYN.WCG.BT.79.9-3146	TWS-INC-05-93-05	Area G Sorption	Syn Pt Sorp. #2				
63	SYN.WCG.BT.74-3147	TWS-INC-05-93-05	Area G Sorption	Syn Pt Sorp. #2				
64	SYN.WCG.BT.74-3148	TWS-INC-05-93-05	Area G Sorption	Syn Pt Sorp. #2				
65	SYN.WCG.BT.79.1-3149	TWS-INC-05-93-05	Area G Sorption	Syn Pt Sorp. #2				
66	SYN.WCG.BT.79.1-3150	TWS-INC-05-93-05	Area G Sorption	Syn Pt Sorp. #2				
67	SYN.WCG.BT.65-3151	TWS-INC-05-93-05	Area G Sorption	Syn Pt Sorp. #2				
68	SYN.WCG.BT.65-3152	TWS-INC-05-93-05	Area G Sorption	Syn Pt Sorp. #2				
69	SYN.WCG.BT.10-3153	TWS-INC-05-93-05	Area G Sorption	Syn Pt Sorp. #2				
70	SYN.WCG.BT.10-3154	TWS-INC-05-93-05	Area G Sorption	Syn Pt Sorp. #2				
71	SYN.WCG.BT.91-3155	TWS-INC-05-93-05	Area G Sorption	Syn Pt Sorp. #2				
72	SYN.WCG.BT.91-3156	TWS-INC-05-93-05	Area G Sorption	Syn Pt Sorp. #2				
73	U.SOR.BT.SYN.WCG.5/3/96 CTR 3143	TWS-INC-05-93-05	Area G Sorption	Syn Pt Sorp. #2				
74	U.SOR.BT.SYN.WCG.5/3/96 CTR 3144	TWS-INC-05-93-05	Area G Sorption	Syn Pt Sorp. #2				
75	U.SOR.BT.SYN.WCG.5/3/96 STD 17	TWS-INC-05-93-05	Area G Sorption	Syn Pt Sorp. #2				
76	U.SOR.BT.SYN.WCG.5/3/96 STD 18	TWS-INC-05-93-05	Area G Sorption	Syn Pt Sorp. #2				

Syn BT Sorp #2

	A	B	C	D	E	F	G	H	I
1	Sample Identification	Sorption Time	Experiment No.	Atmosphere	Desired Pu, Am, Np, U, Tc Tracer Solution Activity, CPM/g	Description of Solid (Bandelier Tuff)	Particle Size, Micrometers (If Sieved)	Sieving Information	Type of Water Used If Wet Sieved
77									
78	SYN.WCG BT.108-3157	2 weeks	Bandelier Sorp SYN WCG#2	.03%CO2	34000 of Tc 95	108.0'-109.5'	< 500	Dry	N/A
79	SYN.WCG BT.108-3158	2 weeks	Bandelier Sorp SYN WCG#2	.03%CO2	34000 of Tc 95	108.0'-109.5'	< 500	Dry	N/A
80	SYN.WCG BT.79.9-3159	2 weeks	Bandelier Sorp SYN WCG#2	.03%CO2	34000 of Tc 95	79.9'-80.0' Fe rich	< 500	Dry	N/A
81	SYN.WCG BT.79.9-3160	2 weeks	Bandelier Sorp SYN WCG#2	.03%CO2	34000 of Tc 95	79.9'-80.0' Fe rich	< 500	Dry	N/A
82	SYN.WCG BT.74-3161	2 weeks	Bandelier Sorp SYN WCG#2	.03%CO2	34000 of Tc 95	74.0'-75.0'	< 500	Dry	N/A
83	SYN.WCG BT.74-3162	2 weeks	Bandelier Sorp SYN WCG#2	.03%CO2	34000 of Tc 95	74.0'-75.0'	< 500	Dry	N/A
84	SYN.WCG BT.79.1-3163	2 weeks	Bandelier Sorp SYN WCG#2	.03%CO2	34000 of Tc 95	79.1'-79.7'	< 500	Dry	N/A
85	SYN.WCG.BT.79.1-3164	2 weeks	Bandelier Sorp SYN WCG#2	.03%CO2	34000 of Tc 95	79.1'-79.7'	< 500	Dry	N/A
86	SYN.WCG BT.65-3165	2 weeks	Bandelier Sorp SYN WCG#2	.03%CO2	34000 of Tc 95	65.0'-66.0'	< 500	Dry	N/A
87	SYN.WCG BT.65-3166	2 weeks	Bandelier Sorp SYN WCG#2	.03%CO2	34000 of Tc 95	65.0'-66.0'	< 500	Dry	N/A
88	SYN. WCG BT.10-3167	2 weeks	Bandelier Sorp SYN WCG#2	.03%CO2	34000 of Tc 95	10.8'-12.0'	< 500	Dry	N/A
89	SYN.WCG BT.10-3168	2 weeks	Bandelier Sorp SYN WCG#2	.03%CO2	34000 of Tc 95	10.8'-12.0'	< 500	Dry	N/A
90	SYN.WCG BT.91-3169	2 weeks	Bandelier Sorp SYN WCG#2	.03%CO2	34000 of Tc 95	91'0	< 500	Dry	N/A
91	SYN.WCG.BT.91-3170	2 weeks	Bandelier Sorp SYN WCG#2	.03%CO2	34000 of Tc 95	91'0	< 500	Dry	N/A
92	Tc.SOR.BT.SYN.WCG 5/30/96 CTR 3157	2 weeks	Bandelier Sorp SYN WCG#2	.03%CO2	34000 of Tc 95	N/A	N/A	N/A	N/A
93	Tc.SOR BT.SYN.WCG 5/30/96 CTR 3158	2 weeks	Bandelier Sorp SYN WCG#2	.03%CO2	34000 of Tc 95	N/A	N/A	N/A	N/A
94	Tc.SOR BT.SYN WCG 5/30/96 STD 19	Only 70 % Efficiency on Scintillation Counter #103476 AUTO-GAMMA							
95	Tc.SOR BT.SYN WCG 5/30/96 STD 20	Only 70 % Efficiency on Scintillation Counter #103476 AUTO-GAMMA							

	A	J	K	L	M	N	O	P	Q	R
1	Sample Identification	Tube + Cap Mass, g	Tube + Cap + Mineral Mass, g	Mineral Mass, g (Col. K-Col. J)	Tube + Cap + Mineral + Water Mass, g	Water Mass, g (Col. M-Col. K)	Julian Date Pretreatment Started '95	Julian Date Pretreatment Ended '96	Period of Pretreatment, Days	Tube + Cap + Mineral + Water after Pretreatment Mass, g
77										
78	SYN.WCG.BT.108-3157	23.12	24.12	1.00	43.89	19.77	250.6146	267.5417	16.9271	43.74
79	SYN.WCG.BT.108-3158	23.18	24.18	1.00	43.99	19.81	250.6146	267.5417	16.9271	43.68
80	SYN.WCG.BT.79.9-3159	22.97	23.97	1.00	43.69	19.72	250.6146	267.5417	16.9271	43.59
81	SYN.WCG.BT.79.9-3160	22.64	23.64	1.00	43.44	19.80	250.6146	267.5417	16.9271	43.31
82	SYN.WCG.BT.74-3161	22.80	23.80	1.00	42.12	18.32	250.6146	267.5417	16.9271	42.03
83	SYN.WCG.BT.74-3162	23.14	24.14	1.00	43.65	19.51	250.6146	267.5417	16.9271	43.56
84	SYN.WCG.BT.79.1-3163	22.65	23.65	1.00	42.86	19.21	250.6146	267.5417	16.9271	42.76
85	SYN.WCG.BT.79.1-3164	22.94	23.94	1.00	43.44	19.50	250.6146	267.5417	16.9271	43.35
86	SYN.WCG.BT.65-3165	22.89	23.89	1.00	43.46	19.57	250.6146	267.5417	16.9271	43.38
87	SYN.WCG.BT.65-3166	23.05	24.05	1.00	43.71	19.66	250.6146	267.5417	16.9271	43.62
88	SYN. WCG.BT.10-3167	22.87	23.86	0.99	43.39	19.53	250.6146	267.5417	16.9271	43.26
89	SYN.WCG.BT.10-3168	22.98	23.98	1.00	43.68	19.70	250.6146	267.5417	16.9271	43.60
90	SYN.WCG.BT.91-3169	23.14	24.14	1.00	43.82	19.68	250.6146	267.5417	16.9271	43.72
91	SYN.WCG.BT.91-3170	23.15	24.14	0.99	43.59	19.45	250.6146	267.5417	16.9271	43.50
92	Tc.SOR.BT.SYN.WCG.5/30/96 CTR 3157	22.89								
93	Tc.SOR.BT.SYN.WCG.5/30/96 CTR 3158	22.73								
94	Tc.SOR.BT.SYN.WCG.5/30/96 STD 19									
95	Tc.SOR.BT.SYN.WCG.5/30/96 STD 20									

	A	S	T	U	V	W	X	Y	Z	AA
1	Sample Identification	% Evaporation during Pretreatment ((Col.N Col.S) /Col.N*100)	Tube + Cap + Mineral + Water after Decantation Mass, g	pH of Water after Pretreatment	Eh of Water after Pretreatment, mV	Julian Date Tracer Solution was Added, '96	Mass after Tracer Solution was Added, g	Mass of Tracer Solution Added, g	Julian Date Sorption Started '96	Julian Date Sorption Ended '96
77										
78	SYN.WCG.BT.108-3157	0.34	25.87	9.98	N/A	268.3431	46.07	20.20	268.3431	282.4167
79	SYN.WCG.BT.108-3158	0.70	25.83		N/A	268.3431	46.06	20.17	268.3431	282.4167
80	SYN.WCG.BT.79.9-3159	0.23		9.98	N/A	268.3431	45.96	45.96	268.3431	282.4167
81	SYN.WCG.BT.79.9-3160	0.30			N/A	268.3431	45.90	45.90	268.3431	282.4167
82	SYN.WCG.BT.74-3161	0.21	25.60	9.96	N/A	268.3431	45.62	20.02	268.3431	282.4167
83	SYN.WCG.BT.74-3162	0.21	25.33		N/A	268.3431	45.50	20.11	268.3431	282.4167
84	SYN.WCG.BT.79.1-3163	0.23	24.97	9.95	N/A	268.3431	45.07	20.10	268.3431	282.4167
85	SYN.WCG.BT.79.1-3164	0.21	25.03		N/A	268.3431	45.12	20.09	268.3431	282.4167
86	SYN.WCG.BT.65-3165	0.18	25.04	9.96	N/A	268.3431	45.22	20.18	268.3431	282.4167
87	SYN.WCG.BT.65-3166	0.21	25.17		N/A	268.3431	45.14	19.97	268.3431	282.4167
88	SYN. WCG.BT.10-3167	0.33	24.75	9.98	N/A	268.3431	44.80	20.05	268.3431	282.4167
89	SYN.WCG.BT.10-3168	0.18	24.72		N/A	268.3431	44.70	19.98	268.3431	282.4167
90	SYN.WCG.BT.91-3169	0.23	25.26	9.97	N/A	268.3431	45.15	19.82	268.3431	282.4167
91	SYN.WCG.BT.91-3170	0.21	25.21		N/A	268.3431	44.73	19.58	268.3431	282.4167
92	Tc.SOR.BT.SYN.WCG.5/30/96 CTR 3157					268.3431	42.90	20.01	268.3431	282.4167
93	Tc.SOR.BT.SYN.WCG.5/30/96 CTR 3158					268.3431	42.60	19.87	268.3431	282.4167
94	Tc.SOR.BT.SYN.WCG.5/30/96 STD 19									
95	Tc.SOR.BT.SYN.WCG.5/30/96 STD 20									

	A	AB	AC	AD	AE	AF	AG	AH	AI	AJ
1	Sample Identification	Period of Sorption, Days	Mass after Sorption Ended, g	% Evaporation during Sorption ((Col X-Col AB) /Col.X*100)	pH of Tracer Solution after Sorption	Eh of Tracer Solution after Sorption	Mass of Counting Vial, g	Mass of Counting Vial + Aliquot of Tracer Solution after Sorption, g	Mass of Counted Tracer Solution after Sorption, g (Col.AI-Col.AH)	Total CPM in Counted Tracer Solution after Sorption
77										
78	SYN.WCG BT.108-3157	14.0736	45.49	1.26	9.82	N/A	2.65	3.67	1.01	26730.00
79	SYN.WCG BT.108-3158	14.0736	45.33	1.58		N/A	2.67	3.67	1.00	26952.00
80	SYN.WCG BT.73.9-3159	14.0736	45.82	0.30	9.81	N/A	2.65	3.66	1.00	25454.00
81	SYN.WCG BT.73.9-3160	14.0736	45.74	0.35		N/A	2.68	3.68	1.00	25721.00
82	SYN.WCG BT.74-3161	14.0736	44.91	0.24	9.8	N/A	2.66	3.67	1.01	27026.00
83	SYN.WCG BT.74-3162	14.0736	45.34	0.35		N/A	2.67	3.68	1.01	27037.00
84	SYN.WCG BT.73.1-3163	14.0736	44.97	0.22	9.81	N/A	2.7	3.70	1.00	26879.00
85	SYN.WCG BT.73.1-3164	14.0736	45.01	0.24		N/A	2.66	3.67	1.01	27169.00
86	SYN.WCG BT.65-3165	14.0736	44.98	0.53	9.81	N/A	2.65	3.65	1.00	27125.00
87	SYN.WCG BT.65-3166	14.0736	45.04	0.22		N/A	2.66	3.67	1.01	27255.00
88	SYN. WCG BT.10-3167	14.0736	44.69	0.25	9.81	N/A	2.7	3.70	1.00	27164.00
89	SYN.WCG BT.10-3168	14.0736	44.58	0.27		N/A	2.65	3.64	0.99	27249.00
90	SYN.WCG BT.91-3169	14.0736	45.04	0.24	9.81	N/A	2.65	3.65	1.00	26833.00
91	SYN.WCG BT.91-3170	14.0736	44.65	0.25		N/A	2.67	3.68	1.01	27090.00
92	Tc.SOR BT.SYN.WCG.5/30/96 CTR 3157	14.0736	42.80	0.23	9.91	N/A	2.65	3.65	1.00	28165.00
93	Tc.SOR BT.SYN.WCG.5/30/96 CTR 3158	14.0736	42.49	0.26		N/A	2.66	3.66	1.00	28196.00
94	Tc.SOR BT.SYN.WCG.5/30/96 STD 19						3.24	4.23	0.99	28265.00
95	Tc.SOR BT.SYN.WCG.5/30/96 STD 29						3.24	4.21	0.97	27258.00

	A	AK	AL	AM	AN	AO	AP	AQ
1	Sample Identification	CPM/g in Counted Tracer Solution after Sorption (Col AL/ Col AK)	Kd (ml/g) of Original Tracer Solution Based on Standards	Kd (ml/g) of Original Tracer Solution Based on Controls	Water ID	Type of Scintillation Cocktail Used	ID of Tracer Solutions Used for Sorption Experiment	Binder where Raw Experimental Data are Located
77								
78	SYN.WCG BT.108-3157	26524.75	2.06E-01	9.09E-02	SYN WCG 9/17/95	N/A	Tc SOR SYN/WCG 9/18/95	Area G Sorption Studies
79	SYN.WCG BT.108-3158	26952.00	4.65E-02	-6.04E-02	SYN WCG 9/17/95	N/A	Tc SOR SYN/WCG 9/18/95	Area G Sorption Studies
80	SYN.WCG BT.79.9-3159	25454.00	2.93E+01	2.90E+01	SYN WCG 9/17/95	N/A	Tc SOR SYN/WCG 9/18/95	Area G Sorption Studies
81	SYN.WCG BT.79.9-3160	25721.00	2.84E+01	2.82E+01	SYN WCG 9/17/95	N/A	Tc SOR SYN/WCG 9/18/95	Area G Sorption Studies
82	SYN.WCG BT.74-3161	26758.42	8.81E-02	-2.60E-02	SYN WCG 9/17/95	N/A	Tc SOR SYN/WCG 9/18/95	Area G Sorption Studies
83	SYN.WCG BT.74-3162	26769.31	7.77E-02	-2.99E-02	SYN WCG 9/17/95	N/A	Tc SOR SYN/WCG 9/18/95	Area G Sorption Studies
84	SYN.WCG BT.79.1-3163	26879.00	-1.40E-01	-2.47E-01	SYN WCG 9/17/95	N/A	Tc SOR SYN/WCG 9/18/95	Area G Sorption Studies
85	SYN.WCG BT.79.1-3164	26900.00	8.33E-02	-2.37E-02	SYN WCG 9/17/95	N/A	Tc SOR SYN/WCG 9/18/95	Area G Sorption Studies
86	SYN.WCG BT.65-3165	27125.00	-1.82E-02	-1.25E-01	SYN WCG 9/17/95	N/A	Tc SOR SYN/WCG 9/18/95	Area G Sorption Studies
87	SYN.WCG BT.65-3166	26935.15	-2.94E-02	-1.35E-01	SYN WCG 9/17/95	N/A	Tc SOR SYN/WCG 9/18/95	Area G Sorption Studies
88	SYN. WCG BT.10-3167	27164.00	7.68E-02	-3.06E-02	SYN WCG 9/17/95	N/A	Tc SOR SYN/WCG 9/18/95	Area G Sorption Studies
89	SYN.WCG BT.10-3168	27524.24	-3.97E-02	-1.44E-01	SYN WCG 9/17/95	N/A	Tc SOR SYN/WCG 9/18/95	Area G Sorption Studies
90	SYN.WCG BT.91-3169	26839.00	9.03E-02	-1.58E-02	SYN WCG 9/17/95	N/A	Tc SOR SYN/WCG 9/18/95	Area G Sorption Studies
91	SYN.WCG BT.91-3170	26821.76	1.38E-01	3.22E-02	SYN WCG 9/17/95	N/A	Tc SOR SYN/WCG 9/18/95	Area G Sorption Studies
92	Tc.SOR BT.SYN.WCG 5/30/96 CTR 3157	28165.00	N/A	N/A	SYN WCG 9/17/95	N/A	Tc SOR SYN/WCG 9/18/95	Area G Sorption Studies
93	Tc.SOR BT.SYN.WCG 5/30/96 CTR 3158	28136.00	N/A	N/A	SYN WCG 9/17/95	N/A	Tc SOR SYN/WCG 9/18/95	Area G Sorption Studies
94	Tc.SOR BT.SYN.WCG 5/30/96 STD 19	28550.51	N/A	N/A	SYN WCG 9/17/95	N/A	Tc SOR SYN/WCG 9/18/95	Area G Sorption Studies
95	Tc.SOR BT.SYN.WCG 5/30/96 STD 20	28096.91	N/A	N/A	SYN WCG 9/17/95	N/A	Tc SOR SYN/WCG 9/18/95	Area G Sorption Studies

	A	AR	AS	AT	AU	AV	AW	AX
1	Sample Identification	Optical Disk where Reduced Data are Located	Subdirectory	File Name				
77								
78	SYN.WCG BT.108-3157	TWS-INC-05-93-05	Area G Sorption	Syn Bt Scrp. #2				
79	SYN.WCG BT.108-3158	TWS-INC-05-93-05	Area G Sorption	Syn Bt Scrp. #2				
80	SYN.WCG BT.79.9-3159	TWS-INC-05-93-05	Area G Sorption	Syn Bt Scrp. #2				
81	SYN.WCG BT.79.9-3160	TWS-INC-05-93-05	Area G Sorption	Syn Bt Scrp. #2				
82	SYN.WCG BT.74-3161	TWS-INC-05-93-05	Area G Sorption	Syn Bt Scrp. #2				
83	SYN.WCG BT.74-3162	TWS-INC-05-93-05	Area G Sorption	Syn Bt Scrp. #2				
84	SYN.WCG BT.79.1-3163	TWS-INC-05-93-05	Area G Sorption	Syn Bt Scrp. #2				
85	SYN.WCG BT.79.1-3164	TWS-INC-05-93-05	Area G Sorption	Syn Bt Scrp. #2				
86	SYN.WCG BT.65-3165	TWS-INC-05-93-05	Area G Sorption	Syn Bt Scrp. #2				
87	SYN.WCG BT.65-3166	TWS-INC-05-93-05	Area G Sorption	Syn Bt Scrp. #2				
88	SYN. WCG BT.10-3167	TWS-INC-05-93-05	Area G Sorption	Syn Bt Scrp. #2				
89	SYN.WCG BT.10-3168	TWS-INC-05-93-05	Area G Sorption	Syn Bt Scrp. #2				
90	SYN.WCG BT.91-3169	TWS-INC-05-93-05	Area G Sorption	Syn Bt Scrp. #2				
91	SYN.WCG BT.91-3170	TWS-INC-05-93-05	Area G Sorption	Syn Bt Scrp. #2				
92	Tc SOR BT.SYN.WCG.5/30/96 CTR 3157	TWS-INC-05-93-05	Area G Sorption	Syn Bt Scrp. #2				
93	Tc.SOR BT.SYN.WCG.5/30/96 CTR 3158	TWS-INC-05-93-05	Area G Sorption	Syn Bt Scrp. #2				
94	Tc SOR.BT.SYN.WCG.5/30/96 STD 19	TWS-INC-05-93-05	Area G Sorption	Syn Bt Scrp. #2				
95	Tc.SOR BT.SYN.WCG.5/30/96 STD 20	TWS-INC-05-93-05	Area G Sorption	Syn Bt Scrp. #2				

Am-241

Mineral ID	kd based on stds	kd based on ctrls	molarity
108.0'-109.5'	2.26E+02	2.06E+02	2.34E-09
108.0'-109.5'	2.18E+02	1.98E+02	2.34E-09
79.9'-80.0' Fe rich	4.20E+02	4.00E+02	2.34E-09
79.9'-80.0' Fe rich	4.69E+02	4.49E+02	2.34E-09
74.0'-75.0'	4.29E+03	4.27E+03	2.34E-09
74.0'-75.0'	4.61E+03	4.59E+03	2.34E-09
79.1'-79.7'	3.62E+02	3.42E+02	2.34E-09
79.1'-79.7'	3.98E+02	3.78E+02	2.34E-09
65.0'-66.0'	1.78E+04	1.77E+04	2.34E-09
65.0'-66.0'	1.52E+04	1.52E+04	2.34E-09
10.8'-12.0'	1.83E+04	1.83E+04	2.34E-09
10.8'-12.0'	2.24E+04	2.23E+04	2.34E-09
91'0	2.03E+04	2.03E+04	2.34E-09
91'0	2.73E+04	2.73E+04	2.34E-09

Np-237

Mineral ID	kd based on stds	kd based on ctrls	molarity
108.0'-109.5'	-6.04E-01	1.66E-01	4.49E-05
108.0'-109.5'	-5.68E-01	1.89E-01	4.49E-05
79.9'-80.0' Fe rich	1.03E-01	8.94E-01	4.49E-05
79.9'-80.0' Fe rich	1.27E+00	2.11E+00	4.49E-05
74.0'-75.0'	2.02E+00	2.88E+00	4.49E-05
74.0'-75.0'	2.13E+00	2.99E+00	4.49E-05
79.1'-79.7'	3.08E-01	1.11E+00	4.49E-05
79.1'-79.7'	1.14E-01	9.01E-01	4.49E-05
65.0'-66.0'	1.98E+00	2.87E+00	4.49E-05
65.0'-66.0'	2.13E+00	2.98E+00	4.49E-05
10.8'-12.0'	5.04E+00	6.04E+00	4.49E-05
10.8'-12.0'	5.32E+00	6.30E+00	4.49E-05
91'0	2.23E+00	3.07E+00	4.49E-05
91'0	1.56E+00	2.38E+00	4.49E-05

Pu-239

Mineral ID	kd based on stds	kd based on ctrls	molarity
108.0'-109.5'	1.17E+00	1.23E+00	2.95E-07
108.0'-109.5'	1.71E+00	1.77E+00	2.95E-07

79.9'-80.0' Fe rich	1.81E+00	1.87E+00	2.95E-07	
79.9'-80.0' Fe rich	1.73E+00	1.79E+00	2.95E-07	
74.0'-75.0'	6.31E+00	6.39E+00	2.95E-07	
74.0'-75.0'	6.64E+00	6.71E+00	2.95E-07	
79.1'-79.7'	1.59E+00	1.65E+00	2.95E-07	
79.1'-79.7'	1.50E+00	1.56E+00	2.95E-07	
65.0'-66.0'	1.72E+01	1.73E+01	2.95E-07	
65.0'-66.0'	1.79E+01	1.80E+01	2.95E-07	
10.8'-12.0'	1.11E+02	1.12E+02	2.95E-07	
10.8'-12.0'	1.08E+02	1.08E+02	2.95E-07	
91'0	1.93E+01	1.94E+01	2.95E-07	
91'0	1.89E+01	1.90E+01	2.95E-07	

U-233

Mineral ID	kd based on stds	kd based on ctrls	molarity	
108.0'-109.5'	2.52E+00	2.39E+00	9.70E-06	
108.0'-109.5'	1.50E+00	1.38E+00	9.70E-06	
79.9'-80.0' Fe rich	2.13E+00	1.99E+00	9.70E-06	
79.9'-80.0' Fe rich	1.63E+00	1.50E+00	9.70E-06	
74.0'-75.0'	3.11E+00	2.97E+00	9.70E-06	
74.0'-75.0'	2.59E+00	2.46E+00	9.70E-06	
79.1'-79.7'	2.07E+00	1.93E+00	9.70E-06	
79.1'-79.7'	2.96E+00	2.82E+00	9.70E-06	
65.0'-66.0'	3.40E+00	3.26E+00	9.70E-06	
65.0'-66.0'	2.40E+00	2.27E+00	9.70E-06	
10.8'-12.0'	2.78E+00	2.65E+00	9.70E-06	
10.8'-12.0'	2.35E+00	2.22E+00	9.70E-06	
91'0	2.97E+00	2.84E+00	9.70E-06	
91'0	3.60E+00	3.46E+00	9.70E-06	

Tc-95

Mineral ID	kd based on stds	kd based on ctrls	molarity	
108.0'-109.5'	2.00E-01	9.09E-02	7.06E-12	
108.0'-109.5'	4.65E-02	-6.06E-02	7.06E-12	
79.9'-80.0' Fe rich	2.93E+01	2.90E+01	7.06E-12	
79.9'-80.0' Fe rich	2.84E+01	2.82E+01	7.06E-12	
74.0'-75.0'	8.11E-02	-2.60E-02	7.06E-12	
74.0'-75.0'	7.77E-02	-2.99E-02	7.06E-12	
79.1'-79.7'	-1.40E-01	-2.47E-01	7.06E-12	

79.1'-79.7'	8.33E-02	-2.37E-02	7.06E-12	
65.0'-66.0'	-1.82E-02	-1.25E-01	7.06E-12	
65.0'-66.0'	-2.94E-02	-1.35E-01	7.06E-12	
10.8'-12.0'	7.68E-02	-3.00E-02	7.06E-12	
10.8'-12.0'	-3.97E-02	-1.44E-01	7.06E-12	
91'0	9.03E-02	-1.58E-02	7.06E-12	
91'0	1.38E-01	3.22E-02	7.06E-12	

RAE-9629/91B-2

RADIOACTIVE WASTE INVENTORY FOR THE TA-54, AREA G PERFORMANCE ASSESSMENT AND COMPOSITE ANALYSIS

Rob Shuman

Prepared for

Los Alamos National Laboratory
CST-14, Solid Radioactive Waste Management
Mail Stop J595
Los Alamos, NM 87545

March 1997

Rogers & Associates Engineering Corporation
P.O. Box 330
Salt Lake City, UT 84110-0330

This page intentionally left blank.

TABLE OF CONTENTS

Chapter		Page No.
1	INTRODUCTION	1-1
2	WASTE CHARACTERIZATION METHODOLOGY	2-1
	2.1 Historic Waste	2-1
	2.2 Future Waste	2-23
	2.2.1 Operational LLW	2-23
	2.2.2 ER and D&D LLW	2-25
	2.2.3 MLLW Residues	2-28
	2.2.4 Total Future Inventory	2-33
3	AREA G INVENTORY PROJECTIONS	3-1
	3.1 Historic Waste	3-1
	3.1.1 Pre-1971 Inventory	3-2
	3.1.2 1971 to September 25, 1988, Inventory	3-21
	3.1.3 September 26, 1988, to 1995 Inventory	3-44
	3.2 Projected LLW Inventory	3-57
	3.2.1 Operational LLW Inventory Projections	3-57
	3.2.2 ER and D&D LLW	3-70
	3.2.3 MLLW Residues	3-70
	3.2.4 Total Future Inventory	3-75
	3.3 Summary of the Area G Radioactive Waste Inventory	3-75
	3.3.1 Radioactive Waste Inventory for the Area G Performance Assessment	3-75
	3.3.2 Radioactive Waste Inventory for the Area A Composite Analysis	3-84
REFERENCES		R-1
APPENDIX A -- RADIONUCLIDES EXCLUDED FROM AREA G INVENTORY PROJECTIONS BASED ON HALF-LIFE CONSIDERATIONS		A-1

This page intentionally left blank.

LIST OF FIGURES

Figure No.		Page No.
2-1	Fractional abundances of MFP radionuclides	2-16
3-1	Historic LLW volumes in pit and shaft waste	3-3
3-2	Historic LLW activities in pit and shaft waste	3-4
3-3	Mean and standard deviation of LLW pit and shaft disposal volumes	3-5
3-4	Mean and standard deviation of LLW pit and shaft activities	3-6
3-5	Historic TRU waste volumes and activities	3-8
3-6	Mean and standard deviation of historic TRU waste volumes	3-9
3-7	Mean and standard deviation of historic TRU waste activities	3-10

This page intentionally left blank.

LIST OF TABLES

Table No.		Page No.
2-1	Operational periods for the disposal pits and shafts at Area G	2-3
2-2	Waste forms for LANL waste streams	2-12
2-3	Information used to allocate MFP activity	2-15
2-4	Information used to allocate MAP activity	2-18
2-5	Material type allocations for the Area G inventory	2-19
2-6	Waste streams assumed to be generated from ER and D&D activities	2-26
2-7	MLLW streams, treatment options, and inventories	2-29
3-1	Total pre-1971 inventory volume and activity projections	3-12
3-2	Pre-1971 radionuclide inventory projections for Area G pits	3-14
3-3	Pre-1971 radionuclide inventory projections for Area G shafts	3-16
3-4	Quantities and radiological characteristics of TRU waste that was non-retrievably disposed of in Pit 6	3-18
3-5	Area G disposal events that are not fully captured by the extrapolation process	3-19
3-6	Additions to the extrapolation-based waste inventory projections for the pre-1971 period	3-20
3-7	Pit and shaft waste volumes and activities disposed of from 1971 to September 25, 1988	3-22
3-8	Pit radionuclide inventories for 1971 through September 25, 1988	3-26
3-9	Shaft radionuclide inventories for 1971 through September 25, 1988	3-42

LIST OF TABLES
(Continued)

Table No.		Page No.
3-10	Quantities of TRU waste that was non-retrievably disposed of between 1971 and September 25, 1988	3-45
3-11	Radionuclide inventories in TRU waste that was non-retrievably disposed of between 1971 and September 25, 1988	3-46
3-12	Pit and shaft waste volumes and activities disposed of from September 26, 1988, to 1995	3-48
3-13	Pit radionuclide inventories for September 26, 1988, through 1995	3-50
3-14	Shaft radionuclide inventories for September 26, 1988, through 1995	3-56
3-15	Major generators of LLW based on total volume	3-58
3-16	Major generators of LLW based on total activity	3-59
3-17	Major generators of LLW based on radionuclide-specific activity	3-60
3-18	Projections of future operations at the major generators of LLW	3-62
3-19	Major generators of LLW between 1990 and 1995	3-64
3-20	Stored and projected inventories of waste with high H-3 activities	3-65
3-21	Projected operational LLW volumes and activities for pits and shafts	3-66
3-22	Projected radionuclide inventories for operational waste disposed of in pits	3-67
3-23	Projected shaft radionuclide inventories for Area G	3-69
3-24	Projected ER and D&D and CMR Upgrade LLW inventories for Area G	3-71

LIST OF TABLES
(Continued)

Table No.		Page No.
3-25	Radionuclide concentrations in ER, D&D, and CMR upgrade waste	3-72
3-26	Radionuclide inventories for ER, D&D, and CMR upgrade waste	3-73
3-27	Projected inventories of uranium chip waste	3-74
3-28	Total future inventory volume and activity projections	3-76
3-29	Total future radionuclide inventories for Area G pits	3-77
3-30	Total future radionuclide inventories for Area G shafts	3-79
3-31	Pit and shaft waste volumes and activities included in the Area G performance assessment inventory	3-80
3-32	Pit radionuclide inventories for the Area G performance assessment	3-81
3-33	Shaft radionuclide inventories for the Area G performance assessment	3-83
3-34	Pit and shaft waste volumes and activities included in the Area G composite analysis inventory	3-85
3-35	Pit radionuclide inventories for the Area G composite analysis	3-86
3-36	Shaft radionuclide inventories for the Area G composite analysis	3-88

This page intentionally left blank.

1. INTRODUCTION

The Los Alamos National Laboratory (LANL) generates radioactive waste as a result of various activities. Operational waste is generated at LANL from a wide variety of research and development activities, including nuclear weapons development, energy production, and medical research. Environmental restoration (ER) and decontamination and decommissioning (D&D) waste is generated as contaminated sites and facilities at LANL undergo cleanup or remediation. The majority of this waste is low-level radioactive waste (LLW) and is disposed of at the Technical Area 54 (TA-54), Area G, disposal facility.

U.S. Department of Energy (DOE) Order 5820.2A requires that radioactive waste be managed, treated, stored, and disposed of in a manner that protects public health and safety, and the environment. To comply with this order, DOE field sites must prepare and maintain a site-specific radiological performance assessment for all LLW disposal facilities.

Additionally, in response to Recommendation 94-2 from the Defense Nuclear Facilities Safety Board, DOE has developed a comprehensive approach for ensuring that Environmental Management (EM) activities will not compromise future radiological protection of the public (DOE, 1996). Under this approach, DOE requires that a composite analysis be performed which accounts for the cumulative impact of active and planned LLW disposal facilities and all other sources of radioactive contamination that could interact with active disposal facilities.

This report characterizes the waste that will be included in the next draft of the performance assessment for TA-54, Area G, and in the composite analysis. In terms of the performance assessment, this waste includes all LLW disposed of at Area G since September 26, 1988, and the LLW projected to require disposal over the remainder of the facility's lifetime. The waste inventory for the composite analysis includes all radioactive waste disposed of at Area G since the disposal facility opened in 1957 and the LLW projected to require disposal in the future. Characteristics of the waste addressed by this report include total volume, total activity, and radionuclide-specific activities. These characteristics

are provided for several different waste forms and for waste disposed of in pits and shafts at Area G.

Chapter 2 of this report summarizes the types and quantities of radioactive waste that have been disposed of at Area G and discusses the methodology used to characterize the waste. Chapter 3 presents the results of the characterization effort.

2. WASTE CHARACTERIZATION METHODOLOGY

This section describes the waste that has been disposed of at Area G (historic waste) and waste that is expected to require disposal in the future (future waste). It discusses the approaches used to estimate characteristics of this waste in a form useful for conducting the Area G performance assessment and composite analysis.

Different approaches were used to characterize historic waste and future waste because the levels of existing information on these wastes differed. The methods used to characterize the historic waste are discussed in Section 2.1, while the approach for estimating future waste characteristics is described in Section 2.2.

2.1 HISTORIC WASTE

Historic waste, as the term is used here, refers to all waste disposed of at Area G since it opened in 1957 through the end of 1995. Area G first began receiving waste in the second quarter of 1957, when its first disposal pit was placed in service (Rogers, 1977). This pit received only non-routine contaminated waste until January 2, 1959, when it began accepting routine contaminated waste. The first shafts used for radioactive waste disposal at Area G were placed in service in April 1966 (Rogers, 1977).

Although the waste currently disposed of at Area G is restricted to LLW, transuranic (TRU) waste was routinely disposed of at Area G prior to 1971. Since that time, most TRU waste has been segregated from the LLW and retrievably stored. Furthermore, prior to 1986, most of LANL's mixed low-level waste (MLLW) was disposed of at the Area G disposal facility. However, since July 1986, when the EPA affirmed its authority over the regulation of the hazardous component of MLLW, this waste has been stored on site or shipped off site for treatment and disposal.

The waste disposed of at Area G includes operational or routine waste, non-routine waste, and waste from ER and D&D activities at LANL. Operational waste consists of a wide range of materials, including compactible trash (e.g., paper, cardboard, and plastic), rubber, glass, disposable protective clothing, solidified powders and ash, animal tissue, and suspect radioactive waste. Non-routine waste includes classified waste, uranium chips from shops at LANL, and pieces of heavy equipment such as dump trucks (Rogers, 1977). ER and D&D waste generally consists of equipment and scrap metal, building debris, soil, asbestos, and polychlorinated biphenyl (PCB)-contaminated materials. The facility does not accept free liquids for disposal.

Thirty-five pits and almost 200 shafts were used for disposal of LLW at Area G through December 31, 1995. These disposal units and their periods of operation are listed in Table 2-1. The periods of operation listed in the table are based on the first and last dates of waste receipt, as indicated in LANL's LLW disposal database or Rogers (1977).

Four of the 35 disposal pits were still open at the end of 1995. Pit 31 is dedicated to the disposal of asbestos waste and will continue to receive moderate amounts of waste in the future. Pits 37, 38, and 39 are used for the disposal of routine, ER, and D&D waste generated at LANL. Fewer than 20 of the disposal shafts active between April 1966 and December 1995 were active at the end of 1995 (Lopez, 1996). In general, concrete caps have been placed over the closed shafts.

The types and quantities of LLW disposed of at Area G are recorded on shipment manifests and entered into the LANL LLW disposal database on a per-package basis. Disposal records from 1971 through the present day have been maintained in the disposal database. The information contained in the database includes the waste form, the volume and total activity of the waste package, and the radionuclide activities in the waste. While disposal records for waste disposed of prior to 1971 are maintained in logbooks, these data are not included in the LLW disposal database.

As discussed earlier, TRU waste was disposed of at Area G prior to 1971. Since that time, the majority of this waste has been segregated and retrievably stored; small quantities of TRU waste were non-retrievably disposed of in pits and shafts through 1979. The types and quantities of TRU waste placed in storage or disposed of are recorded on shipment

Table 2-1. Operational periods for the disposal pits and shafts at Area G.

Disposal Unit	Month of First Delivery	Month of Last Delivery[a]	Current Status
Pits			
1	2nd qtr, 1957	April-61	Closed
2	4th qtr, 1959	July-63	Closed
3	Jun-63	Apr-66	Closed
4	1st qtr, 1966	4th qtr, 1967	Closed
5	Oct-69	Dec-73	Closed
6	1st qtr, 1970	Aug-72	Closed
7	Mar-74	Sep-78	Closed
8	Sep-71	Mar-74	Closed
9	Sep-74	Aug-78	Closed
10	Apr-79	May-80	Closed
12	Jun-72	Nov-75	Closed
13	Nov-76	Sep-77	Closed
16	Jun-72	Jul-75	Closed
17	Aug-72	Mar-74	Closed
18	Feb-78	Oct-79	Closed
19	May-73	Aug-79	Closed
20	Jan-75	Oct-77	Closed
21	Aug-72	Dec-74	Closed
22	Dec-73	Apr-80	Closed
24	Jan-75	Nov-76	Closed
25	Dec-79	Feb-86	Closed
26	Feb-84	Apr-85	Closed
27	May-81	May-86	Closed
28	Jan-81	Feb-86	Closed
29	Mar-83	Oct-86	Closed
30	Oct-88	Jun-90	Closed
31	Sep-90	Present	Active
32	Feb-84	Nov-90	Closed
33	Nov-82	Jul-84	Closed
35	Jun-87	Apr-88	Closed
36	Jun-88	Oct-89	Closed
37	Apr-90	Present	Active
38	Sep-94	Present	Active
39	Aug-93	Present	Active

Table 2-1. Continued.

Disposal Unit	Month of First Delivery	Month of Last Delivery[a]	Current Status
Shafts			
1	Apr-66	Jan-67	Closed
2	Apr-66	Jun-67	Closed
3	Apr-66	Nov-67	Closed
4	Apr-67	Jan-68	Closed
5	Jun-67	Jan-68	Closed
6	Jun-67	Mar-68	Closed
7	Jun-67	Sep-68	Closed
8	Apr-68	Jan-69	Closed
9	Jun-68	Apr-69	Closed
10	Feb-69	Aug-69	Closed
11	Jan-67	Oct-92	Closed
12	Jul-66	Mar-70	Closed
13	Sep-66	Mar-90	Closed
14	Sep-67	Sep-69	Closed
15	Nov-69	Jun-70	Closed
16	Nov-69	Nov-69	Closed
17	Mar-70	Dec-74	Closed
18	Jul-70	Apr-79	Closed
19	Oct-71	Apr-74	Closed
20	May-74	Jun-75	Closed
21	Jan-85	Jan-85	Closed
22	Aug-80	May-93	Closed
23	Apr-80	Apr-80	Closed
24	Sep-69	Apr-72	Closed
25	Sep-69	Feb-71	Closed
26	Dec-69	Jun-70	Closed
27	May-70	Aug-70	Closed
28	Jun-70	Jul-70	Closed
29	Jul-70	Jun-71	Closed
30	Jul-70	Feb-85	Closed
31	Sep-70	Feb-71	Closed
32	May-70	Oct-71	Closed
33	Oct-70	Feb-71	Closed
34	Feb-70	Apr-72	Closed
35	Sep-71	Jul-85	Closed
36	Jun-70	Mar-85	Closed
37	Jun-70	Oct-85	Closed
38	Jun-70	Feb-74	Closed

Table 2-1. Continued.

Disposal Unit	Month of First Delivery	Month of Last Delivery[a]	Current Status
39	Aug-70	Oct-73	Closed
40	Mar-71	May-71	Closed
41	Mar-71	Aug-72	Closed
42	Mar-71	Oct-72	Closed
43	Jul-71	Aug-72	Closed
44	Aug-71	Aug-72	Closed
45	Sep-71	Aug-72	Closed
46	Apr-72	Aug-72	Closed
47	Apr-72	Jul-72	Closed
48	Jun-72	Sep-72	Closed
49	Apr-72	Sep-72	Closed
50	Jun-74	Apr-76	Closed
51	Mar-75	Oct-75	Closed
52	Sep-75	Jun-76	Closed
53	Nov-75	Mar-76	Closed
54	Jul-76	Dec-76	Closed
55	Dec-76	Jan-77	Closed
56	Jan-77	Feb-77	Closed
57	Feb-77	Mar-77	Closed
58	Jul-72	Sep-73	Closed
59	Jul-72	May-74	Closed
60	Dec-72	Dec-74	Closed
61	Jun-73	Feb-74	Closed
62	Apr-74	Jan-76	Closed
63	Jan-76	Jan-76	Closed
64	Jan-76	Aug-77	Closed
65	Aug-76	Oct-77	Closed
66	May-76	Jul-76	Closed
67	Apr-77	Jun-77	Closed
68	Jun-77	Aug-77	Closed
69	Aug-77	Aug-77	Closed
70	Jan-75	Feb-76	Closed
71	Jan-78	Feb-78	Closed
72	Nov-72	Mar-73	Closed
73	Jan-73	Mar-73	Closed
74	Mar-73	Aug-73	Closed
75	May-73	Sep-73	Closed
76	Oct-73	Apr-74	Closed
77	Jan-74	May-74	Closed

Table 2-1. Continued.

Disposal Unit	Month of First Delivery	Month of Last Delivery[a]	Current Status
78	Jun-74	Mar-75	Closed
79	Oct-74	Dec-75	Closed
80	Jun-75	Apr-76	Closed
81	May-75	Jun-76	Closed
82	Feb-78	Apr-78	Closed
83	Feb-78	Apr-78	Closed
84	Mar-78	May-78	Closed
85	May-78	May-78	Closed
86	Sep-77	Oct-77	Closed
87	Oct-77	Nov-77	Closed
88	Nov-77	Nov-77	Closed
89	Dec-77	Jan-78	Closed
90	Jan-78	Jan-78	Closed
91	Sep-77	May-78	Closed
92	Sep-77	Jul-78	Closed
93	Jul-78	Jun-84	Closed
94	Dec-78	Jun-84	Closed
95	Mar-84	Jul-84	Closed
96	May-77	Jan-79	Closed
97	Jul-78	Apr-84	Closed
99	Apr-83	Mar-84	Closed
100	May-83	Jun-83	Closed
101	Sep-80	Jun-81	Closed
102	Jul-82	Aug-83	Closed
103	Dec-81	Jul-82	Closed
104	Oct-82	Dec-82	Closed
105	Jun-82	May-83	Closed
106	Jul-80	Aug-81	Closed
107	Sep-78	Jan-81	Closed
108	Jul-80	May-82	Closed
109	Mar-80	Jul-80	Closed
110	Feb-79	Nov-79	Closed
111	Oct-79	Jun-80	Closed
112	May-78	Oct-79	Closed
114	May-79	Aug-82	Closed
115	Aug-79	Aug-82	Closed
118	Mar-83	Feb-84	Closed
119	Mar-83	Nov-83	Closed
120	Jun-83	Nov-84	Closed

Table 2-1. Continued.

Disposal Unit	Month of First Delivery	Month of Last Delivery[a]	Current Status
121	Jul-84	Apr-85	Closed
122	Aug-84	Jun-85	Closed
123	Mar-84	Aug-84	Closed
124	Feb-84	Aug-91	Closed
125	Oct-84	Dec-84	Closed
126	Mar-85	May-87	Closed
127	Feb-85	Nov-85	Closed
128	Oct-85	Jun-86	Closed
129	Jan-86	Mar-86	Closed
130	Jan-86	Aug-87	Closed
131	Jul-87	Jul-95	Active
132	Mar-87	Jan-93	Closed
133	Mar-86	Jan-87	Closed
134	Jun-86	Oct-86	Closed
135	Oct-86	Mar-87	Closed
136	Sep-86	Aug-95	Closed
137	Sep-87	Sep-92	Active
138	Apr-87	Sep-87	Closed
139	Apr-87	Oct-88	Closed
140	Oct-87	Jul-91	Closed
141	Oct-88	Mar-91	Closed
142	Jan-91	Sep-91	Closed
143	Sep-91	Mar-95	Closed
144	Feb-94	Mar-95	Active
147	Sep-91	May-95	Active
148	Oct-91	May-93	Closed
149	Apr-91	Jan-94	Closed
150	May-76	Mar-79	Closed
151	Jul-79	May-86	Closed
152	Apr-80	Apr-83	Closed
153	Apr-83	Apr-84	Closed
154	Apr-84	Sep-86	Closed
155	Aug-88	Apr-89	Closed
156	Dec-86	Sep-87	Closed
157	Sep-87	Jan-88	Closed
158	Sep-89	Aug-93	Active
159	Apr-89	Apr-89	Active
160	Jun-90	Aug-93	Active
161	Aug-93	Jun-94	Active

Table 2-1. Continued.

Disposal Unit	Month of First Delivery	Month of Last Delivery[a]	Current Status
162	May-95	Sep-95	Active
171	Jun-95	Aug-95	Closed
172	Jul-95	Aug-95	Closed
173	Jul-95	Aug-95	Closed
174	Jun-95	Jul-95	Closed
175	Jul-95	Aug-95	Closed
176	Aug-95	Aug-95	Closed
177	Aug-95	Aug-95	Closed
189	Aug-87	Feb-88	Closed
190	Mar-83	May-84	Closed
191	Oct-84	Dec-86	Closed
192	Feb-84	Sep-87	Closed
196	Aug-89	Aug-93	Active
197	Oct-93	Nov-95	Active
206	Sep-80	Sep-80	Closed
301	Sep-92	Nov-94	Active
307	Feb-92	Aug-94	Active
308	Mar-94	Apr-94	Active
C-1	Sep-80	Sep-80	Closed
C-2	Feb-81	Feb-81	Closed
C-3	Feb-81	Feb-81	Closed
C-4	Feb-81	Feb-81	Closed
C-5	Feb-81	Feb-81	Closed
C-6	Feb-81	Feb-81	Closed
C-7	Feb-81	Feb-81	Closed
C-8	Feb-81	May-82	Closed
C-9	May-82	Sep-84	Closed
C-10	Mar-84	Jul-85	Closed
C-11	Aug-85	Jun-86	Closed
C-12	Jul-86	Oct-90	Closed
C-13	Sep-87	Oct-95	Active
C-14	Nov-92	Nov-92	Active

a. Operational period is current through December 31, 1995.

manifests and entered into the TRU waste database. These detailed records date back to 1971; information about waste disposed of prior to 1971 is maintained in logbooks.

The historic waste inventory for the period spanning 1971 through 1995 was estimated using the data in the LANL LLW disposal database and the TRU waste database. The majority of the Area G inventory for this period was derived from the LLW disposal records. The TRU waste that was non-retrievably disposed of in pits and shafts was added to the LLW inventory to arrive at the total inventory for the period. This TRU waste includes material that was placed in pits 6, 7, 8, 20, and 22 and shafts 17 through 110.

The lack of detailed shipment records for radioactive waste disposed of prior to 1971 required that an alternative means of characterizing this waste be developed. Consequently, the characteristics of a portion of the waste disposed of since 1971 were extrapolated back to the period for which detailed disposal data were unavailable. Specifically, the LLW and TRU waste disposal data for the period of 1971 through 1977 were used to estimate the characteristics of the waste disposed of in pits prior to 1971. Shaft disposal data for 1971 through 1975 were used to characterize the waste disposed of in shafts prior to 1971. The approach taken in selecting these periods is discussed in the following paragraphs.

The period from which disposal data are drawn to estimate the characteristics of the pre-1971 waste strongly influences resulting inventory projections. Thus, the data chosen for the analysis needed to be as representative of the period from 1957 to 1970 as possible. Under ideal conditions, the operations generating waste during the period from which waste characteristics are extrapolated would be identical to the operations generating waste for the period of time for which the waste inventory is being developed. As the period of time from which waste characteristics are extrapolated increases, however, the likelihood of satisfying this condition diminishes. Over time, some operations at LANL are phased out, while new ones begin as the role of LANL evolves. Changes in disposal regulations may also affect the types and quantities of waste undergoing disposal.

With the preceding considerations in mind, the Area G LLW disposal data were examined for the period from 1971 through 1995. The quantities and characteristics of the disposed waste were evaluated to establish LLW disposal patterns and identify any obvious shifts in those patterns. The TRU waste database, which records the types and quantities

of TRU waste disposed of or placed in storage at LANL, underwent a similar evaluation to characterize the TRU component of the waste disposed of prior to 1971. Based on these evaluations, the results of which are discussed in Section 3.1, the periods from 1971 to 1977 and from 1971 to 1975 were selected as reasonable periods for characterizing the waste placed in pits and shafts, respectively, prior to 1971.

The 1971 to 1977 pit data and the 1971 to 1975 shaft data were used to develop average annual disposal quantities for Area G prior to 1971. These averages were multiplied by the number of years the facility accepted waste for disposal in the respective disposal units. The average annual pit inventories were multiplied by 12 years because Area G began accepting routine contaminated waste on January 2, 1959; only non-routine waste was disposed of between the facility's opening in 1957 through the end of 1958. The average annual disposal quantities for the shafts were multiplied by 5 years, consistent with the fact that these units began accepting waste in April 1966.

The extrapolation approach used to estimate the pre-1971 inventory implicitly assumes that the waste disposed of between 1971 and 1977 is similar to that disposed of between 1957 and 1970. While this assumption generally is expected to be valid, some of the wastes generated from 1957 to 1970 and 1971 to 1977 are unique to those periods. A comprehensive examination of the disposal data to identify these unique wastes was beyond the scope of this effort; however, former and current LANL personnel familiar with historic operations at LANL were asked to identify wastes that were unique to either the 1957 to 1970 or 1971 to 1977 period. Waste that was unique to the 1957 to 1970 period was added to the inventory estimated using the extrapolation approach. If waste was generated between 1971 and 1977 under conditions that did not occur prior to that period, the material was removed from the 1971 to 1977 data used to estimate the pre-1971 inventory.

The physical and chemical form of the waste disposed of in the pits and shafts plays an important role in how radioactivity is released to the environment from the disposal units and the rate at which these releases occur. For example, surface contamination on glass may be quickly rinsed from the waste as water percolates through the disposal units, whereas radionuclides sorbed to soils or concrete may be released from disposal units gradually over time. Source-term modeling for the performance assessment accounts for releases from

surface-contaminated waste, soils, concrete and sludges, and bulk-contaminated waste such as activated metals.

Source-term modeling performed in support of the Area G performance assessment and composite analysis requires that the historic inventory data for each pit and shaft be provided in terms of the waste forms discussed above. Thus, all waste streams that belong to a single waste form were grouped. For example, all waste streams which are expected to be surface-contaminated (e.g., glass, trash, plastic) were combined. Data for these waste streams were summed to determine the total volume, total activity, and radionuclide-specific activities to yield the inventory for surface-contaminated waste for the pits and shafts. Inventories were developed similarly for soil, concrete and sludges, and bulk-contaminated waste.

The development of waste-form-specific inventories required that the waste streams disposed of at Area G be categorized in terms of surface-contaminated waste, soils, concrete and sludges, and bulk-contaminated waste. The categories to which the waste streams were assigned are shown in Table 2-2. Each waste stream was conservatively assumed to be surface-contaminated waste unless there was specific knowledge about the waste and its release characteristics that allowed it to be assigned to one of the other three categories. Waste streams encompassing a variety of waste matrices were assumed to fall into several different waste-form or release categories. For example, waste streams consisting of debris were assumed to include surface-contaminated, soil, and concrete components (shown in Table 2-2).

Separate inventories were developed for all pits except pits 1 through 6. Pits 1 through 6 were active prior to 1971, the first year for which detailed disposal data are available. Consequently, a significant portion of the inventory in these disposal units was based on the extrapolation procedure described above. Given the general nature of this procedure, it was not possible to assign individual inventories to these pits.

The waste placed in the Area G disposal shafts was combined into a single shaft inventory. The sheer number of shafts that have been used for waste disposal, and the scattered distribution of these shafts, complicates the development of separate shaft

Table 2-2. Waste forms for LANL waste streams.

Waste Code	Waste Description	Release Mechanism: Surface-Contaminated Waste	Soils	Concrete/ Sludges	Bulk-Contaminated Waste
10	Graphite Solids	X			
11	Graphite Powder	X			
14	Combustible Decon Waste	X			
15	Cellulosics (paper, wood, etc.)	X			
16	Plastics	X			
17	Rubber Materials	X			
18	Combustible Lab Trash (paper, plastic, rubber)	X			
181	Non-Combustible Lab Trash (glass, metal)	X			
19	Combined Combustible/Non-Combustible Lab Trash	X/50%[a]			50%[a]
20	Hydrocarbon Oil (liquid)	X			
21	Silicon-Based Oil (absorbed, no free liquid)	X			
201	Hydrocarbon Oil (absorbed, no free liquid)	X			
211	Silicon-Based Oil (absorbed, no free liquid)	X			
22	Petroleum-Contaminated Soil		X		
23	Aqueous Solution (absorbed, no free liquid)	X			
24	Cemented/Immobilized Residues/Powders			X	
25	Leached Process Residues	X			
26	Evaporator Bottoms/Salts	X			
28	Chloride Salts	X			
30	PN Equipment	X			
31	Non-PN Equipment	X			
32	PN Oversize Equipment	X			
33	Non-PN Oversize Equipment	X			
35	Combustible Building Debris	X			
36	Non-Combustible Building Debris	50%[b]	25%[b]	25%[b]	
40	Combustible Hot Cell Waste	X/50%[a]			50%[a]
41	Non-Combustible Hot Cell Waste	X/50%[a]			50%[a]
45	Uranium Chips and Turnings in Diesel Fuel	X[c]	X[c]		
46	Skull and Oxide	X			
47	Slag and Porcelain	X			
49	Sanitary Sludge			X	
50	Metal Crucibles, Scrap, Dies	X			

Table 2-2. Continued.

Waste Code	Waste Description	Release Mechanism: Surface-Contaminated Waste	Soils	Concrete/ Sludges	Bulk-Contaminated Waste
51	Precious Metals	X			
52	Scrap Metal	X/50%[a]			50%[a]
53	Lead	X			
55	Filter Media	X			
56	Filter Media Residue	X			
60	Other Combustibles	X			
61	Other Non-Combustibles	X			
62	Molecular Sieves	X			
65	Animal Tissue	X			
68	Asbestos	X			
69	Asbestos-Contaminated Debris	50%[b]	25%[b]	25%[b]	
70	Chemical Waste	X			
71	Beryllium	X			
72	Beryllium-Contaminated Debris	50%[b]	25%[b]	25%[b]	
73	Scintillation Vials	X			
74	Ion Exchange Resins	X			
75	Chemical Treatment Sludge			X	
76	Cement Paste			X	
77	PCB-Contaminated Materials	X			
78	PCB-Contaminated Equipment	X			
79	PCB-Contaminated Soil		X		
791	PCB-Contaminated Concrete			X	
80	Irradiation Sources	X			
801	Irradiation Sources in Lead Shielding	X			
85	Firing Point Residues		X		
90	Radioactively-Contaminated Soil		X		
95	Glass	X			
99	Unidentified Material	X			

a. Release of all radionuclides except mixed activation products (MAP) is assumed to occur via rapid rinse; release of MAP is assumed to occur via rapid rinse (50%) and corrosion (50%).
b. Assumed distribution.
c. Historic waste is assumed to be surface-contaminated; future waste is assigned to the soil waste form based on anticipated waste treatment processes.

inventories. The usefulness of separate shaft inventories in terms of the performance assessment and composite analysis is questionable as well.

A portion of the waste disposed of at Area G is listed in the LLW and TRU waste databases as mixed fission products (MFP) or mixed activation products (MAP). Activity from these wastes was allocated to specific radionuclides as part of the inventory development (Vold, 1995). Allocations of MFP were based on fission product yields for thermal and fast neutrons. All radionuclides with an atomic mass number between 78 and 160 and a half-life of at least one year were included in the calculations. In using these fission product yields, it was conservatively assumed that the yield of a given isotope was the maximum of that provided for thermal and fast neutrons. The radionuclides included in the calculations, their half-lives, and their fission yields are listed in Table 2-3.

In many instances, several isotopes of an element may be generated by fission. The allocation of MFP activity was based on the conservative assumption that the entire yield of isotopes of a given atomic number consisted of the long-lived species listed in Table 2-3. No stable isotopes were assumed to be generated in the fission process. In cases where two long-lived isotopes were generated, it was assumed that the isotopic yield of each isotope was half of the total. The fractional correction terms for each fission product are included in Table 2-3.

The information in Table 2-3 was used to calculate the activity of each radionuclide generated per fission. These calculations were conducted assuming the waste was, on average, 2 years old at the time of disposal. This assumption stemmed from the fact that while some LLW is processed and disposed of at Area G within a year of generation, other waste (e.g., that generated through ER and D&D activities) may be disposed of at the facility several years after it was generated. Thus, because detailed information on the times of generation and disposal of the MFP was not available, the 2-year average age was assumed. The radionuclide activities per fission, decay-corrected for 2 years, are included in Table 2-3. These activities were normalized to determine the fractional radionuclide abundances in MFP waste. These fractional abundances, included in Table 2-3 and shown in Figure 2-1, were multiplied by the total MFP activities to yield the radionuclide activities for this waste.

Table 2-3. Information used to allocate MFP activity.

Radionuclide	Half-Life (yr)	Average Fission Yield/ Mass Number	Correction Term	Activity/ Fission at 2 Years	Fractional Abundance (Activity Basis)
Ag-108m	1.3E+02	2.0E-02	1.0E+00	1.1E-04	2.1E-03
Ba-133	1.0E+01	6.5E-02	1.0E+00	3.8E-03	7.4E-02
Cd-109	1.2E+00	1.0E-02	1.0E+00	1.8E-03	3.6E-02
Cd-113m	1.5E+01	1.0E-02	1.0E+00	4.3E-04	8.5E-03
Ce-144	7.8E-01	6.5E-02	5.0E-01	4.9E-03	9.6E-02
Cs-134	2.1E+00	6.5E-02	1.0E+00	1.1E-02	2.2E-01
Cs-135	2.3E+06	6.5E-02	1.0E+00	2.0E-06	3.8E-07
Cs-137	3.0E+01	6.5E-02	5.0E-01	7.2E-04	1.4E-02
Dy-154	1.0E+06	2.0E-03	5.0E-01	6.9E-10	1.4E-08
Eu-150	3.5E+01	1.0E-02	5.0E-01	9.5E-05	1.9E-03
Eu-152	1.3E+01	5.0E-03	1.0E+00	2.4E-04	4.7E-03
Eu-154	8.6E+00	2.0E-03	5.0E-01	6.9E-05	1.3E-03
Eu-155	4.8E+00	1.0E-03	1.0E+00	1.1E-04	2.1E-03
Gd-148	9.3E+01	2.5E-02	1.0E+00	1.8E-04	3.6E-03
Gd-150	1.8E+06	1.0E-02	5.0E-01	1.9E-09	3.8E-08
I-129	1.6E+07	3.0E-02	1.0E+00	1.3E-09	2.6E-08
Kr-81	2.1E+05	7.0E-03	1.0E+00	2.3E-08	4.5E-07
Kr-85	1.1E+01	2.0E-02	1.0E+00	1.1E-03	2.2E-02
La-137	6.0E+04	6.5E-02	5.0E-01	3.8E-07	7.4E-06
Mo-93	3.0E+03	6.5E-02	5.0E-01	7.5E-06	1.5E-04
Nb-92	2.0E+07	6.5E-02	1.0E+00	2.3E-09	4.4E-08
Nb-94	2.0E+04	6.5E-02	1.0E+00	2.3E-06	4.4E-05
Pd-107	6.5E+06	3.0E-02	1.0E+00	3.2E-09	6.3E-08
Pm-144	1.0E+00	6.5E-02	5.0E-01	5.6E-03	1.1E-01
Pm-146	5.5E+00	5.0E-02	5.0E-01	2.4E-03	4.8E-02
Pm-147	2.6E+00	3.5E-02	1.0E+00	5.5E-03	1.1E-01
Ru-106	1.1E+00	4.5E-02	1.0E+00	7.9E-03	1.6E-01
Sb-125	2.7E+00	2.0E-02	1.0E+00	3.1E-03	6.0E-02
Se-79	6.5E+04	2.0E-04	1.0E+00	2.1E-09	4.2E-08
Sm-146	1.0E+08	5.0E-02	5.0E-01	1.7E-10	3.4E-09
Sm-151	9.3E+01	8.0E-03	1.0E+00	5.9E-05	1.2E-03
Sn-121	5.0E+01	1.5E-02	1.0E+00	2.0E-04	4.0E-03
Sr-90	2.9E+01	6.5E-02	1.0E+00	1.5E-03	2.9E-02
Tb-157	1.6E+02	5.0E-04	1.0E+00	2.2E-06	4.2E-05
Tb-158	1.5E+02	2.0E-04	1.0E+00	9.2E-07	1.8E-05
Tc-97	2.6E+06	6.5E-02	1.0E+00	1.7E-08	3.4E-07
Tc-99	2.1E+05	6.5E-02	1.0E+00	2.1E-07	4.2E-06
Zr-93	9.5E+05	6.5E-02	5.0E-01	2.4E-08	4.7E-07

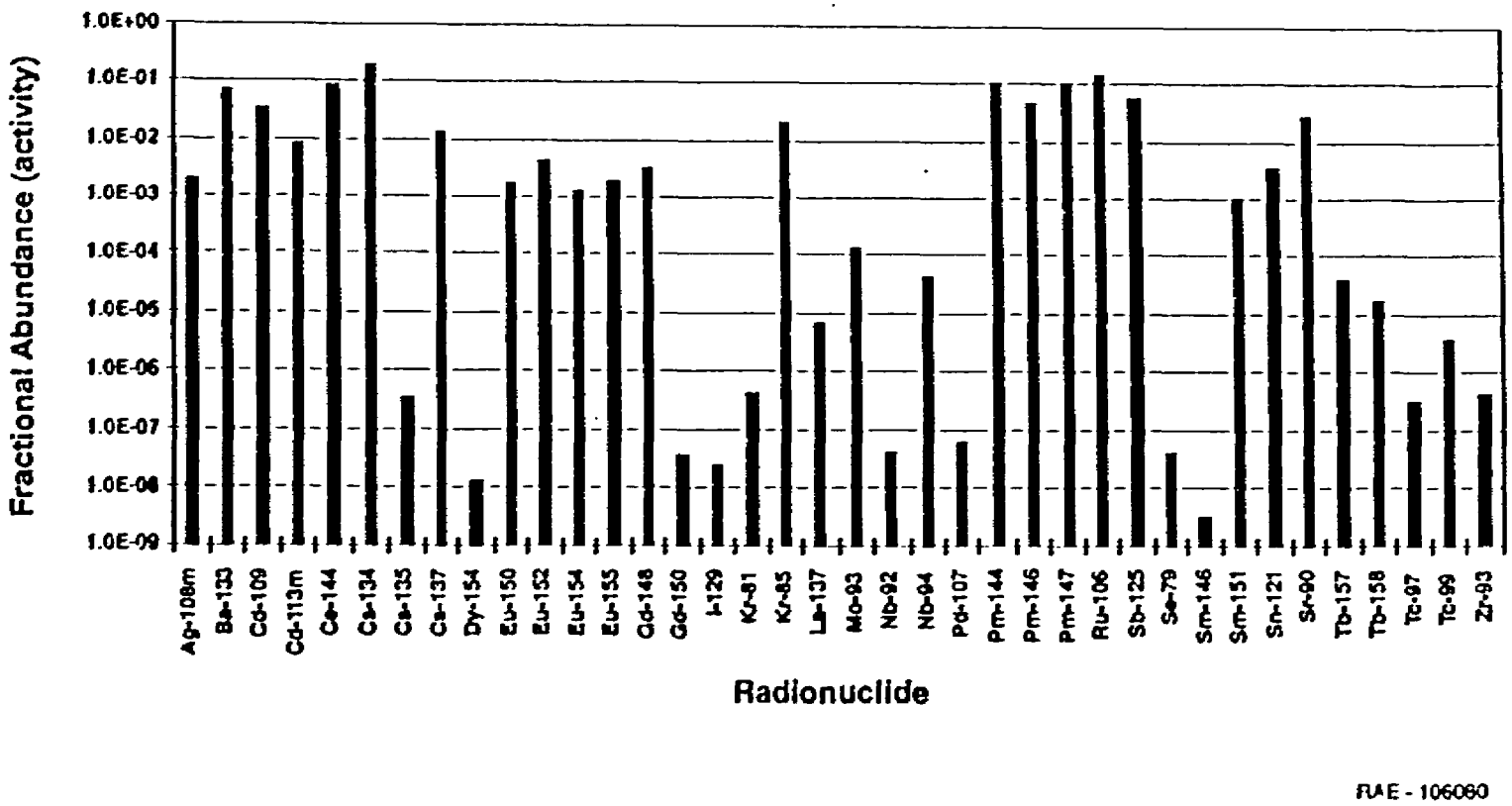

Figure 2-1. Fractional abundances of MFP radionuclides.

A review of the LLW disposal records for Area G indicates that MAP was primarily generated by the Los Alamos Meson Physics Facility (LAMPF), a high-energy accelerator facility (Vold, 1995). Three major waste streams are generated at LAMPF, including trash, targets, and beam-line inserts. The dominant forms of this waste include activated steel, aluminum, and graphite. The radiological characteristics of trash are provided in Table 2-4.

Based on similarities between the trash and the other LLW generated at LAMPF, the fractional abundances listed in Table 2-4 were assumed to apply to all MAP generated at LAMPF (Vold, 1995). The product of the abundances listed in the table and the specific activities of the radionuclides yields the activity of each isotope generated per gram of MAP. Normalizing these activities yields the fractional abundance of each radionuclide on an activity basis (shown in Table 2-4). The activity fractional abundances were multiplied by the total MAP activity to determine the radionuclide-specific activities for that waste.

Several material types have been used in the past to describe the LLW shipped for disposal or the TRU waste placed in storage. Each material type corresponds to specific radionuclide compositions, shown in Table 2-5. These radionuclide abundances were used to develop the Area G inventory projections. Material definitions for PU41, U72, GAMMA, GRALPH, GRBETA, and TRU were unavailable at the time the Area G inventory was prepared; thus, these material types were not included in the inventory projections.

Institutional control over the Area G disposal facility will be maintained for at least 100 years following the end of disposal operations. During this period, persons will be prevented from intruding onto the site for extended periods and measures will be taken to maintain proper facility function. Consequently, it is expected that there will be little or no potential for exposures from radionuclides with short half-lives.

Consistent with the preceding discussion, the Area G inventory was screened to eliminate radionuclides with short half-lives. In general, all radionuclides with half-lives of 5 years or less were removed from the disposal facility inventory. Exceptions include short-lived radionuclides that decay to one or more daughter products with half-lives in excess of 5 years, and radionuclides that are daughters of parents with half-lives in excess of 5 years.

Table 2-4. Information used to allocate MAP activity.

Radionuclide	Mass Fraction[a]	Activity Concentration in MAP (Ci/g)	Fractional Abundance (Activity Basis)
Be-7	3.0E-02	1.1E+04	6.9E-01
Na-22	1.0E-01	6.3E+02	4.1E-02
Mn-54	1.8E-01	1.5E+03	9.5E-02
Co-57	1.2E-01	1.0E+03	6.7E-02
Co-60	4.4E-01	5.0E+02	3.3E-02
Zn-65	1.3E-01	1.1E+03	7.1E-02

a. Source: Roberts (1995).

Table 2-5. Material type allocations for the Area G inventory.

Material Type	Isotopes	Activity Fraction
AM44	Am-241	1.0E+00
AM45	Am-243	1.0E+00
D38	U-234	4.2E-01
	U-235	1.0E-02
	U-236	2.0E-02
	U-238	5.5E-01
GAMMA	—[a]	—[a]
GRALPH	—[a]	—[a]
GRBETA	—[a]	—[a]
PU41	—[a]	—[a]
PU42	Pu-238	6.2E-02
	Pu-239	3.2E-04
	Pu-240	6.5E-03
	Pu-241	9.3E-01
	Pu-242	2.1E-03
	Pu-244	2.0E-09
PU51	Pu-238	7.0E-03
	Pu-239	4.1E-01
	Pu-240	4.9E-02
	Pu-241	5.4E-01
	Pu-242	4.8E-06
PU52	Pu-238	6.1E-03
	Pu-239	2.1E-01
	Pu-240	4.9E-02
	Pu-241	7.4E-01
	Pu-242	2.8E-06
PU53	Pu-238	1.1E-02
	Pu-239	1.2E-01
	Pu-240	4.2E-02
	Pu-241	8.2E-01
	Pu-242	6.1E-06
PU54	Pu-238	8.5E-03
	Pu-239	5.9E-02
	Pu-240	2.8E-02
	Pu-241	9.0E-01
	Pu-242	9.4E-06
PU55	Pu-238	8.9E-03
	Pu-239	4.5E-02
	Pu-240	2.9E-02

Table 2-5. Continued.

Material Type	Isotopes	Activity Fraction
	Pu-241	9.2E-01
	Pu-242	1.0E-05
PU56	Pu-238	8.0E-03
	Pu-239	3.9E-02
	Pu-240	2.9E-02
	Pu-241	9.3E-01
	Pu-242	1.1E-05
PU57	Pu-238	2.7E-02
	Pu-239	1.7E-02
	Pu-240	1.7E-02
	Pu-241	9.4E-01
	Pu-242	2.4E-05
PU83	Pu-238	9.9E-01
	Pu-239	5.0E-04
	Pu-240	1.9E-04
	Pu-241	1.2E-02
	Pu-242	1.4E-07
TH88	Th-232	1.0E+00
U10	U-234	5.0E-01
	U-235	2.2E-02
	U-238	4.7E-01
U11	U-234	2.2E-01
	U-235	5.2E-03
	U-238	7.7E-01
U12	U-234	2.7E-01
	U-235	1.0E-02
	U-238	7.2E-01
U15	U-234	2.9E-01
	U-235	1.3E-02
	U-238	6.9E-01
U18	U-234	4.1E-01
	U-235	2.4E-02
	U-238	5.6E-01
U21	U-234	4.6E-01
	U-235	2.7E-02
	U-238	5.2E-01
U22	U-234	5.1E-01
	U-235	3.1E-02
	U-236	1.6E-03

Table 2-5. Continued.

Material Type	Isotopes	Activity Fraction
	U-238	4.6E-01
U23	U-234	5.7E-01
	U-235	3.5E-02
	U-236	4.1E-03
	U-238	3.9E-01
U24	U-234	6.3E-01
	U-235	3.8E-02
	U-236	6.1E-03
	U-238	3.3E-01
U25	U-234	6.8E-01
	U-235	4.1E-02
	U-236	7.7E-03
	U-238	2.7E-01
U29	U-234	7.7E-01
	U-235	4.4E-02
	U-236	9.5E-03
	U-238	1.8E-01
U31	U-234	8.0E-01
	U-235	4.4E-02
	U-236	1.0E-02
	U-238	1.5E-01
U32	U-234	8.6E-01
	U-235	4.4E-02
	U-236	1.0E-02
	U-238	8.4E-02
U33	U-234	9.1E-01
	U-235	4.1E-02
	U-236	9.1E-03
	U-238	3.6E-02
U34	U-234	9.4E-01
	U-235	3.7E-02
	U-236	7.5E-03
	U-238	1.5E-02
U35	U-234	9.5E-01
	U-235	3.5E-02
	U-236	6.5E-03
	U-238	8.2E-03
U36	U-234	9.6E-01
	U-235	3.3E-02

Table 2-5. Continued.

Material Type	Isotopes	Activity Fraction
	U-236	5.2E-03
	U-238	3.0E-03
U37	U-234	9.6E-01
	U-235	3.1E-02
	U-236	4.3E-03
	U-238	7.0E-04
U38	U-234	9.7E-01
	U-235	3.0E-02
	U-236	4.1E-03
	U-238	2.8E-04
U39	U-234	9.7E-01
	U-235	3.0E-02
	U-236	4.0E-03
	U-238	7.2E-05
U70	U-233	1.0E+00
U72	—[a]	—[a]
U81	U-234	5.1E-01
	U-235	2.2E-02
	U-238	4.7E-01

a. Material type definitions were unavailable and were not included in the inventory projections.

2.2 FUTURE WASTE

Several types of LLW are expected to require disposal at Area G in the future. These include operational waste from ongoing activities at LANL, waste generated from ER and D&D projects, and residues generated from MLLW treatment. The following sections briefly describe these types of waste and discuss the methods used to project future Area G inventories of each. Section 2.2.1 addresses operational waste, Section 2.2.2 discusses ER and D&D waste, and Section 2.2.3 considers residues generated from MLLW treatment processes. Section 2.2.4 discusses the approach used to estimate the entire future inventory for Area G.

2.2.1 Operational LLW

A large portion of the waste disposed of at Area G in the past has resulted from normal operations at the various Technical Areas (TAs) at LANL. This waste is diverse, reflecting the wide array of activities conducted at LANL. In general, operational waste requiring disposal at Area G in the future is expected to resemble that disposed of since 1990. Exceptions will arise, however, as LANL's mission evolves in response to changing research needs and levels of funding.

To estimate the effect that changes in LANL's operations may have upon operational waste characteristics, it is necessary to identify the major generators of waste at LANL and evaluate the potential for operational changes at these facilities. Toward this end, screening calculations were conducted to determine the major generators of LLW at LANL between 1990 and 1995. These screening calculations were based on the total volume, total activity, and radionuclide-specific activities shipped for disposal during this period. TAs whose waste shipments comprised 95 percent of the total volume of waste disposed of at Area G in one or more years were identified as major generators of waste. A similar screen was conducted on the basis of the total activity of waste disposed of between 1990 and 1995. All screening calculations were based on the total amount of LLW disposed of at Area G; no distinction was made between waste buried in pits and waste disposed of in shafts.

Screening calculations based on the total activity of LLW shipped for disposal may overlook TAs that ship waste with low total activities but relatively high activities of specific radionuclides. To avoid this potential oversight, the waste disposal database also was screened with respect to radionuclide-specific activities. TAs whose waste shipments comprised 95 percent of the total radionuclide-specific activity disposed of at Area G in one or more years between 1990 and 1995 also were identified as major generators of LLW. Once again, screening calculations were based on the total amount of LLW disposed of in pits and shafts.

Activities conducted at LANL are grouped according to function within TAs. In general, several buildings or facilities exist within each TA, most of which generate specific types and quantities of waste. The screening procedures used to identify major generators were conducted on the basis of TAs, rather than the individual buildings or facilities within each TA.

Once the major generators of LLW at LANL were identified, estimates of future levels of activity at each were developed. Program and division managers for the TAs were asked to identify operations that generated LLW in the past but are no longer active, and those that have generated LLW in the past and are expected to continue doing so in the foreseeable future. Managers also were asked to identify operations that are expected to begin in the foreseeable future and generate LLW. Finally, personnel familiar with the overall operations of LANL were questioned about future activities at the various TAs. Adjustments to the operational waste inventory were made based on the responses to these interviews.

The projected operational LLW inventory was developed based on the assumption that the waste generated in the future by the TAs identified as major generators would resemble that disposed of at Area G between 1990 and 1995. Specifically, waste data for this period were analyzed to estimate average annual total volumes, activities, and radionuclide activities for each TA. Separate projections were developed for waste disposed of in pits and shafts. The estimates developed for the TAs were summed to yield the total annual averages for all LLW disposed of in pits and all waste placed in shafts. These average waste characteristics were assumed to remain constant over the remainder of the Area G disposal facility's lifetime.

Using historic disposal data to project future generation rates of high-activity tritium waste from LANL tritium operations is inappropriate. The disposal of waste with high tritium activities was discontinued approximately 6 years ago to allow the adequacy of the packaging for this waste to be evaluated. While this evaluation has been completed, the majority of the tritium waste backlog has not been shipped for disposal because the feasibility of recovering the tritium from the waste is being assessed. Most waste that did not contain high activities of tritium was shipped to Area G on a regular basis over the last 6 years.

Given the unique circumstances surrounding the tritium waste, a combination of approaches was used to estimate future disposal activities and volumes for this radionuclide. Disposal data for the period spanning 1990 to 1995 were used to project future tritium disposal rates for operations that continued to ship waste for disposal during this time frame. The quantities of high-activity tritium waste currently in storage were estimated from data supplied by the waste generators (Carlson, 1996; Martinez, 1996). Future waste generation rates of the high-activity tritium waste were estimated using generator-supplied information (Myers, 1996).

A portion of the 1990 to 1995 LLW data used to project future operational waste inventories represents waste generated during ER and D&D activities. Because projections of LLW generated by ER and D&D activities were developed separately, the ER and D&D waste represented in the database was removed to avoid double-counting this waste in the total Area G inventory. While it is extremely difficult to extract all records for ER and D&D LLW from the database, it is reasonable to assume that certain waste codes or streams are generated almost exclusively as a result of cleanup activities. Thus, for the Area G inventory, 11 waste streams were assumed to represent ER and D&D waste. These waste streams, listed in Table 2-6, were excluded from the calculations of future operational waste inventories.

2.2.2 ER and D&D LLW

Waste generated from ER and D&D activities at LANL generally consists of soil, concrete, asphalt, metals, polyvinyl chloride (PVC) piping, and demolition debris. Several sites or facilities are scheduled to undergo ER or D&D in the foreseeable future. The waste

Table 2-6. Waste streams assumed to be generated from ER and D&D activities.

Petroleum-Contaminated Soil
Combustible Building Debris
Non-Combustible Building Debris
Asbestos
Asbestos-Contaminated Debris
Beryllium-Contaminated Debris
PCB-Contaminated Materials
PCB-Contaminated Equipment
PCB-Contaminated Soil
PCB-Contaminated Concrete
Radioactively Contaminated Soil

generated by these activities is expected to include MLLW, hazardous waste, and LLW. Waste volume projections developed for the low-level component of the ER and D&D waste by the ER Project Office (Maassen, 1996) were used for the Area G inventory projections.

The Chemistry and Metallurgy Research (CMR) facility at LANL is undergoing an upgrade to bring it into compliance with DOE Orders. The waste generated during the upgrade was included in the ER and D&D portion of the future inventory. Primary components of the waste include wiring, conduit, electrical panels, and other electrical equipment. An attempt is being made to recycle items such as copper wiring; waste that cannot be recycled will be disposed of at Area G. Volume projections for the CMR upgrade waste provided by Kennicott (1996) were used in the Area G inventory projections.

ERM/Golder (1995) developed estimates of the MLLW inventory for ER waste at LANL. These estimates were based on information on potential release sites contained in the most recent Operable Unit Resource Conservation and Recovery Act (RCRA) Facility Investigation, interviews with former Operable Unit Project Leaders or other knowledgeable team members that were used to refine information contained in the work plans, and data from the Facility for Information Management, Analysis, and Display (FIMAD) database. The first two sources of information were used to determine potential MLLW sites, while the FIMAD database was used to identify waste constituents, concentrations, and activities.

The radiological characteristics of the LLW to be generated by ER and D&D activities have not been developed. Thus, to estimate the contribution of this waste to the Area G inventory, it was assumed that the radionuclide concentrations developed by ERM/Golder (1995) for the mixed ER waste apply to the ER and D&D LLW as well. The projected ER and D&D waste inventory was allocated among the four waste forms used in the source-term modeling analysis. Because detailed information on the forms of the ER and D&D waste and the proportion of each was not available, it was assumed that 50 percent of the LLW generated by these activities was surface-contaminated waste. The remaining waste was assumed to consist of equal proportions of contaminated soils and concrete.

The radiological characteristics of waste from the future CMR Upgrade waste are largely unknown. Thus, it was assumed that the CMR upgrade waste had the same radionuclide concentrations as the ER LLW discussed above. The entire inventory associated

with the CMR upgrade waste was assigned to the surface-contaminated waste form, consistent with the nature of the waste generated from the upgrade.

2.2.3 MLLW Residues

A variety of MLLW streams are in storage or are generated at LANL. These wastes exist as solids, liquids, or compressed gases. The solid waste includes oxidizers, reactive metals, contaminated debris and scrap metal, firing site debris, process residuals, contaminated lead shielding, decontamination waste and debris, and dewatered treatment sludges. Liquid and compressed gas waste includes gas cylinders, ignitable liquids, acids, caustics, reactive liquids, analytical laboratory waste, spent solvents, contaminated wastewaters, metals, photographic fixer solutions, and chemical products. The majority of the MLLW is radiologically contaminated with plutonium or uranium.

Prior to 1986, most of the MLLW generated at LANL was disposed of at the Area G disposal facility. However, since July 1986, when the EPA affirmed its authority over the regulation of the hazardous component of MLLW, this waste has been stored. Since 1988, all containers of MLLW have been tracked in accordance with RCRA recordkeeping requirements.

The RCRA Land Disposal Restriction (LDR) requires DOE sites to treat hazardous waste (including the hazardous component of MLLW) to certain standards before disposal. Storage of hazardous waste or MLLW is generally prohibited if the waste does not meet these LDR requirements. The Federal Facilities Compliance Act (FFCA), signed on October 6, 1992, requires DOE to prepare plans for developing the required treatment capacity for MLLW stored or generated at each of its sites.

In compliance with the FFCA, LANL issued a Draft Site Treatment Plan (STP) that discusses the preferred options for treating MLLW stored or generated at the site (LANL, 1995). Treatment options were identified for a number of waste streams, several of which may result in the generation of LLW (i.e., waste without any hazardous components). The fiscal year 1995 update of this report has been issued in draft form (LANL, 1996). The MLLW streams discussed in the LANL STP Update are listed in Table 2-7 with their

Table 2-7. MLLW streams, treatment options, and inventories.[a]

Waste Stream	Preferred Treatment Option	Volume in Storage as of 9/30/94 (m^3)	Annual Generation Rate (m^3/yr)
Aqueous Wastes:			
Organic Waste	CAI[b]/Evaporative Oxidation	1.7E+00	1.0E-01
Heavy Metal Waste	Chemical Plating	1.9E+00	2.0E-01
Cyanides, Nitrates, Chromates, and Arsenates	Chemical Plating	1.3E-01	2.0E-03
Biochemical Laboratory Waste	TBD[c]	1.3E+00	1.0E-01
Bulk Oils	CAI[b]/Hydrothermal Processing	3.8E+00	6.0E-01
Compressed Gases:			
Gases Requiring Scrubbing	Caustic, Acid, or Water Scrubbing	3.5E-01	2.0E-02
Gases Requiring Oxidation	Gas Oxidation	8.0E-02	2.0E-02
Other Compressed Gases	TBD[c]	1.3E+00	4.0E-01
Corrosive Solutions	Chemical Plating	1.4E+00	1.0E-01
Debris:			
Noncombustible	Macroencapsulation	5.6E+00	6.0E-01
Combustible	CAI[b]/ Macroencapsulation	1.4E+01	3.0E-01
Dewatered Treatment Sludge	Reclassify as LLW	2.7E+02	—
Inorganic Solid Oxidizers	Hydrothermal Processing	2.0E-01	1.0E-02

Table 2-7. Continued.

Waste Stream	Preferred Treatment Option	Volume in Storage as of 9/30/94 (m^3)	Annual Generation Rate (m^3/yr)
IPA Waste	Commercial Thermal Treatment	1.6E+01	3.0E-03
Lead Wastes:			
Surface-Contaminated Lead	Decontamination	5.6E+01	2.5E+00
Activated/Inseparable Lead	Macroencapsulation	1.6E+01	2.0E-01
Lead Requiring Sorting	Sort Based on Treatment	1.0E+01	0.0E+00
Lead Blankets	Commercial Stabilization	7.4E-01	4.0E-02
Other Lead Waste	TBD[c]	5.1E+01	2.0E+00
Mercury Wastes:			
Elemental Mercury	Amalgamation	5.0E-01	1.0E-02
Other Mercury Waste	TBD[c]	1.8E+01	5.1E+00
Nonradioactive/Suspect Waste	Sort, Survey, and Decontaminate	1.4E+01	1.9E+00
Organic Liquids:			
Halogenated	CAI[b]/Hydrothermal Processing	1.7E+01	1.1E+00
Non-Halogenated	CAI[b]/Hydrothermal Processing	1.4E+01	2.0E+00
PCB Waste with RCRA Components	CAI[b]/Hydrothermal Processing	7.4E-01	4.0E-02
Scintillation Fluids	Commercial Thermal Treatment	2.5E+00	8.0E-01

Table 2-7. Continued.

Waste Stream	Preferred Treatment Option	Volume in Storage as of 9/30/94 (m^3)	Annual Generation Rate (m^3/yr)
Soils:			
Contaminated with Heavy Metals	Commercial stabilization	1.1E+01	4.0E-01
Combustible, Contaminated with Organics	CAI[b]/Thermal Desorption	2.8E+01	1.4E+00
ER Soils	Commercial stabilization	3.9E+01	1.3E+01
Non-Combustible, Contaminated with Organics	Thermal Desorption	7.8E+00	1.6E+00
Water-Reactive Waste	Controlled Reaction with Water	6.0E+00	4.0E-02
Totals	—	6.1E+02	3.5E+01

a. Source: LANL, 1996.
b. CAI = controlled-air incineration.
c. TBD = to be determined.

estimated inventories and the quantities of waste projected to be generated between fiscal years 1996 and 2000.

While treatment options continue to be developed for the MLLW streams at LANL, the preferred option for dealing with these wastes is to treat and dispose of them off site. This option is made possible by the increased availability of commercial treatment and disposal capacity and the development of treatment facilities at other DOE sites. Under this preferred option, LANL would continue to develop mobile treatment units only after it determines that no offsite alternatives exist for treating and disposing of the residues.

The quantity of LLW generated by the treatment of MLLW and requiring disposal at Area G is expected to be small, assuming the preferred option of using offsite treatment and disposal facilities is implemented. Consequently, this waste was not included in the Area G inventory projections.

A waste stream that is currently being stored as mixed waste and which is not included in Table 2-7 is uranium chips and turnings. This waste is currently being stored in diesel fuel in 0.1-m^3 drums placed in 0.2-m^3 overpacks. Additional chips and turnings are expected to be generated on a regular basis in the future. Current plans call for treating this waste, stabilizing it in a clay matrix, and disposing of it in Area G. Consequently, this waste must be accounted for in the projected inventory.

Projections of future uranium chip waste inventories were based on the quantities of waste currently in storage and estimates of future levels of activity in the LANL shops that generate the material. Volumes and activities of the waste in storage were taken from the storage database for the waste stream (Brazenger, 1996). Quantities of waste expected to be generated in the future were provided by Hodges (1996a, 1996b). The waste activity was allocated among the various uranium isotopes using the allocation factors for the material type D-38 (shown in Table 2-5).

2.2.4 Total Future Inventory

The total amount of LLW that will be disposed of at Area G will be a function of the rate at which waste is generated and the disposal capacity of the disposal facility. Sections 2.2.1 through 2.2.3 discuss the projected rates of LLW generation. This section discusses the disposal capacity of the Area G disposal facility.

The LLW disposal facility at Area G is quickly approaching its capacity. The waste disposal capacity remaining at the end of fiscal year 1995 was approximately 23,000 m^3. An additional pit has been excavated within the area already reserved for disposal, and current plans call for excavating one more. With these additional pits, the disposal facility is expected to be able to accommodate routine, ER, and D&D LLW into the early part of fiscal year 2001.

An Environmental Assessment (EA) for the expansion of the Area G LLW disposal facility was prepared in January 1994 (LANL, 1994). The EA identified a proposed action and several alternatives for dealing with the impending shortage of disposal capacity. The proposed action called for the expansion of Area G and modifications in waste management and disposal practices. Under the proposed action, disposal operations would expand to approximately 28 additional hectares on Mesita del Buey, increasing disposal capacity by approximately 600,000 m^3. Later plans called for expanding the disposal facility by only 2 ha. The increase in disposal capacity due to expansion would be complemented by the permitting and operation of a 200-ton supercompactor.

The LANL Site-Wide Environmental Impact Statement (SWEIS), currently in preparation, examines a number of options regarding the level of future operations at LANL. If implemented, these alternatives would influence the quantities of waste generated and, hence, the disposal demands placed on Area G. Therefore, while construction of the compactor has proceeded, expansion plans at Area G have been postponed until the SWEIS is completed in fiscal year 1997.

At the time the inventory projections were developed, it was unclear whether the Area G disposal facility would be expanded to accept more LLW and, if so, to what extent expansion would be pursued. Thus, to maximize the utility of the Area G performance

assessment for future LLW disposal operations at the LANL, it was assumed that the disposal facility will continue to accept waste through the year 2044. This operational period was chosen because it is expected to be amenable to all future LLW disposal needs at LANL.

In summary, the total projected inventory for the Area G performance assessment and composite analysis was calculated based on the assumption that the facility will remain operational through 2044. The annual operational waste projections for pits and shafts were multiplied by 49, the number of years between 1996 and 2044, to account for the total inventory of waste placed in these units. All ER and D&D LLW projected to require disposal was assumed to be buried at Area G because the activities responsible for this waste are expected to be completed well before the year 2044.

3. AREA G INVENTORY PROJECTIONS

This chapter presents the Area G inventory projections developed using the methodology described in Chapter 2. Characteristics of historic waste (disposed of between 1957 and the end of 1995) are discussed in Section 3.1. Future LLW projections are provided in Section 3.2.

3.1 HISTORIC WASTE

This section presents the historic Area G inventory in terms of three waste disposal periods: (1) the period from the opening of the Area G disposal facility through 1970, (2) the period from the beginning of 1971 through September 25, 1988, and (3) the period from September 26, 1988, through the end of 1995. Separate inventories were prepared for these periods for two reasons. First, as discussed in Section 2.1, the amount of detailed data available for characterizing the historic waste differs dramatically between the pre-1971 and 1971 to 1995 periods. Maintaining the identities of the pre-1971 and 1971 to 1995 inventories permits evaluation of the uncertainties inherent in each inventory. Second, DOE Order 5820.2A applies to waste disposed of on or after September 26, 1988. Consequently, separate inventories (i.e., waste disposed of through September 25, 1988, and waste disposed of thereafter) must be developed to demonstrate compliance with the Order.

Section 3.1.1 characterizes the waste disposed of from the time the Area G disposal facility began accepting waste through 1970. Sections 3.1.2 and 3.1.3 present the inventories for the periods from 1971 to September 25, 1988, and September 26, 1988, to 1995, respectively.

3.1.1 Pre-1971 Inventory

As discussed in Section 2.1, data from the LANL LLW disposal and TRU waste databases were used to characterize the waste disposed of at Area G prior to 1971. The periods from which data were drawn to characterize this waste are 1971 through 1977 for the disposal pits and 1971 through 1975 for the shafts. These periods were chosen based on evaluations of the disposal and storage patterns between 1971 and 1995 and changes in disposal practices at LANL during this period. The results of these evaluations are discussed in the following paragraphs.

The volumes and activities of LLW disposed of at Area G between 1971 and 1995 are shown in Figures 3-1 and 3-2, respectively, for the disposal pits and shafts. Pit and shaft disposal volumes ranged over an order of magnitude during this period; the majority of the waste, on a volume basis, was placed in the pits. Disposal activities between 1971 and 1995 were much more variable, ranging over several orders of magnitude. The disposal shafts received most of the activity disposed of at Area G.

The sensitivity of the pre-1971 waste characteristics to the amount of data used in making these estimates was evaluated as an aid in selecting a suitable period for extrapolation. Average annual disposal volumes and activities were calculated for pits and shafts for each year from 1971 to 1995. These averages were based on the disposal data for all preceding years (i.e., from 1971 through the year in question). For example, the annual averages for 1973 were based on disposal data for 1971 through 1973, while the averages for 1980 took into account data for 1971 through 1980. Standard deviations were also calculated for the subset of data used to determine annual averages. The results of these calculations are shown in Figures 3-3 and 3-4 for LLW disposal volumes and activities, respectively.

Figure 3-3 shows that the average annual volumes of LLW disposed of in pits at Area G are relatively constant, regardless of the length of time over which the average is calculated (Figure 3-3). Between 1972 and 1975, the average volume of waste disposed of increases from about 4,000 m^3 to 6,000 m^3, and remains at that level until 1982. The gradual decline in average disposal volume after 1982 reflects the downward trend in waste disposal volumes seen in Figure 3-1. This decline is moderated by the increasingly greater number of years included in the calculations of average volume. The average shaft disposal

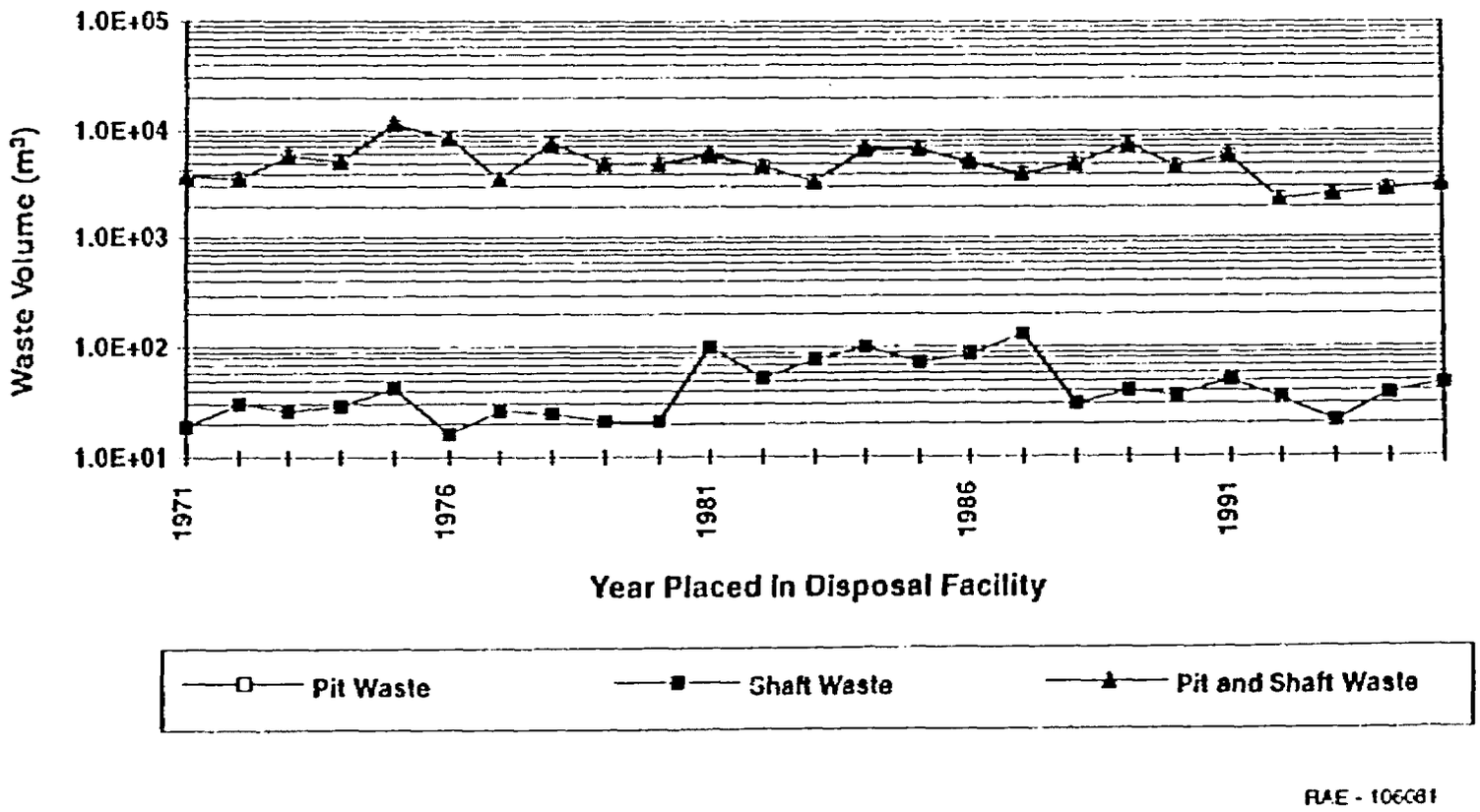

Figure 3-1. Historic LIW volumes in pit and shaft waste.

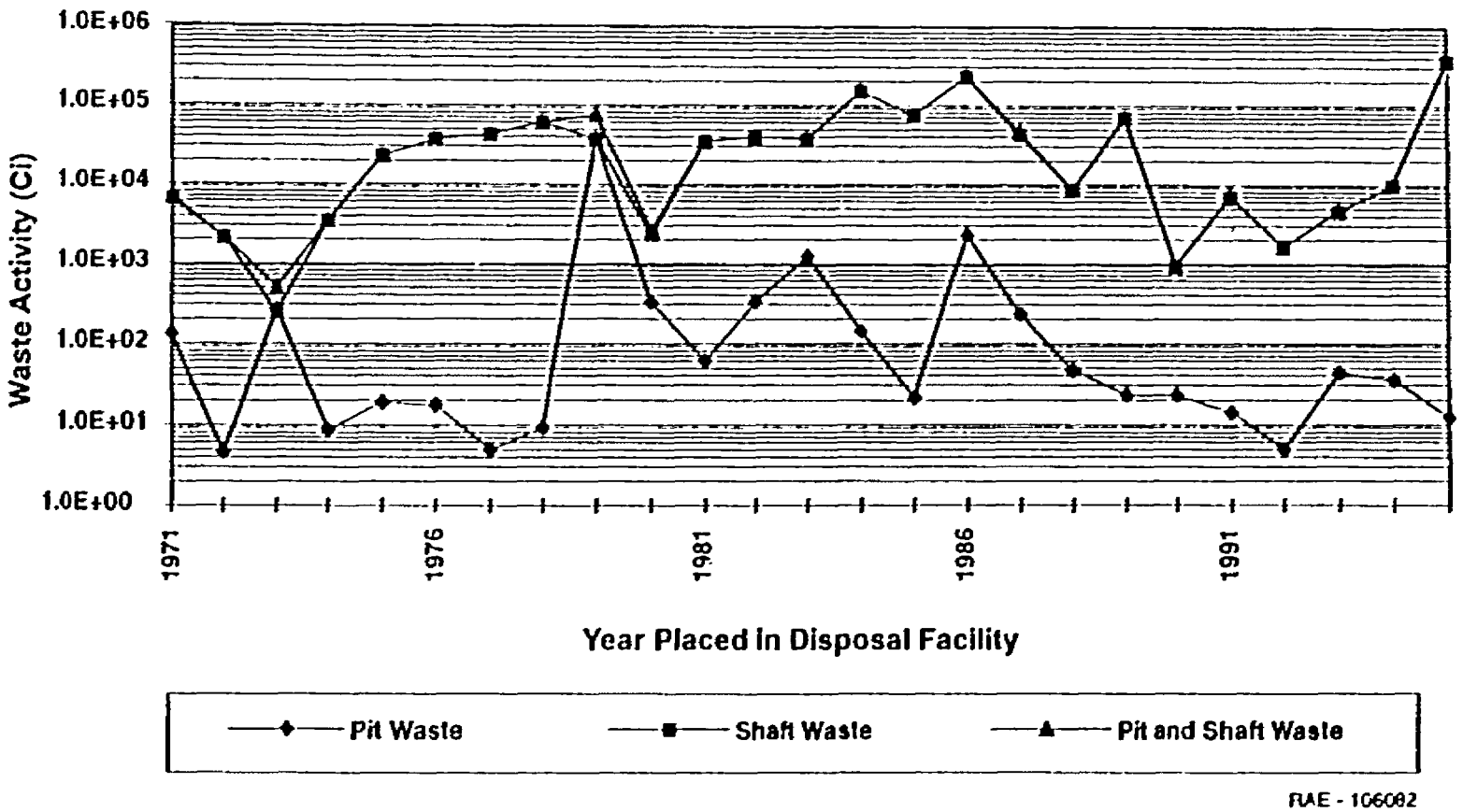

Figure 3-2. Historic LLW activities in pit and shaft waste.

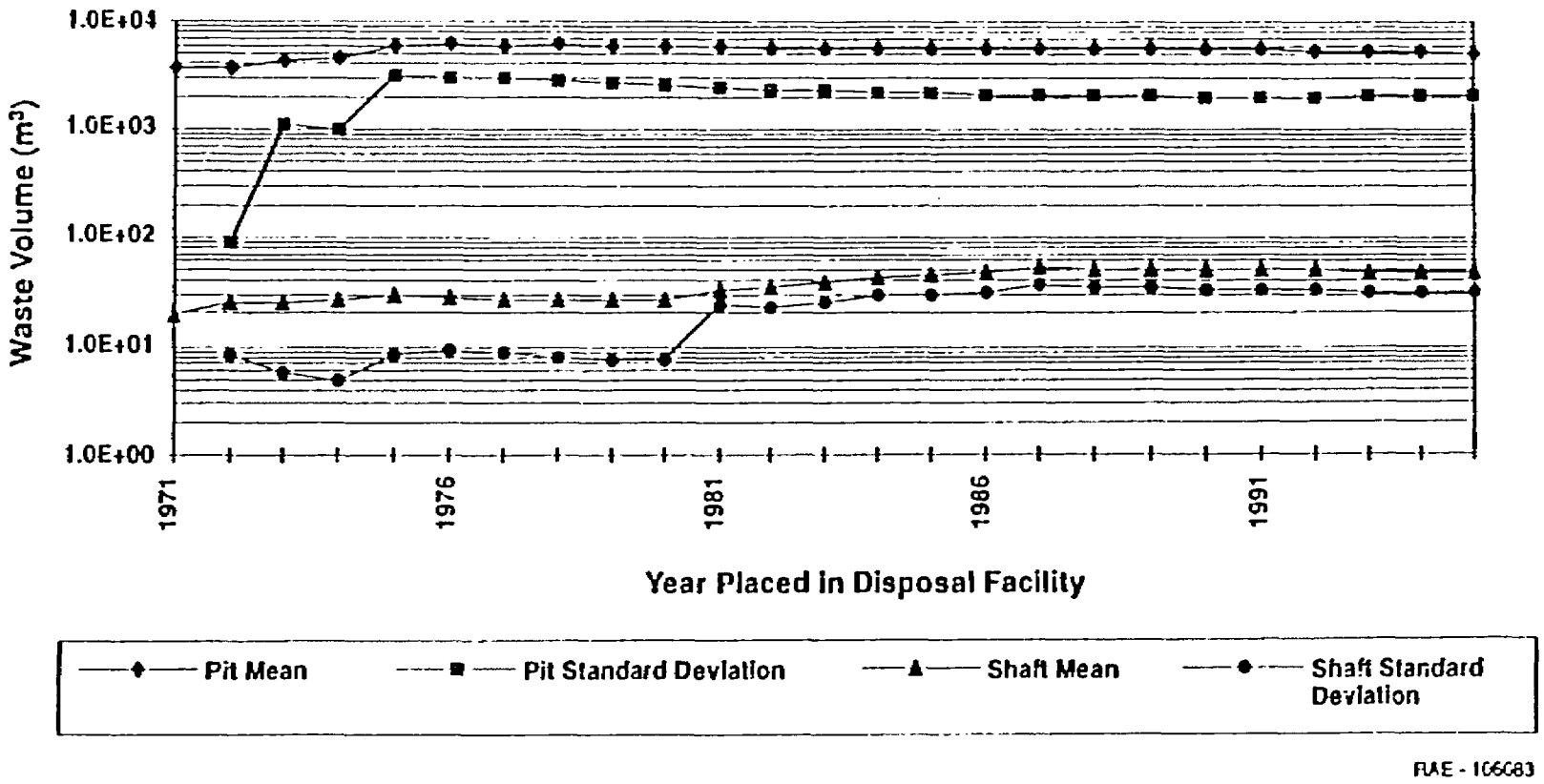

Figure 3-3. Mean and standard deviation of LLW pit and shaft disposal volumes.

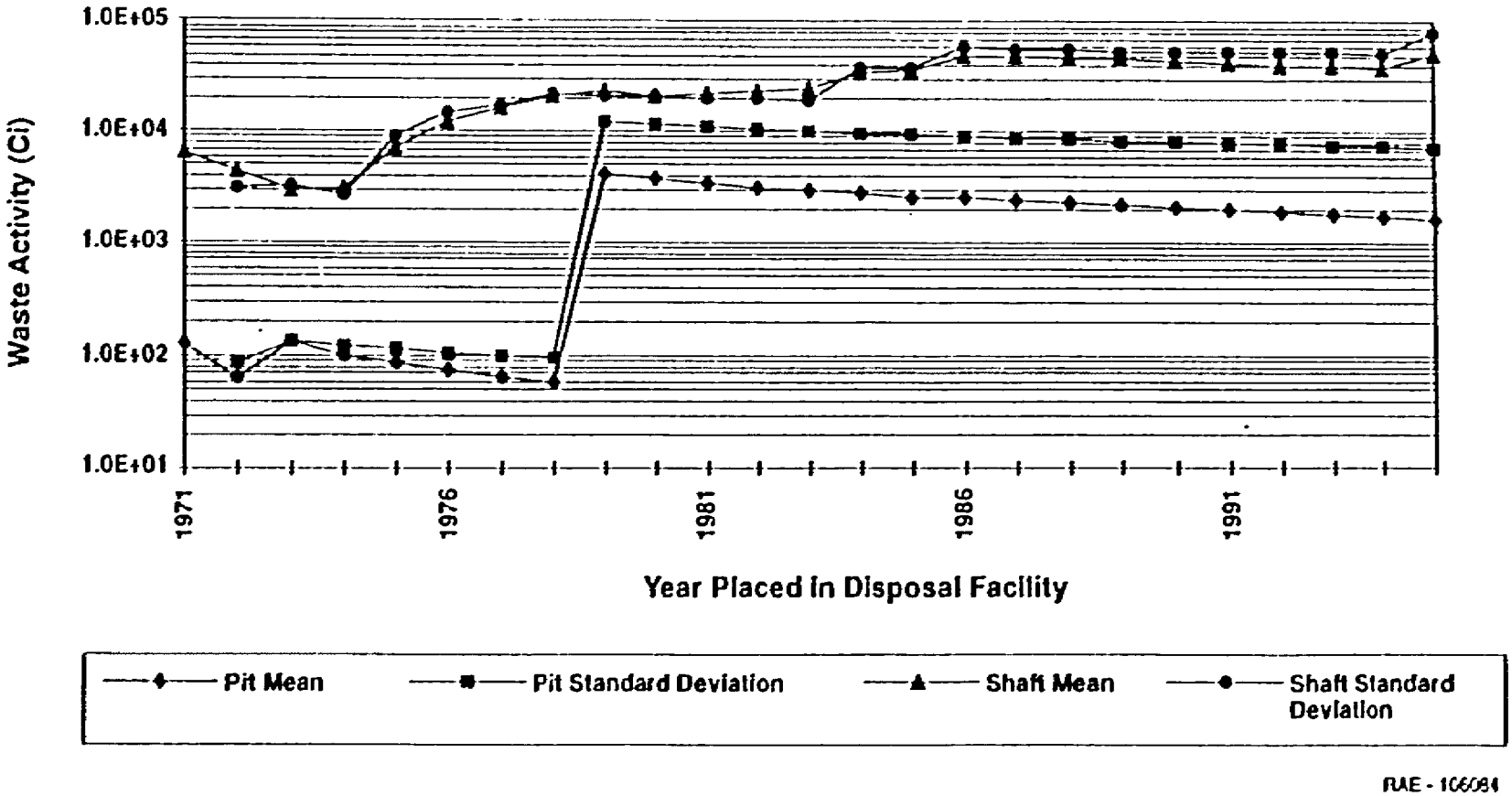

Figure 3-4. Mean and standard deviation of LLW pit and shaft activities.

volume is relatively constant until 1981, at which point a gradual increase begins. This increase corresponds to the elevated rates of disposal occurring from 1981 to 1987 (Figure 3-1).

Figure 3-4 shows that the average annual activity of LLW disposed of in pits remains relatively constant between 1971 and 1978, but increases sharply in 1979 due to the disposal of large activities of H-3, Co-60, Sr-89, and MAP. The average activities decline slowly thereafter as disposal activities return to more normal levels (see Figure 3-2). The effect of waste disposal in 1979 on the average activities, however, is evident for the remainder of the 1971 to 1995 period. Average shaft activities rise almost an order of magnitude as the period under consideration extends from 1974 to 1978. The average remains relatively constant until about 1983, at which point it rises gradually.

The volumes and activities of TRU waste disposed of or placed in storage at Area G between 1971 and 1995 are shown in Figure 3-5. As shown, waste volumes range over about an order of magnitude during the period; activities range over almost three orders of magnitude. The average volumes of TRU waste disposed of or placed in storage increase in the early and late 1970s (see Figure 3-6), remaining relatively constant thereafter. Average TRU waste activities rise dramatically through 1974 and remain relatively constant thereafter (Figure 3-7).

Based on the data presented above and other considerations, the period from 1971 through 1977 was chosen for estimating the pre-1971 waste characteristics for waste placed in disposal pits. The starting point of 1971 was chosen because LANL's operations during that year most closely resemble those that generated waste prior to that time. The quantity of TRU waste placed in storage, and the radionuclide concentrations in the waste, increase substantially in the late 1970s and early 1980s. Consequently, use of a longer extrapolation period would increase the divergence between the extrapolated TRU waste inventory and the actual waste disposed of prior to 1971. The 1971 to 1977 extrapolation period is advantageous in that it excludes a number of unique waste streams associated with D&D and startup activities at LANL, including the decommissioning of the TA-21 plutonium facilities and the startup of TA-55. This period also generally predates a number of changes in disposal operations at Area G, including the implementation of waste compaction in 1977 and the end of MLLW disposal in the mid-1980s.

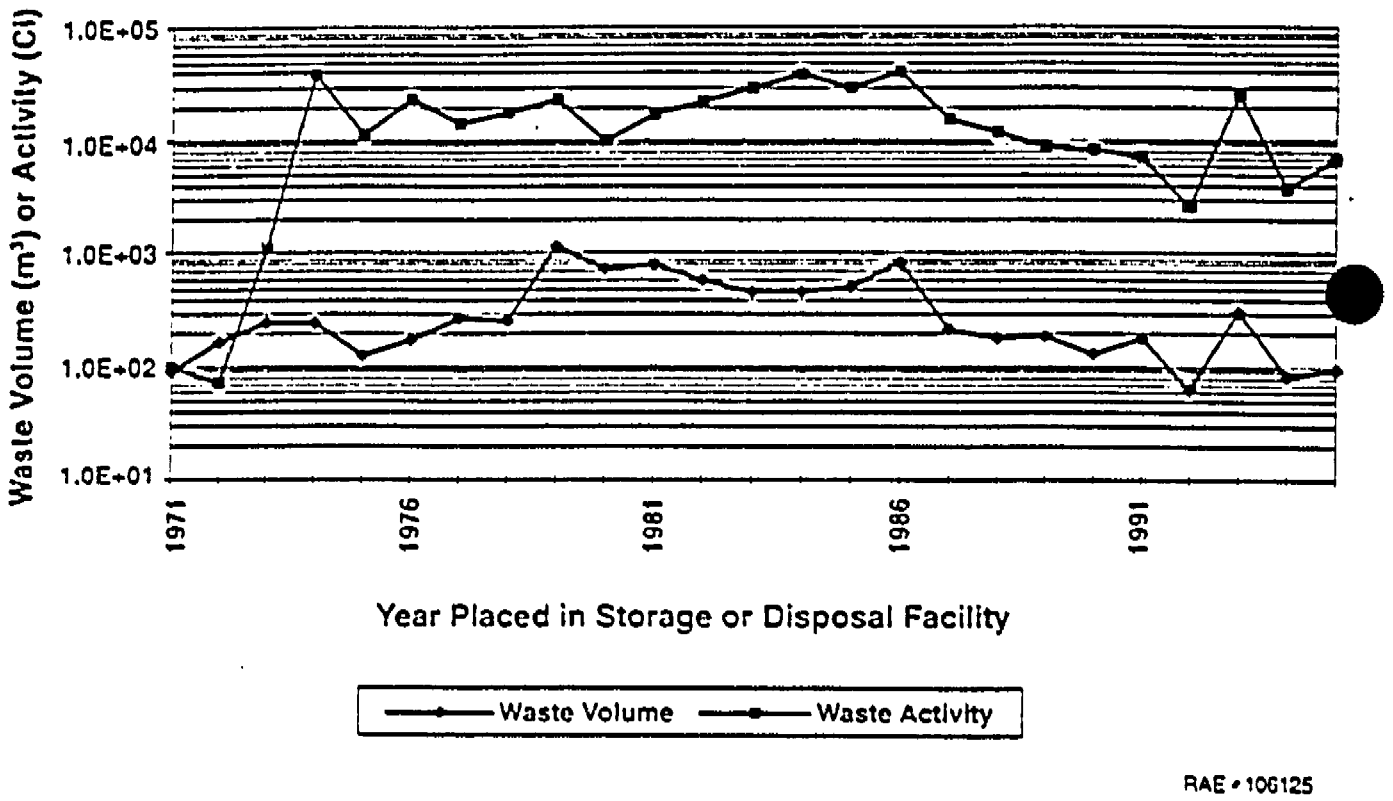

Figure 3-5. Historic TRU waste volumes and activities.

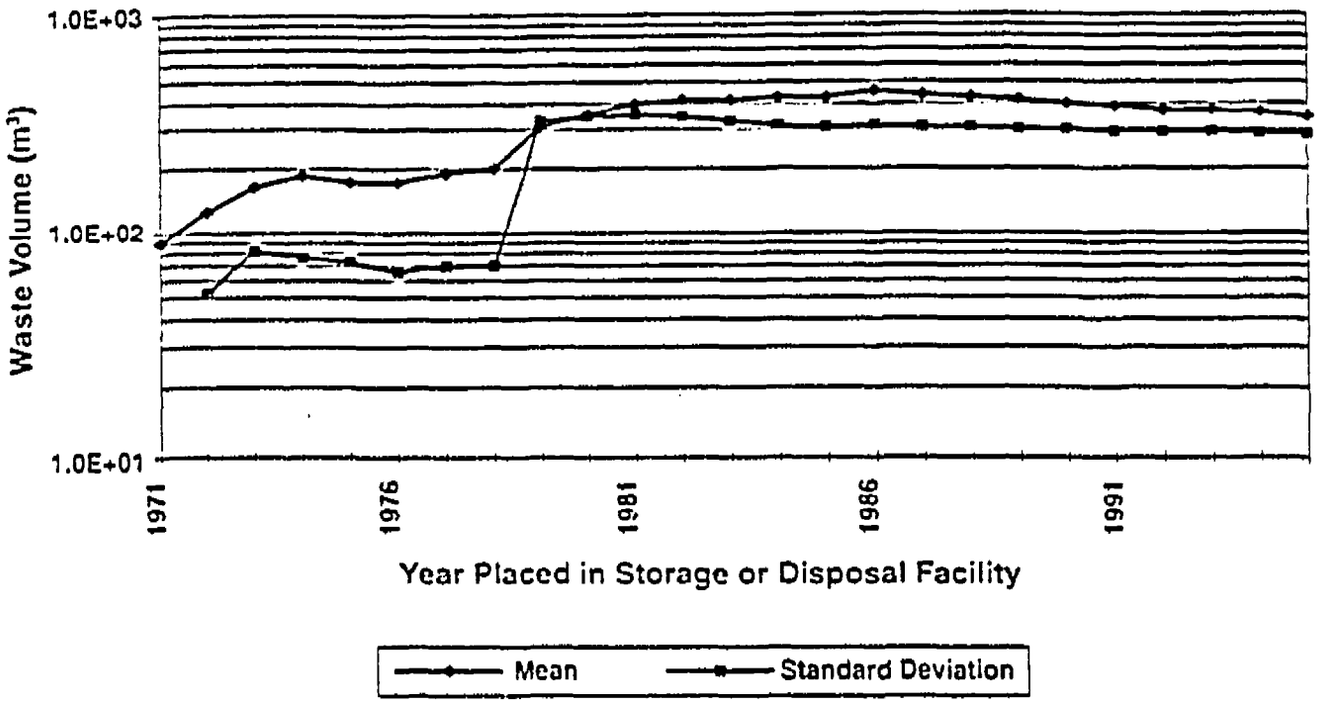

RAE - 106126

Figure 3-6. Mean and standard deviation of historic TRU waste volumes.

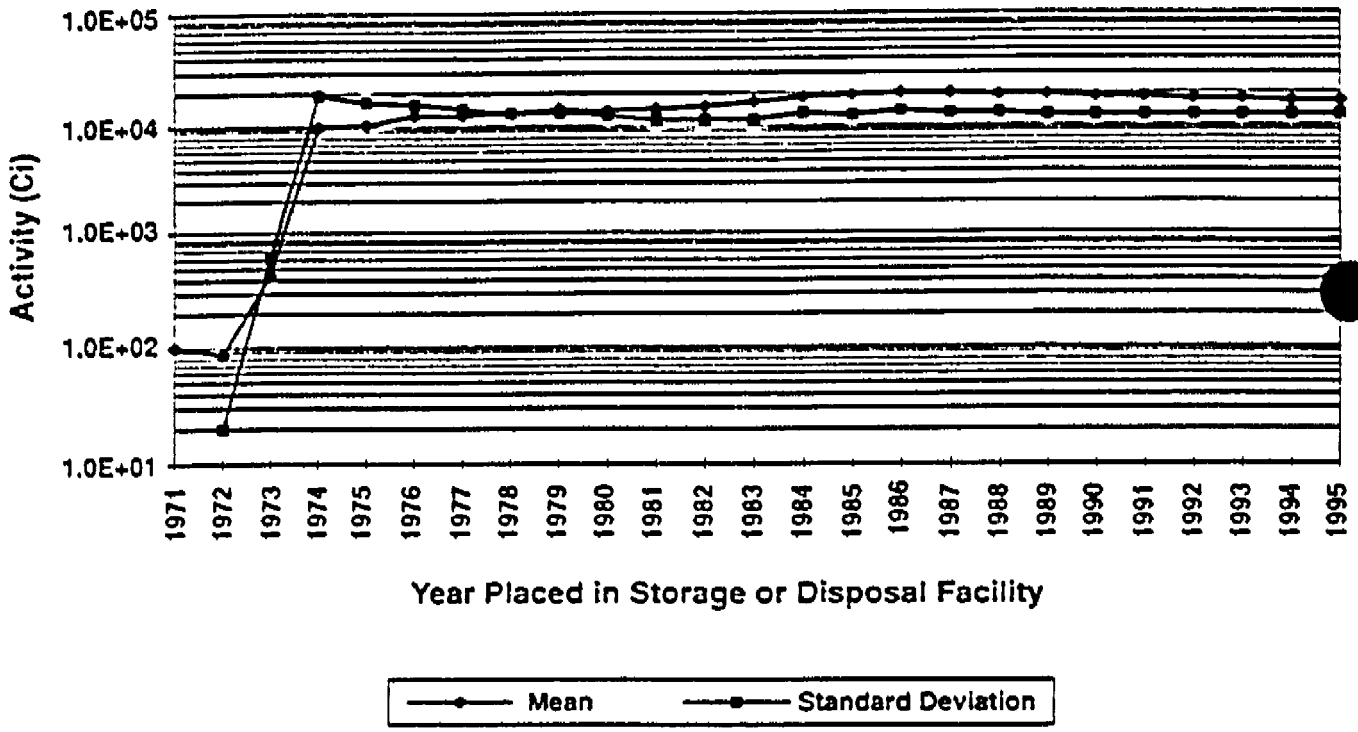

RAE - 106127

Figure 3-7. Mean and standard deviation of historic TRU waste activities.

A five-year period extending from 1971 through 1975 was used for characterizing the pre-1971 waste placed in shafts. In general, the characteristics and quantities of waste disposed of in shafts between 1971 and 1975 are expected to resemble those of the waste placed in the shafts from 1966 to 1970 (Warren, 1996). Ending the extrapolation period in 1975 appears prudent because it excludes the much higher disposal rates observed in 1976 and subsequent years.

The data used for estimating the pre-1971 pit and shaft inventories were examined to identify, to the extent possible, non-routine or special case waste. Based on this analysis, the following wastes were eliminated from the LLW and TRU waste data used to estimate the pre-1971 inventory.

- All waste generated at TA-53, the LAMPF. This waste was excluded because the LAMPF began operations in June 1972.
- LLW and small amounts of TRU waste generated from townsite (TA-1) cleanup activities in the mid-1970s. This waste was excluded because similar activities did not occur prior to 1971.
- LLW generated from the removal of the acid sewer system in 1977. This waste was excluded because similar activities did not occur prior to 1971.
- High-activity Pu-238 and U-233 waste generated at TA-21 and stored in trenches A through C. The Pu-238 waste was shipped to the Savannah River Site (SRS) for disposal prior to 1974. When the SRS stopped accepting the waste, it was retrievably stored in trenches at Area G. LANL did not receive approval to dispose of the U-233 waste until after 1971. Because these wastes were retrievably stored, they were excluded from the estimates of the pre-1971 inventory.

The estimated quantities of waste disposed of at Area G prior to 1971 are listed in Table 3-1 for pits and shafts. Separate inventories are listed for waste projections that were based on LLW disposal records and for waste derived from the TRU waste database. While Pits 5 and 6 received waste prior to and following the start of 1971, the greatest volume of waste was buried before 1971. For convenience, all of the waste placed in these units is included in the pre-1971 inventory. The data listed in Table 3-1 include the waste inventory developed using the extrapolation method and the waste for which disposal records exist.

Table 3-1. Total pre-1971 inventory volume and activity projections.

Disposal Unit/Waste Form	LLW Volume (m^3)	LLW Activity (Ci)	TRU Waste Volume (m^3)	TRU Waste Activity (Ci)	All Waste Volume (m^3)	All Waste Activity (Ci)
Pit Waste						
Surface-Contaminated Waste	4.0E+04	7.4E+02	1.7E+03	1.5E+04	4.2E+04	1.6E+04
Soils	6.0E+03	1.9E+01	1.1E+01	3.7E+01	6.1E+03	3.9E+01
Concrete and Sludges	4.5E+03	4.1E+02	3.0E+03	2.4E+03	7.5E+03	2.8E+03
Bulk-Contaminated Waste	1.1E+01	7.8E-02			1.1E+01	7.8E-02
Shaft Waste						
Surface-Contaminated Waste	1.4E+02	3.5E+04	1.2E+00	8.3E+02	1.5E+02	3.6E+04
Soils	2.1E-02	—[a]			2.1E-02	0.0E+00
Concrete and Sludges	4.4E-01	—[a]			4.4E-01	0.0E+00
Bulk-Contaminated Waste	5.3E-01	5.5E+01			5.3E-01	5.5E+01

a. All disposal activities listed in the data used to project pre-1971 inventories were zero.

Radionuclide-specific inventories are listed in Tables 3-2 and 3-3 for pits and shafts, respectively, for the four waste forms discussed earlier. The waste volumes listed in the tables represent the quantity of waste contaminated with each radionuclide. Because several radionuclides may occur in a single waste package, the sum of these volumes is greater than the total volume of waste disposed of in the pits and shafts.

The radionuclide activities listed in Tables 3-2 and 3-3 represent as-disposed activities and include contributions from MAP, MFP, and the material types discussed in Section 2.1. The radionuclides listed have half-lives greater than 5 years or have parents or daughters with half-lives greater than 5 years. The radionuclides eliminated from the inventory projections based on half-life are listed in Appendix A.

Limited quantities of waste listed in the TRU waste database were disposed of non-retrievably in Pit 6. Table 3-4 lists the total volume, total activity, and radionuclide-specific inventories for the waste in this pit. This information is included in the data presented in Tables 3-1 through 3-3.

Using 1971 to 1977 waste data to infer the quantities and characteristics of the waste placed in Area G prior to 1971 overlooks waste that was not disposed of during the extrapolation period. It is practically impossible to identify all unique disposal events at Area G before 1971. However, Warren (1980) has identified several such events that involved large quantities of specific radionuclides and which were not captured by the extrapolation process. These events are summarized in Table 3-5.

Based on the information presented in Table 3-5, waste data were added to the extrapolation-based inventory projections. The waste form, total volume, total activity, and radiological characteristics of the waste represented by these additions are listed in Table 3-6 and are included in Tables 3-1 through 3-3. These additions were based on a number of assumptions. The sludge generated between 1952 and 1967 was assumed to be disposed of at Areas C and G in equal amounts because the Area G pits did not receive routine operational waste until the late 1950s. The 585 equivalent grams of Pu indicated for this waste were not included because it was unclear as to how to interpret this entry. All of the cement paste disposed of between 1959 and 1968 was assumed to be placed in pits at Area G,

Table 3-2. Pre-1971 radionuclide inventory projections for Area G pits.

Waste Form/Radionuclide	LLW Volume (m^3)	LLW Activity (Ci)	TRU Waste Volume (m^3)	TRU Waste Activity (Ci)	All Waste Volume (m^3)	All Waste Activity (Ci)
Surface-Contaminated Waste						
Ac-227	1.8E+00	1.2E-01	1.9E-01	7.4E-01	2.0E+00	8.6E-01
Ag-108m	3.1E+03	1.6E-03	2.5E+01	2.1E+00	3.2E+03	2.1E+00
Am-241			1.8E+01	4.4E+01	1.8E+01	4.4E+01
Ba-133	3.1E+03	5.7E-02	2.5E+01	7.6E+01	3.2E+03	7.6E+01
Cd-113m	3.1E+03	6.5E-03	2.5E+01	8.7E+00	3.2E+03	8.7E+00
Cf-249	9.7E-01	7.0E-04	3.6E-01	1.7E-03	1.3E+00	2.4E-03
Cf-251			1.5E-01	2.7E-03	1.5E-01	2.7E-03
Cf-252	4.9E-01	1.5E-02			4.9E-01	1.5E-02
Cm-244			3.6E-01	1.7E-03	3.6E-01	1.7E-03
Co-60	7.8E+02	8.7E-03			7.8E+02	8.7E-03
Cs-135	3.1E+03	2.9E-07	2.5E+01	3.9E-04	3.2E+03	4.0E-04
Cs-137	3.2E+03	2.7E-01	2.5E+01	1.4E+01	3.2E+03	1.5E+01
Dy-154	3.1E+03	1.0E-08	2.5E+01	1.4E-05	3.2E+03	1.4E-05
Eu-152	3.1E+03	3.6E-03	2.5E+01	4.8E+00	3.2E+03	4.8E+00
Eu-154	3.1E+03	1.0E-03	2.5E+01	1.4E+00	3.2E+03	1.4E+00
Gd-148	3.1E+03	2.8E-03	2.5E+01	3.7E+00	3.2E+03	3.7E+00
Gd-150	3.1E+03	2.9E-08	2.5E+01	3.9E-05	3.2E+03	3.9E-05
H-3	1.5E+03	2.7E+00			1.5E+03	2.7E+00
I-129	3.1E+03	2.0E-08	2.5E+01	2.6E-05	3.2E+03	2.6E-05
Kr-81	3.1E+03	3.5E-07	2.5E+01	4.7E-04	3.2E+03	4.7E-04
Kr-85	3.1E+03	1.9E-02	2.5E+01	2.3E+01	3.2E+03	2.3E+01
La-137	3.1E+03	5.7E-06	2.5E+01	7.6E-03	3.2E+03	7.6E-03
Mo-93	3.1E+03	1.1E-04	2.5E+01	1.5E-01	3.2E+03	1.5E-01
Nb-92	3.1E+03	3.4E-08	2.5E+01	4.5E-05	3.2E+03	4.5E-05
Nb-94	3.1E+03	3.4E-05	2.5E+01	4.5E-02	3.2E+03	4.5E-02
Np-237			5.5E-01	3.9E-03	5.5E-01	3.9E-03
Pd-107	3.1E+03	4.8E-08	2.5E+01	6.4E-05	3.2E+03	6.5E-05
Pu-238	8.2E+03	7.1E+02	1.2E+03	3.5E+03	9.5E+03	4.2E+03
Pu-239	1.9E+04	1.1E+00	1.4E+03	1.8E+03	2.0E+04	1.8E+03
Pu-240	1.1E+03	3.0E-03	6.2E+02	4.5E+02	1.7E+03	4.5E+02
Pu-241	1.1E+03	4.6E-02	6.2E+02	8.1E+03	1.7E+03	8.1E+03
Pu-242	1.1E+03	1.8E-07	6.2E+02	4.9E-02	1.7E+03	4.9E-02
Se-79	3.1E+03	3.2E-08	2.5E+01	4.3E-05	3.2E+03	4.3E-05
Sm-146	3.1E+03	2.6E-09	2.5E+01	3.5E-06	3.2E+03	3.5E-06
Sm-147	3.1E+03	2.0E-12	2.5E+01	2.7E-09	3.2E+03	2.7E-09
Sm-151	3.1E+03	8.8E-04	2.5E+01	1.2E+00	3.2E+03	1.2E+00
Sr-90	3.1E+03	3.1E-01	2.5E+01	3.0E+01	3.2E+03	3.0E+01
Tb-157	3.1E+03	3.2E-05	2.5E+01	4.3E-02	3.2E+03	4.3E-02
Tb-158	3.1E+03	1.4E-05	2.5E+01	1.9E-02	3.2E+03	1.9E-02
Tc-97	3.1E+03	2.6E-07	2.5E+01	3.5E-04	3.2E+03	3.5E-04
Tc-99	3.1E+03	3.2E-06	2.5E+01	4.3E-03	3.2E+03	4.3E-03
Th-230	1.9E-02	1.6E+01			1.9E-02	1.6E+01
Th-232	5.4E+00	1.7E-03			5.4E+00	1.7E-03

Table 3-2. Continued.

Waste Form/Radionuclide	LLW Volume (m^3)	LLW Activity (Ci)	TRU Waste Volume (m^3)	TRU Waste Activity (Ci)	All Waste Volume (m^3)	All Waste Activity (Ci)
U-234	7.3E+01	2.2E+00			7.3E+01	2.2E+00
U-235	1.8E+04	4.6E-01	1.3E+02	1.9E-04	1.8E+04	4.6E-01
U-236	1.0E+01	9.6E-05			1.0E+01	9.6E-05
U-238	1.3E+04	9.3E+00			1.3E+04	9.3E+00
Zr-93	3.1E+03	3.6E-07	2.5E+01	4.8E-04	3.2E+03	4.8E-04
Soil						
Co-60	1.9E-01	2.8E-04			1.9E-01	2.8E-04
Pu-238	2.4E+03	3.1E-01			2.4E+03	3.1E-01
Pu-239	4.2E+03	3.4E-02	4.5E+00	3.7E+01	4.2E+03	3.7E+01
Th-232	4.9E-03	1.9E-04			4.9E-03	1.9E-04
U-234	5.7E-01	4.2E-01			5.7E-01	4.2E-01
U-235	2.4E+03	1.7E-02			2.4E+03	1.7E-02
U-238	1.3E+03	1.1E+00			1.3E+03	1.1E+00
Concrete and Sludges						
Am-241	1.3E+03	7.2E-01	2.6E+03	2.2E+03	3.9E+03	2.2E+03
Co-60	1.9E-01	2.8E-04			1.9E-01	2.8E-04
Pu-238	2.6E+03	4.0E+02	1.9E+02	1.7E+02	2.8E+03	5.7E+02
Pu-239	4.3E+03	4.5E+00	3.0E+03	7.5E+01	7.3E+03	8.0E+01
U-233			2.5E+03	6.2E+00	2.5E+03	6.2E+00
U-235	1.9E+03	3.4E-03	4.9E+01	8.4E-05	2.0E+03	3.5E-03
Bulk-Contaminated Waste						
Co-60	1.1E+01	2.6E-03			1.1E+01	2.6E-03

Table 3-3. Pre-1971 radionuclide inventory projections for Area G shafts.

Waste Form/Radionuclide	LLW		TRU Waste		All Waste	
	Volume (m^3)	Activity (Ci)	Volume (m^3)	Activity (Ci)	Volume (m^3)	Activity (Ci)
Surface-Contaminated Waste						
Ag-108m	8.8E+00	1.9E+00	1.0E+00	1.6E+00	9.8E+00	3.5E+00
Am-241	2.0E+00	3.4E-08			2.0E+00	3.4E-08
Ba-133	8.8E+00	6.7E+01	1.0E+00	5.7E+01	9.8E+00	1.2E+02
C-14	3.4E-01	1.0E-02			3.4E-01	1.0E-02
Cd-113m	8.8E+00	7.7E+00	1.0E+00	6.5E+00	9.8E+00	1.4E+01
Cf-252	2.3E-01	5.5E+01			2.3E-01	5.5E+01
Cm-244	3.8E-01	1.9E-01			3.8E-01	1.9E-01
Co-60	4.4E+00	1.2E+01			4.4E+00	1.2E+01
Cs-135	8.8E+00	3.5E-04	1.0E+00	2.9E-04	9.8E+00	6.4E-04
Cs-137	9.2E+00	1.3E+01	1.0E+00	1.1E+01	1.0E+01	2.3E+01
Dy-154	8.8E+00	1.2E-05	1.0E+00	1.0E-05	9.8E+00	2.3E-05
Eu-152	8.8E+00	4.3E+00	1.0E+00	3.6E+00	9.8E+00	7.8E+00
Eu-154	8.8E+00	1.2E+00	1.0E+00	1.0E+00	9.8E+00	2.2E+00
Gd-148	8.8E+00	3.3E+00	1.0E+00	2.7E+00	9.8E+00	6.0E+00
Gd-150	8.8E+00	3.4E-05	1.0E+00	2.9E-05	9.8E+00	6.3E-05
H-3	4.5E+01	3.4E+04			4.5E+01	3.4E+04
I-129	8.8E+00	2.3E-05	1.0E+00	1.9E-05	9.8E+00	4.3E-05
Kr-81	8.8E+00	4.1E-04	1.0E+00	3.5E-04	9.8E+00	7.6E-04
Kr-85	8.8E+00	2.0E+01	1.0E+00	1.7E+01	9.8E+00	3.7E+01
La-137	8.8E+00	6.7E-03	1.0E+00	5.6E-03	9.8E+00	1.2E-02
Mo-93	8.8E+00	1.3E-01	1.0E+00	1.1E-01	9.8E+00	2.5E-01
Nb-92	8.8E+00	4.0E-05	1.0E+00	3.4E-05	9.8E+00	7.4E-05
Nb-94	8.8E+00	4.0E-02	1.0E+00	3.4E-02	9.8E+00	7.4E-02
Np-237	4.6E-02	7.1E-05			4.6E-02	7.1E-05
Pd-107	8.8E+00	5.7E-05	1.0E+00	4.8E-05	9.8E+00	1.0E-04
Pu-238	1.4E+01	7.9E-01	1.9E-02	3.0E-01	1.4E+01	1.1E+00
Pu-239	4.8E+01	1.3E+00	1.2E+00	4.9E+01	4.9E+01	5.0E+01
Pu-240			3.8E-03	1.0E+00	3.8E-03	1.0E+00
Pu-241	2.8E-03	7.3E-01	3.8E-03	1.5E+01	6.6E-03	1.6E+01
Pu-242			3.8E-03	5.8E-05	3.8E-03	5.8E-05
Se-79	8.8E+00	3.8E-05	1.0E+00	3.2E-05	9.8E+00	7.0E-05
Sm-146	8.8E+00	3.1E-06	1.0E+00	2.6E-06	9.8E+00	5.7E-06
Sm-147	8.8E+00	2.4E-09	1.0E+00	2.0E-09	9.8E+00	4.5E-09
Sm-151	8.8E+00	1.0E+00	1.0E+00	8.8E-01	9.8E+00	1.9E+00
Sr-90	8.8E+00	2.6E+01	1.0E+00	2.2E+01	9.8E+00	4.8E+01
Tb-157	8.8E+00	3.8E-02	1.0E+00	3.2E-02	9.8E+00	7.0E-02
Tb-158	8.8E+00	1.6E-02	1.0E+00	1.4E-02	9.8E+00	3.0E-02
Tc-97	8.8E+00	3.1E-04	1.0E+00	2.6E-04	9.8E+00	5.7E-04
Tc-99	8.8E+00	3.8E-03	1.0E+00	3.2E-03	9.8E+00	6.9E-03
Th-232	2.7E-01	1.1E-02			2.7E-01	1.1E-02
U-232	3.8E-03	2.1E-01			3.8E-03	2.1E-01
U-233	3.6E-01	4.0E+00			3.6E-01	4.0E+00
U-234	2.9E+00	2.9E-02	1.1E-02	2.1E-02	2.9E+00	4.9E-02

Table 3-3. Continued.

Waste Form/Radionuclide	LLW Volume (m^3)	LLW Activity (Ci)	TRU Waste Volume (m^3)	TRU Waste Activity (Ci)	All Waste Volume (m^3)	All Waste Activity (Ci)
U-235	5.3E+01	5.0E-03	8.9E-01	3.0E-03	5.4E+01	8.0E-03
U-236	6.3E-01	8.8E-05	1.1E-02	8.9E-05	6.4E-01	1.8E-04
U-238	4.2E+01	4.4E+00	1.1E-02	6.0E-06	4.2E+01	4.4E+00
Zr-93	8.8E+00	4.2E-04	1.0E+00	3.6E-04	9.8E+00	7.8E-04
Bulk-Contaminated Waste						
Co-60	5.3E-01	1.8E+00			5.3E-01	1.8E+00

Table 3-4. Quantities and radiological characteristics of TRU waste that was non-retrievably disposed of in Pit 6.

Waste Parameter	Disposal Volume (m^3)	Disposal Activity (Ci)
Waste Form Totals		
Surface-Contaminated Waste		
Soils		
Concrete and Sludges	1.9E+01	6.0E+01
Bulk-Contaminated Waste		
Radionuclide-Specific Inventories		
Pu-238	1.9E+01	5.7E+01
Pu-239	1.9E+01	3.6E+00

Table 3-5. Area G disposal events that are not fully captured by the extrapolation process.

Date of Disposal	Disposal Area	Disposal Units	Quantities of Disposed Radionuclides (g)				Comments
			Pu	Am-241	U-233	Other	
1952-1967	C, G	Pits	3.4E+02			585 equivalent g Pu	Over 3,000 55-gal drums containing weapons-grade Pu disposed of as sludge; generated by the TA-21 treatment plant
1959-1968	C, G	Pits	7.4E+02	6.6E+02	6.5E+02		Approximately 11,800 55-gal drums of weapons-grade material disposed of as cement paste
1951-1963	C, G	Pits	N/A[a]	N/A[a]	N/A[a]		Sludge in 55-gal drums from TA-45 treatment plant
1960	G	Pit 1	6.0E+02				Approximately 30 to 40 30-gal drums containing sand from TA-21 decontamination activities

a. N/A indicates that data were unavailable.

Table 3-6. Additions to the extrapolation-based waste inventory projections for the pre-1971 period.

Waste	Waste Form	Total Volume (m^3)	Total Activity (Ci)	Radionuclide	Radionuclide Activity (Ci)
1952-1967 Sludge	Concrete/Sludge	3.1E+02	1.0E+01	Pu-239	1.0E+01
1959-1968 Cement Paste	Concrete/Sludge	2.5E+03	2.2E+03	Am-241	2.1E+03
				Pu-239	4.5E+01
				U-233	6.2E+00
1960 Soil	Soil	4.5E+00	3.7E+01	Pu-239	3.7E+01

although small quantities of it were probably placed in Area C pits. Finally, all Pu inventories listed in Table 3-5 were assumed to be Pu-239 (Warren, 1996).

3.1.2 1971 to September 25, 1988, Inventory

Twenty-five pits and over 140 shafts were used to dispose of LLW at Area G between 1971 and September 25, 1988. The total volumes and activities of LLW placed in these disposal units during this period are listed in Table 3-7 for the four waste forms described earlier. Individual totals are reported for each pit, while inventories are summed over the shafts.

As discussed in Section 3.1.1, the waste disposed of in Pits 5 and 6 is included in the pre-1971 disposal period for convenience. While these pits received waste prior to and following 1971, the greatest volume of material was buried before 1971. In addition, one shipment of waste was placed in Pit 32 after September 25, 1988. For simplicity, this shipment is included in the waste data presented in this section. Pit 36 and several shafts were used prior to September 26, 1988, and following that date. The data presented in Table 3-7 include the waste that was disposed of in those units through September 25, 1988.

Pit 9 was used for the disposal of LLW and retrievable storage of TRU waste. Although retrieval of the TRU waste will likely entail removal of the LLW as well, the latter is expected to be placed back into a disposal unit at Area G. Consequently, the LLW disposed of in Pit G is maintained in the inventory.

Radionuclide-specific inventories are listed in Tables 3-8 and 3-9 for the pits and shafts, respectively, for the four waste forms discussed earlier. Inventories are provided for each pit, but are summed over all of the shaft disposal units. The volumes provided in the tables are the quantities of waste contaminated with each radionuclide. Because several radionuclides may occur in a single waste package, the sum of these waste package volumes is greater than the total volume of waste disposed of in the pits and shafts. The listed activities include contributions from MAP, MFP, and the material types discussed in Section 2.1.

Table 3-7. Pit and shaft waste volumes and activities disposed of from 1971 to September 25, 1988.

Disposal Unit/Waste Form	Total Disposal Volume (m^3)	Total Disposal Activity (Ci)
Pit 7		
Surface-Contaminated Waste	2.0E+03	1.4E-01
Soils	1.0E+03	2.0E-01
Concrete and Sludges	2.6E+02	2.0E+01
Bulk-Contaminated Waste	2.9E+00	2.6E-02
Pit 8		
Surface-Contaminated Waste	7.7E+02	3.3E-05
Soils	2.8E+02	0.0E+00
Concrete and Sludges	7.8E+02	2.1E+01
Bulk-Contaminated Waste	0.0E+00	0.0E+00
Pit 9		
Surface-Contaminated Waste	4.8E+00	1.2E+00
Soils	0.0E+00	0.0E+00
Concrete and Sludges	0.0E+00	0.0E+00
Bulk-Contaminated Waste	0.0E+00	0.0E+00
Pit 10		
Surface-Contaminated Waste	2.5E+03	6.4E+03
Soils	4.1E+02	1.5E+00
Concrete and Sludges	2.1E+02	1.3E+00
Bulk-Contaminated Waste	1.1E+01	3.8E+02
Pit 12		
Surface-Contaminated Waste	6.4E+02	8.3E-03
Soils	9.3E+02	0.0E+00
Concrete and Sludges	2.4E+02	3.4E-01
Bulk-Contaminated Waste	0.0E+00	0.0E+00
Pit 13		
Surface-Contaminated Waste	1.2E+03	1.7E+00
Soils	2.8E+02	4.2E-01
Concrete and Sludges	4.9E+01	4.3E-06
Bulk-Contaminated Waste	8.9E+00	1.5E-02

Table 3-7. Continued.

Disposal Unit/Waste Form	Total Disposal Volume (m^3)	Total Disposal Activity (Ci)
Pit 16		
Surface-Contaminated Waste	1.6E+03	1.8E+00
Soils	8.9E+01	3.4E-02
Concrete and Sludges	1.6E+00	0.0E+00
Bulk-Contaminated Waste	3.7E+00	4.4E-02
Pit 17		
Surface-Contaminated Waste	3.1E+03	7.0E-02
Soils	3.5E+02	0.0E+00
Concrete and Sludges	3.6E+02	0.0E+00
Bulk-Contaminated Waste	0.0E+00	0.0E+00
Pit 18		
Surface-Contaminated Waste	6.6E+03	3.0E+04
Soils	2.3E+03	6.4E-01
Concrete and Sludges	6.3E+02	2.5E+00
Bulk-Contaminated Waste	1.7E+01	2.1E+00
Pit 19		
Surface-Contaminated Waste	5.3E+01	3.0E-01
Soils	9.0E-01	0.0E+00
Concrete and Sludges	9.0E-01	0.0E+00
Bulk-Contaminated Waste	0.0E+00	0.0E+00
Pit 20		
Surface-Contaminated Waste	1.2E+03	1.4E+00
Soils	1.0E+04	0.0E+00
Concrete and Sludges	2.0E+02	4.9E+00
Bulk-Contaminated Waste	0.0E+00	0.0E+00
Pit 21		
Surface-Contaminated Waste	2.5E+03	5.5E-01
Soils	2.4E+02	0.0E+00
Concrete and Sludges	2.1E+01	0.0E+00
Bulk-Contaminated Waste	0.0E+00	0.0E+00

Table 3-7. Continued.

Disposal Unit/Waste Form	Total Disposal Volume (m^3)	Total Disposal Activity (Ci)
Pit 22		
Surface-Contaminated Waste	1.3E+03	6.0E+02
Soils	1.4E+03	1.8E-01
Concrete and Sludges	1.5E+02	1.0E+00
Bulk-Contaminated Waste	1.8E+01	1.6E-01
Pit 24		
Surface-Contaminated Waste	1.5E+03	1.4E+01
Soils	4.1E+03	2.8E-01
Concrete and Sludges	1.1E+01	5.0E-03
Bulk-Contaminated Waste	3.5E+01	3.7E-01
Pit 25		
Surface-Contaminated Waste	3.8E+03	3.7E+02
Soils	5.4E+02	3.2E-01
Concrete and Sludges	1.9E+02	0.0E+00
Bulk-Contaminated Waste	3.0E+01	6.3E-01
Pit 26		
Surface-Contaminated Waste	2.1E+03	4.9E+01
Soils	1.0E+03	1.9E+00
Concrete and Sludges	5.8E+02	1.7E+01
Bulk-Contaminated Waste	6.2E+01	4.8E+01
Pit 27		
Surface-Contaminated Waste	3.2E+03	1.6E+02
Soils	2.7E+03	9.9E-01
Concrete and Sludges	2.1E+02	6.4E-03
Bulk-Contaminated Waste	2.7E+01	2.6E+01
Pit 28		
Surface-Contaminated Waste	2.0E+03	1.3E+03
Soils	1.4E+03	5.9E-01
Concrete and Sludges	2.6E+02	1.1E-01
Bulk-Contaminated Waste	1.6E+01	6.5E+01

Table 3-7. Continued.

Disposal Unit/Waste Form	Total Disposal Volume (m^3)	Total Disposal Activity (Ci)
Pit 29		
Surface-Contaminated Waste	4.2E+03	2.3E+03
Soils	2.9E+03	3.3E+00
Concrete and Sludges	4.8E+02	2.9E+00
Bulk-Contaminated Waste	1.8E+02	3.7E+00
Pit 32		
Surface-Contaminated Waste	3.0E+03	1.4E+02
Soils	1.3E+03	1.0E+01
Concrete and Sludges	3.1E+02	7.0E+00
Bulk-Contaminated Waste	1.6E+02	4.1E+00
Pit 33		
Surface-Contaminated Waste	4.8E+03	3.8E+01
Soils	1.1E+03	7.0E-01
Concrete and Sludges	6.0E+02	1.3E+00
Bulk-Contaminated Waste	1.1E+02	1.3E+01
Pit 35		
Surface-Contaminated Waste	1.9E+03	7.4E+01
Soils	6.6E+02	5.6E-01
Concrete and Sludges	1.8E+02	1.6E+00
Bulk-Contaminated Waste	1.1E+02	4.0E+00
Pit 36		
Surface-Contaminated Waste	2.1E+03	3.5E+01
Soils	5.2E+02	6.6E-02
Concrete and Sludges	1.7E+02	5.7E-01
Bulk-Contaminated Waste	9.4E+01	1.4E+00
		4.1E+04
Shafts		
Surface-Contaminated Waste	7.7E+02	8.2E+05
Soils	2.2E+01	1.0E+02
Concrete and Sludges	7.1E-01	1.0E+02
Bulk-Contaminated Waste	1.2E+02	6.7E+03

Table 3-8. Pit radionuclide inventories for 1971 through September 25, 1988.

	Waste Form							
	Surface-Contaminated Waste		Soils		Concrete and Sludges		Bulk-Contaminated Waste	
Radionuclide	Volume (m^3)	Activity (Ci)	Volume (m^3)	Activity (Ci)	Volume (m^3)	Activity (Ci)	Volume (m^3)	Activity (Ci)
Pit 7								
Ag-108m	4.0E+02	9.7E-05						
Am-241					1.2E+02	1.3E-01		
Ba-133	4.0E+02	3.5E-03						
Cd-113m	4.0E+02	4.0E-04						
Cf-252	2.8E-01	8.6E-03						
Co-60	2.6E+01	9.3E-04					2.9E+00	8.6E-04
Cs-135	4.0E+02	1.8E-08						
Cs-137	4.0E+02	6.6E-04						
Dy-154	4.0E+02	6.4E-10						
Eu-152	4.0E+02	2.2E-04						
Eu-154	4.0E+02	6.3E-05						
Gd-148	4.0E+02	1.7E-04						
Gd-150	4.0E+02	1.8E-09						
I-129	4.0E+02	1.2E-09						
Kr-81	4.0E+02	2.1E-08						
Kr-85	4.0E+02	1.1E-03						
La-137	4.0E+02	3.5E-07						
Mo-93	4.0E+02	6.9E-06						
Nb-92	4.0E+02	2.1E-09						
Nb-94	4.0E+02	2.1E-06						
Pd-107	4.0E+02	3.0E-09						
Pu-238	1.3E+03	4.7E-02	9.8E+02	1.8E-01	2.4E+02	2.0E+01		
Pu-239	1.9E+03	5.3E-03	1.0E+03	2.0E-02	2.6E+02	4.0E-01		
Pu-240	2.2E+02	1.2E-04						
Pu-241	2.2E+02	1.7E-03						
Pu-242	2.2E+02	6.7E-09						
Se-79	4.0E+02	2.0E-09						
Sm-146	4.0E+02	1.6E-10						
Sm-147	4.0E+02	1.2E-13						
Sm-151	4.0E+02	5.4E-05						
Sr-90	4.0E+02	1.4E-03						
Tb-157	4.0E+02	2.0E-06						
Tb-158	4.0E+02	8.5E-07						
Tc-97	4.0E+02	1.6E-08						
Tc-99	4.0E+02	2.0E-07						
U-235	9.9E+02	8.6E-05			1.9E+02	1.6E-03		
Zr-93	4.0E+02	2.2E-08						
Pit 8								
Am-241					3.1E+02	9.8E-01		
Th-232	1.4E+00	3.3E-05			—			
Pu-238					7.7E+02	1.6E-01		
Pu-239					7.7E+02	3.5E+00		

Table 3-8. Continued.

Radionuclide	Waste Form: Surface-Contaminated Waste Volume (m^3)	Surface-Contaminated Waste Activity (Ci)	Soils Volume (m^3)	Soils Activity (Ci)	Concrete and Sludges Volume (m^3)	Concrete and Sludges Activity (Ci)	Bulk-Contaminated Waste Volume (m^3)	Bulk-Contaminated Waste Activity (Ci)
Pit 9								
Ag-108m	7.6E-03	2.1E-03						
Ba-133	7.6E-03	7.4E-02						
Cd-113m	7.6E-03	8.5E-03						
Cs-135	7.6E-03	3.8E-07						
Cs-137	7.6E-03	1.4E-02						
Dy-154	7.6E-03	1.4E-08						
Eu-152	7.6E-03	4.7E-03						
Eu-154	7.6E-03	1.3E-03						
Gd-148	7.6E-03	3.6E-03						
Gd-150	7.6E-03	3.8E-08						
I-129	7.6E-03	2.6E-08						
Kr-81	7.6E-03	4.5E-07						
Kr-85	7.6E-03	2.2E-02						
La-137	7.6E-03	7.4E-06						
Mo-93	7.6E-03	1.5E-04						
Nb-92	7.6E-03	4.4E-08						
Nb-94	7.6E-03	4.4E-05						
Pd-107	7.6E-03	6.3E-08						
Pu-238	4.8E+00	1.8E-01						
Se-79	7.6E-03	4.2E-08						
Sm-146	7.6E-03	3.4E-09						
Sm-147	7.6E-03	2.7E-02						
Sm-151	7.6E-03	1.2E-03						
Sr-90	7.6E-03	2.9E-02						
Tb-157	7.6E-03	4.2E-05						
Tb-158	7.6E-03	1.8E-05						
Tc-97	7.6E-03	3.4E-07						
Tc-99	7.6E-03	4.2E-06						
Zr-93	7.6E-03	4.7E-07						
Pit 10								
Ag-108m	2.4E+02	1.1E-04						
Am-241	6.2E+01	1.0E-03						
Ba-133	2.4E+02	3.8E-03						
C-14	2.0E+00	9.0E-07						
Cd-113m	2.4E+02	4.3E-04						
Cf-252	2.8E-02	8.0E-06						
Co-60	5.6E+01	1.2E+01	6.2E-01	9.9E-06			1.1E+01	1.2E+01
Cs-135	2.4E+02	2.0E-08						
Cs-137	5.7E+02	2.2E-03	6.2E+01	5.1E-07	1.4E+01	5.0E-07		
Dy-154	2.4E+02	6.9E-10						
Eu-152	2.4E+02	2.4E-04						
Eu-154	2.4E+02	6.8E-05						
Gd-148	2.4E+02	1.8E-04						
Gd-150	2.4E+02	1.9E-09						
H-3	1.4E+02	6.1E+03	1.5E+01	1.3E+00	1.6E+01	1.3E+00		

Table 3-8. Continued.

	Waste Form							
	Surface-Contaminated Waste		Soils		Concrete and Sludges		Bulk-Contaminated Waste	
Radionuclide	Volume (m^3)	Activity (Ci)	Volume (m^3)	Activity (Ci)	Volume (m^3)	Activity (Ci)	Volume (m^3)	Activity (Ci)
I-129	2.4E+02	1.3E-09						
Kr-81	2.4E+02	2.3E-08						
Kr-85	2.4E+02	1.1E-03						
La-137	2.4E+02	3.8E-07						
Mo-93	2.4E+02	7.5E-06						
Nb-92	2.4E+02	2.3E-09						
Nb-94	2.4E+02	2.3E-06						
Pd-107	2.4E+02	3.2E-09						
Pu-238	4.6E+02	2.3E-02						
Pu-239	1.4E+03	5.5E-02	2.6E+02	5.0E-07	1.8E+02	5.0E-07		
Pu-240	1.4E+02	6.3E-04						
Pu-241	1.4E+02	9.5E-03						
Pu-242	1.4E+02	3.6E-08						
Ra-226	2.1E-01	9.9E-02						
Se-79	2.4E+02	2.1E-09						
Sm-146	2.4E+02	1.7E-10						
Sm-147	2.4E+02	1.4E-13						
Sm-151	2.4E+02	5.9E-05						
Sr-90	5.8E+02	2.1E-01	6.4E+01	5.1E-07	2.4E+01	5.0E-07		
Tb-157	2.4E+02	2.1E-06						
Tb-158	2.4E+02	9.2E-07						
Tc-97	2.4E+02	1.7E-08						
Tc-99	2.4E+02	2.1E-07						
Th-232	1.8E+00	4.4E-04						
U-233	1.0E+00	1.9E-05						
U-234	6.8E-01	7.2E-02	1.4E-02	7.0E-03				
U-235	6.9E+02	1.1E-02	1.4E-02	2.7E-04				
U236	2.1E-01	6.3E-08						
U-238	4.5E+02	1.5E+00	1.0E+02	2.1E-01				
Zr-93	2.4E+02	2.4E-08						
Pit 12								
Ag-108m	2.2E+01	1.7E-05						
Ba-133	2.2E+01	5.9E-04						
Cd-113m	2.2E+01	6.8E-05						
Cs-135	2.2E+01	3.1E-09						
Cs-137	2.2E+01	1.1E-04						
Dy-154	2.2E+01	1.1E-10						
Eu-152	2.2E+01	3.8E-05						
Eu-154	2.2E+01	1.1E-05						
Gd-148	2.2E+01	2.9E-05						
Gd-150	2.2E+01	3.0E-10						
I-129	2.2E+01	2.0E-10						
Kr-81	2.2E+01	3.6E-09						
Kr-85	2.2E+01	1.8E-04						
La-137	2.2E+01	5.9E-08						
Mo-93	2.2E+01	1.2E-06						

Table 3-8. Continued.

	Waste Form							
	Surface-Contaminated Waste		Soils		Concrete and Sludges		Bulk-Contaminated Waste	
Radionuclide	Volume (m^3)	Activity (Ci)	Volume (m^3)	Activity (Ci)	Volume (m^3)	Activity (Ci)	Volume (m^3)	Activity (Ci)
Nb-92	2.2E+01	3.5E-10						
Nb-94	2.2E+01	3.5E-07						
Pd-107	2.2E+01	5.0E-10						
Pu-238	1.6E+02	5.6E-05			6.7E+01	2.7E-01		
Pu-239	2.3E+01	4.4E-05			2.4E+02	7.1E-02		
Pu-240	2.3E+01	1.0E-05						
Pu-241	2.3E+01	1.5E-04						
Pu-242	2.3E+01	5.9E-10						
Se-79	2.2E+01	3.3E-10						
Sm-146	2.2E+01	2.7E-11						
Sm-147	2.2E+01	2.1E-14						
Sm-151	2.2E+01	9.2E-06						
Sr-90	2.2E+01	2.3E-04						
Tb-157	2.2E+01	3.4E-07						
Tb-158	2.2E+01	1.4E-07						
Tc-97	2.2E+01	2.7E-09						
Tc-99	2.2E+01	3.3E-08						
Zr-93	2.2E+01	3.7E-09						
Pit 13								
Ag-108m	7.1E+01	3.1E-05						
Ba-133	7.1E+01	1.1E-03						
Cd-113m	7.1E+01	1.3E-04						
Co-60	7.4E+01	6.7E-04	1.1E+00	1.4E-07	1.1E+00	1.4E-07	8.9E+00	5.0E-04
Cs-135	7.1E+01	5.8E-09						
Cs-137	7.1E+01	2.1E-04						
Dy-154	7.1E+01	2.0E-10						
Eu-152	7.1E+01	7.1E-05						
Eu-154	7.1E+01	2.0E-05						
Gd-148	7.1E+01	5.4E-05						
Gd-150	7.1E+01	5.7E-10						
H-3	8.3E+00	5.0E-01						
I-129	7.1E+01	3.8E-10						
Kr-81	7.1E+01	6.8E-09						
Kr-85	7.1E+01	3.3E-04						
La-137	7.1E+01	1.1E-07						
Nb-92	7.1E+01	6.6E-10						
Mo-93	7.1E+01	2.2E-06						
Nb-92	7.1E+01	6.6E-10						
Nb-94	7.1E+01	6.6E-07						
Pd-107	7.1E+01	9.4E-10						
Se-79	7.1E+01	6.3E-10						
Sm-146	7.1E+01	5.1E-11						
Sm-147	7.1E+01	4.0E-14						
Sm-151	7.1E+01	1.7E-05						
Sr-90	7.1E+01	4.4E-04						
Tb-157	7.1E+01	6.3E-07						

Table 3-8. Continued.

	Waste Form							
	Surface-Contaminated Waste		Soils		Concrete and Sludges		Bulk-Contaminated Waste	
Radionuclide	Volume (m^3)	Activity (Ci)	Volume (m^3)	Activity (Ci)	Volume (m^3)	Activity (Ci)	Volume (m^3)	Activity (Ci)
Tb-158	7.1E+01	2.7E-07						
Tc-97	7.1E+01	5.1E-09						
Tc-99	7.1E+01	6.2E-08						
U-234	3.3E+00	9.9E-03	2.8E-02	1.1E-01				
U-235	6.8E+02	3.8E-04	8.0E+01	4.4E-03	3.7E+01	2.5E-10		
U-238	4.6E+02	1.2E+00	1.8E+02	3.0E-01				
Zr-93	7.1E+01	7.0E-09						
Pit 16								
Co-60	1.3E+01	2.6E-03					3.7E+00	1.4E-03
Th-232	1.7E+00	6.5E-04						
U-234	1.1E+01	3.7E-01	2.8E-01	1.7E-02				
U-235	5.7E+02	5.4E-02	2.8E-01	7.4E-04				
U-236	3.8E+00	5.3E-05						
U-238	1.5E+03	1.3E+00	2.8E-01	1.6E-02				
Pit 17								
Ac-227	1.0E+00	7.0E-02						
Pit 18								
Ag-108m	2.9E+02	2.5E-03						
Am-241	1.0E+02	2.7E-04	9.6E+00	2.0E-03	1.3E+02	3.3E-01		
Ba-133	2.9E+02	8.9E-02						
C-14	4.4E+00	2.0E-06						
Cd-113m	2.9E+02	1.0E-02						
Co-60	6.3E+01	1.1E+03	1.5E+00	1.7E-07	3.0E-02	1.7E-07	1.7E+01	7.0E-02
Cs-135	2.9E+02	4.6E-07						
Cs-137	2.9E+02	1.7E-02						
Dy-154	2.9E+02	1.6E-08						
Eu-152	2.9E+02	5.6E-03						
Eu-154	2.9E+02	1.6E-03						
Gd-148	2.9E+02	4.3E-03						
Gd-150	2.9E+02	4.5E-08						
H-3	8.3E+01	1.0E+01	7.3E+00	2.8E-07	7.3E+00	2.8E-07		
I-129	2.9E+02	3.1E-08						
Kr-81	2.9E+02	5.4E-07						
Kr-85	2.9E+02	2.7E-02						
La-137	2.9E+02	8.8E-06						
Mo-93	2.9E+02	1.8E-04						
Nb-92	2.9E+02	5.3E-08						
Nb-94	2.9E+02	5.3E-05						
Pd-107	2.9E+02	7.5E-08						
Pu-238	1.5E+03	1.4E-03	5.5E+01	1.3E-08	1.6E+02	1.2E+00		
Pu-239	3.1E+03	3.1E-02	1.6E+03	6.1E-03	3.1E+02	9.7E-01		
Pu-240	6.3E+02	2.0E-03						
Pu-241	6.3E+02	3.1E-02						
Pu-242	6.3E+02	1.2E-07						

Table 3-8. Continued.

	Waste Form							
	Surface-Contaminated Waste		Soils		Concrete and Sludges		Bulk-Contaminated Waste	
Radionuclide	Volume (m^3)	Activity (Ci)	Volume (m^3)	Activity (Ci)	Volume (m^3)	Activity (Ci)	Volume (m^3)	Activity (Ci)
Se-79	2.9E+02	5.0E-08						
Sm-146	2.9E+02	4.1E-09						
Sm-147	2.9E+02	3.2E-12						
Sm-151	2.9E+02	1.4E-03						
Sr-90	2.9E+02	1.1E+00						
Tb-157	2.9E+02	5.1E-05						
Tb-158	2.9E+02	2.2E-05						
Tc-97	2.9E+02	4.1E-07						
Tc-99	2.9E+02	5.0E-06						
Th-232	6.4E+00	8.7E-04						
U-234	5.0E+00	9.7E-02	3.4E-02	5.8E-02				
U-235	1.1E+02	1.3E-02	6.6E+01	2.2E-03	1.8E+02	2.5E-10		
U-236	2.3E+00	5.3E-06						
U-238	7.6E+02	1.8E+00	1.5E+02	5.8E-01				
Zr-93	2.9E+02	5.6E-07						
Pit 10								
Ag-108m	3.4E-02	6.2E-04						
Ba-133	3.4E-02	2.2E-02						
Cd-113m	3.4E-02	2.5E-03						
Cs-135	3.4E-02	1.2E-07						
Cs-137	3.4E-02	4.2E-03						
Dy-154	3.4E-02	4.1E-09						
Eu-152	3.4E-02	1.4E-03						
Eu-154	3.4E-02	4.0E-04						
Gd-148	3.4E-02	1.1E-03						
Gd-150	3.4E-02	1.1E-08						
I-129	3.4E-02	7.7E-09						
Kr-81	3.4E-02	1.4E-07						
Kr-85	3.4E-02	6.7E-03						
La-137	3.4E-02	2.2E-06						
Mo-93	3.4E-02	4.4E-05						
Nb-92	3.4E-02	1.3E-08						
Nb-94	3.4E-02	1.3E-05						
Pd-107	3.4E-02	1.9E-08						
Se-79	3.4E-02	1.3E-08						
Sm-146	3.4E-02	1.0E-09						
Sm-147	3.4E-02	8.0E-13						
Sm-151	3.4E-02	3.5E-04						
Sr-90	3.4E-02	8.7E-03						
Tb-157	3.4E-02	1.3E-05						
Tb-158	3.4E-02	5.4E-06						
Tc-97	3.4E-02	1.0E-07						
Tc-99	3.4E-02	1.2E-06						
Zr-93	3.4E-02	1.4E-07						

Table 3-8. Continued.

	Waste Form							
	Surface-Contaminated Waste		Soils		Concrete and Sludges		Bulk-Contaminated Waste	
Radionuclide	Volume (m^3)	Activity (Ci)	Volume (m^3)	Activity (Ci)	Volume (m^3)	Activity (Ci)	Volume (m^3)	Activity (Ci)
Pit 20								
Ag-108m	2.2E+02	1.3E-04						
Am-241					1.9E+02	1.0E-01		
Ba-133	2.2E+02	4.8E-03						
Cd-113m	2.2E+02	5.5E-04						
Cf-249	5.7E-01	4.1E-04						
Cf-251	8.5E-02	1.6E-03						
Cs-135	2.2E+02	2.5E-08						
Cs-137	2.2E+02	9.1E-04						
Dy-154	2.2E+02	8.8E-10						
Eu-152	2.2E+02	3.1E-04						
Eu-154	2.2E+02	8.7E-05						
Gd-148	2.2E+02	2.3E-04						
Gd-150	2.2E+02	2.5E-09						
H-3	1.7E+01	6.0E-01						
I-129	2.2E+02	1.7E-09						
Kr-81	2.2E+02	2.9E-08						
Kr-85	2.2E+02	1.4E-03						
La-137	2.2E+02	4.8E-07						
Mo-93	2.2E+02	9.6E-06						
Nb-92	2.2E+02	2.9E-09						
Nb-94	2.2E+02	2.9E-06						
Pd-107	2.2E+02	4.1E-09						
Pu-238	7.9E+02	1.2E-01			2.0E+02	4.2E+00		
Pu-239	1.2E+03	6.5E-01			2.0E+02	5.8E-01		
Pu-240	2.9E+02	5.6E-04						
Pu-241	2.9E+02	8.5E-03						
Pu-242	2.9E+02	3.3E-08						
Se-79	2.2E+02	2.7E-09						
Sm-146	2.2E+02	2.2E-10						
Sm-147	2.2E+02	1.7E-13						
Sm-151	2.2E+02	7.5E-05						
Sr-90	2.2E+02	1.9E-03						
Tb-157	2.2E+02	2.7E-06						
Tb-158	2.2E+02	1.2E-06						
Tc-97	2.2E+02	2.2E-08						
Tc-99	2.2E+02	2.7E-07						
U-235					1.9E+02	4.7E-04		
Zr-93	2.2E+02	3.0E-08						
Pit 21								
U-234	1.8E+00	1.0E-01						
U-235	2.0E+03	1.7E-01						
U-238	2.1E+03	2.7E-01						

Table 3-8. Continued.

	Waste Form							
	Surface-Contaminated Waste		Soils		Concrete and Sludges		Bulk-Contaminated Waste	
Radionuclide	Volume (m^3)	Activity (Ci)	Volume (m^3)	Activity (Ci)	Volume (m^3)	Activity (Ci)	Volume (m^3)	Activity (Ci)
Pit 22								
Ag-108m	1.1E+02	1.2E+00						
Am-241	2.1E-01	3.4E-03			8.0E+01	1.7E-01		
Ba-133	1.1E+02	4.5E+01						
Cd-113m	1.1E+02	5.1E+00						
Co-60	2.4E+01	5.3E-03					1.8E+01	5.3E-03
Cs-135	1.1E+02	2.3E-04						
Cs-137	1.1E+02	8.4E+00						
Dy-154	1.1E+02	8.2E-06						
Eu-152	1.1E+02	2.8E+00						
Eu-154	1.1E+02	8.0E-01						
Gd-148	1.1E+02	2.2E+00						
Gd-150	1.1E+02	2.3E-05						
H-3	1.8E+01	5.0E-05						
I-129	1.1E+02	1.5E-05						
Kr-81	1.1E+02	2.7E-04						
Kr-85	1.1E+02	1.3E+01						
La-137	1.1E+02	4.4E-03						
Mo-93	1.1E+02	8.8E-02						
Nb-92	1.1E+02	2.7E-05						
Nb-94	1.1E+02	2.7E-02						
Pd-107	1.1E+02	3.8E-05						
Pu-238	2.9E+02	6.4E-03			8.4E+01	4.5E-01		
Pu-239	8.4E+02	9.4E-01			1.4E+02	4.1E-01		
Pu-240	9.6E+01	1.2E-03						
Pu-241	9.6E+01	1.9E-02						
Pu-242	9.6E+01	7.2E-08						
Se-79	1.1E+02	2.5E-05						
Sm-146	1.1E+02	2.0E-06						
Sm-147	1.1E+02	1.6E-09						
Sm-151	1.1E+02	6.9E-01						
Sr-90	1.1E+02	1.7E+01						
Tb-157	1.1E+02	2.5E-02						
Tb-158	1.1E+02	1.1E-02						
Tc-97	1.1E+02	2.0E-04						
Tc-99	1.1E+02	2.5E-03						
U-234			1.7E-02	4.9E-02				
U-235	4.3E+02	5.6E-04	1.7E-02	1.9E-03				
U-238	3.1E+02	4.7E-01	2.9E+01	1.3E-01				
Zr-93	1.1E+02	2.8E-04						
Pit 24								
Co-60	8.1E+01	1.7E-02	1.1E-01	1.7E-04	1.1E-01	1.7E-04	3.5E+01	1.2E-02
Cs-137	7.6E-01	1.5E-01						
H-3	3.0E+01	5.0E-01						
Sr-90	7.6E-01	1.7E-01						
Th-230	1.1E-02	9.5E+00						

Table 3-8. Continued.

	Waste Form							
	Surface-Contaminated Waste		Soils		Concrete and Sludges		Bulk-Contaminated Waste	
Radionuclide	Volume (m^3)	Activity (Ci)	Volume (m^3)	Activity (Ci)	Volume (m^3)	Activity (Ci)	Volume (m^3)	Activity (Ci)
Th-232	5.7E-02	3.3E-04	2.8E-03	1.1E-04				
U-234	2.7E+01	7.8E-01	8.5E-03	6.7E-02				
U-235	6.6E+02	3.2E-02	8.5E-03	2.6E-03				
U-236	2.2E+00	3.1E-06						
U-238	1.0E+03	2.2E+00	4.1E+03	2.0E-01				
Pit 25								
Ag-108m	3.5E+02	2.5E-03						
Am-241	1.7E+02	3.1E-03						
Ba-133	3.5E+02	8.9E-02						
Cd-113m	3.5E+02	1.0E-02						
Co-60	2.3E+02	1.2E+02					3.0E+01	2.1E-02
Cs-135	3.5E+02	4.6E-07						
Cs-137	6.9E+02	2.0E+02	7.1E+00	1.0E-09				
Dy-154	3.5E+02	1.6E-08						
Eu-152	3.5E+02	5.6E-03						
Eu-154	3.5E+02	1.6E-03						
Gd-148	3.5E+02	4.3E-03						
Gd-150	3.5E+02	4.5E-08						
H-3	9.9E+01	5.0E+01						
I-129	3.5E+02	3.1E-08						
Kr-81	3.5E+02	5.4E-07						
Kr-85	3.5E+02	2.7E-02						
La-137	3.5E+02	8.8E-06						
Mo-93	3.5E+02	1.8E-04						
Nb-92	3.5E+02	5.3E-08						
Nb-94	3.5E+02	5.3E-05						
Pd-107	3.5E+02	7.5E-08						
Pu-238	7.3E+02	1.6E-03						
Pu-239	2.2E+03	5.5E-02						
Pu-240	2.0E+02	4.6E-04						
Pu-241	2.0E+02	7.0E-03						
Pu-242	2.0E+02	2.7E-08						
Se-79	3.5E+02	5.0E-08						
Sm-146	3.5E+02	4.1E-09						
Sm-147	3.5E+02	3.2E-12						
Sm-151	3.5E+02	1.4E-03						
Sr-90	7.5E+02	4.2E-02	1.6E+01	4.0E-03				
Tb-157	3.5E+02	5.1E-05						
Tb-158	3.5E+02	2.2E-05						
Tc-97	3.5E+02	4.1E-07						
Tc-99	3.5E+02	5.0E-06						
U-234			2.5E-02	2.8E-02				
U-235	9.4E+02	9.9E-03	7.1E+01	1.1E-03				
U-238	8.0E+02	1.0E+00	5.6E+01	2.8E-01				
Zr-93	3.5E+02	5.6E-07						

Table 3-8. Continued.

Radionuclide	Waste Form: Surface-Contaminated Waste Volume (m^3)	Surface-Contaminated Waste Activity (Ci)	Soils Volume (m^3)	Soils Activity (Ci)	Concrete and Sludges Volume (m^3)	Concrete and Sludges Activity (Ci)	Bulk-Contaminated Waste Volume (m^3)	Bulk-Contaminated Waste Activity (Ci)
Pit 26								
Ag-108m					1.9E+02	1.2E-03		
Am-241	1.6E+02	8.2E-04			2.0E+02	1.4E+01		
Ba-133					1.9E+02	4.2E-02		
Cd-113m					1.9E+02	4.8E-03		
Ce-144					1.9E+02	5.4E-02		
Co-60	9.7E+01	2.6E+00					6.2E+01	1.6E+00
Cs-135					1.9E+02	2.2E-07		
Cs-137					1.9E+02	7.9E-03		
Dy-154					1.9E+02	7.7E-09		
Eu-152					1.9E+02	2.7E-03		
Eu-154					1.9E+02	7.6E-04		
Gd-148					1.9E+02	2.0E-03		
Gd-150					1.9E+02	2.1E-08		
H-3	1.1E+02	3.0E-03						
I-129					1.9E+02	1.4E-08		
Kr-81					1.9E+02	2.6E-07		
Kr-85					1.9E+02	1.3E-02		
La-137					1.9E+02	4.2E-06		
Mo-93					1.9E+02	8.3E-05		
Nb-92					1.9E+02	2.5E-08		
Nb-94					1.9E+02	2.5E-05		
Pd-107					1.9E+02	3.6E-08		
Pu-238	2.5E+02	3.4E-03	4.6E+01	7.6E-02	2.0E+02	7.4E-01		
Pu-239	8.8E+02	1.7E-02	2.0E+02	1.6E+00	3.0E+02	1.1E+00		
Pu-240	1.1E+02	8.2E-04	2.1E+01	1.3E-02				
Pu-241	1.1E+02	1.2E-02	2.1E+01	2.0E-01				
Pu-242	1.1E+02	4.7E-08	2.1E+01	7.4E-07				
Se-79					1.9E+02	2.4E-08		
Sm-146					1.9E+02	1.9E-09		
Sm-147					1.9E+02	1.5E-12		
Sm-151					1.9E+02	6.5E-04		
Sr-90	2.1E+02	8.2E-03	5.4E+02	9.3E-02	2.6E+02	1.8E-02		
Tb-157					1.9E+02	2.4E-05		
Tb-158					1.9E+02	1.0E-05		
Tc-97					1.9E+02	1.9E-07		
Tc-99					1.9E+02	2.4E-06		
U-235	5.8E+02	1.5E-01			2.3E+02	7.5E-04		
U-238	3.3E+02	1.1E-01	1.3E+02	1.2E-03				
Zr-93					1.9E+02	2.6E-07		
Pit 27								
Ag-108m	3.7E+02	4.2E-05	1.3E+02	2.3E-05	9.8E+00	1.6E-08		
Am-241	2.0E+02	8.4E-08	3.7E+01	8.5E-06	1.1E+01	2.3E-09		
Ba-133	3.7E+02	1.5E-03	1.3E+02	8.2E-04	9.8E+00	5.8E-07		
Cd-113m	3.7E+02	1.7E-04	1.3E+02	9.4E-05	9.8E+00	6.5E-08		
Co-60	1.1E+02	1.8E+00					2.7E+01	8.4E-01

Table 3-8. Continued.

	Waste Form							
	Surface-Contaminated Waste		Soils		Concrete and Sludges		Bulk-Contaminated Waste	
Radionuclide	Volume (m^3)	Activity (Ci)	Volume (m^3)	Activity (Ci)	Volume (m^3)	Activity (Ci)	Volume (m^3)	Activity (Ci)
Cs-135	3.7E+02	7.9E-09	1.3E+02	4.3E-09	9.8E+00	3.0E-12		
Cs-137	4.8E+02	2.9E-04	1.3E+02	1.6E-04	9.8E+00	1.1E-07		
Dy-154	3.7E+02	2.8E-10	1.3E+02	1.5E-10	9.8E+00	1.1E-13		
Eu-152	3.7E+02	9.6E-05	1.3E+02	5.2E-05	9.8E+00	3.6E-08		
Eu-154	3.7E+02	2.7E-05	1.3E+02	1.5E-05	9.8E+00	1.0E-08		
Gd-148	3.7E+02	7.4E-05	1.3E+02	4.0E-05	9.8E+00	2.8E-08		
Gd-150	3.7E+02	7.7E-10	1.3E+02	4.2E-10	9.8E+00	2.9E-13		
H-3	4.8E+01	1.1E+02	4.2E-01	5.0E-04	3.8E+01	5.0E-04		
I-129	3.7E+02	5.2E-10	1.3E+02	2.8E-10	9.8E+00	2.0E-13		
Kr-81	3.7E+02	9.3E-09	1.3E+02	5.0E-09	9.8E+00	3.5E-12		
Kr-85	3.7E+02	4.6E-04	1.3E+02	2.5E-04	9.8E+00	1.7E-07		
La-137	3.7E+02	1.5E-07	1.3E+02	8.2E-08	9.8E+00	5.7E-11		
Mo-93	3.7E+02	3.0E-06	1.3E+02	1.6E-06	9.8E+00	1.1E-09		
Nb-92	3.7E+02	9.0E-10	1.3E+02	4.9E-10	9.8E+00	3.4E-13		
Nb-94	3.7E+02	9.0E-07	1.3E+02	4.9E-07	9.8E+00	3.4E-10		
Pd-107	3.7E+02	1.3E-09	1.3E+02	7.0E-10	9.8E+00	4.9E-13		
Pu-238	7.0E+02	4.9E-02	3.8E+01	6.9E-04	3.5E+00	4.3E-04		
Pu-239	1.4E+03	2.0E-02	1.8E+03	5.5E-01	8.7E+01	1.2E-02		
Pu-240	2.3E+02	6.7E-04						
Pu-241	2.3E+02	1.0E-02						
Pu-242	2.3E+02	3.9E-08						
Ra-226	1.5E+00	9.7E-02						
Se-79	3.7E+02	8.6E-10	1.3E+02	4.6E-10	9.8E+00	3.2E-13		
Si-32	9.1E+01	1.0E-03						
Sm-146	3.7E+02	7.0E-11	1.3E+02	3.8E-11	9.8E+00	2.6E-14		
Sm-147	3.7E+02	5.5E-14	1.3E+02	3.0E-14	9.8E+00	2.1E-17		
Sm-151	3.7E+02	2.4E-05	1.3E+02	1.3E-05	9.8E+00	8.9E-09		
Sr-90	4.9E+02	9.6E-04	5.7E+02	2.0E-03	1.2E+01	3.5E-04		
Tb-157	3.7E+02	8.6E-07	1.3E+02	4.7E-07	9.8E+00	3.3E-10		
Tb-158	3.7E+02	3.7E-07	1.3E+02	2.0E-07	9.8E+00	1.4E-10		
Tc-97	3.7E+02	7.0E-09	1.3E+02	3.8E-09	9.8E+00	2.6E-12		
Tc-99	3.7E+02	8.5E-08	1.3E+02	4.6E-08	9.8E+00	3.2E-11		
U-234	1.9E+01	1.9E-03	1.7E-02	4.5E-02				
U-235	1.1E+03	6.1E-03	6.2E+01	1.8E-03				
U-236	1.9E+01	9.5E-06						
U-238	5.7E+02	4.8E-01	1.8E+02	3.8E-01				
Zr-93	3.7E+02	9.5E-09	1.3E+02	5.2E-09	9.8E+00	3.6E-12		
Pit 28								
Am-241			3.0E+02	3.0E-06				
Co-60	6.2E+01	2.2E+00					1.6E+01	2.2E+00
H-3	9.8E+01	1.2E+03						
Pu-238	3.9E+02	1.7E-01	3.2E+02	7.5E-02	3.0E+01	7.5E-02		
Pu-239	9.9E+02	1.4E-01	1.2E+03	6.7E-02	1.6E+02	3.9E-02		
Pu-240	1.5E+02	6.2E-04						
Pu-241	1.5E+02	9.4E-03						
Pu-242	1.5E+02	3.6E-08						

Table 3-8. Continued.

	Waste Form							
	Surface-Contaminated Waste		Soils		Concrete and Sludges		Bulk-Contaminated Waste	
Radionuclide	Volume (m^3)	Activity (Ci)	Volume (m^3)	Activity (Ci)	Volume (m^3)	Activity (Ci)	Volume (m^3)	Activity (Ci)
Th-232	5.1E-01	2.3E-02						
U-235	5.4E+02	8.0E-03						
U-238	3.8E+02	6.6E-02	3.4E+01	4.5E-01				
Pit 29								
Ag-108m	4.0E+02	3.6E-02			2.0E+01	3.5E-07		
Am-241	3.4E+02	6.3E-04	1.3E+02	1.2E+00	7.8E+01	2.0E+00		
Ba-133	4.0E+02	1.3E+00			2.0E+01	1.3E-05		
C-14	2.9E+00	2.1E-01						
Cd-113m	4.0E+02	1.5E-01			2.0E+01	1.4E-06		
Co-60	2.4E+02	1.0E-01	2.2E+02	1.6E-03	1.3E+01	1.7E-05	1.8E+02	1.2E-01
Cs-135	4.0E+02	6.6E-06			2.0E+01	6.5E-11		
Cs-137	5.4E+02	8.8E+02	5.5E+02	4.4E-03	4.2E+01	2.9E-03		
Dy-154	4.0E+02	2.3E-07			2.0E+01	2.3E-12		
Eu-152	4.0E+02	8.1E-02			2.0E+01	8.0E-07		
Eu-154	4.0E+02	2.3E-02			2.0E+01	2.3E-07		
Gd-148	4.0E+02	6.2E-02			2.0E+01	6.1E-07		
Gd-150	4.0E+02	6.5E-07			2.0E+01	6.4E-12		
H-3	2.1E+02	5.8E-01						
I-129	4.0E+02	4.4E-07			2.0E+01	4.3E-12		
Kr-81	4.0E+02	7.8E-06			2.0E+01	7.7E-11		
Kr-85	4.0E+02	3.8E-01			2.0E+01	3.8E-06		
La-137	4.0E+02	1.3E-04			2.0E+01	1.2E-09		
Mo-93	4.0E+02	2.5E-03			2.0E+01	2.5E-08		
Nb-92	4.0E+02	7.6E-07			2.0E+01	7.5E-12		
Nb-94	4.0E+02	7.6E-04			2.0E+01	7.5E-09		
Np-237	1.5E+01	7.1E-07						
Pd-107	4.0E+02	1.1E-06			2.0E+01	1.1E-11		
Pu-238	1.0E+03	5.6E-02	2.7E+02	1.1E+00	1.5E+02	3.5E-01		
Pu-239	2.1E+03	2.3E-01	6.1E+02	3.8E-03	1.9E+02	4.9E-01		
Pu-240	5.8E+02	3.5E-02	7.4E+01	1.7E-03	7.4E+01	1.7E-03		
Pu-241	5.9E+02	5.6E-01	7.4E+01	5.4E-02	7.4E+01	5.4E-02		
Pu-242	5.8E+02	2.6E-06	7.4E+01	5.6E-07	7.4E+01	5.6E-07		
Se-79	4.0E+02	7.2E-07			2.0E+01	7.1E-12		
Sm-146	4.0E+02	5.8E-08			2.0E+01	5.8E-13		
Sm-147	4.0E+02	4.5E-11			2.0E+01	4.5E-16		
Sm-151	4.0E+02	2.0E-02			2.0E+01	1.9E-07		
Sr-90	5.3E+02	1.4E+03	4.2E+02	8.9E-02	2.0E+01	4.9E-06		
Tb-157	4.0E+02	7.2E-04			2.0E+01	7.1E-09		
Tb-158	4.0E+02	3.1E-04			2.0E+01	3.0E-09		
Tc-97	4.0E+02	5.8E-06			2.0E+01	5.8E-11		
Tc-99	4.0E+02	7.1E-05			2.0E+01	7.0E-10		
Th-232	1.9E-03	4.9E-05						
U-233	3.5E+00	1.9E-02						
U-234	4.0E+01	3.9E-02						
U-235	7.8E+02	2.4E-01			5.9E+01	5.3E-03		
U-236	4.0E+01	4.5E-05						

Table 3-8. Continued.

	Waste Form							
	Surface-Contaminated Waste		Soils		Concrete and Sludges		Bulk-Contaminated Waste	
Radionuclide	Volume (m^3)	Activity (Ci)	Volume (m^3)	Activity (Ci)	Volume (m^3)	Activity (Ci)	Volume (m^3)	Activity (Ci)
U-238	9.8E+02	1.4E-01	7.3E+02	7.8E-01	1.7E+01	6.3E-05		
Zr-93	4.0E+02	8.0E-06			2.0E+01	7.9E-11		
Pit 32								
Ag-108m	2.9E+02	4.4E-03						
Am-241	2.0E+02	6.0E-02	9.9E+00	3.0E-03	1.3E+02	2.1E+00		
Ba-133	2.9E+02	1.6E-01						
C-14	3.2E+00	1.5E-06						
Cd-113m	2.9E+02	1.8E-02						
Co-60	3.0E+02	2.0E-01	4.1E+00	3.3E-01	3.6E+00	3.3E-05	1.6E+02	1.3E-01
Cs-135	2.9E+02	8.2E-07						
Cs-137	3.0E+02	3.5E-02	3.4E+02	2.1E-03				
Dy-154	2.9E+02	2.9E-08						
Eu-152	2.9E+02	1.0E-02						
Eu-154	2.9E+02	2.9E-03						
Gd-148	2.9E+02	7.7E-03						
Gd-150	2.9E+02	8.1E-08						
H-3	2.0E+02	1.5E+00						
I-129	2.9E+02	5.5E-08						
Kr-81	2.9E+02	9.7E-07						
Kr-85	2.9E+02	4.8E-02						
La-137	2.9E+02	1.6E-05						
Mo-93	2.9E+02	3.1E-04						
Nb-92	2.9E+02	9.5E-08						
Nb-94	2.9E+02	9.5E-05						
Pd-107	2.9E+02	1.3E-07						
Pu-238	7.3E+02	2.2E-02	9.2E+01	1.5E-04	2.1E+02	1.5E+00		
Pu-239	1.5E+03	1.3E-01	3.9E+02	7.3E-02	2.3E+02	3.4E+00		
Pu-240	5.0E+02	6.8E-03	8.6E+01	7.4E-04	7.8E+01	7.2E-04		
Pu-241	5.0E+02	1.1E-01	7.8E+01	1.3E-02	7.8E+01	1.3E-02		
Pu-242	5.0E+02	4.7E-07	7.8E+01	8.1E-08	7.8E+01	8.1E-08		
Ra-226	1.3E-01	1.0E-05						
Se-79	2.9E+02	8.9E-08						
Sm-146	2.9E+02	7.3E-09						
Sm-147	2.9E+02	5.7E-12						
Sm-151	2.9E+02	2.5E-03						
Sr-90	2.9E+02	6.3E-02	2.6E-01	3.1E-04	5.7E-02	2.8E-04		
Tb-157	2.9E+02	9.0E-05						
Tb-158	2.9E+02	3.9E-05						
Tc-97	2.9E+02	7.3E-07						
Tc-99	2.9E+02	8.9E-06						
Th-230	4.2E-02	2.6E-09			—			
Th-232	1.4E-01	1.0E-09						
U-234	6.4E+01	2.1E-02						
U-235	4.6E+02	3.5E-03			5.1E+00	3.2E-05		
U-236	6.4E+01	6.8E-05						

Table 3-8. Continued.

	Waste Form							
	Surface-Contaminated Waste		Soils		Concrete and Sludges		Bulk-Contaminated Waste	
Radionuclide	Volume (m^3)	Activity (Ci)	Volume (m^3)	Activity (Ci)	Volume (m^3)	Activity (Ci)	Volume (m^3)	Activity (Ci)
U-238	6.1E+02	4.1E-01	2.4E+02	3.4E-03				
Zr-93	2.9E+02	1.0E-06						
Pit 33								
Ag-108m	4.8E+02	2.6E-02						
Am-241	4.3E+02	9.5E-01			9.8E+01	9.7E-01		
Ba-133	4.8E+02	9.3E-01						
C-14	1.2E+01	1.5E-02						
Cd-113m	4.8E+02	1.1E-01						
Co-60	2.2E+02	5.9E-01	1.1E+00	8.3E-06	1.1E+00	8.3E-06	1.1E+02	4.4E-01
Cs-135	4.8E+02	4.8E-06						
Cs-137	4.8E+02	1.6E+00	1.5E+00	5.0E-07				
Dy-154	4.8E+02	1.7E-07						
Eu-152	4.8E+02	5.9E-02						
Eu-154	4.8E+02	1.7E-02						
Gd-148	4.8E+02	4.5E-02						
Gd-150	4.8E+02	4.7E-07						
H-3	3.0E+02	4.0E+00	3.2E+01	5.9E-03	1.5E+02	2.6E-03		
I-129	4.8E+02	3.2E-07						
Kr-81	4.8E+02	5.7E-06						
Kr-85	4.8E+02	2.8E-01						
La-137	4.8E+02	9.2E-05						
Mo-93	4.8E+02	1.8E-03						
Nb-92	4.8E+02	5.5E-07						
Nb-94	4.8E+02	5.5E-04						
Pd-107	4.8E+02	7.8E-07						
Pu-238	8.9E+02	1.7E-02	3.6E+01	6.0E-06	1.1E+02	4.4E-02		
Pu-239	1.9E+03	1.4E+00	2.6E+02	5.4E-01	1.7E+02	2.5E-01		
Pu-240	3.5E+02	5.5E-03						
Pu-241	3.5E+02	8.4E-02						
Pu-242	3.5E+02	3.2E-07						
Se-79	4.8E+02	5.2E-07						
Sm-146	4.8E+02	4.2E-08						
Sm-147	4.8E+02	3.2E-11						
Sm-151	4.8E+02	1.4E-02						
Sr-90	4.8E+02	4.9E-01	2.5E+00	1.2E-05				
Tb-157	4.8E+02	5.3E-04						
Tb-158	4.8E+02	2.2E-04						
Tc-97	4.8E+02	4.2E-06						
Tc-99	4.8E+02	5.2E-05						
Th-232	2.3E-02	2.6E-03						
U-234	4.8E+02		5.7E-03	6.3E-04				
U-235	1.5E+03	1.1E-02	6.9E+01	2.5E-05	7.0E+01	1.3E-05		
U-238	9.9E+02	6.2E-01	5.4E+02	1.5E-01	2.2E+01	2.0E-05		
Zr-93	4.8E+02	5.8E-06						

Table 3-8. Continued.

	Waste Form							
	Surface-Contaminated Waste		Soils		Concrete and Sludges		Bulk-Contaminated Waste	
Radionuclide	Volume (m^3)	Activity (Ci)	Volume (m^3)	Activity (Ci)	Volume (m^3)	Activity (Ci)	Volume (m^3)	Activity (Ci)
Pit 35								
Ag-108m	1.4E+02	1.8E-02						
Am-241	1.1E+02	7.5E-05			2.8E+01	4.3E-01		
Ba-133	1.4E+02	6.4E-01						
Cd-113m	1.4E+02	7.3E-02						
Co-60	2.8E+02	2.1E+00	3.5E+01	6.6E-05	1.6E+01	8.3E-09	1.1E+02	1.3E-01
Cs-135	1.4E+02	3.3E-06						
Cs-137	1.4E+02	1.2E-01						
Dy-154	1.4E+02	1.2E-07						
Eu-152	1.4E+02	4.1E-02						
Eu-154	1.4E+02	1.2E-02						
Gd-148	1.4E+02	3.1E-02						
Gd-150	1.4E+02	3.2E-07						
H-3	8.1E+01	1.2E+00						
I-129	1.4E+02	2.2E-07						
Kr-81	1.4E+02	3.9E-06						
Kr-85	1.4E+02	1.9E-01						
La-137	1.4E+02	6.3E-05						
Mo-93	1.4E+02	1.3E-03						
Nb-92	1.4E+02	3.8E-07						
Nb-94	1.4E+02	3.8E-04						
Pd-107	1.4E+02	5.4E-07						
Pu-238	5.9E+02	4.3E-04	9.4E+01	2.8E-03	2.9E+01	3.1E-01		
Pu-239	9.7E+02	3.3E-02	9.4E+01	9.6E-02	4.8E+01	9.1E-01		
Pu-240	3.8E+02	2.4E-03	9.4E+01	2.2E-02				
Pu-241	3.8E+02	3.7E-02	9.4E+01	3.4E-01				
Pu-242	3.8E+02	1.4E-07	9.4E+01	1.3E-06				
Se-79	1.4E+02	3.6E-07						
Si-32	7.3E+00	1.0E-08						
Sm-146	1.4E+02	2.9E-08						
Sm-147	1.4E+02	2.3E-11						
Sm-151	1.4E+02	9.9E-03						
Sr-90	1.4E+02	2.5E-01						
Tb-157	1.4E+02	3.6E-04						
Tb-158	1.4E+02	1.6E-04						
Tc-97	1.4E+02	2.9E-06						
Tc-99	1.4E+02	3.6E-05						
U-235	3.5E+02	1.2E-03						
U-238	3.1E+02	5.7E-02	4.7E+02	1.0E-01				
Zr-93	1.4E+02	4.0E-06						
Pit 36								
Ag-108m	1.5E+02	2.5E-03						
Am-241	5.8E+01	8.7E-05			1.9E+01	1.3E-01		
Ba-133	1.5E+02	9.1E-02						
Cd-113m	1.5E+02	1.0E-02						
Co-60	5.2E+02	8.7E-02					9.4E+01	4.7E-02

Table 3-8. Continued.

	Waste Form							
	Surface-Contaminated Waste		Soils		Concrete and Sludges		Bulk-Contaminated Waste	
Radionuclide	Volume (m^3)	Activity (Ci)	Volume (m^3)	Activity (Ci)	Volume (m^3)	Activity (Ci)	Volume (m^3)	Activity (Ci)
Cs-135	1.5E+02	4.7E-07						
Cs-137	1.6E+02	1.9E-02						
Dy-154	1.5E+02	1.7E-08						
Eu-152	1.5E+02	5.8E-03						
Eu-154	1.5E+02	1.6E-03						
Gd-148	1.5E+02	4.4E-03						
Gd-150	1.5E+02	4.6E-08						
H-3	6.6E+01	3.0E+01						
I-129	1.5E+02	3.1E-08						
Kr-81	1.5E+02	5.6E-07						
Kr-85	1.5E+02	2.7E-02						
La-137	1.5E+02	9.0E-06						
Mo-93	1.5E+02	1.8E-04						
Nb-92	1.5E+02	5.4E-08						
Nb-94	1.5E+02	6.2E-05						
Pd-107	1.5E+02	7.7E-08						
Pu-238	5.5E+02	2.6E-02	5.2E+01	4.0E-04	5.3E+01	6.1E-02		
Pu-239	9.3E+02	8.4E-02	1.1E+02	1.4E-02	7.1E+01	3.8E-01		
Pu-240	4.2E+02	1.7E-02	5.2E+01	3.2E-03				
Pu-241	4.2E+02	2.5E-01	5.2E+01	4.8E-02				
Pu-242	4.2E+02	9.6E-07	5.2E+01	8.0E-06				
Se-79	1.5E+02	5.1E-08						
Sm-146	1.5E+02	4.2E-09						
Sm-147	1.5E+02	3.2E-12						
Sm-151	1.5E+02	1.4E-03						
Sr-90	1.5E+02	3.6E-02						
Tb-157	1.5E+02	5.2E-05						
Tb-158	1.5E+02	2.2E-05						
Tc-97	1.5E+02	4.2E-07						
Tc-99	1.5E+02	5.1E-06						
U-234	2.3E+00	7.9E-04						
U-235	4.3E+02	4.8E-02	1.4E+01	5.7E-07	1.9E+01	5.7E-07		
U-236	2.3E+00	3.4E-06						
U-238	3.0E+02	3.1E-03	1.1E+02	1.5E-06	1.1E+01	2.9E-07		
Zr-93	1.5E+02	5.7E-07						

Table 3-9. Shaft radionuclide inventories for 1971 through September 25, 1988.

	Waste Form							
	Surface-Contaminated Waste		Soils		Concrete and Sludges		Bulk-Contaminated Waste	
Radionuclide	Volume (m^3)	Activity (Ci)	Volume (m^3)	Activity (Ci)	Volume (m^3)	Activity (Ci)	Volume (m^3)	Activity (Ci)
Ag-108m	2.6E+01	1.5E+01						
Am-241	4.6E+00	4.0E+02						
Am-243	2.6E-02	1.1E-05						
Ba-133	2.6E+01	5.5E+02						
C14	5.8E+00	1.1E+00						
Cd-113m	2.6E+01	6.3E+01						
Cf-252	3.3E-01	5.5E+01						
Cm-244	3.9E-01	1.9E-01						
Co-60	1.5E+02	3.0E+03					1.2E+02	2.2E+02
Cs-135	2.6E+01	2.8E-03						
Cs-137	2.7E+01	1.5E+02						
Dy-154	2.6E+01	1.0E-04						
Eu-152	2.6E+01	3.5E+01						
Eu-154	2.6E+01	9.9E+00						
Gd-148	2.6E+01	2.7E+01						
Gd-150	2.6E+01	2.8E-04						
H-3	1.4E+02	8.0E+05	1.1E-01	1.0E+02	5.3E-01	1.0E+02		
Hf-182	2.8E-02	3.1E+01						
I-129	2.6E+01	1.9E-04						
Kr-81	2.6E+01	3.4E-03						
Kr-85	2.9E+01	1.7E+02						
La-137	2.6E+01	5.5E-02						
Mo-93	2.6E+01	1.1E+00						
Nb-92	2.6E+01	3.3E-04						
Nb-94	2.6E+01	3.3E-01						
Ni-63	3.8E+00	4.3E-03						
Np-237	9.2E-02	7.8E-05						
Pd-107	2.6E+01	4.7E-04						
Pu-238	1.2E+02	1.4E+00						
Pu-239	1.6E+02	9.8E+01						
Pu-240	1.3E+01	3.7E+00						
Pu-241	1.3E+01	5.6E+01						
Pu-242	1.3E+01	2.1E-04						
Pu-244	1.9E+00	0.0E+00						
Ra-226	1.4E+00	2.5E+00						
Se-79	2.6E+01	3.1E-04						
Sm-146	2.6E+01	2.5E-05						
Sm-147	2.8E+01	2.0E-08						
Sm-151	2.6E+01	8.5E+00						
Sr-90	2.7E+01	2.2E+02						
Tb-157	2.6E+01	3.1E-01						
Tb-158	2.6E+01	1.3E-01						
Tc-97	2.6E+01	2.5E-03						
Tc-99	2.6E+01	3.1E-02						
Th-232	1.2E+01	1.9E-02						
U-232	3.8E-03	2.1E-01						

Table 3-9. Continued.

	Waste Form							
	Surface-Contaminated Waste		Soils		Concrete and Sludges		Bulk-Contaminated Waste	
Radionuclide	Volume (m^3)	Activity (Ci)	Volume (m^3)	Activity (Ci)	Volume (m^3)	Activity (Ci)	Volume (m^3)	Activity (Ci)
U-233	4.1E-01	4.0E+00						
U-234	2.5E+01	4.7E-01	6.2E+00	2.8E-02				
U-235	9.9E+01	9.9E-01	6.2E+00	1.1E-03				
U-236	7.6E-01	1.9E-04						
U-238	1.6E+02	1.1E+01	8.0E+00	1.8E-01				
Zr-93	2.6E+01	3.5E-03						

TRU waste was non-retrievably disposed of in Pits 6, 7, 8, 20, and 22 and several shafts at Area G between 1971 and 1979. Table 3-10 lists the total volumes and activities of this waste (excluding waste placed in Pit 6) for the four waste forms. Radionuclide-specific inventories for the waste are listed in Table 3-11. In each case, individual totals are reported for the affected pits, while inventory data are summed over the shafts. These TRU waste data are included in Tables 3-7 through 3-9.

The activities listed in Tables 3-8 and 3-9 are the as-disposed activities for radionuclides with half-lives greater than 5 years or radionuclides with parents or daughters with half-lives greater than 5 years. The radionuclides eliminated from the inventory projections based on half-life are listed in Appendix A.

3.1.3 September 26, 1988, to 1995 Inventory

Seven pits and approximately 40 shafts were used for disposal of waste between September 26, 1988, and the end of 1995. The total volumes and activities of LLW placed in these units during this period are listed in Table 3-12. Inventories for the four waste forms are reported for each disposal pit, while inventories are summed over the shafts. As discussed earlier, all but one shipment of waste was placed in Pit 32 prior to September 26, 1988. The entire inventory for this unit is included in the 1971 to September 25, 1988, period (Section 3.1.2). The inventories listed for Pit 36 and the shafts include only the waste that was disposed of on or following September 26, 1988.

Radionuclide inventories for the waste disposed of between September 26, 1988, and the end of 1995 are listed in Tables 3-13 and 3-14 for pits and shafts, respectively. Separate inventories are listed for the pits used during this period, while shaft inventories are summed over all of the individual units. The volumes listed in these tables represent the quantities of waste contaminated with the respective radionuclides. Because several radionuclides may occur in a single waste package, the sum of the volumes is greater than the total volume of waste disposed of in the pits and shafts. The listed activities include contributions from MAP, MFP, and the material types discussed in Section 2.1.

Table 3-10. Quantities of TRU waste that was non-retrievably disposed of between 1971 and September 25, 1988.

Disposal Unit/Waste Form	Total Disposal Volume (m^3)	Total Disposal Activity (Ci)
Pit 7		
Surface-Contaminated Waste		
Soils		
Concrete and Sludges	1.9E+00	6.6E-02
Bulk-Contaminated Waste		
Pit 8		
Surface-Contaminated Waste		
Soils		
Concrete and Sludges	5.8E+01	7.1E+00
Bulk-Contaminated Waste		
Pit 20		
Surface-Contaminated Waste	8.5E-02	1.6E-03
Soils		
Concrete and Sludges		
Bulk-Contaminated Waste		
Pit 22		
Surface-Contaminated Waste	1.1E+01	6.0E+02
Soils		
Concrete and Sludges		
Bulk-Contaminated Waste		
Shafts		
Surface-Contaminated Waste	4.4E+00	2.8E+03
Soils		
Concrete and Sludges		
Bulk-Contaminated Waste		

Table 3-11. Radionuclide inventories in TRU waste that was non-retrievably disposed of between 1971 and September 25, 1988.

	Waste Form							
	Surface-Contaminated Waste		Soils		Concrete and Sludges		Bulk-Contaminated Waste	
Radionuclide	Volume (m^3)	Activity (Ci)	Volume (m^3)	Activity (Ci)	Volume (m^3)	Activity (Ci)	Volume (m^3)	Activity (Ci)
Pit 7								
Pu-238					1.9E+00	6.2E-02		
Pu-239					1.9E+00	3.8E-03		
U-235					1.9E+00	4.9E-05		
Pit 8								
Am-241					4.2E+01	9.3E-01		
Pu-238					5.5E+01	3.6E+00		
Pu-239					5.8E+01	2.6E+00		
Pit 20								
Cf-251	8.5E-02	1.6E-03						
Pit 22								
Ag-108m	1.1E+01	1.2E+00						
Am-241	2.1E-01	3.4E-03						
Ba-133	1.1E+01	4.5E+01						
Cd-113m	1.1E+01	5.1E+00						
Cs-135	1.1E+01	2.3E-04						
Cs-137	1.1E+01	8.4E+00						
Dy-154	1.1E+01	8.2E-06						
Eu-152	1.1E+01	2.8E+00						
Eu-154	1.1E+01	8.0E-01						
Gd-148	1.1E+01	2.2E+00						
Gd-150	1.1E+01	2.3E-05						
I-129	1.1E+01	1.5E-05						
Kr-81	1.1E+01	2.7E-04						
Kr-85	1.1E+01	1.3E+01						
La-137	1.1E+01	4.4E-03						
Mo-93	1.1E+01	8.8E-02						
Nb-92	1.1E+01	2.7E-05						
Nb-94	1.1E+01	2.7E-02						
Pd-107	1.1E+01	3.8E-05						
Pu-239	1.1E+01	9.3E-01						
Se-79	1.1E+01	2.5E-05						
Sm-146	1.1E+01	2.0E-06						
Sm-147	1.1E+01	1.6E-09						
Sm-151	1.1E+01	6.9E-01						
Sr-90	1.1E+01	1.7E+01						
Tb-157	1.1E+01	2.5E-02						
Tb-158	1.1E+01	1.1E-02						
Tc-97	1.1E+01	2.0E-04						
Tc-99	1.1E+01	2.5E-03						
U-235	1.1E+01	9.6E-05						
Zr-93	1.1E+01	2.8E-04						

Table 3-11. Continued.

	Waste Form							
	Surface-Contaminated Waste		Soils		Concrete and Sludges		Bulk-Contaminated Waste	
Radionuclide	Volume (m^3)	Activity (Ci)	Volume (m^3)	Activity (Ci)	Volume (m^3)	Activity (Ci)	Volume (m^3)	Activity (Ci)
Shafts								
Ag-108m	2.0E+00	5.4E+00						
Am-241	2.8E-02	3.4E-03						
Ba-133	2.0E+00	1.9E+02						
Cd-113m	2.0E+00	2.2E+01						
Cm-244	1.9E-03	2.3E-04						
Cs-135	2.0E+00	1.0E-03						
Cs-137	2.0E+00	3.7E+01						
Dy-154	2.0E+00	3.6E-05						
Eu-152	2.0E+00	1.2E+01						
Eu-154	2.0E+00	3.5E+00						
Gd-148	2.0E+00	9.4E+00						
Gd-150	2.0E+00	9.9E-05						
H-3	1.1E+00	0.0E+00						
I-129	2.0E+00	6.7E-05						
Kr-81	2.0E+00	1.2E-03						
Kr-85	2.0E+00	5.8E+01						
La-137	2.0E+00	1.9E-02						
Mo-93	2.0E+00	3.8E-01						
Nb-92	2.0E+00	1.2E-04						
Nb-94	2.0E+00	1.2E-01						
Np-237	4.5E-02	7.1E-06						
Pd-107	2.0E+00	1.6E-04						
Pu-238	2.1E+00	6.3E-01						
Pu-239	4.3E+00	9.7E+01						
Pu-240	1.9E+00	3.7E+00						
Pu-241	1.9E+00	5.6E+01						
Pu-242	1.9E+00	2.1E-04						
Pu-244	1.9E+00	0.0E+00						
Se-79	2.0E+00	1.1E-04						
Sm-146	2.0E+00	8.9E-06						
Sm-147	2.0E+00	7.0E-09						
Sm-151	2.0E+00	3.0E+00						
Sr-90	2.0E+00	7.6E+01						
Tb-157	2.0E+00	1.1E-01						
Tb-158	2.0E+00	4.7E-02						
Tc-97	2.0E+00	8.9E-04						
Tc-99	2.0E+00	1.1E-02						
U-233	4.5E-02	9.6E-04						
U-234	6.8E-02	2.1E-02						
U-235	1.9E+00	5.1E-03						
U-236	1.1E-02	8.9E-05						
U-238	1.1E-01	2.1E-03						
Zr-93	2.0E+00	1.2E-03						

Table 3-12. Pit and shaft waste volumes and activities disposed of from September 26, 1988, to 1995.

Disposal Unit/Waste Form	Total Disposal Volume (m^3)	Total Disposal Activity (Ci)
Pit 30		
Surface-Contaminated Waste	7.5E+03	3.1E+01
Soils	1.7E+03	2.3E+00
Concrete and Sludges	3.7E+02	6.9E-01
Bulk-Contaminated Waste	5.7E+02	2.9E+00
Pit 31		
Surface-Contaminated Waste	2.6E+02	6.6E-02
Soils	1.1E+02	3.3E-02
Concrete and Sludges	1.1E+02	3.3E-02
Bulk-Contaminated Waste	0.0E+00	0.0E+00
Pit 36		
Surface-Contaminated Waste	7.0E+02	1.3E+00
Soils	2.5E+02	1.5E-01
Concrete and Sludges	5.9E+01	1.5E-01
Bulk-Contaminated Waste	3.4E+01	3.9E-01
Pit 37		
Surface-Contaminated Waste	1.2E+04	7.1E+01
Soils	2.1E+03	3.3E+00
Concrete and Sludges	3.9E+02	1.7E+00
Bulk-Contaminated Waste	3.8E+02	3.8E+00
Pit 38		
Surface-Contaminated Waste	8.1E+02	2.8E+01
Soils	1.0E+02	3.8E-02
Concrete and Sludges	1.1E+02	2.2E+00
Bulk-Contaminated Waste	0.0E+00	0.0E+00
Pit 39		
Surface-Contaminated Waste	1.5E+03	1.6E+00
Soils	4.4E+02	1.3E-02
Concrete and Sludges	1.9E+02	6.4E-01
Bulk-Contaminated Waste	0.0E+00	0.0E+00

Table 3-12. Continued.

Disposal Unit/Waste Form	Total Disposal Volume (m^3)	Total Disposal Activity (Ci)
Shafts		
Surface-Contaminated Waste	2.1E+02	4.5E+05
Soils	1.3E+01	2.7E-07
Concrete and Sludges	2.6E+01	4.2E-01
Bulk-Contaminated Waste	2.8E+01	2.8E+03

Table 3-13. Pit radionuclide inventories for September 26, 1988, through 1995.

	Waste Form							
	Surface-Contaminated Waste		Soils		Concrete and Sludges		Bulk-Contaminated Waste	
Radionuclide	Volume (m^3)	Activity (Ci)	Volume (m^3)	Activity (Ci)	Volume (m^3)	Activity (Ci)	Volume (m^3)	Activity (Ci)
Pit 30								
Ag-108m	6.9E+02	3.5E-02	4.3E+01	2.4E-06	1.9E+01	1.6E-06		
Am-241	6.6E+02	7.7E-03	1.6E+01	2.6E-07	4.6E+00	2.6E-07		
Ba-133	6.9E+02	1.3E+00	4.3E+01	8.8E-05	1.9E+01	5.8E-05		
C-14	2.9E+01	2.0E-09						
Cd-113m	6.9E+02	1.4E-01	4.3E+01	1.0E-05	1.9E+01	6.6E-06		
Co-60	1.9E+03	5.5E-01	2.2E+02	1.8E-01	1.2E+02	1.8E-01	5.7E+02	9.6E-02
Cs-135	6.9E+02	6.5E-06	4.3E+01	4.5E-10	1.9E+01	3.0E-10		
Cs-137	1.1E+03	1.1E+00	1.8E+02	4.1E-01	1.5E+02	4.1E-01		
Dy-154	6.9E+02	2.3E-07	4.3E+01	1.6E-11	1.9E+01	1.1E-11		
Eu-152	6.9E+02	8.0E-02	4.3E+01	5.5E-06	1.9E+01	3.7E-06		
Eu-154	6.9E+02	2.3E-02	4.3E+01	1.6E-06	1.9E+01	1.0E-06		
Gd-148	6.9E+02	6.1E-02	4.3E+01	4.2E-06	1.9E+01	2.8E-06		
Gd-150	6.9E+02	6.4E-07	4.3E+01	4.4E-11	1.9E+01	2.9E-11		
H-3	2.1E+02	8.6E-01	4.0E+00	7.2E-04				
I-129	6.9E+02	4.3E-07	4.3E+01	3.0E-11	1.9E+01	2.0E-11		
Kr-81	6.9E+02	7.7E-06	4.3E+01	5.3E-10	1.9E+01	3.5E-10		
Kr-85	6.9E+02	4.2E-01	4.3E+01	2.6E-05	1.9E+01	1.7E-05		
La-137	6.9E+02	1.2E-04	4.3E+01	8.7E-09	1.9E+01	5.7E-09		
Mo-93	6.9E+02	2.5E-03	4.3E+01	1.7E-07	1.9E+01	1.1E-07		
Nb-92	6.9E+02	7.5E-07	4.3E+01	5.2E-11	1.9E+01	3.4E-11		
Nb-94	6.9E+02	7.5E-04	4.3E+01	5.2E-08	1.9E+01	3.4E-08		
Ni-63	8.5E-02	1.0E-05						
Pd-107	6.9E+02	1.1E-06	4.3E+01	7.4E-11	1.9E+01	4.9E-11		
Pu-238	8.6E+02	3.6E-03	2.5E+02	1.6E+00				
Pu-239	3.0E+03	2.6E-01	1.0E+02	2.7E-03	7.6E+01	2.7E-03		
Pu-240	6.7E+02	2.9E-02						
Pu-241	6.7E+02	4.3E-01						
Pu-242	6.7E+02	1.7E-06						
Ra-226	1.3E+01	1.0E-03						
Se-79	6.9E+02	7.1E-07	4.3E+01	4.9E-11	1.9E+01	3.3E-11		
Si-32	5.6E+01	2.1E+00						
Sm-146	6.9E+02	5.8E-08	4.3E+01	4.0E-12	1.9E+01	2.7E-12		
Sm-147	6.9E+02	4.5E-11	4.3E+01	3.2E-15	1.9E+01	2.1E-15		
Sm-151	6.9E+02	1.9E-02	4.3E+01	1.4E-06	1.9E+01	9.0E-07		
Sr-90	7.4E+02	5.6E-01	5.6E+01	3.3E-02	3.2E+01	3.3E-02		
Tb-157	6.9E+02	7.1E-04	4.3E+01	5.0E-08	1.9E+01	3.3E-08		
Tb-158	6.9E+02	3.1E-04	4.3E+01	2.1E-08	1.9E+01	1.4E-08		
Tc-97	6.9E+02	5.8E-06	4.3E+01	4.0E-10	1.9E+01	2.7E-10		
Tc-99	6.9E+02	7.0E-05	4.3E+01	4.9E-09	1.9E+01	3.2E-09		
Th-232	3.5E+00	3.7E-02						
U-234	1.1E+01	2.9E-02						
U-235	1.3E+03	4.1E-01	6.6E+01	5.5E-02	5.4E+01	5.5E-02		
U-236	2.8E-02	1.2E-04						
U-238	1.2E+03	3.5E+00	2.0E+02	3.5E-03	1.5E+01	2.5E-03		
Zr-93	6.9E+02	7.9E-06	4.3E+01	5.5E-10	1.9E+01	3.6E-10		

Table 3-13. Continued.

	Waste Form							
	Surface-Contaminated Waste		Soils		Concrete and Sludges		Bulk-Contaminated Waste	
Radionuclide	Volume (m^3)	Activity (Ci)	Volume (m^3)	Activity (Ci)	Volume (m^3)	Activity (Ci)	Volume (m^3)	Activity (Ci)
Pit 31								
Ag-108m	7.5E+01	2.0E-08	3.7E+01	9.8E-09	3.7E+01	9.8E-09		
Ba-133	7.5E+01	7.1E-07	3.7E+01	3.5E-07	3.7E+01	3.5E-07		
C-14	3.3E+00	3.4E-09	1.6E+00	1.7E-09	1.6E+00	1.7E-09		
Cd-113m	7.5E+01	8.0E-08	3.7E+01	4.0E-08	3.7E+01	4.0E-08		
Co-60	3.1E+00	1.7E-09	1.6E+00	8.3E-10	1.6E+00	8.3E-10		
Cs-135	7.5E+01	3.7E-12	3.7E+01	1.8E-12	3.7E+01	1.8E-12		
Cs-137	8.4E+01	1.4E-07	4.2E+01	6.8E-08	4.2E+01	6.8E-08		
Dy-154	7.5E+01	1.3E-13	3.7E+01	6.5E-14	3.7E+01	6.5E-14		
Eu-152	7.5E+01	4.5E-08	3.7E+01	2.2E-08	3.7E+01	2.2E-08		
Eu-154	7.5E+01	1.3E-08	3.7E+01	6.4E-09	3.7E+01	6.4E-09		
Gd-148	7.5E+01	3.4E-08	3.7E+01	1.7E-08	3.7E+01	1.7E-08		
Gd-150	7.5E+01	3.6E-13	3.7E+01	1.8E-13	3.7E+01	1.8E-13		
H-3	9.5E+00	1.1E-09	4.3E+00	5.5E-10	4.3E+00	5.5E-10		
I-129	7.5E+01	2.4E-13	3.7E+01	1.2E-13	3.7E+01	1.2E-13		
Kr-81	7.5E+01	4.3E-12	3.7E+01	2.2E-12	3.7E+01	2.2E-12		
Kr-85	7.5E+01	2.1E-07	3.7E+01	1.1E-07	3.7E+01	1.1E-07		
La-137	7.5E+01	7.0E-11	3.7E+01	3.5E-11	3.7E+01	3.5E-11		
Mo-93	7.5E+01	1.4E-09	3.7E+01	7.0E-10	3.7E+01	7.0E-10		
Nb-92	7.5E+01	4.2E-13	3.7E+01	2.1E-13	3.7E+01	2.1E-13		
Nb-94	7.5E+01	4.2E-10	3.7E+01	2.1E-10	3.7E+01	2.1E-10		
Pd-107	7.5E+01	6.0E-13	3.7E+01	3.0E-13	3.7E+01	3.0E-13		
Pu-239	7.1E+01	6.5E-02	2.2E+01	3.3E-02	2.2E+01	3.3E-02		
Se-79	7.5E+01	4.0E-13	3.7E+01	2.0E-13	3.7E+01	2.0E-13		
Sm-146	7.5E+01	3.2E-14	3.7E+01	1.6E-14	3.7E+01	1.6E-14		
Sm-147	7.5E+01	2.5E-17	3.7E+01	1.3E-17	3.7E+01	1.3E-17		
Sm-151	7.5E+01	1.1E-08	3.7E+01	5.5E-09	3.7E+01	5.5E-09		
Sr-90	8.4E+01	6.9E-06	4.2E+01	3.4E-06	4.2E+01	3.4E-06		
Tb-157	7.5E+01	4.0E-10	3.7E+01	2.0E-10	3.7E+01	2.0E-10		
Tb-158	7.5E+01	1.7E-10	3.7E+01	8.6E-11	3.7E+01	8.6E-11		
Tc-97	7.5E+01	3.2E-12	3.7E+01	1.6E-12	3.7E+01	1.6E-12		
Tc-99	8.3E+01	2.0E-09	4.2E+01	1.0E-09	4.2E+01	1.0E-09		
Th-232	7.5E+00	4.0E-07	3.7E+00	2.0E-07	3.7E+00	2.0E-07		
U-234	4.7E+01	3.0E-06	2.4E+01	1.5E-06	2.4E+01	1.5E-06		
U-235	1.5E+02	2.6E-04	5.8E+01	1.3E-04	5.8E+01	1.3E-04		
U-238	2.1E+01	2.5E-04	1.0E+01	1.3E-04	1.0E+01	1.3E-04		
Zr-93	7.5E+01	4.4E-12	3.7E+01	2.2E-12	3.7E+01	2.2E-12		
Pit 36								
Ag-108m	5.7E+00	2.1E-05						
Am-241	2.8E+01	1.2E-04						
Ba-133	5.7E+00	7.4E-04						
Cd-113m	5.7E+00	8.5E-05						
Co-60	1.3E+02	1.9E-01	3.4E+01	7.5E-02	3.4E+01	7.5E-02	2.1E+00	1.3E-02
Cs-135	5.7E+00	3.8E-09						
Cs-137	7.4E+01	1.5E-01	3.4E+01	7.5E-02	3.4E+01	7.5E-02		
Dy-154	5.7E+00	1.4E-10						

Table 3-13. Continued.

Radionuclide	Waste Form: Surface-Contaminated Waste Volume (m^3)	Surface-Contaminated Waste Activity (Ci)	Soils Volume (m^3)	Soils Activity (Ci)	Concrete and Sludges Volume (m^3)	Concrete and Sludges Activity (Ci)	Bulk-Contaminated Waste Volume (m^3)	Bulk-Contaminated Waste Activity (Ci)
Eu-152	7.8E+00	4.7E-05						
Eu-154	5.7E+00	1.3E-05						
Eu-152	5.7E+00	2.9E-02						
Gd-148	5.7E+00	3.6E-05						
Gd-150	5.7E+00	3.8E-10						
H-3	3.7E+01	2.9E-01						
I-129	5.7E+00	2.6E-10						
Kr-81	5.7E+00	4.5E-09						
Kr-85	5.7E+00	2.2E-04						
La-137	5.7E+00	7.4E-08						
Mo-93	5.7E+00	1.5E-06						
Nb-92	5.7E+01	4.4E-10						
Nb-94	5.7E+00	4.4E-07						
Pd-107	5.7E+00	6.3E-10						
Pu-238	5.3E+01	2.7E-04						
Pu-239	4.0E+02	1.3E-02						
Pu-240	3.0E+01	2.1E-03						
Pu-241	3.0E+01	3.2E-02						
Pu-242	3.0E+01	1.2E-07						
Se-79	5.7E+00	4.2E-10						
Si-32	9.4E+00	2.0E-09						
Sm-146	5.7E+00	3.4E-11						
Sm-147	5.7E+00	2.7E-14						
Sm-151	5.7E+00	1.2E-05						
Sr-90	5.7E+00	2.9E-04						
Tb-157	5.7E+00	4.2E-07						
Tb-158	5.7E+00	1.8E-07						
Tc-97	5.7E+00	3.4E-09						
Tc-99	5.7E+00	4.2E-08						
U-235	1.5E+02	<.2E-09						
U-238	8.3E+01	6.5E-02						
Zr-93	5.7E+00	4.7E-09						
Pit 37								
Ag-108m	9.4E+02	1.1E-03	6.0E+02	9.3E-07	1.5E+01	1.0E-12		
Al-26	2.8E-02	3.8E-08						
Am-241	1.8E+03	1.1E-01	3.9E+02	2.8E-03	7.3E+01	1.8E-01		
Am-243	2.5E+01	2.5E-05	1.5E+00	2.4E-07	1.5E+00	2.4E-07		
Ba-133	1.0E+03	4.1E-02	6.0E+02	3.3E-05	1.5E+01	3.7E-11		
Bi-207	7.4E-01	2.0E-05						
Bk-247	1.4E+01	5.4E-08						
C-14	2.0E+02	1.7E-02	7.4E+00	3.9E-05	7.1E+00	3.9E-05		
Cd-113m	9.4E+02	4.5E-03	6.0E+02	3.8E-06	1.5E+01	4.2E-12		
Cf-252	1.4E-01	1.4E-05						
Cl-36	1.4E-01	3.7E-04						
Co-60	1.8E+03	6.9E+00	5.2E+01	5.0E-03	2.6E+01	4.8E-05	3.8E+02	1.2E-01
Cs-135	9.4E+02	2.1E-07	6.0E+02	1.7E-10	1.5E+01	1.9E-16		

Table 3-13. Continued.

	Waste Form							
	Surface-Contaminated Waste		Soils		Concrete and Sludges		Bulk-Contaminated Waste	
Radionuclide	Volume (m^3)	Activity (Ci)	Volume (m^3)	Activity (Ci)	Volume (m^3)	Activity (Ci)	Volume (m^3)	Activity (Ci)
Cs-137	1.3E+03	1.6E-01	6.9E+02	9.8E-02	5.3E+01	1.5E-04		
Dy-154	9.4E+02	7.3E-09	6.0E+02	6.1E-12	1.5E+01	6.8E-18		
Eu-152	9.4E+02	2.5E-03	6.0E+02	2.4E-06	1.6E+01	5.0E-09		
Eu-154	9.4E+02	7.2E-04	6.0E+02	6.0E-07	1.5E+01	6.7E-13		
Gd-148	9.4E+02	1.9E-03	6.0E+02	1.6E-06	1.5E+01	1.8E-12		
Gd-150	9.4E+02	2.0E-08	6.0E+02	1.7E-11	1.5E+01	1.9E-17		
H-3	7.6E+02	9.5E+00	2.0E+02	2.8E+00	1.7E+01	1.3E-07		
Hf-182	1.8E+01	6.3E-03						
Ho-163	1.3E+01	3.5E-03						
I-129	9.4E+02	1.4E-08	6.0E+02	1.1E-11	1.5E+01	1.3E-17		
Kr-81	9.4E+02	2.4E-07	6.0E+02	2.0E-10	1.5E+01	2.3E-16		
Kr-85	9.4E+02	1.2E-02	6.0E+02	1.0E-05	1.5E+01	1.1E-11		
La-137	9.4E+02	3.9E-06	6.0E+02	3.3E-09	1.5E+01	3.7E-15		
Mo-93	9.4E+02	7.9E-05	6.0E+02	6.6E-08	1.5E+01	7.4E-14		
Nb-92	9.4E+02	2.4E-08	6.0E+02	2.0E-11	1.5E+01	2.2E-17		
Nb-94	9.4E+02	2.5E-02	6.0E+02	2.0E-08	1.5E+01	2.2E-14		
Ni-59	1.0E+01	3.6E-03						
Ni-63	1.4E-01	1.5E-04						
Np-237	3.3E+01	1.1E-05	1.7E+00	3.5E-08	1.7E+00	3.5E-08		
Pa-231	1.3E+01	9.0E-09						
Pb-210	2.5E+00	9.6E-03						
Pd-107	9.4E+02	3.4E-08	6.0E+02	2.8E-11	1.5E+01	3.1E-17		
Pm-145	1.8E+01	5.7E-04						
Pu-238	2.7E+03	3.5E-02	4.2E+02	4.4E-04	7.6E+01	1.0E+00		
Pu-239	5.9E+03	1.2E+00	4.2E+02	1.5E-01	8.8E+01	4.0E-01		
Pu-240	2.0E+03	2.2E-01	5.6E+00	1.0E-05	1.1E+00	6.3E-14		
Pu-241	2.0E+03	3.4E+00	1.1E+00	1.6E-07	1.1E+00	9.5E-13		
Pu-242	1.9E+03	1.2E-05	1.1E+00	3.6E-18	1.1E+00	3.6E-18		
Ra-226	6.7E+00	2.3E-02	2.3E-01	2.0E-06				
Se-79	9.4E+02	2.2E-08	6.0E+02	1.9E-11	1.5E+01	2.1E-17		
Si-32	2.4E+02	1.2E-02						
Sm-146	9.4E+02	1.8E-09	6.0E+02	1.5E-12	1.5E+01	1.7E-18		
Sm-147	9.6E+02	1.5E-12	6.0E+02	1.2E-15	1.5E+01	1.3E-21		
Sm-151	9.4E+02	6.2E-04	6.0E+02	5.2E-07	1.5E+01	5.8E-13		
Sr-90	1.1E+03	5.2E-02	6.2E+02	1.7E-04	2.9E+01	1.0E-04		
Tb-157	9.4E+02	2.3E-05	6.0E+02	1.9E-08	1.5E+01	2.1E-14		
Tb-158	9.4E+02	9.6E-06	6.0E+02	8.1E-09	1.5E+01	9.0E-15		
Tc-97	9.4E+02	1.8E-07	6.0E+02	1.5E-10	1.5E+01	1.7E-16		
Tc-99	1.1E+03	3.2E-03	6.1E+02	2.6E-06	1.7E+01	1.8E-08		
Th-229	1.3E+01	3.9E-05	1.7E-01	5.2E-07	1.7E-01	5.2E-07		
Th-230	1.5E+01	4.3E-07	1.4E+00	2.9E-09				
Th-232	1.4E+02	4.1E-04	3.6E+00	4.4E-09	3.5E+00	2.5E-10		
Ti-44	7.0E+00	3.0E-04						
U-232	2.0E-01	2.0E-10						
U-233	7.4E+00	1.3E-03	2.0E+00	2.8E-04	2.0E+00	2.8E-04		
U-234	1.3E+03	2.5E-01	6.4E+02	4.1E-03	3.6E+01	1.1E-03		
U-235	4.7E+03	2.8E-01	7.1E+02	1.8E-03	1.7E+02	7.4E-04		

Table 3-13. Continued.

	Waste Form							
	Surface-Contaminated Waste		Soils		Concrete and Sludges		Bulk-Contaminated Waste	
Radionuclide	Volume (m^3)	Activity (Ci)	Volume (m^3)	Activity (Ci)	Volume (m^3)	Activity (Ci)	Volume (m^3)	Activity (Ci)
U-236	1.3E+02	7.2E-04	2.3E+02	4.2E-06	8.9E+00	3.1E-06		
U-238	2.4E+03	6.8E-01	1.0E+03	1.5E-01	1.4E+02	2.1E-02		
Zr-93	9.4E+02	2.5E-07	6.0E+02	2.1E-10	1.5E+01	2.3E-16		
Pit 38								
Am-241	8.0E+01	9.0E-03	1.9E+01	3.5E-04	5.1E+01	3.8E-01		
Am-243	1.8E+01	1.1E-04	1.0E-01	5.7E-05	1.0E-01	5.7E-05		
Bk-247	1.0E+01	1.0E-09						
Co-60	8.1E+01	2.4E+00	7.3E+00	1.4E-03	6.9E+00	1.4E-03		
Cs-135	2.7E+00	4.5E-07						
Cs-137	1.3E+02	5.5E-02	3.4E+01	2.1E-03	1.1E+01	2.1E-03		
Eu-152	1.0E+01	2.8E-07	1.7E-01	6.2E-09				
H-3	3.0E+01	5.0E+00	7.3E+00	8.6E-04	7.0E+00	6.4E-01		
Hf-182	2.5E+01	6.8E-05						
K-40			2.0E-01	5.1E-06				
Kr-85	2.8E-03	7.4E-04						
Nb-94	1.3E+00	6.0E-08	6.7E-01	3.0E-08	6.7E-01	3.0E-08		
Ni-59	2.4E+00	4.5E-03	3.8E-01	1.4E-03	3.8E-01	1.4E-03		
Np-237	7.6E+00	3.1E-11						
Pu-238	9.9E+01	3.4E-03	4.8E+01	2.3E-04	5.8E+01	7.7E-01		
Pu-239	3.3E+02	1.7E+00	4.7E+01	1.4E-02	5.7E+01	3.6E-01		
Pu-240	2.1E-01	1.1E-04	1.0E-01	5.7E-05	1.0E-01	5.7E-05		
Pu-242	5.6E+00	1.1E-04	1.4E+00	5.7E-05	1.4E+00	5.7E-05		
Ra-226			2.0E-01	4.8E-07				
Sr-90	7.1E+01	4.6E-03	1.3E+01	1.4E-03	7.1E+00	1.4E-03		
Tc-99	2.5E+01	1.3E-02						
Th-230	1.0E+01	1.0E-09						
Th-232	1.8E+02	3.8E-04	2.0E-01	6.2E-07				
U-232	2.1E-01	1.1E-04	1.0E-01	5.7E-05	1.0E-01	5.7E-05		
U-233	2.1E-01	1.1E-04	1.0E-01	5.7E-05	1.0E-01	5.7E-05		
U-234	2.6E+02	7.2E-02	6.4E+01	1.4E-02	4.6E+01	7.5E-03		
U-235	4.0E+02	7.9E-03	8.1E+01	2.0E-03	1.1E+02	2.0E-03		
U-236	1.5E+02	1.4E-03	1.0E-01	5.7E-05	1.0E-01	5.7E-05		
U-238	2.7E+02	2.4E-01	3.6E+01	8.2E-03	6.8E+00	3.3E-03		
Pit 39								
Am-241	2.9E+02	5.9E-03	5.0E+01	4.8E-04	2.1E+01	4.5E-02		
Am-243	5.7E-02	1.0E-09						
Ba-133	1.7E-01	3.8E-07						
Bi-207	3.8E-03	7.4E-05						
C-14	2.3E-01	2.7E-05						
Co-60	8.8E+01	2.9E-02	1.9E-01	1.8E-07	1.9E-01	1.8E-07		
Cs-135	3.4E-01	2.0E-05						
Cs-137	8.7E+01	4.5E-03	9.1E+01	9.6E-04	1.9E-01	9.6E-08		
Eu-152	6.2E-01	8.0E-09						
H-3	5.3E+01	5.6E-02	2.7E+01	1.1E-06				
Hf-182	2.3E-01	2.6E-05						

Table 3-13. Continued.

	Waste Form							
	Surface-Contaminated Waste		Soils		Concrete and Sludges		Bulk-Contaminated Waste	
Radionuclide	Volume (m^3)	Activity (Ci)	Volume (m^3)	Activity (Ci)	Volume (m^3)	Activity (Ci)	Volume (m^3)	Activity (Ci)
Ni-59	6.2E+00	2.1E-03						
Ni-63	5.7E-02	1.0E-06						
Np-237	2.1E+01	6.1E-04						
Pu-234	5.7E-02	2.0E-09						
Pu-238	3.3E+02	5.6E-03	5.6E+01	3.1E-04	2.7E+01	5.1E-01		
Pu-239	5.8E+02	1.1E-01	1.7E+02	5.4E-03	5.5E+01	8.4E-02		
Pu-240	1.7E+02	1.9E-02						
Pu-241	1.7E+02	2.8E-01						
Pu-242	1.7E+02	1.1E-06						
Ra-226	2.5E-04	3.9E-09	1.9E-02	1.8E-10				
Si-32	2.5E+00	4.0E-02						
Sr-90	9.6E+00	2.1E-03						
Tc-97	3.4E-01	6.0E-09						
Tc-99	6.6E+01	3.5E-03						
Th-232	4.1E+01	1.4E-03						
U-233	5.5E+00	5.3E-08	1.9E+00	9.5E-11	1.9E+00	9.5E-11		
U-234	2.9E+02	2.6E-01	1.7E+02	3.2E-05	1.3E+02	2.7E-05		
U-235	4.4E+02	1.3E-02	1.8E+02	1.0E-06	1.5E+02	4.6E-05		
U-236	2.3E+01	3.2E-04						
U-238	4.2E+02	6.4E-01	3.8E+01	4.6E-03	2.1E+01	1.2E-05		

Table 3-14. Shaft radionuclide inventories for September 26, 1988, through 1995.

	Waste Form							
	Surface-Contaminated Waste		Soils		Concrete and Sludges		Bulk-Contaminated Waste	
Radionuclide	Volume (m^3)	Activity (Ci)	Volume (m^3)	Activity (Ci)	Volume (m^3)	Activity (Ci)	Volume (m^3)	Activity (Ci)
Ag-108m	6.2E+00	1.2E-01			3.6E+01	1.0E-01		
Am-241	8.8E+00	1.0E-03						
Ba-133	6.2E+00	4.5E+00						
Bi-207	3.8E-03	4.0E-06						
C-14	3.0E+00	8.9E-03						
Cd-113m	6.2E+00	5.1E-01						
Cf-252	3.8E-03	4.5E-08					2.8E+01	9.2E-01
Co-60	6.9E+01	7.7E+02						
Cs-135	8.9E+00	2.8E-05						
Cs-137	1.2E+01	8.3E+01						
Dy-154	6.2E+00	8.2E-07						
Eu-152	6.3E+00	2.8E-01						
Eu-154	6.6E+00	1.8E-01						
Gd-148	6.2E+00	2.2E-01						
Gd-150	6.2E+00	2.3E-06						
H-3	4.6E+01	4.3E+05	7.5E+00	1.5E-07				
I-129	6.2E+00	1.5E-06						
Kr-81	6.2E+00	2.7E-05						
Kr-85	6.2E+00	1.3E+00						
La-137	6.2E+00	4.4E-04						
Mo-93	6.2E+00	8.8E-03						
Nb-92	6.3E+00	4.0E-03						
Nb-94	6.2E+00	2.7E-03						
Ni-63	3.8E-03	3.0E-05						
Pb-210	1.9E-02	2.4E-09						
Pd-107	6.2E+00	3.8E-06			3.6E+01	2.4E-01		
Pu-238	1.7E+01	1.4E-03			3.7E+01	7.7E-02		
Pu-239	2.3E+01	1.3E-02						
Pu-240	4.2E-01	2.8E-03						
Pu-241	4.2E-01	4.2E-02						
Pu-242	4.2E-01	1.6E-07						
Ra-226	8.5E-02	1.5E-05						
Se-79	6.2E+00	2.5E-06						
Sm-146	6.2E+00	2.0E-07						
Sm-147	6.2E+00	1.6E-10						
Sm-151	6.2E+00	6.9E-02						
Sr-90	6.4E+00	6.9E+00						
Tb-157	6.2E+00	2.5E-03						
Tb-158	6.2E+00	1.1E-03						
Tc-97	6.2E+00	2.0E-05						
Tc-99	6.2E+00	2.5E-04						
Th-229	3.8E-03	5.4E-08						
Th-232	9.3E-01	4.1E-04						
U-234	2.8E-01	2.5E-03	1.8E-02	4.7E-08	1.8E-02	4.7E-08		
U-235	1.4E+01	1.2E-03	1.8E-02	1.1E-09	3.6E+01	2.2E-04		
U-236	1.5E-01	5.8E-06	1.8E-02	2.2E-09	1.8E-02	2.2E-09		
U-238	2.2E+01	2.0E-01	1.8E-02	6.1E-08	5.9E-01	4.4E-07		
Zr-93	6.2E+00	2.8E-05						

CORRECTION

START

Table 3-13. Continued.

	Waste Form							
	Surface-Contaminated Waste		Soils		Concrete and Sludges		Bulk-Contaminated Waste	
Radionuclide	Volume (m^3)	Activity (Ci)	Volume (m^3)	Activity (Ci)	Volume (m^3)	Activity (Ci)	Volume (m^3)	Activity (Ci)
Ni-59	6.2E+00	2.1E-03						
Ni-63	5.7E-02	1.0E-06						
Np-237	2.1E+01	6.1E-04						
Pu-234	5.7E-02	2.0E-09						
Pu-238	3.3E+02	5.6E-03	5.6E+01	3.1E-04	2.7E+01	5.1E-01		
Pu-239	5.8E+02	1.1E-01	1.7E+02	5.4E-03	5.5E+01	8.4E-02		
Pu-240	1.7E+02	1.9E-02						
Pu-241	1.7E+02	2.8E-01						
Pu-242	1.7E+02	1.1E-06						
Ra-226	2.5E-04	3.9E-09	1.9E-02	1.8E-10				
Si-32	2.5E+00	4.0E-02						
Sr-90	9.6E+00	2.1E-03						
Tc-97	3.4E-01	6.0E-09						
Tc-99	6.6E+01	3.5E-03						
Th-232	4.1E+01	1.4E-03						
U-233	5.5E+00	5.3E-08	1.9E+00	9.5E-11	1.9E+00	9.5E-11		
U-234	2.9E+02	2.6E-01	1.7E+02	3.2E-05	1.3E+02	2.7E-05		
U-235	4.4E+02	1.3E-02	1.8E+02	1.0E-06	1.5E+02	4.6E-05		
U-236	2.3E+01	3.2E-04						
U-238	4.2E+02	6.4E-01	3.8E+01	4.6E-03	2.1E+01	1.2E-05		

Table 3-14. Shaft radionuclide inventories for September 26, 1988, through 1995.

	Waste Form							
	Surface-Contaminated Waste		Soils		Concrete and Sludges		Bulk-Contaminated Waste	
Radionuclide	Volume (m^3)	Activity (Ci)	Volume (m^3)	Activity (Ci)	Volume (m^3)	Activity (Ci)	Volume (m^3)	Activity (Ci)
Ag-108m	6.2E+00	1.2E-01						
Am-241	8.8E+00	1.0E-03			3.6E+01	1.0E-01		
Ba-133	6.2E+00	4.5E+00						
Bi-207	3.8E-03	4.0E-06						
C-14	3.0E+00	8.9E-03						
Cd-113m	6.2E+00	5.1E-01						
Cf-252	3.8E-03	4.5E-08						
Co-60	6.9E+01	7.7E+02					2.8E+01	9.2E+01
Cs-135	8.9E+00	2.8E-05						
Cs-137	1.2E+01	8.3E+01						
Dy-154	6.2E+00	8.2E-07						
Eu-152	6.3E+00	2.8E-01						
Eu-154	6.6E+00	1.8E-01						
Gd-148	6.2E+00	2.2E-01						
Gd-150	6.2E+00	2.3E-06						
H-3	4.6E+01	4.3E+05	7.5E+00	1.5E-07				
I-129	6.2E+00	1.5E-06						
Kr-81	6.2E+00	2.7E-05						
Kr-85	6.2E+00	1.3E+00						
La-137	6.2E+00	4.4E-04						
Mo-93	6.2E+00	8.8E-02						
Nb-92	6.3E+00	4.0E-03						
Nb-94	6.2E+00	2.7E-03						
Ni-63	3.8E-03	3.0E-05						
Pb-210	1.9E-02	2.4E-09						
Pd-107	6.2E+00	3.8E-06						
Pu-238	1.7E+01	1.4E-03			3.6E+01	2.4E-01		
Pu-239	2.3E+01	1.3E-02			3.7E+01	7.7E-02		
Pu-240	4.2E-01	2.8E-03						
Pu-241	4.2E-01	4.2E-02						
Pu-242	4.2E-01	1.6E-07						
Ra-226	8.5E-02	1.5E-05						
Se-79	6.2E+00	2.5E-06						
Sm-146	6.2E+00	2.0E-07						
Sm-147	6.2E+00	1.6E-10						
Sm-151	6.2E+00	6.9E-02						
Sr-90	6.4E+00	6.9E+00						
Tb-157	6.2E+00	2.5E-03						
Tb-158	6.2E+00	1.1E-03						
Tc-97	6.2E+00	2.0E-05						
Tc-99	6.2E+00	2.5E-04						
Th-229	3.8E-03	5.4E-08						
Th-232	9.3E-01	4.1E-04						
U-234	2.8E-01	2.5E-03	1.8E-02	4.7E-08	1.8E-02	4.7E-08		
U-235	1.4E+01	1.2E-03	1.8E-02	1.1E-09	3.6E+01	2.2E-04		
U-236	1.5E-01	5.8E-06	1.8E-02	2.2E-09	1.8E-02	2.2E-09		
U-238	2.2E+01	2.0E-01	1.8E-02	6.1E-08	5.9E-01	4.4E-07		
Zr-93	6.2E+00	2.8E-05						

CORRECTION

END

Tables 3-13 and 3-14 include radionuclides with half-lives greater than 5 years and those with parents or daughters with half-lives greater than 5 years. The radionuclides eliminated from the inventory projections based on half-life are listed in Appendix A.

3.2 PROJECTED LLW INVENTORY

The projected LLW inventory includes waste from routine operations and ER and D&D waste. Inventory projections for these types of waste are presented in this section. Projected operational waste inventories are discussed in Section 3.2.1, ER and D&D inventory projections are provided in Section 3.2.2, and inventories of MLLW residues are given in Section 3.2.3. The total future inventory is summarized in Section 3.2.4.

3.2.1 Operational LLW Inventory Projections

A total of 26 TAs were identified as major generators of LLW at LANL using the screening process described in Section 2.2.1. The screen based on the total volume of LLW generated identified 19 TAs as major generators of LLW, shown in Table 3-15. Several TAs consistently generated large volumes of waste throughout the 1990 to 1995 period, including TAs 3, 15, 21, 48, 50, 53, and 55. The remainder of the TAs listed in the table qualified as major generators of waste for three or less of the six years.

The results of the screening calculations based on total activity, shown in Table 3-16, indicate that a small number of TAs were responsible for most of the activity disposed of at Area G: seven areas were responsible for 95 percent of the activity disposed of between 1990 and 1995. Of these, TA-48 and TA-53 were the most consistent contributors, qualifying as major generators for five of the six years. All of the TAs identified as major generators of LLW using the total activity screen also were identified as such by the screen based on total waste volume.

The screening calculation based on radionuclide-specific activities identified 28 TAs as major generators of waste between 1990 and 1995 (Table 3-17). The TAs that were

Table 3-15. Major generators of LLW based on total volume.

Technical Area	Year of Disposal[a]					
	1990	1991	1992	1993	1994	1995
TA-0 Unassigned Land Reserve				X		X
TA-2 Omega Site	X				X	
TA-3 South Mesa Site	X	X	X	X	X	X
TA-15 R-Site	X	X	X	X	X	X
TA-16 S-Site			X	X		
TA-18 Parajito Laboratory	X		X			
TA-21 DP-Site	X	X	X	X	X	X
TA-33 HP-Site	X					
TA-35 Ten Site		X				X
TA-36 Kappa Site		X				X
TA-39 Ancho Canyon Site				X		
TA-43 Health Research Lab and DOE Headquarters	X			X		
TA-46 WA Site		X				
TA-48 Radiochemistry Site	X	X	X	X	X	X
TA-50 Waste Management Site	X	X	X	X	X	X
TA-52 Reactor Development Site	X					
TA-53 Meson Physics Facility	X	X	X	X	X	X
TA-54 Waste Disposal Site				X	X	X
TA-55 Plutonium Facility	X	X	X	X	X	X

a. "X" indicates that the waste shipped for disposal by the TA comprised 95 percent of the total volume of waste disposed of in the indicated year.

Table 3-16. Major generators of LLW based on total activity.

Technical Area	Year of Disposal[a]					
	1990	1991	1992	1993	1994	1995
TA-2 Omega Site			X			
TA-3 South Mesa Site	X			X		
TA-21 DP-Site				X		
TA-33 HP-Site					X	X
TA-48 Radiochemistry Site	X	X	X	X	X	
TA-53 Meson Physics Facility	X	X	X	X	X	
TA-55 Plutonium Facility						X

a. "X" indicates that the waste shipped for disposal by the TA comprised 95 percent of the total activity of waste disposed of in the indicated year.

Table 3-17. Major generators of LLW based on radionuclide-specific activity.

Technical Area	Year of Disposal[a]					
	1990	1991	1992	1993	1994	1995
TA-0 Unassigned Land Reserve				X		X
TA-1 Town Site						X
TA-2 Omega Site		X	X		X	
TA-3 South Mesa Site	X	X	X	X	X	X
TA-8 Anchor Site West		X				
TA-9 Anchor Site East						X
TA-11 K-Site	X					
TA-15 R-Site	X				X	X
TA-16 S-Site	X			X	X	
TA-18 Parajito Laboratory	X					X
TA-21 DP-Site	X	X	X	X	X	X
TA-33 HP-Site			X		X	X
TA-35 Ten Site		X	X	X		X
TA-36 Kappa Site						X
TA-39 Ancho Canyon Site			X		X	
TA-41 W-Site			X	X		
TA-43 Health Research Lab and DOE Headquarters				X	X	
TA-46 WA Site		X		X	X	X
TA-48 Radiochemistry Site	X	X	X	X	X	X
TA-50 Waste Management Site	X	X	X	X	X	X
TA-51 Radiation Exposure Facility						X
TA-52 Reactor Development Site	X					
TA-53 Meson Physics Facility	X	X	X	X	X	X
TA-54 Waste Disposal Site				X		X
TA-55 Plutonium Facility	X	X	X	X	X	X
TA-59 OH-Site		X	X	X	X	X
TA-60 Sigma Mesa					X	
TA-64 Central Guard Facility Site						X

a. "X" indicates that the waste shipped for disposal by the TA comprised 95 percent of the total radionuclide-specific activities of waste disposed of in the indicated year.

identified in addition to those revealed through total volume and activity screens include TA-1, TA-8, TA-9, TA-11, TA-41, TA-51, TA-59, TA-60, and TA-64. Of these, TA-60 and TA-64 were dismissed from further consideration. TA-60 was identified as a major generator of waste based on the activity of "gamma emitters" shipped for disposal in 1994. The total activity of this waste, 1.0E-08 Ci, was much less than the disposed activities of important gamma emitters (e.g., Co-60 and Cs-137) in that year (2.2E+02 and 1.5E+01 Ci, respectively). Given this fact, TA-60 was eliminated from consideration as a major generator of waste. The TA-64 waste shipments noted in the database consisted of soil samples collected from other TAs, including TA-1, TA-21, TA-50, and TA-54. Given that the waste was not generated at TA-64 and that the areas from which the contamination originated had already been identified as major generators of waste, this TA was removed from further consideration in the future waste projections.

Estimates of future levels of activity at the TAs identified as major generators of LLW at LANL are provided in Table 3-18. Current operations are expected to continue essentially unchanged for the foreseeable future at several TAs. In contrast, the waste generated at five TAs (TA-0, TA-1, TA-2, TA-33, and TA-52) is expected to consist of primarily ER and D&D waste as closed sites and facilities are remediated. Some or all of the operations are expected to continue at the remaining TAs, although the nature of the LLW generated at these TAs may change as operations evolve. For example, the quantities and types of waste shipped for disposal from TA-21 are expected to change significantly with the D&D of the plutonium and uranium facilities.

Based on the results provided in Table 3-18, LLW generated in the future at TA-0, TA-1, TA-2, TA-33, and TA-52 was assumed to consist solely of ER and D&D waste. These TAs were not considered in the development of projected operational waste inventories. With the exception of TA-54, all of the remaining TAs listed in Table 3-18 were included in the development of projected inventories for routine LLW. While the level of activity at some of these facilities may decline in the future, it was not feasible to use the existing LLW disposal information to identify a subset of the waste generated at a given TA as waste which will no longer be generated. Consequently, a conservative approach was adopted wherein all LLW generated at these TAs is included in the performance assessment and composite analysis. Adjustments to the projected inventory to account for the start of new operations at a small

Table 3-18. Projections of future operations at the major generators of LLW.

Technical Area	Future Operational Status
TA-0 Unassigned Land Reserve	Generation of ER waste only.
TA-1 Town Site	Generation of ER waste only.
TA-2 Omega Site	Reactor has been shut down; generation of ER and D&D waste only.
TA-3 South Mesa Site	Operations will continue.
TA-8 Anchor Site West	Operations will continue.
TA-9 Anchor Site East	Operations will continue.
TA-11 K-Site	Operations will continue.
TA-15 R-Site	Operations will continue.
TA-16 S-Site	Operations will continue.
TA-18 Parajito Laboratory	Operations will continue.
TA-21 DP-Site	D&D of plutonium and uranium facilities expected in future; other operations will continue.
TA-33 HP-Site	Facility closed and scheduled to undergo D&D.
TA-35 Ten Site	Work with radionuclides will decline; D&D of old fission product buildings is scheduled.
TA-36 Kappa Site	Operations will continue.
TA-39 Ancho Canyon Site	Operations will continue.
TA-41 W-Site	Decline in operations handling radionuclides.
TA-43 Health Research Lab and DOE Headquarters	Operations will continue.
TA-46 WA-Site	Operations will continue.
TA-48 Radiochemistry Site	Operations will continue; quantity of fresh fission-product waste will decline.
TA-50 Waste Management Site	Current facilities to operate until new liquid radioactive waste treatment facility is constructed. A moderate increase in the activity of the waste is expected from the more efficient treatment process.
TA-51 Radiation Exposure Facility	Operations will continue.
TA-52 Reactor Development Site	Reactors have undergone D&D; activities now center on non-LANL studies that generate little or no waste.
TA-53 Meson Physics Facility	Operations will continue; new waste streams are expected from the irradiation of targets when studies of accelerator production of tritium begin.
TA-54 Waste Disposal Site	No significant generation of waste expected.
TA-55 Plutonium Facility	Operations will continue; waste streams containing weapons-grade plutonium could increase slightly as LANL increases operational plutonium support for DOE. When fabrication of Pu-238 thermal generators is complete, this plutonium waste will decrease.
TA-59 OH-Site	Operations will continue.

number of TAs were not possible because the radiological characteristics of waste from these operations are unknown.

TA-54 was not assumed to be a major generator of LLW in the future. The waste that is attributed to TA-54 in the LLW database is generally material generated at other TAs. The origin of the waste was listed as TA-54 because the waste underwent special handling at the disposal facility prior to disposal. Quantities of operational LLW actually generated at TA-54 in the future are expected to be small.

In summary, the major generators upon which projections of future operational waste inventories were based are listed in Table 3-19. These generators are expected to account for approximately 95 percent of the operational LLW generated in the future on the basis of total volume, total activity, and radionuclide-specific activities.

As discussed in Section 2.2.1, high-activity tritium waste generated in the past six years is currently being stored while tritium recovery options are being investigated. Because no decision had been made about whether the recovery option would be pursued at the time the inventory was developed, it was assumed that all of this waste in storage and all such waste generated in the future would be sent to Area G for disposal. Table 3-20 lists the total volumes and activities of high-activity tritium waste in storage as of July 1996 and the expected rate of future generation.

The projected operational LLW inventories for Area G are listed in Tables 3-21 through 3-23 for the four waste forms discussed earlier. Table 3-21 lists the volumes and as-disposed activities of waste projected to require disposal for the remainder of the facility's lifetime. Table 3-22 provides the total as-disposed radionuclide inventories for the LLW disposed of in pits, while Table 3-23 provides similar information for the disposal shafts. The waste with high levels of tritium, summarized in Table 3-20, is included in Tables 3-21 through 3-23. Radionuclides with half-lives of 5 years or less have been screened from the projected inventories.

Table 3-19. Major generators of LLW between 1990 and 1995.

TA-3 South Mesa Site

TA-8 Anchor Site West

TA-9 Anchor Site East

TA-11 K-Site

TA-15 R-Site

TA-16 S-Site

TA-18 Parajito Laboratory

TA-21 DP-Site

TA-35 Ten Site

TA-36 Kappa Site

TA-39 Ancho Canyon Site

TA-41 W-Site

TA-43 Health Research Lab and DOE Headquarters

TA-46 WA Site

TA-48 Radiochemistry Site

TA-50 OH-Site

TA-51 Radiation Exposure Facility

TA-53 Meson Physics Facility

TA-55 Plutonium Facility

TA-59 OH-Site

Table 3-20. Stored and projected inventories of waste with high H-3 activities.

Disposal Unit/Waste Form	Volume in Storage (m^3)	Activity in Storage (Ci)	Annual Generation Rate: Volume (m^3)	Annual Generation Rate: Activity (Ci)	Total Waste Inventory: Volume (m^3)	Total Waste Inventory: Activity (Ci)
Pit Waste						
Surface-Contaminated Waste	5.8E+01	5.8E+02			5.8E+01	5.8E+02
Soils						
Concrete and Sludges						
Bulk-Contaminated Waste						
Shaft Waste						
Surface-Contaminated Waste	3.2E+00	6.2E+05	5.7E-01	1.0E+05	3.1E+01	5.5E+06
Soils						
Concrete and Sludges						
Bulk-Contaminated Waste						

Table 3-21. Projected operational LLW volumes and activities for pits and shafts.

Disposal Unit/Waste Form	Average Annual Volume (m^3)	Average Annual Activity (Ci)	Total Volume (m^3)	Total Activity (Ci)
Pit Waste				
Surface-Contaminated Waste	2.2E+03	1.8E+01	1.1E+05[a]	1.4E+03[b]
Soils	9.9E+01	2.1E-02	4.8E+03	1.0E+00
Concrete and Sludges	2.2E+01	7.3E-01	1.1E+03	3.6E+01
Bulk-Contaminated Waste	5.2E+01	3.4E-01	2.5E+03	1.7E+01
Shaft Waste				
Surface-Contaminated Waste	2.3E+01	1.1E+05	1.1E+03[c]	6.1E+06[d]
Soils	—	—	—	—
Concrete and Sludges	4.0E+00	7.0E-02	2.0E+02	3.4E+00
Bulk-Contaminated Waste	2.3E+00	3.3E+02	1.1E+02	1.6E+04

a. Includes 5.8E+01 m^3 of stored high-tritium-activity waste.
b. Includes 5.8E+02 Ci of stored high-tritium-activity waste.
c. Includes 3.2E+00 m^3 of stored high-tritium-activity waste.
d. Includes 6.2E+05 Ci of stored high-tritium-activity waste.

Table 3-22. Projected radionuclide inventories for operational waste disposed of in pits.

	Waste Form							
	Surface-Contaminated Waste		Soils		Concrete and Sludges		Bulk-Contaminated Waste	
Radionuclide	Volume (m^3)	Activity (Ci)	Volume (m^3)	Activity (Ci)	Volume (m^3)	Activity (Ci)	Volume (m^3)	Activity (Ci)
Ag-108m	8.6E+03	2.0E-01						
Al-26	2.3E-01	3.1E-07						
Am-241	1.8E+04	1.1E+00			1.1E+03	4.9E+00		
Am-243	3.5E+02	2.0E-04						
Ba-133	8.8E+03	7.0E+00						
Bi-207	6.0E+00	7.7E-04						
Bk-247	1.5E+02	4.5E-07						
C-14	1.6E+03	1.4E-01						
Cd-113m	8.6E+03	8.0E-01						
Cf-252	1.2E+00	1.2E-04						
Cl-36	1.2E+00	3.1E-03						
Co-60	1.7E+04	2.0E+01			1.2E+00	2.5E-08	2.5E+03	5.5E-01
Cs-135	8.6E+03	2.0E-04						
Cs-137	1.2E+04	2.9E+00			4.9E-01	2.1E-04		
Dy-154	8.6E+03	1.3E-06						
Eu-152	8.7E+03	4.4E-01						
Eu-154	8.6E+03	1.3E-01						
Gd-148	8.6E+03	3.4E-01						
Gd-150	8.6E+03	3.6E-06						
H-3	5.2E+03	7.0E+02			1.9E+00	5.2E+00		
Hf-182	3.5E+02	5.2E-02						
Ho-163	1.1E+02	2.8E-02						
I-129	8.6E+03	2.4E-06						
Kr-81	8.6E+03	4.3E-05						
Kr-85	8.6E+03	2.1E+00						
La-137	8.6E+03	7.0E-04						
Mo-93	8.6E+03	1.4E-02						
Nb-92	8.6E+03	4.2E-06						
Nb-94	8.6E+03	2.1E-01						
Ni-59	1.5E+02	3.9E-02						
Ni-63	2.3E+00	1.3E-03						
Np-237	5.1E+02	5.0E-03						
Pa-231	1.4E+02	7.4E-08						
Pb-210	9.3E-01	7.8E-02						
Pd-107	8.6E+03	5.9E-06						
Pm-145	1.4E+02	6.4E-03						
Pu-238	2.6E+04	3.6E-01			1.1E+03	1.9E+01		
Pu-239	5.7E+04	1.8E+01			1.1E+03	6.8E+00		
Pu-240	1.9E+04	2.0E+00						
Pu-241	1.9E+04	3.1E+01						
Pu-242	1.9E+04	1.1E-04						
Ra-226	1.6E+02	2.0E-01						
Se-79	8.6E+03	4.0E-06						
Si-32	1.6E+03	4.3E-01						
Sm-146	8.6E+03	3.2E-07						

Table 3-22. Continued.

	Waste Form							
	Surface-Contaminated Waste		Soils		Concrete and Sludges		Bulk-Contaminated Waste	
Radionuclide	Volume (m^3)	Activity (Ci)	Volume (m^3)	Activity (Ci)	Volume (m^3)	Activity (Ci)	Volume (m^3)	Activity (Ci)
Sm-147	8.8E+03	2.5E-10						
Sm-151	8.6E+03	1.1E-01						
Sr-90	9.7E+03	3.0E+00						
Tb-157	8.6E+03	4.0E-03						
Tb-158	8.6E+03	1.7E-03						
Tc-97	8.6E+03	3.2E-05						
Tc-99	1.1E+04	1.6E-01						
Th-229	1.1E+02	3.1E-04						
Th-230	1.8E+02	3.5E-06						
Th-232	2.9E+03	1.8E-02						
Ti-44	5.7E+01	2.5E-03						
U-232	1.6E+00	1.6E-09						
U-233	4.5E+01	6.2E-03						
U-234	3.5E+03	3.3E+00	1.9E+03	7.7E-08				
U-235	3.4E+04	4.2E+00	1.9E+03	1.8E-09	1.1E+03	4.5E-03		
U-236	1.8E+03	1.8E-02	1.9E+03	3.7E-09				
U-238	2.2E+04	2.9E+01	4.5E+03	1.0E+00	4.6E+00	1.5E-02		
Zr-93	8.6E+03	4.4E-05						

Table 3-23. Projected shaft radionuclide inventories for Area G.

	Waste Form							
	Surface-Contaminated Waste		Soils		Concrete and Sludges		Bulk-Contaminated Waste	
Radionuclide	Volume (m^3)	Activity (Ci)	Volume (m^3)	Activity (Ci)	Volume (m^3)	Activity (Ci)	Volume (m^3)	Activity (Ci)
Am-241	7.2E+01	8.5E-03			2.9E+02	8.5E-01		
Ba-133	2.5E-01	2.0E-03						
Bi-207	3.1E-02	3.3E-05						
C-14	2.3E+01	2.2E-08						
Cf-252	3.1E-02	3.7E-07						
Co-60	4.1E+02	4.6E+03					1.1E+02	5.3E+02
Cs-135	2.2E+01	3.7E-05						
Cs-137	3.6E+01	6.7E+02						
Eu-152	1.0E+00	1.8E-02						
Eu-154	2.8E+00	7.9E-01						
H-3	1.8E+02	6.0E+06						
Kr-85	9.3E-03	8.2E-03						
Nb-92	9.3E-01	3.3E-02						
Ni-63	3.1E-02	2.5E-04						
Pb-210	1.5E-01	1.9E-08						
Pm-145	1.5E-01	3.2E-13						
Pu-238	1.2E+02	1.1E-02			2.9E+02	2.0E+00		
Pu-239	1.5E+02	1.1E-01			3.0E+02	6.3E-01		
Pu-240	3.4E+00	2.3E-02						
Pu-241	3.4E+00	3.5E-01						
Pu-242	3.4E+00	1.3E-06						
Ra-226	4.6E-01	1.6E-06						
Sm-147	1.5E-01	1.2E-14						
Sr-90	1.6E+00	3.4E+01						
Th-229	3.1E-02	4.4E-07						
Th-232	7.6E+00	3.3E-03						
U-234	9.6E-01	9.9E-04						
U-235	1.1E+02	8.9E-03			2.9E+02	1.8E-03		
U-236	9.6E-01	4.7E-05						
U-238	1.7E+02	1.6E+00			3.4E+00	3.1E-06		

3.2.2 ER and D&D LLW

The volumes of LLW expected to require disposal at Area G due to ER and D&D activities and the CMR upgrade are listed in Table 3-24. All of this waste is expected to be disposed of in pits. The volume of ER waste is based on estimates collected from the various Field Units at LANL. Estimates had been received from about 60 percent of the Units at the time the ER inventory projections were being developed for inclusion in the Area G inventory. These units are expected to account for approximately 85 percent of the total future waste (Maassen, 1996). Consequently, the projections were increased 15 percent to account for the non-responding Field Units. The D&D waste volume projections included in Table 3-24 are based on a specific set of funding assumptions. Waste projections were available through fiscal year 2001 at the time the Area G inventory was being developed; D&D activities may continue beyond this year. The volume estimate for the CMR upgrade waste accounts for the remainder of the projections (Kennicott, 1996).

As discussed in Section 2.2.2, the radionuclide concentrations in the ER, D&D, and CMR upgrade waste were assumed to be the same as those found in mixed low-level ER waste by ERM/Golder (1995). These concentrations are provided in Table 3-25. The as-disposed radionuclide inventories based on these concentrations and the volume information provided in Table 3-24 are shown in Table 3-26. Inventories are listed for radionuclides with half-lives greater than 5 years and for radionuclides that have daughters or parents with half-lives greater than 5 years.

3.2.3 MLLW Residues

The total volume and activity of uranium chips and turnings in storage (i.e., waste plus diesel fuel) through 1995 was 24.8 m^3 and 5.3 Ci, respectively (Brazenger, 1996). Generation rates of uranium chips are expected to increase relative to historic levels as workloads in the LANL shops increase (Hodges, 1996a). The quantities of such waste expected to require disposal as a result of future operations are listed in Table 3-27. The waste was assigned to the soil waste form, based on the fact that the waste currently is expected to be stabilized in a clay matrix following treatment. The radionuclide inventories in the waste also are included in Table 3-27.

Table 3-24. Projected ER and D&D and CMR Upgrade LLW inventories for Area G.

	ER and D&D Waste		CMR Upgrade Waste		Total	
Waste Form	Total Volume (m^3)	Total Activity (Ci)	Total Volume (m^3)	Total Activity (Ci)	Total Volume (m^3)	Total Activity (Ci)
Surface-Contaminated Waste	8.9E+03	6.3E+00	5.2E+03	3.7E+00	1.4E+04	1.0E+01
Soils	4.4E+03	3.1E+00			4.4E+03	3.1E+00
Concrete and Sludges	4.4E+03	3.1E+00			4.4E+03	3.1E+00
Bulk-Contaminated Waste						

Table 3-25. Radionuclide concentrations in ER, D&D, and CMR upgrade waste.[a]

Radionuclide	Concentration (pCi/g)
Ac-227	2.2E+00
Am-241	1.6E+00
Ce-144	5.1E-01
Co-60	2.6E-01
Cs-137	5.0E-01
H-3	6.4E+01
K-40	2.6E+01
Pb-210	4.3E+00
Pb-212	1.4E+00
Pu-238	4.8E-01
Pu-239	8.9E+01
Pu-240	9.5E+01
Ra-226	1.5E+00
Sr-90	8.9E-01
Tc-99	3.0E-01
Th-228	1.4E+00
Th-230	1.1E+00
Th-232	1.8E+00
Th-234	1.9E+00
Tl-208	4.2E-01
U-234	6.5E+00
U-235	5.4E-01
U-238	5.6E+00

a. Source: ERM/Golder, 1995.

Table 3-26. Radionuclide inventories for ER, D&D, and CMR upgrade waste.

	Waste Form							
	Surface-Contaminated Waste		Soils		Concrete and Sludges		Bulk-Contaminated Waste	
Radionuclide	Volume (m^3)	Activity (Ci)	Volume (m^3)	Activity (Ci)	Volume (m^3)	Activity (Ci)	Volume (m^3)	Activity (Ci)
Ac-227	1.4E+04	7.1E-02	4.4E+03	2.2E-02	4.4E+03	2.2E-02		
Am-241	1.4E+04	5.1E-02	4.4E+03	1.6E-02	4.4E+03	1.6E-02		
Co-60	1.4E+04	8.4E-03	4.4E+03	2.7E-03	4.4E+03	2.7E-03		
Cs-137	1.4E+04	1.6E-02	4.4E+03	5.1E-03	4.4E+03	5.1E-03		
H-3	1.4E+04	2.1E+00	4.4E+03	6.5E-01	4.4E+03	6.5E-01		
K-40	1.4E+04	8.3E-01	4.4E+03	2.6E-01	4.4E+03	2.6E-01		
Pb-210	1.4E+04	1.4E-01	4.4E+03	4.4E-02	4.4E+03	4.4E-02		
Pu-238	1.4E+04	1.6E-02	4.4E+03	4.9E-03	4.4E+03	4.9E-03		
Pu-239	1.4E+04	2.9E+00	4.4E+03	9.1E-01	4.4E+03	9.1E-01		
Pu-240	1.4E+04	3.1E+00	4.4E+03	9.7E-01	4.4E+03	9.7E-01		
Ra-226	1.4E+04	4.9E-02	4.4E+03	1.5E-02	4.4E+03	1.5E-02		
Sr-90	1.4E+04	2.9E-02	4.4E+03	9.1E-03	4.4E+03	9.1E-03		
Tc-99	1.4E+04	9.7E-03	4.4E+03	3.1E-03	4.4E+03	3.1E-03		
Th-230	1.4E+04	3.7E-02	4.4E+03	1.2E-02	4.4E+03	1.2E-02		
Th-232	1.4E+04	5.9E-02	4.4E+03	1.9E-02	4.4E+03	1.9E-02		
Th-234	1.4E+04	6.2E-02	4.4E+03	1.9E-02	4.4E+03	1.9E-02		
U-234	1.4E+04	2.1E-01	4.4E+03	6.6E-02	4.4E+03	6.6E-02		
U-235	1.4E+04	1.7E-02	4.4E+03	5.5E-03	4.4E+03	5.5E-03		
U-238	1.4E+04	1.8E-01	4.4E+03	5.7E-02	4.4E+03	5.7E-02		

Table 3-27. Projected inventories of uranium chip waste.

Waste Parameter	Disposal Volume (m^3)	Disposal Activity (Ci)
Total Volumes and Activities		
Stored Waste	2.5E+01	5.3E+00
1996	9.3E-01	1.6E-01
1997-2007	4.4E+01	7.7E+00
2008-2049	9.7E+01	1.7E+01
Radionuclide-Specific Activities		
U-234	1.7E+02	1.3E+01
U-235	1.7E+02	3.0E-01
U-236	1.7E+02	6.0E-01
U-238	1.7E+02	1.7E+01

3.2.4 Total Future Inventory

The total volumes and activities of LLW projected to require disposal at Area G in the future are listed in Table 3-28. Separate totals are provided for the four waste forms considered in source-term modeling and for waste disposed of in pits and shafts. Tables 3-29 and 3-30 list the total projected radionuclide inventories for the pits and shafts, respectively.

3.3 SUMMARY OF THE AREA G RADIOACTIVE WASTE INVENTORY

As discussed in Chapter 1, the Area G performance assessment and composite analysis address different portions of the waste that has been disposed of, and which is expected to require disposal at, the disposal facility. This section summarizes the radioactive waste inventories specific to these two analyses. The Area G inventory for the performance assessment is summarized in Section 3.3.1, while Section 3.3.2 presents the inventory for the composite analysis.

3.3.1 Radioactive Waste Inventory for the Area G Performance Assessment

The Area G performance assessment includes waste disposed of since September 26, 1988, and the waste expected to require disposal over the remainder of the facility's lifetime. The characteristics of this waste are detailed in Sections 3.1.3 and 3.2 of this report. The summary tables that follow are based on the information in those sections.

The total volumes and activities of waste projected to be disposed of between September 26, 1988, and the year 2044 are provided in Table 3-31 for the disposal pits and shafts. These quantities are provided for the four waste forms that will be considered in source-term modeling, and are summed over all pits and shafts receiving waste during this period. The projected radionuclide inventories for this waste are listed in Tables 3-32 and 3-33 for pits and shafts, respectively. The waste volumes listed in these tables represent the quantities of waste contaminated with each radionuclide. Because several radionuclides may

Table 3-28. Total future inventory volume and activity projections.

Disposal Unit/Waste Form	Total Volume (m^3)	Total Activity (Ci)
Pit Waste		
Surface-Contaminated Waste	1.2E+05	1.4E+03
Soils	9.4E+03	3.4E+01
Concrete and Sludges	5.5E+03	3.9E+01
Bulk-Contaminated Waste	2.5E+03	1.7E+01
Shaft Waste		
Surface-Contaminated Waste	1.1E+03	6.1E+06
Soils	—	—
Concrete and Sludges	2.0E+02	3.4E+00
Bulk-Contaminated Waste	1.1E+02	1.6E+04

Table 3-29. Total future radionuclide inventories for Area G pits.

	Waste Form							
	Surface-Contaminated Waste		Soils		Concrete and Sludges		Bulk-Contaminated Waste	
Radionuclide	Volume (m^3)	Activity (Ci)	Volume (m^3)	Activity (Ci)	Volume (m^3)	Activity (Ci)	Volume (m^3)	Activity (Ci)
Ac-227	1.4E+04	7.1E-02	4.4E+03	2.2E-02	4.4E+03	2.2E-02		
Ag-108m	8.6E+03	2.0E-01						
Al-26	2.3E-01	3.1E-07						
Am-241	3.2E+04	1.1E+00	4.4E+03	1.6E-02	5.5E+03	5.0E+00		
Am-243	3.5E+02	2.0E-04						
Ba-133	8.8E+03	7.0E+00						
Bi-207	6.0E+00	7.7E-04						
Bk-247	1.5E+02	4.5E-07						
C-14	1.6E+03	1.4E-01						
Cd-113m	8.6E+03	8.0E-01						
Cf-252	1.2E+00	1.2E-04						
Cl-36	1.2E+00	3.1E-03						
Co-60	3.1E+04	2.0E+01	4.4E+03	2.7E-03	4.4E+03	2.7E-03	2.5E+03	5.5E-01
Cs-135	8.6E+03	2.0E-04						
Cs-137	2.6E+04	2.9E+00	4.4E+03	5.1E-03	4.4E+03	5.3E-03		
Dy-154	8.6E+03	1.3E-06						
Eu-152	8.7E+03	4.4E-01						
Eu-154	8.6E+03	1.3E-01						
Gd-148	8.6E+03	3.4E-01						
Gd-150	8.6E+03	3.6E-06						
H-3	1.9E+04	7.0E+02	4.4E+03	6.5E-01	4.4E+03	5.8E+00		
Hf-182	3.5E+02	5.2E-02						
Ho-163	1.1E+02	2.8E-02						
I-129	8.6E+03	2.4E-06						
K-40	1.4E+04	8.3E-01	4.4E+03	2.6E-01	4.4E+03	2.6E-01		
Kr-81	8.6E+03	4.3E-05						
Kr-85	8.6E+03	2.1E+00						
La-137	8.6E+03	7.0E-04						
Mo-93	8.6E+03	1.4E-02						
Nb-92	8.6E+03	4.2E-06						
Nb-94	8.6E+03	2.1E-01						
Ni-59	1.5E+02	3.9E-02						
Ni-63	2.3E+00	1.3E-03						
Np-237	5.1E+02	5.0E-03						
Pa-231	1.4E+02	7.4E-08						
Pb-210	1.4E+04	2.2E-01	4.4E+03	4.4E-02	4.4E+03	4.4E-02		
Pd-107	8.6E+03	5.9E-06						
Pm-145	1.4E+02	6.4E-03						
Pu-238	4.1E+04	3.8E-01	4.4E+03	4.9E-03	5.5E+03	1.9E+01		
Pu-239	7.1E+04	2.1E+01	4.4E+03	9.1E-01	5.5E+03	7.7E+00		
Pu-240	3.3E+04	5.1E+00	4.4E+03	9.7E-01	4.4E+03	9.7E-01		
Pu-241	1.9E+04	3.1E+01						
Pu-242	1.9E+04	1.1E-04						
Ra-226	1.4E+04	2.4E-01	4.4E+03	1.5E-02	4.4E+03	1.5E-02		
Se-79	8.6E+03	4.0E-06						
Si-32	1.6E+03	4.3E-01						

Table 3-29. Continued.

	Waste Form							
	Surface-Contaminated Waste		Soils		Concrete and Sludges		Bulk-Contaminated Waste	
Radionuclide	Volume (m^3)	Activity (Ci)	Volume (m^3)	Activity (Ci)	Volume (m^3)	Activity (Ci)	Volume (m^3)	Activity (Ci)
Sm-146	8.6E+03	3.2E-07						
Sm-147	8.8E+03	2.5E-10						
Sm-151	8.6E+03	1.1E-01						
Sr-90	2.4E+04	3.0E+00	4.4E+03	9.1E-03	4.4E+03	9.1E-03		
Tb-157	8.6E+03	4.0E-03						
Tb-158	8.6E+03	1.7E-03						
Tc-97	8.6E+03	3.2E-05						
Tc-99	2.5E+04	1.7E-01	4.4E+03	3.1E-03	4.4E+03	3.1E-03		
Th-229	1.1E+02	3.1E-04						
Th-230	1.4E+04	3.7E-02	4.4E+03	1.2E-02	4.4E+03	1.2E-02		
Th-232	1.7E+04	7.7E-02	4.4E+03	1.9E-02	4.4E+03	1.9E-02		
Ti-44	5.7E+01	2.5E-03						
U-232	1.6E+00	1.6E-09						
U-233	4.5E+01	6.2E-03						
U-234	1.8E+04	3.5E+00	6.5E+03	1.3E+01	4.4E+03	6.6E-02		
U-235	4.8E+04	4.2E+00	6.5E+03	3.1E-01	5.5E+03	1.0E-02		
U-236	1.8E+03	1.8E-02	2.0E+03	6.0E-01				
U-238	3.7E+04	2.9E+01	9.1E+03	1.8E+01	4.4E+03	7.2E-02		
Zr-93	8.6E+03	4.4E-05						

Table 3-30. Total future radionuclide inventories for Area G shafts.

	Waste Form							
	Surface-Contaminated Waste		Soils		Concrete and Sludges		Bulk-Contaminated Waste	
Radionuclide	Volume (m^3)	Activity (Ci)	Volume (m^3)	Activity (Ci)	Volume (m^3)	Activity (Ci)	Volume (m^3)	Activity (Ci)
Am-241	7.2E+01	8.5E-03			2.9E+02	8.5E-01		
Ba-133	2.5E-01	2.0E-03						
Bi-207	3.1E-02	3.3E-05						
C-14	2.3E+01	2.2E-08						
Cf-252	3.1E-02	3.7E-07						
Co-60	4.1E+02	4.6E+03					1.1E+02	5.3E+02
Cs-135	2.2E+01	3.7E-05						
Cs-137	3.6E+01	6.7E+02						
Eu-152	1.0E+00	1.8E-02						
Eu-154	2.8E+00	7.9E-01						
H-3	2.4E+02	6.2E+06						
Kr-85	9.3E-03	8.2E-03						
Lu-172	1.1E+01	2.1E+00						
Nb-92	9.3E-01	3.3E-02						
Ni-63	3.1E-02	2.5E-04						
Pb-210	1.5E-01	1.9E-08						
Pm-145	1.5E-01	3.2E-13						
Pu-238	1.2E+02	1.1E-02			2.9E+02	2.0E+00		
Pu-239	1.5E+02	1.1E-01			3.0E+02	6.3E-01		
Pu-240	3.4E+00	2.3E-02						
Pu-241	3.4E+00	3.5E-01						
Pu-242	3.4E+00	1.3E-06						
Ra-226	4.6E-01	1.6E-06						
Sm-147	1.5E-01	1.2E-14						
Sr-90	1.6E+00	3.4E+01						
Th-229	3.1E-02	4.4E-07						
Th-232	7.6E+00	3.3E-03						
U-234	9.6E-01	9.9E-04						
U-235	1.1E+02	8.9E-03			2.9E+02	1.8E-03		
U-236	9.6E-01	4.7E-05						
U-238	1.7E+02	1.6E+00			3.4E+00	3.1E-06		

Table 3-31. Pit and shaft waste volumes and activities included in the Area G performance assessment inventory.

Disposal Unit/ Waste Form	Total Disposal Volume (m^3)	Total Disposal Activity (Ci)
Pits		
Surface-Contaminated Waste	1.5E+05	1.6E+03
Soils	1.4E+04	4.0E+01
Concrete and Sludges	6.8E+03	4.4E+01
Bulk-Contaminated Waste	3.5E+03	2.4E+01
Shafts		
Surface-Contaminated Waste	1.3E+03	6.6E+06
Soils	1.3E+01	2.7E-07
Concrete and Sludges	2.2E+02	3.9E+00
Bulk-Contaminated Waste	1.4E+02	1.9E+04

Table 3-32. Pit radionuclide inventories for the Area G performance assessment.

	Waste Form							
	Surface-Contaminated Waste		Soils		Concrete and Sludges		Bulk-Contaminated Waste	
Radionuclide	Volume (m^3)	Activity (Ci)	Volume (m^3)	Activity (Ci)	Volume (m^3)	Activity (Ci)	Volume (m^3)	Activity (Ci)
Ac-227	1.4E+04	7.1E-02	4.4E+03	2.2E-02	4.4E+03	2.2E-02		
Ag-108m	1.0E+04	2.3E-01	6.8E+02	3.4E-06	7.2E+01	1.6E-06		
Al-26	2.6E-01	3.4E-07						
Am-241	3.5E+04	1.2E+00	4.9E+03	2.0E-02	5.7E+03	5.6E+00		
Am-243	3.9E+02	3.4E-04	1.6E+00	5.7E-05	1.6E+00	5.7E-05		
Be-133	1.1E+04	8.3E+00	6.8E+02	1.2E-04	7.2E+01	5.8E-05		
Bi-207	6.8E+00	8.6E-04						
Bk-247	1.7E+02	5.1E-07						
C-14	1.9E+03	1.5E-01	9.0E+00	3.9E-05	8.8E+00	3.9E-05		
Cd-113m	1.0E+04	9.5E-01	6.8E+02	1.4E-05	7.2E+01	6.6E-06		
Cf-252	1.3E+00	1.3E-04						
Cl-36	1.3E+00	3.4E-03						
Co-60	3.5E+04	3.0E+01	4.8E+03	2.7E-01	4.6E+03	2.6E-01	3.5E+03	7.8E-01
Cs-135	1.0E+04	2.3E-04	6.8E+02	6.3E-10	7.2E+01	3.0E-10		
Cs-137	2.9E+04	4.3E+00	5.5E+03	5.9E-01	4.7E+03	5.0E-01		
Dy-154	1.0E+04	1.5E-05	6.8E+02	2.2E-11	7.2E+01	1.1E-11		
Eu-152	1.0E+04	5.6E-01	6.8E+02	8.0E-06	7.3E+01	3.7E-06		
Eu-154	1.0E+04	1.5E-01	6.8E+02	2.2E-06	7.2E+01	1.1E-06		
Gd-148	1.0E+04	4.0E-01	6.8E+02	5.9E-06	7.2E+01	2.8E-06		
Gd-150	1.0E+04	4.2E-06	6.8E+02	6.2E-11	7.2E+01	3.0E-11		
H-3	2.0E+04	7.1E+02	4.7E+03	3.5E+00	4.5E+03	6.5E+00		
Hf-182	3.9E+02	5.9E-02						
Ho-163	1.2E+02	3.2E-02						
I-129	1.0E+04	2.9E-06	6.8E+02	4.2E-11	7.2E+01	2.0E-11		
K-40	1.4E+04	8.3E-01	4.4E+03	2.6E-01	4.4E+03	2.6E-01		
Kr-81	1.0E+04	5.1E-05	6.8E+02	7.4E-10	7.2E+01	3.6E-10		
Kr-85	1.0E+04	2.5E+00	6.8E+02	3.6E-05	7.2E+01	1.8E-05		
Le-137	1.0E+04	8.3E-04	6.8E+02	1.2E-08	7.2E+01	5.8E-09		
Mo-93	1.0E+04	1.6E-02	6.8E+02	2.4E-07	7.2E+01	1.2E-07		
Nb-92	1.0E+04	5.0E-06	6.8E+02	7.2E-11	7.2E+01	3.5E-11		
Nb-94	1.0E+04	2.3E-01	6.8E+02	1.0E-07	7.2E+01	6.5E-08		
Ni-59	1.7E+02	4.9E-02	3.8E-01	1.4E-03	3.8E-01	1.4E-03		
Ni-63	2.6E+00	1.5E-03						
Np-237	5.8E+02	5.7E-03	1.7E+00	3.5E-08	1.7E+00	3.5E-08		
Pa-231	1.6E+02	8.3E-08						
Pb-210	1.4E+04	2.3E-01	4.4E+03	4.4E-02	4.4E+03	4.4E-02		
Pd-107	1.0E+04	7.0E-06	6.8E+02	1.0E-10	7.2E+01	4.9E-11		
Pm-146	1.6E+02	5.2E-03						
Pu-238	4.5E+04	4.2E-01	5.2E+03	1.6E+00	5.7E+03	2.1E+01		
Pu-239	8.1E+04	2.4E+01	5.2E+03	1.1E+00	5.8E+03	8.6E+00		
Pu-240	3.6E+04	5.4E+00	4.4E+03	9.7E-01	4.4E+03	9.7E-01		
Pu-241	2.2E+04	3.5E+01	1.1E+00	1.6E-07	1.1E+00	9.5E-13		
Pu-242	2.2E+04	2.4E-04	2.5E+00	5.7E-05	2.5E+00	5.7E-05		
Ra-226	1.4E+04	2.7E-01	4.4E+03	1.5E-02	4.4E+03	1.5E-02		
Se-79	1.0E+04	4.7E-06	6.8E+02	6.8E-11	7.2E+01	3.3E-11		
Si-32	1.9E+03	2.6E+00						
Sm-146	1.0E+04	3.8E-07	6.8E+02	5.6E-12	7.2E+01	2.7E-12		
Sm-147	1.1E+04	3.0E-10	6.8E+02	4.5E-15	7.2E+01	2.1E-15		
Sm-151	1.0E+04	1.3E-01	6.8E+02	1.9E-06	7.2E+01	9.0E-07		

Table 3-32. Continued.

	Waste Form							
	Surface-Contaminated Waste		Soils		Concrete and Sludges		Bulk-Contaminated Waste	
Radionuclide	Volume (m^3)	Activity (Ci)	Volume (m^3)	Activity (Ci)	Volume (m^3)	Activity (Ci)	Volume (m^3)	Activity (Ci)
Sr-90	2.6E+04	3.6E+00	5.2E+03	4.3E-02	4.3E+03	4.3E-02		
Tb-157	1.0E+04	4.7E-03	6.8E+02	6.9E-06	7.2E+01	3.3E-06		
Tb-158	1.0E+04	2.0E-03	6.8E+02	2.9E-06	7.2E+01	1.4E-06		
Tc-97	1.0E+04	3.8E-05	6.8E+02	5.6E-10	7.2E+01	2.7E-10		
Tc-99	2.7E+04	1.9E-01	5.1E+03	3.1E-03	4.5E+03	3.1E-03		
Th-229	1.2E+02	3.5E-04	1.7E-01	5.2E-07	1.7E-01	5.2E-07		
Th-230	1.4E+04	3.7E-02	4.4E+03	1.2E-02	4.4E+03	1.2E-02		
Th-232	1.7E+04	1.2E-01	4.4E+03	1.9E-02	4.4E+03	1.9E-02		
Ti-44	6.4E+01	2.8E-03						
U-232	2.0E+00	1.1E-04	1.0E-01	5.7E-05	1.0E-01	5.7E-05		
U-233	5.8E+01	7.7E-03	4.0E+00	3.4E-04	4.0E+00	3.4E-04		
U-234	1.9E+04	4.1E+00	7.4E+03	1.3E+01	4.7E+03	7.5E-02		
U-235	5.6E+04	4.9E+00	7.6E+03	3.7E-01	6.1E+03	6.8E-02		
U-236	2.1E+03	2.1E-02	2.2E+03	6.0E-01	9.0E+00	6.0E-05		
U-238	4.1E+04	3.4E+01	1.0E+04	1.8E+01	4.6E+03	1.0E-01		
Zr-93	1.0E+04	5.2E-05	6.8E+02	7.0E-10	7.2E+01	3.6E-10		

Table 3-33. Shaft radionuclide inventories for the Area G performance assessment.

	Waste Form							
	Surface-Contaminated Waste		Soils		Concrete and Sludges		Bulk-Contaminated Waste	
Radionuclide	Volume (m^3)	Activity (Ci)	Volume (m^3)	Activity (Ci)	Volume (m^3)	Activity (Ci)	Volume (m^3)	Activity (Ci)
Ag-108m	6.2E+00	1.2E-01						
Am-241	8.1E+01	9.5E-03			3.3E+02	9.6E-01		
Ba-133	6.5E+00	4.5E+00						
Bi-207	3.5E-02	3.7E-05						
C-14	2.6E+01	8.9E-03						
Cd-113m	6.2E+00	5.1E-01						
Cf-252	3.5E-02	4.2E-07						
Co-60	4.8E+02	5.4E+03					1.4E+02	6.2E+02
Cs-135	3.1E+01	6.4E-06						
Cs-137	4.8E+01	7.5E+02						
Dy-154	6.2E+00	8.2E-07						
Eu-152	7.3E+00	3.0E-01						
Eu-154	9.4E+00	9.7E-01						
Gd-148	6.2E+00	2.2E-01						
Gd-150	6.2E+00	2.3E-06						
H-3	2.9E+02	6.6E+06	7.5E+00	1.5E-07				
I-129	6.2E+00	1.5E-06						
Kr-81	6.2E+00	2.7E-05						
Kr-85	6.2E+00	1.4E+00						
La-137	6.2E+00	4.4E-04						
Lu-172	1.1E+01	2.1E+00						
Mo-93	6.2E+00	8.8E-03						
Nb-92	7.2E+00	3.7E-02						
Nb-94	6.2E+00	2.7E-03						
Ni-63	3.5E-02	2.8E-04						
Pb-210	1.7E-01	2.2E-08						
Pd-107	6.2E+00	3.8E-06						
Pm-145	1.5E-01	3.2E-13						
Pu-238	1.4E+02	1.3E-02			3.3E+02	2.2E+00		
Pu-239	1.7E+02	1.2E-01			3.3E+02	7.1E-01		
Pu-240	3.8E+00	2.6E-02						
Pu-241	3.8E+00	3.9E-01						
Pu-242	3.8E+00	1.5E-06						
Ra-226	5.5E-01	1.7E-05						
Se-79	6.2E+00	2.5E-06						
Sm-146	6.2E+00	2.0E-07						
Sm-147	6.4E+00	1.6E-10						
Sm-151	6.2E+00	6.9E-02						
Sr-90	8.0E+00	4.1E+01						
Tb-157	6.2E+00	2.5E-03						
Tb-158	6.2E+00	1.1E-03						
Tc-97	6.2E+00	2.0E-05						
Tc-99	6.2E+00	2.5E-04						
Th-229	3.5E-02	5.0E-07						
Th-232	8.5E+00	3.7E-03						
U-234	1.2E+00	3.5E-03	1.8E-02	4.7E-08	1.8E-02	4.7E-08		
U-235	1.2E+02	1.0E-02	1.8E-02	1.1E-09	3.3E+02	2.0E-03		
U-236	1.1E+00	5.3E-05	1.8E-02	2.2E-09	1.8E-02	2.2E-09		
U-238	1.9E+02	1.8E+00	1.8E-02	6.1E-08	4.0E+00	3.5E-06		
Zr-93	6.2E+00	2.8E-05						

occur in a single waste package, the sum of these volumes is greater than the total volume of waste disposed of in the pits and shafts.

3.3.2 Radioactive Waste Inventory for the Area G Composite Analysis

The composite analysis includes all waste disposed of since the Area G disposal facility opened in 1957 and the waste expected to require disposal over the remainder of the facility's lifetime. Estimated quantities, physical forms, and radiological characteristics of this waste are presented and discussed in Sections 3.1 and 3.2 of this report. The information summarized in the tables that follow is based on the data presented in those sections.

The projected quantities of waste disposed of from the beginning of operations at Area G through the year 2044 are provided in Table 3-34 for the disposal pits and shafts. Total volumes and activities are provided for surface-contaminated waste, soils, concrete and sludges, and bulk-contaminated waste. They are summed over all pits and shafts receiving waste during this period. Tables 3-35 and 3-36 list the projected pit and shaft radionuclide inventories, respectively, for the waste included in the composite analysis. The waste volumes listed in these tables represent the quantities of waste contaminated with each radionuclide. Because several radionuclides may occur in a single waste package, the sum of these volumes exceeds the total volume of waste disposed of in the pits and shafts.

Table 3-34. Pit and shaft waste volumes and activities included in the Area G composite analysis inventory.

Disposal Unit/ Waste Form	Total Disposal Volume (m^3)	Total Disposal Activity (Ci)
Pits		
Surface-Contaminated Waste	2.4E+05	5.9E+04
Soils	5.4E+04	1.0E+02
Concrete and Sludges	2.0E+04	2.9E+03
Bulk-Contaminated Waste	4.4E+03	5.7E+02
Shafts		
Surface-Contaminated Waste	2.2E+03	7.4E+06
Soils	3.5E+01	1.0E+02
Concrete and Sludges	2.2E+02	1.0E+02
Bulk-Contaminated Waste	2.6E+02	2.6E+04

Table 3-35. Pit radionuclide inventories for the Area G composite analysis.

	Waste Form							
	Surface-Contaminated Waste		Soils		Concrete and Sludges		Bulk-Contaminated Waste	
Radionuclide	Volume (m^3)	Activity (Ci)	Volume (m^3)	Activity (Ci)	Volume (m^3)	Activity (Ci)	Volume (m^3)	Activity (Ci)
Ac-227	1.4E+04	1.0E+00	4.4E+03	2.2E-02	4.4E+03	2.2E-02		
Ag-108m	1.7E+04	3.7E+00	8.1E+02	2.6E-05	3.0E+02	1.2E-03		
Al-26	2.6E-01	3.4E-07						
Am-241	3.6E+04	4.6E+01	5.4E+03	1.2E+00	1.1E+04	2.2E+03		
Am-243	3.9E+02	3.4E-04	1.6E+00	5.7E-05	1.6E+00	5.7E-05		
Ba-133	1.7E+04	1.3E+02	8.1E+02	9.5E-04	3.0E+02	4.2E-02		
Bi-207	6.8E+00	8.6E-04						
Bk-247	1.7E+02	5.1E-07						
C-14	1.9E+03	3.8E-01	9.0E+00	3.9E-05	8.8E+00	3.9E-05		
Cd-109	3.2E+03	3.7E+01						
Cd-113m	1.7E+04	1.5E+01	8.1E+02	1.1E-04	3.0E+02	4.8E-03		
Cf-249	1.9E+00	2.8E-03						
Cf-251	2.3E-01	4.3E-03						
Cf-252	2.1E+00	2.3E-02						
Cl-36	1.3E+00	3.4E-03						
Cm-244	3.6E-01	1.7E-03						
Co-60	3.8E+04	1.3E+03	5.0E+03	6.0E-01	4.7E+03	2.6E-01	4.4E+03	1.9E-01
Cs-135	1.7E+04	8.7E-04	8.1E+02	4.9E-09	3.0E+02	2.2E-07		
Cs-137	3.6E+04	1.1E+03	6.6E+03	6.0E-01	5.0E+03	5.1E-01		
Dy-154	1.7E+04	2.4E-05	8.1E+02	1.7E-10	3.0E+02	7.7E-09		
Eu-152	1.7E+04	8.4E+00	8.1E+02	6.0E-05	3.0E+02	2.7E-03		
Eu-154	1.7E+04	2.4E+00	8.1E+02	1.7E-05	3.0E+02	7.6E-04		
Gd-148	1.7E+04	6.4E+00	8.1E+02	4.6E-05	3.0E+02	2.0E-03		
Gd-150	1.7E+04	6.7E-05	8.1E+02	4.8E-10	3.0E+02	2.1E-08		
H-3	2.3E+04	8.2E+03	4.7E+03	4.7E+00	4.7E+03	7.7E+00		
Hf-182	3.9E+02	5.9E-02						
Ho-163	1.2E+02	3.2E-02						
I-129	1.7E+04	4.6E-05	8.1E+02	3.2E-10	3.0E+02	1.4E-08		
K-40	1.4E+04	8.3E-01	4.4E+03	2.6E-01	4.4E+03	2.6E-01		
Kr-81	1.7E+04	8.1E-04	8.1E+02	3.8E-09	3.0E+02	2.6E-07		
Kr-85	1.7E+04	4.0E+01	8.1E+02	2.8E-04	3.0E+02	1.3E-02		
La-137	1.7E+04	1.3E-02	8.1E+02	9.4E-08	3.0E+02	4.2E-06		
Mo-93	1.7E+04	2.6E-01	8.1E+02	1.9E-06	3.0E+02	8.3E-06		
Nb-92	1.7E+04	5.2E-05	8.0E+02	5.6E-10	3.0E+02	2.5E-08		
Nb-94	1.7E+04	3.1E-01	8.1E+02	5.9E-07	3.0E+02	2.5E-05		
Ni-59	1.7E+02	4.9E-02	3.8E-01	1.4E-03	3.8E-01	1.4E-03		
Ni-63	2.6E+00	1.5E-03						
Np-237	5.0E+02	9.6E-03	1.7E+00	3.5E-08	1.7E+00	3.5E-08		
Pa-231	1.6E+02	8.3E-06						
Pb-210	1.4E+04	2.3E-01	4.4E+03	4.4E-02	4.4E+03	4.4E-02		
Pd-107	1.7E+04	1.1E-04	8.1E+02	8.0E-10	3.0E+02	3.6E-08		
Pm-145	1.6E+02	5.2E-03						
Pu-238	6.4E+04	4.2E+03	9.6E+03	3.4E+00	1.1E+04	6.4E+02		
Pu-239	1.2E+05	1.8E+03	1.7E+04	4.1E+01	1.6E+04	1.0E+02		
Pu-240	4.2E+04	4.6E+02	4.8E+03	1.0E+00	4.6E+03	9.7E-01		
Pu-241	2.8E+04	8.2E+03	3.2E+02	6.5E-01	1.5E+02	6.7E-02		
Pu-242	2.8E+04	4.9E-02	3.2E+02	6.7E-05	1.5E+02	5.7E-05		
Ra-226	1.4E+04	4.6E-01	4.4E+03	1.5E-02	4.4E+03	1.5E-02		
Se-79	1.7E+04	7.5E-05	8.1E+02	5.3E-10	3.0E+02	2.4E-08		

Table 3-35. Continued.

	Waste Form							
	Surface-Contaminated Waste		Soils		Concrete and Sludges		Bulk-Contaminated Waste	
Radionuclide	Volume (m^3)	Activity (Ci)	Volume (m^3)	Activity (Ci)	Volume (m^3)	Activity (Ci)	Volume (m^3)	Activity (Ci)
Si-32	2.0E+03	2.6E+00						
Sm-146	1.7E+04	6.1E-06	8.1E+02	4.3E-11	3.0E+02	1.9E-09		
Sm-147	1.7E+04	2.7E-02	8.1E+02	3.4E-14	3.0E+02	1.5E-12		
Sm-151	1.7E+04	2.1E+00	8.1E+02	1.5E-05	3.0E+02	6.5E-04		
Sr-90	3.4E+04	1.4E+03	6.8E+03	2.3E-01	4.9E+03	6.1E-02		
Tb-157	1.7E+04	7.5E-02	8.1E+02	5.4E-07	3.0E+02	2.4E-05		
Tb-158	1.7E+04	3.2E-02	8.1E+02	2.3E-07	3.0E+02	1.0E-05		
Tc-97	1.7E+04	6.1E-04	8.1E+02	4.3E-09	3.0E+02	1.9E-07		
Tc-99	3.3E+04	2.0E-01	5.3E+03	3.1E-03	4.7E+03	3.1E-03		
Th-229	1.2E+02	3.5E-04	1.7E-01	5.2E-07	1.7E-01	5.2E-07		
Th-230	1.4E+04	2.6E+01	4.4E+03	1.2E-02	4.4E+03	1.2E-02		
Th-232	1.7E+04	1.5E-01	4.4E+03	1.9E-02	4.4E+03	1.9E-02		
Ti-44	6.4E+01	2.8E-03						
U-232	2.0E+00	1.1E-04	1.0E-01	5.7E-05	1.0E-01	5.7E-05		
U-233	6.3E+01	2.7E-02	4.0E+00	3.4E-04	2.5E+03	6.2E+00		
U-234	2.0E+04	7.8E+00	7.4E+03	1.4E+01	4.7E+03	7.5E-02		
U-235	8.7E+04	6.1E+00	1.0E+04	4.0E-01	9.0E+03	7.9E-02		
U-236	2.2E+03	2.1E-02	2.2E+03	6.0E-01	9.0E+00	6.0E-05		
U-238	6.5E+04	5.5E+01	1.9E+04	2.3E+01	4.7E+03	1.0E-01		
Zr-93	1.7E+04	8.3E-04	8.1E+02	5.9E-09	3.0E+02	2.6E-07		

Table 3-36. Shaft radionuclide inventories for the Area G composite analysis.

	Waste Form							
	Surface-Contaminated Waste		Soils		Concrete and Sludges		Bulk-Contaminated Waste	
Radionuclide	Volume (m^3)	Activity (Ci)	Volume (m^3)	Activity (Ci)	Volume (m^3)	Activity (Ci)	Volume (m^3)	Activity (Ci)
Ag-108m	4.2E+01	1.9E+01						
Am-241	8.8E+01	4.9E-02			3.3E+02	9.6E-01		
Am-243	2.6E-02	1.1E-05						
Ba-133	4.2E+01	6.8E+02						
Bi-207	3.5E-02	3.7E-05						
C-14	3.2E+01	1.1E+00						
Cd-113m	4.2E+01	7.7E+01						
Cf-252	5.9E-01	1.1E+02						
Cm-244	7.7E-01	3.7E-01						
Co-60	6.4E+02	8.5E+03					2.6E+02	8.4E+02
Cs-135	6.7E+01	3.6E-03						
Cs-137	8.6E+01	9.2E+02						
Dy-154	4.2E+01	1.2E-04						
Eu-152	4.3E+01	4.3E+01						
Eu-154	4.5E+01	1.3E+01						
Gd-148	4.2E+01	3.3E+01						
Gd-150	4.2E+01	3.4E-04						
H-3	4.8E+02	7.5E+06	7.6E+00	1.0E+02	5.3E-01	1.0E+02		
Hf-182	2.8E-02	3.1E+01						
I-129	4.2E+01	2.3E-04						
Kr-81	4.2E+01	4.1E-03						
Kr-85	4.5E+01	2.0E+02						
La-137	4.2E+01	6.7E-02						
Lu-172	1.1E+01	2.1E+00						
Mo-93	4.2E+01	1.3E+00						
Nb-92	4.1E+01	3.7E-02						
Nb-94	4.2E+01	4.0E-01						
Ni-63	3.9E+00	4.6E-03						
Np-237	1.4E-01	1.5E-04						
Pb-210	1.7E-01	2.2E-08						
Pd-107	4.2E+01	5.7E-04						
Pm-145	1.5E-01	3.2E-13						
Pu-238	2.7E+02	2.5E+00			3.3E+02	2.2E+00		
Pu-239	3.9E+02	1.5E+02			3.3E+02	7.1E-01		
Pu-240	1.7E+01	4.7E+00						
Pu-241	1.7E+01	7.3E+01						
Pu-242	1.7E+01	2.7E-04						
Ra-226	1.9E+00	2.5E+00						
Se-79	4.2E+01	3.8E-04						
Sm-146	4.2E+01	3.1E-05						
Sm-147	4.4E+01	2.4E-08						
Sm-151	4.2E+01	1.1E+01						
Sr-90	4.5E+01	3.0E+02						
Tb-157	4.2E+01	3.9E-01						
Tb-158	4.2E+01	1.6E-01						
Tc-97	4.2E+01	3.1E-03						
Tc-99	4.2E+01	3.8E-02						
Th-229	3.5E-02	5.0E-07						
Th-232	2.1E+01	3.4E-02						

Table 3-36. Continued.

	Waste Form							
	Surface-Contaminated Waste		Soils		Concrete and Sludges		Bulk-Contaminated Waste	
Radionuclide	Volume (m^3)	Activity (Ci)	Volume (m^3)	Activity (Ci)	Volume (m^3)	Activity (Ci)	Volume (m^3)	Activity (Ci)
U-232	7.6E-03	4.3E-01						
U-233	7.7E-01	8.0E+00						
U-234	2.9E+01	5.2E-01	6.2E+00	2.8E-02	1.8E-02	4.7E-08		
U-235	2.7E+02	1.0E+00	6.2E+00	1.1E-03	3.3E+02	2.0E-03		
U-236	2.5E+00	4.1E-04	1.8E-02	2.2E-09	1.8E-02	2.2E-09		
U-238	3.9E+02	1.7E+01	8.0E+00	1.8E-01	4.0E+00	3.5E-06		
Zr-93	4.2E+01	4.3E-03						

This page intentionally left blank.

REFERENCES

Brazenger, R., 1996, written communication from R. Murphy, Los Alamos National Laboratory, to D. Hollis, Los Alamos National Laboratory, May 15, 1996.

Carlson, R.V., 1996, written communication from R.V. Carlson, Los Alamos National Laboratory, to R. Shuman, Rogers & Associates Engineering Corporation, July 8, 1996, and July 10, 1996.

DOE, 1996, Implementation Plans, DNFSB Recommendation 94-2, rev. 1, April 1996.

ERM/Golder, 1995, "Estimated Inventory of Waste Materials for Disposal at the LANL Mixed Waste Disposal Facility," ERM Program Management Co. and Golder Federal Services, Inc., February 17, 1995.

Hodges, W.W., 1996a, memorandum from W.W. Hodges, Los Alamos National Laboratory, to D. Hollis, Los Alamos National Laboratory, July 23, 1996.

Hodges, W.W., 1996b, written communication from W.W. Hodges, Los Alamos National Laboratory, to R. Shuman, Rogers & Associates Engineering Corporation, July 25, 1996.

Kennicott, M., 1996, personal communication between M. Kennicott, Los Alamos National Laboratory, and R. Shuman, Rogers & Associates Engineering Corporation, June 28, 1996.

LANL, 1994, "Environmental Assessment, Expansion of Area G, Los Alamos National Laboratory, Los Alamos, New Mexico," Revision 5, U.S. Department of Energy, DOE/EA-0866, January 1994.

LANL, 1995, "Proposed Site Treatment Plan," Los Alamos National Laboratory, March 1995.

LANL, 1996, "Los Alamos National Laboratory Federal Facility Compliance Order Annual Site Treatment Plan Update for Fiscal Year 1995, Background Volume," Los Alamos National Laboratory, March 31, 1996.

Lopez, G., 1996, written communication between G. Lopez, Los Alamos National Laboratory, and D. Hollis, Los Alamos National Laboratory, July 24, 1996.

Maassen, L., 1996, written communication from L. Maassen, Los Alamos National Laboratory, to D. Hollis, Los Alamos National Laboratory, June 21, 1996.

Myers, S., 1996, personal communication from R.V. Carlson, Los Alamos National Laboratory, to S. Myers, Benchmark Environmental Corp., June 24, 1996.

Rogers, M.A., 1977, "History and Environmental Setting of LASL Near-Surface Land Disposal Facilities for Radioactive Wastes (Areas A, B, C, D, E, F, G, and T)," Los Alamos Scientific Laboratory, LA-6848-MS, Vol. 1, June 1977.

Vold, E.L., 1995, "Isotopic Compositions of Inventory Designations, Mixed Fission Product and Mixed Activation Product," Los Alamos National Laboratory, Appendix 2E in Performance Assessment of LANL TA-54, Area G, Low-Level Radioactive Waste Disposal Facility, preliminary draft, August 1995.

Warren, J.L., 1980, "Program Status Report: Review of Past Waste Disposal Records," Office Memorandum from J.L. Warren to W. Hansen, Los Alamos Scientific Laboratory, January 2, 1980.

Warren, J.L., 1996, "Report on Review of Proposed Method for Characterizing 1959-1971 MDA-G Disposal Inventory," prepared for the Los Alamos National Laboratory, CST-14, July 1996.

APPENDIX A

RADIONUCLIDES EXCLUDED FROM AREA G INVENTORY PROJECTIONS BASED ON HALF-LIFE CONSIDERATIONS

This page intentionally left blank.

APPENDIX A

RADIONUCLIDES EXCLUDED FROM AREA G INVENTORY PROJECTIONS BASED ON HALF-LIFE CONSIDERATIONS

As discussed in the main report, institutional control over the Area G disposal facility will be maintained for at least 100 years following the end of disposal operations. During this period, persons will be prevented from intruding onto the site for extended periods and measures will be taken to maintain proper facility function. Consequently, at Area G, there will be little or no potential for exposures to result from radionuclides with extremely short half-lives.

Consistent with the preceding discussion, most radionuclides with half-lives of 5 years or less were excluded from the Area G disposal facility inventory. Exceptions include short-lived radionuclides that decay to one or more daughter products with half-lives exceeding 5 years, and radionuclides that are daughters of parents with half-lives greater than 5 years. The radionuclides that were excluded from the inventory are listed in Table A-1.

Table A-1. Radionuclides excluded from the Area G inventory based on half-life considerations.

Radionuclide	Half-Life (yr)	Notes
Ag-110m	7.0E-01	
As-72	3.0E-03	
As-73	2.2E-01	
As-74	4.9E-02	
Ba-139	1.6E-04	
Ba-140	3.5E-02	
Be-7	1.5E-01	
Bk-249	8.6E-01	Included as Cf-249
Ca-45	4.5E-01	
Cd-109	1.2E+00	
Ce-139	3.8E-01	
Ce-141	8.9E-02	
Ce-144	7.8E-01	
Cm-242	4.5E-01	Included as Pu-238
Co-56	2.1E-01	
Co-57	7.4E-01	
Co-58	2.0E-01	
Cr-51	7.6E-02	
Cs-134	2.1E+00	
Cs-136	3.8E-02	
Cu-67	6.7E-03	
Dy-159	4.0E-01	
Eu-149	2.9E-01	
Eu-150	1.4E-03	Included as Gd-150
Eu-155	1.8E+00	
Eu-156	4.2E-02	
Fe-55	2.6E+00	
Fe-59	1.2E-01	
Gd-151	3.3E-01	
Gd-153	6.6E-01	
Ge-68	7.5E-01	
Hf-172	5.0E+00	
Hf-175	1.9E-01	
Hg-203	1.3E-01	
I-125	1.6E-01	
I-131	2.2E-02	
In-114m	1.4E-01	
In-115m	5.1E-04	
Ir-192	2.0E-01	

Table A-1. Continued.

Radionuclide	Half-Life (yr)	Notes
La-140	4.6E-03	
Lu-172	1.8E-02	
Lu-172m	7.0E-06	
Lu-173	1.4E+00	
Lu-174	3.6E+00	
Mn-52	1.5E-02	
Mn-52m	4.0E-05	
Mn-54	8.3E-01	
Na-22	2.6E+00	
Nb-91m	1.8E-01	
Nb-92m	2.8E-02	
Nb-95	9.6E-02	
Nd-147	3.0E-02	Included as Sm-147
Ni-56	1.7E-02	
Ni-65	2.9E-04	
Np-239	6.4E-03	Included as daughter of Am-243
P-32	3.9E-02	Included as Si-32
Pa-233	7.4E-02	Included as daughter of Np-237
Pb-212	1.2E-03	Included as daughter of Th-232
Pm-143	7.3E-01	
Pm-144	9.6E-01	
Pm-146	4.4E+00	
Pm-147	2.6E+00	Included as Sm-147
Po-210	3.8E-01	Included as daughter of Ra-226
Pu-233	3.8E-05	
Pu-234	1.0E-03	
Ra-228	6.7E+00	Included as daughter of Th-232
Rb-82	2.4E-06	
Rb-83	2.3E-01	
Rb-84	9.0E-02	
Rb-86	5.1E-02	
Re-183	2.0E-01	
Re-188	1.9E-03	
Rh-97	1.9E-06	
Rh-99	4.4E-02	
Rh-101	3.0E+00	
Rh-102	5.6E-01	
Ru-103	1.1E-01	
Ru-106	1.0E+00	

Table A-1. Continued.

Radionuclide	Half-Life (yr)	Notes
S-35	2.4E-01	
Sb-124	1.7E-01	
Sb-125	2.7E+00	
Sb-126	3.4E-02	
Sc-43	4.5E-04	
Sc-44	4.5E-04	Included as daughter of Ti-44
Sc-46	2.3E-01	
Se-75	3.3E-01	
Sm-145	9.3E-01	Included as Pm-145
Sn-113	3.2E-01	
Sn-121	3.1E-03	
Sr-82	6.8E-02	
Sr-85	1.8E-01	
Sr-89	1.4E-01	
Ta-179	1.6E+00	
Ta-182	3.2E-01	Included as Hf-182
Ta-183	1.4E-02	
Tc-95	2.3E-03	
Tc-95m	1.7E-01	
Tc-99m	6.9E-04	Included as Tc-99
Th-228	1.9E+00	Included as daughter of Th-232
Th-234	6.6E-02	Included as daughter of U-238
Tl-204	3.8E+00	
Tl-208	5.9E-06	Included as daughter of Th-232
Tm-170	3.7E-01	
Tm-171	1.9E+00	
U-237	1.8E-02	Included as Np-237
U-239	4.5E-05	
V-48	4.4E-02	
V-49	9.0E-01	
V-52	3.8E-06	
W-181	3.8E-01	
W-185	2.1E-01	
Y-88	3.0E-01	
Y-90	7.3E-03	Included as daughter of Sr-90
Yb-169	8.7E-02	
Zn-65	6.7E-01	
Zr-88	2.3E-01	
Zr-95	1.8E-01	

LA-UR-96-4872

Title: Isotopic Compositions of Inventory Designations, 'Mixed Fission Product' and 'Mixed Activation Product'

Author(s): Erik L. Vold

Submitted to: U.S. Department of Energy, as support documentation for the Los Alamos Area G Performance Assessment

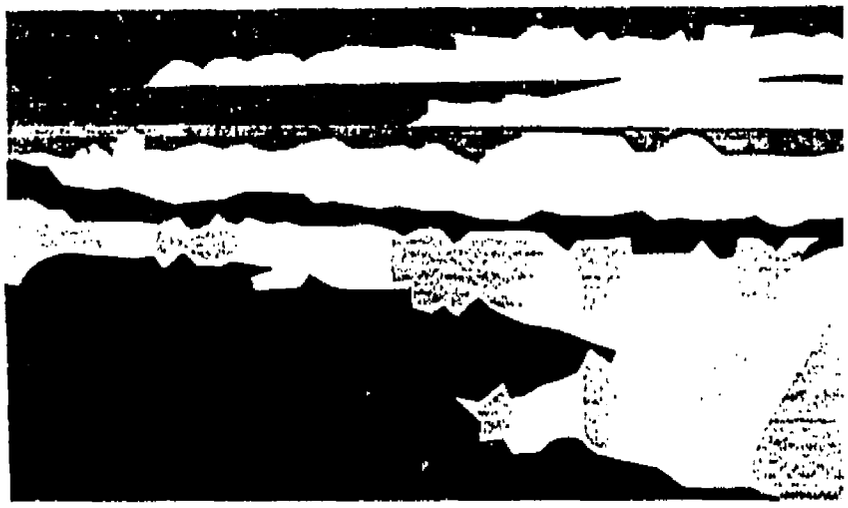

Los Alamos
NATIONAL LABORATORY

Los Alamos National Laboratory, an affirmative action/equal opportunity employer, is operated by the University of California for the U.S. Department of Energy under contract W-7405-ENG-36. By acceptance of this article, the publisher recognizes that the U.S. Government retains a nonexclusive, royalty-free license to publish or reproduce the published form of this contribution, or to allow others to do so, for U.S. Government purposes. The Los Alamos National Laboratory requests that the publisher identify this article as work performed under the auspices of the U.S. Department of Energy.

Isotopic Compositions of Inventory Designations, 'Mixed Fission Product' and 'Mixed Activation Product'

Erik L. Vold

Abstract

The Area G Performance Assessment requires that the entire inventory be specified in terms of specific nuclide activities. The inventory data base has historically allowed some less specific inventory designations including Mixed Fission Products (MFP), Mixed Activation Products (MAP), several Material Type (MT) designations and others. This report describes the assignment of specific nuclide activities from the listed activity amounts in two of the inventory data base categories, MFP and MAP. The MFP nuclide assignment is based on standard fission product yield data and normalized to total activity at two years post-fission. The MAP assignment is based on site-specific analyses conducted by the major generator of the activation products at Los Alamos, the LAMPF.

Mixed Fission Product

The inventory data base for the Los Alamos Area G low level radioactive waste disposal facility contains the entry, 'Mixed Fission Products' (MFP), for waste disposed of prior to 1992. Each MFP waste disposal was assigned a total Curie activity quantity which must be interpreted in terms of activities of specific nuclides for the Performance Assessment.

The data used to define the nuclide composition of MFP is summarized in *Table I: Mixed Fission Product Data Sheet* (last page attached). The listed nuclides were taken from the standard Table of Isotopes (or Chart of the Nuclides, GE Nuclear Energy, San Jose, CA, 1996) including all isotopes in the fission product yield range, atomic mass numbers 78-160, which have a half life of at least one year. This was selected as a practical cut-off to avoid tracking too many shorter lived isotopes. While the PA follows consequences only for nuclides with half life greater than 5 years, the nuclides with half-life between one and five years are important in determining the total activity in the inventory as reported for the waste disposal records.

The column, *FPYM# - ave.* in the Table, is the fission product yield (fractional yield per fission) for each atomic mass number. This was taken from data plots (available in most standard nuclear engineering texts, e.g., see Lamarsh '72) which show yields for thermal and fast neutrons. To be conservative for an unknown fission source we assumed the maximum of the thermal or the fast yield curve. Differences between different fissionable materials are small and neglected. Errors in this term, *FPYM# - ave.*, are small, less than a few tens of a percent.

The next column, *FPY isot. split*, shows the fractional correction for isotopic yield for a given atomic number. This assumes conservatively that all the yield at a given atomic number results in the production (or decay to) the long lived species listed in the table. This assumes no stable isotopes are produced in the yield. In those cases where two long lived nuclides exist at the same atomic mass, one on each side of the stable nuclide curve, then it is assumed that the isotopic yield of each is half. Errors in this term are uncertain but the estimate tends to overestimate production of the long-lived nuclides in the PA.

One possibility wherein this approximation would not be conservative is if a short lived nuclide decays by a process which changes its mass number, then it might contribute to a long lived daughter product at a different mass number. These decay processes were assumed rare and neglected but follow-up work should confirm this. The error associated with this type of decay if it occurs is of the same order as the solution.

The half-lives are taken from the Table of Isotopes (or Chart of the Nuclides, GE Nuclear Energy, San Jose, CA, 1996) and from various editions of the Handbook of Chemistry and Physics (CRC Press). There is not good agreement for this fundamental quantity for some of the more exotic species.

With this data, the activity results are then calculated by nuclide for several assumed values of the fission product age, or time since activation, equal to zero, 2 years, 5 years and 10 years. For each assumed 'age', there are two data columns. The first shows the activity of nuclide, i, per fission product yield (FPY) decay corrected to that age, and this column is summed to get the total MFP activity per FPY at that age. The second column is the nuclide activity at that age, normalized to the total MFP activity at that age. For example, the activity per fission is tabulated with no decay correction (however, nuclides with short half-lives are not considered) in the column, Act/FPY(t0). This is summed to obtain total activity per fission and used to normalize each nuclide contribution to the total activity listed in column, *(Act.i/Act.tot)@t=0* .

It is important to normalize to the total activity at the time that best represents the actual age of the MFP as characterized in the disposed waste. It is assumed that some waste materials are processed in the lab and disposed of in about one year while another significant contribution to the waste will be from clean-up and D&D operations which will occur several years after the MFP was created. A single representative average age for all the MFP is taken to be two years. Thus, the activity per fission for each nuclide was decay corrected to two years in column, *Act/FPY@2yr*. This was summed and again used to normalize the nuclide activities per total activity at two years, as summarized in column, *(Act.i/Act.tot)@2yr*.

Similar data is shown for the age of nuclides equal to 5 years and 10 years. These data can be used to estimate uncertainties associated with the actual age of waste disposed as 'MFP'. Note that the sum of MFP activities at each tabulated age decreases by about a factor of 2 to 3 indicating a large sensitivity of the assessment to the estimated age of the MFP.

Figure 1 shows a log scale of nuclide activity normalized to the total activity evaluated at t = 0 years (top) and at t = 2 years (bottom). A different set of nuclides dominate each case; the shortest lived nuclides which were considered (τ > 1 yr) dominate the evaluation normalized at t = 0. Similar results evaluated at t = 0, are shown on a linear scale in Fig. 2(top) for comparison. The results normalized at t = 2 years were taken to define the MFP content for the analyses in the PA. The activity remaining at 100 years and normalized to the total activity at 2 years is seen in Fig. 2(bottom). These numbers, *(Act.i/sum)@2yr*, times the activity listed as MFP in the disposal inventory represents the present best estimate of the actual nuclide inventory comprising MFP. This is the nuclide assignment used in the site PA.

Figure 3 shows a log scale of nuclide activity remaining at subsequent times, t = 100 yrs (top) and t = 10,000 yrs (bottom) normalized to the total activity evaluated at t = 2 years. Note that Fig. 2(bottom) and Fig. 3(top) show the same data on linear and log plots, respectively. These are the nuclides which could potentially contribute at later times in the assessment period and beyond.

MFP Uncertainty

The nuclide activity sum drops from 0.135 at zero time (no decay correction) to 0.051 with the two year decay correction, or by a factor of almost three, as seen in the Table. This shows the total MFP inventory is sensitive to the estimate of MFP age, and could be used to estimate the inventory uncertainty resulting from a specified age uncertainty.

The estimate for the MFP distribution assumes that the MFP 'total Curie' listed inventory amount is accurately related to the total MFP activity, so that the total activity (at 2 years) is the correct sum for normalizing nuclide amounts. The error in this assumption will depend upon the method used to determine the total MFP activity listed on the waste manifest. For example, calculating total MFP activity from gamma radiation measurements at a distance might reflect mostly just Cs-137 activity, and so the Cs-137 activity would be a better normalization constant in that case. If the waste generator measured Cs-137 activity and assigned that activity as the total MFP activity, then the waste inventory listing of MFP will significantly underestimate the total MFP inventory by an amount equal to the ratio of the MFP total activity to the Cs-137 activity in the first data column at each age group. Resolution of this detail would require interviews with waste generators from the past to determine their method of estimating MFP from some actual measurement.

The cut-off of a one year half-life for fission products evaluated here may contribute to some error. This error will decrease as the 'age' of the MFP increases. The error is expected to be small but requires more detailed analysis including shorter lived fission products to quantify.

Mixed Activation Products

The inventory data base contains the entry, 'Mixed Activation Products' (MAP), for waste disposed of prior to 1992. This needs to be defined in terms of specific nuclides for the Performance Assessment. A review of disposal records indicates MAP was primarily generated at LAMPF (Los Alamos Meson Physics Facility), a high energy accelerator facility. Conversations with current LAMPF staff (John Roberts, LANL, personal communication) lead to the following summary of their waste inventory.

There are three main waste streams from LAMPF, including trash, targets and beam line 'inserts', and targets. Each stream has a similar but distinct waste profile or nuclide composition. Materials in each stream can include activated steel, aluminum, and graphite. Only the 'trash' waste profile has been quantified to date in an ongoing effort between LAMPF and the LANL Health and Safety groups (John Roberts, personal communication). Because the waste streams are similar, this profile will be taken to represent the total profile for inventory listed as MAP.

The MAP profile has been determined to be comprised of the following isotopes by mass fraction.

Nuclide	Mass fraction
Co-57	0.12
Co-60	0.44
Mn-54	0.18
Zn-65	0.13
Na-22	0.10
Be-7	0.03

Based on this mass fraction distribution, the approximate distribution by activity follows.

Nuclide	Ci/gram	Activity fraction
Co-57	1,000	0.065
Co-60	500	0.033
Mn-54	1,450	0.095
Zn-65	1,080	0.072
Na-22	630	0.042
Be-7	10,600	0.693
Total		15,300

The short half-life of Be-7 (τ = 54d) implies that the normalization constant for total activity is changing rapidly in time. It is assumed that the waste inventory previously characterized as MAP was normalized to total activity in the same way as described here, based on the activity fractions shown above. This implies that the waste was previously characterized in the same time frame that the above mass fractions were determined.

Each of these listed nuclides have half-lives less than 5 yr except Co-60. The half-life for Na-22 is 2.6 yr, so it is not evaluated in the PA, although it is important in determining the total MAP. If it is retained as a listed nuclide, the effective PA inventory for N_{MAP} Curies of mixed activation products is ($0.033*N_{MAP}$) Curies of Co-60 and ($0.042*N_{MAP}$) Curies of Na-22. If Na-22 is neglected, the effective PA inventory is just ($0.033*N_{MAP}$) Curies of Co-60.

MAP Uncertainty

The major uncertainty in this inventory is the time at which one chooses to categorize the waste because the total activity depends primarily on the short lived nuclide, Be-7. If one assumes the inventory is assessed accurately in time to within 30 days, then the error in Be-7 activation will be related to the decay exponential expression, $1 - exp(-0.693*30/54) = 1. - 0.68$, or about 32% difference, as a rough estimate of the order of the error.

The beryllium results from graphite activation, sodium from aluminum and the other nuclides result from steel activation. The distribution of activation products is not expected to vary greatly in time or between the different waste streams from LAMPF so this variation introduces smaller uncertainty into the inventory. If this factor introduces a 20%

error, and if the two sources of errors are independent and the dominant error terms, the total error should be small, about 36%.

References

Lamarsh '72 - J.R.Lamarsh, Introduction to Nuclear Reactor Theory, p.93, Addison-Wesley, New York, 1972.

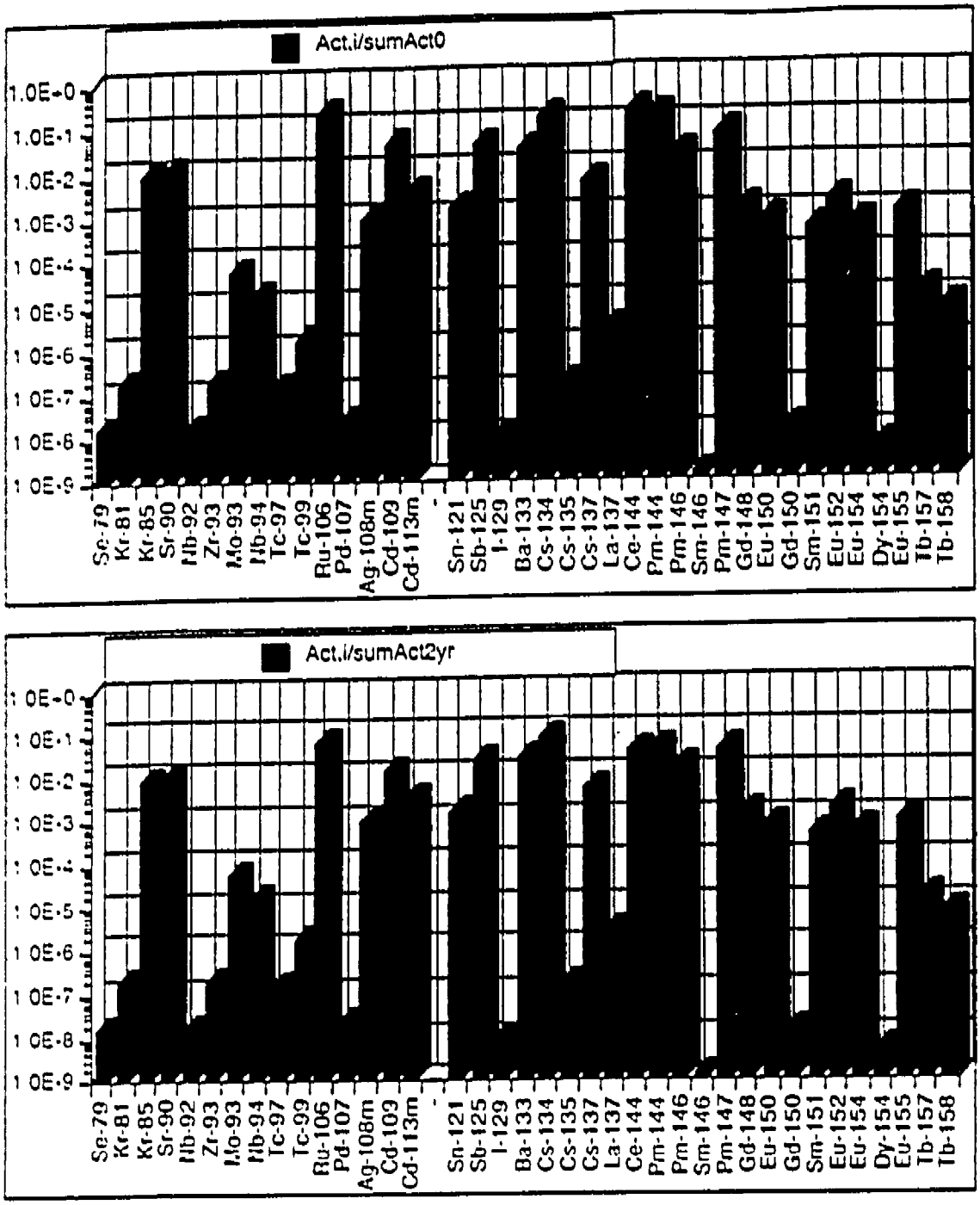

Figure 1 Log scale of nuclide activity normalized to the total activity evaluated at t = 0 years (top) and at t = 2 years (bottom). The evaluation normalized at t = 2 years was taken to define the MFP content for the analyses in the PA.

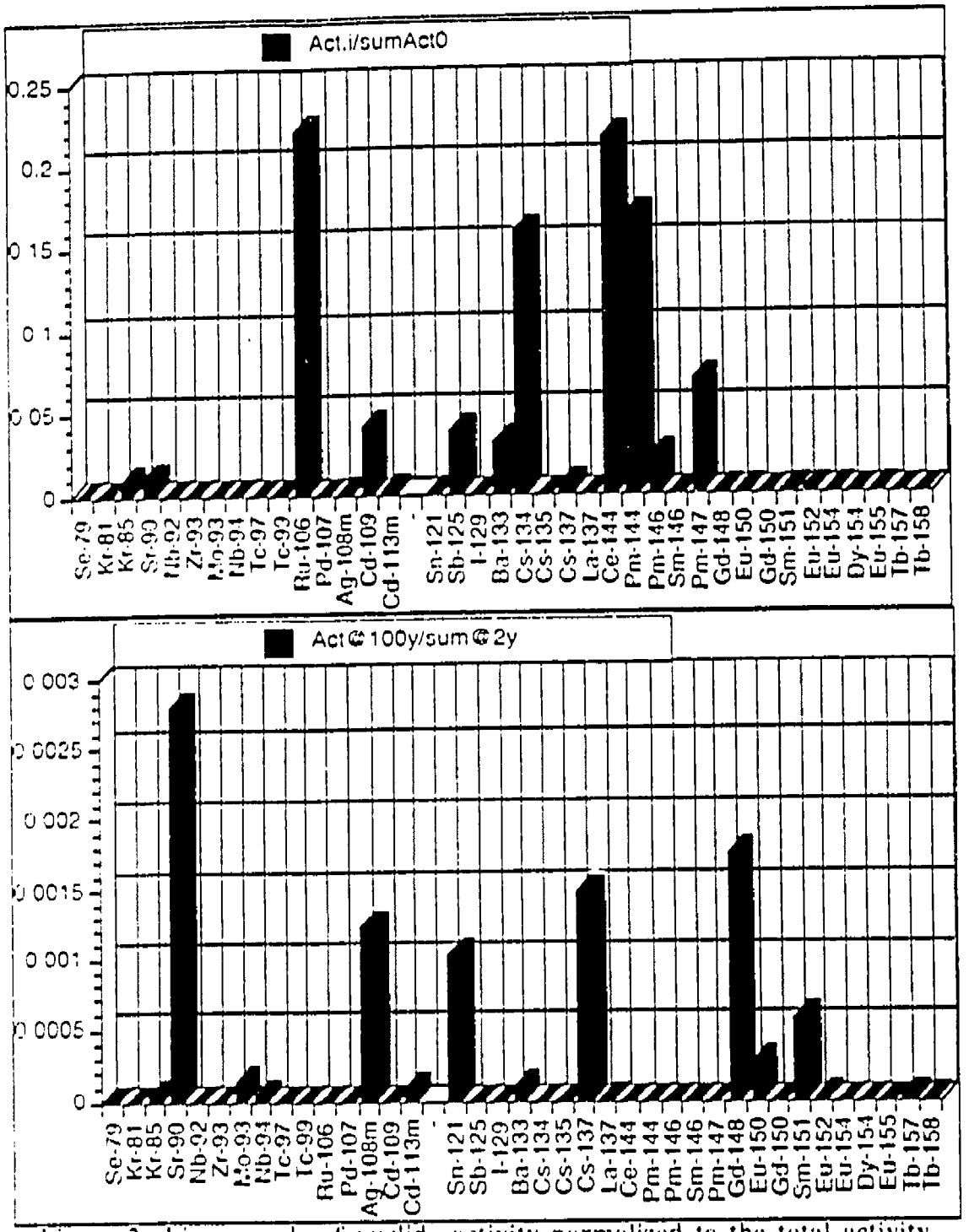

Figure 2 Linear scale of nuclide activity normalized to the total activity evaluated at t = 0 years (top) and the activity remaining after 100 years, normalized to the activity present at t = 2 years (bottom). A different set of nuclides dominate each case; the shortest lived nuclides which were considered ($\tau > 1$ yr) dominate the evaluation normalized at t = 0.

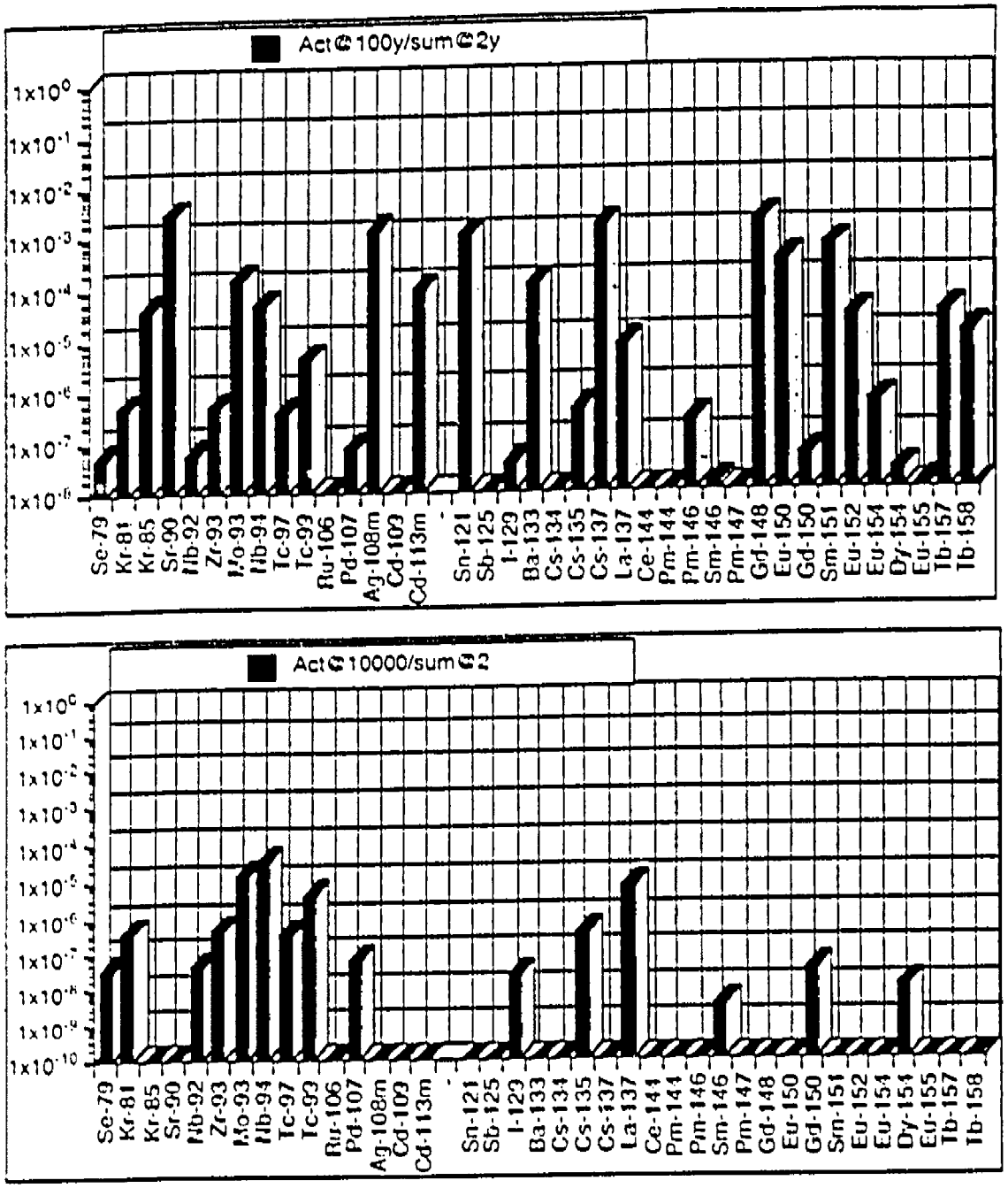

Figure 3 Log scale of nuclide activity remaining at subsequent times, t = 100 yrs (top) and t = 10,000 yrs (bottom) normalized to the total activity evaluated at t = 2 years.

Table I: Mixed Fission Product Data Sheet

Nuclide Data					Activity results by nuclide for several 'fission product ages'							
nuclide, i	M# atom. mass	FPY/M # -ave.	FPY-isot. split	half-life (yrs.)	Act/FPY (t0)	(Act.i/ Act.tot) @t=0	Act/FPY @2 yrs	(Act.i/ Act.tot) @2 yrs	Act/FPY @ 5 yrs	(Act. i/ Act.tot) @ 5 yrs	Act/FPY @ 10 yrs	(Act.i Act.tot) @ 10 yrs
Se-79	79	0.0002	1	6.50E+04	2.13E-09	1.58E-08	2.13E-09	4.18E-08	2.1299E-09	1.0868E-07	2.1298E-09	2.456E-07
Kr-81	81	0.007	1	2.10E+05	2.31E-08	1.71E-07	2.31E-08	4.53E-07	2.31E-08	1.1786E-06	2.3099E-08	2.6638E-05
Kr-85	85	0.02	1	10.7	1.30E-03	9.60E-03	1.14E-03	2.23E-02	0.00094038	0.04798256	0.00068025	0.07844471
Sr-90	90	0.065	1	29	1.55E-03	1.15E-02	1.48E-03	2.90E-02	0.00137544	0.07018097	0.00122054	0.14074965
Nb-92	92	0.065	1	2.00E+07	2.25E-09	1.67E-08	2.25E-09	4.42E-08	2.25E-09	1.1481E-07	2.25E-09	2.5947E-07
Zr-93	93	0.065	0.5	9.50E+05	2.37E-08	1.76E-07	2.37E-08	4.65E-07	2.37E-08	1.2093E-06	2.37E-08	2.733E-06
Mo-93	93	0.065	0.5	3.00E+03	7.51E-06	5.56E-05	7.50E-06	1.47E-04	7.5013E-06	0.00038275	7.4927E-06	0.00086104
Nb-94	94	0.065	1	2.00E+04	2.25E-06	1.67E-05	2.25E-06	4.42E-05	2.2496E-06	0.00011479	2.2492E-06	0.00025938
Tc-97	97	0.065	1	2.60E+06	1.73E-08	1.28E-07	1.73E-08	3.40E-07	1.73E-08	8.8272E-07	1.73E-08	1.995E-06
Tc-99	99	0.065	1	2.13E+05	2.11E-07	1.57E-06	2.11E-07	4.15E-06	2.11E-07	1.0766E-05	2.1099E-07	2.4331E-05
Ru-106	106	0.045	1	1.05	2.97E-02	2.20E-01	7.93E-03	1.56E-01	0.00109543	0.05589372	4.0403E-05	0.00465918
Pd-107	107	0.03	1	6.50E+06	3.20E-09	2.37E-08	3.20E-09	6.27E-08	3.2E-09	1.6328E-07	3.2E-09	3.6902E-07
Ag-108m	108	0.02	1	130	1.07E-04	7.90E-04	1.05E-04	2.07E-03	0.00010419	0.00531602	0.00010145	0.01169848
Cd-109	109	0.01	1	1.24	5.59E-03	4.14E-02	1.83E-03	3.58E-02	0.00034185	0.01744284	2.0906E-05	0.00241081
Cd-113m	113	0.01	1	14.6	4.75E-04	3.52E-03	4.32E-04	8.46E-03	0.00037465	0.01911619	0.0002955	0.03407607
-										0		0
Sn-121	121	0.015	1	50	2.08E-04	1.54E-03	2.02E-04	3.97E-03	0.00019407	0.00990251	0.00018108	0.02088176
Sb-125	125	0.02	1	2.7	5.13E-03	3.80E-02	3.07E-03	6.02E-02	0.00142158	0.07253559	0.00039394	0.04542817

Nuclide Data					Activity results by nuclide for several 'fission product ages'							
nuclide, i	M# atom. mass	FPY/M # -ave.	FPY-isot. split	half-life (yrs.)	Act/FPY (10)	(Act.i/ Act.tot) @t=0	Act/FPY @2 yrs	(Act.i/ Act.tot) @2 yrs	Act/FPY @ 5 yrs	(Act. I/ Act.tot) @ 5 yrs	Act/FPY @ 10 yrs	(Act.i Act.tot) @ 10 yrs
I-129	129	0.03	1	1.60E+07	1.30E-09	9.63E-09	1.30E-09	2.55E-08	1.3E-09	6.6332E-08	1.3E-09	1.4991E-07
Ba-133	133	0.065	1	10.4	4.33E-03	3.21E-02	3.79E-03	7.43E-02	0.00310308	0.15833285	0.00222381	0.25644514
Cs-134	134	0.065	1	2.1	2.15E-02	1.59E-01	1.11E-02	2.17E-01	0.00412907	0.2106837	0.00079299	0.09144579
Cs-135	135	0.065	1	2.30E+06	1.96E-08	1.45E-07	1.96E-08	3.84E-07	1.96E-08	1.0001E-06	1.96E-08	2.2602E-06
Cs-137	137	0.065	0.5	30.1	7.48E-04	5.54E-03	7.15E-04	1.40E-02	0.00066666	0.03401618	0.00059417	0.06851882
La-137	137	0.065	0.5	6.00E+04	3.75E-07	2.78E-06	3.75E-07	7.36E-06	3.7498E-07	1.9133E-05	3.7496E-07	4.3239E-05
Ce-144	144	0.065	0.5	0.78	2.89E-02	2.14E-01	4.88E-03	9.55E-02	0.00034012	0.01735428	4.0027E-06	0.00046159
Pm-144	144	0.065	0.5	1	2.25E-02	1.67E-01	5.63E-03	1.10E-01	0.00070364	0.03590298	2.2005E-05	0.00253757
Pm-146	146	0.05	0.5	5.53	3.13E-03	2.32E-02	2.44E-03	4.78E-02	0.00167272	0.0853496	0.00089393	0.10308582
Sm-146	146	0.05	0.5	1.00E+08	1.73E-10	1.28E-09	1.73E-10	3.40E-09	1.73E-10	8.8272E-09	1.73E-10	1.995E-08
Pm-147	147	0.035	1	2.62	9.26E-03	6.86E-02	5.45E-03	1.07E-01	0.00246745	0.12590026	0.00065748	0.07581978
Gd-148	148	0.025	1	93	1.86E-04	1.38E-03	1.84E-04	3.60E-03	0.0001792	0.00914346	0.00017264	0.01990894
Eu-150	150	0.01	0.5	35	9.90E-05	7.33E-04	9.52E-05	1.87E-03	8.9669E-05	0.00457529	8.1217E-05	0.00936574
Gd-150	150	0.01	0.5	1.80E+06	1.93E-09	1.43E-08	1.92E-09	3.77E-08	1.93E-09	9.8477E-08	1.93E-09	2.2256E-07
Sm-151	151	0.008	1	93	5.96E-05	4.42E-04	5.87E-05	1.15E-03	5.742E-05	0.00292984	5.532E-05	0.00637942
Eu-152	152	0.005	1	13	2.67E-04	1.97E-03	2.40E-04	4.70E-03	0.00020453	0.01043599	0.00015667	0.01806741
Eu-154	154	0.002	0.5	8.6	8.06E-05	5.97E-04	6.86E-05	1.34E-03	5.3871E-05	0.00274874	3.6006E-05	0.00415214
Dy-154	154	0.002	0.5	1.00E+06	6.93E-10	5.13E-09	6.93E-10	1.36E-08	6.93E-10	3.536E-08	6.93E-10	7.9915E-08
Eu-155	155	0.001	1	4.8	1.44E-04	1.07E-03	1.05E-04	2.12E-03	6.9961E-05	0.00356972	3.399E-05	0.00391965
Tb-157	157	0.0005	1	160	2.17E-06	1.60E-05	2.15E-06	4.21E-05	2.1235E-06	0.00010835	2.078E-06	0.00023963

Nuclide Data					Activity results by nuclide for several 'fission product ages'							
nuclide, i	M# atom. mass	FPY/M # -ave.	FPY-isot. split	half-life (yrs.)	Act/FPY (t0)	(Act.i/ Act.tot) @t=0	Act/FPY @2 yrs	(Act.i/ Act.tot) @2 yrs	Act/FPY @ 5 yrs	(Act. i/ Act.tot) @ 5 yrs	Act/FPY @ 10 yrs	(Act.i Act.tot) @ 10 yrs
Tb-158	158	0.0002	1	150	9.24E-07	6.84E-06	9.16E-07	1.80E-05	9.029E-07	4.607E-05	8.8228E-07	0.00010174
				sum(Act/FPY(t0)) 1.35E-01		sum(Act/FPY(2yrs)) 5.10E-02		sum(Act/FPY(5yrs)) 1.96E-02		sum(ACT/FPY(10yrs)) 8.67E-03		

LA-UR-97-155

Title: **Evaluation of Atmospheric Release Sources for Gaseous Phase Contaminants Emanating from the Disposal Facility at Area G**

Author(s): **Erik L. Vold**

Submitted to: U.S. Department of Energy, as support documentation for the Los Alamos Area G Performance Assessment

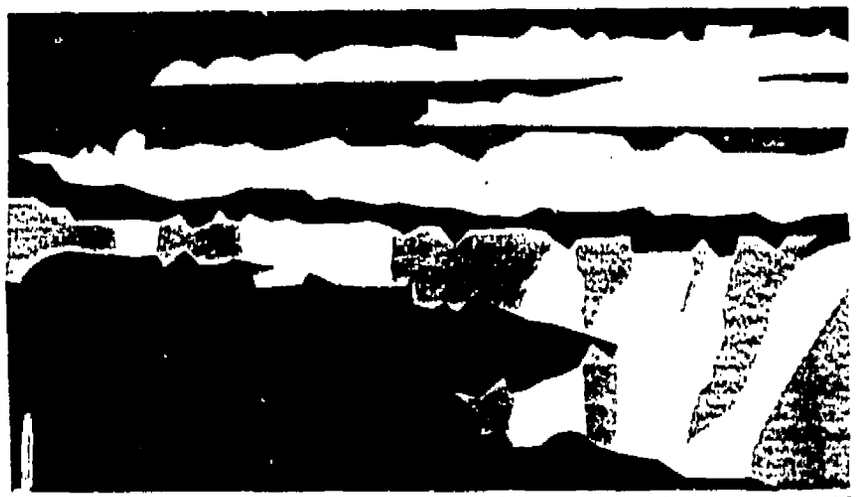

Los Alamos
NATIONAL LABORATORY

Los Alamos National Laboratory, an affirmative action/equal opportunity employer, is operated by the University of California for the U.S. Department of Energy under contract W-7405-ENG-36. By acceptance of this article, the publisher recognizes that the U.S. Government retains a nonexclusive, royalty-free license to publish or reproduce the published form of this contribution, or to allow others to do so, for U.S. Government purposes. The Los Alamos National Laboratory requests that the publisher identify this article as work performed under the auspices of the U.S. Department of Energy.

Evaluation of Atmospheric Release Sources For Gaseous Phase Contaminants Emanating from the Disposal Facility at Area G

Erik Vold

Table of Contents

Abstract 1
Introduction 2
Analysis 3
- Analytic solution 4
- Numeric Analysis and Calibration Against Tritium Field Data 5
- Subsurface Gas and Vapor Phase Diffusion 5

Results 7
- Near-surface Tritium at a 1-D Disposal Unit 7
- Tritium Migration to the Deep Aquifer 9
- Carbon-14 Release 10
- Rn-222 Release 11

Analytic Solutions and Comparison to Numeric Results 13
Conclusions 14
Acknowledgments 15
References 15

Figures 17

Evaluation of Atmospheric Release Sources For Gaseous Phase Contaminants Emanating from the Disposal Facility at Area G

Erik Vold

Abstract

This report summarizes a numerical evaluation of the time dependent atmospheric release source terms for gas and vapor phase contaminants emanating from the disposal facility at Los Alamos Area G over the long term duration. These airborne sources are considered for the site Performance Assessment (PA) and Composite Analysis (CA) to meet U.S. Department of Energy requirements. The model is calibrated to tritium field data. The numerical approach and detailed results described here are compared and serve as a cross-check to the analytic method implemented within the PA dose calculations for representative source terms, including the historical PA inventory sources for radon-222, carbon-14, and tritium.

Effective diffusion coefficients for gases and the vapor phase are determined for migration from disposal unit pits and separately from disposal shafts, based on field data for vapor phase tritium migration from the Area G site. A 1-D numerical diffusion model (along a vertical axis transecting the disposal unit) is described and implemented for representative nuclides to predict time dependent vertical concentration profiles. The numerical results for ground surface efflux of contaminants are a cross-check to the results predicted analytically. Tritium results are first compared to field data and used to calibrate model parameters, including the in-situ diffusion coefficient and a time constant for the release rate of tritium from the waste matrix. Tritium migration is then extrapolated to the saturated aquifer using the vapor phase diffusion coefficient observed in the near-surface tritium diffusion field study. Results show tritium decreases to below background levels before reaching the aquifer.

Carbon-14 is assumed to be released as CO_2 or CH_4 in the biodegradation of organic carbon from two waste forms, each with a characteristic degradation or release rate. The radon-222 source term is generated by the decay of radium-226 which is in turn determined primarily from the listed inventory of radium-226, uranium-234 and uranium-238. Numeric results described here and analytic PA results for the carbon-14 and radon-222 are in close agreement (within 20% and 40%, respectively) and suggest the analytic model implemented in the PA is adequate. The numeric result (in agreement with the measured field data) for the tritium ground surface efflux is about 200 times less than that predicted by the analytic model. The conservative estimate of the release rate projected in the analytic model is attributed to the small release fraction per year from the tritium waste packages which is derived from the field study but is not incorporated into the analytic release estimate.

Evaluation of Atmospheric Release Sources For Gaseous Phase Contaminants Emanating from the Disposal Facility at Area G

Introduction

The airborne contaminant pathway dose assessment requires evaluation of airborne sources from the disposal site which undergo atmospheric transport and dispersion to off-site receptor locations. These sources include gaseous or vapor phase nuclides which diffuse from the disposal unit and are then released as efflux from the ground surface above the disposal unit. This report describes the numerical evaluation of the source release, calibrates the model to field data, and compares the numeric results to analytic results. This serves as a cross-check on the analytic model results implemented within the Area G Performance Assessment (PA) and Composite Analysis (CA) [Shuman 1997].

The air pathway dose assessment includes factors of source concentration, S, source release rate, R, atmospheric dispersion, c/Q, and dose conversion, D_f, related as

$$D[mrem/yr] = S\,[Ci/m3]\; R\left(\frac{Ci/s}{Ci/m3}\right) c/Q\,[s/m3]\; D_f\left(\frac{mrem/yr}{Ci/m3}\right). \qquad (1)$$

The airborne transport, characterized with a dispersion value, c/Q, equal to the receptor location concentration, $c\,[Ci/m3]$, per continuous source term release, $Q\,[Ci/s]$ is described in a separate report [Vold 1996A]. The dose conversion, D_f, includes the inhalation rate for the inhalation dose or for other foodstuffs pathways, it incorporates the deposition velocity for particulate contaminants as described in detail elsewhere [Shuman 1997].

A release model for the time dependent gaseous phase radionuclides source is the subject of this report. This details the numerical evaluation for select nuclides of the source release, which combines a release rate, R, with the disposal unit waste concentrations, S, to produce an integrated ground surface efflux (Ci/s). More generally, one can evaluate the source as an efflux per unit area above a disposal unit (Ci/m2/s or Ci/m2/yr).

Sources of release to the atmosphere include gaseous or vapor diffusion from the waste with subsequent efflux from the surface. A review of the inventory indicates this includes several nuclides. Of these, tritium, carbon-14 and radon-222 were chosen for comparison of numeric and analytic solutions in this study. Small amounts of Kr released from the mixed fission products, and radon-220 have also been considered in the analytic

assessment of the complete atmospheric release for the Area G site Performance Assessment (PA) and Composite Analysis (CA) [Shuman 1997]. Tritium emanates from the waste and is assumed to convert to tritiated water during its diffusion through the subsurface. Carbon-14 is assumed to diffuse from the organic fraction of the carbon-14 waste as it biodegrades primarily to carbon dioxide. Radon-222 emanates from the waste in the decay of Ra-226, which is a listed inventory item and also grows in from decay chains for additional inventory nuclides, most significantly for U-234 and U-238. The source release model for each of these gaseous / vapor sources is unique as described in this report.

Only gaseous or vapor phase contaminants are evaluated in this report. As considered elsewhere, some fraction of the total inventory can be translocated to the disposal unit ground surface via biotic translocation or erosional processes [Vold and Shuman 1997]. Subsequently, this can become airborne as particulate matter via resuspension processes. Particulate matter which becomes airborne by the resuspension of surface soil contamination and its contribution to redeposition is considered elsewhere in the PA [Shuman 1997].

The release models for airborne sources were evaluated by analytic and by numerical methods. The analytic models described in the following were used in the PA and CA dose pathway assessment [Shuman 1997] because of the practicality of implementation. Generally, the analytic solutions are based on simplifying assumptions and are not as accurate representations of the physics. The numerical solutions represent the physics more accurately, when the numerical approximation errors are small. The numerical results described here were calibrated to tritium field data and then used to confirm the analytic model for the selected nuclide release cases and to provide better understanding of the spatial and temporal profiles resulting from the diffusion and efflux boundary problem.

Analysis

The equation governing the production, decay and diffusive transport of a nuclide's gaseous concentration, C_i, is

$$\frac{\partial C_i}{\partial t} + l_i C_i + \nabla \cdot (D_i \nabla C_i) = S_i \qquad (2)$$

where

l_i = radiologic decay constant for nuclide i,

D_i = diffusion coefficient for nuclide through the matrix

S_i = source term for nuclide i.

Analytic solution

An analytic solution is derived for the steady state case in a source free region of thickness, x. This represents the waste cover over a disposal unit pit or disposal shaft at Area G in the off-site release scenario and represents the basement slab in the intruder scenario. In this case, the governing equation (2) reduces to

$$l_i C_i + \nabla\cdot(- D_i \nabla C_i) = 0. \qquad (3)$$

In one dimension, x, for constant diffusion coefficient, the solution is

$$C(x) = C_o \exp (- x \sqrt{l/D}), \qquad (4)$$

where x is now assumed to be the waste disposal unit cover thickness, L_c, and D is the diffusion coefficient within the cover material. Using the flux approximation with a diffusion scale length, $L_d = (\sqrt{l/D})^{-1}$, then the flux, $J(x)$ becomes

$$J(x) = - D \nabla C \sim - D\, C/L_d \qquad (5)$$

and so substituting from the above, the flux magnitude is,

$$|J(x)| = C_o (\sqrt{lD}) \exp (- x \sqrt{l/D}). \qquad (6)$$

This expression is used in the pathways assessment as the 'analytic result' for the atmospheric release term (except for radon-222 as discussed later). A boundary condition

is imposed as the concentration on the waste side fixing $C_o(x=0) = C_w$, where C_w is derived from the total inventory distributed over the total volume, neglecting the effects of diffusion.

This approximation is not entirely self-consistent because the boundary condition $(x=0)$ is derived assuming no diffusion and then used to determine the amount of diffusion loss. It is expected to be conservative since the actual waste concentrations are reduced by the diffusion process. This analytic solution also does not account explicitly for the flux loss at the surface boundary (the ground surface-air interface located at distance, x). Also, the source term, C_o, accounts for all the inventory in an available waste form and does not account for a slow or retarded release rate from the waste package itself, it assumes the whole inventory of this form is available to diffuse. Because of these considerations the numerical solutions are expected to reflect a more accurate solution.

Radon-222 is a special case and the analytic flux is determined by a more detailed expression specifically derived for radon flux from mill tailings [NRC, 1984]. The application of this equation to the Area G PA and CA is summarized in [Shuman, 1997]).

Numeric Analysis and Calibration Against Tritium Field Data

The governing equation for the diffusive transport (Eqn. 2) was solved numerically by implementing standard finite differencing techniques using second order central differencing for the diffusive flux (e.g., see [Anderson,et.al., 1984]. A 3-D code with explicit differencing in time was used to model the tritium migrating from the disposal shafts. This was detailed previously [Vold and Eklund, 1996] and compared to tritium surface efflux measurements in the vicinity [Eklund and Vold, 1995]. Contour results comparing the 3-D numerical results to the field data from [Vold and Eklund, 1996] are reproduced in Fig.1 to show the generally good agreement between the field data and the simple diffusion model results.

From this comparison study, the numeric model was calibrated and the in-situ effective diffusion coefficient for the tritium was found to be 15 m^2/yr. This corresponds to a vapor phase diffusion coefficient of about 1.5 $x10^{-3} m^2/s$ or about 60 times the binary diffusion coefficient for water vapor in still air. This enhanced diffusion observed in-situ was later

attributed to the atmosphere barometric pumping acting in conjunction with the increased effective permeability of the mesa tuff due to the fractured nature of the porous media [Vold, 1996B]. The proposed mechanism for this enhanced diffusion will act the same on any gas or vapor species entrained in the oscillating air flow through the porous spaces in the subsurface region. Therefore, it is assumed that gaseous species other than tritiated vapor diffuse in the tuff media with the same coefficient derived for the tritiated vapor. As discussed below, this diffusion value applies only to sources in the shafts where subsequent diffusion is through the undisturbed tuff. (Note that since the tritium moves by combined vapor and liquid phases the 'effective' tritium diffusion coefficient (15 m^2/yr) is not the same as the in-situ vapor phase diffusion coefficient *($1.5x10^{-3}$ m^2/s = 50,000 m^2/yr)* even though the tritium movement is dominated by the vapor flux. See [Vold and Eklund, 1996] for further detail.)

Subsurface Gas and Vapor Phase Diffusion

Diffusion of gas or vapor occurs from the waste package location within the disposal units through the porous subsurface media to the ground surface. Diffusion coefficients must be characterized which are appropriate for the disposal pits and for the shafts. Values must be distinguished for gases and for water vapor where water vapor is strongly subject to temperature and pressure gradient influences. Tritium released from waste packages is assumed to oxidize in the saturated pore spaces quickly compared to the diffusion transit time, and thus tritium diffuses in the subsurface region as water vapor.

The binary gas diffusion coefficient, D_o, for specific gases diffusing into still isothermal air varies in the range from 1 to 3 $x10^{-5}m^2/s$, with the value of 2.4 $x10^{-5}m^2/s$ for water vapor in air at 8°C [CRC Handbook of Chemistry and Physics]. The simple theory for the in-situ diffusion coefficient in a porous media, D_{ins}, indicates the diffusion is reduced from D_o by the tortuosity, t, and by a factor, e, related to the pore space air volume fraction, q_a, or [Koorevaar,et.al.1987]

$$D_{ins} \sim \frac{e(q_a)\, D_o}{t} . \qquad (7)$$

It is common to take $t \sim 2$, and $e(q_a) \sim q_a$.

In-situ data often indicates this simple theory for porous media diffusion underestimates the actual diffusion [Philips and de Vries,'57]. Following the terminology in that reference, we use h as the ratio of observed diffusion to diffusion predicted by the simple theory in Eqn. 1, so that the in-situ diffusion coefficient for porous media diffusion is written as

$$D_{ins} \sim 0.5\, q_a\, h\, D_o . \qquad (8)$$

In [Philips and de Vries, 1957], they tabulate h from several experimental data sets for water vapor diffusion in porous media, and an average value is found to be $h = 5.9 \sim 6$. Temperature gradient effects were proposed as a dominant factor in the empirical enhancement of the diffusion of water vapor in these studies. It is assumed in our analysis that a similar enhancement of water vapor diffusion occurs in-situ. This is conservative since the enhanced diffusion is driven by temperature gradients which will not propagate more than a few meters into the disposal unit.

Diffusion of tritiated water vapor from the disposal shafts at Area G through the near surface (to 60 ft depth) tuff and to the ground surface has been examined in some detail and an empirically determined coefficient for the in-situ diffusion has been found to be $\sim 1.5 \times 10^{-3} m^2/s$, or about 60 times the binary diffusion coefficient for water vapor [Vold and Eklund, 1996]. This large anomalous enhancement of in-situ diffusion has been attributed to a 'barometric pumping' in a model of atmospheric pressure fluctuation enhanced diffusion [Vold 1996B].

The calibration of the model with field data implies only that the enhanced diffusion is significant for the effective permeability of the fractured media at Area G, and that transport occurs through the connected fracture network. The enhanced diffusion mechanism in the model depends only on the pressure fluctuation driven convective motion of air through the pore spaces within the subsurface region and thus the enhanced diffusion is expected to be similar for any entrained gas or vapor species. Since the diffusion mechanism does not depend upon the properties of the diffusing species, all gases and vapors are expected to diffuse similarly from the shaft disposal units at Area G to the ground surface with the diffusivity of $1.5 \times 10^{-3}\ m^2/s$.

The mechanism for the enhanced diffusion indicates that there is no significant diffusion enhancement for the unfractured Bandelier Tuff matrix properties. Within the pit disposal units, disposal operations include backfill and compaction of crushed tuff surrounding the waste packages which is expected to minimize the effective permeability within the disposal unit, so that it is similar in value to that for the crushed tuff. In this case, diffusion within and from the pit disposal unit is not expected to be enhanced by pressure fluctuations as seen in the shaft diffusion field study.

Gases are expected to diffuse from the pit disposal units with the in-situ diffusion coefficient in Eqn. 8, with $h \sim 1$, while tritium as water vapor will diffuse from pits per Eqn. 8 with $h \sim 6$, consistent with the previous work discussed above. A nominal binary diffusion coefficient value is assumed to apply to all gas species in the pits, $D_0 = 2. \times 10^{-5} m^2/s$. The effective air volume fraction in the pits is taken to be $q_a \sim 0.3$. These values in Eqn. 8 lead to the diffusion coefficients used in the assessment as summarized in this Table 1.

Table I: In-situ diffusion coefficients

	Disposal pits		Disposal shafts
	h	$D_{ins}(m^2/yr)$	$D_{ins}(m^2/yr)$
gas: CO_2, Kr, Rn	1.	100.	50,000.
water vapor, HTO_v	6.	600.	50,000.

Results

Near-surface Tritium at a 1-D Disposal Unit

The governing diffusion equation (2) is solved in 1-D along a vertical axis transecting the disposal unit to project the surface efflux above the disposal unit. The finite differencing

uses implicit methods resulting in a tridiagonal matric to solve at each time step using the standard Thomas algorithm (e.g., see [Press,et.al.,1992]). The top finite difference zone corresponds to the ground surface where the tritium concentrations are assumed to be zero and so the surface efflux evolves self-consistently with the vertical profiles through the disposal unit. The diffusion coefficient used in these calculations is the $15m^2/yr$ derived from the detailed comparison study [Vold and Eklund, 1996] between tritium field data and modeling, (corresponding to the vapor phase diffusion coefficient of 50,000 m^2/yr seen in Table I). The source term is assumed to be distributed uniformly over the depths from 10 to 60 ft for shaft disposal.

Tritium concentration results at three representative points along the vertical profile are shown as functions of time in Fig.2. The tritium concentrations and thus the surface flux both peak at about 10 years post disposal (note this is for a simplified case where the entire inventory is buried at a single time, $t = 0$). At this peak time the tritium near the surface is almost two orders of magnitude below the tritium concentration at 12m depth (near the profile maximum.

Tritium concentration profile results are shown in Fig.3. This indicates at early times (1 yr) the vertical profile shape is still evolving but by 10 yrs the shape is close to the steady state profile which remains self-similar after that time while decreasing in magnitude due to the radiologic decay of the tritium. The vertical distribution of the tritium source is not precisely known, due to emplacement uncertainties associated with the tritium waste in the shafts. Vertical tritium profiles for two assumed distributions of tritium with depth are compared in Fig. 4. In both cases the tritium is uniformly distributed but over different ranges in depth as indicated in the figure legend. The source which is closer to the surface (11-60 ft) results in a greater surface flux and greater near-surface gradient in tritium, as should be expected. These profiles can be compared at least qualitatively to tritium profiles from field data.

Field data collected in bore holes drilled in the tritium disposal shaft area show concentrations of tritiated water from the core soil moisture taken as a function of depth in a test hole shown in Fig. 5. The test hole penetrated 150' vertically and directly transected the center of the tritium plume from these disposal shafts.

Comparing these field data to the computational results allows a 'calibration' of the magnitude of the tritium model source term needed to match the field data. The comparison study between field data and model results indicated that a release time constant for tritium from the disposal shafts, t_{sh}, was about 1000 yrs [Vold and Eklund 1996]. This was derived by modeling the tritium source, S_i, in Eqn. 2 as Q/t_{sh} where Q is the actual tritium inventory concentration and then varying the time constant until the tritium model results matched field data (for example as shown in Fig. 5).

One can compare the vertical profile shapes predicted by the model in Fig. 4 to the observed profiles in Fig.5. The shape and scale lengths for either computed result in Fig. 4 seem to agree qualitatively with the field data in the near surface region above about 60 ft. As detailed previously [Vold and Eklund 1996] this region is where the derived in-situ diffusion coefficient applies. Below 60 ft, the data seems to decrease more rapidly with depth than predicted by the model with this diffusion coefficient. This appears to be consistent with a smaller diffusion coefficient at greater depths [Vold and Eklund 1996]. In fact, since the model ties the in-situ diffusion to the near surface fracture-enhanced effective permeability [Vold 1996], the diffusion coefficient is likely to be much smaller beneath the mesa where the stratigraphy is relatively unfractured until at least the depth of the basalt layers [Krier, et.al., 1995].

The source term derived here was then used in a 1-D model to predict vapor phase transport to the deep aquifer and in the 3-D model to predict vapor phase losses to the sides of the mesa. Tritium in the vapor phase loss to the mesa edges was negligibly small [Eklund and Vold 1995] and is not discussed further.

Tritium Migration to the Deep Aquifer

Although not an atmospheric release, tritium as a vapor may also diffuse down to toward the aquifer. A 1-D diffusion model for tritium in vapor is based on the diffusion equation (2). A vertical axis through the disposal unit is modeled using 100 grid points ($dz = 3m$ per point) from the mesa top down to the top of the deep aquifer. Free flux boundary conditions account for loss at the mesa top and some loss to the mesa sides is modeled as sink terms in the top 30m. Standard numerical solution methods use a tridiagonal solver on the discretized governing equations at each grid point [Press,et.al.,1992].

The model source term is distributed over depths of 9-18 m (model nodes 3-6), and specified as a total of $2x10^5$ Ci with release rate and diffusion coefficient as determined from the above empirical studies. This source strength is the correct order of magnitude and needs to be scaled to the inventory of concern in considering the results. For example, the historical inventory (88-95) of tritium is about $4x10^5$ Ci (as of 1995), and so the model results are a factor of two less than that expected from the historical inventory alone.

The results of the 1-D tritium vapor diffusion calculation are summarized in Fig. 6. This shows tritium concentration verses depth to the main aquifer at several times as labeled in the figure. The model predicts concentrations with an exponential decrease with depth to the aquifer. This is independent of the background level of tritium which is not considered in the model. For comparison, the background level of tritium seen in soil moisture is indicated as the horizontal line. Diffusion solutions below this level are meaningless as the contaminant tritium will blend into the background at this level. The figure shows that this occurs at about 70% of the distance down to the deep aquifer. The vapor phase contaminant moves relatively quickly compared to the aqueous phase and arrives at the background concentration (at this 70% depth point) in the 50-100 year time frame. Liquid phase transport will be relatively small and much slower as discussed in [Vold and Eklund 1996] and as evaluated for the PA [Birdsell, et.al. 1997] (work in progress).

Carbon-14 Release

Model

Carbon-14 in the gaseous phase diffuses from the waste disposal unit as governed by Eqn. 2. The source of gaseous carbon-14 is the biodegradation of the organic fraction of the carbon-14 waste. This was determined to be 4.7 mCi in the historical inventory (1988-1995) based on the waste codes associated with organic carbon waste (100% of waste with waste code 18 and 50% of waste code 19. Waste codes are listed in section 2.3 of the PA main report [Hollis,et.al., 1997].)

It is assumed that the organic carbon waste is half cellulosics and half wood/paper/plastics which are assumed to have two distinct biodegradation characteristic times. These correspond to effective decay constants of 17 years and 550 years, respectively, for organic carbon waste assumed to be 'paper' or 'wood, rubber, plastics' (see Table 3.1 in Appendix

6 to [MacKinnon,et.al., 1994]). This implies the source term for carbon-14 needed in Eqn. 2 is of the form,

$$S(C\text{-}14\ [Ci/m3/yr]) = \frac{(Q_{18} + 0.5\,Q_{19})}{2\,V}\left(\frac{e^{-t/17}}{17} + \frac{e^{-t/550}}{550}\right) \qquad (9)$$

where

Q_{18}, Q_{19} are the inventories (Ci) in waste code groups 18 and 19

V is the inventory volume (m3).

Carbon-14 Results Discussion

The carbon-14 source term for gaseous phase release from the disposal unit, generated by the biodegradation of the organic component of the C14 inventory, is shown in Fig. 7 indicating the contributions from the two waste types. Carbon-14 concentrations (Ci/m3) at the ground surface, at the disposal unit midpoint in depth, and the ground surface tritium efflux (Ci/m2/s) as a function of time after disposal, calculated in the numerical diffusion model are shown in Fig. 8.

The carbon-14 gaseous concentrations and emission fluxes peak immediately after disposal for the assumed biodegradation source of gaseous carbon and for the derived in-situ diffusion coefficient. This peak results from the balance between the biodegradation sources and the diffusive transport losses. The decreasing concentrations in time shows the effect of two source components, corresponding to the two half lives assumed for the biodegradation source term processes. At 100 years the concentrations are more than one order of magnitude below the peak values.

The concentration profiles with depth at four selected times are shown in Fig. 9. The profiles are seen to be very nearly self similar at the different time steps with a slight change from 1 yr to 10 yrs, and so the gradient is not varying in time. This indicates the surface flux will vary directly with the amount of carbon-14 remaining at a given time.

Carbon-14 ground surface efflux (Ci/m2/s) as a function of time after disposal is compared in the numerical diffusion model for two values of the diffusion coefficient in Fig. 10. The base case of 100 m^2/yr is compared to a reduced diffusion of 10 m^2/yr, to examine the effect of a smaller diffusion coefficient. For the latter case, the carbon-14 gaseous emission fluxes peak at 10 - 20 years after disposal for the assumed biodegradation source

of gaseous carbon. The diffusion in that case is small enough that it introduces a significant delay in the flux to the surface and hence the curve maximum is shifted to a later time.

Rn-222 Release

Model

Radon-222 is a sufficiently long lived radon isotope to diffuse from the waste to the surface before decaying, and is used for the numeric and analytic result comparison. Radon-220 is also evaluated in the PA [Shuman 1997]. Radon-222 grows in from the decay of Ra-226. Radium-226 is included in the listed inventory and results from decay chains of the several inventory isotopes including: Pu-238, Pu-242, Ra-226, Th-230, U-234, and U-238. For each of these potential radon contributors, the radon as a function of time was calculated, for a normalized decay chain parent quantity (1 Ci). This was multiplied by the actual historical total inventory and it was found that the resulting radon-222 was dominated by the inventory nuclides, Ra-226 and U-234 (and U-238 at very long times, after 10,000 yrs).

Equation (2) governs the production, decay and diffusive transport of the radon 222 concentration. The source term is evaluated as:

$$S_{222} = f_{em}\, l_{222}\, A_{226} / V_{inv}, \qquad (10)$$

where A_{226} is the Ra-226 activity in the inventory volume, V_{inv}, and f_{em} is an emission fraction to account for radon attachment, absorption, retardation on and diffusion from the interior of soil grains. This was taken to be 1 in the numerical calculations but assumed equal to 0.35 in the final analytic calculations in the dose assessment based [NRC 1984].

Considering the contributing nuclides shown to be significant,

$$A_{226}(t) = A_{226}(t=0)\, exp(-l_{226}\, t) + A_{226}[U234[t]] + A_{226}[U238[t]]. \qquad (11)$$

The time dependence of Ra-226 from U234, $A_{226}[U234[t]]$, is evaluated as the solution to the third generation in a nuclide decay chain. The time dependence of Ra-226 from U238, $A_{226}[U238[t]]$, is evaluated as the solution to the fourth generation in a nuclide decay

chain. It is assumed several intermediate decay products are in secular equilibrium and are negligible in the decay chain calculation. This source term and the contributions from Ra-226, U-234 and U-238 are plotted verses time in Fig. 11.

Numerical Results

Equation 2 was solved numerically in one spatial dimension (vertical) using several grids and comparing output. A standard discretization is used with a tridiagonal subroutine to solve the resulting coupled algebraic equations implicitly as in the previous cases. Reported solutions are for the case using 200 grid points with even spacing, $dz = 0.5\ ft$, allowing 6 nodes throughout the waste cover, and 120 nodes throughout the waste volume. This resolution was adequate to resolve accurate profiles.

The results for Rn-222 concentrations and surface flux are shown as a function of time in Fig. 12. The short decay life for Rn-222 assures secular equilibrium and so the Rn-222 results follow the source activity nearly exactly as compared to Fig. 11. At the waste edge, the Rn-222 concentration is about 60% less than in the waste region interior. At the ground surface, on top of the 1m cover, the Rn-222 concentration is reduced by about a factor of 20 from the concentration in the waste. This result is slightly sensitive to the grid discretization, however, it was determined that the 6 grid points through the waste cover were sufficient to resolve the profile to within a few percent.

The surface efflux (Ci/m2/s) follows as the self-consistently determined boundary condition at the surface grid cell, and this is also shown in the figure. It is this value which can be compared directly to the Rn-222 emission standard of 20 pCi/m2/s. It is seen in the figure that the peak efflux within the first 10,000 years remains at least an order of magnitude below the standard. The model predicts the standard is exceeded at about 50,000 years due to the ingrowth from the U-234 and U-238.

Profiles of Rn-222 concentration verses depth through the disposal unit at four times of interest are shown in Fig. 13. At $t = 100\ yrs$ the source is dominated by the radium 226 inventory, at $t = 5000\ yrs$, the source reaches a local minimum, and at 100,000 yrs the contribution from the U-234 and U-238. The profiles are self-similar at each time step reflecting only the difference in net source strength. A flat profile throughout the waste volume is seen with the roll off in concentration through the top 1m cover and into the deeper tuff below the pit bottom at about 18m depth. This characteristic results from the short half-life of radon-222 relative to the diffusion time through the disposal unit cover.

Analytic Solutions and Comparison to Numeric Results

Analytic calculations of atmospheric release rate for gas or vapor are implemented within the site PA calculations using Eqn. 6. The one exception is for Rn-222, which is calculated from a more specific equation originally derived for emanation from mill tailings as described in [Shuman, 1997]. The analytic calculations are applied to the entire Area G site inventory for the PA and for the CA as detailed in [Shuman 1997].

For cross-checking with the numeric results, the analytic calculation assumptions are summarized as follows and with the inventory as given in Table II. H-3 historic (1988-1995) waste flux is based on a shaft field inventory of 4.29×10^5 Ci, a emplacement efficiency of 0.42, a shaft field factor of 0.107, a waste volume of 272 m3, a cover thickness of 1.37 m and a diffusion coefficient of 50,000 m^2/yr. C-14 historic pit waste flux calculation is based on an inventory of 4.7×10^{-3} Ci, an emplacement efficiency of .36, a waste volume of 3×10^4 m3, a cover thickness of 1.02 m, and a diffusion coefficient of 100 m^2/yr. Rn-222 historic pit waste flux calculation is based on a cover thickness of 1.02 m, a diffusion coefficient of 100 m^2/yr, and a Ra-226 concentration of 0.22 pCi/g.

The ground surface efflux for three important representative gaseous contaminants are compared from the numeric and analytic results in Table II. There is good agreement for radon-222 and for carbon-14, suggesting that the analytic model is a reasonably good approximation for most cases.

The tritium efflux is much higher (~220x) in the analytic estimate than for the numerical estimate. The numerical number agrees fairly well with field observations which measured about 14 Ci/yr total emanating from the ground surface in the vicinity of the high level tritium disposal shafts [Eklund and Vold, 1995], with about 2-3 Ci/yr of that migrating by diffusion through the undisturbed tuff surrounding the shafts. That is, assuming an effective emanation area surrounding the disposal shafts of about 40m by 40m (this area estimate is in good agreement with the tritium plume observed in the field data, as in

Fig.1), then the numerical integrated release would be about 0.002 Ci/m2/yr x 40m x 40m ~ 3 Ci/yr. This suggests the numerical method is calibrated reasonably accurately.

The numerical method includes a source term derived from comparison to the field data which specifies a time constant for tritium release from the shafts. This was found to be about 1000 yrs [Vold and Eklund, 1996] indicating a small fraction of the tritium inventory is actually escaping the waste disposal package in a given year. This release factor is not factored into the analytic source term estimate for tritium release as detailed in [Shuman 1997], the analytic model assumes the entire tritium inventory is available for diffusion to the surface. This factor probably accounts for the discrepancy between the numeric and analytic solutions for the tritium release. The data suggest that the numeric result is probably fairly accurate and the analytic result is a conservative over-estimate of the actual release rate for tritium.

Table II Comparison of atmospheric source terms as surface efflux between the numeric and analytic solutions for representative radionuclides in the Area G inventory.

Nuclide	Historic (88-95) inventory (Ci) [a] evaluated at 1995	Atmospheric Source Term (maximum ground surface efflux)[b] Ci/m2/yr		Difference between analytic and numeric
		Numeric Result	Analytic Result	
H-3	4.3 E05	2. E-03	0.44	220 x
C-14	4.7 E-03 [c]	1.5 E-08	1.9 E-08	20%
Rn-222 [d]	-	6. E-06	(3.5-10) E-06 [e]	40%
Ra-226	2.4 E-02			
U-234	0.6			
U-238	5.3			

a - Inventory in calculation is that for disposal pits except for tritium, which is disposal shaft inventory.

b - Maximum for all time equals the maximum within compliance interval of 1,000 yrs except for Rn-222 which increases beyond 10,000 yr due to ingrowth contributions from U-234 and U-238 decay.

c - This is the estimated 'organic component' of the C-14 waste.

d - Only the Ra-226 listed inventory contributes significantly to the Rn-222 flux at early times.

e - The range for the analytic solution covers a range of values for an 'emanation factor', e_f = 0.35 to 1.0. The numerical solution assumed $e_f = 1$. Note that the maximum value, 1.E-05 Ci/m2/yr, corresponds to 0.3 pCi/m2/s.

Conclusions

The numeric results are in good agreement with the analytic solution implemented in the PA and CA spreadsheet calculations for the atmospheric release of gas or vapor radioactive contaminants from Area G. A discrepancy in the case of tritium is attributable to the small release rate of tritium from the waste packages or from the disposal shaft which is included in the numeric result but is neglected in the analytic result where it is assumed the entire tritium inventory is available for diffusion to the ground surface. This is a very conservative assumption but the analytic PA results still indicate there is no problem from the tritium emanation and subsequent airborne dose pathways.

The numeric results provide insight into the detail of the vertical profiles in concentration and the self-consistently evolved surface efflux for the cases of tritium, carbon-14 and radon-222. Most importantly, they provide a site-specific and field calibrated cross-check on the accuracy of the analytic solution used to determine atmospheric release source terms in the Los Alamos Area G Performance Assessment and Composite Analysis.

Acknowledgments

This work was supported by the U.S. Department of Energy, Waste Management Programs, as part of the Performance Assessment for the disposal facilities at Los Alamos National Laboratory, Area G.

References

[Anderson,et.al. 1987] D.A. Anderson, J.C. Tannehill, R.H. Pletcher, Computational Fluid mechanics and Heat Transfer, Hemisphere Publishing Corporation, New York, 1984.

[Eklund and Vold,95] B. Eklund, and E. Vold, "Measurement of Emission Fluxes from Technical Area 54, Areas G and L", final report 1/4 from RADIAN to LANL- CST-14 under DOE subcontract 6345L0014-31, Los Alamos National Laboratory Report, LA-UR-95-3891, Los Alamos, NM, 1995.

[Hollis, et.al., 1997] D.Hollis, E.Vold, R.Shuman, K.Birdsell, K.Bower, W.Hansen, D.Krier, P.Longmire, B. Newman, D.Rogers, E.Springer, "Performance Assessment and Composite Analysis for the Los Alamos National Laboratory

Material Disposal Area G", Los Alamos National Laboratory Report, LA-UR-97-85, Los Alamos, NM, 1997.

[Koorevaar,et.al.,83]. P. Koorevaar, G. Menelik, C. Dirksen, Elements of Soil Physics, p.200, Elsevier, New York, 1983.

[Krier,et.al., 1995] D. Krier, P. Longmire, R. Gilkeson, H.J.Turin, "Geologic, Geohydrologic, and Geochemical Data Summary of MDA G, TA-54, LANL", Los Alamos National Laboratory Report LA-UR-95-2696, Los Alamos, NM, 1995.

[MacKinnon,et.al., 1994] R.J.MacKinnon, T.M.Sullivan, C.J.Suen, S.A.Simonson, "BLT-EC Breach, Leach, TRansport and Equilibrium Chemistry....Model Description", report NUREG/CR-???, prepared for the U.S. Nuclear Regulatory Commission, August, 1994.

[NRC, 1984] "Radon Attenuation Handbook for Uranium Mill Tailings Cover Design," prepared for the U.S. Nuclear Regulatory Commission by Rogers and Associates Engineering Corporation and Pacific Northwest Laboratory, NUREG/CR-3533, April 1984.

[Philip and de Vries,57] J R.Philip and D.A. de Vries, "Moisture movement in porous materials under temperature gradients", Trans., Amer. Geophysical Union, v38,n2, p222, 1957.

[Press, et.al., 1992] W.H.Press, S.A.Teukolsky, W.T.Vetterling, B.P.Flannery, Numerical Recipes in FORTRAN, Second Edition, Cambridge University Press, New York, 1992.

[R.,Shuman, 1997], "Radiological Dose Assessment for the TA-54, Area G Performance Assessment and Composite Analysis," Rogers and Associates Engineering Corporation, RAE-9148/82-2, January 1997.

[Vold 1996A] E.L. Vold, "Atmospheric Transport in Complex Terrain at Los Alamos, Area G", Los Alamos National Laboratory Report, LA-UR-96-4870, Los Alamos, NM, 1996.

[Vold, 1996B] E.L. Vold, "A Model for the Effective Diffusion of Gas or the Vapor Phase in a Fractured Media Unsaturated Zone Driven by Periodic Atmospheric Pressure Fluctuations", Los Alamos National Laboratory Report, LA-UR-96-4871, Los Alamos, NM, 1996.

[Vold and Eklund,96A] Vold, E.L., and Eklund, B., 'Determination of an In-Situ Vapor Diffusion Coefficient at a Mesa Top Waste Disposal Facility', Los Alamos National Laboratory Report, LA-UR-96-1848, Los Alamos, NM, draft report May 22, 1996.

[Vold and Shuman 1997] E. L. Vold and R. Shuman, "A Model for the Biotic Translocation of Buried Low-Level Radioactive Waste to the Ground Surface in the Presence of Surface Erosion", Los Alamos National Laboratory Report, LA-UR-97-84, Los Alamos, NM, 1997.

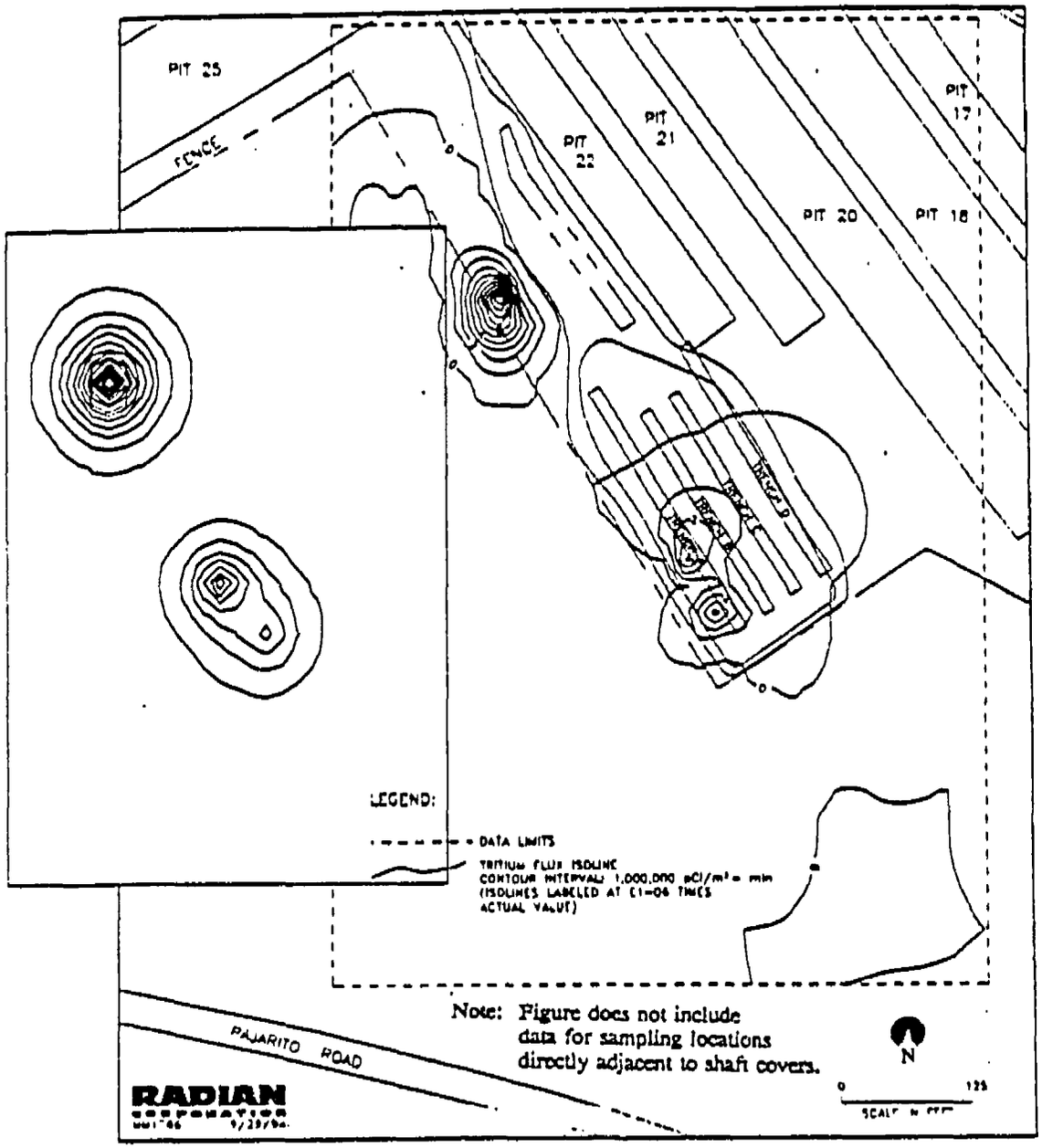

Fig. 1 Contour results of tritium flux in the vicinity of the high level tritium disposal shafts [from Vold and Eklund, 1996]. Field results are shown on the site map, interpolated from sample data as discussed in [Vold and Eklund, 1996]. The inset (left center) shows the computational results for the same area from the 3-D model. The inset window area is *(x,y) = 600' x 800'*, approximately the same area as the dashed region on the map. The contour levels in each plot are relative and not quantitatively comparable between the field and the computational plots.

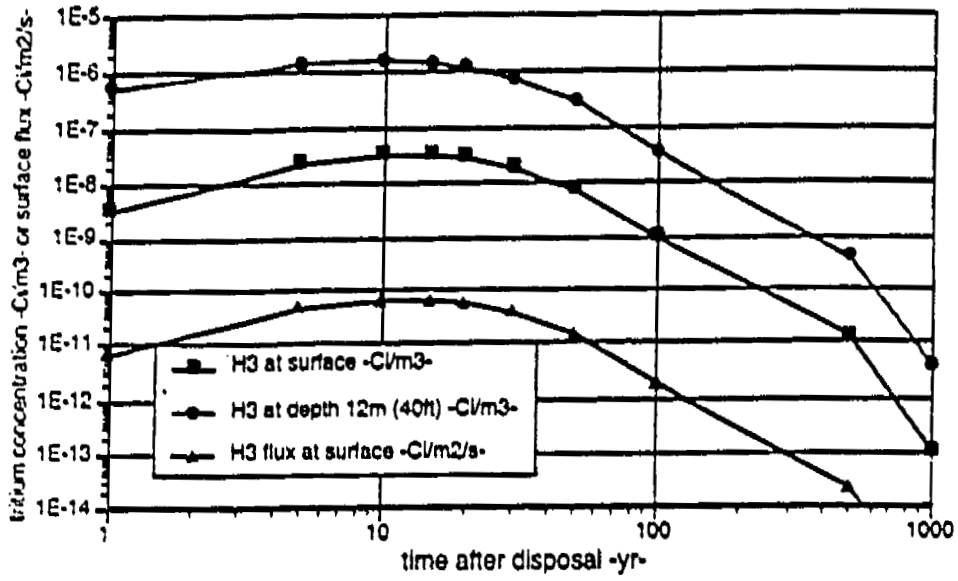

Fig.2 Tritium concentrations (Ci/m3) at the ground surface, at the disposal unit midpoint in depth, and the ground surface tritium efflux (Ci/m2/s) as a function of time after disposal, calculated in the numerical diffusion model.

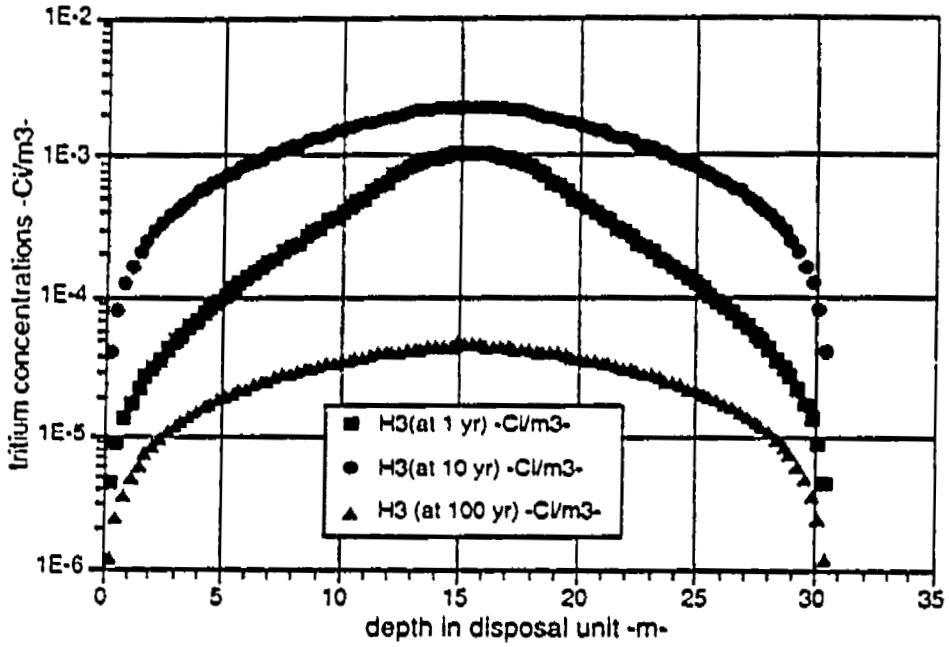

Fig.3 Tritium concentration (Ci/m3) profiles vertically through the disposal unit calculated from the numerical model at three different times.

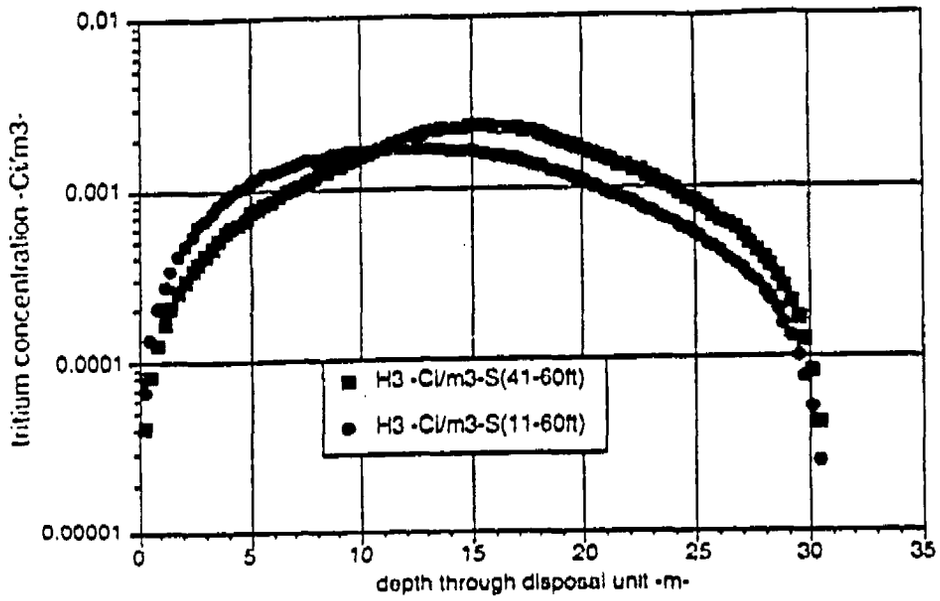

Fig. 4 Tritium concentration profiles (Ci/m3) vertically through the disposal unit calculated from the numerical model for two different distributions of the tritium source along the vertical profile of the disposal unit.

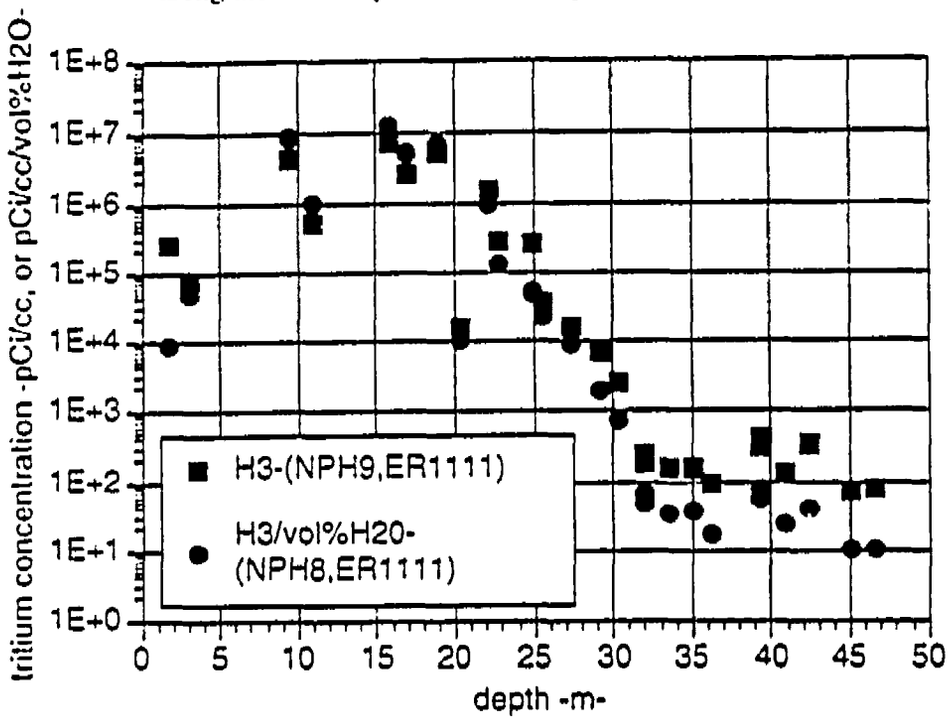

Fig. 5 Profiles of tritium concentration data as measured in borehole core moisture (labeled *H3*, in units of pCi/cc), and tritium concentration per volumetric moisture content (labeled *H3/vol%H2O*, in units of pCi/cc/vol%), in a borehole in the immediate vicinity of the tritium shafts.

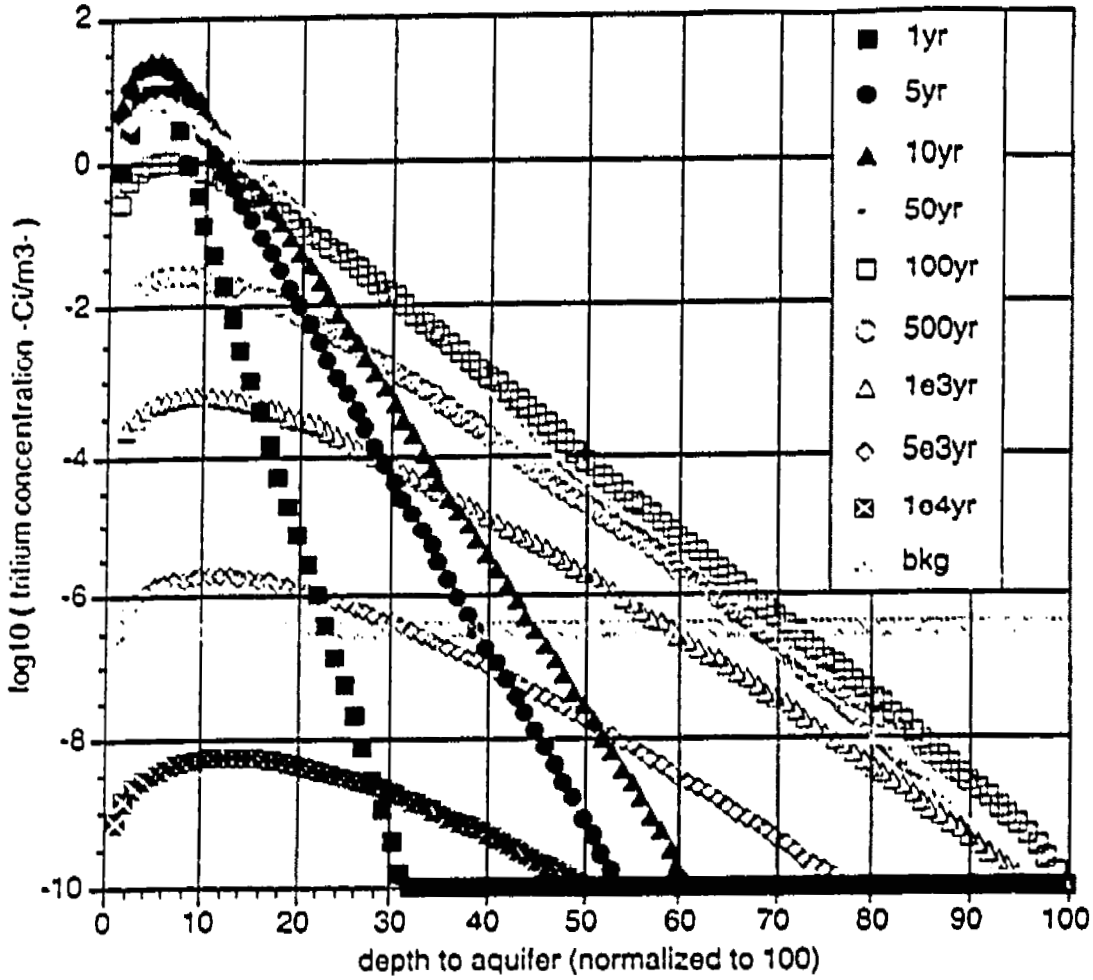

Fig. 6 Tritium concentration verses depth from the mesa top to the deep aquifer at select times assuming tritium migration is dominated by vapor phase diffusion as determined from empirical observations in the near surface unsaturated region at Area G.

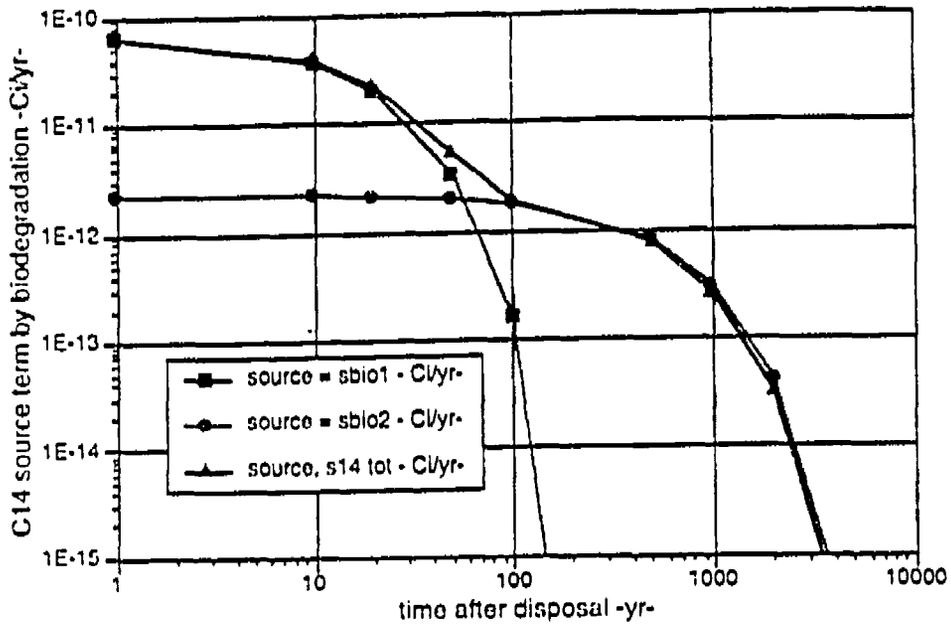

Fig. 7 Carbon-14 source term for gaseous phase release from the disposal unit, generated by the biodegradation of the organic component of the C14 inventory.

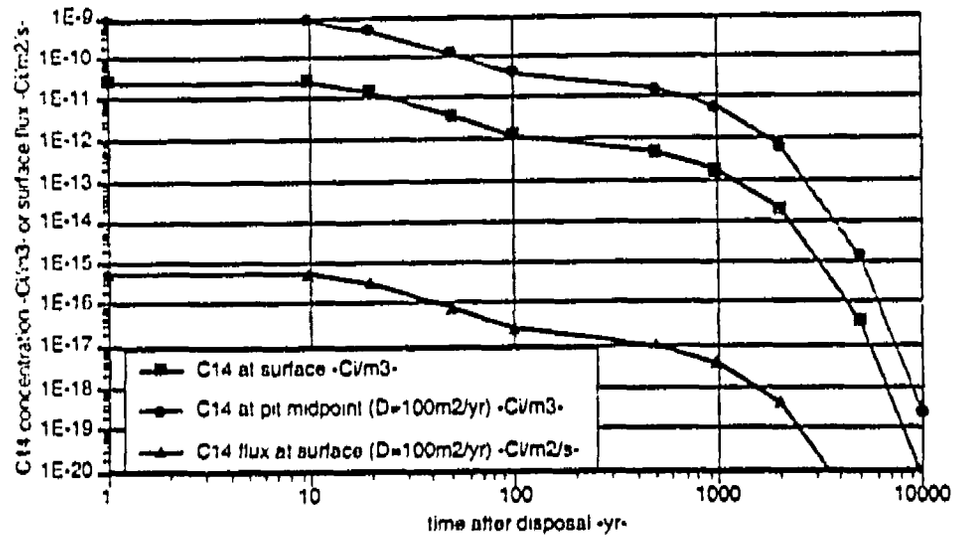

Fig. 8 Carbon-14 concentrations (Ci/m3) at the ground surface, at the disposal unit midpoint in depth, and the ground surface tritium efflux (Ci/m2/s) as a function of time after disposal, calculated in the numerical diffusion model.

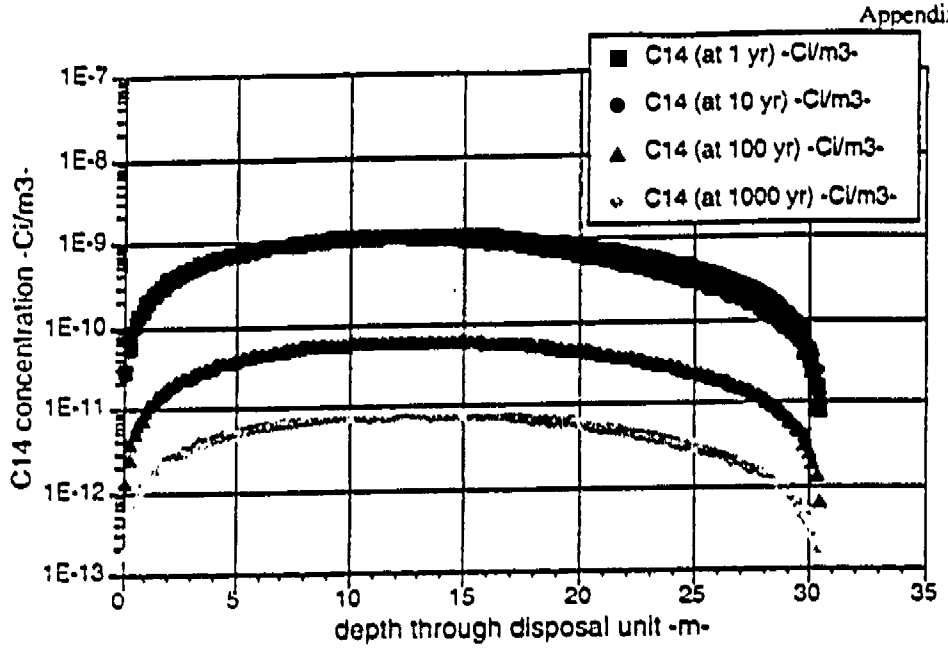

Fig. 9 Carbon-14 concentration (Ci/m3) profiles vertically through the disposal unit calculated from the numerical model at four different times.

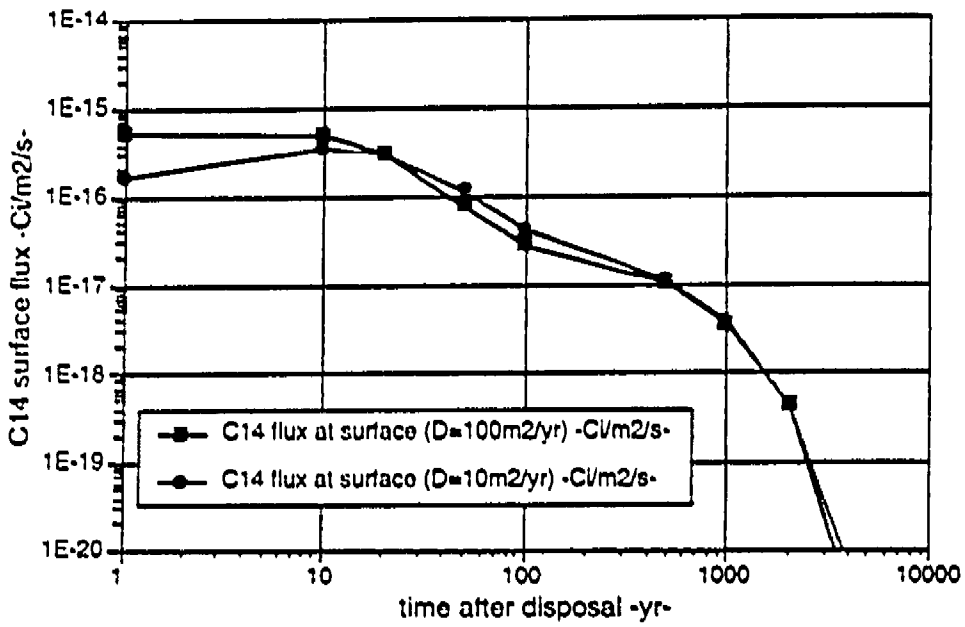

Fig. 10 Carbon-14 ground surface tritium efflux (Ci/m2/s) as a function of time after disposal, calculated in the numerical diffusion model for two values of the diffusion coefficient.

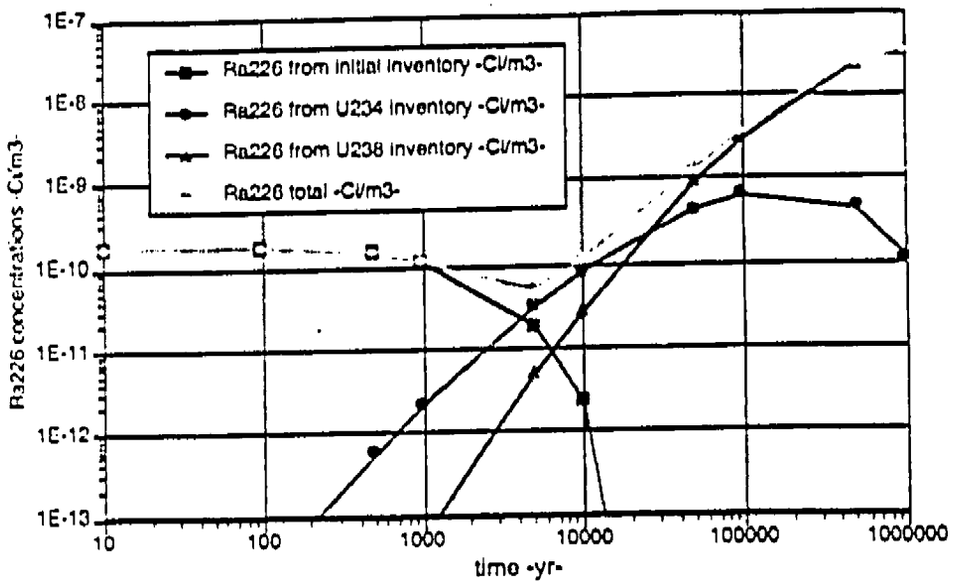

Fig. 11 Radium-226 (source for radon-222 gaseous phase release from the disposal unit) from the three main contributions, Ra-226 initial inventory, U234 inventory, and U238 inventory.

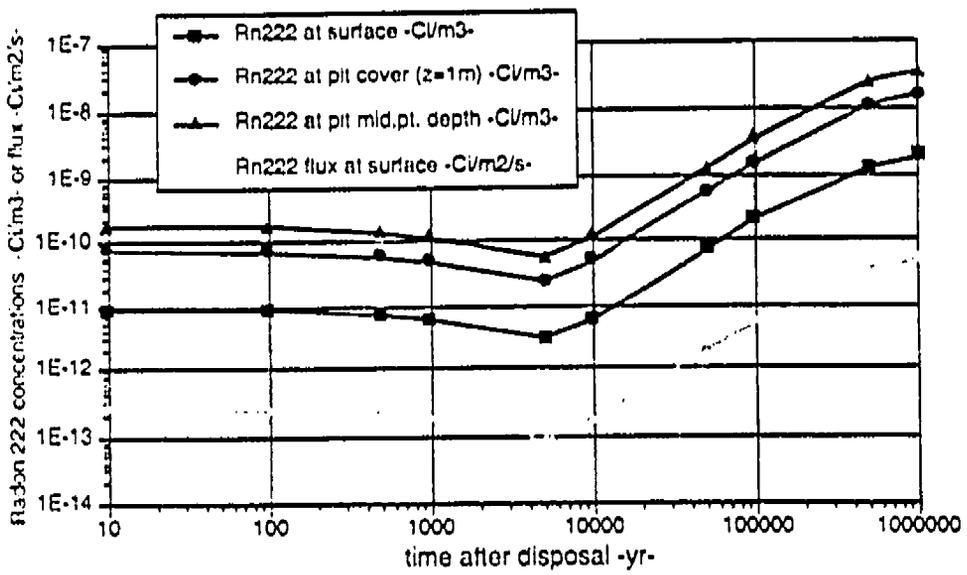

Fig. 12 Radon-222 concentrations (Ci/m3) at the ground surface, at the disposal unit cover depth (1m), at the disposal unit midpoint in depth, and the ground surface tritium efflux (Ci/m2/s) as a function of time after disposal, calculated in the numerical diffusion model.

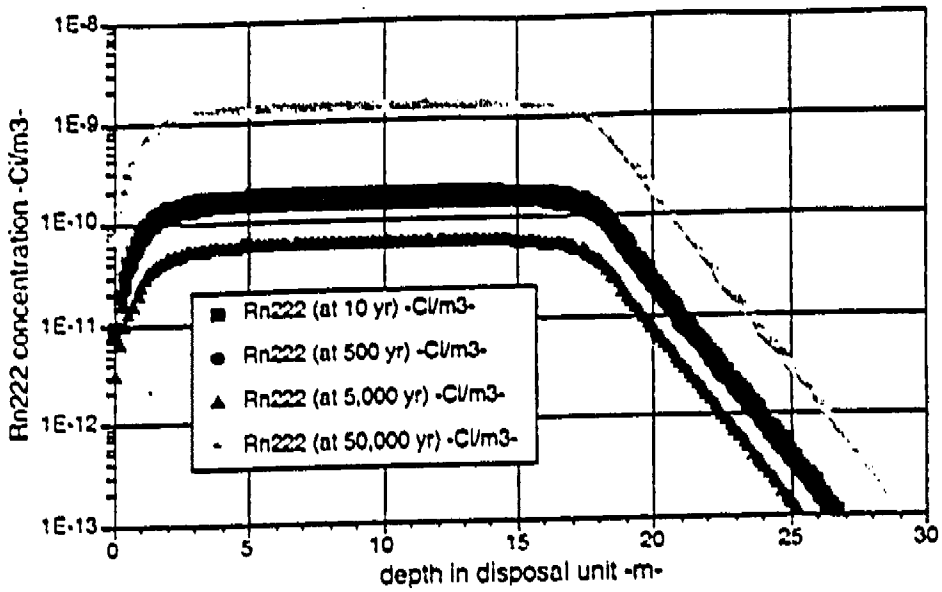

Fig. 13 Radon-222 concentration (Ci/m3) profiles vertically through the disposal unit calculated from the numerical model at four different times.

LA-UR-97-84

Title: A Model for the Biotic Translocation of Buried Low-Level Radioactive Waste to the Ground Surface in the Presence of Surface Erosion

Author(s): Erik L. Vold - LANL

Rob Shuman - RAE

Submitted to: U.S. Department of Energy, as support documentation for the Los Alamos Area G Performance Assessment

Los Alamos
NATIONAL LABORATORY

Los Alamos National Laboratory, an affirmative action/equal opportunity employer, is operated by the University of California for the U.S. Department of Energy under contract W-7405-ENG-36. By acceptance of this article, the publisher recognizes that the U.S. Government retains a nonexclusive, royalty-free license to publish or reproduce the published form of this contribution, or to allow others to do so, for U.S. Government purposes. The Los Alamos National Laboratory requests that the publisher identify this article as work performed under the auspices of the U.S. Department of Energy.

Appendix 3b

A Model for the Biotic Translocation of Buried Low-Level Radioactive Waste to the Ground Surface in the Presence of Surface Erosion

Erik L. Vold - Los Alamos National Laboratory
Rob Shuman - Rogers and Associates Engineering, Inc.

Table of Contents

Abstract....1
BIOTIC TRANSLOCATION MODEL....2
Introduction....2
Analysis....3
Area G Parameters....6
Area G Base Case (most likely biointrusion) Results....8
Area G Biointrusion Model Uncertainty and Sensitivity....8
Area G Biointrusion Model Combined with Erosion....10
Area G PA Implementation....11
Discussion....12
Summary....13
Acknowledgments....13
References....13
Tables I - IV....16
Figures 1- 6....20

A Model for the Biotic Translocation of Buried Low-Level Radioactive Waste to the Ground Surface in the Presence of Surface Erosion

Erik L. Vold - Los Alamos National Laboratory
Rob Shuman - Rogers and Associates Engineering, Inc.

Abstract

Intrusion into buried low-level radioactive waste by plants and burrowing animals may lead to the translocation of contaminants to the ground surface of the disposal facility. Radioactivity brought to the surface is a source term for atmospheric release by surface particle resuspension and for surface water run-off to an off-site receptor location. A simple model for this biotic translocation process, including a modification to account for surface erosion at a specified rate, is described in this report. Site-specific parameter values for the low-level radioactive waste disposal facility at Los Alamos National Laboratory, Area G, are presented. These data are used to model a base case intrusion scenario that is representative of the animal and plant species at this semi-arid site. Two 'bounding cases' characterized by greater degrees of intrusion are also examined in order to understand the uncertainties associated with the base-case intrusion results. The output from the biotic translocation model is a projection of radionuclide-specific surface soil concentrations as a function of time, normalized to the initial waste disposal concentration. These normalized concentrations, C_s/C_{wo}, are used in the environmental transport analyses conducted in support of the Area G Performance Assessment and Composite Analysis.

The translocation of radioactivity is dominated by burrowing animals when the plant uptake factor, B_i, is small (≤0.1). Under these conditions, the projected value of C_s/C_{wo} for the Area G base case ranges from 0.03 to 0.07 and is relatively constant for thousands of years. Considering the Area G bounding cases, an upper limit on this value is likely to be about 0.12 and a lower limit likely to be 0.02 or less. As the value of B_i increases, the surface concentration is controlled by plant uptake until late times. Only five elements present in the waste inventory have large uptake factors, greater than or approximately equal to one, Tc ($B_i = 9.5$), Sr ($B_i = 2.5$), H ($B_i = 0.9$), C ($B_i = 1.3$), and Cl ($B_i = 70$). For these isotopes, the expected values for C_s/C_{wo} are estimated as 2.0, 0.6, 0.25, 0.25, and 10, respectively. The model implementation in the Performance Assessment and Composite Analysis accounts for the detailed radionuclide site inventory and specifies the time dependent biotic translocation including effects of erosion on the penetration depth of plants and burrowing animals in the waste.

BIOTIC TRANSLOCATION MODEL

Introduction

Biotic intrusion into low-level radioactive waste disposed in shallow burial configurations at Los Alamos National Laboratory (LANL), Area G, and the subsequent translocation of contaminants to the surface soil can occur from rooting of plants or burrowing of small animals or insects in the waste volume. A model for this translocation process and the site-specific parameter values used for Area G are described in this report. A simple modification to the model accounts for a specified surface erosion rate which reduces the waste cover thickness. The output from this biotic translocation model is a prediction of surface soil concentration as a function of time. This contaminated surface soil concentration is a source term for atmospheric release by surface particle resuspension and for surface run-off to an off-site receptor location, subsequently used in the dose analysis for the disposal site Performance Assessment and Composite Analysis [Shuman, 1996].

A study of the local plants [Tierney and Foxx, 1987] examined the distribution of root length verses depth for many species indigenous to this area. Most species have nearly exponential decrease in rooting mass with depth with exponential decay lengths of only a few tens of cm. No significant root mass was reported for any species below 2 m depth, even for the larger conifers examined in the study. Conversely, some plants such as the chamisa (a large weedy bush) can grow a tap root to more than 5 m. Translocation of strontium by a chamisa tap root penetrating through at least 14 ft of clean overburden covering an old contaminated site has been described in detail [Fresquez, et.al., 1995c].

Field data used to characterize relevant biotic translocation model parameters for several animals potentially present at an arid or semi-arid site are summarized in Table I, taken from the BIOPORT code documentation (adapted from Table 2.3.1 in [McKenzie, et.al., 1982]). The field work quoted in the literature for biotic translocation by small mammals often refers back to studies on pocket gophers done at Los Alamos [Hakonson, et.al., 1982, Hakonson, et.al., 1992], and so these study results are directly applicable to Area G. Recent field work at Area G suggests that the dominant small mammal species in Area G is the deer mouse [J.Biggs, 95]. Burrowing data for this species is assumed from the literature [Arthur, et.al.,1987] for use in the present modeling.

Environmental surveillance data collected at Area G from vegetation and from small mammals generally shows elevated activities for several nuclides in both the vegetation [Fresquez et.al., 1995a, 1995b, 1996] and in the mammals [Biggs, et.al., 1995]. The contamination levels are low with respect to dose consequences, however, this confirms that the biotic translocation mechanism at Area G is potentially important in off-site migration and should be considered for the all-pathways dose assessment.

Analysis

A simple conceptual model for biotic translocation is shown in Fig. 1 for a representative intruding animal and plant species. Key parameters in the analysis include the waste cover thickness, L_c, the total biotic intrusion depth, L_b, and the overlap in volumes (shown as areas in the figure) of the total biotic intrusion volume and the buried waste volume. (Note that the shape of the depth distribution for the plant is shown as uniform with depth here for example only and that an exponential distribution will be assumed in the analysis.) The extent of overlap of the biotic intrusion volume with the waste disposal volume beneath the waste cover will be unique for each species, however, the overlap can be approximated with a single bounding value for plants and with a second value for animals which represent different distributions in rooting depth or animal burrows, respectively. The bounding values represent a net penetration into the disposed waste volume.

The biotic translocation process yields a surface concentration, C_s, normalized to initial waste concentration, C_{wo}. For more than one biotic intruder species bringing a contaminated soil mass to the ground surface from the subsurface, the normalized surface contamination is given as the average of the surface concentrations, C_{sb}, due to each of nb contributing biotic species, weighted for the soil mass brought to the surface (on an annual rate basis) by each species, or

$$\frac{C_s}{C_{wo}} = \frac{\sum_{b=1}^{b=nb} \dot{m}_b \, (C_{sb}[t] / C_{wo})}{\sum_{b=1}^{b=nb} \dot{m}_b} \qquad (1)$$

where

$$C_{sb}[t] = f_b B_b C_w[t] \qquad (2)$$

and,

$\dot{m}_b$ = mass transfer to the surface soil [kg/m2/yr] for the biota species, b

f_b = fraction of biotic intrusion volume (plant rooting volume or animal burrowing volume) which overlaps the waste volume

B_b = biotic transfer factor. In plants, B_i is an element-specific value for element, i, [(contaminant/kg-plant)/(contaminant/kg-soil)], and depends upon the root uptake. For animals, B_i is taken to be unity.

The waste concentration in the disposal unit is depleted over time due to biotic intrusion as reflected in $C_w[t]$. Each biota species contributes to a time dependent surface contamination concentration with the average given by the above equation.

Each waste layer which is occupied, or intruded upon, by a unique number of biota species, is depleted at a unique rate. This waste layer concentration, C_{iz}, is governed by a continuity equation which can be written in the control volume integral form,

$$A \, L_{iz} \frac{\partial C_{iz}}{\partial t} = - A \sum_{b=1}^{b=nb} \dot{m}_b f_b B_b \frac{C_{iz}}{\rho_s} \qquad (3)$$

where L_{iz} is the vertical dimension of the iz layer and A is the area in the surface plane. For the initial waste layer concentration, C_{wo}, leading to an initial surface concentration of C_{so} and assuming the concentration eventually tends to a steady state value, C_{ss}, this equation has the solution

$$C_{iz} = C_{ss} + (C_{so} - C_{ss}) \exp\left(- \frac{t}{\rho_s L_{iz}} \sum_{b=izb}^{b=nzb} \dot{m}_b f_b B_b \right) \qquad (4)$$

where the summation indices track those biota which intrude in the iz layer.

The steady state concentration, C_{ss}, depends upon the assumed physical processes which determine the long-time characteristics. If one neglects surface erosion and assumes that only the biotic intrusion is modifying the concentration of the surface, then animals act in the long run to mix the waste concentration throughout the biota intrusion depth, while plants continually dilute contaminants by adding new biomass to the surface layers.

Animal Intrusion - For animal intrusion below a cover depth, L_c, the initial contaminant concentration brought to the surface by animals is $f_b\ C_{wo}$. The long term steady state contaminant surface concentration is $\frac{L_b - L_c}{L_b}\ C_{wo}$, representing an eventual complete mixing of the contaminant throughout the (burrow) intrusion depth, L_b. The exponential build-up time constant is given by λ_b, from the solution equation above where $L_{iz} = L_b - L_c$ for the case a single species considered, or

$$\lambda_b = \frac{\dot{m}_b f_b B_b}{\rho_s (L_b - Lc)} . \qquad (5)$$

For these assumptions, and ignoring B_b which is always unity for animals, the time dependent surface concentration due to animal intrusion, expressed as $C_w[t]/C_{wo}$, is

$$C_{sb}[t]/C_{wo} = f_b + \left(\frac{L_b - L_c}{L_b} - f_b\right)(1. - exp(- \lambda_b\ t)) . \qquad (6)$$

Plant Intrusion - For plant intrusion, plants are assumed to biodegrade and deposit their biomass in the soil surface locally and on a time scale short compared to the characteristic time scale ($\tau_b = \lambda_b^{-1}$) for mass transfer rates associated with biotic translocation. The model does not explicitly include a factor, f_f, a 'fixed fraction', which represents the fraction of the biomass production rate which is locally fixed into the soil layer. This number is assumed to be $f_f = 1$, implying all plant biomass produced in locally degraded into the surface soil. These assumptions of local and relatively rapid biodegradation of the plant mass and local mixing in the surface soil are supported directly by a study of translocation by chamisa plants in this area [Fresquez, et.al. 1995c].

The biota time constant, Eqn. 5, for plants is similar to that for animals. However, the plant is adding biomass to the soil which is assumed to be primarily drawn from biosynthesis and not from the original soil mass. Therefore, the contaminant

concentrations are being continually diluted in new biomass and the waste and surface concentrations eventually approach zero.

The equation describing this situation for plant intrusion, again in terms of normalized surface concentration is

$$C_{sb}[t]/C_{wo} = f_b B_i \exp(-\lambda_b t). \qquad (7)$$

Combining the above, Equations 1, 6, and 7 give a model of the time dependent evolution expected for the surface contaminant concentrations for specified combinations of different species of animals or plants. This neglects the effect of surface erosion which acts to reduce the cover thickness, L_c, over time. The model is modified as described in a later section to account in a simple manner for the effect of surface erosion.

Area G Parameters

The Area G Biota Translocation Model considers first a 'base case' or likely expected biota intrusion case. Following that, variations in the base case are considered to cover the range of results expected from the uncertainties in the input data and in the model itself.

The cover thickness is assumed to be 1 m for all historical disposal pits (1.4 m over historical disposal shafts), consistent with past practices in disposal at Area G. Current closure practice dictates that future covers will have a thickness of 2 m. This, combined with the slow surface erosion rate and the maximum biota intrusion depth at Area G of 2 m, indicates there will be no significant biotic translocation from future disposal operations at Area G. The above cover thicknesses are implemented in the biota analysis for the PA [Shuman, 1997] while this study assumes a 1m cover to illustrate the results under 'base case' assumptions.

A base case is chosen to be the most likely scenario at Area G. Characteristics of potential animal intruders were summarized in Table I adapted from [McKenzie, et.al., 1982]. These potential intruders have been compared to species observed at LANL as summarized in the main report. Recently, deer mice have been observed as the main species trapped at Area G disposal site [Biggs, 1995]. Dirt excavation rates for deer mice observed at INEL [Arthur, et.al.,1987] are slightly lower than the values summarized in Table I for similar species, so the tabulated values for pocket mice are used as conservative upper limits.

Burrow data for the pocket mouse is assumed to represent the 'deer mice' since this data for deer mice data are unavailable. Element specific values for the plant uptake factors, B_i, are tabulated from Baes et.al., 1984 with modifications for carbon and hydrogen as described in Shuman, 1996. These values are compiled in Table II.

The Area G Base Case considers a single plant and single animal species that bound the problem. The review of data shows that a 'deer mice' species with a 2m maximum burrow depth bounds animal translocation expected at the Area G site. Insect translocation is expected to be relatively minor. A generic arid plant with 2m rooting depth bounds the plant intrusion expected at Area G (note that a few deep tap roots can be assumed to be included in the model since f_b is conservatively assumed to be 0.3). The model parameter values for the expected intrusion base case are summarized in Table III.

In this most likely base case, parameters for deer mice are $\dot{m}_b = 0.05$ kg/m2/yr, $f_b = 0.1$, and $B_b = 1$. Parameters for the representative plant species are $\dot{m}_b = 0.1$ kg/m2/yr [Hanson and Miera, 1976] and $f_b = 0.3$. This value for f_b is conservative compared to site specific data [Tierney and Foxx, 1987], and could be considered to include a contribution from plants such as chamisa which extend well below the 2m rooting depth used in the model.

A worst case analysis considered intrusion by pocket gophers. Pocket gophers excavation rates are larger by ~20x than that for deer mice or other species. However, they are never reported below 1 m depth which implies they will not intrude in LANL waste which is below at least a 1 m cover over the historical disposal units. Because of the potentially large intrusion if pocket gophers burrow slightly deeper than previously reported, pocket gopher intrusion into the waste is considered in an 'uncertainty bounding case' by adding a pocket gopher species to those species already considered in the base case. Additionally, in the 'uncertainty bounding case', the plant rooting volume intrusion fraction is increased to $f_b = 0.5$ which is taken as an upper limit in lieu of site-specific data. The base case deer mice assumptions remain unchanged in the 'bounding case' because that data are relatively well established empirically.

Area G Base Case (most likely biointrusion) Results

The normalized surface contaminant results for the base case parameter values are shown in Fig. 2. The range in the element-specific root uptake factors, B_i, is shown by plotting results for $B_i = 10, 1, 0.1, 0.01$, and $B_i = 0.001$. This can be compared to the B_i values for specific elements, tabulated in Table II. For large B_i or root uptake, the surface concentration is controlled by the plant uptake until late times. As the value for B_i or root uptake decreases, the surface soil contaminant concentrations are limited by the animal excavation. These concentrations are still increasing at 10,000 years due to the slow excavation rate for the burrowing animal species.

Only a few elements present in the waste inventory, Tc, Sr, C and Cd have uptake factors (B_i) greater than or equal to about one. For all other nuclides the figure shows that the maximum normalized surface contaminant concentration value, C_s/C_{wo}, for all times up to 10,000 - 20,000 years is under about 0.07 or 7%. One reasonable approach to simplify the dose pathway calculations is to assume a constant value for C_s/C_{wo} of 0.07 for all nuclides except for the five listed above. For each of these, a different constant can be read from the graph which bounds the concentrations within the 10,000 year conformance interval. These constant values for C_s/C_{wo} are estimated respectively as 2.0 (Tc, $B_i = 9.5$), 0.6 (Sr, $B_i = 2.5$), 0.25 (H, $B_i = 0.9$), 0.25 (C, $B_i = 1.3$), and 0.1 (Cd, $B_i = 0.5$). Using these surface concentration fractions, the time dependence of the surface soil contaminant concentration is a small variation over the 10,000 yr compliance duration. In the actual PA/CA analysis, these simplifications were not made; the full time-dependent biotic model was implemented.

Area G Biointrusion Model Uncertainty and Sensitivity

The biotic translocation model is sensitive to the assumed species, their depth distribution, and excavation rates as well as several factors which influence the long-term behavior. The variance in results from the biota translocation model is examined by considering two cases which are intended to bound the range of uncertainty in the input parameters. It is assumed that the model itself is giving a reasonable estimate of the likely physical processes.

The first of the two 'bounding cases' increases biointrusion to expected maximum possible levels for all species. These parameter values are shown in Table IV. This case also adds a

pocket gopher species. These animals are never observed to intrude to sufficient depths to penetrate a 1m cover layer so they are excluded from the 'expected intrusion' base case, however, they excavate considerably more dirt than any other species so if they intruded deeper than previously observed, the intrusion results would be expected to be dominated by this species.

The results of this first bounding case are shown in Fig. 3, in a format similar to that described for Fig. 2. The normalized surface concentration values, for small B_i or at late times, have increased to the range 0.09-0.12 compared to the 0.07 value in the base case due to the large animal excavation by the pocket gophers in the present case. In this bounding case, the maximum values of C_s/C_{wo} at large B_i, are actually reduced slightly from the base case, because the plant uptake concentrations are diluted by the increased pocket gopher excavations in this case.

A second bounding case was examined by using the base case parameter values except assuming an increase of a factor of 4 in the plant biomass uptake factor. The base case value of $\dot{m}_p = 0.1$ *kg/m2/yr* is based on LANL site-specific data for vegetative density (kg/m2) [Hanson and Miera, 1976] and assumes perennial plants which renew their biomass once per year. The value of $\dot{m}_p = 0.4$ kg/m2/yr is the default for arid sites recommended in the widely used assessment code, GENII [Pacific Northwest Laboratory, 1988], in lieu of site-specific data. This is likely to be a conservatively large value for the Area G site.

The results of this second bounding case are shown in Fig. 4. For large B_i values where the root uptake dominates, then the C_s/C_{wo} result increases over the base case. However, for most nuclides where $B_i << 1$, then the effect of increased plant biomass production rate is to dilute the surface concentrations dominated by the animal excavations, so that for small B_i, (≤ 0.01) then C_s/C_{wo} goes to < 0.015, compared to the 0.07 value in the base case.

Overall, it is observed in these limited 'bounding cases' that the largest variance exists for the animal intruder dominated nuclides (small B_i). The expected value of C_s/C_{wo} is 0.07 when B_i is small (≤ 0.1) with an upper limit for C_s/C_{wo} likely to be about 0.12 and a lower limit likely to be 0.02 or less. If these limiting cases are assumed to be associated with the

standard deviation of a lognormal distribution, then a crude estimate of parameters describing the distribution for C_s/C_{wo} are geometric mean of 0.07 and geometric standard deviation of about 2.

For the few nuclides with large B_i values, the surface contamination results varied only slightly between the cases. However, the root uptake factors themselves were not varied in this study, and these factors are associated with large uncertainties themselves. Therefore, the surface contamination uncertainty for nuclides with large B_i will be directly related to the underlying uncertainty of the root uptake factors.

Area G Biointrusion Model Combined with Erosion

Over very long times surface erosion could significantly reduce the waste cover thickness and modify the results of the biotic translocation by increasing the intrusion volume with time. The erosion rate is very uncertain and likely to vary with location being largest near the sloped mesa edge and in rivulets and smaller on relatively flat terrain. A net increase in disposal unit cover could result in areas where biomass accumulation and deposition is larger than the erosion. This latter possibility would occur at Area G under the assumed conditions where uniform surface erosion was determined in preliminary analyses [Springer, 1995] to be about 0.024 kg/m^2/yr. This erosion value was reduced even further in the final analysis for the PA [Shuman, 1996], consistent with the final calculated erosion results [Springer, 1996]. The calculated erosion is for surface run-off only and does not account for wind erosion which has been estimated independently for Area G [Kowalewsky, et.al.,1995] as the resuspension value of 0.057 kg/m2/yr. The arid plant biomass production rate, 0.1 kg/m^2/yr, is slightly larger than the combined calculated surface erosion rates. Thus, if most of the biomass production rate is fixed locally in the soil by microbial action, then the net erosion rate would be negative corresponding to a thickening of the waste cover in time due to bioaccumulation.

Considering these uncertainties, the effect of surface erosion on the biotic translocation model was evaluated assuming net erosion is a uniform rate of 0.024 kg/m^2/yr. This corresponds to a constant decrease in time of cover thickness, equal to - 2.e-5 m/yr. To incorporate erosion into the biota translocation model an analytic expression for intrusion volume as a function of cover thickness is developed. This was obtained by using the few

data points available in the literature (Table 1 taken from the BIOPORT code documentation [McKenzie, et.al., 1982]), and obtaining a curve fit to the data as shown in Fig.5 for the Area G generic animal and plant intruder species. Using the resulting analytic expressions for $f_b(Lc)$ and assuming a linear decrease in cover thickness with time for the assumed constant erosion rate, the biotic model is modified to account for the combined translocation-erosion effects in a simple manner by computing $L_c(t)$, then $f_b(Lc(t))$, and using these values in the model Equations 1, 6 and 7. The results are shown in Fig. 6 for several values of B_i, the plant uptake factor.

This combined translocation-erosion model is somewhat adhoc. The biota model was initially developed with assumptions of a constant cover thickness, which is not satisfied when erosion is simultaneously considered. Since the erosion rate is so small, however, the impact of the model simplification is small and within the first 1000 or even 10,000 years the difference in results between this adhoc model and a more rigorous treatment is expected to be negligible for the predicted erosion rates.

One effect of the simplication to the erosion model is a minor inconsistency at long times when the surface erosion first uncovers the disposed waste. The surface contaminant was assumed to be diluted by the relatively clean biomass deposited by plants which are locally fixed into the soil in time. This means that the long time behavior approaches an asymptote given by the mass weighted expression (Eqn. 1) which, for the Area G parameter values, gives a dilution factor at the surface of about 0.3 for nuclides with small B_i. However, on the other hand, one expects that as erosion continues into the waste then one should see the surface contamination equal to the waste concentration for times where the surface cover has completely eroded. This leads to a discontinuity in the model results from C_s/C_{wo} = *0.3 to 1*, at the time when the cover thickness goes to zero. The combined biota-erosion model could be revised to more consistently account for the interactions of the two processes and to reconcile the apparent discontinuity, if the biota translocation leads to significant consequences in the Performance Assessment for the site. However, the discontinuity occurs well past the 1,000 or even the 10,000 year time frame.

Area G PA Implementation

The model equations for biotic translocation in the presence of ground surface erosion have been implemented within the analysis for the site PA in a set of spreadsheet calculations

which incorporate the Area G base case biota parameters. The model implemented in the PA dose analyses is the 'base case' biota translocation model described here with the base case erosion model combined in the manner described in the previous section. The analysis in the PA includes the actual site inventory distinguished by disposal pits and by shafts for each of the four inventory source term groups [Shuman, 1996]. It also considers the varying disposal unit cover thicknesses discussed in this report. The biotic translocation produces a surface soil contamination which contributes to two dose pathways, one, for airborne resuspension of ground surface particulate matter and two, for surface erosion in storm water run-off from the mesa top facility to off-site locations.

Discussion

Translocation of strontium by a chamisa tap root through at least 14 ft of clean overburden soil covering an old contaminated site has been described in detail [Fresquez,et.al., 1995c]. This field work indicated that the nuclide, Sr, has a significant plant uptake factor in chamisa, consistent with the literature value used in the analysis (B_i = 2.5). The study showed the strontium is taken to the surface by the plant, deposited very locally in the litter dropped by the plant and becomes mixed into the top soil, in a region immediately around the deep rooted plant. The field work confirms the basic assumptions of the biotic translocation model presented here for the plant species. The deep root is beyond the expected biotic intrusion depth of 2 m, but the conservatively assumed value of f_b = 0.3, the arid plant overlap fraction of intrusion and waste volumes, accounts for uptake such that the results are not strongly sensitive to the actual rooting depth observed in the field.

As discussed previously, routine environmental surveillance data collected at Area G from vegetation and from small mammals generally shows elevated activities for several nuclides in both the vegetation [Fresquez et.al., 1995a, 1995b, 1996] and in the mammals [Biggs, et.al., 1995]. This supports the notion that the biotic translocation mechanism at Area G is potentially important in off-site migration and for the all-pathways dose assessment. A detailed examination of the field data in comparison to the quantitative predictions of this biotic translocation model has not yet been done but could be used to improve the model predictions.

Summary

This report has described a biota translocation model for application to the Performance Assessment at Area G. Site parameters for the model have been reviewed and presented in a most likely 'base case' and in two bounding cases to explore the sensitivity of the results to the parameter input values. Implications of the model and these representative cases have been discussed in detail.

The model equations for biotic translocation in the presence of ground surface erosion have been implemented within the analysis for the site PA in a set of spreadsheet calculations which incorporate the Area G base case biota parameters. The biotic translocation produces a surface soil contamination which contributes to two dose pathways, one, for airborne resuspension of ground surface particulate matter and two, for surface erosion in storm water run-off from the mesa top facility to off-site locations.

On-going environmental surveillance monitoring provides an opportunity to 'calibrate' the model against field data.

Acknowledgments

This work was supported by the U.S. Department of Energy, Waste Management Programs, as part of the Performance Assessment for the disposal facilities at Los Alamos National Laboratory, Area G.

References

W.J. Arthur, O.D. Markham, C.R. Groves, B.L. Keller, "Radionuclide export by deer mice at a solid radioactive waste disposal area in southeastern Idaho", *Health Phys.*, 52, 45-53, 1987.

C.F. Baes III, R.D. Sharp, A.L. Sjoreen,, and R.W. Shor, "A Review and Analysis of Parameters for Assessing Transport of Environmentally Released Radionuclides through Agriculture", Oak Ridge National Laboratory Report, ORNL-5786, Oak Ridge, TN, September 1984.

J.K. Biggs, personal communication, ESH-20, Ecology Group, Los Alamos National Laboratory, Los Alamos, NM, 1995.

J.K. Biggs, K.D. Bennett, and P.R. Fresquez, "Radionuclide Contaminant Analysis of Small Mammals at Area G, TA-54, 1994," Los Alamos National Laboratory report LA-13015-MS (1995).

P.R. Fresquez, M.A. Mullens, and J.K. Ferenbaugh, "Radionuclides and Radioactivity in Soils Within and Around Los Alamos National Laboratory: 1974 to 1994," Los Alamos National Laboratory report LA-UR-95-3671 (1995a).

P.R. Fresquez, J.B. Biggs, and K.D. Bennett, "Radionuclide Concentrations in Vegetation at Radioactive-Waste Disposal Area G During the 1994 Growing Season," Los Alamos National Laboratory report LA-12954-MS (1995b).

P.R. Fresquez, T.S. Foxx, L. Naranjo, Jr., "Strontium Concentrations in Chamisa (Chrysothamnus nauseous) Shrub Plants Growing in a Former Liquid Waste Disposal Area in Bayo Canyon", Los Alamos National Laboratory Report, LA-13050-MS, Los Alamos, NM, Nov, (1995c).

P.R. Fresquez, E.L. Vold, and L. Naranjo, "Radionuclide Concentrations in/on Vegetation at Radioactive-Waste Disposal Area G during the 1995 Growing Season," Los Alamos National Laboratory report LA-13124-PR (March 1996).

T.E. Hakonson, L.J. Lane, J.G. Steger, G.L. DePoorter, "Some Interactive Factors Affecting Trench Cover Integrity of Low-Level Waste Sites", *Proc. Low-Level Waste Disposal: Site Characterization and Monitoring*, Arlington, VA, June 16-17, 1982, NUREG/CP-0028, CONF-820674, vol2., 1982.

T.E. Hakonson, L.J. Lane, E.P. Springer, in "Biotic and Abiotic Processes", p.112 in *Deserts as Dumps?*, ed., C.C. Reith and B.M.Thomson, Univ. of New Mexico Press, Albuquerque, NM, 1992.

K. Kowalewsky, B. Eklund, E. Vold, "Air Quality Impacts Analysis for Area G", final report 4/4 from RADIAN to LANL under DOE subcontract 6345L0014-31, with CST-14, Los Alamos National Laboratory, NM, 1995.

D.H. McKenzie, L.L. Caldwell, L.E. Eberhardt, W.E. Kennedy Jr., R.A. Peloquin, M.A. Simmons, "Relevance of Biotic Pathways to the Long-Term Regulation of Nuclear Waste Disposal", Pacific Northwest Laboratory, Topical Report on Reference Western Arid Low-Level Sites, U.S. Nuclear Regulatory Commission Report NUREG/CR-2675, Vol. 2, October 1982.

Pacific Northwest Laboratory, "GENII: Environmental Radiation Dosimetry Software System", available as code CCC-601 from Radiation Shielding Information Center, Oak Ridge National Laboratory, Oak Ridge, TN, 1988

R.,Shuman, 1997, "Radiological Dose Assessment for the TA-54, Area G Performance Assessment and Composite Analysis," Rogers and Associates Engineering Corporation, RAE-9148/82-2, January 1997.

E.P. Springer, "Area G Performance Assessment: Surface Water and Erosion", Los Alamos National Laboratory report LA-UR-95-2497, Los Alamos, NM, 1995.

E.P. Springer, "Surface Water and Erosion Calculations to Support the MDA G Performance Assessment: ", Los Alamos National Laboratory report LA-UR-96-4894, Los Alamos, NM, 1996.

G.D. Tierney, T.S. Foxx, "Root Lengths of Plants on Los Alamos National Laboratory Lands", Los Alamos National Laboratory Report, LA-10865-MS, Los Alamos, NM, Jan, 1987.

A Model for the Biotic Translocation of Buried Low-Level Radioactive Waste to the Ground Surface in the Presence of Surface Erosion

Tables I - IV

Table 1 Burrowing Habits of Potential Animal Intruders at the Reference Arid Low-Level Waste Burial Site (from [McKenzie, et.al., 1982]).

Animal	Percent Distribution of Burrow System Below-ground Depth Interval (m)					Density (Animals/ha)		Burrow Volume (m^3)		Estimated Volume of Soil Brought to Surface in First Year (m^3/ha)	Proportion of New Burrow Systems/Year
	0-0.5	0.5-1.0	1.0-1.5	1.5-2.0	>2.0	Range	Average	Range	Ave.		
Ground Squirrels (a)	50	30	15	5	0	5.7 - 74	25	0.008 - 0.077	0.02	0.500	0.50 - 1
Pocket Mice and Kangaroo Rats (a)	50	40	5	5	0	0.8 - 180	25	0.003 - 0.103	0.014	0.350	0.75 - 1
Pocket Gophers (a)	85	15	0	0	0	2 - 124		0.510 - 81.5 (b)	8.3 (b)	8 300	0.75 - 1
Prairie Dogs (a)	20	20	20	20	20	3.5 - 31.9 (c)	10 (c)	.120 - .356	0.196	1.960	0.02
Badgers	70	15	5	5	5	–	–	–	.170	0.211 (d)	1.00
Ants	70	10	10	5	5	–	50 (e)	–	.002 (f)	0.100	0 .10

(a) Represents several species and several sources of information (see Appendix A).
(b) Estimate of volume of soil excavated per hectare.
(c) Represents density in an individual colony.
(d) Estimated 0.17 m^3/burrow x 124 burrows/ha/yr - 21 08 m^3 /ha/yr. However, most of the digging is done in existing prey burrows and the burrow density figure was from an area of very high badger density. For our purposes, we used an estimate of 10% new soil excavation and 10% of reported badger density, therefore 21 08 x .01 - .211 m^3 /ha/yr.
(e) Colonies per hectare
(f) Represents average burrow volume per colony.

Table II - Plant uptake factors [a,b].

Element	Uptake Factor	Element	Uptake Factor
Ac	3.5E-04	Mo	6.0E-02
Ag	1.0E-01	Nb	5.0E-03
Al	6.5E-04	Ni	6.0E-02
Am	2.5E-04	Np	1.0E-02
At	1.5E-01	P	3.5E+00
Ba	1.5E-02	Pa	2.5E-04
Bi	5.0E-03	Pb	9.0E-03
Bk	1.5E-05[c]	Pd	4.0E-02
C	1.3E+00[d]	Pm	4.0E-03
Cd	1.5E-01	Po	4.0E-04
Cf	1.5E-05	Pu	4.5E-05
Cl	7.0E+01	Ra	1.5E-03
Cm	1.5E-05	Sc	1.0E-03
Co	7.0E-03	Se	2.5E-02
Cs	3.0E-02	Si	7.0E-02
Dy	4.0E-03	Sm	4.0E-03
Eu	4.0E-03	Sr	2.5E-01
Fr	8.0E-03	Ta	2.5E-03
Gd	4.0E-03	Tb	4.0E-03
H	0.0E+00[e]	Tc	1.5E+00
Hf	8.5E-04	Th	8.5E-05
Ho	4.0E-03	Ti	3.0E-03
I	5.0E-02	Tl	4.0E-04
K	5.5E-01	U	4.0E-03
Kr	0.0E+00	Y	6.0E-03
La	4.0E-03	Zr	5.0E-04

a Source of parameters is Baes et al., 1984, unless otherwise noted.
b. Plant-soil concentration factors have units of Ci/kg (dry weight) of vegetation per Ci/kg (dry weight) of soil.
c Plant-soil concentration factors and transfer factors are assumed to be the same as the factors for Cf and Cm.
d. Source of plant uptake factors is Sheppard et al., 1991. Source of transfer factors is NRC, 1977.
e Plant uptake of H-3 from soil was not assumed to occur.

Table III
Model parameter values for the Area G expected intrusion base case

site parameters: ρ_s = 1.3e3 kg/m3 L_c = 1.m

biota parameters:

index	species	f_b	L_b	$\dot{m}_b$	B_b	λ_b (yrs^{-1})
1	deer mice	0.1	2.	0.05	1.	3.8e-6
2	and plants	0.3	2.	0.1	B_i(elem.i)	(2.3e-5 B_i)

Table IV
Model parameter values for the Area G maximum biota intrusion case

site parameters: ρ_s = 1.3e3 kg/m3 L_c = 1.m

biota parameters:

index	species	f_b	L_b	$\dot{m}_b$	B_b	λ_b (yrs^{-1})
1	deer mice	0.2	2.	0.05	1.	7.7e-6
2	pocket gophers	0.1	1.2	1.2	1.	4.6e-4
3	and plants	0.5	2.	0.4	B_i(elem.i)	(1.5e-4 B_i)

A Model for the Biotic Translocation of Buried Low-Level Radioactive Waste to the Ground Surface in the Presence of Surface Erosion

Figures 1- 6

[redacted]

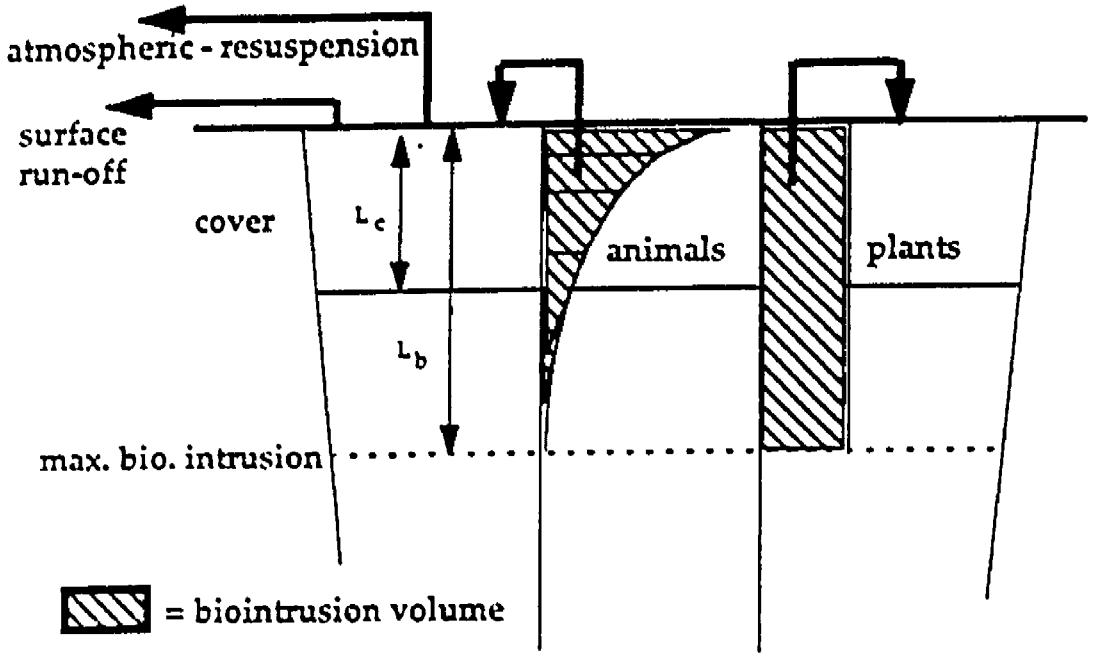

Figure 1 Biotic translocation conceptual model.

Waste is distributed throughout the volume beneath the disposal unit cover of thickness, L_c. Biotic intrusion occurs to an assumed maximum depth, L_b. (Note that the plant rooting volume, sketched as uniform with depth, is actually modeled as an exponential decrease in depth with a maximum intrusion depth.)

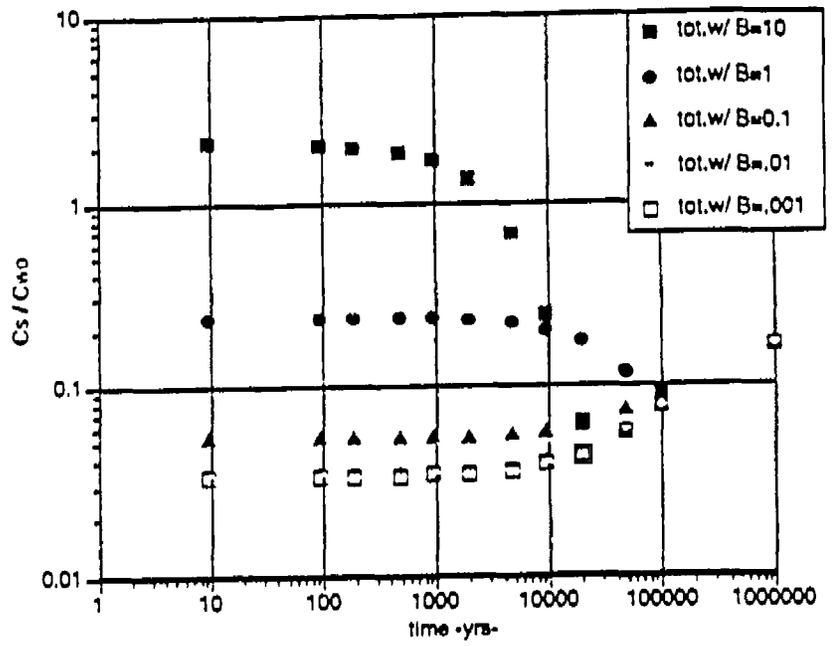

Figure 2 Normalized surface contaminant concentration verses time for the base case, the most likely biota intrusion case; shown for several values of B_i, the plant uptake factor.

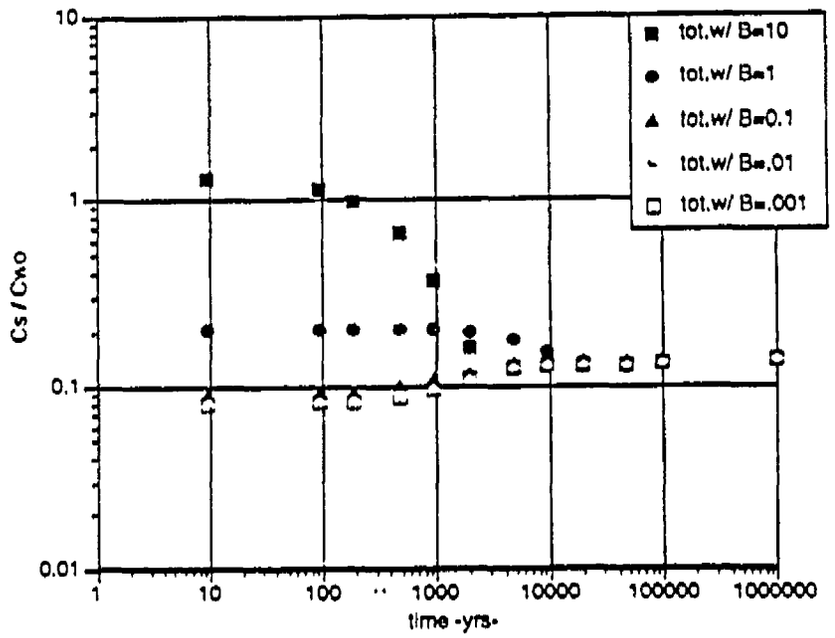

Figure 3 Normalized surface contaminant concentration verses time for the maximum likely biota intrusion case; shown for several values of B_i, the plant uptake factor.

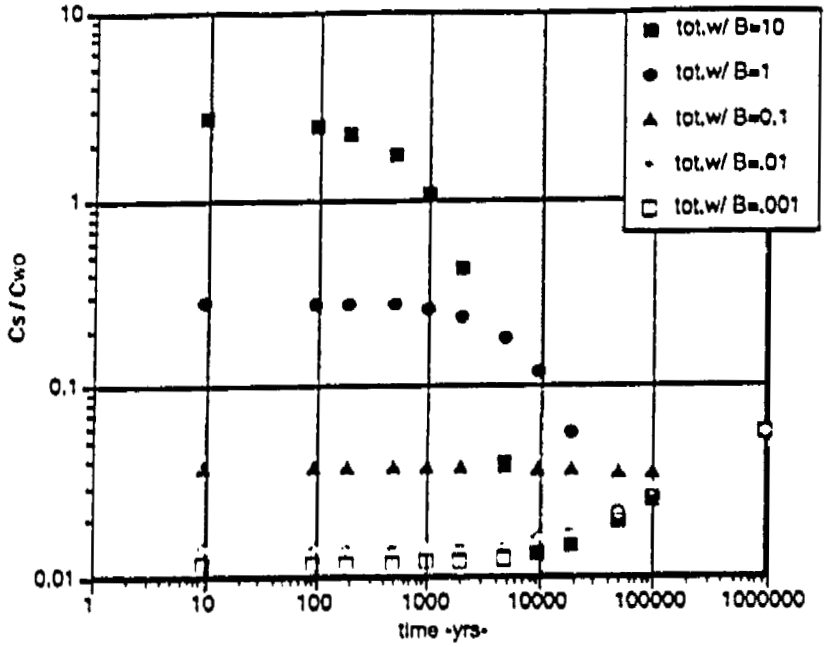

Figure 4 Normalized surface contaminant concentration verses time for the biota intrusion base case parameters but with plant uptake factor increased by a factor of four; shown for several values of B_l, the plant uptake factor.

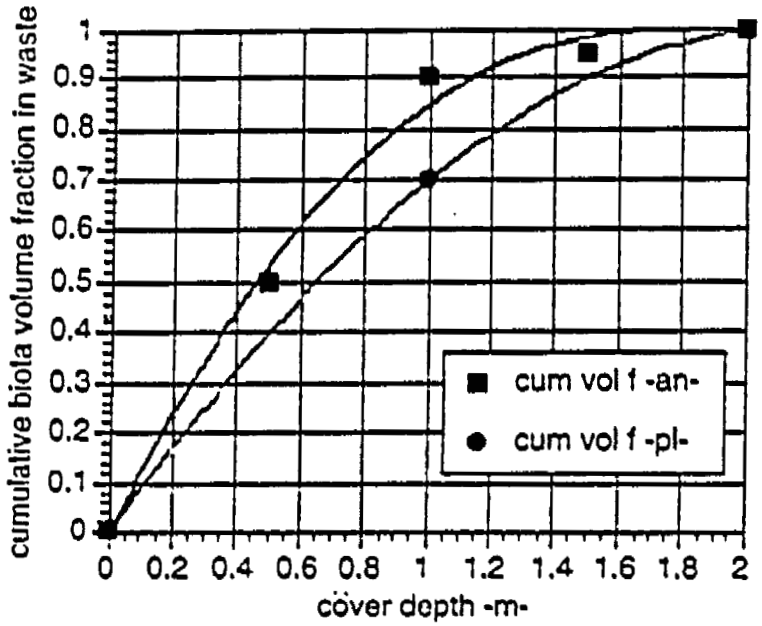

Figure 5 Data points for assumed depth distributions *(cum volf)* of the biota intrusion volume, f_b, and best-fit function profiles to the data for intruder animal species, an, and intruder plant species, pl.

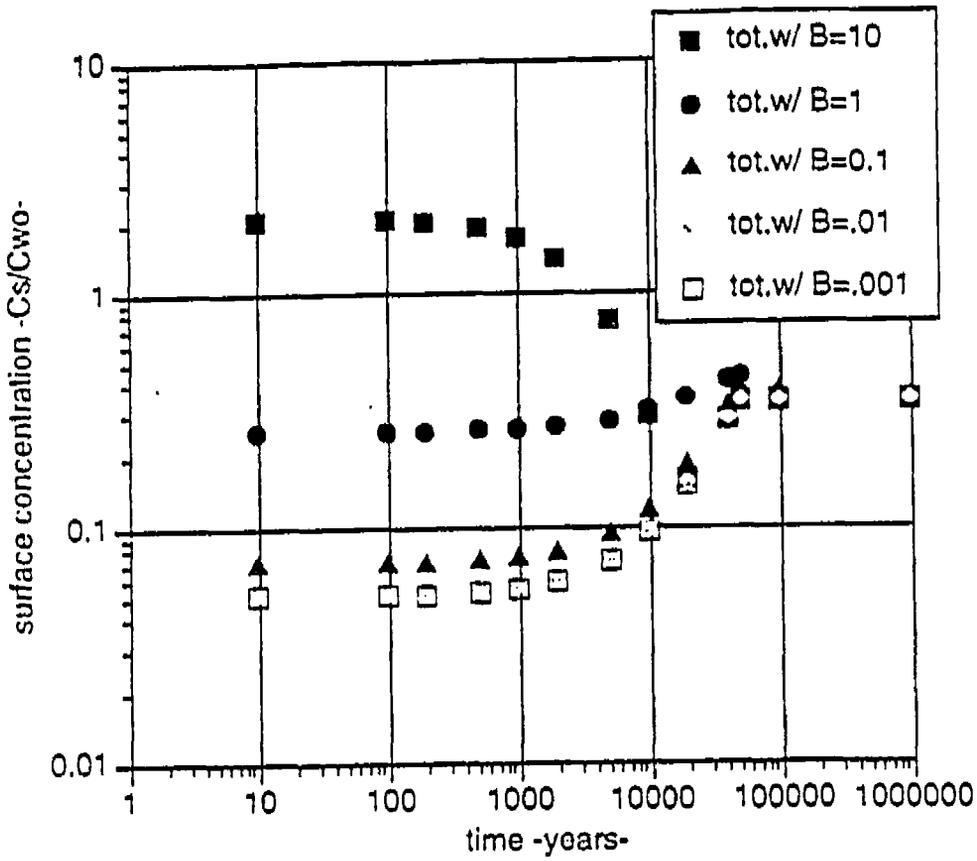

Figure 6 Normalized surface contaminant concentration verses time for the combined base case biota and erosion models, for several values of B_i, the plant uptake factor.

LA-UR- 96- 4894

Approved for public release;
distribution is unlimited.

Title: SURFACE WATER AND EROSION CALCULATIONS TO SUPPORT THE MDA G PERFORMANCE ASSESSMENT

Author(s): E. P. Springer, EES-15

Submitted to: Los Alamos Report

Los Alamos
NATIONAL LABORATORY

Los Alamos National Laboratory, an affirmative action/equal opportunity employer, is operated by the University of California for the U.S. Department of Energy under contract W-7405-ENG-36. By acceptance of this article, the publisher recognizes that the U.S. Government retains a nonexclusive, royalty-free license to publish or reproduce the published form of this contribution, or to allow others to do so, for U.S. Government purposes. Los Alamos National Laboratory requests that the publisher identify this article as work performed under the auspices of the U.S. Department of Energy. The Los Alamos National Laboratory strongly supports academic freedom and a researcher's right to publish; as an institution, however, the Laboratory does not endorse the viewpoint of a publication or guarantee its technical correctness.

Form 836 (10/96)

SURFACE WATER AND EROSION CALCULATIONS TO SUPPORT THE MDA G PERFORMANCE ASSESSMENT

E. P. Springer

INTRODUCTION

The performance of MDA G is dependent on surface hydrological and ecological processes because radionuclide transport by surface runoff can affect human and/or environmental receptors directly and the percolation for the subsurface radionuclide transport pathway is determined by the water balance in the near surface. For subsurface disposal of waste, surface soil erosion reduces the effectiveness of the surface cover and if wastes are exposed, then surface runoff can transport contaminants either in a soluble phase or sorbed to eroded soil particles. The objectives of this section are to estimate the effects at MDA G of surface runoff, soil erosion, and percolation. The conceptual and mathematical models will be reviewed, parameter estimation for the models will be presented and results and sensitivity analyses for a surface cover at MDA G will be presented.

CONCEPTUAL MODEL

Water Balance

The basic conceptual model that governs the surface water pathway is the water balance equation written as

$$\frac{dS}{dt} = P - Q - ET - R \tag{1}$$

where:
S = soil water storage (mm);
P = precipitation (mm);
Q = surface runoff (mm);
ET = evapotranspiration (mm);
R = the deep percolation (mm); and
t = time.

Equation 1 is used to describe the water balance for conceptual cover at disposal pit at MDA G. Precipitation may be either rain or snow. Evapotranspiration is from both soil evaporation and plant transpiration. Deep percolation is defined as that water draining below the pit. Figure 1 presents the conceptual model represented by Equation 1.

One key assumption for this application of Equation 1 to MDA G is that the cover is topsoil over crushed tuff. Cover designs can include a low permeability layer such as clay (Warren et al., 1996) or a capillary barrier (Nyhan et al., 1990) to divert infiltrated water. No credit was taken in the following analyses for any engineered cover design. The model is one-dimensional considering only the vertical coordinate.

Equation 1 is solved by measuring its various terms in field experiments. The following material reviews studies pertinent to the terms in Equation 1 that have been performed at or near MDA G to support the conceptual and mathematical models.

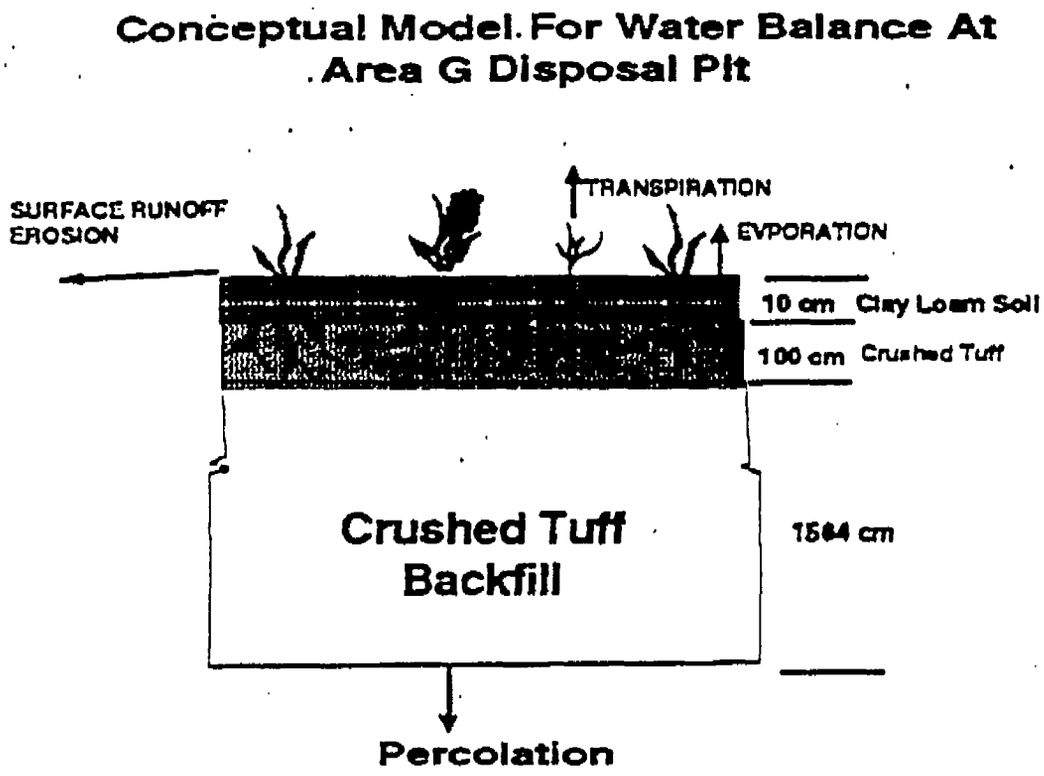

Figure 1. Conceptualization of hypothetical pit at MDA G for surface runoff and erosion assessment.

The focus of the following analyses is surface runoff (Q). Limited measurements of Q have been made for MDA G. Abeele et al. (1981) presented results (for a single event) from a runoff gauging station located at MDA G. Nyhan and Lane (1986b) used rainfall simulation to study surface runoff and soil erosion from different surface cover materials such as gravel mulch and vegetation at Los Alamos. Runoff data are available for one year for MDA G and the major canyons (Pajarito Canyon and Cañada del Buey) that drain the site as part of the Los Alamos stormwater quality program.

Soil moisture measurements have been made for various studies at MDA G. Results of a study by Purtyman are reported in Rogers (1977) for surface covers at Pits 1 and 2 in MDA G. These moisture data are presented in Figures 2 and 3. Note that the water content in Pit 1 is higher than Pit 2. The cause of this difference is unknown. Nyhan et al. (1986) performed a study at MDA G on Pit 25 using four different surface cover designs. One cover design includes the topsoil over crushed tuff like the cover design presented in Figure 1 that was used in this Performance Assessment. The other three cover designs had a biobarrier composed of a layer of either large cobbles or gravel and cobble to prevent plant and animal intrusion. Beneath each cover design, a layer of crushed tuff was placed, and the soil water content was measured in this layer. The temporal distribution of water content in this crushed tuff layer for the different cap configurations is presented Figure 4 which is from Nyhan et al. (1986). Generally, an increase in water content of the tuff layer can be observed for all cover designs early in 1983. A trend of decreasing water content occurs over the rest of 1983 followed by an increase in water content early in 1984 that is coincident with snowmelt period. Data in Figure 4 indicate that water can penetrate to depths greater than 1 meter. Nyhan et al. (1986) examined root penetration of the different designs using a cesium tracer placed in the crushed tuff layer beneath the cover designs. Substantial penetration was observed for the soil over tuff design providing a mechanism for water removal. Some root penetration was noted for the biobarrier designs, but this was not as prevalent as on the conventional design.

Nyhan et al. (1990) reported on a study of conventional and engineered surface covers at TA-51 located approximately 2 km west of MDA G. The conventional design consisted of loam soil over crushed tuff. The engineered design included a capillary barrier of pea gravel beneath the loam top soil and a biobarrier made of large cobble beneath the capillary barrier. The surface slope of these plots was zero in order to maximize infiltration: therefore no runoff occurred. Table 1 (Nyhan et al., 1990) gives the different components of the water balance for the two plot designs. These results indicate the relative distribution of the components in Equation 1 early in the performance period of these surface cap designs. Nyhan et al. (1990) attributed the seepage in the March to April period to snowmelt and low evapotranspiration demand because the vegetation was still dormant at this time of the year.

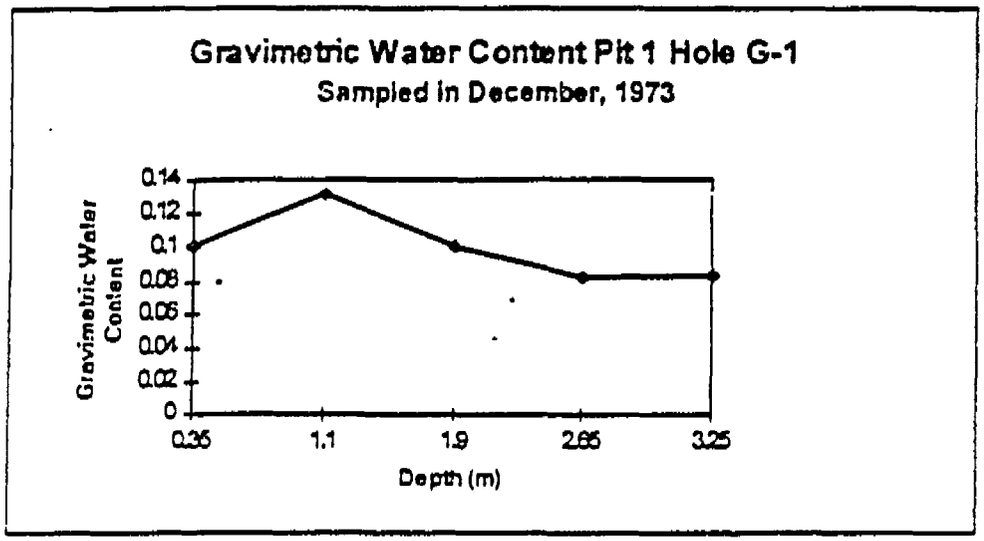

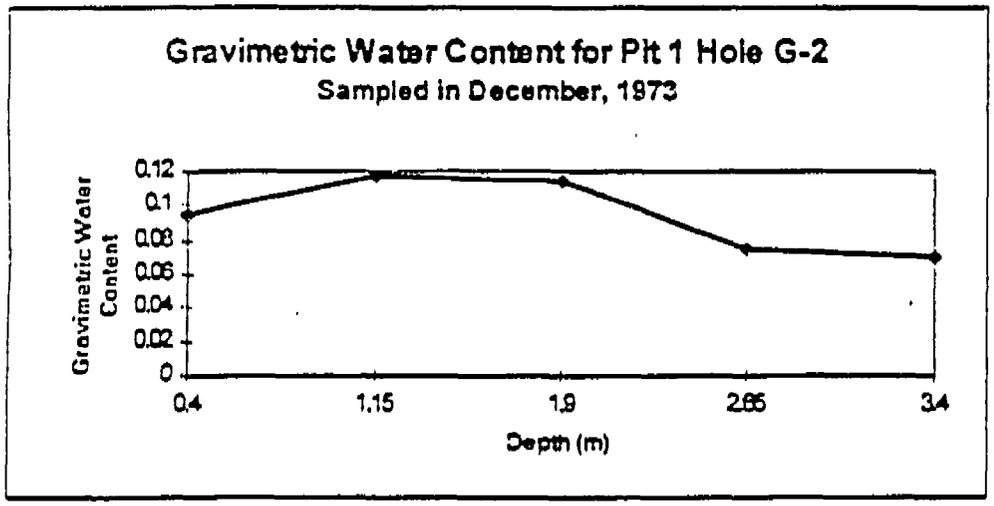

Figure 2. Gravimetric soil water content from two boreholes drilled in cover of MDA G pit number 1.

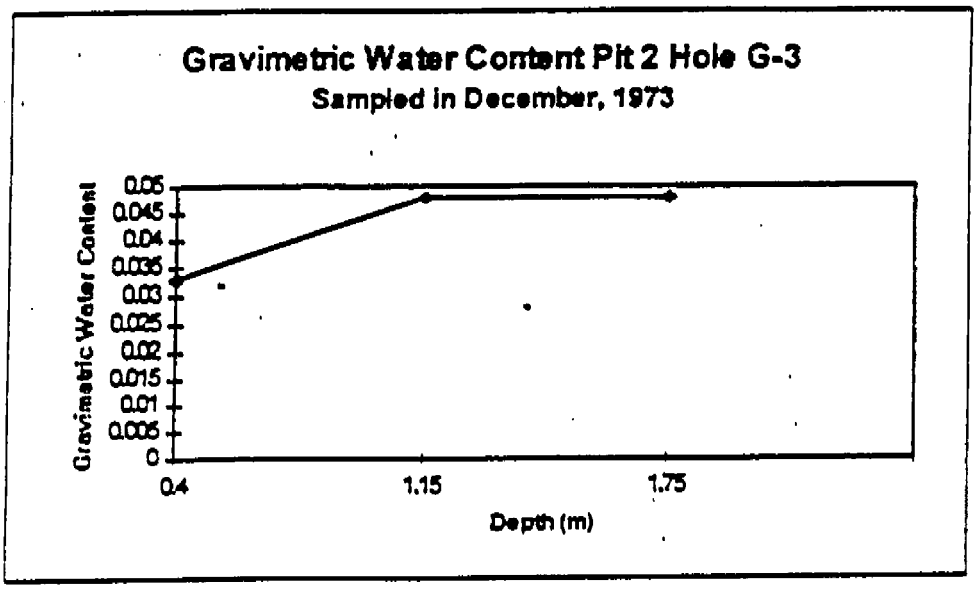

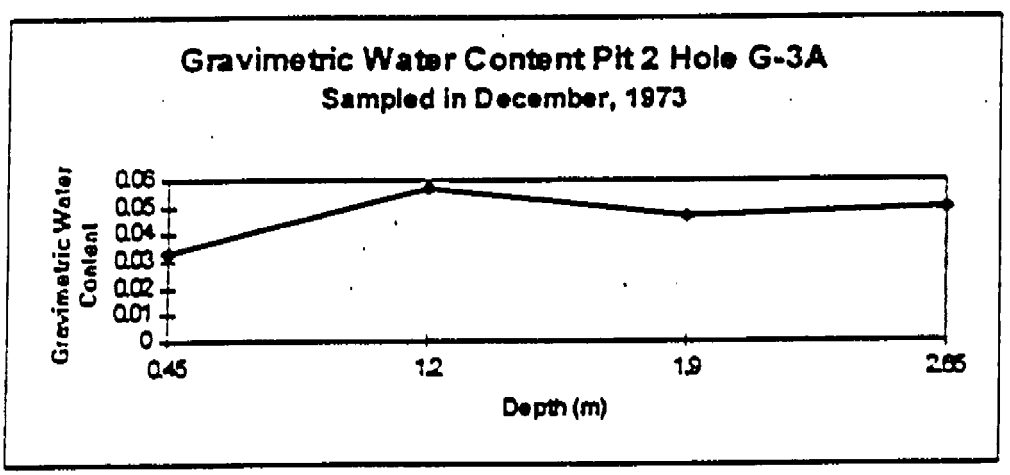

Figure 3. Gravimetric soil water content from two boreholes drilled in cover of MDA G Pit number 2.

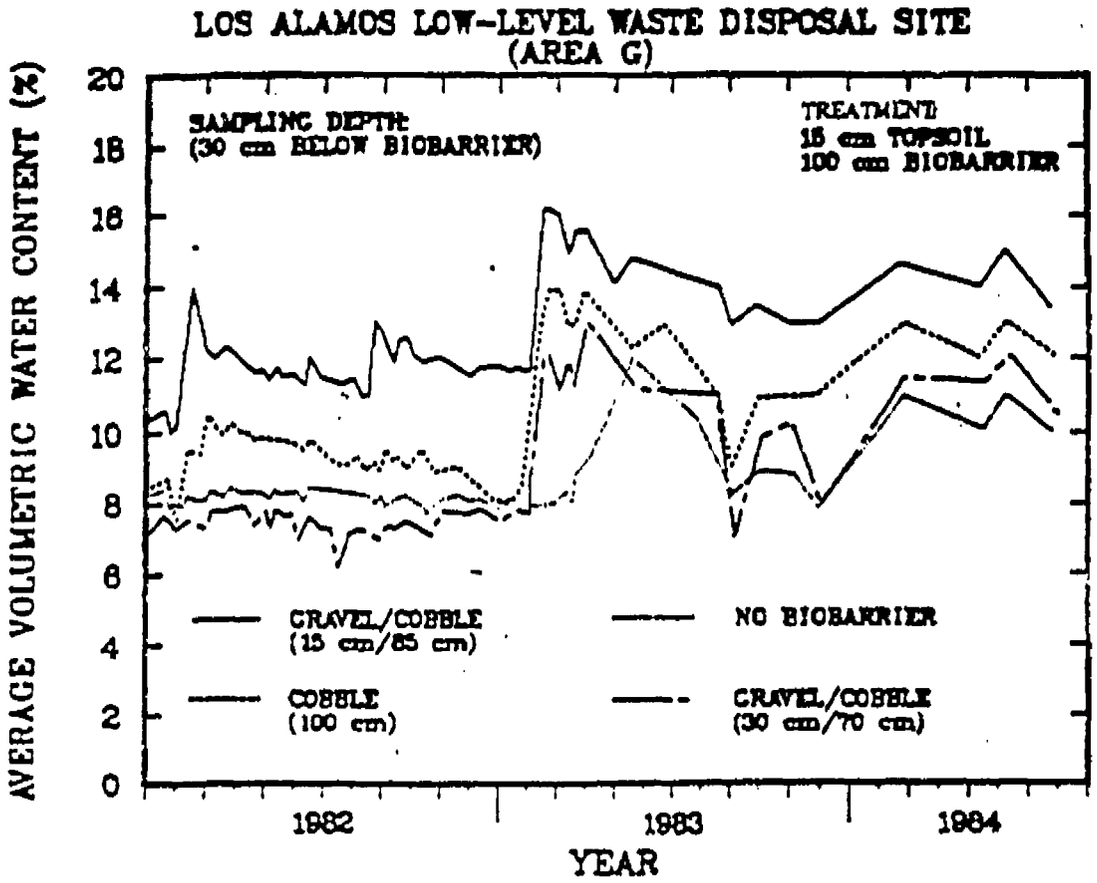

Figure 4. Volumetric water content in crushed tuff layer (137-cm sampling depth) beneath surface covers at MDA G (from Nyhan et al. 1986).

Table 1. Soil water balance components for cover experiment at TA-51 from Nyhan et al. (1990).

	Control Plots		Improved Plots	
	1	2	1	2
Precipitation (cm)	173.72	173.72	173.72	173.72
Soil water increase (cm)	12.09	9.09	4.15	4.43
Interflow (cm)	0	0	0	1.93
Percolation (cm)	10.62	10.63	0	2.64
Evapotranspiration	151.67	154.87	169.57	164.71

The available data suggest that water will penetrate a depth greater than 1 m at MDA G which is the cover thickness assummed in the performance assessment simulations. As vegetation is established, deeper rooted plants can remove moisture from deeper in the profile reducing the percolation. On the negative side, plant root uptake may become a pathway for radionuclides, and dead roots can provide channels for flow.

Soil Erosion

Soil erosion is defined for this problem as the removal of surface material by water. Wind is another agent that can remove surface material, but it is not included here. Soil erosion is included because the removal of surface soil will reduce cap thickness and may eventually expose wastes and because radionuclides adsorbed to soil particles can be transported.

Soil erosion studies on surface covers at Los Alamos were reported by Nyhan et al. (1984) and Nyhan and Lane (1986a). These studies used rainfall simulation technology with plots prepared for different surface cover schemes to determine parameters for the Universal Soil Loss Equation (USLE) (Wischmeier and Smith, 1978). As expected soil erosion was greatest on plots that were recently disturbed and had little or no cover. The soil loss measured by Nyhan et al. (1984) from the natural plots was 2% of that from cultivated plots. Nyhan and Lane (1986a) showed an order of magnitude reduction in the USLE cover management (C) factor when a 70% gravel mulch surface cover was applied compared to the bare soil surface cover. A further factor of two reduction in soil loss was suggested when a vegetation was used in conjunction with the gravel mulch but these results were highly variable. Data from these studies were used by Nyhan and Lane (1986b) to determine parameters for the USLE to apply to shallow land burial sites at Los Alamos.

Soil erosion is a function of soil properties, surface conditions, topography, climate, and land management. The Universal Soil Loss Equation (USLE) uses a multiplicative

expression to relate these factors (Wischmeier and Smith, 1978; Nyhan and Lane, 1986b). The USLE estimates long-term average annual soil loss for a site using a climate factor. For the Performance Assessment, the Modified Universal Soil Loss Equation (MUSLE) was used because daily hydrologic information was available (Williams, 1975).

Biological Intrusion

Intrusion into surface covers by animals and vegetation has important implications for surface runoff and erosion. Intrusion can have positive and negative effects on surface cover performance. Suter et al. (1993) reviewed the effects that vegetation and burrowing animals may have on surface covers. For vegetation, the most detrimental effects are penetrating hydrologic barriers thus reducing their effectiveness, and root uptake of waste material. Vegetation is needed to reduce potential percolation of water and minimize water and wind erosion. Burrowing animals can provide a more direct route for water to the waste, and if the animals penetrate the waste burrowing animals can move contaminated soil or waste to the surface where it can be eroded.

Studies from many different locations were reviewed by Suter et al. (1993). Link et al. (1995) summarized information on vegetation and animal effects for Hanford which is a semiarid site like Los Alamos. Their studies concluded that small mammal burrows have little or no effect on soil moisture content. They cautioned that this result was based on short-term studies.

Sejkora and Alldredge (1989) used rainfall simulation to study the influence of pocket gophers on runoff and erosion. Runoff and soil loss were measured on bare and vegetated plots with and without gophers. The results indicated that introducing gophers reduced runoff by an average of 21% and soil loss by 42% after four weeks of activity by the gophers in the plots. The authors concluded from this short-term study that cumulative impacts of the gophers will increase with time and that the presence of the gophers may affect other factors such as vegetation growth that can further change the relationships between runoff and erosion.

MATHEMATICAL MODEL

The Performance Assessment for surface runoff and soil erosion from MDA G require analyses over a duration of 10,000 years or more, but historical records are available for less than 100 years for the Los Alamos area. To provide the record necessary for this performance assessment, a stochastic climate generator is used to provide precipitation and weather values. A daily water balance model of the pit is employed to provide information on seasonal variations of the response of the disposal pit.

The mathematical models for generation of the weather and solution of the water balance were taken from the SPUR (Simulation of Production and Utilization of

Rangelands) Model (Wight and Skiles 1987). The water balance model for SPUR was based on the CREAMS (Chemical, Runoff, and Erosion from Agricultural Management Systems) model (Knisel 1980) with modifications for snow accumulation and melt. Vegetation dynamics were not included in this application of the model. Vegetation was represented by a leaf area index (LAI) curve that remained constant over each year.

The following mathematical descriptions are taken directly from the pertinent chapters in Wight and Skiles (1987).

Climate Generation

The climate generator is known as CLIMGN. The purpose of this component is to provide daily values of precipitation, maximum and minimum air temperatures, and solar radiation (Richardson et al., 1987). The GENPAR code was used to estimate parameters for CLIMGN with historical records from Los Alamos.

The CLIMGN program generates daily values of precipitation (P), maximum temperature (t_{max}), minimum temperature (t_{min}), and solar radiation (r) for an n-year period at a given location. The model is designed to preserve the dependence in time, the internal correlation, and the seasonal characteristics which exist in actual weather data for the location. Precipitation and wind run are generated independently of the other variables. Maximum temperature, minimum temperature, and solar radiation are generated depending on whether the day is wet or dry.

Precipitation

The precipitation-generation component of CLIMGN is a Markov chain-gamma model. A first-order Markov chain is used to generate the occurrence of wet or dry days. When a wet day is generated, the two-parameter gamma distribution is used to generate the precipitation amount.

With the first-order Markov chain model, the probability of rain on a given day is conditioned on the wet or dry status of the previous day. A wet day is defined as a day with 0.01 inch of precipitation or more. Let $P_i(W/W)$ be the probability of a wet day on day i given a wet day on day i-1, and let $P_i(W/D)$ be the probability of a wet day on day i given a dry day on day i-1. Then:

$$P_i(D/W) = 1 - P_i(W/W)$$
$$P_i(D/D) = 1 - P_i(W/D) \qquad (2)$$

where $P_i(D/W)$ and $P_i(D/D)$ are the probabilities of dry day given a wet day on day i-1 and the probability of a dry day given a dry day on day i-1, respectively. The transition probabilities are, therefore, fully defined given $P_i(W/W)$ and $P_i(W/D)$.

The density function of the two-parameter gamma distribution is given by:

$$f(x) = \frac{x^{\alpha-1} e^{-\frac{x}{\beta}}}{\beta^{\alpha}\Gamma(\alpha)}, \qquad p>0 \tag{3}$$

where α and β are distribution parameters and $\Gamma(\alpha)$ is the gamma function of α. The α and β are shape and scale parameters, respectively. For $0 < \alpha < 1$, the distribution has a reverse "J" shape. This shape is appropriate for precipitation amounts since small amounts occur more frequently than larger amounts. The gamma distribution was shown by Richardson (1982a) to better describe precipitation amounts than the simple exponential distribution.

The values of $P_i(W/W)$, $P_i(W/D)$, α, and β vary continuously during the year for most locations. In CLIMGN, each of the four precipitation parameters is held constant for a given month but vary from month to month. The parameters are used with a Markov chain-generation procedure and the gamma-generation procedure described by Haan (1977) to generate daily precipitation values.

Temperature and Solar Radiation

The procedure used in CLIMGN is based on the weakly stationary generating process given by Matalas (1967). The equation is:

$$x_i(j) = Ax_{i-1}(j) + Bc_i(j) \tag{4}$$

where $x_i(j)$ is a 3 X 1 matrix for day i whose elements are residuals of $t_{max}(j=1)$, t_{min} (j=2), and r(j=3); c_i is a 3 X 1 matrix of independent random components, and A and B are 3 X 3 matrices whose elements are defined such that the new sequences have the desired serial correlation and cross-correlation coefficients. The A and B matrices are given by:

$$A = M_1 M_0^{-1} \tag{5}$$

$$BB^T = M_0 - M_1 M_0^{-1} M_1^T \tag{6}$$

where the superscripts -1 and T denote the inverse and transpose of the matrix. M_0 and M_1 are defined as:

$$M_0 = \begin{bmatrix} 1.0 & p_0(1,2) & p_0(1,3) \\ p_0(1,2) & 1.0 & p_0(2,3) \\ p_0(1,3) & p_0(2,3) & 1.0 \end{bmatrix} \tag{7}$$

$$M_1 = \begin{bmatrix} p_1(1) & p_1(1,2) & p_1(1,3) \\ p_1(2,1) & p_1(2) & p_1(2,3) \\ p_1(3,1) & p_1(3,2) & p_1(3) \end{bmatrix} \tag{8}$$

where $p_0(j,k)$ is the correlation coefficient between variables j and k on the same day, $p_1(j,k)$ is the correlation coefficient between variables j and k with variable k lagged one day with respect to variable j, and $p_1(j)$ is the lag-one-serial-correlation coefficient for variable j.

The correlation coefficients in Equations 7 and 8 were determined by season from 20 years of temperature and solar radiation data for 31 locations in the United States. The seasonal and regional patterns of the correlation coefficients were described by Richardson (1982b). The seasonal and spatial variation in the correlation coefficients are relatively small. If the small variations are neglected and the average values of the correlation coefficients given by Richardson (1982b) are used, the M_0 and M_1 matrices become:

$$M_0 = \begin{bmatrix} 1 & 0.633 & 0.186 \\ 0.633 & 1 & -0.193 \\ 0.186 & -0.193 & 1 \end{bmatrix} \tag{9}$$

$$M_1 = \begin{bmatrix} 0.621 & 0.445 & 0.087 \\ 0.563 & 0.674 & -0.100 \\ 0.015 & -0.091 & 0.251 \end{bmatrix} \tag{10}$$

(The off-diagonal elements were calculated but not reported by Richardson (1982b).)

Using Equations 5 and 6, the A and B matrices become:

$$A = \begin{bmatrix} 0.567 & 0.086 & -0.002 \\ 0.253 & 0.504 & -0.050 \\ -0.006 & -0.039 & 0.244 \end{bmatrix} \tag{11}$$

$$B = \begin{bmatrix} 0.781 & 0 & 0 \\ 0.328 & 0.637 & 0 \\ 0.238 & -0.341 & 0.873 \end{bmatrix} \tag{12}$$

The A and B matrices given in Equations 11 and 12 are used with Equation 4 in CLIMGN to generate new sequences of the residuals of t_{max}, t_{min}, and r, which are

serially correlated and cross correlated with the correlations being constant at all locations.

The final daily generated values of t_{max}, t_{min}, and r are determined by multiplying the residual elements generated with Equation 4 by a seasonal standard deviation and adding a seasonal mean using the equation:

$$t_i(j) = x_i(j)s_i(j) + m_i(j) \tag{13}$$

where t(j) is the daily value of t_{max}(j=1), t_{min}(j=2), and r(j=3); $s_i(j)$ is the standard deviation; and $m_i(j)$ is the mean for day i. The values of $m_i(j)$ and $s_i(j)$ are conditioned on the wet or dry status as determined from the precipitation component of the model. By expressing Equation 13 in terms of the coefficient of variation (c=s/m) rather than the standard deviation, the equation becomes:

$$t_i(j) = m_i(j)[x_i(j)c_i(j) + 1] \tag{14}$$

The seasonal change in the means and coefficients of variation may be described by:

$$u_i = \bar{u} + C\cos\left(360\frac{i-T}{365}\right) \qquad i = 1, 2, \ldots, 365 \tag{15}$$

where u_i is the value of $m_i(j)$ or $c_i(j)$ on day i. $\bar{u}$ is the mean of u_i, C is the amplitude of the harmonic, and T is the position of the harmonic in days. Value of u, C, and T must be determined for the mean and coefficient of variation of each weather variable (t_{max}, t_{min}, r) and for the wet or dry condition. There were no detectable differences in the means and coefficients of variation for t_{min} on wet or dry days.

Some of the parameters in Equation 15 demonstrate location dependence, and other parameters do not change significantly with location. The values of T for all the descriptors of temperature (means and coefficients of variation of t_{max} and t_{min}) are near 200 days for all locations. Similarly, the T values for r are about 172 days (summer solstice) for all locations. Therefore, in CLIMGN, all the T values for temperature are assumed to be 200 days and all the T values for solar radiation are assumed to be 172 days.

The $\bar{u}$ and C values for t_{max} vary with location. The amplitude (C) of the mean of t_{max} for a given location was not significantly different on wet or dry days. The C's for the coefficient of variation of t_{max} are negative because t_{max} is less variable during the summer when the mean t_{max} is greatest. The values of $\bar{u}$ and C for the coefficient of variation of t_{max} are the same for either wet or dry days. The $\bar{u}$ values for the mean of t_{max} on wet days were significantly less than for dry days. The other parameters for t_{max} on wet days were not required since they were not significantly different from the

parameters of t_{max} on dry days. The values of $\bar{u}$ and C for the means and coefficients of variation of t_{min} all have a strong regional pattern.

Similar to t_{max}, C for the mean of r was not significantly different on wet and dry days. The values of u and C for the coefficient of variation of r showed no relationship to station location (Richardson et al. 1987). In CLIMGN, the parameter values are assumed to be constant at the average values.

The following notations will be used for the means ($\bar{u}$) and amplitudes (C) of Equation 15 for t_{max}, t_{min}, and r:

TXMD - mean of tmax (dry), °F,
ATX - amplitude of tmax (wet or dry), °F,
CVTX - mean coefficient of variation of tmax (wet or dry),
ACVTX - amplitude of coefficient of variation of tmax (wet or dry),
TXMW - mean of tmax (wet), °F,
TN - mean of tmin (wet or dry), °F,
ATN - amplitude of tmin (wet or dry), °F,
CVTN - mean of coefficient of variation of tmin (wet or dry),
ACVTN - amplitude of coefficient of variation of tmin (wet or dry),
RMD - mean of r (dry), langley(ly),
AR - amplitude of r (wet or dry), ly,
CVRD - mean of coefficient of variation of r (dry), (assumed to be 0.24 for all locations),
ACVRD - amplitude of coefficient of variation of r (dry), (assumed to be -0.08 for all locations),
RMW - mean of r (wet), ly,
CVRW - mean of coefficient of variation of r (wet), (assumed to be 0.48 for all locations),
ACVRW - amplitude of coefficient of variation of r (wet), (assumed to be -0.13 for all locations).

The GENPAR Program

If users need to generate weather data for a location outside the 48 United States or if they need to develop generation parameters from actual data from a specific location, the GENPAR program may be used. The GENPAR program reads daily values of P, t_{max}, t_{min}, and r and writes the generation parameters which are required by CLIMGN. The number of years of weather data required to develop parameters which are representative of a particular location varies with the climate. In general, at least 20 years of precipitation data and 10 years of temperature and radiation data are required. Longer records of precipitation may be required for arid locations. GENPAR was used with Los Alamos and MDA G weather data to estimate the parameters for CLIMGN.

Solar Radiation Correction for Sloping Terrain

A correction factor for adjusting the radiation values generated by the climate model for a horizontal surface to the actual slope and aspect conditions at the site being simulated is included. The procedure uses the method outlined by Lee (1963) to calculate the potential insolation on both a horizontal and an inclined surface.

Water Balance Model

The water balance component is described by Renard et al. (1987). A snow accumulation and melt component also described here can be found in Cooley et al. (1987).

Soil-Layer Water Storage

The soil profile is divided into layers (user-specified number of layers (up to eight) and layer thickness). Water balance calculations are done on a daily basis using runoff, evapotranspiration, and percolation, as described in Equation 1. Total storage, field capacity, and initial water storage in the various layers are expressed in terms of plant available water and are computed from input parameters as follows:

$$UL_i = (SMO_i - SM15_i)THK_i \tag{16}$$

$$FC_i = (SM3_i - SM15_i)THK_i \tag{17}$$

$$SWO_i = FC_i \bullet STF \tag{18}$$

where:

UL_i = upper limit of water storage in layer i (in),
FC_i = field capacity in layer i (in),
SWO_i = initial soil water in layer i (in),
SMOi = soil porosity for layer i (in/in),
$SM3_i$ = 1/3-bar water content for layer i (in/in),
$SM15_i$ = 15-bar water content for layer i (in/in),
THK_i = soil layer thickness for layer i (in), and
STF = initial soil water content as a fraction of field capacity for the entire soil profile.

Runoff

The traditional three antecedent moisture levels (1 - dry, 2 - normal, 3 - wet), as used by the Soil Conservation Service (SCS), have been modified in the model by allowing soil moisture to be updated daily and by computing daily curve numbers based on soil-water storage, rather than using the three curve numbers associated with their moisture classes. Thus, each day has a curve number (Williams and LaSeur 1976), and the soil moisture changes between runoff events with estimates of evapotranspiration and percolation using routines very similar to those used in CREAMS (Knisel 1980). Using the curve number method, surface runoff or Q in Equation 1 is estimated on a daily basis from:

$$Q = \frac{(P - I_a)^2}{P + s - I_a} = \frac{(P - 0.2s)^2}{P - 0.8s} \tag{19}$$

where:

Q	=	daily runoff (in),
P	=	daily rainfall (in),
s	=	a retention parameter (in), and
I_a	=	0.2s = initial abstraction.

The maximum value, s_{max}, for the retention parameter, s, is computed with the following SCS curve number relationship (USDA 1972):

$$s_{max} = \frac{1000}{CN1} - 10 \tag{20}$$

where CN1 is the dry-antecedent-moisture-condition curve number. If handbook curve numbers are available for the normal moisture condition, CN2, the following polynomial may be used to estimate CN1:

$$CN1 = -16.91 + 1.348CN2 - 0.01379CN2^2 + 0.0001177CN2^3 \tag{21}$$

The soil retention parameter scales from zero to s_{max} and is computed daily as a weighted average of the unused storage in the various soil layers. The retention parameter is:

$$s = s_{max} \sum_{i=1}^{n} \left(W_i \frac{UL_i - SW_i}{UL_i} \right) \tag{22}$$

where:

n	=	number of soil layers,

SW_i = current water storage in layer i (updated daily) (in), and
W_i = weighting factor.

The weighting factors decrease exponentially to give greater dependence of s on the upper soil layers, so:

$$W_i = a e^{-4.606 d_i} \tag{23}$$

where:
d_i = (depth to bottom of layer i)/(depth to bottom of last layer), and

a = constant adjusted so that $\sum_{i=1}^{n} W_i = 1$.

Percolation

The percolation component of SPUR uses a storage routing model combined with a crack-flow model to predict flow through the soil profile. Crack-flow was not implemented for these simulations.

In the following, PL_i is percolation flow out of the bottom layer i from the storage routing model. The variable PL_0 is equal to precipitation minus runoff, and it is the amount of water that enters the first soil layer.

Flow through a soil layer may be restricted by a lower layer which is saturated or nearly saturated. The variable PL_i may exceed the projected available storage in the next layer ($UL_{i+1} - SW_{i+1} + UW_{i+1}$), in which case, PL_i is set to this projected value (see Equation 39 for definition of UW_{i+1}). There is no "succeeding" layer to the bottom layer, and the value for R in Equation 1 is PL_i for the bottom layer.

Storage Routing

The storage routing model uses an exponential function with the percolation computed by subtracting the soil water in excess of field capacity at the end of the day from that at the beginning of the day, or:

$$PL_i = \begin{cases} (SW_i - FC_i)\left(1 - e^{-\frac{\Delta t}{T_i}}\right) & SW_i > FC_i \\ 0 & SW_i \le FC_i \end{cases} \tag{24}$$

where:

PL_i = amount of percolate (in),
SW_i = the soil water content at the beginning of the day for layer i (in)
Δt = time interval (24 h),
T_i = travel time through a particular layer (h),
FC_i = the field capacity water content for layer i, (in), and
i = soil layer number increasing with depth.

The travel time through each soil layer is computed with the linear storage equation:

$$T_i = \frac{SW_i - FC_i}{H_i} \tag{25}$$

where: H_i = the hydraulic conductivity of layer i (in/h).

Hydraulic conductivity is varied from the specified saturated conductivity value by:

$$H_i = SC_i \left(\frac{SW_i}{UL_i}\right)^{\beta_i} \tag{26}$$

where:

SC_i = saturated conductivity for layer i (in/hr), and
β_i = parameter that causes $H_i = 0.0022\ SC_i$ when $SW_i = FC_i$.

The equation for estimating β_i is:

$$\beta_i = \frac{-2.655}{\log\left(\frac{FC_i}{UL_i}\right)} \tag{27}$$

where the constant (-2.655) assures that $H_i = 0.0022\ SC_i$ at field capacity.

Evapotranspiration

The evapotranspiration (ET) component in SPUR is the same as that used in CREAMS and is based on work by Ritchie (1972). Potential evaporation is computed with the equation:

$$E_o = \frac{0.0504\, H_o \Delta}{\gamma + \Delta} \tag{28}$$

where:

E_o = potential evaporation (in),

Δ = slope of the saturation-vapor-pressure curve at the mean air temperature,

H_o = net solar radiation (ly), and

γ = a psychrometric constant.

Δ is computed with the equation:

$$\Delta = \frac{5304}{T_k^2} e^{\left(21.255 - \frac{5304}{T_k}\right)} \tag{29}$$

where: T_k = daily temperature (degrees Kelvin).

The variable H_o is calculated with the equation:

$$H_o = \frac{(1-\lambda)r}{58.3} \tag{30}$$

where:

r = daily solar radiation (ly) and

λ = albedo.

Soil evaporation

The model computes soil evaporation and plant transpiration separately. Potential soil evaporation is computed with the equation:

$$E_{so} = \min\begin{cases} E_o e^{-0.4\,LAI} \\ E_o GR \end{cases} \tag{31}$$

where:

E_{so} = potential evaporation at the soil surface (in),

LAI = Leaf area index defined as the area of plant leaves relative to the soil surface (in^2/in^2), and

GR = mulch (residue) cover factor. (A value of 0.5 is suggested for most range plant communities, and 1.0 for bare soil.)

Actual soil evaporation (E_s) is computed in two stages based on the soil moisture status in the upper soil profile. In stage 1, soil evaporation is limited only by the energy available at the surface, and thus, is equal to the potential (Eq. 31). When the accumulated soil evaporation exceeds the first-stage upper limit, the stage-2

evaporation begins (the reader is referred to Ritchie (1972) for additional explanation of the procedure). The first-stage upper limit is estimated from:

$$U = 1.38(\alpha - 0.118)^{0.42} \tag{32}$$

where:

U = stage-1 upper limit (in) and

α = soil evaporation parameter (CONA) dependent on soil-water transmission characteristics (ranges from 0.13 to 0.22 in/day$^{1/2}$).

Ritchie (1972) suggests using α=0.14 for clay soils, 0.18 for loamy soils, and 0.13 for sandy soils. Similar values were obtained for data from Jackson et al. (1976). A wider distribution of values for most soil textural classes is given by Lane and Stone (1983).

Stage-2 soil evaporation is predicted by:

$$E_s = \alpha\left[t^{\frac{1}{2}} - (t-1)^{\frac{1}{2}}\right] \tag{33}$$

where:

E_s = soil evaporation for day t (in) and

t = days since stage-2 evaporation began.

Plant transpiration

Potential transpiration (E_{po}) from plants is computed with the equations:

$$E_{po} = \frac{E_o LAI}{3} \qquad 0 \le LAI \le 3 \tag{34}$$

$$E_{po} = E_o - E_s \qquad LAI > 3 \tag{35}$$

(If $E_{po} + E_s > E_o$, E_s is reduced so $E_{po} + E_s = E_o$.) Because the LAI is generally less than three in rangeland plant communities that SPUR is intended to consider, Equation 34 will be used most of the time. If soil water is limited, plant transpiration is reduced with the equation:

$$E_p = \frac{E_{po} SW}{0.25FC} \qquad SW \le 0.25FC \tag{36}$$

where:

E_p = plant transpiration reduced by limited soil moisture (in) and

SW = current soil water in the root zone (in).

(If SW > 0.25 (FC), E_p - E_{po}, and if E_p + E_s exceeds available water, E_s is reduced so E_p + E_s = available water.)

Evapotranspiration (ET), then, is the sum of plant transpiration (Eq. 34, 35 or 36) plus soil evaporation (Eq. 32 or 33), and cannot exceed available soil water.

Distribution of ET in the soil profile

Soil-water evaporation is removed uniformly from the soil profile down to a maximum depth (ESD). The variable ESD is set in the SPUR code. If the soil profile does not contain sufficient water to meet soil-water evaporation demand, the actual amount of evaporation is reduced accordingly.

Transpiration is initially distributed through the soil layers by the following equation:

$$v = v_o e^{-v_1 D} \quad (37)$$

where:

v = water-use rate by crop at depth D (in/day),
v_o = water-use rate at the surface (in/day),
V_1 = 3.065, and
D = soil depth/depth to bottom of deepest soil layer with roots.

The total water use within any depth can be computed by integrating Equation 37. The value of v_o is determined for the root depth each day, and the water use in each soil layer is computed with the equations:

$$v_o = \frac{v_1 ET}{1 - e^{-v_1}} \quad (38)$$

$$UW_i = \frac{v_o}{v_1}\left(e^{-v_1 D_{i+1}} - e^{-v_1 D_i}\right) \quad (39)$$

where:

UW_i = water use in layer i (n), and
D_{i+1} and D_i = the fractional depths at the top and bottom layer i.

When calculating actual uptake, transpiration demand for a layer that cannot be satisfied by the available water in that layer is added to the demand of the next layer. This process is continued until the transpiration demand is satisfied or the bottom of the root zone is reached.

The UW_i vector contains the initial estimates of ET which are to be subtracted from the various soil layers. If a layer has insufficient water, the excess ET is taken out of the first layer containing available water and having roots present.)

Soil Erosion

Soil erosion is calculated using the modified Universal Soil Loss Equation (Williams 1975). The equation is

$$Y = \eta\left(Q * Q_p\right)^{0.56} KCPLS \tag{40}$$

where:

Y	=	sediment yield (tons/acre),
η	=	coefficient = 95,
Q	=	runoff volume (in),
Q_p	=	peak flow rate (ft^3/s),
K	=	Universal Soil Loss Equation (USLE) soil erodibility factor,
C	=	USLE cover management factor,
P	=	USLE erosion control practice factor, and
LS	=	USLE slope length and steepness factor.

Snow Accumulation and Melt

The model used for snow accumulation and melt processes is HYDRO-17, developed by Anderson (1973) of the National Weather Service (NWS).

HYDRO-17 incorporates physical processes affecting snow accumulation and melt. Air temperature is used to index energy exchange across the snow-air interface. This is not the same as the degree-day method, which uses air temperature as an index to snowpack outflow. The degree-day method does not explicitly account for freezing of the melt water due to a heat deficit and the retention and transmission of liquid water, both of which cause snowpack outflow to differ from snowmelt.

Accumulation process

The accumulation of snow in the model is simply based on the air temperature and the temperature selected to differentiate rain from snow (PXTEMP). Precipitation is considered to be snow if the air temperature is less than or equal to PXTEMP, and rain if the air temperature is greater than PXTEMP. The amount of new snow is added to the existing snowpack to establish a new total snowpack.

Melt processes

The snowmelt processes are divided into two categories: snowmelt during rain-on-snow and snowmelt during nonrain periods. Snowmelt during rain-on-snow periods is separated from melt during nonrain periods because (1) of the difference in magnitude of the various energy transfer processes during rain-on-snow periods, and (2) the seasonal variation in melt rates is generally different for the two processes.

Rain-on-snow

During rain-on-snow, melt is assumed to occur at the snow surface. Following the development of the model relationships presented by Anderson (1973), the energy balance of a snow cover can be expressed as:

$$\Delta Q = Q_n + Q_m + Q_e + Q_h + Q_g \tag{41}$$

where:

ΔQ = change in the heat storage of the snow cover,
Q_n = net radiation transfer,
Q_m = heat transfer by mass changes (advected heat),
Q_e = latent heat transfer,
Q_h = sensible heat transfer, and
Q_g = heat transfer across the snow-soil interface.

The units of each term in Equation 41 are energy per unit area.

Upon expansion of each term in Equation 41, and elimination of variables made possible by the assumptions listed below, the amount of snowmelt M (mm) during a time period Δt (h) can be determined as follows:

$$M = \Delta t\left[0.612\times10^{-9}(T_a+273)^4 - 3.39\right] + 0.0125\,P_x T_a + 8.5\,UADJ\left[(0.9\,e_{sat} - 6.11) + 0.00057\,P_a T_a\right] \tag{42}$$

where:

T_a = temperature of the air (°C),
P_x = water equivalent of precipitation (mm),
P_a = atmospheric pressure (mb),
e_{sat} = saturation vapor pressure at the air temperature (mb), and
UADJ = average wind function during rain-on-snow periods (mm • mb^{-1} Δt h^{-1}).

The assumptions pertaining to conditions during rain-on-snow events are as follows:

1. The turbulent transfer coefficients for heat and water vapor are equal.

2. The temperature of the snow cover outflow is 0 °C.
3. The heat content of the transferred vapor is negligible; only heat transferred by precipitation is considered.
4. The isothermal snow cover is melting and the snow surface temperature is 0 °C.
5. Heat transfer across the snow-soil interface is negligible compared with energy exchange at the snow surface.
6. The change in heat storage of the snow surface becomes equal to the amount of melt.
7. Incoming longwave radiation is negligible because overcast conditions prevail.
8. Incoming longwave radiation is equal to blackbody radiation at the temperature of the bottom of the cloud cover, which should be close to the air temperature.
9. The relative humidity is quite high (90 percent is used).

Under the conditions described by these assumptions, the wet-bulb temperature is essentially the same as the air temperature. The saturation vapor pressure can be computed as a function of air temperature by the relationship:

$$e_{sat} = 2.749 \times 10^{8} e^{\left[\frac{-4278.6}{T_a + 242.8}\right]} \tag{43}$$

The atmospheric pressure, P_a, is computed for the elevation of the site or area using a "standard atmosphere" altitude-pressure relationship which can be approximated by the expression:

$$P_a = 1012.4 - 11.34\,E_1 + 0.00745\,E_1^{2.4} \tag{44}$$

where E_1 = elevation (hundreds of meters).

The wind-function parameter, UADJ, is determined during the calibration process. In the model, the amount of rain must exceed 6 mm during a 24-hour period before Equation 42 is used; therefore, humid overcast conditions are more likely to have occurred.

Ablation (Nonrain Periods)

Because such a wide variety of meteorological conditions can occur during nonrain periods, the energy balance equations are not used as a basis for estimating snowmelt from air temperature. Rather, an empirical air-temperature-based relationship is used in which snowmelt is determined by:

$$M = M_f(T_a - MBASE) \tag{45}$$

where:

M_f	=	melt factor,
MBASE	=	base temperature (°C) below which no melt is produced, and
T_a	=	air temperature (°C).

The melt factor exhibits a seasonal variation due partly to the variation in incoming solar radiation, and partly to a decrease in the albedo of the snow cover with time since the last snowstorm. Seasonal variations in other meteorological factors like vapor pressure, wind, and cloud cover, also influence the melt factor. A sinusoidal relationship between melt factor and season was developed within the model to account for this variation. This relationship is adequate for use throughout the 48 contiguous United States.

Groundmelt

In some watersheds, a small amount of melt takes place continuously at the bottom of the snowpack. The melt is small on a daily basis, but it can amount to a significant quantity of water when accumulated over an entire snow season. Groundmelt adds to soil moisture storage and helps sustain baseflow throughout the winter. It is added to the snow cover outflow and to rain which falls on bare ground to obtain total rain plus melt.

Model Parameters for Snow Accumulation and Melt

In addition to the data requirements of temperature, and site elevation, values must be set for six major and six minor parameters to use the model. The six major parameters are those which generally have the greatest effect on the simulation results and, therefore, require the most care in determining the proper value. These parameters with their expected range in parentheses are:

1. SCF – (0.8 - 1.4). A snow correction factor which adjusts precipitation for gage-catch errors during periods of snowfall and implicitly accounts for net vapor transfer and interception losses. This parameter depends mainly on the wind speed at the gage site and whether the gage is shielded.
2. MFMAX – (2.0 - 8.0) (mm/°C - 24 h). Maximum-melt factor during nonrain periods. This factor is affected by many climatic and physiographic variables such as radiation intensity, wind, forest cover, and aspect.
3. MFMIN – (0.4 - 3.6) (mm/°C - 24 h). Minimum-melt factor during nonrain periods. The same climatic and physiographic variables that affect MFMAX also effect MFMIN in essentially the same way.
4. UADJ – (0.0 - 0.6) (mm/mb). The average wind function during rain-on-snow periods, which is affected most by density and height of vegetation, and terrain.

5. SI – (200 - 600) (mm). The mean, areal water equivalent above which there is always 100 percent areal snow cover. This value is affected by the snowfall characteristics of the area. If the snow cover is uniform and melts at a uniform rate, the area will remain at 100 percent cover until just before the snow disappears. In contrast, especially where drifting occurs, the snow cover in some areas is so variable that bare ground appears as soon as melt begins.

6. ADPT – Areal Depletion Curve (described more fully later). A curve which defines the areal extent of the snow cover as a function of how much of the original snow cover remains. It also implicitly accounts for the reduction in the melt rate that occurs with a decrease in the areal extent of the snow cover and is closely related to the SI parameter.

The six minor parameters can normally be determined in advance, based on a knowledge of the typical climatic and snow cover conditions for the area. These parameters and their normal range of values in parentheses are:

1. TIPM – (0.1 - 0.5). A factor that determines how much weight is placed on the air temperature for each prior period. A small value corresponds to deep snowpacks and longer periods, while a larger value corresponds to shallow snowpacks and short periods of only a few days.

2. NMF – (0.0 - 2.0)(mm/°C/24 h). The maximum negative melt factor. This factor is assumed to have the same seasonal variability as the surface melt factor. It is affected mostly by snow density, though climate and physiographic variables also affect heat exchange during nonmelt periods.

3. MBASE – (0.0 - 2.0)(°C). Base temperature (normally 0 °C) for snowmelt computations during nonrain periods.

4. PXTEMP – (0.0 - 5.0) (°C). The temperature which differentiates rain from snow (normally 1 to 2 °C).

5. PMWHC – (0.01 - 0.05). Percent liquid-water holding capacity expressed as a decimal. Represents the maximum amount of liquid water in the snowpack which can be held against gravity drainage.

6. DAYGM – (0.0 - 0.5)(mm). Constant rate of melt which occurs at the snow-soil interface whenever the soil is not frozen and snow is present.

The range of values presented are based on information reported by Anderson (1973) and experience in calibrating the model at several sites and climatic regimes. Although upper and lower values are presented, values outside this range can occur. Since the model has been tested over such a wide range of conditions, most of the values should be within the range presented.

PARAMETER ESTIMATION

Springer (1995) performed an initial simulation of MDA G using the same mathematical model. Since that simulation, additional information and data are available to change the estimates of many of the parameters. The following sections provide the estimates for the parameters required by the surface runoff and erosion model that has been presented in the previous section.

Weather Realizations

Daily observations of precipitation at Los Alamos extend back to 1920 with a one-year break during 1944. The Los Alamos precipitation gauge has been moved several times, but Nyhan et al. (1989) found that the location changes have had no effect on annual precipitation. As the Laboratory developed, additional precipitation gauges have been installed at different sites including MDA G and White Rock. The main Los Alamos precipitation gauge was located at TA-59 which is west of MDA G and at a higher elevation, and since 1990 the main Los Alamos gauge has been located at TA-6 which is south of TA-59 In this report, TA-59 will designate the main Los Alamos gauge even though data from TA-6 is included in the analysis.

The longest available record of weather data is from TA-59 or the Los Alamos gauge. The average annual precipitation at TA-59 is 45.7 cm compared to 35.6 cm from MDA G (Bowen 1990). The length of record is relatively short compared to the simulation times involved, but still the TA-59 location was used to estimate the needed parameters for the precipitation realizations. The GENPAR program was used with data from 1951 to 1994 to make the parameter estimates for CLIMGN. For days with missing precipitation, a value of 0.0 was entered. Parameter estimates for TA-59 are given in Table 2. The average annual precipitation using these parameters for a 10000-year simulation was 47.8 cm.

Table 2. Parameters for CLIMGN used to generate precipitation realizations for MDA G simulations.

Month	P(W/W)	P(W/D)	Alpha	Beta
Jan	0.426	0.121	0.759	0.215
Feb	0.389	0.168	0.846	0.146
Mar	0.469	0.166	0.824	0.191
Apr	0.447	0.127	0.732	0.223
May	0.534	0.156	0.797	0.217
Jun	0.477	0.151	0.752	0.254
Jul	0.598	0.347	0.744	0.299
Aug	0.613	0.369	0.788	0.327
Sep	0.518	0.191	0.717	0.294
Oct	0.494	0.120	0.734	0.344
Nov	0.455	0.115	0.796	0.253
Dec	0.420	0.130	0.765	0.236

The Los Alamos precipitation data is adding an additional 10 cm of precipitation on average over that received at MDA G. The advantage of the Los Alamos data is a longer record with better parameter estimates. One approach is to reduce the Los Alamos data by a linear factor so that the average annual precipitation is equal to 35.6 cm. The problem with this approach is the seasonal or monthly dynamics between the sites may be different. Using the White Rock / MDA G precipitation record from 1965 to 1994, a GENPAR estimate of the parameters required for CLIMGN was made. Comparisons between the CLIMGN precipitation parameters from both TA-59 and MDA G for the period of record in which there are values are given in Figures 5-8. The differences between sites appear to be consistent and no crossing in the monthly behavior is obvious between sites. Generally all parameter values for Los Alamos are greater than those from White Rock except the alpha parameter which is consistently larger for White Rock. Richardson et al. (1987) defined the alpha as the shape parameter for the gamma distribution therefore the higher alpha values for White Rock indicate a larger variance or more spread in these data. It was assumed that the consistent differences observed between the parameters in Figures 5-8 permitted the Los Alamos data to be reduced by a constant factor so that average annual precipitation for the 10000-year simulation was 35.6 cm.

Temperature and solar radiation data from TA-54 were used for parameter estimates for the variables in CLIMGN because the nearest weather station is Albuquerque and parameters from Hanson and Richardson (1987) for Albuquerque were not considered adequate. The parameter values used in the simulations are given in Table 3.

Table 3. Temperature and solar radiation parameters for CLIMGN for base case simulation.[1]

Parameter Name	Value
TXMD	62.3
ATX	21.4
CVTX	0.127
ACOTX	-0.074
TXMW	55.51
TN	37.1
ATN	18.6
CVTN	0.203
ACUTN	-0.164
RMD	487.0
AR	196.2
RMW	365.6

[1]Wind run was not used as part of this simulation.

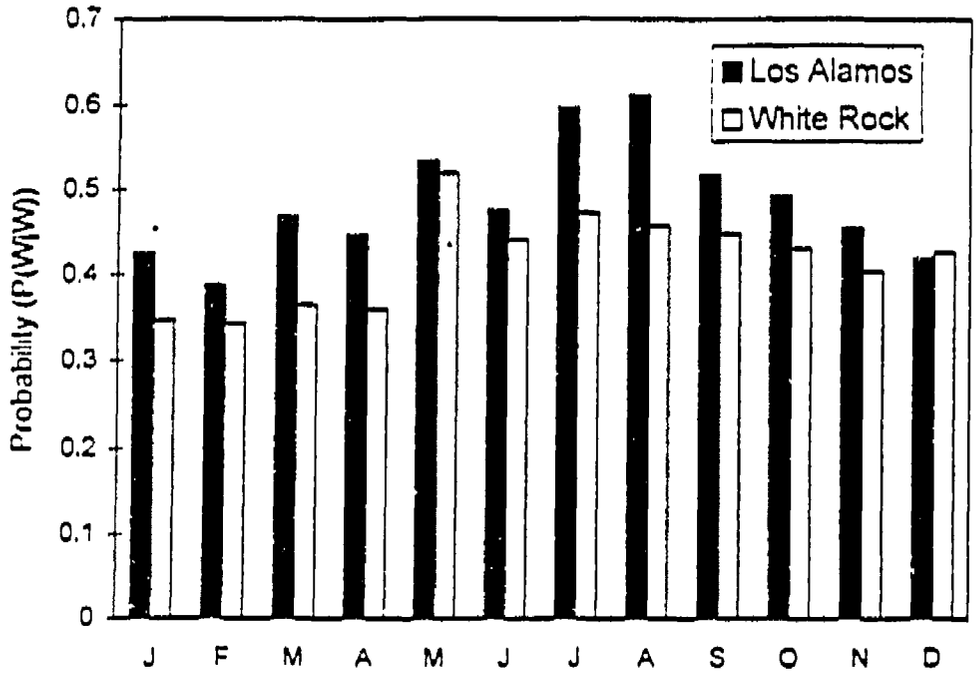

Figure 5. Comparison between Los Alamos and White Rock (MDA G) of probability of a wet day given a wet day.

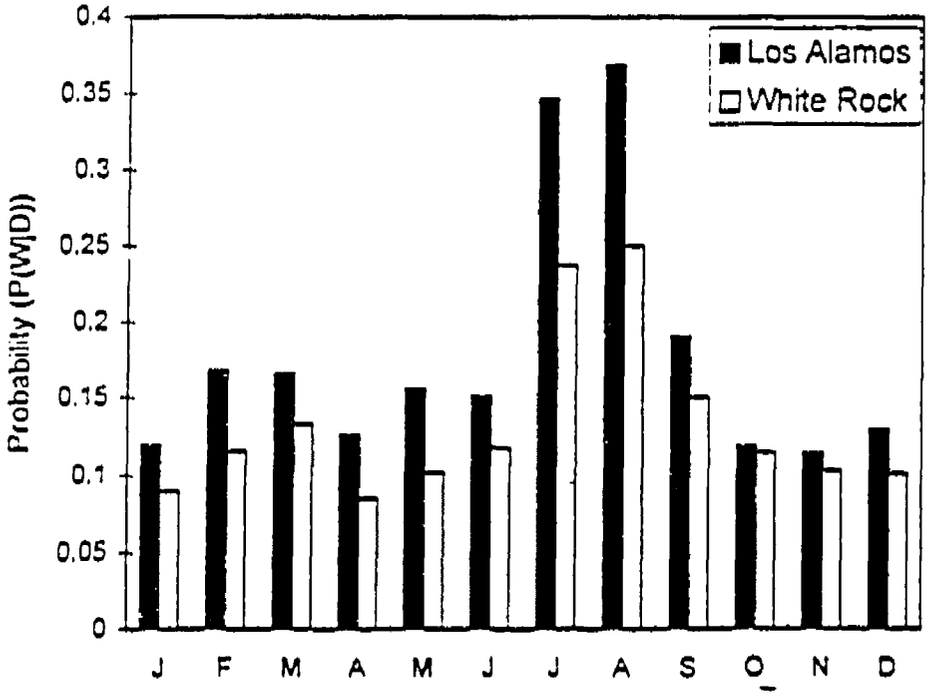

Figure 6. Comparison between Los Alamos and White Rock (MDA G) of the probability of a wet day given a dry day.

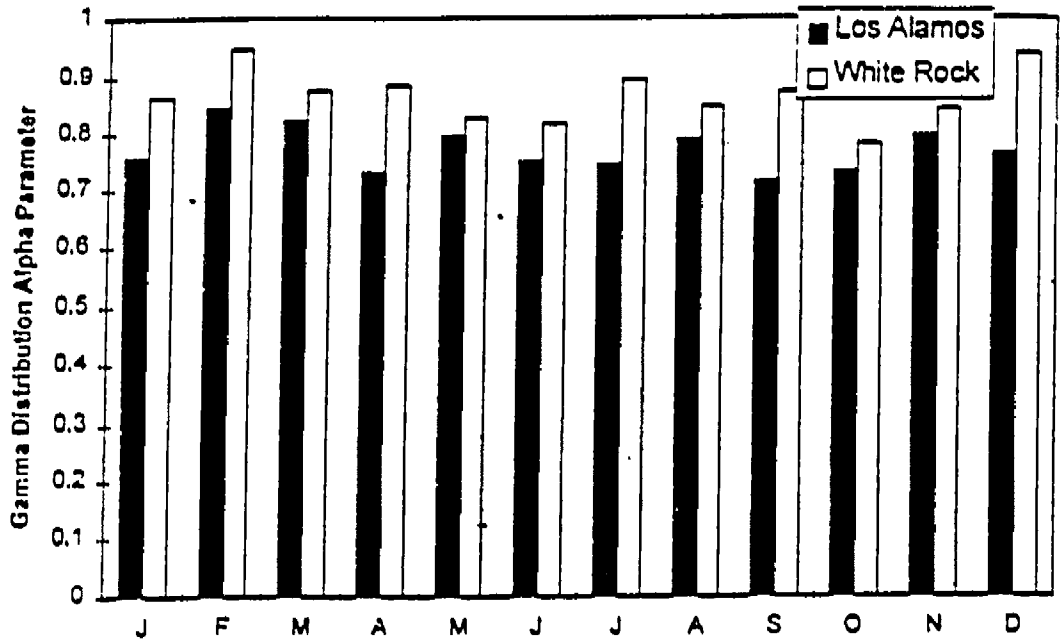

Figure 7. Comparison between TA-59 and TA-54 (MDA G) of the gamma distribution alpha parameter for daily precipitation amount.

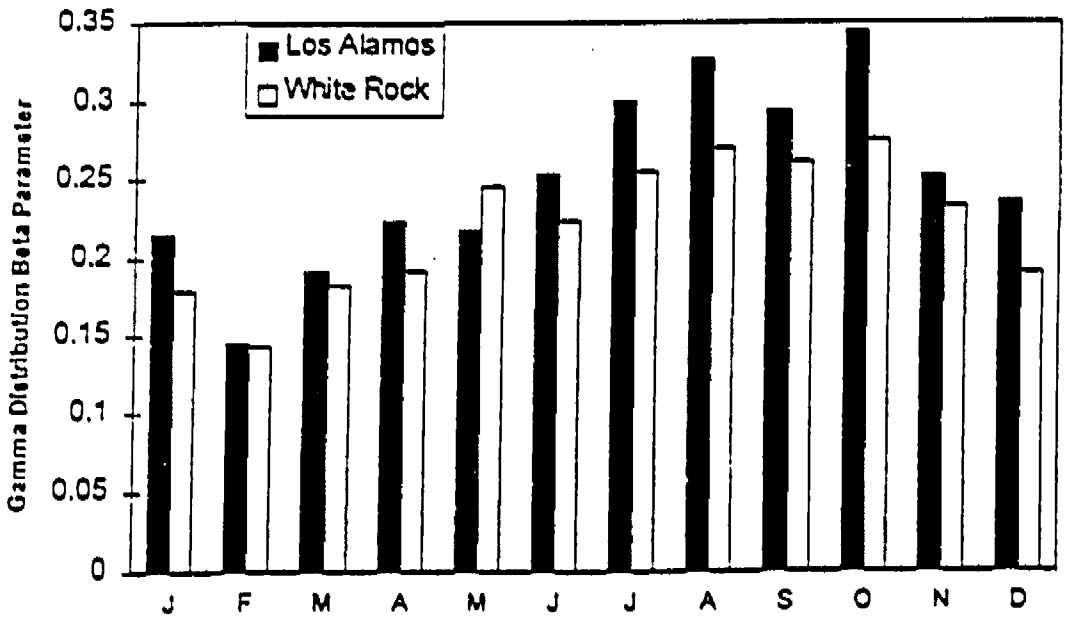

Figure 8. Comparison between TA-59 and TA-54 (MDA G) of the gamma distribution beta parameter for daily precipitation amount.

Soil Properties

The pit for this simulation was given a surface area of 0.41 ha (1 ac) with a length to width ratio of 2:1. The pit was assumed to be sloped along the width dimension for runoff and erosion calculations. The surface slope was 3 percent. The pit with cover was assumed to be 16.25 m (53.3 ft.) deep, but the water balance for the upper 1 m (3 ft.) was simulated for this effort to supply water input for source-term calculations.

A clay loam surface soil was used as most representative of the Hackroy soil series found in this part of Los Alamos (Nyhan et al. 1978). The depth of the topsoil layer was 10 cm (4 in.). The hydrologic properties for the clay loam soil were obtained from Nyhan (1996, pers. comm.) for soil from plots located at TA-51. These data are a better representation than the average values for a clay loam texture class from Springer and Lane (1987) used by Springer (1995). The data from Nyhan (1996, pers. comm.) was in the form of a moisture characteristic and the RETC code from van Genuchten et al. (1991) was used to fit the van Genuchten (1980) function to the data to estimate the 340 cm and 15300 cm volumetric water contents. The parameter estimates from RETC are: saturated water content = 0.493; residual water content = 0.0673; alpha (cm^{-1}) = 0.0115; and N = 1.5031. The values used in the water balance simulations are given in Table 4.

The remaining depth (90 cm) of the pit was filled with crushed Bandelier Tuff which is the common backfill at MDA G. Springer (1995) used the results from van Genuchten et al. (1987) who fit a soil water retention function to data from an instantaneous profile experiment that used crushed Bandelier Tuff in an intermediate-scale facility. The tuff for that intermediate-scale experiment was obtained from the quarry at Los Alamos, and it was most likely from unit 3 of the Bandelier Tuff rather than unit 2 in which most of the pits at MDA G are located. Abeele et al. (1986) characterized the moisture retention on several cores from boreholes at TA-54 including MDA G, but Abeele et al. (1986) did not provide bulk density or porosity data for their samples. Porosity and bulk density estimates for the Bandelier Tuff units characterized by Abeele et al. (1986) were obtained by using the means for the same units from Rogers and Gallaher (1995). The data from Abeele et al. (1986) were analyzed using the RETC code (van Genuchten et al. 1991). The estimated parameters for the van Genuchten (1980) function for the crushed tuff were: saturated water content = 0.479; residual water content = 0.008; alpha (cm^{-1}) = 0.007; and N = 2.004. The parameter estimates for the water balance model are given in Table 4. The estimated saturated hydraulic conductivity for the crushed Bandelier Tuff is the same as that from Springer (1995) because there was no additional data on this parameter.

Table 4. Soil and crushed tuff properties used for MDA G simulation.

	Hackroy Clay Loam	Crushed Tuff
Porosity	0.493	0.479
1/3-bar volumetric water content	0.273	0.1982
15-bar volumetric water content	0.099	0.0122
Saturated hydraulic conductivity (cm/hr)	0.899	1.270

The 1-m soil profile was divided into eight layers. The thickness of layers 1 through 6 was 5 cm (2 in.), layer 7 was 15.2 cm (6 in.), and layer 8 was 55.8 cm (22 in.).

The value for the soil evaporation parameter in Equation 32, CONA, is 3.8 mm/day$^{1/2}$ which is the suggested average value for the clay loam texture class.

Data were available for runoff from MDA G for two subwatersheds that were monitored by the Stormwater Runoff Program operated by ESH-18 at Los Alamos. Data for these subwatersheds denoted G-1 and G-3 are given in Table 5. It can be seen from Table 5 that there were a limited number of events recorded during the 1995 water year. Also, the last column of Table 5 is the estimated curve number parameter using relationships from Springer et al. (1980) to estimate the CN value for a given precipitation - runoff data pair. The lowest CN value observed was 72.5. What is not shown in Table 5 is the number of events where precipitation occurred with no runoff. These data reduced the CN1 to 70 for these simulations of MDA G. This is consistent with the CN2 from Lane (1984) for the Los Alamos CREAMS simulations. Using Equation 21 a CN2 of 85 has an estimated CN1 of 70.2.

Table 5. Runoff data from MDA G watersheds collected by Stormwater Runoff Program at Los Alamos.

Watershed	Date	Precipitation (mm)	Runoff (mm)	Estimated CN
G-1	5/29/95	28.19	0.76	72.5
G-1	8/13/95	14.48	0.18	82.0
G-1	8/29/95	17.02	2.73	89.0
G-1	9/7/95	26.42	2.39	79.9
G-3	8/29/95	17.02	0.38	80.8
G-3	9/7/95	26.42	0.97	75.1
G-3	9/8/95	26.42	1.79	78.1

The LAI distribution was taken from Lane (1984) for his Los Alamos simulation with CREAMS. These values and their Julian date are given in Table 6. Linear interpolation is used between Julian days to determine LAI values between the days listed in Table 6. Rooting depth was assumed to be 0.45 m (1.5 ft.). This parameter was varied for sensitivity analyses because the depth in the soil profile from which water is extracted is

determined by the rooting depth. By removing water deeper from the profile, percolation will be affected.

Table 6. Leaf area index distribution used for MDA G simulation.

Julian Day	Leaf Area Index
1	0.0
91	0.02
121	0.05
152	0.20
182	1.00
213	1.00
244	0.80
274	0.20
305	0.01
366	0.0

For these simulations, rapid or crack flow and return flow were set to zero. The disturbed nature of the pit and packing of crushed materials reduce the opportunity for rapid flow by destroying the structure of the soil and tuff. The design of the base case cover does not include permeability barriers that can create significant lateral flow.

Soil Erosion Parameters

Tables, charts, and data from Nyhan and Lane (1986b) for Los Alamos were used to estimate the parameters for MUSLE (Equation 51). Slope length was 30 m (98.4 ft.) and the slope was 3 percent giving the LS factor a value of 0.28. The K factor was the average value obtained from the 1983 simulations of Nyhan and Lane (1986b) of 0.069 Mg ha h/MJ ha mm (0.52 ton·acre hour/100 acre·ft-ton·inch). The C or cover factor of 0.03 was taken from the 1983 simulator run of Nyhan and Lane (1986b) for their trench cap plots with a gravel and wheatgrass cover.

SIMULATION RESULTS

The surface runoff, soil erosion, and percolation through the 1-m cover at MDA G were predicted using a Monte Carlo approach. A total of 100 realizations that were 10000 years long were generated in this Monte Carlo procedure giving a total of 1000000 annual observations for the response variables. The 10000-year period was selected for sensitivity and uncertainty analyses purposes according to guidance from DOE. The percolation estimates are used by the subsurface transport pathway to predict radionuclide source term behavior and transport from the pits.

The statistics for the annual precipitation from the weather generator were:

mean = 35.56 cm (14.0 in),
standard deviation = 5.97 cm (2.35 in.),
maximum annual = 71.02 cm (27.96 in.), and
minimum annual = 12.29 cm (4.84 in.).

Nyhan et al. (1989) estimated the 100-year annual precipitation event for the Los Alamos gauge to be 83.57 cm (32.9 in.). The Nyhan et al. (1989) estimate compares well with the maximum generated by the stochastic weather generator.

Statistic for the three response variables are given in Table 7. The percolation value is for the bottom of a 1-m profile.

Table 7. Statistics for annual values of percolation, runoff, and soil erosion for 100 Monte Carlo simulations each with a realization length of 10000 years (total of 1000000 observations) for MDA G at Los Alamos.

Variable	Mean	Standard Deviation	Maximum	Minimum
Percolation (mm)	0.99	5.17	129.33	0.0
Runoff (mm)	0.78	1.65	67.49	0.0
Soil erosion (t/ac·yr)	0.002	0.005	0.23	0.0

The large standard deviations relative to the means for each variable are indicative of highly dispersed distributions, and the large maximum values suggest a skewed distribution. These results are consistent with those of Springer (1995) in terms of the relationship between the statistics. The magnitude of the values are lower than those from Springer (1995) because of the reduced mean annual precipitation and changes in the CN1 and soil water properties of the cover profile.

Springer (1995) found that over 80 percent of the annual percolation values were zero. The same results hold for this data set. Some confidence in the simulation results can be gained through the annual distribution of percolation. Nyhan et al. (1990) reported that percolation through a conventional cover was greatest in the late winter and early spring when snowmelt occurred and evapotranspiration was low because the vegetation was not active. Figure 9 is a plot of the monthly mean percolation from the Monte Carlo simulation. The sum of the February and March percolation values is approximately 68 percent of the annual average of 0.99 mm.

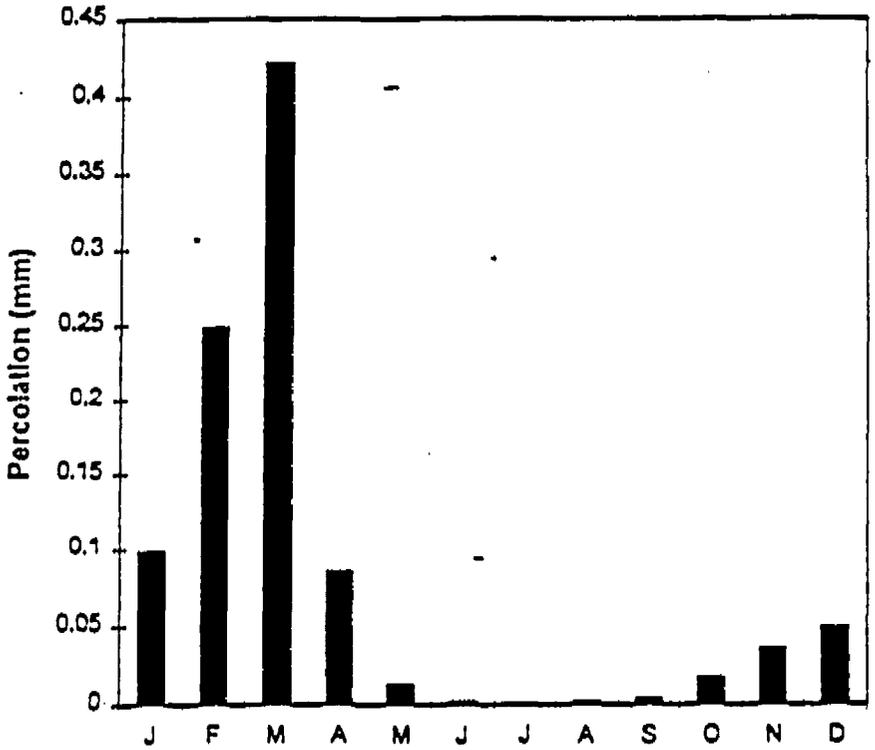

Figure 9. Average monthly percolation for MDA G from 100 Monte Carlo simulations with a realization length of 10000 years.

The average surface runoff in Table 7 is low compared to the available runoff data from MDA G in Table 5. The limited amount of available data cannot be considered representative of long-term response. These data were used to estimate the minimum CN, but this is not an average. To estimate the average, it is estimated that 30 years of data are required. Another issue for runoff generation is the use of a daily precipitation and the CN method. In the Los Alamos area, high intensity rainfall events generate runoff and soil erosion, and the daily precipitation moderates the rainfall intensity effect because rainfall duration is constant for precipitation event. An alternative approach is to use the daily simulation model for the interstorm period and an event based model such as KINEROS (Woolhiser et al., 1990) for the high intensity rainfall events. One complication is that the event based model will require more data on spatial distribution of infiltration and surface hydraulic properties.

The soil erosion in Table 7 is well below the EPA recommended rate of 4.48 mT/ha•yr (2 t/ac•yr). This low erosion rate is directly related to the low runoff. Taking the maximum rate from Table 7, the 1-m surface cover will be erode so that waste is expose in 10000 years (≈ 0.0005 cm/yr). This calculation assume a spatially uniform rate of soil removal and a bulk density of the material of 1.337 g/cm^3 (Abeele 1984).

This result is also dependent on the maintenance of the vegetation and gravel mulch cover that has been shown to be effective at erosion control (Nyhan et al. 1984). The persistence of the gravel mulch and grass cover is unknown.

UNCERTAINTY AND SENSITIVITY

The range of the variables in Table 7 reveals considerable uncertainty. The range of percolation is three orders of magnitude which is similar to the range reported by Springer (1995). Percolation is important because it is used by the subsurface pathway analysis to predict subsurface radionuclide migration. More site specific data from MDA G were used for parameter estimates of the daily water balance model in this simulation than used by Springer (1995), but the uncertainty has not been substantially reduced. Much of the uncertainty in the percolation and runoff results is due to the weather input term, and with realistic parameter estimates in the water balance model little reduction in uncertainty is possible.

Springer (1995) examined the sensitivity of CN1, LAI, rooting depth (RD), and initial soil water content and found that the CN1 and RD parameters were significant relative to surface runoff and percolation response. These results were consistent with those from Lane and Ferreira (1980) for the CREAMS model. Additional data from MDA G has given a better estimate of the CN1 so this parameter has been fixed. RD was increased to a depth of 1 m which decreased the average annual percolation to 0.003 mm and the maximum annual percolation to 69 mm. This parameter remains sensitive, but further refinement is difficult without more controlled experimentation. Also, the data from the chloride profile studies by Newman (1996) supports higher flux rates in this upper zone. LAI was reduced in half with the same temporal distribution and the mean percolation rate was doubled (2.08 mm vs. 0.99 mm). The change of magnitude in LAI had a limited effect on mean surface runoff (0.78 mm vs. 0.99 for the 0.5*LAI case). LAI can be measured reducing uncertainty associated with this parameter. Measurement of LAI will also provide some data on its seasonal distribution which has not been addressed in these simulations.

Long-term dynamics of the vegetation and soil properties remains unknown in these simulations. These effects can be very important to the integrity of surface covers (Suter et al., 1993).

SUMMARY AND RECOMMENDATIONS

The surface runoff, soil erosion, and percolation through a 1-m thick soil cover for the low-level radioactive waste disposal area at Los Alamos, MDA G, were simulated using a stochastic weather generator and a daily water balance model. Soil erosion was predicted using the MUSLE equation. A Monte Carlo approach was used that generated 100 realizations which were 10000 years long.

Precipitation parameters for the stochastic generator were estimated using data from the Los Alamos location rain gauge because the record for this site was longer. The mean annual precipitation was constrained to 35.56 cm which is the mean for the MDA G location from Bowen (1990). The seasonal distribution of the precipitation parameters from the White Rock gauge were compared to the Los Alamos gauge and the patterns were similar for the available data.

The simulated surface was a 1-m thick profile with a 10-cm layer of clayloam topsoil and the remaining depth composed of crushed tuff. Data from the stormwater runoff measuring stations at MDA G were available and the CN1 parameter was estimated from these data. Soil water characteristics and saturated hydraulic conductivity from a field experiment were used in place of soil texture based tabular values for the topsoil. Also, crushed tuff water characteristics were revised using data from MDA G.

Results from the base case simulation showed considerable variability in both percolation and surface runoff. The magnitude of the mean annual surface runoff is low compared with the available data from MDA G. Soil erosion is directly related to surface runoff through the MUSLE equation so the amount of soil erosion is low too. There was considerable variability in the percolation and surface runoff response which is essentially the same as the variability calculated by Springer (1995). Better estimates of key parameters such as soil water characteristics and CN1 did not reduce the uncertainty. Much of the uncertainty enters through the weather input.

The models and parameter values reflect the current appraisal of the lumped system at MDA G. Data such as chloride profiles, stable isotope distributions, and surface runoff are being collected, and these will provide some further constraints on future simulations. Also, MDA G will be closed and no further maintenance will be performed putting this system into an ecological and soil succession process. Parameters that control the hydrology will change with the succession process, but the pattern and magnitude of the change are unknown and not considered in this simulation study.

The following recommendations are made based on the results of this simulation study:

- Continue to collect soil moisture, chloride profile, and stable isotope data to constrain model parameters or replace model inputs. It may be possible to use the chloride profile data to estimate the subsurface flux rate.

- Implement a dynamic model that incorporates changes in vegetation and soil properties over time is needed.

- Consider implementing an event-based surface runoff model to account for the effects of high intensity rainfall events on runoff and erosion and the spatial distribution of soil properties. The current daily water balance model can be used for interstorm periods to predict antecedent conditions. This is expected to be more important for the soil erosion.

REFERENCES

Abeele, W. V. 1984. Geotechnical aspects of Hackroy sandy loam and crushed tuff. Los Alamos National Lab. Report No. LA-9916-MS, 20 pp.

Abeele, W. V., H. R. Fuentes, and J. Hosch. 1986. Characterization of soil moisture characteristic curves in the 30 to 1000 kPa tension range for Bandelier Tuff in waste disposal areas G and L, Technical Area 54, Los Alamos National Laboratory. Report prepared for Environmental Surveillance Group, HSE-8, Los Alamos National Laboratory, Los Alamos, NM, 99pp.

Abeele, W. V., M. L. Wheeler, and B. W. Burton. 1981. Geohydrology of Bandelier Tuff. Los Alamos Nat. Lab. Rep. No. LA-8962-MS, 50 pp.

Anderson, E. A. 1973. National Weather Service river forecast system – snow accumulation and ablation model. NOAA Tech. Memo. NWS HYDRO-17, U.S. Dept. of Commerce, Silver Spring, MD, 217 pp.

Bowen, B. M. 1990. Los Alamos climatology. Los Alamos National Lab. Report No. LA-11735-MS, 254 pp.

Cooley, K. R., E. P. Springer, and A. L. Huber. 1987. Part I. Chapter 4. Hydrology component: snowmelt. Pages 31-40 in J. R. Wight and J. W. Skiles (eds.). SPUR - Simulation of Production and Utilization on Rangelands: Documentation and user guide. U.S. Department of Agriculture, Agricultural Research Service. ARS-63, 367 pp.

Haan, C. T. 1977. Statistical methods in hydrology. Iowa State Univ. Press, Ames, Iowa, 378 pp.

Hanson, C. L., and C. W. Richardson. 1987. Parameter estimation for the climate generator. Pages 300-320 in SPUR: Simulation of Production and Utilization of Rangelands. Documentation and user guide, J. R. Wight and J. W. Skiles, eds. U.S. Department of Agriculture, Agricultural Research Service, ARS 63, 372 pp.

Jackson, R. D., S. B. Idso and R. J. Reginato. 1976. Calculation of evaporation rates during the transition for energy-limiting to soil-limiting phases using albedo data. Water Resources Research 12(1):23-26.

Knisel, W. G. 1980. CREAMS: A field-scale model for Chemicals, Runoff, and Erosion from Agricultural Management Systems. USDA Conservation Res. Rep. No. 26, 643 pp.

Lane, L. J. 1984. Surface water management: A user's guide to calculate a water balance using the CREAMS model. Los Alamos National Laboratory Report No. LA-10177-MS, 49 pp.

Lane, L. J. and J. J. Stone. 1983. Water balance calculations, water use efficiency and aboveground net production. Pages 27-34 in Hydrology and water resources in Arizona and the southwest, Volume 13.

Lane, L. J., and V. A. Ferreira. 1980. Sensitivity analysis. Pages 113-158 in CREAMS: A field scale model for Chemicals, Runoff, and Erosion from Agricultural Management Systems, W. G. Knisel, ed. USDA Conservation Res. Rep. No. 26, 643 pp.

Lee, R. 1963. Evaluation of solar beam irradiation as a climatic parameter of mountain watersheds. Colo. State University Hydrology Papers, No. 2 (August 1963), Ft. Collins.

Link, S. O., L. L. Cadwell, K. L. Petersen, M. R. Sackschewsky, and D. S. Landeen. 1995. The role of plants and animals in isolation barriers at Hanford, Washington. Pacific Northwest Laboratory Report No. PNL-10788, Pacific Northwest laboratory, Richland, WA.

Matalas, N. C. 1967. Mathematical assessment of synthetic hydrology. Water Resources Research 3(4):937-945.

Newman, B. D. 1996. Vadose zone water movement at Area G, Los Alamos National Laboratory, TA-54: Interpretations based on chloride and stable isotope profiles. Los Alamos National Laboratory Report, LA-UR-96-4682, Los Alamos National Laboratory, Los Alamos, NM, 30pp.

Nyhan, J. W., W. V. Abeele, T. E. Hakonson, and E. A. Lopez. 1986. Technology development for the design of waste repositories at arid sites: Field studies of biointrusion and capillary barriers. Los Alamos National Laboratory Rep. No. LA-10574-MS, Los Alamos National Laboratory, Los Alamos, New Mexico, 50 pp.

Nyhan, J. W., R. Beckman, and B. Bowen. 1989. An analysis of precipitation occurrences in Los Alamos, New Mexico, for long-term predictions of waste repository behavior. Los Alamos National Laboratory Rep. No. LA-11459-MS, Los Alamos National Laboratory, Los Alamos, New Mexico, 27 pp.

Nyhan, J. W., G. L. Depoorter, B. J. Drennon, J. R. Simanton, and G. R. Foster. 1984. Erosion of earth covers used in shallow land burial al Los Alamos, New Mexico. J. Environmental Quality, 13(3):361-366.

Nyhan, J. W., L. W. Hacker, T. E. Calhoun, and D. L. Young. 1978. Soil survey of Los Alamos County, New Mexico. Los Alamos Report LA-6779-MS, Los Alamos National Laboratory, Los Alamos, New Mexico, 102 pp.

Nyhan, J. W., T. E Hakonson and B. J. Drennon. 1990. A water balance study of two landfill cover designs for semiarid regions. J. Environmental Quality, 19:281- 288.

Nyhan, J. W. and L. J. Lane. 1986a. Rainfall simulator studies of earth covers used in shallow land burial at Los Alamos, New Mexico. Pagers 39-42 in Proceedings of the Rainfall Simulator Workshop, January 14-15, 1985, Tucson, AZ, Society for Range management, Denver, CO.

Nyhan, J. W., and L. J. Lane. 1986b. Erosion control technology: A user's guide to the use of the Universal Soil Loss Equation at waste burial facilities. Los Alamos Report LA-10262-MS, Los Alamos National Laboratory, Los Alamos, New Mexico, 67 pp.

Renard, K. G., E. D. Shirley, J. R. Williams, and A. D. Nicks. 1987. Part I. Chapter 3. Hydrology component: Upland phases. Pages 17-30 in J. R. Wight and J. W. Skiles (eds.). SPUR - Simulation of Production and Utilization on Rangelands: Documentation and user guide. U.S. Department of Agriculture, Agricultural Research Service. ARS-63., 367 pp.

Richardson, C. W. 1982a. A comparison of three distributions for the generation of daily rainfall amounts, p. 67-78. In Singh, V.P., ed., Statistical Analysis of Rainfall and Runoff. Proceedings of International Symposium on Rainfall-Runoff Modeling, Water Research Publication, 700 p.

Richardson, C. W. 1982b. Dependence structure of daily temperature and solar radiation. Trans. ASAE, 25:735-739.

Richardson, C. W., C. L. Hanson, and A. L. Huber. 1987. Climate generator. Pages 3-16 in SPUR: Simulation of Production and Utilization of Rangelands. Documentation and user guide, J.R. Wight and J.W. Skiles, eds. U.S. Department of Agriculture, Agricultural Research Service, ARS 63, 372 pp.

Ritchie, J. T. 1972. A model for predicting evaporation from a row crop with incomplete cover. Water Resour. Res. 8:1204-1213.

Rogers, D. M. and B. M. Gallaher. 1995. The unsaturated hydraulic characteristics of Bandelier Tuff. Los Alamos National Laboratory Report, LA-12968-MS, Los Alamos National Laboratory, Los Alamos, NM, 132p.

Rogers, M. A. 1977. History and environmental setting of LASL near-surface land disposal facilities for radioactive wastes (Areas A, B, C, D, E, F, G, and T). Los Alamos Scientific Laboratory Rep., LA-6848-MS, Vol. 1.

Sejkora, K. J. and A. W. Alldredge. 1989. Influence of pocket gophers on water erosion and surface hydrology. Final report submitted to Los Alamos National Laboratory by Colorado State University, Department of Fish and Wildlife Biology, Fort Collins, CO, 144pp.

Springer, E. P. 1995. Area G performance assessment: Surface water and erosion. Los Alamos National Laboratory Report No., LA-UR-95-2497, Los Alamos National Laboratory, Los Alamos, NM, 40pp.

Springer, E. P., and L. J. Lane. 1987. Hydrology-component parameter estimation. Pages 260-275 in SPUR: Simulation of Production and Utilization of Rangelands. Documentation and user guide, J.R. Wight and J.W. Skiles, eds. U. S. Department of Agriculture, Agricultural Research Service, ARS 63, 372 pp.

Springer, E. P., B. J. McGurk, R. H. Hawkins, and G. B. Coltharp. 1980. Curve numbers from watershed data. In Watershed Management 1980, p. 938-950. Am. Soc. Civil Engin. Symposium on Watershed Management, Boise, Idaho.

Suter II, G. W., R. J. Luxmoore, and E. D. Smith. 1993. Compacted soil barriers at abandoned landfill sites are likely to fail in the long term. J. Environmental Quality, 22:217-226.

USDA, Soil Conservation Service. 1972. National engineering handbook, hydrology section 4, chapters 4-10.

van Genuchten, M. Th. 1980. A closed form equation for predicting the hydraulic conductivity of unsaturated soil. Soil Science Soc. Am. J. 44:892-898.

van Genuchten, M. Th., F. J. Leij, and S. R. Yates. 1991. The RETC code for quantifying the hydraulic functions of unsaturated soils. U. S. Environmental Protection Agency Rep. No. EPA/600/2-91/065, 85pp.

van Genuchten, M. Th., J. C. Parker, and J. B. Kool. 1987. Analysis and prediction of water and solute transport in a large lysimeter. Pages 4-36 in Modeling Study of Solute Transport in the Unsaturated Zone, Workshop proceedings. U. S. Nuclear Regulatory Comm., Washington, D.C., NUREG/CR-4615 vol. 2, 242 pp.

Warren, R.W., T. E. Hakonson, and K. V. Bostick. 1996. The hydrologic evaluation of four cover designs for hazardous waste landfills at Hill Air Force Base. Federal Facilities Environment Journal, Winter 1995/96, 91- 110.

Wight, J. R. and J. W. Skiles, eds. 1987. SPUR: Simulation of Production and Utilization of Rangelands. Documentation and user guide. U. S. Department of Agriculture, Agricultural Research Service, ARS 63, 372 pp.

Williams, J. R. and W. V. LaSeur. 1976. Water yield model using SCS curve numbers. Journal of the Hydraulics Division, American Society of Civil Engineers, 102(HY9):1241-1253.

Williams, J. R. 1975. Sediment yield prediction with universal equation using runoff energy factor. USDA, Agricultural Res. Service, ARS-S-40, pp. 244-252.

Wischmeier, W. H. and D. D. Smith. 1978. Predicting rainfall erosion losses -A guide to conservation planning. USDA Handbook 537, 58pp.

Woolhiser, D. A., R. E. Smith, and D. C. Goodrich. 1990. KINEROS, A kinematic runoff and erosion model: Documentation and user manual. U. S. Department of Agriculture, Agriculture Research Service, ARS-77, 130pp.

Source Release Modeling for the Los Alamos National Laboratory Material Disposal Area G Performance Assessment and Composite Analysis

Erik Vold - *Los Alamos National Laboratory*
Rob Shuman - *Rogers and Associates Engineering Corporation*

Source Release Modeling for the Los Alamos National Laboratory Material Disposal Area G Performance Assessment and Composite Analysis

Erik Vold - *Los Alamos National Laboratory*
Rob Shuman - *Rogers and Associates Engineering Corporation*

ABSTRACT

A performance assessment (PA) and composite analysis (CA) for the low-level radioactive waste (LLRW) disposal facility at TA-54, Area G, at the Los Alamos National Laboratory (LANL) provide the technical basis for disposal operations and demonstrate the environmental compatibility of those operations. A model was developed to project aqueous phase releases from multiple waste forms of radioactivity to the unsaturated zone for the preliminary PA for the disposal facility at Area G as described in the report, LA-UR-96-368. Based upon the results and findings from Phase One, the model has been refined and improved in Phase Two for application to the current LANL PA/CA, as described in the report, LA-UR-96-4786.

Phase One focused on the development of analytical and numerical aqueous phase release models, and an examination of the release from composite waste forms based on inventory data for the 'historical PA' inventory (1988-1995). Inventory that needed explicit release modeling was reduced with a leachate screening test. Four waste categories were considered in the Phase One analysis to account for characteristics of the waste forms that control aqueous-phase release rates. Results from the preliminary analysis show that peak leachate concentrations were dominated by a single waste form, the 'rapid release' or surface-contaminated waste form.

Phase Two focused on improving the release model for the dominant waste form, surface contaminated waste, to reflect a dissolution time limited by the *in situ* percolation rate. The formulation allowed the inventory-limited release and solubility-limited release models to be applied to each of the individual disposal units at Area G. These aqueous phase source release models are incorporated directly into the 3-D unsaturated zone transport computations and are used to distinguish more than 40 disposal units and 45 nuclides needed to characterize the source releases in the PA/CA.

Uncertainty was addressed in Phase One, in relation to the analytic release model and its parameters. Phase Two modeling examined the effects on the release model and uncertainty associated with percolation transients.

LA-UR-96-4786

Title: Phase Two of the Aqueous Phase Source Release Modeling for the Los Alamos Area G Disposal Facility Performance Assessment

Author(s): Erik L. Vold - LANL

Rob Shuman - RAE

Submitted to:

1. U.S. Department of Energy, as support documentation for the Los Alamos Area G Performance Assessment

2. Waste Management '97
USDOE Conf., Tucson, AZ, March, 1997

Los Alamos
NATIONAL LABORATORY

Los Alamos National Laboratory, an affirmative action/equal opportunity employer, is operated by the University of California for the U.S. Department of Energy under contract W-7405-ENG-36. By acceptance of this article, the publisher recognizes that the U.S. Government retains a nonexclusive, royalty-free license to publish or reproduce the published form of this contribution, or to allow others to do so, for U.S. Government purposes. The Los Alamos National Laboratory requests that the publisher identify this article as work performed under the auspices of the U.S. Department of Energy.

Phase Two of the Source Release Modeling for the Los Alamos Area G Disposal Facility Performance Assessment

Erik Vold - *Los Alamos National Laboratory*
Rob Shuman - *Rogers and Associates Engineering Corporation*

ABSTRACT

Analytic and numerical modeling of the aqueous phase release to the unsaturated zone of low level radioactive waste from a shallow burial disposal facility was initiated last year (Phase One) in support of the preliminary Los Alamos National Laboratory Area G Performance Assessment. This year (Phase Two) the effort is continuing to refine the preliminary results to allow for a rigorous 3-D analysis of the aqueous phase release from over 40 distinct disposal units into the unsaturated zone. The previous results showed that a 'rapid release' or surface contaminated waste form (with solid-liquid phase partition coefficient, $K_d = 0$) dominates peak leachate concentrations and therefore determines the maximum off-site groundwater dose. The model for the dissolution process from the waste compartment solid phase to liquid phase for the rapid release inventory has been improved to reflect a transition limited by the insitu percolation rate. The analytic solution to the previous model is singular for this case; a new solution is derived and applied to the site assessment. A detailed numerical analysis evaluates transient percolation and the resulting leachate concentrations and waste compartment efflux as a function of time in comparison to the analytic source release model output based on an average percolation rate. Transients can be significant locally but attain average values rapidly over local variations in time and space. The site inventory is sorted into groups by time period of interest, allowing analysis of nuclide solubility limits by individual disposal unit. A detailed implementation of the source release model has been incorporated directly into the source term module of the 3-D unsaturated zone computational model used in the site performance assessment.

INTRODUCTION

A Performance Assessment (PA), as required by DOE Orders, is underway for the low level radioactive waste (LLRW) disposal facility at Los Alamos National Laboratory, Area G [1]. This assessment provides the technical basis for disposal operations and for establishing environmental compatibility of those operations. Fig.1A shows a cross-section of the mesa-top disposal facility at Area G with three representative disposal units.

A model for the aqueous phase release of radioactivity to the unsaturated zone by a prescribed percolation rate and the subsequent leaching of contaminants has been evaluated in the preliminary PA [1] with the model development described previously [2] and its application to the preliminary site PA in [3]. This report summarizes results from the previous analyses and describes model improvements and the continuing effort to refine the results in several areas. These include a refined percolation model for the dominant 'rapid release' waste category, an examination of the effects of percolation transients on source release, and a methodology to apply the analytic model results to over 40 specific disposal units across the site, including disposal pits and shaft fields.

Synopsis of Preliminary Source Release Model

The conceptual model for subsurface liquid phase release from a disposal unit is shown in Fig.1B. A representative waste package is shown to the left, and a disposal unit is shown on the right. Waste packages for a given nuclide and for a given package type are distributed more or less randomly throughout the disposal unit volume and thus the leachate through the waste packages approximates a uniform volumetric source term to the disposal unit volume. In the model, radioactive contaminant moves through three compartments (Fig.1C) from the waste package solid phase to the waste package liquid phase by a dissolution process, from the waste package liquid phase to the disposal unit by percolation, and finally from the disposal unit to the unsaturated zone by percolation. Analytic solutions were derived for the three compartments [2]. It is critical to distinguish the waste package solid and liquid phase compartments because the maximum contaminant leachate concentrations occur within the waste package leachate. Therefore, the elemental solubility limit must be applied to the concentrations at that point as detailed previously [2], before dilution occurs throughout the disposal unit volume.

In application to the site Performance Assessment, the solution for the efflux from the waste package liquid phase (compartment 2) has been used directly in the numerical transport model for the unsaturated zone [4], with the waste leachate source term distributed over the computational grid points which represent the disposal unit volumes. Thus, the focus here is on the concentration and efflux solutions from the second compartment in the model. The governing equations of interest are derived as the contaminant mass continuity equation in the control

volume or integral form for each model compartment. The result for the first compartment, the waste package solid phase, is

$$V_s \frac{\partial C_s}{\partial t} = - A_s u_s C_s , \qquad (1)$$

and for compartment 2, the waste package liquid phase,

$$\theta_w V_w \frac{\partial C_w}{\partial t} = \frac{A_s u_s C_s}{R_w} - \frac{A_w q_w C_w}{R_w} , \qquad (2)$$

where subscript s refers to the waste package solid phase, and w refers to waste package liquid (water) phase. C is the contaminant concentration, u_s is a specified dissolution velocity, R is the standard retardation coefficient, $R = (1. + K\rho_m/\theta)$, and θ is the moisture content volumetric fraction, q is a Darcy flux (flux of liquid volume), V is a waste volume from the data base, and A is an area in the horizontal plane. The waste packages have an average height dimension (h_w) taken to be 1m, and $A = h_w/V$.

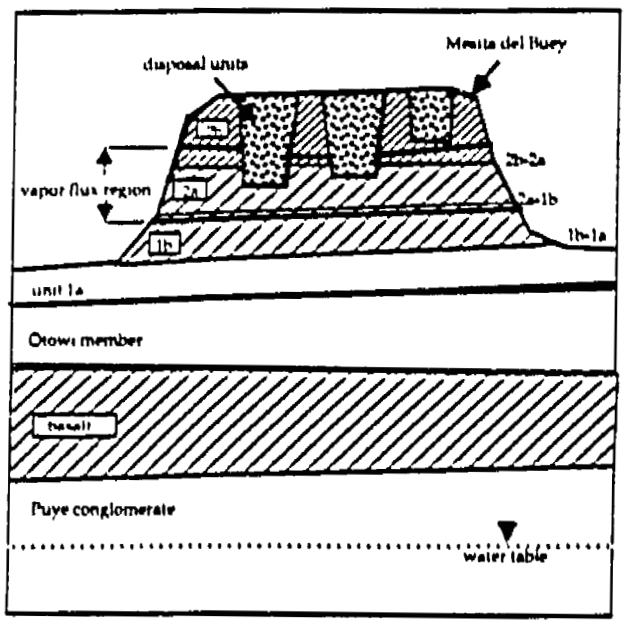

Fig.1A Sketch of the stratigraphy cross-section underlying the disposal facilities at Area G.
The figure dimensions are not to scale; the mesa top to canyon floor distance averages about 100 ft, the canyon floor to the water table is about 800 ft, the mesa width varies from 400 to 1200 ft. The cross-hatched regions indicate the more fractured stratigraphic units. The 'vapor flux region' is discussed in the text.

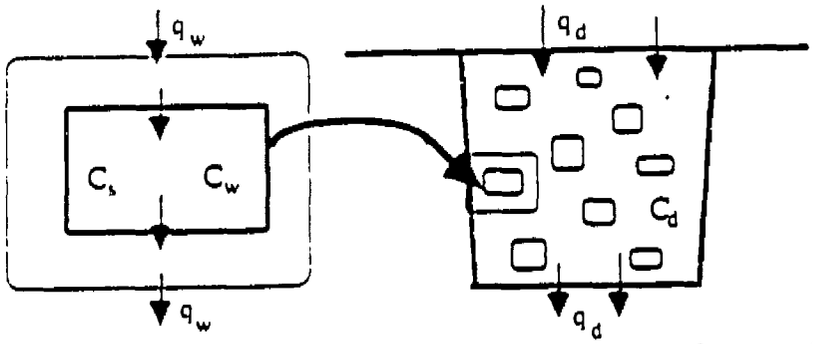

Fig. 1B. Conceptual model for subsurface liquid phase release from a disposal unit. A representative waste package (solid phase, s and liquid or water phase, w) is shown to the left, and a disposal unit (d) containing many randomly distributed waste packages is shown on the right.

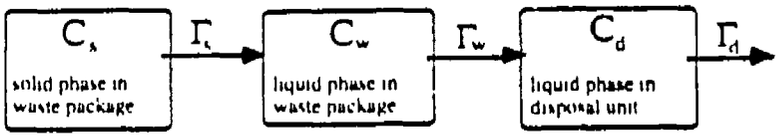

Fig. 1C. The three compartments in the present release model are an equivalent representation of the conceptual model from Fig.1a, showing contaminant concentrations, C, and flux, Γ for the three compartments.

The analytic solution to Eqns.1 and 2 with initial conditions, C_s set to the data base inventory concentration, C_{so}, and $C_w = 0.$, was given [2] as,

$$C_w(t) = \frac{C_{so}}{\theta_w R_w} \frac{\lambda_s}{(\lambda_w - \lambda_s)} \frac{V_s}{V_w} (exp(-\lambda_s t) - exp(-\lambda_w t)) , \qquad (3)$$

with $\lambda_s = \dfrac{A_s u_s}{V_s}$, and $\lambda_w = \dfrac{A_w q_w}{V_w \theta_w R_w}$.

The moisture content, θ, and percolation rate, q, through the waste are assumed the same as through the disposal unit, with $\theta = 0.08$ determined from empirical data [5] and $q \sim 5$ *mm/yr* determined from modeling [6] and analytic sources summarized in a companion paper [7]. Waste and disposal unit dimensions and volume are from the site data base, and to simplify, it is assumed that $A_s = A_w$ and $V_s = V_w$.

Synopsis of Preliminary Model Results

The data base for disposed radionuclides at Area G allows inventory to be sorted by nuclide, by disposal package type (>50 waste codes are available for the waste generator to identify different waste types and process streams), and by disposal unit (DU) location (over 30 disposal pits and 200 disposal shafts over a 60 acre site). The data were grouped in order to simplify the source term to a manageable calculation. The ~50 waste codes were categorized into four release groups, rapid release or surface contamination (K_d = 0 in the waste package), contaminated soil, concrete/solidified sludge, and metal activation or corrosion release. Performance assessment pathway analysis requires that nuclides be distinguished, so the tradeoff for simplification is between waste package forms and waste disposal location. Phase One analysis simplified disposal location while tracking waste forms in detail. Phase Two analysis simplifies waste form as justified in this discussion, and tracks disposal location in detail for input to the 2-D and 3-D unsaturated zone transport model [8].

The preliminary PA analysis (Phase One) focused on a simplification over disposal units where inventory was averaged over those disposal units utilized in the 'historical inventory' (1988-1995). This allowed a detailed sorting and analysis by waste form where the >50 waste codes were approximated by four 'release categories' characterized with distinct parameter values in the source release model. A 'rapid release' category includes the waste inventory where the data base did not have specific enough data to justify any retardation or retention for the waste package form, and so $K_d = 0$, or $R_w = 1$ applies to this waste category, and the 'rapid release' waste is assumed to be leached as soon as water percolates through the closed disposal unit.

The previous analysis demonstrated clearly that only the inventory in the 'rapid release' category is significant in predicting maximum leachate concentrations and thus we need consider only the 'rapid release inventory' to predict the maximum drinking water dose or all pathways dose that eventually occurs after contaminant migration from the site. The specific criteria for comparing release concentrations based on inventory sources across different waste forms is Q_{ij}/R_{ij} where i is the nuclide index, j is the waste form or category index, and Q is the inventory quantity per DU. This was examined in the data base across the entire inventory and the 'rapid release inventory' was confirmed to dominate for all nuclides. For Am-241, even though much of the inventory is in the sludge/concrete waste category, $R \sim 5000$ applies to that waste form [9] and so that waste release category does not contribute to maximum release concentrations. A few nuclide elements including uranium were consistently solubility limited and for these cases, the contributions across waste categories were calculated separately in the site assessment.

This allows us in Phase Two to use only waste inventory in the 'rapid release' category. This justified simplification allows us to evaluate the rapid release

inventory by each disposal unit throughout the mesa top 60 acre Area G site. This provides detailed input to the 3-D unsaturated-saturated transport numerical study.

ANALYSES

Percolation Limited 'Rapid Release'

The characteristic time for waste package inventory to be available for dissolution in the liquid phase of the water percolating through the waste packages within the disposal unit was previously set as a constant based on waste form and empirical data where available. No data are available for the release from the rapid release category under in-situ conditions at Area G; it was assumed in Phase I analysis to be 'rapid' relative to the percolation transit time through the waste package, $T_w = (\theta_w h_w)/q_w$.

Under the more realistic conditions assumed in Phase II analysis for 'rapid release' waste, the transition from the solid to liquid phase by dissolution will be limited by the moisture percolating into the waste package. Thus, this transition is controlled by the same percolation rate which controls the leachate release from the waste package and so the same characteristic time constant applies to the release from compartment 1 or 2. In Eqn. 1 and 2, $R_w = 1$, and $u_s = q_w/\theta$ and so $\lambda_s = \lambda_w$, and therefore the analytic solution in Eqn.3 becomes singular (divides by zero).

For this singular case, the solution to Eqn.1 and 2, is re-derived for $\lambda_s = \lambda_w = \lambda = 1/T_w = q_w/(h_w\theta_w)$, and assuming $V_s = V_w$. The analytic solution for this case, where the solid to liquid phase dissolution process is limited by the moisture percolation into the waste and the leaching from the waste form is controlled by the same percolation rate, becomes

$$C_w(t) = \frac{C_{so}}{\theta_w} \lambda t \; exp(-\lambda t). \qquad (4)$$

It is easily shown that the maximum concentration in the waste compartment liquid phase, $C_{w\text{-}max}$, is given as $C_{so}/\theta_w e$, where e is the natural log constant or, $C_{w\text{-}max} \sim 0.37 C_{so}/\theta_w$. The time this maximum occurs is $t = T_w = 1/\lambda$. The time dependent leachate efflux from the waste, $\Gamma_w(t)$, is

$$\Gamma_w(t) = q_w(t)\, \theta_w(t)\, C_w(t). \qquad (5)$$

For the analytic solution, $C_w(t)$ is given by Eqn.4, and the Darcy flux and moisture contents are approximated as constant values from appropriate time averages.

The result of varying a fixed dissolution time constant, $T_s = 1/\lambda_s$, from Eqn.3 is compared to the singular case solution ($T = T_s = T_w$) from Eqn.4, in Fig.2. The figure

shows a normalized concentration, $C_w/(C_{so}/\theta_w)$, in waste leachate verses time for the 'rapid release' waste category, using several values for T, the transition time from the solid to the liquid phase within the waste. The limit as T goes to zero corresponds to a simple release model where the contaminant concentration is instantaneously mixed into the moisture volume fraction (and thus concentrated in the smaller moisture volume), and subsequently decays in time through percolation from the waste package. The singular solution to Eqn.3 occurs for $T = 16$ *years*. This case is used in the site performance studies and assumes the dissolution transition is limited by the percolation through the waste package.

Transients in Percolation

The source release model includes a set of governing equations and the analytic solutions which apply under simplifying assumptions such as a constant percolation rate. Numerical solutions to the governing equations were obtained for transient percolation rates to evaluate the validity of this assumption. Results for the transient case are found by numerically integrating the governing equations, Eqn.1 and 2, to obtain $C_w(t)$ with $u_s = q_w(t)/\theta_w$ and so the constant q_w is replaced with $q_w(t)$, a given time series for the percolation or Darcy flux. This time series was

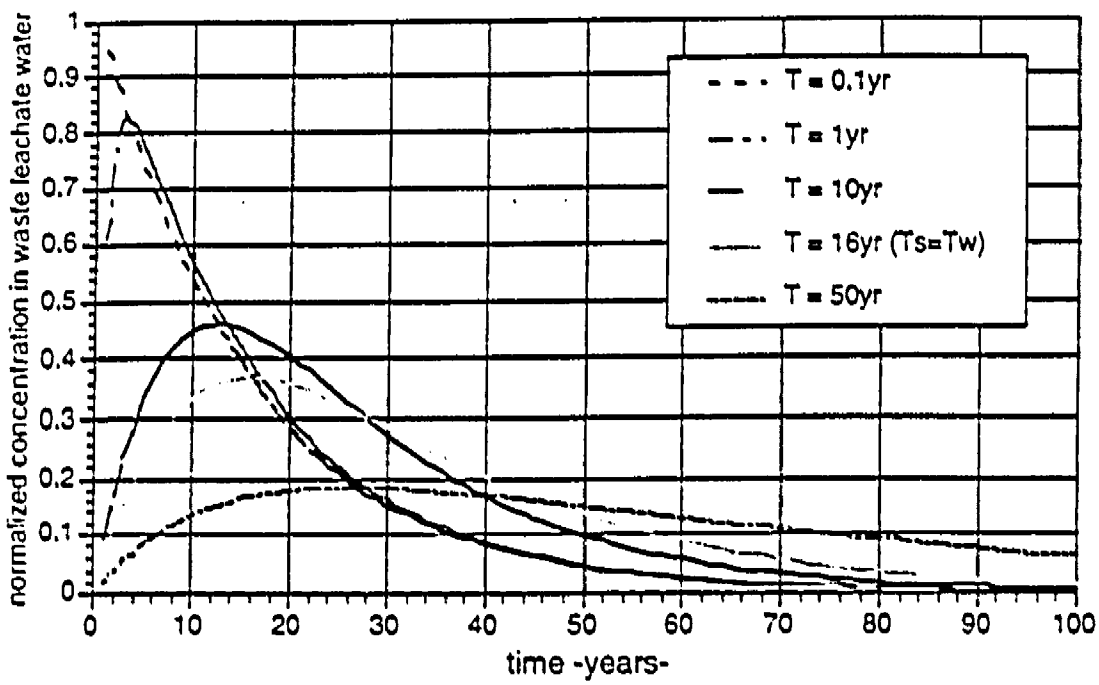

Fig.2 Normalized concentration in waste leachate water for the 'rapid release' waste category, using several values for $T = T_s$, the transition time from the solid to the liquid phase within the waste. The case $(T = T_s = T_w)$ is used in the site performance studies and assumes the transition is limited by the percolation through the waste package. Concentrations are normalized to initial solid phase waste concentration per moisture content, C_{so}/θ_w.

determined from percolation analyses using site precipitation data records [6]. A constant θ_w is still assumed, consistent with small changes observed about the empirical value, and the transient flux is given by Eqn.5. Results from the transient analyses are seen in Fig.3 and 4.

Figure 3 (top) shows the normalized leachate concentration and percolation verses time and compares concentrations for the analytic solution to the averaged percolation rate *(Cw-an-avg)* and the numerical transient solution for the time dependent percolation *(Cw-num-q(t))*, for a particular percolation data 50 yr record. The percolation is very aperiodic and leads to correspondingly aperiodic changes in release concentrations which approximate the smooth curve result for the average percolation rate. This particular percolation data series is unusually dry for the first 25 years, and the transient leachate concentration is displaced accordingly to later times than the solution to the average percolation case.

Figure 3 (bottom) shows normalized leachate concentration versus time comparing concentrations for the analytic solution to the averaged percolation rate for a single 50 yr percolation record *(Cw-an-avg)* and for the average of four 50 yr percolation records *(Cw_an_qave)* and the numerical transient solution for the time dependent percolation averaged over four 50 year time series of percolation data *(Cw_q(t))*. The average percolation for each of the four 50 yr records ranged from 3.8 mm/yr to 9.1 mm/yr and the average over the four records is $q = 6.7\ mm/yr$. The average percolation in the single 50 yr record plotted in the figure is 5.6 mm/yr. Since the average of this single 50 yr record is close to the average of the four records, the two smooth curves are similar however, they would vary in direct proportion to the average percolation over the range from 3.8 mm/yr to 9.1 mm/yr, depending upon the actual time series. The transient solution to the percolation averaged over the four 50 yr records is already beginning to approach the smooth curve given for the average percolation value in the analytic solution.

The waste efflux corresponding to the concentrations in Fig.3 is shown in Fig.4 for the same percolation records. Normalized waste leachate flux verses time (Fig.4 (top)) compares values for the analytic solution to the averaged percolation rate *(flux-w-q(ave))* and the numerical transient solution for the time dependent percolation *(flux-w-q(t))*. The transient flux, given by Eqn.5, is very different from the analytic solution to the averaged percolation rate, owing to the direct dependence of flux on the aperiodic Darcy flux, q(t). The transient flux is nearly an order of magnitude larger than the averaged value at some points in time but occurs only during the occasional percolation years.

Figure 4 (bottom) shows the normalized waste package leachate flux verses time, comparing flux for the analytic solution to the averaged percolation rate for the single 50 yr percolation record *(flux-w-q(ave))* and for the average of the four 50 yr percolation records *(flux_qave)* and the numerical transient solution for the time dependent percolation averaged over four 50 year time series of percolation data

(flux_q(t)). The numerical solution to the transient case for the average of the four records is slowly approaching the analytic solution to the average percolation, however, the transient fluxes still differ from the average case typically by a factor of two and they occur only in the percolation years. Here, the averaging produces flux greater and less than the average flux value while the actual result for a single percolation record will most often exceed the average during percolation years and will be equal to zero in this simple model during years without percolation.

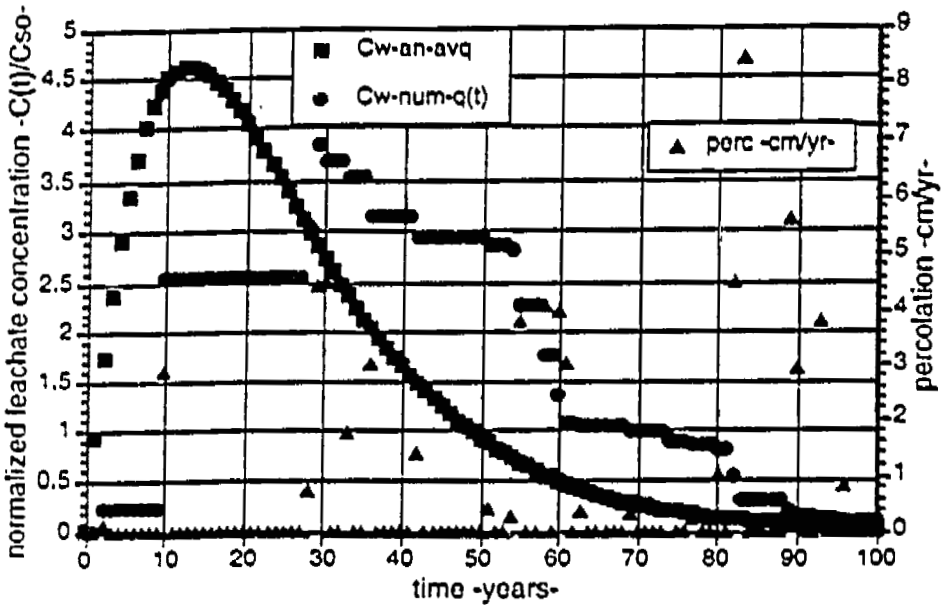

Fig.3 (top) Normalized leachate concentration and percolation verses time comparing concentrations for the analytic solution to the averaged percolation rate (Cw-an-avg) and the numerical transient solution for the time dependent percolation (Cw-num-q(t)).

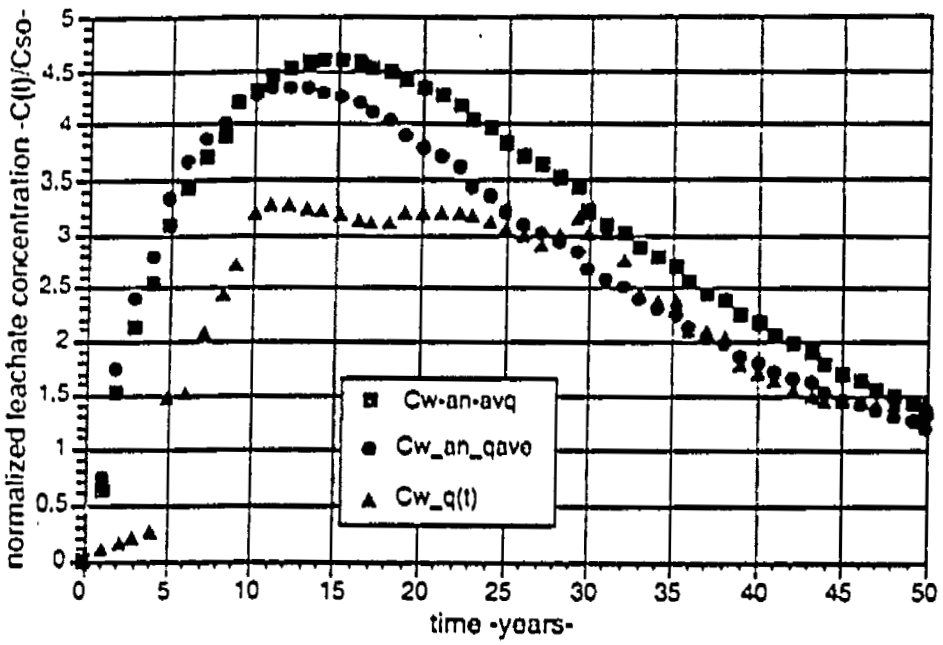

Fig.3 (bottom) Normalized leachate concentration verses time comparing concentrations for the analytic solution to the averaged percolation rate for a single 50 yr percolation record (Cw-an-avg) and for the average of four 50 yr percolation records (Cw_an_qave) and the numerical transient solution for the time dependent percolation averaged over four 50 year time series of percolation data (Cw_q(t)).

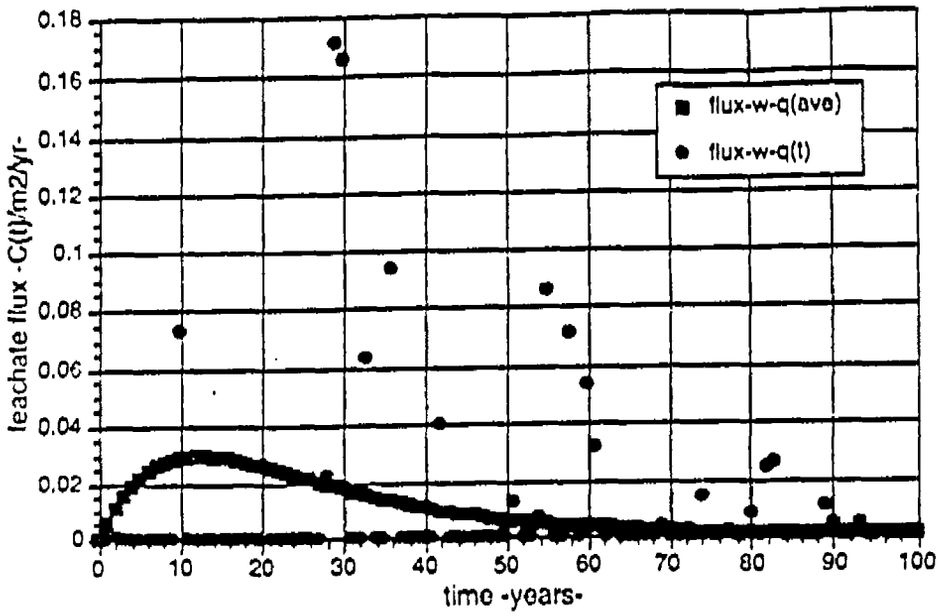

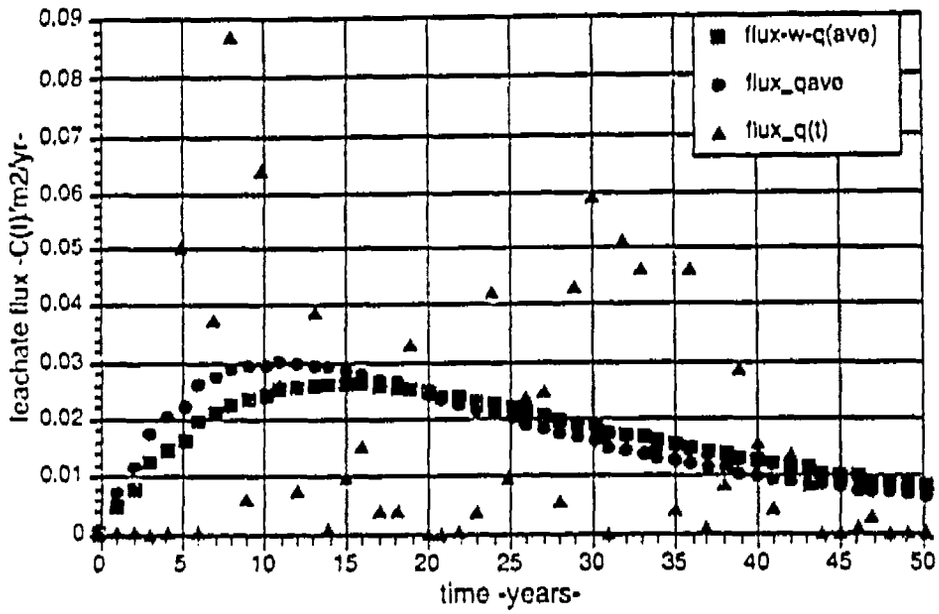

Fig.4 (top) Normalized waste package leachate flux verses time, comparing values for the analytic solution to the averaged percolation rate (flux-w-q(ave)) and the numerical transient solution for the time dependent percolation (flux-w-q(t)).
Fig.4 (bottom) Normalized waste package leachate flux verses time, comparing flux for the analytic solution to the averaged percolation rate for a single 50 yr percolation record (flux-w-q(ave)) and for the average of four 50 yr percolation records (flux_qave) and the numerical transient solution for the time dependent percolation averaged over four 50 year time series of percolation data (flux_q(t)).

DISCUSSION

Transient results show that in conditions approaching the extreme case, which might represent waste in a relatively shallow portion of the disposal unit, that the waste source release term fluctuates considerably and is periodic in time following the particular time sequence of the moisture pulses following individual percolation occurrences. The model however does not represent these extreme conditions accurately because the moisture transit time past a waste package, $T_w = h_w\theta_w/q_w(t)$, is assumed constant in space and is assumed to vary in time only through $q_w(t)$. Actually, there will be variations in space and time associated with each waste package, i.e., $q_w(z,t)$ and $\theta(z,t)$ will vary in time and in space even over the distance associated with the waste package height, h_w. This will tend to average the waste leachate efflux over the transit time and will dampen fluctuations on time scales shorter than the transit time, $T = h_w\theta_w/q_w(t) \sim 16$ *years* in the case for Area G. On the other hand, the transit time for averaging a typical transient (4cm/yr for one year) is much less, $T = (1)(0.08)/0.04) = 2$ *yr*.

As the depth of disposal increases, releases from the waste are expected to approach projected releases based on the steady-state percolation rate. Field data and numerical calculations on variations in moisture content profiles in the near surface unsaturated zone suggest that the percolation fluctuations dampen near the surface and that below about 2 m depth the variations are slight [10] and approach the averaged conditions assumed in the steady state model. Waste packages at different locations throughout the disposal unit will see the moisture transients at various phases of the passing moisture pulse. Leachate efflux from the disposal unit will be averaged over the differences associated with the larger disposal unit volume and will tend to dampen fluctuations on time scales shorter than $T = h_d\theta_d/q_d(t)$, where subscript d refers to 'disposal unit', and the typical height, h_d is 20m, thus tending to average out fluctuations on time scales less than about 300 years.

The results show that the transient solution approaches the analytic solution for the average percolation rate as the percolation sequences are averaged in time. This has two implications. One, the variations for a set of particular percolation sequences represent the envelope of expectations for what will actually occur in the next 50 years which will drive the release from the disposal facility. At the end of site operations, the actual precipitation and percolation data could be used to estimate the actual release. There is a second implication of the transient results if we also assume that the averaging in time is related to averaging in space. The variability in percolation at different points in space is known to be large [7]. If we assume this indicates a real variation over an area comparable to that of a disposal unit then the net efflux from the area of a disposal unit is an average and the actual percolation over space and time will approach that averaged solution for the 'time average' percolation rate. Within and beyond the volume of the disposal unit,

hydrodynamic dispersion will also act to average transients during transport to dose receptor sites.

APPLICATION TO THE AREA G SITE PERFORMANCE ASSESSMENT

The Area G inventory is divided into four segments based on the time of disposal (1959 to 1970, 1971 to 1988, 1988 to 1995, and 1996 to 2044) for dose consequence analyses [11]. The waste disposed of between 1988 and 2044 is included in the Area G Performance Assessment compliance evaluation. All of the waste is considered in analyses which partially satisfy DOE 'Composite Analysis' requirements for active disposal facilities. The four inventory groups are distinguished roughly as: 1959-1970; limited TRU-LLW segregation, no detailed data base records, inventory by extrapolation, 1971-1988; detailed data base for inventory, TRU and LLW distinguished, pre-compliance period, 1988-1995; detailed inventory data base to present date, compliance-driven, 1996-2044; future operations projected throughout the expected lab lifetime, compliance-driven. Inventory from 1971-1995 is segregated by disposal unit for the source release model and for the subsequent transport analyses, distinguishing over 30 disposal pits and four grouped 'shaft fields'. Extrapolated inventory (<71 and >96) is averaged over (past and planned) disposal units.

For each of the source term disposal units, the rapid release component of the waste inventory is specified by waste quantity, $Q_0(Ci)$, and waste package volume, $V(m^3)$. The curie concentration is converted to molar concentration and the maximum leachate concentration, $C_{w\text{-}max} = (0.37C_{so}/\theta)$, is compared to the elemental solubility limit. Where $C_{w\text{-}max}$ is less than the solubility limit, the nuclide is considered to be inventory limited and the integrated release from the waste packages, Φ_w, for a particular nuclide from each disposal unit is calculated by integrating Eqn.4 over waste package area to obtain,

$$\Phi_w[Ci/yr] = Q_0(Ci)\, \lambda_w^2\, t\; e^{-\lambda_w t}. \qquad (6)$$

This release (and subsequent maximum concentrations and dose assessments) depends upon inventory quantity but is independent of inventory volume or concentration.

If $C_{w\text{-}max}$ is predicted to exceed the elemental solubility limit, C_{sl}, the total leachate concentration by element will be limited to C_{sl} and the actual leachate concentration by nuclide will be some fraction of C_{sl} where the fraction, f_{sl}, depends upon the contributions to that elemental solubility limit from other nuclides of the same element. The integrated leachate flux from the waste packages during the solubility limited release is

$$\Phi_w[Ci/yr] = A_w q_w f_{sl} C_{sl} = \frac{V_w}{h_w} q_w f_{sl} C_{sl}. \qquad (7)$$

The duration, Dt_{sl}, of release at this rate is

$$\Delta t_{sl} = \frac{Q_o f_{sl}}{\Phi_w} = \frac{Q_o}{V_w}\frac{h_w}{q_w}\frac{f_{sl}}{f_{sl} C_{sl}} = \frac{h_w}{q_w}\frac{C_o}{C_{sl}}. \qquad (8)$$

Following this duration, the release will be briefly inventory limited and follow Eqn.6. This leads to a rapid decrease in release rate and so the solubility limited release rate can be realistically approximated as a step function with step height given by Eqn.7 and duration ending at Δt_{sl}. This release for solubility limited nuclides scales as the total nuclide inventory volume, V_w, because the release rate is limited to the fixed concentration, C_{sl}. The initial waste concentration (at disposal time), $C_o = Q_o/V_w$, does not play a direct role in the integral source strength for either release case, but does determine the duration of a solubility limited release.

Previous analysis [3] indicated that only a few nuclide elements which were shown to be of significance in the site dose assessment were also consistently solubility limited. These included uranium and thorium. The nuclide fraction of the solubility limit, f_{sl}, is found to be an important correction only for the uranium inventory. This factor is evaluated as a sum over waste forms of the fraction of the elemental solubility limit attributed to a particular nuclide in a particular waste form, normalized to the nuclide quantity (as a volume) in the rapid release waste form category. This allows a straightforward correction for the uranium nuclides from the 'rapid release' inventory tabulated for the source term evaluation by individual disposal unit.

Extending the previous analysis to individual disposal units identifies specific pits and shafts where solubility limits are exceeded. Plutonium and americium become solubility limited in a few disposal units including the shaft fields, often reserved for disposal of waste with greater specific activity. The realistic spatial distribution of the disposal units with the individual source terms which are either inventory or solubility limited serve as input to the detailed 3-D unsaturated zone modeling effort underway as part of the performance assessment [8].

CONCLUSIONS

Phase Two source release modeling acknowledged previous results that the 'rapid release' waste category is critical, and therefore deserves a more self-consistent treatment of the percolation and transition from the solid to the liquid phase in the waste package leachate. This leads to new analytic expressions for the case of inventory limited release which has been applied to the Area G Site Performance Assessment in calculations incorporated directly into the 2-D and 3-D unsaturated zone transport model. Elemental solubility limits dictate which nuclide waste is

'inventory-limited' and which is 'solubility limited' on an individual disposal unit basis. The integrated release for the inventory limited case is proportional to the total inventory in a given disposal unit while the solubility limited release is proportional to the inventory volume and the solubility limited duration is proportional to the waste inventory concentration.

Transients in release rates due to time varying percolation rates were examined and found to potentially impact the results considerably. The results bracket the uncertainty due to percolation, but probably overestimates the variability in the real case. The release model does not accurately represent some detailed aspects of the transient case and many factors in the real situation, including hydrodynamic dispersion and spatial and temporal variability in percolation, are likely to average the actual release rates and tend to smooth the results towards those predicted by the analytic model using the average percolation rates.

ACKNOWLEDGMENT

This work is sponsored by the U.S. Department of Energy, Waste Management Program Office.

REFERENCES

1. D. Hollis, E. Vold, K. Birdsell, J. Turin, P. Longmire, E. Springer, W. Hansen, D. Krier, R. Shuman, "Performance Assessment of LANL TA-54, Area G, LLRW Disposal Facility - Preliminary Draft", Los Alamos National Laboratory, Los Alamos, NM, August, 1995.

2. E. Vold, "A Source Release Model with Application to the LANL LLRW Disposal Site Performance Assessment, Los Alamos National Laboratory Report LAUR-95-2060, see also App 3B to ref.1, Los Alamos, NM, accepted in proceedings of the MRS Symposium on the Scientific Basis for Nuclear Waste Management, Boston, Nov.1995.

3. Vold, E.L., Shuman, R., Hollis. D., Longmire, P., Springer. E., Birdsell, K., The Role of a Detailed Aqueous Phase Source Release Model in the LANL Area G Performance Assessment, proceedings of the USDOE Waste Management Conference, Tucson, AZ, Feb.1996, Los Alamos National Laboratory Report LA-UR-95-3099, Los Alamos, NM, 1995.

4. K. Birdsell, W. Soll, N. Rosenberg, B. Robinson, "Numerical Modeling of Unsaturated Groundwater Flow and Radionuclide Transport at MDA G", Los Alamos National Laboratory Report LA-UR-95-2735, Los Alamos, NM, 1995.

5. Loaiza, D. and Vold, E., Moisture Profile Measurements in Subsurface Monitor Holes at the Los Alamos LLRW Disposal Site, Los Alamos National Laboratory Report LAUR-95-1922, Los Alamos, NM, 1995.

6. E. Springer, "Area G Performance Assessment: Surface Water and Erosion", Los Alamos National Laboratory Report LA-UR-95-2497, see also App.3D to ref.1, Los Alamos, NM, 1995.

7. E. Vold, B. Newman, K. Birdsell, B. Gallaher, D. Krier, P. Longmire, D. Rogers, E. Springer, "Representative Recharge Rates in a Complex Unsaturated Hydrogeology", presented at Waste Management '97, DOE Conference, Tucson, Az., February, 1997, Los Alamos National Laboratory Report LA-UR-96-4787, Los Alamos, NM, 1997.

8. K. Birdsell, W. Soll, K. Bower, A. Wolfsberg, T. Orr, and T. Cherry, "Simulations of Groundwater Flow and Radionuclide Transport in the Vadose and Saturated Zones Beneath Area G", Los Alamos National Laboratory Report LA-UR-97-157, Los Alamos, NM, 1997.

9. D. Krier, P. Longmire, R. Gilkeson, H.J.Turin, "Geologic, Geohydrologic, and Geochemical Data Summary of MDA G, TA-54, LANL", Los Alamos National Laboratory Report LA-UR-95-2696, see also App.2A to ref.1, Los Alamos, NM, 1995.

10. International Technology Corporation, "Hydrologic Assessment of Technical Area 54, Areas G and L, Los Alamos National Laboratory", Final Report, Docket Number NMHWA 001007, Los Alamos National Laboratory, Los Alamos, NM, March, 1987.

11. R. Shuman, "Radioactive Waste Inventory for the TA-54, Area G Perfromance Assessment and Composite Analysis", Rogers and Assoc. Engineering Report, RAE-9148/82-1, Salt Lake City, UT, prepared for the LANL Area G Performance Assessment, Oct., 1996.

LA-UR-96-368

Title: The Role of a Detailed Aqueous Phase Source Release Model in the LANL Area G Performance Assessment

Author(s): E. L. Vold, D. Hollis, P.Longmire, E. Springer, K.Birdsell - LANL

R. Shuman - RAE

Submitted to:

1. U.S. Department of Energy, as support documentation for the Los Alamos Area G Performance Assessment

2. Waste Management '96 USDOE Conf., Tucson, AZ, Feb. 1996.

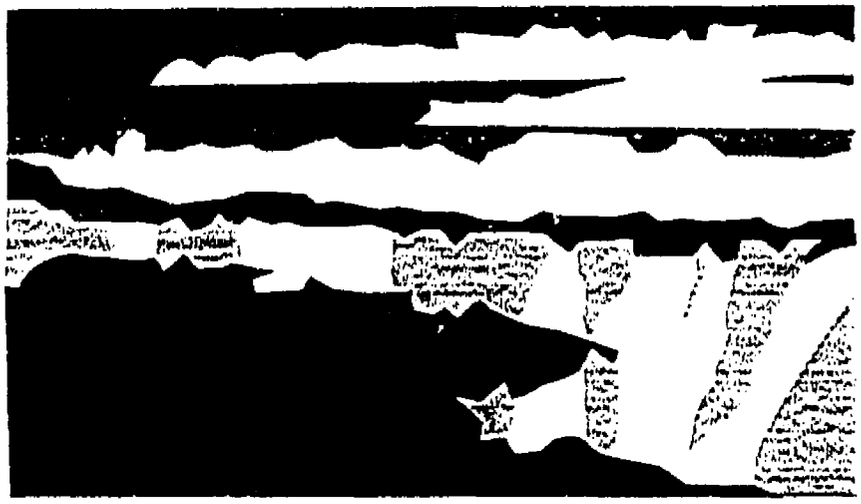

Los Alamos
NATIONAL LABORATORY

Los Alamos National Laboratory, an affirmative action/equal opportunity employer, is operated by the University of California for the U.S. Department of Energy under contract W-7405-ENG-36. By acceptance of this article, the publisher recognizes that the U.S. Government retains a nonexclusive, royalty-free license to publish or reproduce the published form of this contribution, or to allow others to do so, for U.S. Government purposes. The Los Alamos National Laboratory requests that the publisher identify this article as work performed under the auspices of the U.S. Department of Energy.

THE ROLE OF A DETAILED AQUEOUS PHASE SOURCE RELEASE MODEL IN THE LANL AREA G PERFORMANCE ASSESSMENT

E.L. Vold, D. Hollis, P.Longmire, E. Springer, K. Birdsell
Los Alamos National Laboratory, Los Alamos, NM

R. Shuman
Rogers Engineering Assoc., Salt Lake City, UT

ABSTRACT

The Performance Assessment for the LANL Low-Level Radioactive Waste (LLRW) Disposal Facility, Area G, is on-going. A detailed review of the inventory data base records and the existing models for source release led to the development of a new modeling capability to describe the liquid phase aqueous transport from the waste package volumes. Inventory is sorted into four release form categories and screened in a comparison of leachate concentrations to the drinking water limit. Percolation through the disposal unit is prescribed in an independent surface water balance model incorporating site rainfall statistics. Waste package types and the disposal unit matrix have independently specified solubility limits and solid-liquid phase partition coefficients, or Kd values. Analytic solutions for inventory limited release of each nuclide in each of the four different waste package release forms are computed. Isotopic contributions are summed over elements to limit the waste package liquid phase concentrations to the elemental solubility limits. Time dependent releases from the waste packages for each nuclide which may be inventory or solubility limited are specified as model output which is provided as the source term to the unsaturated transport model. The waste package efflux is distributed over the 2-D unsaturated zone model grid points corresponding to the cross-sections for 5 representative disposal units within the mesa top. Results show the Area G release is dominated by the inventory in the 'rapid release waste form' (Kd = 0), which percolates from the waste packages over 5-100 years and from the disposal unit over 50-1000 years. Nuclides in waste package categories with larger Kd values are released proportionately slower. Uranium and thorium are the main nuclides of concern released as solubility limited nuclides from the 'historical inventory' at Area G. The analytic models provide an efficient means to explore the sensitivity of the results to variations and uncertainty in the model parameter values.

INTRODUCTION

A preliminary draft of the site Performance Assessment (PA) for the Los Alamos National Laboratory (LANL) low level radioactive waste (LLRW) disposal facility at Area G has been completed[1] as required per DOE orders. A detailed review of the inventory data base, records and existing models for source release led to the development of a new modeling capability[2] to describe the liquid phase aqueous transport from the waste package volumes. The code output, a time dependent efflux to the disposal unit volume (as detailed in App.3B to ref.[1]), is provided as input to a sophisticated 2-D unsaturated flow model[3] for subsequent transport within the disposal unit and throughout the vadose zone.

The Area G disposal facility is located on the top of a narrow finger-like mesa composed of volcanic tuff (Bandelier Tuff), deposited in stratigraphic layers of ash and solidified volcanic flows. Waste disposed at Area G is placed into pits excavated in the volcanic tuff, crushed in place, and backfilled with the native crushed tuff to about 30% waste package and 70% tuff by volume. These disposal operations are evolving to minimize future disposal volume, and to assure stability of emplaced waste.

Disposal operations at Area G began in 1959 and disposal inventory is established in a detailed electronic data base dating back to 1972. (Disposal for operations prior to that date is recorded in log books currently being transcribed to a new data base.) Nuclide quantities are associated with 50 waste codes, which characterize the physical and chemical form of the waste.

ANALYSES

These waste codes were sorted into four waste package release categories, based on preliminary modeling efforts which indicated the release characteristics of concern. The four release categories include rapid release (with compartment release time of one year, and with solid-liquid phase partition coefficient, Kd, set equal to zero, taking no credit for solid phase reabsorption), soil (Kd for Bandelier tuff at neutral pH), concrete/sludge (Kd for concrete at pH=12, and corrosion associated with metal waste forms (with compartment release time of three hundred years, and with Kd=0).

Of the 60 inventory nuclides listed with half-life greater than 5 years, 30 were screened out in a 'leachate screening', and 30 were followed in detail by the source release model. The leachate screening compared the total inventory concentration in the disposal unit moisture to the drinking water concentrations that result in 4mrem/yr at the standard ingestion rate. Of the 30 nuclides followed in detail, 15 were decay chain parents, with 48 non-secular equilibrium decay chain products evolved self-consistently.

Geochemistry for the waste packages was evaluated in terms of the equilibration coefficients, Kds, and elemental solubility limits, Csl, interpolated from the literature by Longmire[4]. Yucca Mountain Kds[5,6] were used as best estimates for Kds in tuff and as conservative estimates in soil, justified by a favorable comparison of water chemistry between Bandelier and Yucca Mountain tuff samples[4]. Solubility limits for tuff[7] were applied to all waste packages except waste in concrete/sludge, where values taken from the literature[8] were applied. A program to evaluate site-specific Kds under field conditions is underway at Los Alamos. This will include five key nuclides in several Bandelier Tuff stratigraphies and over a range of water chemistry.

Percolation calculations were run with a modified version of the SPUR code[9] which does a detailed water balance at the surface. Results for the base case closure cover, 90 cm of crushed tuff, 10cm soil and a thin gravel-mulch seeded surface, showed an average of 4mm/yr percolation from the disposal unit bottom[10]. Recent results with revised crushed tuff hydrologic properties show an infiltration rate of 5.5mm/yr. The statistical analysis shows the average percolation rate is for a highly skewed distribution composed of 80% values equal to zero. The implications on the source release model of the actual distribution rather than the average value are under investigation. A range of infiltration model parameter variations were evaluated to account for evapotranspiration including rooting depth and leaf area index, and for run-off including surface slope and other factors important in the surface water balance[10].

The waste release model is based on a compartment representation of the package efflux, and depends upon package size, percolation rate or Darcy flux, retardation coefficient, and moisture content. The physical and conceptual flow models are shown in Fig.1, where the concentration and flux symbols are defined. An analytic solution for waste package efflux under inventory-limited conditions (everything which is not solubility limited) is evaluated for each nuclide in each waste package type (or release category). This is described in detail elsewhere[2] with the result for the waste package liquid phase compartment concentration, C_w, written as

$$C_w(t) = \frac{C_{s0}}{\theta_w R_w} \frac{\lambda_s}{(\lambda_w - \lambda_s)} \frac{V_s}{V_w} \left(\exp(-\lambda_s t) - \exp(-\lambda_w t) \right) \qquad (1)$$

with

$$\lambda_s = \frac{A_s u_s}{V_s} = \tau_s^{-1}; \qquad \lambda_w = \frac{A_w q_w}{V_w \theta_w R_w}. \qquad (2)$$

The compartment subscripts are shown in Fig.1, and the λ values are 'compartment clearance rates' derived by a control volume integration of the continuity equation defined in terms of the compartment area, A (horizontal planar area), volume, V,

Darcy percolation rate, q, dissolution velocity, u, moisture volumetric content, θ, and retardation coefficient, R, related in the usual way to the solid-liquid phase partition coefficient, Kd, as $R = 1 + \rho K_d/\theta$. Using this time dependent concentration, the waste compartment efflux, Γ_w, is

$$\Gamma_w = A_w q_w C_w. \quad (3)$$

Nuclide contributions to the same element, including ingrowth from decay chains, are summed to compare to the elemental solubility limits in each waste package type. Waste package concentrations for each nuclide of the solubility limited elements are partitioned to the contributing nuclides. The solubility limited waste package efflux for a nuclide is

$$\Gamma_w = A_w q_w f_{sli} C_{sl}, \quad (4)$$

where C_{sl} is the elemental solubility limit and f_{sli} is the fraction of the solubility limit which is contributed by that specific nuclide. This fraction is assumed equal to the nuclides contribution to the elemental solubility limit at the time when that limit is first exceeded.

Solubility limited effluxes continue until the solid phase waste package concentration is depleted to the point the water phase concentration can no longer exceed a solubility limit, and subsequently the waste package is depleted at the inventory-limited release rate[2]. An algorithm of how the solubility limits are tracked over nuclides, elements and waste package types is included as Table I.

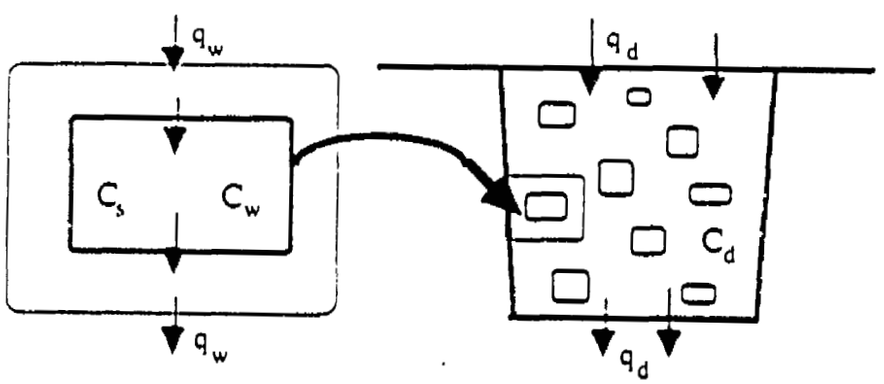

Fig. 1a. Conceptual model for subsurface liquid phase release from a disposal unit. A representative waste package is shown to the left, and a disposal unit is shown on the right.

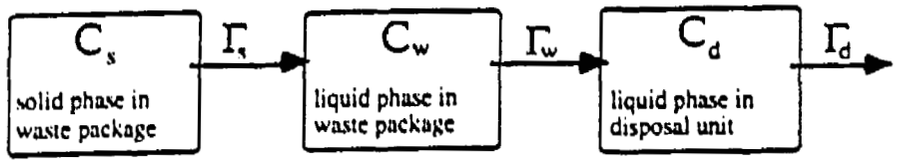

Fig. 1b. The three compartments in the release model are an equivalent representation of the conceptual model from Fig.1a, showing contaminant concentrations, C, and flux, Γ for the three compartments.

Table I
Algorithm for Model Implementation Over Nuclides and Waste Package Forms.

1. Calculate $C_s(t)$, $C_w(t)$, and $C_d(t)$ using inventory release limited equations for all time for each nuclide and for each waste form.
   A. inventory nuclides - analytic solutions
   B. decay chain daughters - numerical solutions

2. Sum all nuclide contributions (inventory and daughter products) to each element concentration for each waste form.

3. Determine time, tsl1, when solubility limit first applies for each waste form, when C_w(for element sum) > C_{sl}(element).

4. Interpolate (in time) to get C_w(tsl1) for each nuclide and each waste form which is solubility limited.

5. Calculate $C_s(t)$ and $C_d(t)$ under solubility limited equations
   A. inventory nuclides - analytic eqns
   B. daughter nuclides - numeric solution to eqns

6. Sum nuclide contributions to elemental concentrations per waste form.

7. Determine time, tsl2, when C_s(element) is depleted to point where solution is no longer solubility limited, when $C_s < C_{sl}\, q_w A_w/(u_s A_s)$.

8. Interpolate in time to get C_w(tsl2) for all nuclides for each waste form.

9. Continue from t = tsl2 to t_{end}, calculating $C_s(t)$, $C_w(t)$, $C_d(t)$ using the inventory limited equations.

The release model was tested extensively as described previously[1,2]. The analytic models described above were supplemented with numerical modeling in two areas. One, the ingrowth of progeny nuclides which can have transport properties different from the parent nuclides makes the analytic solutions to the compartment model impractical. Ingrowth of progeny is calculated numerically in a simple implicit scheme which implements the compartment governing equations with the added complexity of progeny ingrowth. This was used in the present modeling effort to account for 'daughter-product' ingrowth which could contribute to the solubility limit within a waste package. From the perspective of nuclide transport in the site PA work, ingrowth within the packages was considered negligible, and ingrowth was modeled within the disposal unit and in the unsaturated zone within the 2-D unsaturated model[3] because that code has had more extensive QA and verification.

A second numerical modeling effort examined the compartment solutions where the waste package efflux feeds a one-dimensional (vertical axis) representation of the disposal unit. In this case, release from the disposal unit is controlled by the vertical gradient at the disposal unit bottom which evolves consistently along the vertical axis from waste packages homogeneously distributed throughout the disposal unit. This work confirmed that the global or compartment model results were reasonably accurate compared to results with 1-D profile effects in the disposal unit[2].

RESULTS

Figure 2 shows the concentrations verses time inside the waste package matrix. The solid concentration, C_s, is uncorrected for readsorption in the solid phase and corresponds to the case where Kd = 0. The actual solid phase concentration corrected for readsorption inside the waste package and assuming a nuclide with Kd = 0.5 is shown as 'Csmod', based on a governing equation derived elsewhere[2]. Csmod decays over the time scale for 'rapid release' to an equilibrium plateau at a fraction, $(\rho_m Kd/\theta/(1+\rho_m Kd/\theta))$, of the original solid phase concentration. It then decays to zero over the time scale for percolation from the waste package, along with the waste package liquid phase concentration, Cw. If this nuclide becomes solubility limited, the Csmod concentration is needed to accurately track the solubility limited release through the solubility limited release duration.

For the 'historical inventory' (1988 to the present) and site conditions at Area G, most nuclides are found to be inventory limited. An important result observed from the source release model is that for inventory limited nuclides, it is the component of inventory which is considered to be 'rapid release' which dominates the efflux function of time. All other release forms effect slower release rates which therefore reduce the efflux peak in time. The eventual peak in the aquifer concentration is determined by this release model modified by translation and dispersion during transport through the unsaturated and saturated zones.

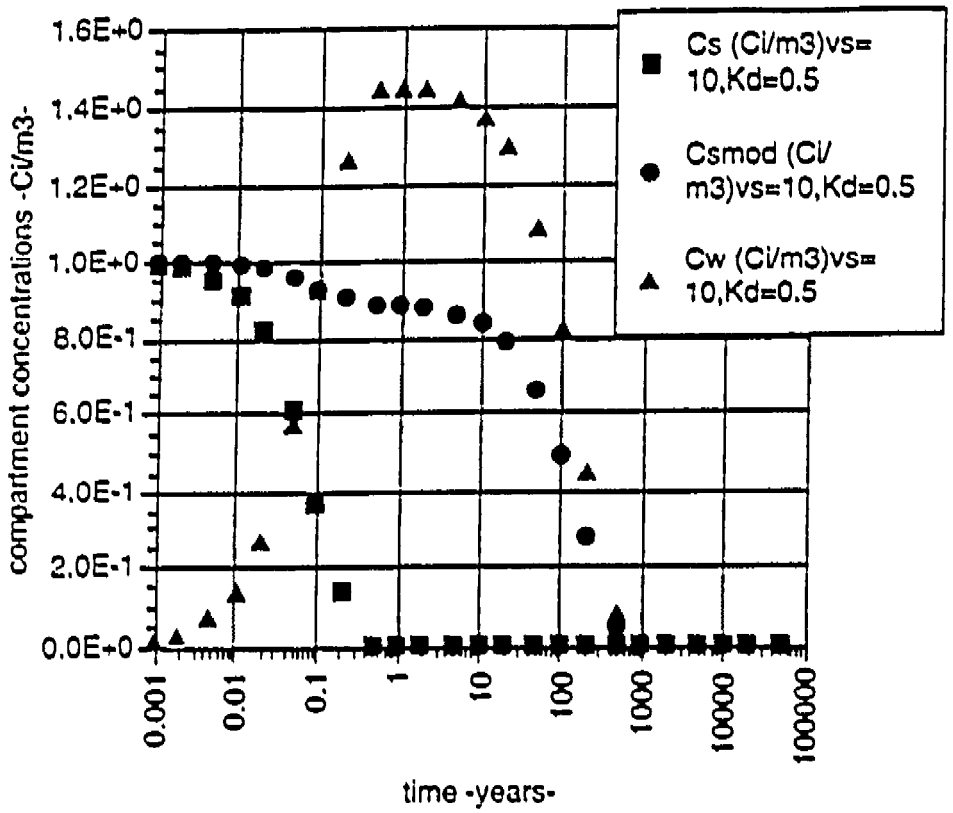

Fig.2 The solid phase concentration, Cs, is modified for reabsorption, Cs-mod, and decays to an equilibrium plateau over the time scale for 'rapid release'. It then decays to zero over the time scale for percolation from the waste package, along with the waste package liquid phase concentration, Cw.

These concepts are illustrated in Fig. 3, which shows the inventory release, Ci/yr, as a function of time for four of the plutonium isotopes in the Area G inventory. The peak release rate for each nuclide is dominated by the 'rapid release' (Kd = 0) waste package source term which occurs at about 3-5 years. Contributions to each nuclide from the other waste package release forms have relatively slower release rates due to effects of solid-liquid partitioning and readsorption (Kd > 0), and are seen in the Figure as the 'bumps' which occur later in time from 200-10,000 years. Because these release rates are so small, the contribution from these waste package types to the peak release rate is small even if their inventory is comparable to that in the 'rapid release' category.

For the Area G inventory and site conditions, the only nuclides which contribute significantly to dose and are solubility limited are uranium and thorium. Uranium is depleted at a solubility limited rate which is sufficient to reduce the concentrations to an inventory-limited release at about 5000 years, after which the

source decreases rapidly to negligible levels. This is illustrated in Fig.4 for three isotopes of uranium. As in the inventory limited case in Fig.3, there are contributions from multiple waste package types. The most inventory is in the 'rapid release' form which is solubility limited until about 5000 years. Imposed on top of this is a contribution from another waste form (concrete/sludge) which is also solubility limited but is depleted at about 500 years. Most of the uranium in this form is U-235, so only that isotope is noticeably influenced by the second waste form.

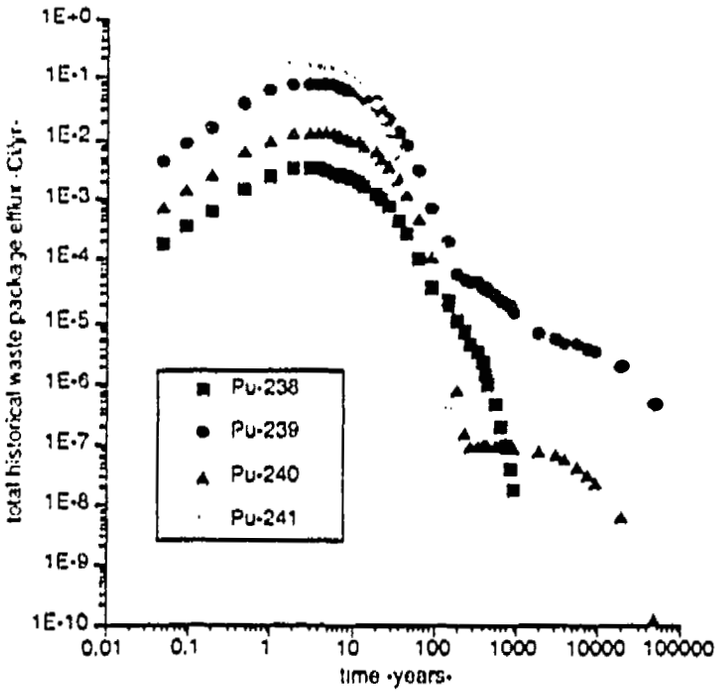

Fig. 3 Area G results for the historical inventory showing the total waste package efflux in Ci/yr for four inventory-limited plutonium isotopes. These curves correspond to the source term (moles/yr) input to the unsaturated zone 2-D transport model of Area G.

The thorium solubility limit is so small that the release remains solubility limited effectively for all time. Plutonium is close to the solubility limit and would become solubility limited under slightly increased disposal concentrations.

Uncertainties in the results are examined via parametric examination of the input variables, and will be discussed in some detail[1,2]. Variability due to transient percolation effects is currently under investigation. Spatial variation in percolation rate or percolation differences within the disposal unit matrix verses within the waste package itself are being evaluated.

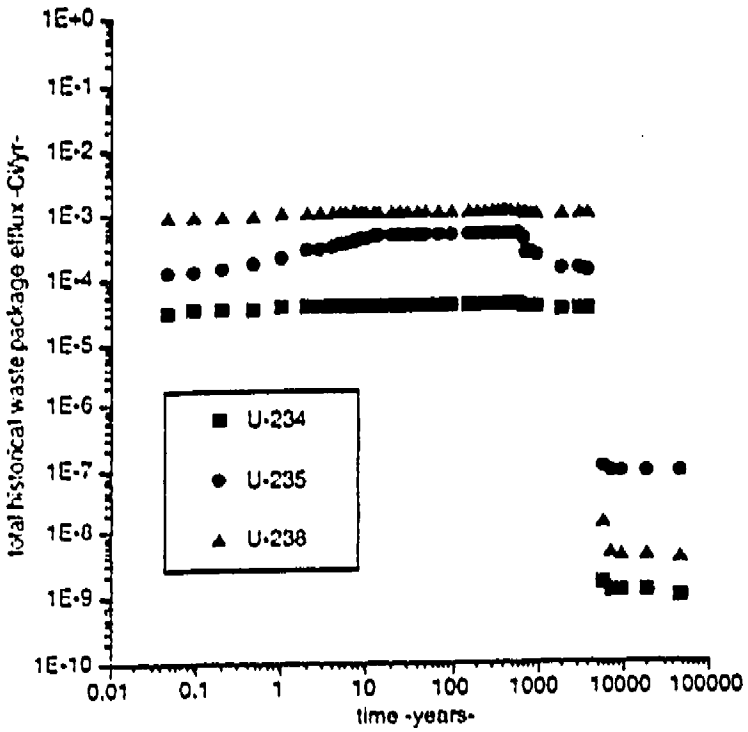

Fig. 4 Area G results for the historical inventory showing the total waste package efflux in Ci/yr for three solubility limited nuclides of uranium. These curves correspond to the source term (moles/yr) input to the unsaturated zone 2-D transport model of Area G.

CONCLUSIONS

The results of a site Performance Assessment depend critically upon the source release model and its input data. The maximum concentrations in the time dependent efflux from the waste package will be integrated over the disposal unit volume and then translated through the vadose zone and diluted in the aquifer while being modified slightly for dispersion and diffusion during the aqueous phase transport. Thus, it is a modification of the time dependent source release which will determine the receptor location concentrations and ingestion dose.

ACKNOWLEDGMENT

This work is sponsored by the U.S. Department of Energy, Waste Management Program Office.

REFERENCES

1. D. Hollis, E. Vold, K. Birdsell, J. Turin, P. Longmire, E. Springer, W. Hansen, D. Krier, R. Shuman, "Performance Assessment of LANL TA-54, Area G, LLRW Disposal Facility - Preliminary Draft", Los Alamos National Laboratory, Los Alamos, NM, August, 1995.

2. E. Vold, "A Source Release Model with Application to the LANL LLRW Disposal Site Performance Assessment, Los Alamos National Laboratory Report LAUR-95-2060, see also App 3B to ref.1, Los Alamos, NM, accepted in proceedings of the MRS Symposium on the Scientific Basis for Nuclear Waste Management, Boston, Nov.1995.

3. K. Birdsell, W. Soll, N. Rosenberg, B. Robinson, "Numerical Modeling of Unsaturated Groundwater Flow and Radionuclide Transport at MDA G", Los Alamos National Laboratory Report LA-UR-95-2735, Los Alamos, NM, 1995.

4. D. Krier, P. Longmire, R. Gilkeson, H.J.Turin, "Geologic, Geohydrologic, and Geochemical Data Summary of MDA G, TA-54, LANL", Los Alamos National Laboratory Report LA-UR-95-2696, see also App.2A to ref.1, Los Alamos, NM, 1995.

5. I.R. Triay, C.R. Cotter, S.M. Kraus, M.H. Huddleston, S.J. Chipera, D.L. Bish, "Report on Radionuclide Sorption in Yucca Mountain Tuffs with J-13 Well Water: Neptumium, Uranium, and Plutonium Milestone #3338", Los Alamos National Laboratory draft report, 12p. Los Alamos, NM 1994.

6. K. Wolfsberg, "Sorptive Properties of Tuff and Nuclide Transport and Retardation" in J.K.Johnstone and K.Wolfsberg, Eds., Evaluation of Tuff as a Medium for Nuclear Waste Repository: Interim Status Report on the Properties of Tuff, Sandia National Laboratory Report SAND80-1464, p.39-48, Albuquerque, NM 1980.

7. Nitsche, H., Gatti, R.C., Standifer, E.M., Lee, S.C., Muller, A., Prussin, T., Deihammer, R.S., Maurer, H., Becraft, K., Leung, S., Carpenter, S.A., "Measured Solubilities and Speciation of Neptumium, Plutonium, and Americium in a Typical Groundwater (J-13) from the Yucca Mountain Region, Milestone Report 3010-WBS 1.2.3.4.1.3.1", Report LA-12562-MS, Los Alamos National Laboratory, Los Alamos, NM 1993.

8. Ewart, F.T., Pugh, S.Y., Wisbey, S.J., Woodwark, D.R., "Chemical and Microbial Effects in the Near Field: Current Status 1989, Harwell Laboratory UKAEA, Report No. G/111, 65p., Harwell, UK 1989.

9. SPUR (Simulation of Production and Utilization of Rangelands) model ref: J.R. Wight, and J.W. Skiles, eds., SPUR (Simulation of Production and Utilization of Rangelands) Documentation and User Guide, U.S. Dept. of Agriculture, Agricultural Research Service, ARS 63, 372 pp., 1987.

10. E. Springer, "Area G Performance Assessment: Surface Water and Erosion", Los Alamos National Laboratory Report LA-UR-95-2497, see also App.3D to ref.1, Los Alamos, NM, 1995.

11. G. Zyvoloski, B. Robinson, Z.Dash, L. Trease, "Models and Methods Summary for the FEHMN Application", Los Alamos National Laboratory Report LA-UR-94-3787, Los Alamos, NM, 1995.

RAE-9629/91B-1

RADIOLOGICAL DOSE ASSESSMENT FOR THE TA-54, AREA G PERFORMANCE ASSESSMENT AND COMPOSITE ANALYSIS

Rob Shuman

Prepared for

Los Alamos National Laboratory
CST-14, Solid Radioactive Waste Management
Mail Stop J595
Los Alamos, NM 87545

March 1997

Rogers & Associates Engineering Corporation
P.O. Box 330
Salt Lake City, UT 84110-0330

This page intentionally left blank.

TABLE OF CONTENTS

Chapter		Page No.
1	INTRODUCTION	1-1
2	DOSE ASSESSMENT METHODOLOGY	2-1
	2.1 Human Exposure Pathways and Scenarios	2-1
	2.1.1 Operational and Active Institutional Control Periods	2-2
	2.1.2 Industrial Use Period	2-7
	2.2 Models and Data	2-18
	2.2.1 Radionuclide Inventory Projections	2-18
	2.2.2 Environmental Transport Pathways	2-22
	2.2.3 Human Exposure and Dose Projections	2-43
3	DOSE ASSESSMENT RESULTS	3-1
	3.1 Performance Assessment	3-1
	3.1.1 Offsite Dose Assessment Results	3-1
	3.1.2 Inadvertent Intruder Dose Assessment Results	3-14
	3.2 Composite Analysis	3-27
	3.2.1 All Pathways - Groundwater Scenario	3-33
	3.2.2 Atmospheric Scenario	3-33
	3.2.3 All Pathways -- Parajito Canyon Scenario	3-37
	3.3 Area G Dose Assessment Summary and Compliance Assessment	3-37
	3.3.1 Performance Assessment Dose Summary and Compliance Evaluation	3-42
	3.3.2 Composite Analysis Dose Summary and Compliance Evaluation	3-45

TABLE OF CONTENTS
(Continued)

Chapter			Page No.
4	SENSITIVITY AND UNCERTAINTY		4-1
	4.1	Offsite Exposure Scenarios	4-2
	4.1.1	Groundwater Resources Protection Scenario	4-3
	4.1.2	Atmospheric Scenario	4-18
	4.1.3	All Pathways Exposure Scenarios	4-30
	4.1.4	Summary of the Offsite Scenario Sensitivity and Uncertainty Analysis	4-43
	4.2	Inadvertent Intruder Exposure Scenarios	4-70
	4.2.1	Radionuclide Inventories	4-71
	4.2.2	Source Releases and Environmental Transport	4-74
	4.2.3	Resource Utilization	4-79
	4.2.4	Radionuclide Dose Conversion Factors	4-79
	4.2.5	Summary of Intruder Sensitivity and Uncertainty Analysis	4-80
REFERENCES			R-1

LIST OF FIGURES

Figure No.		Page No.
3-1	Projected performance assessment doses for the Groundwater Resource Protection Scenario 100 m downgradient of the Area G disposal units	3-3
3-2	Projected performance assessment doses for the Groundwater Resource Protection Scenario in Parajito Canyon	3-4
3-3	Projected performance assessment doses for the All Pathways - Groundwater Scenario	3-6
3-4	Projected performance assessment doses for the Atmospheric Scenario	3-8
3-5	Radionuclide contributions to the peak performance assessment dose for the Atmospheric Scenario	3-10
3-6	Ra-226 and Ra-228 concentrations in historic pit and shaft waste	3-11
3-7	Ra-226 and Ra-228 concentrations in future pit and shaft waste	3-13
3-8	Projected performance assessment doses for the All Pathways - Parajito Canyon Scenario	3-15
3-9	Projected performance assessment doses from historic pit waste for the Intruder-Agriculture Scenario	3-18
3-10	Radionuclide contributions from historic pit waste to the peak performance assessment intruder dose	3-19
3-11	Projected performance assessment doses from historic shaft waste for the Intruder-Agriculture Scenario	3-23
3-12	Radionuclide contributions from historic shaft waste to the peak performance assessment intruder dose	3-24
3-13	Projected performance assessment doses from future pit waste for the Intruder-Agriculture Scenario	3-26
3-14	Radionuclide contributions from future pit waste to the peak performance assessment intruder dose	3-28
3-15	Projected performance assessment doses from future shaft waste for the Intruder-Agriculture Scenario	3-30

LIST OF FIGURES
(Continued)

Figure No.		Page No.
3-16	Radionuclide contributions from future shaft waste to the peak performance assessment intruder dose	3-31
3-17	Projected composite analysis doses for the All Pathways - Groundwater Scenario	3-34
3-18	Projected composite analysis doses for the Atmospheric Scenario	3-36
3-19	Radionuclide contributions to the peak composite analysis dose for the Atmospheric Scenario	3-38
3-20	Projected composite analysis doses for the All Pathways - Parajito Canyon Scenario	3-39
3-21	Radionuclide contributions to the peak composite analysis dose for the All Pathways - Parajito Canyon Scenario	3-40
4-1	Projected performance assessment doses for the Groundwater Resource Protection Scenario east-southeast of the Area G disposal units for different flow conditions	4-13
4-2	Projected performance assessment doses for the Groundwater Resource Protection Scenario in Parajito Canyon for different flow conditions	4-14
4-3	Projected performance assessment doses for the All Pathways - Groundwater Scenario for different flow conditions	4-34
4-4	Projected composite analysis doses for the All Pathways - Groundwater Scenario for different flow conditions	4-35
4-5	Projected performance assessment doses for the All Pathways - Parajito Canyon Scenario for different flow conditions	4-36
4-6	Projected composite analysis doses for the All Pathways - Parajito Canyon Scenario for different flow conditions	4-38

LIST OF TABLES

Table No.		Page No.
2-1	Offsite exposure scenarios for the operational and active institutional control periods	2-3
2-2	Offsite exposure scenarios for the industrial use periods	2-9
2-3	Intruder exposure scenarios considered for the Area G performance assessment	2-14
2-4	Pathway input parameters for food-chain exposure modeling	2-30
2-5	Element-specific input parameters for food-chain exposure modeling	2-31
2-6	Food chain parameters used in the tritium models	2-35
2-7	Ingestion, inhalation, and air immersion dose conversion factors	2-45
2-8	Exposure times for the inadvertent intruder and members of the public	2-50
3-1	Pathway contributions to the peak projected performance assessment dose for the All Pathways - Groundwater Scenario	3-7
3-2	Peak projected radon fluxes for the Area G performance assessment	3-12
3-3	Pathway contributions to the peak projected performance assessment dose for the All Pathways - Parajito Canyon Scenario	3-16
3-4	Pathway contributions to the peak projected intruder dose for the historic pits	3-20
3-5	Projected intruder doses due to the inhalation of radioactive gases	3-21
3-6	Pathway contributions to the peak projected intruder dose for the historic shafts	3-25
3-7	Pathway contributions to the peak projected intruder dose for the future pits	3-29

LIST OF TABLES
(Continued)

Table No.		Page No.
3-8	Pathway contributions to the peak projected performance assessment intruder dose for the future shafts	3-32
3-9	Pathway contributions to the peak projected composite analysis dose for the All Pathways - Groundwater Scenario	3-35
3-10	Pathway contributions to the peak projected composite analysis dose for the All Pathways - Parajito Canyon Scenario	3-41
3-11	Summary of peak projected doses and performance objectives for the Area G performance assessment	3-43
3-12	Summary of peak projected radon fluxes and performance objectives for the Area G performance assessment	3-44
3-13	Summary of peak projected doses and performance objectives for the Area G composite analysis	3-46
4-1	Summary of radionuclide contributions to the peak doses for the Atmospheric, All Pathways - Groundwater, and All Pathways - Parajito Canyon scenarios	4-19
4-2	Sources of uncertainty and associated errors for the Groundwater Resource Protection Scenario	4-45
4-3	Sources of uncertainty and associated errors for the Atmospheric Scenario	4-51
4-4	Sources of uncertainty and associated errors for the radon flux projections	4-58
4-5	Sources of uncertainty and associated errors for the All Pathways - Groundwater Scenario	4-61
4-6	Sources of uncertainty and associated errors for the All Pathways - Parajito Canyon Scenario	4-64
4-7	Summary of radionuclide contributions to peak intruder dose projections	4-72

1. INTRODUCTION

The Los Alamos National Laboratory (LANL) generates radioactive waste from a wide variety of research and development activities and from the cleanup or remediation of contaminated sites and facilities. The majority of this waste is low-level radioactive waste (LLW) and is disposed of at the Technical Area 54 (TA-54), Area G, disposal facility. U.S. Department of Energy (DOE) Order 5820.2A (DOE, 1988a) requires that this waste be managed, treated, stored, and disposed of in a manner that protects public health and safety, and the environment. To comply with this order, DOE field sites must prepare and maintain site-specific radiological performance assessments for all LLW disposal facilities.

In response to Recommendation 94-2 from the Defense Nuclear Facilities Safety Board, DOE has developed a comprehensive approach for ensuring that Environmental Management activities do not compromise future radiological protection of the public (DOE, 1996a). Under this approach, DOE requires that field sites conduct a composite analysis which accounts for the cumulative impacts of active and planned LLW disposal facilities and all other sources of radioactive contamination that could interact with active disposal facilities.

A radiological dose assessment is an integral part of the performance assessment and composite analysis. The assessment is used to project potential doses to persons exposed to radioactivity disposed of in a LLW disposal facility. The projected doses are compared to DOE performance objectives to assess facility compliance, and are used to develop waste acceptance criteria (WAC) for the disposal facility.

The performance objectives are specific to the performance assessment and composite analysis. The objectives for the performance assessment are (DOE, 1988a):

- Protect public health and safety in accordance with standards specified in applicable EH Orders and other DOE Orders.
- Ensure that external exposure to the waste and concentrations of radioactive material which may be released into surface water,

groundwater, soil, plants and animals results in an effective dose equivalent that does not exceed 25 mrem/yr to any member of the public. Ensure that releases to the atmosphere meet the requirements of 40 CFR 61, and that a reasonable effort is made to maintain releases of radioactivity in effluents to the general environment as low as is reasonably achievable.

- Ensure that the committed effective dose equivalents received by individuals who inadvertently intrude into the facility after the loss of active institutional control (100 yr) will not exceed 100 mrem/yr for continuous exposure or 500 mrem for a single acute exposure.

- Protect groundwater resources consistent with federal, state, and local requirements.

These performance objectives were interpreted for the Area G performance assessment as:

- Maximum effective dose equivalent of 25 mrem/yr to any member of the public resulting from external exposure and concentrations of radioactive material released into surface water, groundwater, soil, plants, and animals.

- Maximum effective dose equivalent of 10 mrem/yr to any member of the public from concentrations of radioactive material released to the atmosphere (excluding radon) from Area G and all other facilities at the LANL.

- Maximum flux of radon gas (i.e., Rn-220 and Rn-222) from the undisturbed disposal site of 20 $pCi/m^2/s$ (1.9 $pCi/ft^2/s$).

- Maximum effective dose equivalent of 100 mrem/yr for continuous exposures of individuals who inadvertently intruder into the facility after the loss of active institutional control (100 yr).

- Maximum effective dose equivalent of 500 mrem for acute exposures of individuals who inadvertently intruder into the facility after the loss of active institutional control (100 yr).

- Maximum effective dose equivalent of 4 mrem/yr to any member of the public from the consumption of drinking water drawn from wells outside of the land-use boundary.

These performance objectives are consistent with the intent of DOE Order 5820.2A (DOE 1988a) and the *Interim Format and Content Guide and Standard Review Plan for U.S. Department of Energy Low-Level Waste Disposal Facility Performance Assessment*

(DOE 1996b). Compliance with these performance objectives must be demonstrated for a period of 1,000 yr.

The performance objective for the composite analysis is the DOE primary annual dose limit of 100 mrem effective dose equivalent for members of the public (DOE, 1996c). Doses to the hypothetical receptor must be maintained as low as is reasonably achievable. If the projected dose exceeds 30 mrem/yr, an options analysis must be prepared to consider actions that could be taken to reduce exposures, taking into account the cost of such actions. The 30-mrem/yr dose is used as a dose constraint in evaluating the results of the composite analysis. Compliance with the composite analysis performance objectives must be demonstrated for a period of 1,000 yr (DOE, 1996c).

This report discusses the dose assessment conducted in support of the TA-54, Area G, performance assessment and composite analysis. The methodology used to project potential doses to human receptors is described in Chapter 2. The results of the dose assessment are presented and discussed in Chapter 3. Chapter 4 discusses the uncertainties associated with the dose assessment and their effect on the ability of the Area G disposal facility to comply with the performance objectives summarized above.

This page intentionally left blank.

2. DOSE ASSESSMENT METHODOLOGY

This chapter describes the models and data used to project potential doses to inadvertent intruders and members of the public living in the vicinity of the Area G disposal facility. Section 2.1 discusses the exposure pathways and scenarios used in the dose assessment. Section 2.2 discusses the models and data used in the preparation of the dose projections.

2.1 HUMAN EXPOSURE PATHWAYS AND SCENARIOS

The means through which humans may be exposed to radioactive materials are called exposure pathways. Each exposure pathway includes a source or release from a source, a transport or exposure medium, a location at which the exposure occurs, and an exposure route. The actual exposure pathways that may lead to human exposures will depend upon the patterns of human activity at, and adjacent to, the disposal site. Patterns of human activity may be specified by using a collection of appropriate exposure pathways, generally referred to as an exposure scenario.

The exposure pathways and scenarios through which people may be exposed to radioactivity disposed of at Area G are specific to the period of the facility's lifetime. Thus, to understand the basis for pathway and scenario development, it is necessary to understand the stages of the disposal facility's lifetime. These stages include the:

- Operational period, defined as the period during which waste is placed in disposal pits and shafts. The Area G disposal facility's operational period began in 1957 and, for the analysis described here, was assumed to continue through the year 2044.

- Closure period, during which the final pits and shafts are closed and surface structures are removed from the site. Site closure was assumed to require two years to complete, through the year 2046.

- Active institutional control period, characterized by continuing DOE control over the entire LANL. This period was assumed to last 100 yr, extending from 2047 through 2146.

- Industrial use period, during which active DOE control shifts from the entire LANL to specific facilities, including the Area G disposal facility. This period was assumed to extend throughout the remainder of the 1,000-yr compliance period, or until the year 3046.

Only offsite members of the public may receive radiation exposures during the operational and active institutional control periods. Exposures to these receptors may continue following the end of active institutional control. Furthermore, inadvertent intruders may receive radiation exposures from waste disposed of at Area G for brief periods of time. The exposure pathways and scenarios modeled for each of these periods are discussed below.

2.1.1 Operational and Active Institutional Control Periods

Radioactivity in waste disposed of at Area G may be leached from the waste or released to the atmosphere during the operational and active institutional control periods. Radioactivity leached from the waste may be transported to the regional aquifer underlying Area G. Use of groundwater by members of the public downgradient of the disposal facility may result in exposures during these periods. Similarly, radioactivity released to the atmosphere in the form of gases may be transported off site with prevailing winds. Persons living downwind of the disposal facility may inhale or otherwise be exposed to these airborne contaminants. While a potential exists for particulate releases from the site, any such releases will be very small because of controls placed on facility operations and site maintenance activities.

Exposures of the public during the operational and active institutional control periods were projected using the offsite resident exposure scenarios listed in Table 2-1. The Groundwater Resource Protection Scenario and the All Pathways - Groundwater Scenario were implemented at the boundary of the LANL near the town of White Rock, home to approximately 7,000 people. Projected exposures for the former scenario were limited to the ingestion of contaminated groundwater and were used to assess compliance with the 4-mrem/yr groundwater protection standard. For the All Pathways - Groundwater Scenario,

Table 2-1. Offsite exposure scenarios for the operational and active institutional control periods.

Exposure Scenario	Exposure Pathways and Routes	Point of Exposure
Groundwater Resource Protection	Ingestion of drinking water	LANL boundary adjacent to White Rock
All Pathways - Groundwater	Ingestion of drinking water	LANL boundary adjacent to White Rock
	Ingestion of food crops irrigated with well water	
	Ingestion of meat and milk from animals watered with well water	
	Ingestion of contaminated soils	
	Inhalation of airborne radioactivity	
	Direct radiation from airborne radioactivity	
	Direct radiation from contaminated soils	
Atmospheric	Ingestion of food crops grown in contaminated soils and contaminated by airborne radioactivity	Point of maximum atmospheric exposure outside of LANL boundaries
	Ingestion of contaminated soils	
	Inhalation of airborne radioactivity	
	Direct radiation from airborne radioactivity	
	Direct radiation from contaminated soils	

the receptor was assumed to receive exposures from inhalation and ingestion of radioactivity and direct radiation. Airborne radioactivity suspended from contaminated soil surfaces is inhaled by the individual during the time spent at home. Ingestion doses occur from the consumption of crops grown in contaminated soils, milk and meat from animals raised using water drawn from the resident's well, small amounts of soil, and drinking water. Exposures to direct radiation from airborne contamination at the homestead and radioactivity deposited on the soil add to the internal exposures. The projected doses for this scenario were used to assess compliance with the 25-mrem/yr and 30/100-mrem/yr "all pathways" performance objectives for the performance assessment and composite analysis, respectively.

The Atmospheric Scenario was implemented at the point of maximum atmospheric exposure outside of LANL boundaries and at White Rock, the population center closest to Area G (Table 2-1). The receptor was assumed to inhale radioactive gases (except radon and its daughters) and resuspended dust transported from Area G; ingestion doses were assumed to occur from the consumption of crops contaminated by radioactivity deposited on plant surfaces and the ground surface, and from the consumption of small amounts of soil. External exposures were assumed to result from contaminated soil surfaces and airborne radioactivity. The projected doses for this scenario were used to assess compliance with the 10-mrem/yr atmospheric pathway performance objective for the performance assessment and the 30/100-mrem/yr "all pathways" performance objective for the composite analysis. Radon fluxes from the undisturbed disposal site were projected separately and used to assess compliance with the 20-pCi/m^2/s (1.9 pCi/ft^2/s) performance assessment flux objective.

The locations used to project doses for the offsite exposure scenarios are consistent with DOE restrictions on land use, hydrologic and atmospheric conditions, and land-use patterns in the vicinity of Area G. As discussed in Section 2.1, DOE is expected to retain control of the entire LANL throughout the operational and active institutional control periods. Consequently, the establishment of a residence or well any closer to Area G than the area immediately adjacent to White Rock will be prevented. The area around White Rock lies in the prevailing groundwater flow path and is the first location at which groundwater potentially contaminated by waste disposed of at Area G may be used while site restrictions are in place. Establishment of a well at this location is consistent with current land use patterns in the region insofar as the LANL boundary currently runs along the eastern edge of White Rock. The exposures modeled at the point of maximum atmospheric exposure and

White Rock account for the prevailing meteorological conditions, the complex terrain, and the demographics in the vicinity of Area G. Both of these locations are situated on land outside of the LANL boundaries.

The assessment of exposures to the offsite resident at the locations discussed above is expected to provide reasonably conservative dose estimates for the operational and active institutional control periods. As previously discussed, the location near White Rock is the first point where regular usage of water drawn from the aquifer is possible. If exposures occur during the operational or active institutional control periods from the use of contaminated water, they are expected to be greatest at this location. Groundwater pathway doses further downgradient of the disposal site will diminish as the concentrations of groundwater contamination abate due to dilution and dispersion. By definition, the location of maximum atmospheric exposure will bound doses to offsite individuals resulting from airborne releases from Area G. Concentrations of airborne contaminants will diminish as the distance from the disposal facility increases or as the location of the receptor relative to the site changes.

Groundwater may occur at LANL in the alluvium in canyon bottoms, as zones of perched groundwater, and in the regional aquifer. The source of water used by the offsite resident will directly influence the magnitude of the doses received by the individual from the use of contaminated groundwater. Therefore, the selection of this water source for the Area G performance assessment and compliance analysis is a potentially critical part of the dose assessment.

The source of groundwater used as the basis for projecting doses to the offsite resident must meet three conditions to be pertinent to the Area G dose assessment. First, the water must have a potential for being contaminated by radioactivity leached from the Area G disposal facility. Second, the groundwater must be of adequate quality and supply to furnish the individual's needs. Finally, the water must be accessible to the individual during the operational and active institutional control periods.

Most of the water percolating through the Area G disposal facility is expected to flow vertically until it contacts the regional aquifer located within the Puye Formation. Water in the alluvium in Parajito Canyon and Canada del Buey may become contaminated following lateral transport of radioactivity from the disposal units to the sides of the mesa if the

contamination is washed into the canyon by surface runoff. No contamination of these canyon waters is anticipated from radioactivity leached from the waste and transported downward with the water percolating through the disposal site. Zones of perched water may be present in the canyons and may become contaminated as radioactivity in the alluvium is transported downward; perched groundwater has not been observed beneath Mesita del Buey.

In terms of water quality and supply characteristics, there is no evidence that zones of perched water in the vicinity of Area G are capable of meeting an individual's water requirements. Similarly, the alluvial waters in Canada del Buey and Parajito Canyon are not expected to be capable of supporting average household use. The alluvial water in Parajito Canyon, the more substantial source of water found in the two canyons, would generally be pumped dry during most seasons of the year. Adequate water may be available for short periods of time following snowmelt runoff from April to May and in mid to late summer following runoff from summer thunderstorms. Groundwater within the regional aquifer is of sufficient quality and quantity to meet all water needs of the resident.

The accessibility of the alluvial groundwater and zones of perched water to the offsite resident during the operational and active institutional control periods is limited. These sources of moisture are inaccessible in Parajito Canyon adjacent to Area G due to restrictions placed on site access during the operational and active institutional control periods; they may be accessed near the town of White Rock, approximately 2 km (1.2 mi.) away. Alluvial and perched groundwater within Canada del Buey is accessible to individuals throughout the operational and active institutional control periods because this canyon lies on the border of LANL and San Ildefonso Indian lands.

Based on the preceding information, the regional aquifer was selected as the source of water for the groundwater pathway analysis. While alluvial and perched groundwater in Canada del Buey and Parajito Canyon is accessible in some areas and may be contaminated by radioactivity transported laterally from the disposal units, it is not capable of meeting year-round household water needs. The regional aquifer may be contaminated by radioactivity leached from the waste, is capable of meeting the offsite resident's water needs, and is accessible to members of the public during the operational and active institutional control periods.

The potential exists for an offsite resident to be exposed to radioactivity released from the Area G disposal facility to surface waters adjacent to, and downgradient from, Mesita del Buey. Surface runoff from the mesa may result in contaminated year-round or seasonal flows in Parajito Canyon and Canada del Buey. Separately, contaminated groundwater in the regional aquifer may eventually discharge to the Rio Grande River, approximately 5 km (3.1 mi.) downgradient of Area G.

Exposures resulting from the use of surface water during the operational and active institutional control periods were not considered in the Area G dose assessment. Active controls over the disposal site during these periods will allow measures to be taken to prevent the transport of radioactivity into the adjacent canyons via surface runoff. Projected exposures resulting from the use of contaminated surface water from the Rio Grande River will be bounded by doses contingent on the use of contaminated water drawn from the regional aquifer. Radionuclide concentrations in the river will be lower than concentrations in the regional aquifer because of dispersive effects during the additional time required to transport the radioactivity to the surface water and because groundwater releases will be diluted in the river. Consequently, the potential doses resulting from the use of surface water will be lower than the exposures received by using groundwater closer to the disposal site.

2.1.2 Industrial Use Period

Radionuclide releases to groundwater and the atmosphere will continue following the end of active institutional control and may result in exposures to members of the public. Continued DOE control over the site will allow long-term maintenance of the site, thereby ensuring proper functioning of the disposal system components. Brief lapses in custodial responsibilities at the disposal site may, however, permit releases via additional mechanisms (e.g., particulate releases to the atmosphere) for short periods. Lapses in custodial responsibilities may also provide opportunities for inadvertent intruders to arrive at the site and undertake various activities that may result in their exposure to radioactivity. The exposure scenarios used to quantify the potential doses to offsite individuals and intruders during the industrial use period are discussed below.

Exposures of members of the public during the industrial use period were projected using the offsite exposure scenarios listed in Table 2-2. The Groundwater Resource Protection Scenario was implemented at the point of maximum groundwater exposure east-southeast of the Area G boundary and in Parajito Canyon adjacent to Area G. Doses projected for these locations were used to assess compliance with the 4-mrem/yr groundwater protection standard. The All Pathways - Groundwater Scenario was also implemented at the point of maximum groundwater exposure east-southeast of the Area G fenceline, and was used to assess compliance with the 25- and 30/100-mrem/yr "all pathways" performance objectives for the performance assessment and composite analysis, respectively. The Atmospheric Scenario was used to estimate potential doses for an individual located at the point of maximum atmospheric exposure outside of the Area G disposal facility boundaries and for a person living in the town of White Rock. Results for this scenario were evaluated against the 10-mrem/yr atmospheric pathway performance objective for the performance assessment and the 30/100-mrem/yr "all pathways" performance objective for the composite analysis. The exposure pathways and routes modeled for these three scenarios were identical to those discussed in Section 2.1.1. Radon fluxes from the undisturbed disposal site were projected separately and used to assess compliance with the 20-pCi/m^2/s (1.9-pCi/ft^2/s) performance assessment flux objective.

The All Pathways - Parajito Canyon Scenario (Table 2-2) was used to estimate potential doses resulting from the transport of contamination from Mesita del Buey to the canyons below. The projected doses for this scenario were used to assess compliance with the 25-mrem/yr and 30/100-mrem/yr "all pathways" dose objectives for the performance assessment and composite analysis, respectively.

Radioactivity may be exposed on top of the mesa through a variety of mechanisms, including plant and animal intrusion, soil erosion, and cliff retreat. Rates of erosion at Area G are such that waste will not be exposed until well after the 1,000-yr compliance period. A mean surface erosion rate of 4.0×10^{-7} m/yr (1.3×10^{-6} ft/yr) has been estimated by Springer (1996). Based on this rate, less than 1 percent of the covers placed over the disposal pits and shafts are projected to erode within 1,000 yr.

The unique topographical features of the Area G disposal facility make it susceptible to cliff retreat, wherein portions of the mesa walls collapse into the adjacent canyons. If

Table 2-2. Offsite exposure scenarios for the industrial use period.

Exposure Scenario	Exposure Pathways and Routes	Point of Exposure
Groundwater Resource Protection	Ingestion of drinking water	East-southeast of Area G and Parajito Canyon
All Pathways - Groundwater	Ingestion of drinking water	East-southeast of Area G and Parajito Canyon
	Ingestion of food crops irrigated with well water	
	Ingestion of meat and milk from animals watered with well water	
	Ingestion of contaminated soils	
	Inhalation of airborne radioactivity	
	Direct radiation from airborne radioactivity	
	Direct radiation from contaminated soils	
Atmospheric	Ingestion of food crops grown in contaminated soils and contaminated by airborne radioactivity	Point of maximum atmospheric exposure outside of Area G boundaries
	Ingestion of contaminated soils	
	Inhalation of airborne radioactivity	

Table 2-2. Continued.

Exposure Scenario	Exposure Pathways and Routes	Point of Exposure
	Direct radiation from airborne radioactivity	
	Direct radiation from contaminated soils	
All Pathways - Parajito Canyon	Ingestion of drinking water	Parajito Canyon below the Area G disposal facility
	Ingestion of food crops grown in contaminated soils and irrigated with well water	
	Ingestion of meat and milk from animals watered with well water	
	Ingestion of contaminated soils	
	Inhalation of airborne radioactivity	
	Direct radiation from airborne particulates	
	Direct radiation from contaminated soils	

allowed to continue over extended periods, cliff retreat may result in exposure of the waste disposed of in the pits and shafts. The time required for exposure of the waste to occur will depend upon the rate of cliff retreat, a subject studied by a number of LANL investigators.

The retreat of mesa walls occurs as a result of small rockslides from cliffs, the separation of rocks from slopes, and larger, deep-seated landslides (Reneau, 1993). Landslides typically result in mass-wasting on a much larger scale than that observed from rockfalls. While the cause of landslides may vary across the LANL, seismic shaking was identified as a potentially important triggering mechanism for large-scale mass movement along Parajito Canyon due to the proximity of faults believed capable of generating Magnitude 7 earthquakes (Reneau and Vaniman, 1994). If seismic shaking does play an important role in landslides, then the rate of cliff retreat will be proportional to the recurrence interval of seismic events of sufficient intensity to trigger movement of blocks of tuff. It is unclear, however, what intensity of shaking is sufficient to trigger landslides. While the recurrence interval of Magnitude 7 events in the central portion of the LANL is believed to be greater than 10,000 yr, peak ground accelerations of 0.16 to 0.3 g may occur with 1,000- to 5,000-yr return periods (Wong et al., 1993). Short of complete failure of the 15.2-m (50-ft)-thick tuff walls separating the disposal units from the mesa edge, these recurrence intervals suggest that it is unlikely that waste will be exposed during the 1,000-yr compliance period.

While the loss of blocks of tuff from mesa walls due to cliff retreat is a discrete process, investigators at the LANL have developed estimates of cliff retreat rates assuming cliff retreat is a continuous process (Purtymun and Kennedy, 1971; Reneau, 1993; Reneau and Vaniman, 1994). These estimates range from approximately 3.7×10^{-3} to 3.7×10^{-2} cm/yr (1.5×10^{-3} to 1.5×10^{-2} in./yr). Based on these rates and the design criterion that disposal units be placed no closer than 15.2 m (50 ft) from the edge of the mesa, waste may be exposed between 40,000 and 400,000 yr from the present day. These estimates support the notion that waste will not be exposed during the 1,000-yr compliance period. Consequently, the effects of cliff retreat were not included in the dose assessment.

Based on the preceding discussion, intrusion into the disposed waste by plants and animals was assumed to be the sole mechanism through which radioactivity could be brought to the surface of the disposal facility during the 1,000-yr period of compliance. Inclusion of

this release scenario is expected to be conservative because DOE's long-term control over the Area G disposal facility should prevent widespread establishment of deep-rooted plants and populations of burrowing animals at Area G.

Radioactivity may also be transported laterally by water drawn from the disposal units at Area G to the sides of the mesa. Contamination reaching the mesa sides may subsequently be transported into the canyons below with surface runoff. The contamination in the runoff may sorb to canyons soils or be transported downward via the alluvial groundwater, eventually reaching the regional aquifer. This potential source of contamination of water supplies was also considered in the projection of exposures for the All Pathways - Parajito Canyon Scenario.

The resident in Parajito Canyon was assumed to raise crops and animals to supply a portion of his or her food requirements (Table 2-2). The crops were assumed to be grown in soil contaminated by the radioactivity transported from the mesa top to the canyon floor. Water drawn from the regional aquifer was assumed to be used for crop irrigation and to water animals raised by the resident. The cattle and cows were assumed to be range-fed, such that no crops were grown to feed them. Exposures to radioactivity were assumed to occur through the inhalation of particulates suspended from contaminated soil surfaces in the canyon during the time spent at home, while ingestion doses were assumed to result from the consumption of crops raised at the residence, milk and meat from animals raised at the site, small amounts of contaminated soil, and water drawn from the well. Exposures to direct radiation from airborne contamination at the homestead and radioactivity deposited over the resident's lot were assumed to add to the internal exposures.

As discussed in Section 2.1, DOE is expected to maintain responsibility for the Area G disposal site throughout the 1,000-yr compliance period. Continued control over the site will minimize the potential for contact with the disposed waste. However, if DOE becomes complacent about its custodial responsibilities for a short period of time (e.g., one or two years), a situation may arise where an inadvertent intruder arrives at the site and, through his or her activities, becomes exposed to radioactivity. Given this possibility, an intruder analysis was included in the dose assessment to assess compliance with the intruder dose objectives specified in DOE Order 5820.2A.

Five intruder exposure scenarios, described in Table 2-3, were evaluated for inclusion in the dose projections developed for the Area G performance assessment. The table briefly discusses the activities that were assumed to occur, when they were expected to be feasible, the amount of time each intruder was assumed to be exposed to radioactivity, and the routes of exposure. In general, these exposure scenarios resemble those used by the U.S. Nuclear Regulatory Commission (NRC) in support of 10 CFR Part 61 (NRC, 1986).

Although the Drilling and Post-Drilling exposure scenarios are commonly considered during the development of exposure scenarios for radiological dose assessments, they were excluded from the Area G performance assessment. Both scenarios are based on the assumption that the intruder establishes a well after arriving at the disposal site. Consistent with the Standard Format and Content guidance issued by DOE (1996b), the establishment of a well and subsequent use of groundwater were not assumed to occur.

The time at which the intruder scenarios were considered to be feasible may have significant effects on the projected doses. In general, intrusion into the waste was considered feasible at any time following the 100-yr active institutional control period as long as the waste had decomposed sufficiently to resemble ordinary soil and no barriers to intrusion were encountered. If the intruder encounters intact waste packages, stabilized waste (e.g., grout), or engineered barriers (e.g., concrete caps on disposal shafts), it was assumed that the person would stop all intrusive activities and leave the site.

Conditions necessary to delay intrusion into the disposal pits beyond the 100-yr active institutional control period were not assumed to exist. The potentially rapid decomposition of cardboard boxes and steel drums used to dispose of historic waste minimizes the likelihood of encountering these waste packages in an intact state. While the B-25 boxes to be used for future waste disposal may remain intact for longer periods, their actual lifetimes under Area G disposal conditions are not known. Consequently, it was assumed that these containers do not limit the potential for intrusion into the waste. In terms of waste form, metals and stabilized waste may be recognizable after 100 yr. Once again, however, the rate at which these materials will degrade to forms that are indistinguishable from the remainder of the material in the pits is unknown. Lacking this information, it was conservatively assumed that these waste forms do not prevent intrusion. The other forms of waste disposed of in the pits (e.g., cellulosics, sludges, animal tissues, and filters) truly may be unrecognizable as

Table 2-3. Intruder exposure scenarios considered for the Area G performance assessment.

Exposure Scenario	Scenario Description	Period of Exposure (hr/yr)	Exposure Routes
Intruder-Agriculture	The intruder resides in a house constructed over the closed disposal units. The person works away from the house during the day and spends a portion of their spare time raising crops for personal consumption. Crops are grown in contamination brought to the surface during basement excavation. The scenario may occur any time after the 100-yr active institutional control period for the disposal pits; intrusion into the shafts is prevented for 300 yr by the concrete caps.	6,180*	Ingestion of contaminated food and soil; inhalation of airborne contaminants; direct radiation from airborne contaminants and contaminated soils.
Intruder-Construction	An individual arrives at the disposal site and constructs a house over the closed disposal units. Radioactivity brought to the surface during basement excavation is spread over the house lot. The scenario is considered to be feasible at all times following the 100-yr active institutional control period for the disposal pits; intrusion into the shafts is assumed to be prevented for 300 yr by the concrete caps.	500	Inhalation of airborne contaminants; ingestion of contaminated soils; direct radiation from airborne contaminants and contaminated soils.
Intruder-Discovery	An individual arrives at the disposal site to construct a house. The person encounters an intact barrier, stabilized waste, or a waste package in the course of excavating a basement; determines that the site was used for radioactive waste disposal; and abandons all efforts. The scenario is feasible at the end of the 100-yr active institutional control period for the disposal pits and shafts.	6	Inhalation of airborne contaminants; ingestion of contamination; direct radiation from airborne contaminants and contaminated soils.

Table 2-3. Continued.

Exposure Scenario	Scenario Description	Period of Exposure (hr/yr)	Exposure Routes
Intruder-Drilling	A local well driller is contracted to drill a well through the closed disposal units. Radioactivity brought to the surface with the drill cuttings is spread over a limited area around the drill rig. The scenario may occur any time after the end of the 100-yr active institutional control period for the disposal pits and shafts.	100 or less[b]	Limited inhalation of airborne contaminants; limited direct radiation from air immersion; direct radiation from contaminated drill cuttings.
Intruder-Post-Drilling	An individual resides in a house constructed over the closed disposal units. The person works away from the house during the day and spends a portion of their spare time raising crops for personal consumption. Crops are grown in the contamination brought to the surface during well drilling only. The scenario may occur any time after the 100-yr active institutional control period for the disposal pits and shafts.	6,180[a]	Ingestion of contaminated food, water, and soil; inhalation of airborne contaminants; direct radiation from airborne contaminants and contaminated soils.

a. Time of exposure includes 4,380 hr inside the house and 1,800 hr outside the house.
b. Time required to drill the well is specific to the area geology and depth of the well.

waste within 100 yr of disposal. Finally, intrusion into the pit waste was not assumed to be limited by the presence of engineered barriers because no such features exist.

Containers used to dispose of waste in the disposal shafts were not assumed to prevent intrusion into the waste after the end of the institutional control period for the reasons given with respect to the pits. Similarly, while metallic and concrete waste forms may not be fully degraded within 100 yr, it was conservatively assumed that intrusion is not prevented by these materials. The disposal shaft design incorporates concrete caps to better isolate the waste from the surface environment. The use of these caps to seal the disposal shafts was expected to limit the ability to excavate a basement. While the expected lifetime of these concrete caps is unknown, it was assumed that the concrete caps will resist intrusion for 300 yr. Consequently, the Intruder-Agriculture and Intruder-Construction scenarios were not projected to occur over the disposal shafts until 300 yr after the end of the closure period.

The intruder analysis for the Area G performance assessment was limited to the development of dose projections for the Intruder-Agriculture Scenario. Projected exposures for the Intruder-Construction and Intruder-Discovery scenarios will be lower than those projected for the Intruder-Agriculture Scenario for the reasons discussed below. As stated earlier, the Drilling and Post-Drilling scenarios were excluded from consideration because long-term control over the site is expected to preclude establishment of a well.

The magnitudes of potential intruder exposures are a function of the radionuclide concentrations in contaminated media, the length of time the person is exposed to these media, and the extent to which the individual uses the contaminated resources. The concentrations of radioactivity encountered by the agricultural intruder are the same as those projected for the Intruder-Construction Scenario because the same degree of intrusion into the disposed waste is postulated to occur at the same times relative to disposal facility closure. The projected concentrations of radioactivity contacted in the Intruder-Discovery Scenario are greater than those encountered in the Intruder-Agriculture and Intruder-Construction scenarios for any given time because the waste was not assumed to be exhumed and mixed with clean cover soil.

Times of exposure to radioactivity are greatest for the Intruder-Agriculture Scenario (Table 2-3). The intruder in this scenario was assumed to spend 6,180 hr at the residence,

70 percent of which is spent indoors. In contrast, construction of the house was assumed to require only 500 hr, while the discoverer was assumed to spend 100 hr or less at the disposal site. The individual who resides at the closed disposal facility also makes the greatest use of contaminated resources and, hence, is subject to greater risks of exposure. This person receives exposures through ingestion of contaminated foodstuffs and soil, inhalation of airborne particulates and gases, and direct radiation from airborne and soil contamination. A subset of these potential exposure routes pertains to the remaining intruder scenarios.

When the concentrations of radioactivity encountered, the times of exposure, and the level of resource utilization are taken into consideration, potential exposures will be greatest for the agricultural intruder under all conditions. As such, projected doses for this scenario will result in WAC that are more restrictive than criteria based on projected doses for the Intruder-Construction and Intruder-Discovery scenarios. Consequently, this scenario was chosen as the basis for the intruder analysis conducted in support of the Area G performance assessment. The performance objectives for the composite analysis pertain to potential exposures received by members of the public; they do not apply to persons who may inadvertently intrude into the disposed waste (DOE, 1996c). Thus, no intruder dose assessment was conducted for the Area G composite analysis.

As discussed earlier, the inadvertent intruder analysis was included in the performance assessment to address the possibility that DOE may become complacent in its custodial responsibilities at Area G for a period not exceeding 2 yr (DOE, 1996b). The actual length of exposure is important because it determines the basis for assessing compliance with the DOE Order 5820.2A performance objectives. The pertinent dose objective is 500 mrem for acute exposures, while chronic exposures must not result in doses to the intruder exceeding 100 mrem/yr.

The NRC defines acute exposure events as those that occur for less than 1 yr (NRC, 1986). Based on this definition and on the assumption that complacency on the part of the site custodian could last as long as 2 yr, it was assumed that the Intruder-Agriculture Scenario constitutes a chronic exposure. Consequently, the 100-mrem/yr performance objective was used to assess compliance with DOE Order 5820.2A for the intruder analysis.

The offsite and intruder exposure scenarios used to project potential doses during the industrial use period should be placed in proper perspective with respect to current land use patterns and the need to demonstrate compliance with DOE performance objectives. In terms of future land-use patterns, the exposure scenarios may not accurately portray the ways in which Mesita del Buey and the canyons adjacent to it will be used by their inhabitants in the future. More reasonable expectations would be that this land will revert to uses consistent with the current lifestyle of the San Ildefonso Indians, owners of the lands adjacent to the LANL.

The exposure scenarios were selected to provide reasonably conservative estimates of the potential exposures that may result from the waste disposed of at Area G. To the extent that the scenarios represent more intensive use of potentially contaminated resources than might actually occur, the calculated doses are expected to provide additional assurance that the disposal system will perform at least as well as projected. This approach to modeling exposures facilitates the evaluation of the ability of the disposal facility to comply with the dose objectives for the performance assessment and composite analysis.

2.2 MODELS AND DATA

The models and data used to project doses for members of the public and inadvertent intruders are presented below. Section 2.2.1 discusses the radiological inventories used in the dose assessment and the steps taken to model depletion of radioactivity over time. Section 2.2.2 describes the models and data used to simulate environmental transport of radioactivity to locations accessible to humans. Section 2.2.3 presents the models and data used to project intake of radioactivity by humans and the consequent doses.

2.2.1 Radionuclide Inventory Projections

The performance assessment and composite analysis address different portions of the waste disposed of at Area G since the facility opened in 1957. The performance assessment addresses waste disposed of since September 26, 1988, and waste expected to require disposal

through the end of disposal operations in the year 2044. This inventory was divided into two portions: waste disposed of between September 26, 1988, and the end of 1995, and waste projected to require disposal from 1996 through 2044. Each of these inventories was further divided based on whether the waste was buried in pits or shafts.

The inventory for the composite analysis includes waste disposed of at Area G since the facility opened in 1957 and waste expected to require disposal in the future. As such, the composite analysis inventory includes the segmented performance assessment inventory discussed above. It divides the waste disposed of between 1957 and September 25, 1988, into two segments: the waste disposed of through 1970, and the waste disposed of starting in 1971. Separate inventories for disposal pits and shafts were developed for each disposal period.

Separating the performance assessment and the composite analysis inventories into disposal unit and time-specific segments offers several advantages. It permits evaluation of the contributions the pits and shafts make to the projected scenario doses, and permits more detailed analysis of how uncertainties associated with the inventory projections influence disposal facility projections. In addition, the development of WAC for the Area G disposal facility needs to account for future disposal practices. Because these practices are expected to differ from historic operations, period-specific inventories are required for the performance assessment inventory.

Radionuclide inventories in the disposal units will decline over time as radionuclides undergo radioactive decay, as radioactivity is leached from the units by water percolating through the disposal site, and, for some isotopes, as the radionuclides diffuse upward out of the units as gases. For the Area G dose assessment, depletion of the inventory was assumed to occur only as a result of radioactive decay; no credit was taken for depletion of the inventory due to leaching or gaseous diffusion. In general, depletion due to radioactive decay was calculated as

$$Q_{i,t} = Q_{i,o}\, e^{-\lambda_i t} \qquad (2\text{-}1)$$

where

$Q_{i,t}$ = inventory of radionuclide i at time t (Ci)

$Q_{i,o}$ = initial inventory of radionuclide i (Ci)

λ_i = radioactive decay constant of radionuclide i (yr^{-1})

t = time since disposal (yr).

Adjustments made to account for radioactive decay must reflect the disposal history of the waste. To minimize the need for detailed accounting of disposal dates, all waste disposed of during a given period was assumed to be placed in the disposal units at the end of that period. For example, decay adjustments for waste projected to be disposed of prior to 1971 were based on the assumption that the material was placed in the pits and shafts at the end of 1970. Similarly, decay adjustments for waste disposed of between 1971 and September 25, 1988, and for waste disposed of between September 26, 1988, and 1995 were based on disposal dates of 1988 and 1995, respectively.

The majority of the waste projected to require disposal in the future was assumed to be generated at a constant rate between 1996 and the end of Area G disposal operations. The activity of a given radionuclide in the waste at the end of disposal operations is given by

$$Q_{i,t} = \frac{Q_{i,o}(1-e^{-\lambda_i t})}{\lambda_i t} \qquad (2\text{-}2)$$

The time, t, in Equation (2-2) refers to the length of time the disposal facility is assumed to accept the future waste. The Area G disposal facility was assumed to continue to accept waste through the year 2044, or 49 yr from the end of 1995. Adjustments for radioactive decay of the future inventory remaining in 2044 were made using Equation 2-1.

A portion of the inventory projected to require disposal in the future includes tritium-contaminated wastes that have been in storage for varying lengths of time. Adjustments for radioactive decay of this waste were made based on the date the waste was generated, if available, using Equation (2-1). If the date of generation was unknown, it was assumed that the waste was placed in storage at the end of 1995 and decayed from that time forward.

Several radionuclides included in the Area G dose assessment decay to form radioactive daughter products. The ingrowth of daughter products over time is an important part of the disposal unit inventories and must be accounted for in the projection of doses. The activity of a given daughter product is a function of the half-lives of the parent and daughter radionuclides and the time over which ingrowth is assumed to occur. For the dose assessment, daughters with half-lives that are short relative to those of their parents were assumed to be in secular equilibrium with their parents and, therefore, to have the same activities as the parent radionuclides. The activities of longer-lived daughters were calculated using the Bateman equation.

For the performance assessment, the concentrations of waste radionuclides in the disposal pits and shafts were used in the projection of doses to inadvertent intruders. In general, these concentrations were calculated as the product of the radionuclide concentrations in the waste and the waste emplacement efficiencies for the various disposal units. Waste emplacement efficiencies for the pits and shafts that received waste through 1995 were 36 and 42 percent, respectively. These estimates were based on the average emplacement efficiencies for disposal units that began receiving waste after 1970 and which are now closed. In anticipation of operational practices that will increase pit disposal efficiencies in the future, a waste emplacement efficiency of 50 percent was assumed to apply to all future disposal pits. Changes in operational practices are not expected to affect the waste emplacement efficiency for disposal shafts. Consequently, the waste emplacement efficiency of 42 percent for the historic disposal shafts was applied to the future disposal shafts as well.

The disposal shafts included in the Area G performance assessment and composite analysis are distributed in small groups over a large portion of the disposal facility. This wide-ranging spatial distribution makes projecting doses to the inadvertent intruder difficult. In an attempt to simplify this portion of the dose assessment and to provide a reasonably conservative estimate of potential intruder doses from shaft waste, it was assumed that the disposal shafts are arranged in a shaft field. The dimensions of the shaft field were based on the minimum spacing used in excavating the shafts. Specifically, shafts with diameters of 0.9 m (3 ft) or less were assumed to be arranged to maintain a distance of 2.3 m (7.6 ft) from the centers of adjacent shafts. Larger shafts were assumed to be spaced 5.5 m (18 ft) from the centers of adjacent shafts (Kopp, 1991).

Based on the calculations described above, the portion of the area within the shaft field that consists of shaft disposal units was determined. This calculation indicated that approximately 11 percent of the surface area of the shaft field consists of disposal units. Consequently, the average radionuclide concentrations in historic and future shaft waste were reduced by roughly an order of magnitude prior to using them in projecting doses for inadvertent intruder exposure scenarios.

2.2.2 Environmental Transport Pathways

The disposal of radioactive material may result in the release of radionuclides to the environment. Transport of these releases may result in contamination of ground and surface waters, surface soils, biota, and air. The modeling approaches taken in simulating the environmental transport of radioactivity from the disposal pits and shafts are discussed below.

The following discussion is organized in terms of the environmental media that may become contaminated by releases from the disposal pits and shafts. Section 2.2.2.1 briefly discusses the approach used to model groundwater contaminant transport in the vadose zone and radionuclide dilution in the aquifer. Section 2.2.2.2 describes the models used to calculate levels of contamination in surface soils resulting from intrusion into the waste, erosion, and cliff retreat. The equations used to project radionuclide concentrations in vegetation and animal products are provided in Sections 2.2.2.3 and 2.2.2.4, respectively. Finally, the models used to estimate atmospheric concentrations of radioactivity are discussed in Section 2.2.2.5.

2.2.2.1 Groundwater

Radionuclides leached from the waste may be transported vertically through the unsaturated zone and discharged to the regional aquifer underlying the disposal site, or transported laterally from the disposal units to the sides of the mesa. Groundwater transport of radionuclides through the unsaturated zone underlying Area G and the regional aquifer was modeled by LANL personnel (Birdsell, et al., 1997).

The results of the groundwater transport modeling were used to identify the locations at which the greatest groundwater pathway exposure occurred for the Groundwater Resource Protection and All Pathways - Groundwater exposure scenarios. Projected radionuclide concentrations in the aquifer were multiplied by normalized exposure scenario dose factors and summed at each model node or location. The locations with the greatest total dose were used as the basis for more detailed dose calculations for the two scenarios.

The All Pathways - Parajito Canyon Scenario included an evaluation of the potential impacts of radioactivity that was transported laterally from the disposal units to the sides of the mesa. All contamination reaching the mesa sides was conservatively assumed to be transported into the canyon by surface runoff, and downward to the regional aquifer with water percolating through the canyon alluvium. In lieu of detailed dilution modeling of the contamination entering the aquifer, radionuclide concentrations for the various segments of the performance assessment and composite analysis inventories were simply summed prior to estimating the consequent doses.

The Area G performance assessment was conducted to assess compliance with the DOE Order 5820.2A performance objectives. One of these performance objectives requires the protection of groundwater resources. As discussed in Section 1, this objective was interpreted to mean that concentrations in the regional aquifer must be such that consumption of the water will not lead to a dose greater than 4 mrem/yr. The doses calculated to demonstrate compliance with the groundwater protection standards were based on projected radionuclide concentrations in the aquifer, and did not account for dilution effects created by pumping water over the screened length of the well.

2.2.2.2 Surface Soils

Surface soils may become contaminated from inadvertent intrusion into the disposed waste by humans and intrusion into the waste by plants and burrowing animals. Waste radionuclides may also be exposed following erosion of the cover system placed over the disposal units and cliff retreat along the edges of the mesa. The methods for projecting soil contaminant concentrations from these mechanisms are discussed below.

The inadvertent intruder exposure scenarios considered the potential impacts of excavating a basement into the disposal units. The concentration of radioactivity in surface soils following human intrusion is a function of the extent of intrusion (i.e., the area and depth over which intrusion occurs) and the depth of the cover system placed over the waste. It was assumed that the surface area of the house is 200 m^2 (2,150 ft^2), typical for a reasonably large ranch-style home. The excavation was assumed to be 26 m (85 ft) by 16 m (52 ft) at the ground surface (giving a 1:1 slope for the sides of the hole) and 3 m (9.8 ft) deep (NRC, 1986).

The total amount of material exhumed during basement construction is 906 m^3 (3.2×10^4 ft^3). A portion of this material consists of the earthen cover system placed over the disposal units at the end of operations. The remainder of the material is the crushed tuff/waste mixture placed in the units. Approximately one-third of the exhumed material was assumed to be used as backfill outside of and around the basement walls. The remaining 600 m^3 (2.1×10^4 ft^3) of material were distributed over the 2,300-m^2 (2.5×10^4-ft^2) lot on which the house was constructed, less the area occupied by the house.

Concentrations of radioactivity in the material spread over the intruder's lot were calculated using

$$C_{i,s,t} = C_{i,w,t} \frac{E_w}{E_t} \tag{2-3}$$

where

$C_{i,s,t}$ = soil concentration of radionuclide i at time t (Ci/kg)

$C_{i,w,t}$ = waste concentration of radionuclide i at time t (Ci/kg)

E_w = volume of exhumed material consisting of crushed tuff/waste (m^3)

E_t = total volume of exhumed material (m^3).

Equation (2-3) implicitly assumes that the crushed tuff/waste mixture excavated from the disposal unit(s) is uniformly mixed with the cover material overlying the waste before the material is spread over the lot. The waste radionuclide concentrations, $C_{i,w,t}$, were calculated as the radionuclide inventories in the waste divided by the entire volume of waste disposed

of in the pits or shafts. Average radionuclide concentrations were calculated for the four periods for which inventory data were developed (see Section 2.2.1), taking into account radioactive decay and daughter ingrowth.

The volume of the exhumed material consisting of the crushed tuff/waste mixture, E_w, is equal to the area of the excavation times the excavation depth less the cover thickness. The thickness of the waste placed in the disposal pits is 15 m (49 ft) and 16 m (52 ft) in the shafts, based on the average thickness in historic disposal units included in the performance assessment. The nominal thickness of the interim cover over the historic pits is 1.0 m (3.3 ft), while 1.4 m (4.6 ft) of topsoil, crushed tuff, and concrete are placed over the historic disposal shafts. A uniform cover thickness of 2 m (6.6 ft) was used for all pits and shafts opened for waste disposal after 1995, reflecting recent changes in disposal operations at Area G.

Radioactivity may also be brought to the surface of the disposal facility by animal and plant intrusion into the waste. The burrows of invertebrates and small mammals may extend below the cover placed over the waste, resulting in the incorporation of contaminants in the surface soils. Roots of plants may extend into the waste and provide a pathway for the uptake and assimilation of radioactivity. Following the death of the plant or leaf fall, the radioactivity may be incorporated into the surface soils as the litter decays.

In general, DOE control over the disposal site was expected to reduce the impacts of, but not completely prevent, biointrusion into the disposed waste. The establishment of plant species with extreme rooting depths was assumed to be prevented by removing individuals once they were identified. Similarly, recognizing that complete eradication of burrowing animals may be difficult, nominal levels of burrowing were assumed to occur. The modeling approach used to estimate the transport of radioactivity to the surface of the disposal site by plants and animals is discussed in Vold and Shuman (1997).

Erosion will indirectly and directly affect the concentrations of radionuclides in the surface soils at Mesita del Buey. Erosion of the mesa top will influence the volume of waste exhumed as a result of intrusion into the waste. As the cover system is removed, the proportion of the material brought to the surface through human, animal, and plant intrusion that is waste will increase. If erosion goes unchecked for very long periods, the cover placed

over the disposal pits and shafts may be entirely removed. Under these conditions, radionuclide concentrations in the exposed "surface soils" will be equivalent to the original as-disposed waste concentrations, corrected for radioactive decay and daughter ingrowth.

Work conducted by Springer (1996) indicates a sheet erosion rate of 4×10^{-7} m/yr (1.3×10^{-6} ft/yr). Based on this rate and the 1,000-yr period of compliance, it is evident that erosion will have a limited affect on the cover system placed over the disposal units. Nevertheless, reductions in the thickness of the cover system were accounted for in determining the quantity of waste brought to the surface from human and biotic intrusion.

Surface soils at offsite locations may become contaminated through a variety of mechanisms, including deposition of airborne contaminants, deposition of radioactivity in water used for crop irrigation, and surface water transport of radionuclides. Soil concentrations resulting from the first two processes were modeled using Equations (2-4) and (2-5):

$$C_{i,s,t} = \frac{C_{i,a,t}\, v_d\, 3.15 \times 10^7\, (1 - e^{-\lambda_i t_b})}{d\, \rho_s \lambda_i} \qquad (2\text{-}4)$$

where

$C_{i,a,t}$	=	air concentration of radionuclide i at time t (Ci/m^3)
v_d	=	deposition velocity (m/s)
3.15×10^7	=	seconds per year conversion factor
t_b	=	time over which deposited activity builds up (yr)
d	=	plow depth (m)
ρ_s	=	bulk density of surface soil (kg/m^3).

$$C_{i,s,t} = \frac{C_{i,a,t}\, I_r\, 8760\, f_r\, (1 - e^{\lambda_i t_b})}{d\, \rho_s \lambda_i} \qquad (2\text{-}5)$$

where

$C_{i,w,t}$ = groundwater concentration of radionuclide i at time t (Ci/m^3)

I_r = irrigation rate (m^3/m^2-hr)

8760 = hours per year conversion factor

f_r = fraction of year crops are irrigated.

A deposition velocity of 0.001 m/s (0.04 in./s) (Soldat et al., 1974), a buildup time of 15 yr (NRC, 1977), a plow layer depth of 0.15 m (5.9 in.) (NRC, 1977), and a soil bulk density of 1300 kg/m^3 (81 lb/ft^3) (Abeele, 1984) were used for the Area G dose assessment. Crops were assumed to be irrigated at a rate of 2.1x10^{-4} m^3/m^2-hr (5.2x10^{-3} gal/ft^2-hr) for 27 percent of the year (based on Hansen, 1995a). Equation (2-4) was used to project soil concentrations at the location of maximum atmospheric exposure. Equation (2-5) was used to project soil concentrations at the offsite locations where the resident uses groundwater to irrigate crops.

The Area G dose assessment evaluates potential exposures resulting from the transport of radioactive sediments on the top of Mesita del Buey to Parajito Canyon. The complexity of modeling sediment transport is such that a simpler approach was taken which is expected to bound the potential exposures. In this approach, the radionuclide concentrations in the canyon surface soils are given by

$$C_{i,ca,t} = C_{i,ma,t} \frac{D_m}{D_c} \qquad (2\text{-}6)$$

where

$C_{i,ca,t}$ = surface soil concentration of radionuclide i in the canyon at time t (Ci/kg)

$C_{i,ma,t}$ = surface soil concentration of radionuclide i on the mesa at time t (Ci/kg)

D_m = depth of surface soil on mesa that is transported to the canyon (m)

D_c = depth over which contamination is mixed in canyon soils (m).

The depth of contamination removed from the mesa each year was set equal to 4x10^{-7} m (1.3x10^{-6} ft) (Springer, 1996), which is the depth of soil estimated to be eroded annually by

surface water runoff. The depth of mixing in the canyon soils, D_c, was assumed to be 0.15 m (5.9 in.) (NRC, 1977).

Equation (2-6) implicitly assumes that the area over which contamination is spread in the canyon is equivalent to the area of contamination on the mesa. The actual area over which contamination will spread as it is transported down the sides of the mesa and out onto the central portion of the canyon is unknown. However, the assumption that the area would not be any smaller than that from which the contamination originated is expected to be reasonably conservative.

The unique topographical features of the Area G disposal facility make it susceptible to another form of disruption. Over extended periods of time, waste disposed of in pits and shafts may be exposed as a result of cliff retreat. However, as discussed in Section 2.1.2, the rates of cliff retreat are such that waste at Area G is not expected to be exposed during the 1,000-yr compliance period and, perhaps, for tens or hundreds of thousands of years beyond this period. Consequently, the effects of cliff retreat were not included in the dose assessment.

2.2.2.3 Vegetation

Vegetation may become contaminated with radioactivity due to depositional processes and as a result of root uptake of radioactivity in the soil. Radionuclide concentrations in vegetation are calculated using

$$C_{i,v,t} = \frac{C_{i,a,t}\, I_r\, T_v\, R_w\, (1-e^{-\lambda_w t_w})}{Y_v\, \lambda_w} + C_{i,a,t}\, B_{i,v}\, D_v + \frac{C_{i,a,t}\, R_r\, \rho_s\, d\, V_d\, T_v\, R_w\, (1-e^{-\lambda_w t_w})}{Y_v\, \lambda_w\, 2.8E-04} \qquad (2\text{-}7)$$

where

$C_{i,v,t}$ = vegetation concentration of radionuclide i at time t (Ci/kg)

T_v = vegetation translocation factor

R_w	=	vegetation retention factor
λ_w	=	weathering removal coefficient (hr^{-1})
t_g	=	crop growing season (hr)
Y_v	=	crop agricultural yield (kg/m^2 (wet weight))
$B_{i,v}$	=	soil to plant concentration factor (Ci/kg dry weight vegetation per Ci/kg dry weight soil)
D_v	=	dry-to-wet-weight ratio for vegetation
R_r	=	resuspension factor due to rainsplash (m^{-1})
V_d	=	deposition velocity (m/s)
2.8E-04	=	day per second conversion factor.

The first term in Equation (2-7) accounts for contamination of the plant from irrigating crops with contaminated water, while the second term accounts for root uptake of soil contamination. The final term in the equation calculates plant concentrations resulting from the deposition of radioactivity on plant surfaces from rainsplash. All three modes of contamination were considered in modeling exposures to members of the public. Contamination of food crops as a result of irrigation was excluded from the intruder analysis because this individual was not assumed to use contaminated water.

Radionuclides assimilated by vegetation may undergo radioactive decay during the growing season and the time between harvest and consumption of the crop. The reduction in plant radionuclide concentrations due to decay, however, will be negligible because the length of the growing season plus the holdup period is short compared to the half-lives of the radionuclides being analyzed. Consequently, these secondary effects were ignored.

Equation (2-7) was used to calculate radionuclide concentrations in leafy vegetables, produce (e.g., fruit and non-leafy vegetables), and grain. A variety of pathway and radionuclide- or element-specific data are required to calculate vegetation concentrations. The pathway data used to perform food-chain calculations are summarized in Table 2-4, while element-specific parameter values are given in Table 2-5.

Table 2-4. Pathway input parameters for food-chain exposure modeling.

Input Parameter	Units	Value	Source of Value
Human consumption rate:			
Leafy vegetables	kg/yr	1.6E+01	Yang & Nelson, 1986
Other (protected produce, fruit, etc.)	kg/yr	9.0E+01	Yang & Nelson, 1986
Grain	kg/yr	7.4E+01	Yang & Nelson, 1986
Meat	kg/yr	4.2E+01	Yang & Nelson, 1986
Milk	L/yr	1.0E+02	Yang & Nelson, 1986
Water	L/yr	7.3E+02	EPA, 1989
Soil	kg/yr	3.6E-02	EPA, 1989
Fraction of food eaten that is grown on site	—	5.0E-01	Assumed value
Soil bulk density	kg/m^3	1.3E+03	Abeele, 1984
Vegetation weathering removal constant	hr^{-1}	2.1E-03	NRC, 1977
Vegetation translocation factor:			
Leafy vegetables	—	1.0E+00	Ng et al., 1978
All other crops	—	1.0E-01	Ng et al., 1978
Agricultural productivity (wet weight):			
Leafy vegetables	kg/m^2	2.0E+00	NRC, 1977
Produce	kg/m^2	2.0E+00	NRC, 1977
All other food crops	kg/m^2	6.0E-01	NCRP, 1984
Dry:wet weight fraction:			
Leafy vegetables	—	1.0E-01	Peterson, 1983
All other food crops	—	4.3E-01	Baes et al., 1983
Irrigation rate	m^3/m^2-hr	2.1E-04	Hansen, 1995a
Fraction of year crops are irrigated	—	2.7E-01	Hansen, 1995a
Animal consumption rate:			
Cattle - water	L/d	5.0E+01	NRC, 1977
Milk cow - water	L/d	6.0E+01	NRC, 1977

Table 2-5. Element-specific input parameters for food-chain exposure modeling.[a]

	Plant-Soil Concentration Factor[b]			Transfer Factors	
Element	Leafy Vegetables	Produce	Grain	Forage-to-Meat (d/kg)	Forage-to-Milk (d/L)
Ac	3.5E-03	3.5E-04	3.5E-04	2.5E-05	2.0E-05
Ag	4.0E-01	1.0E-01	1.0E-01	3.0E-03	2.0E-02
Al	4.0E-03	6.5E-04	6.5E-04	1.5E-03	2.0E-04
Am	5.5E-03	2.5E-04	2.5E-04	3.5E-06	4.0E-07
At	1.0E+00	1.5E-01	1.5E-01	1.0E-02	1.0E-02
Ba	1.5E-01	1.5E-02	1.5E-02	1.5E-04	3.5E-04
Bi	3.5E-02	5.0E-03	5.0E-03	4.0E-04	5.0E-04
Bk	8.5E-04[c]	1.5E-05[c]	1.5E-05[c]	3.5E-06[c]	2.0E-05[c]
C	1.3E+00[d]	1.3E+00[d]	1.3E+00[d]	3.1E-02[d]	1.2E-02[d]
Cd	5.5E-01	1.5E-01	1.5E-01	5.5E-04	1.0E-03
Cf	8.5E-04	1.5E-05	1.5E-05	3.5E-06	2.0E-05
Cl	7.0E+01	7.0E+01	7.0E+01	8.0E-02	1.5E-02
Cm	8.5E-04	1.5E-05	1.5E-05	3.5E-06	2.0E-05
Co	2.0E-02	7.0E-03	7.0E-03	2.0E-02	2.0E-03
Cs	8.0E-02	3.0E-02	3.0E-02	2.0E-02	7.0E-03
Dy	1.0E-02	4.0E-03	4.0E-03	5.5E-03	2.0E-05
Eu	1.0E-02	4.0E-03	4.0E-03	5.0E-03	2.0E-05
Fr	3.0E-02	8.0E-03	8.0E-03	2.5E-03	2.0E-02
Gd	1.0E-02	4.0E-03	4.0E-03	3.5E-03	2.0E-05
H	—[e]	—[e]	—[e]	—[e]	—[e]
Hf	3.5E-03	8.5E-04	8.5E-04	1.0E-03	5.0E-06
Ho	1.0E-02	4.0E-03	4.0E-03	4.5E-03	2.0E-05
I	1.5E-01	5.0E-02	5.0E-02	7.0E-03	1.0E-02
K	1.0E+00	5.5E-01	5.5E-01	2.0E-02	7.0E-03
La	1.0E-02	4.0E-03	4.0E-03	3.0E-04	2.0E-05
Mo	2.5E-01	6.0E-02	6.0E-02	6.0E-03	1.5E-03
Nb	2.0E-02	5.0E-03	5.0E-03	2.5E-01	2.0E-02
Ni	6.0E-02	6.0E-02	6.0E-02	6.0E-03	1.0E-03
Np	1.0E-01	1.0E-02	1.0E-02	5.5E-05	5.0E-06
P	3.5E+00	3.5E+00	3.5E+00	5.5E-02	1.5E-02

Table 2-5. Continued.

Element	Plant-Soil Concentration Factor[b]			Transfer Factors	
	Leafy Vegetables	Produce	Grain	Forage-to-Meat (d/kg)	Forage-to-Milk (d/L)
Pa	2.5E-03	2.5E-04	2.5E-04	1.0E-05	5.0E-06
Pb	4.5E-02	9.0E-03	9.0E-03	3.0E-04	2.5E-04
Pd	1.5E-01	4.0E-02	4.0E-02	4.0E-03	1.0E-02
Pm	1.0E-02	4.0E-03	4.0E-03	5.0E-03	2.0E-05
Po	2.5E-03	4.0E-04	4.0E-04	9.5E-03	3.5E-04
Pu	4.5E-04	4.5E-05	4.5E-05	5.0E-07	1.0E-07
Ra	1.5E-02	1.5E-03	1.5E-03	2.5E-04	4.5E-04
Sc	6.0E-03	1.0E-03	1.0E-03	1.5E-02	5.0E-06
Se	2.5E-02	2.5E-02	2.5E-02	1.5E-02	4.0E-03
Si	3.5E-01	7.0E-02	7.0E-02	4.0E-05	2.0E-05
Sm	1.0E-02	4.0E-03	4.0E-03	5.0E-03	2.0E-05
Sr	2.5E+00	2.5E-01	2.5E-01	3.0E-04	1.5E-03
Ta	1.0E-02	2.5E-03	2.5E-03	6.0E-04	3.0E-06
Tb	1.0E-02	4.0E-03	4.0E-03	4.5E-03	2.0E-05
Tc	9.5E+00	1.5E+00	1.5E+00	8.5E-03	1.0E-02
Th	8.5E-04	8.5E-05	8.5E-05	6.0E-06	5.0E-06
Ti	5.5E-03	3.0E-03	3.0E-03	3.0E-02	1.0E-02
Tl	4.0E-03	4.0E-04	4.0E-04	4.0E-02	2.0E-03
U	8.5E-03	4.0E-03	4.0E-03	2.0E-04	6.0E-04
Y	1.5E-02	6.0E-03	6.0E-03	3.0E-04	2.0E-05
Zr	2.0E-03	5.0E-04	5.0E-04	5.5E-03	3.0E-05

a. Source of parameters is Baes et al., 1984, unless otherwise noted.
b. Plant-soil concentration factors have units of Ci/kg (dry weight) of vegetation per Ci/kg (dry weight) of soil.
c. Plant-soil concentration factors and transfer factors are assumed to be the same as the factors for Cf and Cm.
d. Source of plant uptake factors is Sheppard et al., 1991. Source of transfer factors is NRC, 1977.
e. Transfer of H-3 from food to animal products is calculated using a specific activity model.

As discussed earlier, several of the radionuclides included in the Area G dose assessment decay to yield radioactive daughter products. Many of these daughter products are extremely short-lived and will be present at approximately the same activity as their immediate long-lived parent in all environmental media. Food chain transport parameters for these short-lived daughters were assigned the same values as their parents, effectively transporting the daughters at the same rates as their respective parents. Daughters with half-lives that are long relative to the length of the growing season were assigned food chain transport parameters consistent with their own elemental properties.

Special consideration was given to modeling the assimilation of H-3 and C-14 in vegetation. Tritium exhibits minimal sorption onto soil particles and, as a result, is quickly rinsed from surface soils. Consequently, projected levels of H-3 in the soil were not assumed to contribute to the contamination of food crops through either root uptake or resuspension. In scenarios where potentially contaminated water is used to irrigate food crops, a specific activity model was used to estimate H-3 concentrations in plant tissues. Using this model, the concentration in plant tissue is given by (Wood et al., 1994)

$$C_{H\text{-}3,v,t} = C_{H\text{-}3,w,t}\, F_v^w \qquad (2\text{-}8)$$

where

$C_{H\text{-}3,v,t}$ = concentration of H-3 in vegetation at time t (Ci/kg)

$C_{H\text{-}3,w,t}$ = concentration of H-3 in groundwater at time t (Ci/kg)

F_v^w = fraction of water in vegetation.

The fraction of water in the vegetation, F_v^w, was modified to account for the H-3 in the water in plants as well as that organically bound in the produce. The equation used to make this adjustment is (Wood et al., 1994)

$$F_v^{w2} = F_v^w + (1 - F_v^w)\, F_v^H\, 9 \qquad (2\text{-}9)$$

where

F_v^{w2} = effective water fraction in vegetation

F_v^{H} = fraction of hydrogen in vegetation

9 = coefficient to convert H-3 concentration to hydrogen concentration.

Applying Equations (2-8) and (2-9) with the parameters listed in Table 2-6 shows that the H-3 concentrations in leafy vegetation, produce and fruit, and grain were equivalent to 91, 91, and 62 percent of the concentration in the water used for irrigation, respectively.

Root uptake of C-14 was modeled using the results of Sheppard et al. (1991) rather than specific activity models. The plant concentration factor adopted from this work is included in Table 2-5.

2.2.2.4 Animal Products

Radioactivity ingested by animals consuming contaminated water and forage may result in the contamination of animal products such as meat and milk. Cattle and cows raised in the Los Alamos area are typically range-fed, minimizing the potential for the ingestion of contaminated forage. Thus, for the Area G dose assessment, potential sources of radioactivity for animals were assumed to be restricted to contaminated water drawn from area wells. Concentrations of radionuclides in meat were calculated as

$$C_{i,mt,t} = C_{i,w,t}\, Q_w\, f_{i,mt} \qquad (2\text{-}10)$$

where

$C_{i,mt,t}$ = concentration of radionuclide i in meat at time t (Ci/kg)

Q_w = consumption rate of water by animals (kg/d)

$f_{i,mt}$ = forage-to-meat transfer factor for radionuclide i (d/kg).

Table 2-6. Food chain parameters used in the tritium models.[a]

Food Product	Fraction of Water in Food Product	Fraction of Hydrogen in Food Product
Leafy vegetables	8.0E-01	6.3E-02
Produce	8.0E-01	6.3E-02
Grain	1.2E-01	6.3E-02
Meat	---	9.4E-02
Milk	---	8.3E-02

a. Source: Wood et al., 1994.

Contaminant concentrations in milk were calculated similarly using

$$C_{i,mk,t} = C_{i,a,t}\ Q_w\ f_{i,mk} \tag{2-11}$$

where

$C_{i,mk,t}$ = concentration of radionuclide i in milk at time t (Ci/kg)

$f_{i,mk}$ = forage-to-milk transfer factor for radionuclide i (d/kg).

The input parameters needed to implement these equations are included in Tables 2-4 and 2-5. Element-specific properties of daughter products that are in secular equilibrium with their parents were assumed to be identical to those of the parents.

A specific activity model was used to project H-3 concentrations in animal products resulting from the consumption of contaminated water (Napier et al., 1988). Tritium concentrations in meat and milk were calculated using

$$C_{H\text{-}3,mt,t} = \frac{9\ C_{H\text{-}3,a,t}\ Q_w\ F^H_{mt}}{Q_w} \tag{2-12}$$

where

$C_{H\text{-}3,mt,t}$ = concentration of H-3 in meat at time t (Ci/kg)

F^H_{mt} = fraction of hydrogen in meat

and

$$C_{H\text{-}3,mk,t} = \frac{9\ C_{H\text{-}3,a,t}\ Q_w\ F^H_{mk}}{Q_w} \tag{2-13}$$

where

$C_{H\text{-}3,mk,t}$ = concentration of H-3 in milk at time t (Ci/kg)

F^H_{mk} = fraction of hydrogen in milk.

Based on Equations (2-12) and (2-13) and the parameters included in Table 2-6, H-3 concentrations in meat and milk were equivalent to 85 and 75 percent, respectively, of the concentration in the water drawn from the individual's well.

Equations (2-10) through (2-13) were used to model the exposures of members of the public living in the vicinity of Area G. As discussed earlier, the inadvertent intruder was not assumed to use contaminated water drawn from the onsite well. Consequently, the transport mechanisms addressed by these equations were not considered in the intruder analysis modeling.

2.2.2.5 Air

Resuspension of contaminated surface soils and release of radioactive gases to the atmosphere may contaminate the air above the disposal facility. The average air concentration of radioactivity as particulates was calculated for the intruder analysis using an average mass loading approach:

$$C_{i,air,t} = C_{i,s,t}\, m_{at} \qquad \textbf{(2-14)}$$

where

m_{at} = average mass loading (kg/m^3).

Calculated air concentrations were based on an average mass loading of $1x10^{-7}$ kg/m^3 ($6.2x10^{-9}$ lb/ft^3). This value is a conservative approximation of the average background dust loading for nonurban areas in the United States of about $4x10^{-8}$ kg/m^3 ($2.5x10^{-9}$ lb/ft^3) (Anspaugh et al., 1975).

Airborne concentrations of contaminated dust downwind of Area G were calculated using

$$C_{i,air,t} = C_{i,s,t}\, f_r\, A_s\, X/Q \qquad \textbf{(2-15)}$$

where

f_r = resuspension factor ($kg/m^2/s$)

A_s = area of site (m^2)

X/Q = ratio of air concentration to source release rate (s/m^3).

A resuspension factor of 1.8×10^{-9} $kg/m^2/s$ (3.7×10^{-10} $lb/ft^2/s$) was used in this calculation, and was based on site-specific measurements at Area G (Kowalewsky et al., 1995). The area of the site was specific to the inventory under consideration (e.g., the performance assessment or composite analysis inventory). These areas were calculated as the quotient of the as-disposed waste volume and the average depth of the disposal units in which the waste was placed. Waste volumes were derived from the inventory projections (Shuman, 1997); the disposal unit depths of 10 and 12 m (33 and 39 ft) for pits and shafts, respectively, were based on averages for all historic disposal units at Area G. The values for X/Q for the point of maximum atmospheric exposure and the town of White Rock were based on atmospheric transport calculations conducted by Vold (1996a).

Tritium, C-14, krypton, and radon may undergo gaseous release from the Area G disposal facility, leading to exposures of inadvertent intruders and offsite individuals. The fluxes of H-3, C-14, Kr-81, and Kr-85 through a cover placed over the waste were calculated using a model based on simple Fickian diffusion:

$$J_{i,t} = C_{i,g,t}\, e^{-x\sqrt{\lambda_i / D_i}}\, \sqrt{\lambda_i\, D_i} \qquad (2\text{-}16)$$

where

$J_{i,t}$ = flux of radionuclide i at time t ($Ci/m^2/yr$)

$C_{i,g,t}$ = gas concentration of radionuclide i at time t (Ci/m^3)

x = diffusion distance (m)

D_i = diffusion coefficient of radionuclide i (m^2/yr).

To implement Equation (2-16), it was necessary to define the concentrations of H-3, C-14, Kr-81, and Kr-85 available for diffusion as gases. The concentration of H-3 in water vapor depends on the concentration of the radionuclide in the water within the disposal units.

This concentration is simply the concentration in the waste divided by the water content of the waste. A moisture content for the waste of 8 percent by volume (Loaiza and Vold, 1995) was used to calculate H-3 concentrations.

Given the H-3 concentration in soil water, the water vapor concentration was calculated based on the assumption that the radionuclide is evenly distributed between liquid and vapor. The vapor concentration is given by (EPA, 1988a)

$$C_{H\text{-}3,g,t} = C_{H\text{-}3,w,t} \frac{VP\ M}{R\ T} \qquad (2\text{-}17)$$

where

$C_{H\text{-}3,g,t}$	=	concentration of H-3 in water vapor at time t (Ci/m^3)
$C_{H\text{-}3,w,t}$	=	concentration of H-3 in groundwater at time t (Ci/m^3)
VP	=	vapor pressure (atm)
M	=	molecular weight of water (g/mol)
R	=	ideal gas constant ($atm\text{-}m^3/mol\text{-}°K$)
T	=	temperature (°K).

The parameter values used to implement Equation (2-17) include a vapor pressure of 1.2×10^{-2} atm, an ideal gas constant of 8.2×10^{-5} m^3-atm/mol-°K, a temperature of 283°K (10°C), and a molecular weight of water of 18 g/mol.

Only the C-14 present as organic waste was assumed to be available for release as a gas. In actuality, this gas will become available over time as the organic waste matrix decomposes. However, to bound the potential dose from the release of gaseous C-14, it was assumed that all organic C-14 present in the disposed waste would be released as a gas within a single year. The portion of the C-14 inventory identified as organic was based on the assumption that all combustible lab trash (waste code 18) and 50 percent of the combined combustible/non-combustible lab trash (waste code 19) was organic. All other C-14 waste was assumed to be inorganic and unavailable for release as a gas. All Kr-81 and Kr-85 in the waste was assumed to be available for immediate release as gases.

Equations (2-16) and (2-17) were used to estimate fluxes into the inadvertent intruder's house and from the undisturbed site. Intruder flux projections were based on a diffusion distance of 10.2 cm (4 in.), a typical thickness of the floor of the foundation. The diffusion distances for projecting fluxes from the undisturbed site were set equal to the cover depths placed over the pits and shafts, adjusted for erosive effects. The H-3 disposed of in pits was assigned a diffusion coefficient of 600 m^2/yr (6,500 ft^2/yr) in crushed tuff. This coefficient is based on the free diffusion coefficient of water vapor in air, 750 m^2/yr (8,100 ft^2/yr) at 8°C (CRC, 1962), adjusted to account for the effects of soil porosity and tortuosity, and thermal gradients in the porous media (Philip and de Vries, 1957). A diffusion coefficient of 100 m^2/yr (1,100 ft^2/yr) was assigned to C-14, Kr-81, and Kr-85. This coefficient approximates the free diffusion of these gases, adjusted downward for porosity and tortuosity effects. Concrete diffusion coefficients for all gases were conservatively assumed to be equal to those in the crushed tuff/waste mixture.

The diffusion coefficient used for H-3, C-14, and krypton disposed of in shafts was 50,000 m^2/yr (5.38×10^5 ft^2/yr). This value is based on work performed by Vold and Eklund (1996), and takes into account the effects of air movement in the fractured media surrounding the disposal units.

The projected fluxes of H-3, C-14, and krypton into the intruder's house were used to project doses to the individual. These doses are proportional to the radionuclides' concentrations in the air breathed by the intruder. These concentrations were calculated using

$$C_{i,air,t} = \frac{J_{i,t}\,A}{K\,V} = \frac{J_{i,t}}{K\,h} \qquad (2\text{-}18)$$

where

$C_{i,air,t}$ = diluted concentration of radionuclide i in air at time t (Ci/m^3)

A = area of room (m^2)

K = air ventilation rate (air changes/yr)

V = volume of room (m^3)

h = height of room (m).

An average room height of 2.4 m (7.9 ft) and a ventilation rate of 0.5 air changes per hour were assumed for the Area G dose assessment.

The doses calculated based on Equation (2-18) ignore exposures received by the intruder during the time spent outdoors at the disposal site. These doses are expected to be negligible compared to those received during the time spent indoors. Gases released to the atmosphere outside of the individual's home will quickly dissipate and, consequently, pose little risk to the individual.

The concentrations of radioactive gases inhaled by a member of the public downwind of Area G are a function of the fluxes from the disposal facility, the area of the site, and the atmospheric transport characteristics of the site. The fluxes were calculated using Equation (2-16). The site from which the flux originated was specific to the inventory under consideration (e.g., the performance assessment or composite analysis inventory). These areas were estimated as discussed above with respect to dust resuspension and transport. Gas releases from the disposal site were transported to the point of maximum atmospheric exposure using site-specific models (Vold, 1996a).

Radon fluxes from the undisturbed disposal site were projected using the approach given in NRC, 1984. The flux of radon gas from covered waste is given by

$$J_{i,c} = \frac{2\, J_{i,w}\, e^{-b_c x_c}}{\left(1 + \sqrt{a_w/a_c}\ \tanh(b_w x_w)\right) + \left(1 - \sqrt{a_w/a_c}\ \tanh(b_w x_w)\right) e^{-2b_c x_c}} \qquad \textbf{(2-19)}$$

where

$J_{i,c}$ = flux of radionuclide i from covered waste (Ci/m^2-s)

$J_{i,w}$ = flux of radionuclide i from bare waste (Ci/m^2-s)

$b_{i,j}$ = $\sqrt{\lambda/D_{ij}}$ where j refers to cover or waste (m^{-1})

$D_{i,j}$ = diffusion coefficient of radionuclide i in cover or waste (m^2/s)

x_j = thickness of cover or waste layer (m)

a_{ij} = $P_j^2 D_{ij} [1 - (1-k) m_j]^2$ (m^2/s)

P_j = total porosity of cover or waste

k = 0.26 Ci/m^3 in water per Ci/m^3 in air

m_j = fractional moisture saturation of cover or waste as given by $10^{-2} \rho_j M_j/P_j$

ρ_j = bulk density of cover or waste (kg/m^3)

M_j = moisture content of cover or waste (dry weight %).

The flux from uncovered waste, $J_{i,w}$ was calculated using (NRC, 1984)

$$J_{i,w} = R_a \rho_w E \sqrt{\lambda_i D_{i,w}} \tanh(\sqrt{\lambda_i / D_{i,w}}\, x_w) \qquad (2\text{-}20)$$

where

R_a = specific activity of radium in the waste (Ci/kg)

ρ_w = bulk density of waste (kg/m^3)

E = radon emanation coefficient

$D_{i,w}$ = diffusion coefficient of radionuclide i in waste (m^2/s)

x_w = thickness of waste layer (m).

The Ra-226 and Ra-228 activities were determined from the inventory projections (Shuman, 1997), and adjusted for radioactive decay and ingrowth. The diffusion coefficient of radon gas in the pit waste and cover system was assumed to be 100 m^2/yr (1,100 ft^2/yr). This value is based on the approximate free diffusion coefficient of radon, 330 m^2/yr (3,600 ft^2/yr) (Thamer et al., 1980), adjusted downward to account for tortuosity and porosity effects. A diffusion coefficient of 50,000 m^2/yr (5.4×10^5 ft^2/yr) was used for radon in the disposal shafts, based on the work of Vold and Eklund (1996). The bulk density, porosity, and moisture content of the cover and waste were set equal to 1,300 kg/m^3 (81 lb/ft^3) (Abeele, 1984), 0.33, and 0.08 (Loaiza and Vold, 1995), respectively. A radon emanation coefficient of 0.35 (NRC, 1989) was used for Rn-220 and Rn-222.

2.2.3 Human Exposure and Dose Projections

The exposure scenarios used in the Area G dose assessment project potential human exposures for members of the public and the inadvertent intruder. In each scenario, the receptor is postulated to come in contact with contamination and receive a dose through the ingestion, inhalation, or direct radiation exposure routes. The approaches used to model exposures received through these routes are discussed in Sections 2.2.3.1, 2.2.3.2, and 2.2.3.3, respectively.

2.2.3.1 Ingestion Exposure Route

The exposure scenarios included in the dose assessment project potential doses received from the ingestion of soil, food crops, animal products, and water. In general, the activity ingested of a given radionuclide is given by the product of the consumption rate of the contaminated medium, the proportion of the total material ingested that is contaminated, and the radionuclide concentration in the soil, food, or water:

$$I_{i,g,t} = U_m f_m C_{i,m,t} \tag{2-21}$$

where

$I_{i,g,t}$ = intake of radionuclide i through ingestion at time t (Ci/yr)

U_m = consumption rate of contaminated material (kg/yr)

f_m = fraction of consumed material that is contaminated

$C_{i,m,t}$ = concentration of radionuclide i in environmental medium at time t (Ci/kg).

The annual food, soil, and water consumption rates used in the dose assessment are included in Table 2-4. Fifty percent of the food requirements of the intruder or homesteader was assumed to be met by growing crops at his or her residence. All soil inadvertently ingested by the individual was assumed to be contaminated. All water consumed by members of the public was assumed to be drawn from the well downgradient of the disposal site.

The doses received from the ingestion of contaminated materials were calculated as the product of the intake and the radionuclide dose conversion factors for ingestion:

$$D_{i,g,t} = I_{i,g,t} \, D_{i,g} \tag{2-22}$$

where

$D_{i,g,t}$ = whole body effective dose equivalent from the ingestion of radionuclide i at time t (mrem/yr)

$D_{i,g}$ = ingestion dose conversion factor for radionuclide i (mrem/yr/Ci/yr).

The total dose from the ingestion of contaminated material is the sum of the radionuclide doses. The dose conversion factors used in the dose assessment were taken from DOE (1988b) and EPA (1988b), and are listed in Table 2-7. Dose conversion factors were not available in these sources for selected radionuclides; these isotopes were not included in the dose calculations. The ingestion dose conversion factors listed in the table are 50-yr committed dose equivalent factors.

2.2.3.2 Inhalation Exposure Route

The dose assessment included the projection of doses due to the inhalation of radioactivity suspended in the form of particulates or released as gases. The radionuclide intake via inhalation was calculated using

$$I_{i,h,t} = U_{air} \, f_{air} \, C_{i,air,t} \tag{2-23}$$

where

$I_{i,h,t}$ = intake of radionuclide i through inhalation at time t (Ci/yr)

U_{air} = inhalation rate (m^3/yr)

f_{air} = fraction of year individual inhales contaminated air.

Table 2-7. Ingestion, inhalation, and air immersion dose conversion factors.[a]

Radionuclide	Exposure Routes: Ingestion (rem/μCi)	Inhalation (rem/μCi)	Air Immersion (mrem/yr/μCi/m^3)
Ac-225	9.5E-02	1.0E+01	6.8E+01
Ac-227	1.4E+01	6.7E+03	6.3E-01
Ac-228	2.1E-03	2.9E-01	4.8E+03
Ag-108	---[b]	---[b]	8.9E+01
Ag-108m	7.5E-03	2.0E-01	8.2E+03
Al-26	1.3E-02	7.9E-02	1.4E+04
Am-241	4.5E+00	5.2E+02	9.5E+01
Am-243	4.5E+00	5.2E+02	2.6E+02
At-217	---[b]	---[b]	1.2E+00
Ba-133	3.2E-03	6.9E-03	1.8E+03
Ba-137m	---[b]	---[b]	3.1E+03
Bi-207	4.9E-03	1.4E-02	8.0E+03
Bi-210	5.9E-03	1.9E-01	3.8E+00
Bi-211	---[b]	---[b]	2.4E+02
Bi-212	9.9E-04	2.1E-02	9.6E+02
Bi-213	6.8E-04	1.7E-02	7.0E+02
Bi-214	2.4E-04	6.3E-03	8.1E+03
Bk-247	2.3E+00	5.5E+02	5.5E+02
C-14	2.1E-03	2.1E-03	2.6E-02
Cd-113m	1.5E-01	1.4E+00	8.1E-01
Cf-252	9.4E-01	1.3E+02	3.8E-01
Cl-36	3.0E-03	2.0E-02	4.2E-05
Cm-248	1.6E+01	1.9E+03	3.1E-01
Co-60	2.6E-02	1.5E-01	1.3E+04
Cs-135	7.1E-03	4.5E-03	6.6E-02
Cs-137	5.0E-02	3.2E-02	9.0E-01
Dy-154	---[b]	---[b]	---[b]
Eu-152	6.0E-03	2.2E-01	5.9E+03
Eu-154	9.1E-03	2.6E-01	6.5E+03
Fr-221	---[b]	---[b]	1.6E+02
Fr-223	8.6E-03	6.1E-03	2.3E+02
Gd-148	2.1E-01	3.3E+02	0.0E+00
Gd-150	---[b]	---[b]	---[b]
H-3	6.3E-05	6.3E-05	3.9E-02

a. Sources: DOE, 1988b and 1988c; EPA, 1988b.
b. No value provided in cited sources.

Table 2-7. Continued.

Radionuclide	Exposure Routes: Ingestion (rem/μCi)	Inhalation (rem/μCi)	Air Immersion (mrem/yr/μCi/m^3)
Hf-182	1.4E-02	2.8E+00	1.7E+03
Ho-163	—[b]	—[b]	—[b]
I-129	2.8E-01	1.8E-01	4.2E+01
K-40	1.9E-02	1.2E-02	8.1E+02
Kr-81	—[b]	—[b]	5.1E+02
Kr-85	—[b]	—[b]	1.1E+01
La-137	4.3E-04	7.3E-02	4.7E+01
Mo-93	1.3E-03	2.8E-02	3.8E+00
Nb-92	—[b]	—[b]	7.8E+03
Nb-93m	5.3E-04	2.8E-02	6.8E-01
Nb-94	5.1E-03	3.3E-01	8.2E+03
Ni-59	2.0E-04	1.3E-03	1.9E-01
Ni-63	5.4E-04	3.0E-03	0.0E+00
Np-237	3.9E+00	4.9E+02	1.2E+02
Np-239	2.9E-03	2.2E-03	8.4E+02
P-32	7.7E-03	1.3E-02	1.2E+01
Pa-231	1.1E+01	1.3E+03	1.5E+02
Pa-233	3.3E-03	8.6E-03	1.1E+03
Pa-234	2.1E-03	7.4E-04	1.0E+04
Pa-234m	—[b]	—[b]	6.0E+01
Pb-209	2.1E-04	9.0E-05	9.5E-01
Pb-210	5.1E+00	1.3E+01	6.7E+00
Pb-211	4.4E-04	8.0E-03	2.6E+02
Pb-212	4.1E-02	1.6E-01	7.4E+02
Pb-214	5.8E-04	6.7E-03	1.2E+03
Pd-107	1.4E-04	1.3E-02	0.0E+00
Pm-145	4.6E-04	2.7E-02	8.4E+01
Po-210	1.6E+00	8.1E+00	4.4E-02
Po-211	—[b]	—[b]	4.0E+01
Po-212	—[b]	—[b]	0.0E+00
Po-213	—[b]	—[b]	1.6E-01
Po-214	—[b]	—[b]	4.3E-01
Po-215	—[b]	—[b]	7.4E-01
Po-216	—[b]	—[b]	7.6E-02

a. Sources: DOE, 1988b and 1988c; EPA, 1988b.
b. No value provided in cited sources.

Table 2-7. Continued.

Radionuclide	Exposure Routes: Ingestion (rem/μCi)	Inhalation (rem/μCi)	Air Immersion (mrem/yr/μCi/m^3)
Po-218	—[b]	—[b]	5.2E-02
Pu-238	3.8E+00	4.6E+02	4.4E-01
Pu-239	4.3E+00	5.1E+02	4.1E-01
Pu-240	4.3E+00	5.1E+02	4.3E-01
Pu-241	8.6E-02	1.0E+01	8.5E-03
Pu-242	4.1E+00	4.8E+02	3.7E-01
Ra-223	5.5E-01	7.5E+00	6.7E+02
Ra-224	3.3E-01	2.9E+00	5.1E+01
Ra-225	3.1E-01	7.5E+00	3.4E+01
Ra-226	1.1E+00	7.9E+00	3.4E+01
Ra-228	1.2E+00	4.2E+00	3.2E-07
Rn-219	—[b]	—[b]	2.9E+02
Rn-220	—[b]	—[b]	2.6E+00
Rn-222	—[b]	—[b]	2.6E+00
Sc-44	1.4E-03	4.2E-04	1.1E+04
Se-79	8.3E-03	8.9E-03	3.5E-02
Si-32	1.7E-03	1.0E+00	6.1E-02
Sm-146	2.0E-01	7.8E+01	0.0E+00
Sm-147	1.8E-01	7.1E+01	0.0E+00
Sm-151	3.4E-04	2.9E-02	4.6E-03
Sr-90	1.3E-01	1.3E+00	8.8E-01
Ta-182	6.0E-03	3.7E-02	6.7E+03
Tb-157	1.0E-04	9.0E-03	1.3E+01
Tb-158	4.0E-03	2.5E-01	5.5E+03
Tc-97	1.5E-04	4.2E-03	4.7E+00
Tc-99	1.3E-03	7.5E-03	3.6E-03
Th-227	3.6E-02	1.6E+01	5.2E+02
Th-228	3.8E-01	3.1E+02	9.9E+00
Th-229	3.5E+00	2.0E+03	4.3E+02
Th-230	5.3E-01	3.2E+02	2.0E+00
Th-231	1.3E-03	8.1E-04	5.8E+01
Th-232	2.8E+00	1.6E+03	9.3E-01
Th-234	1.3E-02	3.3E-02	3.9E+01
Ti-44	1.9E-02	8.9E-01	6.7E+02

a. Sources: DOE, 1988b and 1988c; EPA, 1988b.
b. No value provided in cited sources.

Table 2-7. Continued.

Radionuclide	Exposure Routes		
	Ingestion (rem/μCi)	Inhalation (rem/μCi)	Air Immersion (mrem/yr/μCi/m^3)
Tl-207	—[b]	—[b]	1.1E+01
Tl-208	—[b]	—[b]	2.0E+04
Tl-209	—[b]	—[b]	1.1E+04
U-232	1.3E+00	6.7E+02	1.3E+00
U-233	2.7E-01	1.3E+02	1.2E+00
U-234	2.6E-01	1.3E+02	7.6E-01
U-235	2.5E-01	1.2E+02	7.7E+02
U-236	2.5E-01	1.2E+02	6.0E-01
U-238	2.3E-01	1.2E+02	5.2E-01
Y-90	1.0E-02	8.2E-03	2.2E+01
Zr-93	1.6E-03	2.1E-03	0.0E+00

a. Sources: DOE, 1988b and 1988c; EPA, 1988b.
b. No value provided in cited sources.

The times the inadvertent intruder and members of the public were assumed to be exposed to airborne radioactivity are listed in Table 2-8. An average inhalation rate of 8,000 m^3 (2.8×10^6 ft^3) of air per year (ICRP, 1975) was assumed. The product of the intakes and the inhalation dose conversion factors yields the radionuclide doses due to inhalation of contaminated air:

$$D_{i,h,t} = I_{i,h,t} \, D_{i,h} \tag{2-24}$$

where

$D_{i,h,t}$ = whole body effective dose equivalent from the inhalation of radionuclide i at time t (mrem/yr)

$D_{i,h}$ = inhalation dose conversion factor for radionuclide i (mrem/yr/Ci/yr).

The total inhalation dose at a given time was calculated as the sum of the radionuclide doses. The inhalation dose conversion factors used in the calculations (taken from DOE, 1988b, and EPA, 1988b) are included in Table 2-7. Radionuclides for which dose conversion factors were unavailable were omitted from the dose calculations. All inhalation dose conversion factors are 50-yr committed dose equivalent factors.

2.2.3.3 Direct Radiation Exposure Route

The inadvertent intruder and members of the public may be exposed to direct radiation from contaminated ground surfaces and from immersion in airborne radioactivity. Direct exposures from contaminated ground surfaces were calculated using

$$D_{i,em,t} = E_{i,t} \, t_e \, 0.75 \tag{2-25}$$

where

$D_{i,em,t}$ = whole body effective dose equivalent from direct radiation from radionuclide i at time t (mrem/yr)

$E_{i,t}$ = exposure rate from ground surface contaminated with radionuclide i in time t (mR/hr)

Table 2-8. Exposure times for the inadvertent intruder and members of the public.

Receptor	Annual Exposure Time (hr)	Source
Agricultural-Intruder		
Outside of house	1.8E+03	NRC, 1986
Gardening	1.0E+02	NRC, 1986
Other activities	1.7E+03	NRC, 1986
Inside of house	4.4E+03	NRC, 1986
Away from house	2.6E+03	NRC, 1986
Offsite Resident[a]		
Outside of house	1.8E+03	NRC, 1986
Gardening	1.0E+02	NRC, 1986
Other activities	1.7E+03	NRC, 1986
Inside of house	4.4E+03	NRC, 1986
Away from house	2.6E+03	NRC, 1986

a. Exposure times for members of the public were assumed to be equivalent to the intruder exposure times.

t_e = time of exposure (hr)

0.75 = conversion factor (mrem/mR).

The factor used to convert from exposure in air to absorbed dose is adopted from ICRP 51 (1987) and pertains to a rotational geometry for a photon energy of 0.2 MeV.

The exposure rates required to implement Equation (2-25) were calculated using the MICROSHIELD computer code (Grove Engineering, 1992). Exposures were modeled using various cylindrical exposure geometries to represent the volume of contamination. Exposures received by the offsite resident and inadvertent intruder were modeled using a cylinder with a radius of 27.1 m (89 ft) and a height of either 15 or 28 cm (11 in.). The cross-sectional area of the cylinder approximates the 2,300-m^2 (2.5×10^4 ft^2) lot upon which the individual was assumed to live. The height of the cylinder is the depth over which radioactivity was mixed in the surface soils. Radioactivity deposited off site following atmospheric deposition, irrigation, or surface runoff from the mesa top was assumed to be mixed to a depth of 15 cm (5.9 in.) (NRC, 1977). The contaminated material spread over the lot following basement excavation results in a layer of material approximately 28 cm (11 in.) thick.

MICROSHIELD simulations were conducted for unit concentrations of all parent and daughter radionuclides included in the Area G dose assessment. These unit-concentration exposure rates were scaled using the projected surface soil concentrations at the receptor locations to estimate the projected doses to the intruder or offsite resident.

Direct exposures received from immersion in airborne radioactivity were calculated using

$$D_{i,ea,t} = C_{i,at,t}\, D_{i,ea}\, f_a \qquad (2\text{-}26)$$

where

$D_{i,ea,t}$ = whole body effective dose equivalent from direct radiation in air for radionuclide i at time t (mrem/yr)

$D_{i,ea}$ = air immersion dose conversion factor for radionuclide i (mrem/yr/Ci/m^3)

f_a = fraction of year receptor is immersed in contaminated air.

The dose conversion factors used in Equation (2-26) were taken from DOE, 1988c and EPA, 1988b. Dose conversion factors were not available in these sources for selected radionuclides; these isotopes were not included in the dose calculations. All air immersion dose conversion factors used in the analysis are included in Table 2-7.

A portion of the time the intruder or homesteader spends at his or her residence will be spent inside the dwelling. Exposures to direct radiation during this time were reduced relative to the time spent outside because the house will shield a portion of the beta and gamma radiation. For the Area G dose assessment, a shielding factor of 0.7 was used (NRC, 1977).

3. DOSE ASSESSMENT RESULTS

This chapter presents the results of the dose assessment conducted in support of the Area G performance assessment and composite analysis. Section 3.1 discusses the dose projections developed for the Area G performance assessment, while the dose estimates for the composite analysis are presented in Section 3.2. In Section 3.3, the results of the dose assessment are summarized and used to evaluate the Area G disposal facility's compliance with DOE requirements.

3.1 PERFORMANCE ASSESSMENT

The exposure scenarios discussed in Section 2.1 address potential exposures to members of the public living in the vicinity of the Area G disposal facility and persons who inadvertently intrude into the disposed waste following the 100-yr active institutional control period. The dose projections for the performance assessment are organized in terms of these two categories of receptors. Section 3.1.1 presents and discusses the dose estimates for members of the public, while Section 3.1.2 discusses the dose projections for persons who inadvertently intrude into the disposal facility.

3.1.1 Offsite Dose Assessment Results

The results of the offsite dose assessment are presented and discussed for each offsite exposure scenario. The dose projections for the Groundwater Resource Protection Scenario are discussed in Section 3.1.1.1, while the All Pathways - Groundwater Scenario dose projections are addressed in Section 3.1.1.2. Section 3.1.1.3 discusses the projected exposures for the Atmospheric Scenario and the radon flux projections for the undisturbed site. The dose projections for the All Pathways - Parajito Canyon Scenario are considered in Section 3.1.1.4.

3.1.1.1 Groundwater Resource Protection Scenario

The projected doses for the Groundwater Resource Protection Scenario are shown in Figures 3-1 and 3-2 for the receptor locations east-southeast of the Area G disposal units and in Parajito Canyon, respectively, for a period of 10,000 yr following facility closure. While the compliance period spans only 1,000 yr, projections are provided for the longer period to provide a more complete understanding of the performance of the disposal facility. Projected doses are shown in Figure 3-1 starting 650 yr after facility closure. Contaminated groundwater may discharge to the aquifer before this time, however, the projected doses to the receptor are extremely small. Doses to the canyon resident occur much earlier, due to the very short groundwater travel time to the regional aquifer.

The doses shown in Figure 3-1 correspond to the point of maximum groundwater exposure approximately 100 m east-southeast of the Area G fenceline. The resident near the town of White Rock is not projected to receive exposures from the groundwater pathway during the active institutional control period because contaminant travel times to this location are much greater than 100 yr. Annual doses at the point of maximum exposure peak between 4,500 and 5,000 yr, reaching a maximum of 1.4×10^{-5} mrem. C-14, Tc-99, and I-129 are the only radionuclides that reach the receptor's well during the period. C-14 is responsible for the majority of the projected doses early in the simulation, while Tc-99 is a major contributor at later times. Projected doses at the receptor location in Parajito Canyon (Figure 3-2) increase to a maximum of 4.5×10^{-5} mrem/yr at about 800 yr post-closure, and then decline for the remainder of the 10,000-yr period. C-14 is the primary contributor to the projected doses for the entire period.

The peak annual dose to the receptor downgradient of Area G during the compliance period is 8.3×10^{-6} mrem. C-14 is responsible for about 88 percent of this dose, while Tc-99 accounts for essentially all of the remainder. As stated above, the peak annual dose to the canyon resident is 4.5×10^{-5} mrem at 800 yr post-closure. C-14 is responsible for 68 percent of the peak dose, Tc-99 contributes 31 percent of the total.

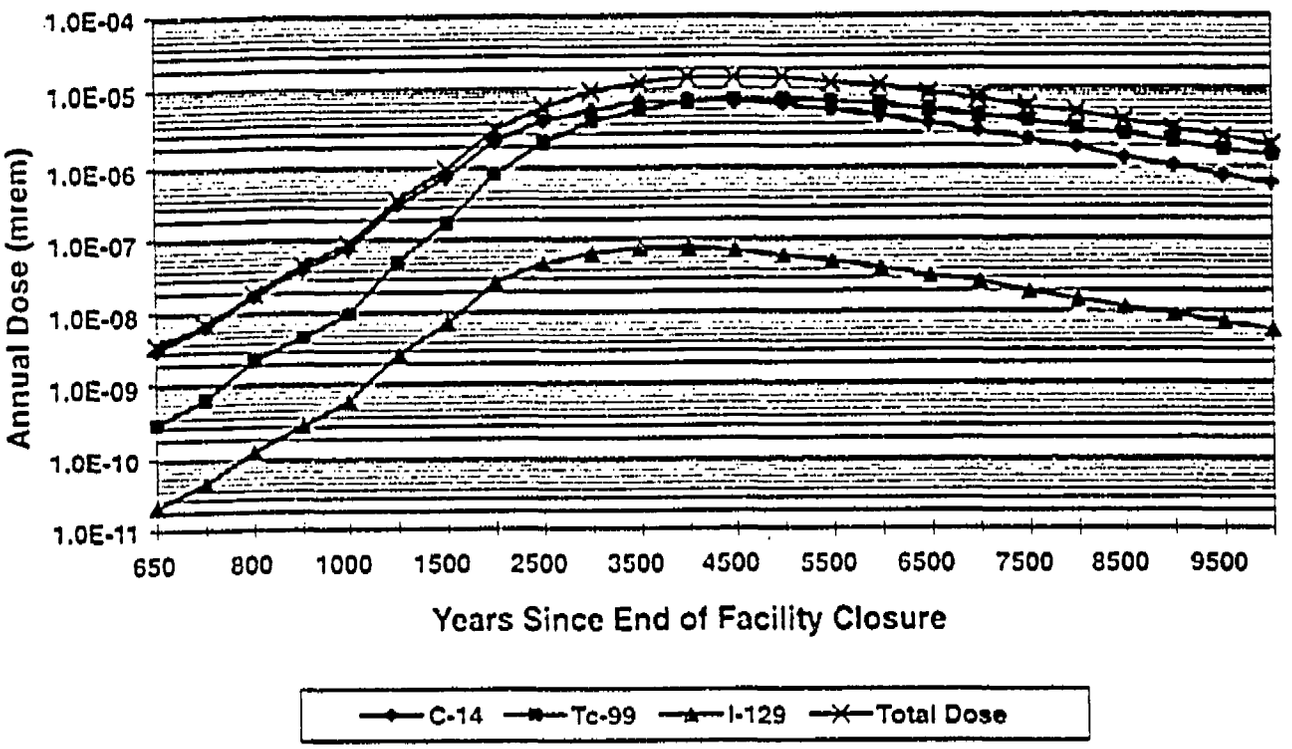

Figure 3-1. Projected performance assessment doses for the Groundwater Resource Protection Scenario 100 m downgradient of the Area G disposal units.

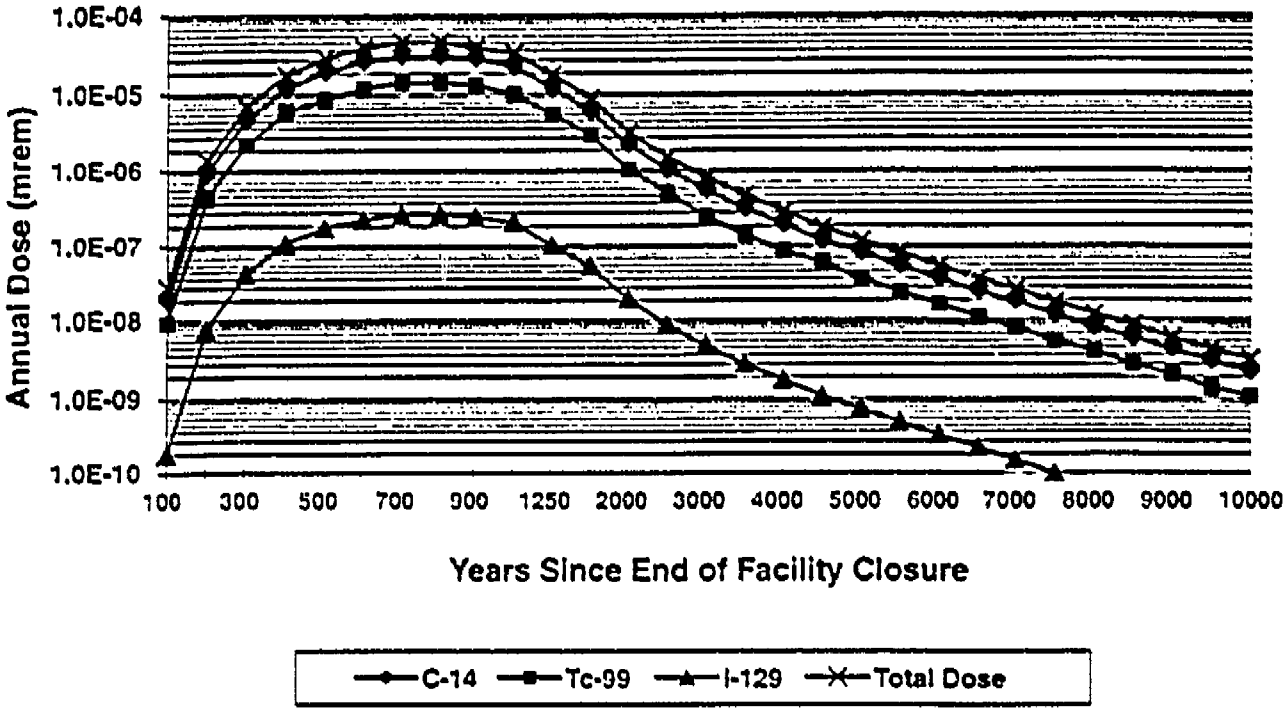

Figure 3-2. Projected performance assessment doses for the Groundwater Resource Protection Scenario in Paraijto Canyon.

3.1.1.2 All Pathways - Groundwater Scenario

No doses are projected to occur for the All Pathways - Groundwater Scenario at the receptor location near the town of White Rock before the end of the active institutional control period because groundwater contaminant transport times to this location exceed 100 yr. The projected annual doses for the offsite resident 100 m (330 ft) downgradient of the Area G fenceline are shown in Figure 3-3 for 10,000 yr following disposal facility closure. These doses, shown starting at 650 yr post-closure, rise to a maximum of 4.2×10^{-5} mrem at 4,500 yr post-closure. C-14 and Tc-99 are the major contributors to the projected doses throughout the period.

The peak annual dose projected for the 1,000-yr compliance period is 2.3×10^{-7} mrem. C-14 and Tc-99 contribute 86 and 14 percent of the peak dose, respectively. The contributions of the various exposure pathways to the peak projected dose are shown in Table 3-1. The ingestion of drinking water and consumption of vegetables irrigated with contaminated well water are responsible for 37 and 60 percent of the peak dose, respectively.

3.1.1.3 Atmospheric Scenario

Gaseous and particulate releases to the atmosphere may result in exposures of members of the public following their transport off site. These exposures were projected for the location of maximum atmospheric exposure, approximately 500 m (16,000 ft) north of Area G in Canada del Buey, and for the town of White Rock. The projected peak exposures at these locations prior to the end of the active institutional control period are 6.6×10^{-2} and 1.6×10^{-2} mrem/yr, respectively. The peak doses are dominated by H-3, which accounts for more than 99 percent of the exposures. The maximum doses are projected to occur at the end of disposal operations, in the year 2044, because inventories of H-3 are highest at this time. The sole exposure route for this dose is the inhalation of tritiated water vapor and C-14 gas.

The doses projected to result from atmospheric transport of contamination brought to the surface from biotic intrusion are shown in Figure 3-4. The peak projected dose at the point of maximum exposure is 9.1×10^{-3} mrem/yr, while the peak annual dose in White Rock is 2.2×10^{-3} mrem. These doses occur at the end of the active institutional control period, the

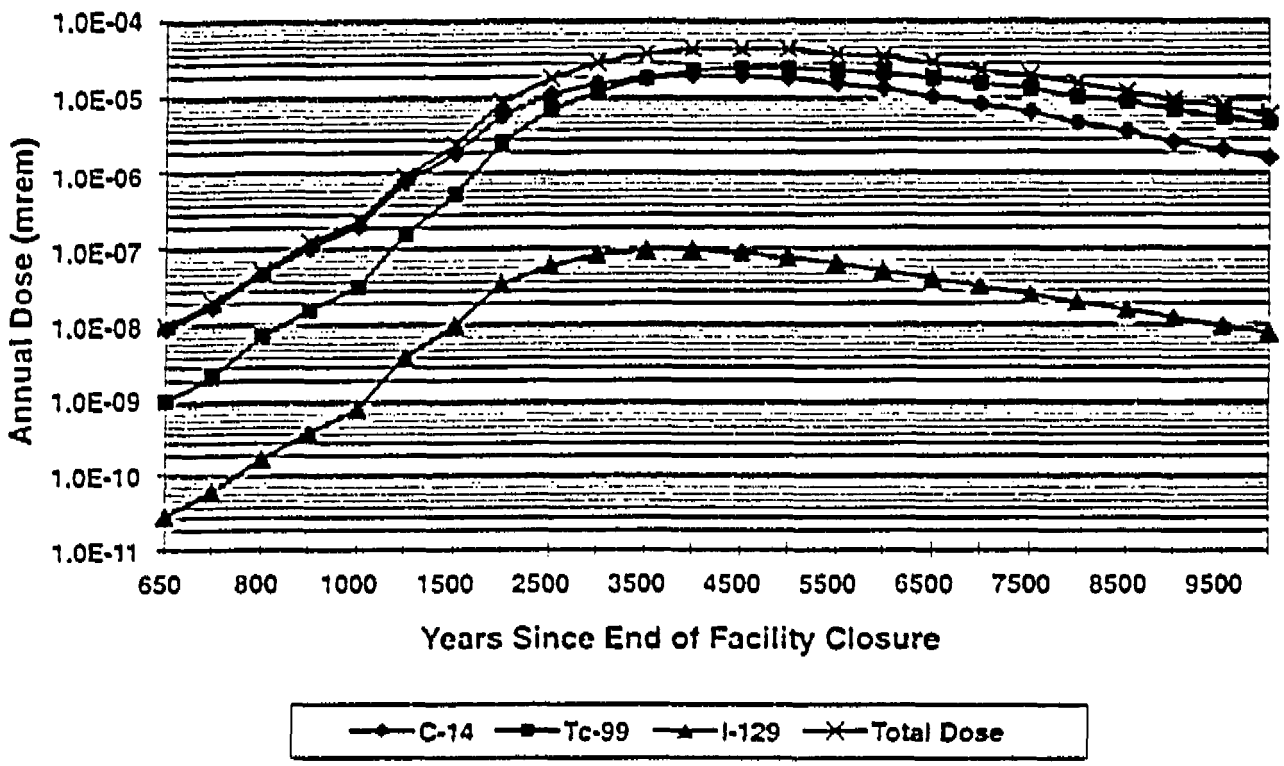

RAE - 106257

Figure 3-3. Projected performance assessment doses for the All Pathways - Groundwater Scenario.

Table 3-1. Pathway contributions to the peak projected performance assessment dose for the All Pathways - Groundwater Scenario.

Pathway	Dose at Peak Time	Percent Contribution
Ingestion of water	8.3E-08	37%
Ingestion of soil	1.6E-10	0%
Ingestion of crops	1.4E-07	60%
Ingestion of meat	3.4E-09	1%
Ingestion of milk	4.1E-09	2%
Inhalation of particulates	3.8E-12	0%
Direct radiation from soils	1.8E-12	0%
Direct radiation from air	3.0E-18	0%
Total Dose	2.3E-07	

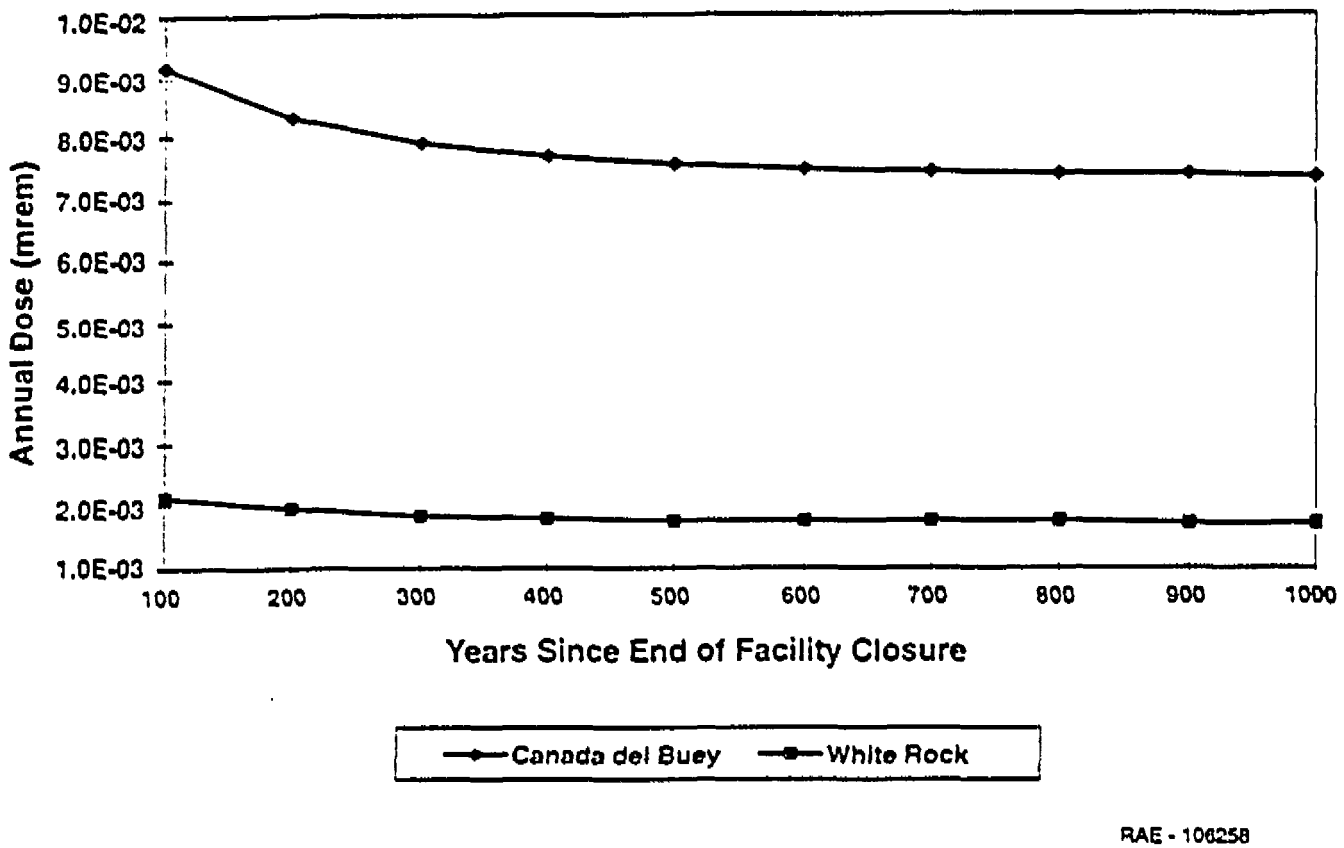

Figure 3-4. Projected performance assessment doses for the Atmospheric Scenario.

time at which biotic intrusion is first expected to be feasible. The radionuclides that contribute to the peak doses during the 1,000-year compliance period are shown in Figure 3-5. Isotopes of americium, plutonium, and uranium account for more than 95 percent of the dose at each location. Inhalation of contaminated dust accounts for essentially all of the projected exposures.

The projected fluxes of radon gas from the undisturbed disposal site depend upon the Ra-226 and Ra-228 concentrations in the waste. Total pit and shaft concentrations of these isotopes in the waste disposed of between September 26, 1988, and the end of 1995 are shown in Figure 3-6 from the end of 1995 through the year 12045 (10,000 yr after the end of disposal operations). Concentrations of Ra-226 decline initially due to radioactive decay, but increase at later times as long-lived parents of the isotope decay. Ra-228 concentrations remain relatively constant over the entire period and are determined almost entirely by the Th-232 inventory in the pits and shafts. The concentrations shown in the figure do not account for the depletion of radionuclides in the waste due to leaching.

The projected peak radon fluxes for the historic waste are presented in Table 3-2. The maximum Rn-222 flux from the historic disposal pits is 1.1×10^{-1} pCi/m^2/s (1.0×10^{-2} pCi/ft^2/s), while the projected fluxes of Rn-220 are negligible throughout the period. The peak projected Rn-222 flux from the historic shafts is 2.5×10^{-2} pCi/m^2/s, (2.3×10^{-3} pCi/ft^2/s), while the peak flux of Rn-220 is 3.1 pCi/m^2/s (2.9×10^{-1} pCi/ft^2/s).

Pit and shaft concentrations of Ra-226 and Ra-228 in the future waste are shown in Figure 3-7 for the 10,000 yr following the end of disposal operations. As demonstrated earlier, Ra-226 concentrations change as initial inventories decay and ingrowth from the isotope's longer-lived parents occurs. Ra-228 concentrations remain essentially constant over the period. The maximum Rn-222 flux during the 1,000-year compliance period for the pit waste is 1.7×10^{-1} pCi/m^2/s (1.6×10^{-2} pCi/ft^2/s), occurring at the end of disposal operations (Table 3-2). Rn-220 fluxes from the pit waste are negligible. The peak projected flux of Rn-222 from the future shaft waste is 2.0×10^{-3} pCi/m^2/s (1.9×10^{-4} pCi/ft^2/s), while the peak Rn-220 flux during the compliance period is 8.1×10^{-1} pCi/m^2/s (7.5×10^{-2} pCi/ft^2/s).

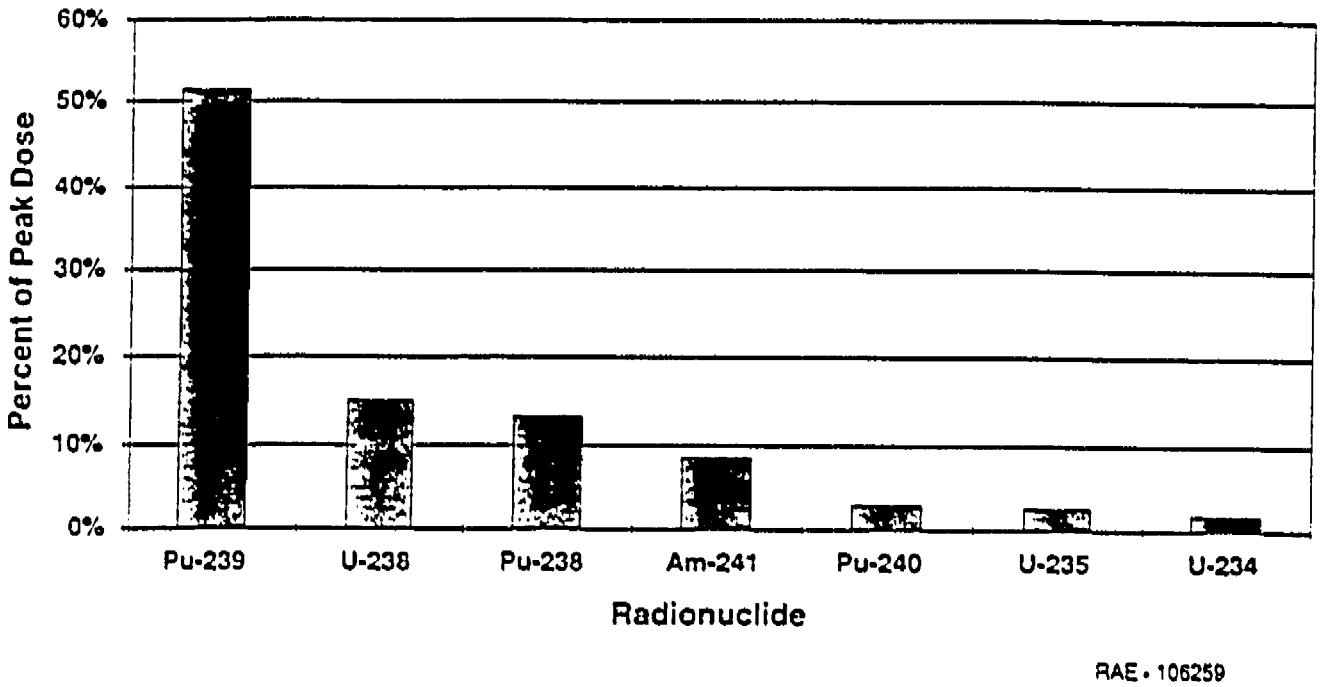

Figure 3-5. Radionuclide contributions to the peak performance assessment dose for the Atmospheric Scenario.

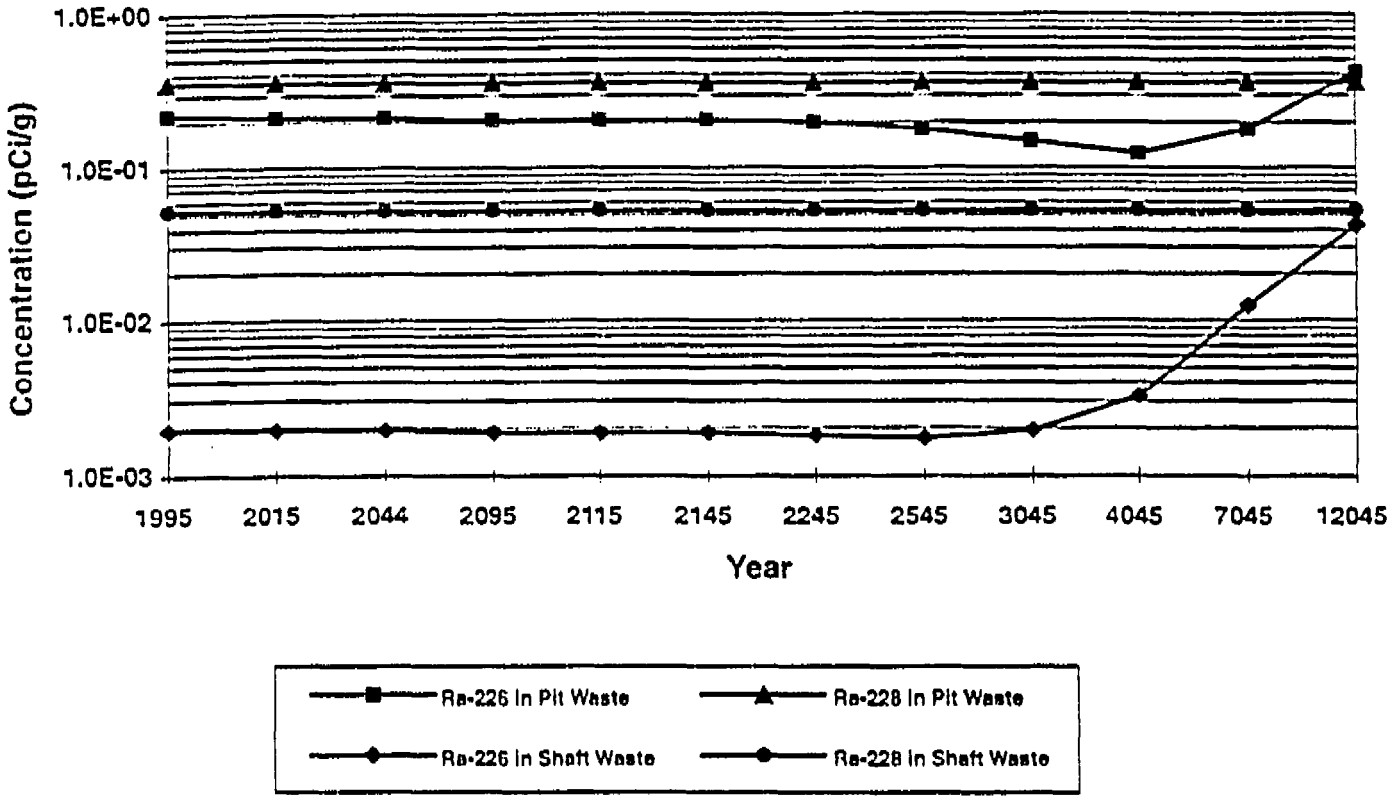

Figure 3-6. Ra-226 and Ra-228 concentrations in historic pit and shaft waste.

Table 3-2. Peak projected radon fluxes for the Area G performance assessment.

Disposal Units/Waste	Peak Projected Flux During Compliance Period		
	Rn-220 ($pCi/m^2/s$)	Rn-222 ($pCi/m^2/s$)	Total ($pCi/m^2/s$)
Disposal Pits			
Historic waste	0.0E+00	1.1E-01	1.1E-01
Future waste	0.0E+00	1.7E-01	1.7E-01
Disposal Shafts			
Historic waste	3.1E+00	2.5E-02	3.1E+00
Future waste	8.1E-01	2.0E-03	8.1E-01

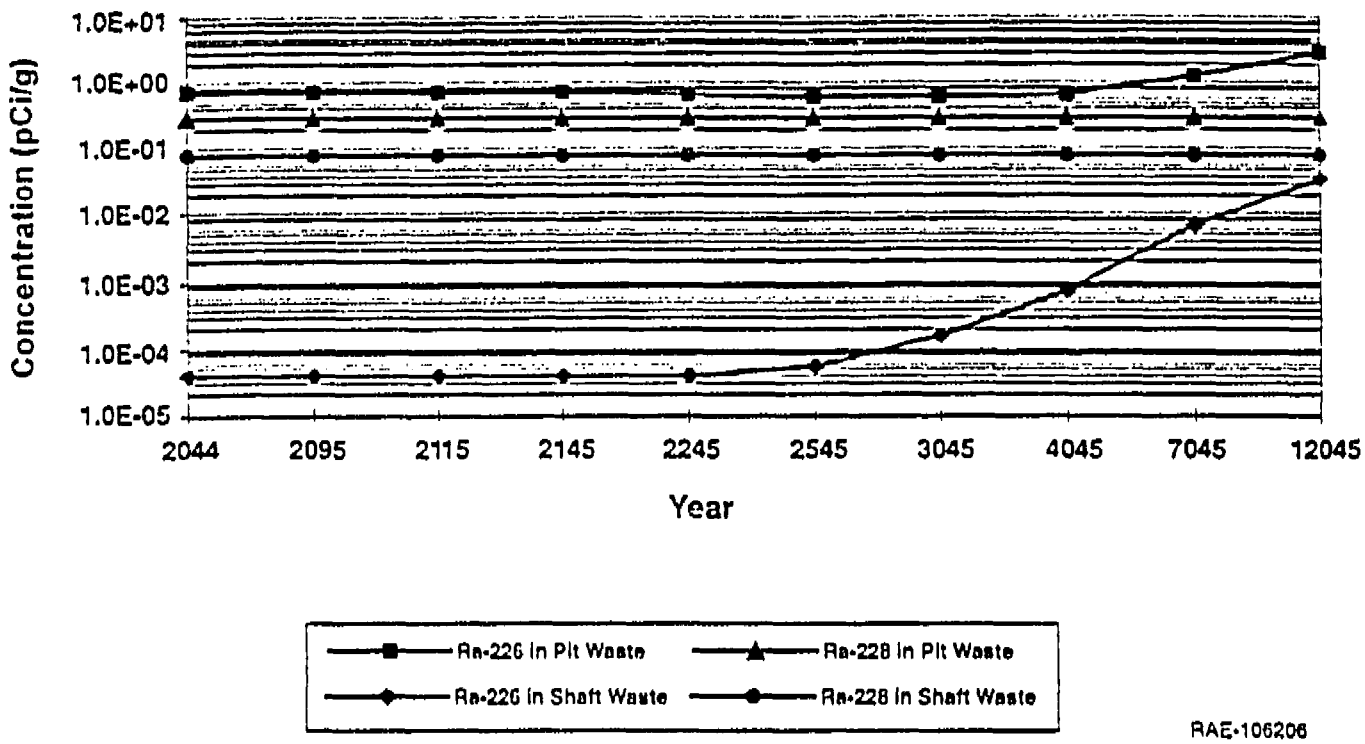

Figure 3-7. Ra-226 and Ra-228 concentrations in future pit and shaft waste.

3.1.1.4 All Pathways - Parajito Canyon Scenario

The projected doses for the All Pathways - Parajito Canyon Scenario are shown in Figure 3-8 for a period of 10,000 yr. Projected annual doses increase from 8.7×10^{-6} mrem at the end of the active institutional control period to a peak of 1.3×10^{-4} mrem at 800 yr post-closure, and decline thereafter. The general increase in the projected doses for the first 800 yr coincides with the arrival of C-14, Tc-99, and I-129 at the resident's well, following their discharge to the sides of the mesa. No other radionuclides are projected to reach the sides of the mesa during the compliance period.

The peak scenario dose is dominated by the radionuclides entering the regional aquifer. C-14 and Tc-99 are responsible for 62 and 34 percent of the dose, respectively. Pu-239 in the canyon soils accounts for 2 percent of the total dose. The ingestion of water and consumption of food crops irrigated with contaminated water account for 34 and 60 percent of the peak dose, respectively (Table 3-3).

3.1.2 Inadvertent Intruder Dose Assessment Results

The Intruder-Agriculture Scenario was used to project potential doses to a person who inadvertently intrudes into the disposed waste after the 100-yr active institutional control period. The nature of the intruder scenario is such that intrusion into one type of disposal unit (i.e., pits or shafts) precludes simultaneous intrusion into the other. Similarly, intrusion into the historic waste by an individual is not consistent with intrusion into the future inventory at the same time. Consequently, separate intruder dose projections were prepared for the historical and future inventories, and for the disposal pits and shafts. These projections account for the inventories disposed of or projected to be disposed of at Area G, as well as the specific characteristics of the disposal units.

The projected doses for the intruder scenarios account for the cumulative dose from all waste radionuclides. Consequently, the dose assessment methodology was implemented at various times after facility closure to ensure that the time-dependent aspects of exposure were accounted for and that the maximum projected doses were identified. With this in mind, intruder doses were projected at the time intrusion into the waste may first occur, at

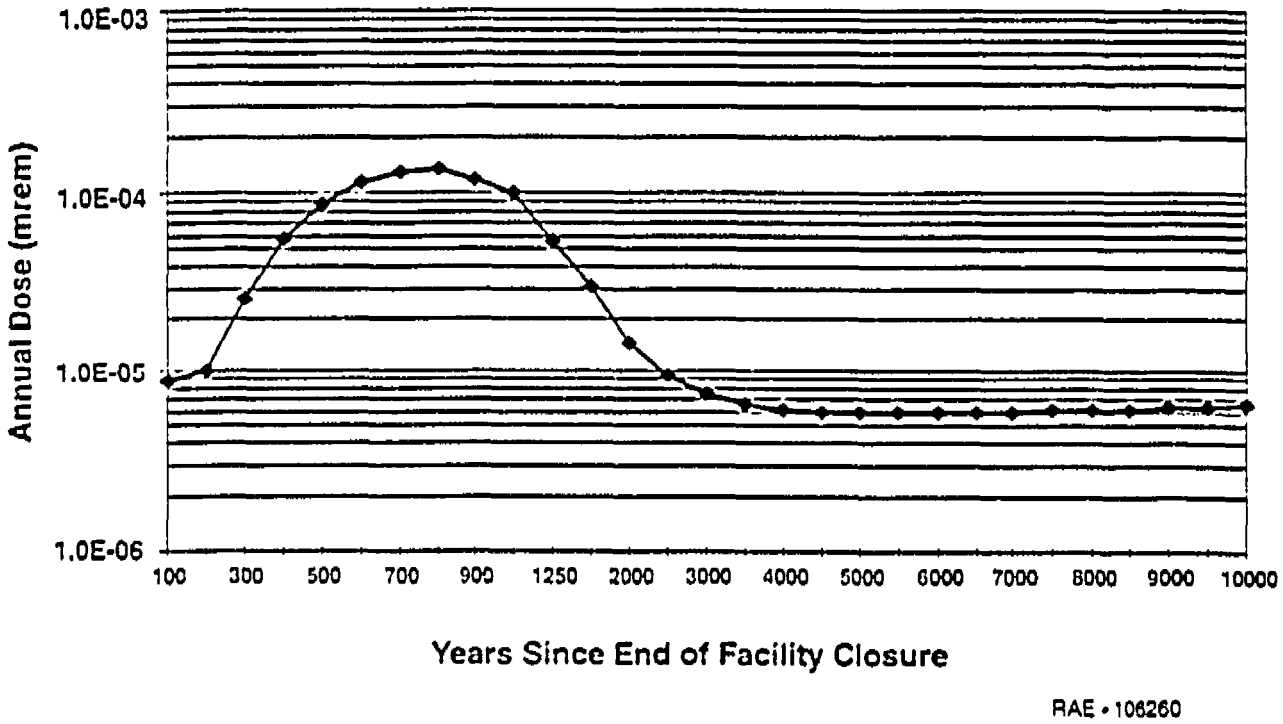

Figure 3-8. Projected performance assessment doses for the All Pathways - Parajito Canyon Scenario.

Table 3-3. Pathway contributions to the peak projected performance assessment dose for the All Pathways - Parajito Canyon Scenario.

Pathway	Dose at Peak Time	Percent Contribution
Ingestion of water	4.5E-05	34%
Ingestion of soil	1.1E-06	1%
Ingestion of crops	8.0E-05	60%
Ingestion of meat	1.5E-06	1%
Ingestion of milk	2.2E-06	2%
Inhalation of particulates	2.4E-06	2%
Direct radiation from soils	1.4E-06	1%
Direct radiation from air	1.6E-13	0%
Total	1.3E-04	

the end of the 1,000-yr compliance period, and at intermediate times to improve the understanding of the disposal facility's performance. As discussed in Section 2.1, the time at which intrusion may first occur differs for the different disposal technologies. Intrusion into the waste was assumed to be feasible at the end of the 100-yr active institutional control period for the disposal pits. In contrast, the presence of concrete caps over the disposal shafts was assumed to prevent the intruder scenario from occurring for 300 yr following closure of the disposal facility.

The dose projections for the Intruder-Agriculture Scenario are presented and discussed below. Section 3.1.2.1 discusses the results for the historic waste, the material disposed of between September 26, 1988, and the end of 1995. Section 3.1.2.2 addresses future waste, the material expected to require disposal between 1996 and 2044, the assumed end of disposal operations at Area G.

3.1.2.1 Intruder Dose Projections for Historic Waste

The doses projected for the Intruder-Agriculture Scenario for the historic disposal pits are shown in Figure 3-9 for 1,000 yr following the end of disposal operations. Projections are shown starting at 100 yr post-closure. This period corresponds to the end of the active institutional control period, and is the earliest time at which intrusion into the disposal pits is feasible.

The peak projected dose shown in Figure 3-9 is 30 mrem and occurs at the end of the active institutional control period. Doses decline to approximately 24 mrem at the end of the compliance period as the shorter-lived radionuclides undergo radioactive decay. The radionuclides making major contributions to the projected dose at 100 yr post-closure are shown in Figure 3-10. Pu-239 and U-238 account for about 53 percent of the total projected dose; Am-241, Th-232, U-235, and Pu-238 are each responsible for about 6 to 9 percent of the total. Inhalation of suspended dust and direct radiation from contaminated soil are responsible for 43 and 29 percent of the peak dose, respectively (Table 3-4).

The projected doses to the intruder from the inhalation of radioactive gases diffusing into the house from the historic pit waste are included in Table 3-5. The peak dose from this

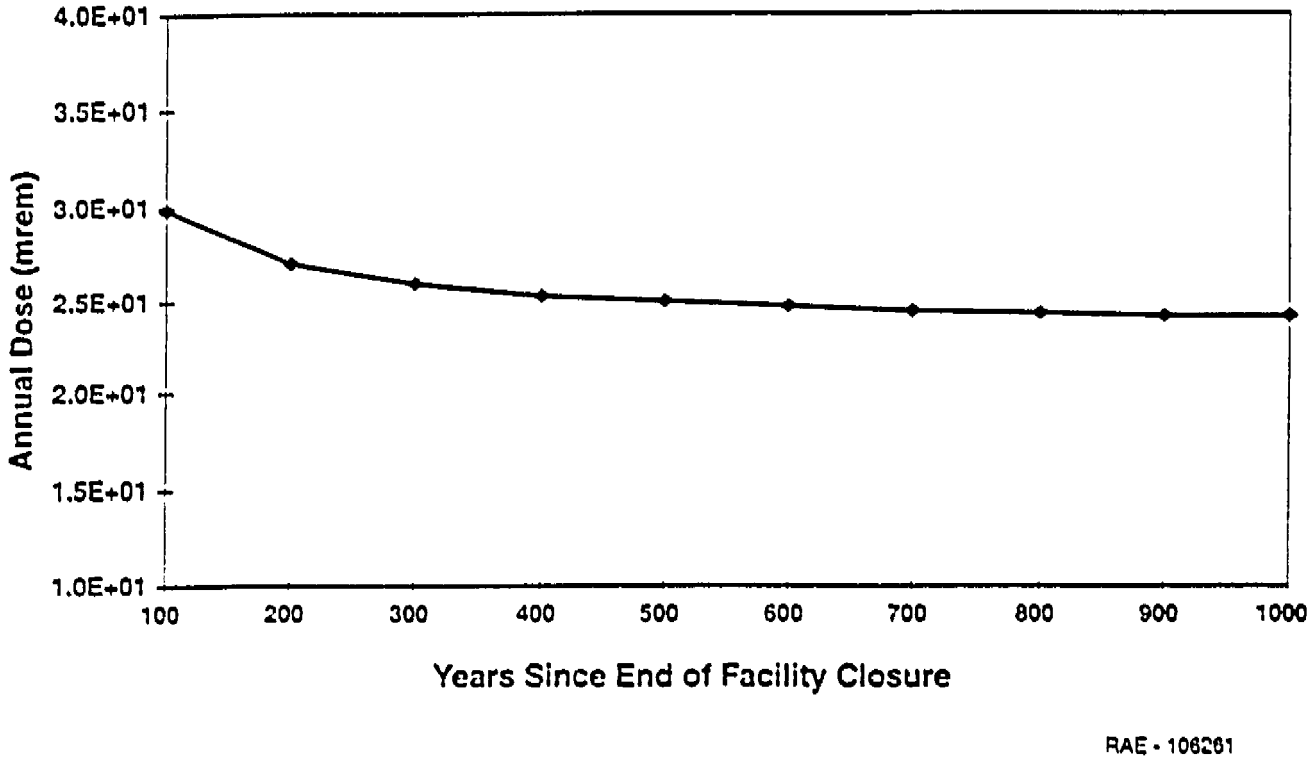

Figure 3-9. Projected performance assessment doses from historic pit waste for the Intruder-Agriculture Scenario.

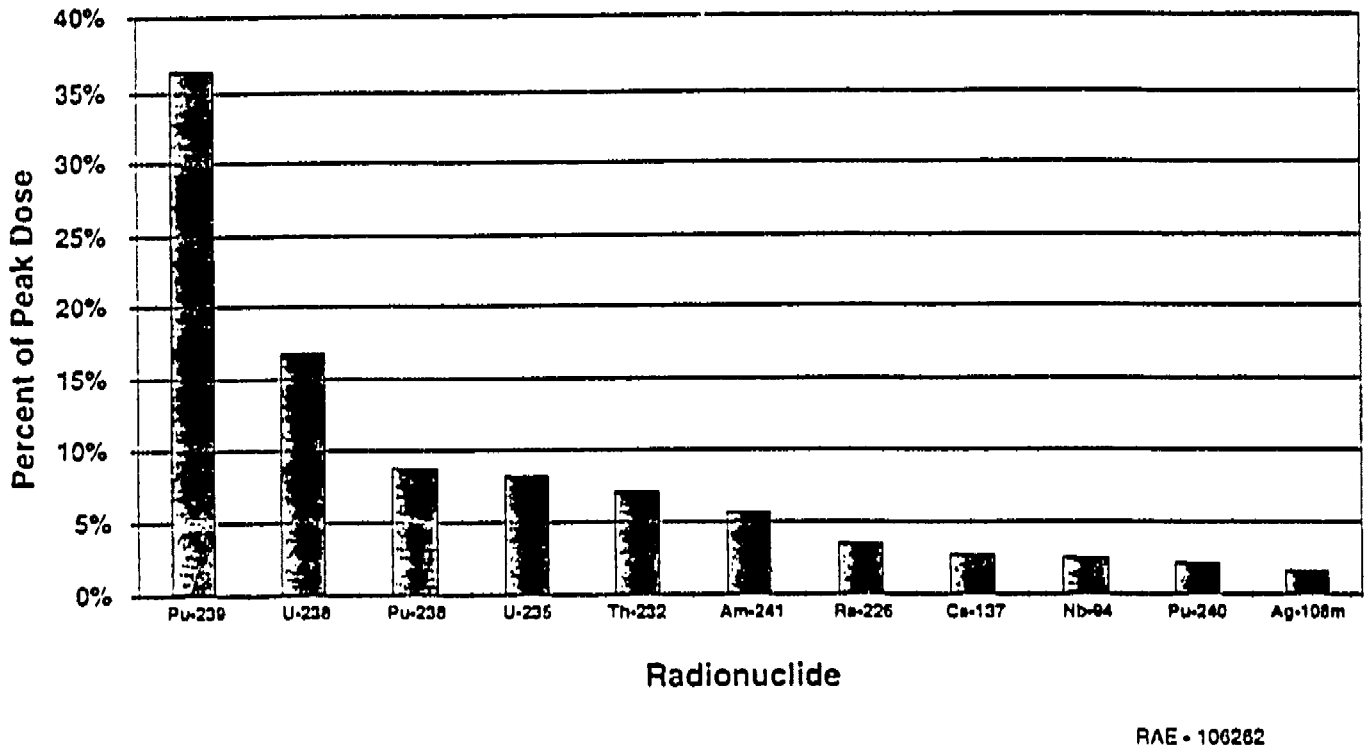

Figure 3-10. Radionuclide contributions from historic pit waste to the peak performance assessment intruder dose.

Table 3-4. Pathway contributions to the peak projected intruder dose for the historic pits.

Exposure Pathway	Dose at Peak Time	Percent of Peak Dose
Ingestion of soil	5.8E+00	20%
Ingestion of crops	2.7E+00	9%
Inhalation of particulates	1.3E+01	43%
Inhalation of gases	1.5E-02	0%
Direct radiation from soils	8.5E+00	29%
Direct radiation from air	8.2E-07	0%
Total Dose	3.0E+01	

Table 3-5. Projected intruder doses due to the inhalation of radioactive gases.

Waste Inventory	Radionuclide H-3 (mrem)	C-14 (mrem)	Total (mrem)
Historic Waste			
Pits	7.5E-07	1.5E-02	1.5E-02
Shafts	2.7E-05	1.9E-01	1.9E-01
Future Waste			
Pits	1.4E-05	2.6E-02	2.6E-02
Shafts	3.5E-04	0.0E+00	3.5E-04

pathway is 1.5×10^{-2} mrem, and is dominated by C-14. This dose is projected to occur immediately following the active institutional control period, based on the conservative assumption that all organic C-14 present in the waste will be released as a gas within a single year. No doses are projected to occur from Kr-81 and Kr-85, as inhalation dose conversion factors were unavailable from DOE (1988b) and EPA (1988b). The inhalation doses listed in Table 3-5 are reflected in Figure 3-9 and Table 3-4.

Dose projections for the Intruder-Agriculture Scenario for the historic disposal shafts are shown in Figure 3-11. Projections are shown starting at 300 yr post-closure; intrusion prior to this time was assumed to be prevented by the placement of concrete caps over the shafts. The maximum projected dose during the 1,000-yr compliance period is 18 mrem, occurring at the time of first intrusion. Projected doses decline to less than 8 mrem by the end of the compliance period, following the decay of the shorter-lived radionuclides in the waste.

The radionuclides that make major contributions to the 300-yr post-closure shaft dose are shown in Figure 3-12. Ag-108m and Cs-137 are responsible for almost 50 percent of the projected dose; Nb-94, Nb-92, Am-241, U-238, and Pu-239 each contribute about 5 to 13 percent of the dose. Direct radiation from contaminated soils accounts for 66 percent of the projected dose, while inhalation of airborne radioactivity accounts for 20 percent of the dose projection (Table 3-6).

The maximum annual dose from the inhalation of radioactive gases generated by the historic shaft waste is 1.9×10^{-1} mrem (Table 3-5). C-14 accounts for essentially all of the projected exposure, which was assumed to occur at 300 yr post-closure. The projected dose due to the inhalation of gases is included in Figure 3-11 and Table 3-6.

3.1.2.2 Intruder Dose Projections for Future Waste

Doses projected for the Intruder-Agriculture Scenario for the future disposal pits are shown in Figure 3-13 for the 1,000-yr compliance period. Model calculations project a dose of 30 mrem at 100 yr post-closure. The doses decline to approximately 25 mrem by the end of the period. Pu-239 and U-238 account for about 50 percent of the projected peak dose

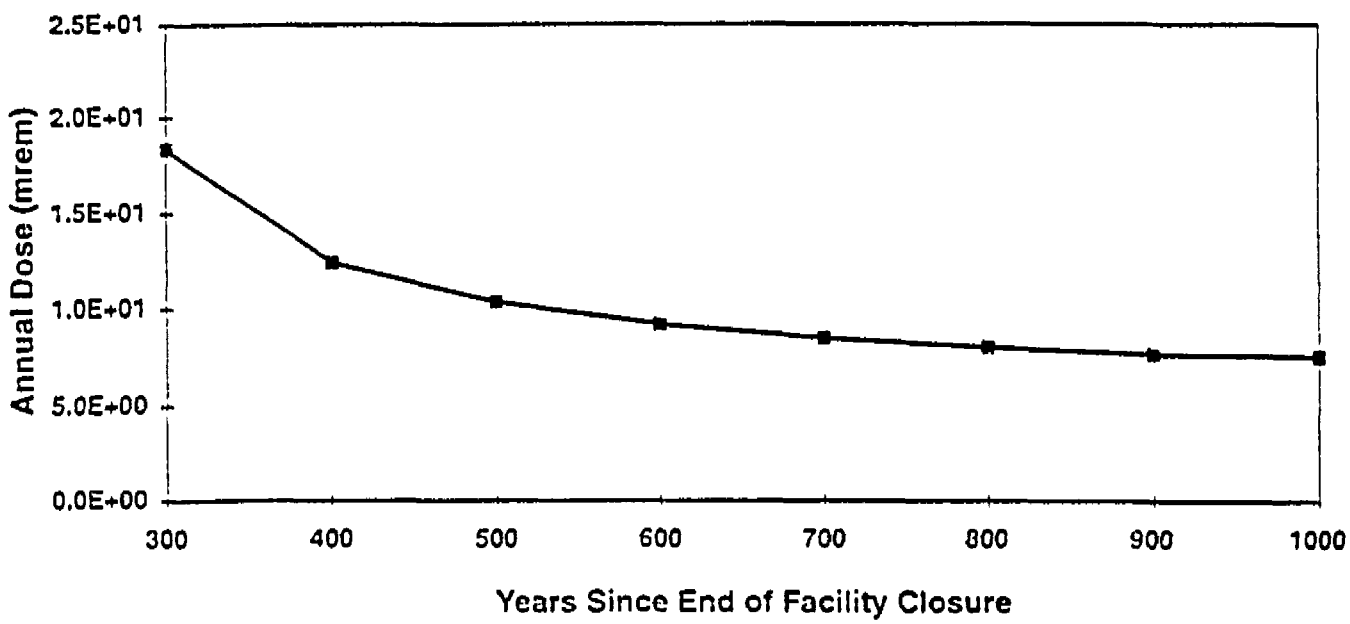

RAE - 106209

Figure 3-11. Projected performance assessment doses from historic shaft waste for the Intruder-Agriculture Scenario.

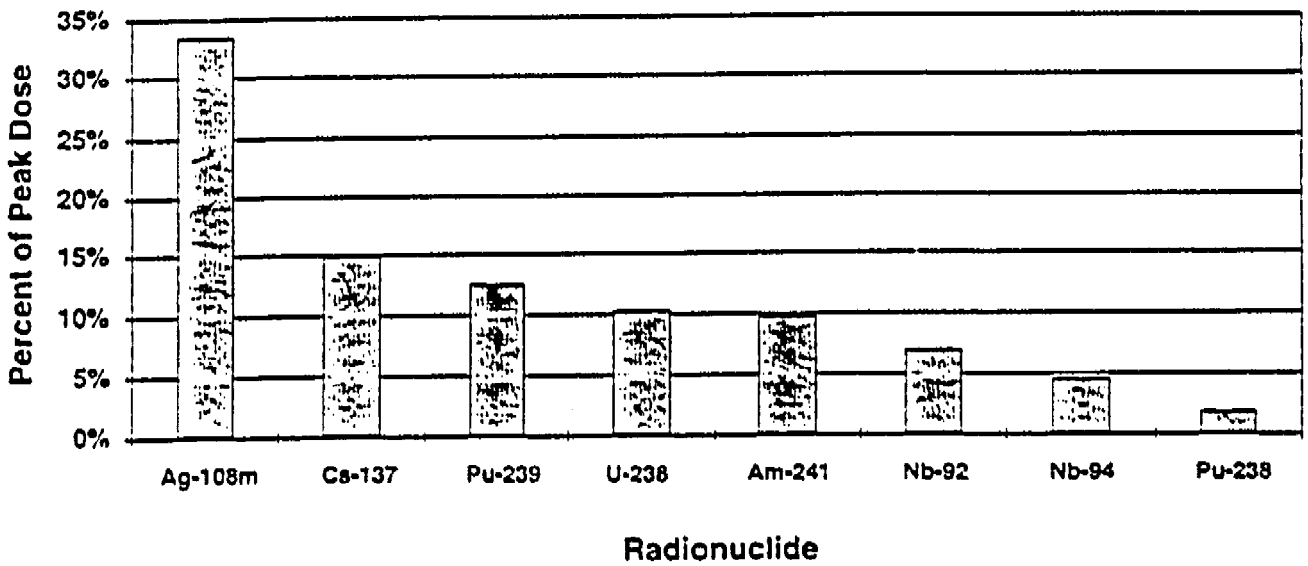

RAE - 106210

Figure 3-12. Radionuclide contributions from historic shaft waste to the peak performance assessment intruder dose.

Table 3-6. Pathway contributions to the peak projected intruder dose for the historic shafts.

Exposure Pathway	Dose at Peak Time (mrem)	Percent of Peak Dose
Ingestion of soil	1.7E+00	9%
Ingestion of crops	6.0E-01	3%
Inhalation of particulates	3.8E+00	20%
Inhalation of gases	1.9E-01	1%
Direct radiation from soil	1.2E+01	66%
Direct radiation from air	1.0E-06	0%
Total Dose	1.8E+01	

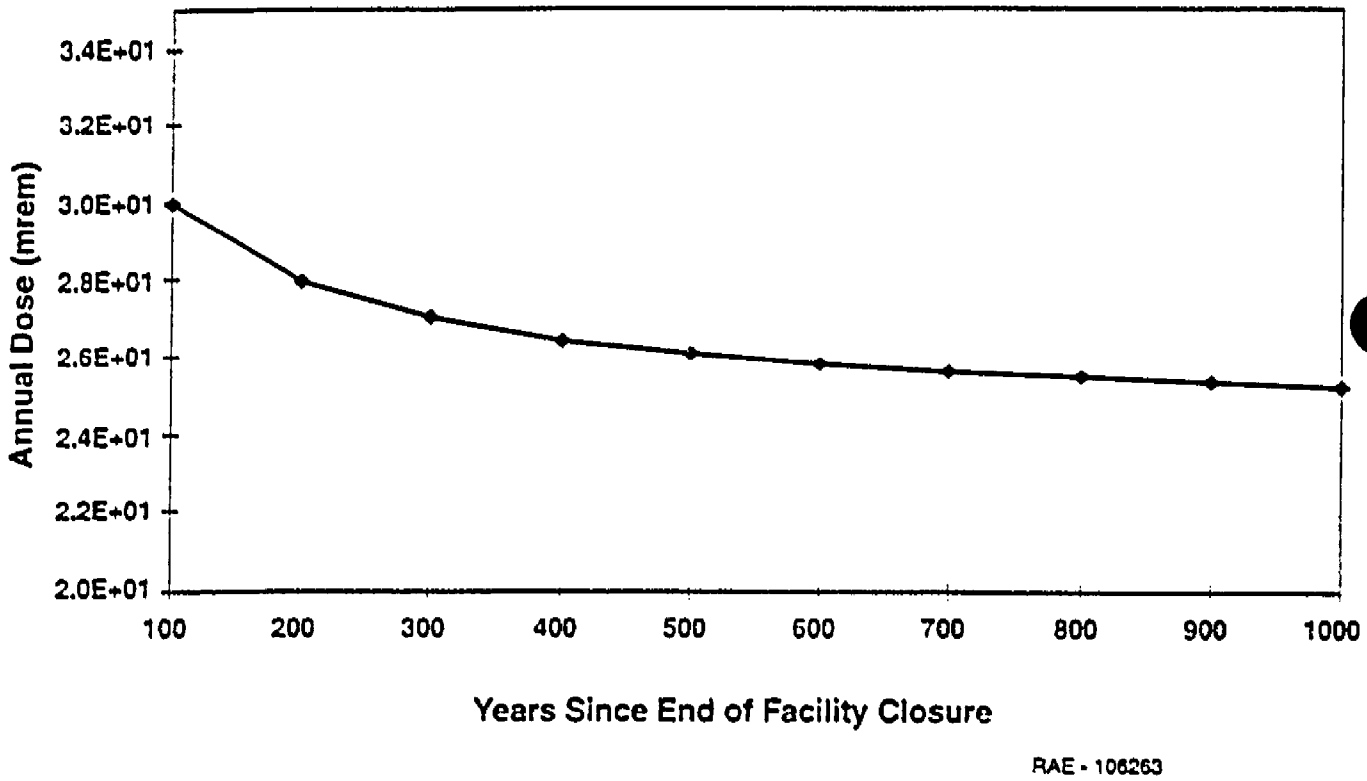

Figure 3-13. Projected performance assessment doses from future pit waste for the Intruder-Agriculture Scenario.

(Figure 3-14). U-234, Ra-226, U-235, Am-241, Pu-238, and Pu-240 are each responsible for about 5 to 7 percent of the total dose. Inhalation of airborne particulates and direct radiation from the ground surface are the dominant exposure pathways, accounting for 69 percent of the peak dose (Table 3-7). The peak dose from the inhalation of radioactive gases is 2.6×10^{-2} mrem (Table 3-5) and is dominated by C-14 generated from organic waste at the end of the active institutional control period. This dose is reflected in the results summarized in Figure 3-13 and Table 3-7.

Dose projections for the Intruder-Agriculture Scenario for the future disposal shafts are shown in Figure 3-15. Projections are shown starting at 300 yr post-closure; intrusion prior to this time was assumed to be prevented by the placement of concrete caps over the disposal units. The maximum projected dose during the 1,000-yr compliance period is about 12 mrem, occurring at the time of first intrusion. Projected doses decline to less than 6 mrem by the end of the compliance period, following the decay of the shorter-lived radionuclides in the waste. Cs-137 accounts for 38 percent of the projected intruder dose; Nb-92, U-238, Am-241, and Pu-239 each contribute about 10 to 17 percent of the total dose (Figure 3-16). Inhalation of airborne radioactivity and direct radiation from contaminated soil account for 83 percent of the projected exposure (Table 3-8). The peak annual dose from the inhalation of radioactive gases is 3.5×10^{-4} mrem (Table 3-5) and is projected to occur immediately after the end of active institutional control. The dose is due solely to tritiated water vapor as no organic C-14 is projected to be present in the future shaft waste.

3.2 COMPOSITE ANALYSIS

The exposure scenarios for the composite analysis, discussed in Section 2.1, address potential exposures to members of the public living in the vicinity of the Area G disposal facility. The dose projections for the analysis are organized in terms of these scenarios. Section 3.2.1 discusses the dose estimates for the All Pathways - Groundwater Scenario, while the dose projections for the Atmospheric Scenario are presented in Section 3.2.2. The projected doses for the All Pathways - Parajito Canyon Scenario are discussed in Section 3.2.3.

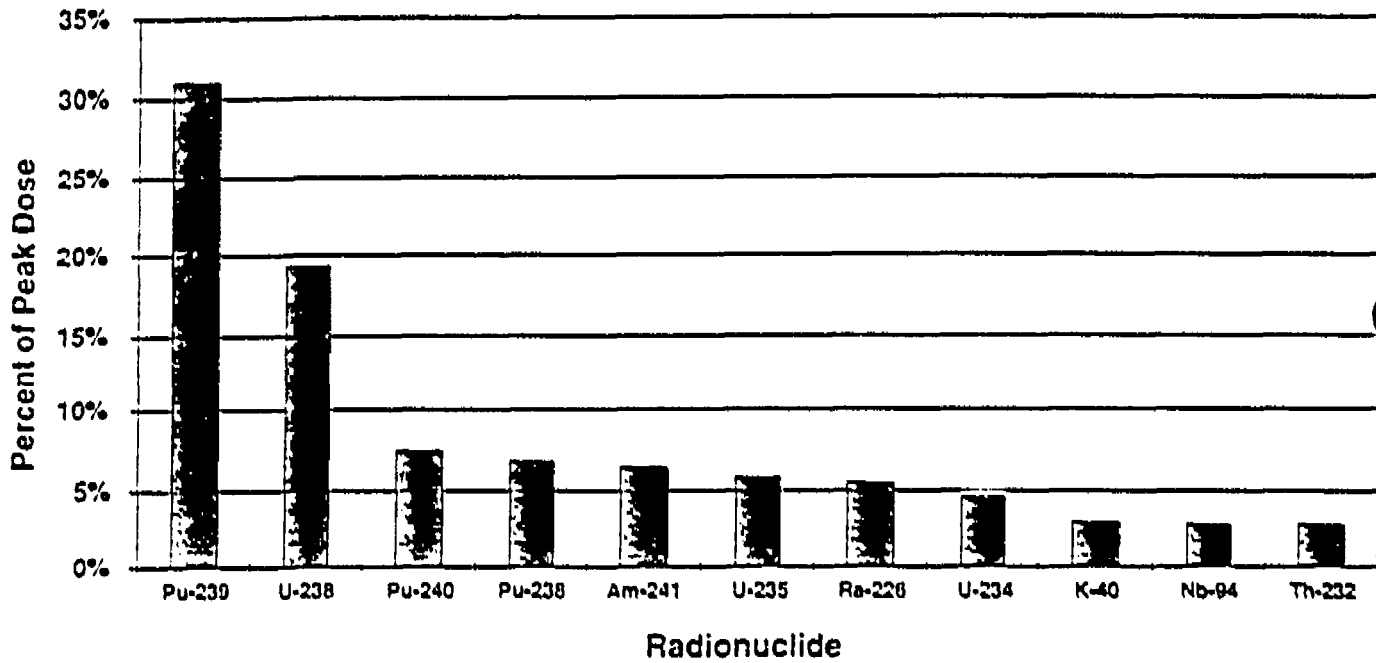

RAE - 108264

Figure 3-14. Radionuclide contributions from future pit waste to the peak performance assessment intruder dose.

Table 3-7. Pathway contributions to the peak projected intruder dose for the future pits.

Exposure Pathway	Dose at Peak Time	Percent of Peak Dose
Ingestion of soil	5.8E+00	19%
Ingestion of crops	3.5E+00	12%
Inhalation of particulates	1.3E+01	44%
Inhalation of gases	2.6E-02	0%
Direct radiation from soil	7.5E+00	25%
Direct radiation from air	7.1E-07	0%
Total Dose	3.0E+01	

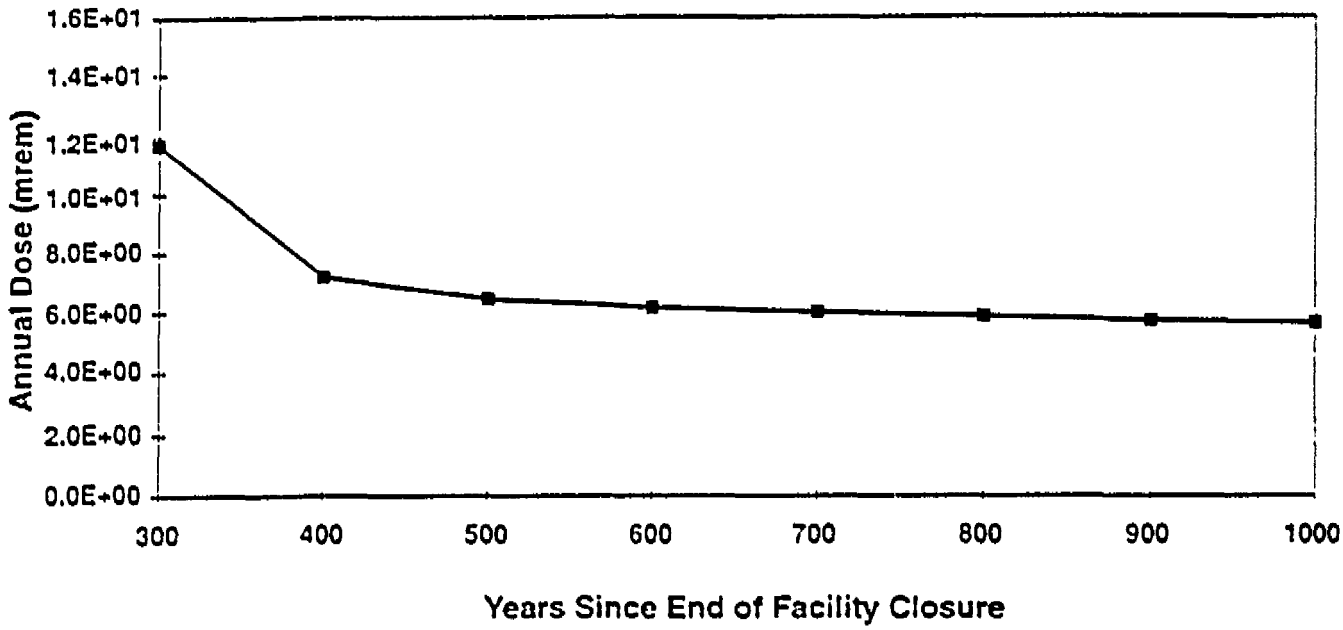

RAE - 106213

Figure 3-15. Projected performance assessment doses from future shaft waste for the Intruder-Agriculture Scenario.

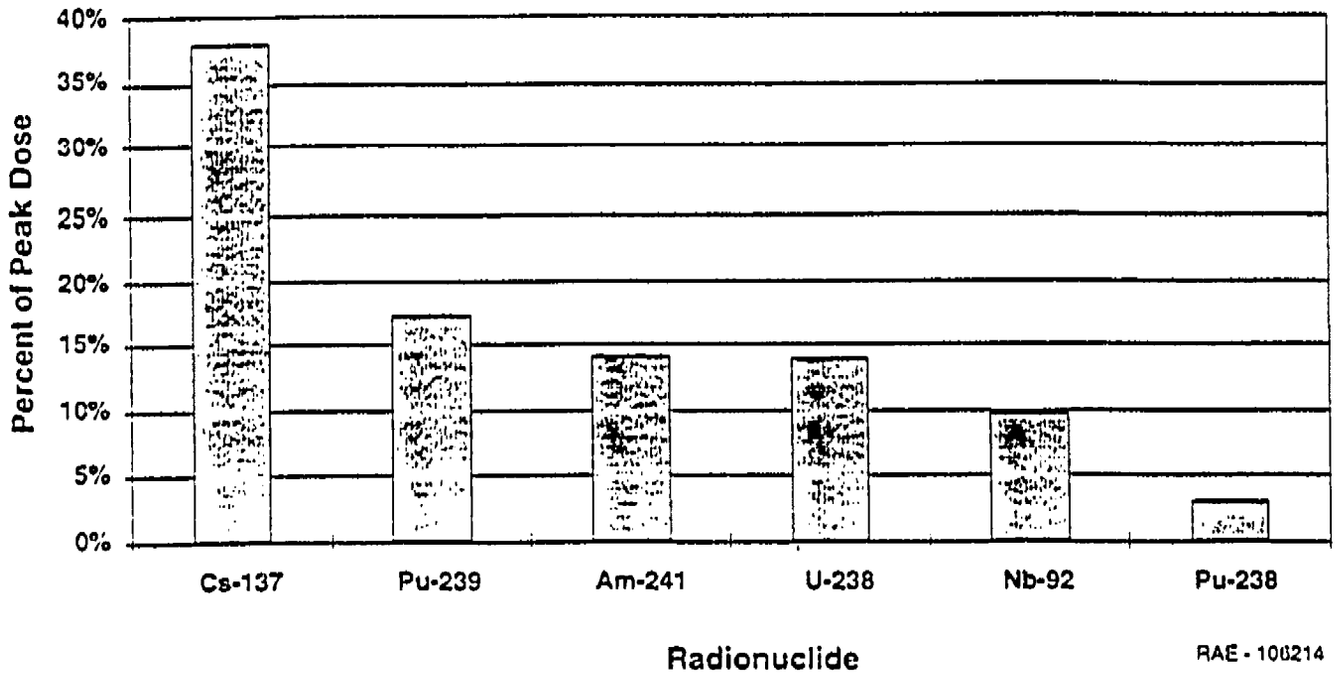

Figure 3-16. Radionuclide contributions from future shaft waste to the peak performance assessment intruder dose.

Table 3-8. Pathway contributions to the peak projected performance assessment intruder dose for the future shafts.

Exposure Pathway	Dose at Peak Time (mrem)	Percent of Peak Dose
Ingestion of soil	1.5E+00	13%
Ingestion of crops	5.1E-01	4%
Inhalation of particulates	3.2E+00	28%
Inhalation of gas	3.9E-04	0%
Direct radiation from soil	6.5E+00	55%
Direct radiation from air	5.8E-07	0%
Total Dose	1.2E+01	

3.2.1 All Pathways - Groundwater Scenario

As noted in Section 3.1.1, the contaminant travel time to the receptor location near the town of White Rock is greater than 100 yr. Consequently, no doses are projected for this location prior to the end of the active institutional control period. The projected doses for the point of maximum exposure 100 m (330 ft) east-southeast of the disposal units are shown in Figure 3-17 for a period of 10,000 yr following closure of the disposal facility. Projected doses are shown beginning 650 yr after the end of active institutional control; annual doses continue to increase until 3,000 yr post-closure, reaching a maximum of 7.3×10^{-4} mrem. C-14, Tc-99, and I-129 are the only radionuclides that are projected to reach the receptor's well within 10,000 yr; C-14 is the primary contributor to the projected doses throughout the period.

The peak annual dose during the 1,000-yr compliance period is 1.2×10^{-5} mrem. C-14 and Tc-99 account for 95 and 3 percent of the this dose, respectively. Exposure pathway contributions to the peak projected dose are shown in Table 3-9. Consumption of water and ingestion of vegetables irrigated with contaminated well water contribute 38 and 59 percent of the peak dose, respectively.

3.2.2 Atmospheric Scenario

The projected peak dose from gas inhalation at the point of maximum exposure is 7.5×10^{-2} mrem/yr, the corresponding dose at White Rock is 1.8×10^{-2} mrem/yr. These doses are projected to occur at the end of facility operations because H-3 inventories are highest at this time. H-3 is responsible for 90 percent of the total doses; C-14 accounts for the remainder. The projected doses are due entirely to the inhalation of tritiated water vapor and C-14 gas.

The doses projected to result from atmospheric transport of contamination brought to the surface from biotic intrusion are shown in Figure 3-18. The peak projected dose for this pathway is 5.5 mrem/yr in Canada del Buey and 1.3 mrem/yr at White Rock. Peak doses at both locations occur at the end of the active institutional control period, the first time at which biotic intrusion is expected to be feasible. Doses decline by the end of the 1,000-yr compliance period as radionuclides in the waste decay. The radionuclides that contribute to

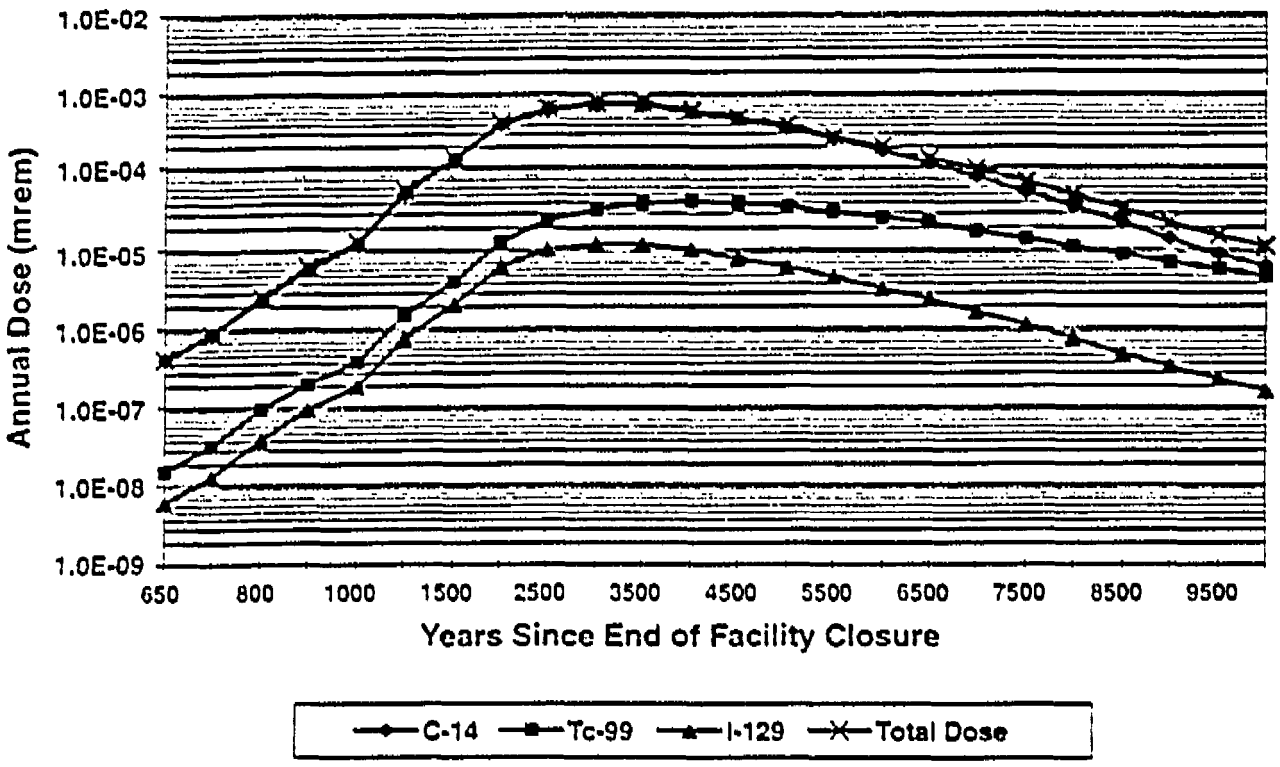

RAE - 106265

Figure 3-17. Projected composite analysis doses for the All Pathways - Groundwater Scenario.

Table 3-9. Pathway contributions to the peak projected composite analysis dose for the All Pathways - Groundwater Scenario.

Exposure Pathway	Dose at Peak Time	Percent of Peak Dose
Ingestion of water	4.6E-06	38%
Ingestion of soil	8.8E-09	0%
Ingestion of crops	7.2E-06	59%
Ingestion of meat	2.0E-07	2%
Ingestion of milk	2.3E-07	2%
Inhalation of particulates	1.5E-10	0%
Direct radiation from soil	3.7E-10	0%
Direct radiation from air	2.2E-16	0%
Total Dose	1.2E-05	

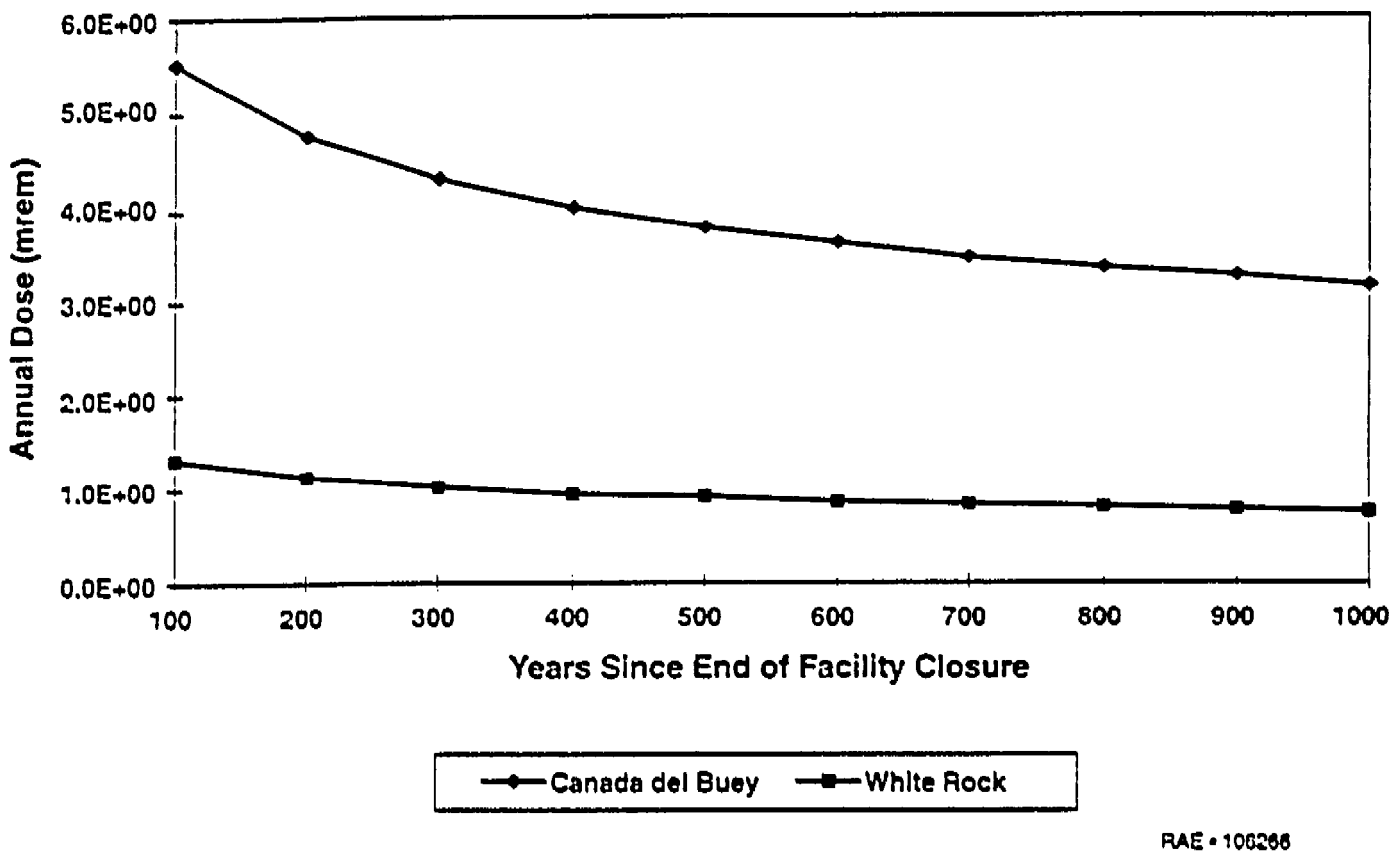

Figure 3-18. Projected composite analysis doses for the Atmospheric Scenario.

the peak dose during the 1,000-yr compliance period are shown in Figure 3-19. Isotopes of americium and plutonium account for more than 95 percent of the total dose at each location. Inhalation of contaminated dust accounts for essentially all of the projected exposures.

3.2.3 All Pathways - Parajito Canyon Scenario

The projected doses for the All Pathways - Parajito Canyon Scenario are shown in Figure 3-20 for the 10,000-yr period following closure of the disposal facility. The projected doses are greatest at the end of the active institutional control period, declining for several hundred years thereafter. Radioactivity brought to the surface by plants and animals is the major contributor to the peak dose. Doses rise slightly to a local maximum at about 800 yr post-closure, coinciding with the arrival of peak concentrations of C-14 and Tc-99 at the receptor's well.

The peak annual dose during the 1,000-yr compliance period is 7.2×10^{-3} mrem and, as stated above, occurs at the end of active institutional control. Hf-182, Ag-108m, and Pu-239 contribute 16 to 37 percent of the peak dose; several radionuclides make contributions ranging from about 2 to 8 percent (Figure 3-21). The inhalation of airborne dust and direct radiation from contaminated soils are responsible for 34 and 43 percent of the maximum dose during the compliance period (Table 3-10).

3.3 AREA G DOSE ASSESSMENT SUMMARY AND COMPLIANCE ASSESSMENT

This section summarizes the results of the Area G dose assessment. These results are used to determine if the disposal facility is in compliance with the performance objectives for the performance assessment and composite analysis. Section 3.3.1 addresses the dose projections for the performance assessment, while Section 3.3.2 discusses the results of the dose assessment for the composite analysis.

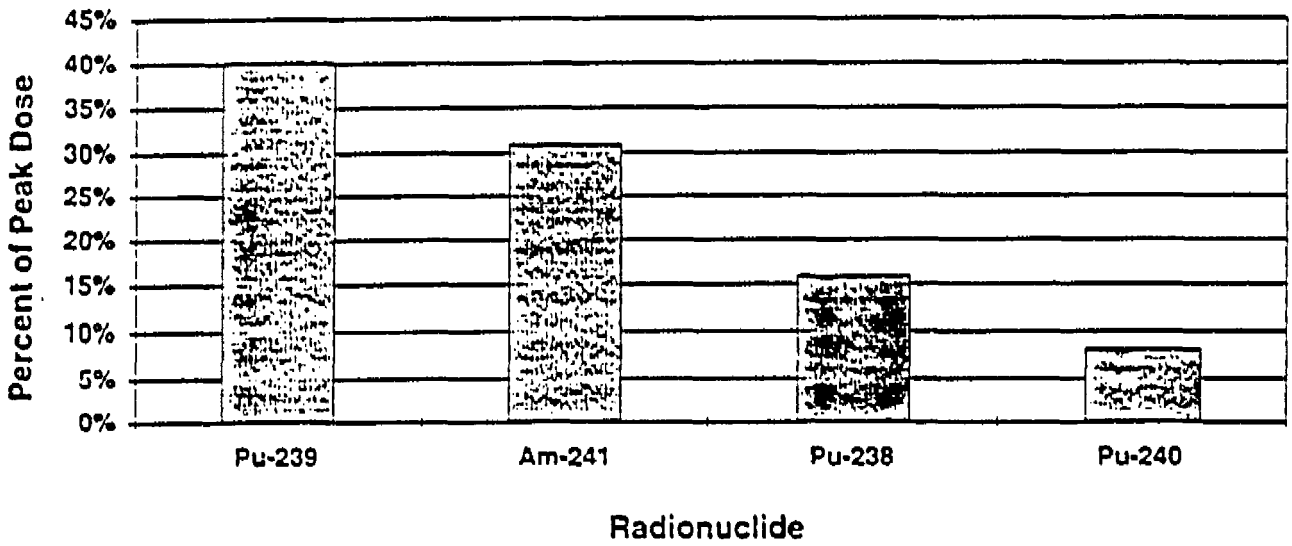

RAE - 106228

Figure 3-19. Radionuclide contributions to the peak composite analysis dose for the Atmospheric Scenario.

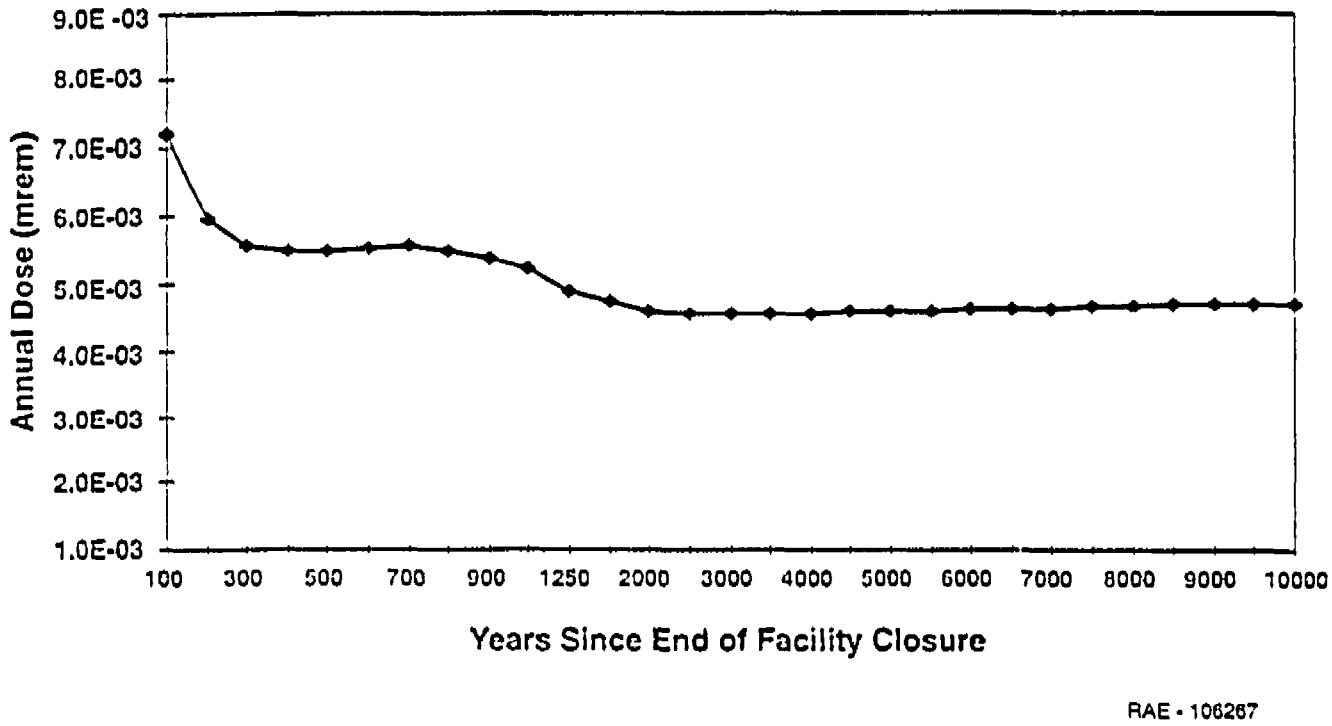

Figure 3-20. Projected composite analysis doses for the All Pathways - Parajito Canyon Scenario.

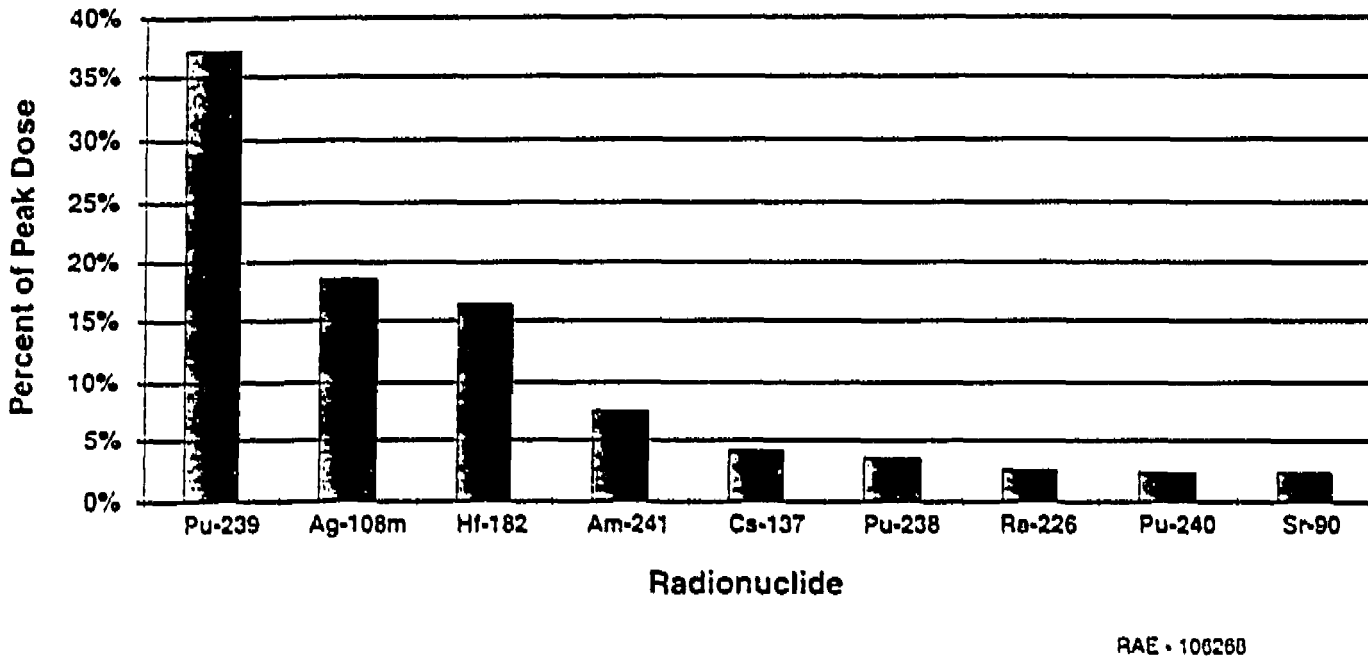

Figure 3-21. Radionuclide contributions to the peak composite analysis dose for the All Pathways - Parajito Canyon Scenario.

Table 3-10. Pathway contributions to the peak projected composite analysis dose for the All Pathways - Parajito Canyon Scenario.

Exposure Pathway	Dose at Peak Time	Percent of Peak Dose
Ingestion of water	1.9E-07	0%
Ingestion of soil	1.3E-03	18%
Ingestion of crops	3.7E-04	5%
Ingestion of meat	7.9E-09	0%
Ingestion of milk	9.5E-09	0%
Inhalation of particulates	2.4E-03	34%
Direct Radiation from soil	3.1E-03	43%
Direct Radiation from air	3.6E-10	0%
Total Dose	7.2E-03	

3.3.1 Performance Assessment Dose Summary and Compliance Evaluation

The peak dose projections for the exposure scenarios included in the performance assessment are summarized in Table 3-11. The peak annual dose for the Groundwater Resource Protection Scenario is 4.5×10^{-5} mrem at the receptor location in Parajito Canyon. Exposures at this location are dominated by C-14. A peak dose of 2.3×10^{-7} mrem is projected for the All Pathways - Groundwater Scenario, and occurs at the end of the compliance period. The maximum annual dose projected for the Atmospheric Scenario is 6.6×10^{-2} mrem at the end of disposal operations, and is due primarily to releases of tritiated water vapor from the facility. The peak dose for the All Pathways - Parajito Canyon Scenario is 1.3×10^{-4} mrem/yr, and occurs 800 yr after the disposal facility closes. Maximum radon fluxes from the historic and future waste range from 1.1×10^{-1} to 1.7×10^{-1} pCi/m^2/s (1.0×10^{-2} to 1.6×10^{-2} pCi/ft^2/s) for the pits and 8.1×10^{-1} to 3.1 (7.5×10^{-2} to 2.9×10^{-1} pCi/ft^2/s) pCi/m^2/s for the shafts (Table 3-12). Finally, the maximum projected doses for the inadvertent intruder range from 12 to 30 mrem/yr for the historic and future waste disposed of in pits and shafts. All peak intruder doses occur at the time of first intrusion, 100 and 300 yr after facility closure for the pits and shafts, respectively (Table 3-11).

The DOE Order 5820.2A performance objectives for the exposure scenarios addressed in the dose assessment are listed in Table 3-11. All projected peak doses are less than the corresponding performance objectives. Peak drinking water doses and "all pathways" doses are small fractions of the pertinent performance objectives. The peak radon fluxes from the historic waste are 6.5 to 180 times smaller than the prescribed flux limit of 20 pCi/m^2/s (1.9 pCi/ft^2/s), while fluxes from future waste are 25 to 120 times smaller than the objective. The projected intruder doses range from 12 to 30 percent of the 100-mrem/yr performance objective for chronic exposures.

The 10-mrem/yr performance objective for the atmospheric scenario represents the maximum effective dose a member of the public may receive from all facilities at the LANL. To demonstrate compliance with this objective, the projected doses for Area G must be added to those projected to occur as a result of releases from other LANL facilities. In compliance with 10 CFR Part 61, the LANL environmental surveillance program includes the projection of maximum individual doses from airborne emissions from LANL facilities (LANL, 1996). Dose calculations based on monitoring data collected in 1994 project a maximum individual

Table 3-11. Summary of peak projected doses and performance objectives for the Area G performance assessment.

Exposure Scenario	Projected Peak Dose (mrem/yr)	Applicable Performance Objective (mrem/yr)
Groundwater Resources Protection Scenario	4.5E-05	4.0E+00
All Pathways - Groundwater Scenario	2.3E-07	2.5E+01
Atmospheric Scenario	6.6E-02	1.0E+01[a]
All Pathways - Parajito Canyon Scenario	1.3E-04	2.5E+01
Intruder-Agriculture Scenario		
Historic pit waste	3.0E+01	1.0E+02
Future pit waste	3.0E+01	1.0E+02
Historic shaft waste	1.8E+01	1.0E+02
Future shaft waste	1.2E+01	1.0E+02

a. Performance objective represents the maximum exposure received by a member of the public from all sources at LANL.

Table 3-12. Summary of peak projected radon fluxes and performance objectives for the Area G performance assessment.

Waste Type	Projected Peak Radon Flux ($pCi/m^2/s$)	Applicable Performance Objective ($pCi/m^2/s$)
Historic pit	1.1E-01	2.0E+01
Future pit	1.7E-01	2.0E+01
Historic shaft	3.1E+00	2.0E+01
Future shaft	8.1E-01	2.0E+01

dose of 3.5 mrem at a location north of TA-53, the Los Alamos Meson Physics Facility. The sum of this dose and the 6.6×10^{-2}-mrem dose projected at the end of Area G disposal operations is about 3.6 mrem. This dose is less than the 10-mrem/yr performance objective.

Strictly speaking, summing the atmospheric contributions in the manner described above is incorrect insofar as these doses are projected to occur at different times and locations. The dose contribution from Area G corresponds to the time of projected facility closure at a location south of TA-53, while the dose calculated to demonstrate compliance with 10 CFR Part 61 is based on data collected in 1994 north of TA-53. However, the projected dose for the Area G disposal facility is expected to bound the actual exposures received by a receptor at the point of maximum atmospheric exposure in 1994 and, generally speaking, for at least the next 100 yr. To the extent that the doses from the other facilities at the LANL do not rise significantly above the 1994 dose estimate, the 10-mrem/yr performance objective will be satisfied.

3.3.2 Composite Analysis Dose Summary and Compliance Evaluation

Table 3-13 summarizes the peak projected doses for the exposure scenarios included in the composite analysis. Peak annual doses for the All Pathways - Groundwater and All Pathways - Parajito Canyon scenarios are 1.2×10^{-5} and 7.2×10^{-3}, respectively. The dose for the former scenario occurs at the end of the 1,000-yr compliance period, while the dose for the canyon resident is projected to occur immediately following the end of active institutional control. The maximum annual dose projected for the Atmospheric Scenario is 5.5 mrem, and occurs at the end of the active institutional control period.

To demonstrate compliance, the projected doses for the composite analysis must be less than 100 mrem/yr. Furthermore, doses greater than 30 mrem/yr indicate the need for an options analysis to identify cost-effective methods of reducing exposures. The results of the dose assessment indicate that the Area G disposal facility complies with the 100-mrem/yr limit, and that there is no need for an options analysis.

Table 3-13. Summary of peak projected doses and performance objectives for the Area G composite analysis.

Exposure Scenario	Projected Peak Dose (mrem/yr)	Applicable Performance Objective (mrem/yr)
All Pathways - Groundwater Scenario	1.2E-05	3.0E+01/1.0E+02
Atmospheric Scenario	5.5E+00	3.0E+01/1.0E+02
All Pathways - Parajito Canyon Scenario	7.2E-03	3.0E+01/1.0E+02

4. SENSITIVITY AND UNCERTAINTY

The dose projections presented in Chapter 3 are the culmination of the modeling conducted to simulate radionuclide release and transport in the Area G disposal environment. The projections are subject to the uncertainties inherent in the modeling analyses, as well as to those introduced by the dose assessment itself. This chapter addresses these uncertainties and discusses their implications in terms of demonstrating compliance with the performance assessment and composite analysis performance objectives.

The sensitivity and uncertainty analysis was performed to develop an understanding of the potential effects modeling and data uncertainties may have on the projected doses. The uncertainties associated with the modeling analyses conducted in support of the performance assessment and composite analysis (i.e., infiltration modeling, source-term modeling, groundwater flow and transport modeling, atmospheric modeling, and dose assessment) were evaluated by each of the subject-matter experts involved in the analyses. This chapter uses the results of these studies to interpret the significance of identified uncertainties in terms of demonstrating compliance with the DOE Order 5820.2A and composite analysis performance objectives.

The discussion of uncertainty is organized in terms of the exposure scenarios included in the performance assessment and composite analysis. Section 4.1 discusses uncertainties and their potential impact on the projection of doses for members of the public living downgradient or downwind of the disposal facility. Section 4.2 addresses uncertainties as they pertain to the inadvertent intruder dose projections.

The sensitivity and uncertainty analysis focused on the projected performance of the disposal facility during the 1,000-year compliance period. However, in some instances, sources of uncertainty are discussed here in terms of their impact over periods of up to 10,000 years. This longer period was taken into consideration to ensure that waste disposed of in the Area G disposal facility will not pose unacceptable risks to human health and the environment.

4.1 OFFSITE EXPOSURE SCENARIOS

The offsite exposure scenarios were used to evaluate the potential impacts of radioactive releases from the Area G disposal facility on members of the public. Releases were assumed to be transported to the receptors via groundwater, the atmosphere, and surface water runoff. The radioactivity in these media resulted in the contamination of foodstuffs and soils used or accessed by the offsite resident. Uncertainties in the models and parameters used to estimate rates of radionuclide release, transport, and exposure will introduce errors into the dose projections. The sensitivity and uncertainty analysis discussed below places quantitative bounds on the magnitude of the errors associated with the projected doses.

The following discussion is organized in terms of the offsite exposure scenarios included in the performance assessment and composite analysis. Section 4.1.1 discusses the uncertainties and their impact on projected doses for the Groundwater Resource Protection Scenario, while the uncertainties associated with the Atmospheric Scenario and the radon flux projections are addressed in Section 4.1.2. The impact of uncertainties associated with the "all pathways" scenarios is discussed in Section 4.1.3. Section 4.1.4 summarizes the results of the sensitivity and uncertainty analysis for the offsite exposure scenarios.

The dose projections for the various exposure scenarios all depend on a consistent set of modeling components or elements. These components include:

- The waste inventory, which defines the total amount of radioactivity buried in the disposal facility.
- Source release mechanisms, which define the mode and rate at which radioactivity is released to the environment from the disposed waste.
- Transport mechanisms, through which radionuclides are transported through the environment to locations accessible to humans.
- Usage factors, which describe the rate of usage of, or time exposed to, contaminated resources.
- Dose conversion factors, which relate intakes of radioactivity to absorbed doses in the receptor.

The discussions of sensitivity and uncertainty that follow are organized in terms of these modeling components.

4.1.1 Groundwater Resources Protection Scenario

A peak dose of 8.3×10^{-8} mrem/yr is projected for the Groundwater Resource Protection Scenario at the receptor location 100 m (330 ft) east-southeast of the Area G fenceline during the 1,000-yr compliance period. The peak annual dose projected for the receptor in Parajito Canyon during this period is 4.5×10^{-5} mrem. C-14, Tc-99, and I-129 are the only radionuclides that contribute to these projected doses; no other radionuclides reach the aquifer during the compliance period. C-14 is the primary contributor to the peak doses, accounting for 68 to 88 percent of the totals. The uncertainties associated with the dose projections for this scenario, and their potential impact on the ability of the Area G disposal facility to comply with the performance objectives, are discussed below.

4.1.1.1 Radionuclide Inventories

The projected doses for the Groundwater Resource Protection Scenario are directly proportional to the activities of radioactive waste disposed of at Area G. The September 26, 1988, to 1995 and 1996 to 2044 performance assessment inventories included in the scenario were projected using information taken from the LLW disposal database (Shuman, 1997). Historic radionuclide inventories were taken directly from the database. The future operational waste inventories were largely extrapolated from 1990 to 1995 disposal records. Waste expected to be generated by environmental restoration and decontamination and decommissioning activities was characterized using independent information from the waste generators.

The historic inventory projections are only as accurate as the recorded data used to estimate them. Errors made in measuring or reporting the volumes and radionuclide activities will misrepresent the actual radionuclide activities and concentrations in the disposal units. Insofar as the future operational waste projections are based on the historic waste disposal records, they are also subject to uncertainties introduced by measurement and

reporting errors. Additional uncertainties are associated with the future waste because these projections assume that waste requiring disposal in the future will have the same general characteristics of LLW shipped for disposal between 1990 and 1995. Changes in the mission of the LANL may dramatically affect the types and quantities of LLW generated at LANL, thus invalidating this assumption. Given the current political climate and state of flux within the DOE, it is reasonable to expect that such changes could occur over the next 50 years.

The magnitude of the errors introduced by uncertainties in the historic and future waste inventory projections are difficult to evaluate in an objective manner. The accuracy of the historic waste shipment data cannot be confirmed short of excavating the disposed waste, an inappropriate course of action by all accounts. While checks on the accuracy of future waste projections will be possible as shipments arrive at Area G for disposal, estimates of the possible errors at this time are speculative. Nevertheless, some general conclusions about these potential errors can be drawn.

All of the radionuclides that contribute to the groundwater dose (i.e., C-14, Tc-99, and I-129) emit low-energy beta particles and/or x-rays and, consequently, are difficult to detect in the waste. Detection is easiest in low-density waste due to the lack of attenuation of radioactive emissions; accurate detection in high-density waste is very difficult. Given these potential problems, it is possible that generators have overlooked these radionuclides in the past. Errors associated with measurements in low-density waste may be on the order of 100 to 200 percent unless the waste is subjected to radiochemical analysis, an approach seldom used to characterize LLW.

The inventories of C-14, Tc-99, and I-129 included in the Groundwater Resource Protection Scenario are dominated by waste projected to be disposed of in the future. For example, the future performance assessment inventory comprises 84 and 90 percent of the total C-14 and Tc-99 inventories, respectively, on an activity basis. The contribution of future waste to the total I-129 inventory is more moderate, accounting for 55 percent of the total. Over 98 percent of the projected inventories of these radionuclides is operational waste. The significant contribution of future operational waste to the projected inventories of C-14, Tc-99, and I-129 highlights the importance of accurately characterizing the level of future operations at LANL.

The rates of waste generation in the future were assumed to be equivalent to the rates implied by the 1990 to 1995 LLW disposal records. Waste generated at these rates was, in turn, assumed to be disposed of at Area G through the year 2044. This period of almost 50 yr was chosen to maximize the benefit of the performance assessment in terms of optimizing waste management operations. This period is expected to be a conservative estimate of the facility's actual lifetime, and may overestimate the remaining operational period by 10 yr or more. Projected groundwater pathway doses will decline from those reported here if the facility closes prior to 2044.

Approximately 60 percent of the projected C-14 inventory in the future waste is based on the disposal of C-14 sources in 1992 and 1994. Sources of this type and activity are disposed of at Area G infrequently. In fact, a review of Area G LLW disposal records indicates that the activity associated with these sources represents more than 99 percent of the total C-14 source activity disposed of since the early 1970s. Based on these results, the projected inventory of C-14 used in the performance assessment is expected to overestimate the actual activity of this radionuclide placed in the disposal facility, perhaps by as much as 50 percent. Given the contribution of C-14 to the peak projected drinking water doses, nearly any reduction in the projected future inventory of this radionuclide will significantly affect the projected scenario exposures.

4.1.1.2 Source Releases

The rate at which radioactivity is leached from the waste is a function of the form of the waste subject to leaching, the amount of water percolating through the waste, and the geochemical conditions within the disposal unit environment. The source-term modeling conducted in support of the Area G dose assessment examined the release characteristics of four waste-forms: surface-contaminated waste, soils, concrete and sludges, and bulk-contaminated waste. The allocation of the period-specific inventories among these waste-forms was performed based on the waste codes supplied by the generator when the waste is shipped for disposal. Waste streams were assumed to be surface-contaminated waste unless there was specific knowledge about the waste and its release characteristics that allowed it to be assigned to one of the other three waste forms (Shuman, 1997).

In general, rates of radionuclide release are greatest for the surface-contaminated waste as water percolating through the disposal units is assumed to rinse or wash the contamination from the waste (Vold and Shuman, 1997). In contrast, releases from soils, concrete, and sludges are inversely proportional to the distribution coefficients of the radionuclides within each matrix. Releases from bulk-contaminated waste are controlled by corrosion rates of the activated metal waste form. Modeled rates of release of C-14, Tc-99, and I-129 considered only the inventories associated with the surface-contaminated waste because prior work indicated that releases from this waste form dominated the projected groundwater doses.

The manner in which radionuclide inventories were allocated among the four waste forms and the simplification of the source release model to consider only the surface-contaminated waste inventories are not expected to significantly affect the projected scenario doses. More than 99 percent of the waste contaminated with C-14, Tc-99, and I-129 was assigned to the rapidly leaching, surface-contaminated waste. Consequently, little opportunity exists for underestimating actual release rates using the allocation approach. While assuming that the vast majority of the C-14, Tc-99, and I-129 waste is surface-contaminated could lead to overestimation of actual release rates, the magnitude of this overestimation is unknown. Consequently, no attempt was made to bound this potential error.

Releases of radioactivity from the waste disposed of at Area G are proportional to the square of the amount of water percolating through the disposal units (Vold and Shuman, 1997). An average percolation rate of 5 mm/yr (0.2 in./yr) on top of Mesita del Buey was used to model source releases and groundwater contaminant transport for the Area G performance assessment and composite analysis. This percolation rate is based on the unsaturated conductivity of crushed tuff at a moisture content of 8 percent, assuming unit gradient conditions. Percolation rates of 1 and 10 mm/yr (0.04 and 0.4 in./yr) are expected to reasonably bound the base-case percolation rate. These values result in radionuclide release rates that are 4 and 300 percent of those projected to occur for the 5-mm/yr (0.2-in./yr) percolation rate.

Near-surface rates of water percolation through Area G are extremely variable and are strongly influenced by the disposal units, surface structures, and other alterations which

have accompanied waste disposal. Given this variability, the selection of a suitable percolation rate for the performance assessment and composite analysis is fraught with uncertainty. Nevertheless, the mean percolation rate of 5 mm/yr (0.2 in./yr) used in the groundwater modeling is expected to be a reasonable, and possibly conservative, approximation of the rate at which water flows through the disposal units. This conclusion is supported by several lines of evidence which indicate that mean percolation rates through the disposal units at Area G range from about 1 to 10 mm/yr (3.9×10^{-2} to 3.9×10^{-1} in./yr) (Newman, 1996; Springer, 1996; Vold, 1996b).

Radionuclide release rates from the surface-contaminated waste are influenced by the transit time of water through the waste packages. In general, peak radionuclide concentrations in the leachate will increase as the transit time decreases. The source-term analysis estimated an average transit time of approximately 16 yr based on an average waste package thickness of 1 m (3.3 ft), a percolation rate of 5 mm/yr (0.2 in./yr) through the disposal units, and a moisture content for the waste of 8 percent (Vold and Shuman, 1997).

The magnitude of the error introduced into the source-term analysis by uncertainties in the water transit time through the waste packages will be relatively small. The sensitivity of peak radionuclide concentrations in the leachate to transit time was examined for transit times ranging from 0.1 to 50 yr (Vold and Shuman, 1997). The peak leachate concentration for a transit time of 1 yr was approximately 2.2 times greater than the peak concentration projected for a transit time of 16 yr. Extending the transit time to 50 yr resulted in a peak leachate concentration about two times lower than the concentration for the 16-yr transit time.

The geochemical conditions within the disposal units play an important role in the release of radionuclides from soils, concrete, and sludges. These conditions ultimately determine the radionuclide sorption characteristics in the units and the solubility limits of waste contaminants in water percolating through the waste. Sorption characteristics influence the release of radioactivity from the soil, concrete, and sludge waste-forms; solubility limits may influence releases from the entire waste inventory.

As discussed above, the majority of the C-14, Tc-99, and I-129 inventories consist of surface-contaminated waste. Insofar as releases from this waste form are unaffected by the

radionuclides' sorption behavior, the geochemical conditions in the disposal units are relatively unimportant in terms of source release modeling. Their importance is diminished further by the fact that the releases of these radionuclides were never of such a magnitude as to exceed the isotopes' solubility limits.

4.1.1.3 Environmental Transport Modeling

The radioactivity leached from the waste was assumed to be subject to vertical transport to the regional aquifer and to lateral migration to the sides of the mesa. Contamination reaching the sides of the mesa was conservatively assumed to be washed immediately into the canyon alluvium and transported downward to the regional aquifer. For each case, groundwater transport modeling was conducted to estimate radionuclide travel times to, and contaminant concentrations at, the receptor's well.

The radionuclide travel time, or time required for radionuclides leached from the waste to reach the receptor's well, is important in that it determines whether exposures will occur during the compliance period and what the magnitude of those exposures will be. Radionuclide travel times are a function of the groundwater travel time and the sorption behavior of the contaminants. Groundwater flow modeling results indicate that the minimum groundwater travel time from the disposal units downward to the regional aquifer is approximately 600 yr (Birdsell et al., 1997). The travel time in the aquifer from the point of discharge to the receptor's well 100 m (330 ft) downgradient of the disposal facility is small in comparison, about 50 yr. The groundwater travel time to the regional aquifer from Parajito Canyon is projected to be about 100 yr. This much shorter travel time reflects the shorter distance from the canyon bottom to the aquifer and greater rates of water percolation through the canyon alluvium. The travel time from the point of discharge into the aquifer to the receptor's well in the canyon was ignored because the well was assumed to be located immediately adjacent to Area G.

Groundwater travel times in the unsaturated zone are proportional to the amount of water percolating through the disposal site. The 600-yr travel time cited above is based on a percolation rate of 5 mm/yr (0.2 in./yr) through the mesa, 1 mm/yr (0.04 in./yr) in Canada del Buey, and 50 mm/yr (2 in./yr) in Parajito Canyon. The effect of changes in percolation

rates on travel time is demonstrated by the results of modeling analyses performed using mesa top percolation rates of 1 and 10 mm/yr (0.04 and .4 in./yr). These percolation rates, which are expected to reasonably bound the base-case percolation rates, were projected to result in groundwater travel times from the disposal units to the aquifer of approximately 3,000 and 300 yr, respectively (Birdsell et al., 1997). Groundwater travel times from the floor of Parajito Canyon to the aquifer are also proportional to the infiltration rate. The 100-yr travel time cited above corresponds to a percolation rate of 50 mm/yr (2 in./yr) in the canyon. Travel times of 250 and 50 yr are projected for canyon infiltration rates of 20 and 100 mm/yr (0.8 and 4 in./yr), respectively.

The hydraulic conductivities and moisture retention characteristics of the geologic strata underlying Area G will determine the velocity at which groundwater moves through the vadose zone. Studies were conducted to evaluate the effect of variations in the hydraulic conductivities of the geologic units underlying Area G on projected groundwater travel times (Birdsell et al., 1997). Particle tracking simulations were conducted using the minimum and maximum reported values of hydraulic conductivities for each unit down to the Cerros del Rio basalts. These variations resulted in changes in the projected groundwater travel times on the order of 25 to 35 percent.

Units 2 and 1v of the Tshirege Member of the Bandelier tuff form the top of Mesita del Buey and are characterized by extensive fracturing (Krier et al., 1995). While these fractures may provide a pathway for deep infiltration, thus shortening the groundwater travel time, they do not appear to play an important role in this regard. The crushed tuff placed in the bottom of the disposal units during pit and shaft excavation tends to seal the fractures immediately below the disposed waste, minimizing the potential for rapid vertical movement of contaminated water. Modeling studies by Soll (1995) indicate that significant flows in fractures are unlikely except under the most extreme infiltration events. Even under these conditions, the simulations indicate that fractures with no coatings or fill are unable to carry water long distances. Finally, the fractures beneath Area G are discontinuous, preventing water from traveling along them for long distances.

The sorption behavior of the waste radionuclides in the unsaturated and saturated zones also affects the time required for radionuclides to reach the receptor's well. The sorption behavior of the radionuclides included in the Groundwater Resource Protection

Scenario was estimated based on site-specific studies and information taken from the open literature. A conservative distribution coefficient of 0 mL/g was chosen for C-14, Tc-99, and I-129 (Longmire et al., 1996). Based on this value, the contaminant travel times for these radionuclides were equivalent to the groundwater travel times. Consequently, groundwater doses for contamination transported vertically through the mesa were first estimated to occur about 650 yr after facility closure (Birdsell et al., 1997). Exposures from radionuclides transported laterally, to the sides of the mesa, were projected to start about 100 yr after facility closure.

Errors in estimating radionuclide travel times to the receptor's well may lead to over- or underestimation of drinking water doses. Overestimates of the contaminant travel times generally will lead to underestimation of the actual groundwater pathway doses. Conversely, underestimates of the times required for radionuclides to reach the well may lead to overestimation of the actual doses received by the person consuming the water. The impact of such errors is expected to be relatively small in terms of the receptor location in Parajito Canyon. As stated earlier, the contaminant travel time to the aquifer via this route is rapid (about 100 yr), providing little opportunity for overestimating the time required for the radionuclides to reach the well. Conversely, while actual travel times may be greater than 100 yr, they would have to be more than three or four times longer to cause significant reductions in the peak drinking water dose projected for the canyon resident.

The travel time of C-14, Tc-99, and I-129 to the well east-southeast of the Area G disposal facility is about 650 yr. The effect of shorter travel times on the projected compliance period doses at this location (i.e., assuming constant rates of radionuclide release) can be approximated using Figure 3-1. As the travel time decreases, all projected doses shown in the figure will occur at earlier times. For example, assume the contaminant travel times for C-14, Tc-99, and I-129 in the vadose zone decrease about 50 percent to 300 yr, consistent with the groundwater travel time observed using a mesa top infiltration rate of 10 mm/yr (0.4 in./yr). In approximate terms, the dose shown in Figure 3-1 at 1,300 yr post-closure would occur at the end of the 1,000-yr compliance period. Under these conditions, the projected peak dose during the compliance period would increase about 5.5 times, after adjusting for radioactive decay.

The preceding discussion demonstrates that the water infiltration rate in the vicinity of the disposal site may have significant effects on the projected drinking water doses. As discussed in Section 4.1.1.2, rates of radionuclide release are proportional to the amount of water percolating through the disposed waste. Furthermore, as discussed above, changes in infiltration rate will influence the radionuclide travel times to the receptor's well. While the effects of changes in the infiltration rate can be estimated based on an understanding of the individual release and groundwater transport models used in the performance assessment, the overall impact of uncertainties in the rate of infiltration on the projected doses is best understood by conducting specific model simulations. Such simulations were conducted as part of the sensitivity and uncertainty analysis, the results of which are discussed in the following paragraphs.

Birdsell et al. (1997) conducted a series of groundwater model simulations for different flow conditions at Area G. The flow conditions included the following:

- A mesa top infiltration of 1 mm/yr (0.04 in./yr), a Canada del Buey infiltration rate of 1 mm/yr (0.04 in./yr), and a Parajito Canyon infiltration rate of 20 mm/yr (0.8 in./yr)
- A mesa top infiltration of 5 mm/yr (0.2 in./yr), a Canada del Buey infiltration rate of 1 mm/yr (0.04 in./yr), and a Parajito Canyon infiltration rate of 20 mm/yr (0.8 in./yr)
- A mesa top infiltration of 10 mm/yr (0.4 in./yr), a Canada del Buey infiltration rate of 1 mm/yr (0.04 in./yr), and a Parajito Canyon infiltration rate of 20 mm/yr (0.8 in./yr)
- A mesa top infiltration of 10 mm/yr (0.4 in./yr), a Canada del Buey infiltration rate of 5 mm/yr (0.2 in./yr), and a Parajito Canyon infiltration rate of 100 mm/yr (4 in./yr)

These flow conditions are expected to reasonably bound the actual infiltration rates at, and in the vicinity of, Area G. As discussed earlier, several investigators (e.g., Newman, 1996; Springer, 1996; Vold, 1996b) have indicated that the mesa top infiltration rate ranges from about 1 to 10 mm/yr (0.04 to 0.4 in./yr). Vold et al. (1996) indicate infiltration rates ranging from less than 1 mm/yr (0.04 in./yr) to 5 mm/yr (0.2 in./yr) in dry canyons such as Canada del Buey, while infiltration rates in wet canyons such as Parajito Canyon appear to be on the order of 50 mm/yr (2 in./yr).

The total fluxes of radionuclides to the aquifer were projected for each of the flow conditions listed above and compared to the fluxes for the base-case flow conditions of 5 mm/yr (0.2 in./yr) infiltration on the mesa top, 1 mm/yr (0.04 in./yr) infiltration in Canada del Buey, and 50 mm/yr (2 in./yr) infiltration in Parajito Canyon (Birdsell et al., 1997). Radionuclide fluxes to the aquifer were smallest when infiltration rates of 1, 1, and 20 mm/yr (0.04, 0.04, and 0.8 in./yr) were assigned to the mesa top, Canada del Buey, and Parajito Canyon, respectively. Conversely, fluxes reached a maximum when the mesa top was assigned an infiltration rate of 10 mm/yr (0.4 in./yr) and infiltration rates of 5 and 100 mm/yr (0.2 and 4 in./yr) were assigned to Canada del Buey and Parajito Canyon, respectively. Potential doses were projected for the drinking water pathway for these low and high flow conditions.

The doses projected for the low and high flow conditions are compared to the base-case dose projections in Figure 4-1 for the receptor location 100 m (330 ft) east-southeast of the Area G disposal facility. Doses for the low flow condition increase throughout the 10,000-yr period shown and are significantly lower than the base-case projections for most of this time. The peak annual dose projected for the low flow condition during the 1,000-yr compliance period is 4.4×10^{-12} mrem, or almost 19,000 times less than the peak dose projected for the base case. Conversely, the higher rates of release and shorter travel times characteristic of the high flow condition result in higher doses at earlier times. The peak annual dose projected for the period, 3.0×10^{-5} mrem, occurs approximately 2,500 years after facility closure. The peak dose during the compliance period for the high flow condition is 3.5×10^{-6} mrem/yr, which is approximately 42 times higher than the maximum compliance period dose for the base case.

The projected drinking water doses for the base-case, low, and high flow conditions at the receptor location in Parajito Canyon are shown in Figure 4-2. Projected doses are lower and peak later for the low flow condition relative to the base case. The peak dose during the 1,000-yr compliance period is 5.3×10^{-6} mrem/yr or 12 percent of the peak dose projected for the base case simulation. Projected doses peak approximately 600 yr after facility closure under the high flow condition, or 200 yr sooner than that seen under the base case conditions. The peak dose during the compliance period is 1.2×10^{-4} mrem/yr, which is about 2.7 times the peak base case dose. This increase in the projected peak dose is less than that observed for the receptor location 100 m east-southeast of Area G, and is due to the existence of

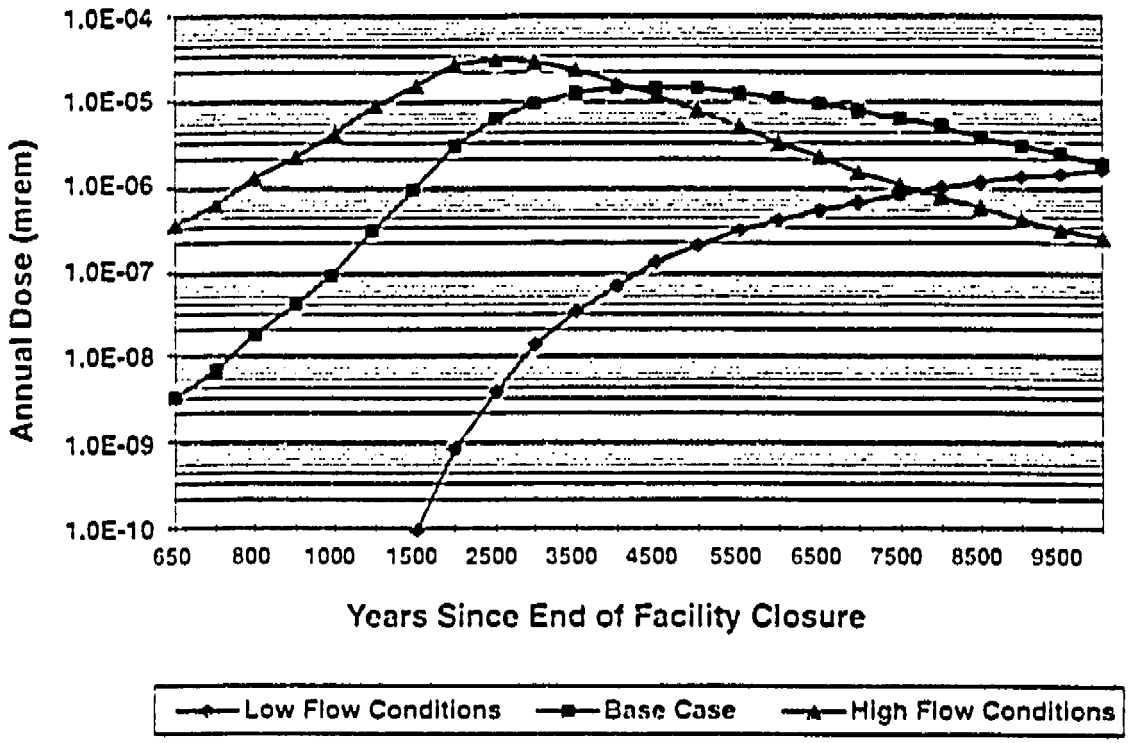

Figure 4-1. Projected performance assessment doses for the Groundwater Resource Protection Scenario east-southeast of the Area G disposal units for different flow conditions.

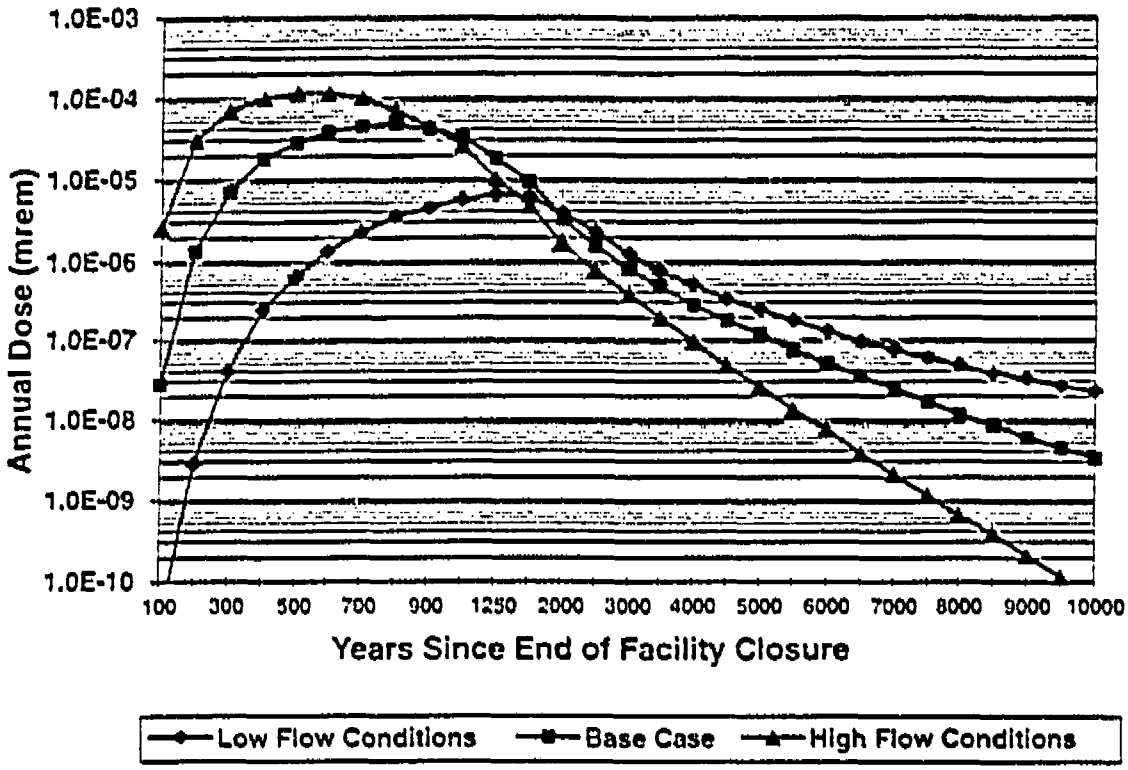

RAE - 106271

Figure 4-2. Projected performance assessment doses for the Groundwater Resource Protection Scenario in Parajito Canyon for different flow conditions.

competing forces in the lateral and vertical directions. The sides of the mesa exert a greater pull on the leachate for the high flow case because there is a fixed low saturation at the mesa edges and an increased moisture content near the disposal units. On the other hand, increased infiltration through the disposal site tends to force water downward, beyond the evaporative "pull" of the mesa sides.

The peak drinking water dose projected to occur following the lateral transport of contamination to the sides of the mesa is expected to be overstated for reasons pertaining to the manner in which lateral transport was modeled and the approach used to estimate aquifer contaminant concentrations. In terms of the groundwater modeling approach, the assignment of a fixed evaporation boundary condition to the sides of the mesa only is not expected to accurately represent the true extent of evaporation within the mesa. Evaporation is also expected to occur within the fractures in the geologic units comprising the top of the mesa. Groundwater moving laterally will encounter fractures in the intact portions of the mesa separating the disposal units from the mesa walls. Under unsaturated conditions, moisture will tend to evaporate at the walls of the fractures, leaving any contamination behind. While saturated flow in the fractures following heavy precipitation or snow-melt may transport the contamination downward, it is improbable that the radioactivity will undergo any additional lateral transport.

The groundwater modeling analysis did not account for the existence of fractures between the disposal units and the sides of the mesa. Consequently, lateral transport of radioactivity was assumed to proceed uninterrupted by fractures in Units 2 and 1vu of the Tshirege Member of the Bandelier tuff, which forms the top of Mesita del Buey. Under these conditions, the quantities of contamination projected to reach the mesa walls are expected to be greater than would actually occur, leading to projected doses to the Parajito Canyon resident that are larger than expected.

Assumptions about how radioactivity is transported from the sides of the mesa to the regional aquifer will also tend to overestimate the actual doses received from drinking contaminated groundwater. Contamination reaching the sides of the mesa along Parajito Canyon was assumed to be carried immediately to the bottom of the canyon by surface runoff. Once there, all radioactivity was assumed to be transported vertically to the regional aquifer with the prevailing flow through the canyon alluvium. It is more likely, however, that

radioactivity will be washed from the sides of the mesa over time. Contamination in the runoff will be distributed along the lower portions of the mesa walls, wherever water may collect, and out onto the canyon floor. It is unlikely that all contamination will enter into alluvial waters and undergo immediate transport downward at the rate projected in the groundwater modeling.

Radioactivity that is not subject to lateral transport was modeled to travel vertically to the regional aquifer. Therefore, overestimates of the amount of contamination transported laterally to the sides of the mesa will underestimate the activities transported vertically to the aquifer and, hence, the doses received by the receptor located east-southeast of the disposal units. The error introduced into the dose projections by this source of uncertainty, however, is expected to be small. Groundwater simulations indicate that the total mass of contamination exiting the sides of the mesa over 10,000 yr is approximately 30 percent of the mass discharged to the aquifer. Based on these results, doses received by the receptor located east-southeast of Area G would be no more than 30 percent greater if all contamination were transported vertically to the regional aquifer.

Radioactivity in the aquifer is diluted as it is transported from the point of discharge to the receptor's well. Uncertainties in the amount of dilution that will actually occur may lead to errors in the projected drinking water doses. Concentrations of radioactivity in the aquifer are a function of the aquifer velocity, the transverse and longitudinal dispersivities, and the mixing depth in the saturated zone. In general, radioactivity in the aquifer will become more diluted as the values of these parameters increase.

The amount of aquifer dilution projected to occur between the disposal site and the receptor 100 m (330 ft) down-gradient of the disposal units may underestimate actual conditions. An aquifer velocity of 16 m/yr (52 ft/yr) was used in the saturated zone modeling. This velocity is small relative to the velocities of 29 and 100 m/yr (95 and 350 ft/yr) cited by Abrahams (1963) for the regional aquifer to the north and south of Area G, respectively. Longitudinal and transverse dispersivities of 20 and 2 m (66 and 6.6 ft), respectively, were used in the saturated zone modeling. These values are also expected to be conservative. Longitudinal dispersivities are expected to range from 24 to 130 m (79 to 426 ft) when the actual distances from the disposal units to the receptor's well are taken into account. Similarly, transverse dispersivities are expected to range from 2.4 to 13 m (7.9 to 43 ft).

Radionuclides discharged to the aquifer were projected to mix over the entire 100 m (330 ft) thickness assumed for the regional aquifer. Abrahams (1963) cites aquifer thicknesses of 530 and 107 m (1,700 and 490 ft) north and south of Area G, respectively. If the aquifer thickness below Area G is greater than 100 m (330 ft), additional dilution would be expected.

Radionuclide concentrations in the regional aquifer below Parajito Canyon were projected separately for the September 26, 1988 to 1995 and 1996 to 2044 performance assessment inventories. The drinking water doses projected for the canyon resident were based on the assumption that an individual consumes water with radionuclide concentrations equal to the sum of the concentrations projected for the historic and future waste. The actual contaminant concentrations encountered by the resident will depend upon the placement of the well relative to the disposal units and the degree to which plumes from the different waste inventories interact with one another. Nevertheless, the approach used is expected to overestimate the actual exposures received by the individual.

4.1.1.4 Resource Utilization

The sole source of exposure for the Groundwater Resource Protection Scenario is the consumption of contaminated water drawn from the well. The individual is assumed to ingest 2 L (5.3×10^{-1} gal) of water per day, including water consumed in the form of juices and other beverages containing tap water. This water consumption rate is consistent with the methodology used to develop the groundwater protection standards and, as such, is appropriate for use in the Area G dose assessment; however, it is expected to overestimate actual rates of consumption for an average individual. The National Academy of Sciences (1977; reported in EPA, 1989) calculated an average per capita water consumption rate of 1.6 L/day (4.2×10^{-1} gal/day) based on a survey of nine literature sources. This source and several others chosen by the EPA (1989) to determine a recommended consumption rate indicate an average adult drinking water consumption rate of 1.4 L/day (3.7×10^{-1} gal/day) and a reasonable worst-case value of 2 L/day (5.3×10^{-1} gal/day).

4.1.1.5 Radionuclide Dose Conversion Factors

The concentrations of radioactivity in groundwater and the rate of water consumption yield the intakes of radioactivity for the groundwater user. These intakes are related to doses using the ingestion dose conversion factors. The projected doses for the Groundwater Resource Protection Scenario are committed effective dose equivalents, representing the total dose equivalent received by the body over a 50-yr period after the intake of radioactivity. The dose conversion factors are based on the recommendations of the International Commission of Radiological Protection (ICRP) as provided in Publications 26, 30, and 48 (ICRP, 1977, 1979-1982, 1986). While uncertainties in the dose conversion factors used to project these doses exist, the impact of these uncertainties is not readily characterized. The impact of these uncertainties upon the dose projections was not considered in the uncertainty analysis.

4.1.2 Atmospheric Scenario

The Atmospheric Scenario was included in the dose assessment for the performance assessment and the composite analysis. Radon fluxes were projected for the undisturbed disposal site for the performance assessment only. The peak performance assessment dose for the scenario in Canada del Buey is 6.6×10^{-2} mrem/yr, due to the inhalation of radioactive gases at the end of disposal operations. The corresponding dose at the exposure location near White Rock is 1.6×10^{-2} mrem/yr. Dust resuspended from the site at the end of active institutional control results in peak doses of 9.2×10^{-3} and 2.2×10^{-3} mrem/yr in Canada del Buey and White Rock, respectively. The radionuclides that contribute 1 percent or more of the peak dose for the inhalation of gases and dust are listed in Table 4-1. Projected peak fluxes of radon gas from the historic pit and shaft waste are 1.1×10^{-1} pCi/m^2/s (1.0×10^{-2} pCi/ft^2/s) and 3.1 pCi/m^2/s (2.9×10^{-1} pCi/ft^2/s), respectively. The maximum flux for the future pit waste is 1.7×10^{-1} pCi/m^2/s (1.6×10^{-2} pCi/ft^2/s), while the peak flux for the future shaft waste is 8.1×10^{-1} pCi/m^2/s (7.5×10^{-2} pCi/ft^2/s).

The peak dose projected for the Atmospheric Scenario using the composite analysis inventory is 5.5 mrem/yr in Canada del Buey and 1.3 mrem/yr near White Rock. These doses are projected to occur at the end of the active institutional control period. Radionuclides making significant contributions to the peak dose are included in Table 4-1. The inhalation

Table 4-1. Summary of radionuclide contributions to the peak doses for the Atmospheric, All Pathways - Groundwater, and All Pathways - Parajito Canyon scenarios.

	Percent Contribution to Peak Dose					
	Performance Assessment			Composite Analysis		
Radionuclide	Atmospheric Scenario	All Pathways Groundwater	All Pathways Parajito Canyon	Atmospheric Scenario	All Pathways Groundwater	All Pathways Parajito Canyon
Ag-108m	—[a]	—[a]	—[a]	—[a]	—[a]	10%
Am-241	9%	—[a]	—[a]	31%	—[a]	8%
C-14	—[a]	86%	62%	10%[b]	95%	—[a]
Cs-137	—[a]	—[a]	—[a]	—[a]	—[a]	4%
Gd-148	1%	—[a]	—[a]	—[a]	—[a]	—[a]
H-3	100%[b]	—[a]	—[a]	90%[b]	—[a]	—[a]
Hf-182	—[a]	—[a]	—[a]	—[a]	—[a]	16%
I-129	—[a]	—[a]	—[a]	—[a]	1%	—[a]
Pu-238	13%	—[a]	—[a]	16%	—[a]	4%
Pu-239	51%	—[a]	2%	40%	—[a]	37%
Pu-240	3%	—[a]	—[a]	8%	—[a]	2%
Pu-241	1%	—[a]	—[a]	4%	—[a]	1%
Ra-226	—[a]	—[a]	—[a]	—[a]	—[a]	3%
Sr-90	—[a]	—[a]	—[a]	—[a]	—[a]	2%
Tc-99	—[a]	14%	34%	—[a]	3%	—[a]
Th-232	2%	—[a]	—[a]	—[a]	—[a]	—[a]
U-234	2%	—[a]	—[a]	—[a]	—[a]	—[a]
U-235	3%	—[a]	—[a]	—[a]	—[a]	—[a]
U-238	15%	—[a]	—[a]	—[a]	—[a]	1%

a. Indicates radionuclide does not contribute 1 percent or more to peak projected dose.
b. Contributions to exposures received from the inhalation of radioactive gases.

of radioactive gases prior to the end of the active institutional control period is projected to result in annual doses of 7.5×10^{-2} and 1.8×10^{-2} mrem in Canada del Buey and White Rock, respectively. The uncertainties associated with all of these projections, and their potential impact on the ability of the Area G disposal facility to comply with the performance objectives, are discussed below.

4.1.2.1 Radionuclide Inventories

As stated earlier, the historic and future performance assessment inventories are based on data taken directly from the LLW disposal database, the extrapolation of historic disposal data to estimate future rates of disposal, and additional information collected from waste generators. The 1957 to 1970 pit and shaft inventories for the composite analysis are based on the extrapolation of LLW and transuranic waste data for the early to mid-1970s. The 1971 to September 25, 1988, composite analysis inventory is based on data in the LLW disposal database.

General comments about the uncertainties associated with the performance assessment inventory projections are provided in Section 4.1.1.1. Many of these same uncertainties will apply to the 1957 to 1970 and 1971 to September 25, 1988, composite analysis inventories. The remainder of this section deals with uncertainties associated with radionuclides that make significant contributions to the projected Atmospheric Scenario doses.

H-3 is difficult to detect and quantify in small quantities unless radiochemical analyses are performed. Measurement errors decline as the activity of the waste increases. For samples with activities on the order of a few curies, off-gassing measurements may be accurate to within a factor of 10. Waste containing hundreds to thousands of curies of H-3 are characterized using ion chamber measurements and calorimetry. The former method may be accurate to within a factor of 2, while the error associated with calorimetry is less than 20 percent. The majority of the H-3 activity disposed of at Area G occurs as packages containing hundreds to tens of thousands of curies of H-3. Thus, based on the information provided above, measurements errors are expected to be less than 20 to 100 percent for the H-3 inventories.

In general, radionuclide activities in weapons-grade plutonium LLW are difficult to detect using non-invasive or non-destructive means. Detection capabilities are closely linked with the activity and density of the waste. Low-density, low-activity waste may have measurement errors as great as 400 to 900 percent associated with it; as the activity increases, errors will tend to fall below 100 to 200 percent. Plutonium activities in high-density, low-activity waste are difficult to detect; errors may reach 900 percent or more. As the density of higher-activity waste decreases, measurement errors may be as high as 100 to 400 percent. These uncertainties can be reduced when sampling and radiochemistry are used to characterize the waste. However, this level of effort is seldom applied to LLW.

While the errors associated with plutonium activity measurements may be quite high, tendencies of generators to overestimate actual activities in LLW may offset all, or a portion of, these errors. Generators of waste contaminated with transuranic radionuclides understand the importance of restricting radionuclide concentrations to less than 100 nCi/g if the material is to be disposed of at Area G. Consequently, in the last three to five years, possibly longer, most major generators of transuranic waste have listed radionuclide activities on their waste disposal records that correspond to the mean activity plus one standard deviation of the mean.

The tendency of generators to overestimate actual activities of plutonium in their waste is especially important in terms of the inventory projected for the performance assessment. This inventory is dominated by operational waste projected to require disposal in the future. As discussed earlier, the assumed characteristics of the future waste were based on the properties of the waste disposed of between 1990 and 1995. Consequently, any tendency to overstate actual activities in the historic waste will also tend to overestimate future inventories.

The plutonium inventories for the composite analysis are dominated by the waste projected to be disposed of prior to 1971. As discussed earlier, these projections were developed by extrapolating waste disposal data for the early to mid-1970s back to the 1957 to 1971 period. The projected inventories of these isotopes are expected to vastly overestimate the actual activities in the disposed waste and, as such, to overestimate the doses for the Atmospheric Scenario. For example, Warren (1980) reports that approximately 9,700 g (21 lb) of plutonium were disposed of at LANL through the end of 1978. In contrast,

the projections developed for the 1957 to 1970 period estimate that over 30,000 g (66 lb) of plutonium was disposed of at Area G alone. Approximately 29,000 g (64 lb) of this quantity was projected to be Pu-239, the radionuclide making the greatest contribution to the projected Atmospheric Scenario dose.

The overestimate of pre-1971 plutonium inventories appears to involve the activities projected for surface-contaminated waste. While this waste form dominates the projected activities, the majority of the plutonium waste generated prior to 1971 is expected to consist of liquid waste. In fact, information provided by Warren (1980) suggests that approximately two-thirds of the plutonium activity was in the form of liquids.

In addition to highlighting possible shortcomings about the pre-1971 waste projections, the form of the waste has important implications in terms of detection uncertainties. In general, the liquid waste in question was characterized by subjecting samples of the waste to radiochemical analysis. As discussed earlier, detection errors are much smaller when this approach is used. Errors associated with these measurements are expected to be on the order of 10 to 50 percent.

Am-241 is relatively easy to detect in low-density matrices; measurement errors for this waste are generally less than 100 to 200 percent. Errors of 900 percent or more may occur in high-density matrices because of matrix attenuation of gamma radiation. Measurement errors may be reduced using sampling and radiochemistry. Given that the majority of the Am-241 in the composite analysis inventory consisted of liquid waste, radiochemical methods were most likely used to quantify activities of this isotope. Pre-1971 inventories of this radionuclide may also be significantly overestimated. A total of 2.2×10^3 Ci of the isotope were projected to be disposed of between 1957 and 1970 using the extrapolation-based approach, while the waste projected from 1971 through the end of disposal operations in 2044 was projected to contain approximately 34 Ci. The large difference between these activities suggests that the 1957 to 1970 inventory of the radionuclide is overstated. However, no firm conclusions may be reached without further investigation into this matter.

Depleted and enriched uranium are relatively easy to detect using non-destructive techniques and can be characterized with errors of 100 to 200 percent. These errors can also

be reduced by sampling the waste and conducting radiochemical analyses. Th-232 is relatively easy to detect because its short-lived daughters emit relatively high-energy gamma radiation. Errors associated with non-destructive analysis are typically within 200 to 300 percent. Detection problems may arise if the isotope has been chemically separated from its daughters.

The projected radon fluxes from the Area G disposal units depend upon the amount of Ra-226 and Ra-228 present in the waste. The inventories of these radionuclides depend, in turn, upon the amount of each isotope disposed of in the pits and shafts and the inventories of the isotopes' long-lived parents. An evaluation of the errors introduced into the flux projections by measurement uncertainties must take into account all of these sources of radon gas.

Ra-226 has been disposed of at Area G in the past, and is projected to require disposal in the future. This radionuclide is characterized by high-energy gamma emissions and is readily detected in LLW. Measurement errors for this radionuclide, using non-destructive analysis, will typically fall within 100 to 200 percent. Contributions to the Ra-226 inventory from the decay of the isotope's long-lived parents are negligible over the 1,000-yr compliance period. Consequently, the measurement errors associated with the parents are unimportant.

Ra-228 has not been reported in Area G disposal records but is generated by the decay of Th-232. No other long-lived parents of the isotopes are projected to result in significant Ra-228 inventories. As discussed above, the detection errors associated with non-destructive analysis of Th-232 are typically within 200 to 300 percent.

4.1.2.2 Source Releases

Two mechanisms of release were considered in the source-term modeling for the Atmospheric Scenario: the diffusion of radioactive gases from the buried waste, and the resuspension of contamination transported to the surface by plants and burrowing animals. The uncertainties associated with each of these release mechanisms are discussed below.

The rates of release of gases from Area G will be proportional to the diffusion coefficients assigned to the waste and cover material. The diffusion coefficients used in the dose assessment are expected to be representative of conditions at Area G. The diffusion coefficients used for H-3 were 600 and 50,000 m^2/yr ($6.5x10^3$ to $5.4x10^5$ ft^2/yr) for pits and shafts, respectively. These values take into account the effects of thermal gradients in the pits (Philip and de Vries, 1957) and barometric pumping effects near the shafts (Vold, 1997). These values are approximately equal to and 65 times greater than, respectively, the free diffusion coefficient of water vapor. The diffusion coefficient used for modeling releases of C-14, krypton, and radon from the disposal shafts was the same as that used for H-3, while a value of 100 m^2/yr (1,100 ft^2/yr) was used for the pits. The pit coefficient was based on the free diffusion coefficient of these gases, adjusted downward to account for the effects of soil porosity and tortuosity.

The H-3 fluxes projected for the scenario are expected to overestimate the actual rates of release observed at the disposal site. The analytical model used in the dose assessment was based on a number of conservative assumptions. It was assumed that all tritiated water vapor in the disposal units at a given time was released from the disposal site within one year's time, that no depletion of the H-3 inventory occurred from groundwater leaching or diffusive losses, and that the entire H-3 inventory was located immediately below the earthen cover placed over the disposal units, thereby minimizing the distance over which the vapor must diffuse.

Vold (1997) used a numerical model to model H-3 fluxes from Area G in a more realistic fashion, avoiding much of the conservative nature of the approach used in the dose assessment. Perhaps most importantly, the analysis includes a time constant of 1,000 yr for tritium release. This constant, based on data collected at Area G, indicates that a small fraction of the H-3 inventory is actually escaping from the waste packages in any given year. The results of these calculations project fluxes from the historic shaft waste that are approximately 200 times less than those projected using the analytical approach.

Assumptions similar to those discussed with respect to H-3 were also applied in the dose assessment to model C-14, Kr-81, and Kr-85 gas fluxes from Area G. Numerical modeling by Vold (1997) took into account the rate of C-14 gas generation based on bio-degradation rates of the organic matrices (i.e., paper and wood) comprising the inventory.

Nevertheless, the projected fluxes using the analytical approach are in general agreement with numerical modeling results. Comparisons between the analytical and numerical models were not conducted for krypton.

The fluxes of radioactive gases to the atmosphere may be affected by the rate of soil erosion at the disposal facility. As erosion of the cover proceeds, the distance through which gases must diffuse to reach the ground surface will decrease, possibly resulting in greater fluxes. Consequently, errors associated with estimates of the erosion rate may lead to errors in the projected releases of gases from the site.

The effect of erosion was not taken into account in modeling H-3 vapor and C-14 gases releases from the disposal site, but was accounted for in the radon flux projections. A mean erosion rate of 4.0×10^{-7} m/yr (1.3×10^{-6} ft/yr) was used in the radon flux model, based on an Area G modeling study conducted by Springer (1996). This erosion rate has associated with it a standard deviation of 1×10^{-6} m/yr (3.3×10^{-6} ft/yr), and a maximum value of almost 5×10^{-5} m/yr (1.6×10^{-4} ft/yr). Based on these statistics, the actual erosion rate is expected to fall within an order of magnitude of the mean rate. Taking these errors into account, however, has only minor effects on the projected radon fluxes.

The release of radon gas from the disposed waste is directly proportional to the emanation coefficient. This coefficient is the fraction of radon that is released from the waste matrix into the pore space. While the actual coefficient will be affected by the characteristics of the waste matrix, the value of 0.35 (NRC, 1989) used in the dose assessment is expected to reasonably represent the soils at LANL. Lacking actual measurements from the site, however, it was assumed that the error associated with the emanation coefficient was 20 percent.

Potentially important sources of uncertainty in the biotic intrusion source release model are specific to the mode of transport of radioactivity to the ground surface (i.e., plant uptake and animal burrowing). Modeling indicates that rates of release to the surface will be dominated by plant uptake and the subsequent decay of plant organic matter for radionuclides with plant uptake factors of 0.1 and greater (Vold and Shuman, 1997). Burrowing animals will be the primary transport vector for radionuclides that are poorly

assimilated by plants. This is, in fact, the case for the isotopes of americium, plutonium, and uranium that dominate the exposures projected for the Atmospheric Scenario.

Rates of release of radionuclides due to plant uptake will depend upon the root distribution of the plants relative to the disposed waste, the rate at which plant organic matter is deposited on the ground surface, the vegetative density, and the plant uptake factors. As a greater proportion of the plant's roots extend into the waste, more radioactivity will be assimilated and, ultimately, incorporated into the surface soils at the site. The source-release modeling was based on a maximum rooting depth of 2 m (6.6 ft). Thirty percent of the roots were assumed to occur below a depth of 1 m (3.3 ft), the approximate thickness of the cover system placed over the historic disposal pits. This assumed root distribution is expected to bound actual rooting depths at the disposal site. As discussed earlier, DOE will continue to maintain the facility. As part of these custodial duties, it is expected that efforts will be taken to prevent the establishment of very deep-rooted species of plants.

The impact of greater penetration into the waste by plant roots on radionuclide concentrations in the surface soil will be influenced by the degree to which plants assimilate the radioactivity. Radionuclides characterized by small plant uptake factors will be poorly assimilated, regardless of the proportion of roots contacting the disposed waste. Given that the primary contributors to the projected doses for the Atmospheric Scenario have small plant uptake factors, the distribution of plant roots in the waste is unimportant in terms of the long-term performance of the disposal facility.

The contamination assimilated by plants was assumed to be deposited on the surface within a year's time due to leaf fall and decay of the above-ground biomass. This rapid recycling is expected to reasonably estimate soil radionuclide concentrations. Less rapid cycling of plant matter would slow the release of radioactivity to the soil, resulting in lower radionuclide concentrations in the soil for a period of time. The vegetative density used for the source modeling was based on site-specific data for vegetative densities at LANL. Much higher densities will result in only moderately higher soil concentrations of radionuclides with high plant uptake factors (Vold and Shuman, 1997). For example, a four-fold increase in the vegetative density would increase soil concentrations of a radionuclide with a plant uptake factor of 1.0 approximately 13 percent. Soil concentrations of radionuclides with small

plant uptake factors will actually decline slightly with increases in vegetative densities because the plant biomass effectively dilutes the contamination excavated by animals.

The radionuclide plant uptake factors determine the extent to which radioactivity in the soil is assimilated by plants via their roots. The plant uptake factors used to project ingestion doses are based on an extensive literature review of terrestrial transport and agricultural parameters by Baes et al. (1984). The plant uptake factors reported in that study take into account the experimental techniques used to generate the literature values, the reliability of the reported data, and their appropriateness for modeling uptake by agricultural crops. The use of generic plant uptake factors for the dose analysis ignores the effects that LANL-specific factors may have upon the assimilation of radionuclides from contaminated soils. However, while LANL-specific uptake factors are available for some elements and plants (e.g., White et al., 1981), a comprehensive set of factors for the radionuclides and crops included in the performance assessment does not exist.

The errors introduced into the dose assessment by uncertainties associated with the plant uptake factors will be limited. Modeling results indicate that releases of contamination to the surface soil for radionuclides with plant uptake factors of 0.01 and 0.1 are approximately 4 and 40 percent greater, respectively, than releases for radionuclides that are transported to the surface solely by burrowing animals. The radionuclides that make the most important contributions to the peak projected doses for the Atmospheric Scenario have plant uptake factors ranging from 4.5×10^{-5} to 2.5×10^{-4}. Based on these uptake factors, even one to two order-of-magnitude increases will have relatively small impacts on the projected doses for the scenario.

The projected releases of radioactivity due to the intrusion of animals into the waste depend upon the burrow distributions of the animal species and the densities of the burrows at the site. The source-release model was based on a burrow distribution representative of the pocket mouse. The burrow characteristics of this species were used to estimate those of the deer mouse, a species of small mammal commonly observed at Area G. Burrows were estimated to extend to a depth of 2 m (6.6 ft); 10 percent of the burrows were assumed to occur below a depth of 1 m (3.3 ft) or the approximate thickness of the cover system placed over closed disposal pits. Burrow densities used in the model were consistent with densities observed for deer mice.

While the extent of burrowing assumed in the source-term model is expected to reasonably represent conditions at Area G, deeper or more extensive burrows could result in increased rates of radionuclide transport to the surface. Vold and Shuman (1997) examined the effect of increasing the level of animal intrusion into the waste to a reasonable maximum. Under the conditions evaluated, surface soil concentrations of radionuclides with small plant uptake factors increase almost three times relative to the nominal level of intrusion assumed for the dose assessment. Concentrations of radionuclides with large plant uptake factors decline because the additional soil brought to the surface by animals dilutes the radioactivity deposited by plants.

The depth to which plants and animals intrude into the disposed waste will also be affected by the surface soil erosion rate at Area G. As erosion progresses, the cover over the waste decreases, thereby allowing plant roots and animal burrows to extend further into the zone of contamination. However, taking the uncertainties associated with the erosion rate into account has a minor effect on the projected rates of contaminant transport to the soil surface during the 1,000-yr compliance period.

4.1.2.3 Environmental Transport

The atmospheric transport model may be characterized by the values of the resuspension factor and dispersion factor used in the dose calculations. These values are based on site-specific information and assumptions about the effects of complex terrain in the vicinity of Area G (Kowalewsky et al., 1995; Vold, 1996a). While there are uncertainties associated with the resuspension and dispersion factors, the magnitude of any error introduced into the projected atmospheric concentrations by these uncertainties is difficult to quantify without additional site data. Kowalewsky et al. (1995) expect that the overall uncertainty in the resuspension factor is less than an order of magnitude. Errors introduced by uncertainties associated with the dispersion factor are expected to be on the order of 100 to 200 percent.

4.1.2.4 Resource Utilization

The inhalation of radioactive gases and dust accounts for more than 99 percent of the projected peak dose for the Atmospheric Scenario. Consequently, the discussion of uncertainties associated with rates of resource utilization focuses on this pathway. The quantity of radioactivity inhaled by the receptor is determined by the rate of inhalation and the fraction of time the individual is exposed to contaminated air. An annual inhalation rate of 8,000 m^3 (2.8×10^5 ft^3) was used in the dose assessment, based on the assumption that the individual spends 16 hr of each day engaged in light activity and 8 hr resting (ICRP, 1975). While changes in activity levels will result in higher or lower inhalation rates, the rate used in the assessment is reasonably conservative as a long-term average. For example, it is 10 percent greater than the annual inhalation rate of 7,300 m^3 (2.6×10^5 ft^3) recommended by the EPA (1989) for continuous-exposure situations in which specific activity patterns are unknown. On the other hand, scenario doses would be about 35 percent higher than projected if the EPA's reasonable worst-case inhalation rate of almost 11,000 m^3/year (3.9×10^5 ft^3) were used.

The offsite resident was assumed to be at home and inhale airborne radioactivity for almost 6,200 hr per year. This value is reasonable for a person who works away from the house but, otherwise, spends little time away from the residence. Data summarized by the EPA (1989) indicate that, on average, an adult spends 64 percent of his or her time at home or in the yard. This equates to approximately 5,600 hours per year, or about 91 percent of the total exposure time used in the dose assessment. While higher occupancy times are possible, it is unlikely that an average adult would spend much more than 80 percent of his or her time at home.

4.1.2.5 Radionuclide Dose Conversion Factors

As stated earlier, essentially all of the projected doses for the Atmospheric Scenario result from the inhalation of airborne radioactivity. The radioactivity inhaled by the receptor is related to doses using inhalation dose conversion factors. The projected doses for the scenario are committed effective dose equivalents, representing the total dose equivalent received by the body over a 50-yr period after the intake of radioactivity. The dose conversion

factors are based on the recommendations of the ICRP (1977, 1979-1982, 1986). While uncertainties in the dose conversion factors used to project these doses do exist, these uncertainties are difficult to quantify and are not considered here.

4.1.3 All Pathways Exposure Scenarios

Two "all pathways" exposure scenarios were included in the Area G performance assessment: the All Pathways - Groundwater Scenario and the All Pathways - Parajito Canyon Scenario. A peak annual dose of 2.3×10^{-7} mrem is projected to occur at the end of the 1,000-yr compliance period for the All Pathways - Groundwater Scenario. The consumption of water and vegetables irrigated with contaminated water accounts for about 97 percent of the peak dose. The peak dose projected for the All Pathways - Parajito Canyon Scenario is 1.3×10^{-4} mrem/yr. The consumption of water and ingestion of food crops irrigated with water drawn from the resident's well are responsible for 34 and 60 percent of the peak dose, respectively. Radionuclides contributing to the peak doses for these scenarios are included in Table 4-1.

The All Pathways - Groundwater and All Pathways - Parajito Canyon scenarios were also included in the composite analysis. The maximum annual dose projected for the former scenario is 1.2×10^{-5} mrem. The ingestion of drinking water and consumption of vegetables irrigated with well water are the dominant exposure pathways in this scenario. The peak dose for the All Pathways - Parajito Canton Scenario is 7.2×10^{-3} mrem/yr. The inhalation of resuspended dust and direct radiation from contaminated soil account for 77 percent of this dose. Radionuclides making significant contributions to these peak doses are listed in Table 4-1. The uncertainties associated with the dose projections for the "all pathways" scenarios are discussed below.

4.1.3.1 Radionuclide Inventories

The uncertainties associated with the waste inventory projections are discussed, in general terms, in Section 4.1.1.1. Furthermore, errors associated with measuring most of the radionuclides that are important in terms of the "all pathways" scenarios have been

estimated. The following discussion addresses measurement errors for radionuclides that are not considered above.

Two fission products, Ag-108m and Cs-137, make significant contributions to the All Pathways - Parajito Canyon Scenario dose for the composite analysis. These radionuclides emit high-energy photons that are readily detected. Hf-182 is also characterized by high-energy gamma emissions and will be readily detected in LLW. Measurement errors for these radionuclides, using non-destructive analysis, will typically fall within 100 to 200 percent. In contrast, Sr-90 is a pure beta emitter and may be difficult to detect in waste matrices. Consequently, it is possible that generators have overlooked, or otherwise underestimated, activities associated with this radionuclide.

The projected inventories of Ag-108m and Cs-137 incorporate uncertainties that were introduced by the methods used to project them. Ag-108m accounts for about 19 percent of the peak dose to the canyon resident for the composite analysis. The projected inventory of this radionuclide is based solely on the factors used to allocate the Mixed Fission Products (MFP) waste to specific radionuclides; no activities were listed in the disposal database specific to this isotope. Consequently, the projected Ag-108m activity is subject to uncertainties associated with the allocation approach (Vold, 1996c). One such uncertainty that may overstate the actual activity of this radionuclide pertains to the assumed age of the MFP waste.

The MFP allocation fractions were based on the assumption that the waste was 2 yr old at the time the activity was recorded. This age was selected realizing that operational MFP waste may have been younger at the time of disposal, while MFP waste from environmental restoration or decontamination and decommissioning activities may have been considerably older. Over 96 percent of the MFP waste disposed of in the historic shafts consists of operational waste from hot-cell activities. As such, it is reasonable to expect that this waste was, in fact, less than 2 yr old at the time of disposal. Under these conditions, the radionuclide allocation fractions used to distribute the MFP waste will overestimate the actual activities of long-lived radionuclides such as Ag-108m, perhaps by as much as a factor of 2.5. Reductions of this magnitude will significantly reduce the doses projected for the canyon resident.

Cs-137 was projected to contribute 4 percent of the peak dose for the All Pathways - Parajito Canyon Scenario for the composite analysis. The projected impact of this waste, however, is expected to overstate the risk posed to the receptor. Almost all of the historic inventory is represented by two irradiation sources encased in stainless steel. While this waste was assumed to be transported to the surface by plants and burrowing animals, it is more likely that it will still be contained in the source jacket at the projected time of exposure. Furthermore, even if the source was no longer sealed, the discrete nature of the waste is such that transport of the material to the surface is unlikely. Consequently, actual doses from the source will tend to be smaller than the projected exposures.

As discussed in Section 4.1.2.1, the americium and plutonium inventories projected for the composite analysis are expected to significantly overestimate the activities actually placed in the Area G disposal facility. These errors are expected to significantly overestimate a portion of the actual doses for the All Pathways - Parajito Canyon Scenario.

4.1.3.2 Source Releases

The uncertainties inherent in the source-release models used to project releases of radioactivity to groundwater are discussed in Section 4.1.1.2. These uncertainties apply to the "all pathways" scenarios as well. Radioactivity was also assumed to be transported to surface soils by plants rooting in the disposed waste and animals burrowing into the disposal units. Possible errors introduced by these uncertainties are discussed in Section 4.1.2.2.

4.1.3.3 Environmental Transport

Uncertainties associated with groundwater transport modeling of radionuclides to the receptor locations east-southeast of the Area G disposal units and in Parajito Canyon are discussed in Section 4.1.1.3. These uncertainties, and their expected impact, apply to the "all pathways" scenarios as well. The following discussion addresses additional sources of uncertainty unique to the All Pathways - Groundwater and All Pathways - Parajito Canyon scenarios.

The infiltration characteristics on top of Mesita del Buey and in the adjacent canyons will play an important role in terms of the doses projected for the All Pathways - Groundwater and All Pathways - Parajito Canyon scenarios. As discussed in Section 2.1.1.3, model simulations were conducted to understand the overall impact of uncertainties in the rate of infiltration on groundwater radionuclide transport and doses to persons using contaminated groundwater (Birdsell et al., 1997). Briefly, simulations were conducted for different sets of mesa top and canyon infiltration rates. Radionuclide fluxes to the regional aquifer were compared among the simulations, and the cases resulting in the smallest and largest fluxes were identified. Doses were projected for groundwater users for these low and high flow conditions.

Figure 4-3 shows the projected performance assessment doses for the All Pathways - Groundwater Scenario under low, base case, and high flow conditions. Projected doses for the low flow condition increase throughout the 10,000-yr period shown. The peak annual dose during the 1,000-yr compliance period is 1.2×10^{-11} mrem, which is about 19,000 times less than the peak compliance period dose projected for the base case simulation. Doses for the high flow condition peak approximately 2,500 yr after facility closure, the maximum compliance period dose is 9.7×10^{-6} mrem/yr. This dose is 42 times greater than the peak base case dose.

Figure 4-4 shows the projected composite analysis doses for the All Pathways - Groundwater Scenario for the different flow conditions. Once again, doses for the low flow condition increase over the 10,000-yr period. A peak dose of 5.3×10^{-11} mrem/yr is projected for the compliance period, this dose is about than 225,000 times less than the dose projected under base case flow condition. Doses for the high flow condition peak about 2,000 yr after facility closure. The peak dose during the 1,000-yr compliance period is 5.8×10^{-4} mrem/yr, which is about 48 times greater than the peak dose projected for the base case flow condition.

The performance assessment doses projected for the All Pathways - Parajito Canyon Scenario are shown in Figure 4-5 for the different flow conditions. Doses for the low flow condition reach a maximum at about 1,250 yr post-closure. The peak annual dose projected for this condition during the 1,000-yr compliance period is 2.0×10^{-5} mrem, which is 6.6 times less than the peak dose projected for the base case flow condition. Higher rates of release and transport accompany the high flow condition. The peak dose of 3.3×10^{-4} mrem/yr is

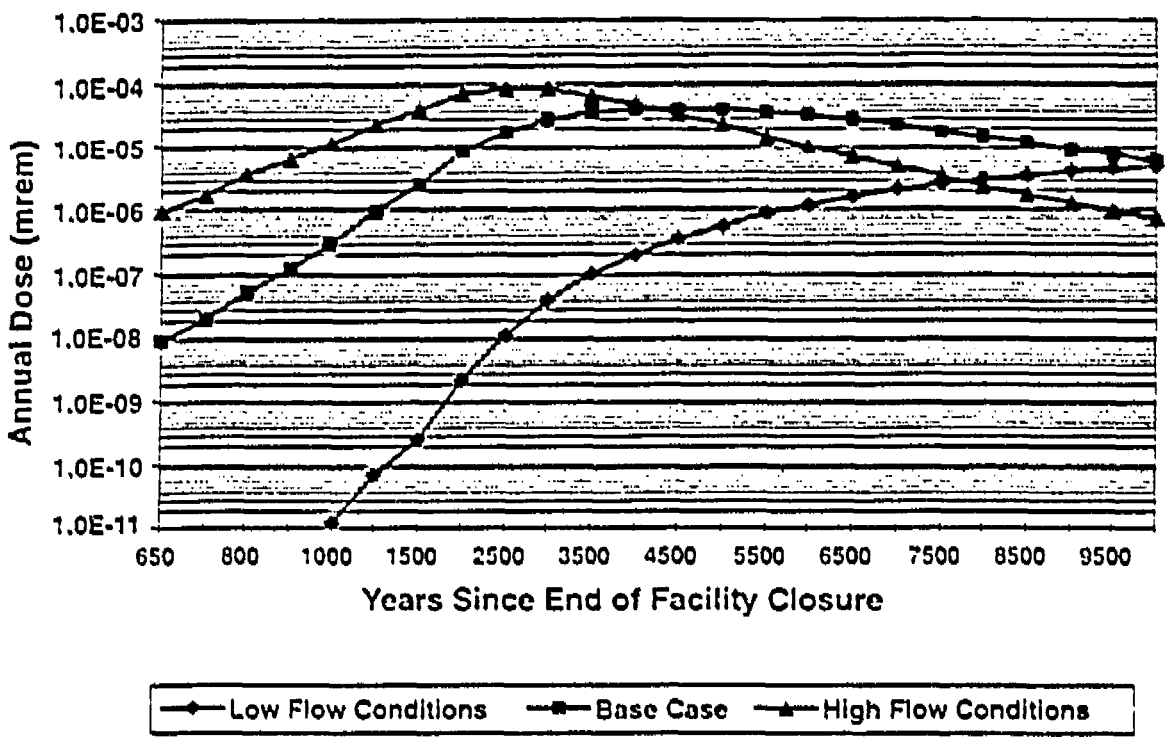

RAE - 106272

Figure 4-3. Projected performance assessment doses for the All Pathways - Groundwater Scenario for different flow conditions.

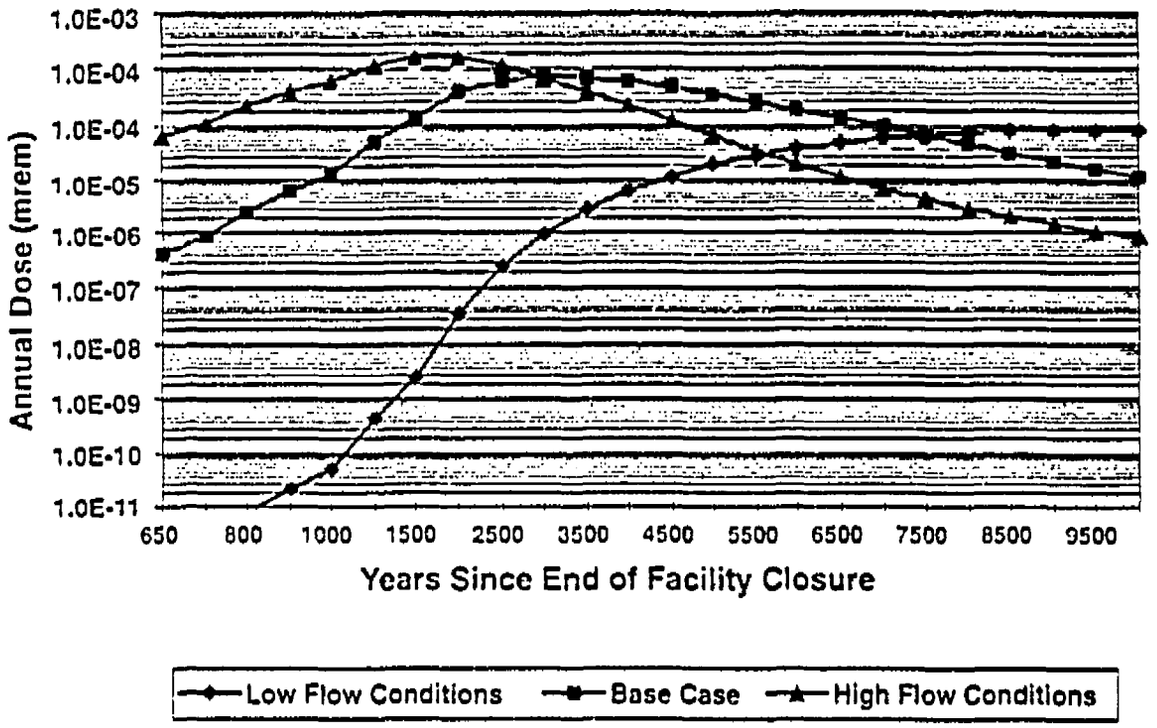

Figure 4-4. Projected composite analysis doses for the All Pathways - Groundwater Scenario for different flow conditions.

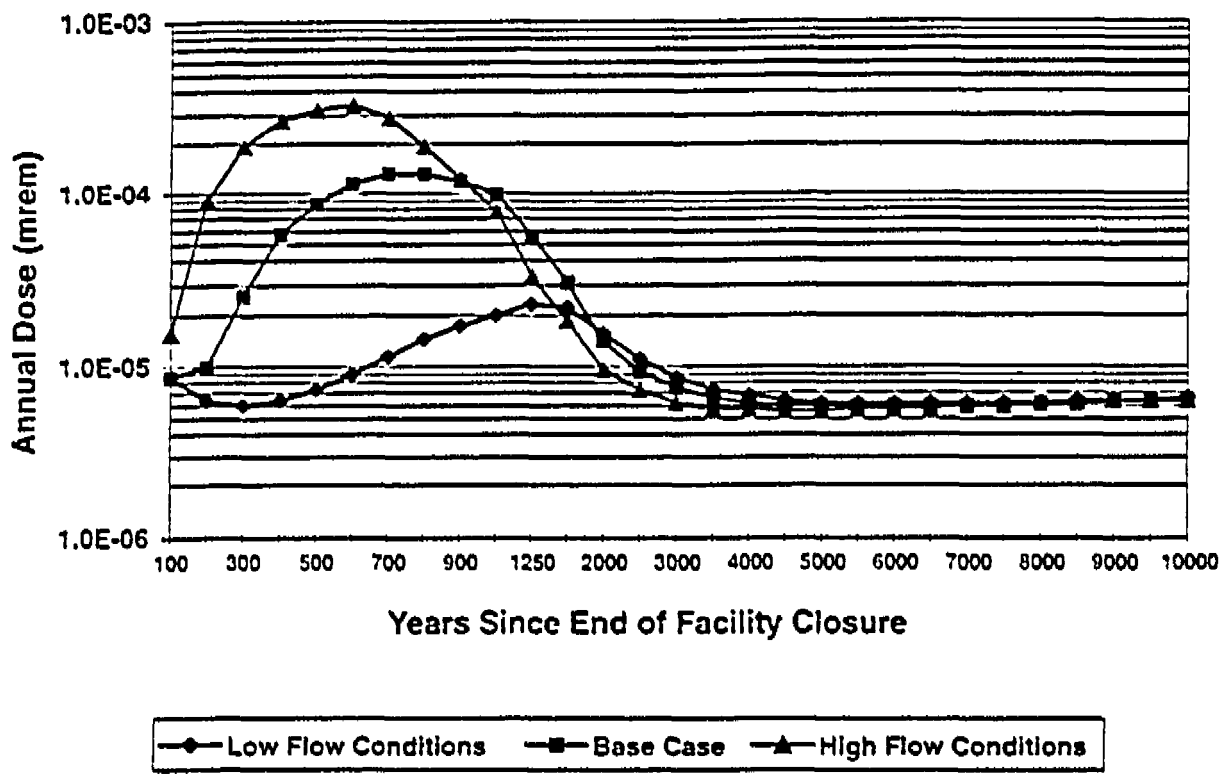

RAE - 106274

Figure 4-5. Projected performance assessment doses for the All Pathways - Parajito Canyon Scenario for different flow conditions.

projected to occur approximately 600 yr after facility closure. This dose is 2.5 times greater than the peak base case dose.

Figure 4-6 shows the projected composite analysis doses for the All Pathways - Parajito Canyon Scenario for the different flow conditions. The peak doses for the base case, low, and high flow conditions all occur at the end of the active institutional control period, when biotic intrusion into the disposed waste is first expected to be feasible. Dose contributions from C-14, Tc-99, and I-129 increase between 100 and 1,000 yr post-closure as infiltration rates through the mesa top and Parajito Canyon rise.

The two "all pathways" receptors were assumed to raise food crops and animals to supply a portion of the their food requirements. While the consumption of contaminated food crops contributes as much as 60 percent of the projected peak doses, the consumption of milk and beef is responsible for less than 4 percent of the total doses. Consequently, the following discussion addresses the uncertainties associated with the former pathway.

The food crops grown by the All Pathways - Groundwater Scenario receptor were assumed to be contaminated by radioactivity deposited on plant surfaces during irrigation, as a result of rainsplash, and by root uptake of contamination reaching the ground. The root uptake pathway was the more significant of the three, accounting for more than 85 percent of the dose projected for the food ingestion pathway. The crops grown by the "all pathways" receptor in Parajito Canyon were also assumed to be grown in contamination washed into the canyon from the mesa top.

The soil concentrations of C-14, Tc-99, and I-129 due to irrigation are expected to be overestimated by the models used in the dose assessment. A soil buildup time of 15 yr was assumed to apply to all radionuclides applied in the irrigation water. While accounting for buildup may be appropriate for radionuclides that sorb to soils, these highly mobile radionuclides will tend to be transported downward with water percolating through the garden. As the contamination is rinsed from the soils, it will become unavailable for root uptake by plants.

The degree to which C-14, Tc-99, and I-129 build up in soils following irrigation will depend upon the radionuclides' sorption behaviors in the offsite soils. However, it is

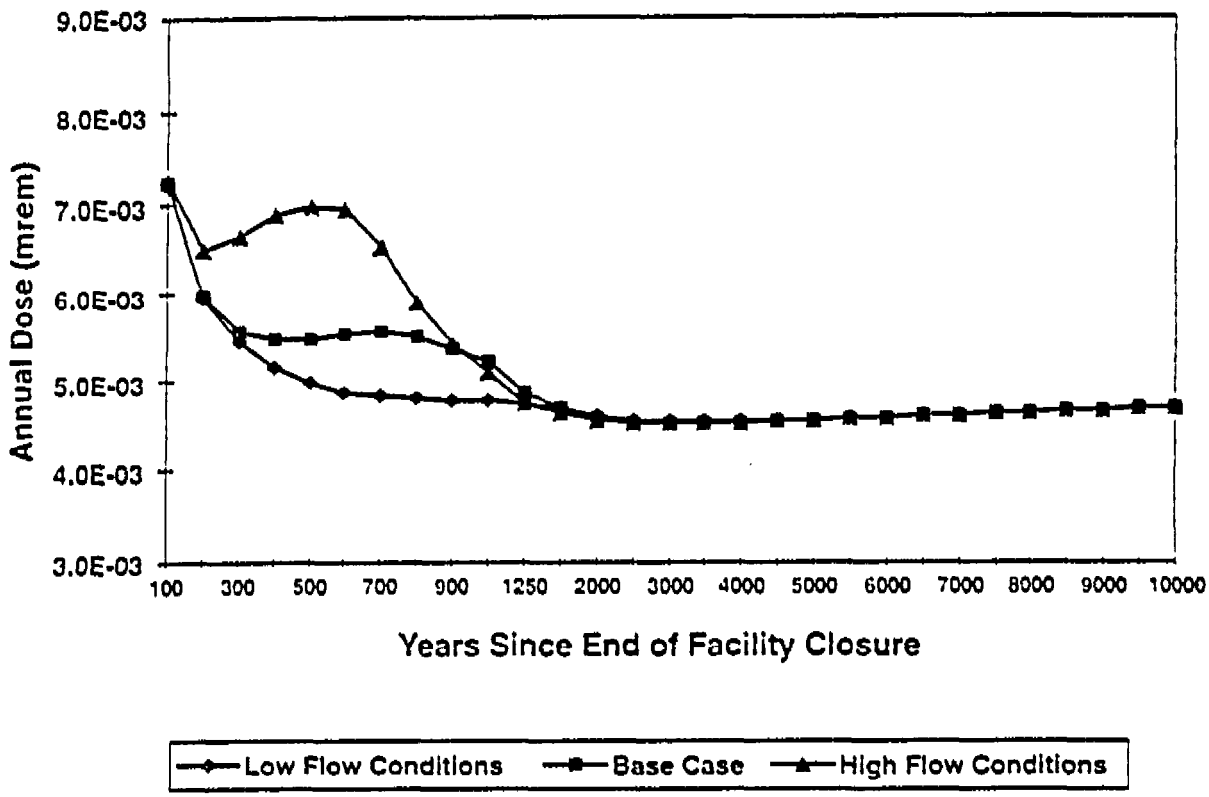

RAE - 106275

Figure 4-6. Projected composite analysis doses for the All Pathways - Parajito Canyon Scenario for different flow conditions.

reasonable to expect that these contaminants will demonstrate mobility similar to that projected for mesa top soils. Based on this assumption, a buildup time of 1 yr is expected to be appropriate for projecting soil radionuclide concentrations. Under these conditions, the plant radionuclide concentrations of C-14 and Tc-99 would be 19 and 16 percent, respectively, of the projected values. Concentrations of I-129 would be about 80 percent of the modeled values.

Errors in the projected doses due to uncertainties associated with the plant uptake factors will be limited for the "all pathways" scenarios. The uptake factors used in the dose assessment for C-14 and Tc-99 both exceed 1.0, indicating plant radionuclide concentrations exceeding those observed in soils. Moderately higher uptake factors for these radionuclides (e.g., two times the nominal values) would result in food pathway doses that are almost two times higher than projected. However, these higher doses would increase the peak scenario doses by less than 20 percent. The uptake factors for I-129 would need to increase by 100 times or more to have significant effects on the peak receptor doses. Radionuclides transported into the canyon by surface runoff make relatively small contributions to the food pathway doses. Those that do have very small plant uptake factors. Increases in these uptake factors greater than one to two orders of magnitude would be needed to significantly affect projected doses for the canyon resident.

The plant radionuclide concentrations resulting from the assimilation of radioactivity directly from the irrigation water are a function of the amount of water applied to the crops, crop yields, the plant translocation factor, the fraction of the radioactivity deposited on the plant that is initially retained, and the rate at which radioactivity deposited on plant surfaces is removed due to weathering. The amount of water that was assumed to be applied to the crops is based on information for the greater Los Alamos area and, as such, is expected to reasonably approximate the amount of water applied to food crops. While rates of water application could vary for short periods, the total amount of water applied to the crops over the course of a growing season is not expected to change substantially.

The crop yields used in the dose assessment are expected to be reasonable for the northern New Mexico region. While decreased yields could result in higher concentrations of radionuclides in plants, these differences are expected to be minor. All radioactivity deposited on plants was assumed to be transferred to the edible portions of leafy vegetables

grown by the resident, while 10 percent of the activity deposited on protected produce, fruit, and grain was assumed to be assimilated into the edible portion. Moderate increases in the translocation factor for protected produce, fruit, and grain will have limited impacts on the projected ingestion doses, given the small contribution that contamination deposited directly on the plants makes to the peak projected doses. For example, a five-fold increase in the translocation factor for non-leafy vegetables results in food pathway doses that are about 20 percent greater than those projected for the nominal case

The amount of radioactivity initially retained by a plant during irrigation and the rate at which it is weathered from plant surfaces are not easily quantified. The fraction of activity initially retained will depend largely upon the rate at which water is applied to the crops and the morphology of the plants. The rate of weathering will vary with meteorological conditions at the site and characteristics of the food crops. While the magnitude of the error introduced by these uncertainties is unknown, it is not expected to be significant.

A large component of the composite analysis doses projected for the Parajito Canyon resident is ultimately determined by canyon soils that become contaminated following surface runoff. Radionuclide concentrations in the canyon soils are proportional to the quantity of contamination removed from the mesa top by surface runoff, the area over which the contamination disperses during runoff, and the depth to which the radioactivity is mixed at the resident's home. The doses projected for this receptor are based on the assumption that a thickness of soil equivalent to the projected surface erosion rate would be transported from the mesa each year. As discussed earlier, a mean erosion rate of 4.0×10^{-7} m/yr (1.3×10^{-6} ft/yr) was used in the dose assessment (Springer, 1996). The actual erosion rate is expected to fall within an order of magnitude of the mean rate. Hence, doses to the canyon resident would increase by 10 times or less due to errors in the erosion rate estimate.

Radioactivity transported into the canyons by surface runoff was assumed to uniformly disperse over an area that is equivalent to the area of contamination on the mesa. In actuality, relatively high contaminant concentrations are expected to occur in local depressions where surface runoff collects, while little or no contamination may occur in other areas. While the actual distribution of contamination across the landscape will influence the projected exposures for the canyon resident, it is not readily projected. Consequently, the error introduced by this source of uncertainty is not quantified.

The contamination transported to the canyon floor was assumed to be mixed to a depth of 15 cm (6 in.) over the resident's entire lot. This depth is expected to be reasonable for the individual's garden, but may overestimate the mixing depth over the remainder of the lot and, therefore, radionuclide concentrations in surface soil. Under worst-case conditions, however, reduced mixing depths will result in no more than a ten-fold increase in the projected doses.

4.1.3.4 Resource Utilization

The uncertainties associated with the consumption rate of drinking water and inhalation rate of air used in the dose assessment are discussed in Sections 4.1.1.4 and 4.1.2.4, respectively. Conclusions reached in those sections regarding the impact of uncertainties on the ability of the disposal facility to comply with the performance objectives apply equally as well to the "all pathways" scenarios. The ingestion of soil and food and exposure to contaminated soils also play important roles in terms of the projected "all pathways" doses. The potential impact of uncertainties associated with the use of, or exposure to, these resources is considered below. The consumption of contaminated beef and milk from animals raised by the resident contributes 4 percent or less to the projected peak doses, and is not considered below.

The rate of inadvertent soil ingestion used in the dose assessment, 100 mg/day (3.5×10^{-3} oz/day), is expected to overestimate actual exposures because it reflects an adult with a high tendency to ingest soil (EPA, 1989). Rates of ingestion for individuals with low to moderate tendencies to ingest soil range from 1 to 10 mg/day (3.5×10^{-5} to 3.5×10^{-4} oz/day). The rates of ingestion used for leafy vegetables, grain, and produce are based on national averages for the United States (Yang and Nelson, 1986). These consumption rates generally agree with the annual consumption rate of 190 kg (420 lb) of fruit, grain, and vegetables cited by the NRC (1977) for an average individual. The rates also generally agree with data developed by Rupp (1980) which indicate annual consumption rates of vegetables, other produce, and grains of about 18, 140, and 35 kg (40, 310, and 77 lb), respectively. Finally, the total consumption rate used in the dose assessment is similar to the consumption rate of 190 kg/yr cited by the NRC (1977), but is three to four times smaller than that cited for modeling doses received by the maximally exposed individual.

The assumption that one-half of the resident's food requirements is met by crops and animals raised at the site is expected to overestimate the actual amount of food raised by a typical individual. The EPA (1989) indicates that, on average, 25 percent of vegetables is home grown, while 20 percent of fruit is grown at home. Reasonable worst-case values cited by the EPA for the amount of home grown vegetables and fruit in the intruder's diet are 40 and 30 percent, respectively.

The offsite resident was assumed to be at home for almost 6,200 hr per year, during which time the person was assumed to be exposed to direct radiation and inhale airborne radioactivity. As discussed in Section 4.1.2.4, this time of exposure exceeds the time recommended by the EPA (1989) for an average adult by about 10 percent. Although higher occupancy times are possible, it is unlikely that the average adult would spend more than 80 percent of his or her time at home.

Direct radiation exposures will be attenuated by the individual's house during the time spent indoors. A shielding factor of 0.7 was used in the dose assessment to account for these shielding effects. In essence, this means that 70 percent of the direct radiation incident upon the house contributes to the resident's projected exposure. This shielding factor, which is expected to overestimate the exposure of the individual, is suggested by the NRC (1977) for projecting doses to the maximum individual; the value suggested for the average individual is 0.5.

4.1.3.5 Radionuclide Dose Conversion Factors

The "all pathways" receptors are projected to receive internal exposures from the inhalation and ingestion of radioactivity. These exposures were estimated using 50-yr committed effective dose equivalents, representing the total dose equivalent received by the body over a 50-yr period after the intake of radioactivity. These dose conversion factors are based on the recommendations of the ICRP (1977, 1979-1982, 1986). While uncertainties in the dose conversion factors used to project these doses exist, these uncertainties are difficult to quantify and are not considered here.

The dose conversion factors used to estimate exposures from direct radiation from contaminated soils were developed using the MICROSHIELD computer code (Grove Engineering, 1992). This code accounts for the source geometry and shielding configuration (i.e., excluding the individual's house) appropriate for the "all pathways" scenarios and, as such, is expected to provide reasonable estimates of the actual exposures. The exposures calculated by the code were converted to radionuclide doses using a conversion factor of 0.75 mrem/mR. This factor was adopted from ICRP 51 (1987) and pertains to a rotational geometry for a photon energy of 0.2 MeV. While the precise conversion factor will depend upon the photon energy and exposure geometry, it is not expected to vary by more than 20 percent for most exposure conditions.

4.1.4 Summary of the Offsite Scenario Sensitivity and Uncertainty Analysis

The uncertainties associated with the offsite exposure scenarios are discussed in Sections 4.1.1 through 4.1.3. Considered alone, none of the sources of uncertainty are expected to compromise the ability of the Area G disposal facility to comply with the performance objectives discussed in Chapter 1. However, the errors introduced by the uncertainties discussed above will propagate through the different modeling components, increasing the potential impacts on the projected doses. Therefore, to adequately demonstrate compliance with DOE Order 5820.2A and the DOE Implementation Order, the potential impact of these propagated errors must be evaluated.

The manner in which errors are propagated for a given scenario is an important factor in determining the overall error in the dose estimates. Propagation must take into account how the projected doses are affected by each parameter and must account for any interdependencies that exist between parameters. While analytical procedures are available for estimating the effects of error propagation, numerical techniques such as the Monte Carlo approach and Latin Hypercube Sampling are often applied to large-scale problems.

The complete set of data required for an extensive evaluation of uncertainties using numerical techniques is not available at this time. Therefore, a simpler approach to estimating the overall error associated with the dose estimates was adopted. Under this approach, approximations were made of the extent to which doses may be under- or

overestimated due to the uncertainties associated with the parameters and models used in their calculation. Parameters and models that may, because of associated uncertainties, underestimate the actual doses received by a receptor were assigned errors greater than 1.0. If a given parameter was expected to overestimate doses, and the magnitude of this error could be approximated, an error of less than 1.0 was assigned. Parameters and models that were not expected to significantly over- or underestimate actual doses, or have errors associated with them that are not easily quantified, were assigned errors of 1.0.

The errors assigned to account for parameter and model uncertainties were combined to arrive at a conservative estimate of the overall error associated with the projected doses. Errors related to specific radionuclides or exposure pathways were weighted by the fraction of the total scenario dose for which they were responsible. The estimate of total error was multiplied by the projected peak scenario doses to yield estimates of the greatest and smallest scenario exposures that could reasonably be expected. These worst- and best-case doses were used to evaluate the potential impact of uncertainties on the ability of the Area G disposal facility to comply with the performance objectives.

The potential impacts of the propagated error on the ability of the disposal facility to meet the performance objectives are discussed below. Section 4.1.4.1 addresses the impacts as they pertain to the Groundwater Resource Protection Scenario, while Section 4.1.4.2 discusses potential errors for the Atmospheric Scenario. The All Pathways - Groundwater and All Pathways - Parajito Canyon scenarios are considered in Section 4.1.4.3.

4.1.4.1 Groundwater Resource Protection Scenario

Section 4.1.1 discusses the sources of uncertainty associated with the doses projected for the Groundwater Resource Protection Scenario. These uncertainties and the estimated errors associated with them are summarized in Table 4-2. The errors listed for the parameters in the table are estimates of the extent to which doses could reasonably be under- or overestimated by each parameter's associated uncertainty. The rationale used in assigning these errors is summarized in the table and in the following paragraphs. The reader is referred to Sections 4.1.1.1 through 4.1.1.5 for additional details.

Table 4-2. Sources of uncertainty and associated errors for the Groundwater Resource Protection Scenario.

Source of Uncertainty	Uncertainty Factor for Underestimating Dose[a]	Rationale for Values Assigned	Uncertainty Factor for Overestimating Dose[b]	Rationale for Values Assigned
Radionuclide Inventories				
C-14	3.0E+00	Waste is disposed of at projected rate, detection error equals 200 percent.	4.2E-01	No sources are generated in the future; disposal facility closes after 40 yr, no detection error.
Tc-99	3.0E+00	Waste is disposed of at projected rate; detection error equals 200 percent.	8.4E-01	Disposal facility closes after 40 yr; no detection error.
I-129	3.0E+00	Waste is disposed of at projected rate; detection error equals 200 percent.	9.0E-01	Disposal facility closes after 40 yr; no detection error.
Source Releases				
Allocation of waste forms	1.0E+00	All waste assigned to waste form with greatest release rates.	1.0E+00	Factor cannot be assigned lacking release characteristics of waste streams allocated to surface contaminated waste.
Concentration on surface-contaminated waste	1.0E+00	Waste included in dose assessment accounts for more than 99 percent of total projected inventories of C-14, Tc-99, and I-129.	1.0E+00	Waste included in dose assessment accounts for more than 99 percent of total projected inventories of C-14, Tc-99, and I-129.
Infiltration Rate				
East-Southeast of Area G	4.2E+01	Ratio of peak compliance period dose for high flow conditions to peak compliance period dose for base case flow conditions.	5.3E-05	Ratio of peak compliance period dose for low flow conditions to peak compliance period dose for base case flow conditions.
Parajito Canyon	2.7E+00	Ratio of peak compliance period dose for high flow conditions to peak compliance period dose for base case flow conditions.	1.2E-01	Ratio of peak compliance period dose for low flow conditions to peak compliance period dose for base case flow conditions.
Water Transit Time in Waste	2.2E+00	Transit time of 1 yr.	7.5E-01	Estimate to account for a transit time greater than 16 yr and less than 50 yr.

Table 4-2. Continued.

Source of Uncertainty	Uncertainty Factor for Underestimating Dose[a]	Rationale for Values Assigned	Uncertainty Factor for Overestimating Dose[b]	Rationale for Values Assigned
Geochemical Properties	1.0E+00	All radionuclides are assigned distribution coefficients of 0 ml/g; solubility limits are not exceeded.	1.0E+00	Significantly higher distribution coefficients and lower solubility limits for C-14, Tc-99, and I-129 are unlikely.
Environmental Transport				
Radionuclide Travel Time:				
East-Southeast of Area G	4.2E+01	Ratio of peak compliance period dose for high flow conditions to peak compliance period dose for base case flow conditions.	5.3E-05	Ratio of peak compliance period dose for low flow conditions to peak compliance period dose for base case flow conditions.
Parajito Canyon	2.7E+00	Ratio of peak compliance period dose for high flow conditions to peak compliance period dose for base case flow conditions	1.2E-01	Ratio of peak compliance period dose for low flow conditions to peak compliance period dose for base case flow conditions.
Lateral Transport Modeling:				
East-Southeast of Area G	1.3E+00	Based on proportion of total flux transported laterally over a 10,000 year period.	1.0E+00	Inclusion of lateral transport cannot overestimate exposure at this location
Parajito Canyon	1.0E+00	Modeling approach is not expected to be capable of underestimating dose.	1.0E+00	Factor may be zero if lateral flow is prevented by fractures; conservatively set equal to 1 for the analysis.
Sorption Behavior	1.0E+00	All radionuclides are assigned distribution coefficients of 0 ml/g.	1.0E+00	Significantly higher distribution coefficients are unlikely for C-14, Tc-99, and I-129.
Aquifer Dilution	1.0E+00	Modeling approach is not expected to be capable of underestimating dose.	5.0E-01	Conservative estimate based on observed aquifer characteristics in the vicinity of Area G
Combination of Lateral Sources				
East-Southeast of Area G	—[c]		—[c]	
Parajito Canyon	1.0E+00	Modeling approach is not expected to be capable of underestimating dose.	6.0E-01	Estimate based on relative contributions of historic and future performance assessment inventories

Table 4-2. Continued.

Source of Uncertainty	Uncertainty Factor for Underestimating Dose[a]	Rationale for Values Assigned	Uncertainty Factor for Overestimating Dose[b]	Rationale for Values Assigned
Resource Utilization				
Rate of Water Consumption	1.0E+00	Rate of consumption used is a reasonable worst-case maximum.	7.0E-01	Factor based on estimated per capita water consumption rate.
Radionuclide Dose Conversion Factors				
Ingestion Factors	1.0E+00	Uncertainties are not considered for parameter.	1.0E+00	Uncertainties are not considered for parameter.
Total Propagated Error				
East-Southeast of Area G	3.6E+02		7.7E-06	
Parajito Canyon	1.8E+01		1.0E-02	

a. The factors listed represent the degree to which the projected scenario doses may be underestimated due to errors in the associated models and parameters under conditions approaching worst-case.
b. The factors listed represent the degree to which the projected scenario doses may be overestimated due to errors in the associated models and parameters under optimal conditions.
c. No error was assigned as the parameter does not contribute significantly to the projected doses.

Uncertainties that may cause doses for the Groundwater Resource Protection Scenario to be underestimated include those associated with radionuclide inventories, rates of water infiltration on the mesa and in the adjacent canyons, the water transit time in the waste, radionuclide travel times, and the modeling approach used to estimate rates of lateral transport. An error term of 3 was assigned to C-14, Tc-99, and I-129 based on the assumptions that all future waste projections were correct and that measured activities always underestimate the actual activities by 200 percent. The error terms associated with the water infiltration rates are based on the results of the groundwater simulations for high flow conditions, discussed in Section 4.1.1.3. These error terms account for the effects that increased infiltration has on rates of radionuclide leaching from the waste and contaminant travel times to the receptor's well. While the same errors are listed for radionuclide travel times, they were considered only once in the propagation of errors. The error term of 2.2 assigned to the water transit time is based on the conservative assumption that water passes through the waste packages in the disposal units in a year's time. More rapid transit times may occur if the moisture content of the waste was greater than projected or the amount of infiltration in the disposal units was increased. Finally, an error of 1.3 was assigned to lateral flow modeling for the receptor location east-southeast of Area G. This term is based on the assumption that, in the event that no lateral transport occurs, all radioactivity leached from the waste may reach this receptor's well.

A number of sources of uncertainty may also cause the actual doses for the Groundwater Resource Protection Scenario to be overestimated. The error terms included in Table 4-2 were assigned to account for this possibility. The error terms assigned for inventory uncertainties are based on the assumptions that all waste activities were measured accurately and that the Area G disposal facility ceases operation after 40 yr rather than 49 yr. This error term was reduced further for C-14 to account for the possibility that no C-14 sources, the dominant contributor to the projected inventory, will be generated at the Laboratory. The error terms associated with the water infiltration rates take into account the results of the groundwater simulations for low flow conditions, discussed in Section 4.1.1.3. These same error terms are listed for radionuclide travel times, but were considered only once in error propagation. The error term of 0.75 for water transit time was estimated based on the assumption that the time required for water to travel through the waste packages is greater than 16 yr but less than 50 yr. Such a condition may exist, for instance, if drier conditions prevailed in the disposal units. Uncertainties associated with aquifer

dilution modeling may overestimate the actual dose by a factor of two or more, a factor of two was assumed for the sensitivity and uncertainty analysis. An error term of 0.6 was assigned to the Parajito Canyon receptor location to account for uncertainties introduced by combining lateral releases from the historic and future performance assessment inventories. This factor was estimated as the ratio of the dose contributed by the future inventory to the total peak dose from the entire performance assessment inventory. Finally, the rate of water consumption was assigned an error of 0.7 to account for the fact that the 2-L/day (0.5-gal/day) consumption rate is higher than average per capita consumption rates.

Error terms of 1.0 were assigned to all other sources of uncertainty associated with the Groundwater Resource Protection Scenario. The assignment of this value signifies that the parameters and modeling approaches used are not expected to significantly under- or overestimate actual exposures, or that they have errors associated with them that are not easily quantified.

The propagated errors for the Groundwater Resource Protection Scenario provide bounds on the degree to which the dose projections prepared for the performance assessment may under- or overestimate actual exposures of the receptors. The results shown in Table 4-2 indicate that the parameters and modeling approaches used in the performance assessment may underestimate doses to the receptor east-southeast of the disposal facility by as much as 360 times, and by as much as 18 times at the Parajito Canyon location. Based on these results and on the doses projected for the receptor located 100 m downgradient of Area G, the peak annual dose expected under worst-case conditions during the 1,000-yr compliance period is expected to be 3.0×10^{-5} mrem/yr. Similarly, the peak annual dose under worst-case conditions for the receptor in Parajito Canyon is expected to be 8.1×10^{-4} mrem. Even under these unfavorable conditions, the projected peak doses for the Groundwater Resource Protection Scenario still constitute only small fractions of the 4-mrem/yr performance objective.

The parameters and models used for the performance assessment may also result in overestimates of the actual drinking water pathway doses. Based on the results shown in Table 4-2, doses for the receptor may be overestimated by several orders of magnitude, while doses for the Parajito Canyon resident may be overstated by a factor of 100. Hence, under conditions approaching best-case, the peak projected dose for the receptor east-southeast of

the disposal facility is 6.4×10^{-13} mrem/yr. Similarly, the peak annual dose projected for the person in Parajito Canyon is 4.5×10^{-7} mrem.

The propagated errors and the consequent dose estimates discussed above represent conditions approaching worst and best-case. More sophisticated analyses take into account the statistical distribution of model parameters and recognize that many of the parameters and modeling constructs operate independently of one another. The simpler analysis employed here ignores these complexities, combining important sources of error to maximize and minimize their impact on the projected doses. Consequently, the actual doses resulting from the disposal of radioactive waste at Area G are expected to fall between these projected endpoints.

4.1.4.2 Atmospheric Scenario

The sources of uncertainty associated with the Atmospheric Scenario are discussed in Section 4.1.2. These uncertainties and the maximum errors expected to be introduced into the projected doses as a result of them are summarized in Table 4-3. These errors are estimates of the extent to which doses could be under- or overestimated by each parameter's or model's associated uncertainty. The bases for assigning these errors are summarized in the table and in the following paragraphs. The reader is referred to Sections 4.1.2.1 through 4.1.2.5 for additional details.

The uncertainties that may cause the projected scenario doses to be underestimated include those associated with the projected inventories of several radionuclides; the extent of animal burrowing at the site; the values used for the resuspension and dispersion factors; the inhalation rate of the receptor; and the time the receptor is exposed to airborne radioactivity. The errors assigned to these parameters are based on the discussions in Section 4.2. The errors assigned to the projected performance assessment inventories of radionuclides are based on the measurement uncertainties discussed earlier. The composite analysis inventory for Am-241 was assumed to be subject to a 30 percent measurement uncertainty, consistent with the detection errors associated with radiochemical measurement techniques. The plutonium isotopes were assigned errors of 1.0 to account for measurement errors and the vast overestimation of inventories that is expected to result from the

Table 4-3. Sources of uncertainty and associated errors for the Atmospheric Scenario.

Source of Uncertainty	Uncertainty Factor for Underestimating Dose[a]			Uncertainty Factor for Overestimating Dose[b]		
	Performance Assessment	Composite Analysis	Rationale for Values Assigned	Performance Assessment	Composite Analysis	Rationale for Values Assigned
Radionuclide Inventories						
Am-241	3.0E+00	1.3E+00	Detection error of 200 and 30 percent for performance assessment and composite analysis inventory, respectively.	8.5E-01	1.0E+00	Factor for performance assessment reflects no detection error and disposal facility closure after 40 yr; factor for composite analysis set equal to 1 as magnitude of overestimate is unknown.
H-3	2.0E+00	2.0E+00	Detection error of 100 percent	8.5E-01	8.5E-01	Disposal facility closes after 40 yr; no detection error.
Pu-238	3.0E+00	1.0E+00	Detection error of 200 percent for performance assessment waste; factor for composite analysis reflects balance between detection errors and overestimate of pre-1971 inventory.	8.5E-01	3.3E-01	Factor for performance assessment reflects no detection error and disposal facility closure after 40 yr; factor for composite analysis reflects three fold overestimate of pre-1971 plutonium inventories.
Pu-239	3.0E+00	1.0E+00	Detection error of 200 percent for performance assessment waste; factor for composite analysis reflects balance between detection errors and overestimate of pre-1971 inventory.	8.5E-01	3.3E-01	Factor for performance assessment reflects no detection error and disposal facility closure after 40 yr; factor for composite analysis reflects three-fold overestimate of pre-1971 plutonium inventories.
Pu-240	3.0E+00	1.0E+00	Detection error of 200 percent for performance assessment waste; factor for composite analysis reflects balance between detection errors and overestimate of pre-1971 inventory.	8.0E-01	3.3E-01	Factor for performance assessment reflects no detection error and disposal facility closure after 40 yr; factor for composite analysis reflects three fold overestimate of pre-1971 plutonium inventories.

Table 4-3. Continued.

Source of Uncertainty	Uncertainty Factor for Underestimating Dose[a]			Uncertainty Factor for Overestimating Dose[b]		
	Performance Assessment	Composite Analysis	Rationale for Values Assigned	Performance Assessment	Composite Analysis	Rationale for Values Assigned
Pu-241	3.0E+00	1.0E+00	Detection error of 200 percent for performance assessment waste; factor for composite analysis reflects balance between detection errors and overestimate of pre-1971 inventory.	8.5E-01	3.3E-01	Factor for performance assessment reflects no detection error and disposal facility closure after 40 yr; factor for composite analysis reflects three-fold overestimate of pre-1971 plutonium inventories.
Th-232	3.0E+00	—[c]	Detection error of 200 percent	8.5E-01	—[c]	Disposal facility closes after 40 yr; no detection error.
U-234	2.0E+00	—[c]	Detection error of 100 percent	8.0E-01	—[c]	Disposal facility closes after 40 yr; no detection error.
U-235	2.0E+00	—[c]	Detection error of 100 percent.	8.5E-01	—[c]	Disposal facility closes after 40 yr; no detection error.
U-238	2.0E+00	—[c]	Detection error of 100 percent.	8.5E-01	—[c]	Disposal facility closes after 40 yr; no detection error.
Source Releases						
Rate of Gas Generation	1.0E+00	1.0E+00	Modeling approach is not expected to underestimate doses.	1.0E+00	1.0E+00	Magnitude of overestimate is unknown.
Rate of Diffusion	1.0E+00	1.0E+00	Modeling approach is not expected to underestimate doses.	1.0E+00	1.0E+00	Estimated diffusion coefficient of significant radionuclides based on site-specific data.
Plant Root Distribution	1.0E+00	1.0E+00	Plant root distribution expected to bound actual distribution; important radionuclides are affected by animal burrowing only.	1.0E+00	1.0E+00	Surface soil concentrations of important radionuclides are unaffected by plant uptake.
Vegetative Density and Decay Rate	1.0E+00	1.0E+00	Soil concentrations of significant radionuclides are determined by animal burrowing.	1.0E+00	1.0E+00	Surface soil concentrations of important radionuclides are unaffected by plant uptake.

Table 4-3. Continued.

Source of Uncertainty	Uncertainty Factor for Underestimating Dose[a]			Uncertainty Factor for Overestimating Dose[b]		
	Performance Assessment	Composite Analysis	Rationale for Values Assigned	Performance Assessment	Composite Analysis	Rationale for Values Assigned
Plant Uptake Factors	1.0E+00	1.0E+00	Increases in uptake factors needed to significantly impact doses are unlikely.	1.0E+00	1.0E+00	Surface soil concentrations of important radionuclides are unaffected by plant uptake.
Animal Burrow Distributions	2.9E+00	2.9E+00	Reflects maximum expected extent of burrowing at disposal site.	1.0E+00	1.0E+00	Factor may be zero if no intrusion into the disposed waste occurs; conservatively set equal to 1 for the analysis.
Surface Erosion Rate	1.0E+00	1.0E+00	Order of magnitude change in projected erosion rate has no effect on radionuclide releases.	1.0E+00	1.0E+00	Lower erosion rates have no impact on projected doses.
Environmental Transport						
Resuspension Rate	3.2E+00	3.2E+00	Error selected to reflect a total error of 10 for the resuspension and dispersion factors.	3.2E-01	3.2E-01	Error selected to reflect a total error of 10 for the resuspension and dispersion factors.
Dispersion Factor	3.2E+00	3.2E+00	Error selected to reflect a total error of 10 for the resuspension and dispersion factors.	3.2E-01	3.2E-01	Error selected to reflect a total error of 10 for the resuspension and dispersion factors.
Resource Utilization						
Inhalation Rate	1.4E+00	1.4E+00	Based on reasonable worst-case inhalation rate.	9.0E-01	9.0E-01	Reflects average annual inhalation rate recommended by EPA for continuous exposure situations in which activity patterns are unknown.
Time of Exposure	1.1E+00	1.1E+00	Based on 80 percent occupancy at the disposal site.	9.0E-01	9.0E-01	Reflects average amount of time spent at home by an adult.

Table 4-3. Continued.

Source of Uncertainty	Uncertainty Factor for Underestimating Dose[a]			Uncertainty Factor for Overestimating Dose[b]		
	Performance Assessment	Composite Analysis	Rationale for Values Assigned	Performance Assessment	Composite Analysis	Rationale for Values Assigned
Dose Conversion Factors						
Inhalation Factors	1.0E+00	1.0E+00	Uncertainties are not considered for parameter.	1.0E+00	1.0E+00	Uncertainties are not considered for parameter.
Total Propagated Error						
Gas Inhalation	9.8E+00	9.8E+00		2.2E-01	2.2E-01	
Dust Inhalation	1.3E+02	4.9E+01		6.9E-02	4.4E-02	

a. The factors listed represent the degree to which the projected scenario doses may be underestimated due to errors in the associated models and parameters under conditions approaching worst-case.
b. The factors listed represent the degree to which the projected scenario doses may be overestimated due to errors in the associated models and parameters under optimal conditions.
c. No error was assigned as the parameter does not contribute significantly to the projected doses.

extrapolation-based projection method. The error of 2.9 assigned to animal burrow distributions reflects uncertainty about the extent of intrusion into the disposed waste. An error of 3.2 was assigned to the resuspension and dispersion factors to reflect a total error of 900 percent. This error was assumed to apply to the point of maximum exposure in Canada del Buey and to the receptor location in the town of White Rock. An error of 1.4 was assigned to the inhalation rate based on a comparison of the inhalation rate used in the dose assessment to a reasonable worst-case value. Finally, an error term of 1.1 was assigned to the time of exposure to reflect an 80 percent occupancy rate at the disposal site.

Uncertainties associated with the projected radionuclide inventories, the resuspension and dispersion factors used in atmospheric modeling, the inhalation rate of the resident, and the amount of time the individual spends at home may cause the projected doses to be overestimated. Errors assigned to the projected inventories for the performance assessment reflect a reduction in the operational period of the disposal facility and accurate measurement of radionuclide activities. Plutonium inventories are estimated to be overstated by at least a factor of three, based on the comparison of the extrapolation-based pre-1971 inventories to the independent estimates of the amount of plutonium that had been disposed of at Area G through the late 1970s. Errors were assigned to the resuspension and dispersion factors to reflect a total uncertainty of 900 percent for the Canada del Buey and White Rock receptor locations. An error factor of 0.9 was assigned to the inhalation rate and the time of exposure to reflect average breathing rates and occupancy times.

The propagated errors shown in Table 4-3 indicate that the performance assessment doses projected to occur from the inhalation of radioactive gases may be underestimated by about 10 times and overestimated by 4.5 times. When applied to the projected peak doses, these errors translate into annual doses of 6.5×10^{-1} and 1.5×10^{-2} mrem at the point of maximum exposure in Canada del Buey. Corresponding doses for the White Rock location are 1.5×10^{-1} and 3.4×10^{-3} mrem/yr. Doses resulting from the inhalation of resuspended dust may be underestimated by 130 times under worst-case conditions, or may be overestimated by a factor of about 15 times under conditions approaching best-case. These estimated errors yield a maximum dose of 1.2 mrem/yr, and a minimum dose of 6.3×10^{-4} mrem/yr in Canada del Buey. The worst-case dose projected for the receptor location at White Rock is 2.8×10^{-1} mrem/yr, while a dose of 1.5×10^{-4} mrem/yr is estimated for optimal conditions. None of these

projected doses threaten the ability of the disposal facility to comply with the 10-mrem/yr performance objective.

The total errors listed in Table 4-3 indicate that the Atmospheric Scenario doses projected for the composite analysis may be underestimated by 9.8 and 49 times for radioactive gases and resuspended dust, respectively. Based on these worst-case conditions, the maximum annual doses projected to occur following the release of radioactive gases from the disposal site are 7.4×10^{-1} mrem at the point of maximum exposure and 1.7×10^{-1} mrem at White Rock. The maximum doses from the resuspension of contaminated dust are estimated to be 2.7×10^{2} and 64 mrem/yr in Canada del Buey and at White Rock, respectively. Doses projected for the gas and dust inhalation pathways may overestimate actual doses by about 4.5 and 23 times, respectively. These errors translate into doses of 1.6×10^{-2} and 3.9×10^{-3} for radioactive gases for the receptor locations in Canada del Buey and White Rock, respectively. The dust inhalation dose is reduced to 2.4×10^{-1} mrem/yr in Canada del Buey and 5.8×10^{-2} mrem/yr in White Rock.

As discussed earlier, the doses based on the propagated errors are expected to represent worst and best-case conditions. Actual doses are expected to fall in between these estimates. Nevertheless, it is evident from the results for the composite analysis that a potential exists for doses from dust inhalation to exceed the 30 and 100 mrem/yr performance objectives. Consequently, further examination of the uncertainties associated with the projected doses for this pathway is warranted.

Uncertainties associated with the projected inventories of Am-241 and plutonium, the extent of animal intrusion into the disposed waste, the resuspension factor, and the dispersion factor are expected to be the dominant influences on the dust inhalation doses projected for the composite analysis. While the error terms assigned to the projected inventories are small, it is evident from the discussion in Section 4.1.2.1 that the actual inventories of americium and plutonium disposed of prior to 1971 are highly uncertain. For example, the projected inventory of Pu-239 in the pre-1971 waste may be overestimated by more than three-fold. Based on the relative activities of Am-241 disposed of before and after 1971, the inventories for this isotope also appear to vastly overstated. It is apparent from these results and the sensitivity of the atmospheric dose modeling to the pre-1971 inventory projections that better characterization of this early waste is warranted.

The error term assigned to the distribution of animal burrows at Area G accounts for modeling results using what are considered to be reasonable worst-case estimates of animal intrusion at the DOE-controlled disposal site. Under most circumstances, site maintenance activities are expected to reduce levels of animal intrusion to levels far below the modeled conditions. Given the importance of this source release mechanism to the projected Atmospheric Scenario doses, however, the accuracy of the modeling conducted to date should be evaluated.

The sensitivity and uncertainty analysis assigned an error of ±900 percent to account for uncertainties associated with the resuspension and dispersion factors used in the atmospheric modeling. Kowalewsky et al. (1995) indicated that the total uncertainty associated with the resuspension factor was "certainly less than ± one order of magnitude", while Vold (1996a) has identified several potential sources of uncertainty in the dispersion factor. Nevertheless, these uncertainties have not been quantified to date. Given their potential impact on the projected doses when the total error of these parameters is constrained to ± 900 percent, further investigation into these uncertainties is necessary.

While several sources of uncertainty are associated with the projected composite analysis doses for the Atmospheric Scenario, certain characteristics of the portion of Area G used for the disposal of pre-1971 waste may significantly limit atmospheric pathway doses. Transuranic waste storage facilities have been constructed over the pits used for waste disposal between 1957 and 1970. As part of the construction of these facilities, a total of 3.3 m (10 ft) of cover material was placed over the disposal units. If maintained over this portion of Area G, this additional cover would effectively prevent biotic intrusion into the 1957 to 1970 waste inventory. Given that this portion of the composite analysis inventory contributes approximately 98 percent of the peak composite analysis dose projected for the Atmospheric Scenario, peak exposures would decline to about 0.1 mrem/yr. This reduction would, in turn, significantly reduce the worst-case dose of 270 mrem/yr reported above. Under these conditions, the 30-mrem/yr performance objective would easily be met.

The sources of uncertainty associated with the radon flux projections are discussed in Section 4.1.2. These uncertainties and the errors expected to be introduced into the projected fluxes as a result of them are summarized in Table 4-4. These errors estimate the extent to which fluxes could be under- or overestimated by each parameter's associated uncertainty.

Table 4-4. Sources of uncertainty and associated errors for the radon flux projections.

Source of Uncertainty	Uncertainty Factor for Underestimating Flux[a]	Rationale for Values Assigned	Uncertainty Factor for Overestimating Flux[b]	Rationale for Values Assigned
Radionuclide Inventories				
Ra-226				
Historic Pit Waste	2.0E+00	Detection error of 100 percent.	1.0E+00	No detection error.
Historic Shaft Waste	2.0E+00	Detection error of 100 percent.	1.0E+00	No detection error.
Future Pit Waste	2.0E+00	Detection error of 100 percent.	8.0E-01	Disposal facility closes after 40 yr; no detection error.
Future Shaft Waste	2.0E+00	Detection error of 100 percent.	8.0E-01	Disposal facility closes after 40 yr; no detection error.
Th-232				
Historic Pit Waste	3.0E+00	Detection error of 200 percent.	1.0E+00	No detection error.
Historic Shaft Waste	3.0E+00	Detection error of 200 percent.	1.0E+00	No detection error.
Future Pit Waste	3.0E+00	Detection error of 200 percent.	8.0E-01	Disposal facility closes after 40 yr; no detection error.
Future Shaft Waste	3.0E+00	Detection error of 200 percent.	8.0E-01	Disposal facility closes after 40 yr; no detection error.
Source Releases				
Rate of Diffusion	1.0E+00	Substantially higher diffusion coefficients are not expected.	1.0E+00	Estimated diffusion coefficient of significant radionuclides based on site-specific data.
Emanation Coefficient	1.2E+00	Factor reflects a 20 percent increase in the emanation factor.	8.0E-01	Factor reflects a 20 percent decrease in the emanation factor.

Table 4-4. Continued.

Source of Uncertainty	Uncertainty Factor for Underestimating Flux[a]	Rationale for Values Assigned	Uncertainty Factor for Overestimating Flux[b]	Rationale for Values Assigned
Surface Erosion Rate	1.0E+00	Ten-fold increase in surface erosion rate has negligible effect on projected fluxes over 1,000 yr.	1.0E+00	Lower erosion rates have no impact on projected fluxes.
Total Propagated Error				
Historic Pit Waste	2.4E+00		8.0E-01	
Historic Shaft Waste	2.4E+00		8.0E-01	
Future Pit Waste	3.6E+00		6.4E-01	
Future Shaft Waste	3.6E+00		6.4E-01	

a. The factors listed represent the degree to which the projected fluxes may be underestimated due to errors in the associated models and parameters under conditions approaching worst-case.

b. The factors listed represent the degree to which the projected fluxes may be overestimated due to errors in the associated models and parameters under optimal conditions.

The rationale used in assigning these errors is summarized in the table and in the following paragraphs.

Sources of uncertainty that may cause the projected radon fluxes to be underestimated include those associated with the projected inventories of Ra-226 and Th-232 and the emanation coefficient. The errors assigned to the projected radionuclide inventories are based on the measurement uncertainties discussed earlier. An error term of 1.2 was assigned to the radon emanation coefficient in lieu of site-specific data for this parameter. Uncertainties associated with these same parameters may also overestimate the actual radon fluxes.

The propagated errors shown in Table 4-4 indicate that the radon fluxes for the historic performance assessment waste may be underestimated by 2.4 times, while fluxes for the future waste inventories may be 3.6 times higher. Applying these errors to the projected peak fluxes, radon fluxes of 2.6×10^{-1} and 6.1×10^{-1} pCi/m^2/s (2.4×10^{-2} and 5.7×10^{-2} pCi/ft^2/s) are projected for the historic and future pit waste, respectively. The worst-case fluxes for the historic and future disposal shafts are 7.4 and 2.9 pCi/m^2/s (6.9×10^{-1} and 2.7×10^{-1} pCi/ft^2/s), respectively. These fluxes are less than the 20 pCi/m^2/s (1.9 pCi/ft^2/s) flux objective. Fluxes may be overestimated by factors ranging from 1.2 to 1.6 times (Table 4-4). These errors translate into projected fluxes of 8.8×10^{-2} and 1.1×10^{-1} pCi/m^2/s (8.2×10^{-3} and 1.0×10^{-2} pCi/ft^2/s) for the historic and future disposal pits, respectively. The corresponding fluxes for the historic and future shaft waste are 2.5 and 5.1×10^{-1} pCi/m^2/s (2.3×10^{-1} and 4.8×10^{-2} pCi/ft^2/s), respectively.

4.1.4.3 All Pathways Scenarios

The uncertainties associated with the All Pathways - Groundwater and All Pathways - Parajito Canyon scenarios are considered in Section 4.1.3. These uncertainties and the maximum errors that may occur as a result of them are summarized in Tables 4-5 and 4-6, respectively. The errors listed in the tables are estimates of the extent to which doses could reasonably be under- or overestimated by each parameter's or model's associated uncertainty. The rationale used in assigning these errors are summarized in the table and discussed in the following paragraphs. Additional information about these uncertainties may be found in Sections 4.1.3.1 through 4.1.3.5.

Table 4-5. Sources of uncertainty and associated errors for the All Pathways - Groundwater Scenario.

Source of Uncertainty	Uncertainty Factor for Underestimating Dose[a]			Uncertainty Factor for Overestimating Dose[b]		
	Performance Assessment	Composite Analysis	Rationale for Values Assigned	Performance Assessment	Composite Analysis	Rationale for Values Assigned
Radionuclide Inventories						
C-14	3.0E+00	3.0E+00	Waste is disposed of at projected rate; detection error equals 200 percent.	4.2E-01	9.4E-01	No sources are generated in the future; disposal facility closes after 40 yr; no detection error.
Tc-99	3.0E+00	3.0E+00	Waste is disposed of at projected rate; detection error equals 200 percent.	8.4E-01	8.7E-01	Disposal facility closes after 40 yr; no detection error.
I-129	3.0E+00	3.0E+00	Waste is disposed of at projected rate; detection error equals 200 percent.	9.0E-01	1.0E+00	Disposal facility closes after 40 yr; no detection error.
Source Releases						
Allocation of waste forms	1.0E+00	1.0E+00	All waste assigned to waste form with greatest release rates.	1.0E+00	1.0E+00	Factor cannot be assigned lacking release characteristics of waste streams allocated to surface-contaminated waste.
Concentration on surface-contaminated waste	1.0E+00	1.0E+00	Waste included in dose assessment accounts for more than 99 percent of total projected inventories of C-14, Tc-99, and I-129.	1.0E+00	1.0E+00	Waste included in dose assessment accounts for more than 99 percent of total projected inventories of C-14, Tc-99, and I-129.
Infiltration Rate	4.2E+01	4.8E+01	Ratio of peak compliance period dose for high flow conditions to peak compliance period dose for base case flow conditions.	5.2E-05	4.4E-06	Ratio of peak compliance period dose for low flow conditions to peak compliance period dose for base case flow conditions.
Water Transit Time in Waste	2.2E+00	2.2E+00	Transit time of 1 yr.	7.5E-01	7.5E-01	Estimate to account for a transit time greater than 16 yr and less than 50 yr.
Geochemical Properties	1.0E+00	1.0E+00	All radionuclides are assigned distribution coefficients of 0 mL/g; solubility limits are not exceeded.	1.0E+00	1.0E+00	Significantly higher distribution coefficients and lower solubility limits for C-14, Tc-99, and I-129 are unlikely.

Table 4-5. Continued.

Source of Uncertainty	Uncertainty Factor for Underestimating Dose[a]			Uncertainty Factor for Overestimating Dose[b]		
	Performance Assessment	Composite Analysis	Rationale for Values Assigned	Performance Assessment	Composite Analysis	Rationale for Values Assigned
Environmental Transport						
Radionuclide Travel Time	4.2E+01	4.8E+01	Ratio of peak compliance period dose for high flow conditions to peak compliance period dose for base case flow conditions.	5.2E-05	4.4E-06	Ratio of peak compliance period dose for low flow conditions to peak compliance period dose for base case flow conditions.
Lateral Transport Modeling	1.3E+00	1.3E+00	Based on proportion of total flux transported laterally over a 10,000-year period.	1.0E+00	1.0E+00	Factor may be zero if lateral flow is prevented by fractures; conservatively set equal to 1 for the analysis.
Sorption Behavior	1.0E+00	1.0E+00	All radionuclides are assigned distribution coefficients of 0 ml/g.	1.0E+00	1.0E+00	Significantly higher distribution coefficients for C-14, Tc-99, and I-129 are unlikely.
Aquifer Dilution	1.0E+00	1.0E+00	Modeling approach is not expected to be capable of underestimating dose.	5.0E-01	5.0E-01	Conservative estimate based on observed aquifer characteristics in the vicinity of Area G.
Soil Concentrations from Irrigation	1.0E+00	1.0E+00	Use of a 15 yr buildup time is expected to overestimate soil concentrations of mobile radionuclides.	2.0E-01	2.0E-01	Reflects a soil buildup time of 1 yr.
Plant Uptake Factors	1.9E+00	1.9E+00	Reflects a two-fold increase in plant uptake factors for C-14, Tc-99, and I-129.	1.0E+00	1.0E+00	Plant uptake factors may be smaller, but the magnitude of the error is unknown.
Plant Uptake from Irrigation	1.2E+00	1.2E+00	Based on a five-fold increase in the translocation factor for non leafy vegetables.	1.0E+00	1.0E+00	Translocation factors are assumed to be correct.

Table 4-5. Continued.

Source of Uncertainty	Uncertainty Factor for Underestimating Dose[a]			Uncertainty Factor for Overestimating Dose[b]		
	Performance Assessment	Composite Analysis	Rationale for Values Assigned	Performance Assessment	Composite Analysis	Rationale for Values Assigned
Resource Utilization						
Rate of Soil Consumption	1.0E+00	1.0E+00	Rate of consumption used reflects a high tendency to ingest soil.	1.0E-02	1.0E-02	Factor reflects a low tendency to ingest soil.
Rate of Water Consumption	1.0E+00	1.0E+00	Rate of consumption used is a reasonable worst-case maximum.	7.0E-01	7.0E-01	Factor based on estimated per capita water consumption rate.
Rate of Vegetable Consumption	1.0E+00	1.0E+00	Rates of consumption are consistent with national averages.	1.0E+00	1.0E+00	Rates of consumption used are consistent with national averages.
Proportion of Food Crops Grown by Resident	1.0E+00	1.0E+00	Proportion used exceeds reasonable worst-case proportion.	6.0E-01	6.0E-01	Factor based on national average of home-grown portion of food requirements.
Radionuclide Dose Conversion Factors						
Ingestion Factors	1.0E+00	1.0E+00	Uncertainties are not considered for parameter.	1.0E+00	1.0E+00	Uncertainties are not considered for parameter.
Inhalation Factors	1.0E+00	1.0E+00	Uncertainties are not considered for parameter.	1.0E+00	1.0E+00	Uncertainties are not considered for parameter.
Total Propagated Error	6.3E+02	7.1E+02		3.5E-05	5.0E-07	

a. The factors listed represent the degree to which the projected scenario doses may be underestimated due to errors in the associated models and parameters under conditions approaching worst-case.

b. The factors listed represent the degree to which the projected scenario doses may be overestimated due to errors in the associated models and parameters under optimal conditions.

Table 4-6. Sources of uncertainty and associated errors for the All Pathways - Parajito Canyon Scenario.

Source of Uncertainty	Uncertainty Factor for Underestimating Dose[a]			Uncertainty Factor for Overestimating Dose[b]		
	Performance Assessment	Composite Analysis	Rationale for Values Assigned	Performance Assessment	Composite Analysis	Rationale for Values Assigned
Radionuclide Inventories						
Am-241	—[c]	1.3E+00	Detection error of 30 percent.	—[c]	1.0E+00	Factor set equal to 1 as magnitude of overestimate is unknown.
Ag-108m	—[c]	2.0E+00	Detection error of 100 percent.	—[c]	4.0E-02	Overestimate of inventory based on the age of the waste; no detection error.
C-14	3.0E+00	—[c]	Waste is disposed of at projected rate; detection error equals 200 percent.	4.2E-01	—[c]	No sources are generated in the future; disposal facility closes after 40 yr; no detection error.
Cs-137	—[c]	1.0E+00	Form of waste is not expected to promote translocation to surface soils.	—[c]	9.5E-01	Disposal facility closes after 40 yr; no detection error.
Hf-182	—[c]	2.0E+00	Waste is disposed of at projected rate; detection error equals 100 percent.	—[c]	1.0E+00	Disposal facility closes after 40 yr; no detection error.
I-129	3.0E+00	—[c]	Waste is disposed of at projected rate; detection error equals 200 percent.	9.0E-01	—[c]	Disposal facility closes after 40 yr; no detection error.
Pu-238	—[c]	1.0E+00	Factor reflects balance between detection errors and overestimate of pre-1971 inventory.	—[c]	3.3E-01	Factor reflects three-fold overestimate of pre-1971 plutonium inventories.
Pu-239	—[c]	1.0E+00	Factor reflects balance between detection errors and overestimate of pre-1971 inventory.	8.5E-01	3.3E-01	Factor for performance assessment reflects no detection error and disposal facility closure after 40 yr; factor for composite analysis reflects three-fold overestimate of pre-1971 plutonium inventories.
Pu-240	—[c]	1.0E+00	Factor reflects balance between detection errors and overestimate of pre-1971 inventory.	—[c]	3.3E-01	Factor reflects three-fold overestimate of pre-1971 plutonium inventories

Table 4-6. Continued.

Source of Uncertainty	Uncertainty Factor for Underestimating Dose[a]			Uncertainty Factor for Overestimating Dose[b]		
	Performance Assessment	Composite Analysis	Rationale for Values Assigned	Performance Assessment	Composite Analysis	Rationale for Values Assigned
Pu-241	—[c]	1.0E+00	Factor reflects balance between detection errors and overestimate of pre-1971 inventory.	—[c]	3.3E-01	Factor for performance assessment reflects no detection error and disposal facility closure after 40 yr; factor for composite analysis reflects three-fold overestimate of pre-1971 plutonium inventories.
Ra-226	—[c]	2.0E+00	Waste is disposed of at projected rate; detection error equals 100 percent.	—[c]	1.0E+00	Disposal facility closes after 40 yr, no detection error.
Sr-90	—[c]	3.0E+00	Waste is disposed of at projected rate; detection error equals 200 percent.	—[c]	1.0E+00	Disposal facility closes after 40 yr; no detection error.
Tc-99	3.0E+00	—[c]	Waste is disposed of at projected rate; detection error equals 200 percent.	8.4E-01	—[c]	Disposal facility closes after 40 yr; no detection error.
Th-232	—[c]	—[c]		8.5E-01	—[c]	Disposal facility closes after 40 yr; no detection error.
U-235	—[c]	—[c]		8.5E-01	—[c]	Disposal facility closes after 40 yr; no detection error.
U-238	—[c]	2.0E+00	Waste is disposed of at projected rate; detection error equals 100 percent.	8.5E-01	9.0E-01	Disposal facility closes after 40 yr; no detection error.
Source Releases						
Allocation of waste forms	1.0E+00	—[c]	All waste assigned to waste form with greatest release rates.	1.0E+00	—[c]	Factor cannot be assigned lacking release characteristics of waste streams allocated to surface-contaminated waste.
Concentration on surface-contaminated waste	1.0E+00	—[c]	Waste included in dose assessment accounts for more than 99 percent of total projected inventories of C-14, Tc-99, and I-129.	1.0E+00	—[c]	Waste included in dose assessment accounts for more than 99 percent of total projected inventories of C-14, Tc-99, and I-129.
Infiltration Rate	2.5E+00	—[c]	Ratio of peak compliance period dose for high flow conditions to peak compliance period dose for base case flow conditions.	1.5E-01	—[c]	Ratio of peak compliance period dose for low flow conditions to peak compliance period dose for base case flow conditions.

Table 4-6. Continued.

Source of Uncertainty	Uncertainty Factor for Underestimating Dose[a]			Uncertainty Factor for Overestimating Dose[b]		
	Performance Assessment	Composite Analysis	Rationale for Values Assigned	Performance Assessment	Composite Analysis	Rationale for Values Assigned
Water Transit Time in Waste	2.2E+00	—[c]	Transit time of 1 yr.	7.5E-01	—[c]	Estimate to account for a transit time greater than 16 yr and less than 50 yr.
Geochemical Properties	1.0E+00	—[c]	All radionuclides are assigned distribution coefficients of 0 ml/g; solubility limits are not exceeded.	1.0E+00	—[c]	Significantly higher distribution coefficients and lower solubility limits for C-14, Tc-99, and I-129 are unlikely.
Vegetative Density and Decay Rate	—[c]	1.0E+00	Soil concentrations of significant radionuclides are determined by animal burrowing.	1.0E+00	1.0E+00	Surface soil concentrations of important radionuclides are unaffected by plant uptake.
Plant Uptake Factors	—[c]	1.0E+00	Increases in uptake factors needed to significantly impact dose are unlikely.	1.0E+00	1.0E+00	Surface soil concentrations of important radionuclides are unaffected by plant uptake.
Animal Burrow Distributions	—[c]	2.9E+00	Reflects maximum expected extent of burrowing at disposal site.	1.0E+00	1.0E+00	Factor may be zero if no intrusion into the disposed waste occurs; conservatively set equal to 1 for the analysis.
Surface Erosion Rate	—[c]	1.0E+00	Order of magnitude change in projected erosion rate has no effect on radionuclide releases.	1.0E+00	1.0E+00	Lower erosion rates have no impact on projected doses.
Environmental Transport						
Radionuclide Travel Time	2.7E+00	—[c]	Ratio of peak compliance period dose for high flow conditions to peak compliance period dose for base case flow conditions.	1.2E-01	—[c]	Ratio of peak compliance period dose for low flow conditions to peak compliance period dose for base case flow conditions.
Lateral Transport Modeling	1.0E+00	—[c]	Modeling approach is not expected to be capable of underestimating dose.	1.0E+00	—[c]	Factor may be zero if lateral flow is prevented by fractures; conservatively set equal to 1 for the analysis.
Sorption Behavior	1.0E+00	—[c]	All radionuclides are assigned distribution coefficients of 0 ml/g.	1.0E+00	—[c]	Significantly higher distribution coefficients for C-14, Tc-99, and I-129 are unlikely.

Table 4-6. Continued.

Source of Uncertainty	Uncertainty Factor for Underestimating Dose[a]			Uncertainty Factor for Overestimating Dose[b]		
	Performance Assessment	Composite Analysis	Rationale for Values Assigned	Performance Assessment	Composite Analysis	Rationale for Values Assigned
Aquifer Dilution	1.0E+00	—[c]	Modeling approach is not expected to be capable of underestimating dose.	1.0E+00	—[c]	Errors in dilution estimates are expected to be small given the short distance from the points of contaminant discharge to the well
Soil Concentrations from Irrigation	1.0E+00	—[c]	Use of a 15 yr buildup time is expected to overestimate soil concentrations of mobile radionuclides.	2.0E-01	—[c]	Reflects a soil buildup time of 1 yr.
Plant Uptake Factors	1.9E+00	1.0E+00	Factor for performance assessment reflects a two-fold increase in plant uptake factors for C-14, Tc-99, and I-129; magnitude of increase necessary to affect composite analysis doses is unlikely.	1.0E+00	1.0E+00	Plant uptake factors may be smaller, but the magnitude of the error is unknown.
Plant Uptake from Irrigation	1.1E+00	—[c]	Based on the effect of a five fold increase in the translocation factor.	1.0E+00	—[c]	Translocation factors are assumed to be correct.
Surface Erosion Rate	—[c]	1.0E+01	Bounds statistical uncertainty in projected erosion rate.	1.0E+00	1.0E+00	Significantly lower erosion rates appear to be unlikely.
Contamination Mixing Depth	—[c]	1.0E+01	Bounds order of magnitude decrease in mixing depth.	1.0E+00	1.0E+00	Greater mixing depth over extent of property is unlikely.
Resource Utilization						
Rate of Soil Consumption	—[c]	1.0E+00	Consumption rate reflects a high tendency to ingest soil.	1.0E-02	1.0E-02	Factor reflects low tendency to ingest soil.
Rate of Water Consumption	1.0E+00	—[c]	Rate of consumption used is a reasonable worst-case maximum.	7.0E-01	—[c]	Factor based on estimated per capita water consumption rate.
Rate of Vegetable Consumption	1.0E+00	1.0E+00	Rates of consumption are consistent with national averages.	1.0E+00	1.0E+00	Rates of consumption used are consistent with national averages.
Proportion of Food Crops Grown by Resident	1.0E+00	1.0E+00	Proportion used exceeds reasonable worst-case proportion.	5.0E-01	5.0E-01	Factor based on national average of home-grown portion of food requirements.

Table 4-6. Continued.

Source of Uncertainty	Uncertainty Factor for Underestimating Dose[a]			Uncertainty Factor for Overestimating Dose[b]		
	Performance Assessment	Composite Analysis	Rationale for Values Assigned	Performance Assessment	Composite Analysis	Rationale for Values Assigned
Inhalation Rate	—[c]	1.4E+00	Based on reasonable worst-case inhalation rate.	9.0E-01	9.0E-01	Reflects average annual inhalation rate recommended by EPA for continuous exposure situations in which activity patterns are unknown.
Time of Exposure	—[c]	1.1E+00	Based on 80 percent occupancy at the disposal site.	9.0E-01	9.0E-01	Reflects average amount of time spent at home by an adult.
Shielding Factor	—[c]	1.0E+00	Shielding factor used is a reasonable worst-case maximum.	7.0E-01	7.0E-01	Based on suggested shielding factor for the average individual.
Radionuclide Dose Conversion Factors						
Ingestion Factors	1.0E+00	1.0E+00	Uncertainties are not considered for parameter.	1.0E+00	1.0E+00	Uncertainties are not considered for parameter.
Inhalation Factors	—[c]	1.0E+00	Uncertainties are not considered for parameter.	1.0E+00	1.0E+00	Uncertainties are not considered for parameter.
Direct Radiation from Soils	—[c]	1.2E+00	Adjustment to account for other exposure geometries and gamma energies.	1.0E+00	1.0E+00	Exposure geometry assumed to be correct
Total Propagated Error	2.7E+01	5.4E+02		1.2E-01	2.8E-01	

a. The factors listed represent the degree to which the projected scenario doses may be underestimated due to errors in the associated models and parameters under conditions approaching worst-case.
b. The factors listed represent the degree to which the projected scenario doses may be overestimated due to errors in the associated models and parameters under optimal conditions.
c. No error was assigned as the parameter does not contribute significantly to the projected doses.

The sources of uncertainty that may significantly impact the projected scenario doses for the All Pathways - Groundwater Scenario generally resemble those discussed earlier for the Groundwater Resource Protection Scenario. Section 4.1.4.1 contains a brief discussion of the errors assigned to common parameters and models. In terms of parameters unique to this scenario, uncertainties in plant uptake factors and the amount of radioactivity in irrigation water that is assimilated by crops may cause projected doses to be underestimated. An error of 1.9 was assigned to plant uptake factors to reflect the impact a two-fold increase in the plant uptake factors for C-14, Tc-99, and I-129 will have on projected food pathway doses. The error of 1.1 assigned to plant uptake from irrigation reflects a five-fold increase in the translocation factor for non-leafy vegetables.

Unique sources of uncertainty that may cause the projected doses for the All Pathways - Groundwater Scenario to be overestimated include soil radionuclide concentrations resulting from irrigation, the rate of soil consumption, and the proportion of the resident's food requirements that is raised by the individual. An error of 0.2 is assigned to the soil radionuclide concentrations, which is consistent with a more reasonable buildup time of 1 yr for C-14, Tc-99, and I-129. The error of 0.01 assigned to the soil consumption rate is based on average soil consumption rates in adults that have a low tendency to eat soil. The proportion of food requirements grown at the resident's home is assigned an error of 0.5 based on the national averages for this parameter.

The propagated errors listed in Table 4-5 indicate that the doses for the All Pathways - Groundwater Scenario may be underestimated by a factor of 630 for the performance assessment and 710 composite analysis. The products of these errors and the projected peak doses for the performance assessment and composite analysis yield worst-case doses of 6.1×10^{-3} and 4.1×10^{-1} mrem/yr, respectively. These doses are small fractions of the performance objectives pertinent to these analyses. The models and data used in the All Pathways - Groundwater Scenario may also overestimate the actual doses by several orders of magnitude (Table 4-5). The propagated errors listed in the table translate to projected doses of 8.0×10^{-13} and 6.0×10^{-12} mrem/yr for the performance assessment and composite analysis, respectively.

The sources of uncertainty that may have significant impacts on the projected scenario doses for the All Pathways - Parajito Canyon Scenario include many of those discussed above.

Additional sources of uncertainty include the rate of erosion, the soil mixing depth in the canyon, and the soil consumption rate. An error of 10 was assigned to the first two parameters based on the discussions in Section 4.1.3.3. The error of 0.01 assigned to the soil consumption rate takes into account the intake of soil in adults with a low tendency to ingest soil.

The total errors estimated for the All Pathways - Groundwater Scenario indicate that the performance assessment doses may be underestimated by a factor of 27 and overestimated by 8.3 times (Table 4-6). These propagated errors yield annual doses of 3.5×10^{-3} and 1.6×10^{-5} mrem, respectively. Composite analysis doses for this scenario may be underestimated by 540 times, and overestimated by 3.6 times. The doses corresponding to these errors are 3.9 and 2.0×10^{-3} mrem/yr. The worst-case doses are all much less than the appropriate performance objectives.

4.2 INADVERTENT INTRUDER EXPOSURE SCENARIOS

Exposures of the inadvertent intruder are projected to occur when the individual contacts or uses contaminated environmental media. These media include soils, crops and animal products, and air. The magnitude of the projected intruder doses depends upon the extent to which the intruder uses or is exposed to soil, foodstuffs, and air; the radionuclides present in the contaminated media; and the concentrations of these radionuclides in the media.

Uncertainties in the models and parameters used in the intruder analysis contribute to uncertainties in the dose projections. The following discussion considers these uncertainties semi-quantitatively, focusing on the exposure scenarios and parameter values used in the analysis (DOE, 1996b). Assumptions and parameter values used in the intruder analysis that determine resource utilization rates, exposure times, and radionuclide concentrations are discussed relative to "real-world" conditions to provide insight into the level of assurance with which the Area G disposal facility can safely contain the disposed waste.

The intruder sensitivity and uncertainty analysis is discussed in terms of the basic modeling components that comprise the dose assessment. As discussed in Section 4.1, these components include the inventory, source-release mechanisms, transport mechanisms, usage factors, and dose conversion factors. The nature of the intruder-agriculture scenario is such that a clear distinction between the source-release and transport mechanisms is difficult to establish. Consequently, these components are merged in the following discussion.

4.2.1 Radionuclide Inventories

The projected doses for the intruder exposure scenarios are directly proportional to the activities of radioactive waste disposed of at Area G. The uncertainties associated with the historic and future performance assessment inventories are discussed in general terms in Section 4.1.1. The uncertainties associated with inventories of the radionuclides that make significant contributions to the intruder doses will ultimately determine the potential errors inherent in the dose projections. The radionuclides that contribute 1 percent or more of the peak intruder doses are summarized in Table 4-7.

Measurement errors associated with all of the radionuclides listed in Table 4-7 except K-40, Nb-92, and Nb-94 are discussed in Section 4.1. K-40 is relatively easy to detect because it emits relatively high-energy gamma radiation. Measurement errors for this isotope using non-destructive analysis are typically within 200 to 300 percent. Nb-92 and Nb-94 are fission products and emit high-energy photons that are readily detected. Consequently, reported activities for these isotopes will tend to accurately reflect the actual inventories in the waste.

Cs-137 is projected to make significant contributions to the projected intruder doses for the historic and future disposal shafts. While the uncertainties associated with the projected inventories of this radionuclide are addressed in Section 4.1.3.5, they deserve additional discussion here. As discussed earlier, most of the projected historic inventory is represented by two irradiation sources encased in steel. While this waste was assumed to be mixed with cover soil and spread around the intruder's lot, it is more likely that the waste will still be contained in the source jacket at the time of intrusion. Furthermore, the discrete nature of the sources reduces the likelihood that the waste will be contacted during basement

Table 4-7. Summary of radionuclide contributions to peak intruder dose projections.

Radionuclide	Percent Contribution to Peak Dose			
	Historic Pit Waste	Historic Shaft Waste	Future Pit Waste	Future Shaft Waste
Ag-108m	2%	34%	1%	---[a]
Am-241	6%	10%	6%	14%
C-14	---[a]	1%	---[a]	---[a]
Cs-137	3%	15%	---[a]	38%
K-40	---[a]	---[a]	3%	---[a]
Nb-92	---[a]	7%	---[a]	10%
Nb-94	3%	5%	3%	---[a]
Pu-238	9%	2%	7%	3%
Pu-239	36%	13%	31%	17%
Pu-240	2%	---[a]	7%	---[a]
Pu-241	---[a]	---[a]	1%	---[a]
Ra-226	4%	---[a]	5%	---[a]
Th-232	7%	1%	3%	2%
U-234	1%	---[a]	5%	---[a]
U-235	8%	---[a]	6%	---[a]
U-238	17%	10%	19%	14%

a. Indicates the radionuclide did not contribute 1 percent or more to the projected peak dose.

excavation. Based on these factors, the actual doses from Cs-137 are expected to be smaller than projected.

The Cs-137 sources also form the basis for the projected disposal of large activities of Cs-137 in the future. The extrapolation process is expected to significantly overestimate future disposal because Cs-137 sources are generated infrequently at LANL. A review of the LANL disposal records indicates that only one other Cs-137 source with an activity in excess of 1 Ci (41.7 Ci) was disposed of between 1971 and 1995. The future dose projections implicitly assume that more than 13 Ci/yr of Cs-137 sources will be disposed of in the shafts over the remainder of the disposal facility's lifetime. Consequently, intruder doses for the future shaft waste are expected to be much less than estimated.

Projected intruder doses are directly proportional to the radionuclide concentrations in the disposed waste. The higher the concentration of waste in the disposal unit, the greater the amount of waste that will be brought to the surface by the intruder and, thus, the greater the potential doses. Concentrations of radioactivity in the waste are determined by the radionuclide inventories and the waste emplacement efficiency, defined as the fraction of a disposal unit that is filled with waste.

The historic pit and shaft waste emplacement efficiencies used in the dose assessment are 0.36 and 0.42, respectively, based on average efficiencies in closed disposal units. These efficiencies range from less than 10 to almost 60 percent for pits, and from less than 10 to almost 100 percent for shafts. The waste emplacement efficiency for pit waste disposed of in the future is 0.5, a value that accounts for changes in waste disposal operations which should allow tighter packing of the waste in the pits. The waste emplacement efficiency assumed for future shaft waste is the historic value of 0.42 because no changes in disposal operations are expected that would affect these units.

The historic and future waste emplacement efficiencies used in the dose assessment indicate that one-third to one-half of the pits and shafts are filled with waste. Given this, the errors introduced by uncertainties associated with these efficiencies are limited. Even with significant increases in emplacement efficiency, the projected doses would increase by less than a factor of 2. Actual efficiencies lower than those modeled would yield lower projected doses.

4.2.2 Source Releases and Environmental Transport

The nature of the intruder scenario is such that source releases are difficult to define. In essence, the "release" of radioactivity from the disposed waste occurs through the actions of the person constructing the house. That is, the excavation of the basement "releases" the radioactivity, bringing it to the soil surface. Given this definition of release, the uncertainties associated with the source-release modeling pertain to the degree of intrusion that is assumed to occur, as measured by the quantity of waste brought to the surface.

The extent to which intrusion into the waste was assumed to occur in the Intruder-Agriculture Scenario is expected to overestimate the actual amount of radioactivity distributed across the ground surface. Long-term DOE control of LANL in general, and of Area G in particular, will prevent individuals from disrupting the disposed waste. Should the DOE become complacent in its custodial responsibilities for a short period (e.g., one to two yr), the land occupied by the LANL would likely revert to uses consistent with the current lifestyle of the Native American landowners living adjacent to the Laboratory. Under these conditions, it is unlikely that an individual would arrive at the site and construct a house. It is more likely that the site would be used for ceremonial purposes or hunting, as it has been in the past. If a person were to choose to reside over the site, it is not clear that his or her construction activities would include excavating a 3-m (10-ft)-deep basement, as many of the homes built in the region are constructed on slab foundations and lack basements.

The intruder doses projected for the shaft waste are based on the conservative assumption that all shafts at Area G are arranged in a shaft field, the dimensions of which were based on the distances that typically separate adjacent shafts. Using this approach, approximately 11 percent of the surface area of the intruder's basement was projected to contact disposed waste. This degree of intrusion is expected to overestimate the actual quantities of waste contacted by the individual because, in fact, the shafts are widely scattered over Area G.

The amount of radioactivity brought to the surface by the intruder is influenced by the time at which intrusion occurs. The activities of short-lived radionuclides in the waste will be smaller at later times due to radioactive decay, resulting in lower surface soil contaminant

concentrations. Due to ingrowth, higher activities of daughter radionuclides may be encountered as the time of intrusion is delayed. The time at which intrusion was postulated to occur differs between the pits and shafts. Intrusion into the pits was assumed to be feasible at the end of the 100-yr active institutional control period. Intrusion into the disposal shafts was assumed to be prevented by the concrete caps placed over the closed shafts for an additional 200 yr.

The time of intrusion has a significant effect on the doses projected for the waste disposed of in the historic and future shafts. In terms of the historic shaft waste, the projected intruder scenario doses rise from 18 mrem/yr to 320 mrem/yr as the time of intrusion is reduced from 300 to 100 yr post-closure. Annual doses increase more dramatically for the future shaft waste with the same change, from 12 to 470 mrem. These doses are well in excess of the intruder analysis performance objective of 100 mrem/yr. If intrusion were to occur at 200 yr post-closure, the annual intruder dose would be about 50 mrem for both shaft inventories.

The assumption that intrusion into the disposal shafts is delayed for 300 yr after facility closure is based on the fact that concrete caps placed over the units will prevent individuals from excavating a basement. The period over which the caps will actually be effective in preventing intrusion will depend upon rates of concrete degradation at the disposal site. Detailed analyses of rates of degradation were not undertaken as part of the Area G performance assessment. However, given the importance of the concrete caps' effectiveness, further investigation into this issue is recommended.

The ingestion of soil and food crops grown by the intruder is responsible for significant fractions of the projected intruder doses. These doses are proportional to the radionuclide concentrations in these media and the rates of intake. The surface soil and plant concentrations of radioactivity, in turn, are directly proportional to the degree to which the exhumed waste is mixed with clean soil prior to being spread over the intruder's lot. The waste was assumed to be completely mixed with the cover material removed at the time of basement excavation. As a result, contamination levels in soils were 58 and 26 percent of the disposal unit concentrations over the historic and future pits, respectively. The greater dilution noted for the future pits reflects the use of 2 m (6.6 ft) of cover rather than 1 m (3.3 ft). Surface soil concentrations over the historic and future shafts were 4.9 and 2.7 percent,

respectively, of the disposal unit concentrations. The shaft dilution factors are about an order of magnitude smaller than the pit factors because they account for the limited cross-sectional area of the disposal units.

While it is unlikely that the exhumed waste will be uniformly mixed with the clean cover soil, the approach used to model surface soil concentrations is expected, on average, to provide reasonably conservative ingestion dose estimates. For instance, while a portion of the individual's garden may have higher-than-average concentrations of radioactivity, other portions may contain little or no radioactivity. When the disposal pit dilution factors were considered in conjunction with the waste emplacement efficiencies, the intruder's garden was assumed to contain 13 to 21 percent waste on a volume basis. Based on the assumption that only a small fraction of the garden soil could be waste if the garden was to be fertile, this range appears reasonable. When the effect of shaft spacing is ignored, the proportion of waste in the intruder's garden over the shafts is 11 to 19 percent. Once again, this range appears reasonable.

Factors influencing the concentrations of radioactivity in the edible portions of the crops grown by the intruder include radionuclide concentrations in the soil; agricultural yields of leafy vegetables, produce, and grain; the plant weathering removal coefficient; the resuspension factor due to rainsplash; the atmospheric deposition velocity; plant translocation factors; plant radionuclide uptake factors; dry-to-wet weight ratios for vegetation; and soil radionuclide concentrations. The first five factors influence the assimilation of radioactivity deposited on the plant from rainsplash, while the plant uptake factors and the dry-to-wet weight ratios were used in modeling plant radionuclide concentrations from root uptake. The uncertainties associated with projecting soil radionuclide concentrations are discussed in earlier portions of this chapter.

Rainsplash may be an important mechanism of plant contamination. Splash from the impact of raindrops carries detached soil particles radially and upward to be intercepted by nearby plants (e.g., Foster et al., 1985). If the soil is contaminated, this mechanism may deposit radioactivity on plant surfaces. While the significance of rainsplash in terms of projecting overall levels of plant contamination is unclear, some investigators have concluded that surface deposition is an important process for radionuclides that are strongly sorbed to soil particles. Hansen (1995b) concluded that rainsplash is an important process in terms

of plant concentrations of plutonium isotopes. He proposed the use of effective plant concentration factors that include the effects of root uptake and depositional processes.

The dose assessment results indicate that rainsplash is secondary in importance to root uptake in determining plant radionuclide concentrations. For example, contamination in plants due to rainsplash accounts for about 1 percent of the peak food ingestion dose projected for the historic pits, the disposal units for which this pathway yields the highest doses. However, with respect to plutonium isotopes, these results are contradicted if the effective plant concentration factors proposed by Hansen (1995b) are used to project plant concentrations. For example, the projected ingestion doses for the historic pits increase almost four-fold when plutonium food-chain doses are calculated using these factors. The peak projected dose for the intruder-agriculture scenario as a whole increases approximately 85 percent as a result of this modification.

While the effects of rainsplash noted for the plutonium isotopes are obviously significant, it is not apparent that other radionuclides will be similarly affected. For example, White et al. (1981) estimate that the component of Cs-137 contamination of squash and beans that is due to rainsplash ranges from 2 to 52 percent, depending upon the plant tissue under consideration. Thus, for Cs-137, rainsplash appears to be less significant in terms of plant contaminant concentrations relative to the situation noted above for plutonium isotopes, where it may account for essentially all of the observed levels of radioactivity. These results indicate a need for further investigation into the importance of rainsplash as a mechanism of plant contamination for other radionuclides included in the Area G inventory.

Based on the rainsplash modeling results discussed above, the uncertainties associated with crop agricultural yields, the plant weathering removal coefficient, the rainsplash resuspension factor, the atmospheric deposition velocity, and plant translocation factors will have little overall impact on the ingestion pathway dose. Consequently, a detailed discussion of these uncertainties is not warranted. The impact of the uncertainties associated with these parameters should, however, be considered as part of the re-evaluation of the entire rainsplash pathway.

The radionuclide uptake factors determine the extent to which radioactivity in the soil is assimilated by plants via their roots. Given the potential importance of plant uptake of

radionuclides from soil, it is important that the rates at which uptake are projected are reasonably accurate. As discussed in Section 4.1.2.2, the plant uptake factors used to project ingestion doses are based on an extensive literature review of terrestrial transport and agricultural parameters by Baes et al. (1984). While the use of generic plant uptake factors for the dose analysis ignores the effects that LANL-specific factors may have upon the assimilation of radionuclides from contaminated soils, a comprehensive set of factors for the radionuclides and crops included in the performance assessment does not exist.

Lacking exhaustive site-specific information, the data compiled by Baes et al. (1984) are expected to provide a reasonably consistent set of factors. Nevertheless, it should be recognized that these data are highly variable. Uptake factors for a given element may range over several orders of magnitude. Order-of-magnitude changes in the uptake factors used for the dominant radionuclides will have significant effects on the projected intruder scenario doses.

The plant uptake factors used in the dose assessment relate radionuclide concentrations in plants to concentrations in soils on a dry-weight basis. To determine the concentration of radioactivity on a wet-weight basis, which is more representative of the food eaten by the intruder, the plant concentrations were multiplied by the dry-to-wet-weight fraction. For the dose assessment, this parameter was assigned values of 0.1 for leafy vegetables (based on Peterson, 1983) and 0.43 for all other vegetation (Baes et al., 1984). These values are expected to reasonably estimate wet-weight conversions for the food crops grown by the intruder. The value for leafy vegetables is the approximate average of dry-to-wet weight conversion factors for 12 species of vegetables. The value of 0.43 used for all other produce is the weighted average of factors for various classes of vegetables. It exceeds the average dry-to-wet-weight factors for exposed produce (0.13) and protected produce (0.22), but is about half of the value for grain (0.88).

Airborne concentrations of radioactive dust are a function of the surface soil concentrations of the waste radionuclides and the dust loading factor. The factors upon which soil concentrations depend, and the uncertainties associated with these factors, are discussed in Section 4.2.2. A dust loading factor of 1×10^{-7} kg/m^3 (6.2×10^{-9} lb/ft^3) was used to project particulate concentrations in air at the intruder's residence, and is expected to result in a reasonably conservative estimate of actual airborne concentrations of radioactivity.

It is 2.5 times larger than the background dust loading for nonurban area in the United States, as reported by Anspaugh et al. (1975). While the intruder may encounter higher concentrations during a portion of the time spent gardening, this period comprises less than 2 percent of the total time spent by the intruder at the site. Furthermore, while it was assumed that all resuspended dust is contaminated and respirable, some of the resuspended particles will originate outside of the zone of contamination and will be too large to be inhaled.

Direct radiation exposures are an important contributor to the projected intruder doses. Exposures to the intruder during the time spent indoors will be attenuated by the individual's house. As discussed in Section 4.1.3.4, this shielding factor is expected to overestimate actual exposures of the individual.

4.2.3 Resource Utilization

The level of resource utilization by the intruder and the amount of time the individual was exposed to contaminated media are the same as those assumed for the offsite receptors. The uncertainties associated with air inhalation rates, soil and food ingestion rates, and the periods the intruder is exposed to contaminated air and soil are discussed in earlier sections of this chapter.

4.2.4 Radionuclide Dose Conversion Factors

Internal and external exposures to radioactivity were converted to doses using inhalation, ingestion, and external dose conversion factors. As discussed earlier, while there are uncertainties associated with these factors, they are difficult to quantify and, for the most part, were not taken into consideration in the sensitivity and uncertainty analysis. The uncertainties associated with the dose conversion factors used to estimate direct radiation exposures from contaminated soils are discussed in Section 4.1.3.5.

4.2.5 Summary of Intruder Sensitivity and Uncertainty Analysis

The sensitivities of the intruder dose projections to the modeling assumptions and input parameters used in the dose assessment are discussed in Sections 4.2.1 through 4.2.3. Based on these results, the uncertainties associated with the radionuclide inventories in the historic and future waste, the degree of intrusion into the disposed waste, the effective plant uptake factors for food crops, and the time of intrusion into the disposal shafts are expected to have the greatest potential impact on the ability of the Area G disposal facility to comply with the 100-mrem/yr intruder dose objective. The waste inventories are subject to uncertainties associated with measurement errors and the assumptions used to project future rates of waste generation. Many of the radionuclides that make significant contributions to the projected doses are difficult to measure. While measurement errors for the readily detected isotopes may be 100 to 200 percent or less, measurements of other radionuclides may have errors of 900 percent or more associated with them.

The projected doses for the agricultural intruder are expected to overestimate the actual doses received by an intruder. This conclusion is based on the assumption of long-term DOE control over the disposal site, current land-use patterns, the limited surface area of the disposal shafts, and construction techniques prevalent in the area. In contrast, doses due to the ingestion of contaminated crops may be underestimated because of the manner in which rainsplash was modeled. Further investigation into the importance of this mechanism of plant uptake is warranted to reduce the uncertainties in the projected intruder doses. The projected intruder doses for shaft waste increase significantly as the time of intrusion is moved from 300 to 100 yr post-closure, exceeding the intruder performance objective at the earliest time. These results underscore the importance of the long-term performance of the concrete caps placed over the closed shafts.

The uncertainties associated with other modeling assumptions and parameter values used in the dose assessment are expected to have a relatively limited impact on the projected doses. In some cases, this is due to the fact that the assumption made or parameter used is quite conservative by all but the most pessimistic accounts. In other instances, the parameters used in the dose analysis have limited ranges over which they may vary, thereby limiting their impacts on the projected doses.

REFERENCES

Abeele, W.V., 1984, "Geotechnical Aspects of Hackroy Sandy Loam and Crushed Tuff," Los Alamos National Laboratory, LA-9916-MS, 20 pp.

Abrahams, J.H., 1963, "Physical Properties and Movement of Water in the Bandelier Tuff, Los Alamos and Santa Fe Counties, New Mexico," U.S. Geological Survey, Albuquerque, NM, January 1995.

Anspaugh, L.R., et al., 1975, "Resuspension and Redistribution of Plutonium in Soils," Health Physics 29, 571.

Baes, C.F. et al., 1984, "A Review and Analysis of Parameters for Assessing Transport of Environmentally Released Radionuclides through Agriculture," Oak Ridge National Laboratory, ORNL-5786, September 1984.

Birdsell, K.H., et al., 1997, "Simulations of Groundwater Flow and Radionuclide Transport in the Vadose and Saturated Zones Beneath Area G, Los Alamos National Laboratory," Los Alamos National Laboratory Report, LA-UR-97-157, Los Alamos National Laboratory, Los Alamos, NM.

CRC, 1962, "CRC Handbook of Chemistry and Physics," 43rd edition.

DOE, 1988a, "Radioactive Waste Management," DOE Order 5820.2A, September 26, 1988.

DOE, 1988b, "Internal Dose Conversion Factors for Calculation of Dose to the Public," U.S. Department of Energy, DOE/EH-0071, July 1988.

DOE, 1988c, "External Dose-Rate Conversion Factors for Calculation of Dose to the Public," U.S. Department of Energy, DOE/EH-0070, July 1988.

DOE, 1996a, Implementation Plan, Defense Nuclear Facilities Safety Board Recommendation 94-2, Conformance with Safety Standards at Department of Energy Low-Level Nuclear Waste and Disposal Sites, Rev. 1, April 1996.

DOE, 1996b, "Interim Format and Content Guide and Standard Review Plan for U.S. Department of Energy Low-Level Waste Disposal Facility Performance Assessments," U.S. Department of Energy, October 31, 1996.

DOE, 1996c, "Guidance for a Composite Analysis of the Impact of Interacting Source Terms on the Radiological Protection of the Public from DOE LLW Disposal Facilities," April 1996.

EPA, 1988a, "Superfund Exposure Assessment Manual," U.S. Environmental Protection Agency, EPA/540/1-88/001.

EPA, 1988b, "Limiting Values of Radionuclide Intake and Air Concentration and Dose Conversion Factors for Inhalation, Submersion, and Ingestion," U.S. Environmental Protection Agency Federal Guidance Report 11, EPA 520/1-88-020, September 1988.

EPA, 1989, "Exposure Factors Handbook," U.S. Environmental Protection Agency, EPA/600/8-89/043.

Foster, G.R., et al., 1985, "A Model for Splash and Retention of Sediment and Soil-Borne Contaminants on Plants," Transactions of the ASAE, Vol. 28(5): September-October, 1985.

Grove Engineering, 1992, "MicroShield Version 4, User's Manual," Grove Engineering, Inc.

Hansen, W.R., 1995a, "Parameters for Irrigation Rates at Los Alamos," memo from W.R. Hansen, Los Alamos National Laboratory, to R. Shuman, Rogers and Associates Engineering Corporation, June 6, 1995.

Hansen, W.R., 1995b, Personal communication from W.R. Hansen, Los Alamos National Laboratory, to R. Shuman, Rogers and Associates Engineering Corporation, Inc., May 23, 1995.

ICRP, 1975, "Report of the Task Group on Reference Man," International Commission of Radiological Protection, Publication 23, 1975.

ICRP, 1977, "Recommendations of the International Commission on Radiological Protection," ICRP Publication 26, Pergamon Press, New York, NY.

ICRP, 1979-1982, "Limits for Intakes of radionuclides by Workers," ICRP Publication 30, Part 1 (and subsequent parts and supplements), Vol. 2, No. ¾ through Vol. 8, No. 4, Pergamon Press, New York, NY.

ICRP, 1986, "The Metabolism of Plutonium and Related Elements," ICRP Publication 48, Vol. 16, No. 2/3, Pergamon Press, New York, NY.

ICRP, 1987, "Data for Use in Protection Against External Radiation," International Commission on Radiological Protection, Publication 51, March 1987.

Kopp, B., 1991, Personal communication between B. Kopp, Los Alamos National Laboratory, and R. Shuman, Rogers & Associates Engineering Corporation.

Kowalewsky, K., et al., 1995, "Air Quality Impacts Analysis for Area G," Final report 4/4 from RADIAN to CST-14, Los Alamos National Laboratory under DOE subcontract 6345L0014-31, Los Alamos National Laboratory, Los Alamos, NM.

Krier, D., et al., 1995, "Geologic, Geohydrologic, and Geochemical Data Summary of Material Disposal Area G, Technical Area 54, Los Alamos National Laboratory," Los Alamos National Laboratory report LA-UR-95-2696, Los Alamos National Laboratory, NM.

LANL, 1996, "Environmental Surveillance at Los Alamos during 1994," Environmental Assessments and Resource Evaluations Group, Los Alamos National Laboratory report LA-1304/ENV, July 1996.

Longmire, P., et al., 1996, "Batch Sorption Results for Americium, Neptunium, Plutonium, Technetium, and Uranium Transport through the Bandelier Tuff, Los Alamos, New Mexico," Los Alamos National Laboratory report LA-UR-96-4716, Los Alamos National Laboratory, Los Alamos, NM.

Napier, B.A., et al., 1988, "GENII - The Hanford Environmental Radiation Dosimetry Software System, Volume I: Conceptual Representation," Pacific Northwest Laboratory, PNL-6584, vol. 1, December 1988.

NCRP, 1984, "Radiological Assessment: Predicting the Transport, Bioaccumulation, and Uptake by Man of Radionuclides Released to the Environment," National Council on Radiation Protection and Measurements, Report No. 76, March 1984.

Newman, B.D., 1996, "Vadose Zone Water Movement at Area G, Los Alamos National Laboratory, TA-54: Interpretations Based on Chloride and Stable Isotope Profiles," Los Alamos National Laboratory Report, LA-UR-96-4682, Los Alamos National Laboratory, Los Alamos, NM.

Ng, Y.C., et al., 1978, "Methodology for Assessing Dose Commitment to Individuals and to the Population from Ingestion of Terrestrial Foods Contaminated by Emissions from a Nuclear Fuel Reprocessing Plant at the Savannah River Plant," Lawrence Livermore Laboratory, UCID-17743, March 1978.

NRC, 1977, "Regulatory Guide 1.109, Calculation of Annual Doses to Man from Routine Release of Effluents for the Purpose of Evaluating Compliance with 10 CFR Part 50, Appendix I," U.S. Nuclear Regulatory Commission, revision 1, October 1977.

NRC, 1984, "Radon Attenuation Handbook for Uranium Mill Tailings Cover Design," prepared for the U.S. Nuclear Regulatory Commission by Rogers and Associates Engineering Corporation and Pacific Northwest Laboratory, NUREG/CR-3533, April 1984.

NRC, 1986, "Update of Part 61 Impacts Analysis Methodology, Methodology Report," U.S. Nuclear Regulatory Commission, NUREG/CR-4370, Vol. 1, January 1986.

NRC, 1989, "Regulatory Guide 3.64, Calculation of Radon Flux Attenuation by Earthen Uranium Mill Tailings Covers," U.S. Nuclear Regulatory Commission, June 1989.

Peterson, H.T., Jr., 1984, "Terrestrial and Aquatic Food Chain Pathways," in Radiological Assessment, A Textbook on Environmental Dose Analysis, J.E. Till and H.R. Meyer, eds., NUREG/CR-3332.

Philip, J., and D.A. de Vries, 1957, "Moisture Movement in Porous Materials under Thermal Gradients," Transactions, American Geophysical Union, 38(2):222-232.

Purtymun, W.D., and W.R. Kennedy, 1971, "Geology and Hydrology of Mesita del Buey," Los Alamos National Laboratory, LA-4660.

Reneau, S.L., 1993, "Geomorphic Characterization of Technical Area 21, Los Alamos National Laboratory, New Mexico," Los Alamos National Laboratory, LAUR 93-2028.

Reneau, S.L., and D.T. Vaniman, 1994, "Fracture Characteristics in a Disposal Pit at Mesita del Buey," Los Alamos National Laboratory, unpublished report, March 21, 1994.

Rupp, E.M., 1980, "Age Dependent Values of Dietary Intake for Assessing Human Exposures to Environmental Pollutants," Health Physics 39, 151.

Sheppard, M.I., et al., 1991, "Mobility and Plant Uptake of Inorganic ^{14}C and ^{14}C-Labelled PCB in Soils of High and Low Retention," Health Physics, 61(4): pp. 481-492.

Shuman, R., 1997, "Radioactive Waste Inventory for the TA-54, Area G Performance Assessment and Composite Analysis", Los Alamos National Laboratory report LA-UR-97-156, Los Alamos National Laboratory, NM.

Soldat, J.K., N.M. Robinson, and D.A. Baker, 1974, "Models and Computer Codes for Evaluating Radiation Doses," Pacific Northwest Laboratory, report BNWL-1754.

Soll, W.E., 1995, "Influence of Fracture Fills and Fracture Coatings on Flow in Bandelier Tuff," Los Alamos National Laboratory report LA-UR-95-2695, Los Alamos National Laboratory, NM.

Springer, E.P., 1996 "Surface Water and Erosion Calculations to Support the MDA G Performance Assessment," Los Alamos National Laboratory Report, LA-UR-96-4894, Los Alamos National Laboratory, Los Alamos, NM.

Thamer, B.J., et al., 1980, "Radon Diffusion and Cover Material Effectiveness for Uranium Tailings Stabilization," prepared for the U.S. Department of Energy by Ford, Bacon & Davis Utah, Inc., FBDU 258.

Vold, E.L., 1996a, "Atmospheric Transport in Complex Terrain at Los Alamos, Area G," Los Alamos National Laboratory Report LA-UR-96-4870, Los Alamos National Laboratory, Los Alamos, NM.

Vold, E.L., 1996b, "Analysis of Liquid Phase Transport in the Unsaturated Zone at a Mesa Top Disposal Facility," Los Alamos National Laboratory Report, LA-UR-96-370, Los Alamos National Laboratory, Los Alamos, NM.

Vold, E.L., 1996c, "Isotopic Compositions of Inventory Designations, 'Mixed Fission Product' and 'Mixed Activation Product'," Los Alamos National Laboratory Report, LA-UR-96-4872, Los Alamos National Laboratory, Los Alamos, NM.

Vold, E.L., 1997, "Evaluation of Atmospheric Release Sources for Gaseous Phase Contaminants Emanating from the Disposal Facility at Area G," Los Alamos National Laboratory report LA-UR-97-155, Los Alamos National Laboratory, NM.

Vold, E.L., et al., 1996, "Representative Recharge Rates in a Complex Unsaturated Hydrogeology," Los Alamos National Laboratory report, Los Alamos National Laboratory, NM.

Vold, E.L., and B. Eklund, 1996, "Determination of an In-Situ Vadose Zone Vapor Phase Diffusion Coefficient at a Mesa Top Waste Disposal Facility," Los Alamos National Laboratory, LA-UR-96-1848, Draft I-052296.

Vold, E.L., and R. Shuman, 1996, "Phase Two of the Source Release Modeling for the Los Alamos Area G Disposal Facility Performance Assessment," Los Alamos National Laboratory Report, LA-UR-96-4786, Los Alamos National Laboratory, Los Alamos, NM.

Vold, E.L., and R. Shuman, 1997, "A Model for the Biotic Translocation of Buried Low-Level Radioactive Waste to the Ground Surface in the Presence of Surface Erosion," Los Alamos National Laboratory, LA-UR-97-84, Los Alamos National Laboratory, Los Alamos, NM.

Warren, J.L., 1980, "Program Status Report: Review of Past Waste Disposal Records," Office Memorandum from J.L. Warren to W. Hansen, Los Alamos Scientific Laboratory, January 2, 1980.

White, G.C., et al., 1981, "Factors Affecting Availability to Vegetables Grown at Los Alamos," Journal of Environmental Quality, Vol. 10, No. 3, 1981.

Wood, M.I., et al., 1994, "Performance Assessment for the Disposal of Low-Level Waste in the 200 West Area Burial Grounds," Westinghouse Hanford Company, WHC-EP-0645, November 1994.

Wong, I., et al., 1993, "Deterministic and Probabilistic Seismic Hazard Evaluation of the Los Alamos National Laboratory," Proceedings of the Fourth DOE Natural Phenomena Hazards Mitigation Conference, Atlanta, GA, DOE Report CONF-9310102, Vol. 1.

Yang, Y.Y. and C.B. Nelson, 1986, "An Estimation of Daily Food Usage Factors for Assessing Radionuclide Intakes in the U.S. Population," Health Physics, 50 (2): pp. 245-257.

This page intentionally left blank.

LA-UR-96-4870

Title: ATMOSPHERIC TRANSPORT IN COMPLEX TERRAIN AT LOS ALAMOS, AREA G

Author(s): Erik L. Vold

Submitted to: U.S. Department of Energy, as support documentation for the Los Alamos Area G Performance Assessment

Los Alamos
NATIONAL LABORATORY

Los Alamos National Laboratory, an affirmative action/equal opportunity employer, is operated by the University of California for the U.S. Department of Energy under contract W-7405-ENG-36. By acceptance of this article, the publisher recognizes that the U.S. Government retains a nonexclusive, royalty-free license to publish or reproduce the published form of this contribution, or to allow others to do so, for U.S. Government purposes. The Los Alamos National Laboratory requests that the publisher identify this article as work performed under the auspices of the U.S. Department of Energy.

ATMOSPHERIC TRANSPORT IN COMPLEX TERRAIN AT LOS ALAMOS, AREA G

Erik L. Vold

Abstract

This report documents the atmospheric dispersion model used in the LANL Area G Performance Assessment for off-site airborne dose calculations. Potential airborne contaminants from the mesa top disposal facility disperse in the complex terrain dominated by narrow mesas parallel to narrow canyons. The dispersion is characterized by site-specific values of χ/Q $[(Ci/m^3)/(Ci/s)]$ at each of two designated receptor locations, a 'maximum off-site dose' location and a nearby population center (White Rock, NM). The values of χ/Q in each of the sixteen wind sectors are first estimated with the CAP-88 computer code using 1992 annual meteorologic data from Area G and assuming an area source for release. The data captures the dominant wind direction on the mesa tops from the SSW. These dispersion parameters are assumed to apply to open, flat terrain and must be corrected for channeling and velocity effects due to the complex mesa and canyon terrain surrounding the Area G site. Additional meteorologic data have been collected over two years from six remote temporary meteorological stations operated on the mesas and in the canyons immediately around Area G. These data indicate that the wind flow in the canyons is exclusively bimodel, flowing up canyon during the day and down canyon at night:. It is conservatively assumed that all ground level releases from Area G which blow out across an adjacent canyon become entrained in the canyon flow. This effectively combines the contaminant release for several sectors into a single canyon flow which is upstream during the day or downstream at night. This canyon channeling mechanism is implemented in the model by summing the wind sector dispersion factors over those sectors appropriate to the geometry for a release from Area G toward either adjacent canyon. The result is that the location of the 'maximum off-site' individual is found to be up canyon to the north (in Canada del Buey, limited by daytime flow) where the maximum dispersion parameter is $(\chi/Q)_{max} = 5.5x10^{-5}s/m^3$. The maximum dispersion parameter at a population center, $(\chi/Q)_{pop}$, is in White Rock to the ESE (limited by nighttime down canyon flow), where $(\chi/Q)_{pop} = 1.3x10^{-5}s/m^3$. At both locations the analysis indicates the canyon channeling effect increases χ/Q by about a factor of 2.4 over that expected in any single downwind sector. Uncertainties are examined in some detail.

ATMOSPHERIC TRANSPORT IN COMPLEX TERRAIN AT LOS ALAMOS, AREA G

Introduction

Atmospheric transport is evaluated from a source at the Los Alamos National Laboratory LLRW disposal site, Area G, to an off-site receptor at a location of maximum contaminant concentration and to a receptor at a population center (White Rock). Part of the assessment is to determine the location of maximum airborne concentrations, which is complicated by the local complex terrain.

The air pathway assessment can be written in terms of the factors including source strength, S, source release rate, R, atmospheric dispersion, χ/Q, and a pathway and scenario dependent dose conversion, D_f, related as

$$D[mrem/yr] = S\,[Ci/m3]\,R\left(\frac{Ci/s}{Ci/m3}\right)\,\chi/Q\,[s/m3]\,D_f\left(\frac{mrem/yr}{Ci/m3}\right). \qquad (1)$$

Airborne transport is characterized with a dispersion value, χ/Q, equal to the receptor location concentration, χ *[Ci/m3]*, per continuous source term release, Q *[Ci/s]*, assumed to be valid for a quasi-steady state release. This report details the site-specific specification of the χ/Q values for the critical receptor locations near Area G used in the site Performance Assessment (PA).

The main report on the site PA describes the airborne source nuclide strength, S, which has been sorted from the disposal inventory. A separate report [Vold,96] describes detailed numerical calculations to determine the time dependent release rate, $R[t]$, for three nuclide sources. These were chosen to bound the range of releases and to compare to airborne releases calculated in the simpler steady state analytic solutions implemented within the PA as a cross check on accuracy of the solutions. The output from the atmospheric transport and dispersion model combined with the source and source release terms is the airborne concentration at the critical receptor location which becomes input to the dose assessment model for immersion, inhalation, and deposition pathways.

Estimation of atmospheric dispersion of pollutants has an established history using a Gaussian plume solution with the plume spreading related to the Pasquill-Gifford classification system of atmospheric stability [Slade,68]. This method of determining atmospheric pollutant concentration has been implemented in computer codes [CAP-88] as required for assessments by the U.S.EPA [EPA - 40 CFR 61]. The method and the stability classification system was developed for dispersion in relatively flat open terrain. The focus of the present study is to document the CAP-88 results at Area G and the correction factors that are used to apply the results to the complex terrain, a network of mesas and canyons.

An important issue for the complex terrain dispersion correction factor is what fraction of the airborne material released from a ground level source on the mesa top becomes entrained in the adjacent canyon wind flow. Recent simulations [Costigan,et.al.96] suggest this fraction may be less than one, but these simulations do not completely and accurately reproduce the distinct mesa top and canyon flow fields. A tracer study conducted in the local area suggests only limited 'channeling' by the canyon wind flows [Archuleta,et.al.,78], and thus the canyon entrainment fraction would be less than one. To be conservative, this study assumes the maximum, a fraction equal to one, and this is incorporated as a correction factor to the Gaussian plume dispersion factor as detailed in this study.

Data Review

An aerial view in Fig.1 of northern New Mexico from the NNE sector shows the NNE - SSW orientation of the Rio Grande valley between the Jemez Mountains to the west and the Sangre de Cristo mountains to the east. A computer generated surface of the Los Alamos terrain near Area G is seen in Fig.2 (with enhanced vertical scale) which shows the complex finger-like mesas predominantly spanning from the west or NW to the east or SE. The disposal facilities are on top of the narrow finger mesa, Mesita del Buey. The local canyons include Canada del Buey to the north of Area G and Pajarito Canyon to the south, which both channel a nighttime drainage wind. The mesa top (Area G) annual wind rose (for day and night time observations combined) is shown in Fig.3 for use in this analysis. The dominant daytime winds observed at Los Alamos from the south or southwest (channeled by the Rio Grande valley) are seen in the day time windrose in Fig.4. The mesa top nighttime windrose (Fig.5) shows that the mesa top flow is generally consistent with

the canyon drainage although there is a large variation in the mesa top nighttime wind direction. Meteorologic data is summarized annually in the Los Alamos Environmental Surveillance Reports (e.g., see ref.ESR'94) and was described in some detail previously [Bowen,90].

The computer generated view of the topography surrounding Area G (Fig.2) shows six remote meteorological towers which have been collecting 15 minute averaged field data since early 1994. As part of an assessment to understand the flow field and thus dispersion in the local complex terrain, these six portable meteorological towers (of a type originally designed for monitoring at the Nevada Test Site) were sited, two at mesa top locations, one just east of the site where the mesas have dissipated to mild ridges, and three in the canyons adjacent to the disposal site mesa. Since then, the towers have collected horizontal wind velocities, pressure, temperature, relative humidity and a radiation gamma reading every fifteen minutes. In an on-going effort, the data base is being analyzed for trends [Vold,et.al.,95] and to provide a basis for comparison to computational modeling efforts to predict the flow fields [Costigan,et.al.,96, and Celada and Vold,96].

The mesa top flow is seen to be similar at different points, while the mesa top and canyon flows are observed to be quite different from each other. The dominant daytime mesa top wind flow is from the S to SW (with a lesser component in the opposite direction), directed by the Rio Grande canyon between the Jemez and the Sangre de Cristo mountains. This flow has a large variance in direction. The mean and variance can be approximately inferred from the histogram chart in Fig.6a. This plot shows the frequency distribution of wind over the two variables of wind direction (labeled *degree*, the angle wind is from, with zero degrees being to the north) and the hour of day, compiling all 15 minute data from the month of June, 1995 (taken to be a 'typical' or characteristic month).

Similar plots of wind frequency distribution for wind direction and time of day are shown in Fig.6b for one of the canyon locations. The local canyon flows are seen to be very 'precisely bi-modal', meaning flow is directly up canyon during the day, down canyon at night, and with an abrupt change, within 1-2 15-min. sample intervals, for either transition. The nighttime mesa top flow slowly rotates to follow the canyon drainage direction on a variable time scale, some nights never really 'catching up' to the canyon drainage flow. More detailed analyses of the canyon verses mesa top meteorological data is available [Vold, et.al. 95].

An implication for atmospheric transport is that to the extent an airborne release from a mesa top site (Area G) crosses an adjacent canyon, it can become entrained in the canyon flow field, and thus contaminant contributions from several mesa top wind sector directions potentially add together into a canyon flow. In this case, several wind rose sectors may impact a single downwind canyon receptor location. It is assumed to be conservative for this study, that canyon channeling of airborne contaminant above the canyon becomes entrained within the canyon.

A comparison of the mesa top wind roses, and the results from the canyons, was made with respect to the actual geometry of the canyons. Daytime windrose sectors from the WSW to the ESE sectors transport airborne contaminants toward the Mesita del Buey canyon to the north and some fraction of those contaminants will be entrained in the up-canyon daytime flow, and thus end up at a single downwind location in the bottom of Mesita del Buey canyon, which is up-canyon from Area G. Each canyon adjacent to the Area G mesa top site will then have a significant contaminant concentration enhancement due to this canyon channeling effect. A simple quantification of these effects from the complex terrain is described in the following. Based on the appropriate weighting of the site wind roses, the point of maximum off-site concentrations of a disposal site source is determined to be up Mesita del Buey canyon and to the north of the disposal site mesa.

Complex Terrain Atmospheric Transport Model

Critical Off-site Location

The atmospheric transport in complex terrain is assumed to be characterized by a dispersion value, $(\chi/Q)_C$, appropriate to a critical canyon location estimated as

$$\left(\frac{\chi}{Q}\right)_C = \left(\frac{u_m}{u_c}\right) \sum_{\theta} f_\theta \left(\frac{\chi}{Q}\right)_{GP\text{-}\theta} . \qquad (2)$$

where

$\left(\frac{\chi}{Q}\right)_{GP\text{-}\theta}$ is the Gaussian plume dispersion into wind sector, θ, determined for the appropriate source geometry and mesa-top meteorology data, and evaluated at the receptor location distance,

$\left(\frac{u_m}{u_c}\right)$ is the ratio of annual averaged wind speed observed on the mesa top, m, to that in the canyon, c,

$\sum_{\theta} f_\theta$ is a sum over wind sectors, θ, of the fraction, f_θ, of the mesa top release which becomes entrained in the canyon flow, and thus is channeled by the canyon towards the receptor location, c.

The summation accounts for the increase in concentration by canyon channeling over long term releases, that is, dispersion from several mesa top wind sectors add together in the canyon stream flow. The above expression does not include effects of a 'rotor' wind pattern which may result in deeper canyons and could further increase the canyon site concentrations by increasing the canyon residence time for an air parcel.

An important issue is the number of sectors which the summation should include In an examination of the wind rose from the mesa top location with the area map, the range of sectors likely to contribute to flow into either adjacent canyon during the day or the night were determined. The greatest frequency in the wind rose data clearly involves those sectors blowing towards Canada del Buey to the north (dominated by the daytime flow) and the geometry shows sectors from the WSW to the ESE are likely contributors.

For a ground level release it is conservatively assumed that $f_\theta = 1$, that all the release becomes caught in the 'downwash' leeward of the mesa and then moves with the canyon flow. During the day this will be up canyon and during the night this will be down canyon. At Area G, flow towards Canada del Buey is more frequent in the daytime than in the night so the critical receptor will be upstream in Canada del Buey due primarily to daytime conditions in the canyon. The available data for dispersion, χ/Q, is based on the annual averaged data (for day and night time conditions combined) so then the canyon dispersion must be corrected for the daytime frequency in the specified sector range relative to that for the total day and night time data.

his allows us to rewrite the above equation for practical evaluation at Area G as

$$\left(\frac{\chi}{Q}\right)_C = \left(\frac{u_m}{u_c}\right)\frac{cdf_{day}}{cdf_{an}}\sum_{\theta=ESE}^{\theta=WSW}\left(\frac{\chi}{Q}\right)_{GP} \qquad (3)$$

where $\left(\frac{\chi}{Q}\right)_{GP}$ is the Gaussian plume dispersion for a given wind sector, θ, evaluated from the annual averaged data base, and cdf_{day} is the wind cumulative distribution frequency over the sectors of concern evaluated for daytime hours only, and cdf_{an} is the annual cumulative frequency distribution evaluated over the 24 hr data base. Thus,

$$cdf_{day} = \sum_{\theta=ESE}^{\theta=WSW} df_{day}\ , \text{ and } \quad cdf_{an} = \sum_{\theta=ESE}^{\theta=WSW} df_{an}\ . \qquad (4)$$

where df is the distribution frequency or (wind rose sector percentage/100) for the daytime hours (day) or for all hours (an). Examination of the data for the annual, daytime and nighttime Area G wind roses (Fig.3-5) shows that $cdf_{an}(\theta=ESE,WSW) = 0.39$ and $cdf_{day}(\theta=ESE,WSW) = 0.53(0.5)$, since 53% of the daytime occurrences are from this range of wind sectors. It is assumed that half of the total occurrences are recorded on the 'daytime' windrose, and that the actual bimodal behavior observed in the canyons is split in time similarly to the split which defines 'daytime' or nighttime' conditions in establishing the windrose data. This gives $(cdf_{day}/cdf_{an}) = 0.68$ or 68% of the southerly winds whi impact the Canada del Buey upstream critical receptor occur during the day. simplification ignores the different distributions of stability class which exist in th compared to all hours.

Data from the three canyon locations at Area G and a fourth nearby car Alamos Canyon) were pooled to get a canyon average speed, u_C, Data from the four meteorological towers identified as lo (including two near White Rock where the mesas have dis immediate vicinity of Area G were pooled to get the mes m/s. The ratio of speeds needed in the above equatio

An atmospheric transport assessment f [Kowalewsky,et.al., 1995] in which the Gaussian

CORRECTION

START

$\left(\frac{u_m}{u_c}\right)$ is the ratio of annual averaged wind speed observed on the mesa top, m, to that in the canyon, *c*,

$\sum_{\theta} f_{\theta}$ is a sum over wind sectors, θ, of the fraction, f_{θ}, of the mesa top release which becomes entrained in the canyon flow, and thus is channeled by the canyon towards the receptor location, *c*.

The summation accounts for the increase in concentration by canyon channeling over long term releases, that is, dispersion from several mesa top wind sectors add together in the canyon stream flow. The above expression does not include effects of a 'rotor' wind pattern which may result in deeper canyons and could further increase the canyon site concentrations by increasing the canyon residence time for an air parcel.

An important issue is the number of sectors which the summation should include. In an examination of the wind rose from the mesa top location with the area map, the range of sectors likely to contribute to flow into either adjacent canyon during the day or the night were determined. The greatest frequency in the wind rose data clearly involves those sectors blowing towards Canada del Buey to the north (dominated by the daytime flow) and the geometry shows sectors from the WSW to the ESE are likely contributors.

For a ground level release it is conservatively assumed that $f_{\theta} = 1$, that all the release becomes caught in the 'downwash' leeward of the mesa and then moves with the canyon flow. During the day this will be up canyon and during the night this will be down canyon. At Area G, flow towards Canada del Buey is more frequent in the daytime than in the night so the critical receptor will be upstream in Canada del Buey due primarily to daytime conditions in the canyon. The available data for dispersion, χ/Q, is based on the annual averaged data (for day and night time conditions combined) so then the canyon dispersion must be corrected for the daytime frequency in the specified sector range relative to that for the total day and night time data.

This allows us to rewrite the above equation for practical evaluation at Area G as

$$\left(\frac{\chi}{Q}\right)_C = \left(\frac{u_m}{u_c}\right)\frac{cdf_{day}}{cdf_{an}}\sum_{\theta=ESE}^{\theta=WSW}\left(\frac{\chi}{Q}\right)_{GP} \qquad (3)$$

where $\left(\frac{\chi}{Q}\right)_{GP}$ is the Gaussian plume dispersion for a given wind sector, θ, evaluated from the annual averaged data base, and cdf_{day} is the wind cumulative distribution frequency over the sectors of concern evaluated for daytime hours only, and cdf_{an} is the annual cumulative frequency distribution evaluated over the 24 hr data base. Thus,

$$cdf_{day} = \sum_{\theta=ESE}^{\theta=WSW} df_{day}\ , \text{ and } \quad cdf_{an} = \sum_{\theta=ESE}^{\theta=WSW} df_{an}\ , \qquad (4)$$

where df is the distribution frequency or (wind rose sector percentage/100) for the daytime hours $(_{day})$ or for all hours $(_{an})$. Examination of the data for the annual, daytime and nighttime Area G wind roses (Fig.3-5) shows that $cdf_{an}(\theta=ESE,WSW) = 0.39$ and $cdf_{day}(\theta=ESE,WSW) = 0.53(0.5)$, since 53% of the daytime occurrences are from this range of wind sectors. It is assumed that half of the total occurrences are recorded on the 'daytime' windrose, and that the actual bimodal behavior observed in the canyons is split in time similarly to the split which defines 'daytime' or nighttime' conditions in establishing the windrose data. This gives $(cdf_{day}/cdf_{an}) = 0.68$ or 68% of the southerly winds which impact the Canada del Buey upstream critical receptor occur during the day. This simplification ignores the different distributions of stability class which exist in the daytime compared to all hours.

Data from the three canyon locations at Area G and a fourth nearby canyon (TA 41 in Los Alamos Canyon) were pooled to get a canyon average speed, u_C, found to be 1.55 m/s. Data from the four meteorological towers identified as located on 'mesa-top sites' (including two near White Rock where the mesas have dissipated to mild ridges) in the immediate vicinity of Area G were pooled to get the mesa-top average wind speed of 2.63 m/s. The ratio of speeds needed in the above equation is 1.7.

An atmospheric transport assessment for Area G was recently completed [Kowalewsky,et.al., 1995] in which the Gaussian plume dispersion from an area source at

CORRECTION

END

Area G was determined using a version of CAP-88 [ref: CAP-88]. The results include a table of (χ/Q) values by sector (wind towards) and by downwind distance, shown in Table I. The source area used in the calculation was 60 acres corresponding to the whole Area G site. For a dispersed area source this large, the code does not compute receptor locations any closer than 500m. Considering the dimensions of Area G and that of the mesa and adjacent canyons (see Fig.2 for example, noting that Area G as indicated in that figure is almost 2 km long) it is reasonable to take 500m as a minimum distance to a critical receptor location. The actual geometry is simplified by assuming this down wind distance applies to each of the wind sectors contributing to the canyon flow.

Summing the ESE to WSW values of (χ/Q) for the 500m, location in the table, multiplying by the wind speed ratio of 1.7, and the daytime occurrence frequency of 0.68 gives the final dispersion value for the critical canyon receptor location corrected for the complex terrain, of $\left(\frac{\chi}{Q}\right)_C = 5.5x10^{-5}\ s/m3$.

It is interesting to note that the Gaussian plume maximum dispersion in any single wind sector over this range is $1.35x10^{-5}$ m3/s (to the ENE). With the 1.7 wind speed correction, this means that a canyon channeling factor,

$$\sum_{\theta} f_\theta \left(\frac{\chi}{Q}\right)_{GP} / (\chi/Q)_{sector\text{-}max} / (u_m/u_c) = 5.5x10^{-5}/1.35x10^{-5}/1.7 = 2.4,$$

or the canyons can channel contaminants from Area G to concentrate long term averages to about two and one half times that expected from a Gaussian plume prediction. This concentration only applies to long term chronic releases, so that the annual average wind rose applies.

Dispersion values, χ/Q, in a single sector at distances closer than the 500m critical receptor location are not expected to greatly exceed the χ/Q values at 500m due to the large area source. Thus, for example the dose to a receptor at 100m will be limited by the frequency of wind in a single sector which is less than 11% of the time for any sector. This supports the critical off-site location as being in the canyon, assuming the validity of the canyon flow entrainment of mesa top releases.

Population Center Location

A similar analysis can be applied to the nearest population center assumed to be 2 km from Area G in the (E-ESE) direction (present boundary of White Rock). In this case, dispersion from the W sector contributes directly for all hours. During the night time conditions, wind from the WNW through the E sectors is assumed to drain into Pajarito Canyon which is then assumed to flow down canyon and to the receptor location at White Rock.

The same analysis as above for the Canada del Buey receptor location is applied to the WR location, summing Gaussian dispersion at 2 km over θ = WNW to E, correcting for the nighttime wind frequency occurrence and for the canyon flow speed, and now adding the full time dispersion contribution from the W sector. The nighttime occurrence for the sector range, $\theta = WNW\ to\ E$, is evaluated from the wind roses to be 0.57. Summing and correcting this range of Gaussian dispersion values from Table I gives $\chi/Q = 1.7 \times 10^{-5}$ and 5.4×10^{-6} $s/m3$ respectively, at distances of 1500m and 3000m. Interpolating to the population center location at 2000m gives $\chi/Q = 1.3 \times 10^{-5}$ $s/m3$. This is the value used in the analysis of the population center dose assessment.

This dispersion value which accounts for complex terrain can be compared to the maximum dispersion along a single sector (to the SE) which is $\chi/Q = 3. \times 10^{-6}$ $s/m3$ evaluated at 2000m. The complex terrain increases the Gaussian dispersion at this location by $1.3 \times 10^{-5}/3. \times 10^{-6} = 4.3$. Since 1.7 is the correction factor due to wind speed reduction in the canyons, canyon channeling contributes an increase at this location of $4.3/1.7 = 2.5$. This is nearly identical to the case for the critical receptor in Canada del Buey and shows the canyon channeling can increase the Gaussian plume predictions by about 2.5 for the daytime maximum (upstream in Canada del Buey) or for the nighttime maximum downstream in Pajarito Canyon.

The canyon wind speed reduction may not be applicable at the White Rock receptor location because the canyons have essentially dissipated to nearly level terrain there. If we neglect

the canyon wind speed reduction correction then the White Rock location χ/Q value would be closer to $1.7 \times 1.3 \times 10^{-5}$ s/m3 = 2.2×10^{-5} s/m3.

The ratio in χ/Q values between the two sites (Canada del Buey and White Rock) is about $5.5/1.3 \approx 4.2$. This appears to be small compared to a ratio of about 10 expected between two points at 500m and 2000m under the same meteorologic conditions. This is attributed to the difference in day and night dispersion, with less dispersion at night at the White Rock site, increasing the concentration there, and thus reducing the ratio of concentrations at the Canada del Buey to White Rock locations.

Uncertainties

The data base for both the mesa top wind conditions and for the canyon conditions are relatively good and the uncertainties in the annual averages are probably negligibly small. The dominant uncertainty enters from the model itself, both in the Gaussian plume dispersion and in the formulation of the complex terrain correction given by the sector summation equation above. Predicting flow and pollutant dispersion in complex terrain is part art and part science. Major sources of uncertainty identified with this model follow.

1. The choice of area input as the model source is somewhat arbitrary compared to various conceivable area sources from Area G in the long term future transport and waste exposure scenarios. The sensitivity to this parameter is not known but could be explored by several CAP-88 runs.
2. The critical receptor location is at 500m. The sensitivity here is related to that in item 1 and these could be evaluated together.
3. The canyon-entrained flow fraction, f_0, may be less than unity as was assumed here to be conservative. This could be evaluated from tracer field studies or from 2D or 3D simulations. This may overestimate the off-site concentrations by a factor of 2 to 5 (assuming at least 20% of the release is entrained in the canyon flow).
4. The wind sectors to be included in the flow contribution to the critical canyon receptor may be different or may be fractional values of some sectors. Similarly to #3 this could be evaluated by simulations.
5. The Gaussian plume parameter values may be different at Los Alamos than the standard Pasquill-Gifford values used in CAP-88. Some analysis in this direction [Bowen,90] indicates that the dispersion is larger at Los Alamos than the default Pasquill-Gifford values, the result of increased turbulence from the enhanced surface roughness in the mesa-riddled terrain.
6. The complex terrain correction may include other factors, or may need to include the factors in better ways. This is subject to future research.

7. Reduction of the canyon dispersion by the wind speed factor of 1.7 at the White Rock location may be inappropriate since the canyons essentially dissipate at this location. This becomes a 70% uncertainty term.
8. The simplification used to evaluate cdf_{day}/cdf_{an} ignores the different distributions of stability class which exist in the daytime compared to all hours. An improvement in this area would be to generate the Gaussian plume dispersion parameters separately for the daytime and for the night time observations. This would allow a more accurate summation of the canyon channeling effects. The separation of day or night hour observations could be defined to coincide with the time observed for the reversal of the canyon flow direction to improve the model.

Qualitative judgment regarding these uncertainty sources and the magnitude of uncertainty in Gaussian plume approximations [Slade,'68] suggest the dispersion estimate is good to within a factor of about 2-3. If a log, normal distribution is assumed to characterize the estimates of the offsite dispersion, then the estimates given can be considered as the geometric values with geometric standard deviation of 2-3.

Discussion

More detailed assessments utilizing 2D modeling [Celada and Vold] and 3D modeling [Costigan and Bossert, 96] are in process. The 2D studies are expected to shed light on the canyon partition function, f_θ. Fig. 7 [from Bossert, 1995] shows a 3D simulation for a potential pollutant dispersing during daytime from a Los Alamos mesa top site. It is seen that the pollutant blows first to the NE in the dominant mesa top flow and is then channeled up canyon before being dispersed from the canyon and carried on to the north in the mesa top flow again. The meteorological field data from around Area G suggests that the strong canyon driven flow will yield similar results for an Area G release. This simulation result is consistent with the critical receptor location identified for the Area G Performance Assessment.

Simulations have recently been performed for the Area G site [Costigan and Bossert,96], showing similar results to the example in Fig. 7 in some instances, while showing less effect of the channeling by the canyons in other instances. These simulations suggest that the assumption made in this study of canyon channeling, which decreases the atmospheric dilution in the critical canyon locations, will be conservative compared to atmospheric dispersion in the real world.

Acknowledgment

This work was supported by the U.S. Department of Energy, Waste Management Programs and was conducted as part of the Performance Assessment for the disposal facilities at Area G.

References

Archuleta, J., Barr, S., Clements, W.E., Gedayloo, T., Wilson, S.K., "Some Atmospheric Tracer Experiments in Complex Terrain at LASL", Los Alamos National Laboratory Report LA-7198-MS, Vol.I, Los Alamos, NM, March, 1978.

Bossert, J., personal communication, EES-5, Los Alamos National Laboratory, Los Alamos, NM, 1995.

Bowen, B.M., Los Alamos Climatology, Los Alamos National Laboratory Report LA-11735-MS, Los Alamos, NM, 1990.

CAP-88, available as CCC-542 from Radiation Shielding and Information Center, Oak Ridge National Laboratory, Oak Ridge, TN 37831.

Celada, R. and Vold, E., The Simple Atmospheric Model (SAM): Development and Preliminary Environmental Transport Applications at a Waste Disposal Site, in preparation as a Los Alamos National Laboratory Report, Los Alamos, NM, 1995.

Costigan, K.R., and Bossert, J.E., "Three-dimensional modeling study of atmospheric circulations and dispersion at TA-54", Los Alamos National Laboratory Report LAUR-96-4793, Los Alamos, NM, 1996.

EPA - 40 CFR 61 - Code of Federal Regulations, Volume 40 - Protection of the Environment, Part 61 - National Emission Standards for Hazardous Pollutants, subpart 61.93.

ESR-94 - Environmental Surveillance at Los Alamos during 1994, Los Alamos National Laboratory Report LA-13047-ENV, Los Alamos, NM, 1996.

Kowalewsky, K., Eklund, B., Vold, E., Air Quality Impacts Analysis for Area G, final report 4/4 from RADIAN to LANL under DOE subcontract 6345L0014-31, with CST-14, Los Alamos National Laboratory, NM, 1995.

Slade, D.H., ed., Meteorology and Atomic Energy 1968, U.S. Atomic Energy Commision, report TID-24190, NTIS, U.S.Dept. of Commerce, Springfield, VA, 22161.

Vold, E.L., Chan, M., Sanders, L., Preliminary Results from the Los Alamos TA 54 Complex Terrain Atmospheric Transport Study, Los Alamos National Laboratory Report LAUR-95-2222, Los Alamos, NM, 1995, and in preprint volume of the AMS Ninth Joint Conf. on the Applic. of Air Pollution Meteorology, paper 8A.9, p.464, Atlanta, Jan. 28, 1996, American Meteorological Society, Boston, MA.

Vold, E.L., "Evaluation of Atmospheric Release Sources for Gaseous Phase Contaminants Emanating from the Disposal Facility at Area G", Los Alamos National Laboratory

Report LAUR-97-155, (also included as a separate Appendix to the Area G PA), Los Alamos, NM, 1997.

Table I

GROUND-LEVEL χ/Q VALUES WITH NO DEPOSITION
χ/Q (SEC/CUBIC METER) TOWARD INDICATED DIRECTION
(for TA 54/WR 1992 meteorologic data)

	Distance (kilometers)					
Dir	0.5	1.5	3.	6.	11.5	25.
N	5.593E-06	6.825E-07	2.134E-07	7.610E-08	2.981E-08	1.079E-08
NNW	3.338E-06	3.461E-07	1.058E-07	3.661E-08	1.436E-08	5.310E-09
NW	2.589E-06	3.229E-07	9.821E-08	3.422E-08	1.389E-08	5.456E-09
WNW	2.965E-06	3.292E-07	9.785E-08	3.285E-08	1.324E-08	5.187E-09
W	3.766E-06	4.885E-07	1.464E-07	4.989E-08	2.027E-08	8.021E-09
WSW	5.946E-06	6.161E-07	1.867E-07	6.393E-08	2.525E-08	9.492E-09
SW	8.900E-06	1.276E-06	3.997E-07	1.445E-07	5.781E-08	2.205E-08
SSW	1.220E-05	1.640E-06	5.226E-07	1.946E-07	7.933E-08	3.109E-08
S	1.473E-05	2.019E-06	6.474E-07	2.440E-07	1.009E-07	4.070E-08
SSE	1.995E-05	2.316E-06	7.442E-07	2.815E-07	1.170E-07	4.784E-08
SE	2.381E-05	3.887E-06	1.251E-06	4.762E-07	1.989E-07	8.204E-08
ESE	2.372E-05	3.237E-06	1.040E-06	3.951E-07	1.647E-07	6.766E-08
E	1.786E-05	2.475E-06	7.943E-07	3.017E-07	1.256E-07	5.127E-08
ENE	1.354E-05	1.499E-06	4.799E-07	1.813E-07	7.501E-08	3.027E-08
NE	1.088E-05	1.622E-06	5.178E-07	1.931E-07	7.883E-08	3.099E-08
NNE	8.802E-06	1.257E-06	3.969E-07	1.438E-07	5.676E-08	2.071E-08

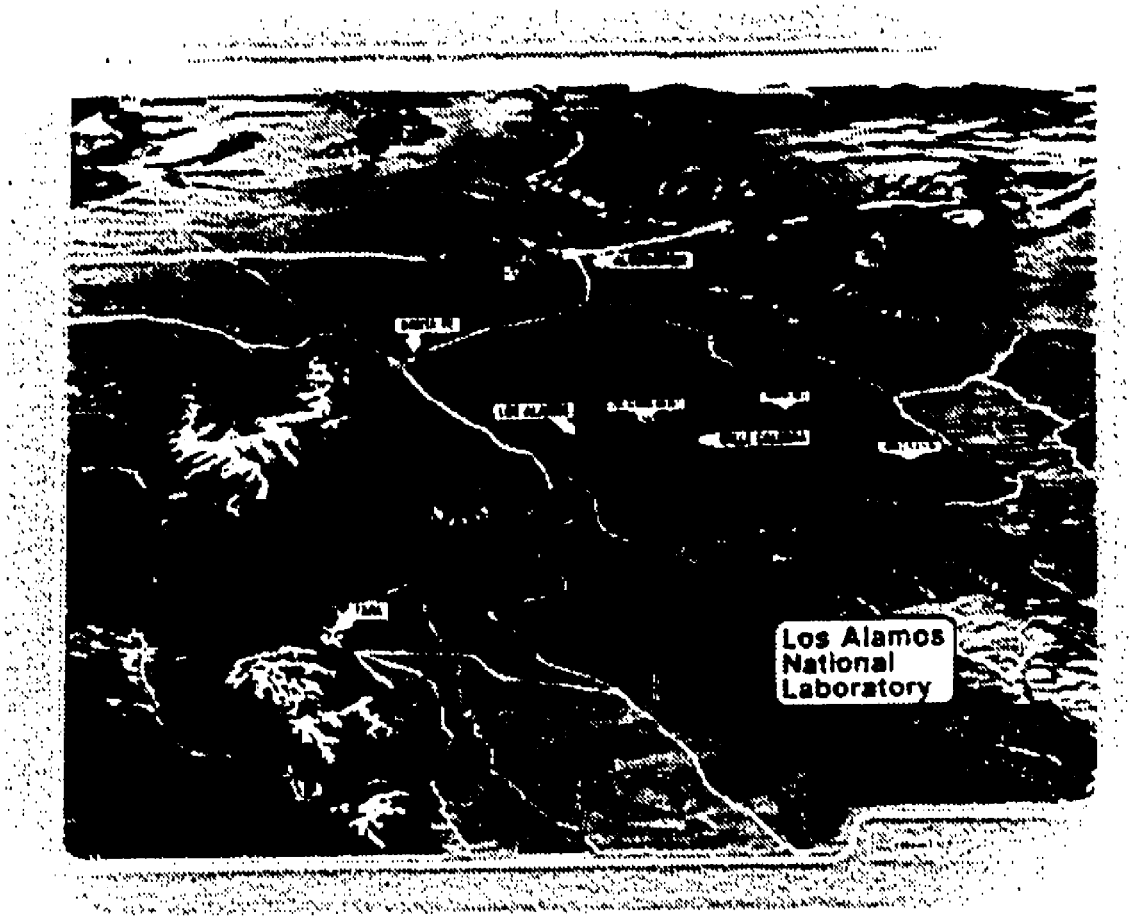

Fig.1 Northern New Mexico from the NNE. The Rio Grande valley lies between the Sangre de Cristo's Range to the east (left in the figure) and the Jemez and Valles Caldera to the west of Los Alamos. This channels the wind to be predominantly from the SSW.

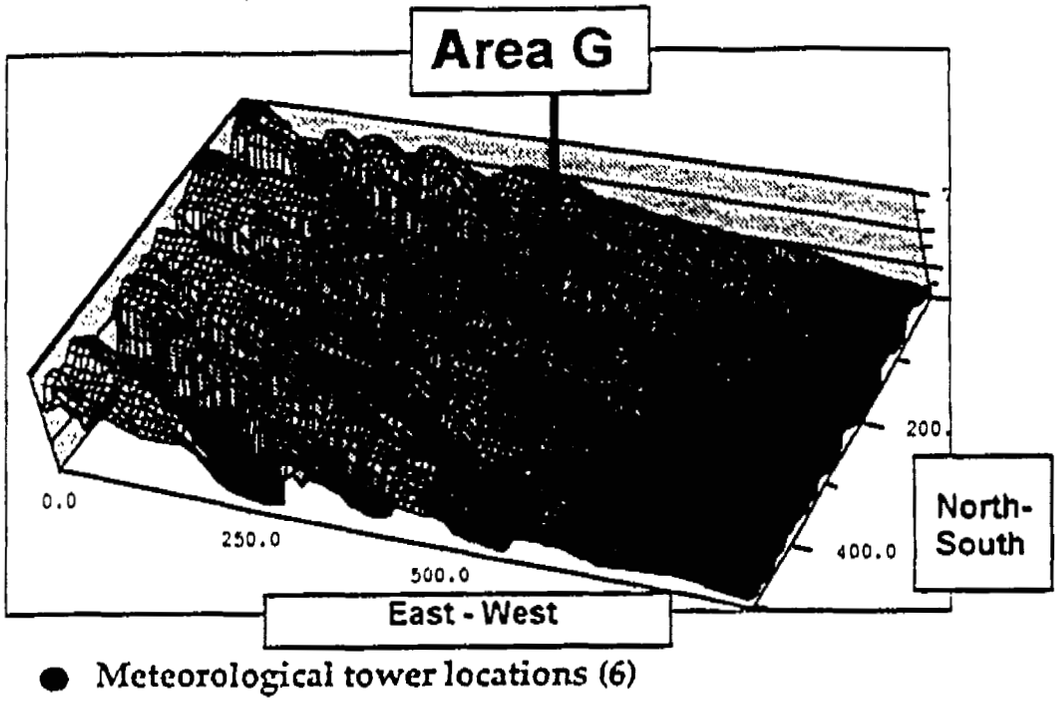

Fig.2 Area G complex terrain and remote meteorological station locations.
Axis scale: units = 20 ft. The whole area shown is about 4 km (E-W) by 2 km (N-S).

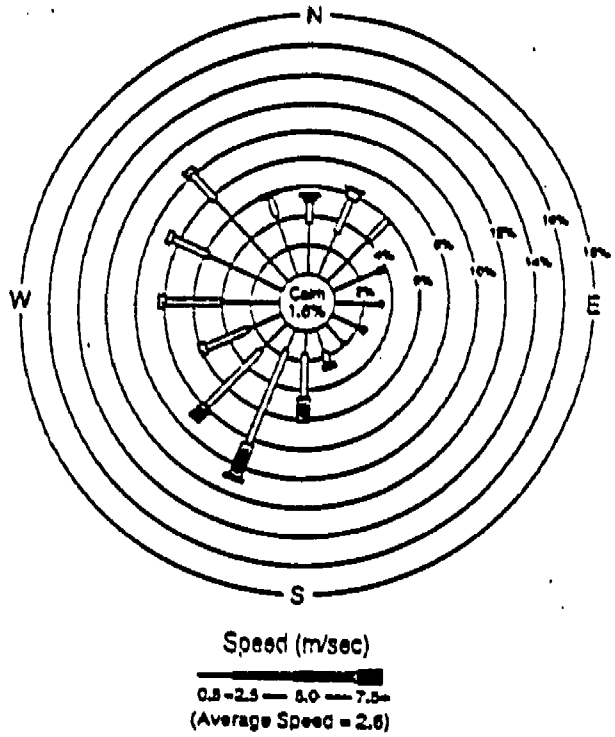

Fig.3 Annual average windrose - Area G 1992.

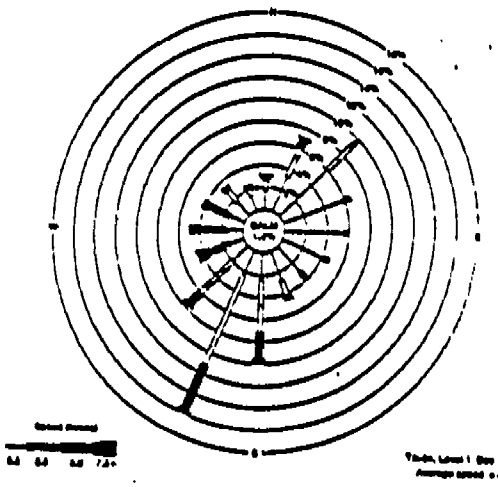

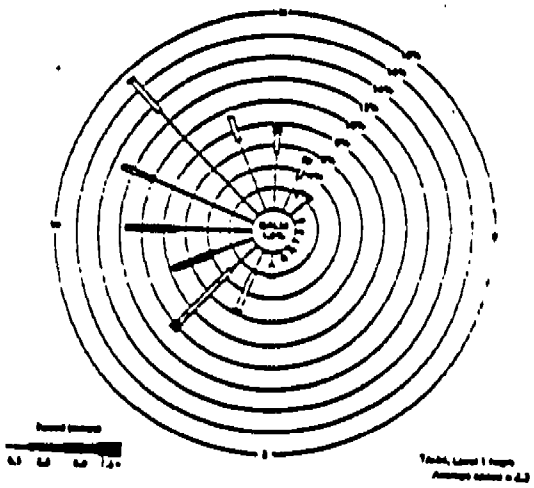

Fig. 4 Day time wind rose for Area G 1992 Fig.5 Night time wind rose.

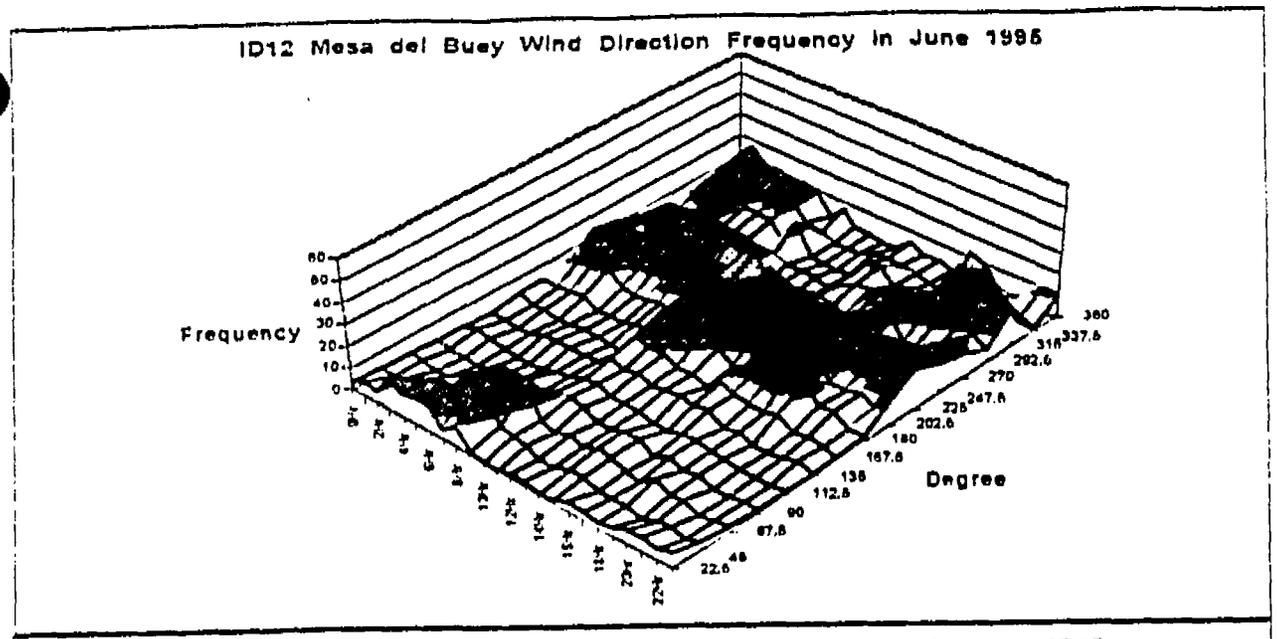

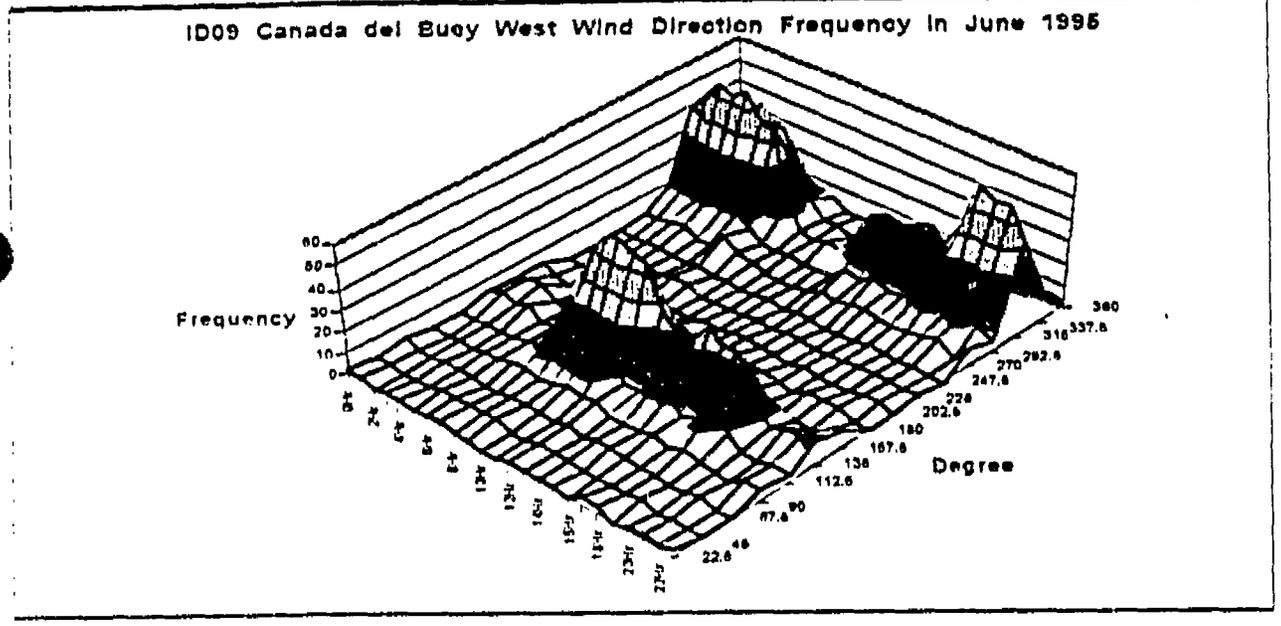

Fig. 6a (top) shows the frequency distribution for wind direction and time of day in June 1995 at the mesa top location at Area G (shown in Fig.2).

Fig.6b (bottom) shows the frequency distribution for wind direction and time of day in June 1995 at a canyon location (Canada del Buey as shown in Fig.2).

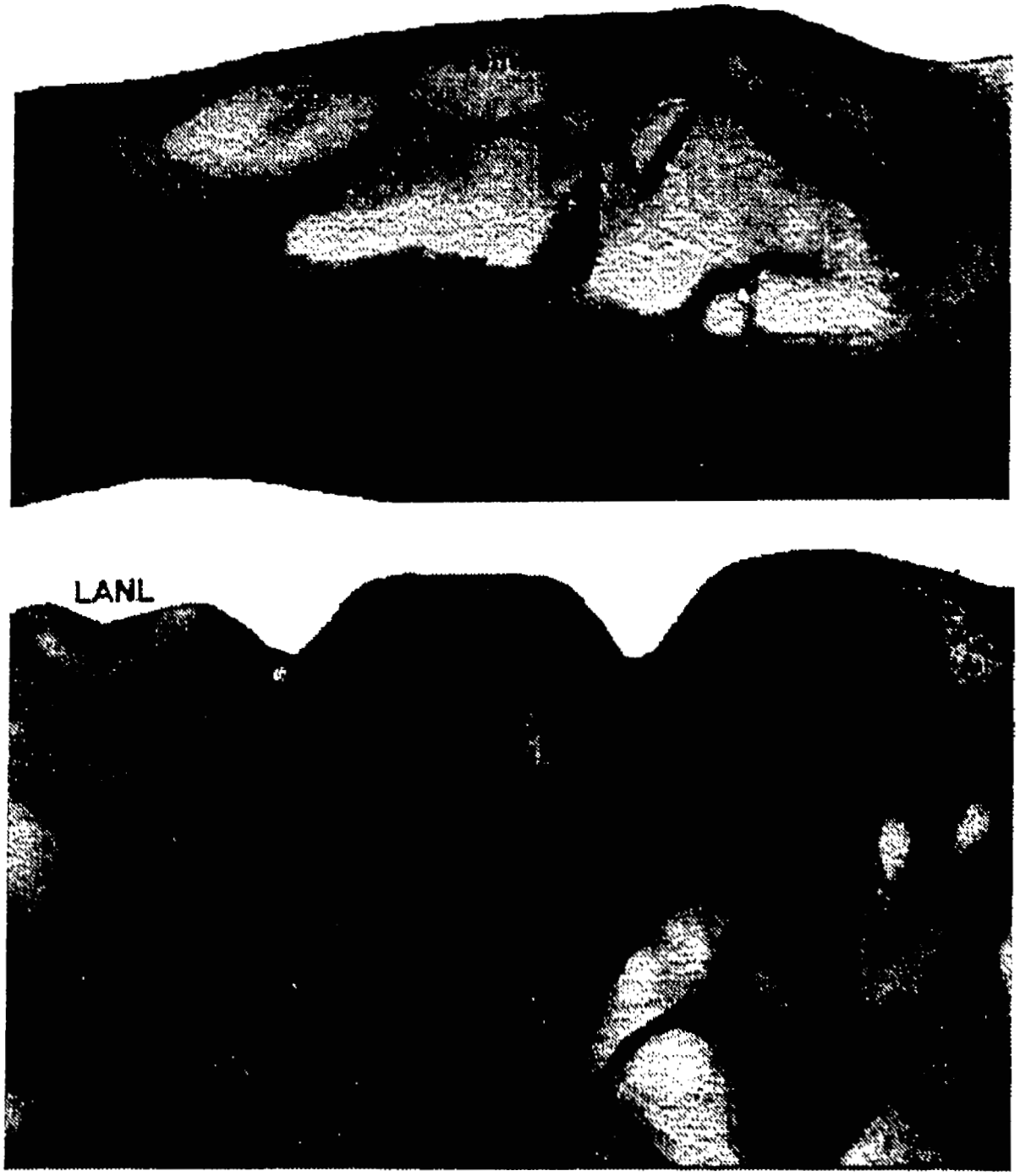

Fig. 7 Atmospheric simulation in Los Alamos complex terrain shown on two different scales (ref: J. Bossert, personal communication). Both views are facing due west. A normalized source is located at TA-21. Similar results are expected from Area G, TA-54.

LA-UR-97-157

Title: SIMULATIONS OF GROUNDWATER FLOW and RADIONUCLIDE TRANSPORT in the VADOSE AND SATURATED ZONES BENEATH AREA G, LOS ALAMOS NATIONAL LABORATORY

Author(s): Kay H. Birdsell, EES-5
Wendy E. Soll, EES-5
Kathleen M. Bower, EES-5
Andrew V. Wolfsberg, EES-5
Tade W. Orr, University of Arizona
Terry A. Cherry, EES-5

Submitted to: CST-14

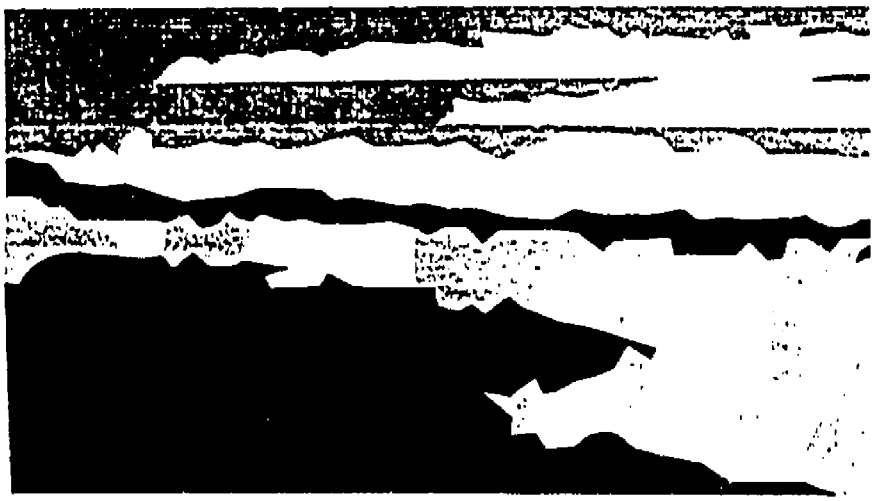

Los Alamos
NATIONAL LABORATORY

Los Alamos National Laboratory, an affirmative action/equal opportunity employer, is operated by the University of California for the U.S. Department of Energy under contract W-7405-ENG-36. By acceptance of this article, the publisher recognizes that the U.S. Government retains a nonexclusive, royalty-free license to publish or reproduce the published form of this contribution, or to allow others to do so, for U.S. Government purposes. The Los Alamos National Laboratory requests that the publisher identify this article as work performed under the auspices of the U.S. Department of Energy.

SIMULATIONS OF GROUNDWATER FLOW AND RADIONUCLIDE TRANSPORT IN THE VADOSE AND SATURATED ZONES BENEATH AREA G, LOS ALAMOS NATIONAL LABORATORY

by

Kay H. Birdsell, Wendy E. Soll, Kathleen M. Bower,
Andrew V. Wolfsberg, Tade W. Orr, and
Terry A. Cherry

ABSTRACT

Numerical simulations are used to predict the migration of radionuclides from the disposal units at Material Disposal Area G through the vadose zone and into the main aquifer in support of a radiological performance assessment and composite analysis for the site. The calculations are performed with the finite element code, FEHM. The transport of nuclides through the vadose zone is computed using a three-dimensional model which describes the complex mesa top geology of the site. The model incorporates the position and inventory of thirty-some disposal pits and shafts located at Area G as well as for proposed future pits and shafts. Only three nuclides, C-14, Tc-99 and I-129, proved to be of concern for the groundwater pathway over a 10,000 year period. The spatial and temporal flux of these three nuclides from the vadose zone is applied as a source term for the three-dimensional saturated zone model of the main aquifer which underlies the site. The movement of these nuclides in the aquifer to a downstream location is calculated and aquifer concentrations are converted to doses. Doses related to aquifer concentrations are six or more orders of magnitude lower than allowable DOE performance objectives for low level radioactive waste sites.

Numerical studies were used to better understand vadose zone flow through the dry mesa-top environment at Area G. These studies helped define the final model used to model flow and transport through the vadose zone. The study of transient percolation indicates that a steady flow vadose-zone model is adequate for computing contaminant flux to the aquifer. The fracture flow studies and the investigation of the effect of basalt and pumice properties helped us define appropriate hydrologic properties for the modeling. Finally, the evaporation study helped to justify low infiltration rates.

ACKNOWLEDGMENTS

The authors would like to thank the following individuals for their assistance. Bruce Robinson for writing the subroutines which calculate the source term and the flux between the vadose-zone and saturated-zone models. Bruce Robinson and George Zyvoloski for technical discussions and for assistance with running FEHM. Carl Gable for grid generation and graphics. Mira Bussod-Dimitrijevic for defining surface boundary conditions based on topography. David Rogers for reviewing the document and providing many useful comments. The entire Area G PA team (Diana Hollis, Rob Shuman, Erik Vold, Everett Springer, Don Krier, David Rogers, Pat Longmire and Brent Newman) for the many technical and organizational discussions which have lead to the success of this project. This work was conducted under the support of the U.S. Department of Energy, Waste Management Programs, Contract No. W-7405-ENG-36.

TABLE OF CONTENTS

1. INTRODUCTION 1
2. STUDIES OF SPECIFIC FLOW PROCESSES 2
    2.1 Addition of Deeper Vadose Zone Units 2
        2.1.1 Introduction and Problem Description 2
        2.1.2 Hydrologic Properties and Their Effects 3
    2.2 Effects of Transient Percolation 9
        2.2.1 Modeling Approach 10
        2.2.2 Transient Flow Results 12
        2.2.3 Transient Transport Results 14
        2.2.4 Summary of Transient Results 15
    2.3 Fracture Flow 16
        2.3.1 Single Fracture Modeling 16
        2.3.2 Dual-Permeability Fracture Modeling 18
    2.4 Evaporation 18
        2.4.1 From Mesa Sides and Fractures 18
        2.4.2 From Surge Beds 21
3. THREE-DIMENSIONAL VADOSE ZONE MODEL 23
    3.1 Vadose Zone Model Definition 23
        3.1.1 Stratigraphy 23
        3.1.2 Grid 24
        3.1.3 Boundary Conditions 24
        3.1.4 Hydrologic Properties 28
        3.1.5 Transport Properties 28
        3.1.6 Source Term 31
    3.2 Vadose Zone Flow Results 32
    3.3 Vadose Zone Transport Results 35
        3.3.1 Downward Transport toward the Water Table 36
            3.3.1.1 Base Case Flow Field 36
            3.3.1.2 Other Flow Fields 39
        3.3.2 Lateral Transport toward the Mesa Sides 41
            3.3.2.1 Base Case Flow Field 41
            3.3.2.2 Other Flow Fields 44
4. THREE-DIMENSIONAL SATURATED ZONE MODEL 47
    4.1 Saturated Zone Model Definition 47
        4.1.1 Geology and Hydrogeology 47
        4.1.2 Grid 48
        4.1.3 Boundary Conditions 49
        4.1.4 Hydrologic and Transport Properties 50
    4.2 Saturated Zone Flow Results 50
    4.3 Saturated Zone Transport Results 51
        4.3.1 Downward Transport toward the Water Table 51
        4.3.2 Lateral Transport toward the Mesa Side 52
        4.3.3 Dose Assessment 53
5. UNCERTAINTY 55
    5.1 Vadose Zone Flow 55
    5.2 Saturated Zone Flow 56
    5.3 Transport Properties 56
6. CONCLUSIONS 58
7. REFERENCES 59
APPENDIX 1
APPENDIX 2

LIST OF FIGURES

Figure.1-1. Cross section of Western MDA G used for 2-dimensional simulations.

Figure 2.1-2. Comparison of site data to calculated steady-state saturation profiles for several infiltration rates. Calculated profiles are located at the center of the cross section.

Figure 2.1-3. Comparison of site data to calculated steady-state saturation profiles at 1 mm/yr using various hydrologic properties for the Guaje Pumice and the Cerros del Rio Basalts. Calculated profiles are located at the center of the cross section.

Figure 2.1-4. Simulated solute pathways for the two-dimensional cross section shown inFigure 2.1-1. a) particle release only at mesa top, matrix-type basalt properties, b) particle release at mesa top and canyon floor, matrix-type basalt properties, c) particle release at mesa top, fracture-type basalt properties.

Figure 2.1-5. Contaminant plume with and without lateral flow along the Guaje Pumice Bed.

Figure 2.1-6. Flux vs. time curves at the water table for the plumes shown in Figure 2.1-5. The equivalent continuum basalt properties give more conservative transport results.

Figure 2.2-1. Two-dimensional cross section used for numerical simulations, modified to indicate five waste disposal pits.

Figure 2.2-2. Variation in saturation with time for the steady and four transient simulations at various depths.

Figure 2.2-3. Source term for the C-14 decay chain based on pit infiltration rate of 4 mm/yr.

Figure 2.2-4. Cumulative breakthrough curve for C-14 to the Guaje Pumice for four transient infiltration simulations and one steady infiltration simulation.

Figure 2.3-1. System Configuration for Fracture Flow Study.

Figure 2.4-1. Problem set-up for the study of evaporative effects from mesa sides and from fractures.

Figure 2.4-2. Resulting Saturation Profiles for Evaporation along a Mesa Edge and from fractures with 5-m and 10-m spacing, Unit 2.

Figure 2.4-3. Resulting Saturation Profiles for Evaporation along a Mesa Edge and from fractures with 5-m and 10-m spacing, Unit 1v-u.

Figure 2.4-4. Resulting saturation profile for evaporation along the surge beds at the Unit 2/1v-u interface compared to that for infiltration alone.

Figure 2.4-5. Resulting capillary pressure profile for evaporation along the surge beds at the Unit 2/1v-u interface compared infiltration alone and to data from Rogers et al. (1995) for Borehole G-5.

Figure 3.1-1. Three-dimensional stratigraphy for the vadose zone model of Area G.

Figure 3.1-2. Pit Boundaries, Internal Pit Nodes, and Mesa Edge Nodes for the Three-Dimensional Vadose Zone Calculations.

Figure 3.1-3. Boundary Condition Map of the Topographic Surface for the Vadose Zone Flow and Transport Calculations.

Figure 3.1-4. Bottom boundary divided into 28 regions for which temporally and spatially dependent flux from the vadose zone calculation is reported.

Figure 3.1-5. Velocity dependent portion of the rapid release source term.

Figure 3.2-1. Steady-state vadose zone saturation field (top view) for the base case flow field.

Figure 3.2-2. Saturation profiles near Pit 1 for the three mesa-top infiltration rates.

Figure 3.2-3. Saturation profiles for the base case flow rate at the three locations of interest.

Figure 3.3-1. I-129 Plumes (concentration, moles/liter) in the vadose zone at 1000 years for the four different source regions, base case flow field.

Figure 3.3-2. Total Flux of C-14 from the vadose zone to the saturated zone from the four source regions, base case flow field.

Figure 3.3-3. Total Flux of I-129 from the vadose zone to the saturated zone from the four source regions, base case flow field.

Figure 3.3-4. Total Flux of Tc-99 from the vadose zone to the saturated zone from the four source regions, base case flow field.

Figure 3.3-5. Total flux of the historical I-129 inventory from the vadose zone to the saturated zone for various flow cases.

Figure 3.3-6. Total flux of (a) C-14, (b) I-129, and (c) Tc-99 from the vadose zone to the saturated zone for the highest flow case (10_5_100) from the four source regions.

Figure 3.3-7. Total flux of (a) C-14, (b) I-129, and (c) Tc-99 from the vadose zone to the saturated zone for the lowest flow case (1_1_20) from the four source regions.

Figure 3.3-8. Total Lateral Flux of C-14 toward the Mesa Sides along (a) Cañada del Buey and (b) Pajarito Canyon from the four source regions, base case flow field (5_1_50).

Figure 3.3-9. Total Lateral Flux of I-129 toward the Mesa Sides along (a) Cañada del Buey and (b) Pajarito Canyon from the four source regions, base case flow field (5_1_50).

Figure 3.3-10. Total Lateral Flux of Tc-99 toward the Mesa Sides along (a) Cañada del Buey and (b) Pajarito Canyon from the four source regions, base case flow field (5_1_50).

Figure 3.3-11. Generic Total Flux from the canyon floors through the Vadose Zone to the Saturated Zone for an Extreme Case of Lateral Transport. Pajarito Canyon (south) flow rate is 50 mm/yr. Cañada del Buey (north) flow rate is 1 mm/yr.

Figure 3.3-12. Generic Total Flux from the Floor of Pajarito Canyon through the Vadose Zone to the Saturated Zone for an Extreme Case of Lateral Transport. Pajarito Canyon flow rates are 100 mm/yr, 50 mm/yr and 20 mm/yr.

Figure 4.1-2. Saturated zone model configuration.

Figure 4.3-2. Concentrations in the Saturated zone for the I-129 Historic Inventory at the Point of Maximum Concentration and at the 100-m Compliance Point.

Figure 4.3-3. Time Dependent Concentration plots for the location of maximum concentration in the saturated zone for the generic rapid release of contaminant.

LIST OF TABLES

Table 2.1-1. Hydrologic Properties

Table 2.2-1. Statistics of Pit Percolation over the First 5000 years used for Transient Simulations.

Table 2.2-2. Comparison of C-14 arrival times and peak concentrations for the steady and four transient flow simulations.

Table 3.1-1. Infiltration Rates (mm/yr) used as Upper Boundary Conditions.

Table 3.1-2. Median Distribution coefficients for Nuclides on Intact Tuff in the Vadose Zone

Table 3.1-3. Median Distribution coefficients for Nuclides within the Pits

Table 3.1-4. Median Distribution coefficients for Nuclides in the Saturated Zone and for the Unsaturated Puye Conglomerate

Table 3.1-5. Disposal Unit Classification and Location

Table 3.3-1. Scale factors to correct generic concentration breakthrough curve for each nuclide and waste category using the base case flow field (5_1_50).

Table 3.3-2. Scale factors to correct generic concentration breakthrough curve for each nuclide and waste category using the highest flow rate (10_5_100).

Table 3.3-3. Scale factors to correct generic concentration breakthrough curve for each nuclide and waste category using the lowest flow rate (1_1_20).

Table 4.3-1. Maximum Ground Water and All Pathways Doses for the PA and CA wastes, Base Case Flow Field.

1. INTRODUCTION

Transport calculations are used to predict the long-term migration rates of water soluble radionuclides at Material Disposal Area G at Los Alamos National Laboratory (LANL) to the main aquifer which underlies the site. The calculations support a radiological performance assessment (PA) and composite analysis (CA) for this low-level radioactive solid waste (LLW) site (Hollis et al., 1997). The PA considers those wastes buried since September, 1988 and projected to be buried through facility closure, which is projected to be in 2044. The CA considers all radioactive wastes buried at the site since its inception in 1957 through facility closure. The distinction of these wastes is driven by regulatory considerations as described in the formal Area G PA/CA (Hollis et al., 1997). The calculations span a 10,000-year time period in order to predict transport to the aquifer for the required 1,000-year compliance period along with a 10,000-year uncertainty period. We examine the flow behavior of the site in order to subsequently make predictions of radionuclide migration from the site through the vadose or unsaturated zone and into the main aquifer which underlies Area G. All calculations presented in this report are run with the finite element code FEHM (Zyvoloski, 1995) which simulates fluid flow, heat transport, and contaminant transport through porous and fractured media.

Before the vadose zone calculations are performed, we study some of the factors that complicate the prediction of flow and transport in the vadose-zone (Section 2.0 of this report). These factors include 1) uncertainties in hydrologic properties for the deeper vadose-zone units (Section 2.1), 2) the effects of transient percolation through the mesa top, including the disposal pits (Section 2.2), 3) the effects of infiltration into fractures (Section 2.3), and 4) the effects of evaporation from the mesa sides, fractures and surge beds (Section 2.4). These studies helped to determine 1) the hydrologic properties that are used for the final vadose-zone flow and transport calculations, 2) that a steady flow model is adequate to perform the PA/CA simulations, 3) that transport through fractures has a minimal effect on the calculation of flux to the saturated zone, and 4) that evaporative effects can reasonably account for the low moisture contents observed in the mesa-top units at the site and justify a small infiltration value. These results support the subsequent assumptions used for predictions of flow and transport of radionuclides through the vadose zone .

The PA/CA calculations are performed in two parts. In Section 3, we compute the transport of nuclides through the vadose zone using a three-dimensional model which describes the complex mesa-top geology of the site. Infiltration is assumed to be steady although the mesa top and two canyons that border Area G receive different infiltration rates. Results for a base case flow field are compared to those for some variations on the flow field as part of an uncertainty analysis. The model incorporates the position and inventories of the thirty-some disposal pits and shafts already located at Area G along with those of future pits and shafts. Two pathways are considered. One is downward migration through the vadose zone to the aquifer. The other is lateral migration to the mesa sides, deposition into the nearby canyon, and subsequent migration through the vadose zone to the aquifer. In these simulations, only three nuclides, C-14, I-129 and Tc-99, reach the water table by either of the two pathways during the 10,000-year period considered in this study. These nuclides are nonsorbing. The remainder of the nuclides have distribution coefficients which retard their migration so that they remain within the vadose zone for a period greater than 10,000 years. Time- and spatially-dependent results for the flux of the three nuclides from the vadose zone feed the saturated zone model.

In Section 4, the continued migration of nuclides into the main aquifer is calculated again using a three-dimensional steady-flow model. This model has a simple configuration, but maintains the spatial and temporal distribution of nuclide flux from the vadose zone. Preliminary results for the PA and CA dose assessments are made. Simulated doses related to aquifer concentrations are several orders of magnitude smaller than DOE performance objectives for LLW sites. In Section 5, we discuss the uncertainties associated with the predictions presented in this report. Finally the conclusions are summarized in Section 6.

2. STUDIES OF SPECIFIC FLOW PROCESSES

2.1 ADDITION OF DEEPER VADOSE ZONE UNITS

2.1.1 Introduction and Problem Description

This introduction summarizes a previous work (Birdsell et al., 1995) in order to explain the need for adding detail to the model of the deep, vadose-zone hydrologic units. To choose appropriate infiltration rates for Area G, simulated saturation profiles for a number of different infiltration rates were compared to site field data. The study used a two-dimensional cross section defined by Krier (Krier et al., 1996) as shown in Figure 2.1-1. We assumed uniform, steady infiltration along the mesa top. Several infiltration rates were applied uniformly over the top of the mesa as shown in Figure 2.1-1: 1.0 cm/yr, 0.1 cm/yr, 0.01 cm/yr, 0.001 cm/yr and 0.0 cm/yr.

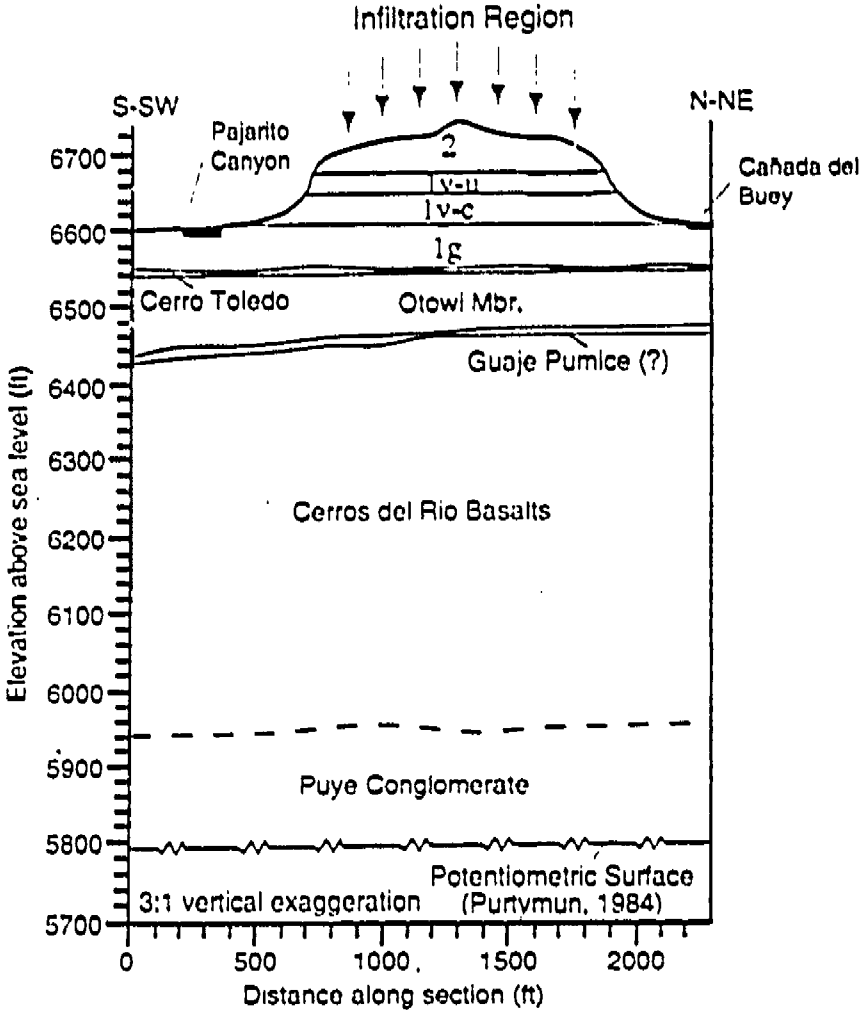

Figure. 2.1-1. Cross section of Western MDA G (based on Krier et al., 1996) used for the two-dimensional simulations.

Evaporation and runoff from the mesa top were indirectly accounted for in the assumed low infiltration rates which are much lower than the average precipitation rate measured at MDA G, 35.6 cm/yr (Bowen, 1990). Mean hydrologic properties (Krier et. al, 1995) were assigned from Units 2 down through the Otowi Member. These properties are shown in Section 2.1.2. Originally,

hydrologic properties for the Otowi Member were assigned to the Guaje Pumice, the Cerros del Rio basalts, and the Puye Conglomerate as no information was available for those units.

Figure 2.1-2 shows calculated steady-state saturation profiles at the center of the mesa for the 5 infiltration rates discussed above. The measured in-situ saturation data are also shown. The simulation results are compared to saturation data from Unit 2 down through the Otowi Member. Here we see that the shape of the curves mimic the shape of the data (e.g. saturations decrease from Unit 2 to Unit 1v-u and then increase again in Unit 1v-c, etc.). However, no single infiltration rate fits through the entire set of saturation data. Results for the lowest infiltration rates (0.001 and 0.0 cm/yr) most closely match the site saturation data in Units 2 and 1v-u, the two mesa-top units. Higher infiltration rates (0.1 and 0.01 cm/yr) are needed to match the saturation data from Units 1v-c and 1g, and an even higher rate (~1 cm/yr) is needed to match the data in the Cerro Toledo and Otowi Member.

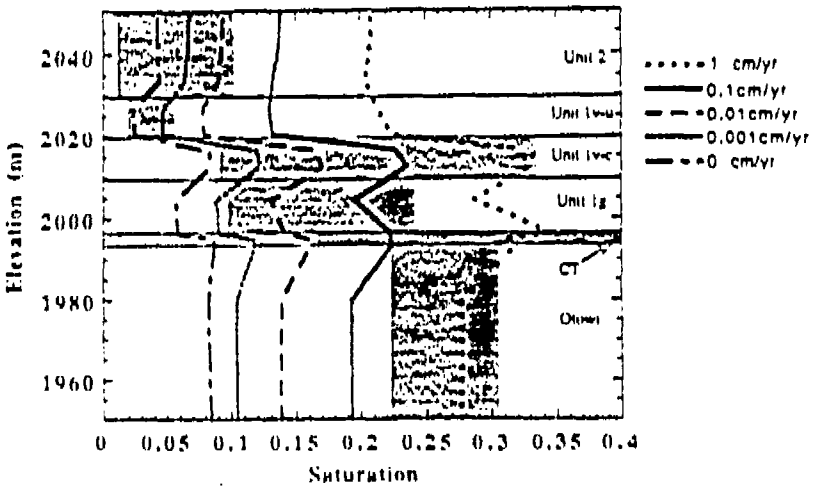

Figure 2.1-2. Comparison of site data (gray boxes) to calculated steady-state saturation profiles for several infiltration rates. Calculated profiles are located at the center of the cross section.

In the current study, we build upon the previous study by assigning hydrologic properties to the three deepest vadose-zone units, the Guaje Pumice, the Cerros del Rio Basalt and the Puye Conglomerate, to test the effect of the addition of these layers on flow (specifically its effect on the calculated saturation in the Otowi Member) and on transport at the site. This addition was suggested by a DOE Peer Review Committee (Hollis et al., 1997) after reviewing a previous draft of the PA.

2.1.2 Hydrologic Properties and Their Effects

As mentioned above, the mean hydrologic properties supplied by Krier et al. (1996) are used for Units 2 down through the Otowi Member. Unsaturated hydrologic parameters for a single core of Guaje pumice were measured and added to the model. These properties, as well as those used for the deeper units, are given in Table 2.1-1. In addition, estimates of in-situ saturation in the Guaje Pumice bed are now available. Gravimetric moisture measured for samples from the Gauje Pumice bed in wells 54-1015 and 54-1016 (Krier, personal communication) range from 13.7% to 28.3%. Using a bulk density and porosity measured on a different sample (Springer, personal communication), this converts to saturations ranging from 0.17 to 0.34.

Table 2.1-1. Hydrologic Properties

Unit	Ksat (cm/s)	porosity	van Genuchten θ_r, α (cm^{-1}), n
Unit 2[a]	4.27×10^{-4}	0.481	0.013, 0.0060, 1.890
Unit 1v-u[a]	1.48×10^{-4}	0.517	0.002, 0.0030, 1.932
Unit 1v-c[a]	1.67×10^{-4}	0.509	0.009 0.0033,1.647
Unit 1g[a]	1.88×10^{-4}	0.480	0.006, 0.0053, 1.745
Cerro Toledo[a]	8.65×10^{-4}	0.473	0.008, 0.0152, 1.506
Otowi Member[a]	2.49×10^{-4}	0.435	0.0188, 0.0059, 1.713
Guaje Pumice[b]	1.5×10^{-4}	0.667	0.0, 0.00081, 4.0264
Puye Formation[d,e]	4.6×10^{-3}	0.25	0.045, 0.145, 2.68
Cerros del Rio basalts[c] *(matrix only)*	9.7×10^{-5}	0.228	6.6×10^{-6}, 0.0384, 1.474
Cerros del Rio basalts[c] (fracture properties) *(equivalent continuum)*	9.7×10^{-5} 9.7×10^{2}	1×10^{-4} 1×10^{-4}	6.6×10^{-6}, 0.0384, 1.474 3.0×10^{-6}, 0.0384, 1.474

[a]Mean values from Krier et. al, 1996, [b]E. Springer (personal communication), [c]Bishop (1991), [d]Purtymun (1984), [e]Carsel and Parrish (1988).

Very little hydrologic data are available for the Cerros del Rio Basalts or for the Puye Conglomerate. Samples collected from the basalts display wide variability (Turin, 1995) ranging from extremely dense with no apparent porosity, to highly fractured, to so vesicular as to appear foamy. This variability leads to large uncertainty in calculating flow and transport through this unit because, without further characterization, we cannot predict whether water flow in this unit is controlled by the matrix or the fracture hydrologic properties.

Our method for modeling the basalt has evolved as our understanding of the system sensitivity to this unit's properties has increased. Originally, the basalt was modeled as an intact matrix material with properties based on analysis of a vesicular basalt located beneath Idaho National Engineering Laboratory (Bishop, 1991) (Table 2.2-1, *matrix only*). The air entry pressure, $1/\alpha$, for the matrix basalt material is significantly greater than for the overlying pumice in our study. Also the saturated hydraulic conductivity is slightly lower. These two factors lead to significant lateral flow in the overlying pumice bed which yields high pumice saturations and increased saturation in the Otowi Member as shown in Figure 2.1-3. The saturation in the Guaje Pumice bed reaches a value of 0.8 which is significantly higher than the data suggest.

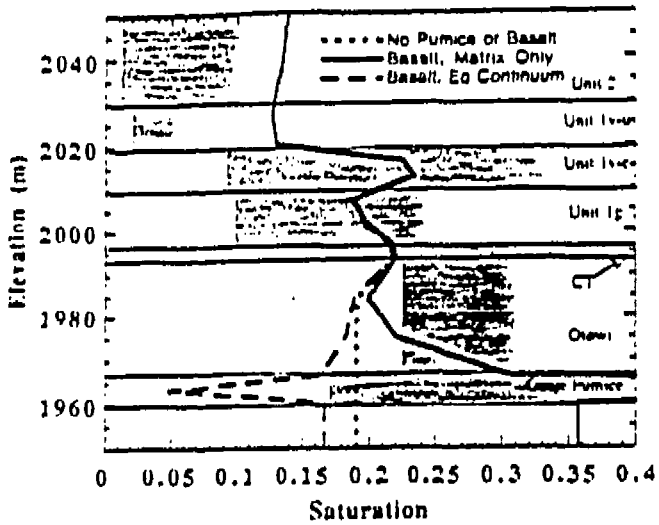

Figure 2.1-3. Comparison of site data (gray boxes) to calculated steady-state saturation profiles at 1 mm/yr using various hydrologic properties for the Guaje Pumice and the Cerros del Rio Basalts. Calculated profiles are located at the center of the cross section.

In the two-dimensional cross section (Figure 2.1-1) the water flows down dip through the pumice bed until it encounters water entering from Pajarito Canyon where it is diverted vertically. The position of this diversion is highly sensitivity to the infiltration rates through the mesa top and in the two canyons. Figure 2.1-4 shows results for particle tracking calculations performed on the two-dimensional cross section. In Figure 2.1-4.a, particles released from the center of the mesa travel vertically to the Guaje Pumice then downdip laterally in the pumice bed. Their lateral movement ceases, and they move vertically again when they encounter the effects of flow coming in from Pajarito Canyon. This is demonstrated in Figure 2.1-4.b where particles are released in Pajarito Canyon as well as from the mesa top using the same flow field. The particles from the canyon travel vertically and laterally to the location where the mesa top particles stop traveling laterally, thus indicating the divide for the water coming from the two source locations. All of the particles are forced downward at the location where the mesa-top and canyon flow fields merge. The no-flow side boundary plays an important role in this result. Figure 2.1-4.c, to be discussed later, shows the effects on particle transport when the fracture permeability of the basalts is increased. In the three-dimensional model of the site, the pumice bed dips toward the south-west. Simulated flow runs laterally toward the south-west end of the grid where it is diverted downward along the no-flow western boundary. This is demonstrated with the plume shown in Figure 2.1.-5.a.

Because the lateral flow in both the two- and three-dimensional simulations is so strongly controlled by the no-flow side boundary conditions, the behavior is considered to be unsatisfactory. Our uncertainty about the flow field in these two layers prompted the sensitivity study performed by Soll that is presented in Appendix 1. Soll considered a three layered system consisting of the Otowi Member, the Guaje Pumice, and the Cerros del Rio Basalt. Various system characteristics were varied such as the thickness, slope and hydraulic conductivity of the pumice bed and the hydraulic conductivity of the basalt layer to determine which factors most strongly affect lateral flow in the pumice bed. The simulations show that the basalt conductivity has the strongest influence on lateral flow. With the matrix properties shown in Table 2.2-1, the basalt acts as a barrier thus diverting flow laterally in the overlying pumice bed. By increasing the

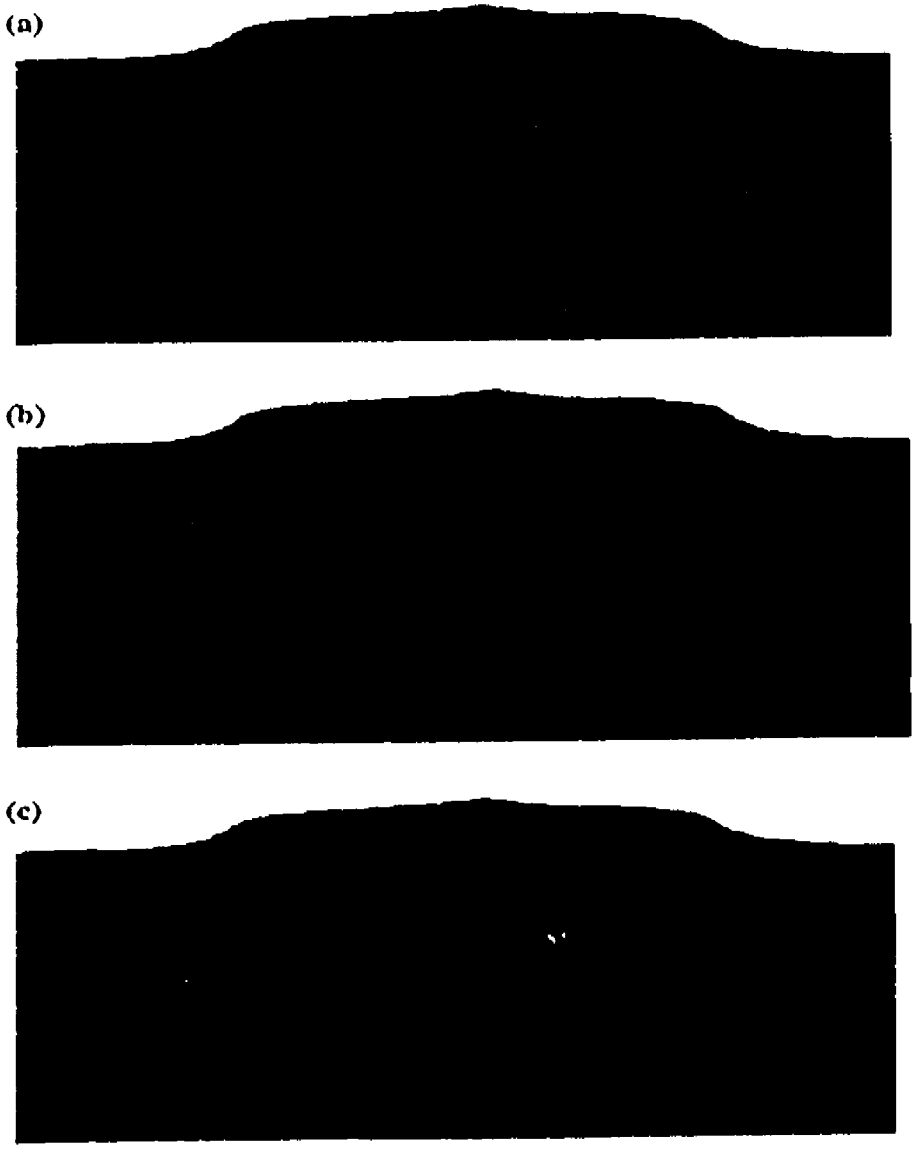

Figure 2.1-4. Simulated solute pathways for the two-dimensional cross section shown inFigure 2.1-1, a) particle release only at mesa top, matrix-type basalt properties, b) particle release at mesa top and canyon floor, matrix-type basalt properties, c) particle release at mesa top, fracture-type basalt properties.

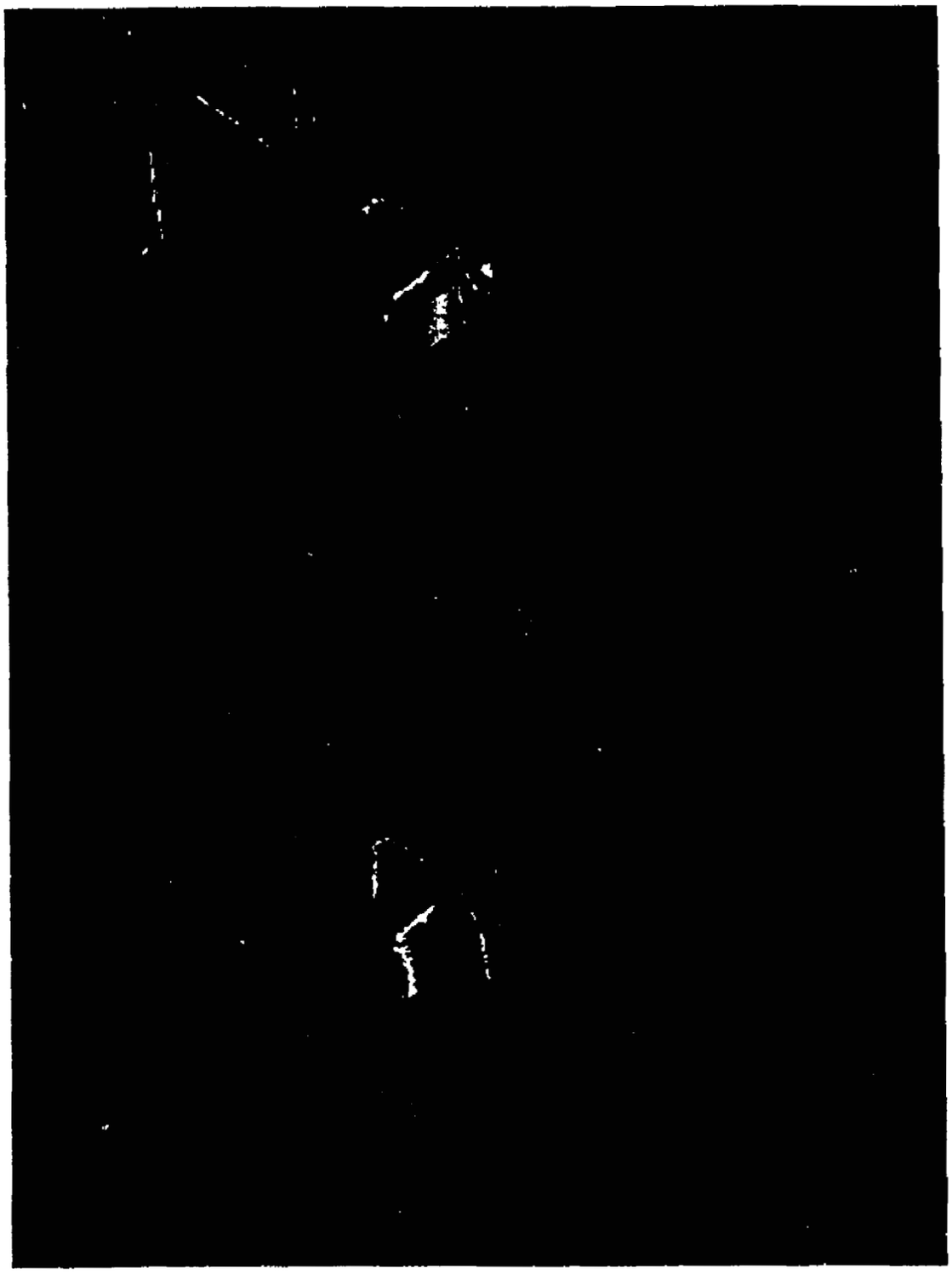

Figure 2.1-5. Contaminant plume with and without lateral flow along the Guaje Pumice Bed.

basalt conductivity or adding fracture characteristics, fluid can more readily enter the basalt thus minimizing the diversion. Sensitivities to the thickness, slope, and conductivity of the pumice layer were secondary.

We expect that dense, unfractured basalt acts as a barrier which promotes lateral flow in the pumice bed in some places while fractured basalt acts as a conduit for fast vertical flow in others, but the spatial distribution of basalt properties at this site is unknown. There is probably some lateral transport in the Guaje Pumice bed with a corresponding increase in the saturation of the overlying Otowi Member. However, this is a conceptualization and cannot be quantified with available data. Therefore, we have chosen to assign equivalent continuum properties that are dominated by fracture flow to the basalt. This modification leads to fast travel times through the basalt and eliminates lateral flow in the pumice layer, thus resulting in conservative transport results. However, as shown in Figure 2.1-3, this also yields pumice saturations that are lower than the measured values and decreases the calculated saturation in the Otowi Member. The matrix only and equivalent continuum curves shown in Figure 2.1-3 represent the end members for flow regimes in these deeper units: the basalt acting as a barrier to flow and the basalt acting as a conduit. Because the pumice saturation lies between these two end members, our hypothesis that the behavior of the basalt lies between these two extremes is supported.

In order to obtain the fast basalt travel times, the basalts are treated as an equivalent continuum medium (Klavetter and Peters, 1986) made up of both fractures and matrix material (Table 2.2-1, *equivalent continuum)* . With the equivalent continuum approximation, a set of matrix and fracture characteristic curves are combined into a single set of characteristic curves which represent matrix flow at low saturations and fracture flow at higher saturations. The fractures are assigned a high permeability and porosity which favor vertical flow from the pumice into the basalts. This serves to minimize lateral flow within the pumice as explained previously. With this set of parameters in the model, a permeability barrier to vertical flow and transport at the top of the basalt is virtually impossible to model. Figures 2.1-4.c and 2.1-5.b respectively show the resulting two-dimensional particle tracking profile and a three-dimensional plume using these modified basalt properties. The flow and transport are effectively prescribed to occur only in the fractures of the basalt by specifying a fracture-like porosity of 10^{-4} for the basalt equivalent continuum. Since pore velocity increases as porosity decreases for the same Darcy flux, this yields rapid groundwater travel times of between 1 and 5 years through the basalts. Figure 2.1-6 shows flux versus time curves at the water table for the two plumes in Figure 2.1-5. This result shows that using the fracture-dominated, equivalent continuum basalt properties yields conservative transport results through the vadose zone. These basalt properties produce conservative transport results in the saturated zone as well. The dose assessment considers saturated zone concentrations at a location 100 meters down gradient from the Area G fence line, as is discussed further in Section 4.3.3. That location is east of Area G. As shown in Figure 2.1-5, the plume that travels downward lies closer to the eastern end of Area G. This plume would reach the monitoring point more quickly and undergo less dilution and dispersion than the plume that flows laterally toward the west along the unsaturated pumice bed. Using the equivalent continuum, basalt properties is therefore a good approach for handling the uncertainty associated with this unit's properties.

Adding additional conservatism to the model, the porosity of 10^{-4} may be up to two orders of magnitude lower than the fracture porosity of the Cerros del Rio basalts (Rogers, personal communication) leading to simulated ground water travel times up to 100 times faster than might actually occur in this unit. With better characterization of the Cerros del Rio basalts, less conservative travel times could be simulated in which solute retarding processes of matrix flow and transport, diffusion from fractures to matrix material, and lateral diversion at the pumice/basalt interface are incorporated in the model.

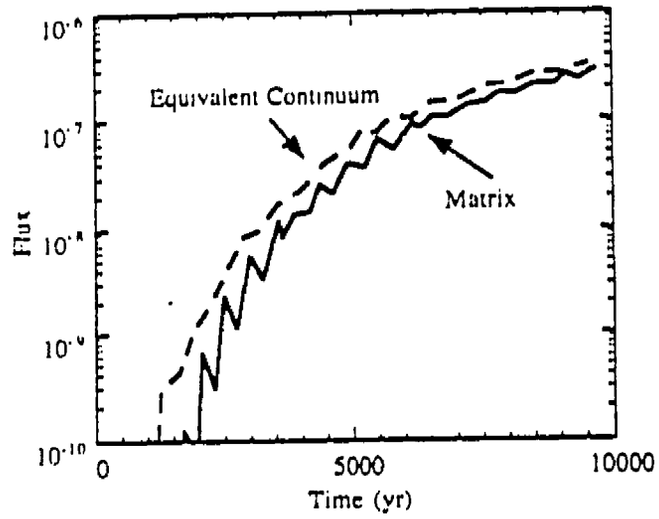

Figure 2.1-6. Flux vs. time curves at the water table for the plumes shown in Figure 2.1-5. The equivalent continuum basalt properties give more conservative transport results.

Although hydrologic properties for the Puye Conglomerate are unknown, we expect flow through this unit to be similar to that through a coarse sand. Therefore, we estimate properties which lead to a conservative (faster than expected) travel time through the Puye Conglomerate that is not virtually instantaneous, as it is in the basalts. The layer is modeled as a coarse sand (Carsel and Parrish, 1988) with the porosity reduced by 60% (from 0.43 to 0.25) to account for cobbles and gravel that reduce the available pore space.

2.2 EFFECTS OF TRANSIENT PERCOLATION

The near surface moisture balance in the mesa tops on the Pajarito Plateau is controlled by alternating periods of episodic infiltration and normal drying cycles (Rogers et al., 1997, Turin et al., 1995). Results presented by Springer (1996) indicate that such episodic events lead to transient percolation rates through the disposal pits at Area G. In this section the system response to transient flow is estimated by applying transient percolation rates to the pits as well as to the undisturbed, upper surface of the mesa. The effects of the transients on the saturation distribution throughout the mesa and on radionuclide transport to the base of the Otowi Member are examined with these simulations. The value of such calculations is to evaluate the efficacy of the steady state assumption against the transient conditions. Namely, these calculations serve to investigate whether the steady flow approximation conservatively predicts contaminant transport rates even though moisture actually enters the system episodically.

An assumption of this study is that if fluctuations in flow are damped at depth and if cumulative contaminant flux for the transient runs is similar to that for the steady flow run, then the subsequent dose calculated from the transient flow and steady flow simulations will be similar. The purpose is to determine whether the transient and steady results are essentially the same. If the results prove to be similar, then steady flow simulations can be run to address compliance issues. Use of a steady flow field for these simulations is desirable because the time step size for the transient flow runs is limited by the yearly or possibly daily fluctuations in the flow field. This time step limitation makes the transient flow runs far more computationally intensive than the steady flow runs. As a result, it would prove difficult to complete the entire suite of simulations required for the Area G PA using transient flow fields.

2.2.1 Modeling Approach

In order to study the effects of transient percolation on flow and transport at Area G a number of transient flow simulations are run, and the results are compared to those for a steady flow simulation which uses the average percolation rate. Moisture profiles at various depths and solute transport rates are compared. C-14 is one of the fastest moving nuclides because it is nonsorbing. Cumulative breakthrough to the Guaje Pumice for this nuclide under steady and transient flow conditions is calculated. The simulations are performed for 5000 years which proved to be a long enough time period for saturations to dampen at depth and for the cumulative breakthrough curves to level out.

The computational grid for these studies is also based on the north-south two-dimensional cross section of Krier (1996) shown in Figure 2.1-1. This study also uses the hydrologic properties shown in Table 2.1-1 with the "matrix only" properties for the Cerros del Rio Basalts. The calculations were performed prior to the choice of the equivalent continuum basalt properties for the final vadose-zone flow model, as described in Section 2.1.2. However, the basalt properties are not of great importance here because the analysis is based on breakthrough at the top of the Guaje Pumice bed. The extensive lateral flow in the pumice layer which occurs for the given pumice and basalt properties complicates the interpretation of breakthrough to the deeper layers or to the water table. If contaminant fluxes compare well at this horizon, they should compare well at deeper horizons.

In this study, it is assumed that fracture flow is not induced, even during high flow years, because sustained high flow rates would be required to increase the very low saturations at the site to near saturated conditions. Therefore fracture properties are not considered. This issue has been further studied by Orr through some one-dimensional modeling and is presented in Appendix 2. The study looks at steady and transient flow through this same system using a dual permeability approach (Zyvoloski, 1995) which accounts for fractures in the two upper units (Unit 2 and Unit 1v-u). With these studies, we find that groundwater travel times to the top of the basalt layer through the fractured system do not vary by more than 100 years from the unfractured system, even when applying transient infiltration rates. Therefore, the two-dimensional calculations are performed with matrix only properties.

Although the matrix only properties may seem to misrepresent the system and limit the study, many studies performed for the Yucca Mountain Site Characterization Project (Klavetter and Peters, 1984; Wang and Narisimhan, 1987; Montazar and Wilson, 1984) indicate that high threshold matrix saturations (often close to full saturation) are required before the induction of fracture flow in volcanic tuffs. With in-situ saturations generally less than 10% in the upper two units of the mesa, which are the only highly fractured tuff units, it seems unlikely that transient pulses would elevate matrix saturations high enough to reach the threshold values. Also, Soll's (1995) simulation results for flow in a single fracture indicate that extremely high flow rates or ponded conditions are required to sustain fracture flow in the Bandelier Tuff. This study also concluded that water flowing from unsaturated crushed tuff into fractured tuff, as is the case of water flowing through the disposal units, is unlikely to induce fracture flow.

The system starts with an initial saturation distribution that results from long-term steady infiltration at 1 mm/yr applied uniformly over the top of the mesa. The simulation is then modified to include the five disposal pits shown in Figure 2.2-1. Transient percolation, with an average of 5.5 mm/yr into the disposal units and an average of 1 mm/yr over the undisturbed mesa top, is applied to the previous steady flow field. The steady runs use a flow field that has equilibrated with the 5.5 mm/yr pit infiltration rate and the 1.0 mm/yr infiltration rate for the undisturbed mesa top.

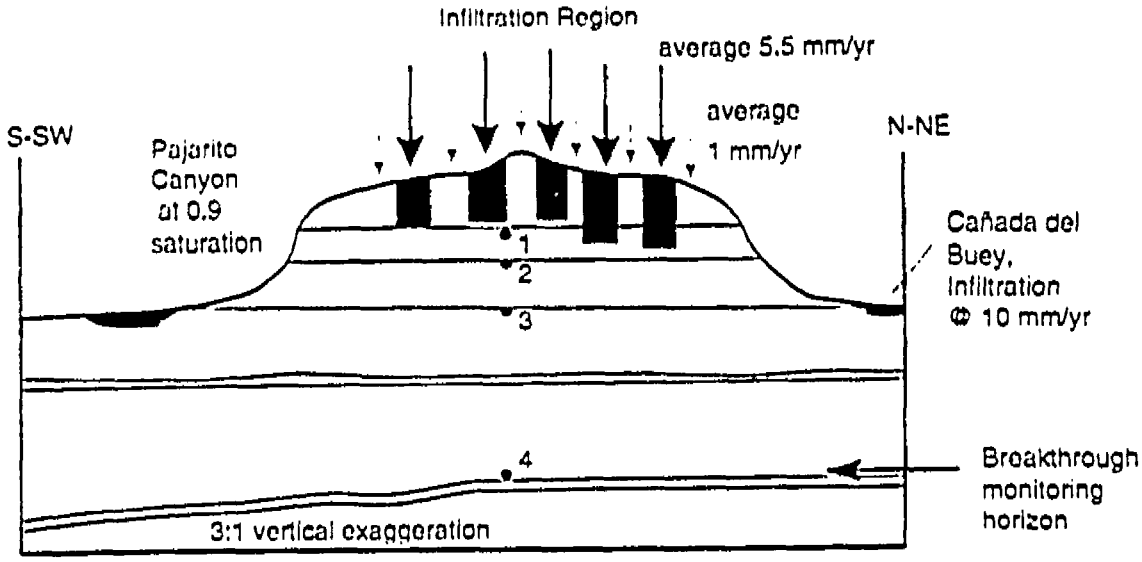

Figure 2.2-1. Two-dimensional cross section used for numerical simulations, modified to indicate five waste disposal pits.

The transient realizations of percolation were determined by the water balance algorithm from the SPUR model (Wight and Skiles, 1987). Precipitation input used a stochastic weather generator with precipitation parameters derived from the Los Alamos gauge at TA-6 (just south of TA-59). The average annual precipitation at TA-6 is approximately 457.2 mm (18 in.) as opposed to the 355.6 mm (14 in.) average annual precipitation at Area G (Bowen, 1990). The pit had a depth of 15.2 m (50 ft.). The upper 0.1 m was topsoil, and the remaining depth was crushed Bandelier Tuff. A plant rooting depth of 0.457 m (18 in.) was assumed. The percolation response was estimated by performing 100 simulations that were 10000 years long using the stochastic weather generator to provide input. More details on the model and the parameters are available in Springer (1996).

Each realization of pit percolation extends for 10,000 years and has an average percolation rate close to 5.5 mm/yr with most years (approximately 72%-75%) having no net percolation. Maximum annual percolation rates are near 100 mm/yr. A yearly transient was applied to the upper surfaces of the pits. A similar transient percolation rate but of decreased magnitude to average 1 mm/yr was applied to the undisturbed mesa-top infiltration regions. Only four of the one hundred realizations were actually run: Cases 1, 2, 6, and 17. Cases 6 and 17 were suggested by Springer. Case 6 has ten consecutive years of non-zero flow, and Case 17 has the highest number of years with non-zero flow. Some statistics for these four cases are given in Table 2.2-1. The statistics apply for 5000 years rather than the full 10,000 years because that is the duration over which these transient studies were performed.

Transport parameters are required for the calculations of C-14 migration. Recent studies by Conca (1992) show that the diffusion coefficient decreases with decreasing saturation. The diffusion coefficient was modeled in this fashion and decreases parabolically from 10^{-9} m^2/s at full moisture to 10^{-15} m^2/s at a moisture content of 0.001. The dispersivity is 1 m in the vertical direction and 0.1 m in the horizontal direction.

Table 2.2-1. Statistics of Pit Percolation over the First 5000 years used for Transient Simulations.

	Case 1	Case 2	Case 6	Case 17
Average Pit Percolation Rate (mm/yr)	5.49	5.27	5.50	5.81
Maximum Pit Percolation Rate (mm/yr)	99.2	88.1	90.8	105.4
Percentage of years with non-zero Percolation	26.4%	26:1%	26.4%	27.4%

2.2.2 Transient Flow Results

Simulated saturations at four locations are examined for 3000 years in order to understand the propagation of transient infiltration through the mesa. These locations represent (1) the top of Unit 1v-u, (2) the top of Unit 1v-c, (3) the top of Unit 1g, and (4) the base of the Otowi Member, as shown in Figure 2.2-1. The time dependent saturation plots are given in Figure 2.2-2.

Recall that for the transient calculations the initial flow field is the result of a steady 1-mm/yr infiltration rate. At each horizon, we can see the saturation front (caused by the higher pit infiltration rate) arrive. There is scatter on the order of 200 years for the arrival time of this front at each horizon due to variations in the applied transient infiltration rate. Case 1 has an average infiltration rate near 10 mm/yr for the first 100 years, which is reflected in the early arrival time of the saturation front at the various depths for this case. Distinct transient responses in saturation are seen for the three more-shallow locations with fluctuations less than 3%. However, these fluctuations are damped near the base of the Otowi Member, which is directly above our contaminant flux monitoring horizon. Once the initial front has arrived at each level the mean saturation for each transient simulation is very close to the mean for the steady simulation. The steady simulation has equilibrated with the pit infiltration rate of 5.5 mm/yr therefore the arrival of the saturation front is absent in the steady solution. As shown in Table 2.2-1, Case 17 has the highest average flow (5.81 mm/yr) and Case 2 has the lowest average flow (5.27 mm/yr). This is reflected as slightly higher and lower average saturations respectively as seen in Figure 2.2-2.

The percolation estimates used in these simulations are intentionally conservative (high). Actual percolation rates are expected to be lower based on lower precipitation rates and deeper rooting depths. Springer's (1996) base case pit percolation estimate has evolved as more data have become available. His current estimate of the mean pit percolation rate is 0.99 mm/yr based on a 1-m rooting depth. In a previous study (Birdsell et al., 1995) the effects of applying various single 5-year pulses to various steady flow fields were examined for this same cross section. That study showed that with a lower background flow rate (0.01 mm/yr), damping of an increased flow pulse (10 mm/yr) occurred at higher elevations within the mesa top than for the same pulse applied to a 1-mm/yr steady flow field. This implies that transient pulses should dampen at higher elevations for lower (more realistic) percolation estimates for the site.

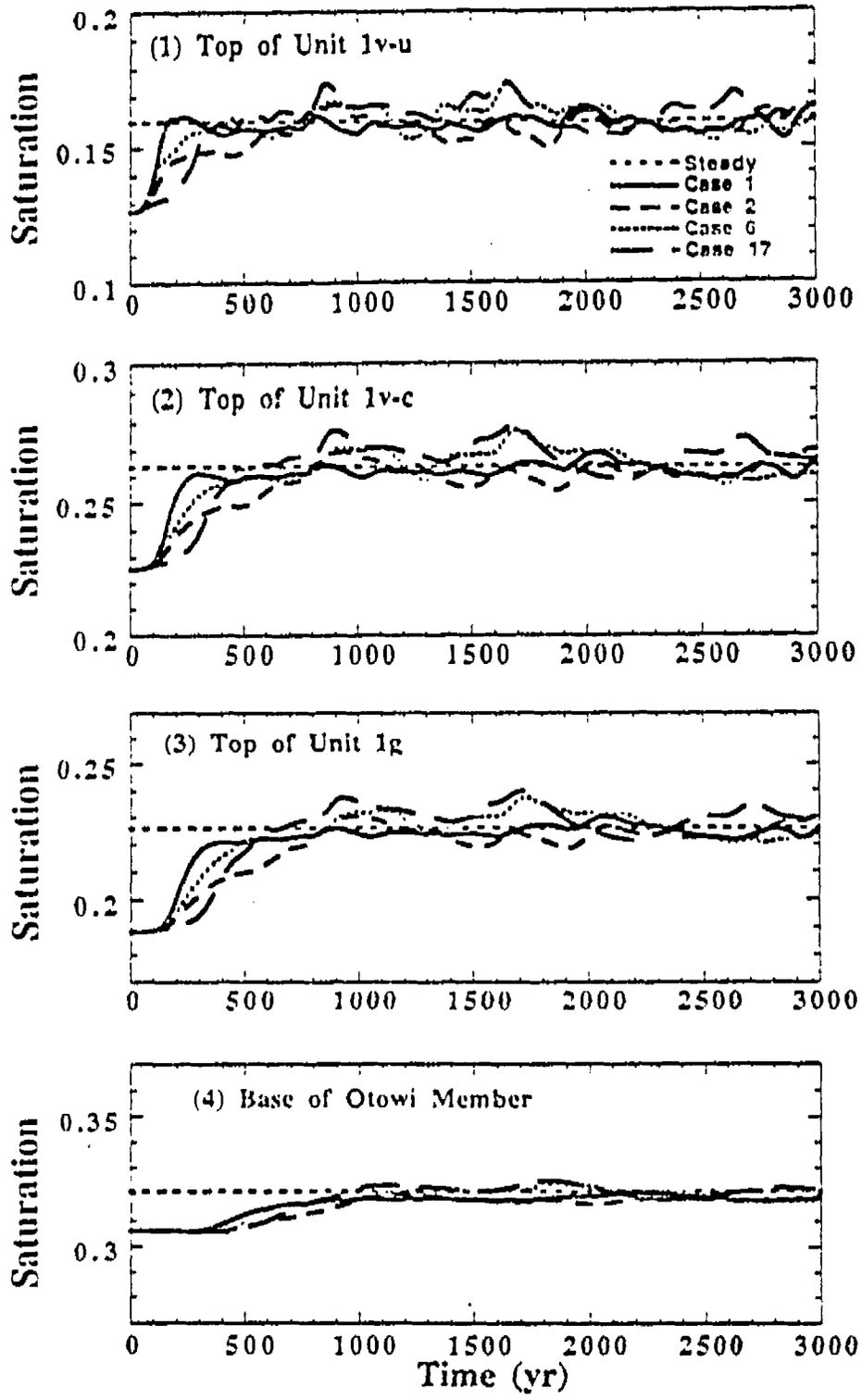

Figure 2.2-2. Variation in saturation with time for the steady and four transient simulations at various depths.

2.2.3 Transient Transport Results

Figure 2.2-3 shows the source term for the flux of liquid-phase C-14 from the waste package to the disposal units. It assumes that the steady flow rate of 4 mm/yr calculated to be passing through the disposal unit (Springer, 1995) is also the percolation rate through the waste package (Vold, 1995). We assume this is an adequate representation of the source for these calculations since the water velocity through individual waste packages is unknown and expected to be highly variable. Nearly the entire C-14 inventory (99%) is released over an 80-year period. If the source term were recalculated to account for the higher percolation rate, this mass would be released over a shorter time frame of approximately 60 years, since the release is proportional to the ratio of the flow rates. In either case, most of the mass is released from the waste packages over a time frame that is short compared to the simulation time. The flux of C-14 from the disposal units (pits) is dependent on the water velocity through the pits and is calculated self-consistently with respect to the transient infiltration in the simulations. Solubility limited species such as Uranium may have significantly higher fluxes from the waste to the disposal unit when the water flow rate is high, but these species have long travel times (Birdsell et al., 1995) compared to the 10,000-yr uncertainty period.

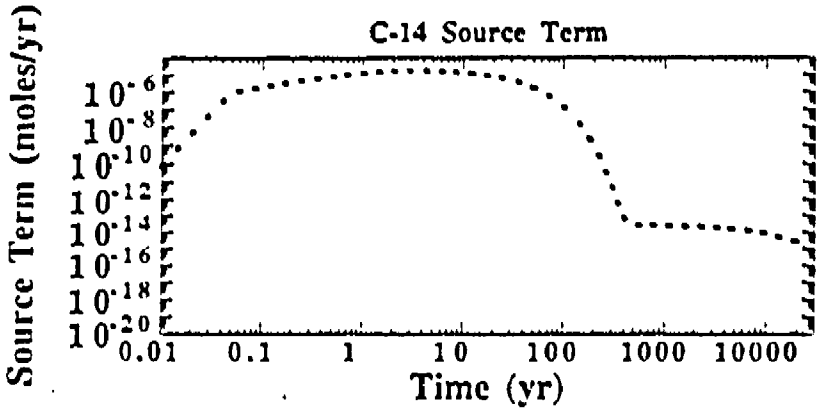

Figure 2.2-3. Source term for the C-14 decay chain based on pit infiltration rate of 4 mm/yr.

Figure 2.2-4 shows the C-14 cumulative breakthrough curves for the steady-flow case and the four transient flow cases. These curves represent the total number of moles that have reached the Guaje Pumice (see Figure 2.2-1). There is some scatter in the arrival of mass to the Guaje Pumice but the curves converge. Table 2.2-2 shows values for time of first arrival at the pumice layer (taken as 1% of the total moles at 5000 yrs) and for the total moles to reach the pumice at 5000 years. Earliest breakthrough occurs for the steady flow simulation because the flow field is in equilibrium with the higher pit infiltration rate. First breakthrough for Case 1 proceeds the other transient cases because it has a higher average flow rate for the first 100 years. The greatest cumulative flux at 1000 years is for the steady flow case because the flow field has already equilibrated with the higher pit percolation rate. The cumulative moles reaching the pumice layer at 5000 years for the transient simulations agree within 3% to that calculated for the steady flow case with the steady flow case having the highest value. The steady solution provides a conservative estimate for both the time of first arrival and for the cumulative breakthrough. From a performance standpoint, all of the simulations behave similarly and the overall agreement is considered to be very good.

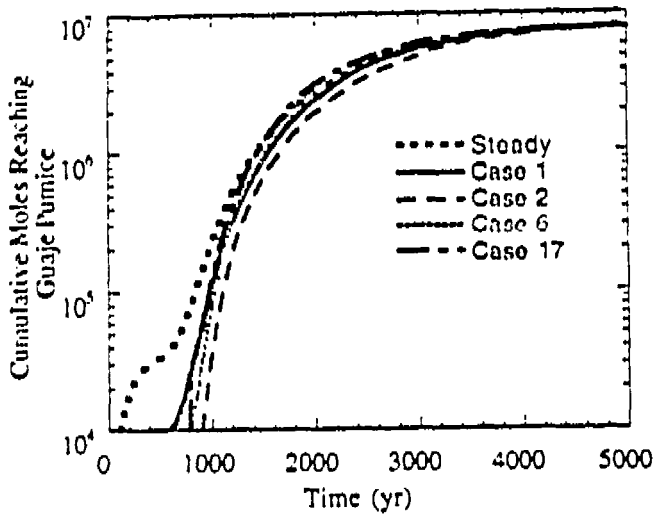

Figure 2.2-4. Cumulative breakthrough curve for C-14 to the Guaje Pumice for four transient infiltration simulations and one steady infiltration simulation.

Table 2.2-2. Comparison of C-14 arrival times and peak concentrations for the steady and four transient flow simulations.

Case	First Arrival (yr)	Cumulative Moles to Pumice at 5000 years
Steady	800	8.05e6
Case 1	940	7.81e6
Case 2	1080	7.55e6
Case 6	1000	7.88e6
Case 17	950	7.99e6

2.2.4 Summary of Transient Results

In order to study the effects of transient percolation on flow and transport at Area G four transient flow simulations are run, and the results are compared to those for a steady flow simulation which uses the average percolation rate. Prior to performing these calculations on the two-dimensional cross sections, a set of preliminary one-dimensional calculations were performed to examine whether fractures needed to be explicitly accounted for. These preliminary calculations were performed using the dual permeability model which permits different fluxes in the fractures and matrix. The dual permeability formulation is also appropriate for these scoping calculations related to the effect of transient percolation because it does not force capillary pressure equilibrium between the matrix and fracture material. The results of these dual permeability transient flow scoping calculations show for the fracture characteristic curves derived from parallel plate theory of fracture flow, flow and transport in the upper layers of this system tend to remain in the matrix material. Simulations of steady state and transient percolation with and without the dual permeability formulation all yielded approximately the same travel times.

The investigation of transient percolation flux was extended to the two-dimensional cross section. For these calculations, the matrix, hydrologic properties were used, thereby neglecting rapid transport in fractures. Moisture profiles at various depths are compared. The simulations show that fluctuations in infiltration produce distinct responses in saturation (less than 3%) through Unit 1g

that dampen at the base of the Otowi Member. Damping would presumably continue as the water percolates through the deeper units toward the water table.

Transport of C-14 is modeled along with the transient flow in the two-dimensional system. The steady flow solution provides a conservative estimate for both the time of first arrival and for the cumulative breakthrough of the C-14. From a performance standpoint, all of the simulations behave similarly and the overall agreement is considered to be very good. The simulations are for a conservative radionuclide and are based on an average percolation rate which is thought to be quite high for this site. Higher sorption coefficients delay the arrival time of the contaminant but yield results having similar spread in arrival time. Lower percolation rates are expected to produce results with even better agreement.

The one- and two-dimensional modeling of transient and steady state percolation with or without the dual permeability formulation support the use of matrix properties and the steady flow assumption when calculating radionuclide transport at Area G. However, the investigation of the role of fractures was limited in scope to a set of characteristic curves based on the theoretical parallel plate fracture model. We must point out that other than the deep basalt only the upper two geologic units, Unit 2 and Unit 1v-u, are considered to be significantly fractured. The disposal pits are excavated through Unit 2, therefore waste can only really travel in fractures through Unit 1v-u until it reaches the basalt. These studies have shown that the matrix material damps transient pulses. Even if transient pulses propogate through the fractures in Unit 1v-u, the tuff units below will most likely attenuate them. Additional support for our conceptual model of very little sustained fracture flow is further supported with the study of flow in a single fracture that is described in the following section.

2.3 FRACTURE FLOW

2.3.1 Single Fracture Modeling

We have performed another study using FEHM to analyze the influence of different characteristics of a fractured system on the movement of fluids in the subsurface. The study focuses on conditions that are relevant to our local system, particularly the influence of fracture coatings and fracture fills on infiltration of water, and on the extent of matrix-fracture communication. This work is described in full by Soll (1995) but the results are summarized here as they pertain to the development of the flow model for MDA G.

In an attempt to isolate behaviors, we have chosen a system that is a single vertical fracture centered in an otherwise uniform block of matrix (Figure 2.3-1). There are four parts of the system: the matrix, the fracture, the fracture coating and the fracture fill. The matrix characteristics represent Bandelier Tuff properties from Mesita Del Buey, Unit 1v-u. The fracture aperture and spacings are average values from local measurements (Krier et al., 1996). In this study the fracture is given the hydrologic properties of a highly porous and highly permeable sand. This assumption allows us to study a fractured system using a porous media simulator, but the results must be interpreted in context with field observations and measurements.

The system is discretized such that a thin coating layer can be assigned along the walls of the fracture. For simulations where no coating is present these elements are assigned matrix properties, thus maintaining the 5-mm fracture aperture through all simulations. Fracture fill can be emplaced by replacing the fracture's hydrologic properties with fill properties for some given length of the fracture. When present, fracture coatings and fracture fills are assigned clay parameters. We use clay parameters from the literature because there are no values available for the local clays and caliches.

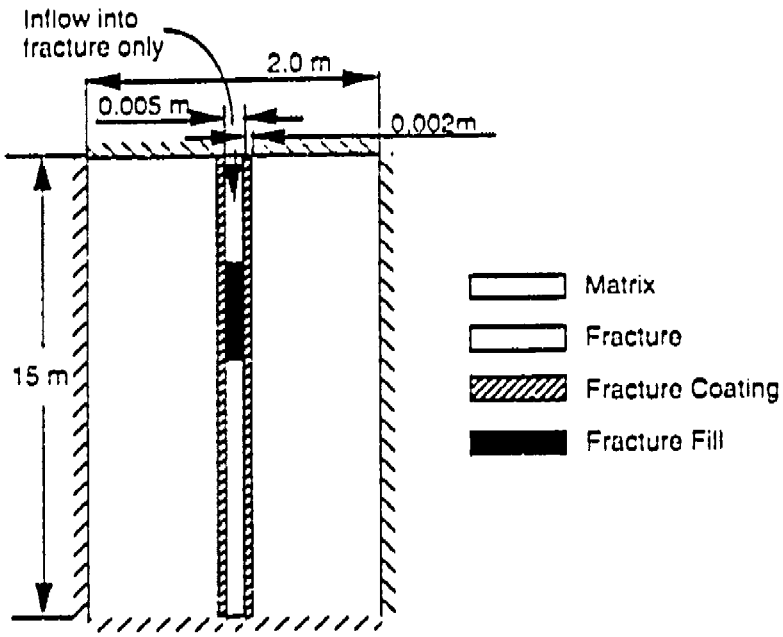

Figure 2.3-1. System Configuration for Fracture Flow Study.

Two different inflow conditions are used at the top of the fracture. One inflow condition assumes a constant influx, at a rate of 5 cm/day, which we considered to be representative of an extreme event for a single day. However, this inflow rate was applied for the entire time period of the simulations, often up to 100 days. The other inflow condition used was a ponded condition at the top of the fracture applied for 0.5 days, followed by removal of the source. This was effectively an infinite source of water for 0.5 days with infiltration rates controlled by the fracture-matrix system. Both of these inflow conditions result in an amount of water entering the system in a matter of days that far exceeds the amount of precipitation seen at Los Alamos over a period of years. These extreme conditions allow us to focus on absolute worst cases.

The most dominant observation from the simulations is that in all but the most extreme infiltration events, fractures in the Bandelier Tuff of MDA G do not appear to provide a 'fast flow path' for liquids. Even under extremely high infiltration events, fractures with no coatings or fills are not able to carry liquids very far, and the invading saturation front looks very similar to that observed in a non-fractured system with point injection.

We found that the effect of a coating along the walls of the fracture is dependent on the relative conductivities of the coating and the matrix. A coating with only 2 orders of magnitude less conductivity than that of the matrix does virtually nothing to prevent liquid in the fracture from being imbibed by the matrix. When there is a larger (4 orders of magnitude) reduction in conductivity at the fracture-matrix interface, water is strongly channeled in the fracture. Any conductivity reduction acts to spread the infiltrating front further down the matrix, allowing water to penetrate deeper during an infiltration event. However, a discontinuity in the low conductivity coating interrupts the fast flow down the fracture. This suggests that the high capillarity of the Bandelier tuff will rapidly draw water into the matrix near any break in a fracture coating. The simulations also show that fracture flow driven by the ponded boundary condition ceases once the source is removed.

When we consider the role of fills in affecting water infiltration, we find that fractures that are filled at the exposed surface of the fracture are effective barriers to inflow into the fracture. These observations are in agreement with Rosenberg et al. (1993). Fills below the surface are effective barriers to continuous flow down the fracture. With no coating or only minimal conductivity reduction above the fill, water entering the fracture is simply imbibed into the matrix and proceeds down as matrix flow. When a continuous, low conductivity coating is present, the water does not

pass beyond the fill, and simply ponds at the surface. A fracture that ends within a unit of the Tshirege Member, or at the interface between two units will behave like a fracture that is filled at that level. The path for the water in the fracture is eliminated, and the water must find an alternate route through the subsurface.

We have also run a simulation where a 1 meter "cap" of matrix material is placed across the entire fracture-matrix system. This condition represents the current surface cap at MDA G and the conditions at the floor of the waste disposal pits both of which are comprised of crushed (unfractured) tuff. The matrix cap was then held at saturations ranging from 50% to 90%. In none of the simulations did water break into the fracture, although it moved as a steady front through the remaining matrix material. These results are consistent with results obtained by Rosenberg et al. (1993) using a different numerical model.

Although most of these results indicate that fractures do not play a significant role in moving water from the surface to the water table, there are reasonable, possible local conditions that may be sufficient to produce significant flow. There are high influx conditions such as snow melt or large runoff events or ponding of runoff due to surface disturbances such as buildings, roads, soil compaction and removal of vegetation that could cause water to move a significant distance in a fractured system. There is some evidence for such flow at other LANL locations (Turin, 1995). It must also be kept in mind that there is wide variation between the different fractures, and that it is possible for one or two fractures to be carrying water while most others do not.

We do not expect fractures to be a fast path for contaminants out of the bottom of the pits because these fractures are covered with crushed tuff. However, if water is able to pond within the pit it may be possible for that water to exit the pit through fractures on the face of the pit, which are not filled or covered. Fractures that are not directly beneath the pits may play an indirect role in the movement of water and contaminants from the pits. Increases in matrix saturation as a result of water moving in the fractures are a potential source of water beneath the pits. As observed in the simulations, water that enters the matrix rapidly redistributes throughout the matrix block toward a uniform saturation. This can act to increase saturation beneath the pit, thus raising the hydraulic conductivity and allowing more rapid movement through the matrix.

2.3.2 Dual-Permeability Fracture Modeling

The fractured system can also be modeled with FEHM using a dual permeability formulation (Zyvoloski et al., 1995). For this formulation, an identical numerical grid is constructed for the matrix and fracture materials so that a one-to-one correspondence exists between a fracture node and the matrix node at that same position. Fluid flow occurs within each continuum, and a transfer term accounts for fluid flow and contaminant transport between the fracture and matrix. Orr (1996) has run a number of one-dimensional simulations with this model that are presented in Appendix 2. Fracture properties are defined for Units 2 and 1v-u based on parallel plate theory. Travel times to the top of basalt for both steady and transient simulations show no significant variation with the addition of the fractures to the model. Orr shows interesting variations in saturation and travel times at different depths within the one-dimensional column for the transient simulations. The reader is referred to Appendix 2 for more details.

2.4 EVAPORATION

2.4.1 From Mesa Sides and Fractures

Very low net infiltration rates are required to match the field observed saturation in the two mesa-top units, Units 2 and 1v-u. Evaporation from the top and sides of the mesa and possibly from fractures is a likely player in keeping the mesa dry. Some data (Rogers et al., 1995, Rogers and Gallaher, 1995) suggest that groundwater flow may be upward toward the volcanic surge beds located at the base of Unit 2. This flow could be driven by evaporation occurring in the surge beds. Some simple simulations are used to study these effects.

First we consider evaporation from the mesa sides and from vertical fractures with both 10-m and 5-m fracture spacing. A two-dimensional rectangular grid (25 m wide, 5 m tall) composed of a homogeneous material, either Unit 2 or Unit 1v-u, is used. Figure 2.4-1 shows the problem

configuration. Uniform infiltration of 0.1 cm/yr occurs along the upper boundary. This infiltration rate accounts for evaporation from the mesa top, but is higher than the flow rates found previously to best match the in-situ saturations of Units 2 and 1v-u (0 to 0.001 cm/yr). We compare the resulting vertical saturation profiles for the following cases: infiltration only, infiltration with evaporation occurring along the right boundary (mesa edge), and infiltration with evaporation along the right boundary and from fractures of either 10-m or 5-m spacing. For the infiltration only case, the right boundary is impermeable. The evaporative boundary is modeled by fixing the saturation at that boundary to a low saturation corresponding to 50% relative humidity. For the fracture runs, the fractures are also held at a low saturation corresponding to 50% relative humidity which is close to the average annual relative humidity for the area. The corresponding saturation values are 0.032 for Unit 2 and 0.00892 for Unit 1v-u.

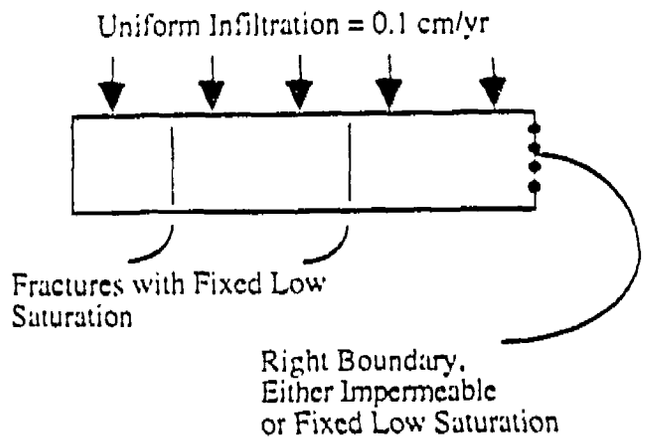

Figure 2.4-1. Problem set-up for study of evaporative effects from mesa sides and from fractures.

Figures 2.4-2 and 2.4-3 show the simulated saturation profiles for a horizontal slice through the center of the grid for Units 2 and 1v-u respectively. For both units, it appears that evaporation affects the saturation profile to a distance of about 7 m from the mesa edge; not much for a mesa that is over 300 m wide. However, assuming that fractures with 5-m spacing act as conduits for air flow, evaporative effects may decrease saturations throughout both units in the mesa top. With fractures spaced 5 m apart, average saturation decreases by ~0.03. From Figure 2.1-2 we see that this order decrease in saturation corresponds to approximately an order of magnitude decrease in the net steady infiltration rate. Actual fracture spacing in these units is 1.0 to 1.3 m, but only a fraction of these may be open to airflow. Some air flow would be required to remove water vapor from tuff, as the relative humidity of the air in a non-flowing fracture would equilibrate with that of the surrounding matrix. It is quite possible that fluctuations in the barometric pressure (Nilson et al., 1991), thermal gradients, and topographic effects (Weeks, 1987) could drive such air flow in a fractured system located on a mesa top.

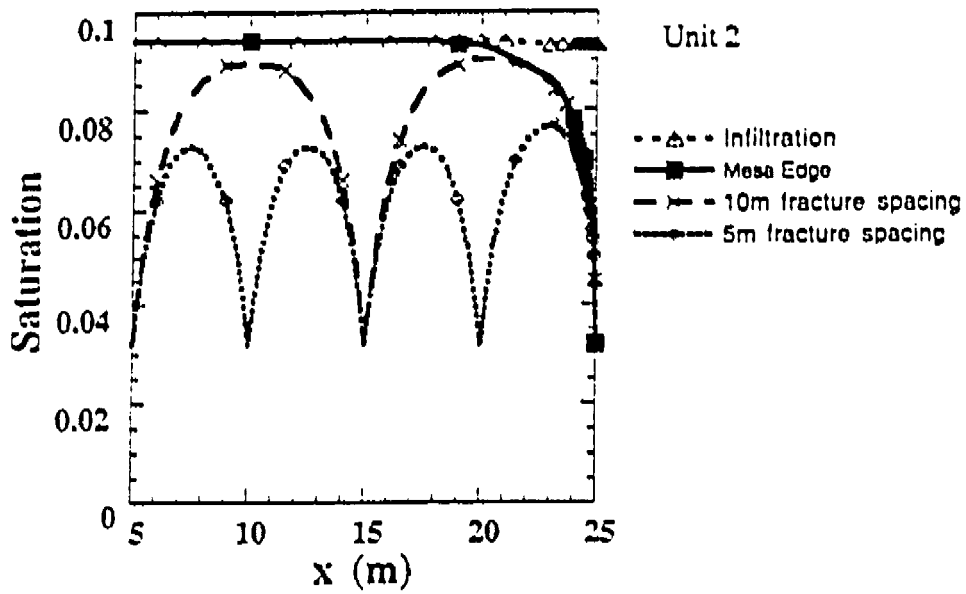

Figure 2.4-2. Resulting Saturation Profiles for Evaporation along a Mesa Edge (right side) and from fractures with 5-m and 10-m spacing, Unit 2.

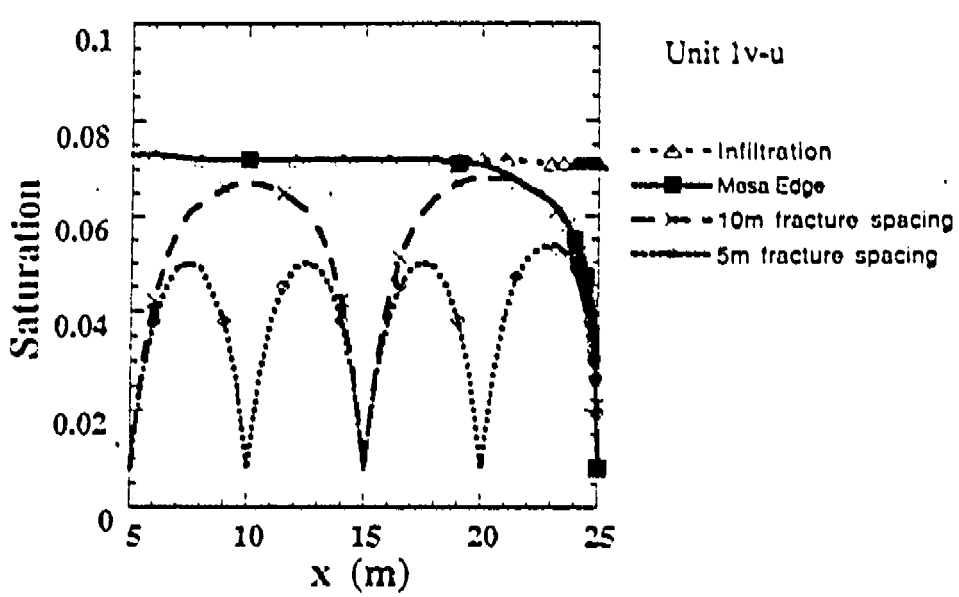

Figure 2.4-3. Resulting Saturation Profiles for Evaporation along a Mesa Edge (right side) and from fractures with 5-m and 10-m spacing, Unit 1v-u.

We note here that evaporation in these simulations and the one that follows is modeled as an isothermal process with saturations fixed at low values corresponding to a relative humidity of 50%. These results are nearly identical to simulated results, also calculated with FEHM, under non-isothermal conditions which account for vapor pressure lowering and binary diffusion of air and water vapor. For these examples, evaporation results in a simple capillary pressure driven wicking toward the drier, atmospheric boundary. Water vapor contributes less than 1% of the mass in the system for these particular examples which were held at or very close to 20°C, even for the non-

isothermal simulations. However, the more complex processes may have a larger effect under more realistic non-isothermal conditions (e.g., geothermal gradients or solar heating of the mesa sides).

2.4.2 From Surge Beds

The next test examines the hypothesis that air flow through the volcanic surge beds located at the base of Unit 2 can cause upward moisture flux from Unit 1v-u. The surge beds are a thin interval of fine sand-sized material which are attributed to deposition from the basal surge associated with violent eruptions (Krier et al., 1996). There is some evidence that this interval is conductive to higher air flow rates than is the rest of the mesa interior. Two layers, Units 2 and 1v-u, are modeled with their appropriate hydrologic properties and thicknesses. Uniform infiltration at a rate of 0.1 cm/yr is applied along the upper boundary. Again we compare the results with infiltration alone to results which include evaporation along the surge bed. The surge bed is modeled simply as a set of low saturation nodes, corresponding again to a relative humidity of 50%, along the interface of the two layers. Figures 2.4-4 and 2.4-5 show the steady-state saturation and capillary pressure profiles for this case. Saturation values throughout both units are significantly lowered by the fixed low saturation at the interface. In Figure 2.4-5, the calculated values are compared to suction data reported by Rogers et al. (1995) for Borehole G-5, which is located at MDA G. The data are translated spatially to force the surge bed to align with that from the simulation. We see that the calculated capillary pressure lies between the two data sets reported by Rogers.

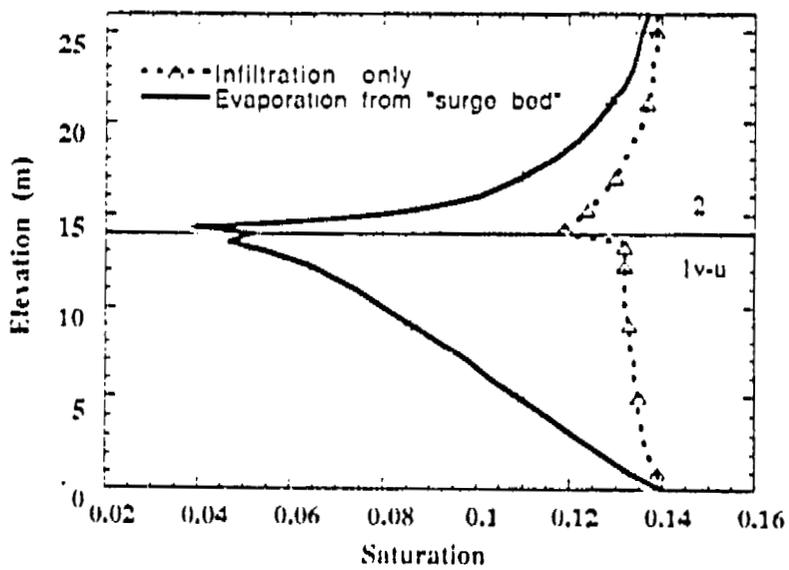

Figure 2.4-4. Resulting saturation profile for evaporation along the surge beds at the Unit 2/1v-u interface compared to that for infiltration alone.

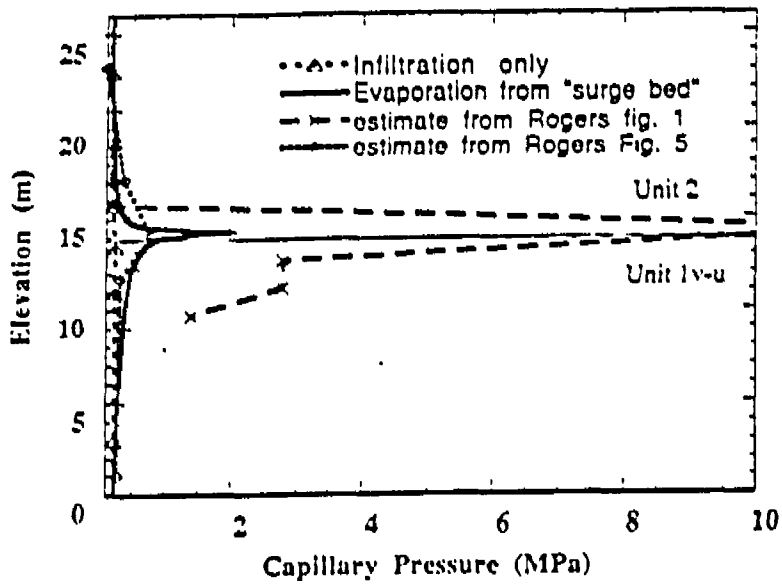

Figure 2.4-5. Resulting capillary pressure profile for evaporation along the surge beds at the Unit 2/1v-u interface compared infiltration alone and to data from Rogers et al. (1995) for Borehole G-5.

These simulations show that evaporation along fractures and surge beds can contribute to significant drying of the mesa top units, possibly causing the very low saturations seen in these units. We feel that the mesa may act as a natural dry barrier which substantially blocks deeper penetration of liquid flow as described in the site conceptual model (Rogers et al., 1997). This theory needs to be substantiated with more data and modeling studies.

3. THREE-DIMENSIONAL VADOSE ZONE MODEL

3.1 VADOSE ZONE MODEL DEFINITION

The vadose zone model is based on a three-dimensional representation of the site which describes the complex mesa-top geology. Infiltration is assumed to be steady although the mesa top and two canyons that border Area G receive different infiltration rates. Results for a base case flow field are compared to those for some variations on the flow field as part of an uncertainty analysis. The model incorporates the position and inventories of the thirty-some disposal pits and shafts already located at Area G along with those of future pits and shafts. Two pathways are considered: downward migration through the vadose zone to the aquifer, and lateral migration to the mesa sides, deposition into the nearby canyon, and subsequent migration through the vadose zone to the aquifer. Time- and spatially-dependent results for nuclide flux from the vadose zone feed the saturated zone model. The simulations are run for 10,000 years to cover the 1000-year compliance period and the 10,000-year uncertainty analysis.

The assumptions used for the vadose zone model rely heavily on the studies of specific flow processes presented in Section 2.0. The equivalent continuum parameters chosen to represent the basalts in Section 2.1 are used. These properties produce fast travel times through the basalt in order to compensate for the lack of hydrologic information about the unit. All flow is forced vertically through the basalt thereby eliminating lateral diversion at the basalt-pumice interface.

In section 2.2, we studied the effects of transient percolation on vadose-zone transport at Area G and found that, at the flow rate considered, transient pulses are damped with depth and cumulative contaminant flux results at depth are similar under transient and steady flow fields. Steady infiltration is also assumed in PA calculations used for other sites (Barnard and Dockery, 1991, and Wood et al., 1994). By using a high, steady infiltration rate and other conservative assumptions concerning flow at the site, the subsequent transport calculations are expected to yield conservative results assuming that fracture flow is not induced.

The fracture flow studies presented in Section 2.3 indicate that transport through fractures has a minimal effect on contaminant flux at depth. Therefore, fractures are not included in the three-dimensional vadose zone model. In Section 2.4 we found that evaporative effects can reasonably account for the low moisture contents observed in the mesa-top units at the site and justify a small infiltration value.

Previous modeling studies for Area G assumed that the pit percolation rate was likely to be higher than the percolation rate for the undisturbed mesa top (Birdsell et al., 1995 and Section 2.2 of this report). The pit density at Area G is high enough that the area can almost be considered "one big pit" in terms of infiltration (see Figure 3.1-2). Recent studies by Newman (1996), Vold (1996), and Springer (1996) show enough variability and overlap in estimates of pit and undisturbed mesa top percolation rates that a single value for the pit and mesa top rates is justifiable and is therefore used in this study. However, we do consider three different rates as described in Section 3.1.3.

3.1.1 Stratigraphy

The stratigraphy was constructed from various sources. The topography and the bases of the Otowi Member (Qbo) and the Tshirege Member (Qbt or Unit 1g) were obtained at 15.24 m (50 ft) spacings (northing and easting) from the LANL site wide geologic model (Vaniman, et al., 1996). Well-log picks were used to define Units 2, 1v-c, the Cerro Toledo, and the Guaje Pumice. Data for wells 54-1102, 54-1105, 54-1106, 54-1107, 54-1108, G-2, 54-1110/G-3, 54-1111/G-4, 54-1112, 54-1114, 54-1115, 54-1116, 54-1117, 54-1120, 54-1121, 54-1123, 54-1124, 54-1125, 54-1126, 54-1128, 54-1001, 54-1002, 54-1003, 54-1004, 54-1005, 54-1006, 54-1008, 54-1009, 54-1015, and 54-1016 (Vaniman, et al., 1996) were used. Some of these holes are inclined, and the northing, easting and depth values required corrections. Surface observations for the contact between Units 2 and 1v-u obtained from Broxton (unpublished data) were used to further constrain this contact. A data point from Well TH-5 (Purtymun, 1995) was also used to constrain the Guaje Pumice layer. The overall number of data points that were available in the vacinity of MDA G for

each of the surfaces was 76 for Unit 2, 30 for Unit 1v-c, 25 for Unit 1g, 14 for the Cerro Toledo, and 4 for the Guaje Pumice.

The data set was interpolated at 45.72 m (150 ft) intervals with the Stratagraphic Geocellular Modeling (SGM) Software (Version 3.10, Copyright 1994, Stratamodel, Inc.). The topographic surface truncates any surface that it crosses. The Guaje Pumice was calculated by adding the layer thickness to the Qbo unit rather than by using its elevation because so few data are available to constrain this unit. Likewise the Cerro Toledo Unit was calculated as a thickness below Unit 1g. The surface for the base of 1v-u was poorly defined by the well-log elevation data resulting in unrealistic undulations that caused overlapping of layers above and below. This surface was ultimately defined as a surface parallel to Unit 1v-c with a thickness of 7.62 m (25 ft) as suggested by Krier who said that this interface is difficult to identify in core samples. Some other minor modifications were made to the surfaces to avoid unphysical crossing of surfaces. The Puye Conglomerate is defined as a 30.48 m (100 ft) thick flat unit within the vadose zone at the base of the model. This layer is probably thicker than 30.48 m (100 ft) in the vadose zone (Krier, 1996), but again too few data are available to justify a more sophisticated representation. The Cerros del Rio Basalts occupy the region between the Guaje Pumice and the Puye Conglomerate. The water table is defined as a flat surface at an elevation of 1767.8 m (5800 ft) although it actually dips downward at the eastern end of the mesa.

Figure 3.1-1 shows the resulting three-dimensional stratigraphic, vadose-zone model. The strata from Unit 2 through the Cerro Toledo dip and generally thin toward the east. The Otowi Member and the Gauje Pumice dip and thicken toward the west.

3.1.2 Grid

The surfaces generated with SGM were used to construct the three-dimensional grid. The grid is generated with the Geomesh/X3D software (Gable, et. al, 1995). An initial grid based on the stratigraphy is constructed with 45.72 m (150 ft) grid spacing. This grid is then refined to include the 38 waste disposal pits and to better define the mesa sides. The final grid is made of 41,542 nodes and 254,614 tetrahedral elements. The surface definition for the pits was obtained from the Facility for Information Management, Analysis, and Display (FIMAD) at LANL. Each pit is assumed to be 10.7 m (35 ft) deep. Pit regions are defined by a set of nodes which outline several adjacent pits both at the surface and at a 13.7 m (45 ft) depth. A set of internal nodes is added down the centerline of each pit at a depth of 7.62 m (25 ft). The volume associated with these nodes approximates true pit volumes. Because the volume of finite element nodes extends half-way to the next node, the resulting pit depth is the desired 10.7 m (35 ft). These internal pit nodes are assigned hydrologic properties for crushed tuff and are the nodes that release waste during the transport calculations. Figure 3.1-2 shows the outline of the waste disposal pits, the internal pit nodes, as well as the nodes that were added to outline the mesa.

3.1.3 Boundary Conditions

The mesa/canyon setting in which MDA G exists leads to a complicated set of boundary conditions. A very low net percolation rate (1 to 10 mm/yr) is thought to occur within the mesa. Pajarito Canyon is quite wet with an estimated percolation rate of 10 to 100 mm/yr while Cañada del Buey is dry with a percolation rate similar to the mesa top. The mesa sides are steep enough that they should represent an evaporative region (water sink) rather than a source region. For these reasons, the top surface nodes of the grid are categorized by position so that various boundary conditions can be applied to the mesa top, to Pajarito Canyon, to Cañada del Buey and to the mesa sides. Figure 3.1-3 shows a boundary condition map for the topographic surface. The lighter blue portion of the grid receives the mesa-top percolation rate and the darker blue portion receives canyon percolation rates. The outline of the mesa is clearly defined in this figure by the yellow-green evaporative boundary nodes. The evaporative nodes are held at a fixed saturation of 0.03 which is equivalent to an ambient relative humidity near 50%. Some nodes are not categorized

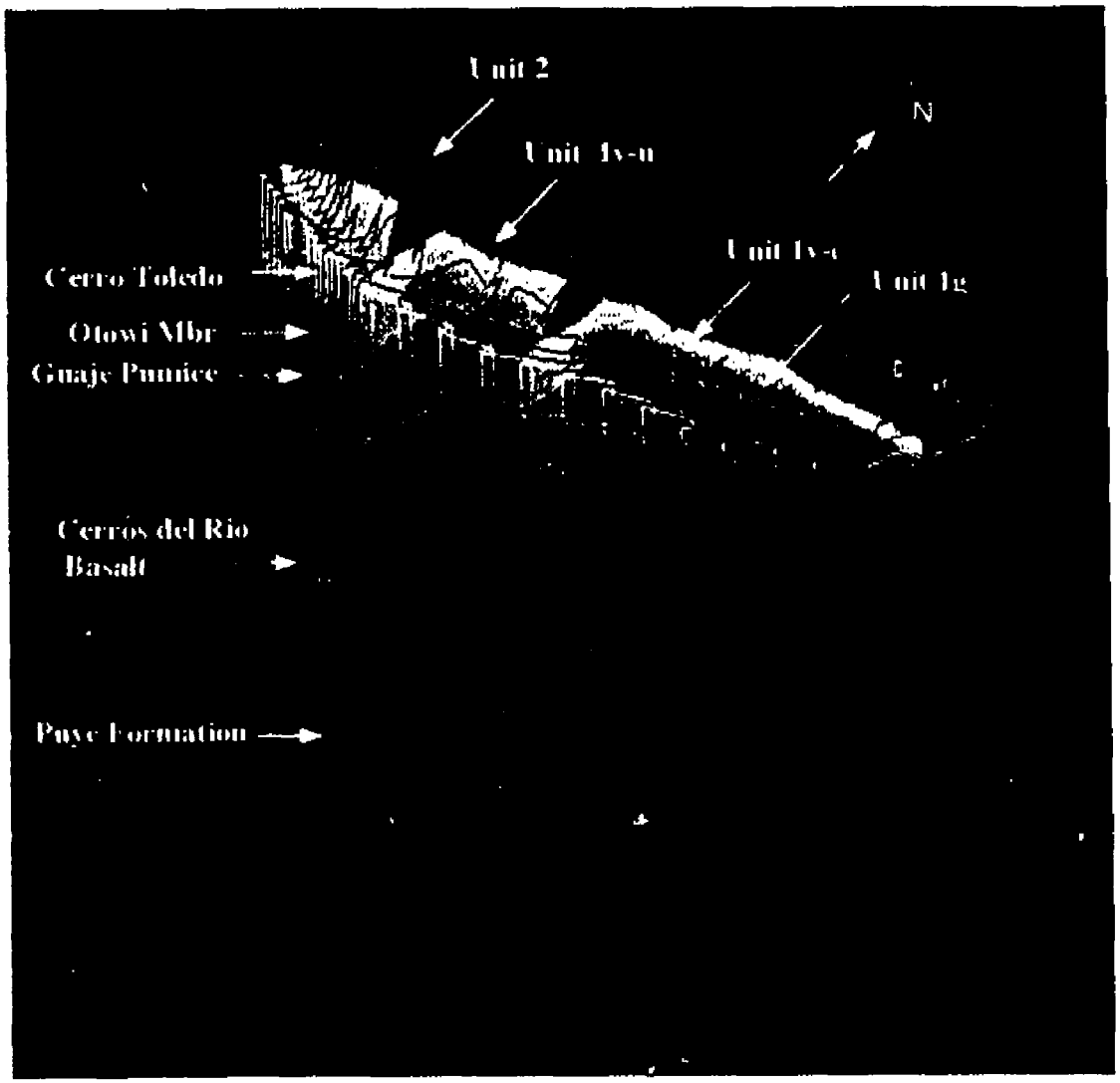

Figure 3.1-1. Three-dimensional stratigraphy for the vadose zone model of Area G.

and are assigned no-flow boundary conditions These nodes are red in the figure and act as buffers between the different boundary regions.

Five different flow fields are considered in order to study the sensitivity of the calculated saturation fields and the transport results to background flow rates. Three mesa-top flow rates are used (1 mm/yr, 5 mm/yr and 10 mm/yr), two flow rates for Cañada del Buey are considered (1 mm/yr and 5 mm/yr), and three flow rates for Pajarito Canyon are used (20 mm/yr, 50 mm/yr and 100 mm/yr). Table 3.3-1 summarizes the five cases. The base case, 5_1_50, is thought to be conservative for the site. Using chloride flux estimates, Newman (1996) reports near-surface, mesa-top flux rates of 3 to 6 mm/yr, mid-mesa flux rates ranging from 0.03 to 1.5 mm/yr, and sub-mesa flux rates near 5 mm/yr. Vold (1996) gets similar results using moisture profile analysis. Springer (1996) estimates a mean pit percolation rate of 0.99 mm/yr using a water balance algorithm. Simulated moisture profiles (Figure 2.1-2) show that the range 1 mm/yr to 10 mm/yr conservatively fit the available moisture data. Rogers et al. (1996) estimate recharge at 4.4

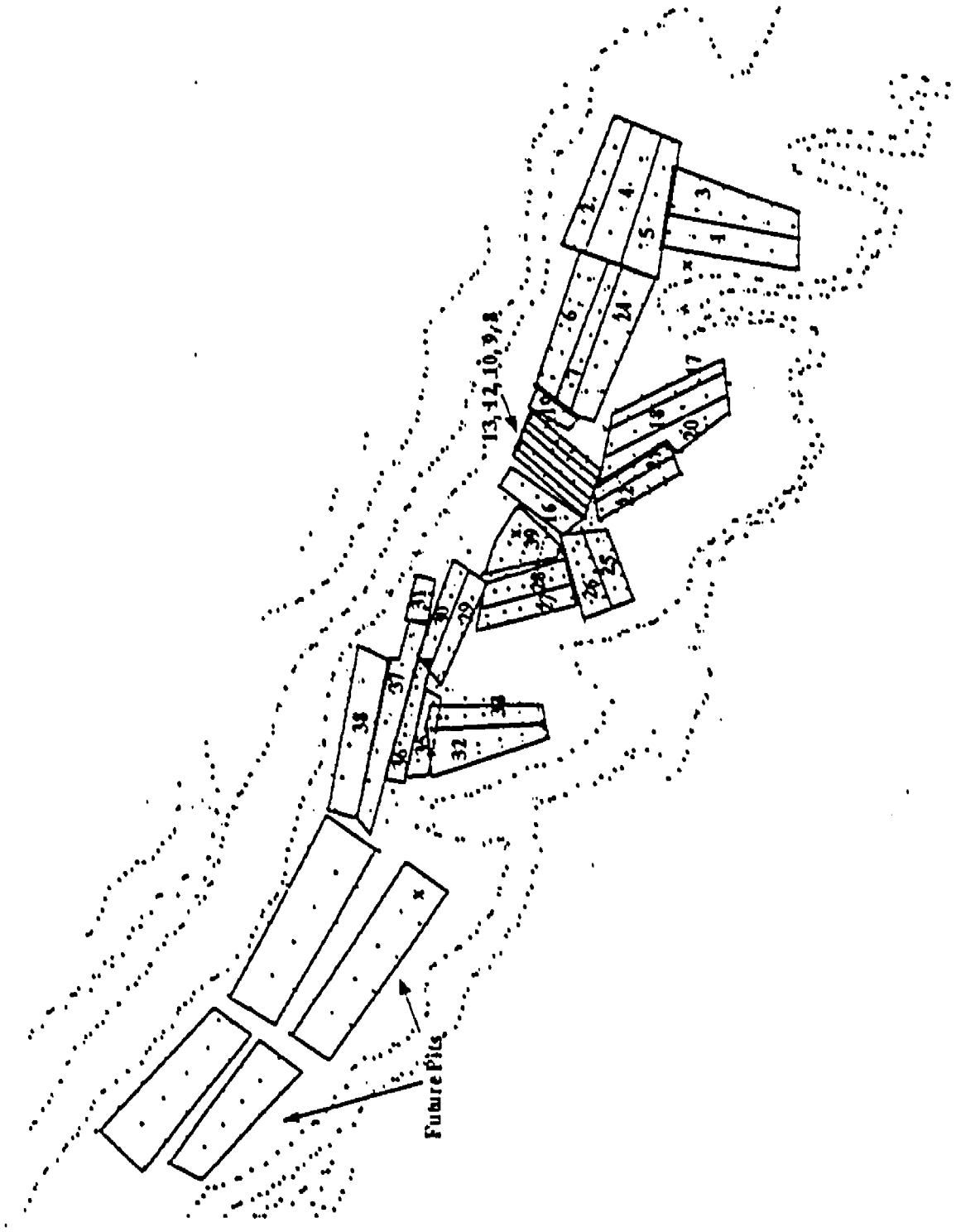

Figure 3.1-2. Pit Boundaries, Internal Pit Nodes, and Mesa Edge Nodes for the Three-Dimensional Vadose Zone Calculations.

mm/yr in Cañada del Buey and 20 to 100 mm/yr in Mortandad Canyon, which is considered to be hydrologically similar to Pajarito Canyon.

Figure 3.1-3. Boundary Condition Map of the Topographic Surface for the Vadose Zone Flow and Transport Calculations (light blue is mesa top, dark blue is canyon, light green is evaporative boundary, red is no-flow buffer zone).

Table 3.1-1. Infiltration Rates (mm/yr) used as Upper Boundary Conditions.

	Mesa Top	Cañada del Buey	Pajarito Canyon
1_1_20 (Lowest Flow Case)	1	1	20
5_1_20	5	1	20
5_1_50 (Base Case)	5	1	50
10_1_20	10	1	20
10_5_100 (Highest Flow Case)	10	5	100

No-flow boundary conditions are applied to the sides of the grid. The bottom boundary represents the water table with a fixed saturation of 0.99. Both water and radionuclides can exit this boundary. Time-dependent radionuclide flux through the bottom of the vadose-zone grid is recorded at each time step to be used as input to the saturated zone model. In order to supply an adequate spatial flux distribution, the bottom boundary is divided into 28 regions for which fluxes of radionuclides are reported as shown in Figure 3.1-4.

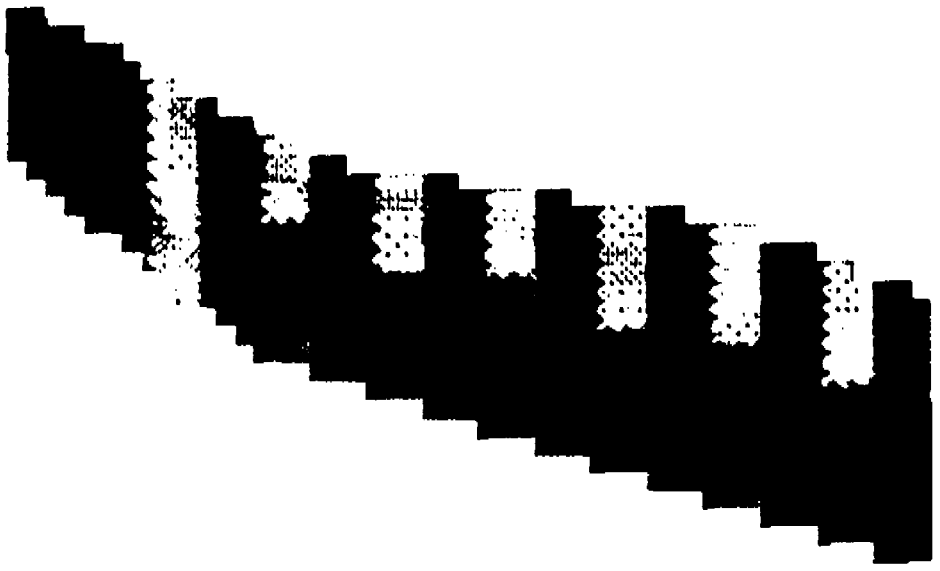

Figure 3.1-4. Bottom boundary divided into 28 regions for which temporally and spatially dependent flux from the vadose zone calculation is reported.

3.1.4 Hydrologic Properties

The hydrologic properties for the units are given in Table 2.1-1. As described in Section 2.1.2, conservative basalt properties are chosen which favor rapid vertical transport through the fractures of this unit. The basalts are treated as an equivalent continuum medium (Klavetter and Peters, 1986) made up of both fractures and matrix material. The fractures are assigned a high permeability and porosity which favor vertical flow from the pumice into the basalts. This serves to minimize lateral flow within the pumice as explained previously. With this set of parameters in the model, a permeability barrier to vertical flow and transport at the top of the basalt is virtually impossible to model. Further, the porosity of the basalt continuum is set equal to 10^{-4}, the estimated volume fraction of fractures, since we desire that most flow occurs in the fractures. This yields extremely rapid groundwater travel times of between 1 and 5 years through the basalts, as would be expected of fracture flow.

Although hydrologic properties for the Puye Conglomerate are also unknown, we expect that our intuition for flow through this unit is better. The layer is modeled as a coarse sand (Carsel and Parrish, 1988) with the porosity reduced by 60% (from 0.43 to 0.25) as described in Section 2.1.2. This should lead to conservative (faster than expected) travel times through the Puye Conglomerate .

3.1.5 Transport Properties

Recent studies by Conca (1992) show that the diffusion coefficient decreases with decreasing saturation. The diffusion coefficient was modeled in this fashion and decreases parabolically from 10^{-9} m^2/s at saturation to 10^{-15} m^2/s at a moisture content of 0.001. The dispersivity is 1 m in the vertical direction and 0.1 m in the horizontal direction.

Table 3.1-2 gives the distribution coefficients (Kd) for the nuclides that apply for the Bandelier Tuff in the vadose zone. The values for Am, Np, Pu, Tc and U were measured at a pH of 9.8 on Bandelier Tuff samples, using a sodium-bicarbonate-carbonate-rich synthetic solution representing pore water extracted from the tuff (Longmire et al., 1996). The remaining values are based largely on sorption measurements for Yucca Mountain tuffs (Krier et al. 1996). These distribution coefficient values apply from Unit 2 down through the Guaje Pumice Bed. No distribution

coefficient is applied in the basalt layer in order to be consistent with the assumption of rapid transport through that unit.

Table 3.1-2. Median Distribution coefficients for Nuclides on Intact Tuff in the Vadose Zone

Radionuclide	Kd (ml/g)
Ac-227	130
Ag-108m	90
Am-241, Am-243	2359
Ba-133	946
C-14	0
Cd-113m	80
Cf-249, Cf-252	130
Cm-244	50
Co-60	0.45
Cs-137	428
Eu-152, Eu-154	50
Gd-148	50
H-3	0
Hf-182	500
I-129	0
K-40	15
Mo-93	4
Nb-93m, Nb-94	100
Np-237	2.25
Pa-231	50
Pb-210	25
Pu-238, Pu-239, Pu-240 Pu-241, Pu-242	4.13
Ra-226, Ra-228	200
Si-32	35
Sm-147, Sm-151	50
Sr-90	116
Tc-95m, Tc-99	0
Th-229, Th-230, Th-232	500
Ti-44	500
U-233, U-234, U-235 U-236, U-238	2.43

Different values for the distribution coefficients of Am, Np, Pu, Tc, and U are applied in the waste disposal pits and are shown in Table 3.1-3. These values were measured on four samples of Bandelier Tuff Unit 2 from a depth interval of 3.3 to 3.7 m (10.8 to 12 ft) and are representative of the crushed tuff that is used to fill the disposal units (Longmire et al., 1996). For radionuclides that are not specifically identified in Table 3.1-3, distribution coefficients listed in Table 3.1-2 are used in the pits.

Table 3.1-3. Median Distribution coefficients for Nuclides within the Pits

Radionuclide	Kd (ml/g)
Am-241, Am-243	2050
Np-237	7.5
Pu-238, Pu-239, Pu-240 Pu-241, Pu-242	711
Tc-95m, Tc-99	0
U-233, U-234, U-235 U-236, U-238	2.61

Also, distribution coefficients have been measured for Am, Np, Pu, Tc, and U that are representative values for the saturated zone. These are shown in Table 3.1-4. These values were measured on Bandelier Tuff samples at a pH of 7.3 using Water Canyon Gallery groundwater (Longmire et al., 1996) which is expected to be closer to the pH of the saturated zone waters. These values are applied to the saturated zone and also to the deep vadose zone for the Puye Conglomerate, which we presume has pore water more similar to the saturated zone than to the shallow vadose zone. Again for radionuclides that are not specifically identified in Table 3.1-4, distribution coefficients listed in Table 3.1-2 are used in the saturated zone.

Table 3.1-4. Median Distribution coefficients for Nuclides in the Saturated Zone and for the Unsaturated Puye Conglomerate

Radionuclide	Kd (ml/g)
Am-241, Am-243	141
Np-237	0.151
Pu-238, Pu-239, Pu-240 Pu-241, Pu-242	13.95
Tc-95m, Tc-99	0
U-233, U-234, U-235 U-236, U-238	4.85

3.1.6 Source Term

The source term models to calculate time dependent total nuclide release rate, Φ (moles/yr), from each disposal unit (Vold et al., 1996; Vold and Shuman, 1996) are incorporated directly into FEHM for the three-dimensional simulations. Two source term models are included: rapid release and solubility limited. The rapid release model takes the form $\Phi = Q\,\lambda^2 t e^{-\lambda t}$, where Q is the total inventory (moles) of the nuclide in the disposal unit, and λ is the release constant ($\lambda = q/\theta h$) where q is the Darcy flux through the waste package, θ is the average moisture content of the disposal unit (taken to be 0.08), and h is the representative height of a waste package (taken to be 1 m). The rapid release source term is highly dependent on the Darcy flux through the waste package (q) as shown in Figure 3.1-5. For the 10 mm/yr flux most of the source is released over a 60-year period, while for the 1 mm/yr flux a similar quantity is released over about 360 years. The solubility limited model takes the form $\Phi = f_{ij} V q C_{sl}/h$ where V is the total initial nuclide waste volume in the disposal unit and C_{sl} is the nuclide solubility limit. The fraction f_{ij} is a correction factor for the solubility limit contributions from multiple nuclides, i, of the same element and from multiple waste forms, j. This was determined to be a significant correction factor only for uranium (Vold and Shuman, 1996). The maximum pore water concentration of each nuclide is compared to its solubility limit to determine the appropriate source release model for each nuclide in each disposal unit. The Darcy flux (q) is set equal to the fixed mesa-top infiltration rate (1, 5 or 10 mm/yr) for the flow field of interest. Source term information describing the total inventory (Q), source release model, initial nuclide waste volume (V), and solubility limit (C_{sl}) were obtained from Vold and Shuman (1996) which in turn was derived from the complete inventory analysis (Shuman, 1996).

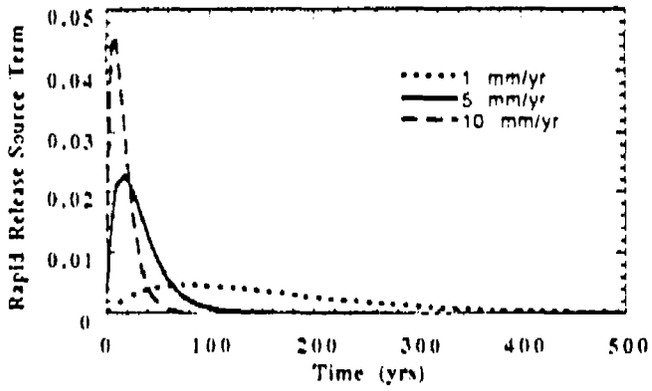

Figure 3.1-5. Velocity dependent portion of the rapid release source term ($\lambda^2 t e^{-\lambda t}$).

The source term information described above was supplied for each of the 4 disposal unit classifications and are described in Table 3.1-5. Shaft fields were added as surface nodes near their true location: Oldest shafts are 2 nodes located west of pits 2 and 4, 71-88 shafts are 4 nodes located west of pit 16, historical shafts are 3 nodes located west of pit 22, and future shafts are 2 nodes located west of the two eastern-most future pits.

Table 3.1-5. Disposal Unit Classification and Location

Disposal unit classifications	Referred to in Text by	Locations
Extrapolated 1957 - 1970	Oldest	Pits 1 through 6 and in shafts located to the west of Pits 2 and 4
Recorded 1971 - 1988	71 to 88	Pits 7 through 36, except for pits 30 and 31, and in shafts located to the west of Pit 16
Recorded 1988 - 1995	Historic	Pits 30, 31 and 36 through 39 and in shafts located to the west of Pits 22
Projected 1996 - 2044	Future	Four large pits and in shafts to the west of Pits 37 and 38

The inventory information (Shuman, 1996) for the Oldest and Future wastes are extrapolated or projected values. For each nuclide in these inventory classes, a total inventory and waste volume is given for all of the pits combined and also for the shafts. In this case, the pit inventory is distributed between all of the pit nodes for the waste class (Oldest or Future), and solubility limited wastes are then considered to be solubility limited in all of the pits. Inventory and waste volume are known in greater detail for the 71 to 88 and for the historic wastes. For each nuclide in these inventory classes, a total inventory and waste volume is given for each individual pit and for the shafts. The individual pit inventory is distributed between the pit nodes for the appropriate waste disposal pit. Wastes may be solubility limited in some pits or shaft fields and rapid release in others depending on the inventory and waste volume in the particular pit or shaft field.

3.2 VADOSE ZONE FLOW RESULTS

The base case flow model uses a 5 mm/yr percolation rate for the mesa top, which includes the undisturbed mesa top as well as the pit areas. Percolation for the adjacent canyons is fixed at 1 mm/yr for Cañada del Buey and 50 mm/yr for Pajarito Canyon. These flow rates are varied in order to quantify the effects of uncertainty in flow rate on dose assessment results. Figure 3.2-1 shows the saturation field looking down on the mesa for the base case flow field. The outline of the mesa top is evident from the low saturation (dark blue) boundary conditions applied along the mesa edge. A higher saturation (green) is also evident in Pajarito Canyon where the infiltration rate is the highest. This figure shows how well the grid captures the topography of the site and also the application of the boundary conditions.

Saturation profiles as a function of depth at three locations are developed for the various infiltration boundary conditions shown in Table 3.1-1. The three locations are shown with x's on Figure 3.1-2 and are near the eastern end of the proposed future pits, at the eastern end of the historic pits beneath Pit 39, and at the eastern end of Area G just west of Pit 1. The purpose of looking at saturation as a function of depth at these locations is to determine whether modeling the three-dimensional geometry of the topography and of the gently dipping beds coupled with the combination of canyon and mesa infiltration rates can predict the in-situ saturation measured in the Cerro Toledo and Otowi Member. The relatively high saturations in these units proved difficult to match with the two-dimensional simulations presented in Section 2.1.

Figure 3.2-2 shows saturation profiles at three different mesa infiltration rates but the same canyon infiltration rates (1_1_20, 5_1_20 and 10_1_20) for the location near Pit 1. This figure indicates results similar to those shown in Figure 2.1-2. An increase in the mesa-top infiltration rate leads to increased saturations throughout the depth of the vadose zone. An increase in mesa infiltration from 1 mm/yr to 10 mm/yr results in an approximate increase in saturation on the order of 0.03 to

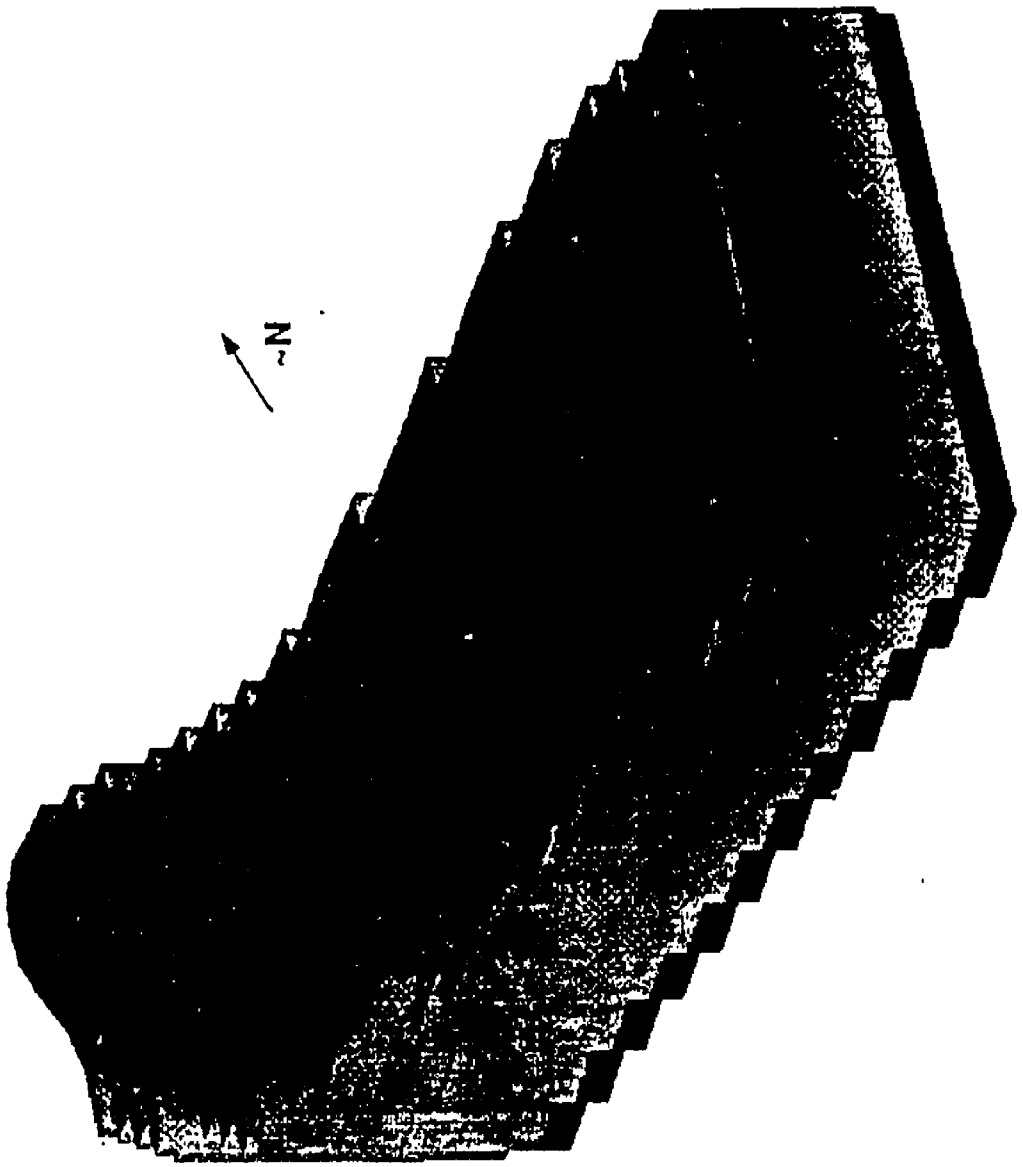

Figure 3.2-1. Steady-state vadose zone saturation field (top view) for the base case flow field (dark blue - saturation is ~0.03, light blue - saturation is ~0.2, green - saturation is ~0.5).

0.1. Figure 3.2-3 shows saturation profiles at the three locations of interest for the base case flow rate (5_1_50). The three saturation profiles differ from one another, on the order of 0.02 to 0.05 in saturation, for the same flow field, which is about half the variation seen for the change in flow rate from 1 mm/yr to 10 mm/yr at the location near Pit 1. These results show that in-situ saturation is not only controlled by the infiltration rate but that the local topographic and stratigraphic configuration are also controlling factors. This suggests that calculated saturation profiles at various locations might better be compared to saturation measurements made at like locations (i.e., individual borehole measurements) than to ensemble average saturation values.

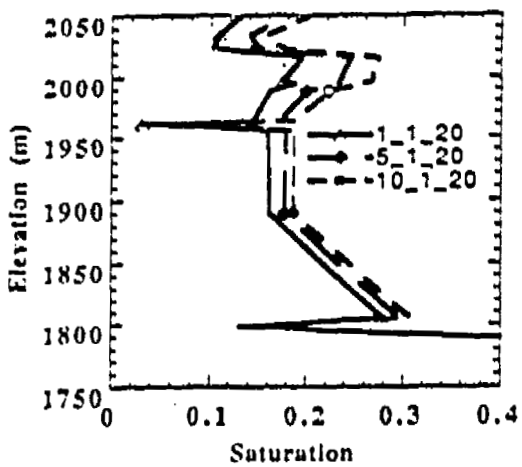

Figure 3.2-2. Saturation Profiles near Pit 1 for three mesa-top infiltration rates.

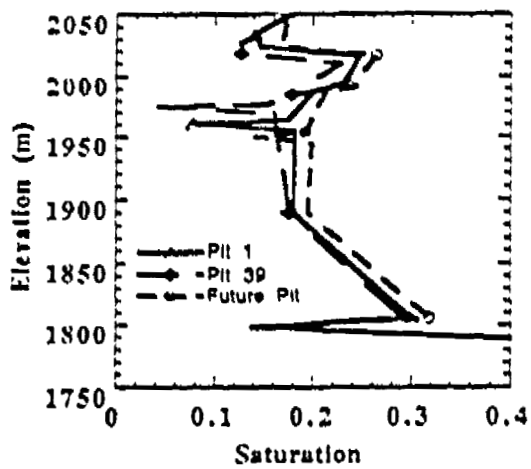

Figure 3.2-3. Saturation Profiles for the base case flow rate (5_1_50) at the three locations of interest.

We also examined the effect of canyon flow rates on the saturation profiles at the three locations. A change in infiltration from 1 mm/yr to 5 mm/yr in Cañada del Buey shows no effect on sub-mesa saturations even in the units that lie beneath the canyon floor. However, a variation in infiltration in Pajarito Canyon does affect saturations slightly for the units from the Otowi Member down to the water table at the location near the future pits. For example, saturations calculated for the Otowi Member at this location increase by about 0.02 with an increase in the Pajarito Canyon infiltration rate from 20 mm/yr to 100 mm/yr. This increase in almost indistinguishable at the other two locations. There are some geological differences at the location near the historic pits that may explain why the saturation at depth responds more strongly to the boundary condition on Pajarito Canyon than at the other two locations. The mesa narrows, the canyon floor is quite steep, and the canyon cuts the strata differently at the western end of Area G. All of these factors may contribute to a more lateral distribution of canyon flows beneath the mesa top. The location near the future pit is also the closest to Pajarito Canyon of the three sites, and proximity to the canyon may also be a factor.

In general, the calculations indicate that variations in mesa-top flow rate and in monitoring location more strongly affect saturation profiles beneath the mesa than do canyon flow rates. This agrees with a previous two-dimensional modeling study (Birdsell et al., 1995) for the site which considered the effects of canyon flow on sub-mesa saturation profiles. However, the results of this current study and the two-dimensional study do not include a component of lateral flow at the pumice/basalt interface. The inclusion of lateral diversion of flow within the pumice bed not only leads to increased saturation in the Otowi Member, as discussed in Section 2.1, but also leads to calculated sub-mesa saturation profiles that do depend on canyon flow rates. Recent stable isotope studies (Newman, 1996) indicate that canyon waters may flow laterally beneath the mesa. A better

understanding of the mechanisms and hydrologic properties that control flow in the deep vadose zone will help to clarify issues related to the interaction of the canyon and mesa flow fields.

3.3 VADOSE ZONE TRANSPORT RESULTS

Vadose-zone transport calculations were run for C-14, I-129, Np-237, Tc-99 and U-238 using the base case, steady flow field (5 mm/yr for the mesa top, 1 mm/yr in Cañada del Buey, and 50 mm/yr in Pajarito Canyon). These nuclides were chosen because of their low distribution coefficients, ranging from zero to 2.43 in most of the vadose zone, as shown in Tables 3.1-2 through 3.1-4. Downward flux to the water table and lateral flux to the mesa sides were examined. Interestingly, only C-14, I-129 and Tc-99, the nonsorbing nuclides (Kd=0), show any breakthrough to either the water table or to the mesa side over the 10000-year time frame considered. This result enables us to eliminate the remaining nuclides (except for Co-60 and H-3) from consideration in the dose assessment because their distribution coefficients are larger than those of either Np-237 or U-238, which did not break through to either the water table or to the mesa sides. This screening technique includes the consideration of all daughter products in the radionuclide decay chains. Calculations of Np-237 and U-238 transport using the maximum flow field (10 mm/yr for the mesa top, 5 mm/yr in Cañada del Buey, and 100 mm/yr in Pajarito Canyon) also showed no breakthrough, thus showing that the screening technique applies at the higher flow rates considered in this study. Co-60 and H-3 are eliminated from the analysis because of their short half-lives of 5.26 years and 12.3 years respectively.

Figures 3.3-1 show the simulated I-129 plumes for the four source regions (described in Table 3.1-5) after 1000 years. The infiltration rate at each source region is the same, 5 mm/yr. Therefore, the difference in plume concentration (note different scales on the color bars) and migration depth is attributed only to geologic variations and different radionuclide flux rates out of the pits and shafts. The distribution of radionuclide inventory in each disposal unit varies substantially leading to significantly different flux rates of radionuclides into the subsurface. For example, the historic shafts located near the southern edge of the mesa (left side of the figure) concentrate nearly 80% of the I-129 historic inventory into a very small source location. This leads to a high I-129 flux out of the shafts producing the large plume volume shown in the southern extent of the figure. The plumes associated with the historic pits (same figure) do not penetrate as deep due to less concentrated inventories. For the simulation of the future waste, the plume does not migrate particularly deep, partly due to the uniformly distributed, projected future inventory. For the three cases in which the simulated plume reaches the horizontal plane, located near the bottom of the basalt, it is clear where the vertical, fracture dominated flow starting at the top of the basalt governs plume migration. Once the plumes reach the basalt, they migrate quickly through the basalt due to the hydrologic properties discussed in Section 2.1. In the future scenario, the plume has not reached the basalt partly due to the distributed source and partly due to the thicker tuff units located between the land surface and the top of the basalt.

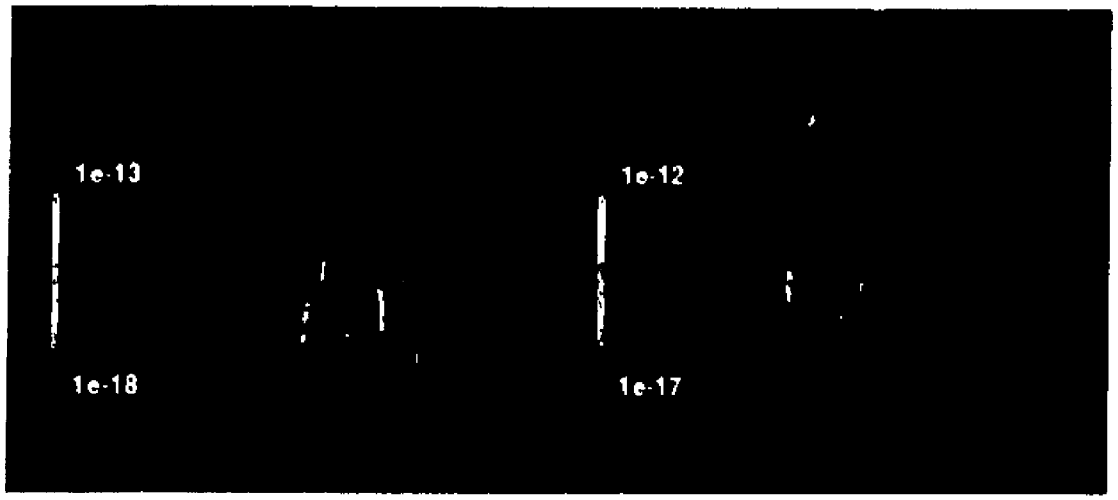

(a) Oldest (b) 71 to 88

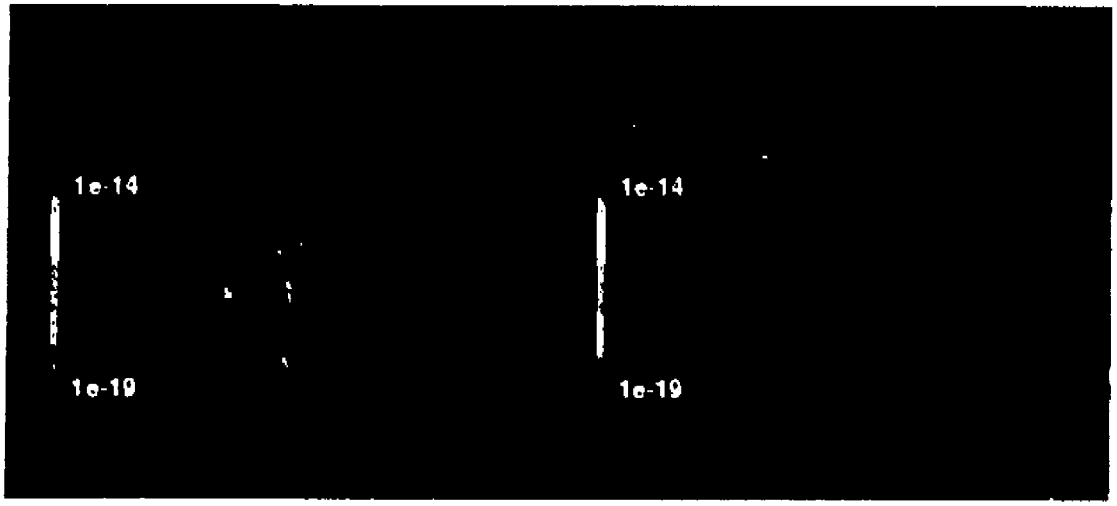

(c) Historic (d) Future

Figure 3.3-1. I-129 Plumes (concentration, moles/liter) in the vadose zone at 1000 years for the four different source regions, base case flow field.

3.3.1 Downward Transport toward the Water Table

3.3.1.1 *Base Case Flow Field*

Figures 3.3-2 through 3.3-4 show the total time-dependent flux of C-14, I-129 and Tc-99 from the vadose zone to the saturated zone for the four source classifications using the base case, steady flow field (5_1_50). The release of all three nuclides is controlled by the exponential rapid release model described in section 3.1.5. This produces flux vs. time curves which peak in less than 10,000 years. A solubility limited release would produce flat flux curves with no peak that extend for the duration of the inventory lifetime. The transient flux information is supplied as input to the saturated zone model, but is broken into 28 spatial footprints as shown in Figure 3.1-4, so that the spatial distribution produced by the various source regions is maintained.

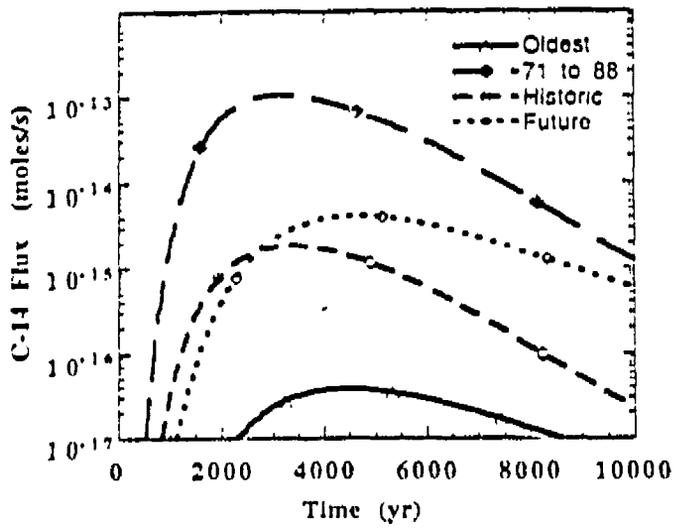

Figure 3.3-2. Total Flux of C-14 from the vadose zone to the saturated zone from the four source regions, base case flow field (5_1_50).

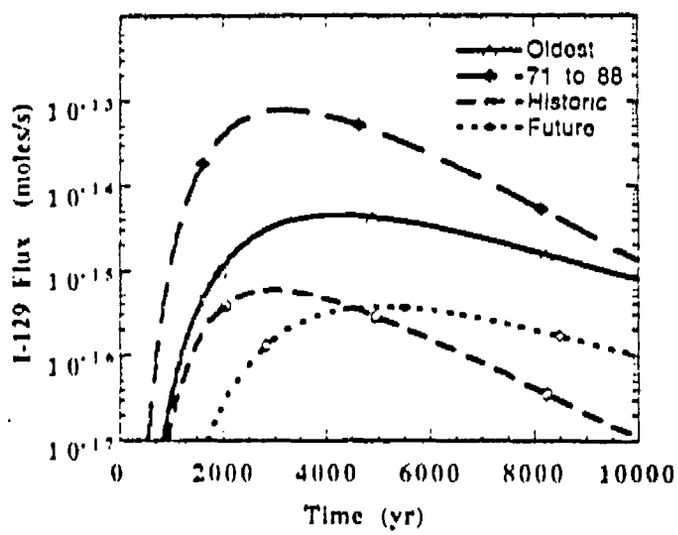

Figure 3.3-3. Total Flux of I-129 from the vadose zone to the saturated zone from the four source regions, base case flow field (5_1_50).

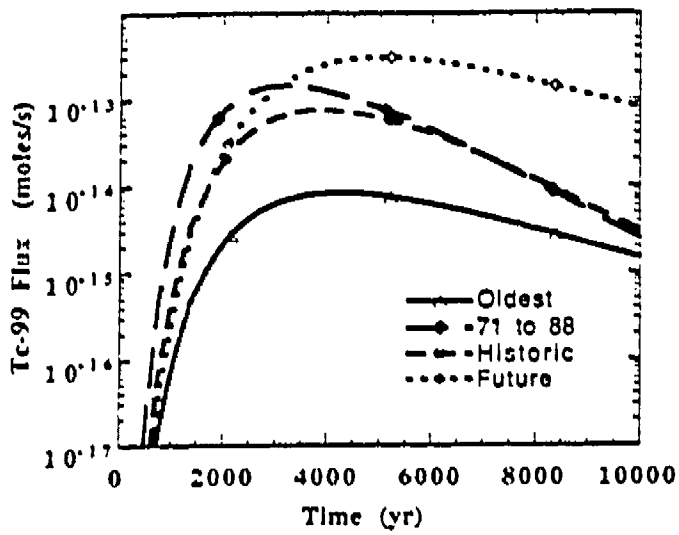

Figure 3.3-4. Total Flux of Tc-99 from the vadose zone to the saturated zone from the four source regions, base case flow field (5_1_50).

For each nuclide and each waste category, the flux is increasing at 1000 years causing the 1000-year peak dose to occur at 1000 years. During the 1,000-year to 10,000-year uncertainty time frame, the peaks in the curves occur at various times making the prediction of time of maximum dose over this time period less straightforward. For each of the three nuclides, the future inventory arrives latest at the base of the vadose zone because of the increased vadose-zone thickness at the western end of Area G.

3.3.1.2 *Other Flow Fields*

In order to assess the uncertainty in flow rate at the site on the transport results, we examined the transport of I-129 for the historical source for different flow rates and compared the flux from the vadose zone. Figure 3.3-5 shows the total flux of I-129 for five different flow rates as described in Table 3.3-1: 1_1_20, 5_1_20, 5_1_50, 10_1_20 and 10_5_100. By comparing the 1_1_20 case, the 5_1_20 case, and the 10_1_20 case, we see that an increased percolation rate through the mesa results in faster transport through the vadose zone and increased flux to the saturated zone. This flux dependency is compounded by the source release rate which is highly flux dependent, as shown in Figure 3.1-1. The flux at 1000 years for the lowest flow case (1_1_20) is some five to seven orders of magnitude less than the other cases considered. This case is investigated further to estimate a lower bound dose as part of the uncertainty analysis. By comparing the 5_1_20 case to the 5_1_50 case, we see that additional water in Pajarito Canyon results in faster transport through the vadose zone and increased flux to the saturated zone. The 10_5_100 case represents the flow field with the most water added to the system. This case yields the fastest transport through the vadose zone, the highest flux rate to the saturated zone and consequently will yield the highest dose over the first 1000 years. For this reason, we study this case further in the uncertainty analysis to estimate an upper bound dose as part of the uncertainty analysis.

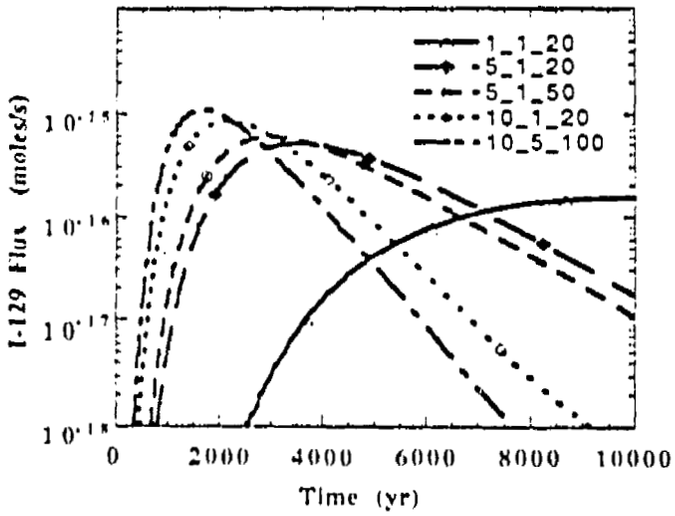

Figure 3.3-5. Total flux of the historical I-129 inventory from the vadose zone to the saturated zone for various flow cases.

Figures 3.3-6 show the total time-dependent flux of C-14, I-129 and Tc-99 from the vadose zone to the saturated zone for the four source regions for the highest-flow case (10_5_100). If these results are compared to those shown in Figures 3.3-2 through 3.3-4 for the base case flow rate, we see that the high-flow case yields curves that peak earlier and have higher contaminant fluxes to the vadose zone. For the base case calculations, the time of first arrival was estimated to be at about 600 years. For the high-flow case, this time has decreased to about 300 years.

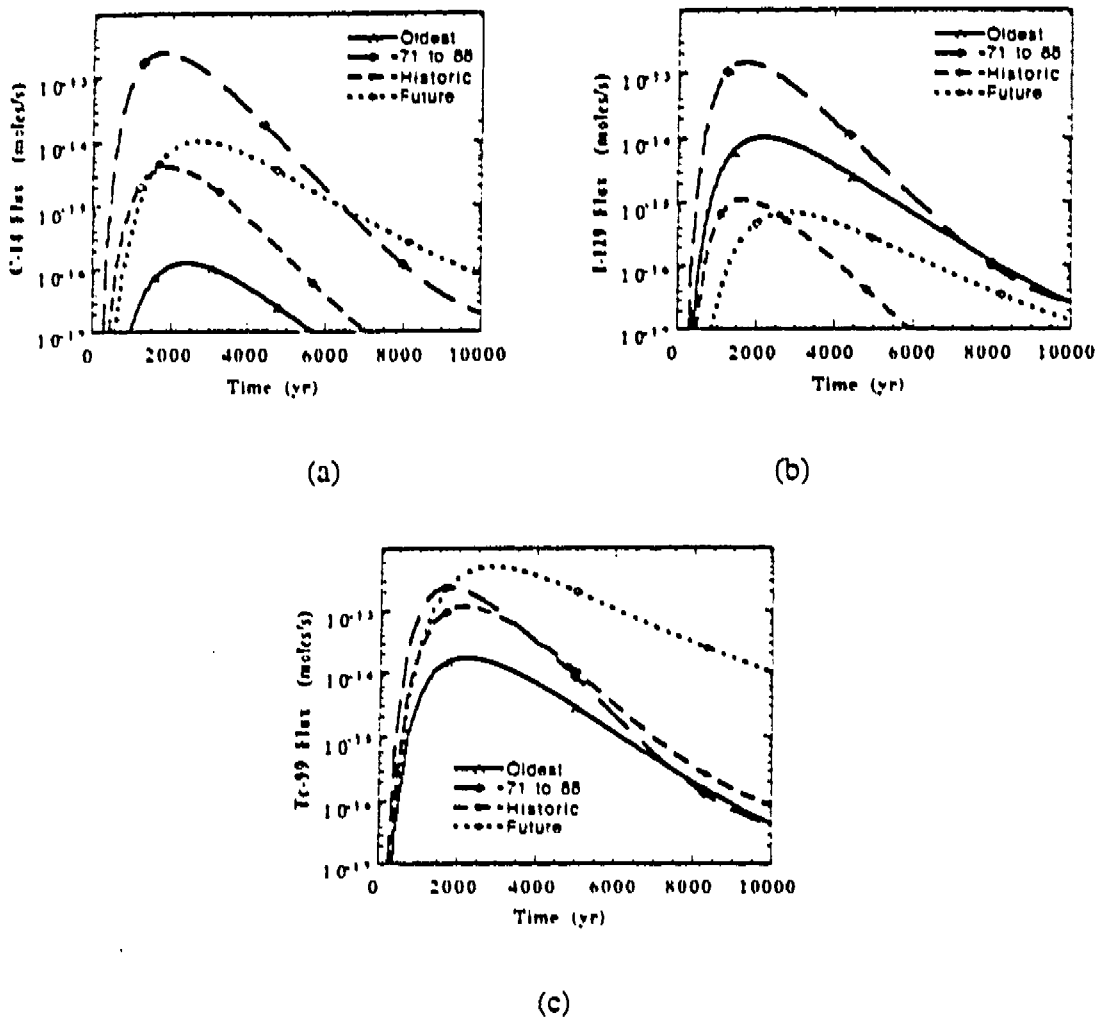

Figure 3.3-6. Total flux of (a) C-14, (b) I-129, and (c) Tc-99 from the vadose zone to the saturated zone for the highest flow case (10_5_100) from the four source regions.

Figures 3.3-7 show the total time-dependent flux of C-14, I-129 and Tc-99 from the vadose zone to the saturated zone for the four source regions for the lowest-flow case (1_1_20). If these results are compared to the base case results (Figs. 3.3-2 to 3.3-4), we see that the peak flux values for the low-flow case occur later than 10,000 years. For the base case calculations, the time of first arrival was estimated to be at about 600 years. For the low-flow case, this time has increased to about 2000 years, which is later than the 1000-year compliance period.

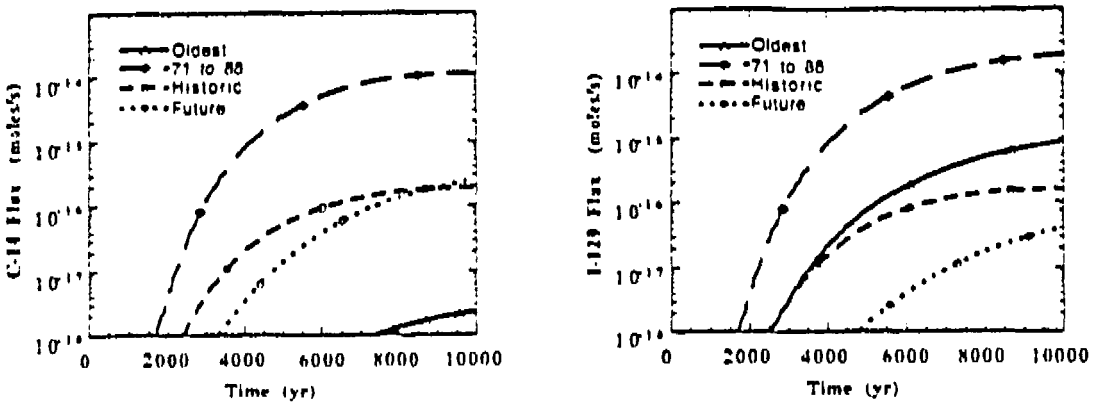

(a) (b)

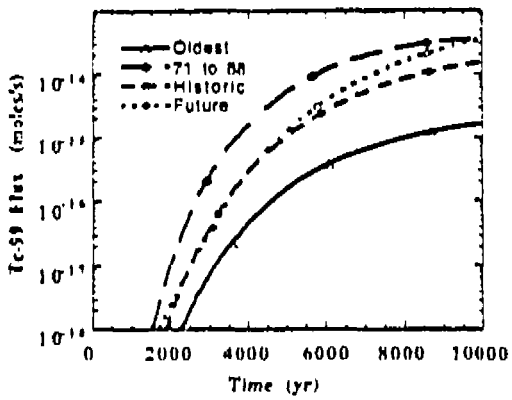

(c)

Figure 3.3-7. Total flux of (a) C-14, (b) I-129, and (c) Tc-99 from the vadose zone to the saturated zone for the lowest flow case (1_1_20) from the four source regions.

3.3.2 Lateral Transport toward the Mesa Sides

3.3.2.1 *Base Case Flow Field*

Figures 3.3-8 through 3.3-10 show the simulated results of lateral flux toward the north (Cañada del Buey) and south (Pajarito Canyon) mesa sides for C-14, I-129 and Tc-99. These calculated flux values are expected to be extremely conservative (high) compared to the true flux that occurs at the site for two reasons. First, the simulated lateral transport of the nuclides occurs because of the evaporative boundary condition imposed along the mesa sides. The very low, fixed saturation along the mesa sides causes a strong lateral pressure gradient which pulls water and subsequently the nuclides from the mesa interior toward the edges. Our hypothesis of evaporative processes at Area G is that evaporation occurs ubiquitously within the fractures in the mesa-top units and also along surge beds as discussed in Section 2.4. This hypothesis is supported by the extremely dry mesa-top tuff units (Krier, et al, 1996), by recent chloride and $\delta^{18}O$ profile analyses (Newman, 1996) and by high suction measured along the surge beds (Rogers et al, 1995, also see Figure 2.4-5 this report). If drying occurs throughout the mesa (as we hypothesize) instead of only at the mesa exterior, the resulting lateral pressure gradient is much weaker leading to less contaminant transport toward the mesa sides.

Second, the flux is calculated as though the nuclides exit the system as they reach the mesa edge. In this case, the nuclides would be available for surface transport, perhaps via surface runoff. It is more likely that nuclides would accumulate along the mesa edge rather than moving beyond. Pore water evaporates but the heavy, non-volatile nuclides will tend to concentrate. This same process happens along other evaporation sites (e.g., fractures) again resulting in less flux at the exterior of the mesa than shown in the calculations. Longmire et al. (1996) have observed elevated chloride, sulfate, and sodium concentrations in pore waters extracted from unsaturated-zone Bandelier tuff samples. They suggest that evaporation leads to the concentration of dissolved species. Newman's (1996) data on chloride and stable isotope concentrations also support this discussion.

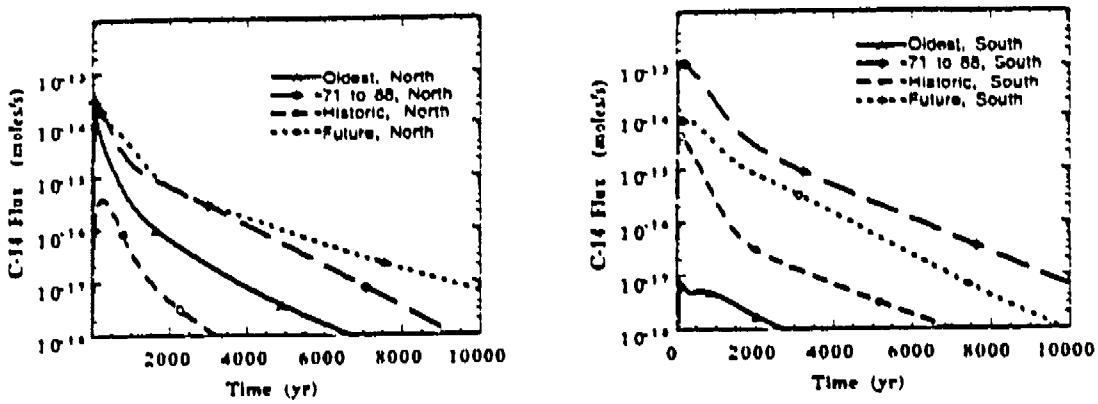

(a) (b)

Figure 3.3-8. Total Lateral Flux of C-14 toward the Mesa Sides along (a) Cañada del Buey and (b) Pajarito Canyon from the four source regions, base case flow field (5_1_50).

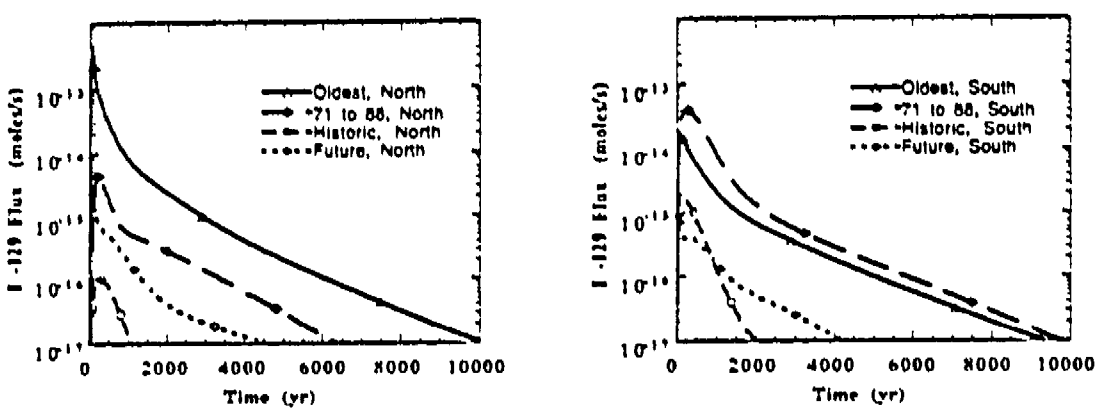

(a) (b)

Figure 3.3-9. Total Lateral Flux of I-129 toward the Mesa Sides along (a) Cañada del Buey and (b) Pajarito Canyon from the four source regions, base case flow field (5_1_50).

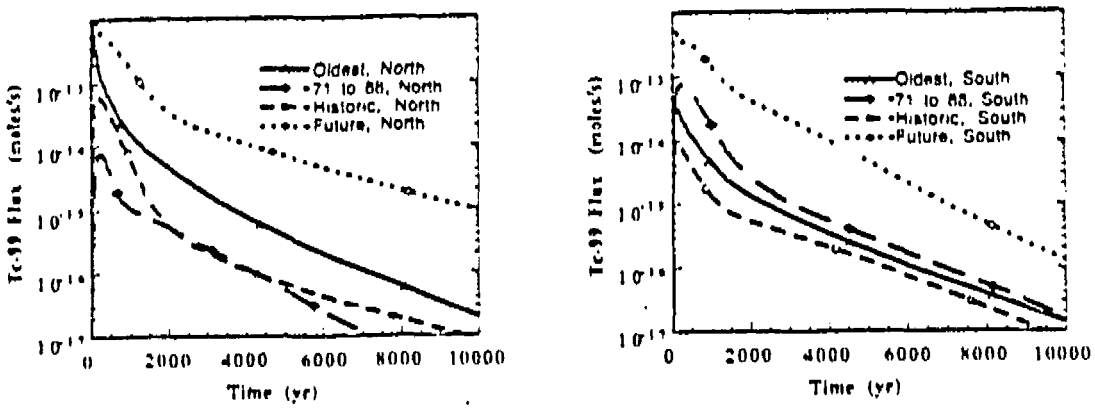

(a) (b)

Figure 3.3-10. Total Lateral Flux of Tc-99 toward the Mesa Sides along (a) Cañada del Buey and (b) Pajarito Canyon from the four source regions, base case flow field (5_1_50).

The next step in this analysis is to consider the migration of this laterally transported waste to the water table from the two canyon floors adjacent to the site. For the simulations, we conservatively assume that the radionuclide flux out of the mesa sides is immediately available for transport from the canyon floors. This is performed for some generic cases and later scaled to estimate results for the specific cases. As seen in Figures 3.3-8 through 3.3-10, a flux of 10^{-13} moles/s is a typical peak lateral flux value. This value is chosen to represent the generic source term. These figures also indicate a peak flux occurring for a period of about 500 years. Therefore, a generic rapid release source is modeled as a constant flux of 10^{-13} moles/s for a period of 500 years. The source release begins immediately so that no lag time for the nuclides to reach the mesa sides and then deposit in the canyon floors is included in the analysis.

Separate calculations are run for the two canyons, Pajarito Canyon (south) with a percolation rate of 50 mm/yr and Cañada del Buey (north) with a percolation rate of 1 mm/yr. The flux is applied over areas in the two canyons that represent the areas adjacent to the historic pits (Recorded 1988-1995 wastes). Figure 3.3-11 shows the resulting flux vs. time curves at the base of the vadose zone for this set of calculations. The contaminant that is placed in Pajarito Canyon (south) reaches the water table more quickly than that placed in Cañada del Buey (north) because of the higher percolation rate in Pajarito Canyon. The peak flux occurs after 750 years. The simulated nuclide flux from the vadose zone for waste placed in Pajarito Canyon is used as input to the saturated zone model so that the maximum possible dose for this mechanism can be predicted. These results are presented in Sections 4.3.2 and 4.3.3. The saturated zone results for the generic rapid release case (flux rate of $1.\times10^{-13}$ moles/s into Pajarito Canyon) are scaled by the approximate peak flux values for each of the three nuclides and each of the four waste categories from Figures 3.3-8 through 3.3-10. These scale factors, shown in Table 3.3-1, are used in the formal dose assessment (Shuman, 1997).

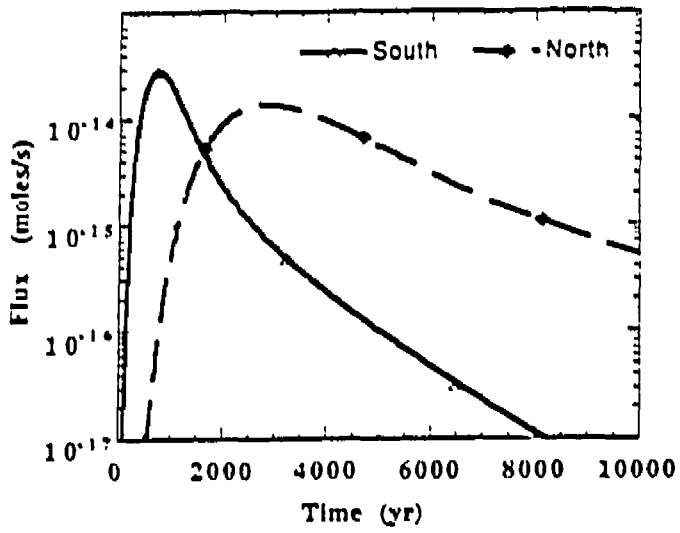

Figure 3.3-11. Generic Total Flux from the canyon floors through the Vadose Zone to the Saturated Zone for an Extreme Case of Lateral Transport. Pajarito Canyon (south) flow rate is 50 mm/yr. Cañada del Buey (north) flow rate is 1 mm/yr.

Table 3.3-1. Scale factors to correct generic concentration breakthrough curve for each nuclide and waste category using the base case flow field (5_1_50).

	C-14	I-129	Tc-99
Oldest	0.0001	0.2	0.4
71 to 88	1.0	0.5	0.8
Historic	0.04	0.02	0.1
Future	0.09	0.005	3.5

3.3.2.2 *Other Flow Fields*

For the high flow case (10_5_100), the simulated lateral transport toward the mesa side is quite similar to the base case predictions shown in Figures 3.3-8 through 3.3-10. Slightly higher peak fluxes (1 to 4 times higher) of shorter duration are calculated. At this higher flow rate, the mesa-top saturation is higher. This produces a larger saturation gradient between the mesa-top units and the side evaporative (fixed low saturation) boundary, causing a stronger capillary pull of contaminated water toward the mesa sides than for the base case. There is, however, a competing advective force. The higher flow rate carries the contaminated water downward twice as fast as in the base case, thus moving it beyond the strong capillary forces exerted along the mesa edges. These factors help to explain the higher peak fluxes of shorter duration. The generic flux curve from Pajarito Canyon to the water table for this case is shown in Figure 3.3-12. The high- and low-flow flux rates shown in Figure 3.3-12 are calculated similarly to that for the base case (a constant source of 10^{-13} moles/s for a period of 500 years with no lag time) except for the background flow field. There is faster breakthrough to the water table because of the higher canyon flow rate of 100 mm/yr. The peak flux

occurs after 580 years. Scale factors are shown in Table 3.3-2 for this higher flow case. These are used in the formal dose assessment to scale results for the generic case of flow through Pajarito Canyon to estimate a worst case release.

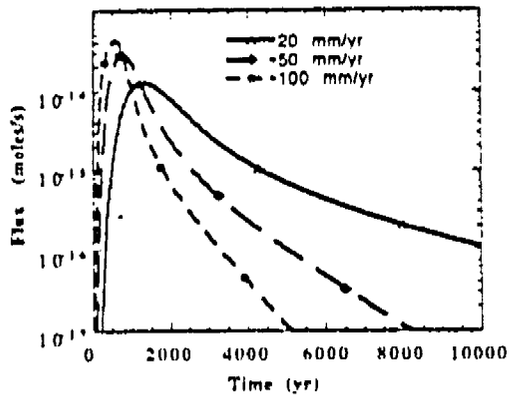

Figure 3.3-12. Generic Total Flux from the Floor of Pajarito Canyon through the Vadose Zone to the Saturated Zone for an Extreme Case of Lateral Transport. Pajarito Canyon flow rates are 100 mm/yr, 50 mm/yr and 20 mm/yr.

Table 3.3-2. Scale factors to correct generic concentration breakthrough curve for each nuclide and waste category using the highest flow rate (10_5_100).

	C-14	I-129	Tc-99
Oldest	0.0001	0.3	0.5
71 to 88	2.0	0.6	0.9
Historic	0.06	0.03	0.1
Future	0.2	0.007	6.0

For the low flow case (1_1_20), the simulated lateral transport toward the mesa side is also similar to the base case predictions shown in Figures 3.3-8 through 3.3-10. Slightly lower peak fluxes (2 to 4 times lower) with delayed arrival times and of longer durations are calculated . At this lower flow rate, the effects of the capillary and advective forces are the opposite of those explained in the previous paragraph for the high flow case. Compared to the base case, the capillary pull toward the mesa edge is weaker because the internal mesa-top saturation is lower. The downward advective transport is five times slower than for the base case. The weaker capillary force helps to explain the delayed arrival time and the lower peak values. With the lower flow rate, the contaminated water remains within the strong capillary gradient for a longer time which causes the longer duration of the flux curve. The generic flux curve from Pajarito Canyon to the water table (Figure 3.3-12) shows slower breakthrough to the water table because of the lower canyon flow rate of 20 mm/yr. The peak flux occurs after 1290 years. Scale factors are shown in Table 3.3-3 for this lower flow case. These are used in the formal dose assessment to scale results for the generic case of flow through Pajarito Canyon to estimate a lower bound release.

Table 3.3-3. Scale factors to correct generic concentration breakthrough curve for each nuclide and waste category using the lowest flow rate (1_1_20).

	C-14	I-129	Tc-99
Oldest	6×10^{-5}	0.04	0.09
71 to 88	0.5	0.2	0.4
Historic	0.01	0.005	0.05
Future	0.03	0.002	1.0

As in the base case, these calculated flux values are expected to be extremely conservative (high) compared to the true lateral flux that occurs at the site for the two reasons discussed in Section 3.3.2.1.

4. THREE-DIMENSIONAL SATURATED ZONE MODEL

4.1 SATURATED ZONE MODEL DEFINITION

The groundwater that percolates through Area G is assumed to flow predominantly downward through the vadose zone and then to enter the main aquifer which underlies the Pajarito Plateau at Los Alamos National Laboratory. This vadose-zone groundwater may be a source of radionuclide contamination to the main aquifer which in turn may flow to the Rio Grande. The potential levels of contamination in the main aquifer must be predicted in order to perform the PA and CA dose assessments for the site. These predictions of potential contaminant levels are made by modeling the groundwater flow and radionuclide transport with the finite element code FEHM (Zyvoloski et al., 1995). The calculations span a 10,000-year time period in order to predict doses in the aquifer for the required 1,000-year compliance period and the 10,000-year uncertainty period.

While an understanding of the geology and groundwater system under the Pajarito Plateau is still being developed, one hypothesis (Purtymun, 1995) is that the groundwater in the main aquifer beneath Area G flows in a southeasterly direction until it flows into the Rio Grande. The numerical model of the saturated flow beneath Area G assumes that groundwater flow is southeasterly and that the hydrologic properties of the aquifer are homogeneous and isotropic. The groundwater is assumed to discharge from the aquifer to the Rio Grande. The radionuclides potentially entering the main aquifer are assumed to have traveled downward through the vadose zone from Area G. The flux of radionuclides from the vadose zone is predicted (Section 3.3.1) and applied as an upper boundary condition to the saturated zone model. Although the flow system is simple, we have chosen to use a three-dimensional model in order to maintain the spatial distribution of the four disposal unit classifications (Section 3.1.6).

4.1.1 Geology and Hydrogeology

This brief description of the geology of the Pajarito Plateau is heavily dependent on Purtymun (1995). Purtymun (1984) states that the Rio Grande depression contains over 4570 m (15,000 ft) of volcanics and sediments that overlie the Precambrian crystalline rock. The upper part of the Pajarito Plateau consists of the Tshirege Member, the Otowi Member, the Guaje Member, the Fanglomerate member of the Puye Conglomerate, the Totavi Lentil, the Chaquehui Formation, the Chamita Formation, and the Tesuque Formations interbedded with basaltic rocks of the Chino Mesa and other basalts. The Tschicoma Formation is found to the west of the Pajarito Plateau.

Groundwater under the Pajarito Plateau can be found in the shallow alluvium near the surface, in perched water found above the main aquifer, and in the main aquifer. The main aquifer exists within the Puye Conglomerate (composed of the Fanglomerate member and the Totavi Lentil) and the Santa Fe Group (composed of the Chaquehui Formation, the Chamita Formation, and the Tesuque Formation). It may be unconfined toward the west, but in the east, it appears to be confined and under artesian and semiartesian conditions along the Rio Grande (Purtymun, 1984).

The main aquifer is thought to exist to great depth under the Pajarito Plateau but contains usable water (TDS less than 1000 mg/l) to a depth of 1830-2130 m (6000-7000 ft). Salinity of the aquifer increases with depth (Purtymun, 1984). There is no evidence of perched groundwater under Area G or between Area G and the Rio Grande (Devaurs, 1985; Devaurs and Purtymun, 1985).

Waste that enters the saturated zone beneath Area G will enter the fanglomerate member of the Puye Conglomerate. It is expected that the waste will not enter any of the deeper units and will remain contained within the fanglomerate member. This unit consists of volcanic debris with pumice cobbles to boulders in a matrix of silts, clays, and sands. Clay, silt and pumice lenses are common. The fanglomerate is widespread beneath the Pajarito Plateau. The basalts of the Chino Meso consist of a thick sequence of basaltic to andesitic rock and interflow breccias. They are interbedded with the Chaquehui Formation and the Fanglomerate member.

Wells located directly to the northwest of Area G are PM-2, PM-4, and PM-5 within the Pajarito well field. There is no information from wells or outcroppings in the area of interest between wells PM-2, PM-4, and PM-5 and near the Rio Grande where outcropping and water levels found in the river and nearby springs give further information.

In the Pajarito well field, the average saturated thickness of the main aquifer penetrated by the wells is 552 m (1810 ft). The average specific capacity of the field is about 6.46×10^{-3} m^2/sec (31.2 gpm/ft) of drawdown, transmissivity is 1.35×10^{-2} m^2/sec (93,800 gpd/ft) and the field coefficient of permeability is 2.52×10^{-5} m/sec (53.4 gpd/ft^2) (Purtymun, 1995). Purtymun has calculated the rate of movement of water in the top of the main aquifer near Area G as 9.2×10^{-7} m/sec (95 ft./yr) based on hydrologic characteristics of the supply and test wells in the Pajarito well field.

Purtymun (1995) states that, based on pumping tests over the screened length of the PM-2 well, the hydraulic conductivity is 1.3×10^{-5} m/sec (28 gpd/ft^2). Over the screened length of the PM-4 well the hydraulic conductivity is 1.1×10^{-5} m/sec (24 gpd/ft^2). Over the screened length of the PM-5 well the hydraulic conductivity is 2.5×10^{-6}.m/sec (5.3 gpd/ft^2).

Springs exist at the Rio Grande in the Totavi Lentil, the Chaquehui, and the Tesuque. Spring 4A outcrops in the Totavi Lentil at an elevation of 1698 m (5570 ft). Spring 4 outcrops in the Totavi Lentil at an elevation of 1698 m (5570 ft). Spring 3AA outcrops in the Totavi Lentil at 1664 m (5460 ft). Spring 5 outcrops in the Totavi Lentil at 1698 m(5570 ft). Spring 3B outcrops in the Tesuque at 1611 m (5450 ft). Spring 5A outcrops in the Chaquehui at 1644 m (5395 ft). (Purtymun, 1995, p.287).

Rogers et al. (1996) estimate that canyon infiltration rates for the Pajarito Plateau at 0.01-0.20 cm/yr beneath dry canyons and 0.01-0.10 cm/yr beneath wet canyons. A rough water balance estimate shows that the volume of vadose-zone water entering the aquifer near Area G is negligible compared to the aquifer volume. Thus, water flux from the vadose zone to the aquifer is not included in the model.

4.1.2 Grid

It is apparent from the preceding discussion of the geology and geohydrology of the Pajarito Plateau that 1) due to interbedded basalts and deltaic and streambed deposition of sediments there is a great deal of variation of the lithology of the area, and 2) in the area between Area G and the Rio Grande there are no outcrops or wells to give information about the detailed geology. Therefore, very little geometric detail of the formations is known about this area. For the saturated model of flow beneath Area G, a complicated model is not justified by the current knowledge of the geology and geohydrology. However, a three-dimensional model is warrented to capture the spatial distribution of radionuclide flux from the vadose zone and to approximate dispersive effects.

A rectangular-shaped grid is used to model the saturated zone; 9773 m (32063 ft) long extending from just west of Area G to the Rio Grande, 1280 m (4199 ft) wide, and 100 m (328 ft) deep (Figure 4.1-1). These dimensions are chosen to capture any potential contamination leaving Area G and moving toward the Rio Grande. The grid is made up of 19,580 nodes and 102,960 tetrahedral elements. Only the upper 100 m of the main aquifer is modeled which mainly encompasses the bottom of the fanglomerate member. The vertical element width decreases with elevation to better model contaminant plumes entering the top of the saturated zone from the vadose zone. Under Area G, the grid is refined in order to model the solute transport of any radionuclides entering the main aquifer from the unsaturated zone. These elements are 20 m in the groundwater flow direction and 44 m perpendicular to it. This element size was chosen to limit numerical dispersion in the solute transport calculations in the area beneath Area G. We expect an accurate flow solution throughout the grid with an accurate transport solution in the area of interest but some numerical dispersion in the less refined region which extends toward the Rio Grande. The model is oriented at -23° from the x-axis (Figure 4.1-2) in order to be approximately perpendicular to the groundwater equipotentials as shown in Purtymun (1995).

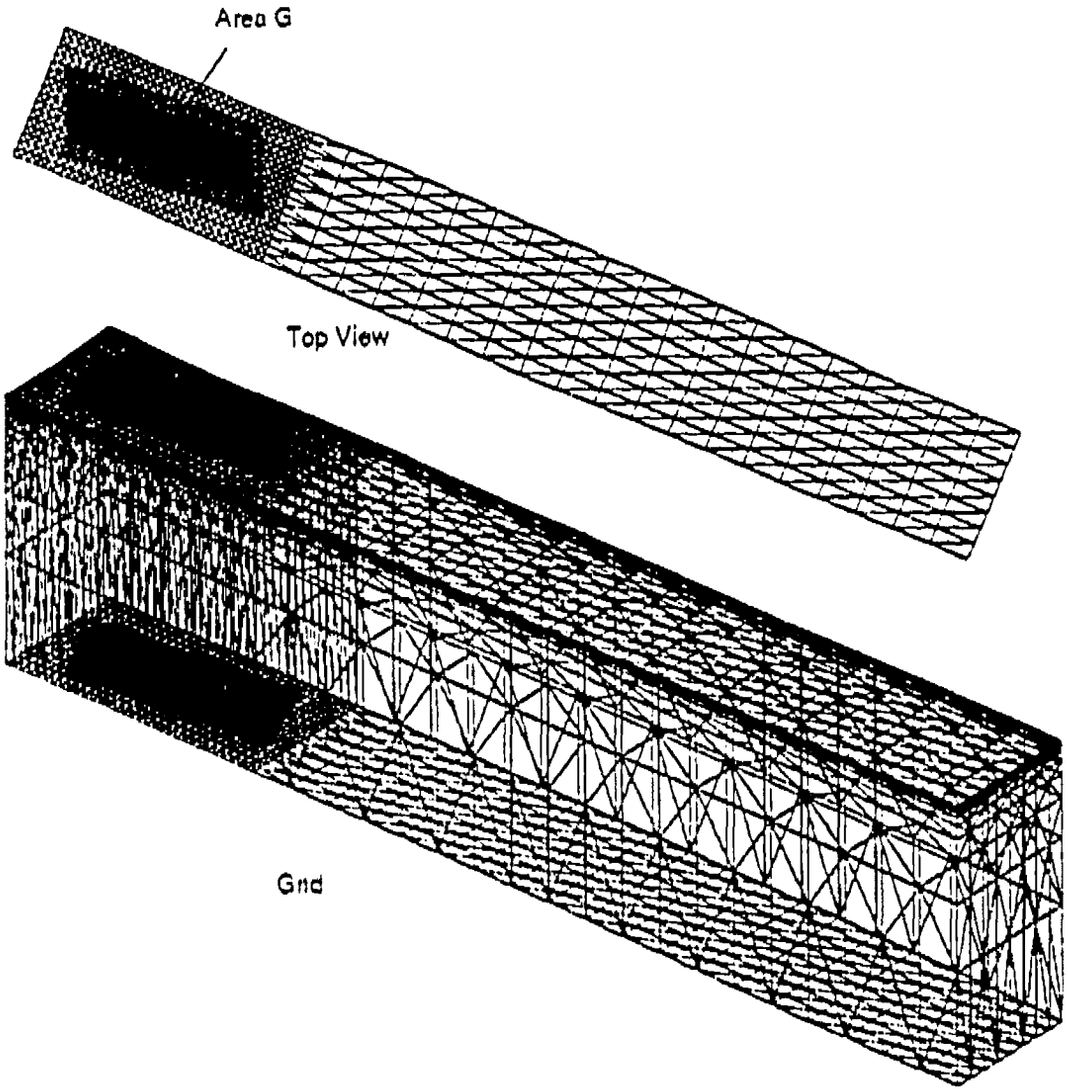

Figure 4.1-1. Three-dimensional finite element grid used for the saturated zone flow and transport calculations.

4.1.3 Boundary Conditions

Groundwater flow in the main aquifer is thought to be confined near the Rio Grande and unconfined further west. As an approximation, the main aquifer is modeled as entirely confined. This has a small effect on the total volume of flow through each cross section of the model but the groundwater velocities, which control the movement of the contaminant plume, are unchanged. The boundary conditions of the model are no flow on top and bottom, no flow along the north and south sides, and fixed pressure along the east and west sides of the model. The pressures at the east and west sides of the model increase with depth to represent constant head conditions and can be related to the equipotentials of the groundwater system by (Strack, 1989):

$$\phi = p/\rho g + \text{elevation}$$

where ϕ is the equipotential, p is the water pressure, ρ is the water density, and g is the gravitational constant. The change in equipotential from east to west is set at 101 m which corresponds to Purtymun's (1995) equipotentials. Time and position variant contaminant flux from the unsaturated zone is added to the upper boundary as a boundary condition for the transport solution.

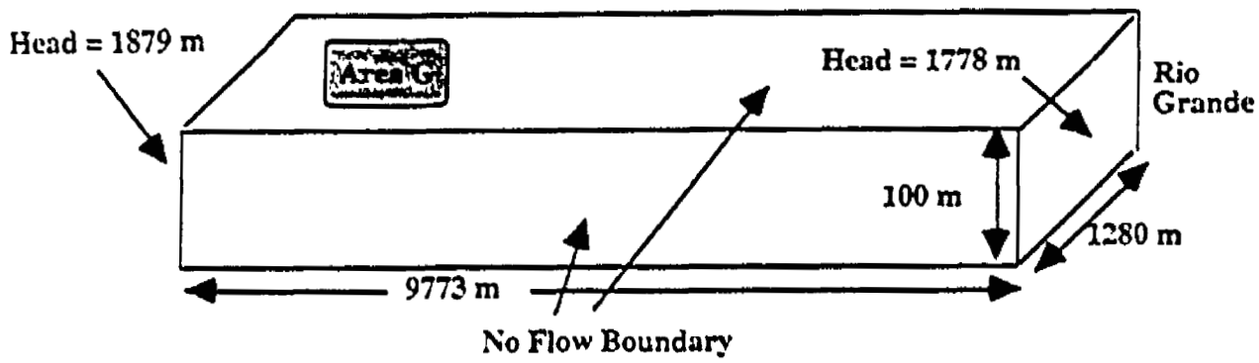

Figure 4.1-2. Saturated zone model configuration

4.1.4 Hydrologic and Transport Properties

Purtymun (1984) estimates that the hydraulic conductivity of the Puye Conglomerate is equal to 4.6×10^{-5} m/sec. This results in an intrinsic permeability equal to 4.72×10^{-12} m^2. The material is assumed to be isotropic and homogeneous for the modeling with a porosity of 0.25, as described in Section 3.1.4.

The diffusion coefficient for the saturated zone is assumed to be 10^{-9} m^2/s which is the same value used in the vadose zone at full saturation. Field studies have shown that the dispersivity increases with scale (Neuman, 1990; Gelhar et al, 1992). A dispersivity value of 20 m in the direction of flow and 2 m transverse to the flow are used for the simulations. These values are estimated using an empirical fit to field data developed by Neuman (1990) based on a length scale of interest of approximately 100 m which is the distance from the Area G boundary to the compliance point. Even larger dispersivity values are justifiable and the effect is discussed further in the uncertainty analysis presented in Section 5.0. The dispersivity limits the grid spacing to approximately 20 m (see Section 4.1.2). Table 3.1-4 gives the distribution coefficients that apply in the saturated zone.

4.2 SATURATED ZONE FLOW RESULTS

A saturated-zone flow field is run to steady state using the boundary conditions described in Section 4.1.3. This results in a Darcy velocity of 52 ft/yr and a linear pressure profile along the direction of flow. The velocity is in the range of those calculated by Purtymun (1995).

4.3 SATURATED ZONE TRANSPORT RESULTS

4.3.1 Downward Transport toward the Water Table

As discussed in Section 3.3.1, the radionuclide source term for the saturated zone model is the simulated, time and position variant radionuclide flux which exits the base of the vadose zone model. Nodes corresponding to the 28 spatial footprints shown in Figure 3.1-4 are defined for the saturated zone model. This retains the spatial distribution of the four disposal unit classifications described in Table 3.1-5. Figure 4.3-1 shows the simulated aquifer plumes for the historic I-129 inventory assuming the base case flow field in the vadose zone at 1000 years and 10,000 years.

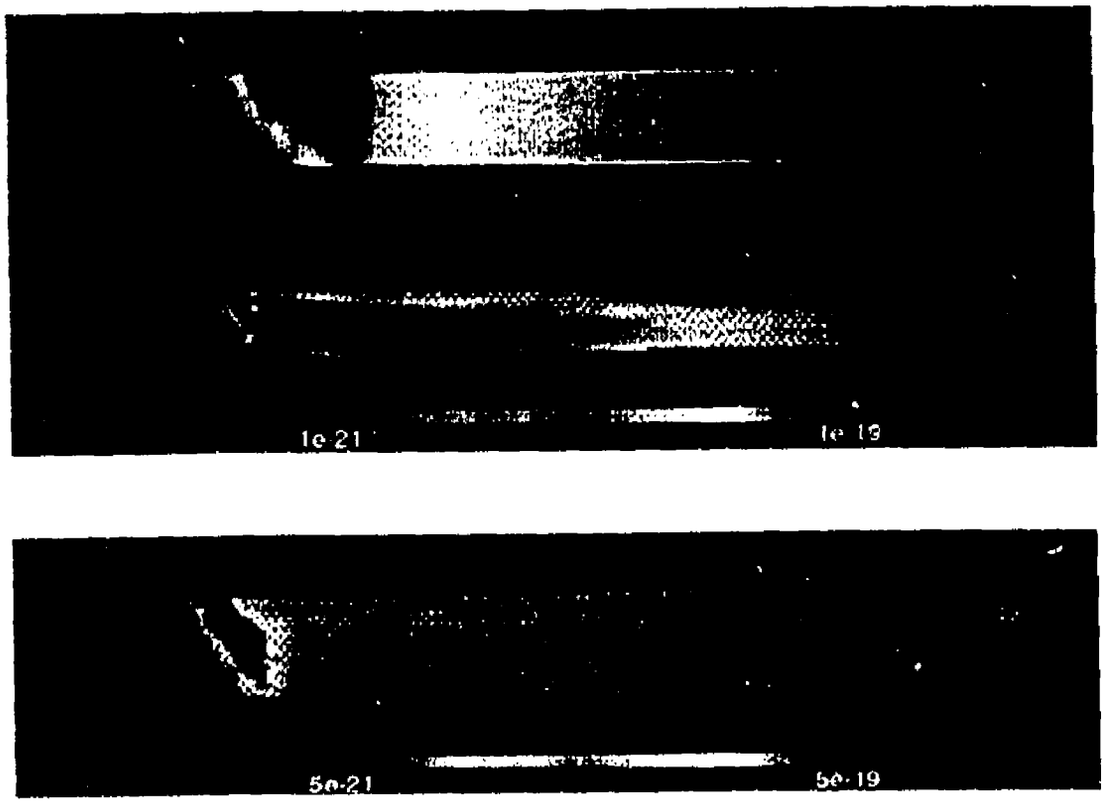

Figure 4.3-1. Historic I-129 Plume (concentration, moles/liter) in the aquifer for the base case, vadose-zone flow field: (top) side view at 1000 years, (middle) top view at 1000 years, (bottom) top view at 10,000 years.

The side view at 1000 years shows that the plume disperses throughout the 100-m depth of the model soon after entering the saturated zone. Concentration profiles at the 100 m compliance point show a nearly uniform contaminant distribution with the highest concentration at the water table. This trend applies for the other I-129 source classifications and for the C-14 and Tc-99 simulations. The top views show that the inventory from the historic shafts dominates the aquifer concentration at

1000 years, while the aquifer concentration is controlled by the various other pit inventories at 10,000 years.

Figure 4.3-2 shows concentration profiles at two locations in the saturated zone again for the historic I-129 inventory. The locations represent the point of maximum dose for the PA waste and the 100 m downstream compliance point. This point is 100 m downstream from the Area G fence line, but approximately 800 m from the location of the historic inventory. This information was submitted to be used in the formal dose assessment (Shuman, 1997; Hollis et al., 1997). The two curves have the same shape with dilution and mixing decreasing the concentration by a factor of about 3 at the 100 m distance. The curves reflect the vadose-zone contaminant flux curve as shown in Figure 3.3-3. Similar results apply for the other nuclides and source terms. The dilution factor at the 100 m location increases as distance increases (i.e. the future inventory is more diluted at the 100 m compliance point than is the oldest inventory.) Aquifer dilution of vadose zone concentrations is approximately a factor of 500 between the maximum vadose zone concentration and the concentration at the 100 m compliance point.

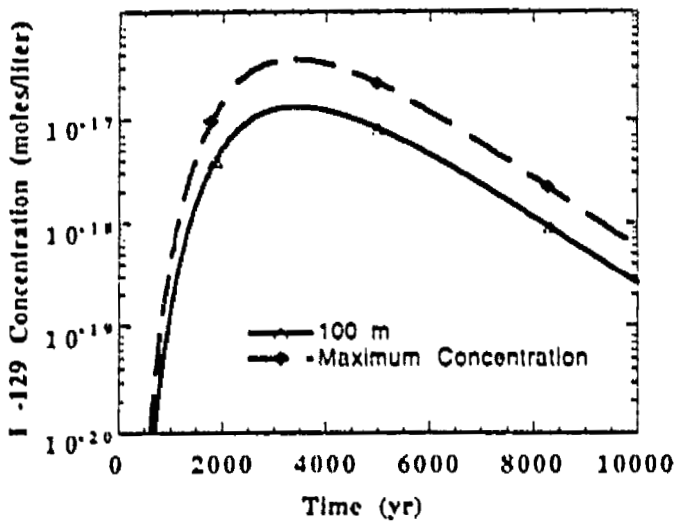

Figure 4.3-2. Concentrations in the Saturated Zone for the I-129 Historic Inventory at the Point of Maximum Concentration and at the 100-m Compliance Point with the base case flow field in the vadose zone.

4.3.2 Lateral Transport toward the Mesa Side

As shown in Figure 3.3-11, waste that is transported laterally through the vadose zone toward the mesa side and then desposited into Pajarito Canyon reaches the water table more quickly and at a higher flux over the first 1000 years than waste that is transported laterally and deposited into Cañada del Buey. For this reason, this saturated zone study focuses on the waste that migrates toward Pajarito Canyon to calculate possible contamination from lateral transport at the water table. Three concentration breakthrough curves are shown in Figure 4.3-3. These represent the time variant aquifer concentration at the location of maximum dose in the saturated zone for the three generic rapid release cases (flux rate of $1.x10^{-13}$ moles/s into Pajarito Canyon): the base case (5_1_50), the highest flow case (10_5_100) and the lowest flow case (1_1_20). These results are scaled by the approximate peak flux values for each of the three nuclides and each of the four waste categories as shown in Tables 3.3-1, 3.3-2 and 3.3-3. The base case breakthrough curve closely mimics that from the vadose zone (Figure 3.3-11) with a lag time of approximately 50 years, the time for the nuclides to travel through the vadose zone at the canyon flow rate of 50 mm/yr. For each of the three vadose zone flow cases, this pathway results in higher aquifer concentrations than

the downward pathway during the first 1000 years because we assume an instantaneous release into the canyon floor where the flow rate is higher than through the mesa. The scale factors along with the concentration breakthrough curves are used as part of the formal dose assessment.

The generic concentration curves represent the maximum concentration in the saturated zone beneath Pajarito Canyon adjacent to the historical pits and shafts. The scale factors (Tables 3.3-1 through 3.3-3) are applied to this curve not only for the historic wastes but also for the other three wastes categories. In the formal dose assessment, the displacement of the different wastes is not taken into account (i.e., all of the wastes are assumed to enter the saturated zone at the same location), which again overestimates the dose for this pathway. Because the concentration is reported at a location directly beneath the canyon source rather than at a downstream location, the plume is not completely mixed. The concentration at a depth of 100 meters is approximately 10% that at the top of the aquifer.

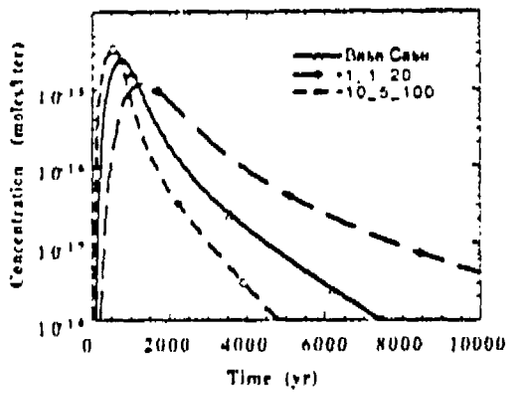

Figure 4.3-3. Time Dependent Concentration plots for the generic case of lateral transport at the location of maximum concentration in the saturated zone.

4.3.3 Dose Assessment

Dose factors were applied to the three-dimensional C-14, I-129 and Tc-99 saturated-zone concentration fields to obtain dose fields. These dose fields were summed to obtain the total ground water dose and the all pathways dose (for the water component) for the Entire PA Inventory (historic plus future waste) and the Composite Analysis Inventory (CA or all wastes). These calculations were performed in support of the formal dose assessment in order to locate the positions of maximum dose for various combinations of waste inventories. The concentrations of C-14, I-129 and Tc-99 at the locations of the maximum entire PA doses beneath Area G, maximum CA doses beneath Area G, and the maximum entire PA and CA doses at a distance 100 m downstream of Area G were supplied for the formal dose assessment. Table 4.3-1 shows the performance objectives along with the calculated maximum dose values for the base case flow field and the 10_5_100 flow field at 1000 years. It also shows the peak doses during the 10,000 year uncertainty period which occurs at about 4500 years for the PA waste and 3000 years for the CA waste for the base case flow rate. All doses calculated for nuclides traveling downward through the vadose zone are six or more

orders of magnitude lower than the performance objectives. For the low flow case, doses are negligible because well over 99% of the inventory remains in the vadose zone as shown in Figure 3.3-7.

Table 4.3-1. Maximum Ground Water and All Pathways Doses for the PA and CA wastes, Base Case Flow Field (mrem/yr).

	PA - Ground Water	PA - All Pathways	CA - All Pathways
Performance Objective	4	25	100
1000 yr (Base Case)	2.4×10^{-7}	6.5×10^{-7}	3.7×10^{-5}
Peak Dose (Base Case)	3×10^{-5} @ ~4500 yrs	1×10^{-4} @ ~4500 yrs	2×10^{-3} @ ~3000 yrs
1000 yr (10_5_100)	8.0×10^{-6}	2.2×10^{-5}	1.4×10^{-3}
1000 yr (1_1_20)	9×10^{-12}	2×10^{-11}	1×10^{-10}

The full dose assessment for the site is presented in Shuman (1997). Shuman calculated a higher dose during the first 1000 years from the waste that is transported laterally to the mesa side than from waste that follows the continuous downward path to the water table. For example, the peak aquifer dose for the base case vadose zone flow field caused by lateral migration toward the mesa side and subsequent desposition into Pajarito Canyon occurs after 800 years. The PA groundwater dose is 4.5×10^{-5} and the PA all pathways dose is 1.3×10^{-4}. These doses are higher than those reported in Table 4.3-1, but five to six orders of magnitude lower than the performance objectives. As explained in section 4.3.2, the earlier arrival time and higher aquifer concentrations for this pathway are due to the assumption of immediate source release into Pajarito Canyon and the corresponding fast canyon recharge rate.

Recall from Section 3.3.2.1, that this pathway is thought to be vastly overestimated. Even still doses from this route are five to six orders of magnitude less than the performance objectives. A mass balance comparison of the downward and lateral pathways was performed to calculate the possible impact of overestimating the lateral pathway. Over 10,000 years, approximately 30% of the mass leaves laterally compared to that which exits at the base of the vadose zone. If this mass were transported downward instead, we would roughly predict a 30% increase in the dose for the downward pathway. As shown in Table 4.3-1, a 30% increase in dose for this pathway is insignificant to the dose assessment.

5. UNCERTAINTY

As in any predictions of the long-term migration of solutes through the subsurface, the results of these transport simulations contain intrinsic uncertainty. Here we will assess what we believe are the more important uncertainties and discuss their impact on the results. The greatest uncertainties associated with predicting aquifer related doses from Area G are related to our understanding of the mechanisms that control flow and transport within the vadose zone and our ability to model these mechanisms. At this point, we feel that uncertainty associated with the hydrologic processes themselves (conceptual model uncertainty) dominates our ability to make predictions of transport at the site more so than uncertainty associated with the hydrologic and geochemical properties (data uncertainty). However, even with these uncertainties, predicted doses are so comfortably low that we do not expect that the uncertainties discussed below can elevate doses to levels of concern.

5.1 VADOSE ZONE FLOW

In-situ saturation data is difficult to match with any single infiltration rate using our current vadose zone models, as was shown in Sections 2.1 and 3.2. Environmental tracer data (Newman, 1996) indicate distinct zones of varying flux with very low mid-mesa water flux rates (0.03 to 0.8 mm/yr) and increased sub-mesa flux rates (0.2 to 5 mm/yr). It is possible that the mesa and the sub-mesa units are not strongly connected hydrologic systems. The wetter saturations beneath the mesa may be the result of recharge from a different source region than from percolation through the mesa top or could represent a wetter climatic period of higher recharge than the present (e.g., during the Pleistocene). Evaporation is clearly an important mechanism controlling mid-mesa flux rates, yet it is only indirectly incorporated into the flow modeling through the application of low infiltration rates of one to ten mm/yr. Under this steady, low infiltration rate, the simulations predict a slow but smooth migration of waste through the vadose zone. However, by directly including evaporation in the simulations, the calculated migration of waste through the mesa may behave similarly to that seen with the environmental tracers such as chloride (Newman, 1996) which accumulate within the mesa and have estimated travel times on the order of 1,000 to 17,000 years through the Bandelier Tuff. The mesa itself may act as a dry barrier to downward migration of waste which could lead to enhanced waste isolation. If this is the case, we expect that the dose estimates made in this report would be higher than if these effects are included.

The mesa-top infiltration rate is the strongest control on the calculated downward migration of waste through the vadose zone. It controls the source release of waste from the disposal units and the subsequent downward migration. We quantified this uncertainty somewhat by considering not only a base case flow field, but also high and low flow cases. As shown in Table 4.3-1, a variation in mesa-top infiltration rate from 1 mm/yr to 10 mm/yr results in a difference in the 1000-year groundwater related doses of six orders of magnitude. Clearly a good understanding of this key parameter is important to the dose assessment. However, because doses are so much less than the performance objectives, a conservative yet realistic value seems adequate for this site.

Other uncertainties are related to flow within the deeper vadose zone units for which very little hydrologic data are available. Is there lateral flow in the Guaje Pumice bed? Do fractures control water flow through the basalts? The simulation results take almost no credit for transport times through the Cerros del Rio Basalts because we have no knowledge of the flow regime for this unit. Because the basalts make up more than 50% of the vadose zone, this assumption is extremely conservative. The inclusion of more realistic flow and transport properties for this unit is likely to add hundreds if not thousands of years to transport times, and to result in lower peak concentrations in the saturated zone. Again, doses related to the groundwater pathways at Area G are orders of magnitude less than the PA or CA performance objectives (Shuman, 1997). An understanding of the mechanisms that govern flow in the deeper vadose zone units would greatly enhance our understanding of flow and transport at Area G. However, because the model assumptions concerning flow through these units add conservatism to the very low predicted doses, a more comprehensive model of the deep vadose zone would probably result in further reduction of predicted doses and is therefore not necessary.

The PA and CA transport calculations are based on the steady flow assumption and on the use of matrix hydrologic properties for all but the basalts at the site. Our understanding of the response of this fractured system to transient flow events is another uncertainty in modeling of the site. The transient calculations (Section 2.2) indicate that the steady flow assumption is adequate because fluctuations in both saturation and contaminant flux rates dampen with depth even when including fractures in the upper two units. The single fracture infiltration study lead us to the conclusion that fracture flow is difficult to initiate (e.g. requires a large source of water) and is short lived once the water source is removed. This conclusion helps justify the use of the matrix hydrologic properties for the transport calculations. Again, we should note that only the upper two tuff units are considered to have significant fracturing (Krier et al., 1996), and that the uppermost unit is excavated during disposal operations. The waste travels through only one highly fractured unit (Unit 1v-u) above the basalts and even if fracture flow dominates there, the matrix units below will help to attenuate any transient pulses.

Mean values were chosen for the hydrologic properties used in the modeling. Clearly there is some variability in hydrologic properties at the site. In Appendix 2, Orr performed a sensitivity analysis using the minimum and maximum reported hydraulic conductivity values for the units above the Guaje Pumice. In these one-dimensional simulations, he found that vadose-zone travel times vary by approximately ± 25% from that calculated using mean values. If travel times are shorter in response to higher conductivity values, predicted doses would be higher because the simulated flux from the vadose zone would be further along the flux vs. time curves (see for example Figures 3.3-2 through 3.3-4). This could not elevate doses by more than two orders of magnitude which is still four orders of magnitude below the performance objectives. However, it is important to point this out as an indicator of our assumptions being less than conservative in favor of our best estimate of the actual system behavior. Heterogeneity in hydrologic properties could lead to preferential flow paths through the vadose zone which could possibly produce faster travel times and regions with more concentrated flux at the base of the vadose zone. However, this waste would be diluted and dispersed in the aquifer, and it is again unlikely that this affect could elevate doses by the six orders of magnitude required to surpass the performance criteria.

5.2 SATURATED ZONE FLOW

The saturated zone is modeled as a homogeneous and isotropic, single medium. However, the true system has interbedded basalts in the Puye Conglomerate. As described above, heterogeneity can lead to preferential flow paths which can yield higher aquifer concentrations. Aquifer concentrations are, however, limited by the flux of nuclides through the vadose zone and even at the point of maximum calculated dose in the aquifer, doses are again six orders of magnitude less than acceptable limits.

The aquifer velocity used in the simulations is 16 m/yr. Purtymun's (1995) estimated aquifer velocity of 29 m/yr would advect the plume more quickly toward the compliance point. However, the plume would be diluted by approximately a factor of two from the current calculation. Again this effect is small because of the very fast travel time through the aquifer. One other uncertainty is related to the modeled aquifer depth. The plume disperses throughout the entire modeled depth of 100 meters. Had the depth been increased, the plume would have dispersed even further with a corresponding decrease in concentration. This aquifer depth produces conservative (higher) concentrations.

5.3 TRANSPORT PROPERTIES

The transport simulations are very sensitive to the value of the distribution coefficient, Kd. Uncertainty in this parameter for weakly sorbing nuclides is a data uncertainty that can play an important role in the results of the transport simulations and the subsequent human dose assessment calculations. According to our simulations, a nuclide with a Kd of approximately 2.5 or higher will not reach the saturated zone within 10,000 years. Previous simulations (Birdsell et al., 1995) indicate that a Kd value as low at 0.3 will retard nuclides sufficiently to prevent breakthrough to the aquifer within 1000 years. Site specific values for several nuclides (Longmire et al., 1996) which have large inventories or were expected to have low distribution coefficients were measured in order

to decrease the uncertainty in the transport predictions that results from data uncertainty for this parameter.

Longitudinal and transverse dispersivity values of 20 m and 2 m were used for the saturated zone modeling. Larger dispersivity values are justifiable based on the distance of the pits to the 100-m compliance point. For example, the oldest pits are located approximately 180 m from the compliance point while the future pits are on the order of 1300 m from the compliance point. These distances lead to longitudinal dispersivity values ranging from 24 m to 130 m and transverse values ranging from 2.4 to 13 m based on Neuman's (1990) empirical fit to field data. Source appropriate dispersivity values for the four source regions could have been applied. The effect of increasing the dispersivity on the simulated concentrations is that an increase in longitudinal dispersivity would result in a faster arrival time for the plume's leading edge and a lower peak concentration. An increase in the transverse dispersivity would also lead to a lower peak concentration. The dispersivity values used for the saturated zone modeling yield conservative results for the dose assessment.

6. CONCLUSIONS

Numerical simulations are used to predict long-term migration rates of radionuclides for the Area G performance assessment and composite analysis. Results of the calculations show that only the three nonsorbing nuclides C-14, I-129 and Tc-99 reach the aquifer during the 1000-year compliance period or the 10,000-year uncertainty period. Doses resulting from the aquifer concentrations of these three nuclides are six or more orders of magnitude less than the performance objectives for the site. As in any predictions of the long-term migration of solutes through the subsurface, the results of these transport simulations contain intrinsic uncertainty. However, even with these uncertainties, predicted doses are so comfortably low that we do not expect that the uncertainties described above can elevate doses to levels of concern.

These predictions require calculations of transport through the vadose and saturated zones. The two domains are simulated separately with the spatial and temporal flux leaving the vadose zone applied as input to the saturated zone. Both domains use steady flow fields. A range of vadose zone flow rates were simulated in order to address the effect of uncertainty in the infiltration rate on aquifer concentrations. All flow fields produced very low aquifer concentrations.

Numerical studies were used to better understand vadose zone flow through the dry mesa-top environment at Area G. These studies helped define the final model used to model flow and transport through the vadose zone. The study of transient percolation indicates that a steady flow vadose-zone model is adequate for computing contaminant flux to the aquifer. The fracture flow studies and the investigation of the effect of basalt and pumice properties helped us define appropriate hydrologic properties for the modeling. Finally, the evaporation study helped to justify low infiltration rates.

7. REFERENCES

Barnard, R.W. and H.A. Dockery, "Technical Summary of the Performance Assessment Calculation Exercises for 1990 (PACE90)," Sandia National Laboratories Report SAND 90-2726, 1991.

Birdsell, K.H., W.E. Soll, N.D. Rosenberg, and B.A. Robinson, "Numerical Modeling of Unsaturated Groundwater Flow and Radionuclide Transport at MDA G", Los Alamos National Laboratory Report LA-UR-95-2735, 1995.

Bishop, C.W., "Hydrologic Properties of Vesicular Basalt", Masters Thesis, University of Arizona, Tucson, AZ 1991.

Bowen, B.M., "Los Alamos Climatology," Los Alamos National Laboratory Manuscript LA-MS-11735, 1990.

Carsel, R.F. and R.S. Parrish, " Developing Joint Probability Distributions of Soil Water Retention Characteristics," *Water Resources Research* 24:755-769, 1988.

Conca, J.L., and J. Wright, "Diffusion and Flow in Gravel, Soil, and Whole Rock", *Applied Hydrogeology*, Vol 1, No. 1, pp. 5-24, 1992.

Devaurs, M., "Core analyses and observation well data from Mesita del Buey waste disposal areas and in adjacent canyons," Los Alamos National Laboratory Report LA-UR-85-4003, 1985.

Devaurs, M., and W. D. Purtymun, "Hydrologic characteristics of the alluvial aquifers in Mortandad, Cañada del Buey, and Pajarito Canyons," Los Alamos National Laboratory Report LA-UR-85-4002, 1985.

Frenzel, P.F., Geohydrology and Simulation of Groundwater Flow near Los Alamos, North-Central New Mexico USGS, Water-Resources Investigations Report 95-4091, 1995.

Gable, C.W., T. Cherry, H. Trease, and G. A. Zyvoloski, "GEOMESH Grid Generation", Los Alamos National Laboratory Report LA-UR-95-4143, 1995.

Gelhar, L.W., C Welty, K.T. Rehfeldt, "A Critical Review of Data on Field Scale Dispersion in Aquifers," Water Resource Research 28: 1955-1974, 1992.

Hollis, D., E. Vold, R. Shuman, K. Birdsell, K. Bower, W. Hansen, D. Krier, P. Longmire, B. Newman, D. Rogers, E. Springer, "Performance Assessment and Composite Analysis for the Los Alamos National Laboratory Disposal Area G," Los Alamos National Laboratory Document LA-UR-97-85, Report-54G-013, 1997.

Klavetter, E.A. and R.R. Peters, "Estimation of Hydrologic Properties of an Unsaturated Fractured Rock Mass", Sandia National Laboratory Report SAND84-2642, 1986.

Krier, D., R. Longmire, and H.J. Turin, "Geologic, Geohydrologic and Geochemical Data Summary of MDA G, TA-54, Los Alamos National Laboratory", Los Alamos National Laboratory Report LA-UR-95-2696, 1996.

Longmire, P., C.R. Cotter, I.R. Triay, J.J. Kitten, C. Hall, J. Bentley, D. Hollis, and A.I. Adams, "Batch Sorption Results for Americium, Neptunium, Plutonium, Technetium, and Uranium Transport through the Bandelier Tuff, Los Alamos, New Mexico" Los Alamos National Laboratory report LA-UR-96-4716, 1996.

Montazar, P., and Wilson, W.E., "Conceptual Hydrologic Model of Flow in the Unsaturated Zone, Yucca Mountain, NV", Water Resources Investigations Report 84-4355, U.S. Geological Survey, 1984.

Neuman, S.P., "Universal Scaling of Hydraulic Conductivities and Dispersivities in Geological Media", Water Resources Research 26: 1749-1758, 1990.

Newman, Brent, "Vadose Zone Water Movement at Area G, Los Alamos National Laboratory, TA-54: Interpretations Based on Chloride and Stable Isotope Profiles," Los Alamos National Laboratory report LA-UR-96-4682, 1996.

Nilson, R.H., E.W. Peterson, K.H. Lie, N.R. Burkhard, and J.R. Hearst, "Atmospheric Pumping: A Mechanism Causing Vertical Transport of Contaminated Gases Through Fractured Permeable Media", J. of Geophysical Research, Vol. 96, B13, pp. 21933-21948, 1991.

Purtymun, W.D., "Geologic and Hydrologic Records of Observation Wells, Test Holes, Test Wells, Supply Wells, Springs, and Surface Water Stations in the Los Alamos Area, " Los Alamos National Laboratory manuscript LA-12883-MS, 1995.

Purtymun, W.D., "Hydrologic Characteristics of the Main Aquifer in the Los Alamos Area: Development of Groundwater Supplies," Los Alamos National Laboratory manuscript LA-9957-MS, 1984.

Rogers, D.B. and B.M. Gallaher, "The Unsaturated Hydraulic Characteristics of the Bandelier Tuff, Los Alamos National Laboratory Manuscript LA-12968-MS, 1995.

Rogers, D.B., E.L. Vold, and B. M Gallaher, "Bandelier Tuff Hydraulic Characteristics from Los Alamos National Laboratory Borehole G-5 at MDA G, TA-54", New Mexico Geologic Society Guidebook, 47th Field Conference, The Jemez Mountains Region, pp. 413-420, 1996.

Rogers, D.B., B.M. Gallaher, E.L. Vold, "Vadose Zone Infiltration Beneath the Pajarito Plateau at Los Alamos National Laboratory," Los Alamos National Laboratory report LA-UR-96-485, 1996.

Rogers, D.B., P. Longmire, B.D. Newman, K.H. Birdsell, W.E. Soll, and E.L. Vold, "Conceptual Model for Subsurface Transport at MDA G", Los Alamos National Laboratory report LA-UR-97-179, 1997.

Rosenberg, N.D., W.E. Soll, and H.J. Turin, "Potential Transport of PCBs Through Fractured Tuff at Area G", Los Alamos National Laboratory report LA-UR-94-28, 1993.

Shuman, Rob, "Radioactive Waste Inventory for the TA-54, Area G Performance Assessment and Composite Analysis", Rogers and Associates Engineering Corp. report, RAE-9148/82-1, 1996.

Shuman, Rob, "Radiological Dose Assessment for the TA-54, Area G Performance Assessment and Composite Analysis", Rogers and Associates Engineering Corp. report, RAE-9148/82-2, 1997.

Soll, W.E., "Influence of Fracture Fills and Fracture Coatings on Flow in Bandelier Tuff", Los Alamos National Laboratory report LA-UR-95-2695, 1995.

Springer, E. P., "Area G Performance Assessment: Surface Water and Erosion", Los Alamos National Laboratory report LA-UR-95-2497, 1995.

Springer, E. P., "Surface Water and Erosion Calculations to Support the MDA G Performance Assessment", Los Alamos National Laboratory report LA-UR-96-4894, 1996.

Strack, O.D.L., *Groundwater Mechanics*, Prentice Hall, New Jersey, 1989.

Turin, H. J., "Subsurface Transport Beneath MDA G: A Conceptual Model", Los Alamos National Laboratory report LA-UR 95-1663, 1995.

Vaniman, D., G. Cole, J. Gardner, J. Conaway, D. Broxton, S. Reneau, M. Rice, G. WoldeGabriel, J. Blossom, and F. Goff, "Development of a Site-Wide Geologic Model for Los Alamos National Laboratory", Los Alamos National Laboratory report LA-UR-96-? 1996.

Vold, E.L., D. Hollis, P. Longmire, E. Springer, K. Birdsell, and R. Shuman, "The Role of a Detailed Aqueous Phase Source Release Model in the LANL Area G Performance Assessment", Los Alamos National Laboratory report LA-UR-96-368, 1996.

Vold, Erik, "Analysis of Liquid Phase Transport in the Unsaturated Zone at a Mesa Top Disposal Facility", Los Alamos National Laboratory report LA-UR-96-370, 1996.

Vold, Erik and Rob Shuman, "Phase Two of the Source Release Modeling or the Los Alamos Area G Disposal Vacility Performance Assessment", Los Alamos National Laboratory report LA-UR-96-4786, 1996.

Wang, J.S., and T.N. Narisimhan, "Hydrologic Modeling of Vertical and Lateral Movement of Partially Saturated Fluid Flow in a Fault Zone at Yucca Mountain, NV", Technical Report SAND87-7070 (Sandia National Laboratory) and LBL-23510 (Lawrence Berkeley National Laboratory), 1987.

Weeks, E.P., "Effect of Topography on Gas Flow in Unsaturated Fractured Rock", Flow and Transport Through Unsaturated Fractured Rock, AGU Geophysical Monograph #42, pp. 165-170, 1987.

Wight, J.R. and J.W. Skiles, eds., "SPUR: Simulation of Production and Utilization of Rangelands. Documentation and User Guide," U.S. Department of Agriculture, Agricultural Research Service, ARS 63, 1987.

Wood, M.I., R. Khaleel, P.D. Rittmann, A.H. Lu, S.H. Finfrock, R.J. Serne, K.J. Cantrell, T.H. DeLorenzo, "Performance Assessment for the Disposal of Low-Level Waste in the 200 West Area Burial Grounds," Westinghouse Hanford Company report WHC-EP-0645, 1994.

Zyvoloski, G. A., B. A. Robinson, Z. V. Dash, and L. L. Trease, "Models and Methods Summary for the FEHMN Application", Los Alamos National Laboratory report LA-UR-94-3787, Rev. 1, 1995.

Zyvoloski, G. A., B. A. Robinson, Z. V. Dash, and L. L. Trease, "User's Manual for the FEHMN Application", Los Alamos National Laboratory report LA-UR-94-3788, Rev. 1, 1995.

APPENDIX 1:

DISCUSSION OF THE INFLUENCE OF BASALT AND GUAJE PUMICE CHARACTERISTICS ON INFILTRATION TO THE WATER TABLE

by
W.E. Soll

Overview of Sensitivity Study:

Within the subsurface under MDA G, there are a number of geologic and hydrogeologic factors that may influence infiltration of water from the surface to the water table. In some cases enough geohydrologic information is available to provide a basis for making reasonable assumptions as to how the system behaves. In other cases, there is virtually no information. The latter is the situation concerning the Guaje pumice and Cerros del Rio basalt layers underlying the Otowi member under MDA G. The lack of data on stratigraphic conditions and hydrogeologic properties makes it difficult to pinpoint representative parameters for a large scale flow and transport study of the area. The computing requirements for these large scale simulations make it unreasonable to study the influence of a range of parameter values for these layers.

We have undertaken a sensitivity analysis on the Otowi, Guaje, and basalt layers. In this analysis a number of unknown characteristics were varied to identify the influence of the different conditions. Characteristics that were varied included: the thickness of the Guaje pumice layer, the slope of the pumice layer (pumice/basalt interface), the saturated conductivity of the basalt, and the saturated conductivity of the Guaje pumice. The effect of a pinching out pumice layer was also considered. There is reason to believe that the Guaje pumice does, in fact, pinch out towards the Eastern end of MDA G. Table 1 shows the different parameters used in the simulations. The 3.7 meter thickness of the Guaje Pumice is the "reported" value based on available data. The 1.0 degree slope is the reported slope, based on stratigraphic measurements. Nominal, base saturated hydraulic conductivity used for the pumice was the reported average of 1.33×10^{-6} m/s (all reported values based on Krier et al., 1996)

Slope GP / Bas [degr]	GP Thickness [m]	K(Bas) $=8.7 \times 10^{-7}$ [m/s]	K(Bas) $=8.7 \times 10^{-5}$ [m/s]	K(Bas) = Fracd [m/s]	K(Guaje) $=8.7 \times 10^{-5}$ [m/s]	K(Bas)& K(Guaje) $=8.7 \times 10^{-5}$ [m/s]
0.0	0.0	X	X	X	-	
0.0	1.0	X	X	X	X	
0.0	3.7	X	X	X	X	
0.0	12.0	X	X	X	X	
1.0	0.0	X	X	X	-	
1.0	1.0	X	X	X	X	
1.0	3.7	X	X	X	X	
1.0	12.0	X	X	X	X	
2.0	3.7	X	X	X	X	
2.0	12.0	X	X	X	X	
Ot=1.0 GP=-0.5	3.7	X	X	X	X	X

Table 1: System parameter variations included in this study. Xs in boxes denote the simulations that were run.

A basalt saturated conductivity of 8.7×10^{-7} m/s was used in the large scale simulations. This value was taken from reported, measured values from other basalts (Bishop, 1991; DBS&A, 1994). At this time there is basically no information on the hydrogeologic properties of the basalt that underlies the Guaje pumice layer at LANL. The only local information is a single measurement by Dan B. Stephens and Associates

(1994) on a core that consisted entirely of basalt matrix (no fractures existed in the core). Bishop (1991) did an extensive analysis of basalt properties using samples from a block of basalt from the Snake River region Both studies showed relatively low values for hydraulic conductivity. However, because of the nature of the laboratory measurements it is necessary to have a relatively well consolidated sample. This would tend to neglect the role of fractures, vugs, and unconsolidated regions that occur naturally and frequently in the local basalts (based on core observations). For the field scale simulations that were run, the highest reported value of hydraulic conductivity, 8.7×10^{-7} m/s, was used. During field scale simulations using a sloped pumice layer, significant lateral flow was observed in the pumice layer, above the pumice basalt interface, indicating that the basalt properties did not allow significant infiltration into the basalt from the pumice. This provided much of the motivation for this study.

System Configuration:

The simulations were run in a rectangular system with dimensions 1000m x 200m (see Figure 1). The Otowi layer was nominally 27.4m thick, as reported by Krier et al. (1996). The basalt extended from the base of the Guaje (or Otowi in cases where Guaje thickness was 0.0) to -200m. For cases where the Guaje layer sloped, the Otowi thickness increased from right to left. The Guaje Pumice thickness was constant for any given simulation, and ranged from 0.0m to 12.0m as shown in Table 1. For the case where the pumice layer had a 2.0 degree slope it was not possible to run a 1.0m thickness because a suitable grid could not be generated (due to grid aspect ratios). Also, no 0.0m thick pumice layer was run for 2.0 degree slope because it was believed that the results from the other two slopes would be sufficient to extrapolate the behavior. For simulations in which the Guaje layer pinched out, the top of the basalt, and thus the Otowi / basalt interface, sloped at 1.0 degrees, while the Otowi / Guaje interface sloped at -0.5 degrees, with the pinch point occurring at the center of the model. Infiltration occurred over the central 100m of the system at a constant rate of 1mm/yr. The pinched out Otowi / Guaje system was an exception in that infiltration occurred over the central 200m of the system, also at a constant rate of 1mm/yr. The larger infiltration region was used so that infiltration would occur over a less centralized area right at the pinchout point. The remainder of the top boundary condition was no flow. The side boundary conditions were no flow over the Otowi and Basalt materials, and fixed saturation of 0.3 in the pumice (based on field data). The reasoning behind these lateral boundary conditions is described in Section 5. The bottom boundary condition was a water table condition - fixed saturation at 0.99.

All simulations were run to steady state. The steady state saturations as a function of depth are shown in figures 2-4. After steady state was reached, a particle tracking simulation was done to visualize the flow pattern. The particle movement information was critical to assessing the influence of the different parameters. Relative degree of lateral flow, as described below, was determined by comparing saturation distributions at steady state, and time history of particle distribution and movement.

The following sections describe the influence of the parameters on resulting infiltration behavior. There is some overlap in discussions because of the natural overlap in cause and effect of parameter variation. Following each of the individual descriptions, the overall trends are described.

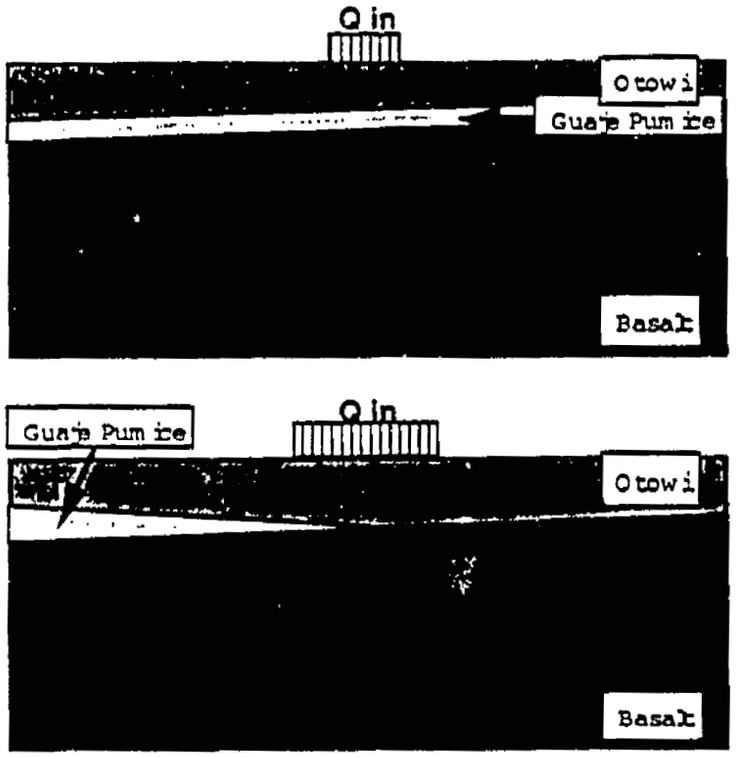

Figure 1: System configurations used for the numerical simulations. The top configuration was used for the majority of the simulations, while the bottom figure shows the configuration for the Guaje Pumice pinchout simulations.

Role of Slope of Guaje / Basalt interface:

The nominal reported slope of the Guaje pumice layer is approximately 1 degree (Krier et al., 1996). In this study three different slopes were used: 0, 1, and 2 degrees. An additional simulation was run in which the pumice layer pinched out into the Otowi layer.

There was an increase in the extent of lateral flow between sloped and non-sloped Guaje / basalt interface for the lower conductivity basalt, observed through an increase in the percent of particles leaving the system through the lateral boundaries at a given time. Although the extent of lateral flow was much greater for the 1 degree slope than for the 0 degree slope, there was little difference between 1 and 2 degree slopes. For the 3.7m thick pumice, the percentage of particles that left the system through all boundaries by $t=10^4$ years was 35% for the 0 slope, 86% for the 1 degree slope, and 81% for the 2 degree slope. A similar trend held for the 12m thick pumice layer. Figures 5 and 7 show particle movement for the low conductivity basalt, 3.7 m pumice layer, and 1 degree and 0 degree slope, respectively.

There was almost complete lateral flow, with little infiltration into the basalt, when using a low conductivity basalt layer. Figure 5 shows the particle movement for the 1 degree slope, 3.7m thick pumice layer. Infiltration into the basalt occurred mostly after the lateral flow had reached the lateral boundaries of the system. Not surprisingly, for the non-sloped system, all water movement was uniform about the centerline of the system, while for the sloped systems, all infiltration in the pumice layer was downslope. For this case, increased slope correlated with slightly decreased saturation, on the order of 0.05 for each degree increase, in the pumice layer. There was an exception to this trend only for the 12m thick pumice layer. For the thickest pumice, the saturation rose between the 1 degree slope and the 2 degree slope. The cause for this rise in saturation is unclear at this time, but may be either a grid effect or a boundary effect caused by the somewhat extreme slope.

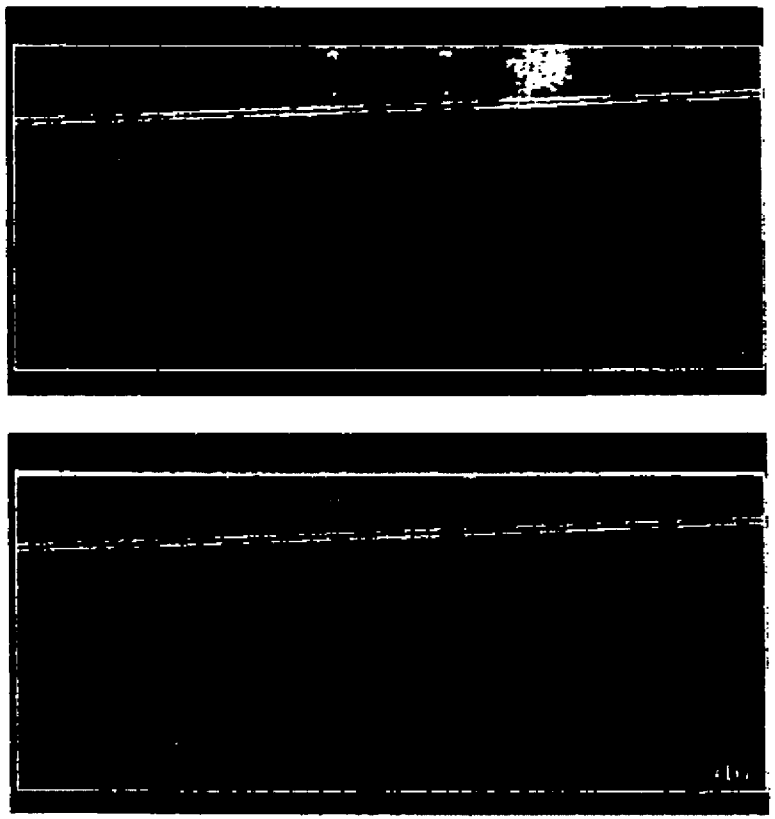

Figure 5: Particle tracking for the run with 3.7 m thick, 1 degree slope Guaje Pumice, and basalt conductivity of 8.7e-7 m/s.
a) t=9, b) t=10

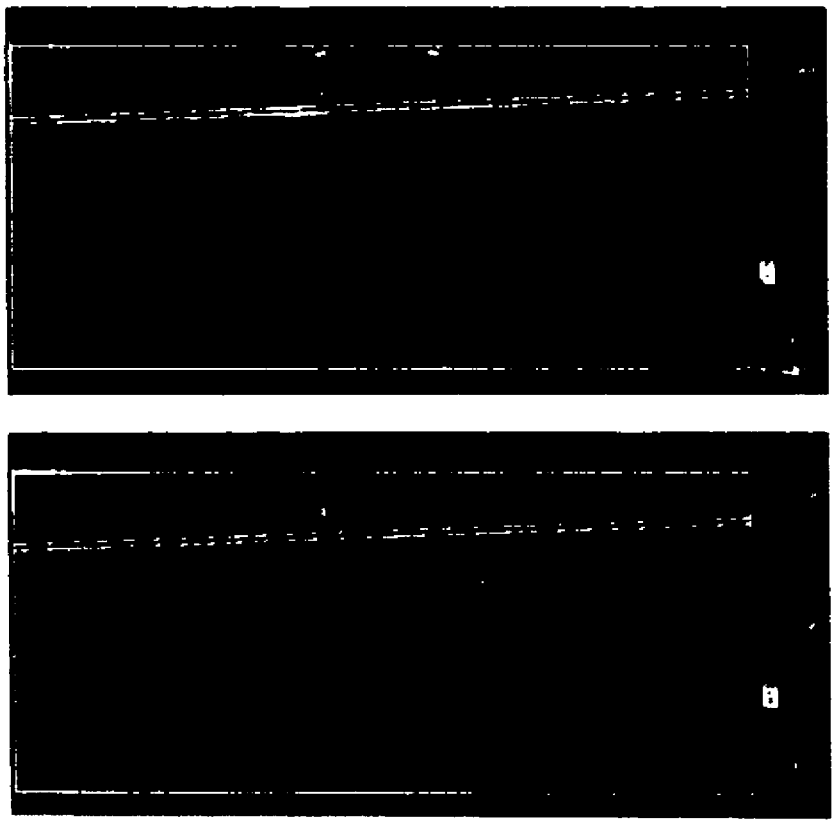

Figure 6: Particle tracking for the run with 3.7 m thick, 1 degree slope Guaje Pumice, and basalt conductivity of 8.7e-5 m/s.
a) t=9, b) t=10

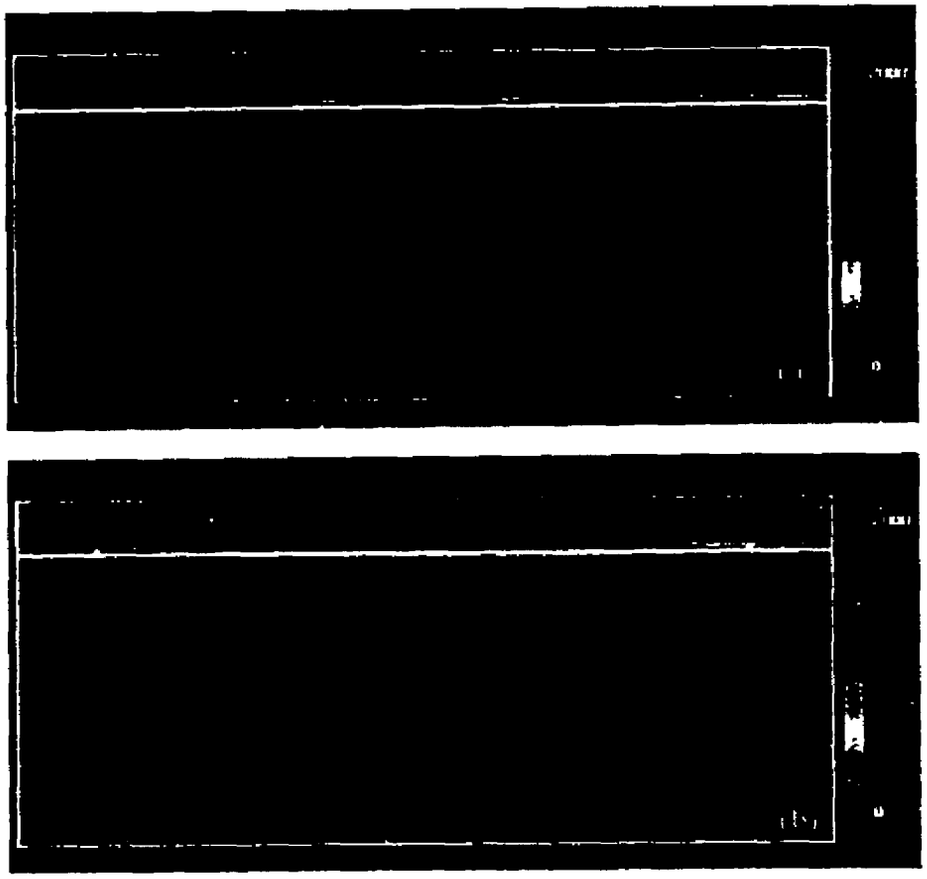

Figure 7: Particle tracking for the run with 3.7 m thick, 0 degree slope Guaje Pumice, and basalt conductivity of 8.7e-7. a)t=9, b)t=10

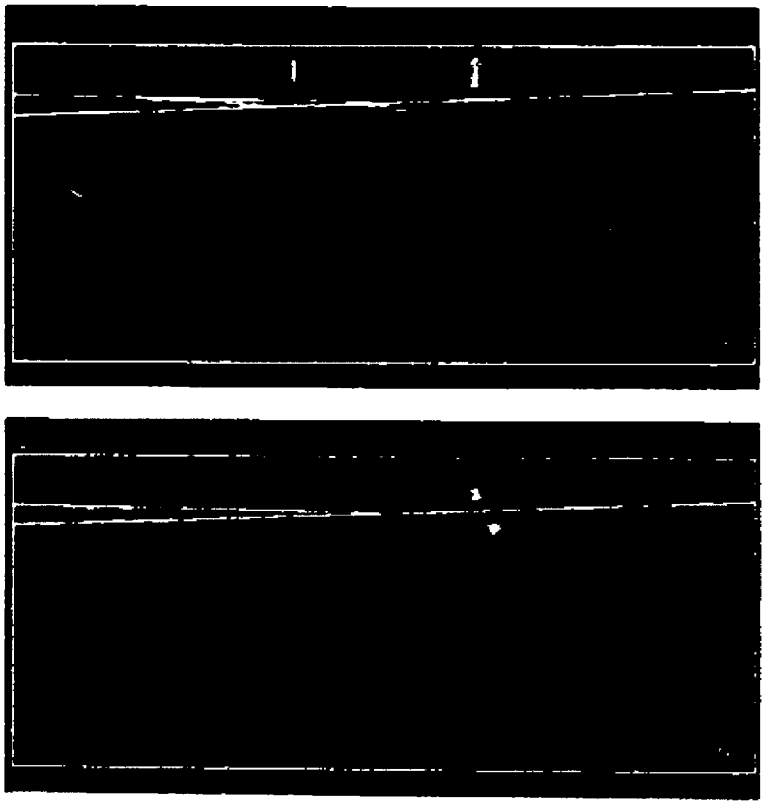

Figure 8: Particle tracking from the run with Guaje Pumice layer pinching out, and basalt conductivity of 8.7e-7. a) t=9, b) t=10

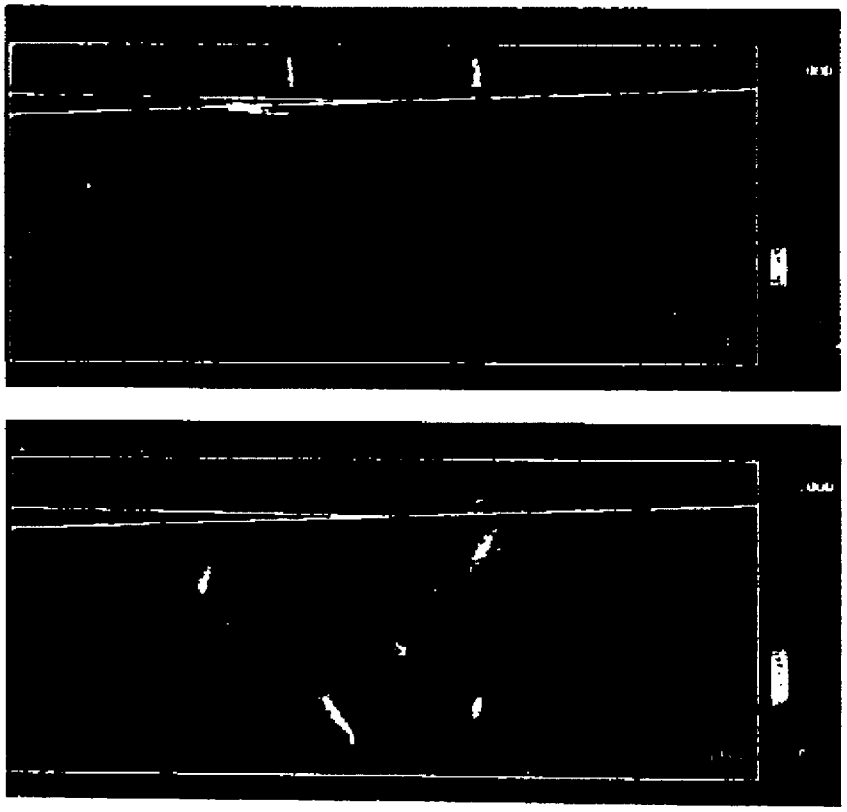

Figure 9: Particle tracking from the run with Guaje Pumice layer pinching out, and basalt conductivity of 8.7e-5. a) t=9, b) t=10

There was no apparent affect of slope on lateral movement with the higher conductivity ($K=8.7x10^{-5}$ m/s) basalt layer, as demonstrated in Figure 6. There was also virtually no effect of slope on saturation distribution.

When the conductivity of the Guaje pumice layer was increased, little change was seen in the saturation profile with increasing slope, independent of the thickness of the pumice. There was some decrease in saturation (0.05) between 1 degree and 2 degrees for the 3.7m thick layer, but an increase in saturation for the 12m thick layer. Again, in the case of the thickest layer this may be a gridding or boundary effect. However, there was a arlger decrease in the saturation of the pumice layer in this case than with the lower conductivity pumice when the pumice was underlain by the lower conductivity basalt. Saturation differences ranged from 0.1-0.2. The increase in conductivity of the pumice layer provided a higher conductivity conduit with which to carry flow away from the center. Thus, the water did not have the opportunity to mound above the basalt layer, but rather was carried away laterally. For the largest slope, lower saturations may result because the influence of gravity is commensurate with the influence of the conductivity.

Role of basalt saturated conductivity:
Sensitivity of the flow to basalt conductivity was tested using three different conductivities, as shown in Table 1. The lowest basalt conductivity used was $8.7x10^{-7}$ m/s, as that value already resulted in almost complete lateral diversion of the infiltrating water. A two order of magnitude increase in the conductivity, to $8.7x10^{-5}$ m/s, was sufficient to allow for significant infiltration of water from the pumice into the basalt. Although some lateral flow in the pumice layer was still observed, all of the water was able to infiltrate prior to the flow hitting the lateral boundaries. Figures 5 and 6, and Figures 8 and 9 demonstrate the particle travel for the different basalt conductivity systems. The increase in basalt conductivity resulted in a decrease in saturation in the pumice layer of approximately 0.3, more or less independent of slope or layer thickness. We anticipate that any further increase in basalt conductivity would provide complete infiltration of water into the basalt from the pumice, with insignificant lateral diversion.

Another set of simulations was run for which the basalt was characterized as a fractured medium. In this case the basalt matrix properties were unchanged from the base case, but there was potential for flow through fractures in the basalt. The fractured basalt properties were determined by varying basalt properties in two-dimensional field scale simulations until lateral flow was eliminaryed but simulated pumice saturation was close to the field-observed value of 0.30. The results of simulations using a fractured basalt description were indistinguishable from the results from the higher conductivity, unfractured basalt ($K=8.7x10^{-5}$ m/s).

Role of Thickness of Guaje layer:
The overall trend, with increasing thickness of the Guaje pumice layer, was toward slightly decreasing saturations in the pumice layer with approximately similar amounts of lateral flow. With the lower conductivity basalt ($8.7x10^{-7}$ m/s) there was little observable difference in lateral flow as a function of pumice thickness. The rate of lateral flow appeared smaller with increasing layer thickness due to the larger volume of pumice available to handle lateral flow. The slower lateral flow was particularly apparent in the 12m thick layer. This is because the lateral flow is caused by the conductivity barrier at the pumice / basalt interface, and the time to initiate lateral flow in the pumice was delayed by the travel time of the water through the pumice layer. For the higher conductivity basalt ($8.7x10^{-5}$ m/s) there was a slight observable difference in lateral flow. The thinner pumice layers tended to produce slightly greater lateral movement prior to the water infiltrating into the basalt. Differences in lateral extent of flow were slight, less than the resolution of the grid. These differences are likely due to the rate of movement of water from the pumice into the basalt being slower than the travel time through the pumice for the thinner layers. However, for the higher K basalt, the greatest extent of lateral flow was only

approximately 25% of the width of the system. All particles passed from the pumice into the basalt far from the lateral boundary.

The thickest pumice layer, 12.0m, showed a significant gradient in saturation with increasing depth, and showed relatively high saturations at the bottom contact with the basalt. This saturation profile is due to gravitational influence in the thicker layers, along with an increase in total water volume contained in the Guaje with increasing layer thickness. Thus more water was available for ponding at the basalt interface.

The saturation of the Otowi layer was basically unaffected throughout the simulations, at approximately 0.18-0.20. The basalt saturation was also basically unaffected by changes in the pumice layer thickness, remaining at approximately 0.22. Trends in saturation with layer thickness can be seen in each of the figures 2, 3, and 4, a-c, where each of the lines in the figures are for a different thickness, with all other parameters the same. The one exception was the case where the pumice layer did not exist (0.0m thick), and the basalt conductivity was low (8.7×10^{-7} m/s). In this case the basalt saturation increased significantly, ranging from 0.3-0.34. For the cases where the pumice layer did not exist the particle movement shows that water was easily able to infiltrate from the Otowi into the basalt. When the pumice layer existed and the basalt conductivity was low, water did not tend to infiltrate into the basalt, but rather moved laterally within the pumice layer.

Pinch out of the Guaje layer:
The system configuration for these runs is shown in Figure 1b. A wedge of Guaje Pumice pinches out into the Otowi layer at the center of the system. As noted previously, infiltration was over the central 200m of the system.

None of the simulations in this system indicated any lateral flow from the Otowi layer into the Guaje layer across the pinch out point (system center). In fact, the general behavior was that of two different systems placed side by side - one with a pumice layer and one without. The half of the system where there was no pumice allowed the water to infiltrate down into the basalt in all cases, with the rate of infiltration varying with basalt conductivity. The half of the system where pumice existed responded like any other simulation with a pumice layer. The particle distribution for the basalt $K=8.7 \times 10^{-7}$ m/s is shown in Figure 8, while Figure 9 is for basalt $K=8.7 \times 10^{-5}$. No lateral flow along the Otowi / pumice interface was observed for either of the pumice conductivities used. It is possible that such flow could occur if the pumice conductivity was reduced. It is also possible, though less likely, that such lateral flow would occur if the slope of the Otowi / pumice interface was increased. This is less likely because there is no apparent deflection of water for this slope, and the infiltration does not appear to be perceptibly delayed by the existing interface. However, slight increases in saturation at the Otowi / pumice interface were observed in some of the other simulations, so the potential for a minor barrier cannot be eliminated.

There was no flow from the pumice towards the Otowi contact point due to the slope of the pumice / basalt interface draining in the opposite direction. Whether water would flow into the Otowi from the pumice if the pumice / basalt interface slope was reversed was untested.

Importance of boundary conditions in simulations:
Selecting lateral boundary conditions (BCs) was a difficult part of this study. Initially there was no information available about the in situ saturation of the Guaje pumice to help define appropriate conditions. A number of different lateral BCs were tested, including no flow, constant saturation, constant pressure, and vertical drains. (Vertical drains were high conductivity zones defined along the lateral edges that would allow flow to move straight down and exit out of the bottom of the basalts when it hit the lateral edge). These tests were undertaken because the initially chosen no-flow BC, also used in the field scale study, proved to dominate the system by allowing water to pile up against the lateral edge in the pumice layer for the low conductivity basalt runs, and dominate the system. Fixed saturation BCs

were also found to dominate the system saturation, with higher boundary saturations resulting in higher internal saturations. These observations were consistent regardless of the system width. Lateral drains were tested to emulate an "open outflow" boundary, where any water reaching the lateral edge could directly flow out. These worked particularly well in the wide system that was finally used. However, during the course of this study some data on the pumice saturations became available. Another BC was then tested, for which the lateral boundaries in the Otowi and basalt layers were made no-flow, and the lateral boundaries in the pumice were assigned constant saturations at the reported values. This BC also gave reasonable results with respect to known saturations in the Otowi and Guaje. Both the fixed saturation and vertical drain BCs gave similar results in the central portion of the system, over which infiltration was occurring.

A relatively wide system, with respect to the length of the infiltration region, and depth of the system, was chosen to minimize boundary effects. 200m, 500m, and 1000m wide systems were all tested. It was necessary to go to the widest system, with infiltration over only the central 100m, to eliminate the influence of the boundary. When looking at saturation distributions only the central portion of the system should be considered, because the outer regions primarily reflect boundary effects.

Summary of Findings:

By far the strongest influence on the flow field and saturation is the (saturated) hydraulic conductivity of the basalt underlying the Guaje pumice. Using a basalt conductivity that is at the high end of reported basalt matrix values (8.7×10^{-7} m/s) results in the basalt largely being a barrier to vertical flow. This results in almost exclusively lateral flow in the Guaje pumice layer, and saturations in the pumice layer as much as 0.3 greater than for a conductive basalt. When the basalt conductivity is modified so that fluid can readily pass from the pumice into the basalt, lateral flow is minimal, and pumice saturations remained relatively low. In the case of these simulations, the pumice saturation was slightly lower than the few reported measurements (0.22 instead of 0.3), but that may reflect using only a simple three-layer model, with steady state infiltration.

Thickness of the pumice layer had a mild effect on saturation in the pumice, but no effect on saturation of the Otowi or the basalt. However, pumice saturation tended to vary by only approximately 0.05. Pumice thickness also had only mild effect on lateral flow, with thicker layers producing slower lateral flow, due to increased flow area. Relative saturation as a function of layer thickness was more or less insensitive to slope or hydraulic conductivities. The influence of pumice layer slope on saturations was approximately as strong as the influence of layer thickness (approx. 0.05 range). However, the effect of slope was strongly correlated to the inability of the water to move either vertically (low basalt conductivity) or laterally.

Conclusions:

Based on this study, the flow field is observed to strongly depend on some of the as yet unknown characteristics of the lower stratigraphic layers underlying MDA G. For example, a relatively impermeable basalt could result in significant lateral flow of contaminants. This suggests possibly needing a much larger scale model to consider compliance for contaminants reaching the water table. A more permeable basalt produces flow fields that are better represented by the current field scale model being used (rapid, vertical flow). A distinctly sloped pumice layer could also result in the need to consider a much larger areal domain in the modeling effort. It is possible that lateral flow could result in longer groundwater travel times, through increased travel time in the pumice, but it could also result in shorter travel times if the flow shortcuts the large basalt and Puye materials and drains into a spring.

The choice of a higher basalt conductivity than those reported in laboratory analyses is justifiable. Laboratory core measurements require a certain level of integrity of the material to get valid pressure-saturation-permeability measurements. A basalt sample without sufficient integrity would not be tested, but would be likely to have a higher conductivity. Also, for similar reasons, the role that fractures and vugs play in the basalts may be missed in standard laboratory tests. In situ well tests of conductivity in

basalts have resulted in variations in measured hydraulic conductivity of over 10 orders of magnitude (Magnuson, 1995). Evidence from basalt cores at the LANL core storage facility, as well as in situ evidence of extensive airflow, suggests that the basalts underlying the Pajarito Plateau may be very impermeable in some locations, and wholly without integrity at others. These observations, in conjunction with the observed importance of basalt conductivity in defining saturation distributions in the lower layers, indicate the need for more hydrogeologic information on the pumice and basalt layers.

References:

Bishop, C. W. Hydraulic Properties of Vesicular Basalt. M.Sc. Thesis, University of Arizona, 1991.

Daniel B. Stephens and Associates. Laboratory Analysis of Soil Hydraulic Properties of SHB Soil Samples. Report #0933-4824-94, August 1994.

Krier, D. P. Longmire, R. Gilkeson, and H. J. Turin. Geologic, Geohydrologic, and Geochemical Data Summary of Material Disposal Area G, TA-54, Los Alamos National Laboratory. Los Alamos National Laboratory Report LA-UR-95-2696, in press. 1996.

Magnusen, S. M. Personal Communication, Idaho National Engineering Laboratory, 1995.

APPENDIX 2:

MODELING FRACTURE PROPERTIES AT MDA G, LOS ALAMOS NATIONAL LABORATORY

by

Tade W. Orr

Modeling Fracture Properties at MDA G, Los Alamos National Laboratory

Tade W. Orr

October 3, 1996

Abstract

Numerical groundwater flow simulations were conducted on two one-dimensional columns. One column represents regions surrounding the waste disposal pits at MDA G, while the other represents the disposal pits themselves. Columns are vertical cross sections of the mesa underlying the disposal area.

Initial steady-state simulations were conducted without fracture properties to establish a base for comparison of saturations and groundwater travel times through the various members to those of subsequent runs. Simulated saturations in the upper two layers of the columns were significantly higher than those observed in the field. Saturations in all other layers for which field data is available was within or very near ranges of saturations observed in the field.

A sensitivity analysis was also performed with the matrix-only columns in which hydraulic conductivities were varied in each layer to establish minimum and maximum potential groundwater travel times through the units. Conductivities used in this analysis were the minimum and maximum values taken from field data.

Fracture properties were then added to units where such data was available. Simulations were conducted to ensure the modeling method did not affect groundwater travel times in layers without fractures. Steady state runs with fractures simulated in the upper layers of each column showed no change in saturations profiles or groundwater travel times through the columns.

A preliminary sensitivity analysis based on varying selected fracture properties was conducted with the disposal pit column. One

combination of van Genuchten n and α for fractures yielded significant fracture flow in the fractured layer of this column. Saturation in the matrix material of the affected layer was reduced by approximately three percent, but was still significantly higher than that observed in the field. Groundwater travel times were slightly reduced.

Finally, transient simulations were conducted with the fractured columns to determine whether or not fractures would provide a fast flow path to lower layers during high infiltration events. Problems were encountered with the column representing the areas adjacent to the disposal pits, and results obtained were inaccurate. Results for the disposal pit columns indicated that saturation profiles and groundwater travel times do not change appreciably in the modeled scenario.

1 Introduction

Several numerical simulations were performed using two one-dimensional cross sections representing the low-level radioactive disposal area at MDA G. The first column represents the areas surrounding the waste disposal pits, with the top layer corresponding to Unit 2 of the Tshirege Member of the Bandelier Tuff. The second column represents the disposal pits themselves, with the top layer corresponding to the crushed tuff used to fill the pits. The simulations were performed with the finite element code FEHM (Zyvoloski et. al, 1995).

Initial simulations were steady-state and used a matrix-only representation to determine baseline saturation profiles for the columns. Transport calculations were also performed using conservative particle tracking to determine groundwater travel times through the various units. Average hydrologic parameters were assigned to each layer for these simulations.

A sensitivity analysis was then conducted on these columns in which minimum and maximum hydraulic conductivities were assigned to each layer. Maximum and minimum groundwater travel times through each unit were calculated, as well as the overall maximum and minimum groundwater travel times to the top of the lowest (basalt) layer. Travel times were calculated to the basalt layer in lieu of to the water table because little hydrologic data is available for the basalt layer. Travel times through this layer would therefore be inaccurate. Travel times to the top of the basalt layer may be used as a conservative estimate of travel times to the water table until more accurate

data on the basalt layer can be obtained.

Fracture properties were next added to the two columns. Preliminary simulations were run where fracture properties in all layers were set equal to matrix properties. This was done to ensure that the representation of non-fractured layers would not be altered by using the dual porosity/dual permeability (dpdp) macro of FEHM. The column representing regions adjacent to the waste disposal pits was then given fracture properties in its upper two layers. The column representing the disposal pits was given fracture properties in its second layer only. Simulations were conducted with fracture properties added to the upper layers of the two columns. Saturation profiles and groundwater travel times through each unit were observed and compared to the matrix-only simulations, as well as to saturation data from field observations.

A preliminary sensitivity analysis was conducted on the column that represents the disposal pits in which fracture permeability, van Genuchten n, and van Genuchten α were varied. Ratios of matrix liquid flux rates to fracture liquid flux rates were compared to those obtained using fracture parameters calculated using parallel plate theory . The saturation profile as well as the groundwater travel time to the basalt layer were observed in one case where significant fracture flow occurred. This data was also compared to the matrix-only simulations, as well as to saturation ranges observed in the field.

Finally, transient simulations were conducted with the fractured columns. The purpose of these simulations was to investigate whether or not fractures serve as conduits for rapid flow under higher-than-average infiltration rates, or whether lower-than-average infiltration rates lead to drying of the upper units in the columns.

2 Modeling Studies

2.1 Representation of Columns

Two one-meter wide, one-dimensional cross-sectional columns were used in the numerical groundwater flow simulations (Figure 1). The first column represents areas adjacent to the waste disposal pits, and has an upper layer consisting of intact tuff. This layer was assigned hydrologic properties of Unit 2 of the Tshirege Member of the Bandelier Tuff. For the steady-state

simulation, an infiltration rate of 1 mm per year was applied to the top two nodes in this column. For the transient simulation, an infiltration profile developed by Springer (1995) was used (Figure 2). The rates in this profile represent an average infiltration rate of 5.5 mm per year, so these rates were scaled to an average rate of 1 mm per year for this column.

The upper layer of the column corresponding to the disposal pits was assigned hydrologic properties of the crushed tuff used to fill the pits. An infiltration rate of 5.5 mm per year was applied to the top of this column for the steady-state simulation. There is little vegetation over the filled disposal pits, and thus there is much less evapotranspiration from the upper region of the pits. Therefore a higher net infiltration rate was used for the crushed tuff columns. For the transient simulation, the infiltration profile developed by Springer was again used. The rates were not scaled in this case as they correspond to an average infiltration rate of 5.5 mm per year.

2.2 Grid Parameters

The computational grid used for both columns is identical. For the steady-state simulations, the grid consists of 210 nodes arranged in two columns situated one meter apart. Vertical node spacing in all layers except the basalt layer is approximately one meter. Vertical node spacing in the basalt layer is approximately 20 meters.

Grid resolution was increased for the fractured column studies in order to reduce errors in the numerical solution. This grid consists of 664 nodes arranged in two columns situated one meter apart. Vertical node spacing in the upper two fractured layers is approximately 0.1 meters. Node spacing in the next five layers is approximately one meter. Vertical node spacing in the basalt layer is approximately 20 meters.

2.3 Steady-State Matrix-Only Simulations and Sensitivity Analysis

Initial steady-state models were run using a matrix-only representation of the system in order to determine saturation profiles for each column for comparison to later runs with fracture parameters included. These simulations were run to 20,000 years to ensure that equilibrium had been reached. These runs also established a steady-state representation of the system from which

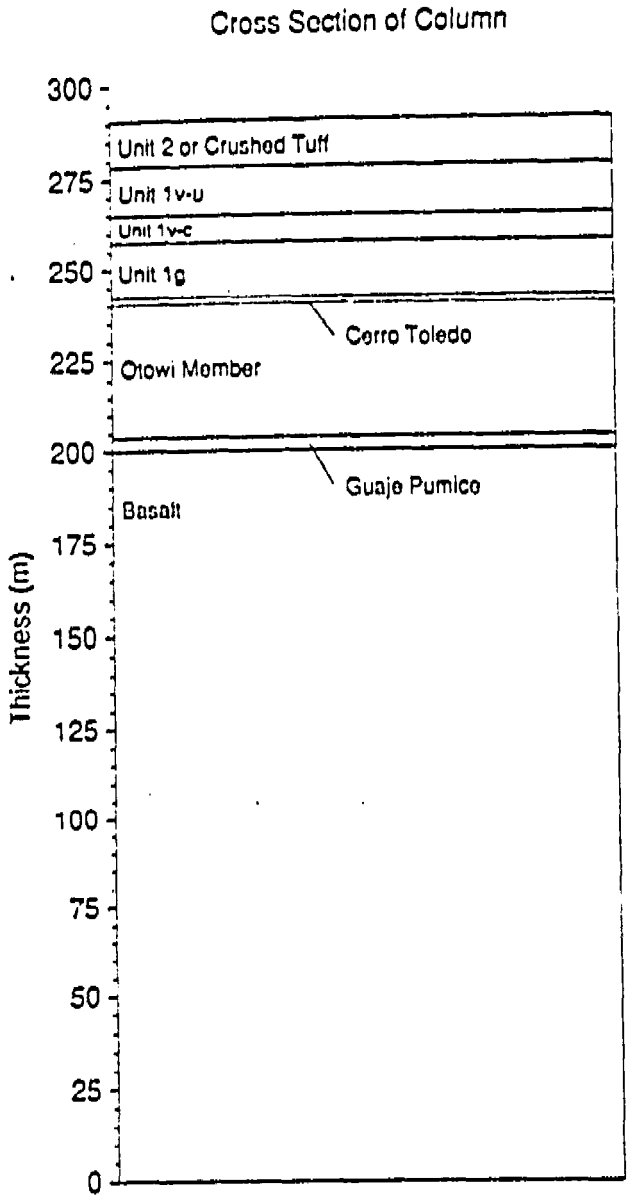

Figure 1: Column cross section.

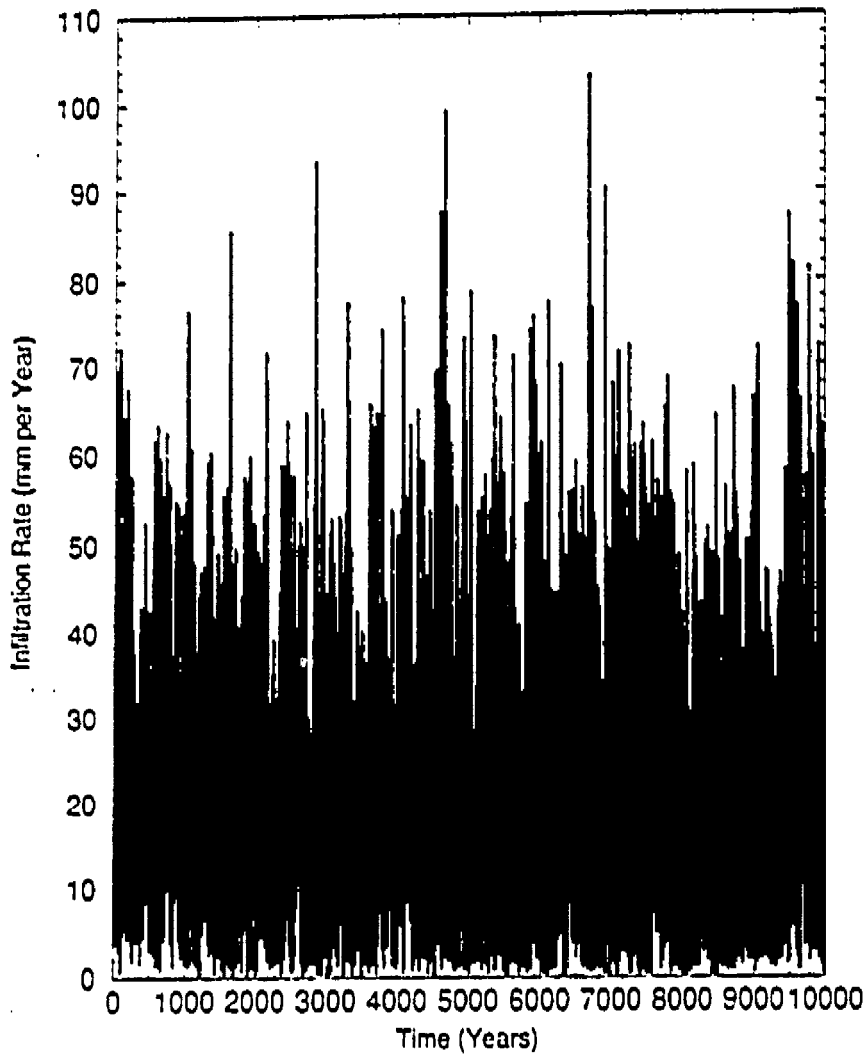

Figure 2: Transient infiltration profile, 5.5 mm per year average (74 percent of years have zero infiltration). (Springer, 1995).

particle tracking runs could be initiated. Saturation profiles were also compared to those observed in the field in layers for which such data is available. All field saturation data was obtained from Krier et. al. (1995). Field saturation data was not available for the crushed tuff, Guaje pumice, or the basalt layer.

Several steady-state flow simulations with conservative particle tracking were then run for both columns to determine the minimum, average and maximum groundwater travel times through each geologic unit at Area G. Groundwater travel times were determined by observing the transport of 100,000 particles injected into the top two nodes of each column during the first 30 days of the simulation. Conservative, non-sorbing liquid-phase particles were simulated with advection as the only transport mechanism to obtain a conservative estimate of travel times. Particle tracking simulations were started with an initial saturation distribution derived from the 20,000 year steady-state simulations, using the appropriate steady-state infiltration rate for the column under consideration.

The average groundwater travel times through each layer and to the basalt layer were computed by assigning average observed hydraulic conductivities to each layer in the column under investigation. Minimum groundwater travel times through a given layer were calculated by assigning the maximum observed saturated hydraulic conductivity to the layer while assigning mean values of saturated hydraulic conductivity to all other layers. Similarly, maximum groundwater travel times were calculated by assigning the minimum observed saturated hydraulic conductivity to the layer under study while holding all other layers at their mean values. Overall maximum and minimum groundwater travel times to the top of the basalt layer were also calculated by assigning minimum and maximum saturated hydraulic conductivities, respectively, to all layers simultaneously. Mean, minimum and maximum hydrologic properties for each of the units are given in Table 1.

2.4 Steady-State Fracture Simulations and Preliminary Sensitivity Analysis

After baseline saturations and groundwater travel times through the matrix-only columns were determined, fracture parameters were added to Unit 2 and Unit 1v-u in the intact tuff column. Fracture parameters were added to Unit 1v-u in the crushed tuff column. Fractures were modeled using the dual

Unit	K_{sat} min (m^2)	K_{sat} avg (m^2)	K_{sat} max (m^2)
Crushed Tuff†	1.05×10^{-13}	2.95×10^{-13}	9.40×10^{-13}
Unit 2†	9.63×10^{-14}	4.46×10^{-13}	4.01×10^{-12}
Unit 1v – u†	8.48×10^{-14}	1.51×10^{-13}	1.01×10^{-12}
Unit 1v – c†	2.18×10^{-14}	1.70×10^{-13}	1.49×10^{-12}
Unit 1g†	3.44×10^{-14}	1.92×10^{-13}	4.47×10^{-12}
Cerro Toledo†	5.39×10^{-14}	8.82×10^{-13}	4.93×10^{-12}
Otowi Member†	1.26×10^{-14}	2.53×10^{-13}	8.94×10^{-12}
Guaje Pumice‡	no data	1.53×10^{-13}	no data
Basalt*	no data	1.00×10^{-13}	no data

†Mean values from Krier et. al, 1995.
‡from Everett (1995).
*from Bishop (1991).
All minimum and maximum values from Rogers et. al, 1995.

Table 1: Hydrologic properties of the Bandelier Tuff.

porosity/dual permeability macro (dpdp) of FEHM.

Field data indicates that fractures in Unit 2 and Unit 1v-u have a spacing (a) of 1.0 to 1.3 meters, with a median aperature (b) of 3 mm (Krier et. al, 1995). An average fracture spacing of 1.15 meters was assumed. Parallel plate theory was used to calculate fracture porosity (ϕ_{frac}), permeability (k_{frac}), length scale (L), and van Genuchten alpha (α_{frac}) from this data for use in the FEHM simulation. From parallel plate theory:

$$\phi_{frac} = b/a$$

$$k_{frac} = b^2/12$$

$$L = a/2$$

$$\alpha_{frac} = b\rho g/2\gamma$$

where ρ is the density of water (1000 kg/m^3), g is gravitational acceleration (9.81 m/sec^2), and γ is 0.072 kg/sec^2. Thus $\phi_{frac} = 2.6 \times 10^{-3}$, $k_{frac} = 7.5 \times 10^{-7}$ m^2, $L = 0.575$ m, and $\alpha_{frac} \simeq 230$ m^{-1}. The van Genuchten n for the intact tuff column was set at 3, based on similar systems being modeled for the Yucca Mountain Project. The van Genuchten n for the crushed tuff column was set at 1.62, the maximum value that could be used in conjunction with the large α_{frac} while allowing the simulation to converge.

Fracture properties also had to be assigned to non-fractured layers when using the dpdp macro of FEHM. It was determined that fracture parameters for any non-fractured layer should be set equal to the matrix properties for that layer. Fracture porosities for these layers were set to small values (1×10^{-4}). A simulation was conducted for each column in which the dpdp macro was used and all layers were modeled as non-fractured. Groundwater travel times through each layer were calculated and compared to the previous matrix-only simulations. The travel times were equal within the time resolution of the simulations, and thus this approach to modeling non-fractured layers with the dpdp macro was deemed valid.

Difficulties were encountered in achieving convergence in the flow simulations of the fractured columns. The problems encountered were due to the use of large α_{frac} values. In order to obtain a solution with the appropriate value of α_{frac}, solutions first had to be obtained using smaller values for this variable. The results of these solutions were then used to re-start a simulation using a slightly higher value of α_{frac}. The value for α_{frac} was incremented in this fashion until the desired value was in place. A typical progression for α_{frac} was from 3 m^{-1} to 7 m^{-1} in steps of 1, from 7 m^{-1} to 27 m^{-1} in steps of 10, from 27 m^{-1} to 42 m^{-1} in steps of 3 to 10, and from 42 m^{-1} to the desired value (approximately 230 m^{-1}) in steps of 40 to 100.

Values of van Genuchten n had to be adjusted from 3 to 1.5 in order to progress past an α_{frac} value of 7 m^{-1} in the crushed tuff column. The value of n was then increased to 1.62 once an α_{frac} value of 230 m^{-1} was achieved. Convergence could not be obtained in the crushed tuff column using both a high value for α_{frac} and a van Genuchten n of 3 in layer 1v-u. With a van Genuchten n of 3, the highest value of α_{frac} that would converge was approximately 6 m^{-1}.

Once the desired column representations were obtained, simulations were conducted to determine saturation profiles in the matrix material and in the fractures. Groundwater travel times through the various units and to the top of the basalt layer were also computed. Particle tracking was conducted in these columns using the same method as in the matrix-only simulations. Additionally, the flxo macro of FEHM was used to compare liquid flux in the matrix material to liquid flux in the fractures. The steady-state infiltration into the columns was routed entirely into the top two fracture nodes of the columns. This was done to maximize the possibility of fracture flow, which could reduce groundwater travel times to lower layers.

After simulations were conducted using fracture parameters derived from

Van Genuchten n	α_{frac} (m^{-1})	k_{frac} (m^2)	Difference†
3	3	7.5×10^{-8}	5
3	3	7.5×10^{-6}	3
3	3	7.5×10^{-3}	2
3	3	7.5×10^{-1}	2
2	3	7.5×10^{-8}	1
1.5	3	7.5×10^{-8}	0

†Difference is expressed as orders of magnitude more matrix liquid flux than fracture liquid flux.

Table 2: Fracture parameter variations and resulting order of magnitude ratio of matrix liquid flux to fracture liquid flux for preliminary sensitivity analysis of crushed tuff column.

parallel plate theory, a preliminary sensitivity analysis was conducted in which the values of van Genuchten n, α_{frac} and k_{frac} were systematically varied in the crushed tuff column. The fixo macro was again used to compare liquid flux in the matrix material to liquid flux in the fractures. A saturation profile and groundwater travel time to the basalt layer was observed for one case in which significant fracture flow occurred. A summary of the fracture parameter variations as well as resulting flux differences is presented in Table 2. Further sensitivity analysis is being conducted on this column as well as the intact tuff column.

2.5 Transient Fracture Simulations

Once steady-state saturation profiles and groundwater travel times were established for the fractured columns, transient infiltration simulations were conducted. An infiltration profile developed by Springer (1995) was used (Figure 2) for these runs. The rates in this profile were developed for an average infiltration rate of 5.5 mm per year, so these rates were scaled to an average rate of 1 mm per year for the intact tuff column. Again, infiltration was routed entirely into the top fracture nodes of the columns. The simulations were started using the saturation distributions obtained in the steady-state fracture simulations for the appropriate column.

Simulations were run to approximately 5000, 6000 and 7000 years. Saturation profiles for both the matrix material and the fractures were observed

at these selected times. Saturation as a function of time at selected nodes in the upper two layers and the bottom layer of each column were also observed from 5000 to 7000 years. The flxo macro was again used to compare the ratio of liquid flux in the matrix and fractures. Liquid flux was observed as a function of time at selected nodes in the upper two layers and bottom layer of each column from 5000 to 7000 years. Again, particle tracking was conducted to determine groundwater travel times through the units, using the same methods as in previous steady-state simulations. Particle tracking in the transient simulations was started at the first flow event in the transient infiltration profile.

Problems were encountered with the simulations involving the intact tuff column. Solutions were difficult to achieve, and did not work well with the existing transient infiltration package used with FEHM. Approximately 10 percent of the flow in the profile developed by Springer was not accounted for in these simulations. Analysis of the results of these simulations is pending until modifications to the transient package are made.

3 Results

3.1 Steady-State Matrix-Only Simulations and Sensitivity Analysis

Saturation profiles were obtained for both the intact tuff and the crushed tuff columns, and are presented in Figures 3 and 4 along with ranges of saturations obtained from field data for available units. Simulated saturations in the upper two units are significantly higher than those observed in the field. Simulated saturations in lower units are within or very near those ranges observed in the field.

The minimum and maximum groundwater travel times calculated through each layer varied by approximately 25 percent from their average calculated values for both columns. Similar variations from the average groundwater travel time to the top of the basalt layer were observed when the minimum and maximum hydrologic properties were used for all layers simultaneously. Because minimum and maximum saturated hydraulic conductivity values were only available for the upper six units, sensitivity analysis was performed only on these layers. Minimum, average and maximum groundwater travel times through individual layers for the intact tuff column are summarized in

Table 3. Minimum, average and maximum groundwater travel times through individual layers for the crushed tuff column are summarized in Table 4. Finally, minimum, average and maximum groundwater travel times to the basalt layer based on varying all layer properties simultaneously for each case are presented in Table 5.

3.2 Steady-State Fracture Simulations and Preliminary Sensitivity Analysis

An initial simulation was conducted to validate the method used to simulate non-fractured layers with the dpdp macro of FEHM. Fracture parameters in all layers were set equal to matrix parameters, with a small (1.0×10^{-4}) fracture porosity. Groundwater travel times were calculated through each layer and to the top of the basalt layer and compared with those found in previous matrix-only simulations. Travel times in this case were the same as those found in the matrix-only simulations, and thus the method was justified.

Fracture properties were then added to the appropriate layers in each column. Groundwater travel times were observed through each layer and to the basalt layer and compared to the matrix-only simulations. Layer-by-layer groundwater travel times for the fractured intact tuff column are given in Table 6. Layer-by-layer groundwater travel times for the fractured crushed tuff column are given in Table 7.

Arrival times for 10 percent and 50 percent total particle concentration are given, and in most cases the travel times to each layer in the matrix-only case fall within the given arrival range for the fractured case. Travel times in the upper 3 layers of the intact tuff column are approximately 100 years faster (for 50 percent concentration arrival) than in the matrix-only case. This difference is most likely due to differences in time step resolution between the matrix-only and fracture simulations. The identical arrival times at the tops of the Cerro Toledo Member and the Otowi Member for both fractured columns is also due to time step resolution in the fracture simulations.

Saturation profiles were also calculated for the matrix material and for the fractures in both columns. The profile for the intact tuff column is given in Figure 5. The profile for the crushed tuff column is given in Figure 6. Ranges of saturation values observed in the field are presented as well for available units. Groundwater travel times to the basalt layer are also graph-

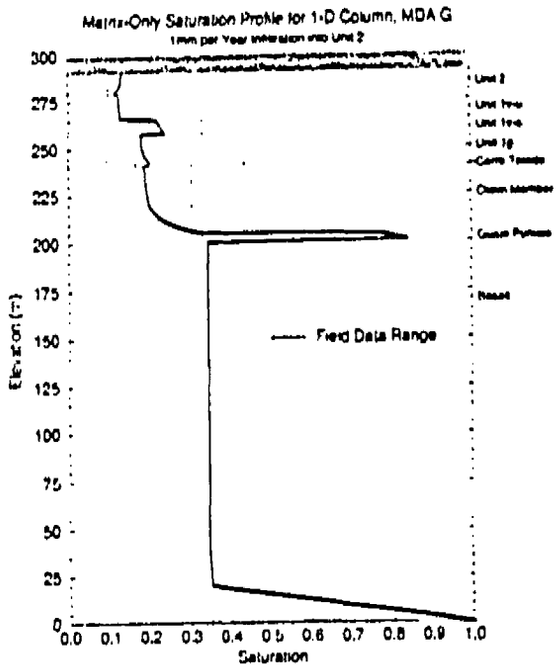

Figure 3: Steady-state saturation profile (matrix only), 1 mm per year infiltration into Unit 2.

Unit	T_{min} (Years)	T_{avg} (Years)	T_{max} (Years)
Unit 2†	600	700	900
Unit 1v – u‡	770	800	900
Unit 1v – c‡	800	800	1000
Unit 1g†	1150	1200	1700
Cerro Toledo‡	100	150	190
Otowi Member†	2900	3300	4900

†100-year resolution, ‡10-year resolution.

Table 3: Groundwater travel time sensitivity analysis, 1 mm per year infiltration into Unit 2.

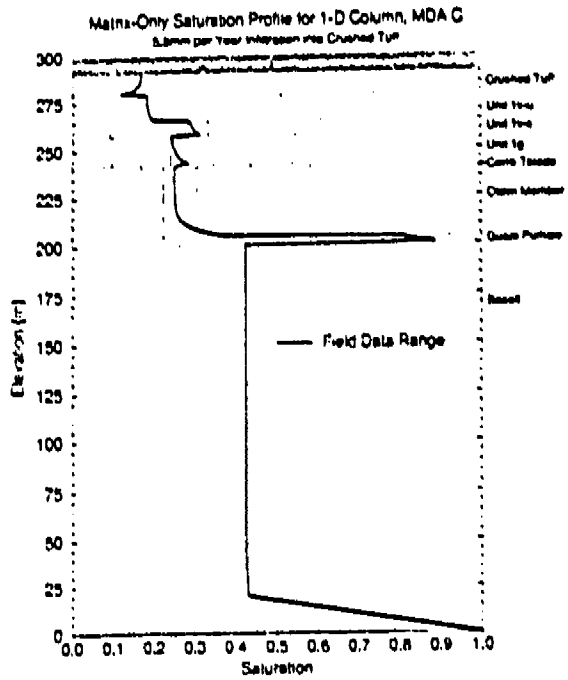

Figure 4: Steady-state saturation profile (matrix only), 5.5 mm per year infiltration into Crushed Tuff.

Unit	T_{min} (Years)	T_{avg} (Years)	T_{max} (Years)
Crushed Tuff	130	160	190
Unit 1v-u	190	230	250
Unit 1v-c	180	200	250
Unit 1g	260	320	420
Cerro Toledo	40	40	50
Otowi Member	570	750	1160

10-year resolution for all units.

Table 4: Groundwater travel time sensitivity analysis, 5.5 mm per year infiltration into Crushed Tuff.

Case	T_{min} (Years)	T_{avg} (Years)	T_{max} (Years)
1 mm per year into Unit 2†	7500	9500	12,500
5.5 mm per year into Crushed Tuff‡	1600	2130	2900

†100-year resolution, ‡10-year resolution.

Table 5: Groundwater travel times to basalt layer, simultaneous conductivity variation.

To Top of Unit	T_{frac} 10% (Years)	T_{frac} 50% (Years)	T_{nofrac} (Years)
Unit 1v-u	250	700	800
Unit 1v-c	1000	1600	1700
Unit 1g	1800	2400	2600
Cerro Toledo	3300	4300	3900
Otowi Member	3300	4300	4100
Guaje Pumice	7000	7500	7500
Basalt	9000	9500	9500

Table 6: Groundwater travel times, 1 mm per year infiltration into Unit 2, layer-by-layer comparison of matrix-only and fractured cases.

To Top of Unit	T_{frac} 10% (Years)	T_{frac} 50% (Years)	T_{nofrac} (Years)
Unit 1v-u	160	170	170
Unit 1v-c	400	410	410
Unit 1g	600	620	620
Cerro Toledo	950	970	950
Otowi Member	950	970	1000
Guaje Pumice	1750	1800	1760
Basalt	2100	2150	2140

Table 7: Groundwater travel times, 5.5 mm per year infiltration into crushed tuff, layer-by-layer comparison of matrix-only and fractured cases.

ically depicted in these figures. The saturation profiles for both columns are almost identical to those of their non-fractured counterparts. Additionally, saturations in the upper two layers remained significantly higher than those reported in field data. Groundwater travel times to the basalt layer are the same as those calculated in the matrix-only simulations.

An analysis of the columns was conducted using the fixo macro of FEHM,

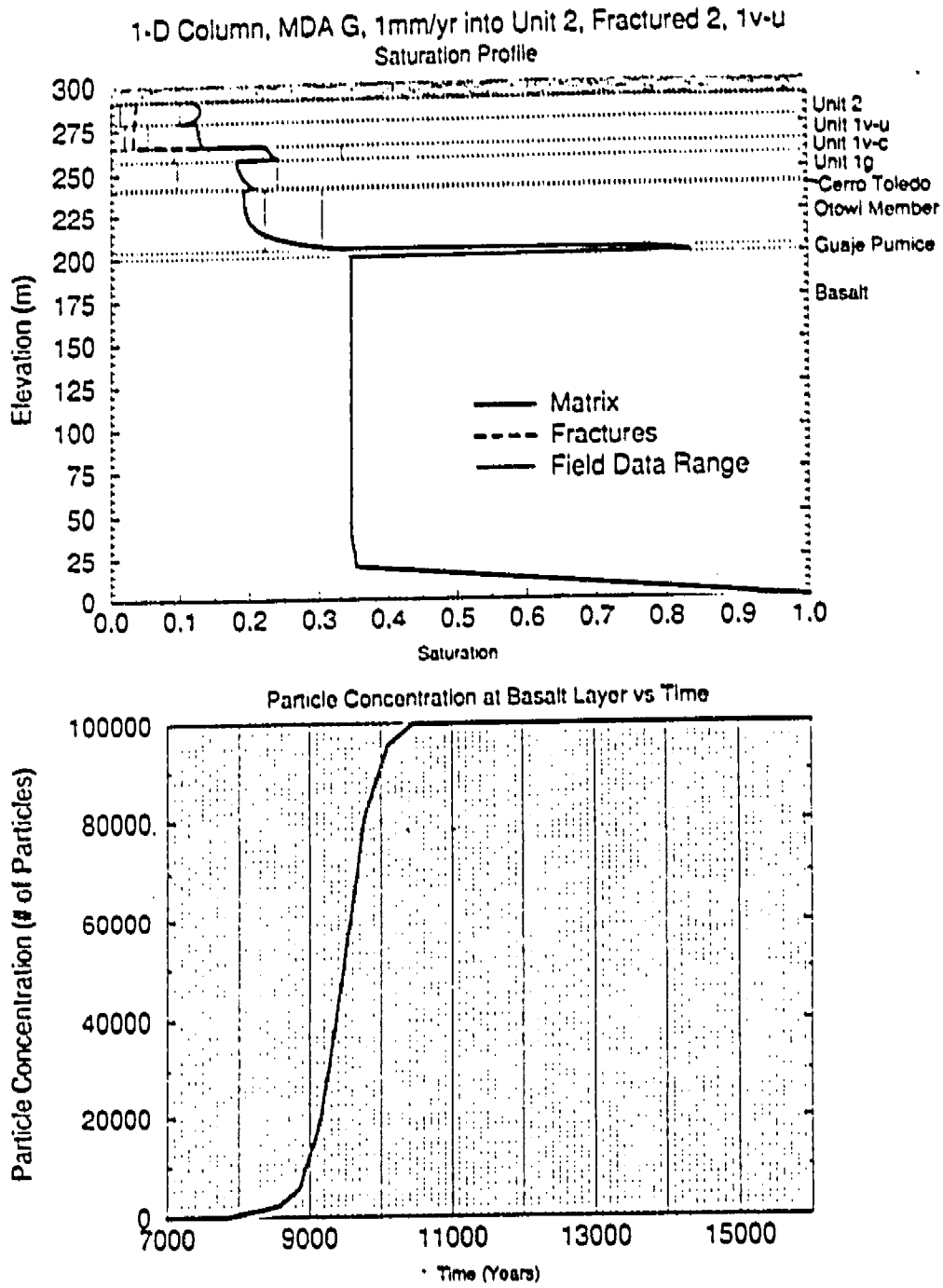

Figure 5: Steady-state saturation profile (fracture simulation), 1 mm per year infiltration into Unit 2, with groundwater travel time to basalt layer.

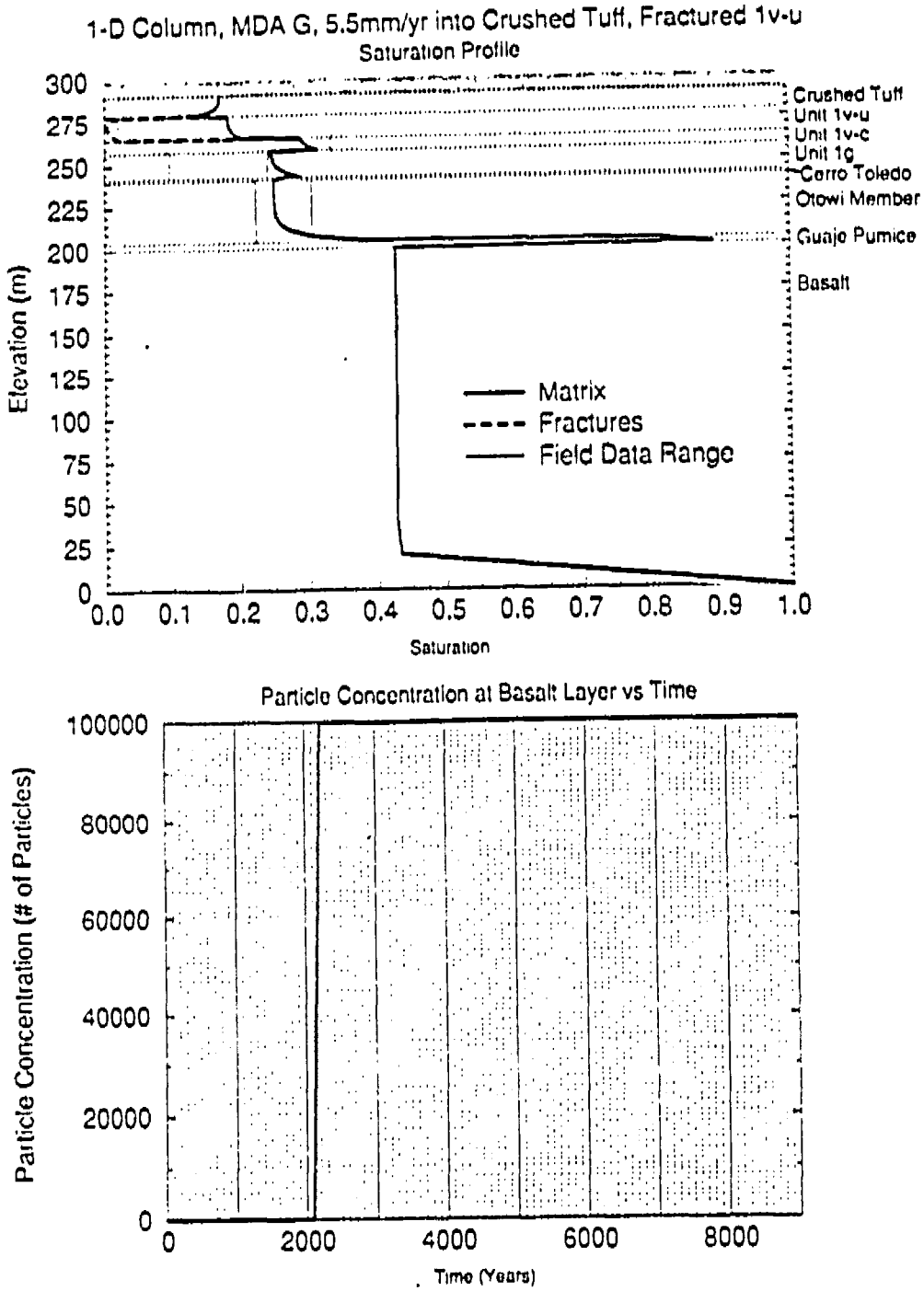

Figure 6: Steady-state saturation profile (fracture simulation), 5.5 mm per year infiltration into crushed tuff, with groundwater travel time to basalt layer.

which reports liquid flux rates between adjacent specified nodes. Flux was observed between several vertical pairs of nodes in the matrix material and between the corresponding fracture nodes in the fractured layers. Liquid flux rates in the fractures were approximately five orders of magnitude lower than liquid flux rates in the corresponding matrix material for both columns. Thus, essentially no fracture flow takes place in either column with fracture parameters calculated using parallel plate theory and steady infiltration profiles.

A preliminary sensitivity analysis of selected fracture parameters was conducted on the crushed tuff column. Van Genuchten n, α_{frac} and k_{frac} were varied in the fractured layer, and the resulting ratio of matrix liquid flux to fracture liquid flux was observed using the fixo macro. Parameter variations as well as flux differences are presented in Table 2.

One case with both a low van Genuchten n (1.5) and a low α_{frac} (3 m^{-1}) showed significant fracture flow. A saturation profile was determined for this scenario, and the difference between this profile and the steady-state profile obtained using fracture parameters calculated with parallel plate theory was computed. These profiles are presented in Figures 7 and 8. A positive value on the difference plot indicates that region is less saturated in the sensitivity analysis than in the base steady-state case. This scenario resulted in an approximately three percent lower saturation in Unit 1v-u. However, the matrix saturation in this layer is still higher than that observed in the field.

Groundwater travel time to the basalt layer was also computed for this scenario, and is depicted graphically in Figure 9. Fracture flow in this case resulted in a 300-year reduction in the arrival time of the first particles in comparison to the base steady-state case. The arrival time for 50 percent particle concentration was reduced by only 100 years.

3.3 Transient Fracture Simulations

Results are presented for only the crushed tuff column due to the problems encountered with the intact tuff column. The transient infiltration profile presented in Figure 2 was applied to the upper two fracture nodes in the crushed tuff column. Saturation profiles were observed at the end of 5014 years, 6000 years and 7000 years and are presented in Figures 10, 12 and 14. The differences between the steady-state fractured column saturation profiles and the three transient saturation profiles were also computed, and are presented in Figures 11, 13 and 15. In these figures, a positive value indicates

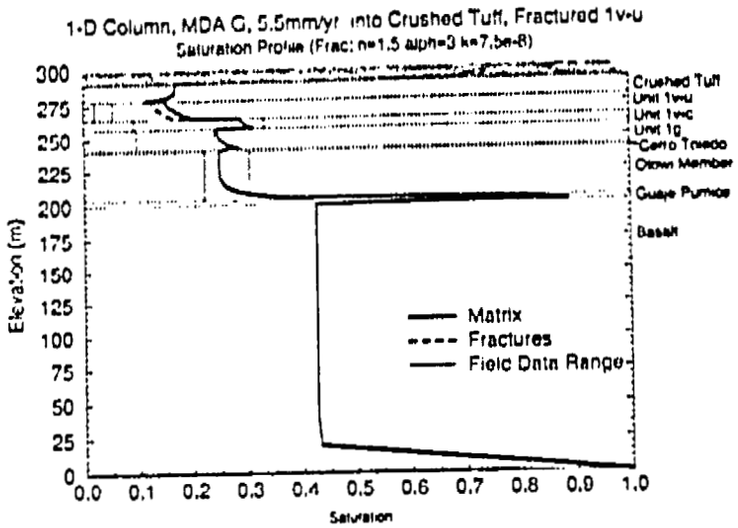

Figure 7: Saturation profile for crushed tuff column, fractured steady-state sensitivity analysis (n = 1.5, α_{frac} = 3 m^{-1}, k_{frac} = 7.5 x 10^{-8} m^2 in Unit 1v-u).

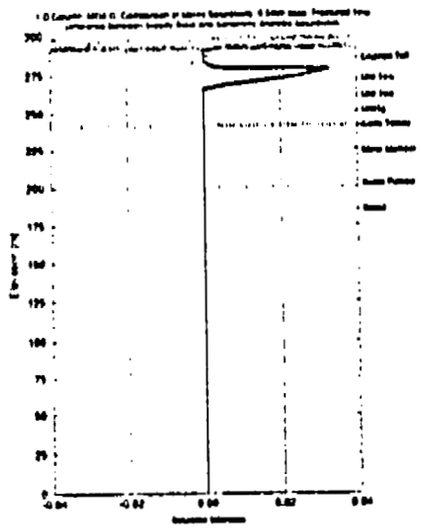

Figure 8: Difference between saturation profiles of steady-state base case and sensitivity analysis case (n = 1.5, α_{frac} = 3 m^{-1}, k_{frac} = 7.5 x 10^{-8} m^2 in Unit 1v-u) for fractured crushed tuff column.

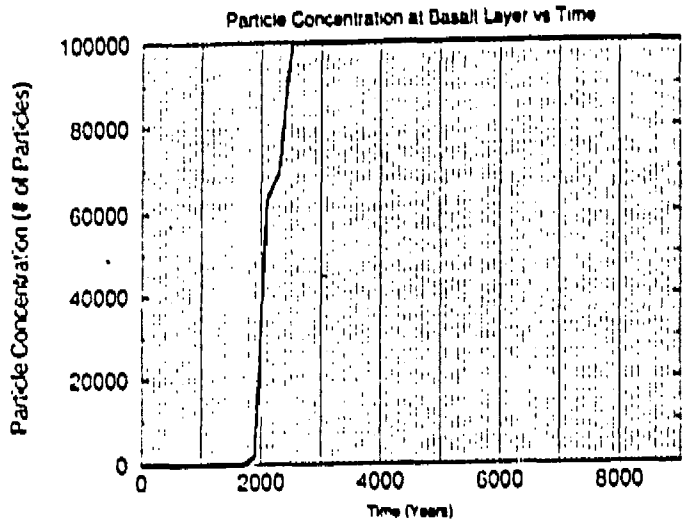

Figure 9: Groundwater travel time to basalt layer in crushed tuff column, fractured steady-state sensitivity analysis (n = 1.5, α_{frac} = 3 m^{-1}, k_{frac} = 7.5 x 10^{-8} m^2 in Unit 1v-u).

that area is less saturated in the transient simulation than in the steady-state simulation, while a negative value indicates that area is more saturated in the transient simulation. Groundwater travel time to the top of the basalt layer was calculated from the start of the first infiltration event in the transient profile, and is presented graphically in Figure 16.

Saturation as a function of time from 5000 years to 7000 years was observed for three nodes each in the crushed tuff, Unit 1v-u, and basalt layers, and is presented in Figures 17, 18 and 19. Both fracture and matrix nodes were observed in Unit 1v-u (the only fractured layer). Damping of the transient input is clearly observed in progressively deeper nodes.

Finally, vertical liquid flux rates between three pairs of adjacent nodes in the crushed tuff, Unit 1v-u, and basalt layers were observed and are presented in Figures 20, 21 and 22. Again, damping of the transient infiltration is evident at progressively deeper nodes. In Unit 1v-u (the only fractured layer), liquid flux rates between the observed fracture nodes were five to six orders of magnitude lower than liquid flux rates between the corresponding matrix nodes. Thus it was concluded that fracture flow is not a significant transport

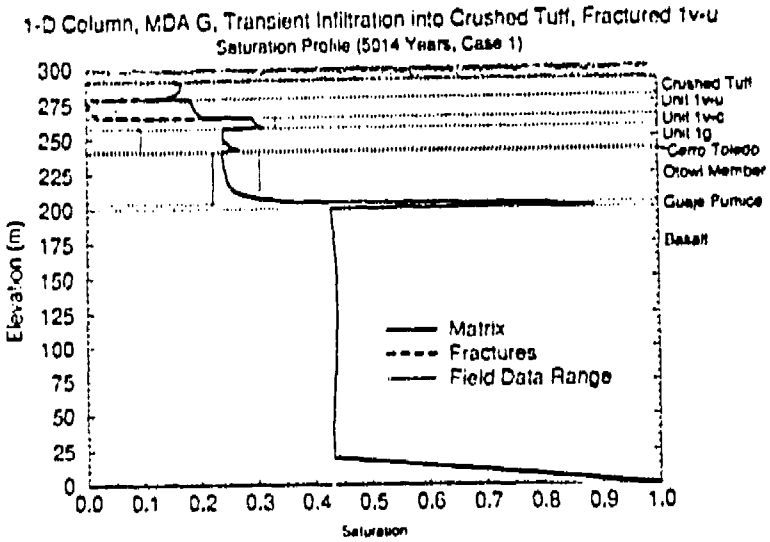

Figure 10: Saturation profile for crushed tuff column, 5014 years into transient simulation (5.5 mm per year average infiltration).

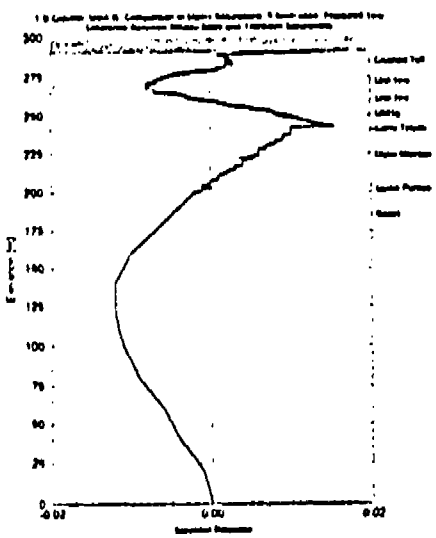

Figure 11: Difference between saturation profiles of steady-state and transient fracture simulations for crushed tuff column at 5014 years into transient simulation (5.5 mm per year average infiltration).

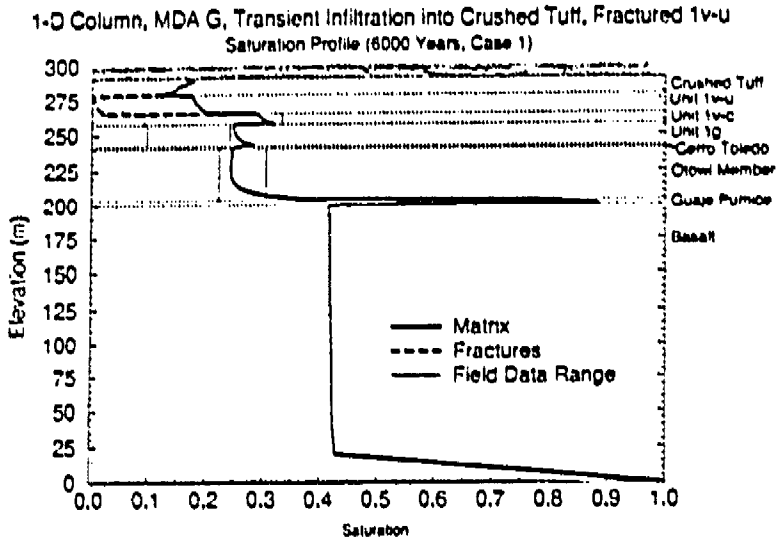

Figure 12: Saturation profile for crushed tuff column, 6000 years into transient simulation (5.5 mm per year average infiltration).

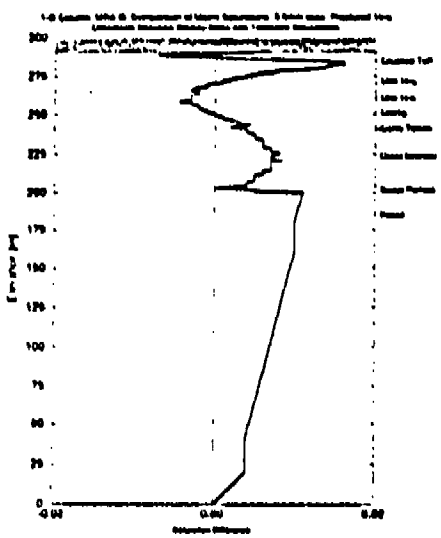

Figure 13: Difference between saturation profiles of steady-state and transient fracture simulations for crushed tuff column at 6000 years into transient simulation (5.5 mm per year average infiltration).

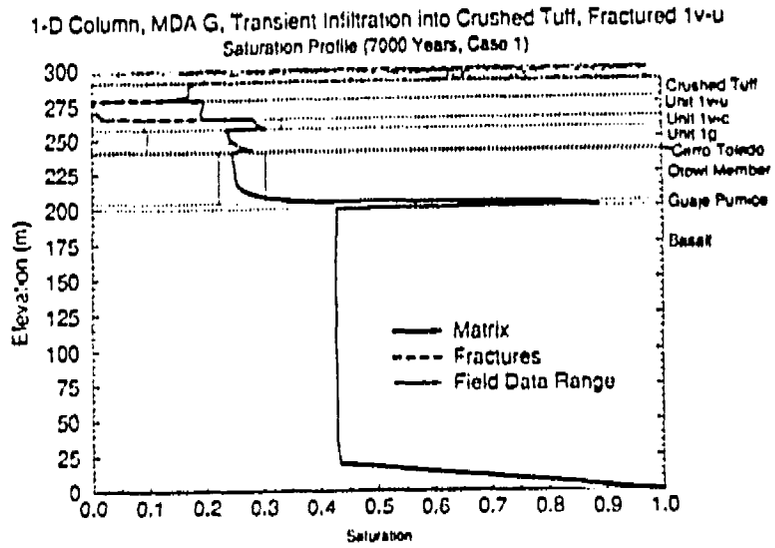

Figure 14: Saturation profile for crushed tuff column, 7000 years into transient simulation (5.5 mm per year average infiltration).

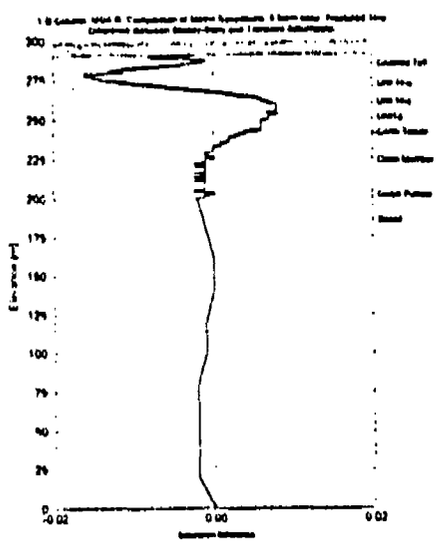

Figure 15: Difference between saturation profiles of steady-state and transient fracture simulations for crushed tuff column at 7000 years into transient simulation (5.5 mm per year average infiltration).

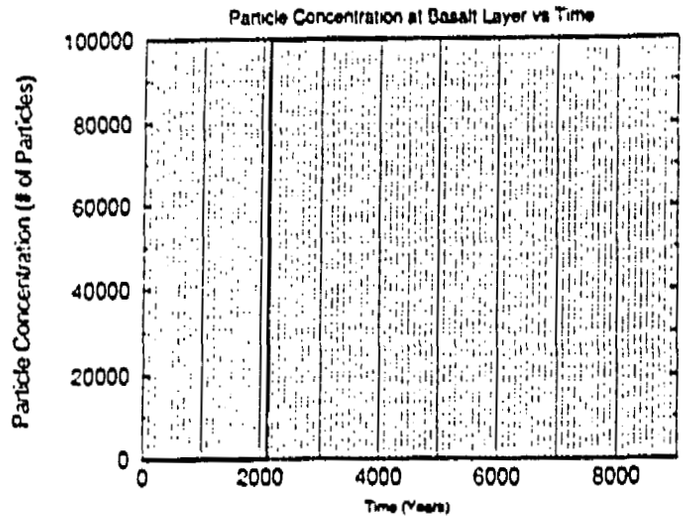

Figure 16: Groundwater travel time to basalt layer in crushed tuff column, transient simulation (5.5 mm per year average infiltration).

mechanism in the transient scenario using the given infiltration profile with fracture parameters calculated using parallel plate theory.

Liquid flux variations in the basalt layer are much lower than saturation variations in that layer. These results agree with observations made by Birdsell et. al. (1996) in a previous study that transient impulses are damped in the lowest units at MDA G.

4 Discussion and Conclusions

Matrix-only saturation profiles as well as groundwater travel times through the various layers in the two simulated columns were first determined to serve as a baseline comparison to subsequent fractured column simulations. Matrix saturations in this case were significantly higher than saturations observed in the field in the upper two units in the columns. Sensitivity analysis was also performed on these columns to determine the effects of using bounding hydraulic conductivity values on groundwater travel times through each of the individual units and to the top of the basalt layer. Travel times were found to vary by approximately 25 percent from average when maximum or

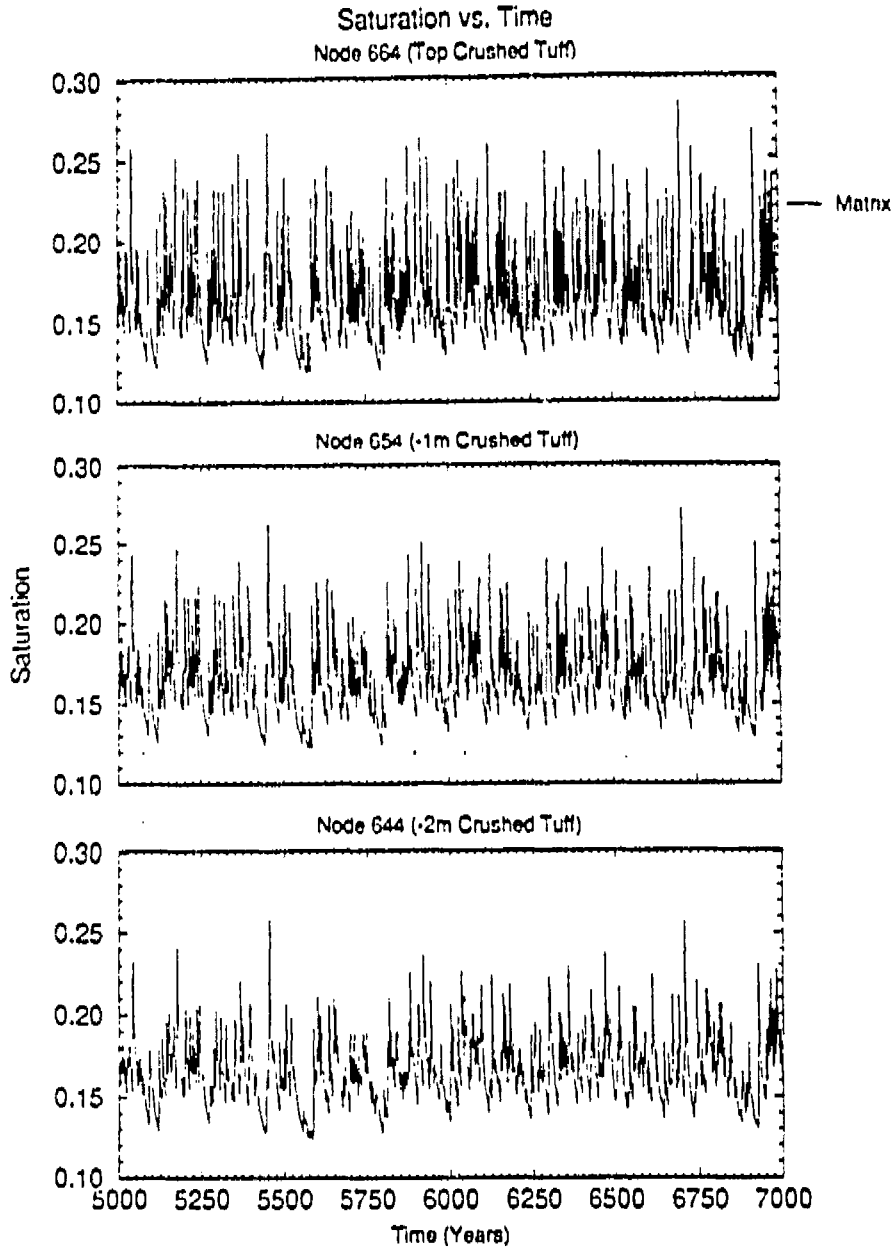

Figure 17: Saturation vs. time, crushed tuff layer, crushed tuff column, transient simulation (5.5 mm per year average infiltration).

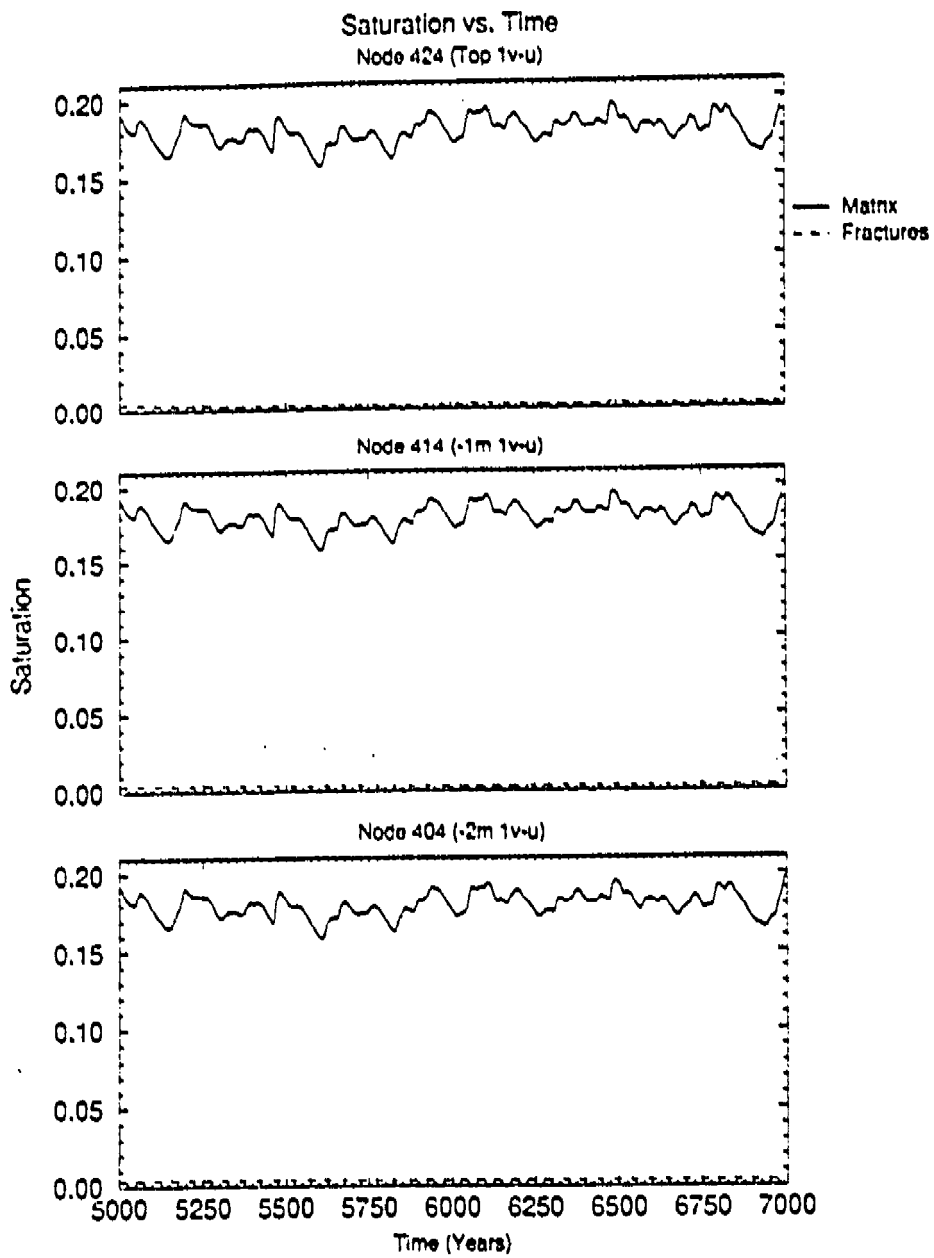

Figure 18: Saturation vs. time, Unit 1v-u, crushed tuff column, transient simulation (5.5 mm per year average infiltration).

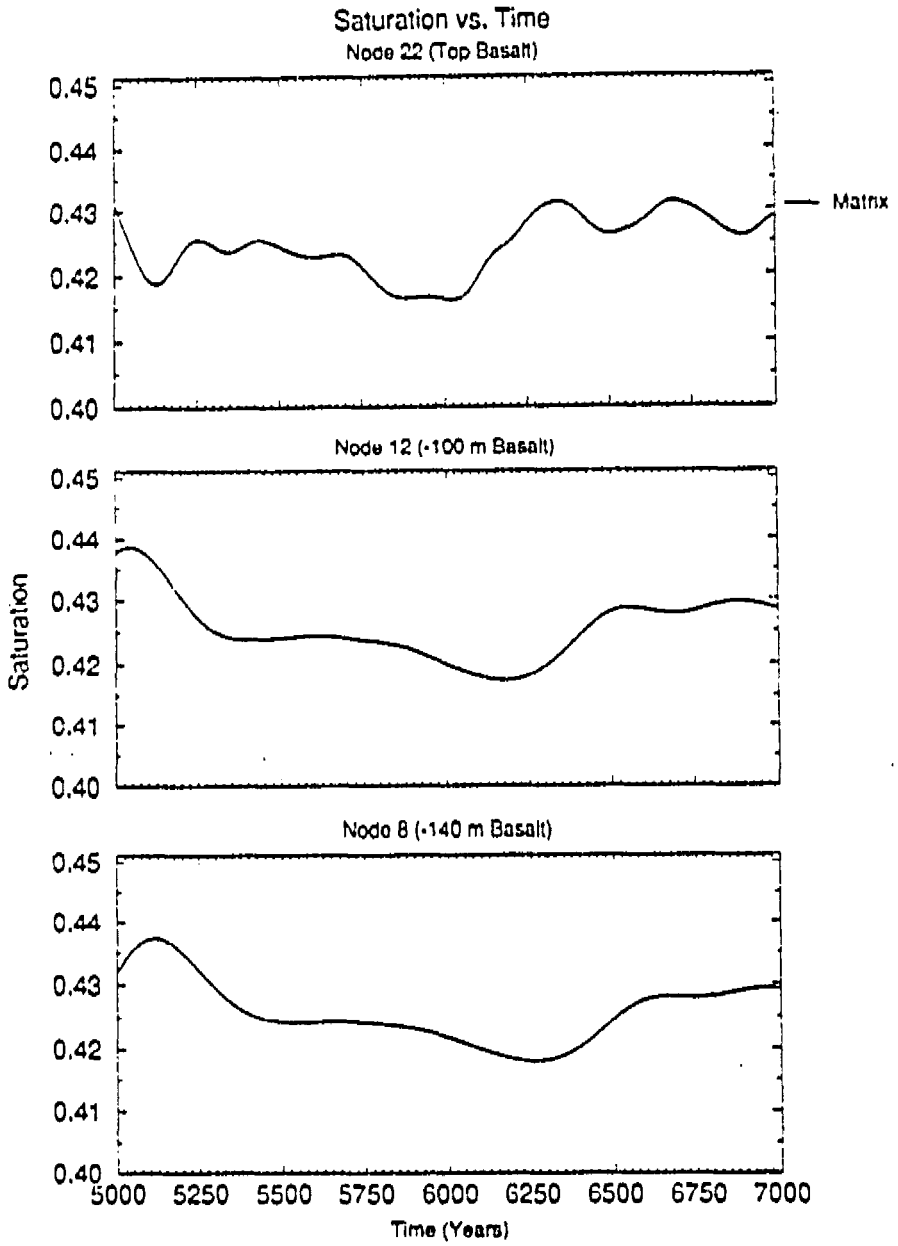

Figure 19: Saturation vs. time, basalt layer, crushed tuff column, transient simulation (5.5 mm per year average infiltration).

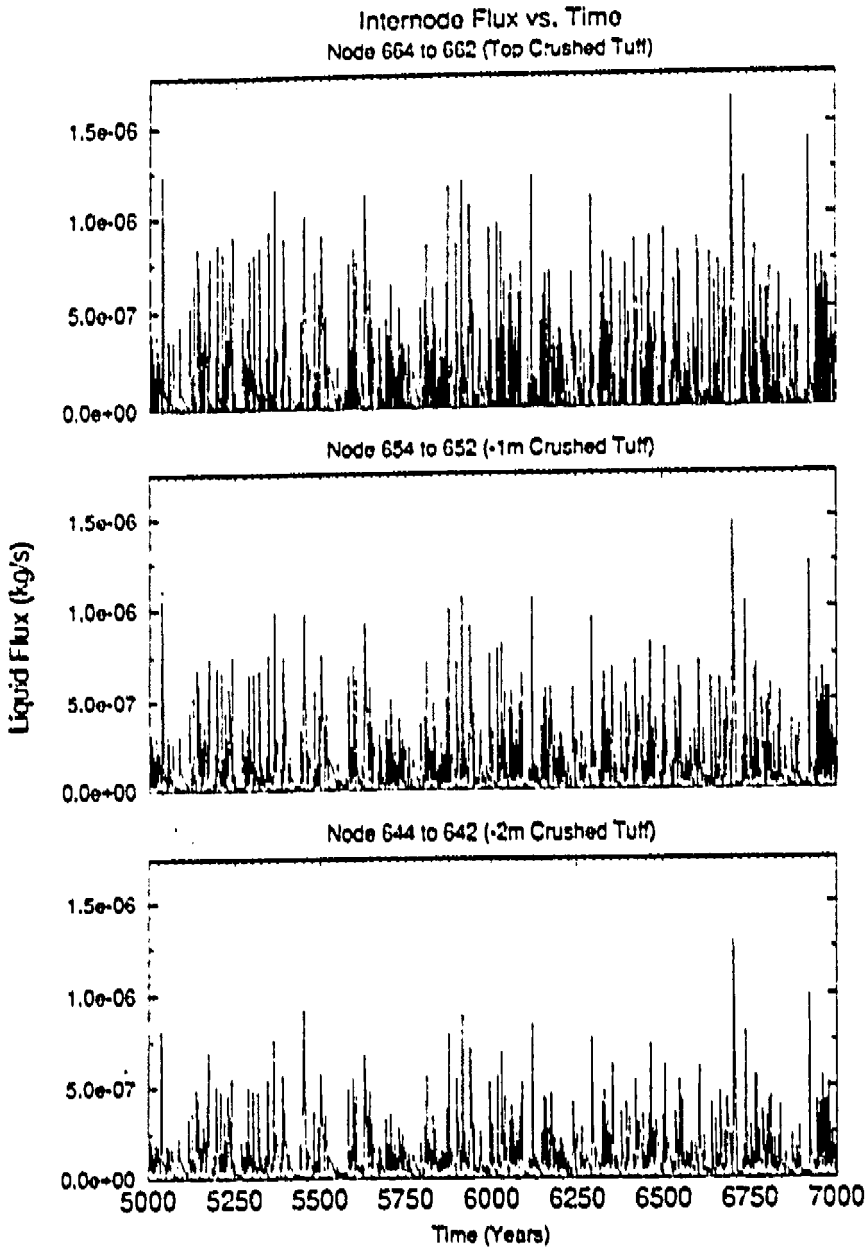

Figure 20: Liquid flux vs. time in matrix, crushed tuff layer, crushed tuff column, transient simulation (5.5 mm per year average infiltration).

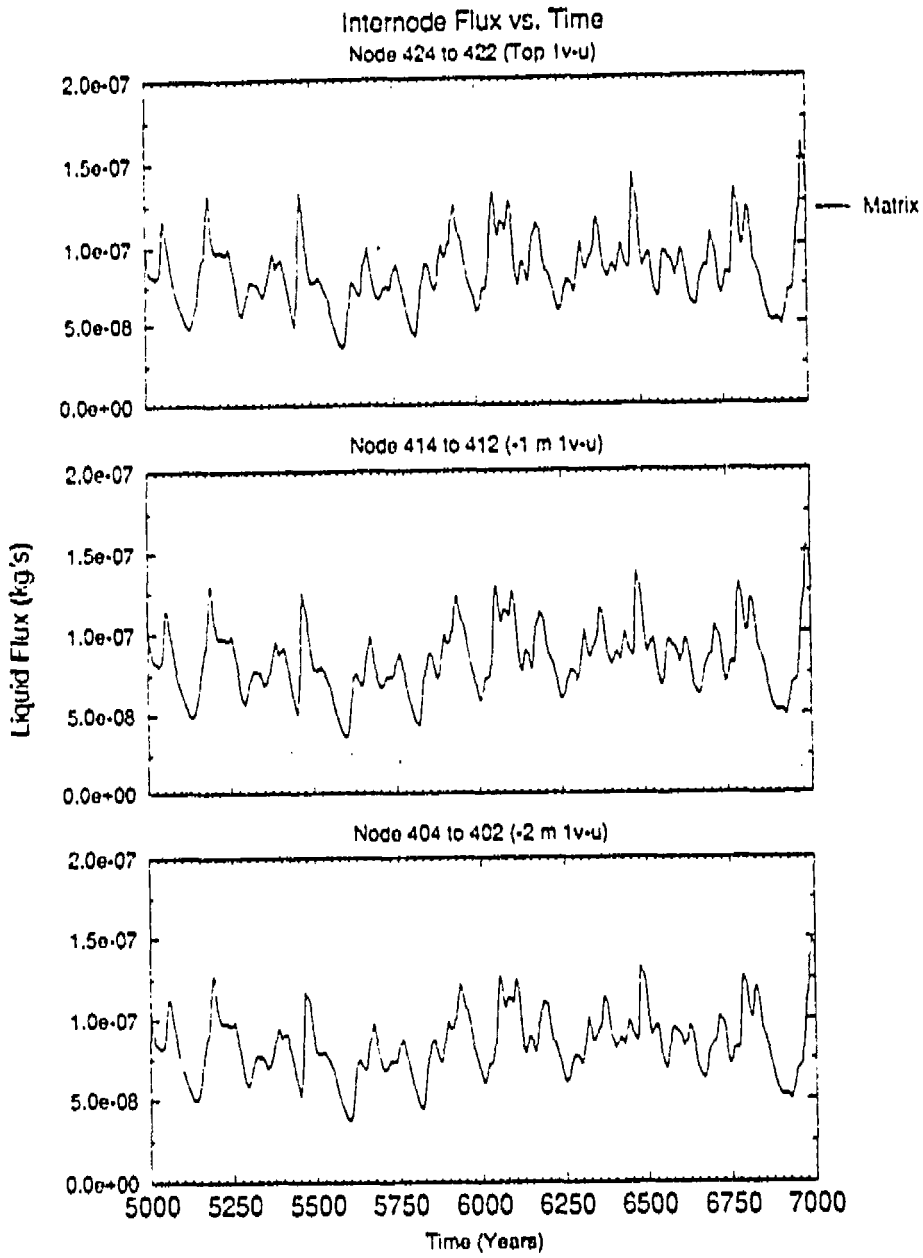

Figure 21: Liquid flux vs. time in matrix, Unit 1v-u, crushed tuff column, transient simulation (5.5 mm per year average infiltration).

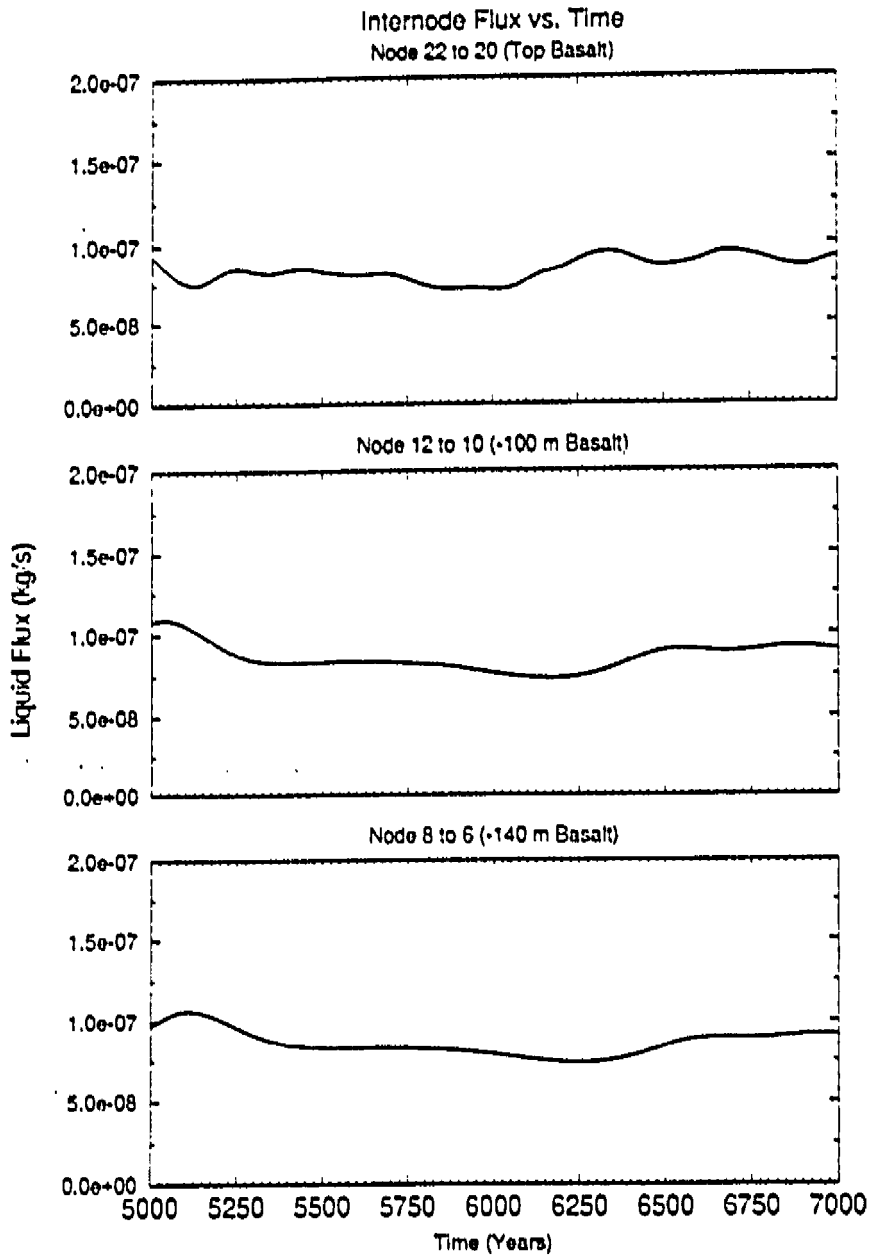

Figure 22: Liquid flux vs. time in matrix, basalt layer, crushed tuff column, transient simulation (5.5 mm per year average infiltration).

minimum conductivities were used in a given unit.

Steady-state fracture simulations were then conducted to investigate the effects of fractures in the upper units of the columns on saturation profiles and groundwater travel times. It was found that fracture flow did not occur in the steady-state simulations with the fracture parameters calculated using parallel plate theory. Saturation profiles did not differ from those obtained in the matrix-only simulations. Furthermore, groundwater travel times remained the same through each unit and overall to the basalt layer.

A sensitivity analysis was performed on the crushed tuff column, where selected fracture parameters were varied in an attempt to induce fracture flow. A combination of low van Genuchten n (1.5) and low α_{frac} (3 m^{-1}) lead to high liquid flux rates in the fractures in Unit 1v-u. Saturations and groundwater travel times were investigated for this scenario. Matrix saturation was reduced by approximately three percent in the fractured layer, but was still higher than saturations observed in the field for this unit. Groundwater travel time was slightly reduced in this scenario. Initial particle arrival was approximately 300 years earlier in this case than in the base steady-state simulation. Arrival time for 50 percent particle concentration was reduced by approximately 100 years. Further sensitivity analysis of fracture parameters in both the crushed tuff and intact tuff columns will be performed.

Transient fracture simulations were finally conducted to determine whether or not unusually high episodic flow events would lead to fracture flow and thus reduced groundwater travel times to lower units. While the intact tuff case with fractured Units 2 and 1v-u could not be adequately solved by the current FEHM transient flux package, the crushed tuff case with fractured Unit 1v-u yielded usable results. Fracture flow did not occur in the transient simulations for this column. Groundwater travel times to the basalt layer were the same as in the steady-state fractured and matrix-only simulations.

Based on the results of these simulations, it appears unnecessary to conduct two- or three-dimensional flow simulations with transient infiltration, considering the much larger required computer resources for such simulations. Transient simulations using fracture parameters obtained from steady-state sensitivity analyses that allow fracture flow to take place will be undertaken to verify this conclusion. Final analysis of transient intact tuff case studies must also be performed in order to support this conclusion.

Further studies will be conducted using a two-dimensional cross-sectional representation of the mesa containing the disposal pits. This representation will be similar to that used by Birdsell et. al. (1995) in a previous study

of the area, except it will incorporate fracture properties in the upper units of the mesa using the dpdp package of FEHM. Differential heating will be applied to the north and south mesa sides along with an atmospheric air pressure gradient. It is hoped that this scenario will induce air flow in the fractured upper units, thus increasing evaporation and decreasing simulated matrix saturations in the upper mesa units.

References

[1] K. H. Birdsell, K. Bower, A. Wolfsberg, W. Soll, T. Orr, and T. Cherry. Simulations of Groundwater Flow and Radionuclide Transport in the Vadose and Saturated Zones Beneath Area G. In progress, 1996.

[2] K. H. Birdsell, W. E. Soll, N. D. Rosenberg, and B. A. Robinson. Numerical Modeling of Unsaturated Groundwater Flow and Radionuclide Transport at MDA G. Technical Report LA-UR-95-2735, Los Alamos National Laboratory, 1995.

[3] C. W. Bishop. Hydrologic Properties of Vesicular Basalt. Master's thesis, University of Arizona, Tucson, AZ, 1991.

[4] Everett, 1995. Get reference.

[5] D. Krier, P. Longmire, and H. J. Turin. Geologic, Geohydrologic and Geochemical Data Summary of MDA G, TA-54, Los Alamos National Laboratory. Technical Report LA-UR-95-2696, Los Alamos National Laboratory, 1995.

[6] D. B. Rogers. The Unsaturated Hydraulic Characteristics of the Bandelier Tuff. Technical Report LA-12968-MS, Los Alamos National Laboratory, 1995.

[7] E. P. Springer. Area G Performance Assessment: Surface Water and Erosion. Technical Report LA-UR-95-2497, Los Alamos National Laboratory, 1995.

[8] G. A. Zyvoloski, B. A. Robinson, Z. V. Dash, and L. L. Trease. User's Manual for the FEHMN Application. Technical Report LA-UR-94-3788, Rev. 1. Los Alamos National Laboratory, 1995.

LA-UR-97-179

Title:

Conceptual Model for Subsurface Transport at MDA G

Author(s):

David B. Rogers, ESH-18

Patrick Longmire, CST-7

Brent D. Newman, EES-15

Kay H. Birdsell, EES-5

Wendy E. Soll, EES-5

Erik L. Vold, EM-SWM

Submitted to: January, 1997

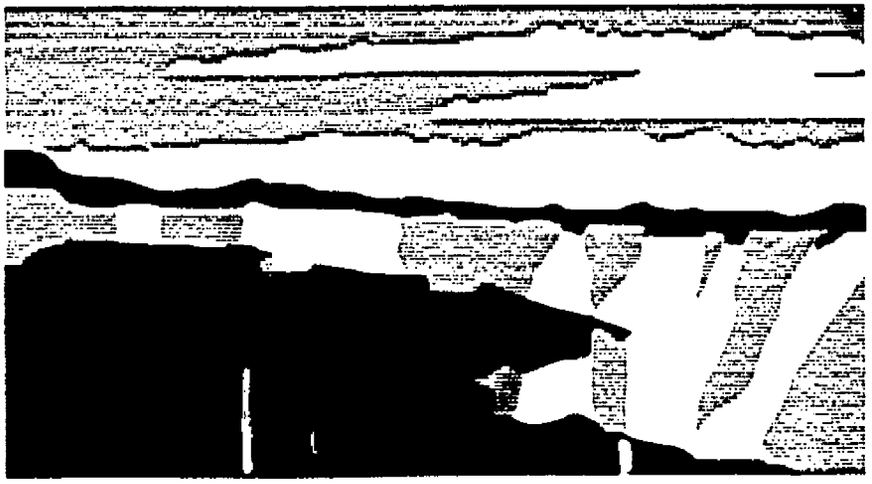

Los Alamos
NATIONAL LABORATORY

Los Alamos National Laboratory, an affirmative action/equal opportunity employer, is operated by the University of California for the U.S. Department of Energy under contract W-7405-ENG-36. By acceptance of this article, the publisher recognizes that the U.S. Government retains a nonexclusive, royalty-free license to publish or reproduce the published form of this contribution, or to allow others to do so, for U.S. Government purposes. The Los Alamos National Laboratory requests that the publisher identify this article as work performed under the auspices of the U.S. Department of Energy.

Form No. 836 R5
ST 2629 10/91

Conceptual Model for Subsurface Transport at MDA G

David B. Rogers, Patrick Longmire, Brent D. Newman, Kay H. Birdsell, Wendy E. Soll, and Erik L. Vold

Introduction

This conceptual model discussion covers aspects of hydrogeology and geochemistry bearing on solute transport beneath MDA G and is an update of that provided by Turin (1995). MDA G occupies part of Mesita del Buey, a narrow, southeast trending mesa on the Pajarito Plateau. The mesa is formed from two ignimbrite (ash flow) eruptions which comprise the Bandelier Tuff. Canyons have cut down 50 to 100 ft. into the tuff below the sides of the mesa. The tuff is underlain by the Cerros del Rio basalts, the Puye Conglomerate, and sediments of the Santa Fe Group. Water in the regional aquifer beneath the Pajarito Plateau occurs in the Puye Conglomerate and the Santa Fe Group, at a depth of about 1050 ft below the western end of Mesita del Buey, and 850 ft below the eastern end (Purtymun and Kennedy, 1971).

Hydrogeologic Conceptual Model for the Pajarito Plateau

To provide a context for the MDA G conceptual model, we briefly present the LANL facility-wide hydrologic conceptual model, taken from the LANL Hydrogeologic Workplan (Water Quality & Hydrology Group, 1996). The document was prepared in response to the New Mexico Environment Department's (NMED) May 30, 1995 denial of LANL's groundwater monitoring waivers for LANL's regulated units (under 40 CFR 265 Subpart G) including MDA G and MDA L at TA-54, and in response to NMED's August 17, 1995 requirement for a comprehensive hydrogeologic workplan for LANL (under 40 CFR 265 Subpart F). The Hydrogeologic Workplan was written by an interdisciplinary LANL team, coordinated by LANL's Water Quality & Hydrology Group (ESH-18), at DOE request. The workplan's hydrogeologic characterization activities are directed at developing an enhanced understanding of the Laboratory's hydrogeologic setting, with the intention of providing a basis for extending LANL's groundwater monitoring system.

For purposes of describing a conceptual model for Los Alamos National Laboratory, the hydrogeology of the Pajarito Plateau is broken into four components. Two of the components relate to physiography: mesas and canyons. Mesa tops are for the most part

dry (Figure 1). Canyons are divided into wet and dry; the wet canyons contain ephemeral streams and contain groundwater in the canyon bottom alluvium (Figure 2). Dry canyons have less stream flow and may lack alluvial groundwater. A third component, intermediate perched groundwater, is found at depths ranging from 100 to 400 ft. and is controlled by lithology. The fourth component, the Regional Aquifer, is found at depths of about 600 to 1200 ft. Important aspects of each component of the hydrogeologic system are listed below.

In the context of the LANL facility-wide conceptual model, Mesita del Buey (occupied in part by MDA G) is one of the drier of the mesas found on the Laboratory. It is located well east of the Jemez Mountains at low elevation, in the portion of the Laboratory where evapotranspiration rates are highest and precipitation is lowest. Pajarito Canyon, to the south of Mesita del Buey, is a canyon that heads in the Jemez Mountains and is one of the wetter canyons (though not the wettest) at the Laboratory. Cañada del Buey, north of Mesita del Buey, heads on the Pajarito Plateau and is one of the driest canyons at LANL. Intermediate perched groundwater has not been observed beneath MDA G (Devaurs and Purtymun, 1985). Intermediate perched groundwater may be present within the Bandelier Tuff beneath Pajarito Canyon, based on results from drilling wells SHB-4 (Gardner et al., 1993) and PM-2 (Cooper et al., 1965). The following sections summarize the four components of the LANL facility-wide hydrogeologic conceptual model (Water Quality & Hydrology Group, 1996).

LANL Facility-wide Conceptual Model: Mesas

Relatively small volumes of water move beneath mesa tops under natural conditions, due to low rainfall, high evaporation, and efficient water use by vegetation. Atmospheric evaporation may extend within mesas, further inhibiting downward liquid flow.

The amount of mesa top recharge along the western portion of the Laboratory is uncertain. Higher rainfall, increased vegetative cover, and increased welding and jointing of the tuff might lead to different recharge rates than those observed in better studied portions of the Laboratory.

Mesa top recharge can be locally significant under disturbed surface conditions. Such change occurs when the soil is compacted, when the vegetation is disturbed, or when more water is artificially added to the hydrologic system by features such as blacktop, lagoons, or effluent disposal.

Hydrogeologic Conceptual Model for Mesas

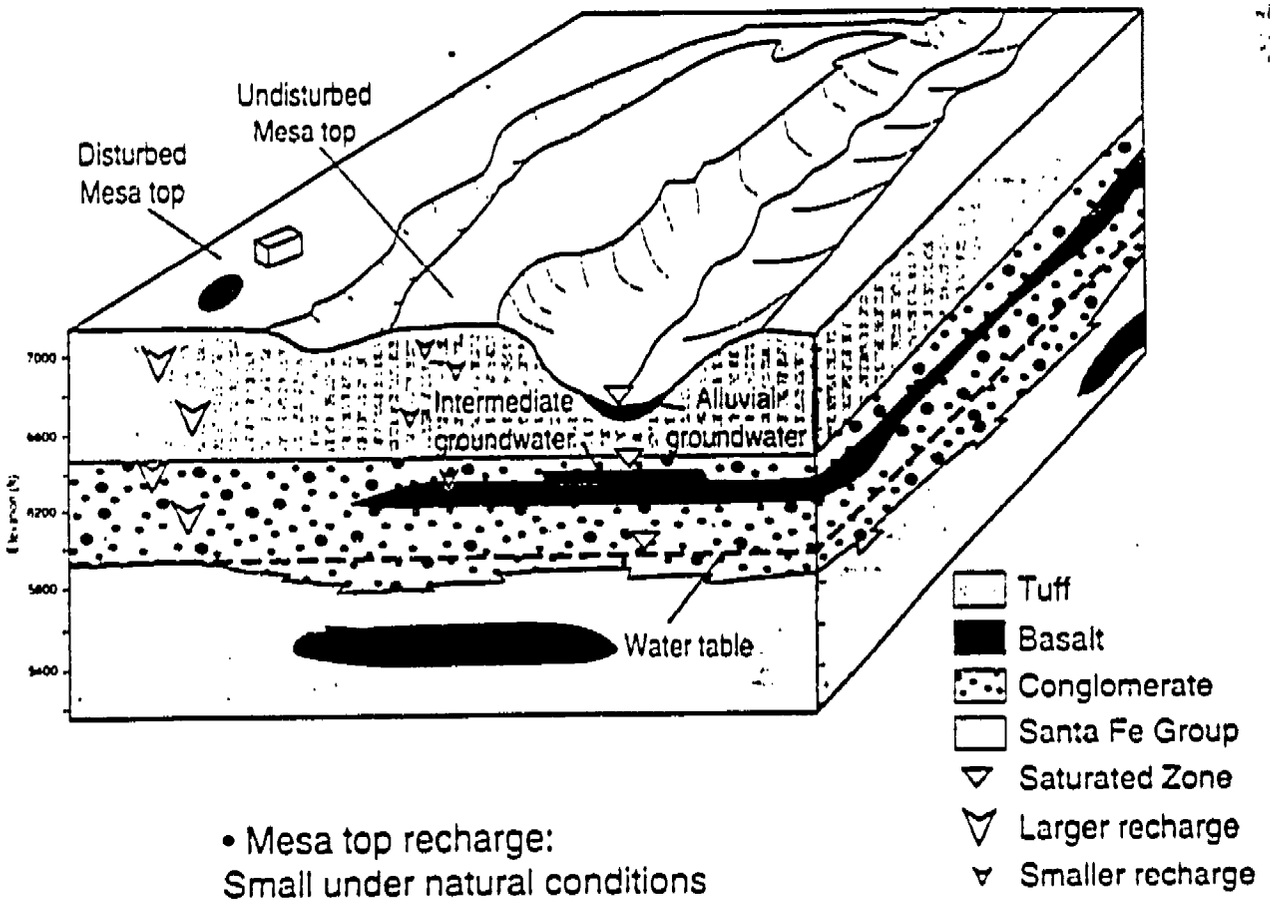

- Mesa top recharge:
  Small under natural conditions
  Significant under disturbed surface
  Fractures don't enhance unless saturated

- Air movement may dry mesa interior

- Vapor phase contaminant movement possible

Figure 1. Hydrogeologic conceptual model for mesas (from Water Quality & Hydrology Group, 1996).

Hydrogeologic Conceptual Model for Canyons

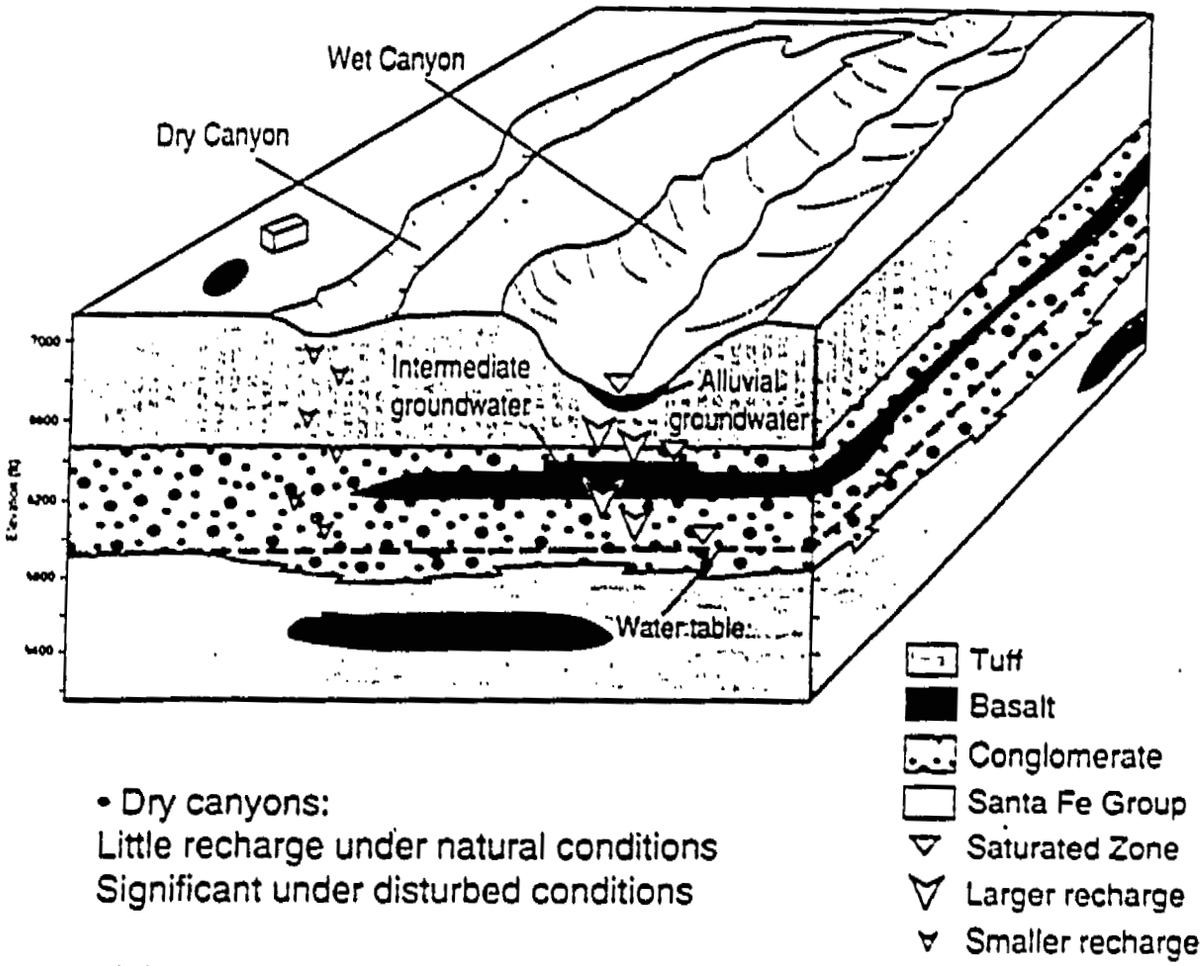

- Dry canyons:
  Little recharge under natural conditions
  Significant under disturbed conditions

- Wet canyons:
  Source of recharge to intermediate groundwater and main aquifer

- Intermediate groundwater:
  Significant contaminant transport path
  Source of recharge to main aquifer
  Occurs in larger canyon systems
  Exists beneath canyons, not mesas?
  Laterally extensive near Jemez Mountains?
  Controlled by subsurface lithology

Figure 2. Hydrogeologic conceptual model for canyons (from Water Quality & Hydrology Group, 1996).

Fractures within mesas do not enhance the movement of dissolved contaminants unless saturation develops.

Contaminants in vapor form readily migrate through mesas. Vapors denser than air will sink.

LANL Facility-wide Conceptual Model: Alluvial Groundwater

In drier canyon bottoms, groundwater may occur seasonally in the alluvium, depending on the volume of surface flow from snowmelt, thunderstorm runoff, and Laboratory NPDES-permitted effluents. As water in the alluvium moves down the canyon, it is depleted by evapotranspiration and infiltration into the underlying rocks.

In wetter canyon bottoms, infiltration of NPDES-permitted effluents and natural runoff reaching the stream channel may maintain a shallow body of groundwater in the alluvium. Water levels are highest in late spring from snowmelt runoff and in late summer from thundershowers. Water levels decline during the winter and early summer when runoff is at a minimum.

Alluvial groundwater zones are a source of recharge to underlying intermediate perched zones, usually by unsaturated flow.

Dry canyon bottoms contribute relatively little recharge under natural conditions. Long-term addition of effluent to naturally dry canyon bottoms may result in recharge to intermediate perched zones.

In a few cases where saturated flow might occur, faults that underlie alluvial saturated zones or intermediate perched zones could provide pathways for downward water movement.

LANL Facility-wide Conceptual Model: Intermediate Perched Groundwater

Intermediate perched zones occur beneath major canyon systems, particularly those that head in the Jemez Mountains. Intermediate perched zones may receive recharge from watersheds west of the Laboratory.

In addition to availability of recharge from overlying alluvial groundwater, the location of intermediate perched zones is controlled by hydrogeologic characteristics of subsurface units, mainly variations in lithology and permeability. In some cases, such as with

interlayered basalts and conglomerates, perched zones could occur at several depths beneath a canyon.

The perched zones have not been observed to extend laterally beneath mesas. However, some lateral spreading of perched groundwater may occur down gradient, if the canyon course and the dip of the perched zone do not coincide.

Some hydrologic evidence suggests the existence of an intermediate perched zone within the Bandelier Tuff along the western portion of the Laboratory, but this can not be confirmed without further study.

Contaminant concentrations in water entering these perched zones are diluted. Lateral, down-canyon flow within intermediate perched zones could contribute to significant transport of contaminants away from their surface source.

LANL Facility-wide Conceptual Model: Regional Aquifer

The slope of the top of the Regional Aquifer suggests that the flow of groundwater is generally towards the east or southeast, and towards the Rio Grande.

Intermediate perched zone and alluvial groundwater bodies may be minor sources of recharge to the Regional Aquifer. The hydraulic connection between the Regional Aquifer and the land surface is not strong.

Regional Aquifer groundwater within the eastern portion of the Pajarito Plateau (generally along the Rio Grande) appears to be of different recharge origin than under the central part of the Plateau.

Sources of recharge to the Regional Aquifer are uncertain. Geochemical data show that the Valles Caldera is not the source of major recharge, contrary to statements in earlier LANL reports. Major recharge may occur by southerly flow along the late Miocene trough of Purtymun (1984).

If present, Laboratory-derived contaminants in the Regional Aquifer are likely to vary in concentration. The contaminant concentrations are probably below maximum contaminant levels (MCLs) for drinking water because (1) Regional Aquifer underflow dilutes contaminant concentrations in recharge, and (2) contaminant concentrations in alluvial and intermediate perched zone groundwater are expected to decrease with depth due to dilution and geochemical attenuation along vertical migration pathways.

MDA G Hydrologic Considerations

The most important aspect of hydrology related to subsurface transport at MDA G regards the magnitude of recharge within the mesa (Vold et al., 1996). The downward flux of water provides the vehicle for carrying solutes to the water table beneath the mesa. The recharge fluxes found in arid or semiarid regions may be small and are difficult to quantify using ordinary hydrologic techniques. The measurement uncertainties in standard techniques obscure the small recharge values in dry regions (Allison et al., 1994). As a result, recharge must be estimated using a combination of geochemical methods and model analysis.

Several aspects of the lithology and structure underlying MDA G pose significant uncertainties to modeling unsaturated flow. Figure 3 shows longitudinal and transverse cross sections through the mesa occupied by MDA G. The Tshirege and Otowi Members of the Bandelier Tuff form the mesa and underlie the canyon bottoms to the north and south of the mesa. The base of the Bandelier Tuff directly overlies the Cerros del Rio Basalts and has a westerly dip beneath the mesa (Broxton and Reneau, 1996). The Guaje Pumice bed, which forms the bottom of the Otowi Member, appears to pinch out to the east. The characteristics of this interface may have significant consequences for lateral diversion of groundwater flow, and are addressed below. The hydrologic characteristics of the Cerros del Rio Basalts, which make up a substantial portion of the vadose zone beneath MDA G, are an important unknown aspect of the flow system, and are also addressed here.

Near-surface mesa water balance

Mean annual precipitation at MDA G is about 14 in (35.6 cm), with a mean at nearby White Rock of 13.2 in. (33.5 cm) (Bowen, 1990). A large proportion of the precipitation at MDA G is removed by evapotranspiration (ET). Nyhan et al. (1990) determined for two control plots located about a mile northwest of MDA G that over a three year period, ET was about 87% to 89% of precipitation. Vold and Eklund (1996) determined that evapotranspiration rates were 69% to 78% of precipitation, but this was based on a set of 4-hour measurements rather than a long-term water balance study. As a result, little water is left over for recharge. Springer (1995) provides a detailed analysis of the partitioning of precipitation between runoff, evapotranspiration, and percolation (or recharge).

Figure 3. Stratigraphic cross sections through MDA G (based on Krier, et al., 1995).

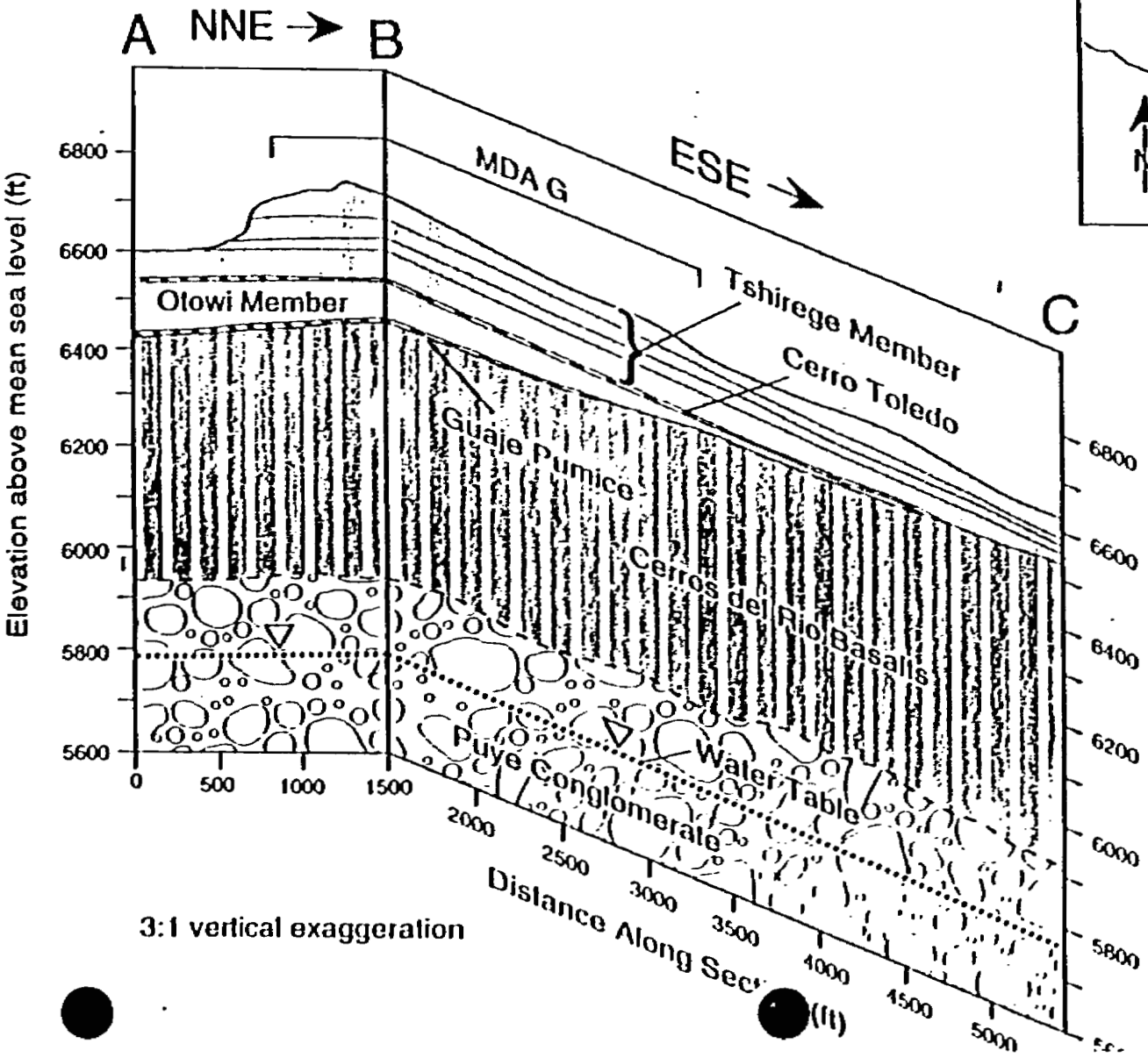

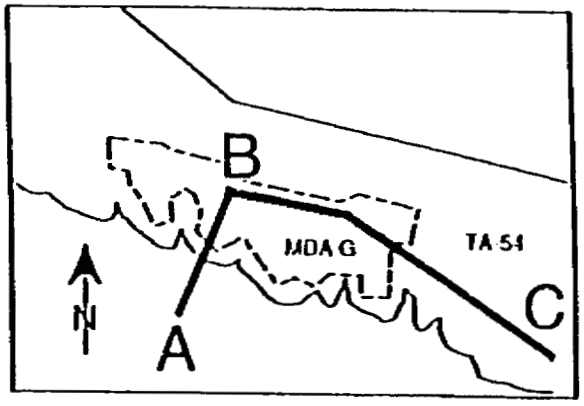

General near-surface moisture trends

Moisture content measurements do not give a measure of water flux, and flux may still occur under steady state moisture conditions. However, moisture content measurements do provide a suggestion of the overall water balance, from which recharge might be inferred. Profiles collected by Kearl et al. (1986) show that volumetric moisture content decreases from 8% to 16% near the surface of Mesita del Buey to about 0.5% to 2% by a depth of 4 to 5 m. There are variations from this general trend: it appears that in areas of surface disturbance such as roads or pits, near-surface moisture contents are higher and these higher moisture contents extend deeper than in undisturbed areas of the mesa (Vold, 1996a). The extent of such disturbances and their effects on moisture profiles is not always evident. Seasonal changes in evapotranspiration and precipitation at MDA G appear to influence measurable moisture content variations within only the shallowest few meters of the mesa top.

Abeele et al. (1981) collected periodic neutron probe moisture content measurements from several holes at MDA G. Data from one hole within the fill overlying a disposal pit indicated "significant seasonal fluctuations in moisture content to a depth of about 4 m, with a downward moisture flux below that depth." For holes drilled in undisturbed tuff within the shaft disposal field, Abeele et al. (1981) found "seasonal fluctuations in moisture content in the upper 4 m, with no significant changes below that depth" and concluded that the "regions of essentially constant moisture content" below 4 m implied "essentially steady state conditions". The low moisture content values below 4 or 5 m, when considered along with moisture retenuon relationships (Rogers and Gallaher, 1995; Rogers et al., 1995; Rogers et al., 1996), indicate that very low liquid water fluxes (of magnitude 10^{-11} cm/sec) occur in this region.

Effect of disposal pits on near-surface moisture

The waste disposal pits at MDA G are generally excavated to near the base of Tshirege Unit 2. Moisture content data collected within pit fill has generally shown moisture levels higher than for surrounding undisturbed tuff (Abeele et al., 1981; Rogers, 1977; Loaiza and Vold, 1995). In 1976 cores were collected from horizontal boreholes drilled to pass through Tshirege Unit 2 about 1 m beneath a pit that had been closed in 1966 (Purtymun et al., 1978; Purtymun et al., 1980). Analysis of these cores indicated that concentrations of ^{90}Sr, ^{137}Cs, ^{238}Pu, $^{239,240}Pu$, and ^{241}Am were below the minimum detection limits. The authors concluded that no traces of radionuclides had migrated

from the pits. In 1992 the boreholes were reentered and moisture measurements made with a neutron probe (McLin, 1994). Volumetric moisture content values beneath the pits were in the range of 1% to 4%, and were generally 1% to 2% higher beneath the pit than moisture levels away from the pit. These measurements suggest that pit excavation might have a small effect on moisture contents beneath the pits.

Hydrologic processes within the mesa

Approximately the uppermost 300 ft of the subsurface beneath the top of Mesita del Buey consists of the Bandelier Tuff and the Cerro Toledo interval. Rogers (1995) summarized unsaturated characteristics of the tuff beneath Mesita del Buey based on laboratory core measurements. The results show that for each unit of the Tshirege Member and for the Otowi Member, the hydraulic properties (moisture characteristic curves and unsaturated hydraulic conductivity relationships) are relatively uniform, with larger differences between units. For this reason, each stratigraphic unit is represented in the transport model as having uniform hydraulic characteristics. The exception to this uniformity is the Cerro Toledo interval, probably due to its fluvial and volcaniclastic origin, which would lead to large textural variations. Nonetheless, the Cerro Toledo interval is also represented as having uniform hydraulic characteristics.

Most moisture profiles on the mesa near MDA G (Abeele et al., 1981; Kearl et al., 1986; Rogers and Gallaher, 1994; Louiza and Vold, 1995) show a decrease in volumetric moisture content with depth from 8% to 16% near the surface to about 0.5% to 2% by a depth of 4 to 5 m, as described above. This decrease occurs within Tshirege Unit 2, which houses most of the waste disposal pits. We hypothesize that the low moisture content zone observed near the base of Unit 2 and in the upper part of Tshirege Unit 1v is caused by evaporation related to air movement within the mesa. This air movement apparently occurs along surge beds at the base of Unit 2 and along cooling joints within Unit 2 and the upper part of Unit 1v. From the bottom of Unit 2 and downward through Unit 1v, volumetric moisture content gradually increases to about 5% to 20% at the Unit 1v- Unit 1g contact (the vapor phase notch).

Fractures and mesa drying

At MDA G, cooling joints ("fractures") within some units of the Tshirege Member of the Bandelier Tuff may play an important role in the water balance within the mesa. Fractures could act as a pathway aiding deeper infiltration of precipitation. At the same

time, by permitting enhanced air movement and evaporation, fractures might dry out the mesa interior.

In their summary of lithology at MDA G, Krier et al. (1995) listed observed fracture densities for Tshirege Unit 2 and the upper part of Unit 1v. For the lower part of Unit 1v and Unit 1g they noted that there were no data available, but mentioned that few fractures were observed in outcrop.

The driest zone within the mesa generally occurs within the lower part of Tshirege Unit 2 and the upper part of Unit 1v, coincident with the observed fracture occurrence. Estimates of matric suction based on laboratory evaluation of moisture retention curves (Rogers and Gallaher, 1995; Rogers et al., 1995) and chilled mirror psychrometer measurements on core samples (Rogers and Gallaher, 1994; Rogers et al., 1995) show that this dry region also is generally a zone of high matric suction and a hydraulic head minimum. The interpretation is that moisture is being drawn towards this depth from above and below. The driving force for this movement may be evaporation aided by air movement along the fractures within these units or along the more permeable surge beds found at the base of Unit 2. Vold (1996b) concluded that in this dry region, water transport in the vapor phase was greater than liquid phase transport.

Birdsell et al. (1995) carried out two sets of simulations to evaluate the possibility that the hypothesized evaporation mechanisms of air movement along fractures or surge beds might contribute to the observed low moisture contents in the upper mesa interior. They concluded that evaporation along these pathways could contribute to significant drying of the mesa interior as observed.

Fractures and mesa infiltration

Hydrologists believe that fractures in dry rock do not act as effective conduits for infiltration, because water is imbibed into the surrounding dry rock matrix (Montazer and Wilson, 1984; Peters and Klavetter, 1988). Low-permeability fracture coatings can reduce the rate of imbibition into the surrounding rock matrix and increase the depth of infiltration, however (Thoma et al., 1992).

Soll (1995) performed a modeling study to evaluate whether fractures might act as a conduit for episodic deep infiltration at MDA G. The study focused on the possible effects of fracture coatings and fracture fills, which have been observed within fractures in the upper part of the mesa (Davenport, 1993; Newman, 1996a). The study modeled

fractures with hydraulic properties equivalent to a loose sand, and some of the results may be sensitive to this choice. Soll (1995) found that the presence of low permeability fracture fills inhibited movement of infiltration from the surface into a fracture. In the case of fractures uniformly coated with a material having permeability two orders of magnitude lower than the matrix (standard clay values), the penetration depth of infiltration with a ponded upper boundary condition was about 10 m. However, the amount of water required to achieve this depth of infiltration was four times the annual precipitation at MDA G. For fractures uniformly coated with a material having permeability four orders of magnitude lower than the matrix, the water was confined to the fracture. Fractures with discontinuous coatings were not effective at channeling water deep into the mesa. Soll (1995) concluded that except in the case of continuous, very low permeability fracture coatings, deep channeling of infiltration at MDA G was unlikely.

High moisture content at the vapor phase notch

High moisture content values (10 to 20% volumetric) are observed at the vapor phase notch throughout the Laboratory, regardless of elevation or relationship to other geographic features such as canyon bottom elevation (Turin, 1995). This boundary is a phase boundary between vapor phase altered (devitrified) and unaltered Bandelier Tuff, rather than a time-stratigraphic or flow boundary. At such a boundary, significant changes in mineralogy, mineral surface properties, and porosity related to mineral alteration would be expected to exert a significant effect on properties such as moisture retention and hydraulic conductivity. The zone is sufficiently narrow that its hydraulic properties have not been characterized in detail from cores.

Another possible explanation for the high moisture contents is that the vapor phase notch is conducting moisture laterally beneath the mesa. One possible argument against this idea is that wells drilled along the base of the mesa in Pajarito Canyon found no saturation near the mesa walls (Devaurs and Purtymun, 1985). Based on the geologic map of Purtymun and Kennedy (1971), the vapor phase notch lies within a few tens of feet below the canyon floor along much of the southern edge of the mesa. These boreholes were installed following a spring (March to May) which had over three times the thirty-year average precipitation for that period. However, the authors did not determine moisture contents for cores from the boreholes. The authors concluded (Devaurs and Purtymun, 1985, p. 12) that groundwater in Pajarito Canyon "is confined to the alluvium in the stream channel, and does not extend to the flank of the canyon".

Benten et al. (1994) found by field measurements with a tension infiltrometer that the unsaturated hydraulic conductivity of the Bandelier Tuff was lower just above the vapor phase notch, and suggested that the higher moisture contents observed might occur above this low permeability zone. Geddis (1992) modeled unsaturated flow beneath Mortandad Canyon, an analogous situation where lateral moisture migration along the highly permeable Cerro Toledo interval at the base of the Tshirege Member beneath a mesa might be expected. Based on his results, Geddis suggested that vertical flow was dominant, and that lateral diversion of flow along the Cerro Toledo interval did not occur. Geddis (1992) did note that this conclusion might change in the case of dipping strata, although ponding or water contents near saturation (a prerequisite to lateral flow diversion) did not occur at layer boundaries.

As the high moisture content values are observed at the vapor phase notch throughout the Laboratory, regardless of its relationship to other geographic features, these moisture content peaks there are probably due to changes in hydraulic properties related to vapor phase alteration. Due to the present lack of sufficient data, however, the hypothesis of lateral movement of moisture at this interface, which would have major consequences for moisture balance and contaminant transport, cannot be entirely ruled out. Newman (1996b) suggests that stable isotope comparisons between pore waters in the vapor phase notch and alluvial groundwater in Pajarito Canyon might indicate whether the latter is a source for the former.

Geochemical profiles within the mesa

Newman (1996b) determined chloride and stable isotope (deuterium and ^{18}O) profiles using cores from four boreholes at MDA G. There appears to be lateral heterogeneity based on differing chloride ages and apparent flux rates between the four wells examined. There is evidently a mesa-wide increase in pore water chloride concentrations at the bottom of Tshirege Unit 2 through the upper part of Unit 1v, and these chloride bulges suggest very low flux rates through this zone. This zone of high chloride concentrations is consistent with the zone of low moisture contents discussed earlier, and supports the hypothesis that the mesa is being dried out by air movement at this depth. Evaluation of chloride concentrations down to about the vapor phase notch suggest that it took between 2000 and 17000 years to accumulate the quantity of chloride present in the mesa. There is some uncertainty regarding these ages due to uncertainty about chloride input rate and evaporative loss of water in the intermediate (low moisture content) zone. However, any correction for these two factors would increase the ages. These accumulation ages are

thus minimum values and indicate that water movement through the mesa has been quite slow for several thousand years.

Stable isotope results also support the deep evaporation hypothesis. Isotopically heavy water is present in the same depth range as the high chloride concentrations, which is below the depths where surface-related evaporation occurs. At depths near the vapor phase notch, isotope values become much lighter and do not appear to be affected by deep evaporation. Chloride concentrations become quite dilute at the vapor phase notch as well. One possible conclusion is that the water at and below the vapor phase notch was recharged during past periods of higher precipitation such as during the Pleistocene or early-mid Holocene. On the other hand, the light waters may have come from lateral flow along a pathway which was not subject to deep evaporation.

Implications of mesa hydrology for modeling

At MDA G there are several lines of evidence to suggest that recharge beneath the mesa is not occurring at present, and may not have occurred for thousands of years. Most moisture profiles observed beneath MDA G and nearby MDA L on Mesita del Buey show three moisture content zones. The fact that different apparent recharge rates are required to explain moisture content variations within the mesa suggests that there are significant sources or sinks of moisture at different depths. However, these sources and sinks are not fully understood. The drying within the middle depths of the mesa interior is likely the result of evaporation connected with air movement along fractures and the surge beds near the base of Tshirege Unit 2.

The strongest evidence in support of this drying hypothesis comes from evaluation of chloride and stable isotope profiles within the mesa. The results support a picture where liquid phase water movement from the top of the mesa has been stopped at about the base of Unit 2 for the last 2000 to 17,000 years. Thus there is a documented hydrologic disconnect within the mesa, which is a significant barrier to recharge passing through the mesa under natural conditions.

The moisture source inferred from increased moisture at the vapor-phase notch could be lateral moisture movement coming from the canyon bottoms. However, the moisture variations are most likely the result of variations in capillary retention properties at lithologic transitions. Similar high moisture content at the Tsankawi/Cerro Toledo

interval and the Guaje Pumice bed might be related to lateral flow of moisture along a dipping interface where hydraulic properties change.

Because the source and sink mechanisms are not yet sufficiently understood, it is not possible to prescribe recharge rate variations with depth in transport modeling of the unsaturated zone beneath MDA G. In addition, most of the waste disposal pits are excavated to near the top of the hypothesized evaporative zone, and the relationship of flow within the pits to this dry zone is unclear at present. Therefore, a vertical recharge rate which is constant with depth has been assumed, and this rate prescribes the surface moisture flux boundary conditions in the transport modeling.

Hydrologic processes beneath canyon bottoms

Two canyons border the Mesita del Buey. To the north, Cañada del Buey contains an intermittent stream. The alluvium is thin and contains no perennial saturation (Purtymun and Kennedy, 1971; Devaurs and Purtymun, 1985). Pajarito Canyon, to the south, also contains an intermittent stream, but the larger flow in this canyon supports a perennial groundwater body in the alluvium (Devaurs and Purtymun, 1985).

The rate of infiltration beneath the canyons to the north and south of MDA G is an important boundary condition for hydrologic modeling. For Cañada del Buey, this infiltration rate was estimated using in situ moisture contents and hydrologic properties determined from cores in a borehole (Rogers et al., 1996). The infiltration rates determined in this report assumed that the equivalent vertical unsaturated hydraulic conductivity was equal to the harmonic mean of the core values. Subsequent discussion with other hydrologists (Jim Smith, University of Arizona, personal communication, 1996) led to the conclusion that the geometric mean unsaturated hydraulic conductivity was a better estimate. The geometric mean conductivity is approximately one order of magnitude larger than the harmonic mean, leading to recharge rates that are one order of magnitude greater than listed in Rogers et al. (1996).

The corresponding recharge rate determined for borehole CDBM-1 in Cañada del Buey is 0.44 cm/yr. This value agrees well with estimates derived from chloride profiles in the same borehole (Bruce Gallaher, Los Alamos National Laboratory, personal communication, 1996). A similar means of estimating fluxes beneath Pajarito Canyon is not available due to lack of data. For this canyon, we used an analogy with a similar canyon, Mortandad Canyon. Estimates of recharge rates from borehole MCM-5.9A

(similarly adjusted from Rogers et al. (1996) using geometric mean unsaturated hydraulic conductivities) range from 2 to 10 cm/yr.

Hydrologic processes beneath the Bandelier Tuff

Choosing unsaturated hydrologic properties for the Cerros del Rio Basalts presents a problem in our modeling. There are numerous studies available which provide large (km) scale estimates of saturated hydraulic conductivity for basalts. Large scale unsaturated properties are another matter. Basalts are highly variable in texture at the meter scale, containing joints and vesicles. At a slightly larger scale, basalt flows include interflow deposits and sections of scoria. In many cases, these features may be lined with deposits of secondary minerals. These large spatial variations in texture can be expected to lead to large spatial variability in unsaturated hydrologic characteristics. Where there are laboratory measurements of unsaturated hydrologic properties for basalts, the measurements have often been done on samples of intact basalt matrix, and do not account for the effects of the larger irregularities described here.

For our modeling, basalt properties are described using an equivalent continuum approximation (Klavetter and Peters, 1986) for the characteristic curves (capillary pressure vs. saturation and relative permeability vs. saturation). With the equivalent continuum approximation, a set of matrix and fracture characteristic curves are combined into a single set of characteristic curves which represents matrix flow at low saturation and fracture flow at higher saturation. Matrix properties are based on a vesicular basalt located beneath the Idaho National Engineering Laboratory (Bishop, 1991). In order to induce rapid flow and transport through the basalt layer, the fractures are assigned a high permeability and porosity (Birdsell et al., 1996). These properties result in travel times through the basalt layer of less than five years. Because of the high uncertainty associated with flow through the basalt we chose properties that lead to a nearly instantaneous travel time, which results in a conservative transport result (Birdsell et al., 1996).

Beneath the Cerros del Rio Basalts lies the Puye Conglomerate. For unsaturated properties, this formation was presumed to have characteristics of a sand, with reduced porosity due to a mixture of grain sizes.

Flow diversion at the Guaje Pumice bed

Lateral diversion of flow has been shown to be potentially significant in unsaturated fractured rock settings (Montazer and Wilson, 1984). Lateral diversion of unsaturated flow might occur at dipping lithologic interfaces where there are large contrasts in permeability and moisture retention properties. There are several lithologic interfaces beneath MDA G where lateral flow might occur, including the vapor phase notch, the Cerro Toledo interval, the Guaje Pumice bed, and the base of the Cerros del Rio Basalts. Such lateral diversion of flow might significantly alter groundwater flow pathways and thus change the location of resultant doses.

The modeling problem is made more difficult by lack of knowledge of subsurface properties, for example, the permeability of the Cerros del Rio Basalts, and of the precise lithology of the interface between the basalt and the Guaje Pumice bed. For example, thin clayey soils are observed to lie between these two units in outcrop. The extent and properties of such soil units could exert a major influence on water flow at this contact.

In order to investigate the potential for lateral flow along the Guaje Pumice bed, Birdsell et al. (1996) did a sensitivity study of what combinations of structure and permeability might lead to lateral flow. They found that the strongest influence on the flow field and moisture content is the (saturated) hydraulic conductivity of the basalt underlying the Guaje Pumice bed. Under an assumption of intact basalt (that is, no fractures), using a basalt conductivity at the high end of reported basalt matrix values (8.7×10^{-7} m/s) results in the basalt largely being a barrier to vertical flow. This results in almost complete lateral flow diversion in the overlying Guaje Pumice bed. When the basalt conductivity is either increased two orders of magnitude or modified to include fractures, fluid can readily pass from the pumice into the basalt, and lateral flow is minimal.

The thickness of the Guaje Pumice bed had a mild effect on moisture content in the pumice, but no effect on moisture content of the Otowi Member or the basalt. The influence of Guaje Pumice bed slope on moisture content was approximately as strong as the influence of layer thickness.

Saturated zone model

Water in the regional aquifer beneath MDA G flows in an east-southeasterly direction towards the Rio Grande (Purtymun, 1984). The top of the regional aquifer lies within the interlayered basalts and fanglomerate member of the Puye Conglomerate (Purtymun,

1995). Birdsell, et al. (1996) constructed a simple model of the regional aquifer beneath MDA G for the purpose of evaluating the combined effects of modeled radionuclide transport from the overlying waste pits. In this saturated zone model, the aquifer is assumed to be homogeneous and isotropic. Boundary conditions utilize heads determined by Purtymun (1984), and overall flow is based on travel times for the aquifer that Purtymun (1984) determined from pump test results.

Radionuclide adsorption

An important aspect of modeling the migration of radionuclides concerns quantifying the geochemical interactions between the radionuclides and the Bandelier Tuff. The sorption of radionuclides on Bandelier Tuff is controlled by (1) the surface area and mineralogy of the tuff and (2) by the water chemistry of the solution in contact with the tuff. Longmire et al. (1996) inferred that the dominant adsorbates within the Bandelier Tuff are glass, hematite, smectite, amorphous $Fe(OH)_3$, kaolinite, and possibly calcite.

Distribution coefficients were experimentally determined using two model pore waters. Water Canyon Gallery (WCG) groundwater, discharging from the Bandelier Tuff at a pH of 7.3, is relatively oxidizing and is characterized by a calcium-sodium-bicarbonate ionic composition with a TDS content less than 130 mg/L. Vadose-zone pore water was extracted from Bandelier Tuff cores collected from beneath Mesita del Buey using an Unsaturated/Saturated Flow Apparatus. This pore water is characterized by a sodium-carbonate-bicarbonate solution with a TDS content of greater than 1300 mg/L. The pH values of these pore water samples range from 9.2 to 9.8 and the solutions are oversaturated with respect to calcite.

The distribution coefficients for radionuclides measured on the Bandelier Tuff, at a pH value of 7.3, decrease in the following order: Am(III) >> Pu(V) > U(VI) >> Np(V) > Tc(VII) (Longmire et al., 1996). The distribution coefficients for radionuclides measured on the tuff samples using the synthetic pore water, at a pH value of 9.8, decrease in the following order: Am(III) >> Pu(V) > U(VI) > Np(V) >Tc(VII). The distribution coefficients for Tc(VII) are all negative and therefore, they are assumed to be zero. The distribution coefficients for Am(III) and Np(V) using synthetic pore water are higher than the distribution coefficients for these two radionuclides using WCG groundwater. We postulate that calcite was precipitated from the synthetic pore water, which enhanced the sorptive capacity of the Bandelier Tuff for Am(III) and Np(V). Calcite occurs within the matrix of the Bandelier Tuff (Broxton et al., 1995).

Based on results of computer simulations using the geochemical computer program MINTEQA2, the dominant aqueous complexes of Am(III) and Np(V) are predicted to include $Am(CO_3)_3^{3-}$ and $NpO_2(CO_3)_3^{5-}$, respectively (Longmire et al., 1996). The synthetic pore water is predicted to be undersaturated with respect to $Am(OH)_3(s)$, $Am(OH)_3(am)$, $AmOHCO_3$, $NpO_2OH(am)$, $NpO_2OH(aged)$, $NaNpO_3 \cdot 3.5H_2O$, and $NaNpCO_3$. Enhanced sorption of Am(III) and Np(V) carbonate complexes on calcite is possible through surface exchange with carbonate and bicarbonate functional groups present on the calcite surface.

The pore water chemistry of core hole 1107 at MDA G suggests that evaporation is an important process for concentrating dissolved species within the vadose zone of the Bandelier Tuff. Observations from other parts of the Laboratory support the concept that evaporation is an important process within mesas. Vaniman and Chipera (1995) report the occurrence of evaporite minerals such as gypsum ($CaSO_4 \cdot 2H_2O$) and halite (NaCl) within fractures at TA-69.

Under the low moisture conditions in the Bandelier Tuff, precipitation of sorptive phases such as calcite and amorphous $Fe(OH)_3$, with high surface areas, is enhanced. This means that conditions for development of the dominant adsorbates are favorable beneath MDA G. These phases have been observed in fracture fill material across the Laboratory (Davenport, 1993; Longmire et al., 1995). Iron, in the forms of amorphous $Fe(OH)_3$ and hematite, and aluminum, concentrated within smectite, kaolinite, and possibly amorphous $Al(OH)_3$, are also elevated within the fracture fill material relative to the Bandelier Tuff at TA-46 (Longmire et al., 1995). Longmire et al. (1995) showed that naturally occurring trace elements (As, Be, Mn, and U) are concentrated within fracture fill material at TA-46, which is consistent with adsorption or possibly coprecipitation being an effective process for removing trace metals from solution.

Summary of Conceptual Model

Most of the water that falls on the mesa at MDA G is lost to evapotranspiration or runoff. Seasonal wetting and drying maintain slightly higher moisture contents in the top few meters of the mesa than are found deeper. While recharge through fractures near the mesa surface may occasionally occur, model studies suggest this does not account for large quantities or great depths of recharge.

Extremely low moisture contents found 4 to 5 m below the mesa surface appear to be the result of evaporation caused by air flow through the mesa. Air flow is enhanced by the

presence of fractures and surge beds. This hypothesis is supported by moisture content, matric suction, stable isotope, and chloride profile data. Despite the evidence for evaporative effects within the mesa, we have not incorporated it in our hydrological model, as we have insufficient physical information to accomplish this at present. Instead we have assumed a uniform, though low, rate of infiltration through the mesa. This may be a reasonable choice because the bottom of the waste disposal pits is near the top of the dry zone, and the effect of pits on underlying moisture contents is not well understood.

The movement of liquid water downward through the mesa is by unsaturated flow, although at some depths vapor transport may be of equal magnitude. Liquid flow appears to be predominantly vertical and one-dimensional, although lateral diversion of flow at several lithologic interfaces such as the Guaje Pumice bed might be important. Groundwater flow in the regional aquifer beneath MDA G appears to be towards the Rio Grande to the east-southeast.

Different hydrologic properties are used for each unit of the Tshirege Member and for the Otowi Member of the Bandelier Tuff. Lateral variability of hydrologic properties within each lithologic unit is ignored. We conceptualize the hydrologic properties of each lithologic unit within both the vadose zone and the saturated zone as being homogeneous and isotropic.

References

Abeele, W. V., M. L. Wheeler, and B. W. Burton, Geohydrology of Bandelier Tuff, 50 pp., Los Alamos Scientific Laboratory Report LA-8962-MS, October 1981.

Allison, G. B., G. W. Gee, and S. W. Tyler, Vadose-zone techniques for estimating groundwater recharge in arid and semiarid regions, Soil Science Society of America Journal, 58, 6-14, 1994.

Benton, L. D., H. J. Turin, B. P. Wilcox, and N. L. Gotti, Field measurements of saturated and unsaturated conductivity, Geological Society of America Abstr., 26(7), p. 443 (Los Alamos National Laboratory Report LA-UR-94-2311), Presented at GSA National Meeting, Seattle, October 1994.

Birdsell, K. H., W. E. Soll, N. D. Rosenberg, and B. A. Robinson, Numerical modeling of unsaturated groundwater flow and radionuclide transport at MDA G, 49 pp., Los Alamos National Laboratory Report LA-UR-95-2735, September 1995.

Birdsell, K. H., Bower, K., Wolfsberg, A., Soll, W., Orr, T., Cherry, T., Simulations of groundwater flow and radionuclide transport in the vadose and saturated zones beneath Area G, Los Alamos National Laboratory Report (in progress), 1996

Bishop, C.W., Hydrologic Properties of Vesicular Basalt, Masters Thesis, University of Arizona, Tucson, AZ, 1991.

Bowen, B. M., Los Alamos climatology, 254 pp., Los Alamos National Laboratory Report LA-11735-MS, May 1990.

Broxton, D. E. and S. L. Reneau, Buried early Pleistocene landscapes beneath the Pajarito Plateau, Northern New Mexico, New Mexico Geological Society Guidebook, 47th Field Conference, The Jemez Mountains Region, pp. 325-334, 1996.

Broxton, D. E., G. Heiken, S. J. Chipera, and F. M. Byers Jr., Stratigraphy, petrography, and mineralogy of Bandelier Tuff and Cerro Toledo deposits: *in* Earth Science Investigations for Environmental Restoration- Los Alamos National Laboratory, Technical Area-21, Los Alamos National Laboratory Report LA-12934-MS, pp. 33-63, 1995.

Conca, J. and J. Wright, Find Transport Data Faster, Soil and Groundwater Cleanup, p. 14-26, December 1995.

Cooper, J. B., W. D. Purtymun, and E. C. John, Records of water-supply wells Guaje Canyon 6, Pajarito Mesa 1, and Pajarito Mesa 2, Los Alamos, New Mexico, U. S. Geological Survey Open-File Report, July 1965.

Davenport, D. W., Micromorphology, mineralogy, and genesis of soils and fracture fills on the Pajarito Plateau, New Mexico, Ph.D. Dissertation, Texas Tech University, Lubbock, 1993.

Devaurs, M., and W. D. Purtymun, Hydrologic characteristics of the alluvial aquifers in Mortandad, Cañada del Buey, and Pajarito Canyons, Los Alamos National Laboratory Report LA-UR-85-4002, 1985

Gardner, J. N., T. Kolbe, and S. Chang, Geology, drilling, and some hydrologic aspects of seismic hazards program core holes, Los Alamos National Laboratory, New Mexico, 19 pp., Los Alamos National Laboratory Report LA-12460-MS, January 1993.

Geddis, A. M., Preliminary modeling of moisture movement in the tuff beneath Mortandad Canyon, Los Alamos National Laboratory, Los Alamos National Laboratory Report LA-UR-12460, August 1992.

Kearl, P. M., J. J. Dexter, and M. Kautsky, Vadose zone characterization of Technical Area 54, waste disposal areas G and L, Los Alamos National Laboratory, New Mexico, Report 4: Preliminary assessment of the hydrologic system through Fiscal Year 1986, Report GJ-54, UNC Technical Services, Inc., December 1986.

Klavetter, E. A. and R. R. Peters, Estimation of Hydrologic Properties of an Unsaturated Fractured Rock Mass, Sandia National Laboratories Report SAND84-2642, 1986.

Krier, D. J., P. Longmire, R. Gilkeson, and H. J. Turin, Geologic, geohydrologic, and geochemical data summary of Material Disposal Area G, TA-54, Los Alamos National Laboratory, Los Alamos National Laboratory Report LA-UR-95-2696, July 1995

Louiza, D. and E. Vold, Moisture profile measurements in subsurface monitor holes at the Los Alamos LLRW disposal site, Los Alamos National Laboratory Report LA-UR-95-1922, June 1995.

Longmire, P., C. R. Cotter, I. R. Triay, J. J. Kitten, C. Hall, J. Bentley, D. Hollis, and A. I. Adams, Batch sorption results for americium, neptunium, plutonium, technetium, and uranium transport through the Bandelier Tuff, Los Alamos, New Mexico, Los Alamos National Laboratory Report LA-????-MS, 1996.

Longmire, P., S. Reneau, P. Watt, L. McFadden, J. Gardner, C. Duffy, and R. Ryti, Natural background geochemistry, geomorphology, and pedogenesis of selected soil profiles and Bandelier Tuff, Los Alamos, New Mexico, Los Alamos National Laboratory Report LA-12913-MS, 1995.

McLin, S. G., Horizontal borehole data gathered with SEAMIST, Los Alamos National Laboratory Memo ESH-8/WQ&H-94-571 to Erik Vold, November 22, 1994.

Montazer, P., and W. E. Wilson, Conceptual hydrologic model of flow in the unsaturated zone, Yucca Mountain, Nevada: U. S. Geological Survey, Water-Resources Investigations Report 84-4345, 55 p, 1984.

Newman, B. D., Geochemical investigations of calcite fracture fills and mesa-top water dynamics on the Pajarito Plateau, New Mexico, Los Alamos National Laboratory Report

LA-UR-96-1441, Ph. D. Dissertation, New Mexico Institute of Mining and Technology, Socorro, 1996a.

Newman, B., Vadose zone water movement at Los Alamos National Laboratory, TA-54, Area G: Interpretations based on chloride and stable isotope profiles, Los Alamos National Laboratory Report LA-UR-96-4682, 1996b.

Nyhan, J. W., T. E. Hakonson, and B. J. Drennon, A water balance study of two landfill cover designs for semiarid regions, Journal of Environmental Quality, 19, p. 281-288, 1990.

Peters, R. R., and E. A. Klavetter, A continuum model for water movement in an unsaturated fractured rock mass, Water Resources Research, 24, p. 416-430, 1988.

Purtymun, W. D., Hydrologic characteristics of the main aquifer in the Los Alamos area: development of ground water supplies, 44 pp., Los Alamos National Laboratory Report LA-9957-MS, January 1984.

Purtymun, W. D., Geologic and hydrologic records of observation wells, test holes, test wells, supply wells, springs, and surface water stations in the Los Alamos area, 339 pp. Los Alamos National Laboratory Report LA-12883-MS, January 1995.

Purtymun, W. D., and W. R. Kennedy, Geology and hydrology of Mesita del Buey, 12 pp., Los Alamos National Laboratory Report LA-4660, May 1971.

Purtymun, W. D., M. L. Wheeler, and M. A. Rogers, Geologic description of cores from holes P-3 MH-1 through P-3 MH-5, Area G, Technical Area 54, Los Alamos Scientific Laboratory Report LA-7308-MS, May 1978.

Purtymun, W. D., M. A. Rogers, and M. L. Wheeler, Radiochemical analyses of samples from beneath a solid radioactive waste disposal pit at Los Alamos, New Mexico, Los Alamos Scientific Laboratory Report LA-8422-MS, June 1980.

Rogers, D. B., Unsaturated hydraulic characteristics of the Bandelier Tuff at TA-54, 38 pp., Los Alamos National Laboratory Report LA-UR-95-1777, May 1995.

Rogers, D. B., and B. M. Gallaher, Moisture and Matric Suction Profiles for 1994 MDA G Wells, 7 pp. and 3 figures, Los Alamos National Laboratory Memo ESH-18/WQ&H-94-632, December 19, 1994.

Rogers, D. B., and B. M. Gallaher, The Unsaturated Hydraulic Characteristics of the Bandelier Tuff, Los Alamos National Laboratory Report LA-12968-MS, September 1995.

Rogers, D. B., E. L. Vold, and B. M. Gallaher, Bandelier Tuff Hydraulic Characteristics from Los Alamos National Laboratory Borehole G-5 at MDA G, TA-54, 23 pp., Los Alamos National Laboratory Report LA-UR-95-3129, August 1995.

Rogers, D. B., B. M. Gallaher, and E. L. Vold, Vadose zone infiltration beneath the Pajarito Plateau at Los Alamos National Laboratory, New Mexico Geological Society Guidebook, 47th Field Conference, The Jemez Mountains Region, pp. 413-420, 1996.

Rogers, M. A., History and environmental setting of LASL near-surface land disposal facilities for radioactive wastes (Areas A, B, C, D, E, F, G, and T), Los Alamos Scientific Laboratory Report LA-6848-MS, 1977.

Soll, W. E., Influence of fracture fills and fracture coatings on flow in Bandelier Tuff, Los Alamos National Laboratory Report LA-UR-95-2695, August 1995.

Springer, E. P., Area G Performance Assessment: surface water and erosion, 40 pp., Los Alamos National Laboratory Report LA-UR-95-2497, 1995.

Thoma, S. G., D. P. Gallegos, and D. M. Smith, Impact of fracture coatings on fracture/matrix flow interactions in unsaturated, porous media, Water Resources Research, 28, p. 1357-1367, 1992.

Turin, H. J., Subsurface transport beneath MDA G: A conceptual model, 28 pp., Los Alamos National Laboratory Report LA-UR-95-1663, May 1995.

Vaniman, D. and S. Chipera, Mesa-penetrating fractures, fracture mineralogy, and projected fault traces at Pajarito Mesa, in Geological Site Characterization for the Proposed Mixed Waste Disposal Facility, Los Alamos National Laboratory, Los Alamos National Laboratory Report LA-13089-MS, p. 71-85, 1995.

Vold, E., Analysis of liquid phase transport in the unsaturated zone at a mesa top disposal facility, Los Alamos National Laboratory Report LA-UR-96-370, 1996a.

Vold, E., An analysis of vapor phase transport in the unsaturated zone with application to a mesa top disposal facility, Part 1, Los Alamos National Laboratory Report LA-UR-96-973, 1996b.

Vold, E., and B. Eklund, Preliminary summary of evaporation measurements made at Los Alamos, Area G, Los Alamos National Laboratory Report LA-UR-96-3499, 1996.

Vold, E., B. Newman, K. Birsdell, B. Gallaher, D. Krier, P. Longmire, D. Rogers, and E. Springer, Representative recharge rates in a complex unsaturated hydrogeology, Los Alamos National Laboratory Report LA-UR-96-????, 1996.

Water Quality & Hydrology Group (ESH-18), Hydrogeologic Workplan, Los Alamos National Laboratory, Draft Revision 1.0, December 6, 1996.

List of Figures

Figure 1. Hydrogeologic conceptual model for mesas (from Water Quality & Hydrology Group, 1996).

Figure 2. Hydrogeologic conceptual model for canyons (from Water Quality & Hydrology Group, 1996).

Figure 3. Stratigraphic cross sections through MDA G (based on Krier, et al., 1995).